

Conference Program and Technical Digest



The Joint International Symposium on

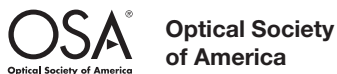
Optical Memory and Optical Data Storage

13-17 July 2008

Hilton Waikoloa Village
Waikoloa, Hawaii, USA



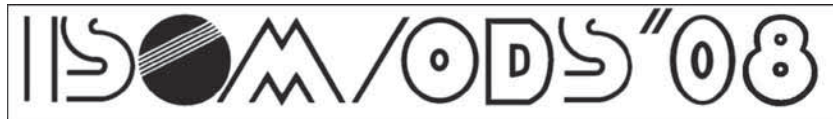
Sponsored by



Co-sponsored by



Technical
Digest



The Joint International Symposium on

Optical Memory and Optical Data Storage

Topical Meeting and Tabletop Exhibit

13-17 July 2008

Hilton Waikoloa Village
Waikoloa, Hawaii, USA



Contents

Chairs' Letter	4
ISOM/ODS 2008 Organizing Committees	5
Agenda of Sessions	6
Courses	7–8
Invited Speakers	9
Conference Program	10–22
Technical Digest	23–480
MA: Keynote Session	23
MB: 3D Storage	30
MP: Poster Session I	49
MC: Special Session on Nano-Photonics	178
TuA: Drive Technologies	189
TuB: Components and Hybrid Recording	202
TuP: Poster Session II	221
TuC: Special Session on Applications	370
WA: New and Related Technologies	386
WB: Media and Applications	402
ThA: Coding and Signal Processing	421
ThB: Holographic I	440
ThC: Holographic II and Super Resolution	459
Key to Authors and Presiders	481–483



Hilton Waikoloa Village - Aerial View



Hilton Waikoloa Village - Golf and Beach

Message from the Chairs

Welcome to ISOM/ODS'08! Reflecting the international nature of the interest and work in optical memory and optical data storage, these two conferences are held jointly every third year. The unparalleled setting of this year's conference provides an outstanding opportunity to share the latest information in this dynamic field with your international colleagues.

ISOM/ODS'08 will provide an opportunity for exchanging information on the status, advances, and future directions in the field of optical memory and optical data storage. New developments in holographic, volumetric, near-field, superresolution, and hybrid recording technologies for fourth-generation systems will be the main focus at this conference.

This year there are 149 papers, except for postdeadline papers, from 14 different countries covering a wide range of topics including two special sessions on Nano Photonics and Applications. Other topics include holographic, drive technologies, components and hybrid recording, new and related technologies, media and applications, and coding and signal processing. The Program Committee has organized a rich program that includes 24 invited, 34 oral and 91 poster presentations spread over three and one half days of technical sessions held Monday through Thursday. Wednesday afternoon has been left free for you to enjoy the beautiful Big Island of Hawaii.

In addition, a series of Short Courses will be held on Sunday to educate both newcomers and veterans about the latest information on optical memory and optical data storage with short courses on Holographic Storage: Advanced Systems and Media, Heat Assisted Magnetic Recording (HAMR), Basics of Servo Technology for Optical Disk, and Near-Field Recording Technology.

We welcome you to actively participate in all aspects of the conference and hope you will benefit from these interactions and enjoy beautiful Waikoloa, Hawaii.

ISOM and ODS Committee Chairs

Cooperating Organizations

The Institute of Electronics, Information and Communication Engineers

The Chemical Society of Japan

Information Processing Society of Japan

The Institute of Electrical Engineers of Japan

The Institute of Image Electronics Engineers of Japan

The Institute of Image Information and Television Engineers

The Japan Society of Precision Engineering

The Laser Society of Japan

Organizing Committees

ODS General Chairs

Tim Rausch, Seagate Technology (USA)
Kimihiro Saito, Sony Corp. (Japan)

ODS Technical Program Committee

Chair: **Kevin R. Curtis**, InPhase Technologies (USA)

Chair: **Luping Shi**, Data Storage Institute (Singapore)

Sumio Ashida, Toshiba Corp. (Japan)

B.V.K. Vijaya Kumar, Carnegie Mellon Univ. (USA)

In-Ho Choi, LG Electronics Inc. (South Korea)

Atsushi Fukumoto, Sony Corp. (Japan)

Lambertus Hesselink, Stanford Univ. (USA)

Tzuan-Ren Jeng, Industrial Technology Research Institute (Taiwan)

Takashi Kikukawa, TDK Corp. (Japan)

Rie Kojima, Matsushita Electric Industrial Co., Ltd. (Japan)

Kyung-Guen Lee, Samsung Electronics Co., Ltd. (South Korea)

Masud Mansuripur, Univ. of Arizona (USA)

Robert R. McLeod, Univ. of Colorado (USA)

Hiroyuki Minemura, Hitachi Ltd. (Japan)

Susanna Orlic, Technische Univ. Berlin (Germany)

Long-Fa Pan, Tsinghua Univ. (China)

Masataka Shinoda, Sony Corp. (Japan)

Paul J. Wehrenberg, Apple Computer, Inc. (USA)

ISOM Technical Program Committee

Chair: **H. Tokumaru**, NHK (Japan)

Co-Chair: **S. Higashino**, Sony Corp. (Japan)

Co-Chair: **T. Iida**, Pioneer (Japan)

Co-Chair: **Y. Kawata**, Shizuoka Univ. (Japan)

I.-H. Choi, LG (South Korea)

T. C. Chong, DSI (Singapore)

C. Davies, Plasmon Data Systems (United Kingdom)

S. Hasegawa, Fujitsu Labs (Japan)

A. Hirao, Toshiba (Japan)

D.-R. Huang, ITRI (Taiwan)

S. Ichiura, Sanyo (Japan)

M. Irie, Osaka Sangyo Univ. (Japan)

K. Itoh, Ricoh (Japan)

M. Itonaga, JVC Ltd. (Japan)

T. Kikukawa, TDK Ltd. (Japan)

J.-H. Kim, Samsung (South Korea)

Y.-J. Kim, Yonsei Univ. (South Korea)

T. Milster, Univ. of Arizona (USA)

H. Miyamoto, Hitachi Ltd. (Japan)

K. Nishikawa, Canon (Japan)

T. Okumura, Sharp (Japan)

I.-S. Park, Samsung (South Korea)

N.-C. Park, Yonsei Univ. (South Korea)

T. E. Schlesinger, Carnegie Mellon Univ. (USA)

T. Shimura, Univ. of Tokyo (Japan)

D.-H. Shin, Samsung (South Korea)

M. Takeda, Sony Corp. (Japan)

R. Tamura, Hitachi Maxell (Japan)

K. Tanaka, Teikyo-Heisei Univ. (Japan)

S. Tanaka, Pioneer (Japan)

C.-H. Tien, Nat'l Chiao Tung Univ. (Taiwan)

J. Tominaga, AIST (Japan)

Y. Tomita, Pioneer (Japan)

D. P. Tsai, Nat'l Taiwan Univ. (Taiwan)

T. Tsujioka, Osaka Kyoiku Univ. (Japan)

K. Ueyanagi, JST (Japan)

S. Wang, Ritek (Taiwan)

P. Wehrenberg, Apple (USA)

D. C. Wright, Univ. of Exeter (United Kingdom)

S. Yagi, NTT (Japan)

N. Yamada, Matsushita (Japan)

Y. Yamanaka, NEC (Japan)

K. Yokoi, Ricoh (Japan)

ODS Advisory Committee

Chair: **Bernard W. Bell**, InPhase Technologies (USA)

Chair: **Takeshi Shimano**, Hitachi Ltd. (Japan)

Chong Tow Chong, Data Storage Institute (Singapore)

David H. Davies, DataPlay, Inc. (USA)

Der-Ray Huang, Industrial Technology Research Institute (Taiwan)

Isao Ichimura, Sony Corp. (Japan)

Ryuichi Katayama, NEC Corp. (Japan)

Jooho Kim, Samsung Electronics Co., Ltd. (South Korea)

Takeshi Maeda, Hitachi Ltd. (Japan)

Thomas D. Milster, Univ. of Arizona (USA)

Naoyasu Miyagawa, Matsushita Electric Industrial Co., Ltd. (Japan)

Michael P. O'Neill, Cellular Bioengineering, Inc. (USA)

Young-Pil Park, Yonsei Univ. (South Korea)

Isao Satoh, Unaxis Balzers AG (Japan)

Barry H. Schechtman, Information Storage Industry Consortium (USA)

Tuviah E. Schlesinger, Carnegie Mellon Univ. (USA)

Yun-Sup Shin, LG Electronics Inc. (South Korea)

Din-Ping Tsai, National Taiwan Univ. (Taiwan)

ISOM Organizing Committee

Chair: **Y. Tsunoda**, Hitachi Maxell (Japan)

R. Ito, Meiji Univ. (Japan) Exofficio

Y. Mitsuhashi, JST (Japan) Exofficio

M. Onoe, Prof. Emeritus, Univ. of Tokyo (Japan) Exofficio

Y. Sakurai, Prof. Emeritus, Osaka Univ. (Japan) Exofficio

T. Toshima, NTT Elec. (Japan) Exofficio

I. Fujimura, Ricoh (Japan)

K. Itoh, Osaka Univ. (Japan)

T. Iwanaga, NEC (Japan)

K. Kime, Mitsubishi (Japan)

M. Kume, Sanyo (Japan)

S. Matsumura, Pioneer (Japan)

H. Miyajima, MSJ (Japan)

M. Nakamura, Hitachi Ltd. (Japan)

K. Nishitani, Sony Corp. (Japan)

Y. Odani, OITDA (Japan)

K. Ohta, Sharp (Japan)

H. Sakaki, JSAP (Japan)

S. Tanaka, Matsushita (Japan)

H. Tokumaru, NHK (Japan)

T. Uchiyama, Fujitsu Labs. (Japan)

H. Yamada, Toshiba (Japan)

H. Yoshida, Mitsubishi Chem. (Japan)

ISOM Steering Committee

Chair: **I. Fujimura**, Ricoh (Japan)

Co-Chair: **T. Maeda**, Hitachi Ltd. (Japan)

Co-Chair: **S. Sugiura**, Pioneer (Japan)

H. Kanbara, NTT (Japan)

R. Katayama, NEC (Japan)

H. Kobori, Toshiba (Japan)

Y. Murakami, Sharp (Japan)

K. Sano, Matsushita (Japan)

M. Shinoda, Mitsubishi (Japan)

T. Tanabe, Ibaraki National College of Technology (Japan)

K. Tezuka, Fujitsu Labs. (Japan)

M. Toishi, Sony Corp. (Japan)

H. Tokumaru, NHK (Japan)

Y. Tsuchiya, Sanyo (Japan)

E. Watanabe, Japan Women's Univ. (Japan)

ISOM Advisory Committee

D. Chen, Chen & Associates Consulting (USA)

K. Fushiki, Nikkei BP (Japan)

K. Goto, Tokai Univ. (Japan)

Y. Ichioka, Nara National College of Technology (Japan)

N. Imamura, TeraHouse (Japan)

A. Itoh, Nihon Univ. (Japan)

K. Itoh, Fujitsu Labs. (Japan)

U. Itoh, AIST (Japan)

T. Kondo, JVC (Japan)

T. Kubo, T. Kubo Engineering Science Office (Japan)

S. Kubota, Sony Corp. (Japan)

M. Mansuripur, Univ. of Arizona (USA)

M. Mori, NatureInterface (Japan)

T. Murakami, OITDA (Japan)

K. Ogawa, Univ. of Tokyo (Japan)

T. Ohta, Ovonic Phase-change Lab. (Japan)

M. Ojima, Hitachi Ltd. (Japan)

Y. Okino, Kansai Univ. (Japan)

Y.-P. Park, Yonsei Univ. (South Korea)

J. Saito, Nikon (Japan)

H.-P. Shieh, Nat'l Chiao Tung Univ. (Taiwan)

H. Ukita, Ritsumeikan Univ. (Japan)

F. Yokogawa, Pioneer (Japan)

Agenda of Sessions

Sunday 13 July

7:00 am to 5:00 pm	Registration Open
8:30 am to 12:30 pm	SC917: Holographic Storage: Advanced Systems and Media
8:30 am to 12:30 pm	SC919: Basics of Servo Technology for Optical Disk
1:30 to 5:30 pm	SC918: Heat Assisted Magnetic Recording (HAMR)
1:30 to 5:30 pm	SC920: Near-Field Recording Technology

Monday 14 July

7:00 am to 5:00 pm	Registration Open
7:30 to 8:30 am	Continental Breakfast
8:45 to 9:00 am	Opening Remarks
9:00 to 10:00 am	MA: Keynote Session
10:00 to 10:30 am	Coffee Break
10:30 am to 12:30 pm	MB: 3D Storage
12:30 to 2:00 pm	Lunch (on your own)
2:00 to 3:30 pm	MP: Poster Session I
3:30 to 6:30 pm	MC: Special Session on Nano-Photonics

Tuesday 15 July

7:00 am to 5:00 pm	Registration Open
7:30 to 8:30 am	Continental Breakfast
8:30 to 10:00 am	TuA: Drive Technologies
10:00 to 10:30 am	Coffee Break
10:30 am to 12:30 pm	TuB: Components and Hybrid Recording
12:30 to 2:00 pm	Lunch (on your own)
2:00 to 3:30 pm	TuP: Poster Session II
3:30 to 6:30 pm	TuC: Special Session on Applications
7:00 to 8:30 pm	Welcome Reception · Lagoon Lanai

Wednesday 16 July

7:00 am to 12:30 pm	Registration Open
7:30 to 8:30 am	Continental Breakfast
8:30 to 10:00 am	WA: New and Related Technologies
10:00 to 10:30 am	Coffee Break
10:30 am to 12:30 pm	WB: Media and Applications
	Afternoon Free

Thursday 17 July

7:00 am to 5:00 pm	Registration Open
7:30 to 8:30 am	Continental Breakfast
8:30 to 10:00 am	ThA: Coding and Signal Processing
10:00 to 10:30 am	Coffee Break
10:30 am to 12:30 pm	ThB: Holographic I
12:30 to 2:00 pm	Lunch (on your own)
2:00 to 4:00 pm	ThC: Holographic II and Super Resolution
4:00 to 4:30 pm	Coffee Break
4:30 to 5:30 pm	ThD: Post Deadline Session
5:30 to 6:00 pm	Closing Remarks

8:30 am to 12:30 pm

Holographic Storage: Advanced Systems and Media

SC917

Instructor: **Kevin R. Curtis**, InPhase Technologies Inc.

Course Level: Intermediate

CEU: 0.35

Member Price \$225 / Non-member Price \$300

COURSE DETAILS

This course addresses the fundamental principles and design issues pertaining to digital holographic data storage (HDS). The fundamental principles of holography, including formation of and diffraction from thick diffraction gratings, are explained. Multiplexing techniques for thick gratings based on Bragg, momentum, or correlation techniques are discussed and explained with an introduction to k-space analysis.

The system architecture of phase conjugate polytopic-angle based systems is presented and their key design issues explained. The monocular architecture version of angle-polytopic is also explained. The metrics used to determine basic system performance and limitations are discussed. Write strategies and record scheduling for achieving high capacity in HDS systems are described. The concepts and issues with mastering and replication of holographic media are also explained. For angle multiplexing based systems, the servo systems and tolerances are discussed. These include thermal compensation and disk position and tilts. Key system component (laser, SLM (Spatial Light Modulator), optical design, and detector) requirements for high performance HDS systems are discussed.

The data channel for HDS systems is particularly different than conventional optical storage systems. The key issues such as over-sampled detection, interleaving, and error correction are presented.

HDS media requirements are explained and related to drive performance. Techniques for testing basic media parameters are also presented.

LEARNING OUTCOMES

This course will enable you to:

- explain and use the basic principles of HDS
- estimate achievable performance of basic HDS systems and media
- design basic HDS systems including servo systems and data channel
- list the key issues, limitations, and tradeoffs in HDS system design
- list the key issues, limitations, and tradeoffs in HDS media design
- test basic media parameters
- summarize the latest results in HDS performance
- compare HDS against conventional optical data storage systems

INTENDED AUDIENCE

This course is intended for engineers and scientists interested in high density optical data storage systems. Attendees are expected to have a Bachelors degree in engineering or science, or equivalent experience, and to have familiarity with optics concepts and optical storage systems. Rudimentary knowledge of holography or holographic recording materials is helpful, but not required.

INSTRUCTOR

Kevin Curtis is Chief Technology Officer and founder of InPhase Technologies in Longmont, Colorado. In this role, Kevin manages and provides the technical direction for the advanced research and development of InPhase's holography-based technologies and products for storage. Prior to founding InPhase, Kevin was a member of the technical staff at Bell Laboratories where he directed the efforts of the holographic storage program upon which InPhase was founded. This included business development and raising the Series A investments to start InPhase. Kevin has worked at Caltech, Northrop and Bell Labs on holographic optical systems for over 17 years. Dr. Kevin Curtis received his B.S., M.S., and Ph.D. degrees in electrical engineering in 1990, 1992 and 1994, respectively, all from the California Institute of Technology, Pasadena, California. He has authored 70+ publications and talks and has over 50 U.S. Patents awarded on holographic storage.

1:30 to 5:30 pm

Heat Assisted Magnetic Recording (HAMR)

SC918

Instructor: **James A. Bain**, Carnegie Mellon Univ.

Course Level: Intermediate

CEU: 0.35

Member Price \$225 / Non-member Price \$300

COURSE DETAILS

This course provides attendees with a working knowledge of heat assisted magnetic recording and the main technical constraints in developing a commercially viable system. The focus of this course will be on the thermo-magnetic aspects of HAMR - essentially the recording physics. The discussion will be developed by first looking at issues of system design from the standpoint of areal density and the thermal stability of magnetic bits. The various HAMR topologies (wide heat, narrow field vs narrow heat, wide field) will then be examined, and the viability of each discussed. Finally, the resulting requirements for HAMR small thermal spots will be discussed, along with how they can be generated. Supplementary material will be covered on the other important aspects of HAMR systems vis a vis traditional recording, such as lubrication, optical delivery, etc. The course will conclude with a review of the current research agenda for future HAMR systems.

LEARNING OUTCOMES

This course will enable you to:

- explain the main design drivers for heat assisted magnetic recording systems
- estimate parameters of the system that are consistent with a particular areal density
- compute required spot sizes and thermal parameters for a HAMR system
- identify recording systems issues in HAMR systems beyond thermo-magnetic physics
- summarize novel approaches to HAMR that are under development

INTENDED AUDIENCE

This material is intended for those with some familiarity with magnetic or optical recording, but without detailed familiarity with the design drivers and constraints in the implementation of HAMR.

INSTRUCTOR

James Bain is a Professor of Electrical and Computer Engineering at Carnegie Mellon University, where he is the Associate Director of the Data Storage Systems Center. Prof Bain has over 100 refereed publications in magnetic and electronic devices for data storage. He has been active in HAMR recording for the last decade and is a member of the IEEE Magnetics Society.

Courses · Sunday 13 July

8:30 am to 12:30 pm

Basics of Servo Technology for Optical Disk

SC919

Instructor: **Kiyoshi Ohishi**, Nagaoka Univ of Technology (Japan)

Course Level: Intermediate

CEU: 0.35

Member Price \$225 / Non-member Price \$300

COURSE DETAILS

This course provides attendees with a basic knowledge of tracking servo control design for optical disk drive systems. The course concentrates on the theory and structure of feedback control, robust control, feedforward control and disturbance observer for optical disk drive systems. Many practical and useful examples are included throughout. You will become fluent with how one designs tracking servo controllers for many varied applications.

LEARNING OUTCOMES

This course will enable you to:

- gain a basic knowledge of servo control design for your application
- design feedback control, robust control, feedforward control and disturbance observer
- construct the robust feedforward control for optical disk drive system
- construct the sudden disturbance observer for optical disk drive system

INTENDED AUDIENCE

This course is intended for anyone who needs to learn how to design tracking servo control. Those who either design their own controller or who work with servo designers will find this course valuable.

INSTRUCTOR

Kiyoshi Ohishi is a full professor at Nagaoka University of Technology in Japan, and has been involved in tracking servo control design and engineering for over 25 years. He received the B.E., M.E., and Ph.D. degrees in electrical engineering from Keio University, Yokohama, Japan, in 1981, 1983, and 1986, respectively. He received the Outstanding Paper Award at IECON'85 and Best Paper Awards at IECON'02 and IECON'04 from the IEEE Industrial Electronics Society, as well as the Best Paper Award from the Institute of Electrical Engineers of Japan in 2002. Dr. Ohishi is a member of IEEE and IEEJ.

1:30 to 5:30 pm

Near-Field Recording Technology

SC920

Instructor: **Tom D. Milster**, College of Optical Sciences/The Univ. of Arizona

Course Level: Introductory

CEU: 0.35

Member Price \$225 / Non-member Price \$300

COURSE DETAILS

Topics to be discussed include an introduction to near-field recording, both solid immersion lens (SIL) and transducer based technology, and the theory of data readout and gap control. In addition, a number of real-world examples and demonstrations will be provided, including working examples of very high NA (1.4 – 2.0) lenses (design, manufacturing and testing), and a Near-Field set-up with an actuated SIL: light path, optical components and control signals, in particular for gap control. We will also cover topics on recording, such as gap signal normalization, chromatic aberration, first-surface and cover-layer protected media, and experimental results.

LEARNING OUTCOMES

This course will enable you to:

- review SIL and transducer technology for data storage
- classify the effects of evanescent and propagating near-field energy
- describe the principles of data readout and gap control with SILs
- summarize design and manufacturing considerations for very high NA Near-Field lenses
- discuss the basic layout of a Near-Field light path and its components
- describe an NFR gap servo system

INTENDED AUDIENCE

University degree in Physics or Electronics, or equivalent. Some familiarity with conventional optical data storage systems like CD and DVD is recommended, but not required.

INSTRUCTOR

Tom Milster's work involves studying the physical optics effects of high performance optical systems, like those used in optical data storage and lithography. For example, he did pioneering work on differential optical servo systems, data detection using magnetic circular dichroism and lens design for volumetric memories. He has also been very active in studying the properties of near-field scanning optical microscopes. More recently, he has developed a theory and simulation technique to explain the interaction of a focused laser beam and evanescent gaps, like the ones used with solid immersion lenses (SILs). An extreme ultraviolet spectrometer designed by Milster was part of the scientific package that flew in the space shuttle with Sen. John Glenn. Prof. Milster holds 5 U.S. Patents and has published well over 100 scientific articles. He is active in organizing professional society meetings, like ODS and ISOM. He is a Fellow of both the SPIE and the OSA.

Invited Speakers

Motoichi Ohtsu, Univ. of Tokyo (Japan)
Nanophotonics and application to future storage technology
[TD05-01]

Masud Mansuripur, College of Optical Sciences/
The Univ. of Arizona
Can future storage technologies benefit from existing or emerging nano-tools and techniques? [TD05-02]

Edwin P. Walker, Call/Recall, Inc.
Terabyte recorded in two-photon 3D disk [TD05-03]

Brian L. Lawrence, GE Global Research
Micro-holographic storage and threshold holographic recording materials [TD05-06]

Susumu Noda, Kyoto Univ. (Japan)
Recent progress in photonic crystals for manipulation of photons
[TD05-10]

Marko Loncar, Harvard Univ.
Nano optics [TD05-11]

Kristian Helmerson, National Institute of Standards and Technology
Optical manipulation of microscopic containers for chemistry with single molecules [TD05-12]

Lambertus Hesselink, Stanford Univ.
Applications of C-apertures to optical data storage [TD05-13]

Min Gu, Swinburne Univ. of Technology (Australia)
Nanophotonics-based optical data storage [TD05-14]

Hideharu Mikami, Hitachi, Ltd. (Japan)
Readout-signal amplification by homodyne detection scheme
[TD05-15]

Kyung-Geun Lee, SAMSUNG Electronics Co., Ltd. (South Korea)
System technology for achieving 200GB drive with 5-layer disc
[TD05-16]

Nobuyuki Hashimoto, Citizen Technology Ctr. Co., Ltd. (Japan)
Liquid crystal active optics and its application to optical pickups
[TD05-19]

Cal Hardie, Seagate Technology LLC
The challenges of heat assisted magnetic recording head integration
[TD05-23]

Kunimaro Tanaka, Teikyo Heisei Univ. (Japan)
Toward adoption of optical disks for preservation of digitized cultural heritage [TD05-25]

Tim Rausch, Seagate Technology LLC
Trends in the digital home: why 'IMG0064.jpg' is the new blinking 12:00 [TD05-26]

Tuviah E. Schlesinger, Carnegie Mellon Univ.
Applications for 4th generation optical storage [TD05-27]

Shoji Taniguchi, Pioneer Corp. (Japan)
DVD-download [TD05-28]

Barry H. Schechtman, Information Storage Industry Consortium
Optical storage in 2008: Where is the competition heading? [TD05-29]

Luping Shi, Data Storage Institute (Singapore)
Fundamental exploration of the solutions for ultra-high density optical recording [TD05-30]

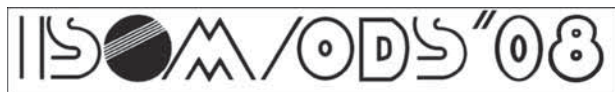
Masaki Takata, The Institute of Physical and Chemical Research (RIKEN) (Japan)
Challenge to snap shot structural visualization of the phase change
[TD05-35]

Thomas D. Milster, College of Optical Sciences/
The Univ. of Arizona
Applications of ODS technology to lithography [TD05-40]

Masaaki Hara, Sony Corp. (Japan)
Linear signal processing for a holographic data storage channel using coherent addition [TD05-47]

Atsushi Fukumoto, Sony Corp. (Japan)
Development of a coaxial holographic data recording system
[TD05-49]

Nikolay I. Zheludev, Univ. of Southampton (United Kingdom)
Optical super-resolution through super-oscillations [TD05-57]



The Joint International Symposium on

Optical Memory and Optical Data Storage

Conference TD05 · Room: Monarchy Ballroom · Monday-Thursday 14-17 July 2008

Conference Chairs: **Kevin R. Curtis**, InPhase Technologies; **Luping Shi**, National Univ. of Singapore/Data Storage Institute (Singapore); **Haruki Tokumaru**, NHK Science & Technical Research Labs. (Japan)

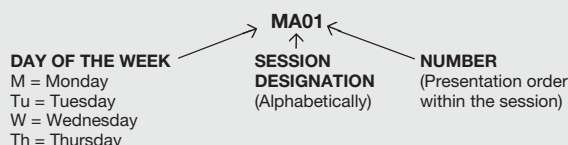
Explanation of Session Codes

The first part of the code designates the day of the week (Monday = M, Tuesday = Tu, Wednesday = W, Thursday = Th)

The next part indicates the session within the particular day the talk is being given. Each day begins with the letter A and continues alphabetically.

The number on the end of the code signals the position of the talk within the session (first, second, third, etc.)

For example, a presentation numbered MA01 indicates that this paper is being presented on Monday during the 1st session (A) and that it is the first paper presented in session MA.



Monday 14 July

Opening Remarks

Room: Monarchy Ballroom · Mon. 8:45 to 9:00 am

Session Chairs: **Tim Rausch**, Seagate Technology LLC; **Kimihiko Saito**, Sony Corp. (Japan); **Koichi Ogawa**, The Univ. of Tokyo (Japan); **Itaru Fujimura**, Ricoh Co., Ltd. (Japan)

SESSION MA: Keynote Session

Session Chairs: **Kevin R. Curtis**, InPhase Technologies Inc.; **Haruki Tokumaru**, NHK Science & Technical Research Labs. (Japan)

Room: Monarchy Ballroom

Mon. 9:00 to 10:00 am

MA01 · 9:00 am Invited

Nanophotonics and application to future storage technology (*Invited Paper*), Motoichi Ohtsu, Univ. of Tokyo (Japan) . . . [TD05-01]

This paper describes the principles and history of nanophotonics, which utilizes the energy transfer of a virtual exciton-polariton. The true nature of this field of study is to realize "qualitative innovation" in optical technology, including photonic devices, fabrications, and information storage. Application to optical near-field magnetic-hybrid recording at a 1-Tb/inch² density is reviewed. For the future development of storage technology, two directions are proposed: one follows the technical roadmap to increase the storage density to 1-Pb/inch² utilizing nanophotonic devices, while the other deviates from the roadmap. High-security information transfer is one example of the latter.

MA02 · 9:30 am Invited

Can future storage technologies benefit from existing or emerging nano-tools and techniques? (*Invited Paper*), Masud Mansuripur, College of Optical Sciences/The Univ. of Arizona . . . [TD05-02]

Certain ideas and techniques are being developed outside the field of optical/magnetic/electronic recording, but the storage community could benefit from these developments once we become sufficiently familiar with the new concepts and methodologies. Aside from nano-photonics, which is the subject of Professor Ohtsu's keynote address, developments in the areas of bio-photonics, fluorescence microscopy, quantum-dots, optical tweezers, micro- and nano-fluidic systems, femto-second fiber lasers, etc., have the potential to influence future generations of data storage systems.

Coffee Break
10:00 to 10:30 am

SESSION MB: 3D Storage

Session Chairs: **Kimihiko Saito**, Sony Corp. (Japan); **Yoshimasa Kawata**, Shizuoka Univ. (Japan)

Room: Monarchy Ballroom

Mon. 10:30 am to 12:30 pm

MB01 · 10:30 am Invited

Terabyte recorded in two-photon 3D disk (*Invited Paper*), Edwin P. Walker, Call/Recall, Inc.; Alexander S. Dvornikov, Call/Recall, Inc. and Univ. of California/Irvine; Kenneth D. Coblentz, Call/Recall, Inc.; Peter M. Rentzepis, Univ. of California/Irvine . . . [TD05-03]

1TB has been recorded in 200 layers in one of our two-photon 120mm diameter x 1.2mm thick form factor 3D disks utilizing our very stable and efficient two-photon materials. Each layer contains 5GB of information.

MB02 · 11:00 am

Multi-layer 400 GB optical disk, Ayumi Mitsumori, Takanobu Higuchi, Takuma Yanagisawa, Masakazu Ogasawara, Satoru Tanaka, Tetsuya Iida, Pioneer Corp. (Japan) . . . [TD05-04]

We confirmed the feasibility of a multi-layer 400 GB optical ROM disk by using a wide range spherical aberration compensator and low absorption reflective materials.

MB03 · 11:15 am Invited

Micro-holographic storage and threshold holographic recording materials (*Invited Paper*), Brian L. Lawrence, Victor P. Ostroverkhov, Xiaolei Shi, Kathryn L. Longley, Eugene P. Boden, GE Global Research . . . [TD05-06]

The limits of micro-holographic storage using standard holographic materials are demonstrated. New threshold holographic materials are being developed to overcome these limits, and preliminary threshold micro-hologram recording results are presented.

MB04 · 11:45 am

Direct servo error signal detection method from recorded micro-reflectors, Hirotaka Miyamoto, Hisayuki Yamatsu, Kimihiko Saito, Norihiro Tanabe, Toshihiro Horigome, Goro Fujita, Seiji Kobayashi, Hiroshi Uchiyama, Sony Corp. (Japan) . . . [TD05-07]

A novel tracking servo error signal detection method for a micro-reflector drive is proposed. The method realizes better performance regarding recording medium interchangeability.

Conference TD05

MB05 · 12:00 pm:

Microholographic data storage towards dynamic disk recording, Susanna Orlic, Enrico Dietz, Sven Frohmann, Jonas Gortner, Alan Guenther, Jens Rass, Technische Univ. Berlin (Germany) . . [TD05-08]

Dynamic recording of microholographic reflection gratings is reported. The current development status and operation of our microholographic drive system is presented.

MB06 · 12:15 pm

Three-dimensional recording with electrical beam control, Ryuichi Katayama, Shin Tominaga, Yuichi Komatsu, Mizuho Tomiyama, NEC Corp. (Japan) [TD05-09]

A concept of an optical storage system without mechanics having high-reliability and low-power-consumption characteristics was proposed and demonstrated by using liquid crystal beam control elements.

Lunch Break
12:30 to 2:00 pm

SESSION MP: Poster Session I

Session Chairs: **Luping Shi**, National Univ. of Singapore/Data Storage Institute (Singapore); **Takashi Kikukawa**, TDK Corp. (Japan); **Yun-Sup Shin**, LG Electronics Inc. (South Korea)

Room: Queen's Ballroom
Mon. 2:00 to 3:30 pm

Poster authors may display their posters beginning at morning coffee break on the day of their presentation, push pins will be provided.

Authors must remain in the vicinity of the poster board for the duration of the session to answer questions.

Posters must be removed at the end of the day after the oral sessions. Posters not removed by 7:00 pm will be considered unwanted and will be discarded.

MP01

Properties of new fluorinated holographic recording material for collinear holography, Kazuyuki Satoh, Daikin Industries, Ltd. (Japan) and Toyohashi Univ. of Technology (Japan); Kazuko Aoki, Makoto Hanazawa, Nami Matsuda, Takashi Kanemura, Daikin Industries, Ltd. (Japan); Pang-Boey Lim, Mitsuteru Inoue, Toyohashi Univ. of Technology (Japan) [TD05-60]

This paper reports the evaluation results of the properties of a new fluorinated holographic recording material for Collinear Holography.

MP02

Holographic recording with blue colorated diarylethene dye doped PMMA, Xinan Liang, Xuewu Xu, Minghua Li, Sanjeev Solanki, Minghui Hong, Chong-Tow Chong, Data Storage Institute (Singapore) [TD05-61]

Blue light illuminated diarylethene dye B1536 doped PMMA were investigated for holographic recording. High sensitivity and refractive index change were achieved.

MP03

ZrO₂ nanoparticle-polymer composite media for volume holographic recording, Toshihiro Nakamura, Sokoh Koda, Kohji Ohmura, Yasuo Tomita, The Univ. of Electro-Communications (Japan); Kentaro Ohmori, Motohiko Hidaka, Nissan Chemical Industries, Ltd. (Japan) [TD05-62]

Volume holographic recording in highly transparent zirconia nanoparticle-polymer composite media is described. Recording sensitivity enhancement and hologram multiplexing are also presented.

MP04

Improved photopolymer for holographic data storage, Yuxia Zhao, Xiaojun Wan, Feipeng Wu, Technical Institute of Physics and Chemistry (China); Huanyong Wang, Pengfei Liu, Shiquan Tao, Beijing Univ. of Technology (China) [TD05-63]

Improved photopolymer for holographic data storage containing a novel broad-band absorption photosensitizer was developed for both 457 nm and 532 nm application.

MP05

Holographic correlator for video image files, Eriko Watanabe, Reiko Akiyama, Kashiko Kodate, Japan Women's Univ. (Japan) [TD05-64]

We have proposed a video identification system using holographic correlator. Taking advantage of fast data processing capability of FARCO, we examined high speed recognition system by registering the optimized video image file. We demonstrate that the processing speed of our optical holographic calculation is remarkably higher than that of the conventional digital signal processing architecture.

MP06

Polarization and random phase modulated reference beam for high-density holographic recording with 2D shift-multiplexing, Sanjeev Solanki, Xuewu Xu, Minghua Li, Xinan Liang, Chong-Tow Chong, Data Storage Institute (Singapore) [TD05-65]

Shift-multiplexing with polarization modulated reference beam is reported with recording of 4kbits data with media shift of 1/2.5 micron along x/y axis.

MP07

Rotational random phase multiplexing, Shih-Hsin Ma, Xuan-Hao Lee, Ye-Wei Yu, Tun-Chien Teng, Ching-Cherng Sun, National Central Univ. (Taiwan) [TD05-66]

An out-of-plane rotational random phase multiplexing is proposed. The rotational sensitivity is enhanced and can be tuned over a large range.

MP08

Parallel realization of two-dimensional discrete Walsh transform in volume holographic storage system, Qiang Ma, Kai Ni, Qingsheng He, Liangcai Cao, Guofan Jin, Tsinghua Univ. (China) [TD05-67]

As an application of the volume holographic storage system, a method that can parallelly perform 2D discrete Walsh transform is theoretically and experimentally described.

MP09

Phase-only correlation for high speed image retrieval in holographic memories, Satoshi Honma, Akiyoshi Katsumata, Univ. of Yamanashi (Japan); Tohru Sekiguchi, NEC Corp. (Japan); Shinzo Muto, Univ. of Yamanashi (Japan) [TD05-68]

We focus on that it is possible to record the phase distribution in the holographic memories and propose a new image matching system.

MP10

Selective erasure of multiplexed holograms using beam amplification by mutually-pumped phase conjugate mirror, Takayuki Sano, Atsushi Okamoto, Hokkaido Univ. (Japan); Kunihiro Sato, Hokkai-Gakuen Univ. (Japan) [TD05-69]

We propose a novel selective erasure using MPPCM. We show the effective selective erasure can be realized by amplified phase conjugate beams due to MPPCM.

Conference TD05

MP11

Spatial resolution of phase-modulated signal detection method using photorefractive two-wave mixing for holographic data storage, Masanori Takabayashi, Atsushi Okamoto, Hokkaido Univ. (Japan). [TD05-70]

A spatial resolution of the phase-modulated signal detection using photorefractive two-wave mixing is considered. We confirmed the operation of a few hundreds micrometers of pixel.

MP12

Micro-integrated r/w-head for WORM-type holographic data storage, Matthias Gruber, Udo Vieth, Univ. of Hagen (Germany). [TD05-71]

The micro-integration of setups for write-once-read-many-type volume holographic data storage is discussed and a particular r/w-head architecture based on planar integration is proposed.

MP13

Simulation technique for diffraction efficiency characteristics in holographic data storage system based on FFT-BPM, Junya Tanaka, Atsushi Okamoto, Motoki Kitano, Hokkaido Univ. (Japan). [TD05-72]

We propose a new simulation method based on FFT-BPM to analyze for diffraction efficiency characteristics in holographic data storage system and visualize an angular selectivity.

MP14

Numerical simulation of retrieving characteristics in holographic data storage by two-wave encryption, Motoki Kitano, Atsushi Okamoto, Takayuki Sano, Hokkaido Univ. (Japan). [TD05-73]

We estimate the effective key space and the shift tolerance to the random phase mask in two-wave encryption and discuss the security and the practicality.

MP15

Analysis of diffraction characteristics of photopolymers by using beam propagation method, Shuhei Yoshida, Manabu Yamamoto, Tokyo Univ. of Science (Japan). [TD05-74]

In this study, we simulated formation of holographic grating in photopolymer based on diffusion model, and analyzed diffraction characteristics by using beam propagation method.

MP16

Modeling and detection of linear and threshold microholograms, Fergus J. Ross, Victor P. Ostroverkhov, Xiaolei Shi, Kenods Welles, Brian L. Lawrence, GE Global Research. [TD05-75]

Linear and threshold material microholographic storage tradeoffs are investigated by simulation. Kogelnik's plane-wave diffraction formula at thickness $Z_0/2$ accurately predicts microholographic diffraction efficiency.

MP17

Optical characterization of photopolymer materials for microholographic data storage, Timo Feid, Enrico Dietz, Sven Frohmann, Christian Mueller, Jens Rass, Susanna Orlic, Technische Univ. Berlin (Germany). [TD05-76]

Different photopolymer materials are investigated for microholographic storage to optimize the interaction between the material itself and the write/read system. Media tester system is presented.

MP18

Data recovery from severely damaged optical media using wavelet transforms, Swetha Kannan, Y. Li, Sashi K. Kasanavesi, Pramod K. Khulbe, Tom D. Milster, Warren L. Bletscher, Delbert Hansen, College of Optical Sciences/The Univ. of Arizona. . . [TD05-77]

Wavelet-transform-based algorithms are developed that increase by at least a factor of two the quality of the recovered signals from badly damaged media.

MP19

Laser diode feedback signal for position sensing using self-mixing interference, Meng-Yen Tsai, Tzong-Shi Liu, National Chiao Tung Univ. (Taiwan); Tuvia E. Schlesinger, Carnegie Mellon Univ. [TD05-78]

We utilize laser diode (LD) package as sensor mounted on DVD pickup. Smaller rotation driven by tilting coil in DVD pickup makes feedback signal distinct.

MP20

High resolution semiconductor inspection by using solid immersion lenses, Jun Zhang, College of Optical Sciences/The Univ. of Arizona; Yullin Kim, Infrared Labs., Inc.; Thomas D. Milster, College of Optical Sciences/The Univ. of Arizona; David M. Dozor, Infrared Labs., Inc. [TD05-79]

A subsurface (100 μ m) microscope is presented with NA=2.45 by using a silicon SIL. The application is IC inspection. Gap and tilt servo are also discussed.

MP21

Photochromic memory with electronic functions II, Tsuyoshi Tsujioka, Osaka Kyoiku Univ. (Japan). [TD05-80]

Various aspects of photochromic memory with electronic function is introduced. Combination of electrical carrier separation and isomerization via hole transportation would achieve high recording sensitivity.

MP22

Chalcogenide layers for optically guided mechanical recording-readout, Mihail Trunov, Uzhgorod National Univ. (Ukraine); Peter Nagy, Erika Kalman, Chemical Research Ctr. (Hungary); Viktor Takats, Sandor J. Kokenyesi, The Univ. of Debrecen (Hungary). . . . [TD05-81]

The giant negative photoplastic effect (giant photosoftening) in amorphous chalcogenide layers was observed and applied to the optically guided nanoindentation experiments. Results can be used in a Millipede-type data recording device.

MP23

Online face recognition system using holographic optical correlator, Akiyama Reiko, Sayuri Ishikawa, Eriko Watanabe, Kashiko Kodate, Japan Women's Univ. (Japan). [TD05-82]

We have proposed and improved a face recognition system based on the algorithm for the Fast Face Recognition Optical Correlator system (FARCO).

MP24

Characteristic of the tracking error signal of a novel multi-level read-only disc, Mingming Yan, Jing Pei, Longfa Pan, Yi Tang, Tsinghua Univ. (China). [TD05-83]

The uniformity and symmetry of the DPD signal of the novel ML-RLL disc by using signal wave-shape modulation is better than the former ML-RLL disc.

Conference TD05

MP25

Symmetric driving coils design for three-axis actuator with low interference force, Buqing Zhang, Jianshe Ma, Longfa Pan, Xuemin Cheng, Hua Hu, Yi Tang, Tsinghua Univ. (China) [TD05-84]

A novel magnetic circuit consisting of symmetric driving coils is developed. This configuration reduces the crosstalk forces in the main moving directions, and improves the driving sensitivity of the actuator used in super multi DVD drive.

MP26

Off axis astigmatic reflector for compact optical pickup, Ya-Ni Su, Cheng-Huan Chen, National Tsing Hua Univ. (Taiwan) [TD05-85]

An optical pickup with all its components stacked up layer by layer and based mostly on reflective optical components has been proposed as a compact and high efficiency solution.

MP27

Inorganic reflective achromatic quarter-waveplate for OPU applications, Kim L. Tan, Karen D. Hendrix, Curtis R. Hruska, Nada A. O'Brien, JDSU. [TD05-86]

An all-inorganic reflective QWP that is achromatic for the three laser wavelengths of an OPU is designed and demonstrated. Implementation into an OPU is described.

MP28

Estimation method of the archival lifetime for optical recordable disks, Mitsuru Irie, Osaka Sangyo Univ. (Japan); Yoshihiro Okino, Kansai Univ. (Japan); Takahiro Kubo, T. Kubo Engineering Science Office (Japan) [TD05-87]

This paper presents a simple estimating method for the archival life expectancy of optical disks in order to apply a rough clarification of archival grade disks.

MP29

Super-trellis-based noise predictive detection for high-density optical storage, Xiao-Ming Chen, Oliver Theis, Deutsche Thomson oHG (Germany) [TD05-88]

Super-trellis based noise prediction was investigated for high density optical storage. Performance gain obtained by the proposed detector increases as storage density increases.

MP30

Channel coding and signal detection for multi-level DVD player system, Hua Hu, Yi Tang, Haibo Yuan, Longfa Pan, Tsinghua Univ. (China) [TD05-89]

Channel coding and signal detection for multi-level DVD player system are introduced, including error correction code, modulation code, timing recovery and adaptive PRML detection.

MP31

Error-correcting coded indices for multimode balanced conservative codes for holographic storage, Yongguang Zhu, Ivan J. Fair, Univ. of Alberta (Canada) [TD05-90]

We present two error-correcting coding schemes for providing error protection for the control array indices required in multimode balanced conservative codes for holographic storage.

MP32

An improved chase decoder for turbo product codes over partial-response channels, Zhiliang Qin, Songhua Zhang, Kui Cai, Xiaoxin Zou, Data Storage Institute (Singapore) [TD05-91]

An improved Chase decoder is proposed based on the concept of local search neighborhood for turbo product codes over partial-response channels.

MP33

Two-dimensional 5:8 modulation code for holographic data storage, Jinyoung Kim, Bongil Lee, Jaejin Lee, Soongsil Univ. (South Korea) [TD05-92]

The proposed two-dimensional 5:8 modulation code is very simple and removes all the isolated 2D ISI patterns.

MP34

Hybrid image processing for holographic data storage system, Jang Hyun Kim, Hyunseok Yang, Jin-Bae Park, Young-Pil Park, Yonsei Univ. (South Korea) [TD05-93]

In this paper, we propose hybrid image processing method in holographic data storage system.

MP35

Gaussian sum approximation approach to Blu-ray disk channel equalization, Gyuyeol Kong, Hyunmin Cho, Sooyong Choi, Yonsei Univ. (South Korea) [TD05-94]

A new equalization method is proposed, which incorporates the Gaussian Sum Approximation into a Kalman filtering framework to mitigate inter-symbol interference in optical recording channels.

MP36

One-dimensional PRML detection with two-dimensional equalizer for holographic data storage, Jinyoung Kim, Donghyuk Park, Jaejin Lee, Soongsil Univ. (South Korea) [TD05-95]

We present a partial response maximum likelihood (PRML) detection with two-dimensional equalizer scheme for holographic data storage channel.

MP37

Optical recording channel equalization using a bilinear recursive polynomial system, Hyunmin Cho, Gyuyeol Kong, Sooyong Choi, Yonsei Univ. (South Korea) [TD05-96]

A new equalizer based on bilinear recursive polynomial models is proposed to improve the performance and simplify the structure of the conventional equalizers for high density optical channels.

MP38

Sum-product decoding of multiple-parallel-concatenated single-parity-check codes over partial-response channels, Xiaoxin Zou, Zhiliang Qin, Kui Cai, Songhua Zhang, Data Storage Institute (Singapore) [TD05-97]

We propose an efficient implementation of a serialized sum-product decoding algorithm for multiple-parallel-concatenated single-parity-check (M-PC-SPC) codes over partial-response channels.

MP39

RMTR constrained parity-check codes for high-density blue laser disk systems, Cai Kui, Kees A. S. Immink, Songhua Zhang, Zhiliang Qin, Xiaoxin Zou, Data Storage Institute (Singapore) [TD05-98]

New constrained codes that satisfy the repeated minimum transition runlength (RMTR) constraint and the parity-check (PC) constraint are proposed for high-density blue laser disk systems.

MP40

Parallel multitrack Viterbi detector for 2D optical storage systems, Timothy S. Yao, The Univ. of Texas at El Paso; Lee Yang, Qingyang Wu, Semiconductor Manufacturing International Corp. (China) [TD05-99]

The proposed parallel Viterbi detector can enhance the bit detection performance of the two-dimensional optical system and processing speed. The algorithm can also be applied to the 3D recording system.

Conference TD05

MP41

Super-resolution near-field disk with phase-change Sn-doped GST mask layer, Irene Lee, Agency for Science, Technology and Research (Singapore); K. T. Yong, Chee Lip Gan, Nanyang Technological Univ. (Singapore); S. M. Daud, L. H. Ting, L. P. Shi, Agency for Science, Technology and Research (Singapore)[TD05-100]

A new mask layer of Sn_{7.0}Ge_{20.6}Sb_{20.7}Te_{51.7} was developed and used on Super-resolution near-field phase change optical disks. The thermal and optical properties of the mask layer were investigated. The recording performance of the new structure is discussed.

MP42

Nonlinear modeling of super-resolution near-field structure, Manjung Seo, Sungbin Im, Jaejin Lee, Soongsil Univ. (South Korea) [TD05-101]

This paper presents a nonlinear modeling of Super-RENS (Super-Resolution Near Field Structure) read-out signal using neural networks. The experiment results indicate that the NARX (Nonlinear AutoRegressive eXogenous) model considered in this study is superior to the NLMS (Normalized Least Mean Square) FIR (Finite Impulse Response) adaptive filter, which is one of linear modeling approaches.

Posters: Postdeadline

Room: Queen's Ballroom
Mon. 2:00 to 3:30 pm

A selection of post deadline poster papers will be included in the Final Technical Program giving the participants the opportunity to hear new and significant material in rapidly advancing areas.

SESSION MC: Special Session: Nano-Photonics

Session Chairs: **Masud Mansuripur**, College of Optical Sciences/The Univ. of Arizona; **Kevin R. Curtis**, InPhase Technologies Inc.

Room: Monarchy Ballroom
Mon. 3:30 to 6:30 pm

MC01 · 3:30 pm Invited

Recent progress in photonic crystals for manipulation of photons (Invited Paper), Susumu Noda, Kyoto Univ. (Japan) [TD05-10]

Recent progresses in photonic crystals are reviewed. First of all, ultra-high Q nanocavity and its dynamic control are discussed. Then, a very unique photonic crystal laser operating at blue-violet wavelengths will be described.

MC02 · 4:00 pm Invited

Nano optics (Invited Paper), Marko Loncar, Harvard Univ. [TD05-11]

Coffee Break
4:30 to 5:00 pm

MC03 · 5:00 pm Invited

Optical manipulation of microscopic containers for chemistry with single molecules (Invited Paper), Kristian Hermerson, Carlos Mariscal-Lopez, Jiayong Tang, Rani B. Kishore, National Institute of Standards and Technology [TD05-12]

We detect and perform chemistry with only a few number of molecules confined in submicron-sized water droplets, which can be manipulated with optical tweezers.

MC04 · 5:30 pm Invited

Applications of C-apertures to optical data storage (Invited Paper), Lambertus Hesselink, J. B. Leen, Paul Hansen, Yao-Te Cheng, Xiaobo Yin, Yin Yuen, Stanford Univ. [TD05-13]

This invited paper describes our latest work towards fully describing the operation of C-aperture light sources and using these sources to write nano-sized marks on optical recording media. During the last decade we have developed and refined a highly efficient nano-sized aperture that, under ideal conditions, increases power throughput by three orders of magnitude compared with round and square apertures producing the same optical spot size. As presented in ODS 2007, these apertures can be mounted on a solid state laser to produce a very high intensity nano-beam having a size of less than 80 nm [1]. In this paper we discuss the theoretical and practical aspects of applying C-apertures to optical data storage as well as our latest results related to using C-shaped nano apertures for optical data storage.

MC05 · 6:00 pm Invited

Nanophotonics-based optical data storage (Invited Paper), Min Gu, Swinburne Univ. of Technology (Australia) [TD05-14]

This talk will present our recent advance in the nanoparticle-assisted optical data storage technology where the information can be stored in five dimensions.

Tuesday 15 July

SESSION TuA: Drive Technologies

Session Chairs: **Ryuichi Katayama**, NEC Corp. (Japan); **Kyunggeun Lee**, SAMSUNG Electronics Co., Ltd. (South Korea)

Room: Monarchy Ballroom
Tues. 8:30 to 10:00 am

TuA01 · 8:30 am Invited

Readout-signal amplification by homodyne detection scheme (Invited Paper), Hideharu Mikami, Takeshi Shimano, Takahiro Kurokawa, Tatsuro Ide, Jiro Hashizume, Koichi Watanabe, Harukazu Miyamoto, Hitachi, Ltd. (Japan) [TD05-15]

Optical signal amplification by using homodyne detection scheme was newly proposed and demonstrated experimentally. Optical pickup for reliably obtaining amplified optical disk readout-signal was designed.

TuA02 · 9:00 am Invited

System technology for achieving 200GB drive with 5-layer disc (Invited Paper), Kyunggeun Lee, Inoh Hwang, Nakhyun Kim, Hyun-Soo Park, Hui Zhao, Tao Hong, Insik Park, SAMSUNG Electronics Co., Ltd. (South Korea) [TD05-16]

We report the feasibility for achieving 200GB with 40GB per layer and 5-layer disc for the first time. bER of lower than 10⁻³ were experimentally obtained respectively using this new data reproducing scheme which shows the possibility of reducing one order of bER. With more improvement of media characteristics, less than 10⁻⁴ of bER can be achieved.

TuA03 · 9:30 am

Stable rotation of optical disks over 15000 rpm, Tomoharu Mukasa, Naofumi Goto, Takeharu Takasawa, Yoshiyuki Urakawa, Nobuhiko Tsukahara, Sony Corp. (Japan) [TD05-17]

We confirmed high-speed-rotation of disks without vibrations up to 20000 rpm and tracking servo control at 17000 rpm using the double-boosted high-gain servo controller.

Conference TD05

TuA04 · 9:45 am

A high-density recording by a near-field optical system using a medium with a top layer with a high refractive index, Ariyoshi Nakaoki, Kimihiro Saito, Takeshi Yamasaki, Tomomi Yukumoto, Tsutomu Ishimoto, Sunmin Kim, Takao Kondo, Takeshi Mizukuki, Osamu Kawakubo, Sony Corp. (Japan); Miwa Honda, Noriyasu Shinohara, Norihiko Saito, JSR Corp. (Japan) [TD05-18]

A coated medium comprised of resin with a high refractive index of 1.83 was examined using a near-field optical disc system of NA 1.84.

Coffee Break
10:00 to 10:30 am

SESSION TuB: Components and Hybrid Recording

Session Chairs: **Paul J. Wehrenberg**, Apple Computer, Inc.; **No-Cheol Park**, Yonsei Univ. (South Korea)

Room: Monarchy Ballroom
Tues. 10:30 am to 12:30 pm

TuB01 · 10:30 am Invited

Liquid crystal active optics and its application to optical pickups (*Invited Paper*), Nobuyuki Hashimoto, Citizen Technology Ctr. Co., Ltd. (Japan) [TD05-19]

We describe optical properties of liquid crystals for optical pickups, liquid crystal GRIN lenses and liquid crystals with sub-wavelength structures.

TuB02 · 11:00 am

A novel deformable mirror for spherical aberration compensation, Sunao Aoki, Masahiro Yamada, Tamotsu Yamagami, Sony Corp. (Japan) [TD05-20]

By using conventional MEMS processes, we have successfully developed a highly accurate and easily controllable deformable mirror with a simple structure.

TuB03 · 11:15 am

Single longitudinal mode blue-violet laser diode for data storage, Christophe Moser, Lawrence Ho, Frank Havermeyer, Ondax, Inc. [TD05-21]

Experimental demonstration of a single mode longitudinal TO-can blue-violet laser with over 1 meter coherence length.

TuB04 · 11:30 am

Designs and tolerances of two-element NA 0.8 objective lenses for page-based holographic data storage systems, Yuzuru Takashima, Lambertus Hesselink, Stanford Univ. [TD05-22]

Two-element NA 0.8 objectives, usable for both holographic and surface recordings, are designed in conjunction with analysis of optical tolerances for holographic removable media systems.

TuB05 · 11:45 am Invited

The challenges of heat assisted magnetic recording head integration (*Invited Paper*), Cal Hardie, Duane C. Karns, William A. Challenger, N. J. Gokemeijer, Tim Rausch, Michael A. Seigler, Edward C. Gage, Seagate Technology LLC. [TD05-23]

The explosion of digital content has created a global demand for storage products that will only increase as the world becomes more digitally oriented and connected. This ever increasing demand for storage capacity has placed significant challenges on the magnetic recording industry. To extend recording densities to beyond 1Tb/in², the industry must find solutions to the superparamagnetic limit which imposes a signal-to-noise ratio, thermal stability, and writability tradeoff. Heat assisted magnetic recording (HAMR) is a technology for achieving these high areal densities. A successful

integration of the HAMR technology will be shown. This integration process is compatible with existing thin film magnetic recording fabrication which includes thin film wafer process, slider lapping, and head/gimbal assembly. A demonstration of 200Gb/in² areal density will be shown as well as a path to increase the areal density capability of HAMR using Near Field Transducer (NFT) technology.

TuB06 · 12:15 pm

HAMR head with spot size converter and triangular aperture, Masakazu Hirata, Manabu Oumi, Majung Park, Seiko Instruments Inc. (Japan) [TD05-24]

This HAMR head has affinity to conventional HDD head and high throughput integrated optics with spot size converter, triangular aperture and mirror.

Lunch Break
12:30 to 2:00 pm

SESSION TuP: Poster Session II

Session Chairs: **Tuviah Ed Schlesinger**, Carnegie Mellon Univ.; **Yoshimi Tomita**, Pioneer Corp. (Japan); **Yoshimasa Kawata**, Shizuoka Univ. (Japan)

Room: Queen's Ballroom
Tues. 2:00 to 3:30 pm

Poster authors may display their posters beginning at morning coffee break on the day of their presentation, push pins will be provided.

Authors must remain in the vicinity of the poster board for the duration of the session to answer questions.

Posters must be removed at the end of the day after the oral sessions. Posters not removed by 7:00 pm will be considered unwanted and will be discarded.

TuP01

Misalignment compensation and equalization for holographic data storage, Haksun Kim, Daewoo Electronics Corp., Ltd. (South Korea) and Daewoo Electronics Corp., Ltd. and Daewoo Electronics Corp., Ltd.; Pilsang Yoon, Joo Youn Park, Heungsang Jung, Daewoo Electronics Corp., Ltd. (South Korea); Gwitae Park, Korea Univ. (South Korea) [TD05-102]

In this paper, misalignment compensation and equalization for holographic data storage is developed and evaluated. Experimental results are shown to verify the proposed algorithm's effectiveness.

TuP02

Improvement of bit error rate by FIR filter, Yuichiro Sasa, Hiroshi Oto, Manabu Yamamoto, Tokyo Univ. of Science (Japan) . [TD05-103]

This paper studies the effects of FIR filter based on genetic algorithm. It is made clear that the best FIR coefficients can be provided by genetic algorithm.

TuP03

Filter structures of write compensation for holographic data storage systems, Takaya Tanabe, Ryu Suzuki, Iwao Hatakeyama, Ibaraki National College of Technology (Japan) [TD05-104]

High pass filters of write compensation are compared and evaluated in simulations. The write compensation with five-pixel pattern shows the best in SNR.

TuP04

Inter-page cross-talk noise in collinear holographic memory, Tsutomu Shimura, Masaru Terada, Yojiro Sumi, Ryushi Fujimura, Kazuo Kuroda, The Univ. of Tokyo (Japan) [TD05-105]

We revealed that signal-to-noise ratio of multiplexed holographic memory is inversely proportional to square root of the multiplied recorded pages theoretically as well as numerical simulation.

Conference TD05

TuP05

Design and test of channel board for holographic data storage, Pilsang Yoon, Daewoo Electronics Corp., Ltd. (South Korea) and Korea Univ. (South Korea); Haksun Kim, Joo Youn Park, Heungsang Jung, Daewoo Electronics Corp., Ltd. (South Korea); Gwitae Park, Korea Univ. (South Korea) [TD05-106]

The hardware channel board for holographic data storage has been designed and implemented with FPGA. A data interface between PC and channel board was adopted in the channel board for data interface. An experiment for real-time recording and reading was performed successfully.

TuP06

Tracking servo control using pole placement based on Luenberger observer for holographic data storage system, Yong Hee Lee, Sang-Hoon Kim, Jang Hyun Kim, Hyunseok Yang, Young-Pil Park, Yonsei Univ. (South Korea); Joo Youn Park, Daewoo Electronics Corp., Ltd. (South Korea) [TD05-107]

In this paper, we focus on effects of radial deviation on the disk and propose a tracking error compensation method for the holographic data storage system.

TuP07

Tilt error measurement and compensation method for the holographic data storage system, Sang-Hoon Kim, Jang Hyun Kim, Yong Hee Lee, Hyunseok Yang, Yonsei Univ. (South Korea); Joo Youn Park, DAEWOO Electronics Corp. (South Korea); Young-Pil Park, Yonsei Univ. (South Korea) [TD05-108]

Tilt error measurement system using external photo detector is suggested and measuring experiments are conducted. A servo controller to compensate tilt error is designed and the performance of it is confirmed.

TuP08

Design of a relay lens with telecentricity in holographic storage system, Yung Sung Lan, National Chiao Tung Univ. (Taiwan); Kuang-Vu Chen, Ping-Jung Wu, Wen-Hung Cheng, Chih-Cheng Hsu, Chin-Tsia Liang, Kuo-Chi Chiu, Tzuan-Ren Jeng, Industrial Technology Research Institute (Taiwan) [TD05-109]

In this paper, we revealed a doubly telecentric Fourier 4f relay for the holographic recording system, which is including six lenses and a PBS. It provides a zero distortion and the wavefront error within $1/4$ (≈ 532 nm).

TuP09

Optimal aperture size for maximizing the capacity of holographic data storage systems, Oliver Malki, Frank Przygodda, Joachim Knittel, Heiko Trautner, Hartmut Richter, Deutsche Thomson oHG (Germany) [TD05-110]

Determination of the optimal spatial filtering of the object beam by an aperture placed in the focal plane in order to optimize the storage capacity of a holographic data storage system.

TuP10

Angular interval scheduling for angle-multiplexed holographic data storage, Nobuhiro Kinoshita, Tetsuhiko Muroi, Norihiko Ishii, Koji Kamijo, Naoki Shimidzu, NHK Science & Technical Research Labs. (Japan) [TD05-111]

We demonstrate an angular interval scheduling for closely stacking holograms. With our scheduling for multiplex number of 300, low bERs across all datapages were obtained.

TuP11

Shift selectivity of the collinear holographic storage system, Ye-Wei Yu, Chih-Yuan Cheng, Shu-Ching Hsieh, Tun-Chien Teng, Ching-Cherng Sun, National Central Univ. (Taiwan) [TD05-112]

The paraxial solution of the shift selectivity of the collinear holographic storage system is proposed, which is a powerful tool for simulation.

TuP12

Isoplanatic lens design for phase conjugate storage systems, Bradley J. Sissom, Alan C. Hoskins, Tolis Deslis, Kevin R. Curtis, InPhase Technologies Inc. [TD05-113]

A new lens design concept for holographic data storage is introduced that improves phase conjugation and enables relaxed assembly tolerances and asymmetric reader/writer architectures.

TuP13

Focus sensing method using far-field diffracted waves and its application to holographic data discs, Teruo Fujita, Hayato Horikoshi, Fukui Univ. of Technology (Japan) [TD05-114]

A far-filed focus sensor was studied by simulation and experiment. A way to suppress the offset of this sensor and optics implemented with it for holographic discs are proposed.

TuP14

Aberration holograms and multiplexing: how to manage spherical aberration in microholographic data storage, Enrico Dietz, Sven Frohmann, Jonas Gortner, Alan Guenther, Jens Rass, Susanna Orlic, Technische Univ. Berlin (Germany) [TD05-115]

We investigate the impact of spherical aberration on microholographic storage and present the concept of so-called aberration holograms and experimental results that demonstrate its viability.

TuP15

Ultra-high density holographic search engine using sub-Bragg and sub-Nyquist recordings, Joby Joseph, Indian Institute of Technology Delhi (India); David A. Waldman, DCE Aprilis, Inc. [TD05-116]

We propose and demonstrate a holographic data storage device meant for search only purposes, having exceptionally huge data density through sub-Bragg and sub-Nyquist holographic recordings.

TuP16

Detection of reproduced image distortion using FFT cross-correlation method in holographic memory, Yuta Kajiwara, Takumi Sano, Manabu Yamamoto, Tokyo Univ. of Science (Japan) [TD05-117]

This paper studies the analysis method of reproduced image distortion. The image distortion was detected by the marker positions in the data area using FFT cross-correlation method.

TuP17

Tilt compensation method for holographic data storage, Sangwoo Ha, Jae-Sung Lee, Na Young Kim, Jeong-Kyo Seo, In-Ho Choi, Byung-Hoon Min, LG Electronics Inc. (South Korea) [TD05-118]

In this paper, we propose the way to detect and compensate the radial/tangential disc tilt. The compensation result by this method is also demonstrated.

TuP18

Dynamic recording and readout of micro-holograms in GE dyedoped thermoplastic, Zhiyuan Ren, Victor P. Ostroverkhov, Xiaolei Shi, Mark A. Cheverton, James Lopez, Brian L. Lawrence, Michael R. Durling, GE Global Research. [TD05-119]

We have implemented recording and readout of micro-holograms in dyedoped thermoplastic in our new dynamic system that utilizes five-axial servos to compensate rotating tilting/run-out.

TuP19

Subwavelength focus by radial polarization through metallic thin film with annular illumination, Tzu-Hsiang Lan, Chung-Hao Tien, National Chiao Tung Univ. (Taiwan) [TD05-120]

With objective of NA = 0.75 and 85% apodized annular pupil, a non-diffraction focused beam has FWHM of 0.37 and more than 2 penetration depth.

Conference TD05

TuP20

Surface plasmon antenna nano-source, Haifeng Wang, Baoxi Xu, Chong-Tow Chong, Data Storage Institute (Singapore) . . . [TD05-121]

A 30nm light spot is generated by illuminating a novel surface plasmon optical antenna with a micron sized focused red light with a wavelength of 650nm.

TuP21

Picometer-scale accuracy in position measurements of dots in a 31 G dot/in² pattern, Donald A. Chernoff, David L. Burkhead, Advanced Surface Microscopy, Inc. [TD05-122]

Picometer scale accuracy in position measurements using standard commercial AFM and SEM with offline calibration/measurement software. Measured Dot pitch 143.895 ± 0.040 by AFM.

TuP22

Study on transparency mechanism of bimetallic Bi/In film, Sihai Cao, Chuanfei Guo, Zhuwei Zhang, Yongsheng Wang, Junjie Miao, Qian Liu, The National Ctr. for Nanoscience and Technology of China (China) [TD05-123]

Transparent mechanism of Bi/In film as potential storage medium was investigated. Oxidation and laser ablation were demonstrated to be main reasons for the transparent conversion.

TuP23

Strategies for employing nano-heterostructures in a near-field enhanced super-resolution optical disk, Yang Wang, Qingling Qu, Yiqun Wu, Fuxi Gan, Shanghai Institute of Optics and Fine Mechanics (China) [TD05-124]

Strategies for employing nano-heterostructures in a near-field enhanced super-resolution optical disk was proposed and numerically investigated.

TuP24

Recovery and reconstruction of the intensity distribution of nano-sized light field obtained with NSOM, HongXing Yuan, Baoxi Xu, M. D. Sofian, Chong-Tow Chong, Data Storage Institute (Singapore) [TD05-125]

Deconvolution techniques is adopted to recover and reconstruct the NSOM for correct characterization of nano-sized light field. Deviation with and without correction is also presented.

TuP25

Pupil plane characteristics and filtering for optical data storage using circular polarization, Junyeob Yeo, Moon-Seok Kim, Narak Choi, Seoul National Univ. (South Korea); Tom D. Milster, College of Optical Sciences/The Univ. of Arizona; Jaisoon Kim, Seoul National Univ. (South Korea) [TD05-126]

Pupil plane beam characteristics and filtering at high-NA and circular polarization are investigated in order to achieve readout signal enhancement.

TuP26

Aberration compensation in near field optics for multi-layer data storage, Kwan-Hyung Kim, Kitak Won, Hyeong-Ryeol Park, Narak Choi, Seoul National Univ. (South Korea); Sam-Nyol Hong, Jeong-Kyo Seo, LG Electronics Inc. (South Korea); Kwang-Sup Soh, Jaisoon Kim, Seoul National Univ. (South Korea) [TD05-127]

The electric component and lens systems are investigated in order to apply for multi-layer data storage in NFR system with high NA.

TuP27

GaP solid immersion lens based on diffraction, Youngsik Kim, Jun Zhang, Thomas D. Milster, College of Optical Sciences/The Univ. of Arizona [TD05-128]

Hybrid solid immersion lens system (SIL) with a spherical lens attached micro gallium phosphide SIL and a diffractive optical element, and its aberration correction mechanisms are discussed.

TuP28

Assembly and evaluation of SIL optical head for high NA cover-layer incident near-field recording, Yong-Joong Yoon, Taeseob Kim, Cheol-Ki Min, Wan-Chin Kim, No-Cheol Park, Young-Pil Park, Yonsei Univ. (South Korea); Tao Hong, Kyunggeun Lee, SAMSUNG Electronics Co., Ltd. (South Korea) [TD05-129]

In this paper, we show the assembly and evaluation results of the SIL optical head with the high refractive index cover layer disc and compare them with simulation ones. Through this research we can improve the effective NA as 1.84 which is the highest NA that has been reported and we can also increase the data recording density per layer such as the surface recording NFR in cover layer incident NFR.

TuP29

Improvement of protection process using observer, Hyun-Woo Hwang, Sang-Hoon Kim, Joong-Gon Kim, Tae-Wook Kwon, Hyun-Seok Yang, No-Cheol Park, Young-Pil Park, Yonsei Univ. (South Korea); Jeong-Kyo Seo, In-Ho Choi, Byeong-Hoon Min, LG Electronics Inc. (South Korea) [TD05-130]

We propose an improved protection process with a mode switching servo method using a Luenberger observer. The protection process based on velocity and gap distance is more powerful than the protection process based only on the gap distance.

TuP30

Improved air gap controller for SIL based near-field recording servo system, Joong-Gon Kim, Min-Seok Kang, Won-Ho Shin, No-Cheol Park, Hyun-Seok Yang, Young-Pil Park, Yonsei Univ. (South Korea) [TD05-131]

This paper describes improved gap controller for near field recording system using an internal model principle and a dead-zone controller. Gap control system is susceptible to disturbances due to small air gap. Therefore, air gap controller should have effective disturbance rejection performance.

TuP31

Effects of surface and mechanical properties of cover-layer on near-field optical recording, Jin-Hong Kim, Jun-Seok Lee, Jungshik Kim, Ki-Chang Song, Jung-Kyo Seo, LG Electronics Inc. (South Korea) [TD05-132]

Several types of cover-layers for NFR media were prepared and characterized.

TuP32

Design of compatible optics for near-field recording and Blu-ray disc using relay lens, Hyun Choi, Jong-Pil Kim, Yong-Joong Yoon, Wan-Chin Kim, No-Cheol Park, Young-Pil Park, Yonsei Univ. (South Korea) [TD05-133]

We designed compatible optics for solid immersion based near-field recording system and Blu-ray disc using the relay lens.

TuP33

Collision between media surface and solid immersion lens in near-field recording, Hyokune Hwang, Jinmoo Park, Sung Hoon Lee, Jung-Kyo Seo, Seung Hun Yoo, In-Ho Choi, Byung-Hoon Min, LG Electronics Inc. (South Korea) [TD05-134]

Harsh collision between media surface and SIL could make permanent deformation causing optical issues. Research to overcome these issues is described in this paper.

Conference TD05

TuP34

The near-field optical module and the tilt compensation method of gap servo near-field recording system, Do-Hyeon Son, Bong-Sik Kwak, Mi Hyeon Jeong, In Gu Han, Jeong-Kyo Seo, In-Ho Choi, Byung-Hoon Min, LG Electronics Inc. (South Korea) [TD05-135]

In this paper, we present the latest results of the LGE NF optical module and the tilt compensation method applying for the NF deck system.

TuP35

L10 ordering of (001)-oriented FePt thin films and its possible application in hybrid recording, Bin Ma, Chaolin Zha, Zongzhi Zhang, Qingyuan Jin, Fudan Univ. (China) [TD05-136]

The L10 ordered phase has been formed in FePt films, deposited on heated MgO substrate or on SrTiO₃, MgO and a 1 nm-FeOx underlayered Si substrate. FePt/TbFeCo bilayered structure is also discussed.

TuP36

Nano-optical characteristics of double-sided grating structure for HAMR application, Dong-Soo Lim, Hyun-Suk Oh, Young-Joo Kim, Yonsei Univ. (South Korea) [TD05-137]

The surface plasmon phenomenon of double-sided grating structure with nano-slit aperture was studied to understand the enhancement of near-field optical throughput for HAMR application.

TuP37

Magnetic and magneto-optical properties of hybrid recording media on porous alumina underlayer, Junbing Yan, Zuoyi Li, Fang Jin, K. F. Dong, Gengqi Lin, X. S. Miao, Huazhong Univ. of Science and Technology (China). [TD05-138]

A self-ordered hexagonal array of nanopores has been fabricated by anodizing a thin film of Al on the glass, the hybrid recording media were sputtered on the porous alumina underlayer, the magnetic properties and magneto-optical properties of TbFeCo film on this underlayer were studied as an example.

TuP38

Study of recorded mark width change with laser power in HAMR, Baoxi Xu, HongXing Yuan, M. D. Sofian, Rong Ji, Jun Zhang, Qide Zhang, Chong-Tow Chong, Data Storage Institute (Singapore) [TD05-139]

The dependence of the recorded mark width on the laser power for heat assisted magnetic recording is studied experimentally and theoretically.

TuP39

Near-field optical coupling and enhancement in the surface plasmon assisted HAMR (SPA) media, Dong-Soo Lim, Young-Joo Kim, Yonsei Univ. (South Korea) [TD05-140]

New structure of 'surface plasmon assisted HAMR (SPA) media' was studied to increase the near-field optical throughput with metal and dielectric interface in magnetic media.

TuP40

Design and performance evaluation of light delivery for heat-assisted magnetic recording, Eun-Hyung Cho, Samsung Advanced Institute of Technology (South Korea); Sung-Mook Kang, Yonsei Univ. (South Korea); John B. Leen, Stanford Univ.; Sung-Dong Suh, Jin-Seung Sohn, Samsung Advanced Institute of Technology (South Korea); Lambertus Hesselink, Stanford Univ.; No-Cheol Park, Young-Pil Park, Yonsei Univ. (South Korea) [TD05-141]

We present a description of the design, fabrication and evaluation of light delivery using a C-shaped nano-aperture for heat assisted magnetic recording

TuP41

Patterning for ultra-high density multi-dimensional multi-level ROM storage, Jia Y. Sze, Luping Shi, Data Storage Institute (Singapore); Diana N. Sutanto, Nanyang Technological Univ. (Singapore); Chun Yang Chong, Jianming Li, Gaoqiang Yuan, Lung Tat Ng, Data Storage Institute (Singapore); Chee Lip Gan, Nanyang Technological Univ. (Singapore); Chong-Tow Chong, Data Storage Institute (Singapore) [TD05-142]

The paper examined the patterning methodology using phase change materials for forming multi-depth pits. The design and fabrication of multi-depth pit for multi-dimensional multi-level ROM disc was also investigated.

TuP42

Application of polynomial regression and re-sampling method to estimate life time of optical disk, Kunimaro Tanaka, Keisuke Fujiwara, Teikyo Heisei Univ. (Japan) [TD05-143]

Re-sampling and linear regression is used for optical disk life estimation. However, Arrhenius plot bends sometimes. Experimental result of application of polynomial regression is reported.

TuP43

Crystallization kinetics and recording mechanisms of a-Ge/Ni bilayer for write-once blue-ray disk, Yung-Chiun Her, Jyun-Hung Chen, National Chung Hsing Univ. (Taiwan) [TD05-144]

The crystallization kinetics and recording mechanism of a-Ge/Ni bilayer recording film for write-once blue ray disk were studied.

TuP44

Preparation and optical storage properties of novel metal hydrazone organic materials for recordable Blu-ray disc, Yiqun Wu, Zhimin Chen, Shanghai Institute of Optics and Fine Mechanics (China) and Heilongjiang Univ. (China); Donghong Gu, Yang Wang, Fuxi Gan, Shanghai Institute of Optics and Fine Mechanics (China) [TD05-145]

New metal hydrazone organic materials as recording media for recordable blu-ray disc have been presented. Optical, thermal and recording properties were involved.

TuP45

Crystallization and melting kinetics of Zn-doped fast-growth Sb₇₀Te₃₀ phase-change recording films, Yung-Sung Hsu, Ying-Da Liu, Yung-Chiun Her, National Chung Hsing Univ. (Taiwan); Shun-Te Cheng, Song-Yeu Tsai, Industrial Technology Research Institute (Taiwan) [TD05-146]

In order to obtain sufficiently high recording sensitivity and archival stability, while maintain adequate initialization ability for the rewritable optical memories, the optimum Zn concentration in Sb₇₀Te₃₀ recording film should be located between 5.3 and 17.9%.

TuP46

Crystallization time dependence on SbTe based phase change films measured by rotating disc techniques, Robert E. Simpson, Paul Fons, Alex Kolobov, Masashi Kuwahara, Junji Tominaga, National Institute of Advanced Industrial Science and Technology (Japan) [TD05-147]

Dynamic measurements of growth dominated and nucleation dominated materials are presented as a function of mark length and film depth. Bismuth doping of these films is found to increase the crystallization rate of the growth dominated materials through a corresponding decrease in the material's viscosity.

Conference TD05

TuP47

Cyclability improvement on super-resolution BD-like ROM disks based on the high-contrast semiconductor InSb, Joseph Pichon, Fabien Laulagnet, Marie-Françoise Armand, Olivier Lemonnier, Bérangère Hyot, Bernard André, Commissariat à l'Energie Atomique (France) [TD05-148]

We present our recent improvements of InSb-based Super-Resolution BD-like ROM disks in terms of cyclability, as investigated by dynamic and static testing.

TuP48

Improvement of aerodynamic stability in flexible optical disk system with cylindrically concaved stabilizer, Yasunori Sugimoto, Shozou Murata, Yasutomo Aman, Masaru Shinkai, Nobuaki Onagi, Ricoh Co., Ltd. (Japan); Daiichi Koide, Yohimichi Takano, Haruki Tokumaru, Japan Broadcasting Corp. (Japan) [TD05-149]

The effects of both disk thickness and material were investigated in order to improve aerodynamic stability in flexible optical disk system with cylindrically concaved stabilizer.

TuP49

Multi-level read-only DVD using signal waveform modulation, Yi Tang, Jing Pei, Longfa Pan, Hua Hu, Haibo Yuan, Buqing Zhang, Mingming Yan, Tsinghua Univ. (China) [TD05-150]

A novel multi-level read-only DVD using signal waveform modulation is proposed and implemented on DVD platform. A raw BER of less than 1e-4 is achieved.

Posters: Postdeadline

Room: Queen's Ballroom
Tues. 2:00 to 3:30 pm

A selection of post deadline poster papers will be included in the Final Technical Program giving the participants the opportunity to hear new and significant material in rapidly advancing areas.

SESSION TuC: Special Session: Applications

Session Chairs: **Susanna Orlic**, Technische Univ. Berlin (Germany); **Mitsuru Irie**, Osaka Sangyo Univ. (Japan)

Room: Monarchy Ballroom
Tues. 3:30 to 6:30 pm

TuC01 · 3:30 pm Invited

Toward adoption of optical disks for preservation of digitized cultural heritage (*Invited Paper*), Kunimaro Tanaka, Teikyo Heisei Univ. (Japan) [TD05-25]

Digital archive is important for preservation and usage of present culture. Recent status and requirement for optical disks for this purpose is described.

TuC02 · 4:00 pm Invited

Trends in the digital home: why 'IMG0064.jpg' is the new blinking 12:00 (*Invited Paper*), Tim Rausch, S. Iren, D. Seekins, Ernest P. Riedel, Seagate Technology LLC [TD05-26]

Technology has become more ubiquitous and accessible than ever before, but it still remains out of reach of many everyday individuals. People struggle with technology and content management in the home on a regular basis. Using design research techniques, we went into the homes of families and spent time with them, observing their successes and failures with digital data. As a result of the study we identified several trends in the digital home and barriers between individuals and their technology.

Coffee Break
4:30 to 5:00 pm

TuC03 · 5:00 pm Invited

Applications for 4th generation optical storage (*Invited Paper*), Tuvia E. Schlesinger, Bruch H. Krogh, Tshuan Chen, Carnegie Mellon Univ. [TD05-27]

Optical data storage provides inexpensive, removable, easily replicated medium. Only applications requiring these will use optical storage. Advanced imaging and control systems are applications that could require the next generation of optical data storage systems.

TuC04 · 5:30 pm Invited

DVD-download (*Invited Paper*), Shoji Taniguchi, Pioneer Corp. (Japan) [TD05-28]

DVD-Download provides a new distribution channel of DVD-Video discs via internet download and centralized production. This paper describes its distribution models and format outline.

TuC05 · 6:00 pm Invited

Optical storage in 2008: Where is the competition heading? (*Invited Paper*), Barry H. Schechtman, Information Storage Industry Consortium [TD05-29]

Optical storage applications are discussed, and the status and outlook are reviewed for other technologies that compete with optical storage for these applications.

Wednesday 16 July

SESSION WA: New and Related Technologies

Session Chairs: **Thomas D. Milster**, College of Optical Sciences/The Univ. of Arizona; **Jooho Kim**, SAMSUNG Electronics Co., Ltd. (South Korea)

Room: Monarchy Ballroom
Wed. 8:30 to 10:00 am

WA01 · 8:30 am Invited

Fundamental exploration of the solutions for ultra-high density optical recording (*Invited Paper*), Luping Shi, Chong-Tow Chong, Boris S. Luk'yanchuk, Jianming Li, Haifeng Wang, Gaoqiang Yuan, Jia Y. Sze, Data Storage Institute (Singapore) [TD05-30]

The possible solutions to achieve ultra-high density optical recording are explored fundamentally, including the ways further reducing spot size to overcome diffraction limit, volumetric recording using real space, imagine space and parameter spaces, and making use of the interaction effect of light and matters. The challenges and limitations are discussed.

WA02 · 9:00 am

Plasmonic nano-structures for optical data storage, Masud Mansuripur, College of Optical Sciences/The Univ. of Arizona; Aramais R. Zakharian, Andrey Kobayakov, Corning, Inc.; Jerome V. Moloney, College of Optical Sciences/The Univ. of Arizona. [TD05-31]

We describe a method of optical data storage that relies on the small dimensions of metallic nano-structures and/or nano-particles to achieve high storage densities. The resonant behavior of these particles (as individuals and in small clusters) in the presence of ultraviolet, visible, and near-infrared light may be used to retrieve pre-recorded information using far-field spectroscopic optical detection.

WA03 · 9:15 am

Towards femto-Joule nanoparticle phase-change optical memory, Andrey I. Denisyuk, Kevin F. MacDonald, Nikolay I. Zheludev, Univ. of Southampton (United Kingdom) [TD05-32]

Phase-change functionality in gallium nanoparticles offers an innovative conceptual basis for the development of high density, low energy, non-volatile optical memories.

Conference TD05

WA04 · 9:30 am

Nanophotonic hierarchical hologram: demonstration of the physical hierarchy, Naoya Tate, Wataru Nomura, The Univ. of Tokyo (Japan); Takashi Yatsui, Japan Science and Technology Agency (Japan); Makoto Naruse, National Institute of Information and Communications Technology (Japan) and The Univ. of Tokyo (Japan); Motoichi Ohtsu, The Univ. of Tokyo (Japan) [TD05-33]

We experimentally demonstrated the concept of proposed "nanophotonic hierarchical hologram" which works both in optical far-fields and near-fields. The hierarchy is attributed to near-fields interactions.

WA05 · 9:45 am

Higher sensitivity for the analysis of bio-entities with changes in thicknesses of multilayered BioDVD structure, Gopinath Subash Chandra Bose, Awazu Koichi, Kumar K. R. Penmetcha, Junji Tominaga, National Institute of Advanced Industrial Science and Technology (Japan) [TD05-34]

Increased the sensitivity of optical based detection of bio-molecular interactions on BioDVD surfaces with manipulations of multilayered structure.

Coffee Break
10:00 to 10:30 am

SESSION WB: Media and Applications

Session Chairs: **Rie Kojima**, Matsushita Electric Industrial Co., Ltd. (Japan); **Chong-Tow Chong**, Data Storage Institute (Singapore)

Room: Monarchy Ballroom
Wed. 10:30 am to 12:30 pm

WB01 · 10:30 am

Invited

Challenge to snap shot structural visualization of the phase change (*Invited Paper*), Yoshito Tanaka, The Institute of Physical and Chemical Research (RIKEN) (Japan); Yoshimitsu Fukuyama, Nobuhiro Yasuda, Jungeun Kim, Haruno Murayama, Shigeru Kimura, Japan Synchrotron Radiation Research Institute (Japan); Kenichi Kato, The Institute of Physical and Chemical Research (RIKEN) (Japan); Shinji Kohara, Japan Synchrotron Radiation Research Institute (Japan); Yutaka Moritomo, Tsukuba Univ. (Japan); Toshiyuki Matsunaga, Rie Kojima, Noboru Yamada, Matsushita Electric Industrial Co., Ltd. (Japan); Hitoshi Tanaka, Japan Synchrotron Radiation Research Institute (Japan); Masaki Takata, The Institute of Physical and Chemical Research (RIKEN) (Japan) [TD05-35]

The first time-resolved structure investigation of phase change process of DVD materials was achieved by SR diffraction experiment coupled with simultaneous photo reflectivity measurement.

WB02 · 11:00 am

What is the origin of activation energy in phase-change film?, Junji Tominaga, Takayuki Shima, Paul Fons, Robert E. Simpson, Masashi Kuwahara, Alexander Kolobov, National Institute of Advanced Industrial Science and Technology (Japan) [TD05-36]

We reveal and discuss the origin of the activation energy, which initiates the transition from the amorphous to crystalline state, based on a GeSbTe-superlattice model by ab-initio local density approximation.

WB03 · 11:15 am

Reliable measurement of optical constants for molten phase-change thin film, Daisuke Eto, Kazuhiko Aoki, Shuichi Ohkubo, NEC Corp. (Japan) [TD05-37]

We found out optical constants of molten InSb thin film are nearly independent of thickness and interface layer material, while melting point depends on thickness.

WB04 · 11:30 am

A two-color photopolymer system for high-capacity multilayer optical data storage, Benjamin A. Kowalski, Robert R. McLeod, Timothy F. Scott, Univ. of Colorado at Boulder [TD05-38]

A novel two-color photopolymer system is demonstrated, which suppresses polymerization at the periphery of recording while maintaining high writing sensitivity at the focus. This enables both increased storage density and increased signal via suppression of out-of-focus exposure.

WB05 · 11:45 am

Phase aberration limits to three-dimensional optical data storage in homogeneous media, Robert R. McLeod, Univ. of Colorado at Boulder [TD05-39]

An analytic expression for the phase aberrations of multi-layer optical storage disks is derived and used to calculate a limit on the total number of layers.

WB06 · 12:00 pm

Invited

Applications of ODS technology to lithography (*Invited Paper*), Thomas D. Milster, College of Optical Sciences/The Univ. of Arizona [TD05-40]

As demands for ever smaller and more powerful computer circuits increase, technologists are planning to decrease the minimum feature size fabricated on Si wafers to less than 16 nm by 2020. This Herculean task may be accomplished with exposure tools operating at the soft x-ray wavelength of 13.5 nm and advanced processing techniques. A significant problem with this plan is that, as the minimum feature size decreases, the cost of the exposure and processing systems increases. This paper addresses the possibility of applying optical data storage (ODS) technology to lithographic exposure, in order to reduce cost of the components and provide a path for fabrication of 10 nm features.

Thursday 17 July

SESSION ThA: Coding and Signal Processing

Session Chairs: **Satoru Higashino**, Sony Corp. (Japan); **Seiji Kobayashi**, Sony Corp. (Japan)

Room: Monarchy Ballroom
Thurs. 8:30 to 10:00 am

ThA01 · 8:30 am

Signal-readout system for optical pickup with homodyne detection scheme, Takahiro Kurokawa, Hideharu Mikami, Tatsuro Ide, Koichi Watanabe, Harukazu Miyamoto, Hitachi, Ltd. (Japan) [TD05-41]

We developed a signal-readout system for optical pickups using a homodyne detection scheme. By using the system, a signal amplification rate of 3.6 was obtained.

ThA02 · 8:45 am

Turbo equalization with RLL (1,9) and LDPC code for SuperRENS ROM discs with 60nm minimum mark length, Oliver Theis, Xiao-Ming Chen, Dietmar Hepper, Gael Pilard, Deutsche Thomson oHG (Germany) [TD05-42]

Low complexity super-trellis detection for an enhanced (1,9) RLL modulation code with application to turbo equalization for next generation optical discs is presented.

Conference TD05

ThA03 · 9:00 am

Study of ITR-PLL with linearly constrained adaptive pre-filter for high-density optical disc, Yoshiyuki Kajiwara, Junya Shiraishi, Shohei Kobayashi, Tamotsu Yamagami, Sony Corp. (Japan). [TD05-43]

Digital phase lock loop with linearly constraint adaptive pre-filter has studied to improve qualities of phase error calculation by adaptive equalized signal with enough stability.

ThA04 · 9:15 am

Adaptive writing strategy based on bits-indexed writing parameters, Hui Zhao, Hyun-Soo Park, Inoh Hwang, Kyunggeun Lee, Insik Park, SAMSUNG Electronics Co., Ltd. (South Korea) . [TD05-44]

A new bits-indexed writing parameters organization method and an adaptive writing strategy are proposed. The performance is proved by 40GB Blu-ray Disc experiment.

ThA05 · 9:30 am

Reduced state sequence estimation with level adaptation (RESSELA) for high density disc, Hyun-Soo Park, Hui Zhao, Inho Hwang, Kyunggeun Lee, Insik Park, SAMSUNG Electronics Co., Ltd. (South Korea). [TD05-45]

We report the new data reproducing scheme for high density over 40GB with a commercial Blu-ray recordable disc. bER of 1×10^{-6} and 1.3×10^{-4} and 2.6×10^{-3} and 9×10^{-3} with 40GB, 45GB, 47.5GB and 50GB were experimentally obtained respectively using this new data reproducing scheme which shows the possibility of achieving 50GB with a commercial single-layer Blu-ray disc.

ThA06 · 9:45 am

Analysis on SNR improvement by multi-tone demodulation, Atsushi Kikukawa, Hiroyuki Minemura, Hitachi, Ltd. (Japan) [TD05-46]

SNR improvement by using multi-tone demodulation was theoretically investigated. The input bandwidth and the ADC clock jitter are the major factors that limit the efficiency.

Coffee Break
10:00 to 10:30 am

SESSION ThB: Holographic I

Session Chairs: Lambertus Hesselink, Stanford Univ.; Tsutomu Shimura, The Univ. of Tokyo (Japan)

Room: Monarchy Ballroom
Thurs. 10:30 am to 12:30 pm

ThB01 · 10:30 am

Invited

Linear signal processing for a holographic data storage channel using coherent addition (*Invited Paper*), Masaaki Hara, Kazutatsu Tokuyama, Kenji Tanaka, Kazuyuki Hirooka, Atsushi Fukumoto, Sony Corp. (Japan). [TD05-47]

A linear channel model and linear signal processing are available for a holographic data storage channel when coherent addition is applied in a reproduction process.

ThB02 · 11:00 am

Homodyne detection of holographic data pages, Mark R. Ayres, Kevin R. Curtis, InPhase Technologies Inc. [TD05-48]

A method for homodyne detection of holographic data pages is presented. The optical phase-matching problem is solved algorithmically, rather than optically.

ThB03 · 11:15 am

Invited

Development of a coaxial holographic data recording system (*Invited Paper*), Atsushi Fukumoto, Sony Corp. (Japan) [TD05-49]

Based on our recent progress in high-density and high data-transfer-rate recordings using coaxial holographic recording testers, the prospects for performance improvement in future systems are discussed.

ThB04 · 11:45 am

A reflective counter-propagating holographic setup, Joachim Knittel, Frank Przygodda, Oliver Malki, Heiko Trautner, Hartmut Richter, Deutsche Thomson-Brandt GmbH (Germany) [TD05-50]

We present a reflective counter-propagating holographic setup for optical data storage that makes efficient use of the laser light.

ThB05 · 12:00 pm

Practical holography, Ken E. Anderson, Edeline Fotheringham, Friso Schlottau, Paul C. Smith, Keith W. Farnsworth, Jason R. Ensher, Kevin R. Curtis, InPhase Technologies Inc. [TD05-51]

We review the evolution of InPhase Technologies' holographic storage drive and discuss technical obstacles that we have overcome to bring our product to market.

ThB06 · 12:15 pm

Material consumption and crosstalk characteristics of different holographic storage concepts, Frank Przygodda, Joachim Knittel, Oliver Malki, Heiko Trautner, Hartmut Richter, Deutsche Thomson-Brandt GmbH (Germany). [TD05-52]

Three holographic data storage concepts (plane wave, collinear, counter-propagating beam setup) are investigated by numerical simulations regarding their material consumption, diffraction efficiency and crosstalk characteristics.

Lunch Break
12:30 to 2:00 pm

SESSION ThC: Holographic II and Super Resolution

Session Chairs: Robert R. McLeod, Univ. of Colorado at Boulder; Satoru Tanaka, Pioneer Corp. (Japan)

Room: Monarchy Ballroom
Thurs. 2:00 to 4:00 pm

ThC01 · 2:00 pm

Wobble alignment for angularly multiplexed holograms, Mark R. Ayres, Alan C. Hoskins, Paul C. Smith, John Kane, InPhase Technologies Inc. [TD05-53]

A method for dynamic alignment adjustment in an angle-multiplexed holographic storage system is presented. A wobble servo corrects readout beam angle, pitch, and wavelength.

ThC02 · 2:15 pm

Three-dimensional Fourier optics analysis of holographic optical data storage systems, George Barbastathis, Massachusetts Institute of Technology [TD05-54]

A theoretical method for analysis and design of holographic memories is presented. The memory is expressed as a 3D pupil in an imaging system. It is shown how practical memory performance metrics, such as interpage---intrapage crosstalk and defocus tolerance, can be understood and optimized using this approach.

Conference TD05

ThC03 · 2:30 pm

Intra-signal modulation in holographic memories, Mark R. Ayres, InPhase Technologies Inc.; Robert R. McLeod, Univ. of Colorado at Boulder [TD05-55]

An analysis of intra-signal noise in volume holography is presented. Estimates of the coherent and incoherent limiting cases are derived for ASK and PSK modulation.

ThC04 · 2:45 pm

Sparse modulation codes for channel with media saturation, Lakshmi D. Ramamoorthy, Vijayakumar Bhagavatula, Carnegie Mellon Univ. [TD05-56]

Channel model with media saturation was built to simulate data pages. We observed a trade off between the relative write transfer rates and bit error rate.

ThC05 · 3:00 pm

Invited

Optical super-resolution through super-oscillations (*Invited Paper*), Nikolay I. Zheludev, Univ. of Southampton (United Kingdom) [TD05-57]

To achieve optical sub-wavelength concentrations of light beyond the near-field, the concept of super-oscillations recently flagged by Berry and Popescu, and demonstrated by our group using a quasi-crystal array of holes, provides a viable and less technologically challenging alternative to the approach based on negative-index super-lenses exploiting recovery of the evanescent fields.

ThC06 · 3:30 pm

Comparison of a semiconductor and a phase-change material for application in a super-resolution ROM disk, Gael Pilard, Larisa Pacearescu, Herbert Hoelzemann, Christophe Féry, Deutsche Thomson oHG (Germany) [TD05-58]

Super-resolution ROM disks based on InSb or AIST were manufactured. A BER of $1e-3$ was found with InSb on random patterns having 40nm channel bit length. We demonstrate why the decoding with AIST is not possible.

ThC07 · 3:45 pm

Super resolution media with significantly high read stability, Shuichi Ohkubo, Kazuhiko Aoki, Eiji Kariyada, Daisuke Eto, NEC Corp. (Japan) [TD05-59]

Read stability of $1e+6$ times has been confirmed with Super-Resolution ROM media with phase change mask layer by developing new protective and inter-face layers.

Coffee Break
4:00 to 4:30 pm

SESSION ThD: Postdeadline Session

Session Chairs: **Barry H. Schechtman**, Information Storage Industry Consortium; **Junji Tominaga**, National Institute of Advanced Industrial Science and Technology (Japan)

Room: Queen's Ballroom

Thurs. 4:30 to 5:30 pm

A selection of post deadline oral papers will be included in the Final Technical Program giving the participants the opportunity to hear new and significant material in rapidly advancing areas.

Closing Remarks

Session Chairs: **Kevin R. Curtis**, InPhase Technologies Inc.; **Luping Shi**, Data Storage Institute (Singapore); **Haruki Tokumaru**, NHK Science & Technical Research Labs. (Japan)

Room: Monarchy Ballroom

Thurs. 5:30 to 6:00 pm

SESSION MA: Keynote Session

Monarchy Ballroom
9:00 to 10:00 am

Kevin R. Curtis, InPhase Technologies Inc.
Haruki Tokumaru, NHK Science & Technical Research Labs. (Japan)

Nanophotonics and application to future storage technology

M. Ohtsu

Department of Electronics Engineering, the University of Tokyo
2-11-16 Yayoi, Bunkyo-ku, Tokyo 113-8656, Japan

ABSTRACT

This paper describes the principles and history of nanophotonics, which utilizes the energy transfer of a virtual exciton–polariton. The true nature of this field of study is to realize “qualitative innovation” in optical technology, including photonic devices, fabrications, and information storage. Application to optical near-field magnetic-hybrid recording at a 1-Tb/inch² density is reviewed. For the future development of storage technology, two directions are proposed: one follows the technical roadmap to increase the storage density to 1-Pb/inch² utilizing nanophotonic devices, while the other deviates from the roadmap. High-security information transfer is one example of the latter.

Keywords: nanophotonics, optical near field, virtual, exciton, polariton, magnetic recording, nano-patterned media

1. INTRODUCTION

Nanophotonics, proposed by the author in 1993, is an innovative technology utilizing the optical near field, which is the virtual exciton–polariton that mediates the interaction between nanometric particles located in close proximity to each other [1]. It enables novel photonic devices, fabrications, and systems to meet the requirements for future optical technology. These requirements include increasing the integration of photonic devices, the resolution of fabrication, and information storage density, which can be called “quantitative innovation.” However, the true nature of nanophotonics is to realize “qualitative innovation” by utilizing novel functions and phenomena caused by the energy transfer of a virtual exciton–polariton and subsequent dissipation of the energy. Several qualitative innovations in photonic devices, optical nano-fabrications, and photonic systems have already been demonstrated [2]. This paper describes the history of nanophotonics and application to ultrahigh density/capacity storage technology.

2. HISTORY OF NANOPHOTONICS

In Japan, the study of optical near fields began in the early 1980s, separate from European and American research [3]. In the early 1990s, a reliable, reproducible, and selective chemical etching technology was established for fabricating high-quality fiber probes, with which optical near fields were generated and detected [4]. Using these fiber probes, optical storage to photochromic thin film was demonstrated [5]. A novel theory was developed based on the interaction and energy transfer between nanometric particles via optical near fields. This perspective is essential because the interaction, energy transfer, and subsequent dissipation are indispensable for nanophotonic devices, fabrication, and information storage and readout. Theoretical work described the local electromagnetic interactions as the exchange of a virtual exciton–polariton, which was expressed by a Yukawa function that represents the localization of the optical near field around the nanometric particles, like an electron cloud around an atomic nucleus. Its decay length is equivalent to the material size [6]. Nanophotonics is the technology utilizing the exchange of a virtual exciton–polariton to realize novel devices, fabrications, and information storage. Nanophotonics undoubtedly has the advantage of exceeding the diffraction limit of light, *i.e.*, “quantitative innovation.” However, note that the most essential advantage is to realize “qualitative innovation,” meaning novel functions and phenomena, which are impossible as long as propagating light is used.

Based on these considerations, research and development has examined nanophotonic devices, fabrications, and systems, with several examples of qualitative innovations having been demonstrated [7]. For application to optical storage, extremely efficient fiber probes were developed by controlling the interference of transmission modes in the tapered core of the fiber [8]. The throughput of optical near-field generation was increased 1000 times over conventional fiber probes. Furthermore, this control technology was applied to develop a high-throughput pyramidal silicon probe and a contact slider, which were used to demonstrate high-density recording and fast readout using a phase-change medium [9].

3. 1-TB/INCH² DENSITY OPTICAL NEAR-FIELD MAGNETIC-HYBRID RECORDING

As an application to magnetic recording with a density as high as 1 Tb/inch², beyond the limit set by thermal instability using conventional technology, an optical near field was used to heat nano-patterned media. This technology was named heat-assisted magnetic recording or optical near-field magnetic-hybrid recording. This is an example of quantitative innovation, and was realized as part of a national project in Japan supervised by the author. This project developed three main technologies:

(1) *Near-field storage media technology*: Two or three rows of magnetic dots were aligned circumferentially in guide grooves that were drawn using an electron beam mastering method, and a process for flattening surfaces was also developed. Nano-patterned media 20 nm in diameter at 30-nm intervals were fabricated on which individual magnetic dots could be observed; a self-assembly method was developed for circumferential alignment using a Si master disk. In addition, regularly aligned dot patterns were obtained with block copolymers, Co/Pd multilayers were developed that had a perpendicular anisotropy of 9.2×10^6 erg/cc, and a magnetization reversal size of 20 nm was obtained by patterning the film into dots.

(2) *Recording technology*: A device made of baked metallic plate, named a “nano-beak,” was developed for generating an optical near field with a spot diameter of 20 nm [10]. A near-field optical slider head was then fabricated to mount the nano-beak and a solid immersion lens. The slider head ran in a stable manner, maintaining a flying height of 20 nm. An isolated dot 20 nm in diameter was recorded on a Co/Pd multilayer magnetic nano-patterned medium.

(3) *Nano-mastering technology*: The electron beam (EB) technique was developed to converge the EB spot diameter to 20 nm with a current density of 8 kA/cm². Using it, master disks were fabricated for 1-Tb/inch² class storage with a groove width of 15 nm and track pitch of 30 nm. The standard deviation of the track pitch was within 1.5 nm. Moreover, the formatter was improved for high-speed drawing and high accuracy.

4. TOWARD THE FUTURE

Several routes lead toward future storage technology. One is to increase the storage density. A consortium has been organized for setting a technology roadmap for 1-Pb/inch² storage technology to be realized by the year 2030. One candidate technology for 1 Pb/inch² is to utilize the interaction between a polarized optical near field and electron spin. Furthermore, for increasing speed recording and readout, the rotating disk should be removed and a solid-state memory developed, for which nanophotonic devices can be used advantageously [11]. Another direction is toward technology off the roadmap; that is, instead of increasing the storage density, adding another degree of freedom would be advantageous. One example utilizes hierarchy in optical near-field interactions, which means that optical near fields exhibit different physical behavior at different scales [12]. By combining the hierarchy property, a novel traceable optical memory can be developed that records memory access events to each bit. It can be useful for applications such as high-security information transfer.

5. SUMMARY

This paper describes the principles and history of nanophotonics. Application to high-density storage technology is also reviewed. For future development of storage technology, two directions are proposed: one follows the technical roadmap to increase the storage density to 1-Pb/inch² using nanophotonic devices; the other deviates from the technology roadmap, with high-security information transfer being one example. Figure 1 summarizes the present and future of storage technology using nanophotonics.

ACKNOWLEDGEMENTS

The author acknowledges Profs. T. Kawazoe, T. Yatsui, and M. Naruse, and postdoctoral fellows K. Nishibayashi, N. Tate, and W. Nomura for their collaboration. Part of this study was supported by JST, MEXT, and NEDO, Japan. MA

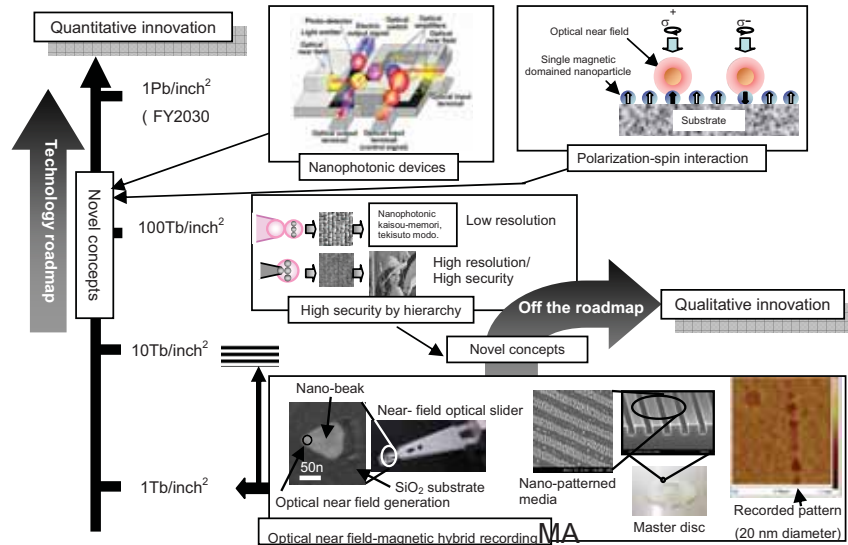


Fig. 1. Future directions for storage technology using nanophotonics.

REFERENCES

- [1] Ohtsu, M. (ed.), [Progress in Nano-Electro-Optics V], Springer-Verlag, Berlin, VII-VIII (2006): Based on “nanophotonics” proposed by Ohtsu in 1993, OITDA (Optical Industry Technology Development Association, Japan) organized the nanophotonics technical group in 1994, and discussions on the future direction of nanophotonics were started in collaboration with academia and industry.
- [2] Ohtsu, M., Kawazoe, T., Yatsui, T., and Naruse, M., [Principles of Nanophotonics], Taylor & Francis, London, 1-222 (2008).
- [3] Zhu, X. and Ohtsu, M. (ed.), [Near-Field Optics: Principles and Applications], World Scientific. Publishing Co., Singapore, 1-8 (2000).
- [4] Ohtsu, M. (ed.), [Near-Field Nano/Atom Optics and Technology], Springer-Verlag, Berlin, 33-69 (1998).
- [5] Jiang, S., Ichihashi, J., Monobe, H., Fujihira, M., and Ohtsu, M., “Highly localized photochemical processes in LB films of photochromic material by using a photon scanning tunneling microscope,” *Opt. Commun.*, 106 (3-5), 173-177 (1994).
- [6] Ohtsu, M. and Kobayashi, K., [Optical Near Fields], Springer-Verlag, Berlin, 109-120 (2004).
- [7] Ohtsu, M., “Nanophotonics in Japan,” *J. Nanophotonics*, 1, 011590 (2007).
- [8] Yatsui, T., Kourogi, M., and Ohtsu, M., “Increasing throughput of a near field optical fiber probe over 1000 times by the use of a triple-tapered structure,” *Appl. Phys. Lett.*, 73(15), 2090-2092 (1998).
- [9] Yatsui, T., Kourogi, M., Tsutsui, K., Takahashi, J., and Ohtsu, M., “High-density-speed optical near-field recording-reading with a pyramidal silicon probe on a contact slider,” *Opt. Lett.*, 25(17), 1279-1281 (2000).
- [10] Nishida, T., Matsumoto, T., Akagi, F., Hieda, H., Kikitsu, A., Naito, K., Koda, T., Nishida, N., Hatano, H., and Hirata, M., “Hybrid recording on bit-patterned media using a near-field optical head,” *J. Nanophotonics*, 1, 011597 (2007).
- [11] Ohtsu, M., Kobayashi, K., Kawazoe, T., Sangu, S., and Yatsui, T., “Nanophotonics: Design, Fabrication, and Operation of Nanometric Devices Using Optical Near Fields,” *IEEE J. Selected Topics in Quantum Electron.*, 8(4), 839-862 (2002).
- [12] Naruse, M., Yatsui, T., Kawazoe, T., Akao, Y., and Ohtsu, M., “Design and Simulation of a Nanometric Traceable Memory Using Localized Energy Dissipation and Hierarchy of Optical Near-Field Interactions,” *IEEE Trans. On Nanotechnol.*, 7(1), 14-19 (2008).

Can future storage technologies benefit from existing or emerging nano-tools and techniques?

Masud Mansuripur

College of Optical Sciences, The University of Arizona, Tucson, Arizona 85721

masud@optics.arizona.edu

Abstract: Certain ideas and techniques are being developed outside the field of optical/magnetic/electronic recording, but the storage community could benefit from these developments once we become sufficiently familiar with the new concepts and methodologies. Developments in the areas of nano- and bio-photonics, fluorescence microscopy, quantum-dots, optical tweezers, micro- and nano-fluidics, femtosecond lasers, etc., have the potential to influence future generations of data storage systems.

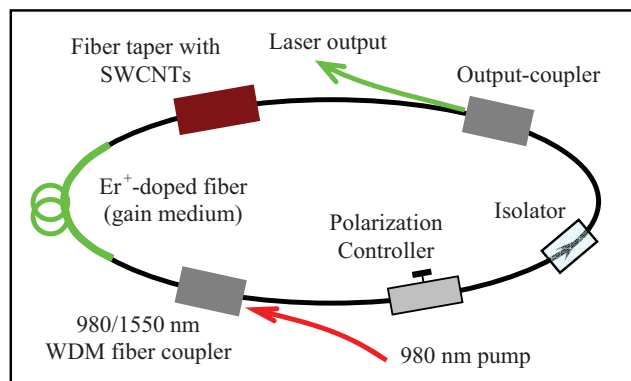
1. All-optical magnetic recording. Magnetization reversal in thin films of GdFeCo has been induced by ultra-short, circularly-polarized laser pulses ($\tau \sim 40$ fs, $\lambda = 800$ nm, $f = 1$ kHz). No external magnetic field is required for switching, and the stable final state of the magnetization is determined by the helicity of the laser pulse, as shown in Fig. 1. This finding reveals an ultrafast and efficient pathway for writing magnetic bits at record-breaking speeds, paving the way for a new generation of ultrafast magnetic recording devices [1].

Fig. 1. Effect of single 40 fs circularly-polarized laser pulses on the magnetic domains of Gd₂₂Fe_{74.6}Co_{3.4}. The 20 μ m domains were obtained by sweeping at 5 cm/s a right (σ^+) or left (σ^-) circularly-polarized beam (~ 29 pJ/ μ m²) over the surface [1].



2. Femtosecond fiber lasers. In a ring fiber laser, a short length of core-pumped Er-doped fiber acts as the gain medium. A saturable absorber (or polarization-sensitive element exploiting the effects of non-linear polarization rotation) embedded within the cavity favors mode-locked operation over continuous-wave laser activity. Pulse duration may be controlled by a variable dispersion control unit. The passively mode-locked ring oscillator can easily generate ultrashort pulses (≤ 150 fs) at a center wavelength of 1.55 μ m with a repetition rate of 100 MHz. With the high gain available from Er-doped fibers, the optical power extracted from the oscillator may be used to seed one or more optical amplifiers. The pulse train typically exhibits an average power of more than 250 mW or 2.5 nJ/pulse. Since these ultrashort pulses are generated in single-mode fibers, their transverse profile has a perfect TEM₀₀ shape, which can be focused to diffraction-limited spots. Several options further enhance the scope of femtosecond fiber lasers: Integrating a highly non-linear fiber into the ring allows the generation of an octave-spanning super-continuum from 1050 nm to 2100 nm. Pulse compression of this broad-band spectral distribution to sub-30 fs pulses and tunable frequency-doubling into the visible or near-infrared regime open new avenues for application. A frequency-doubling module connected directly to the amplifier output allows efficient conversion to 775 nm with output powers exceeding 60 mW or 0.6 nJ/pulse. (Adapted from *Toptica Photonics* website at www.toptica.com.)

Fig. 2: Passively mode-locked, all-fiber ring laser. The gain medium is a 2 m-long Er-doped fiber. A short segment of a fiber taper embedded in a single-walled carbon nanotube/polymer composite acts as a saturable absorber, providing the nonlinear mechanism for mode-locking. The ring consists of 12 m of Corning's SMF28 and ~ 1 m of Flexcor fiber in the WDM coupler [2].



3. Supercontinuum generation (SCG) in photonic crystal fibers (PCFs). In this process a short (typically sub-picosecond) laser pulse is converted to light with a very broad spectral bandwidth. While temporal coherence is lost in the process, spatial coherence usually remains high. The spectral broadening is accomplished by propagating optical pulses through a highly nonlinear medium such as a PCF, whose unusual chromatic dispersion allows strong nonlinear interaction over a significant length of the fiber; see Fig. 3. Even with fairly moderate input powers, very broad spectra can be achieved. Although SCG can be observed in a drop of water given enough pumping power, PCFs are ideal media for SCG as the dispersion can be designed to facilitate continuum generation in a specific band [3]. PCFs with a large nonlinear coefficient are available with a wide range of unique zero-dispersion wavelengths. For single-transverse-mode operation, the fibers are typically designed with relatively small air-holes. (Adapted from R. Paschotta, www.rp-photonics.com.)

A potential application of supercontinuum pulsed lasers to optical data storage involves plasmonic nanostructures tuned to specific wavelengths within a broad range of optical frequencies [4]. By providing simultaneous access to UV, visible, and near IR wavelengths, high-repetition-rate super continuum pulses may hold the key to substantial increases in storage density as well as data-transfer rates.

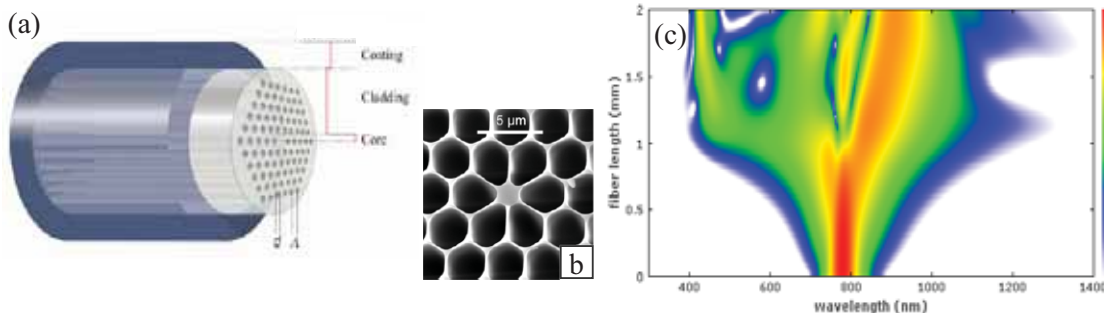


Fig. 3. (a) Photonic crystal fiber (PCF) guides the light in a solid core embedded within a triangular lattice of air holes. (b) SEM picture of a multi-mode PCF with zero dispersion at visible wavelengths. (c) Nonlinear evolution of the spectrum of a femtosecond pulse along the length of a PCF (vertical axis); spectral broadening comes to a halt after ~1 mm of propagation due to significant reductions in the peak power.

4. Macromolecular data storage. Massively parallel writing of data into a DNA backbone has recently been demonstrated [5]. With reference to Fig. 4, using the four natural bases of DNA (identified by the letters G,C,A,T) one can create, for example, 1024 different segments using 5-base sequences. A 5120-base-long sequence then forms a standard 1 kilo-bit template, where the location of each data-bit (0 or 1) in a 1 Kb block will have a unique address. The data-bits are short DNA segments that complement the address of each location in the template (C and A complement G and T, respectively). For instance, if a given location's designated address is TCGAG, the data-bit associated with that location will be AGCTC. The "1" bits have an attachment (e.g., a protein molecule), while the "0" bits have no attachments at all.

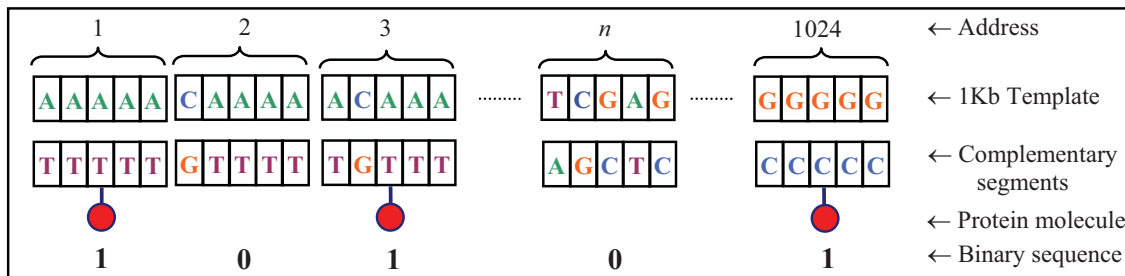
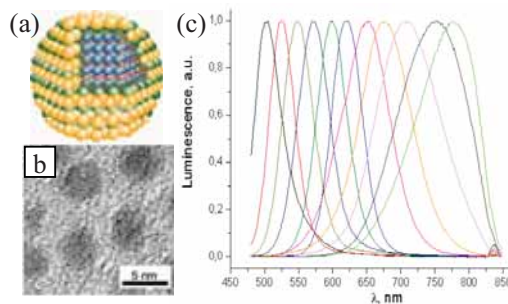


Fig. 4. Massively parallel writing of binary data onto a single-stranded DNA template. The letters G,C,A and T represent the four natural bases of DNA. The 1 kilo-bit template is a string of 1024 distinct 5-base sequences. Each data bit (0 or 1) is associated with a short segment of DNA that complements the address of a specific location on the template. The "1" bits have an attachment (e.g., a protein), while the "0" bits have no attachments at all [5].

To create a specific sequence of 0s and 1s, the short segments having protein attachments must be released into a solution that contains a single copy of the template. The released segments automatically find their complements on the template and get attached at the intended locations. It is this automatic binding of the data-bits onto the template that forms the basis for massively parallel writing in the proposed scheme of macromolecular data storage. An enzyme (DNA polymerase) then fills the gaps that are left open between the “1” segments by “writing” onto the template the complements of the remaining segments (i.e., 0s of the binary sequence). In the final step, the double-stranded DNA molecule with its complete sequence of 1s and 0s (i.e., with and without attached proteins) is transferred to an assigned location within the macromolecular storage system. (Note that increasing the size of a data-block from 1 Kb to, say, 2 MB, would require the assignment of only 12 DNA bases to each segment corresponding to a single bit, because $4^{12} = 16,777,216$ bits = 2 MB.) Creating a practical macromolecular data storage system is a challenge that will require advances in microfluidics, nano-scale integration, bio-chemistry on a chip, and advanced opto-electronic methods of single-molecule detection and manipulation [6].

5. Quantum dots. Due to strong confinement of charge carriers (i.e., electrons and holes), nano-crystals of semiconductors such as CdSe, CdTe, ZnSe, Si, InAs, and PbSe differ substantially in their opto-electronic properties from their bulk crystalline counterparts. Nano-crystalline Q-dots with typical diameters of 2–10 nm contain anywhere from 10^2 to 10^5 atoms. Large quantities of Q-dots may be produced via colloidal synthesis, which is by far the cheapest and least toxic of the various synthetic routes. Colloidal nano-particles are synthesized by first dissolving the precursor compounds and organic surfactants in an appropriate solvent. Monomer concentration and temperature of the growth chamber are critical factors in determining the quality and the opto-electronic properties of the emerging nano-particles [7].

Fig. 5. (a) A typical Q-dot is a nanometer-scale crystallite of a semiconductor, e.g., CdSe, with a dielectric protective layer, such as ZnS. (b) Transmission electron micrograph of 5 nm-diameter doped ZnSe nanocrystals. (c) Emission spectra of CdTe quantum dots of different sizes (2-5 nm) upon excitation by a short-wavelength (e.g., ultraviolet) light source.



Quantum dots of the same material but different sizes emit light of different colors: while smaller Q-dots fluoresce in the blue, the larger ones tend to fluoresce in the red and near-infrared. Larger dots have more energy levels which are also more closely spaced, thus allowing the Q-dot to absorb and emit less energetic photons. In modern biological analysis, Q-dots are considered superior to traditional organic dyes due to their brightness (owing to high quantum yield) and stability (much less photo-destruction). In some applications, such as single-particle tracking, the irregular blinking of Q-dots could be a drawback, although solutions to this problem (e.g., in the form of surface passivation) have been forthcoming. Q-dots are being used in light-emitting diodes to make displays and other light sources. They also have the potential to increase the efficiency and reduce the cost of today's silicon photovoltaic cells. PbSe Q-dots, for instance, can produce as many as seven excitons from one high-energy photon of sunlight (7.8 times the bandgap energy), rather than just one exciton, whose high-kinetic-energy carriers lose energy as heat.

Possible applications of Q-dots to optical data storage include novel light sources and detectors. It is also conceivable that a read-only memory can be built from Q-dots studded with specific ligands, which attach selectively to designated areas on a master disk, before being transferred to a CD-like substrate.

1. C. D. Stanciu et al, "All-optical magnetic recording with circularly polarized light," *Phys. Rev. Lett.* **99**, 047601 (2007).
2. K. Kieu and M. Mansuripur, "Femtosecond laser pulse generation with a fiber taper embedded in carbon nanotube/polymer composite," *Opt. Lett.* **32**, 2242-44 (2007); "All-fiber bidirectional passively mode-locked ring laser," *Opt. Lett.* **33**, 64-66 (2008).
3. A. L. Gaeta, "Nonlinear propagation and continuum generation in microstructure optical fibers," *Opt. Lett.* **27**, 924 (2002).
4. M. Mansuripur et al, "Plasmonic nano-structures for optical data storage," Paper TD05-31, this conference.
5. G. Skinner, K. Visscher, M. Mansuripur, "Biocompatible writing of data into DNA," *J. Bionanoscience* **1**, 1-5 (2007).
6. P. K. Khulbe, M. Mansuripur, and R. Gruener, "DNA translocation through α -hemolysin nano-pores with potential application to macromolecular data storage," *J. Appl. Phys.* **97**, 104317-1:7 (2005).
7. Y. Yin and A. P. Alivisatos, "Colloidal nanocrystal synthesis and the organic-inorganic interface," *Nature* **437**, 664-70 (2005).

SESSION MB: 3D Storage

Monarchy Ballroom
10:30 am to 12:30 pm

Kimihiro Saito, Sony Corp. (Japan)
Yoshimasa Kawata, Shizuoka Univ. (Japan)

Terabyte recorded in two-photon 3D disk

Ed Walker^{1*}, Alexander Dvornikov^{1,2}, Ken Coblenz¹, Peter Rentzepis²

¹Call/Recall, Inc., 6160 Lusk Blvd., Suite C-206, San Diego CA, 92121

²Department of Chemistry, University of California, Irvine, CA 92617

<http://www.call-recall.com>

*Corresponding author ewalker@call-recall.com

ABSTRACT: 1TB has been recorded in 200 layers in one of our two-photon 120mm diameter x 1.2mm thick form factor 3D disks utilizing our very stable and efficient two-photon materials. Each layer contains 5GB of information.

Keywords: Optical data storage, volumetric optical data storage, two-photon, 3d, bit-wise volumetric, large capacity, multilayer optical data storage, two-photon materials, high NA objective lens

1. Introduction

Call/Recall, Inc. has developed a series of efficient and stable two-photon 3D recording materials using photochromic fluorescence compounds that are well suited as media for 3D optical storage memory devices [1-10]. This paper summarizes a milestone achievement for high capacity optical, (HCO), data storage with a fully recorded 1TB optical disk. The media consist of photochromic organic molecules, designed and synthesized by Call/Recall scientists, that change their structure upon two-photon excitation to the first allowed upper state, f , of the molecule using a virtual, v , intermediate excited state, as shown in the energy level diagram of Fig. 1. The unwritten photochromic molecules are uniformly dispersed in a polymer matrix enabling the disks to be of low cost and formed by either compression or injection molding.

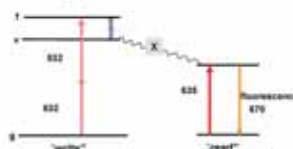


Fig. 1. Energy band diagram picture of the single laser beam two-photon 3D recording.

A 3D bit is recorded in the volume of the media only at regions with sufficient temporal and spatial photon density. High temporal photon density is achieved by means of pulsed laser systems having sufficient pulse energy and peak power, and high spatial photon density through the use of a single tightly focused laser beam. For recording we use objective lenses having numerical apertures (NA) in the 0.5-1.0 range. Recording occurs only within a small volume around the focus of the objective lens due to the two-photon I^2 dependence. Where the irradiance, I , is proportional to the 3D point spread function of the objective lens and input recording laser wavefront [11]. The recorded bits are read by fluorescence that is emitted when excited by a laser diode in a single-photon absorption process whose wavelength lies within the absorption band of the written form.

2. Recording system

We are beginning to experiment with Nichia 445nm and 405nm laser diodes for recording with a laser diode format and will report the results obtained with these lasers in the near future. Figure 2a and 2b show an updated version of our single-beam two-photon recording and one-photon readout spin-stand system. The updated layout is evolving into a typical arrangement of an optical head to facilitate further evolution into a portable prototype of a TB class WORM HCO data storage system. Experimentally, we use a HighQLaser system Picotrain series 532nm Nd:Vanadate laser which emits pulses with 6.5ps pulse width, $\sim 7\text{nJ/pulse}$ energy at a repetition rate of 75MHz. An Isomet Acoustic-Optic modulator modulates the recording laser in the desired data pattern controlled through a standard LabView interface. An automated computer program controls the tracking/layer addressing, objective lens movements and motor speed control. The recording laser beam passes through a beam expander on its way to the objective lens assembly that focuses the recording laser on the media inside the volume of the spinning disk where data is recorded. Several motors are available to spin our storage disks including a Seagull high precision air-bearing spindle, Chiba motor, and standard optical disk motors. After recording, a 635nm CW BlueSky circular laser diode operating at $<0.5\text{mW}$ is used to induce fluorescence by a one-photon, linear, process from the recorded data MA

bits. The fluorescence is then picked up by the same objective lens and focused onto a detector such as a Hamamatsu R7400U PMT, with a $25\mu\text{m}$ confocal pinhole that is used to decrease layer and tracking crosstalk from adjacent tracks and layers, or other high gain APD commercially available detectors. Using our 1.0NA objective lens designed, built, and integrated into our automated recording teststand for multi-layer media[10, 13], we were able to fully record 1TB of test patterns in one of our two-photon 3D disks.

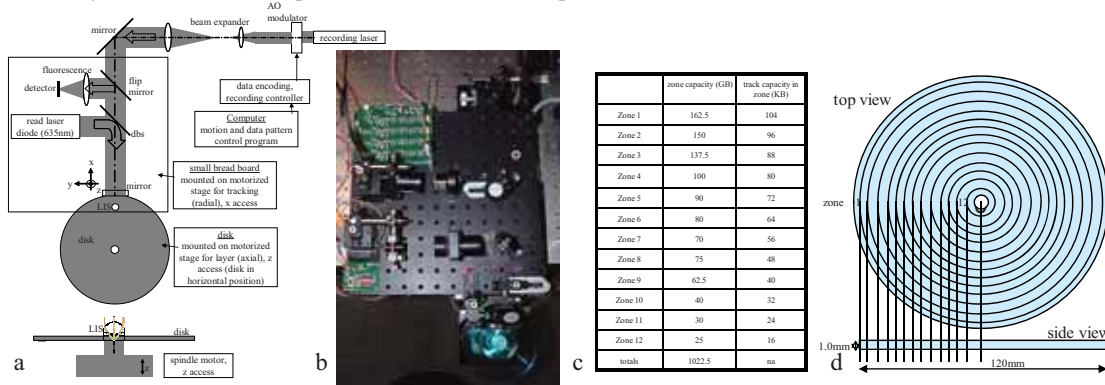


Fig. 2. Single-beam two-photon recording system diagram and Layout of tracks and zones in table form and pictorial layout for a zoned CLV (constant linear velocity) approach to maximize layer capacity in a 120mm diameter disk recording having a capacity of 1TB with a track pitch of $0.8\mu\text{m}$, layer pitch $5\mu\text{m}$, and 200 layers.

3. Experiment

Utilizing the progress that we have made on materials and systems [1-10], we have recorded 1.0TB in a 120mm diameter 1.2mm thick disk having a track pitch of $0.8\mu\text{m}$ and layer spacing of $5\mu\text{m}$, using the 1.0NA objective lens that we have previously developed. This is the first time in the world, to the author’s knowledge, that a two-photon 3D disk, or any other type of removable disk has been fully recorded and reported, especially at such high, TB, bit density. Figure 2c and 2d show the layout of track capacities and zonal capacities for a zoned CLV (constant linear velocity) approach where within each zone the bit pitch along the track varies from $0.3\mu\text{m}$ to $0.5\mu\text{m}/\text{bit}$. Full CLV will be implemented and will be reported elsewhere shortly. Figure 3a shows the fully recorded disk where the energy to record a bit is $7\text{nJ}/\text{bit}$ for the 1.0NA objective lens. Each layer in the 1TB recording has the equivalent capacity of a DVD.

Figure 3a shows a photograph of the disk. Figure 3b depicts a typical xy confocal microscope scan of test tracks recorded in the 1TB recording of the 120mm diameter 1.2mm thick disk at a recording data rate of $5\text{Mbit}/\text{s}$. The data recorded is a series of single tone pulse position modulated, ppm, test tracks of $2\text{T} \rightarrow 8\text{T}$ patterns at a recording energy of $7\text{nJ}/\text{bit}$ of recording energy with the 1.0NA objective lens. Figure 3b shows a typical xz confocal microscope scan of ~ 20 layers separated by $5\mu\text{m}$. Testing at higher single channel data rates of $25\text{-}100\text{Mbit}/\text{s}$ is in progress and we are now able to record with a single pulse from the 75MHz HighQLaser system and anticipate repeating TB recording at these higher recording data rates in the very near future.



Fig. 3. Photograph of 120mm diameter disk after recording. typical xy confocal microscope scan throughout the different layers and xz confocal microscope scan of ~ 20 layers. Track pitch of $0.8\mu\text{m}$ and layer spacing of $5\mu\text{m}$ recorded in the 120mm diameter disk recorded at $7\text{nJ}/\text{bit}$ from a single pulse of a 75MHz repetition rate laser.

The readout signal quality of the 2T and 3T test patterns were found to have a CNR of 30-34dB measured in a 3KHz rbw. The readout signal quality is expected to improve as these results are obtained from a collimated 635nm laser beam into the LIS, that is designed for 532nm, that when focused by the LIS has several waves of spherical aberration due to the spherochromatism of the LIS. Several solutions to the color correction that are needed for the LIS are presently being considered and are in the process of being implemented experimentally. Figure 4 shows some oscilloscope traces and signal spectra from some of the test patterns. We are proceeding to increase both the recording and readout data single channel data rates and the preliminary results of thin scratch resistant coatings low coefficient of friction interface and non contact lens system is encouraging.

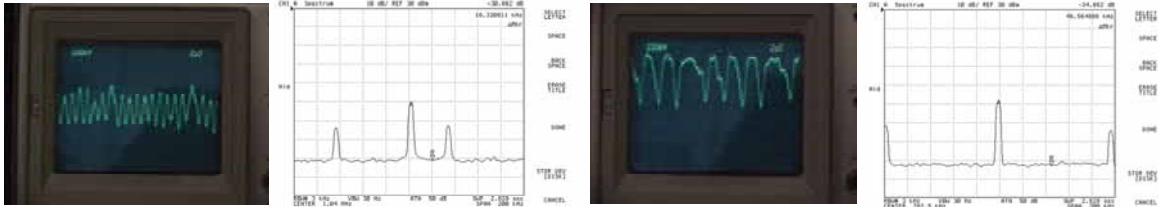


Fig. 4. Oscilloscope traces and signal spectrum on some of the test patterns recorded.

4. Conclusion

The very first full optical disk recording of 1TB has been performed in two-photon 3-d optical data storage materials with very low energy per bit 7nJ/bit. With further improvements in material sensitivities we anticipate being able to record with 100's of pJ/bit that will enable the use of alternative recording laser formats that have a more desirable package such as the Nichia 445nm and 405nm laser diodes that we are using now for high density recording experiments. Full disk recordings are planned that will test at higher single channel data rate recording of 25-100Mbit/s similar to the single pulse recording from the 75MHz HighQLaser system.

Acknowledgements

This effort was partially supported as part of the High Density Optical Data Storage program, sponsored by the US Army Research Office under Contract DAAD19-03-C-0136. MDA sponsorship under Contract W9113M-04-C-0086 is gratefully acknowledged. The US government is authorized to reproduce and distribute reprints for governmental purposes notwithstanding any copyright annotation thereon. We also acknowledge collaboration with Nichia Corporation for providing us with 445nm and 405nm laser diodes. We are grateful to David Stroup for valuable help with the automated recording software/hardware.

5. References

1. D. A Parthenopoulos and P. M. Rentzepis, "Three-Dimensional Optical Storage Memory," *Science* **245**, 843-845, (1989).
2. A. S. Dvornikov, I. Cokgor, M. Wang, F. B. McCormick, S. E. Esener and P. M. Rentzepis, "Materials and Systems for Two Photon 3D ROM Device," *IEEE TCPMT - Part A* **20**, 200-212, (1997).
3. Yongchao Liang, A.S. Dvornikov and P. M. Rentzepis, "Synthesis of novel photochromic fluorescing 2-indolylfulgimides," *Tetrahedron Lett.* v. **40**, 8067-8069, (1999).
4. A.S. Dvornikov, T.D. Milster, E. Walker, P. M. Rentzepis, "Two-photon 3D high-density optical storage media: optical properties, temperature, radiation, and fatigue studies," *Proceedings of SPIE*, **6308**, (2006).
5. Masaharu Akiba, Alexander S. Dvornikov, and Peter M. Rentzepis, "Formation of oxazine dye by photochemical reaction of N-acyl oxazine derivatives," *J. Photochem. Photobiol. A*, **190**, 69-76, (2007).
6. A. S. Dvornikov, Yongchao Liang and P. M. Rentzepis, "Dependence of the Fluorescence of a Composite Photochromic Molecule on a Structure and Viscosity," *J. Mater. Chem.*, **15**, 1072-1078, (2005).
7. Yi Zhang, A. Dvornikov, Y. Taketomi, E.P. Walker, P. Rentzepis, S. Esener, "Towards ultra high density multi-layer disk recording by two-photon absorption," *Proceedings of SPIE*, **5362**, 1-9, (2004).
8. A. S. Dvornikov, Y. C. Liang, P. M. Rentzepis, "Ultra high density non-destructive readout, rewritable molecular memory," *Res. Chem. Intermed.*, **30**, 4-5, 545-561, (2004).
9. A.S. Dvornikov, Y. Liang, C. S. Cruse, P. M. Rentzepis, "Spectroscopy and Kinetics of a Molecular Memory with Non-Destructive Readout for Use in 2D and 3D Storage Systems," *J. Phys. Chem. B*, **108**, 8652-8658, (2004).
10. E. Walker, A. Dvornikov, K. Coblentz, S. Esener, and P. Rentzepis, "Toward terabyte two-photon 3D disk," *Optics Express*, **15**, Issue 19, 12264-12276 (2007).
11. E. P. Walker and T. D. Milster, "Beam shaping for optical data storage," in *Laser Beam Shaping Applications*, F. M. Dickey, S. C. Holswade, D. L. Shealy, eds. (CRC Press Taylor & Francis Group, 2006), 157-181.
12. Ed Walker, W. Feng, Y. Zhang, H. Zhang, F. McCormick, S. Esener, "3-D parallel readout in a 3-D multilayer optical data storage system," *ISOM/ODS meeting Hawaii (2002) paper # TuB4*.
13. H. Zhang, A. Dvornikov, Ed Walker, N. Kim, F.B. McCormick, "Single-beam two-photon-recorded monolithic multi-layer optical disks," *Proceedings of SPIE*, **4090**, 174-178 (2000).

Multi-layer 400 GB Optical Disk

A. Mitsumori, T. Higuchi, T. Yanagisawa, M. Ogasawara, S. Tanaka and T. Iida
Corporate Research and Development Laboratories, Pioneer Corporation
1-2, Fujimi 6 chome, Tsurugashima, Saitama, 350-2288, Japan
Tel: +81-49-279-2300, FAX: +81-49-279-1512
E-mail: ayumi_mitsumori@post.pioneer.co.jp

ABSTRACT

We confirmed the feasibility of a multi-layer 400 GB optical ROM disk by using a wide range spherical aberration compensator and low absorption reflective materials.

Keywords: Multi-layer, 400 GB, ROM, spherical aberration, transparent stamper

1. INTRODUCTION

Multi-layer structure is one of the most promising technology to realize an optical disk capacity as large as 500 Gbytes (GB). According to the road map of the optical memory explained in ISOM2006, the multi-layer disk would be have 500 GB in 2010. ^[1] Until now, a quadruple-layer 100 GB ROM disk ^[2] and an octa-layer 200 GB ROM disk ^[3] have already been reported. In this paper, we report a way to approach 500 GB capacity by using an improved compensator for the spherical aberration and a low absorption material for its information layers.

2. EXPERIMENTAL SETUP

Figure 1 shows the schematic diagram of evaluation optics for the multi-layer disk. We modified a conventional Blu-ray Disc (BD) tester to evaluate a disk containing over octa-layers. We used a blue-violet laser as a light source and a 0.85 NA objective lens. A Kepler-type beam expander was adopted to compensate the spherical aberration caused by the difference of the cover layer thickness. A pinhole was located in the focal point between two lenses of the expander optics, which had an effect to reduce the interlayer cross talk to obtain a focus error signal clearly. Therefore, the designed compensation range of this pick-up head was wider than that of the conventional optics. The compensation range was achieved up to +/- 100 μm range. Figure 2 shows a structure of the 16-layer disk. The thickness of the spacer layer between each information layer was varied to reduce the multi reflection effect. The total thickness of spacer layers was set to approximately 200 μm , which matches for the compensation range of the spherical aberration of the optics. The average thickness of the spacer layer was approximately 13 μm . The information layers were formed using a UV-curable resin, and a transparent resin stamper using a spin method. In this method, the interlayer and the information pits were formed simultaneously. The signal pits patterns were duplicated onto the surface of the UV-curable resin by using the transparent resin stamper. A dielectric thin film was formed over pits patterns as the reflective layer using a sputtering method. We duplicated the information layers 16-times. Finally, a protective layer was formed on pits patterns using the UV-curable resin. The minimum pit length and the track pitch were 149 nm and 320 nm, respectively. The capacity of each information layer was 25 GB for a 120 mm diameter. The duplication method in this experiment is suitable for the mass production because that is a similar process to BD duplication.

3. EXPERIMENTAL RESULT

Figure 3 shows the focus-sum and focus error signal. The stray lights from adjacent layers were reduced by the pinhole. Therefore, we obtained separated signals clearly. Figure 4 indicates jitter values of each layer. The jitter values of 3rd-

layer to 10th-layer signals were less than 9%. The 7th-layer is located in the center of the compensation range of the spherical aberration, and the spherical aberration is almost perfectly compensated in several layers around the 7th-layer. On the other hand, the jitter values of other layers were degraded approximately by 1%. The pick-up head of this tester has the wider dynamic range to compensate the spherical aberration than that of a conventional BD tester. However, the off-axis aberration of the objective lens restricts the ability to compensate the spherical aberration. We think that some residual aberration degraded the jitter values in these layers. Figure 5 shows eye-patterns of several layers after equalization with a limit equalizer. Each signal waveform was clear. From these results we confirmed that sufficiently high signal quality were obtained in all layers of the 16-layer disk. The difference of the jitter values between the 7th layer of the 16-layer disk and the single layer disk was approximately 3%. We used the same stamper to duplicate these disks. We consider this degradation is caused due to the interlayer cross talk. The average thickness of spacer layers of the 16-layer disk was set to approximately 13 μm . The interlayer cross talk from adjacent layers is not perfectly negligible with this thickness.

4. CONCLUSION

We evaluated the 16-layer 400 GB ROM disk using the modified tester for the conventional BD. As a result, we obtained jitter values of 9 - 10% from all layers. We think this result shows that the 16-layer 400 GB ROM disk is promising and feasible. We expect to obtain lower jitter values by optimizing the disk structure and adopting a compensator of a residual spherical aberration. We believe the possibility to realize over 500 GB capacity by using the multi-layer technology.

REFERENCES

- [1] ISOM Optical Memory Roadmap Report 2006
- [2] N. Shida, T. Higuchi, Y. Hosoda, H. Miyoshi, A. Nakano and K. Tsuchiya, Jpn. J. Appl. Phys., 43, pp.4983-4986, (2004)
- [3] I. Ichimura, K. Saito, T. Yamasaki and Kiyoshi Osato, Applied Optics, 45-8, pp.1794-1803, (2006)

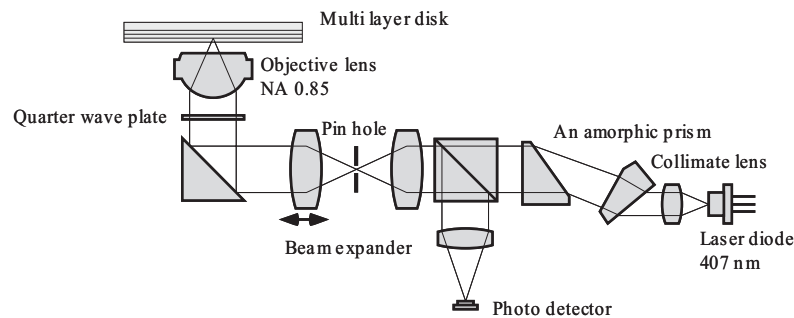


Fig. 1. Schematic diagram of the optical pick-up head with the wide range spherical aberration compensator.

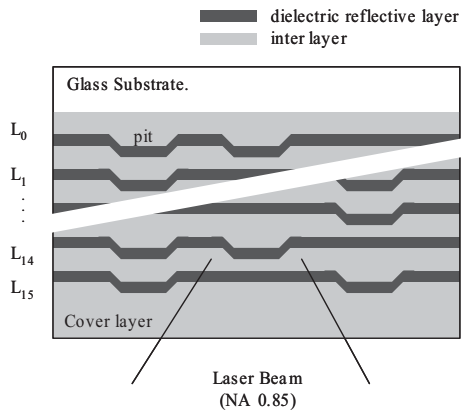


Fig. 2. 16-layer ROM disk structure.

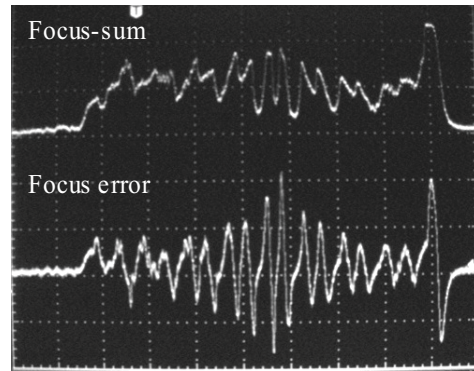


Fig. 3. Focus-sum and focus error signals.

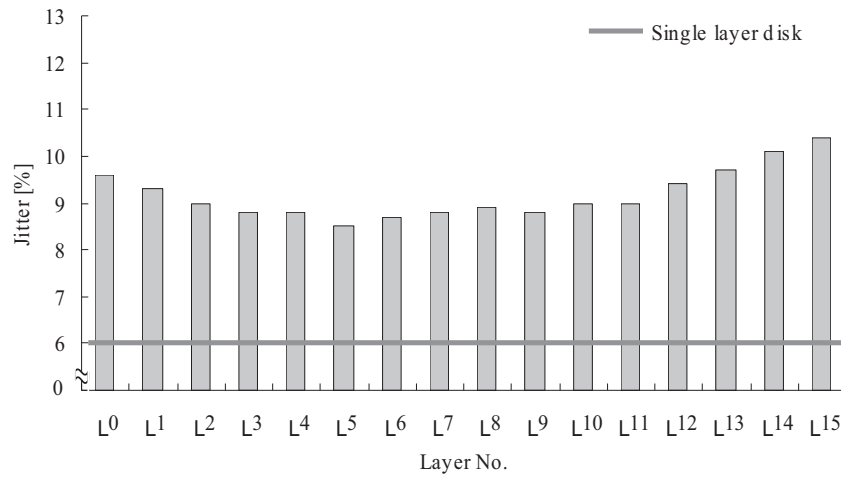


Fig. 4. Measured jitter values of each layer.

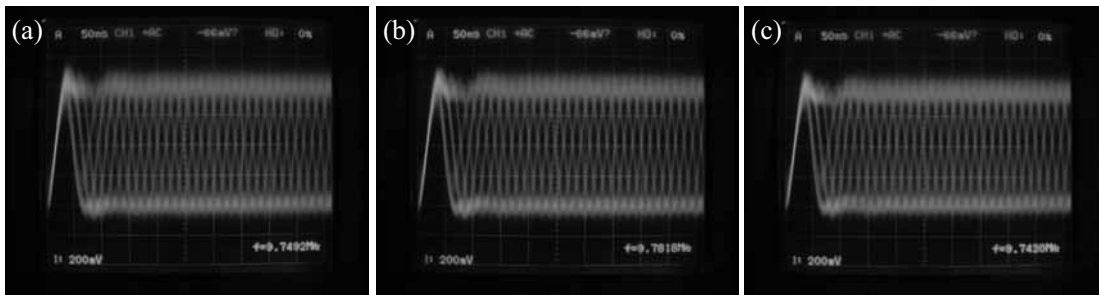


Fig. 5. Eye-pattern images of a 16-layer disk (after the limit equalizer). (a) Layer 0, (b) Layer 8, (c) Layer 15.

Micro-holographic storage and threshold holographic recording materials

Brian Lawrence^{*}, Victor Ostroverkhov, Xiaolei Shi, Kathryn Longley, and Eugene P. Boden
General Electric Global Research, 1 Research Circle, Niskayuna, NY 12309

1. INTRODUCTION

Micro-holographic approaches to optical data storage have been investigated by several groups over the last decade [1-4]. Relative to more traditional page-based holographic techniques, micro-holographic storage offers advantages in system tolerances and sensitivity to environmental conditions while maintaining the ability to achieve high capacities. In this approach, data is stored in virtual layers spread throughout the volume of the media that are written and read-out with beams focused to diffraction limited waists. Consequently, individual layers see multiple exposures during the recording process and as a result standard holographic materials in which the refractive index changes linearly with incident fluence may not be suitable for achieving optimum performance. Recent micro-holographic recording experiments using linear dye-doped thermoplastic materials demonstrated the performance limitations.[4] These results showed that the recorded micro-holograms had lateral dimensions that were larger than the recording beam and had depths that exceeded theoretical predictions. In addition, the results showed that the repeated exposures of adjacent layers during the recording process reduced the diffraction efficiency of each layer by a factor of N^2 , where N was the number of layers. The combination of increased hologram size and reduced efficiency due to repeated exposures severely restricts the achievable capacity of micro-holographic storage in linear materials.

To overcome these limitations, new holographic materials are needed. Recent efforts to develop new materials with nonlinear refractive index changes have used two-photon absorption processes or the oxygen-inhibition effects observed in photopolymers.[5,6] However, these material approaches require high-power lasers or do not provide adequate functionality to be used in practical micro-holographic systems. This paper presents results of micro-holographic recording experiments in new materials with threshold optical functionality. In addition, these results are compared to similar measurements performed on linear materials to demonstrate the potential advantages.

2. EXPERIMENTAL SETUP AND RESULTS

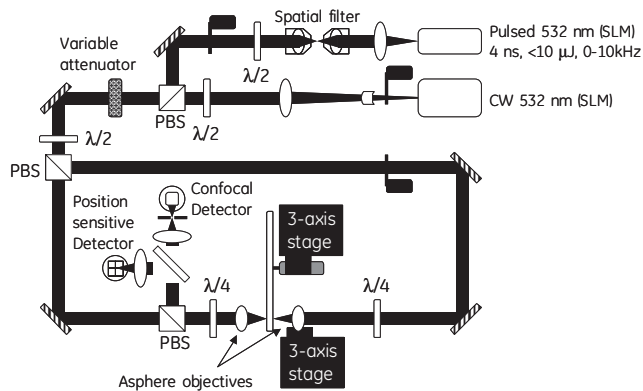


Figure 1: Experimental setup

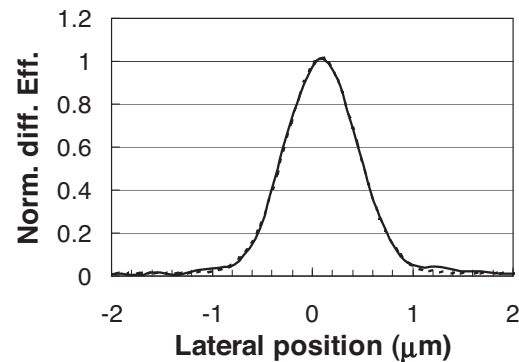


Figure 2: Lateral dimensions of linear micro-hologram

The experimental setup used for static recording of micro-holograms is shown in Figure 1. The system uses both CW and Q-switched 532 nm lasers for flexibility during recording and read-out. Exposure is controlled via fast mechanical shutters. A variable attenuator is used to reduce the power level during read-out to minimize hologram erasure. The two counter-propagating beams are focused into the recording material by identical aspheric lenses with a NA of 0.4. The NA of the focused beams can be reduced by altering the size of the beam entering the lens. The sample and the signal lens are mounted on 3-axis positioning systems with 25 nm accuracy. A position-sensitive detector on the reference side of the

^{*} lawrencb@research.ge.com; phone: (518) 387-4577; fax: (518) 387-5592

sample is used to align the signal lens for optimized recording. During read-out, the reference beam is reflected by the micro-holograms and is incident on a calibrated photodiode in a confocal geometry to provide an absolute measure of the diffraction efficiency.

The samples used in the experiments were 1.2 mm thick injection molded discs. The linear dye-doped materials were the same materials used previously in micro-holographic recording experiments.[4] The threshold materials were also based on modified thermoplastics, engineered to provide the threshold functionality. Micro-holograms were recorded with the cw laser in the linear materials at a NA of 0.21 and the lateral and depth dimensions were measured. The lateral dimension, shown in Figure 2, was measured to be $0.8 \mu\text{m}$ ($\text{HW}1/e^2\text{M}$) and the depth was measured to be $12.9 \mu\text{m}$ (FWHM), after index correction. In addition, arrays of micro-holograms were recorded at spacings of 2.5, 2.0, and $1.5 \mu\text{m}$. Arrays of holograms at the three different spacings are shown in Figures 2(a), 2(b), and 2(c).

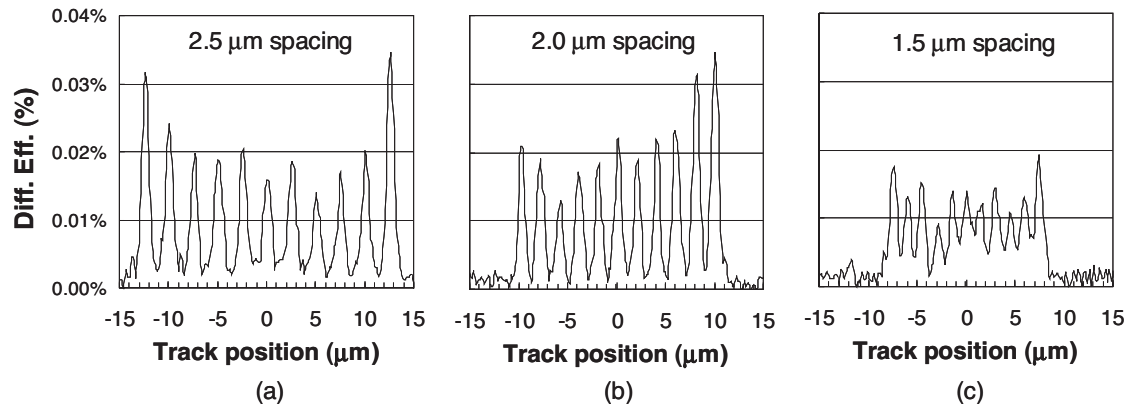


Figure 3: Arrays of 3 adjacent micro-holograms at spacings of: (a) $2.5 \mu\text{m}$, (b) $2.0 \mu\text{m}$, and (c) $1.5 \mu\text{m}$

The measurement system described in this paper uses an optimized confocal detection system resulting in lateral dimensions that are comparable to the calculated recording beam waist of $0.81 \mu\text{m}$, and depth dimensions that are approximately equivalent to twice the calculated Rayleigh range of $12.1 \mu\text{m}$. In addition, the results in Figure 3 show that the adjacent micro-holograms are clearly identifiable at spacings of $2.5 \mu\text{m}$ and $2 \mu\text{m}$. At a spacing of $1.5 \mu\text{m}$, the holograms show significant overlap, which may generate errors during the readout process, limiting the minimum achievable spacing and therefore limiting the capacity.

Micro-holograms were also recorded in both the linear and threshold materials using the pulsed laser setup. To simplify the pulsed recording process, the NA of the recording beams was reduced to 0.2. Holograms were recorded in both materials with pulse energies up to $1.2 \mu\text{J}$. The diffraction efficiency was then read-out with the cw laser at a power of less than $1 \mu\text{W}$ and an NA of 0.16. Figure 4 shows the measured diffraction efficiency as a function of recording pulse energy for both the linear and threshold materials. In addition to diffraction efficiency, the erasure of the micro-holograms during read-out was also evaluated. For the erasure measurement, the micro-holograms were read-out continuously while the reflected signal was monitored. The erasure results for both the linear and threshold materials are shown in Figure 5.

The results shown in Figure 4 clearly indicate that the linear materials show a linear dependence of the diffraction efficiency on recording pulse energy. In extrapolated back to a recording energy of 0 and it corresponds to a diffraction efficiency of 0, which is again indicative of a linear material. The diffraction efficiency measured at the highest recording energy deviates from the line, which may be a result of saturation of the index change. On the other hand, the threshold materials clearly show a nonlinear behavior with reduced diffraction efficiency for recording pulse energies of less than $0.5 \mu\text{J}$. The nonzero diffraction efficiency at low powers is due to the fact that these preliminary threshold materials do not have a perfect threshold and some linear degradation persists. The threshold recording energy in this system appears to be approximately $0.5 \mu\text{J}$, which is far higher than the 5-10 nJ/pulse that can be achieved with standard laser diodes. However, these measurements were conducted at a NA of 0.2, and if the NA is scaled to a more practical 0.7, the focal spot size shrinks by a factor of $(0.7/0.2)^2 = 12$, resulting in a 12-fold reduction in recording energy, reducing the threshold to 50 nJ. A pulse energy of 50 nJ is still greater than the pulse energy produced by a standard laser diode and additional work is proceeding on reducing the threshold energy. The erasure measurement shown in Figure 5 also shows marked differences between linear and threshold materials. The threshold materials show a hologram lifetime improvement of over a factor of 100 over the linear materials. These threshold materials still show long-term decay in the signal that may be attributed to the same slow linear mechanism in the material that causes the imperfect threshold observed in figure 3.

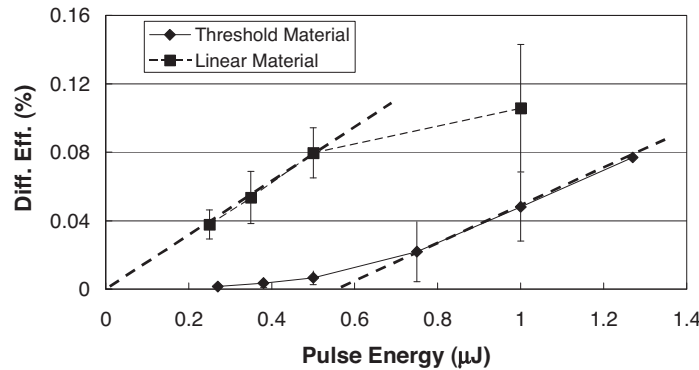


Figure 4: Diffraction efficiency as a function of recording pulse energy for linear and threshold materials

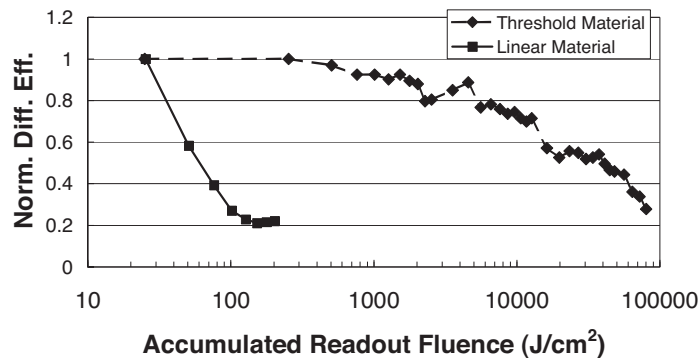


Figure 5: Micro-hologram lifetime/stability measurements for linear and threshold materials.

3. CONCLUSION

This paper discusses the limits of linear holographic materials in micro-holographic storage and presents preliminary results of micro-hologram recording in a new class of materials with threshold optical functionality. The results of hologram erasure studies show a 100-fold improvement in lifetime using threshold materials, demonstrating the benefit of these materials. However, the preliminary threshold materials demonstrated in this paper show a slow linear decay mechanism that results in an imperfect threshold and long-term decay during read-out. In addition, the micro-holograms were recorded with over 0.5 μJ of energy per pulse in a 0.2 NA system, corresponding to over 50 nJ/pulse in a system with a more practical NA of 0.7. Next-generation material development is underway to eliminate any linear index change mechanisms and reduce the recording energies to enable truly practical micro-holographic systems.

REFERENCES

- [1] Eichler, H. J., Kuemmel, P., Orlic, S., and Wappelt, A., "High-Density Disk Storage by Multiplexed Microholograms", *IEEE J. Sel. Top. Quantum Electron.*, 4(5), 840-848, (1998)
- [2] McLeod, R., Daiber, A., McDonald, M., Robertson, T., Slagle, T., Sochava, S., and Hesselink, L., "Microholographic multilayer optical disk data storage," *Appl. Opt.*, 44, 3197-3207 (2005)
- [3] Saito, K., Horigome, T., Miyamoto, H., Yamatsu, H., Tanabe, N., Hayashi, K., Fujita, G., Kobayashi, S., Kudo, T., Uchiyama, H., "Drive system and readout characteristic of Micro-Reflector optical disc", MB1, ODS 2007
- [4] Wu, P., Shi, X., Lawrence, B., Ren, Z., Smolenski, J., Erben, C., Boden, E., and Longley, K., "Micro-holograms Recorded in a New Thermoplastic Medium for Holographic Data Storage," WC2, ODS 2006.
- [5] Akiba, M., Takizawa, H., and Inagaki Y., "Highly Sensitive Two-photon Absorption Recording Materials for Volumetric Optical Data Storage Media," Mo-B-01, ISOM 2008
- [6] McLeod, R., "Localized Recording Approaches and Phase Metrology for Holographic Storage," MB2, ODS 2007

Direct Servo Error Signal Detection Method from Recorded Micro-Reflectors

Hiroataka Miyamoto^a, Hisayuki Yamatsu^a, Kimihiro Saito^a, Norihiro Tanabe^a, Toshihiro Horigome^a,
Goro Fujita^a, Seiji Kobayashi^a, and Hiroshi Uchiyama^b

^a*Optical Storage Laboratory, Materials Laboratories, Sony Corporation
4-14-1 Asahi-cho, Atsugi, Kanagawa, 243-0014, Japan*

^b*Optical Disc Media Product Development Departmen., Disc & Memory Device Division,
Chemical Device Business Group, Sony Corporation*

TEL: +81-46-202-8883, FAX: +81-46-202-6735, Hiroataka.Miyamoto@jp.sony.com

Abstract: A novel tracking servo error signal detection method for a micro-reflector optical disc drive is proposed. Tracking servo error signals are directly obtained from recorded marks in the newly developed method. We studied push-pull signal behavior by simulation and implemented a tracking servo system based on the new idea to our readout drive. The tracking servo system was confirmed to be very effective to improve recording medium interchangeability.

OCIS codes: (210.4770) Optical recording

1. Introduction

Micro-reflector optical disc, or micro-holographic optical disc, is based on well-established bit-wise recording in a monolithic recording medium [1]. These features make it one of the most practical candidates for the post Blu-ray optical memory. Many technologies from the conventional optical disc field can be applied to a micro-reflector optical disc drive because of the similarity between the two architectures. On the other hand, of course, some novel technologies must be developed to handle the issues which are characteristic to the new principle. Three dimensional addressing of recorded marks, or focusing and tracking servo techniques for volumetric recording in other words, is among them.

We have been working on the original servo system using recording media with a reference layer in the past couple of years [2]. The focusing and tracking positions of the two opposed objective lenses were precisely controlled by the five-axis servo system using servo error signals obtained from the reference layer. We succeeded in recording as many as ten layers in the monolithic recording medium with excellent RF signals [3]. However, it still had room to be improved concerning recording medium interchangeability. This was because the servo error signals were not directly obtained from the recorded marks and the servo system was not robust enough against recording medium tilt or decentering.

In this paper, we propose a novel tracking servo error signal detection method from recorded marks. A simulation result is shown to verify the basis of the new method. We implemented a tracking servo system based on the new idea to our micro-reflector optical disc readout drive. The servo system was confirmed to be very effective to improve RF signal quality and a powerful tool to realize recording medium interchangeability.

2. Servo Error Signal Simulation

First, we wanted to confirm if the new tracking servo error signal detection method really works or not. Therefore, a calculation was conducted to simulate tracking servo error signals before getting into experiments.

We assumed the micro-reflector optical disc readout drive described in the next section. The detailed calculation is shown in reference [4]. The light field distributions diffracted by three continuous tracks of holographic index modulation with 1.1 μm -pitch were simulated and a push-pull signal based on them was calculated as shown in figure 1. The result showed that the reflected light field distributions and the push-pull signal are quite similar to those in the conventional optical disc drives, indicating the push-pull signal can be used as a tracking servo error signal.

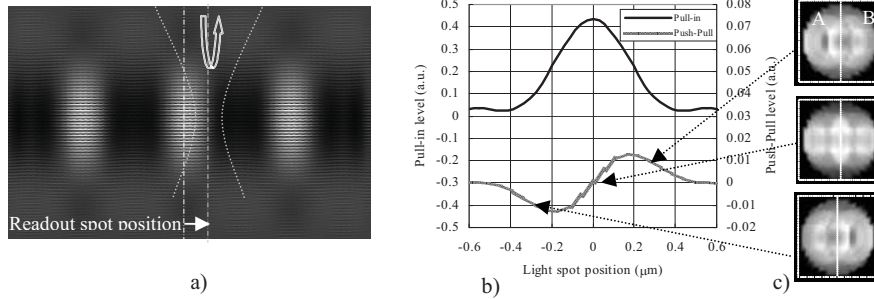


Fig. 1. a): Schematic of the calculation model. $\lambda=405\text{nm}$, $\text{NA}=0.51$. b): Calculated pull-in and push-pull signals. c): Reflected light field distributions on the pupil.

3. Experimental Results and Discussion

Figure 2 shows a schematic of our micro-reflector optical disc readout drive. The objective lens numerical aperture (NA) is 0.51. The primary laser diode (LD), whose wavelength is 405nm, is for RF signal readout and tracking servo. The secondary LD, whose wavelength is 660nm, is for focusing servo. The recording medium is composed of photopolymer and has a reference layer for the conventional focusing servo as shown in figure 3. The reference layer is transparent to a 405nm laser beam, while it is reflective to a 660nm laser beam. The reference layer has guide grooves for the conventional tracking servo. This is to compare the new tracking servo with the conventional one using the 660nm LD.

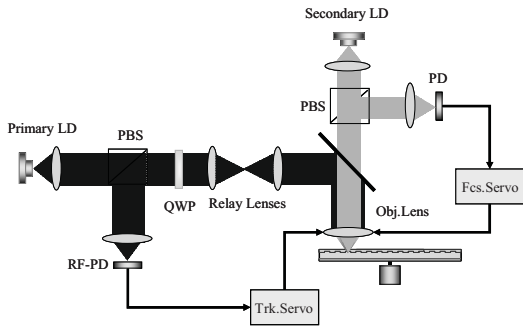


Fig. 2. Schematic of the micro-reflector optical disc readout system.

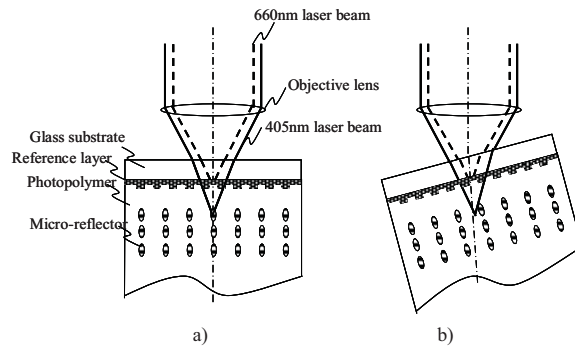


Fig. 3. Schematic of the recording medium with a reference layer. a) With no perturbation. b) With a tilt.

The recording medium has the micro-reflectors recorded beforehand by the two lens recording system about which we explained in the past ISOM and ODS [2, 3, 5]. The laser wavelength for recording is 405nm same as the one for readout. In the readout process, a push-pull tracking servo error signal is generated from the reflected 405nm laser beam by recorded marks. On the other hand, a focusing servo error signal is obtained from the reflected 660nm laser beam by the reference layer. The readout spot position, normally several tens to hundreds of microns below the reference layer, can be controlled by varying the focusing position of the 405nm laser beam by the relay lenses.

Figure 4 shows the observed tracking servo error signals. The upper signal was obtained from the guide grooves on the reference layer by the conventional tracking servo system. The lower signal was obtained directly from the marks recorded at $30\mu\text{m}$ below the reference layer by the new tracking servo system. There was no significant difference between the two signals from the view point of signal to noise ratio (SNR). As the simulation had predicted, a good enough quality tracking servo error signal was generated directly from the recorded marks.

Figure 5-a) shows the RF signal obtained with the conventional tracking servo system, while the one in figure 5-b) was obtained with the new tracking servo system. In each case, the recording medium had the

same order of, but a different amount of tilt or decentering compared with the ones in the recording process to confirm recording medium interchangeability. Apparently, the RF signal in figure 5-b) had better SNR.

Figure 6 shows the RF signals observed in a much longer period than in figure 5 cases. The upper one was obtained with the conventional tracking servo system, while the lower one was obtained with the new tracking servo system. The new tracking servo system dramatically improved the amplitude fluctuation.

From the experimental results, we confirmed that the new tracking servo system improved RF signal quality, therefore recording medium interchangeability. This can be explained as follows. In the conventional tracking servo system case, three dimensional addressing of the recorded marks was achieved through the information from the reference layer. The relative positions of the optical spot, the reference layer, and the recorded marks were expected to be fixed throughout recording and readout. The servo system was vulnerable to recording medium tilt or decentering occurred after recording, each of which changed the relative positions (see figure 3-b). On the other hand, direct addressing of the recorded marks was achieved by the new tracking servo system and the robustness against perturbations was improved a lot.

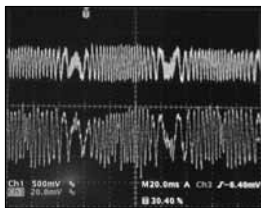


Fig. 4. Tracking servo error signals.

Upper: From the guide grooves on the reference layer.
Lower: From the recorded micro-reflectors.

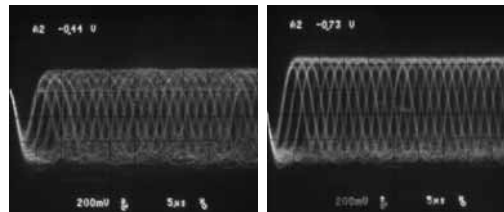


Fig. 5. RF signals.

a) With the conventional tracking servo system.
b) With the new tracking servo system.
The recording and readout conditions are as follows.
Modulation code: 1-7 pp, Chanel clock: 552kHz,
Linear velocity: 0.154m/s, Track pitch: 1.1 μ m.

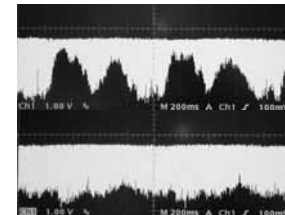


Fig. 6. RF signals in a longer period

Upper: With the conventional tracking servo system.
Lower: With the new tracking servo system.

4. Conclusion

A direct tracking servo error signal detection method from recorded micro-reflectors was proposed. A simulation was conducted to verify the validity of the new method at first. Then, a tracking servo system based on the new idea was implemented to the micro-reflector optical disc readout drive. We confirmed that the drive with the new tracking servo system had better RF signal quality compared with the one with the conventional tracking servo system when the recording medium had a tilt or a decentering after recording. This means that the new tracking servo system improves recording medium interchangeability.

Currently, we are preparing a focusing servo system based on a similar servo error signal detection method discussed in this paper. The effect of the new focusing servo system will be reported in the conference.

4. Acknowledgement

We would like to thank Nippon Paint Co., Ltd. very much for providing their excellent photopolymer to us.

References

- [1]H.J. Eichler et al., Proc. of SPIE, Vol. 3109, pp. 239244 (1997).
- [2]T. Horigome et al., Tech. Digest of ISOM 2006, Mo-D-02 (2006)
- [3]T. Horigome et. al. Submitted to Jpn. J. Appl. Phys.
- [4]K. Saito et al., Proc. of SPIE, Vol. 6282, 628213-1 (2006)
- [5]K. Saito et al., Proc. of SPIE, Vol. 6620, 66200B-1 (2007)

Microholographic data storage towards dynamic disk recording

Susanna Orlic, Enrico Dietz, Sven Frohmann, Jonas Gortner, Alan Guenther, Jens Rass

Optical Technologies Lab, Technical University Berlin, Strasse des 17. Juni 135, 10623 Berlin, Germany

orlic@opttech.tu-berlin.de, www.opttech.tu-berlin.de

Abstract: Dynamic recording of microholographic reflection gratings is reported. Preliminary results have been achieved in linearly translating samples with a moderate velocity. Microholographic lines with varying lengths have been written in two different regimes: in the quasi-dynamic or stop-and-go regime and in the full dynamic regime. The shortest quasi-dynamic mark length is about 200 nm. The length of dynamically written microholographic lines varies down to 300 nm while the length variation of 70 nm can be detected. The current development status and operation of our microholographic drive system is presented.

2007 Optical Society of America

OCIS codes: 210.2860 Holographic and volume memories, 090.7330 Volume holographic gratings, 090.2900 Holographic recording materials, 210.4590 Optical disks

1. Microholographic storage between promise and challenge

In the last couple of years the microholographic recording/readout method came out in as a powerful and promising method to overcome the data density limit of the conventional optical disk technology [1,2,3]. Multilayer recording scheme is a viable technological solution for high density, high capacity data storage on a rapidly rotating disk media. Development and technological implementation paths are largely similar to those undertaken in DVD and BluRay technology.

Previously we have been successful in demonstrating the performance of microholographic recording in terms of data density as well as performing depth multiplexing with high number of layers. Continuous and extensive improvements of the microlocalized recording setup made it possible to record and read out microholograms as small as 300 nm resulting in data marks of about 150 nm. Depth multiplexing has also been demonstrated at the optical resolution limit with 75 layers spaced by 4 microns through a 300 micron thick Aprilis photopolymer. Nevertheless, the microholographic storage approach still meets several heavy challenges that set a series of tough requirement on the optoelectronic write/read system and photopolymer medium, as well.

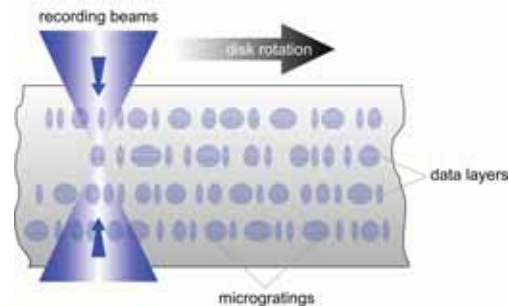


Figure 1. Microholographic multilayer storage scheme: Microholographic gratings are written dynamically with pulse width modulated length in the rotation direction.

One primary challenge concerns the areal data density to be realized in a single microholographic layer as this parameter represents a basis for the envisioned superior system performance. Furthermore, microholographic storage holds the promise of a large number of data layers distributed through the depth of a photopolymer. Probably the most serious challenge for microholographic data storage concerns dynamic recording as required in a dynamic disk and drive technological implementation scheme. Volume holograms have to be recorded with diffraction limited laser beam in a moving rapidly rotating holographic disk while all requirements on the areal and total data density remains the same. The response of the photopolymer recording medium is still a crucial issue in achieving readout signals similar to eye-pattern known from DVD and BD technology. Unfortunately photopolymers are "living" media when exposed to light and current materials are still far from being perfectly homogenous. As a consequence the response of the material shows significant local changes resulting in diffraction efficiency strongly

varying among a plenty of microgratings. The lack of perfect photosensitive media has to be compensated by advanced solution in the realization of the optoelectronic drive system and by sophisticated recording algorithms, as well.

In this paper we report different activities on dynamic recording of resolution limited microholograms in linearly moving photopolymer samples and in a rotating disk, as well. Dynamic drive setup is presented and further development paths are discussed.

2. High density dynamic recording of microholographic data marks.

Statically written microholographic gratings with a diameter of less than 300nm have been created and detected demonstrating the potential of the technology in terms of data density. Our goal yet was transition to dynamically created gratings of this size. Dynamic recording of so-called microholographic lines, i.e. dynamically induced microgratings of variable length is a premise for applying an EFM+ like coding scheme. Such a coding scheme allows an increase of the data density and performance, as well. Data density of a coding scheme that maps one bit with one point-like holographic grating is limited by the size of these gratings. This limit is overcome by the EFM+ coding where the data density is also determined by the accuracy with which the extension and variation of the physical data structures can be measured.

There are several issues that could inhibit the creation of dynamically written microholographic lines. High mechanical stability is necessary in order to create these gratings. Even small vibrations in the direction of the write beam axis will reduce the diffraction efficiency dramatically. The stability of the complete write/read system and active control of its individual components is decisive in creating a resolution limited structure with clearly localized microholographic lines. Another interesting question is whether the microholographic lines can be written in the same distance and with the same spatial resolution as statically generated microgratings. Also the signal noise ratio of statically and dynamically created microgratings is crucial to evaluate the performance of the system. Therefore different bit-pattern recording regimes have been tested starting by quasi-static generation of microholographic lines to transfer to a real dynamic recording regime. In this case microholograms are written in a continuously translating sample while their individual length is controlled by the modulated pulse width, i.e. exposure time.

Improvements and advanced solutions implemented in our microlocalized write/read setup have allowed for recording and error-free detection of microholographic structure as small as the wavelength in both the quasi-dynamic and dynamic regime. The effective size of a single microholographic data mark is even smaller than the wavelength; the same applies to the spacing between neighboring microgratings or lines along a track.

3. Results

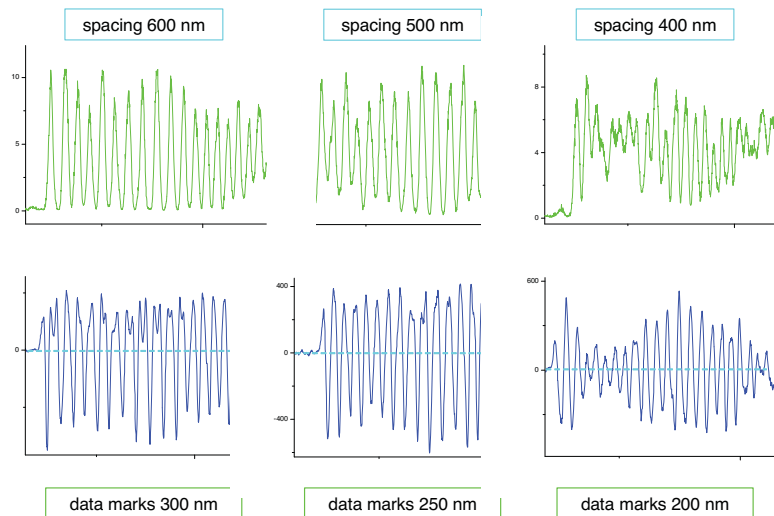


Figure 2. Quasi-dynamic recording of bit pattern with peak-to-peak spacing between successive microgratings of 600 nm, 500 nm, and 400 nm, respectively in a Aprilis D type sample. Readout is performed dynamically while detected signal variations indicate 200 nm as a minimum length of written data mark.

Quasi-dynamic recording has been realized in different samples of Aprilis photopolymer D type (sensitive @ 532 nm) and E type (sensitive @ 407 nm) resulting in tracks filled with microholographic lines that are in their

dimensions even smaller than the wavelength of light. In figure 2 the microholographic lines of same length have been recorded in different peak-to-peak distances going down from 600 nm to 400 nm only. The minimum achieved resulting data mark length is 200 nm.

Dynamic recording of length coded microgratings has also been realized at the optical resolution limit: Microholographic lines with variable lengths are recorded in tracks spaced by 500 nm. The shortest micrograting lines representing 3T are between 300 and 350 nm while the optical in track resolution is less than 100 nm.

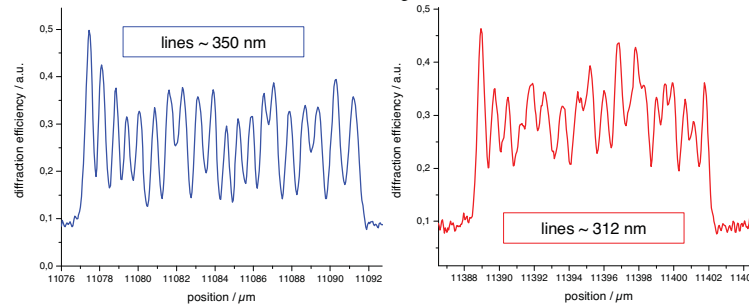


Figure 3. Length of dynamically written microholographic lines has been reduced stepwise down to 312 nm. Recording and readout are performed at 532 nm in a 300 μm thick Aprilis D type sample. The achieved results correspond to the optical resolution limit at this wavelength.

4. Drive system development

A first disk & drive system has been developed for the dynamic operation regime. Recording and readout algorithms have been appropriately adapted. Further improvements concern the overall control and the stability of the optoelectronic and mechanical subsystems. The operational scheme of our microholographic drive system is depicted in Figure 4.

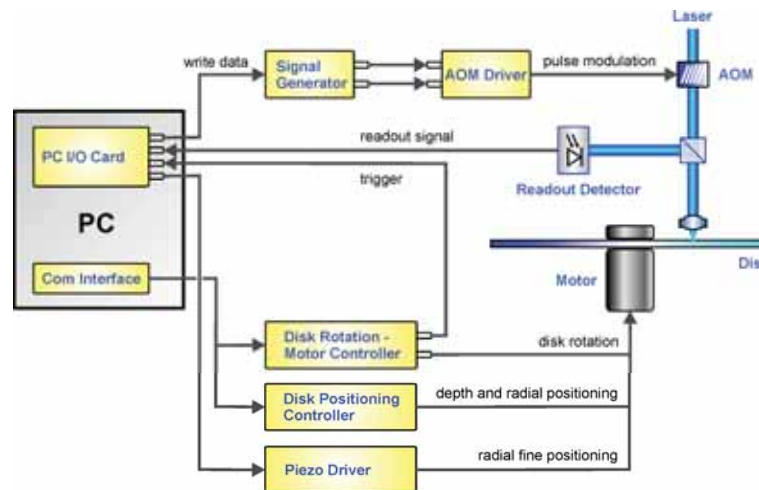


Figure 4. Basic design of the microholographic drive system: A microcontroller system controls the positioning system of the disk and the motor controller and synchronizes the signal generator and the detection system with the motor position and the data acquisition system.

5. Acknowledgement

The work has been supported by the European Commission within the MICROHOLAS project. Holographic polymer samples and disks have been provided by Dr. Dave Waldman, DCE Aprilis.

6. References

- [1] S. Orlic, S. Ulm, H. J. Eichler, "3D bit-oriented optical storage in photopolymers", J. of Optics A: Pure and Applied Optics, vol. 3, 2001.
- [2] R. McLeod et al, "Microholographic multilayer optical disk data storage", Appl. Opt. Vol. 44, 2005.
- [3] K. Saito et al, "Drive system and readout characteristics of Micro-reflector optical disk", Optical Data Storage, Technical Digest, May 2007.
- [4] S. Orlic, E. Dietz, S. Frohmann, J. Gortner, Ch. Müller, "Microholographic multilayer recording at DVD density", Optical Data Storage, Technical Digest, May 2007.

Three-Dimensional Recording with Electrical Beam Control

Ryuichi Katayama, Shin Tominaga, Yuichi Komatsu and Mizuho Tomiyama
 System Jisso Research Laboratories, NEC Corporation
 1753, Shimonumabe, Nakahara-ku, Kawasaki 211-8666, Japan
 Phone: +81-44-431-7581, Fax: +81-44-431-7592, E-mail: r-katayama@bl.jp.nec.com

1. Introduction

Currently, as professional online, nearline and archival storage systems, magnetic storage systems are generally used. However, reliability and power consumption of mechanics in the systems are serious issues. To solve these issues, we propose a concept of a novel optical storage system which has high-reliability and low-power-consumption characteristic, as well as large-capacity characteristic comparable to that of magnetic storage systems. The former is achieved by controlling a light beam focused in a recording medium electrically instead of mechanically, while the latter is achieved by three-dimensional recording. This paper describes an optical configuration and experiments for demonstrating this “green storage” concept.

2. Optical Configuration

Figure 1 shows the optical configuration. It is based on a configuration used in microholographic recording[1]-[4]. A light beam emitted by a laser is split into Beams 1 and 2. A shutter is open during recording and closed during readout. Recording operation is done by focusing two beams facing each other at the same position in the medium, and forming a diffraction grating around the focal position. Readout operation is done by focusing Beam 1 in the medium, and detecting a light beam reflected by the diffraction grating by a photodetector. The medium is card-shaped. A position of focused spots in the medium is varied by electrical beam control elements placed in the optics in both in-plane and vertical directions, without moving the objective lenses or the medium mechanically. For the demonstration of the concept, liquid crystal deflectors and liquid crystal variable focus lenses are used as the electrical beam control elements.

3. Structure of Liquid Crystal Elements

Figures 2 and 3 show structures of the liquid crystal deflector for in-plane beam control and the liquid crystal variable focus lens for vertical beam control, respectively. Each of them has a liquid crystal layer between two substrates with transparent electrodes. One of the electrodes is divided into many regions and adjacent regions are connected by resistors. The liquid crystal deflector has a linear electrode pattern. When voltages $V1(=V0+\Delta V)$ and $V2(=V0-\Delta V)$ are applied to the uppermost and the lowermost electrodes, respectively, a linear voltage distribution is generated over the surface. On the other hand, the liquid crystal variable focus lens has a circular electrode pattern. When voltages $V1$ and $V2$ are applied to the outermost and the innermost electrodes, respectively, a quadratic voltage distribution is generated over the surface.

Figures 4 and 5 show operations of the liquid crystal deflector and the liquid crystal variable focus lens, respectively. The arrows indicate directions of liquid crystal molecules and a polarization direction of an incident light. In Fig. 4, if $\Delta V < 0$ or $\Delta V > 0$, the liquid crystal molecules are tilted toward in-plane or vertical directions around the top and toward vertical or in-plane directions around the bottom, so that the light is deflected upward or downward, respectively. To deflect the light in orthogonal two (X and Y) directions, two deflectors with orthogonal electrode patterns are combined. On the other hand, in Fig. 5, if $\Delta V < 0$ or $\Delta V > 0$, the liquid crystal molecules are tilted toward in-plane or vertical directions around the periphery and toward vertical or in-plane directions around the center, so that the light is diverged or converged, respectively.

4. Experimental Results

First, operation characteristics of the liquid crystal deflector and the liquid crystal variable focus lens were measured. Results at a wavelength of 532nm are shown in Figs. 6 and 7. A deflection angle and a reciprocal of a focal length were proportional to the driving voltage ΔV within a range of $\pm 0.5V$, with proportionality constants of 0.58mrad/V and 1.1/m/V, respectively.

Next, an optics shown in Fig. 1 was constructed, and recording and readout experiments were carried out.

A wavelength of the laser was 532nm, a numerical aperture of the objective lenses was 0.55, and photopolymer was used as a material of the medium. The position of focused spots in the medium was varied by the liquid crystal elements, and 2 bits in in-plane direction and 3 bits in vertical direction were recorded and read out with intervals of 2 μ m and 12.5 μ m, respectively. Readout signals are shown in Figs. 8 and 9. It was observed that signals from corresponding diffraction gratings were well separated in each direction.

5. Conclusions

A concept of a novel optical storage system combining three-dimensional recording with electrical beam control, which features high reliability and low power consumption as well as large capacity, has been proposed. It has been experimentally demonstrated by using liquid crystal elements for beam control. Future work includes a development of faster and more widely variable electrical beam control elements.

References

- [1] H. J. Eichler et al.: IEEE J. Sel. Top. Quantum Electron., Vol. 4, No. 5, pp. 840-848 (1998).
- [2] R. R. McLeod et al.: Appl. Opt., Vol. 44, No. 16, pp. 3197-3207 (2005).
- [3] M. Dubois et al.: Jpn. J. Appl. Phys., Vol. 45, No. 2B, pp. 1239-1245 (2006).
- [4] T. Horigome et al.: Int. Symp. Optical Memory 2007 Tech. Dig., pp. 34-35 (2007).

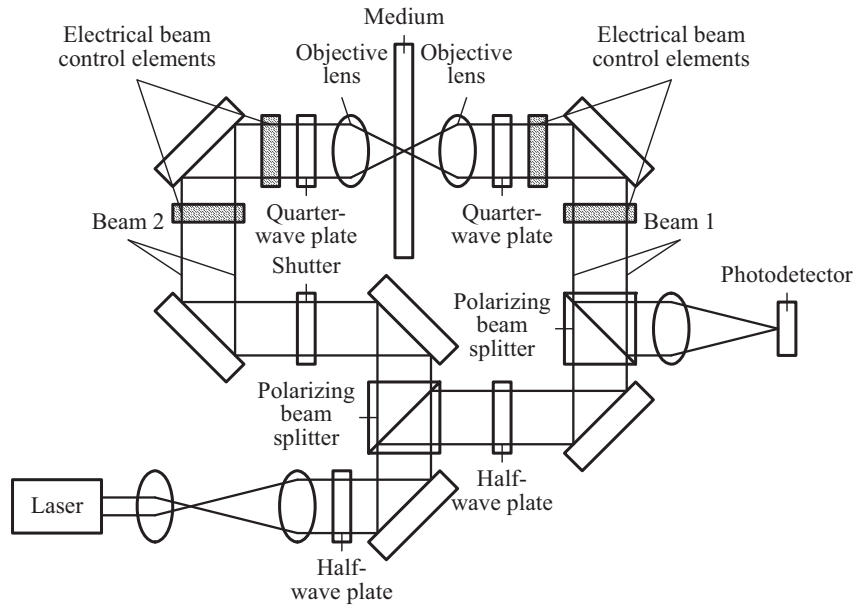


Fig. 1 Optical configuration.

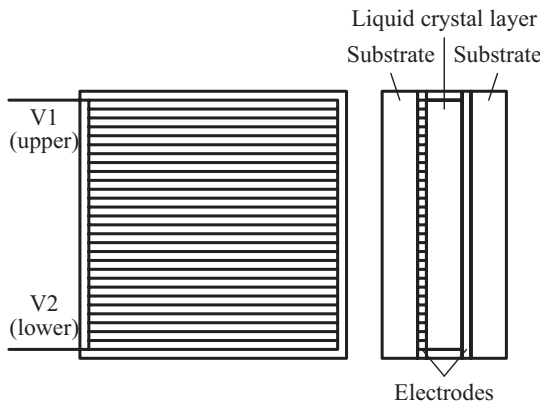


Fig. 2 Structure of liquid crystal deflector.

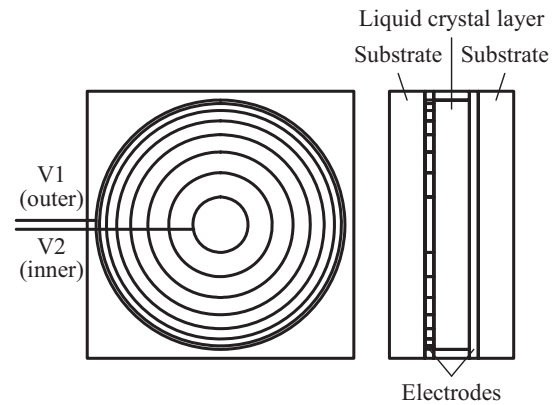


Fig. 3 Structure of liquid crystal variable focus lens.

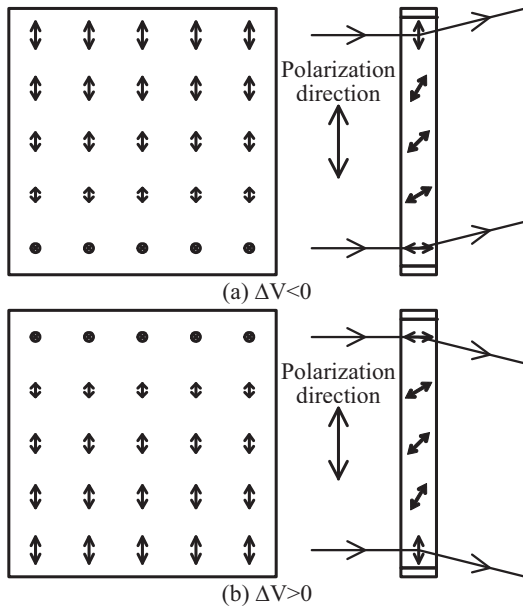


Fig. 4 Operation of liquid crystal deflector.

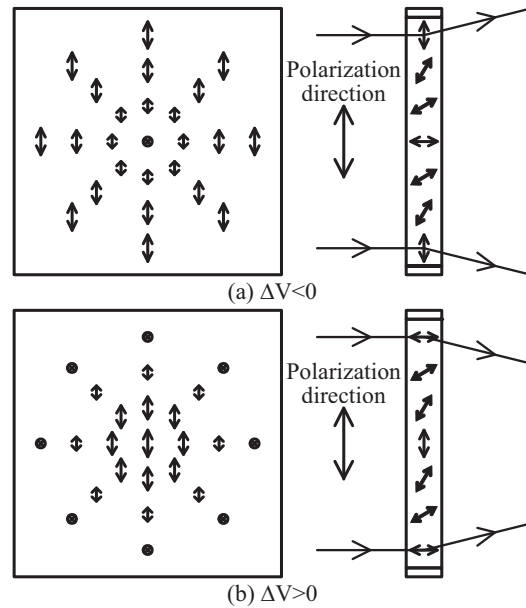


Fig. 5 Operation of liquid crystal variable focus lens.

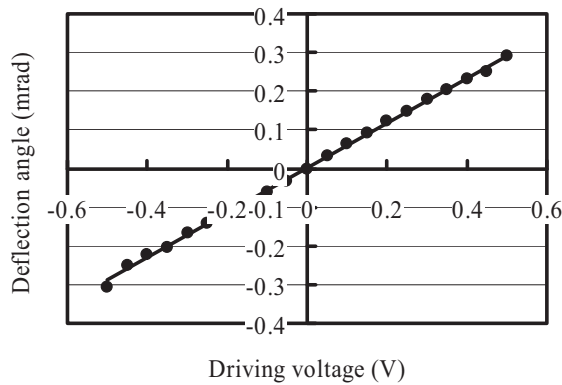


Fig. 6 Operation characteristics of liquid crystal deflector.

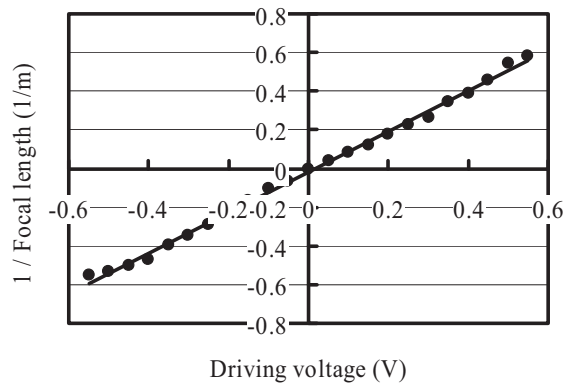


Fig. 7 Operation characteristics of liquid crystal variable focus lens.

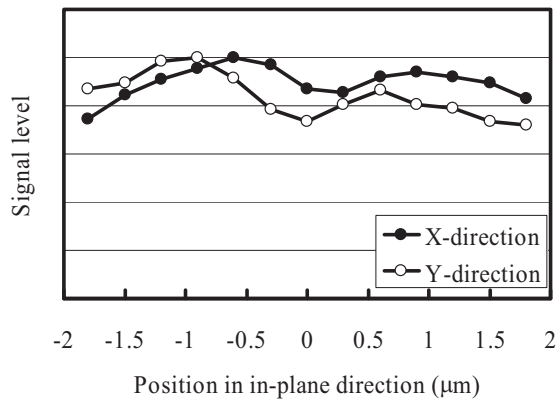


Fig. 8 Readout signals in in-plane direction.

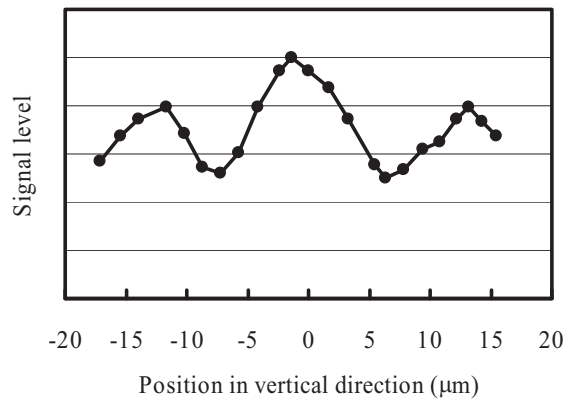


Fig. 9 Readout signals in vertical direction.

SESSION MP: Poster Session I

Queen's Ballroom
2:00 to 3:30 pm

Luping Shi, National Univ. of Singapore/Data Storage Institute (Singapore)
Takashi Kikukawa, TDK Corp. (Japan)
Yun-Sup Shin, LG Electronics Inc. (South Korea)

Properties of New Fluorinated Holographic Recording Material for Collinear Holography

K. Satoh^a, K. Aoki^a, M. Hanazawa^a, N. Matsuda^a, T. Kanemura^a, P. B. Lim^b, M. Inoue^b

^aFundamental Research Dept. Chemical Div., DAIKIN INDUSTRIES, LTD.

1-1 Nishi Hitotsuya, Settsu-shi Osaka, 566-8585, Japan

Phone: +81-6-6349-4196, Fax: +81-6-6349-4751, E-mail: kazuyuki.satou@daikin.co.jp

^bToyohashi University of Technology

1-1 Hibarigaoka, Tempaku, Toyohashi-shi, Aichi 441-8580, Japan

Phone / Fax: +81-532-47-0120, E-mail: inoue_mitsuteru@eee.tut.ac.jp

ABSTRACT

We report here, for the first time, multiplexing hologram recording number as a function of shift distance and Error-Map of a 0.4 mm-thick, 120-mm-diameter photopolymer disc. Increasing the shift distance increases the storage capacity. We studied several novel fluorinated holographic recording materials as 532 nm optical data storage candidates. Their fundamental properties, such as the relationship between shift distance and the Bit Error Rate (BER) and the effect of holographic recording thickness are characterized. This paper reports the evaluation results of the properties of a new fluorinated holographic recording material for Collinear Holography. The material is shown to offer significantly better performance than existing alternatives.

Keywords: Fluorinated holographic recording material, Shift distance, Error-Map, 120-mm-diameter photopolymer disc, Collinear Holography, Multiplexing hologram

1 . INTRODUCTION

Holographic digital data storage has been attracting attention and has become one of the most promising candidates for the next generation optical data storage system. Various research bodies are actively targeting this area. Holographic photopolymer materials are attractive candidates for write-once-read-many-times data storage applications because they can be designed to have large refractive-index contrast, high photosensitivity, high resolution, long-term hologram retention, and easy processing [1-3]. To meet the emerging demands for radically higher recording densities, photopolymers with high Δn are the most attractive candidates. However, hydrocarbon-based photopolymer materials have a practical limit. In order to overcome that barrier, we have investigated non-hydrocarbon-based holographic recording materials that use low refractive index fluorinated components. Multiplexing is probably the most attractive approach to realizing higher capacity. Several methods, such as angle- or shift-multiplex recording have been proposed and tested in hologram performance evaluations. However, with these methods, it is difficult to estimate the ultimate recording density possible. We propose the shift distance method, which uses the inherent shift selectivity of the recording medium to record different streams of holographic data at different shift distances. The ultimate recording density of the new media can be easily estimated.

This paper describes multiplexing hologram recording number as a function of the shift distance and Error-Map of a 0.4 mm-thick, 120-mm-diameter photopolymer disc created using a new holographic recording material with a low refractive index fluorinated component.

2 . EXPERIMENT

2.1 Material and media

An acrylate-based radical-polymerizable monomer dispersed polymer composed of low refractive index fluorinated component was used as a holographic recording layer (400 μm thick); the layer was sandwiched between substrates for hologram recording experiments. Both substrates were glass with a sputter layer of SiO_2 , 532 nm Anti-Reflection

treatment (Tokiwa Optical LTD., SHOT B270). The structure of the coupon sample for the S-VRD is shown in Figure 1. A static type of collinear holographic test system, S-VRD / SHOT-1000G (Toyohashi University of Technology / PULSTEC INDUSTRIAL CO.,LTD.), equipped with a pulse laser (10 ns with wavelength of 532nm), was used to record / read multiplex holograms (Figure 2). Changing the frequency of the laser pulses changed the recording light energy which yielded near-equivalent diffraction efficiencies for each hologram. Holograms were recorded and read out using shift distances of 0.1 μm / 1 μm / 3 μm . The spatial light modulator (SLM) pattern used for hologram recording is 1024 \times 768 pixels.

In the second experiment, a dynamic type of collinear HVD-prototype-drive-system (OPTWARE CO., LTD.), equipped with a pulse laser (with wavelength of 532 nm), was used to record / read holograms.

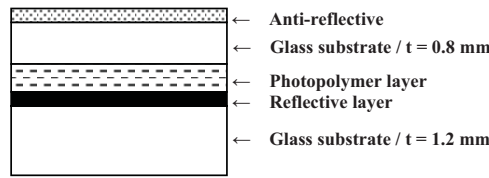


Fig. 1. Structure of the coupon sample.

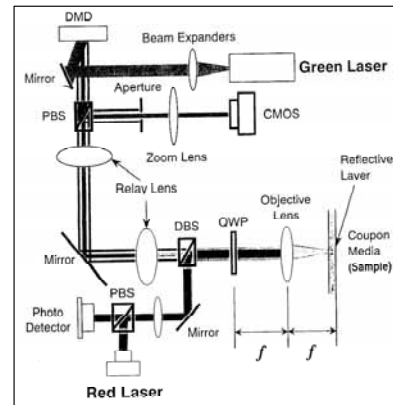


Fig. 2. Optical configuration

3 . RESULTS AND DISCUSSION

3.1 Multiplexing hologram recording number versus shift distance for static collinear holography

The BER values of ten-stream multiplex holograms with shift distances of 1 μm are shown in Figure 3. Prototype coupon samples were fabricated using the following conditions: recording power was 3 $\text{mW}/\text{cm}^2 \times 1000$ pulse (= 5.4 mJ/cm^2), and the reconstruction power is 0.5 $\text{mW}/\text{cm}^2 \times 40$ pulse (= 0.04298 mJ/cm^2). Both powers were kept constant regardless of the frequency of the laser pulses used. The shift distances examined yielded BER values under E-02 on the X-Y plane of the coupon sample. Therefore, the shift distance method can realize high density holographic storage.

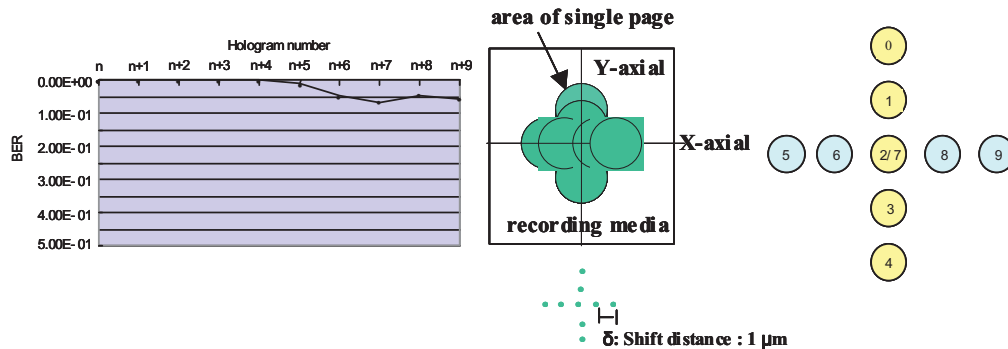


Fig. 3. The BER values of multiplexing holograms with shift distances of 1 μm in X-Y plane of coupon sample.

3.2 Disc Error-map for dynamic type Collinear holography

The error-map of single holograms holding 480 pages on each track on the disc are shown in Figure 4. The track pitch is $1.6 \mu\text{m}$. The track number ranged from 400 to 20200. Shift distances were ca. $321.85 \mu\text{m}$ at disc diameter of 25 mm and ca. $638.99 \mu\text{m}$ at disc diameter of 50 mm. The average error rate was 1.61 % for the disc sample. Therefore, area of single page falls on the top of each page data in 25 mm diameter, and it does not fall on the top / bottom of page data in 50 mm diameter.

Prototype disc samples recorded and tested under the following conditions: the recording power was $\text{HWP } 50000 \times 3$ pulse ($= 0.141 \text{ mJ/cm}^2$), and the reconstruction power was $\text{HWP } 33300 \times 1$ pulse ($= 0.186 \mu\text{J/cm}^2$).

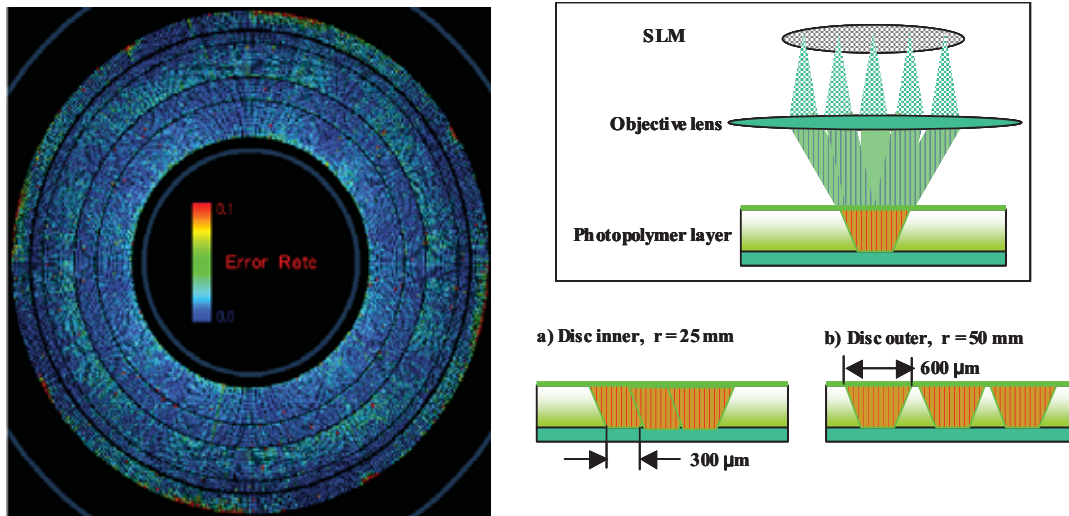


Fig. 4. The error-map of single holograms with 480 pages per track on disc.

4 . CONCLUSION

In this study, we proposed the shift distance method, where several holographic data streams are recorded at different shift distances as determined on the recording medium. Our use of a fluorinated component in the hologram recording layer offers improved recording density. The proposed technique yielded BER values under E-02 in the X-Y plane of coupon samples, and the new holographic recording material with low refractive index fluorinated component improved error-maps as evidenced by 0.4 mm-thick, 120-mm-diameter photopolymer discs. The average error rate was 1.61 % for the disc sample.

This proposal will allow visible wavelength-sensitive photopolymer media to realize high density recording systems that can replace tape media and are as reliable as traditional archival systems.

REFERENCES

- [1] Holographic Data Storage, H. J. Coufal, D. Psaltis, and G. T. Sincerbox eds., Springer Series in Optical Sciences, vol.76, p.10 (2000).
- [2] D. A. Waldman, R. T. Ingwall, P. K. Dal, M. G. Horner, E. S. Kolb, H.-Y.S. Li, R. A. Minns, and H. G. Schild, "Cationic ring-opening photopolymerization methods for volume hologram recording", *PROC. SPIE*, 2689, 127-141 (1996).
- [3] L. Dhar, K. Curtis, M. Tackitt, M. Schilling, S. Campbell, W. Wilson, A. Hill, C. Boyd, N. Levinos, and A. Harris, "Holographic storage of multiple high-capacity digital data pages in thick photopolymer systems", *Opt. Lett.*, vol.23, no.21, 1710-1712 (1998).

Holographic Recording with Blue Colored Diarylethene Dye doped PMMA

X.A. Liang¹, X.W. Xu¹, M.H. Li¹, S. Solanki¹, M.H. Hong¹, T.C. Chong^{1,2}

¹Data Storage Institute, Agency for Science, Technology and Research,
DSI Building, 5 Engineering Drive 1, Singapore 117608

²Optical Crystal Lab, Department of Electrical & Computer Engineering,
National University of Singapore, 4 Engineering Drive 3, Singapore 117576

Phone: +65-68745089, Fax: +65-67778517

E-mail: Liang_Xinan@dsi.a-star.edu.sg

1. Introduction

Holographic data storage is one of the most promising candidates for next generation optical data storage. Recently, rapid progress has been made in the development of both media and drive system [1,2]. For media, most of the efforts were on WORM type media. Regarding rewritable media, different materials have been studied for this application, such as photo-addressable polymer [3], photorefractive polymer, photorefractive crystal and reversible photochromic materials [4].

Various photochromic materials have been studied for optical data storage [5]. Diarylethene derivatives with the heterocyclic ring have attracted many research attention as these compounds show great performance of resistance to fatigue and coloration/decoloration cycles ($>10^4$) [6]. It usually has two isomers, i.e. open-ring form and closed-ring form. When illuminated with UV light or visible light, the conversion between the open-ring and closed-ring can be realized reversibly. It is therefore suitable for rewritable optical recording. Figure 1 shows the photoisomerization of one diarylethene dye. Several authors have studied the holographic storage performance with this kind of photochromic compound. It is well known that UV light is harmful to human's health and UV optics is more expensive than the one for visible light. If visible light can be used to induce the conversion from open-ring to close-ring form, the system can be much cheaper and safer.

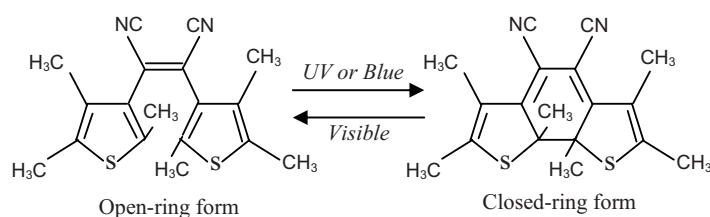


Fig.1 Photoisomerization of B1536.

Among diarylethene photochromic dyes, 1,2-dicyano-1,2-bis(2,4,5-trimethylthiophen-3-yl)ethane (CMTE, also called B1536) can be colored by the illumination of both blue light (405 nm) and UV light, and this will cause a strong absorption at around 532 nm. This dye also shows excellent thermal stability

(> 90 days at $80\text{ }^\circ\text{C}$) and fatigue resistance [6]. The rewrite cycles can achieve as high as $> 10^4$ times. Its performance for two-photon optical recording has been reported [7]. But to our best knowledge, the holographic recording performance for this dye has not been reported.

In this paper, the authors studied the absorption difference between blue and UV light illumination, and the holographic recording performance of B1536 doped PMMA film in terms of diffraction efficiency, sensitivity and fatigue resistance.

2. Experiments

10 wt.% PMMA (Methacrylic Acid Methyl Ester) polymer particles (molecular weight 13500~14000, size around several hundred micrometers) were ultrasonically dissolved into toluene (> 99%, Sigma-Aldrich) solution. 10% B1536 dye (> 98.0 %), which was purchased from TCI (Tokyo Chemical Industry) without any purification, was dissolved ultrasonically in the PMMA toluene solution. A spin coating machine was used to spin the solution onto a $20 \times 20 \text{ mm}^2$ quartz substrate at a speed of 2000 rpm for 60 s. Then, the film was put into an oven in air at $120 \text{ }^\circ\text{C}$ for 2 hours to remove the residual solvent.

The coloration and decoloration effects were examined by measuring the transmission spectra with a Shimadzu UVPC-3100 UV-VIS-NIR spectrophotometer after UV, blue or green light illumination. The holographic recording performance was investigated with a conventional transmission geometry recording setup. A Second Harmonic Generation (SHG) Nd:YAG laser beam at 532 nm was split by a non-polarization beam splitter into two laser beams with same intensities. The two beams were then directed by mirrors and intersected each other. The angle between the two incident laser beams was around 30 degree. During recording, one beam was blocked from time to time to monitor the diffraction light. Before the recording experiment, the film was illuminated with UV or blue light for 5~10 minutes. The UV source was from a Hamamatsu L8333-01 UV lamp equipped with a 300 ~ 400 nm filter; the blue light source was from a 405 nm laser diode (Model: LDCU12/7610 Power Technology Inc.).

3. Results and discussion

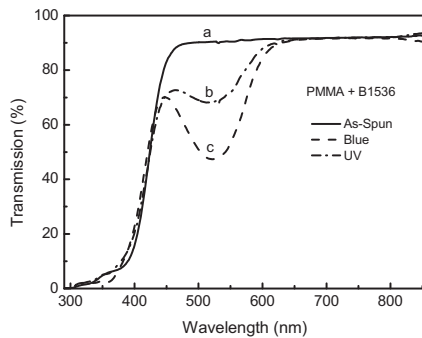


Fig.2 Transmission spectra of doped PMMA (a) as-spun; (b) after UV illumination; (c) after blue illumination.

Figure 2 shows the coloration / decoloration effects of the B1536 doped PMMA film. The as-spun film was yellowish in color. The spectrum is shown in Fig. 2(a). From 475 ~ 830 nm, the curve is almost flat, no obvious absorption was observed. From 300 ~ 475 nm, there is a strong absorption, compared with pure PMMA film with similar thickness of 10 μm . Upon the illumination with blue laser (405 nm), the film color changed to reddish brown. The spectra are shown in Fig. 2(c). A strong absorption peak appears at 522 nm. The absorption band covers a range from 447 ~ 629 nm. This peak corresponds to the closed-ring form of B1536. As mentioned in reference [8], the quantum efficiency can be 1 at 546 nm, which implies that a high recording sensitivity can be achieved with SHG Nd:YAG laser.

We also checked the UV light illumination effect. The spectrum is shown in Fig. 2(b). By comparing curves (b) and (c), the illumination with blue light is more effective, the transmission at the absorption peak of curve (c) is lower than curve (b) by 21%. It means with the blue light illumination, more open-ring form molecules change to its closed-ring counterpart.

The holographic recording performance of the blue and UV colored film was investigated respectively. Before the recording, the film was illuminated with blue (405 nm) or UV light for 10 minutes with light intensity of 63.7 mW/cm^2 . The recording experiments were then carried out with 532 nm green laser with light intensity of 1.67 mW/cm^2 for each beam. Figure 3 shows the recording performance of the blue-colored (■) and UV-colored (Δ) B1536 doped PMMA films. For blue illuminated sample, the film shows a fast response to the green light. Within 130 seconds, it reaches the saturated diffraction efficiency of 1.4%, which corresponds to a refractive index change Δn of about 1.97×10^{-3} . The refractive index change calculation is based on the Kogelnik's two-wave coupled wave

theory [9]. The calculated sensitivity is 0.71 cm/mJ, which is at the same order of magnitude reported in some commercial holographic recording media. This high sensitivity can be attributed to the high quantum efficiency of B1536 in the green wavelength range [8]. However, for the UV illuminated film, under the same recording conditions, the diffraction efficiency achieved was only 1/4 of its blue illuminated counterpart. The sensitivity achieved was 0.22 cm/mJ, which was 3 times lower than the value obtained from the blue colored sample. This may be due to the lower quantum efficiency of the dye for UV light, which resulted in less closed-ring forms available in the UV illuminated sample. The dependence of saturated diffraction efficiency on the recording light intensity was also examined. The recording experiment carried out with 532 nm laser beam with recording intensities of 1.12, 1.37, 1.67 and 2.01 mW/cm² for each beam, respectively. When the light intensity is higher than 1.37 mW/cm², all the saturated diffraction efficiencies achieved at different recording intensities are 1.4%.

However the readout was volatile. During the readout period, the diffraction efficiency dropped exponentially. This is because the uniform illumination of the reference beam erases the recorded grating by converting the closed-ring form to the open-ring form. From the transmission spectrum, one can see that there is very less absorption at wavelength > 630 nm. Therefore it is possible to use a red laser as the readout beam to realize nonvolatile readout of the grating recorded by the green laser. The rewritability was also examined for this film. After 100 times recording and erasing, no obvious degrade of the diffraction efficiency was observed.

4. Summary

1,2-dicyano-1,2-bis(2,4,5-trimethylthiophen-3-yl) ethane doped PMMA was investigated for rewritable holographic recording. It is found that the blue light illumination is more efficient than UV illumination. Both the refractive index change Δn and sensitivity S at 532 nm could be increased greatly after the blue illumination. Sensitivity of 0.71 cm/mJ and refractive index change of 1.97×10^{-3} were achieved. The material also showed good rewritability. In the future work, the approaches to achieve nonvolatile readout will be explored. The thickness of the film needs to be increased for practical applications.

References

1. K. Anderson and K. Curtis, *Opt. Lett.* **29**, 1402 (2004).
2. K. Tanaka, H. Mori, M. Hara, K. Hirooka, A. Fukumoto, K. Watanabe, *ISOM 2007, Oct. 21-25, 2007, Singapore*, Mo-D-03.
3. R. Hagen and T. Bieringer, *Adv. Mater.* **13**, 1805 (2001).
4. S. Luo, K. Chen, L. Cao, G. Liu, Q. He, and G. Jin, *Opt. Exp.* **13**, 3123 (2005).
5. S. Kawata and Y. Kawata, *Chem. Rev.* **100**, 1777 (2000).
6. M. Irie *Chem. Rev.* **100**, 1685 (2000).
7. A. Toriumi, S. Kawata, M. Gu, *Opt. Lett.* **23**, 1924 (1998).
8. Y. Nakayama, K. Hayashi, M. Irie, *Bull. Chem. Soc. Jpn.* **64**, 202 (1991).
9. H. Kogelnik *Bell Syst. Tech. J.* **48**, 2909 (1969).

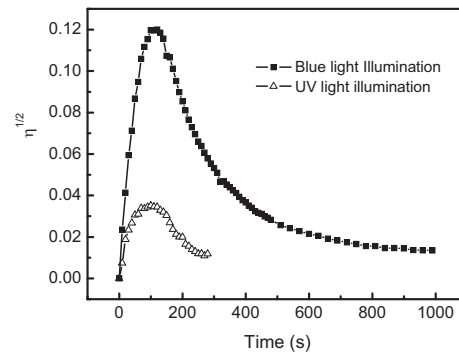


Fig. 3 Holographic recording and readout performance of B1536 doped PMMA films illuminated by blue light (■) and UV light (Δ).

ZrO₂ nanoparticle-polymer composite media for volume holographic recording

Toshihiro Nakamura, Sokoh Koda, Kohji Ohmura, and Yasuo Tomita
Department of Electronics Engineering, University of Electro-Communications
1-5-1 Chofugaoka, Chofu, Tokyo 182-8585, Japan
ytomita@ee.uec.ac.jp

Kentaroh Ohmori and Motohiko Hidaka
Chemical, Research Laboratories, Nissan Chemical Industries, Ltd.
722-1 Tsuboi Funabashi, Chiba 274-8507, Japan

ABSTRACT

We present volume holographic recording in highly transparent ZrO₂ nanoparticle-polymer composite media in the green. It is shown that the refractive index modulation as high as 0.01 is obtained at the nanoparticle concentration of 35 vol.%. The incorporation of ZrO₂ nanoparticles also provides substantive suppression of polymerization shrinkage and improved thermal stability of recorded holograms. Recording sensitivity enhancement by incorporating hydrogen donor/acceptor agents is achieved. Peristrophic multiplexing of 100 plane-wave holograms is demonstrated. The measured dynamic range (M/#) is 1.2 for the composite film of approximately 50- μ m thickness.

Keywords: Holographic recording materials, Holographic and volume memories, Holography

1. INTRODUCTION

Holographic data storage has paid much attention because it is considered to meet the ever-increasing need for mass storage systems with high data transfer speed [1]. For this purpose holographic dry photopolymers have been considered as a possible candidate and studies for almost four decades. Because they possess several attractive properties such as large refractive index modulation (Δn), ease-to-process, high form flexibility and low cost. So far, we have proposed a new nanoparticle-polymer composite material for volume holographic recording. It includes inorganic or organic nanoparticles that are uniformly dispersed to host (meth)acrylate monomers in order to increase Δn and improve the dimensional stability as well [2-4]. Recently, we have also introduced highly transparent ZrO₂ nanoparticle-polymer composite system for volume holographic recording [5]. In this paper we describe improved performance of the ZrO₂ nanoparticle-polymer composite system that has large Δn and a high holographic recording sensitivity by incorporation of hydrogen donor/acceptor sensitizing agents. Hologram multiplexing using a peristrophic multiplexing method [6] is also demonstrated.

2. SAMPLE PREPARATION

ZrO₂ nanoparticles having the average diameter of 3 nm were prepared by the liquid-phase synthesis [7] and were dissolved in a toluene solution. Some chemical treatment to the surface of the nanoparticle was made to avoid unwanted aggregation in a host monomer. As a result, surface-treated ZrO₂ nanoparticles had the effective refractive index of 1.72 at a wavelength of 589 nm. The ZrO₂ sol was dispersed to acrylate monomer [2-propenoic acid, (octahydro-4,7-methano-1H-indene-2,5-diyl)bis(methylene) ester] whose refractive indices were 1.50 in the liquid phase and 1.53 in the solid phase, respectively, at 589 nm. A photo-initiator titanocene (Irgacure784, Chiba) of 1 wt.% was also doped to provide the photosensitivity at wavelengths shorter than 550 nm. Such mixture on a spacer-loaded glass plate was dried at 80°C for approximately 60 min in an oven and was finally covered with another glass plate to make samples for holographic measurements. It was found that the scattering loss coefficient was approximately 1 cm⁻¹ in the green, indicating high transparency of the sample film.

3. EXPERIMENTS

3.1 Diffraction properties

Two mutually coherent beams from a Nd:YVO₄ laser operating at 532nm were used to record a plane-wave volume grating in a sample. An He-Ne laser beam operating at 632.8 nm was employed to monitor the buildup dynamics of the grating. All the beams were s-polarized. Figure 1 shows a dependence of Δn_{sat} on the volume fraction of ZrO₂ nanoparticles at several recording intensities. It can be seen that there exists the optimum value for the volume fraction (~ 35 vol.%) to maximize Δn_{sat} (~ 0.01), more or less independently of recording intensity. Improved thermal stability of recorded holograms is also confirmed by measuring a temperature dependence of Bragg-angle change.

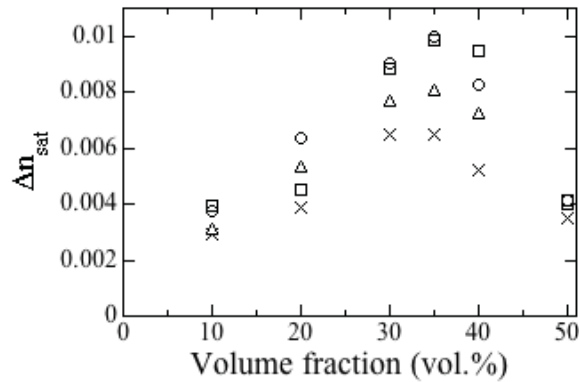


Fig. 1. Dependence of saturated Δn (Δn_{sat}) on volume fraction of ZrO₂ nanoparticles at different recording intensities (\times :10mW/cm², Δ : 50mW/cm², \circ : 100mW/cm², \square : 200mW/cm²). The recorded grating spacing was 1 μm .

3.2 Recording sensitivity enhancement

Hydrogen donor/accepter sensitizers, 3,3'-bismethoxycarbonyl-4,4'-tert-butyl peroxy carbonyl benzophenone (BT2) and N-phenylglycine (NPG) [8] were used to increase the recording sensitivity. It was found that doping of the sensitizers does not induce any substantive absorption loss. For example, doping of BT2 (2 wt.%) and NPG (1 wt.%) gave the absorption coefficient of 8 cm⁻¹, implying the corresponding skin depth of 1.25 mm. Figure 2 shows a dependence of the material recording sensitivity S (defined as $1/LI d\eta^{1/2}/dt|_{t=T}$, where L , I , T and η are a sample's thickness, a recording intensity, the induction time period and the diffraction efficiency, respectively) [9] on concentration of BT2 for samples doped with ZrO₂ nanoparticles of 35 vol.% and with NPG of 1 wt.%. It can be seen that S increases by approximately a factor of two (three) with BT2 concentrations higher than 4 wt.% at a recording intensity of 50 (20) mW/cm².

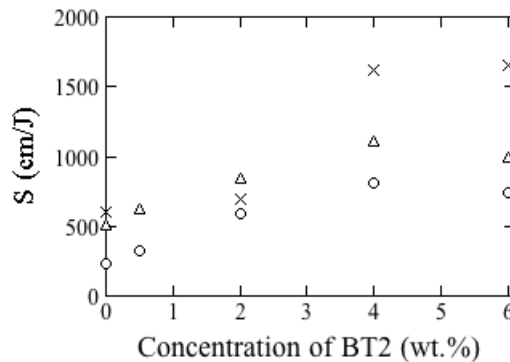


Fig. 2. Dependence of material recording sensitivity on concentration of BT2 for samples doped with ZrO₂ nanoparticles of 35 vol.% and with NPG of 1 wt.% at several recording intensities (\times : 20mW/cm², Δ : 50mW/cm², \circ : 150mW/cm²).

3.3 Peristrophic hologram multiplexing

Figure 3 shows a histogram of diffraction efficiencies for peristrophically multiplexed 100 holograms in a 50- μm -thick film with the ZrO_2 nanoparticle concentration of 35 vol.% after three iterative exposure scheduling procedures [10]. It can be seen that the average diffraction efficiency is approximately 1.4×10^{-4} and the calculated M/# is 1.2. This implies that M/# is 12 or larger with the diffraction efficiency of $\sim 10^{-6}$ per hologram to record 10,000 holograms in our ZrO_2 nanoparticle-polymer composite media of the thickness of 500 μm or thicker.

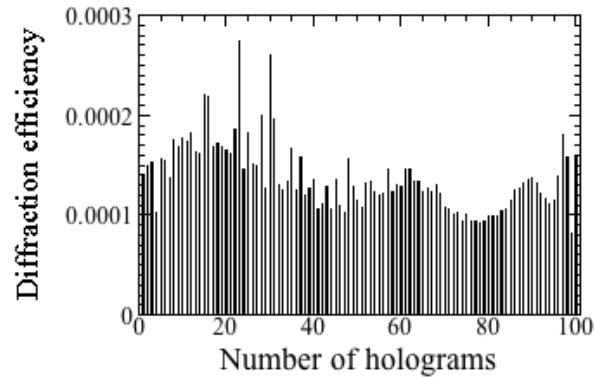


Fig. 3. Diffraction efficiency vs. the number of holograms stored in a 50- μm -thick sample with the 35 vol.% dispersion of ZrO_2 nanoparticles. 100 plane-wave holograms of 1-mm grating spacing were recorded by the peristrophic multiplexing method.

4. CONCLUSION

We have demonstrated volume holographic recording in highly transparent ZrO_2 nanoparticle-polymer composite media. We have shown that the refractive index modulation as large as 0.01 is achieved at a grating spacing of 1.0 μm and the enhancement of the recording sensitivity by use of NPG and BT2 is possible. Peristrophic hologram multiplexing with iterative exposure scheduling yields 100 hologram multiplexing with M/# of 1.2 for a 50- μm -thick sample.

REFERENCES

1. H.J. Coufal, D. Psaltis and G.T. Sincerbox, eds, *Holographic Data Storage*, (Springer, Berlin, 2000).
2. N. Suzuki and Y. Tomita, *Appl. Phys. Lett.* **81**, 4121 (2002).
3. N. Suzuki and Y. Tomita, *Appl. Opt.* **43**, 2125 (2004).
4. Y. Tomita, K. Furushima, K. Ochi, K. Ishizu, A. Tanaka, M. Hidaka, and K. Chikama, *Appl. Phys. Lett.* **88**, 071103-1 (2006).
5. N. Suzuki, Y. Tomita, K. Ohmori, M. Chikama, *Opt. Express.* **14**, 12712 (2006).
6. K. Curtis, A. Pu and D. Psaltis, *Opt. Lett.* **19**, 993 (1994).
7. K. P. Jayadevan and T.Y. Tseng, "Oxide nanoparticles," in *Encyclopedia of Nanoscience and Nanotechnology*, H.S. Nalwa, ed. (American Scientific Publishers, Stevenson Ranch, Calif., 2004), Vol.8, pp.333–376.
8. S. Ikeda and S. Murata, *Journal of Photochemistry and Photobiology A: Chemistry* **149**, 121-130(2002).
9. L. Hesselink, S. S. Orlov and M. C. Bashaw, *Proc. IEEE* **92**, 1231 (2004).
10. A. Pu, K. Curtis, and D. Psaltis, *Opt. Eng.* **35**, 2824 (1006).

Summary

Improved photopolymer for holographic data storage

Yuxia Zhao^a, Xiaojun Wan^a, Feipeng Wu^a, Huanyong Wang^b, Pengfei Liu^b, Shiquan Tao^b

^aTechnical Institute of Physics and Chemistry, Chinese Academy of Sciences, Beijing 100080, China; ^bCollege of Applied Science, Beijing University of Technology, Beijing 100022, China
Contact author: Yuxia Zhao, e-mail: yuxia.zhao@mail.ipc.ac.cn; phone: 86-10-82543571, fax: 86-10-82543491.

Novel photopolymers for holographic storage were investigated by combining acrylate monomers or vinyl monomers as recording media and liquid epoxy resins plus an amine harder as binder. Two combinations, aliphatic monomer with aromatic epoxy resin and aromatic monomer with aliphatic epoxy resin, were investigated. A newly synthesized dye **DEAMC** (shown in Fig.1) was used as sensitizer. Compared to Monroe et al reported photosensitizer 2,5-bis{[4-(diethylamino)-phenyl]methylene}-cyclopentanone (**BDEA**)^[1], **DEAMC** has a broad absorption band within 400-600 nm (shown in Fig. 2) and can induce photopolymerization of acrylate monomers or vinyl monomers under exposure of both 457 nm and 532 nm light. Moreover, **DEAMC** shows higher photosensitizing activity than **BDEA** (shown in Fig. 3) combining with initiator of **HABI**.

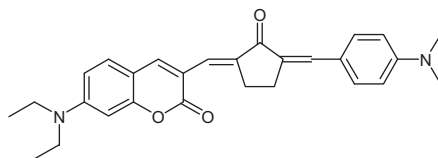


Fig 1 The structure of **DEAMC**

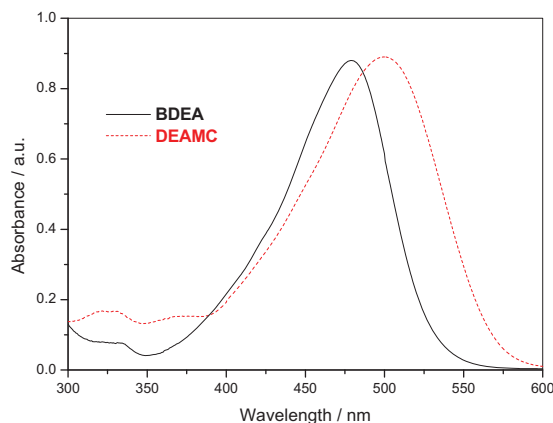


Fig 2 UV-vis spectra of two dyes in chloroform.

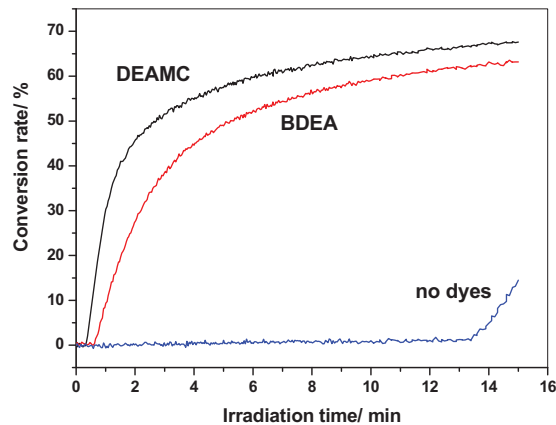


Fig 3 Double-bond conversion rate of samples versus irradiation time (the absorbency of two samples containing different dyes are adjusted exactly same under exposure wavelength).

A series of samples with thickness of 500 μm were prepared by adjusting components and their maximum diffraction efficiencies were studied by two 457 nm laser beams as recording beams and a 632 nm laser as probe beam. The refractive index modulation was then calculated by using the coupled-wave theory. The results are listed in Table 1. It shows that high diffraction efficiency and refractive index modulations are obtained by both combinations of acrylate monomer with aromatic epoxy resin and N-vinyl carbazole monomer with aliphatic epoxy resin.

In order to investigate the noise property, measurements of image quality through the samples were carried out, with the samples inserted into near the Fourier spectrum plane in a standard $4f$ imaging system. The signal-to-noise ratio (SNR) of images before and after coherent illumination were measured and the decrease of SNR in dB (loss of SNR , or $LSNR$) was used to assess the degradation of image quality due to scattering noise^[2]. The term “3dB $LSNR$ exposure dose” in Table 1 is defined as the exposure dose that causes the signal-to-noise ratio of an image through the photopolymer sample to be decreased by 3dB ($LSNR=3\text{dB}$). A very interesting result is presented from Table 1 that the loss of signal-to-noise ratio ($LSNR$) of samples using **DEAMC** as sensitizer are quite lower than samples using **BDEA** as sensitizer, which indicates that this new dye has very nice miscibility with main components. We also used Monroe et al reported recipe^[1] to study **DEAMC**. The same result is obtained. When substituting **DEAMC** for **BDEA** as sensitizer, the 3 dB $LSNR$ exposure dose of sample increased 90 times. This indicates that these improved materials have large potentiality for high-density holographic data storage. Further study is underway.

Table 1 Holographic properties of samples

Sample No.	1	2	3	4	5	6	7	8	
A1	58.4	0	0	0	0	0	0	0	
A2	0	58.4	58.4	58.4	58.4	0	0	0	
A3	0	0	0	0	0	53.1	0	0	
A4	0	0	0	0	0	0	53.1	53.1	
A5	0	0	0	0	0	5.3	5.3	5.3	
Component ^a (wt%)	MMA	0	0	0	0	21.2	21.2	21.2	
	NVC	21.2	21.2	21.2	21.2	0	0	0	
	B1	15.9	15.9	15.9	15.9	15.9	15.9	15.9	
	BDEA	0	0	0.012	0	0.006	0.006	0.012	
	DEAMC	0.006	0.006	0	0.012	0	0	0	
	HABI	0.64	0.64	0.64	0.64	0.64	0.64	0.64	
	MMT	0.64	0.64	0.64	0.64	0.64	0.64	0.64	
	DMF	3.2	3.2	3.2	3.2	3.2	3.2	3.2	
Diffraction efficiency (%)		41.7	66.9	50.3	64.0	68.1	23.8	19.3	63.4
Refractive index modulation ($\times 10^{-4}$)		2.62	3.57	2.94	3.45	3.62	1.9	1.72	3.43
3dB LSNR exposure dose (mJ/cm ²)		430	320	23	260	53	8	7	11

^a**A1** is 1,3-propanediol diglycidyl ether, **A2** is 1,4-butanediol diglycidyl ether, **A3** is Bisphenol F epoxy resin, **A4** is Bisphenol A epoxy resin, **A5** is 3,4-Epoxy cyclohexylmethyl-3,4-epoxycyclohexane-carboxylate, **B1** is Triethylenetetraamine, **HABI** is 1,1',2,2'-bis(o-chlorophenyl)-4,4',5,5'-tetraphenyl-bisimidazole, **MMT** is 4-methyl-4H-1,2,4-triazole-3-thiol.

This work is supported by the National Science Foundation of China under Grant No.60477004, and Natural Science Foundation of Beijing under Grant No.4071001.

References

- [1] Monroe B M, Smother W K, Keys D E, et al. Improved photopolymers for holographic recording. I. imaging properties [J]. *J. Imaging Sci. Tech.*, 1991, **35**: 19-25.
- [2] Wan Y H, Yuan W, Liu G Q, et al. Study on the characteristics of scattering noise in photorefractive holographic storage [J]. *Chinese Journal of Lasers*, 2003, **30** (6): 529-532.

Holographic correlator for video image files

Eriko Watanabe, Reiko Akiyama and Kashiko Kodate

Japan Women's University, Mejirodai 2-8-1, Bunkyo, Tokyo, 112-8681 Japan

Phone: +81-3-5981-3615/Fax: +81-3-5981-3615 E-mail: facer@fourier.jwu.ac.jp

ABSTRACT

We have developed a video identification system based on a holographic correlator. Making the best use of fast data processing capacity of FARCO, high speed recognition system was established by registering optimized video image files. This paper demonstrates that the processing speed of our optical holographic calculation is remarkably higher than that of the conventional digital signal processing architecture.

Keywords: video identification, optical correlator, holographic memory, coaxial holography, image search

1. INTRODUCTION

The volume of information we handle is dramatically increasing as a result of the change from text data to still and moving image files. Free internet video-sharing sites such as YouTube, where moving images can be posted, are becoming considerably popular around the world. More than 100 million videos are viewed each day on the video sharing site. However, the main criticism often targeted at these sites is that many programs are often posted without permissions from copyright holders.

It is widely acknowledged that the current image retrieval technology is restricted to text browsing and index data searching. For unknown images and videos, the searching process can be highly complicated. As a result, the technology for this kind of image searching has not been established.

In order to improve the above-mentioned situations surrounding illegal uploading of images, we proposed and constructed a new optical correlator[1-2] that integrated the optical correlation technology used in our face recognition system[3-6] and holographic memory[7]. In the preliminary holographic correlation experiments using the co-axial coupon type optical set-up, excellent performance of high correlation peaks and low error rates was observed. This system is called Fast Recognition Optical Correlator (FARCO). In FARCO, a large amount of data can be stored in the holographic optical disc in the form of matched filter patterns. In the case of the correlation process where an input image on the same position is illuminated by the laser beam, the correlation signal penetrates through the matched filter and appears on the output plane. The optical correlation process accelerates by simply rotating the disc at higher latency.

In this paper, we propose a video identification system using a holographic correlator. Taking advantage of fast data processing capacity of FARCO, we constructed high speed recognition system by registering the optimized video image file. Experiments on the system demonstrated that the processing speed of our optical holographic calculation is remarkably higher than that of the conventional digital signal processing architecture.

2. CONCEPT OF HOLOGRAPHIC VIDEO FILTER

No storage device has yet been found, which meets both conditions: transfer speed and data capacity. DRAM has high speed data transfer rate, yet with limited data capacity up to several GB. The typical secondary storage devices include hard disk drive, optical disc drive and magnetic tape streamer devices. HDD technology has been making significant progress in expanding data capacity. Recently, the capacity of HDD data storage has expanded to more than 1TB. However, even if a RAID (Redundant Arrays of Inexpensive Disks) system is used, the maximum transfer rate of a conventional HDD system is limited to the order of G bps. Typically, the input digital data is first transferred from HDD to the DRAM, followed by calculation of correlation. Therefore, conventional image search correlation with large image database has a weakness in its image data transmission speed. It is demonstrated that the processing speed of our optical holographic calculation is remarkably higher than that of the conventional digital signal processing architecture. We propose video identification system using ultra high speed holographic optical correlator sever with a web interface. The schematic of video identification FARCO sever is shown in figure 1 below.

1. Registering process of video contents in holographic matched filters

The users post the video contents to the FARCO server by the web interface as shown in Fig. 1(a). The video contents on the FARCO server are preprocessed (i.e. normalization, color information and other feature extraction) and transferred as binary data. These binary data are recorded in the form of matched filtering

patterns.

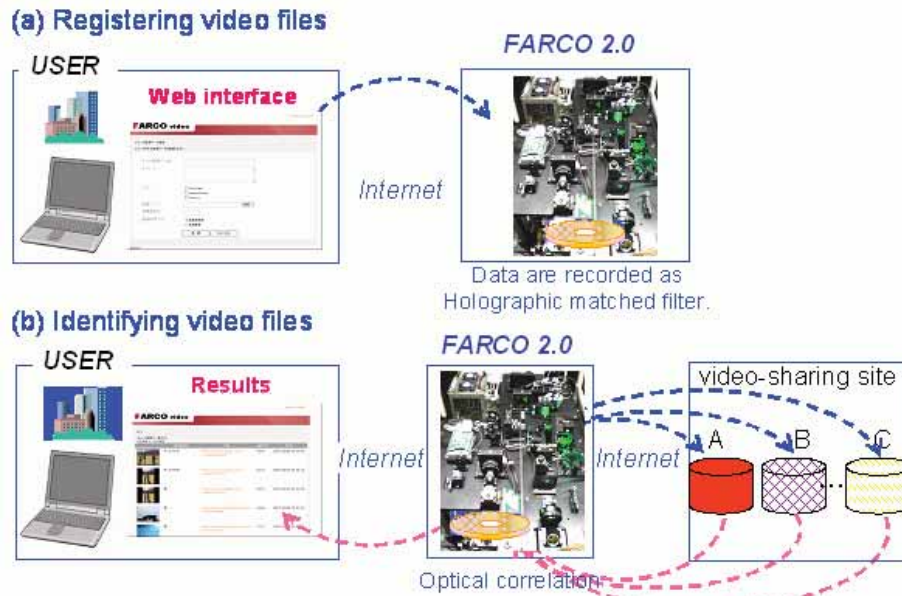


Fig.1 The concept of video filtering system

2. Video identification by holographic optical correlator

Users log in to the website via video identification system shown in Fig.1 (b). Firstly, key words narrow down the list of video files on several video sharing sites, and subsequently, input video data are downloaded. Input video data are preprocessed and correlated. Finally, correlation results are sorted, and the results on the web browser will be displayed. (Fig. 1 (b))

The correlation speed of a holographic matched filter

These preprocessed video images are recorded on a co-axial holographic system. The correlation speed of multiplexed recording is given by:

$$V_c = \frac{2\pi r}{d} \cdot \frac{R}{60}$$

where r [mm], d [mm] and R [rpm] represent the diameter of the disc, the recording pitch and the rotating speed, respectively. In a conventional correlation calculation which uses a digital computer, the data transfer and correlation calculation are achieved separately. In this system, if 240×320 pixel information is written onto a holographic disc at 10 micrometer pitch and at 2,400 rpm, this is equivalent to data transfer of more than 100 G bps. An important point is that the correlation result is applied to an image of 320×240 bits, and the output signal of the correlation operation requires only 1.3 Mbps against the data transfer of 100 Gbps.

3 EXPERIMENTS

In our experimental system, each image file taken from DVD is registered as a video file, while the input video image file is downloaded from video sharing sites.

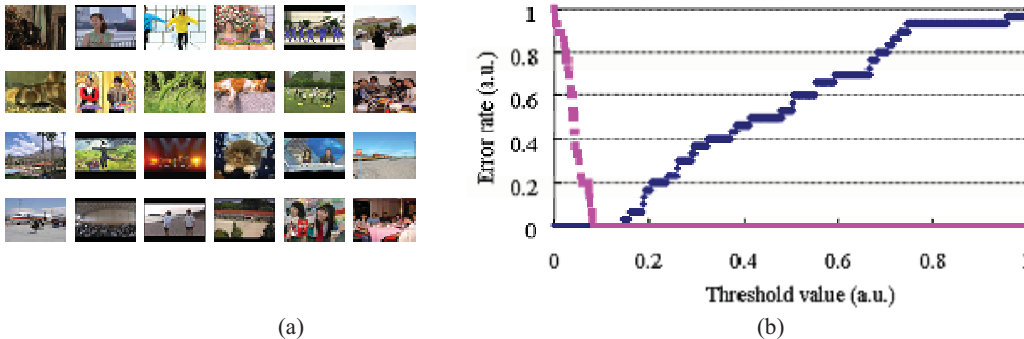
3.1 Database image design

When co-axial hologram is recorded, the space frequency of a Fourier plane varies according to its reference point, as each interference fringe differs. Thus, the reference points have to be carefully designed, considering frequency distribution of each video image. Simulation can be carried out based on hologram analysis, applying Kogelnik's couple wave theory to two dimensional cases. A wave front from each pixel can be considered to be spherical wave before the lens, through which becomes plane wave. In the recording material, plane waves interact with one another. Therefore, couple waves were made by interference of two beams, as a result of the

recording in the media and a pair of pixels. All diffraction gratings were considered as possible pairs in the recording, from which all plane wave diffractions were calculated. Diffraction efficiency was computed based on the Kogelnik equation. Distance from the reference point was normalized against the distance between the central point and the edge of each facial image. In each direction, the images were repositioned identically in the database.

3.2 Experiments using a holographic system

We performed a correlation experiment using a co-axial holographic memory system. The examples registered video image files are shown in Fig.2(a). The intensities of the correlation peaks are compared with the threshold for verification. Figure 2 shows the dependence of the recognition error rates on the threshold: (a) false-match rate and false non-match rate and (b) the correlation between identical images. The intersection of lines (a) represents the equal error rate (EER) (when the threshold is chosen optimally), and in this experiment an EER of 0% was achieved. This ultra high-speed system can achieve a processing speed of 25 microseconds/correlation at a multiplexing pitch of 10 micron and rotational speed of 300rpm.



(a) Frame image examples
 (b) Experimental results using holographic matched filter.

4 CONCLUSIONS

We have proposed a holographic video filtering system using a holographic correlator. Taking advantage of fast data processing capacity of FARCO, we explored the possibility of realizing high speed recognition system by registering the optimized video image file. The results demonstrated that the processing speed of our optical holographic calculation was remarkably higher compared to the conventional digital signal processing architecture.

ACKNOWLEDGMENTS

This study is partly supported by the Cooperative Program of Practical Application of University R&D Results Under the Matching Fund Method (R&D) of NEDO.

References

- [1] E. Watanabe and K. Kodate, Jpn. J. Appl. Phys., 45, 8B, 6759-6761 (2006).
- [2] Y. Ichikawa, E. Watanabe, M. Ohta and K. Kodate: POF&MOC 2006, p.156. (2006)
- [3] E. Watanabe and K. Kodate, Appl. Opt. 44, 666-676 (2005).
- [4] R. Inaba, E. Watanabe and K. Kodate, Opt., Rev. 10, 4, 255 (2003).
- [5] S. Ishikawa, E. Watanabe and K. Kodate, POF&MOC 2007 Technical Digest, G6, 130-131 (2007).
- [6] S. Ishikawa, E. Watanabe, M. Ohta and K. Kodate, 5th International Conference on Optics-photonics Design & Fabrication, 7PS4-49, 305-306 (2006).
- [7] H. Horimai, X. Tan, and J. Li, Appl. Opt. 44, 2575-2579 (2005).

Polarization and Random Phase Modulated Reference Beam for High-Density Holographic Recording with 2D Shift-Multiplexing

Sanjeev Solanki¹, Xuewu Xu¹, Minghua Li¹, Xinan Liang¹, and Tow-Chong Chong^{1,2}

¹Data Storage Institute, Agency for Science, Technology and Research, DSI Building, 5 Engineering Drive 1, Singapore 117608

²Optical Crystal Lab, Department of Electrical & Computer Engineering, National University of Singapore, 4 Engineering Drive 3, Singapore 117576

Phone: +65-68745089, Fax: +65-67778517

Sanjeev_solanki@dsi.a-star.edu.sg

1. Introduction

Holographic data storage [1-3] has become a viable technology in recent years with the commercial availability of enabling components like high-speed SLM, CMOS and compact laser source. One of the challenging tasks is to achieve Tb/in² and higher density by recording more holograms closer to each other reliably.

In this contribution we report how to achieve high areal density of >1 Tbits/in² using low capacity 4 Kbits data pages by combining shift [4], phase-coded [5] and reference beam polarization multiplexing together with reflection geometry. Polarization multiplexing allows either to record two holograms at same location or recording of one more hologram with orthogonal polarization at the middle of two holograms recorded with same polarization along both x-axis and y-axis, respectively. Reflection type of recording geometry allows the use of crystal media in disk-type architecture [6].

2. Experimental method and results

The holographic recording setup is shown in Figure 1., in which converging signal and diverging reference beams enter into recording Cu:Ce:Tb:CLN crystal media from opposite faces. The crystal media face was oriented to be perpendicular to reference beam and mounted on a high-resolution xyz stage with resolution of 0.1 μ m along all three axes.

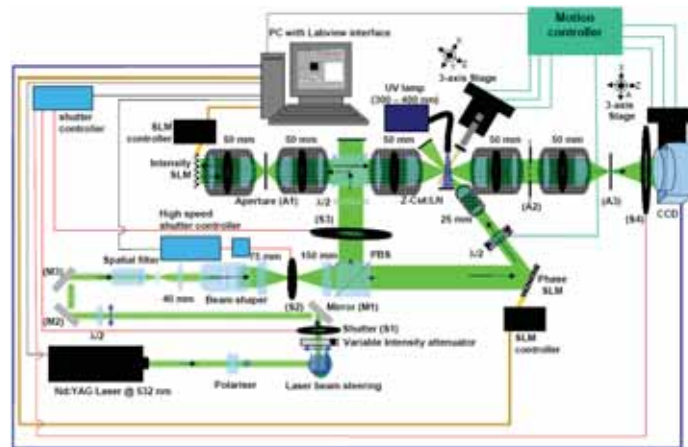


Fig. 1. Holographic recording setup.

The crystal media was sensitized for 20 minutes before recording holograms. The translation and rotation stages for media, CCD and wave-plate were controlled by PC interface. Shutters and laser were also controlled through same interface. The signal beam was focused into the recording media using a focal length of 50mm lens and the reference beam was focused 3mm before it entered into the crystal using a focal length of 25mm lens. The signal beam after passing through the crystal media was imaged onto CCD with pixel-to-pixel matching. The NA of

the signal and reference lenses was 0.16 and 0.27, respectively. Green recording wavelength at 532 nm from a Nd:YAG laser source at 200 mW output power was used for recording holograms.

The binary random phase-code and one of the 4 Kbits data pages are shown in Figure 2. Each bit corresponds to 16x16 pixels and each pixel is of size 8.1 μm . The central data carrying part (1024x1024 pixels) of SLM were imaged onto 2048x2048 pixels of CCD. The page detection was done by binning 2x2 pixels of CCD.

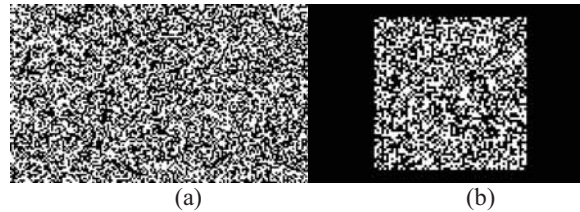


Fig. 2. Random phase-coded array for the reference beam (a), and data page with capacity of 4 Kbits for the signal beam.

One half wave-plate mounted to a rotation stage and placed between phase-SLM and 25mm lens to rotate the polarization of random phase-coded reference beam. First hologram with the capacity 4 Kbits was then recorded and the diffraction efficiency in terms of histogram area was measured with polarization of reference beam. Figure 3 shows the diffracted power with half wave-plate rotation angle. The minimum appears exactly at 45° rotation of wave-plate, which means at 90° rotation of polarization. Continuing rotation of wave-plate brought back the data page at 90° rotation.

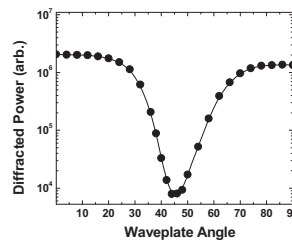


Fig. 3. Diffracted power measured with the rotation of waveplate.

At the location of minimum the hologram reconstruction completely disappears as can be seen in Figure 4 (a) and (b). Two holograms of capacity 4 Kbits data page were recorded next at same location and the reconstructions of both data pages are shown in Figure 4 (c) for data page recorded without rotation of wave-plate and in Figure 4 (d) for data page recorded with rotation of wave-plate by 45°.

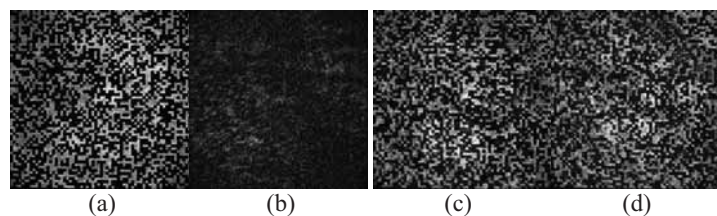


Fig. 4. Reconstructed one data page: (a) same polarization, (b) after 90° rotation; and reconstructed two data pages at same location: (c) same polarization, (d) after 90° rotation.

Next one hologram was recorded and the reconstruction of hologram was checked along x-axis at $\pm 1\mu\text{m}$ and along y-axis at $\pm 2.5\mu\text{m}$ without and with the polarization rotation. The results are shown in Figure 5 for $+1\mu\text{m}$ for x-axis and $+2.5\mu\text{m}$ for y-axis for both polarizations. Further, two new holograms were recorded at $+1\mu\text{m}$ along x-axis and $+2.5\mu\text{m}$ along y-axis relative to the location of first hologram recorded with reference beam polarization rotated by 90° relative to the polarization of first recorded hologram. The reconstructed holograms at $+1\mu\text{m}$ along x-axis and $+2.5\mu\text{m}$ along y-axis can be seen in Figure 6 (a) and (b), respectively.

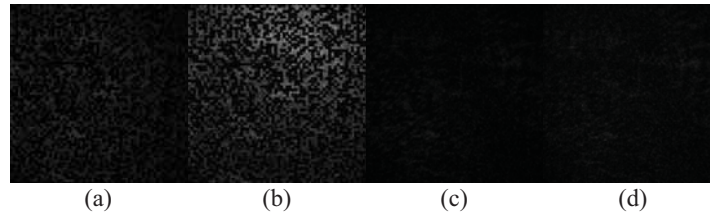


Fig. 5. Reconstructed one data page at (a) $+1\mu\text{m}$ along x-axis with same polarization, (b) $+2.5\mu\text{m}$ along y-axis with same polarization, (c) $+1\mu\text{m}$ along x-axis after 90° rotation and (d) $+2.5\mu\text{m}$ along y-axis after 90° rotation.

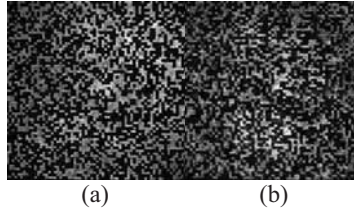


Fig. 6. Reconstructed data page recorded at (a) $+1\mu\text{m}$ along x-axis and (b) $+2.5\mu\text{m}$ along y-axis.

3. Discussion and conclusions

It is very important to develop robust approaches to achieve high density holographic recording. One of the solutions is to add more multiplexing parameters on reference beam to improve the selectivity of recorded hologram and record holograms closer with low noise.

Improving over work presented during ODS2007 [7], together with random phase-coded and shift-multiplexing, the polarization multiplexing is also implemented by modulating polarization of the reference beam into two orthogonal states. Two approaches to improve the recording density by two times or more are demonstrated. First approach includes recording two polarization-multiplexed holograms at one location that doubles the recording density. Second approach is to reduce the shift-selectivity along the x-axis and y-axis by recording alternate holograms along x-axis and y-axis with orthogonal polarizations. Using this approach the shift-selectivity between two recorded holograms with orthogonally polarized reference beams is half of the holograms that are recorded with same polarization.

Therefore, by adding polarization modulation of reference beam we are able to achieve the shift-selectivity of $1\mu\text{m}$ along x-axis and $2.5\mu\text{m}$ along y-axis and recorded hologram with these shifts shows no cross talk. Based on x- and y-axis selectivity of $1\mu\text{m}$ and $2.5\mu\text{m}$ and 4 Kbits of data page capacity the recording density of 1 Tb/in^2 is achievable.

5. References

- [1] L. Hesselink, S. S. Orlov, and M. C. Bashaw, "Holographic data storage systems", *Proc. IEEE*, **92**, 1231-1280 (2004).
- [2] H. Horimai, X. Tan, "Collinear technology for a holographic versatile disk", *Appl. Opt.*, **45**, 910-914 (2006).
- [3] K. Curtis, "Holographic Professional Archive Drive", ISOM conference October 2006, Kagawa Japan.
- [4] G. Barbastathis, M. Levene, D. Psaltis, "Shift multiplexing with spherical reference beam", *Appl. Opt.*, **35**, 2403-2417, (1996).
- [5] C. Denz, G. Pauliat, G. Roosen, T. Tschudi, "Phase-coded hologram multiplexing for high capacity data storage", *Opt. Commn.*, **85**, 171-176 (1991).
- [6] O. Matoba, Y. Yokohama, Masato iura, K. Nitta, T. Yoshimura, "Reflection-type holographic disk memory with random phase shift multiplexing", *Appl. Opt.*, **45**, 3270-3274 (2006).
- [7] S. Solanki, Xu. Xuewu, M. Li, X. Laing, T.C. Chong, "Random Phase 3D-Shift Multiplexing with Spherical Signal-Reference Waves in Reflection Geometry", *Proc. Of SPIE*, 6620, 66201D-6 (2007).

Rotational random phase multiplexing

Shih-Hsin Ma, Xuan-Hao Lee, Ye-Wei Yu, Tun-Chien Teng, and Ching-Cherng Sun*
 Department of Optics and Photonics, National Central University, Chung-Li 320, Taiwan

Phone : +886-3-4276240, E-mail : ccsun@dop.ncu.edu.tw

ABSTRACT

An out-of-plane rotational random phase multiplexing is proposed. The rotational sensitivity is enhanced and can be tuned over a large range. Thus, we can find out an optimum condition for both alignment tolerance and angular selectivity.

Keywords: rotational random phase multiplexing, holographic storage, ground glass

1. INTRODUCTION

Various multiplexing methods are applied to enlarge the capacity of volume holography optical storage [1], including random phase multiplexing. In this paper, we propose and demonstrate a new method to perform random phase multiplexing. In contrast to the previous random phase multiplexing with ground glasses, the proposed scheme is to perform out-of-plane rotation with a ground glass, and the characteristic is the selectivity of the volume holographic optical element is adjustable with change of the radius of rotation so that we can find out an optimum condition for both alignment tolerance and angular selectivity. The theoretical calculation as well as the corresponding experimental results is presented and demonstrated.

The proposed structure for rotational multiplexing by a ground glass is shown in Fig. 1. The ground glass will rotate out-of plane if the ground glass is just attached on the rotation center. Otherwise, if the ground glass is connected to the rotation center with a rod, the ground glass will move around a circular path around the rotation center when the stage rotates. A collimated light is incident on the ground glass, and the passing light serves as the reference beam in the writing process for constructing the grating, and another plane wave serves as the signal. In the reading processing, the light passing through the ground glass serves as the probe beam incident on the recorded medium. In the presented case, the ground glass is moved around the stage with a circular path with a radius equal to the distance between the ground glass and the rotation center of the stage. Since the length is adjustable so that the angular selectivity can be different. In development of the theory, we first regard the scattering lights from the ground glass as the lights emitted from a set of point sources across the ground glass. The initial phase of the point phase relates to the optical path length inside the ground glass. Since the surface variation of a ground glass is unpredictable, the distribution of the initial phase is assumed random across the ground glass. As shown in Fig. 2, the coordinates on the ground glass in the writing process and the reading process are denoted as (x_1, y_1, z_1) and (x_2, y_2, z_2) respectively, and the coordinates at the center of the recorded medium is denoted as (x_3, y_3, z_3) . Upon a rotational angle θ of the stage, the relation between the coordinates of the ground glass before and after the rotation can be written

$$x_2 = x_1 \times \cos \theta - (z_1 + \Delta z) \times \sin \theta,$$

$$y_2 = y_1,$$

$$z_2 = (z_1 + \Delta z) \times \cos \theta + x_1 \times \sin \theta, \quad (1)$$

where Δz is the distance between the ground glass and the rotation center of the stage, and here we call it the radius of rotation. Based on VOHIL (Volume hologram being integrator of light emitted from elementary light sources) model [2], the diffraction light can be written

$$D = \int_{-d/2}^{d/2} \int_{-d/2}^{d/2} \int_{-d/2}^{d/2} \int_{-d/2}^{d/2} \int_{-d/2}^{d/2} \frac{\cos \theta}{r_1 r_2} B \exp \{j\phi(x_2, y_2) - j\phi(x_1, y_1)\} \exp \{jk(z_2 - z_1)\} \exp \{jk(r_2 - r_1)\} dx_1 dy_1 dx_2 dy_2 dz_3, \quad (2)$$

where k is the wave number, d is the diameter of the beam width on the ground glass, θ is the rotational angle of the stage, $r_1 = \left\{ (x_3 - x_1)^2 + (y_3 - y_1)^2 + (z_3 - z_1)^2 \right\}^{1/2}$, and $r_2 = \left\{ (x_3 - x_2)^2 + (y_3 - y_2)^2 + (z_3 - z_2)^2 \right\}^{1/2}$, L is the thickness of the recording medium along diffraction light the and ϕ denotes the initial phase of the reference and the probe beams. Since the useful area of the ground glass in the reading process is the same as that in the writing, the area outside the useful area of the ground glass is set dark in the simulation. The simulation result of the rotational tolerance with respect to the radius of rotation is shown in Fig. 3, where the rotational tolerance is the rotation angle for the diffracted light intensity from the maximum (at Bragg condition) to the first zero. We find that the rotational tolerance dramatically decreases when the radius of rotation increases. The reason is that the increase of the length of the rod, the larger horizontal displacement is introduced, which is the most sensitive direction. [3-4] Fig. 3 also shows that we can tune the rotation tolerance in a large range, from several degrees to one thousandth degrees with adjusting the radius of the rotation.

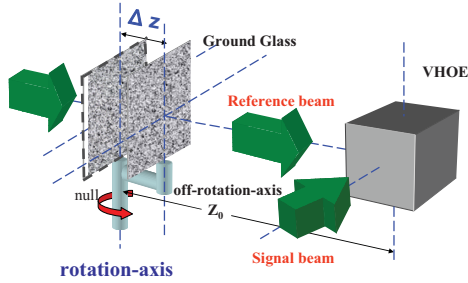


Fig. 1 Schematic diagram of the rotational random phase multiplexing.

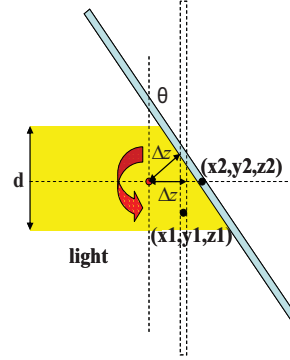


Fig. 2 Geometrical relation of the points on the ground glass before and after the rotation.

The experimental setup of the rotational random phase multiplexing is shown in Fig. 4. An Agron ion laser at 514.5 nm of Innova 300 made by Coherent Inc. was used as the coherent light source. After beam expanded and collimated, it was split into two parts. One was as the signal beam, and the other was the reference, which passed through a ground glass attached on a rotational stage through a rod. A Fe: LiNbO₃ in dimensions of 10×10×10 mm³ was used as the recording medium. The distance between the crystal and the ground glass (denoted z_0) was 10 cm. The diameter of the illumination on the ground glass was 10 mm. In the reading processing, the signal beam was blocked by a shutter, and the diffracted lights were incident on a detector with a power meter.

The intensity measurements with respect to the rotational angle in different radii of the rotation are shown in Fig. 5. The experimental measurements shown in Fig. 5 are close to the theoretical calculation. Since the light distribution across the ground glass is a factor associated with the accuracy of simulation, the measured light distribution on the ground glass was a parameter in the calculation.

The advantage of the presented scheme is that rotational sensitivity is adjustable. The presented experiment and simulation shows that the range of sensitivity is from 0.05° to 10° when z_0 is 10 cm and d is 10 mm. In the study of random phase encoding with a planar ground glass, the shorter distance or the larger illumination diameter on the ground glass may increase the Bragg selectivity so that the rotation selectivity is larger. The further simulation shows when z_0 is reduced to 5 cm, d is 10 mm, the rotational tolerance is 0.02°

for $\Delta z=5$ mm; when z_0 is kept 10 cm, and d is increased to 20 mm, the rotational tolerance is 0.03° for $\Delta z=5$ mm. The both cases show more sensitive in rotation.

This study was sponsored by the Ministry of Economic Affairs of the Republic of China with the contract no. 95-EC-17-A-07-S1-011 and the National Science Council with the contract no. NSC 96-2221-E-008-031. The authors would like to thank S. H. Lin and T. H. Yang for their comments on the study.

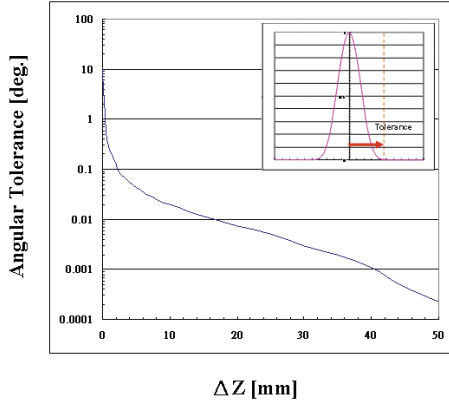


Fig. 3 Rotation tolerance vs. the radius of rotation when $d=10$ mm and $z_0=10$ cm.

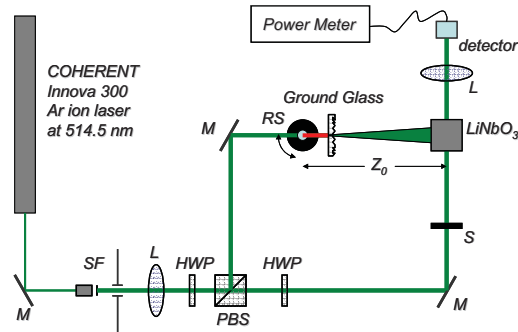


Fig. 4 The experiment setup. SF, spatial filter; L, lens; HWP, half-wave plate; PBS, polarized beam splitter; M, mirror; RS, rotational stage; S, shutter.

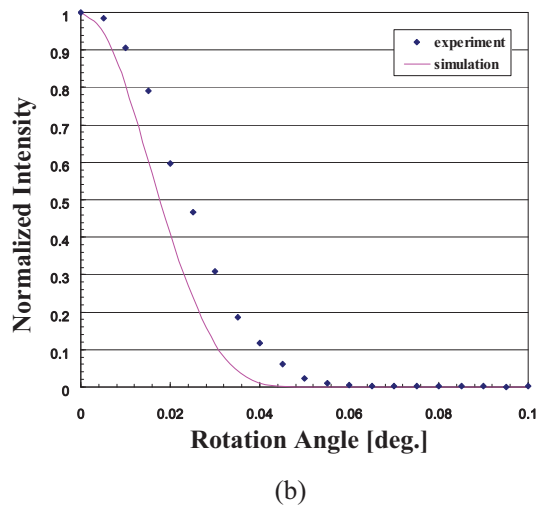
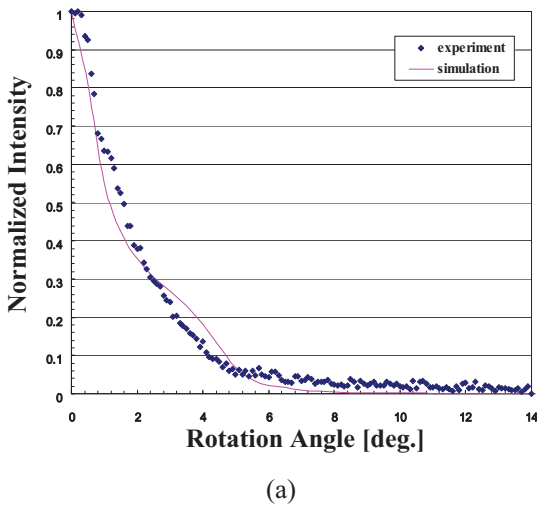


Fig. 5 Theoretical calculation (line) and the corresponding experimental measurement (dots) of the normalized diffraction intensity vs. rotation. (a) $\Delta z=0$. (b) $\Delta z=5$ mm.

REFERENCES

- [1] for example, G. Barbastathis and D. Psaltis, *Volume Holographic Multiplexing Methods*, in H. J. Coufal, D. Psaltis and G. T. Sincerbox, eds, *Holographic Data Storage*, Springer, 2000.
- [2] C. C. Sun, "A Simplified Model for Diffraction analysis of Volume Holograms," *Opt. Eng.* **42**, 1184-1185 (2003).

- [3] C. C. Sun, W. C. Su, B. Wang and Y. Ouyang, "Diffraction Sensitivity of Holograms with Random Phase Encoding," *Opt. Commun.* **175**, 67-74 (2000).
- [4] C. C. Sun, and W. C. Su, "Three-dimensional shifting selectivity of random phase encoding in volume holograms," *Appl. Opt.* **40**, 1253-1260 (2001).

Parallel realization of two-dimensional discrete Walsh transform in volume holographic storage system

Qiang Ma^{*a}, Kai Ni, Qingsheng He, Liangcai Cao, Guofan Jin

^a State Key Laboratory of Precision Measure Technology and Instruments, Tsinghua University, Beijing 100084 China, maqiang00@mails.tsinghua.edu.cn, +86-010-62781204

INTRODUCTION

Volume holographic storage, whose two most commonly noted advantages are its potential for large storage and high data rates, has generated widespread recent interest as a possible next-generation storage technology.

A volume holographic storage system (VHSS) can be considered as a multi-channel optical correlator based on high density holographic storage. It can parallelly perform correlation calculations of one input image with all the stored images which are recorded in a common volume of a crystal by angular multiplexing. The output of each calculation result is a side-lobe suppressed 2D correlation distribution surrounding its central point which represents the 2D inner product. When the distribution area is small enough, the correlation function over it can be integrated to approximate the inner product. There are several methods used to make the approximate more accuracy [1-4].

In this paper, a method that uses VHSS to parallelly perform 2D discrete Walsh transform (DWT) is suggested. Because of the characteristics of VHSS, the method has a possibility to reach a high processing rate. Furthermore, it has a flexibility to perform other orthogonal transforms.

PRINCIPLE

The 2D DWT of a data array $x_{i,j}$ of $N \times N$ points is [5]

$$X_{m,n} = \frac{1}{N^2} \sum_{i=0}^{N-1} \sum_{j=0}^{N-1} x_{i,j} WAL(m,n,i,j), \quad m,n = 0,1,\dots,N-1 \quad (1)$$

where $WAL(m,n,i,j)$ is the 2D Walsh function, and (m,n) is the order of it. Eq.(1) shows that $X_{m,n}$ is a data array with $N \times N$ points as well, and each element of $X_{m,n}$ is the inner product of $x_{i,j}$ and $WAL(m,n,i,j)$.

In VHSS, when the correlation distribution area becomes small enough by the use of speckle modulation [3], the diffraction field on the output plane can be expressed as

$$g(x_c = -x_m, y_c = -y_m) \propto \int dx_0 dy_0 f'(x_0, y_0) f_m(x_0, y_0), \quad m = 1, 2, 3, \dots \quad (2)$$

where $f'(x_0, y_0)$ is the input image, $f_m(x_0, y_0)$ is the stored image of the m th channel. Eq.(2) shows that the diffraction field of each channel is the inner product of $f'(x_0, y_0)$ and $f_m(x_0, y_0)$. Comparing Eq.(1) and Eq.(2) we have that the processing of inner products in DWT is similar to that in the VHSS. If $x_{i,j}$ and $WAL(m,n,i,j)$ are encoded to $f'(x_0, y_0)$ and $f_m(x_0, y_0)$ respectively, then VHSS can be used to perform the inner product of $x_{i,j}$ and $WAL(m,n,i,j)$.

The amplitude-modulation SLM which is used to upload images can only express nonnegative real quantities. In order to encode $WAL(m,n,i,j)$, it should be decomposed as

$$WAL(m,n,i,j) = WAL^0(m,n,i,j) + (-1)WAL^1(m,n,i,j) \quad (3)$$

where $WAL^0(m,n,i,j)$ and $WAL^1(m,n,i,j)$ are all nonnegative quantities. For simply, assuming $x_{i,j}$ to be nonnegative, Eq.(1) can therefore be expressed as

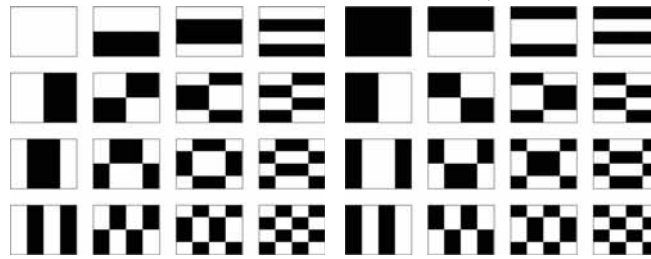
$$X_{m,n} = \frac{1}{N^2} [x_{i,j} \square WAL^0(m,n,i,j) - x_{i,j} \square WAL^1(m,n,i,j)] \tag{4}$$

where the symbol \square represents the inner product calculation.

For each order (m,n), $WAL^0(m,n,i,j)$ and $WAL^1(m,n,i,j)$, each of which has N^2 elements, can be encoded to two binary basis images $f_{m,n}^0$ and $f_{m,n}^1$ respectively. There are 16 Walsh functions when N=4. For example,

$$WAL(1,1,i,j) = \begin{bmatrix} 1 & 1 & -1 & -1 \\ 1 & 1 & -1 & -1 \\ -1 & -1 & 1 & 1 \\ -1 & -1 & 1 & 1 \end{bmatrix}, \text{ then } WAL^0(1,1,i,j) = \begin{bmatrix} 1 & 1 & 0 & 0 \\ 1 & 1 & 0 & 0 \\ 0 & 0 & 1 & 1 \\ 0 & 0 & 1 & 1 \end{bmatrix} \text{ and } WAL^1(1,1,i,j) = \begin{bmatrix} 0 & 0 & 1 & 1 \\ 0 & 0 & 1 & 1 \\ 1 & 1 & 0 & 0 \\ 1 & 1 & 0 & 0 \end{bmatrix}.$$

The 32 basis images that represent them are shown in Fig.1. Fig.1(a) are $f_{m,n}^0$, and Fig.1(b) are $f_{m,n}^1$.

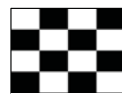


(a) (b)
Fig.1 basis images

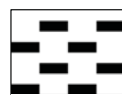
$x_{i,j}$ can be also represented by one binary data image f' . f' is divided into N^2 blocks as well. As the values of elements in $x_{i,j}$ are not only 0 and 1, here the ratio of white pixels to all pixels in each block is used to represent the normalized value of an element. Examples of two data images representing two different 4×4 data array $x_{i,j}$ are shown in Fig.2. Fig.2(a) represents

$$x_{i,j} = \begin{bmatrix} 1 & 0 & 1 & 0 \\ 0 & 1 & 0 & 1 \\ 1 & 0 & 1 & 0 \\ 0 & 1 & 0 & 1 \end{bmatrix}$$

$$x_{i,j} = \begin{bmatrix} 1 & 0.5 & 1 & 0.5 \\ 0.5 & 1 & 0.5 & 1 \\ 1 & 0.5 & 1 & 0.5 \\ 0.5 & 1 & 0.5 & 1 \end{bmatrix}$$



(a)



(b)

Fig.2 data images

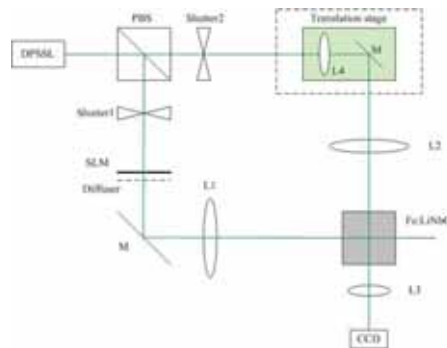


Fig.3 experimental setup

EXPERIMENT

The experiment setup is shown in Fig.3. A diode-pumped solid-state laser (DPSSL, $\lambda = 532\text{nm}$) is the light source. A holographic diffuser of 0.2° scattering angle used as a speckle modulation device [3] is inserted behind the SLM. The holographic recording material is a Fe:LiNbO₃ crystal. Multiple holograms are recorded in the crystal by angle multiplexing. A CCD camera (MINTRON MTV-1881EX) is used to read the output.

In the experiment, the 2D Walsh-ordered DWT of a 4×4 data array is performed. The 16 2D Walsh functions are decomposed respectively. The 32 basis images used to represent them are shown in Fig.1. Fig.2(b) shows the data image that represent the 4×4 data array to be transformed. To improve the accuracy of the inner product calculation, all the basis images and the data image are preprocessed by the use of 2D interleaving method [4].

The 32 interleaved basis images are stored into a common volume of the Fe:LiNbO₃ crystal by angle multiplexing. To perform DWT of the data array, the interleaved data image that represents it is input to VHSS, and the output read by the CCD is shown in Fig.4. The 32 output spots are corresponding to the 32 channels.



Fig.4 output spots

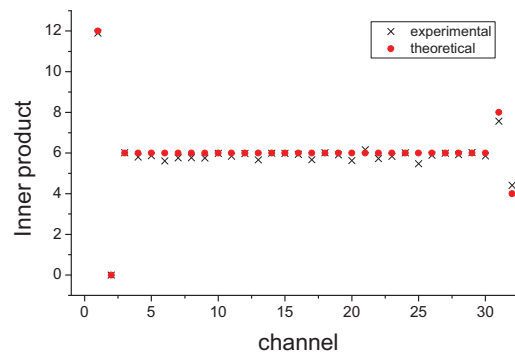


Fig.5 theoretical and experimental inner products

Fig.5 shows the theoretical and experimental inner products of the data array and the decomposed Walsh functions. The error is mainly caused by the nonlinearity and background noise of the CCD. The correspondence of theoretical and experimental results proves that the method can parallelly perform 2D DWT correctly.

CONCLUSION

The correspondency between the theoretical and experimental results shows that the VHSS can parallelly realize the DWT. Furthermore, orthogonal transforms which can be considered as a set of a data array and a series of orthogonal functions can also be realized by the method.

REFERENCES

1. Gu C, Fu H, Lien JR, "Correlation patterns and cross-talk noise in volume holographic optical correlators," J. Opt. Soc. Am. A **12**, 861 (1995).
2. Levene M, Steckman GJ, Psaltis D, "Method for controlling the shift invariance of optical correlators," Appl. Opt. **38**, 394 (1999).
3. Ouyang C, Cao LC, He QS, Liao Y, Wu MX, and Jin GF, "Sidelobe suppression in volume holographic optical correlators by use of speckle modulation," Opt. Lett. **28**, 1972 (2003).
4. K. Ni, Z. Qu, L. Cao, P. Su, Q. He, and G. Jin, "Improving accuracy of multichannel volume holographic correlators by using a two-dimensional interleaving method," Opt. Lett. **32**, 2972 (2007).
5. K. G. Beauchamp, *Walsh Functions and Their Applications* (Academic Press, 1975).

Phase only correlation for high speed image retrieval in holographic memories

Satoshi Honma¹, Akiyoshi Katsumata¹, Tohru sekiguchi², Shinzo Muto¹

1. Interdisciplinary Graduate School of Medicine and Engineering, Yamanashi University, Takeda, 4-3-11, Kofu, Yamanashi, 400-8511, Japan

2. NEC corporation Broadcast and Video Equipment div.,

Phone: +81-55-220-8412, Fax: +81-55-220-8412, Email: shonma@yamanashi.ac.jp

1. Introduction

High speed image retrieval and matching systems are expected to be developed for perception of objects and authentication systems using face images, fingerprints, iris freckles and finger veins. Holographic memories are promising technique to realize high capacity storage for next-generation storage system. One of the most remarkable functions is batch recording/readout of two-dimensional data. The disk type holographic memory has achieved 1-10Gbps transfer rate. Its characteristics have been used for some applications for high speed parallel processing technologies. For example, the face recognition system has potential to achieve operation speed of more than 100,000 faces/s¹.

Spatial information of phase as well as intensity can be recoded in the holographic materials. But only intensity information is, in general memories, used for data storage because it is difficult to detect the phase distribution. In this paper, we focus on that it is possible to record the phase distribution of light in the holographic memories and propose a new image matching system based on phase only correlation. The phase distribution corresponding to the reference images with Fourier transformation are preliminarily recoded in the holographic memory. The data are readout in sequence and these are inputted to a programmable phase modulator. After adding the phase distribution of the search objects on the reconstructed beam, we implement Fourier conversion via optical lens. We can obtain the correlation results with much shaper peak depending on the degree of similarity between the two image data using this technique comparing with that using conventional correlator. Our technique also make possible to perform multiple image matching. It will have a large increase in speed of image retrieval processing. We explain the principle of our technique and demonstrate on the basic image matching.

2. Phase only correlation for high speed image retrieval in holographic memories

The calculation process of cross-correlation is following. The object and reference image are given by $f(x,y)$ and $g(x,y)$, respectively. We calculate the 2D Fourier transformation of both images as

$$F(u,v) = \mathfrak{F}[f(x,y)] \quad G(u,v) = \mathfrak{F}[g(x,y)] \quad (1)$$

, where \mathfrak{F} denotes the Fourier transform. Then we calculate the cross-power spectrum by taking the complex conjugate of the second result, multiplying the Fourier transformation together elements

$$R = F(u,v)G(u,v)^* \quad (2)$$

, where the asterisk indicate the complex conjugate. Applying the inverse Fourier transform, we obtain the cross-correlation

$$r(x,y) = \mathfrak{F}^{-1}\{F(u,v)G(u,v)^*\} \quad (3)$$

Phase only cross-correlation is also calculated by

$$r_{POC}(x,y) = \mathfrak{F}^{-1}\left\{\frac{F(u,v)}{|F(u,v)|} \cdot \frac{G(u,v)^*}{|G(u,v)|}\right\} \quad (4)$$

The output result using phase correlation has much shaper peak corresponding to the degree of similarity of the two image data comparing with using normal correlation.

3. Phase cross-correlation with holographic memories

Fig. 1 shows the conceptual diagram of the phase correlation with holographic memories. In recording process, we previously calculate the phase distribution of 2D Fourier transform of the reference image $G(u,v)/|G(u,v)|$. The hologram is recoded by the writing beam 1 and 2 to which the phase distribution $G(u,v)/|G(u,v)|$ is given by the spatial light modulator (SLM). After that, the position or angle of the holographic media is changed, and then the phase data of the different reference images are recoded by repeating the same process.

In image matching process, the reading beam counter-propagating with the writing beam 2 is radiated to the memory. The reconstructed beam has the phase conjugated pattern $G(u, v) */ |G(u, v)|$. When the phase pattern corresponding to $F(u, v) / |F(u, v)|$ is displayed as the object data on SLM, the transmitted beam has the phase distribution $F(u, v) G(u, v) */ |F(u, v)| |G(u, v)|$. The phase only cross-correlation result between $f(x, y)$ and $g(x, y)$ is obtained by Fourier transformation via lens at the CCD camera. The hologram data are readout in sequence by shifting the recording media. We compare the peak intensity of the output signal at the camera with the threshold value for verification.

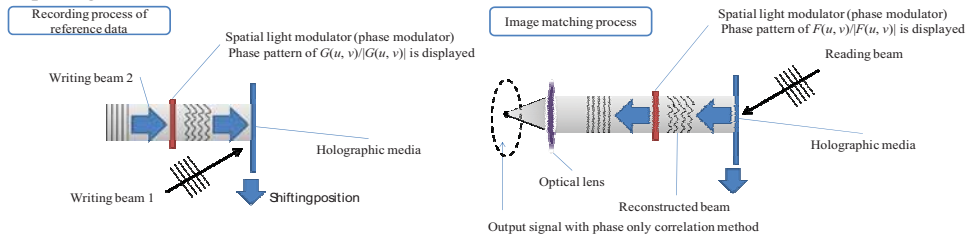


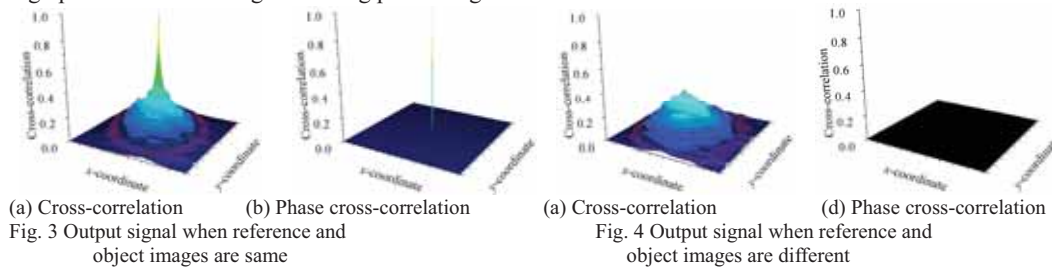
Fig. 1 Conceptual diagram of image correlator based on phase only correlation with holographic memories

4. Simulation of image matching processing

Fig. 2 shows the face images used in our simulation as the reference and input images. We extracted the facial part from each image and implemented edge extraction by using Laplacian filter. The output results of the cross-correlation $r(x, y)$ and the phase only cross-correlation $r_{POC}(x, y)$ calculated by Eq. (3) and (4) are shown in Fig. 3, where it is assumed that the reference image and input signal are same. We found that output signal had peak at $x=y=0$ as shown in both figures. Fig. 4 shows the correlation result in case that the reference image and signal image are different. The noise is generated in figure (a). On the other hand, the noise is not generated in figure (b). Obtaining the maximum value of output signal I_s and I_n of Fig. 3 and Fig. 4 respectively, we calculated the intensity ratio I_s/I_n about each correlation method. The intensity ratios were respectively 5 and 30 in case of normal correlation and phase only correlation. Comparing r_{POC} with r , the result using phase only correlation had much shaper peak depending on the degree of similarity between the two image data. The results imply that the phase only correlation method offer high performance of image matching processing.



Fig. 2 Example image of reference and object image for simulation and experiment



5. Experiment on image matching with phase correlation

The pixel size of the spatial modulator used in our experiment is not small enough. The optical noise outputs at the central position of the detector although the object image is different from the reference image. In order to extract the output signal from the noise, we add the lineally shifted phase distribution on the reference data. Fig. 5 shows the making process of the data. When the phase distribution of $\exp j(au+bv)$ is added on the reference data, the correlation signal outputs at $x=a, y=b$.

Fig. 6 shows the experimental setup. In the writing process, optical shutter SH_1, SH_2 were opened and SH_3 was closed. Here the polarization of the beam was not rotated by HWP_3 . The reference phase pattern was given on SLM. The hologram was recoded by the writing beam 1 and 2 in the photorefractive $LiNbO_3$ crystal. After that the position of the crystal was shifted and new hologram

corresponding to other reference data was recorded.

In the retrieval process, SH₃ was opened and SH₁ and SH₂ were closed. The angle of HWP₃ was rotated by 45[deg.]. The reading beam counter-propagating with the writing beam 2 reconstructed the recorded data as a phase conjugated beam. The reconstructed beam was reflected by SLM on which the phase distribution corresponding to the object data was displayed, and the beam transmitted through the optical lens was obtained at CCD camera.

Fig. 7 shows the output correlation results, where the phase distribution corresponding to (a) same recorded pattern $G(u, v)/|G(u, v)|\exp j(au+bv)$ (b) different pattern $H(u, v)/|H(u, v)|$ (c) phase pattern without phase code $G(u, v)/|G(u, v)|$ are given at SLM, respectively. We found that the noise was generated at the central position in figure (b) which is caused by low resolution of the SLM. Of course, the intensity was smaller than that of the output signal in figure (a). But the noise often causes failure of verification. We also found that the correlation signal could be obtained at side positions in figure (c). In this experiment, $a=\pi$ and $b=0$ are given as phase code.

6. Multiple image matching method

The output signal is almost 0 by phase-only correlation when the object and reference image are different as shown in Fig. 4. By using the property, we can make a reference data for some images. Fig. 8 shows the making process of the reference pattern for multiple image matching. Calculating Fourier transformation of each image and its phase pattern, we add the phase code having different values of a and b on it. The reference pattern is made of the summation of these phase patterns. In image matching process, using the reference pattern, the correlation results for each image outputs at different positions which is determined by value of a and b . The technique make possible to perform multiple image matching. The processing time will be improved by increasing the number of phase patterns multiplexed on a reference pattern.

7. Conclusions

We have demonstrated on the image matching processing based on phase only correlation using the holographic memory. We have shown the improvement of processing speed is achieved by multiplexing the phase distribution of the reference images on a hologram. In this experiment, we used the plane-wave for writing beam to record holograms. We also used shift-multiplexing technique in order to multiplex the reference holograms. When the technique is used, it is difficult to achieve high density recording. In future, we have to consider proper multiplexing technique of holograms.

References

1. E. Watanabe, M. Ohta, Y. Ichikawa and K. Kodate., ;Proc. of ISOM 2006, pp. 272-273 (2006)

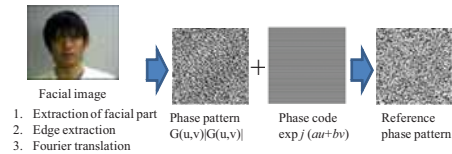


Fig. 5 Making process of reference data

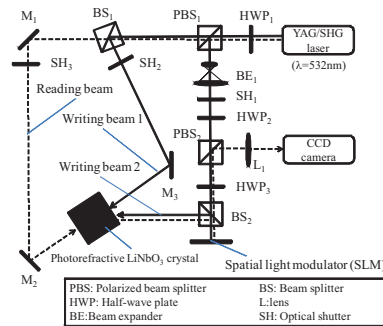


Fig. 6 Experimental setup

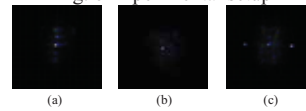


Fig. 7 Output result of correlator on CCD camera

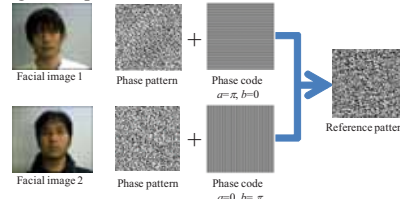


Fig. 8 Making process for multiple image matching process

Selective Erasure of Multiplexed Holograms Using Beam Amplification by Mutually Pumped Phase Conjugate Mirror

Takayuki Sano*^a, Atsushi Okamoto^a, and Kunihiro Sato^b

^a Grad. School of Information Science and Technology, Hokkaido Univ., Kita14-Nishi9, Kita-ku, Sapporo, 060-0814, Japan

Phone: +81 11 706 6522, Fax: +81 11 706 7836, E-mail: s_taka@optnet.ist.hokudai.ac.jp

^b Faculty of Eng., Hokkai-Gakuen University, Sapporo, Japan.

ABSTRACT

We propose a novel selective erasure of multiplexed holograms recorded in a photorefractive medium by using a MPPCM. We show the effective selective erasure can be realized by amplified phase conjugate beams due to the MPPCM.

Keywords: selective erasure, holographic memory, photorefractive, mutually pumped phase conjugate mirror

1. INTRODUCTION

Photorefractive materials, such as BaTiO₃ have been considered as suitable media for a rewritable holographic memory, which attracts much attention because of its high storage density and fast data access. The selective erasure is necessary and achieved by overwriting the π -phase shifted hologram on the recorded hologram for a rewritable holographic memory [1]. In conventional selective erasure method, a liquid-crystal phase modulator or a piezo-mirror is used for overwriting π -phase shifted hologram [2-3]. These methods require the high-precision alignment because the beams must be incident to the strictly same position. Furthermore, it is difficult to apply these methods to a removable holographic memory because the phase of the recorded hologram is not known.

We proposed the selective erasure for multiplexed holograms by using phase conjugator [4]. Two photorefractive crystals are used; one is a main memory and the other is a phase conjugator. In this method, the reading beam incident to the main memory and its reconstructed beam are returned to main memory by the phase conjugator. A phase conjugate beam automatically propagates through the same pass as the incident beam. Therefore, the selective erasure can be realized without the high precision alignment and the hologram recorded in removable holographic memory can be selectively erased. However, the efficient selective erasure cannot be realized by the method which is used four-wave mixing as a phase conjugator in Ref.4. This is because the intensity of the reconstructed beam is small and that of the phase conjugate beam becomes too small to erase the hologram selectively.

In this paper, we use mutually pumped phase conjugate mirror (MPPCM) as a phase conjugator. MPPCM can return the incident beam as a phase conjugate beam and amplify the phase conjugate beam by optimizing the intensity of the pump beams[5]. We show that the decay of other multiplexed holograms is reduced drastically by using MPPCM. In the analytical conditions, the decay is reduced by four times of the case using four-wave mixing.

2. SELECTIVE ERASURE USING MPPCM

The beams used in the selective erasure of one hologram works as the incoherent illumination for other multiplexed holograms. Figure 1 shows the analytical result of Q in the selective erasure process and the incoherent erasure process. Here Q is proportional to the depth of index grating induced by photorefractive effect. The hologram is recorded during $t=0-4$ [sec] and erased from $t=4$ [sec]. It is understood that other multiplexed holograms are slightly erased when the selective erasure process for a hologram is completed. In the selective erasure, it is required to reduce this decay of other multiplexed holograms. Then, we propose a new selective erasure method using a MPPCM.

Figures.2(a)-(b) shows the arrangement for selective erasure using a MPPCM as a phase conjugator. In this method, two photorefractive crystals are used: one is a main memory and the other is a phase conjugator. The direction of the c-axis of the main memory is set to the direction as the energy transfers from the object beam to the reference beam. In this condition, there is π -phase shift between the object beam O_n and the reconstructed beam O'_n .

In the recording process, the hologram is recorded in the main memory by the object beam O_n and the reference beam R_n as shown in Fig. 1(a). In the selective erasure process, the hologram to be erased is retrieved by the incidence of the reading beam R_n . There is a phase difference of π between the interference pattern formed by O_n and R_n , and that by the reconstructed beams O'_n and R_n . By returning the phase conjugate beams of O'_n and R_n to the main memory, the hologram is selectively erased.

In this method, a hologram is erased by the interference between O'_n and R_n , and O''_n and R'_n in the main memory. The decay of other multiplexed holograms is reduced by adjusting the intensity ratio of selective erasure beams to 1:1. However, when the multiplicity of the holograms increases, the diffraction efficiency of main memory becomes small and the intensity ratio of O'_n to R_n becomes worth. Therefore, the decay becomes large. Then, in this method, this decay is improved by amplifying the intensity of O''_n and R'_n by MPPCM. MPPCM can amplify the phase conjugate beam by adjusting the light intensity ratio of a forward pump to a backward pump beam. Furthermore, even when the propagation lengths of O'_n and R_n are changed, the relative phase between O''_n and R'_n can be kept constant in the main memory by a phase conjugator because phase conjugate beams are used as selective erasure beams.

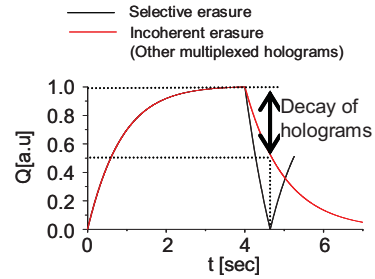


Fig.1 Selective erasure and incoherent erasure

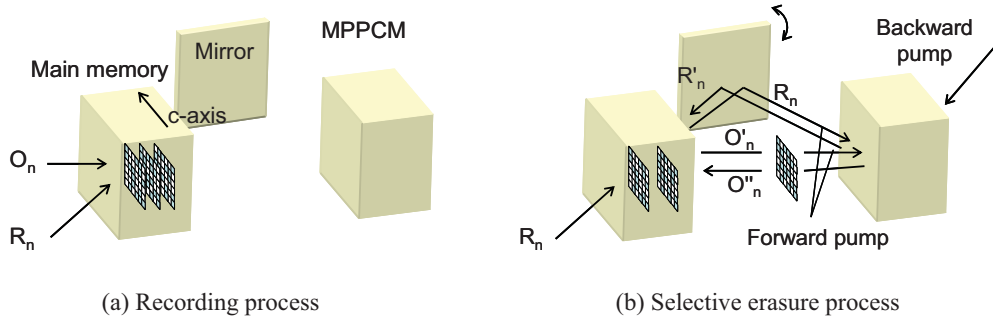


Fig.2 The arrangement for selective erasure using a MPPCM

3. ANALYSIS

We show the decay of other multiplexed holograms is reduced when the gain of MPPCM becomes large. Figure.3 shows the analytical model. In the analysis, we assume that a MPPCM is formed and the amplified phase conjugate beams are returned to the main memory. Furthermore, we assume that all the incident beams are extraordinary polarized plane waves, only the transmission grating is formed in the PRC, and the material absorption is negligible. Under these assumptions, the interactions between the beams are expressed by the following coupled-wave equations.

$$\frac{\partial A_1}{\partial z} = -Q A_2, \quad (1)$$

$$\frac{\partial A_2}{\partial z} = Q^* A_1, \quad (2)$$

$$\frac{\partial A_3}{\partial z} = Q A_4, \quad (3)$$

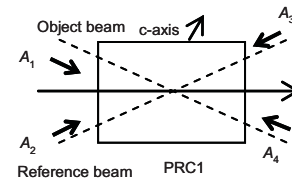


Fig.3 Analytical model

$$\partial A_4 / \partial z = -Q^* A_3, \quad (4)$$

$$\tau \partial Q / \partial t + Q = \gamma (A_1 A_2^* + A_3 A_4^*) / I_0. \quad (5)$$

A_j is the complex amplitude, τ is the time constant of the photorefractive crystal, I_0 is the total light intensity and γ_j is the coupling coefficient of the crystal. Q is proportional to the space charge field and means depth of index grating induced by the photorefractive effect. The boundary conditions in the recording process are given by

$$A_1(0) = 50[mW/cm^2], \quad (6)$$

$$A_2(0) = 50[mW/cm^2], \quad (7)$$

$$A_3(L) = A_4(L) = 0[mW/cm^2]. \quad (8)$$

The boundary conditions in the selective erasure process are given by

$$A_1(0) = 50[mW/cm^2], \quad (9)$$

$$A_2(0) = 0[mW/cm^2], \quad (10)$$

$$A_3(L) = G \times A_2(L), \quad (11)$$

$$A_4(L) = G \times A_1(L), \quad (12)$$

where G represents the gain of the MPPCM. The coupling efficiency is $300[m^{-1}]$ and the crystal thickness L is $5[mm]$.

Figure.4 shows the analytical results in the case of the gain of the MPPCM is 1.0. In this case, it is found that other multiplexed holograms decay to 20% when the selective erasure is completed. Figure.5 shows the decay of other multiplexed holograms when the selective erasure is completed in the case of changing the gain of MPPCM. When the gain is larger than 1.0, the improvement of the decay becomes large. In these analytical conditions, when the gain of MPPCM is larger than 10, we can reduce the decay of other multiplexed holograms to about 0.6.

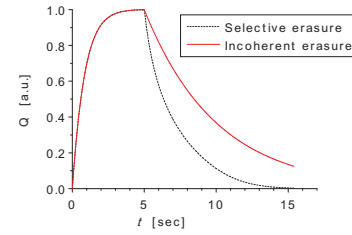


Fig.4 Selective erasure using MPPCM in the case of gain is 1.0

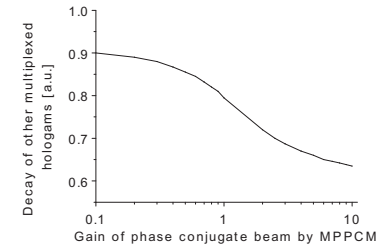


Fig.5 Decay of other multiplexed holograms in the case of gain of MPPCM is 0.1-10.

4. CONCLUSIONS

We proposed the selective erasure using beam amplification by MPPCM. The hologram is selectively erased without high precision alignment and this method enables to erase the hologram recorded in a removable holographic memory because of photorefractive effect and phase conjugate mirror. Furthermore, we analytically show the decay of other multiplexed hologram is reduced drastically by using MPPCM which has large gain. The gain of MPPCM is changed the coupling strength of photorefractive crystal. Therefore, in the future, if the photorefractive crystal which has large coupling strength is developed, our method will greatly contribute a practical use of a rewritable holographic memory.

REFERENCES

- [1] H.V. Alvarez-Bravo, L. Arizmendi, "Coherent erasure and updating of holograms in LiNbO₃," Opt. Mater. 4, pp.419-422, 1995
- [2] H.Sasaki, J.Ma, Y.Fainman, S.H.Lee, Y.Taketomi, "Fast update of dynamic photorefractive optical memory", Opt.Lett, vol.17, no.20, pp1468-1470, 1992.
- [3] Y.Taketomi, "Dynamics of a composite grating in photorefractive crystals for memory application," J. Opt. Soc. Am, A, vol. 11, No. 9, pp.2456-2470, 1994
- [4] T. Sano, A Okamoto, K. Sato, M. Bunsen, "Selective Erasure for Multiplexed Holograms in Photorefractive Crystal Using Phase Conjugator," JJAP, vol. 46, no. 6B, pp. 3822-3827, 2007
- [5] N. V. Bogodaev, V. V. Eliseev, L. I. Ivleva, A. S. Korshunov, S. S. Orlov, N. M. Polozkov, A. A. Zozulya, "Double phase-conjugate mirror: experimental investigation and comparison with theory," JOSA B, vol. 9, Issue 8, pp. 1493-1498, 1992.

Spatial Resolution of Phase-Modulated Signal Detection Method using Photorefractive Two-Wave Mixing for Holographic Data Storage

Masanori Takabayashi and Atsushi Okamoto

Graduate School of Information Science and Technology, Hokkaido University,

Kita 14-Nishi 9, Kita-ku, Sapporo, 060-0814, Japan

Phone: +81 11 706 6522, Fax: +81 11 706 7836, E-mail: takabayashi@optnet.ist.hokudai.ac.jp

1. INTRODUCTION

Holographic data storage is widely studied as next-generation optical memory after Blu-ray Disc. Holographic recording with two dimensional (2D) page data and hologram multiplexing at the same volume can achieve fast data rate and high recording density, respectively. The main ways to express the 2D page data include intensity modulation method and phase modulation method. In conventionally, the page data are modulated in intensity mode for geometric simplification. However the intensity-based system has some problems, such as the consumption of the recording material dynamic range for the reason of the existence of a strongly intense dc peak on the Fourier plane. To achieve the homogeneous intensity distribution on the Fourier plane, the use of phase masks [1] and phase-modulated signals [2, 3] are available. Especially the use of phase-modulated signals predominates because of the lossless of the light power on a spatial light modulator (SLM) whereas the light power of the dark pixels in the intensity-modulated signals is wasted. From these reasons the phase-based holographic data storage can achieve higher recording density and faster data rate than the intensity-based holographic data storage. However the phase-modulated signals cannot be directly detected by imagers without ingenuity.

We have proposed a phase-modulated signal detection method using photorefractive two-wave mixing (PR-TWM) [4, 5]. The reconstruction amplification in PR-TWM provides high energy efficiency. Furthermore alignment of position between the signal beam and pump beam is not required because the refractive index gratings are dynamically induced. In this paper, we characterize a spatial resolution of the phase-modulated signal detection method using PR-TWM. In the experiment, we visually evaluate the operation by shooting the picture of the output beam distribution with four patterns of pixel size. This evaluation allows us to make the connection between the pixel size of signal beam and the detection accuracy because the density and size of the reconstructed image is important in phase-only holographic data storage. If the spatial resolution of this system is revealed, the high density signal can be detected.

2. PHASE-ONLY HOLOGRAPHIC DATA STORAGE USING PHOTOREFRACTIVE TWO-WAVE MIXING

Figure 1 shows the schematic optical geometry of the phase-only holographic data storage system using PR-TWM. In reading process, a phase image is reconstructed from a holographic recording medium by illuminating a reference beam. To convert the phase image into the amplitude image, the transmitted reference beam and the reconstructed phase image is entered the PR medium which is located behind the holographic recording medium.

Photorefractive two-wave mixing is caused by an energy coupling between two beams. When two beams enter the PR medium, a refractive index grating with a spatial phase shift of $\pi/2$ is induced and then one beam is amplified [5]. After that the signal with phase difference of π enters, the output intensity of PR-TWM is reduced to 0. The schematic views of this phenomenon are shown in Fig. 2. To explain this phenomenon we assume a signal α and a signal β and the phase shift value between these two beams is π . Also, the induced refractive index grating by α and β is called g^α and g^β , respectively. When the signal α and the pump beam enter the PR medium, g^α is induced and α is amplified in a detector port. After that the signal β and the pump beam enter the PR medium, however, the signal β is not amplified in the detector port

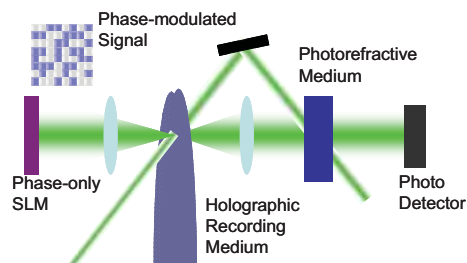


Fig. 1 Schematic optical geometry of phase-only holographic data storage using PR-TWM

because g^β have not been induced yet. Therefore the output intensity is drastically reduced by a destructive interference in the detector port. Subsequently the output intensity in the detector port is reduced to 0 when the amplitude of the transmitted signal β and that of the diffracted pump beam are balanced. Finally the signal β is amplified by g^β . In Fig. 3 (a), the temporal response of output intensity in PR-TWM with the phase shift of π is shown. Furthermore this theory can apply for detection of multi-levelled phase modulated signal because the output intensity in the detector port depends on the phase shift value of the signals. Also, the ratio of the intensity after the signal phase changing to the intensity before the signal phase changing is proportional to cosine function [6, 7] as shown in Fig. 3 (a).

Consequently, we can not only distinguish where the signal phase changes but determine its phase shift value by observing the output intensity in PR-TWM [4]. In addition, the detection accuracy tends to be progressed in the case that time-domain over sampling for holographic reconstruction rates are used.

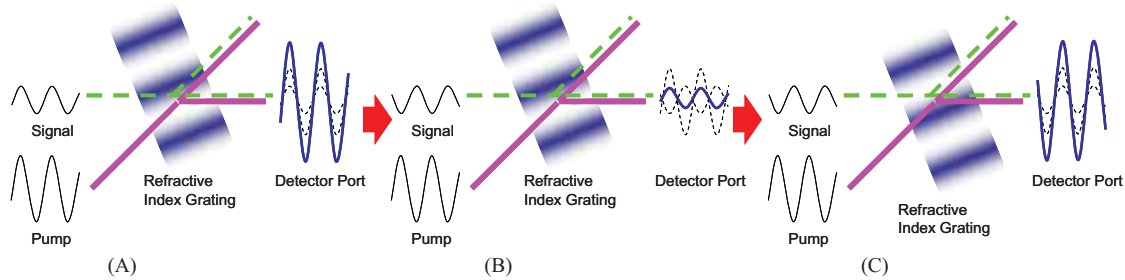


Fig. 2 The principle of phase-modulated signal detection method using PR-TWM.

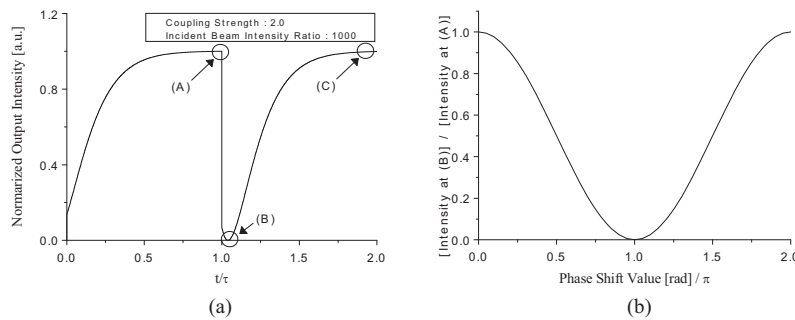


Fig. 3 (a) Time response in PR-TWM with phase change of π at $t/\tau=1$. (b) The relationship between contrast (Intensity at (B)/ Intensity at (A)) and phase shift value at $t/\tau=1$.

3. EXPERIMENT

Figure 4 shows experimental setup for evaluation of spatial resolution in phase-modulated signal detection method using PR-TWM. In this experiment we clear up the spatial resolution, how small pixels can we detected in our method. The beam from Ar^+ laser is split into a signal beam and a pump beam. Then the signal beam is modulated in phase mode on the SLM. The phase-modulated signal beam and the pump beam enter a $BaTiO_3$ crystal. The chessboard-like patterns were provided as the signals. In the detector port, the intensity distribution at $t=T_c$ was measured, where T_c is the time signal was changed. We demonstrated proof-of-principle

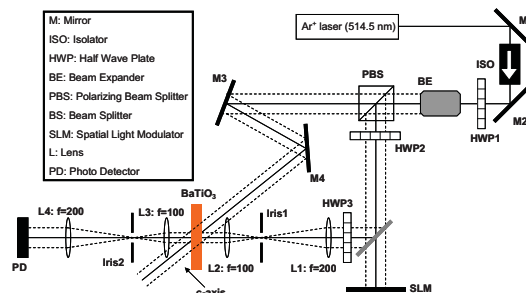


Fig. 4 Experimental setup

experiments with the different pixel sizes, $7*7\text{mm}^2$, $2.3*2.3\text{mm}^2$, $1.3*1.3\text{mm}^2$ and $0.28*0.28\text{mm}^2$. Here, the intensity ratio $I_{\text{pump}}(0)/I_{\text{signal}}(0)$ was 125 and the PR coupling strength γL was 1.5.

The results are shown in Fig. 5 (A). Here the intensity nonuniformity was caused by the defect of the PR crystal. We could confirm the intensity reduction in each case. The spatial resolution of this system probably depends on that of PR-TWM. However one of the problems of phase-modulated signals includes the edge lacking effect as shown in Fig. 5 (B). The edge lacking effect is caused by the destructive interference between neighboring pixels when these pixels have phase difference. As the pixel size is smaller, the influence of this effect becomes severe. Therefore the spatial resolution of phase-modulated signal detection method is worse than that of PR-TWM. Nonetheless, we could evaluate the phase detection of a few hundreds micrometers of pixel in this experiment. The phase detection of smaller pixels will also be achievable.

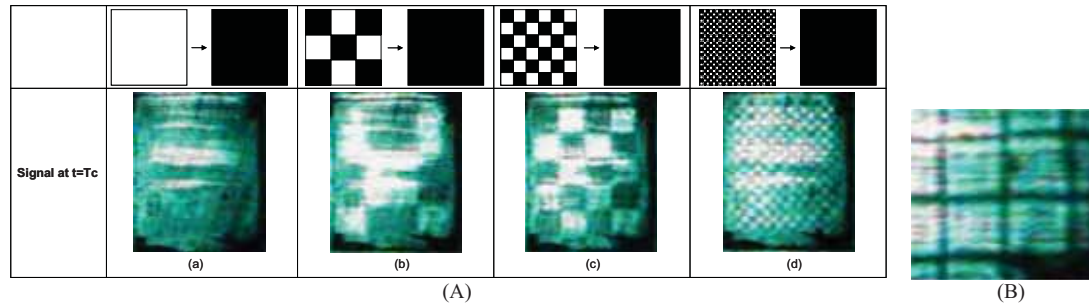


Fig. 5 (A) Results of the experiment. (a) $7*7\text{mm}^2$. (b) $2.3*2.3\text{mm}^2$. (c) $1.3*1.3\text{mm}^2$. (d) $0.28*0.28\text{mm}^2$. (B) Edge lacking effect

4. CONCLUSIONS

We characterized the spatial resolution of the phase-modulated signal detection method using PR-TWM. By shooting the picture of the output beam distribution with four patterns we confirmed the operation of a few hundreds micrometers of pixel. In principle, the operating condition of this method is independent of the pixel sizes of the reconstructed signal because each pixel is independently detected in this method. In practical system, however, the spatial resolution is restricted by two reasons. One is the beam fanning in the PR medium which causes the degradation of the spatial resolution of this method. The beam fanning can be attenuated by the lower PR coupling strength, while the detection accuracy is affected. The other is the edge lacking effect. The spatial resolution of phase-modulated signal detection method is inferior to that of PR-TWM by this effect. We can solve this problem by using larger PR medium.

5. REFERENCES

- [1] C. B. Burckhardt, "Use of a Random Phase Mask for the Recording of Fourier Transform Holograms of Data Masks," *Appl.Opt.* **9**, 695 (1970).
- [2] J. Joseph, D. A. Waldman, "Homogenized Fourier transform holographic data storage using phase spatial light modulators and methods for recovery of data from the phase image," *Appl.Opt.* **45**, 6374 (2006).
- [3] P. Koppa, "Phase-to-amplitude data page conversion for holographic storage and optical encryption," *Appl.Opt.* **46**, 3561 (2007).
- [4] M. Takabayashi, A. Okamoto, and T. Ito, "Time-domain differential detection using photorefractive two-wave mixing in phase-only holographic data storage system," *The 7th Pacific Rim Conference on Lasers and Electro-optics (CLEO/Pacific Rim 2007)*, no.ThP_091, Seoul, Korea (2007).
- [5] P. Yeh, *Introduction to Photorefractive Nonlinear Optics*, (Wiley, 1993).
- [6] T. R. Moore, et al, "Holographic interferometer with photorefractive recording media," *Appl.Opt.* **37**, 5176 (1998)
- [7] M. Sedlatscek, et al, "Differentiation and subtraction of amplitude and phase images using a photorefractive novelty filter," *Appl.Psys.B.* **68**, 1047 (1999)

Micro-integrated r/w-head for WORM-type holographic data storage

Matthias Gruber*, Udo Vieth

Opt. Microsystems Group, University of Hagen, Universitaetsstr. 27, 58097 Hagen, Germany

ABSTRACT

The micro-integration of setups for write-once-read-many-type volume holographic data storage is discussed and a particular r/w-head architecture based on planar-integrated free-space optics is proposed.

Keywords: holographic data storage, micro-optics, planar integration

1. INTRODUCTION

Volume holographic storage approaches for digital data have several characteristic features that are of high interest for high-volume and high-speed information processing applications. Due to the truly 3-dimensional nature of the method a very high storage capacity and density can be achieved. In addition, parallel, page-oriented and optionally associative (i.e. content-addressable) data access is possible^{1,2}. In recent years, many of the technological problems concerning suitable storage materials and laser light sources have been solved with the consequence that a commercial use of the holographic storage principle is imminent³. Suitable commercial devices have to be sufficiently robust and compact, and need to have a reasonable price. MEMS-type micro-integration approaches have the potential to satisfy these requirements. After a short general discussion of this issue from the perspective of optical systems design we propose a particular r/w-head architecture based on planar integration for write-once-read-many-type (WORM-type) volume holographic data storage.

2. HOLOGRAPHIC DATA STORAGE AND RETRIEVAL

Basically, holographic data storage and retrieval works as depicted in Fig. 1. A laser beam is encoded with the information to be stored, relayed as signal beam S to the holographic storage medium, and superimposed with a reference beam R to generate an interference pattern that is recorded in form of a hologram. The stored information is retrieved by using the very same reference beam R as address beam. Diffraction from the hologram will then regenerate the original signal beam S. For digital data storage applications volume holography is usually employed, due to its high Bragg selectivity this method enables multiplexing and thus a high storage density.



Fig. 1. Conventional holographic recording and read-out process; writing and reading operation are unidirectional.

Holography as depicted in Fig. 1 can obviously be considered as a unidirectional method in the sense that data are transferred into the storage medium on one side and retrieved from it from the opposite side. This may be a practical advantage in laboratory experiments because hardware components used for "writing" and "reading" can be separated, there is enough space, and functional contentions are unlikely. However, due to the high Bragg sensitivity, optical components on both sides need to be (kept) adjusted very accurately, which is undesirable for a commercial device.

The mechanical complexity of a holographic r/w-head can be lower and the setup more compact if a bidirectional systems approach is used, i.e. writing and reading is carried out from the same side. Two possibilities to achieve this are shown in Fig. 2. The more general approach is to use a phase-conjugating mirror PCM. Using the phase-conjugate version R^* of the original reference beam R as address beam will generate the phase-conjugate version S^* of the signal beam, which propagates in the opposite direction of S. A simpler alternative is based on a conventional mirror. It is

equivalent to the PCM approach if a suitable reference wave form (e.g. plane waves) is used and if the system is perfectly adjusted such that R' becomes the counter-propagating version of the reference beam used during recording.

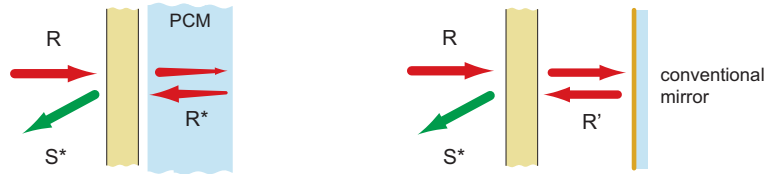


Fig. 2. Writing and reading operation are bidirectional if a (true or effective) phase-conjugate mirror is used for read-out.

An additional advantage of the bidirectional PCM approach is that optical aberrations in the signal beam are irrelevant since they are reversed and disappear through the read-out operation. Now we present a micro-integrated system architecture that implements the PCM approach for holographic data storage and retrieval; it adopts the design concept of planar-integrated free-space optics (PIFSO).

3. PLANAR-INTEGRATED FREE-SPACE OPTICS

The idea of PIFS⁴ is to miniaturize and "fold" a free-space optical system with a certain desired functionality into a transparent substrate of a few millimeters thickness in such a way that all optical components fall onto the plane-parallel surfaces. Passive components like lenses or beam deflectors can then be integrated into the surfaces, for example through surface relief structuring, the implementation as diffractive optical components offers an almost unlimited design freedom. Active components like optoelectronic I/O devices can be bonded on top of the plane-parallel substrates. Reflective coatings ensure that optical signals propagate along zigzag paths inside the substrate. Since all passive components are arranged in a planar geometry the optical system can be fabricated as a whole using mask-based techniques. Lithographic precision for the lateral positioning of components is thereby ensured.

Due to the monolithic integration into a rigid substrate the optical system remains perfectly adjusted and long-term stable and it is well protected against disturbing environmental influences. The application of replication techniques and the use of plastic substrate materials allow one to keep the fabrication cost of PIFS⁴ systems potentially low.

4. PLANAR-INTEGRATED R/W-HEAD

We apply the PIFS⁴ principle for the construction of a read/write head for holographic storage disks⁵. Fig. 2 shows the proposed bidirectional Fourier optical system architecture in the recording and the read-out mode. The designated storage material is a novel photopolymer, phenanthrene-quinone-doped polymethylmethacrylate (PQ:PMMA)⁶, that allows one to fabricate disks of nearly arbitrary size and thickness with a comparatively low technological effort.

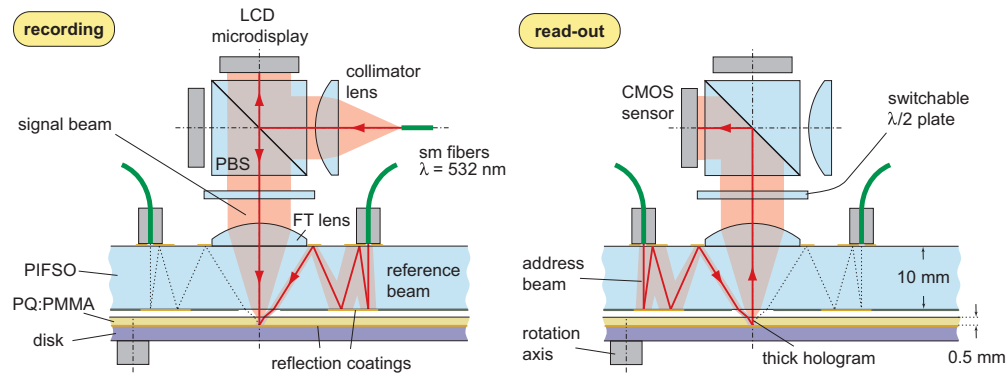


Fig. 3. Schematic setup of the PIFS⁴-type reflection holographic r/w-head depicting it in the recording and in the read-out mode. Reference and address beam are exactly counter-propagating along zigzag paths inside the PIFS⁴ substrate. The FT lens performs an optical Fourier transformation from the LCD and the CMOS sensor to the holographic layer on the storage disk.

One can recognize an orthogonal signal beam and skew reference and address beam paths that intersect at a target position on the reflective lower side of the photosensitive layer of the storage disk in which the hologram is recorded. All beams originate from the same laser source from which they are coupled into the PIFSO system by single-mode optical fibers. The relay of the signal beam from the fiber end to the disk is carried out by a 4-f system; in its Fourier plane the expanded beam is 2-D spatially modulated by a LCD micro-display. To be able to record a complete signal page without loss the diameter of the reference beams has to be matched to the width of the signal spectrum at the disk. Reference and address beam are furthermore perfectly collimated and counter-propagating so that they can be considered as mutually phase-conjugate. Hence, if the reference beam is used for the recording of a hologram then a read-out with the address beam will generate the phase-conjugate version of the original signal beam; this reconstructed beam propagates through the 4-f system in opposite direction and is projected onto a CMOS sensor.

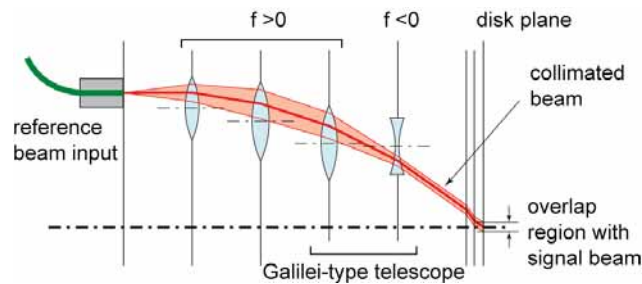


Fig. 4. Unfolded version of the optical system that relays the reference beam to the holographic disk. The four lenses effectively implement a collimator and a Galilei-type telescope in series.

The reference/address beam relay is carried out by an assembly of diffractive lenses that are operated off-axis to achieve a beam inclination of 30 degrees. From Fig. 4, which depicts an unfolded version of this optical subsystem, one can recognize that the beam width is adjusted by a Galilei-type telescope formed by the two lenses next to the disk plane.

REFERENCES

- [1] P. J. van Heerden, "Theory of optical information storage in solids," *Appl. Opt.* 2, 393-400 (1963).
- [2] D. Psaltis and F. Mok, "Holographic memories," *Sci. Am.* 273, 70-76 (1995).
- [3] D. Sarid, B. H. Schechtman, "A roadmap for optical data storage applications," *Optics & Photonics News* 18, 34-37 (2007).
- [4] M. Gruber, J. Jahns, "Planar-integrated free-space optics – from components to systems", Ch. 13 in: J. Jahns, K.-H. Brenner (Eds.), *Microoptics—from technology to applications*, Springer, New York (2004).
- [5] M. Gruber, U. Vieth, K.-Y. Hsu, S.-H. Lin, "Design of a planar-integrated r/w-head for holographic data storage," *Proc. DGaO* (2007), http://www.dgao-proceedings.de/download/108/108_p47.pdf
- [6] S. H. Lin, Y.-N. Hsiao, P.-L. Chen and Ken Y. Hsu, "Doped poly(methyl methacrylate) photopolymers for holographic data storage," *J. Nonlin. Opt. Phys. and Mat.* 15, 239-247 (2006).

Simulation technique for diffraction efficiency characteristics in holographic data storage system based on FFT-BPM

Junya Tanaka, Atsushi Okamoto, and Motoki Kitano

Graduate School of Information Science and Technology, Hokkaido University, N14-W9, Kita-Ku, Sapporo, 060-0814, Japan, phone: +81-11-706-6522, Fax: +81-11-706-7836

E-mail: j-tanaka@optnet.ist.hokudai.ac.jp

1. INTRODUCTION

Holographic data storage system (HDSS) [1] is expected to be a next generation optical data storage system because it is capable of achieving a high storage density and high data transfer rate. But various requirements have been left in order to realize HDSS. One of them is the establishment of a 3-dimensional simulation method for the diffraction efficiency characteristics. Kogelnik's Coupled-Wave Analysis (CWA) [2] and Rigorous Coupled-Wave Analysis (RCWA) [3] have been used to analyze for the diffraction efficiency characteristics in HDSS. They can accurately solve for a simple holographic grating. However, in a practical HDSS, holograms are recorded as 3-D interference fringes of a signal beam which has a 2-D data page and a reference beam, and many holograms are multiplexed in the same position of a recording medium. Therefore, the recording medium has a complex 3-D holographic grating and these methods can not solve for them.

In this paper, we propose a new simulation method based on Fast Fourier Transform-Beam Propagation Method (FFT-BPM) [4] to analyze in HDSS. This is a methods applying Fast Fourier Transform (FFT) toward the propagation direction of the beam. It is able to calculate an inhomogeneous refractive-index distribution and apply in the simulation of the various recording method in HDSS. Consequently, FFT-BPM is the very effective method to analyze in HDSS. It also has great advantages compared with Finite-Difference Time-Domain Method (FDTD-Method) [5] because it can simulate a more extensive analytic region and practical parameter.

We select an angular-multiplexing from the several recording methods in HDSS and analyze for the diffraction efficiency characteristics in an angular multiplexing holographic memory. We record the three 2-D data pages which have "H", "D", and "S" by illuminating the reference beam at three difference angles. We show that each recorded image is reproduced when the readout beam illuminates at the same angle in recording and as the angle of the readout beam is shifted from recording angles, the image gradually fade away.

2. SIMULATION MODEL

In this analysis, we defined the angle of the readout beam as θ_2 and calculate the diffraction efficiency characteristics. The Analysis model and simulation flow are shown in Fig.1, Fig.2.

We applied the plane wave expansion (PWA) to the calculation of wave front of the beam in a homogeneous medium. In an inhomogeneous medium, we calculate it by FFT-BPM. There are four steps in FFT-BPM.

Step1. The spectrum function $\tilde{\phi}(u, v, z_0)$ is represented by FFT of the complex amplitude $\phi(x, y, z_0)$ as

$$\tilde{\phi}(u, v, z_0) = \int_{-\infty}^{\infty} \int_{-\infty}^{\infty} \phi(x, y, z_0) \exp[-j2\pi(ux + vy)] dx dy \quad (1)$$

Step2. The spectrum function $\tilde{\phi}(u, v, z_0 + \Delta z/2)$ is calculated by the effect of propagation in the homogeneous medium as

$$\tilde{\phi}(u, v, z_0 + \Delta z/2) = \phi(u, v, z_0) \exp\left(-jk\Delta z/2 \sqrt{1 - (\lambda_e u)^2 - (\lambda_e v)^2}\right) \quad (2)$$

where $k = 2\pi/\lambda_e$, u and v must be satisfied in the range $(\lambda_e u)^2 + (\lambda_e v)^2 \leq 1$.

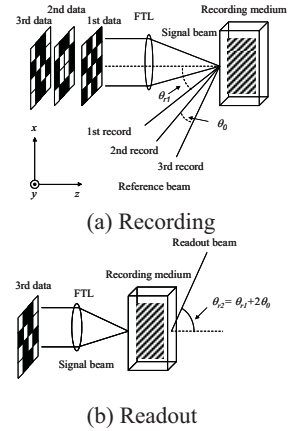


Fig.1. Schematic diagram of angular-multiplexing in HDSS.

Step3. The complex amplitude $\phi(x, y, z_0 + \Delta z / 2)$ is obtained by inverse FFT of equation (2) and the multiplication of phase shift $\exp(-jk_0 \Delta n \Delta z)$ as

$$\phi(x, y, z_0 + \Delta z / 2) = \int_{-\infty}^{\infty} \int_{-\infty}^{\infty} \tilde{\phi}(u, v, z_0 + \Delta z) \exp[j2\pi(ux + vy)] du dv \times \exp(-jk_0 \Delta n \Delta z) \quad (3)$$

Step4. The spectrum function $\tilde{\phi}(u, v, z_0 + \Delta z)$ is obtained by FFT of equation (3) and the effect of propagation in the homogeneous medium.

Therefore, the beam distribution in the inhomogeneous medium is given by repeating their steps at all z .

In the first recording, the interference fringes of the signal beam and reference beam are recorded as the refractive-index distribution $n_1(x, y, z)$.

In the Nth recording ($N=2, 3, \dots$), the propagation of the signal beam and reference beam in the recording medium which has $n_{N-1}(x, y, z)$ is calculated by FFT-BPM, and $n_N(x, y, z)$ is obtained. For the calculation of the refractive-index distribution, it is saturated exponentially with exposure energy so that we assumed a photopolymer as the recording medium and is given by

$$n(x, y, z) = n_{\max} \left\{ 1 - \exp\left(-\frac{I(x, y, z) \cdot t}{E_{\text{sat}}}\right) \right\} \quad (4)$$

where n_{\max} is the depth of refractive-index, $I(x, y, z)$ is the light intensity [W/cm^2], t is the exposure time [s], E_{sat} is the saturation energy flux density [J/cm^2].

In the readout, the propagation of the readout beam in the recording medium having $n_N(x, y, z)$ is calculated by FFT-BPM and the signal beam is obtained by the diffraction of the readout beam as the output image.

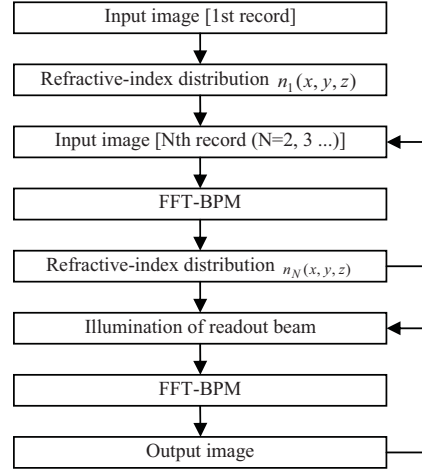


Fig.2. Simulation flow.

3. ANALYSIS

3.1 Angular selectivity by the plane wave

To confirm the fundamental angular selectivity in the angular-multiplexing, we used the plane wave as the signal beam and reference beam before using the 2-D data page. First, we recorded the single hologram by illuminating the signal beam and reference beam at $\theta_s = -10^\circ$ and $\theta_{r1} = 10^\circ$, respectively, and compared with Kogelnik's CWA. Figure.3 shows that the signal beam is obtained by the diffraction of the readout beam. Figure.4 shows that the diffraction efficiency decreases with the form of sinc function as θ_{r2} shifting from θ_{r1} and nearly corresponds with CWA. The peak of the diffraction efficiency is obtained at $\theta_{r2} = 10^\circ$, which is the same angle in the recording. Next, we recorded the three holograms at $\theta_s = -10^\circ$ and $\theta_{r1} = 10^\circ, 12.5^\circ, 15^\circ$. Also, we plotted for several values of dz to examine the difference of the calculation results, where dz is the step size of the beam propagation direction. In Fig.5, the peak of the diffraction efficiency is obtained at $\theta_{r2} = 10^\circ, 12.5^\circ, 15^\circ$, the magnitudes of the diffraction efficiency did not obtain at $dz = 20\mu\text{m}$, accurately. This is thought that the spatial frequency on z direction is increasing by illuminating the reading beam at difference angles in recording.

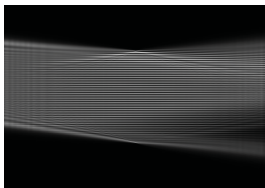


Fig.3. Diffraction of the readout beam.

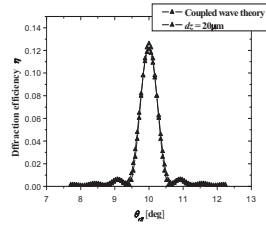


Fig.4. Diffraction efficiency characteristics in the single recording.

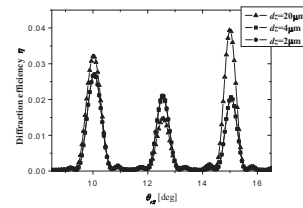


Fig.5. Diffraction efficiency characteristics in three multiplexing.

3.2 Angular selectivity by 2-D data page

We recorded the three 2-D data pages which have “H”, “D”, and “S” by illuminating the signal beam and reference beam at $\theta_s = 0^\circ$ and $\theta_l = 8^\circ, 9.25^\circ, 10.5^\circ$, respectively, and showed the angular selectivity. Figure.6 shows the diffraction efficiency characteristics as well as using the plane wave. The peak of diffraction efficiency corresponded with the recording angles. In the other angles, the diffraction efficiency decreases severely. Figure.7 shows that “H”, “D”, and “S” are reproduced selectively according to the diffraction efficiency characteristics in Fig.6, visually. The image appeared clearly at $\theta_r = 8^\circ, 9.25^\circ, 10.5^\circ$. As the angle of the readout beam is shifted from recording angles, the image is gradually faded away and next the image appears. We can calculate the correlation between the each data page and determine the minimum separation angle in the angular multiplexing from this result.

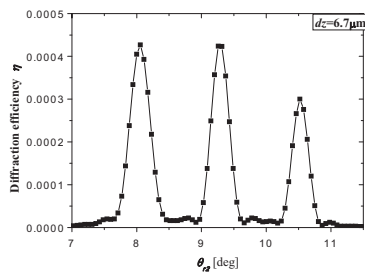


Fig.6. Diffraction efficiency characteristics in recording 2-D data pages.

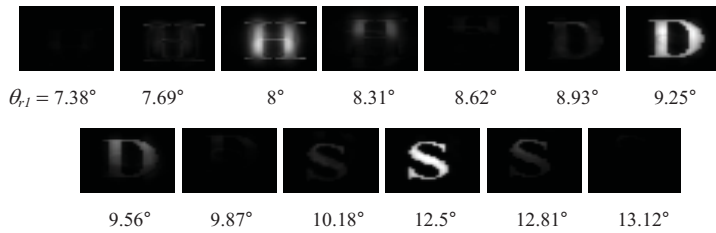


Fig.7. Result that the 2-D data pages is reproduced selectively.

Wavelength(λ)	514.5 μ m
index(n_0)	1.5
refractive index modulation depth(Δn)	4.0×10^{-3}
Medium Size($W_x \times W_y \times W_z$)	617 \times 617 \times 800 μ m
Oversampling ratio(N_1)	4
Zero-padding ratio(N_2)	4
Intensity ratio(I_{sig}/I_{ref})	3
Number of pixel($N_{px} \times N_{py}$)	32 \times 32
Pixel size($l_{px} \times l_{py}$)	20 \times 20 μ m
focal length(f)	6.0×10^{-3}
Total recording power(P_{in})	1mW
Exposure time(t)	0.1seconds
E_{sat}	195J/cm ²

Table.1. Parameters in recording 2-D page data.

4. CONCLUSION

We proposed the new simulation method based on FFT-BPM to analyze for the diffraction efficiency characteristics in HDSS and demonstrated the angular selectivity. The results showed that recorded image is reproduced clearly only when the readout beam illuminates at same angle in the recording. As the angle of the readout beam is shifted from the recording angles, the image is gradually faded away. By using FFT-BPM, we can calculate correlation with the adjacent data pages and determine the minimum separation angle in angular-multiplexing. Also, we apply this method to the simulation of the other recording method in HDSS. Therefore, FFT-BPM is the very effective method in the simulation of HDSS.

REFERENCES

- [1] L. Hesselink, S. S. Orlov, and M. C. Bashaw, “Holographic Data Storage System,” Proc. IEEE, Vol. 92, No. 8, pp.1231 – 1280(2004).
- [2] H. Kogelnik, “Coupled-wave theory for thick hologram gratings,” Bell Sys. Tech. J. Vol. 48, No. 9, pp. 2909 – 2947 (1969).
- [3] M. G. Moharam and T. K. Gaylord, “Rigorous coupled-wave analysis of planar-grating diffraction,” J. Opt. Soc. Am. Vol. 71, No. 7, pp. 811 – 818(1981).
- [4] M. Yamamoto, Y. Tsuji, M. Koshihara, “Reformulation of FFT-BPM for Highly Accurate Analysis,” IEICE, Vol. J81 – C – I, No. 1, pp.24 – 29(1998).
- [5] N. Kinoshita, H. Shiino, N. Ishii, N. Shimidzu, and K. Kamijo, “Integrated simulation technique for volume holographic memory using finite-difference time-domain method,” JJAP Vol. 44, No. 5B, pp. 3503 – 3507 (2005).

Numerical Simulation of Retrieving Characteristics in Holographic Data Storage by Two-Wave Encryption

Motoki Kitano, Atsushi Okamoto, and Takayuki Sano

Graduate School of Information Science and Technology, Hokkaido University N14-W9, Kita-ku, Sapporo, 060-0814, Japan

Phone: +81 11 706 6522, Fax: +81 11 706 7836, E-mail: kitano@optnet.ist.hokudai.ac.jp

1. INTRODUCTION

Encryption plays essential role in information security. Optical encryption [1,2] has drawn much attention due to high speed and parallel processing, and high degree of freedom for encryption key such as phase, polarization, and wavelength. Holographic data storage (HDS) [3] can make use of these advantages because of high transfer rate and all optical processing. There are three main types of optical encrypted HDS system. In the first type, an image is encrypted to encode the object beam [1]. In the second type, a stored image is protected from an illegal access to encode the reference beam [2]. In the third type, both object beam and reference beam is encoded.

We have proposed two-wave encryption as the second type [2]. In this encryption, random phase masks (RPMs) are used for encryption and decryption key. Data is recorded as white noise information due to the randomness of the encryption mask. It is impossible that the original data are retrieved without the correct decryption mask. The output intensity becomes almost zero with the incorrect mask. By monitoring the output intensity, the recorded images can be protected from readout with the incorrect mask. This point is great advantage compared with double-random phase encoding [1].

In this report, we analyze the fundamental retrieving characteristics of two-wave encryption by Fast Fourier Transform Beam Propagation Method (FFT-BPM). Several numerical methods, that based on the coupled wave theory [4] and Finite Difference Time Domain Method (FD-TDM) [5], have been proposed to characterize the readout in HDS. However it is difficult to calculate the interference between the modulated signal beam and the reference beam in a practical size of the recording medium due to the complexity of the interference pattern or the need of huge calculation amount. On the other hand, FFT-BPM can apply the complex interference in the practical size of the recording medium. In the calculation, the 32×32 pixels image with the 4 oversampling is encrypted by the 2313 pixels mask. We estimate the effective key space and the tolerance to shift RPM. The observed output intensity declined by a factor of 10 and the retrieved image is like white noise in the reading with the incorrect mask. The shift tolerance of the random phase mask is $6 \mu\text{m}$.

2. PRINCIPLE

Figure 1 shows schematic diagrams of two-wave encryption. RPMs, which modulates phase randomly and spatially, act as encryption and decryption key. In encryption process as shown in Fig. 1(a), the object beam with an image data are modulated by the RPM1 and the reference beam are modulated by the RPM2. The RPM2 works as encryption mask. The interference pattern of the object and the reference beam induced refractive index in a recording medium. The original data is stored as white noise hologram due to the RPM1. In decryption process as shown in Fig. 1(b), the reading beam enters the recording medium from the opposite direction of the reference beam. RPM3 works as decryption mask. To retrieve the encrypted data correctly, it is necessary that the wave front of the reading beam modulated by RPM3 is phase



Fig.1 Schematic diagrams of two-wave encryption (a) encryption process, (b) decryption process

conjugate to the wave front of the reference beam modulated by RPM2. The output beam is diffracted from different interaction areas in the recording medium. If the two wave fronts do not match, the phases of the individual diffracted components are randomly overlapped. Thus the output intensity declines greatly.

3. ANALYSIS

3.1 Numerical method

Figure 2 shows an analysis model. The analytical region consists of three-dimensional lattice cells. In the SLM (Spatial Light Modulator) plane and the imager plane, Δx_1 and Δy_1 represents the cell size in x and y direction, respectively. N_{px} is the number of pixels of an input image, N_1 is oversampling ratio. In the incidence plane and mask plane, Δx_2 and Δy_2 represents the mesh size of x and y direction, respectively. Δx_1 and Δx_2 are related by

$$\Delta x_2 = \frac{\lambda f}{N_2 N_1 N_{px} \Delta x_1} \quad (1)$$

where λ is the wavelength in free space, f is the focal length of the objective lens. N_2 represents zero padding ratio which increases the calculation accuracy by padding the signal beam profile in the SLM plane with zero.

In the calculation of the encryption process, firstly, the incidence conditions of the recording medium are calculated. The incidence conditions are the sum of the complex amplitude of the signal beam and the reference beam. The signal beam profile in the incidence plane is converted by 2D-FFT (2Dimensional-FFT) of the signal beam profile in SLM plane due to the function of the objective lens. From scalar diffraction theory, light propagation in a homogeneous medium is calculated by the product of the incidence conditions and the transfer function in the spatial frequency domain. Thus the reference beam profile in the incidence plane is obtained by calculating the product of the reference beam profile in the mask plane and the transfer function of free space in the spatial frequency domain. Next, the interference pattern of the signal and reference beam in the recording medium is also obtained by the scalar diffraction of the interference pattern in the incidence plane.

For the calculation of the refractive index distribution, we assume photopolymer as recording medium and the refractive index of the photopolymer is saturated exponentially with the light intensity and is given by

$$\Delta n = n_2 \left\{ 1 - \exp\left(-\frac{I(x, y, z) \cdot T}{E_{sat}}\right) \right\} \quad (2)$$

where n_2 is the refractive index modulation depth, $I(x, y, z)$ is the light intensity [W/m^2], T is the exposure time [s], E_{sat} is the saturation energy flux density [J/m^2] which is the value when Δn reaches $0.63n_2$.

In the calculation of the decryption process, firstly, we obtained the reading beam profile in the transmission plane by calculating the scalar diffraction from the same mask plane as the reference beam. This is because we can easily compare the decryption mask distribution with the encryption mask distribution. Next, the distribution in the incidence plane obtained from the reading beam profile in the transmission plane by FFT-BPM [6]. Finally, the retrieved image is converted by the 2D-Inverse FFT of the output beam profile in the incidence plane.

We evaluated the effect of the mask mismatch and a mask displacement on the output. The mask mismatch is

Wavelength (λ)	514.5nm
Number of pixels (N_{px}, N_{py})	32
Oversampling ratio (N_1)	4
Zero-padding ratio (N_2)	4
Medium size ($W_x \times W_y \times W_z$)	$617 \times 617 \times 450 \mu\text{m}$
Focal length (f)	6mm
Distance of medium from mask (d)	$500 \mu\text{m}$
Angle of reference beam (θ)	8°
Intensity ratio (I_{ref} / I_{sig})	1.8
Total recoding power (P_{in})	1mW
Reference beam width	$284 \mu\text{m}$
Aperture size (D)	$284 \mu\text{m}$
n_1	1.5
n_2	1.0×10^{-3}
E_{sat}	$27 \text{ J}/\text{m}^2$
Exposure time (T)	0.1 seconds

Table 1 Parameter values

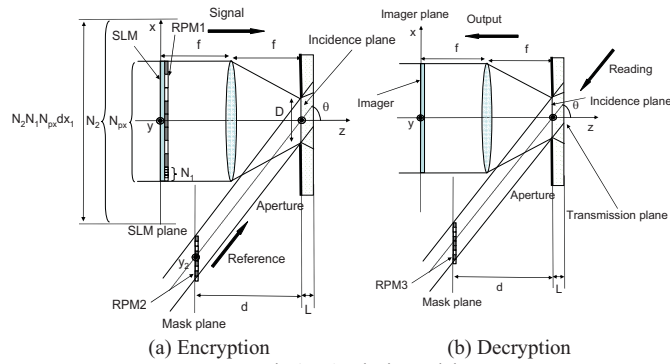
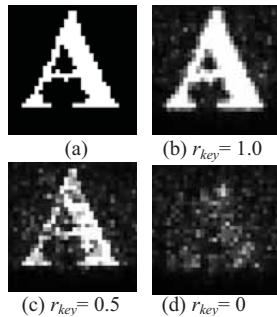


Fig.2 Analysis model



(a) $r_{key}=0.5$ (b) $r_{key}=1.0$
(c) $r_{key}=0.5$ (d) $r_{key}=0$

Fig. 3 Input image and reconstructed images

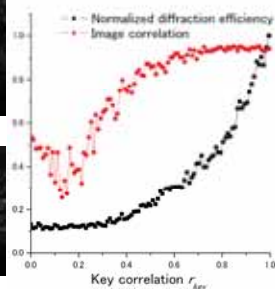


Fig.4 Effect of mask mismatch on output

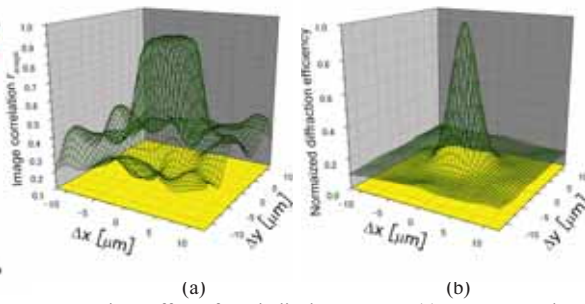


Fig.5 Effect of mask displacement on (a) reconstructed image quality, (b) output intensity

estimated by the key correlation r_{key} that is defined as a correlation coefficient between the encryption key and decryption key. The output is estimated by the diffraction efficiency and the reconstructed image quality. The reconstructed image quality is represented as a correlation coefficient r_{image} between the original image and the reconstructed image. In the simulation, we used the parameter values shown in Table 1. The phase of RPM is distributed 0 or π , the number of mask pixels is 2313.

3.2 Simulation results and discussions

We simulated the recoding with image “A” shown in Fig. 3(a). Figures 3(b), (c), and (d) are the reconstructed image when r_{key} is 1.0, 0.5, and 0 respectively. Figure 4 shows the reconstructed image quality and the output beam intensity as a function of the key correlation r_{key} . The reconstructed image is like white noise and the diffraction efficiency is declined by a factor of 10 when key correlation r_{key} is less than 0.2. According to Ref. 2, the probability of generating the decryption key whose r_{key} is over 0.2 is of the order of 10^{-6} when the number of mask pixels is $32 \times 32 (=1024)$. Thus, the generating probability in the parameter we used is less than 10^{-6} . The original image may not be retrieved using most of keys that can be generated by brute force attack. Figure 5 shows the reconstructed image quality and the diffraction efficiency as the function of the mask displacement. When the decryption mask position is displaced greatly from the encryption mask position, the reconstructed image quality is degraded. The diffraction efficiency falls rapidly to 0.1 when mask displacement reaches about 6 μm in spite of the mask pixel size is about 5 μm . This is because the mask pixel is so small that the reading beam in the incidence plane widely is spread by Fraunhofer diffraction.

4. CONCLUSION

We analyzed the retrieving characteristics in two-wave encryption by proposed simulator based on FFT-BPM. In the incorrect decryption key whose r_{key} is less than 0.2, the diffraction efficiency declines by a factor of 10 and the reconstructed image is like white noise. Thus the illegal access can be detected easily by monitoring the output intensity. In practical terms, the mask displacement need to be set within about 6 μm to retrieve correctly when the pixel size of the mask is about 5 μm .

REFERENCES

- [1] B. Javidi, G. Zhang and J. Li, “Encrypted optical memory using double-random phase encoding,” Appl. Opt., Vol.36, no.5, pp. 1054-1058 (1997).
- [2] A. Okamoto, A. Mita, H. Funakoshi, K. Moritake and T. Sano, “Secure holographic memory by two-wave encryption method with a photorefractive crystal”, Journal of Modern Optics, Vol. 54 No. 4 pp.599 (2007).
- [3] L. Hesselink, S. S. Orlov, and M. C. Bashaw, “Holographic Data Storage Systems,” Proc. IEEE, Vol. 92, no. 8, pp.1231-1280 (2004).
- [4] N. Kinoshita, H. Shiino, N. Ishii, N. Shimidzu and K. Kamijo, “Integrated Simulation Technique for Volume Holographic Memory Using Finite-Difference Time-Domain Method” JJAP Vol. 44, No. 5B, pp. 3503–3507 (2005)
- [5] M. Miura, O. Matoba, K. Nitta, and T. Yoshimura “Image-based numerical evaluation techniques in volume holographic memory systems” J. Opt. Soc. Am. B, Vol. 24, No. 4 pp.792-798 (2007)
- [6] M. D. Feit and J. A. Fleck, Jr., “Light propagation in graded-index optical fibers”, Appl. Opt., 17, 3990(1978)

Analysis of Diffraction Characteristics of Photopolymers by Using Beam Propagation Method

Shuhei Yoshida and Manabu Yamamoto

Tokyo University of Science, 2641 Yamasaki, Noda, Chiba, 278-8510 Japan

E-mail: j8107653@ed.noda.tus.ac.jp

Abstract: In this study, we simulated formation of holographic grating in photopolymer based on diffusion model, and analyzed diffraction characteristics by using beam propagation method.

1. Introduction

In holographic memories, photopolymer is a hopeful material as a recording medium. To use a photopolymer for holographic memories as practical recording media, it is necessary to clarify the design condition of recording/reproduction characteristics.

The coupled-wave analysis [1] (CWA) and the rigorous coupled-wave analysis [2] (RCWA) are widespread methods to analyze diffraction characteristics of volume holographic gratings. However, holographic grating is more complex than simple grating that is presumed in CWA and RCWA, in a practical holographic memory.

In this study, we analyzed characteristics of photopolymer based on a diffusion model and clarified the diffraction characteristics by using the Beam Propagation Method (BPM).

2. Diffusion Model of Photopolymer

In this study, we supposed that reaction of photopolymer is based on diffusion model [3],

$$\frac{\partial m(\mathbf{r}, t)}{\partial t} = D(\mathbf{r}, t) \nabla^2 m(\mathbf{r}, t) - F(\mathbf{r}, t) m(\mathbf{r}, t), \quad (1)$$

$$\frac{\partial p(\mathbf{r}, t)}{\partial t} = F(\mathbf{r}, t) m(\mathbf{r}, t), \quad (2)$$

where m and p are density of monomer and polymer, D and F are diffusion and reaction coefficient that is given by

$$D(\mathbf{r}, t) = D_0 \exp(-aFt), \quad (3)$$

$$F(\mathbf{r}, t) = \kappa \{ I \exp(-\alpha z) [1 + V \cos(\mathbf{K}_g \cdot \mathbf{r})] \}^{1/2}, \quad (4)$$

$$= F_0 [1 + V \cos(\mathbf{K}_g \cdot \mathbf{r})]^{1/2}$$

where D_0 is the initial value of diffusion coefficient, a is the decrease coefficient, κ is the polymerization coefficient, I is the intensity of exposure, α is the absorption coefficient, V is the visibility and \mathbf{K}_g is the grating vector.

refractive index of medium is defined by [4]

$$\frac{n^2 - 1}{n^2 + 2} = m \left(\frac{n_m^2 - 1}{n_m^2 + 2} \right) + p \left(\frac{n_p^2 - 1}{n_p^2 + 2} \right) + b \left(\frac{n_b^2 - 1}{n_b^2 + 2} \right) \quad (9)$$

where n_m , n_p and n_b are refractive index of monomer, polymer and binder, b is the density of binder and defined by $b=1-m-p$.

3. Analysis of Diffraction Characteristics of Volume Holographic Grating

BPM [5] is based on Helmholtz equation

$$\frac{\partial^2 E_y}{\partial x^2} + \frac{\partial^2 E_y}{\partial z^2} + k_0 n^2 E_y = 0, \quad (5)$$

$$\frac{\partial}{\partial x} \left(\frac{1}{n^2} \frac{\partial H_y}{\partial x} \right) + \frac{\partial}{\partial z} \left(\frac{1}{n^2} \frac{\partial H_y}{\partial z} \right) + k_0 H_y = 0, \quad (6)$$

Equation (5) is equation of TE mode, and eq. (6) is TM mode.

Equations (5) and (6) are elliptic partial differential equations (PDE). In general, iterative methods are used to solve elliptic PDEs numerically, for example, Gauss-Seidel method, successive over-relaxation (SOR) method, conjugate gradient method and so on. However, it is necessary to iterate until numerical solutions convergent and its computational complexity is $O(N^3)$ in the worst case. Therefore, BPM takes the approximation that is called slowly varying envelope approximation (SVEA) to transform elliptic PDE to parabolic PDE.

In paraxial region, wave equation is given by

$$2jn_r k_0 \frac{\partial \phi}{\partial z} = P\phi, \quad P = \begin{cases} \frac{\partial^2}{\partial x^2} + k_0^2 (n^2 - n_r^2) & \text{TE mode} \\ n^2 \frac{\partial}{\partial x} \left(\frac{1}{n^2} \frac{\partial}{\partial x} \right) + k_0^2 (n^2 - n_r^2) & \text{TM mode} \end{cases}, \quad (7)$$

where ϕ is E_y in TE mode or H_y in TM mode, n_r is reference refractive index, n is refractive index and k_0 is wave number in vacuum. Equation (7) is parabolic PDE. We formulate eq. (7) as finite differential equation by Crank-Nicolson method and use Thomas algorithm to solve numerically. By using Thomas algorithm, we can obtain numerical solutions quickly and its computational complexity is $O(N)$. In paraxial region, term of $\partial^2 \phi / \partial z^2$ is disregarded, but, in this study, we used formulation by Pade(1,1) to calculate accurately.

4. Simulation Result

Table I shows simulation condition and Fig. 1 shows simulation model, where λ is the wavelength and L is the thickness of holographic grating.

Table I. Simulation condition

Δx	0.1λ
Δz	0.1λ
L	375λ
$m(\mathbf{r},0)$	0.3
$p(\mathbf{r},0)$	0.0
n_m	1.50
n_p	1.54
n_h	1.47

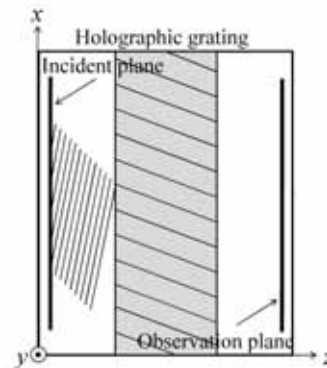


Fig. 1. Simulation model

Figure 2 shows relationship between exposure energy and diffraction efficiency. Where ξ is the non-dimensional parameter that shows energy defined by $\xi = F_0 t$ and R is the ratio of diffusion coefficient and reaction coefficient that is defined by $R = D_0 K_g^2 / F_0$.

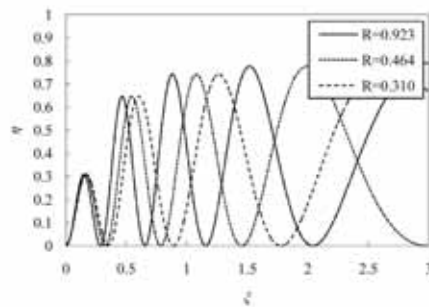


Fig.2. Relationship between ξ and η (TE mode)

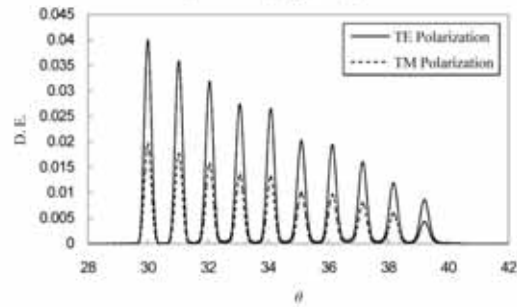


Fig. 3. Diffraction Characteristics of multiplexed hologram

5. Conclusion

As shown in this study, we confirmed that the BPM is effective in analysis of diffraction characteristics of photopolymers and we could obtain the diffraction characteristics of complex volume holographic gratings, which is difficult to deal by conventional methods.

In addition, parameters specific to the medium, such as diffusion coefficient and reaction coefficient greatly affect diffraction efficiency.

Reference

- [1] Herwig Kogelnik "Coupled wave theory for thick hologram gratings," The Bell System Technical Journal, Vol. 48, no. 9, pp. 2909-2947, Nov. 1969.
- [2] M. G. Moharam and T. K. Gaylord, "Rigorous coupled-wave analysis of planar-grating diffraction," J. Opt. Soc. Am, Vol. 71, no. 7, pp. 811-818.
- [3] G. Zhao and P. Mouroulis, "Diffusion model of hologram formation in dry photopolymer materials," J. Mod. Opt., Vol. 41, Issue 10, pp. 1929-1939, Oct. 1994.
- [4] J. T. Sheridan and J. R. Lawrence, "Nonlocal-response diffusion model of holographic recording in photopolymer," J. Opt. Soc. Am. A, Vol. 17, Issue 6, pp. 1108-1114, Jun. 2000.
- [5] Y. Chung and N. Dagli. "An assessment of finite difference beam propagation method," IEEE J. Quantum Optics, Vol. 26, Issue 8, pp. 1335-1339, Aug. 1990.

Modeling and Detection of Linear and Threshold Microholograms

Fergus Ross, Victor Ostroverkhov, Xiaolei Shi, Ken Welles, Brian Lawrence
 GE Global Research, 1 Research Circle, Niskayuna, NY, 12309
 rossf@research.ge.com

1. INTRODUCTION

The microholographic concept was introduced by Eichler, et. al. [2], and has since received attention from many researchers [1,3,4,6,7]. Modeling work published to date assumes linear materials, materials in which the refractive index change is a linear function of incident optical fluence. Unfortunately, linear materials have significant drawbacks: microholograms spread throughout the material, increasing intersymbol interference during readout; data read and ambient light slowly bleach the disk; and writing consumes dynamic range throughout the material, reducing the usable dynamic range of the material, and results in lower DE [8]. Alternatively, threshold materials [3] are being designed that limit the index change to much smaller volumes and prevent low-intensity bleaching. We believe threshold materials are ultimately desired but much is learned from current simulation and experimental work with linear materials. A microholographic diffraction model based on the Born approximation was created to investigate system trade-offs. In the following, various observations from this model are discussed and a simple threshold model is introduced.

2. MODEL

The microholographic diffraction model employed is based on that of Nagy et al [1], with a slight modification. The computer model assumes counterpropagating Gaussian beams, E_r and E_s , to write the microhologram, and a Gaussian probe beam, E_p , to read the microhologram. The diffracted electric field at a point x_1, y_1, z_1 with probe offset $\Delta x, \Delta y, \Delta z$, is

$$E_{diff}(x_1, y_1, z_1, \Delta x, \Delta y, \Delta z) = \iiint \frac{k^2}{4\pi} E_p(x + \Delta x, y + \Delta y, z + \Delta z) \cdot \left(2 \frac{\delta n(x, y, z)}{n} \right) \cdot \frac{\exp\left(ik \sqrt{(x_1 - x)^2 + (y_1 - y)^2 + (z_1 - z)^2} \right)}{\sqrt{(x_1 - x)^2 + (y_1 - y)^2 + (z_1 - z)^2}} dx dy dz$$

where

$$E_p(x, y, z) = \frac{\sqrt{2}}{\sqrt{\pi} w(z)} \exp\left(-\frac{x^2 + y^2}{w(z)^2} \right) \exp\left(ik \frac{x^2 + y^2}{2R(z)} + ikz - i\Phi(z) \right),$$

$\delta n(x, y, z)$ is the profile of the refractive index change as a result of hologram recording; $\delta n(x, y, z) = \delta n_{max} |E_r + E_s|^2 / 4$, approximated by $\delta n_{max} E_r^* E_s / 4$ for linear materials, where δn_{max} is the maximum refractive index change and E_r and E_s are given by

$$E(x, y, z) = \frac{w_0}{w(z)} \exp\left(-\frac{x^2 + y^2}{w(z)^2} \right) \exp\left(ik \frac{x^2 + y^2}{2R(z)} + ikz - i\Phi(z) \right).$$

3. SIMULATION STUDY

Diffraction efficiency (DE), the ratio of reflected signal power to incident probe power, is a system requirement that drives material design [6]. DE must be high enough to allow the use of low-power sources and inexpensive detectors, but weak enough to allow substantial probe illumination and signal propagation at lower layers [7]. The relationship between DE and numerical aperture is a consideration in system design. The grating must be small for large storage capacities, favoring high NA, however DE is inversely proportional to NA. The analysis of Kogelnik gives $DE = \tanh^2(\pi \delta n d_K / \lambda)$ for plane-wave holograms perpendicular to the disk plane under perfect probe alignment, where d_K is the grating thickness [5]. The Kogelnik formula predicts $DE \sim NA^4$, and the numerical model is in agreement, Fig 1. This relationship also drives aspects of material design. It was also noted that DEs calculated by numerical integration were equal to the Kogelnik formula at $d_K = z_0/2$.

Perfect alignment of writing beams is a practical concern, both for the maximum achievable DE as well as for alignment losses during readout. The calculated DE vs. lateral probe offset for an example with $1\omega_0$ horizontal separation between the write beams is shown in Fig. 3. The maximum DE was reduced by 40% and the probe finds this maximum when it is centered between the two write beam locations.

Adjacent microhologram interference strongly influences track and layer spacing. To estimate adjacent bit interference with our numerical model, we first investigated appropriate limits of integration by expanding a nominal integration region in steps and plotting DE vs. y-offset curves to note convergence, as shown in Fig. 2. The nominal box was based on beam parameters: $2z_0$ in depth and $2z_0 \tan(\sin^{-1}(NA/n))$ in both horizontal dimensions. The curves show a scale factor of 5 is reasonable for most offsets of interest. Smaller integration regions underestimate the interference from linear microholograms.

The signal energy along a disk track was estimated by adding the electric field components of offset microholograms. For example, the detected signal from a single track of microholograms without added noise is shown in Fig. 4. Error rates of 3% occurred at a spacing of $1\omega_0$ whereas a spacing of $1.5\omega_0$ produced no errors. Insisting that bit 0 followed all bit patterns of 110 removed all bit errors in the noise-free $1\omega_0$ -spaced channel. Optical and electronic noise was added to the model and the diffracted electric field from each bit was phase modulated to account for bit position variance as the track moves. Results to be discussed include the significant error rate increase caused by vertical bit variation.

Delivering 1TB capacity from a DVD-sized disk requires an average volume per bit of less than $1.7\mu\text{m}^3$ (and realistically around $1\mu\text{m}^3$), also motivating interest in threshold materials. In the simplest threshold model, a threshold is set at the intensity, $|E_r + E_s|^2$, that produces the desired 'threshold' volume. Refractive index change occurs when $|E_r + E_s|^2$ exceeds this threshold. For example, with $\omega_0 = 0.3\mu\text{m}$, a volume of $1.7\mu\text{m}^3$ is produced when the threshold occurs at an x,y extent of +/- $0.3\mu\text{m}$ as this limits the z extent to +/- $2.2\mu\text{m}$, Fig. 5. Various threshold and diffusion models are currently under consideration. Preliminary results show binary threshold models and models with limited diffusion obtain more rapid diffraction decay with lateral offset than linear models at a cost of reduced peak DE. Note that Fig. 2 anticipates this trend.

REFERENCES

- [1] Nagy, Z., Koppa, P., Dietz, E., Frohmann, S., Orlic, S., Lorincz, E., "Modeling of Multilayer Microholographic Storage", *Applied Optics*, 46(5), 753-761, (2007)
- [2] Eichler, H. J., Kuemmel, P., Orlic, S., and Wappelt, A., "High-Density Disk Storage by Multiplexed Microholograms", *IEEE J. Sel. Top. Quantum Electron*, 4(5), 840-848, (1998)
- [3] Lawrence, B., Invited Talk, ISOM/ODS (2008)
- [4] Saito, K., Horigome, T., Miyamoto, H., Yamatsu, H., Tanabe, N., Hayashi, K., Fujita, G., Kobayashi, S., Kudo, T., Uchiyama, H., "Drive system and readout characteristic of Micro-Reflector optical disc", MB1, ODS 2007
- [5] Kogelnik, H., "Coupled Wave Theory for Thick Hologram Gratings", *Bell Sys. Tech. J.*, 48(9), 2909-2945, (1969)
- [6] Shi, X., Erben, C., Lawrence, B., Boden, E., Longley, K., "Improved sensitivity of dye-doped thermoplastic disks for holographic data storage", *J. App. Phys.*, 102, 014907, (2007)
- [7] Saito, K. and Kobayashi, S., "Analysis of Micro-Reflector 3-D optical disk recording", *Proc. SPIE Vol. 6282*, 628213, (2006)
- [8] Dubois, M. et al, "Characterization of microholograms recorded in a thermoplastic medium for three-dimensional optical data storage", *Optics Letters*, Vol.30, No. 15, 1947-1949 (2005)

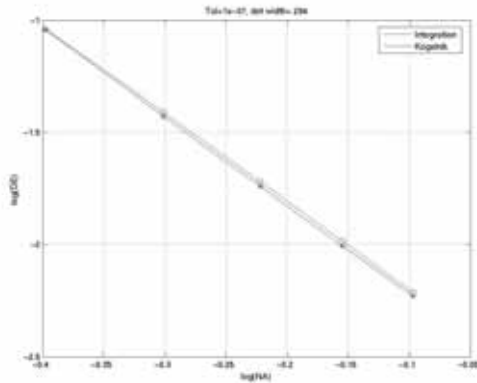


Fig. 1. DE vs. NA

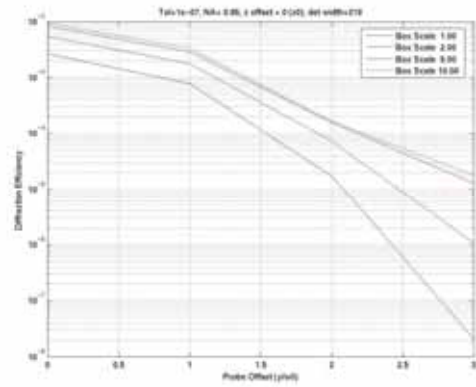


Fig. 2. DE vs horizontal probe offset & integration region

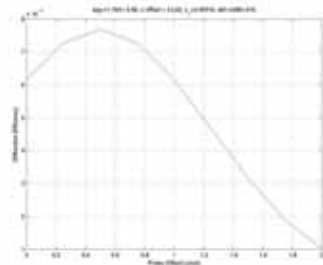


Figure 3. Signal lateral offset by $1\omega_0$. Probe finds maximum DE at $0.5\omega_0$.

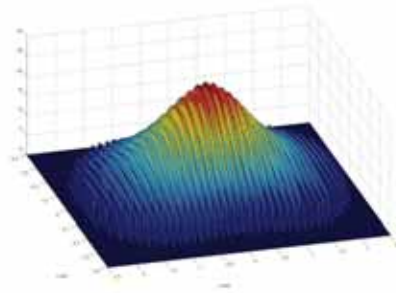


Figure 5. Threshold modulation at x-z plane.

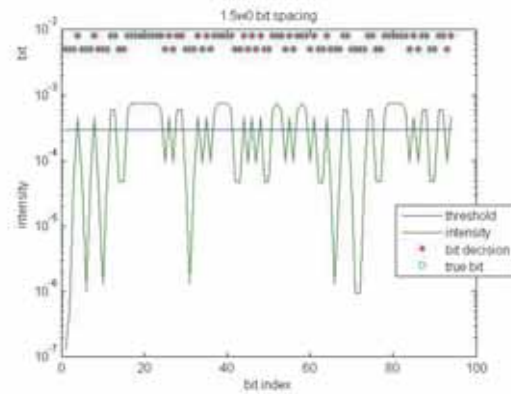
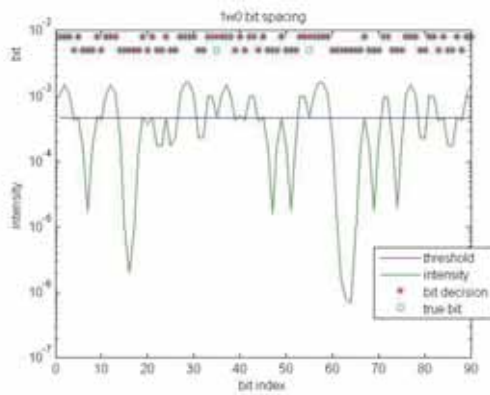


Figure 4. Single-track modeling: 3% error at $1\omega_0$, no errors at $1.5\omega_0$.

Optical characterization of photopolymer materials for microholographic data storage

Timo Feid, Enrico Dietz, Sven Frohmann, Christian Mueller, Jens Rass, Susanna Orlic

Optical technologies Lab, Technical University Berlin, Strasse des 17. Juni 135, 10623 Berlin, Germany

orlic@opttech.tu-berlin.de, www.opttech.tu-berlin.de

Abstract: We investigate different classes of organic photosensitive materials in order to optimize the interaction between the material itself and an optoelectronic system around. Some exemplary applications are microholographic data storage, 3D nano and micro structurization, optical patterning for advanced security features, etc. Key issues include dynamic material response, spectral and temporal grating development, influence of the light intensity distribution, effects of pre-exposure and post-curing by light, etc. Materials under investigation are cationic ring opening and free radical polymerization systems, liquid crystalline polymer nanocomposites, and photoresist systems.

2007 Optical Society of America

OCIS codes: 210.2860 Holographic and volume memories, 090.7330 Volume holographic gratings, 090.2900 Holographic recording materials, 210.4590 Optical disks

1. Photopolymers for microholographic data storage

Many and diverse photonic applications rely on optical patterning of suitable photosensitive materials. Diffractive optical elements with application specific and tailored properties can be fabricated by light induced alternation of the material's refractive index or absorption. Holographic polymers or photoresists are typically used for permanent optical structurization. New emerging applications such as very high density mass capacity data storage, optical sensing, recognition, and security technology set strict requirements on the performance of photosensitive materials. By the availability of supporting technologies, photostructurable media become core elements of photonic systems with extended and innovative capabilities.

In particular, a photopolymer medium represents a core element of the microholographic storage system. The response and dynamics of the recording material are crucial for the overall system performance. High density recording of diffraction limited microholograms combined with a high number of data layers sets strong requirements on the optical quality of the photopolymer material. The two parameters of foremost importance for the system storage performance, i.e. the areal data density achieved in a single layer of microgratings and the total number of multiplexed depth layers, are strongly coupled to each other by the capability of the photopolymer. The knowledge on the dynamic material behavior and its optical properties is therefore a premise for achieving an optimum storage performance in terms of data density and data transfer rates, as well. Investigations on different photopolymer materials and related dynamic grating formation processes represent an important effort to further advance the microholographic storage method. Photosensitivity and spectral response, temporal behavior and dynamics of the grating build up process, grating stability and selectivity, influences of pre-exposure and post-curing are only some of issues under investigation.

2. Media tester system

In order to study the temporal behavior, response and sensitivity of the diverse photopolymers tested for microholographic storage we have designed and developed a versatile optical system, the so called "Media Tester", which has continuously been improved during the past three years. The setup allows writing microgratings in photopolymers in various recording regimes. Different exposure schedules can easily be applied to find an optimum range of exposure parameters. Two main working principles are possible: Either two independent tunable writing beams or a single beam that is reflected back from a retro reflecting unit after passing through the sample can be used. The numerical aperture, the intensity of the laser beams and the exposure scheme can be varied over several orders of magnitude to the current desired values. For the writing process a 405 nm external cavity diode laser system is being used. The Media Tester offers many ways to study and understand the behavior of the created gratings. A CCD Camera, a high sensitivity photodetector and a spectrometer can be used to detect and study the signal diffracted by the gratings. Along with the writing laser a Xe-flash lamp is used for readout and spectral measurements.

Basic data of a new photopolymer sample is collected by writing single microgratings with exposure energies successively rising from detection limit up to saturation level. Each time the reflected signal is scanned temporally but also spatially resolved. Microholographic response of the material is then mapped by selecting and putting

together diffraction efficiencies of gratings written with characteristic exposure energies, observed after specific time periods. Repeating such measurements with different laser beam powers, a multi-dimensional dataset is created representing a typical behavior of a specific material. Changing the focal length of both objective lenses within the write region of the setup affects spatial dimensions and focal beam intensity at the same time. Working with different beam focus spots offers two important opportunities: First dimensionality of the collected data is extended thus allowing better insight and separation of complex interaction between all adjustable parameters.

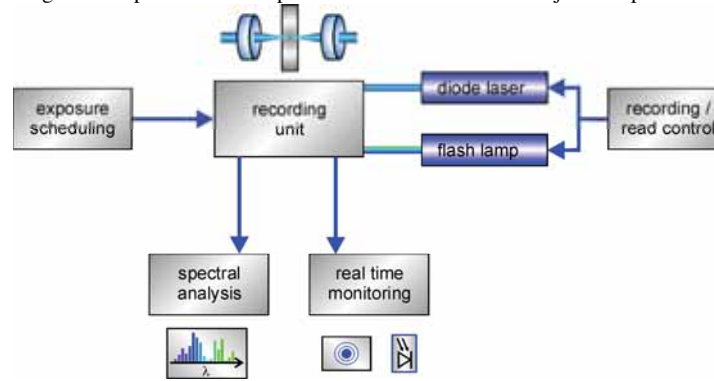


Figure 1. Operation scheme of the versatile media tester system for investigating photopolymer recording materials.

2. Characterization of photopolymer materials

Many and diverse photopolymer materials have been investigated with respect to their suitability for microholographic data storage including commercially available samples from InPhase and Aprilis.

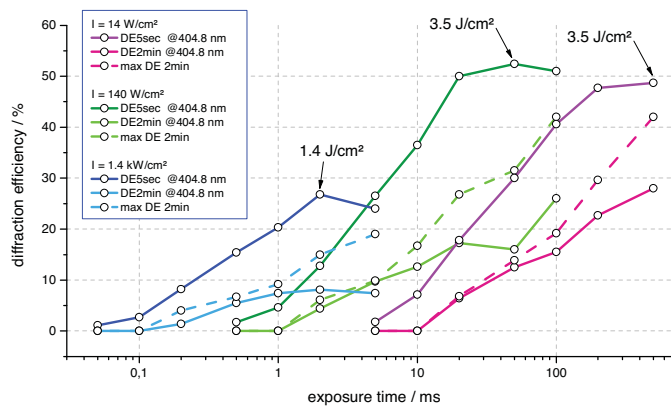


Figure 2. Response map of a Aprilis E type photopolymer #2.

In the following results obtained on two violet-sensitive E-Type CROP (cationic ring opening polymerization) photopolymers from Aprilis are presented. Since this type of material is comparatively new, considerable changes show up between samples of different generations which result in strongly varying behavior of the polymers. The gratings have been written using the two-beam configuration as well as the retro-reflector setup and have been analyzed spectrally by readout with the pulsed white light from the flash lamp. The blue-sensitive E-Type photopolymer of the first generation responded to recording energies between 300 mJ/cm² and 10 J/cm², which in our experiments were generated by laser pulses with intensities of 26 W/cm² and 260 W/cm², respectively.

Sensitivity of the second generation E-Type photopolymer is slightly better, so that we could already write and detect weak gratings at exposure energy of 160 mJ/cm². Three different beam powers (3 μW, 30 μW, 300 μW) have been chosen for this photopolymer to constitute specific exposure energy. Resulting write beam intensities calculate to 14 W/cm², 140 W/cm² and 1.4 kW/cm².

Furthermore, gratings have been scanned over an appropriate period of time to collect information about their spectral response and lifetime in this material. Figure 2 compares the temporal and spectral development of Aprilis

E-type photopolymers of the first and second generation. The left graph of Figure 3 shows the observation of spectral response of a grating recorded with 4.7 J/cm^2 during a period of 24 hours in a first generation E-Type polymer. The life time of such gratings is limited: Already 40 minutes after exposure the peak diffraction efficiency is only half of its initial value. The evaluation of the center wavelength is not straight forward since the single peak splits up into a double peak structure after 3 hours. The right hand side shows the 24 hour measurement of a grating written with recording energy of 3 J/cm^2 and laser intensity of 140 W/cm^2 in a second generation E-Type photopolymer. Right after exposure the grating yields a diffraction efficiency of about 45 %. Two minutes later the diffraction efficiency falls significantly to a value of 20 %. The grating then starts to stabilize 10 minutes after exposure at a value of around 10 %. From this time on the shrinkage process seems to start. After 24 hours the peak position of the spectrum is found at 401 nm. Peak shift of 4 nm compared to the laser wavelength corresponds to 1 % optical shrinkage of the material. Compared to results in the first photopolymer, the spectrums do not show any secondary peaks and also spatial homogeneity is better in this polymer.

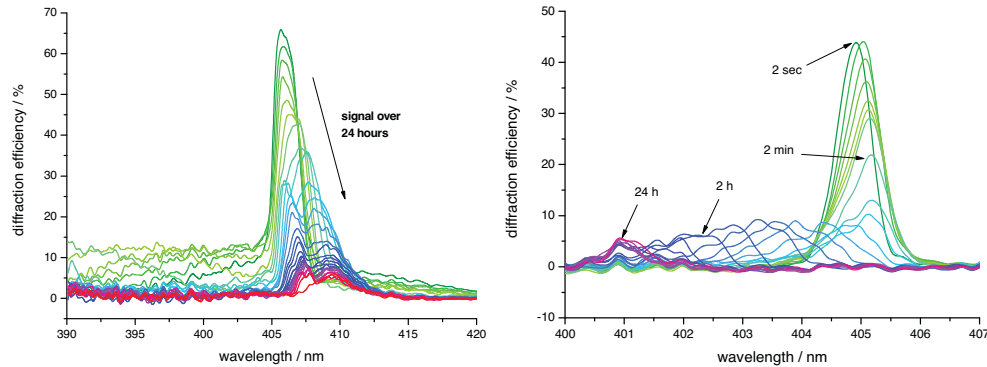


Figure 3. Spectral and temporal development of microgratings recorded with 3 J/cm^2 ($I = 140 \text{ W/cm}^2$) in an Aprilis HMC E-Type photopolymer of the first (left) and second generation (right).

In order to analyze dependency between spectral shift and exposure condition in more detail several spectral measurements as shown in Figure 3 have been evaluated in a way to yield the time resolved shift of the peak wavelength. Such curves are shown in the left graph of Figure 4. Curves of constant exposure energy are grouped by similar color. As a first obvious result, changing laser power at constant energy has no influence on shrinkage of the material. Moreover, all graphs show a decrease of the center wavelength after exposure. Gratings written with energies lower than 1.5 J/cm^2 show a subsequent optical shrinkage during the first 3 minutes. Acquiring equal data for period of 24 hours, as shown in the right graph of Figure 4, gives more insight into the development of exposed regions within this photopolymer. Here the whole extent of wavelength shift becomes apparent. Independent of the exposure energy the spectra suffered from blue shifting by about 1 % of the laser wavelength, after initial increase of the wavelength of about 0.1 %.

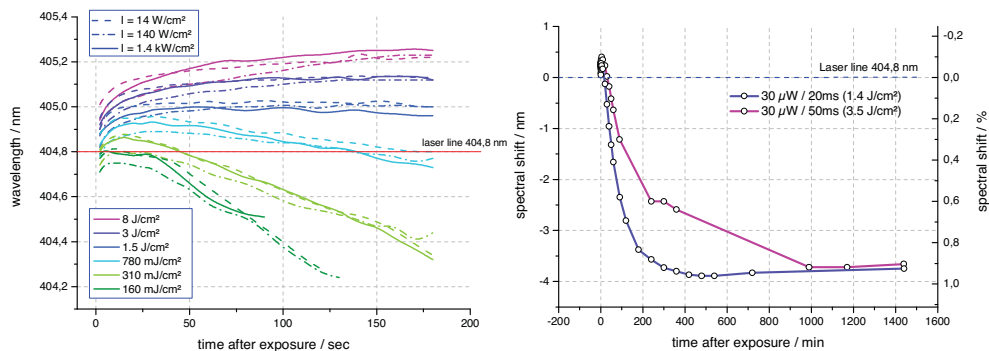


Figure 4. Temporal resolved spectral reflectivity of certain microgratings.

5. Acknowledgement

The work has been supported by the European Commission within the MICROHOLAS project.

Data Recovery from Severely Damaged Optical Media using Wavelet Transforms

S. Kannan, Y. Li, S. Kasanavesi, P. Khulbe, T. D. Milster, W. Bletscher and D. Hansen
 College of Optical Sciences, University of Arizona, Tucson, Arizona U.S.A.
 Swetha.kannan@gmail.com, milster@arizona.edu

I. INTRODUCTION

Optical storage devices, like compact disc (CD) systems, are manufactured to be insensitive to minor scratches and other damages occurring on the surface of the disc due to everyday usage. However, it is not uncommon to partially destroy a CD by accidentally causing deep scratches or breaking the CD into pieces. Regular CDs have a flat and smooth transparent substrate with a thickness of $1.2\text{mm} \pm 100\mu\text{m}$ [1]. The research contained in this paper discusses methods to recover data from CDs with sudden depth changes in the substrate that go beyond $100\mu\text{m}$, like that encountered with a deep scratch. The results of this research could be applied to less severe surface alterations in order to improve readout in commercial drives.

Kasanavesi [2] discusses a three-step modular approach in recovering data from damaged CDs using microscope images. In his approach, a readout signal is derived from the images. Then, data bytes are recovered from the signal. Finally, these bytes are arranged in a user-defined sequence. A similar approach is used in this paper, except that the first step in signal recovery and the associated signal processing are different. Kasanavesi's method of recovery from microscopic images takes approximately 500 hours to recover data from a CD size area [3]. This method is very useful in the case of CDs that are broken into fragments of very small size. However, for CD fragments larger than 25mm in length, it is possible to recover data at a much faster rate. An optical spin-stand (OSS) developed for this purpose is described in this paper. This research uses raw data from the spin stand to test various signal processing algorithms for data recovery.

A standard low speed (1X) CD readout detector current is a sinusoidal narrow-band radio frequency (RF) signal whose frequency varies from 196 kHz to 720 kHz. It consists of distinct frequencies corresponding to the nine possible lengths of data marks. This non-stationary signal exhibits a frequency content that varies randomly, depending on the occurrence of different runlengths. Further, the occurrence of defects on the surface of the disc cause sudden changes in the frequency content of the signal. The wavelet transform (WT) provides an intuitive way of analyzing such non-stationary signals [5].

WT analyzes signals in the scale-time domain. The term scale is similar to the term scale on maps. Higher scales correspond to a non-detailed global view (of the signal) and lower scales correspond to a detailed view (of the signal), *i.e.*, higher frequencies are present in lower scales and vice versa. Wavelet transforms give poor frequency resolution at lower scales (higher frequencies) but a detailed view of the signal in time domain (good time resolution) and good frequency resolution at higher scales (lower frequencies) with a non-detailed global view of the signal in time domain (poor time resolution). A discrete two-channel WT is used in this research. It is implemented by passing the signal through a bank of half band filters that meet regularity conditions [6] - [8].

For WT, the signal is simultaneously passed through a set of low pass (H_0) and high pass (H_1) filters. The half-band filters result in signals that are halved in bandwidth but are individually equal to the input signal length. Since these signals would require more memory than the original signal, signals are downsampled by a factor of 2 by omitting every other sample. The resulting lower frequency coefficients are called approximation coefficients (C_A) and the higher frequency coefficients are called detail coefficients (C_D).

The signal is reconstructed from these coefficients by performing the reverse process, where the coefficients are interpolated with zeros to upsample by a factor of 2. Then, the upsampled signals are passed through inverse filters F_0 and F_1 , and the signal is reconstructed by adding the two outputs. Perfect reconstruction is achieved by using a correct choice of filters.

The research presented in this paper uses finite impulse response (FIR), causal, orthogonal, nearly symmetric filters designed by Abdelnour [9] with $K=2$ and $L=6$. This filter is chosen in particular, because it allows perfect reconstruction of the signal while using orthogonal filter bases. Orthogonal filter bases give uncorrelated coefficients. Symmetric filters give perfect reconstruction. Filter bases cannot be orthogonal and symmetric at the same time. By using WT in this application, the C_A causing defects are identified. These coefficients are altered to correct the defects, and the signal is reconstructed back from these altered coefficients. Use of this method greatly improves performance of the data recovery process.

II. EXPERIMENT

The optical spin stand system (OSS) for the experiment imitates the optoelectronics of a commercial CD player. It also includes custom electronics and sturdy mechanics. The RF data signal from the optical head assembly is converted directly with an 8-bit high speed 100Mbps National Instruments digitizer that is mounted on an acquisition and control computer.

The performance of the OSS and the signal processing algorithms used in the recovery of the data mark and land lengths are tested by recovering data from CDs that underwent severe damage. In the first part of the experiment, two such types of damage, knurling and scratches, a total of three samples are investigated. In the second part of the experiment, a CD written with approximately 600MB of user data is broken into three pieces. The OSS is used to recover as much information as possible from the three sections.

III. RESULTS

In the first part of the experiment, the probability of error $(P_E)_i, i \in \{3-11\}$ is calculated by dividing the area under the Gaussian of a particular group i outside its decision points by the total area of the best-fit Gaussian. The total P_E is the sum of the $(P_E)_i$'s weighted by the probability of occurrence $(P_C)_i$ of each runlength. $(P_C)_i$ is determined by dividing the area under its Gaussian fit by the area under the sum of all Gaussians. Total probability of error P_E defines an approximate statistical measure for a performance comparison of the signal processing algorithms explained in this section. In this section, several processing techniques are described, including simple threshold, dynamic threshold, exclusion technique and wavelet transform algorithms. A comparison of P_E for different algorithms is provided in Table I.

Once the runlengths are reliably decoded, the runlength streams are assigned corresponding EFM patterns and grouped into EFM frames [2]. Since the EFM frame is the basic information unit of data written on a CD, the above mentioned signal processing algorithms are compared by finding the number of errant EFM frames that occur in the recovered EFM frames. Recovery statistics are analyzed by considering 5M samples of the sampled RF signal from Samples 1-3. In Table II, comparisons of the different signal processing algorithms are based on the number EFM frames affected by long runs and the number of other errant EFM frames. Errant frames containing long runs are very significant, since defects are very often misjudged as longer-than-usual runlengths and data at these areas are missed. As a result, several EFM frames have data missing. The number of such EFM frames affected by long runs for each case is entered under the column named LR in Table II.

In the second part of experiment we used OSS to recover data from three broken pieces of CD having approximately 600 MB user data. In OSS a rotating custom chuck mounted on the spindle shaft holds one disc fragment at a time. Collection time and data length from the track is determined by the operator based on the length of the track in fragment and the desired data segment. Data are saved as binary files from each track. The largest file size in our experiment was 3.5MB, which was from the outermost track of the largest fragment. The data file size from innermost track of smallest fragment was 420KB. Read signals from all files are thresholded and the boundaries of data marks and lands are determined via WT processing. A statistical analysis of the quality of the signal is checked by plotting histograms of data mark and land lengths into nine groups corresponding to runlengths from $3T - 11T$. The grouping is done by automatic bin segmentation on the data marks and the lands. In this experiment each track was read four times. The total time to read data from all three fragments was approximately 60 hours. It took

approximately two weeks to extract the user data from RF current signal.

TABLE I: COMPARISON OF PROBABILITY OF ERROR, P_E OF DECODING RUNLENGTHS FOR THE THREE TYPES OF SIGNAL PROCESSING ALGORITHMS

Sample used	Simple Threshold		Dynamic Threshold / Exclusion Technique		Wavelet Processing	
	Data marks	Lands	Data marks	Lands	Data marks	Lands
Sample 1 (Dye-side knurling)	0.022875	0.0013	0.022875	0.0013	0.000675	0.000125
Sample 2 (Substrate-side knurling)	0.016133	0.003033	0.001433	0	0.001067	0
Sample 3 (Scratched substrate)	0.034725	0.082225	0.000337	0.004181	0.0000458	0.00113

TABLE II: COMPARISON OF RECOVERY STATISTICS

	Simple Threshold (No. of EFM frames)			Dynamic Threshold (No. of EFM frames)			Wavelet-based-algorithms (No. of EFM frames)		
	LR	Errant	Total	LR	Errant	Total	LR	Errant	Total
Sample 1 (Dye-side knurling)	89.25	66	574.25	89.25	66	574.25	5.5	29.75	584.5
Sample 2 (Substrate-side knurling)	42	102.33	584.67	13.67	62.67	587	4	45	583.67
Sample 3 (Scratched substrate)	100	193	505	29	109	507.33	25	59	508

REFERENCES

1. *Information technology – Data interchange on read-only 120mm optical data discs (CD-ROM)*, ISO/IEC International Standard 10149, 2nd Ed. - 1995.
2. S. Kasanavesi, T. D. Milster, D. Felix, T. Choi, "Data Recovery from a Compact Disc Fragment," *Proc. SPIE*, 5777(1): pp. 116-127, September 2004.
3. S. Kasanavesi, T. D. Milster, D. Felix, T. Choi, "An approach to graphs of linear forms (Unpublished work style)," unpublished. "Fundamentals of erbium-doped fiber amplifiers arrays (Periodical style—Submitted for publication)," *IEEE J. Quantum Electron.*, submitted for publication. "A note on reflector arrays (Periodical style—Accepted for publication)," *IEEE Trans. Antennas Propagat.*, to be published. {unpublished/submitted/accepted – all three formats for later use}
4. T.D. Milster, "Optical Data Storage," in *The Optics Encyclopedia: Basic Foundations and Practical Applications*, T.G. Brown, K. Creath, H. Kogelnik, M. A. Kriss, J. Shchmit, M.J. Weber, (eds.), Berlin:Wiley-VCH, 2004.
5. R. Polikar (2001, January 12). The Engineer's Ultimate Guide to Wavelet Analysis [Online]. Available:<http://users.rowan.edu/~polikar/WAVELETS/WTutorial.html> (URL)
6. G. Strang, and T. Nguyen, *Wavelets and Filter Banks*, Wellesley-Cambridge Press, 1997
7. M. Vetterli, "Wavelets and Filter Banks: Theory and Design", *IEEE transactions on signal processing*, Vol. 40, No. 9, September 1992.
8. M. Vetterli, "Filter Banks allowing Perfect Reconstruction", *Signal Processing* 10 (1986), pp. 219-244.
9. A. F. Abdelnour, and I. W. Selesnick, "Nearly Symmetric Orthogonal Wavelet Bases", *Proc. IEEE Int. Conf. Acoust., Speech, Signal Processing (ICASSP)*, May 2001.
10. F. Li, "Data recovery from various damaged optical media", Master's thesis, University of Arizona, Department of Electrical and Computer Engineering, 2005
11. P. R Hoffman. Scratch / Dig Optical Surface Specifications [Online]. Available: <http://www.prhoffman.com/technical/scratch-dig.htm> (URL)
12. The Smithsonian Astrophysical Observatory & The University of Arizona Steward Observatory (1997, October 9). Optical Surface Specifications [Online]. Available: http://www.mmt.org/MMTpapers/pdfs/f_9manfspecs.pdf (URL)
13. Application notes of optical profiler Wyko NT8000. Surface Measurement Parameters for Wyko Optical Profilers (AN505) [Online]. Available: <http://www.veeco.com> (URL)
14. A. Papoulis, and S. U. Pillai, *Probability, random variables, and stochastic processes*, 4th ed., New Delhi: Tata McGraw-Hill Publishing Company Limited, 2002, pp. 354-367.
15. D. L. Donoho, and I. M. Johnstone, "Adapting to Unknown Smoothness via Wavelet Shrinkage", *J. Am. Stat. Assoc.*, 90, 1200 (1995).

Laser diode feedback signal for position sensing using self-mixing interference

M. Y. Tsai*^a, T. S. Liu^a and T. E. Schlesinger^b

^aDepartment of Mechanical Engineering, Chiao Tung University, Hsinchu 30010, R. O. C.

^bDepartment of Electrical Engineering, Carnegie Mellon University, PA 15213, USA

ABSTRACT

This paper presents the conformity between the output voltage and the target surface displacement from a laser diode package using the self-mixing effect.

Keywords: laser diode, self-mixing, DVD pickup

1. INTRODUCTION

For position sensing, self-mixing interference (SMI) systems are cheaper than conventional interferometers, since many optical elements like a beam splitter, reference mirror, and external photo-detector are not required. Self-mixing interferometry has been used to measure the distance and displacement. Fast Fourier transform (FFT) analysis technique can be used to detect the signal phase and increase the measurement precision of SMI [1]. Experimentally, displacement was measured with a precision of $\lambda/50$. A double external cavity was proposed [2] with FFT technology. A distance resolution of 1 mm and displacement resolution down to 10 nm can be obtained.

A four-wire pickup head is one type of recording storage [3]. Near-field recording is a promising approach to achieving higher storage density. A laser diode (LD) height control system for near-field recording was developed and constructed by using the laser position sensor installed on a conventional biaxial DVD pickup. And a position accuracy of 9 nm was achieved when a glass disk with a runout of 16 μm at a speed of 1500 rpm. The approach limit that the laser can achieve was estimated to be around 25 nm when the laser size was reduced to 100 μm [4]. Since the noise frequency was much higher than 100 kHz, the residual error was able to be further reduced to ± 4 nm by means of a signal amplifier with a bandwidth of 100 kHz for filtering out noise and increasing the signal-to-noise ratio [5]. Experimental results by using a photodiode (PD) at the back facet of the LD show that the effective spot size was approximately 1 μm [6]. The LDs were mounted on commercial DVD actuators and a control system was constructed. The control system could operate both in the near and far fields, and a controlled approach from the far to near field was demonstrated using a fringe jump controller. This height control system based on feedback in a LD was capable of servo control with up to 1 nm accuracy and over distances ranging from over 10 μm to the nano-scale regime [7].

A flying slider pickup head is another type of recording storage device [8]. There was a measurement by using LD attached to a flying slider and a semi-transparent rotating disk mirror for an extremely-short-external-cavity configuration [9].

2. SYSTEM CONFIGURATION AND SETUP

The present system is measured by means of an actuated surface test system, as shown in Fig. 1. The system consists of DVD pickup mounted LD package with a PD shown in Fig. 2, target wafer fixed on a PZT transducer, and LDV (Laser Doppler Vibrometer) system. Operation current of the laser driver is set 40 mA to enter LD. Peak-to-peak voltage of the function generator is set 158.8 mV, waveform is triangle, and frequency is 10 Hz to enter the PZT driver. Signal of oscilloscope (OSC) channel one is PD signal through an amplifier, and signal of OSC channel two is LDV signal. Both sensors are used to measure displacement of a silicon wafer attached onto a PZT actuator.

*a. dreamyatsai.me94g@nctu.edu.tw; phone +886-3-571-2121; fax +886-3-572-0634

3. RESULTS AND CONCLUSION

Fig. 3 shows measured displacement of the silicon wafer where LDV signal in channel two is $2 \mu\text{m}$ per volt, and PD signal in channel one is $\lambda/2$ per complete interference fringe. Therefore, the signal is a periodic function of the distance with the maximum amplitude of 1.69 V and the pitch, a fringe, corresponds to a displacement of $\lambda/2$, which is 317.5 nm in this case. Although within a fringe, the signal varies nonlinearly with respect to the displacement, it can be approximated as a linear function in the middle region, as shown in Fig. 3. The slope of the linear function represents the sensitivity of the signal with respect to the signal amplitude. The slope in the linear region of this laser sensor is 100mV/nm.

The SMI signal contains multi-frequency components as shown in Fig. 4, for which the FFT method can extract the resonance frequencies. An AD/DA card at 10 kHz sampling rate catches the PD signal. The experimental setup is shown in Fig. 5. Fig. 6(b) shows the Fourier spectra of the SMI signal in Fig. 6(a). The low harmonic component corresponds to 10 Hz of frequency imported to PZT driver by function generator, which are 10 Hz, 20 Hz, and 40 Hz. There is a frequency measured as 275 Hz. By smoothing the original data of green dash-dotted line in Figs. 5 and 6, the frequency of 275 Hz is filtered out by the number of data points in the average is thirty-five shown in Figs. 6 and 7 blue curves.

This paper presents the conformity between the output voltage and the target surface displacement from a laser diode package using the SMI. Moreover, we have presented that tilting motion by using a tilting coil in a DVD pickup validates SMI signal, where the linear region is 100mV/nm. Filtering the frequency of 275 Hz is helpful in improving the SMI feedback signal for position control in the future.

4. REFERENCES

- [1] M. Wang, "Fourier transform method for self-mixing interference signal analysis", *Optics & Laser Technology* 33, 409-416 (2001).
- [2] M. Wang and G. Lai, "A self-mixing interferometer using an external dual cavity", *Institute of Physics Publishing, Measurement Science Technology* 14, 1025-1031 (2003).
- [3] C.-P. Chao, J.-S. Huang, C.-W. Chiu, and C.-Y. Shen, "Design and experimental study of an observer-based controller for a three-DOF four-wire type optical pickup head", *American Control Conference*, 2457-2462 (2005).
- [4] J.-Y. Fang, P. Herget, J. A. Bain, and T. E. Schlesinger, "Laser diode active height control system for data storage application", *Proc. of SPIE Vol. 6282*, 62820P(8) (2003).
- [5] J.-Y. Fang, C.-H. Tien, H.-P. D. Shieh, P. Herget, J. A. Bain, and T. E. Schlesinger, "Optical feedback height control system using laser diode sensor for near-field data storage applications"
- [6] P. Herget, J.-Y. Fang, J. A. Bain and T. E. Schlesinger, "Laser diode feedback sensor characterization experiments for data storage applications", *IEEE*, 144-146 (2006).
- [7] P. Herget, T. Ohno, J. A. BAIN, K. Takatani, M. Taneya, W. C. Messner and T. E. Schlesinger, "Laser diode active height control for near field optical storage", *Japanese Journal of Applied Physics*, Vol. 45, No. 2B, pp. 1193-1196 (2006).
- [8] C.-C. Hsiao, T.-S. Liu and S.-H. Chien, "Adaptive inverse control for the pickup head flying height of near-field optical disk drives", *Smart Materials Structures* 15, 1632-1640 (2006).
- [9] H. Ukita and Y. Karaki, "A wavelength and spectrum measurement of an extremely-short-external-cavity laser diode by precisely controlling slider flying height", *Optical Review*, Vol. 11, No. 3, 188-192 (2004).

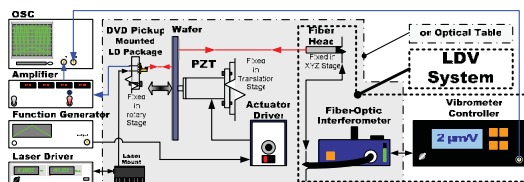


Fig. 1. Experimental setup for feedback signal characterization.

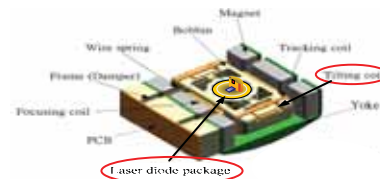


Fig. 2. DVD pickup with LD package.

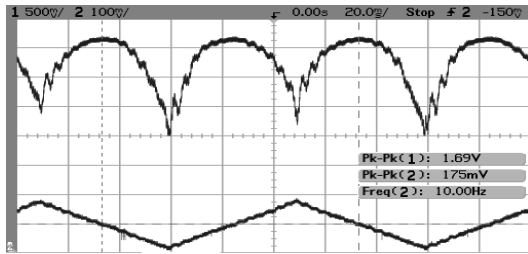


Fig. 3. Measured signals from (1) PD and (2) LDV with tilting pickup head and moving PZT.

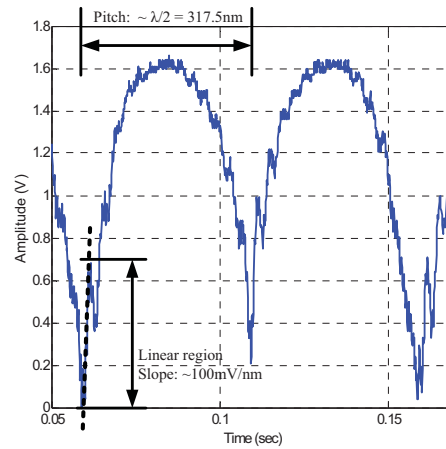


Fig. 4. Enlarged view of Fig. 3.

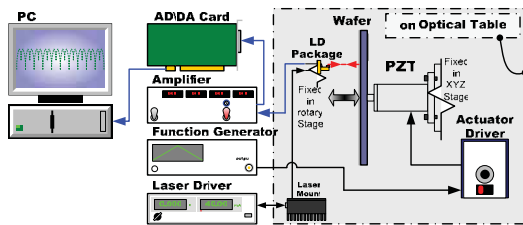


Fig. 5. Experimental setup for feedback signal on AD/DA card.

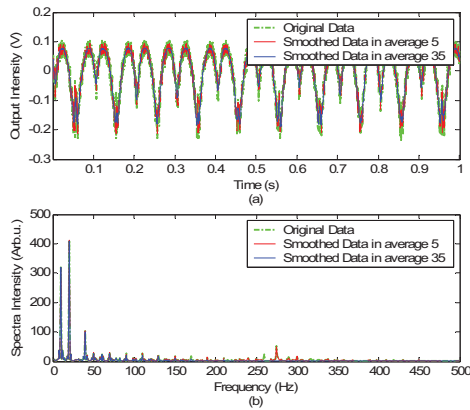


Fig. 6. (a) Interference fringe signal and (b) Fourier spectra of the interference fringe signal with moving PZT only.

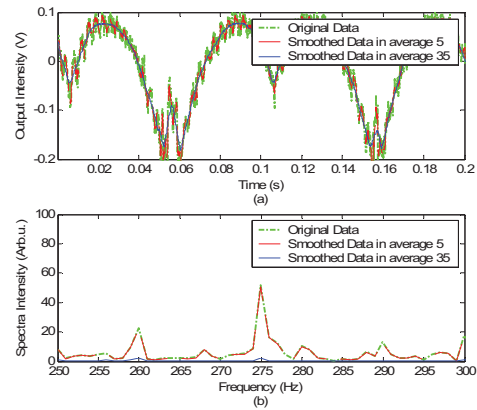


Fig. 7. Enlarged view of Fig. 6 from (a) 0 to 0.2 s and (b) 250 to 300 Hz.

High Resolution Semiconductor Inspection by Using Solid Immersion Lenses

Jun Zhang¹, Yullin Kim², Tom Milster¹, and Dave Dozer²

¹College of Optical Sciences, University of Arizona, Tucson, AZ, 85721, USA

²IRLabs, Inc., Tucson, AZ, 85719, USA

Email: jzhang@optics.arizona.edu

1. Introduction

Integrated circuit (IC) technology has achieved minimum pattern size on the chip around 45nm. There is a need to image subsurface features with a high lateral resolution. The current flip-chip configuration normally has many opaque metal layers and structures above the semiconductor pattern, thereby hindering the topside inspection of the buried surface. Thus, backside imaging through the IC silicon substrate is often preferred. However, due to the absorption of silicon, the wavelength of the illumination light for backside inspection is larger than 1 μ m, which results in a poor lateral resolution for the conventional subsurface microscope according to the diffraction limit $\lambda/(2\times NA)$. *State-of-art* subsurface microscopes have a typical spatial resolution around 1 μ m. In order to further increase the resolution of the subsurface microscope, a solid immersion lens (SIL) or numerical aperture increasing lens (NAIL) is used to increase the NA of the system by a factor of n or n^2 [1][2]. Unlike data storage applications, this application requires imaging over an area of the object.

Ippolito *et al.* have demonstrated a confocal microscope with lateral spatial resolution of better than 0.23 μ m using an aplanatic NAIL [3], which shows the potential to use near-field imaging for semiconductor inspection, failure analysis, and thermal distribution of the IC flip-chips. But the aplanatic NAIL which they used requires a very tight tolerance for the sample surface quality and the thickness between the pattern and the backside of the chips. A hemispherical SIL is welcome because of its loose tolerance. Chen *et al.* have also demonstrated a near-field solid immersion lens microscope at visible light using the induced polarization signal to control the air gap between the sample and the SIL [4][5]. Ishimoto *et al.* have demonstrated a gap and tilt servo for the near-field recording system [6].

Here we present a near-field subsurface microscope using a modified silicon solid immersion lens with NA=2.45 when illuminated with 1.2 μ m wavelength light source. The microscope uses a specific infrared objective with NA=0.7, the latest infrared detector, and is optimized for patterns underneath the surface (around 100 μ m deep) which matches up with current IC technology nodes. The object is located at the center of the solid immersion lens, as shown in Figure 1. A prototype gap and tilt servo for the subsurface microscope is under investigation.

2. Gap and tilt servo simulation

Current subsurface microscopes using SILs have very good spatial resolution, but they normally require the sample and the SIL to be polished very well and make zero gap thickness contact for imaging. Thus, the images have to be taken locally, and then stitched together to give the topology of the pattern. In order to have a dynamic measurement by

the microscope, which is preferred for IC inspection and failure analysis, a gap and tilt servo is needed. In our experimental setup, as shown in Figure 1, we use the induced polarization signal technique [5][6] for gap and tilt control. A linear polarized light source illuminates the pattern through the objective and the silicon solid immersion lens. After reflection, frustrated total internal reflection (FTIR) occurs, the induced polarization reflection is collected for the gap and tilt control. The reflected power of the induced polarization component changes monotonically with the air gap, as shown in Figure 2. The native polarization signal changes with air gap thickness and is also given Figure 2. The simulation model is based on a vector plane-wave decomposition of light emitted from the exit pupil [7][8][9]. *OptiScan* software is used to generate the images [10].

Tilt is a major issue in SIL technology. Normally the SIL is chamfered at a certain angle to reduce area of the bottom surface and improve tilt tolerance of the system. In addition, a small pedestal can be fabricated at the center of the bottom surface by etching [5]. The tilt servo is designed using the radial tilt error signal (RTES) and tangential tilt error signal (TTES) [6]. Simulated radial tilt and tangential tilt induced polarization pupil images at a tilt angle 20° are given in Figure 3. The pupil image is divided into four components A,B,C,D, as shown in Figure 3. The TTES and RETS are defined as the following, $TTES = (A+D)-(B+C)$ and $RETS = (A+B)-(C+D)$.

The relationships between the normalized RETS, normalized TTES and tilt angle are given in Figure 4, where the tilt direction is the same as the radial direction.

3. Experiment setup

A prototype gap and tilt servo is constructed and is being tested. The setup is shown in Figure 5. A parallelogram flexure design, as shown in Figure 6, is used to control the gap between SIL and sample. The encoder utilizes a glass scale that gives 1.2nm resolution, which when combined with a piezo crystal gives 6nm-resolution repeatability based off of the number of image counts. Total movement range is $60\mu\text{m}$.

4. Conclusion

We present a near-field solid immersion lens microscope with the lateral resolution around 300nm at the wavelength $1.2\mu\text{m}$. As the pattern size continues to shrink in the semiconductor industry, the need for subsurface imaging with submicron resolution is greatly increased. A SIL system has unique advantages to satisfy these imaging requirements. Combined with gap and tilt servo technology to achieve the dynamic imaging, it has very promising applications for IC inspection and failure analysis in the semiconductor industry.

5. References

- [1] S. M. Mansfield and G.S. Kino, *Appl. Phys. Lett.* **57**, 2615 (1990)
- [2] S. B. Ippolito, B.B. Goldberg and M.S. Unlu, *J. of Appl. Phys.* **97**, 053105 (2005)
- [3] S. B. Ippolito, B.B. Goldberg and M.S. Unlu, *Appl. Phys. Lett.* **78**, 26 (2001)
- [4] T. Chen, T. Milster, S.K. Park, B. McCarthy and D. Sarid, *Opt. Eng.* **45**, 10 (2006)
- [5] T. Chen, T. Milster, S.H. Yang and D. Hansen, *Opt. Lett.* **32**, 2 (2007)
- [6] T. Ishimoto, S. Kim, K. Saito, T. Kondo, A. Nakaoki and O. Kawakubo, *ISOM* (2007)
- [7] B. Richards and E. Wolf, *Proc. R. Soc. London, Ser. A* **42**, 2719 (2003)
- [8] D.G. Flagello, T. Milster and A.E. Rosenbluthk, *J. Opt. Soc. Am. A* **13**, 53 (1996)
- [9] T. Milster, J.S. Jo and K. Hirota, *Appl. Opt.* **38**, 5046 (1999)
- [10] T. Milster, *ODS* (1997)

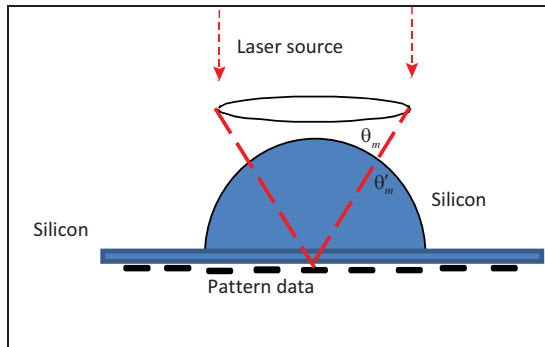


Figure. 1 Solid immersion lens and substrate.

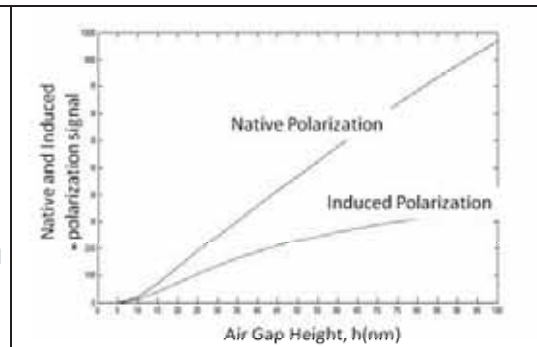
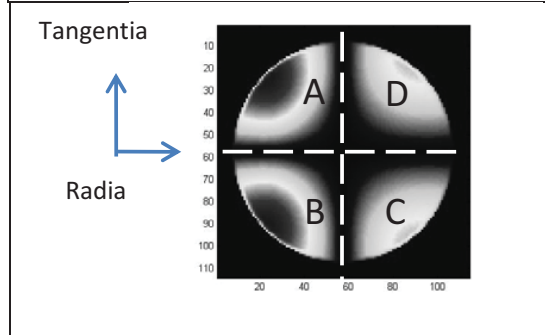
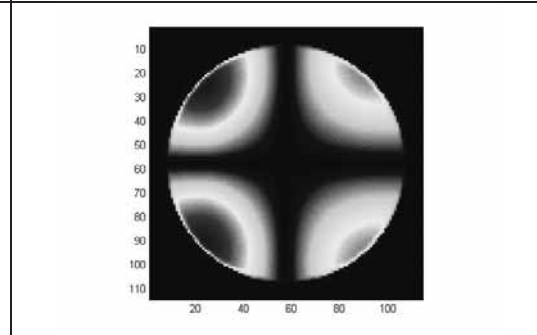


Figure. 2 Induced and native polarization signal.

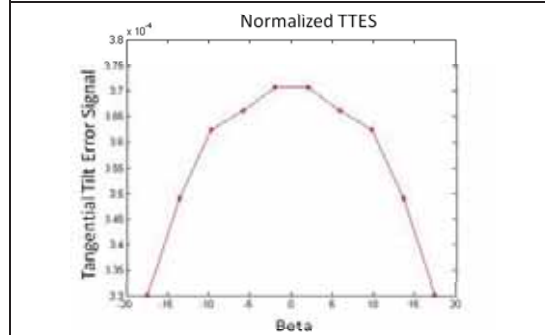


(a)

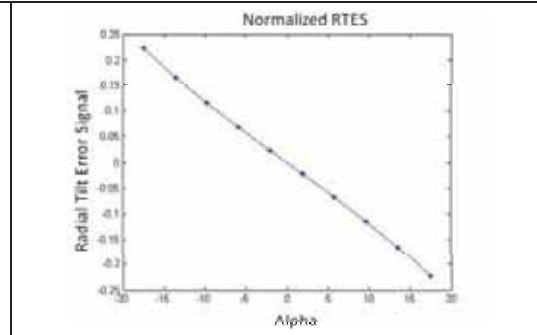


(b)

Figure.3 tilt angle 20° (a) radial tilt induced polarization pupil image, (b) tangential tilt pupil image.



(a)



(b)

Figure. 4 (a) Normalized TTES vs tilt angle, (b) Normalized RTES vs tilt angle.

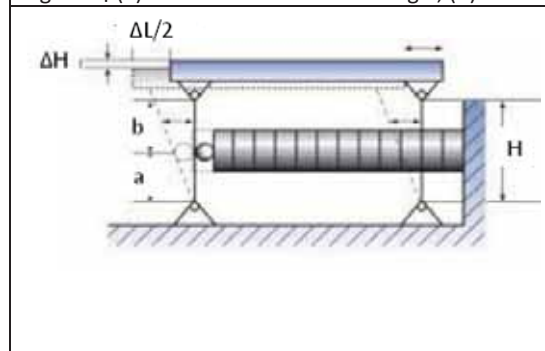


Figure. 5 Parallelogram flexure sketch.

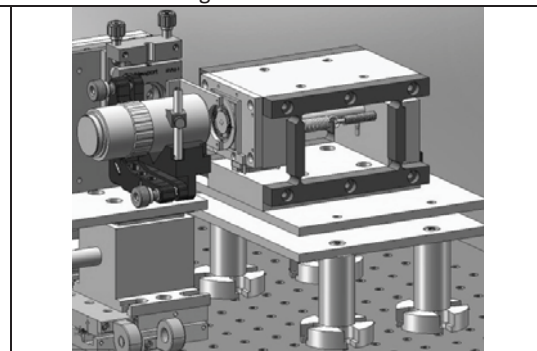


Figure. 6 Solidwork test setup.

Photochromic Memory with Electronic Functions II

Tsuyoshi Tsujioka

*Department of Arts and Sciences, Osaka Kyoiku University
Asahigaoka 4-698-1, Kashiwara, Osaka 582-8582, Japan
Email: tsujioka@cc.osaka-kyoiku.ac.jp*

Photochromic memory has been interested as a candidate of future high density optical memory ¹⁾²⁾. Photochromism is defined as a reversible transformation between two isomers with different absorption spectra upon photo-irradiation. Based on the photoisomerization not only the absorption spectra but also other molecular properties, such as refractive indices, dielectric constants, and ionization potential are changed reversibly. Recently, we found electronic functions of the molecule as well as optical property can be applied to information storage ³⁾⁴⁾⁵⁾. Functional combinations of optical and electronic properties will give new aspects in the field of information storage and will open new potentiality of functions and applications. In this paper, we report new and various aspects of such a photochromic memory with electronic functions.

Incorporation to electronic axis to photochromic memory gives two-dimensional aspects in information storage field using photosensitive molecules (Table 1). We have already discussed a possibility of photosensitivity control by electric field ⁶⁾. In that study, the photo-excited state of the molecule has the electron and hole are on the LUMO (the lowest unoccupied molecular orbital) level and the HOMO (the highest occupied molecular orbital) level, respectively. When the electric field is applied to the excited molecule, these carriers are able to be separated from the molecule and the molecule returns to the ground state, as shown in Fig. 1. This means that the recording sensitivity of the photochromic memory is able to be controlled (reduced) by applying the electric field. The experimental was carried out using a sample structure with a photochromic diarylethene (DAE) memory layer, and external current generated by carrier separation was observed. According to our estimation, the separation efficiency will come up to the value of unity asymptotically at the electric field strength around $1\sqrt{V/nm}$. This means the sensitivity of photon-mode recording would be reducible by the electric field at that field strength. Under the condition of the unity separation efficiency, the perfect nondestructive readout would be possible.

We have also proposed a principle of organic semiconductor memory using DAE molecules ⁴⁾. In that memory the isomerization by electrical carrier injection is used instead of photo excitation. This is a just inverse process of the carrier separation described above as shown in Fig. 2. On the research about organic semiconductor memory, the isomerization

reaction of the DAE memory layer by, hole injection, not by both of hole and electron, was also found to be possible ⁷⁾. Figure 3 illustrates the continuous isomerization by transporting holes in the DAE layer. Figure 4 shows the applied voltage dependence of isomerization. Current decrease originates in the ionization potential change based on isomerization and therefore lower voltage application enables the more efficient reaction (lower current and voltage). That is, reaction of many molecules follows to a single hole transportation. Such a reaction via cationic state has been known for some DAEs.

This phenomenon would be applicable to obtain not only semiconductor memory, but also, optical memory. Figure 5 shows a schematic example for increasing sensitivity of optical recording. Recording laser is focused into the memory layer consist of photochromic molecules. Then, a molecule in the memory layer absorbs a photon in the beam, and is transformed into the excited state. Electric field applied to the memory layer separates carriers from the molecule, and the generated hole is transported in the layer. The hole being transported, therefore, can make to react with many other molecules and the efficient recording will be achieved. This principle would be applied to various kind of high density memory including two-photon absorption memory.

In conclusion, two-dimensional aspects of photochromic memory with electronic function were introduced. The isomerization of photochromic molecule by using electrical carrier injection was reported. Furthermore the isomerization of molecule via a hole injection was demonstrated. Recording sensitivity would be controlled by electric field. The photochromic memory with electronic function will incorporate a variety of potentiality into the field of high density data storage.

References

- 1) M. Irie, Chem. Rev. 100, 1685 (2001).
- 2) M. Irie, T. Fukaminato, T. Sasaki, N. Tamai and T. Kawai, Nature 420, 759 (2002).
- 3) T. Tsujioka, Y. Hamada, K. Shibata, A. Taniguchi and T. Fuyuki, Appl. Phys. Lett. 78, 2282 (2001).
- 4) T. Tsujioka and H. Kondo, Appl. Phys. Lett., 83, 937 (2003).
- 5) T. Tsujioka, K. Masui and F. Otoshi, Appl. Phys. Lett., 85 (2004)
- 6) T. Tsujioka, K. Masui, and R. Takagi, Technical digest of ISOM/ODS 2005, MP19.
- 7) T. Tsujioka, N. Iefuji, A. Jiapaer, M. Irie, S. Nakamura, Appl. Phys. Lett. 89, 222102 (2006)

Table 1 Two-dimensional aspect for the function of photochromic memory

<u>Optical memory by photon absorption</u>	<u>Electronics by photon absorption</u>
Photoisomerization	Electronic characteristic change
Conventional photon-mode optical memory	Nondestructive readout of photon-mode memory
<u>Optical function by electric current/field</u>	<u>Electronics by electric current/field</u>
Recording sensitivity control by electron	Organic semiconductor memory

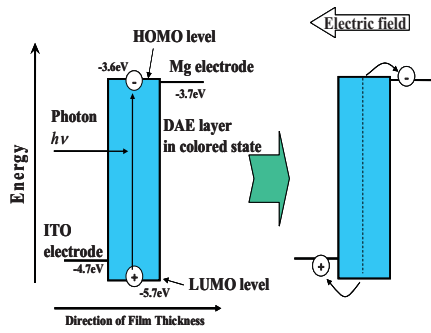


Fig. 1 Principle of electric carrier separation

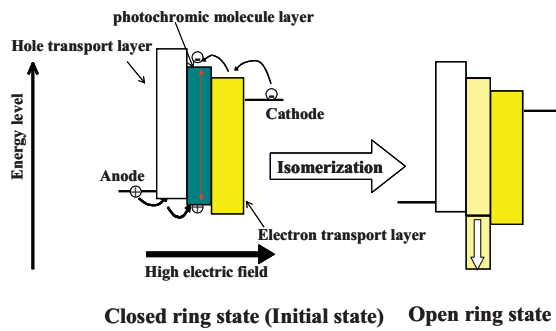


Fig. 2 Principle of isomerization by carrier injection

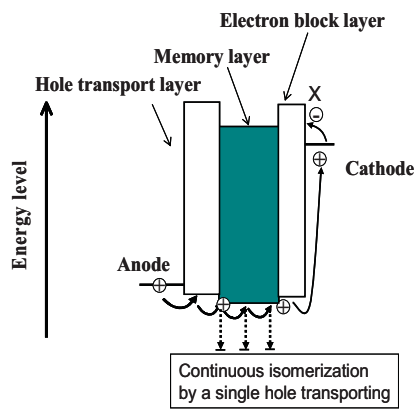


Fig. 3 Illustration of efficient isomerization by hole transportation

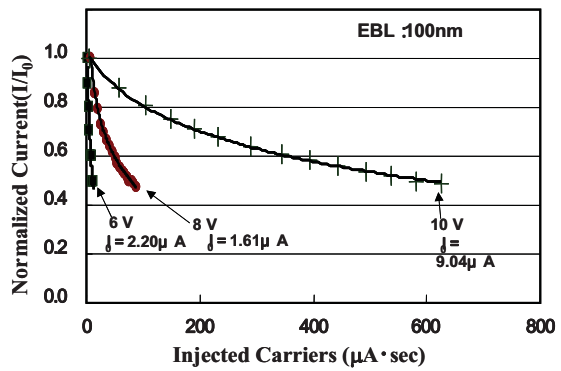


Fig. 4 Current decrease by hole transportation

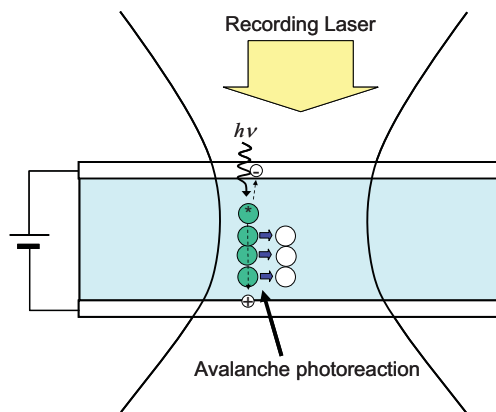


Fig. 5 Schematic illustration of avalanche reaction using hole transportation generated by photon absorption in photochromic layer.

Chalcogenide layers for optically guided mechanical recording-readout

^aM. Trunov, ^bP. Nagy, ^bE. Kalman, ^cV. Takats, ^cS. Kokenyesi

^aUzhgorod National University, Pidhirna str. 46, Uzhgorod, Ukraine 88000

^bInstitute of Surface Chemistry and Catalysis, Pusztaszeri út 59-67, Budapest, Hungary H-1525

^cDept. of Experm. Phys., University of Debrecen, Bem sq. 18/a, Debrecen, Hungary 4026

ABSTRACT

The giant negative photoplastic effect (giant photosoftening) in amorphous chalcogenide layers was observed and applied to the optically guided nanoindentation experiments by means of pyramidal Bercovich nanoindenter. The low-intensity, non-heating He-Ne laser beam ($\lambda=633$ nm) was used to change the viscosity of the sensitive media during the recording, which can result 30 – 350 nm deep and 200 nm wide pyramidal holes under 0.1 - 10 GPa pressure in a model $As_{0.2}Se_{0.8}$ layer. After the recovery time (a few s) the layer became again hard, the marks are stable at room temperature conditions and can be readout mechanically. The best compositions were determined in the As-Se system, which has optimum sensitivity to the illumination by ~ 2 eV photons, while other systems can be driven at different wavelengths.

Keywords: chalcogenide glasses, photoplasticity, indentation, mechanical relief recording

1. INTRODUCTION

Essential changes of optical transparency and refraction occur in a number of amorphous chalcogenide layers due to the illumination in the spectral range of the fundamental optical absorption edge [1,2]. These changes are less or more reversible and connected to the certain structural transformations within the amorphous state of the recording media, the mechanism of which is not fully explained up to now. What is more, small residual changes of the structure causes different solubility in illuminated and non-illuminated regions, what is used for surface pattern fabrication, high resolution lithography, holography and CD master disk recording [3].

The spatial resolution of this type of optical data recording is diffraction limited to the few hundreds of nanometers. Further increase of the resolution to the nanometer scale can be realized involving new physical effects in these materials. One of the most interesting one is the so called photoplastic effect [4] (other name is photofluidity [5]) which reveals itself in essential photoinduced reduction of the viscosity. Since chalcogenide glasses and amorphous layers are rather “soft” materials, in many aspects similar to polymers, the unique changes of mechanical parameters during illumination can be connected with their peculiar chainy-layered structure, specific character of light interaction with it [6], but the real mechanism of these effects is far from completeness. Just for this reason systematic investigations of compositional dependence of the photoplastic effect, its' dependence on experimental conditions of nanoindentation were started and used in the present work as a possible basis for a mechanical, millipede-type memory device, where the heat-driven pit recording can be replaced by light-driven process.

1. METHODOLOGY

Amorphous chalcogenides from As_xSe_{1-x} ($0 \leq x \leq 0.4$) system were investigated because they exhibit giant photoplasticity effect [7] under the influence of the red laser light, are rather simply prepared by vacuum thermal deposition on oxide glass or sapphire substrata. The

preservation of the composition was checked by EDAX measurements (Hitachi S-4300). The thickness d of the homogeneous layers was 1-2 μm , what was necessary to ensure the possibility of full range measurements by Hysitron Triboscope-type nanohardness meter equipped with AFM, which gives us additional possibility to provide *in situ* laser illumination of the examined area and to make AFM pictures of the deformed surface. The surface of the samples was smooth, average surface roughness of the layers was about 0.5 nm as measured by NT-MTD type AFM and so not influenced the accuracy of the deformation measurements. Illumination was provided by He-Ne laser or laser diode with $\lambda=635$ nm and the incident power did not exceed of $50 \text{ mW}\cdot\text{cm}^{-2}$.

2. DATA

First of all the best experimental conditions were investigated for the measurements of deformation parameters. The dynamical response of the media on the pressure induced by the Berkovich indenter was studied using several different loading functions, including the different peak load (from $60 \mu\text{N}$ to 1 mN) and different combinations of rise time and holding time. The typical load-displacement curves are presented in Fig.1. It should be mentioned that the used intensities are not influencing the temperature of the sensitive layer, i.e. we are working with a pure athermal process.

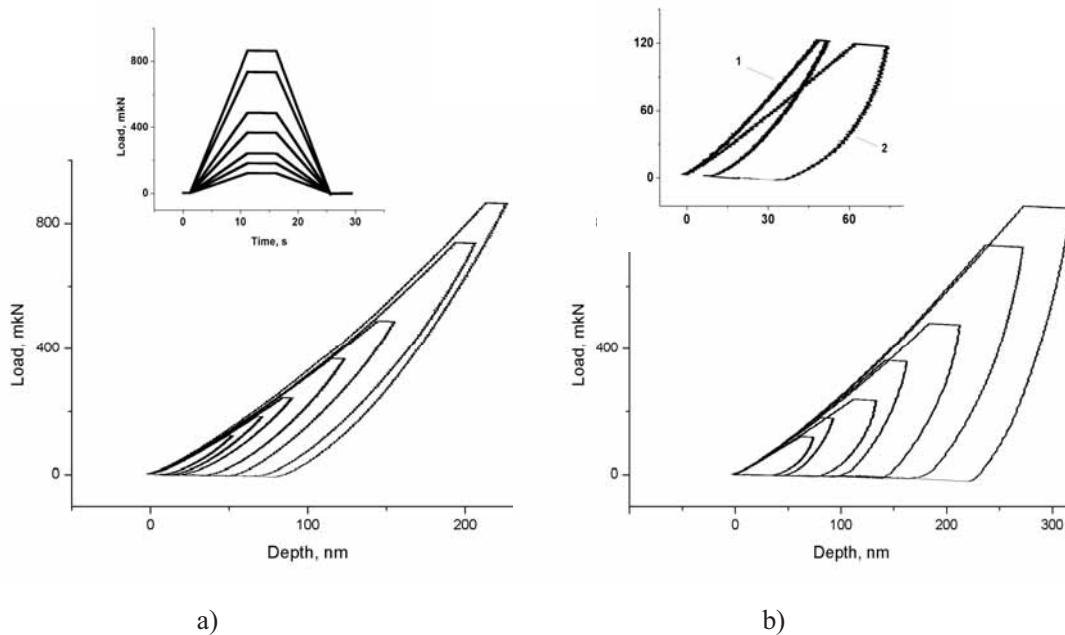


Fig.1 Penetration curves of a Berkovich indenter in annealed amorphous $\text{As}_{0.2}\text{Se}_{0.8}$ film under continuously increasing-decreasing load: a) in darkness and b) upon illumination at the same loading schemes. In inset: (a) loading schemes and (b) response of the film to a load of $120 \mu\text{N}$ in darkness (1) and under illumination (2).

The compositional dependence of the maximum deformation (hole depth) under the same pressure and illumination conditions appeared to be just opposite to the known photo-darkening effect, which is increasing from pure Se towards $\text{As}_{0.5}\text{Se}_{0.5}$ composition. We have

not taken into consideration the pure selenium layer, since it is rather unstable at 293 K, especially under illumination, which causes crystallization [6]. Introduction of 5-10 at% of As essentially stabilize the amorphous state of such binary glass [6] and make it perfectly suitable for nanoindentation measurements.

It was established that compositions with 6-20 at% of As possessed the largest photoplasticity effect, and the $As_{0.2}Se_{0.8}$ composition was chosen as the best for further development of optically guided pit recording. The possible scheme of such recording is presented in Fig. 2.

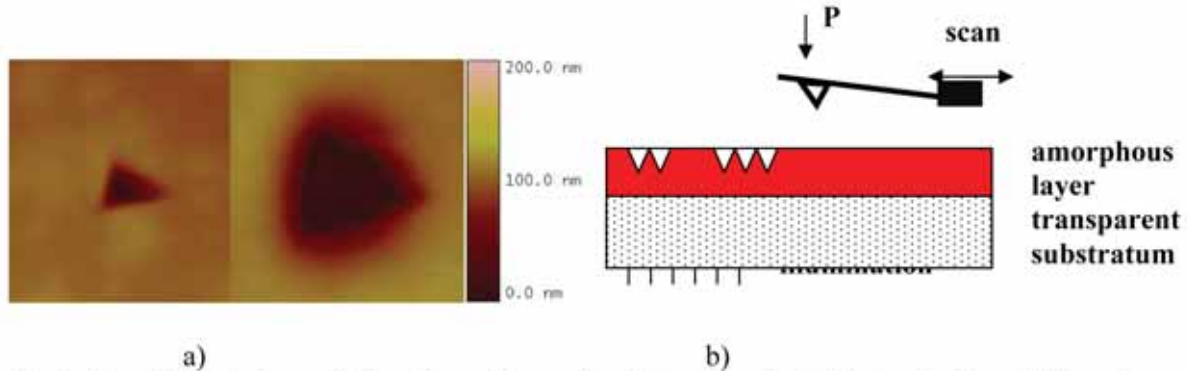


Fig.2. The AFM pictures of the pits on the surface (a) in the dark/after irradiation (left) and under irradiation (right) for load $P = 1\text{mN}$ and (b) the scheme of the optically guided nano-mechanical recording-readout .

The switch-on time in the $As_{0.2}Se_{0.8}$ layer was a few seconds for the used illumination intensities and the minimal width of the imprint in our experiments was 20 nm. So the whole system can be used as archival memory with total or addressable illumination at the recording stage. Since other glass compositions, for example in As-S system, also exhibit photoplastic effect to a certain extent in different spectral regions according to their optical absorption edges, they can be used for similar purposes, but further experiments are necessary to find the optimum materials in each case.

3. CONCLUSIONS

We conclude that amorphous As-Se layers can be used as memory materials for archival, mechanical recording optically guided by low intensity, non heating red laser illumination.

ACKNOWLEDGEMENT

This work has been supported by the Hungarian-Ukrainian UA-14/2006 and OTKA K67685 grants.

REFERENCES

1. J.Singh, K.Shimakawa, *Advances in Amorphous Semiconductors*, CRC Press, (2003).
2. Kikineshi A. *Optical Memory and Neural Networks*, v.4, N3, pp.177-183 (1995).
3. J. Teteris *Current Opinion Sol. State and Mater. Sci* 7 (2003) 127-134.
4. M.L.Trunov *J. Non-Cryst. Solids* 192/193 (1995) 431.
5. H. Hisakuni, K. Tanaka *Science* 270 (1995) 974.
6. A.Feltz, *Amorphe und Glasartige Anorganische Festkorper*, Akademie-Verlag, Berlin, 1983.
7. M.L. Trunov, V.S Bilanich, S.N. Dub, R.S. Shmegeera *JETP Letters* 82 (2005) 562.

Online face recognition system using holographic optical correlator

Reiko Akiyama, Sayuri Ishikawa, Eriko Watanabe and Kashiko Kodate

Japan Women's University, Mejirodai 2-8-1, Bunkyo, Tokyo, 112-8681 Japan

Phone: +81-3-5981-3615, Fax: +81-3-5981-3615 E-mail: facer@fourier.jwu.ac.jp

ABSTRACT

We have proposed and improved a face recognition system based on the algorithm for the Fast Face Recognition Optical Correlator system (FARCO). When it is used as an online search engine for facial images, recognition requires 10ms due to data translation and the limited capacity of RAM for storing digital reference images. In order to accelerate the speed, we have developed a holographic optical correlator system that integrates coaxial holography and the optical correlation technology used in FARCO. Optical correlation of 10μs/face is expected, on the assumption that 37,680 faces per second can be achieved with 20 μm pitch of hologram in one track rotating at the speed of 1,000 rpm. This system can be applied to different types of image search engines.

Keywords: face recognition, image search, coaxial holography, optical correlator, holographic optical memory

1. INTRODUCTION

Today various forms of information and data are exchanged online, and safeguarding information and privacy is one of the major challenges to building a safer society. Personal authentication technology based on biometrics is considered to be an effective means to prevent disguise or counterfeit, and therefore essential in an IT-based society. To keep up with high demands for such tools and constant innovation, we have developed and improved a highly accurate face recognition optical correlator system called FARCO (1000faces/s)^[1], based on the principles of mat filtering and phase information. In order to apply FARCO to the online environment, the system had to be readjusted. This article describes procedures of constructing such a system that can correlate at ultra high speed with large data storage capacity by integrating coaxial holography and the optical correlation technology.

2. ONLINE FACE RECOGNITION SYSTEM

2.1 The face recognition algorithm for FARCO system

An algorithm for the FARCO system is shown below (Fig.1). Through pre- and post-processing using a PC, the S/N ratio and the robustness can be greatly enhanced^[2]. The procedures consist of three stages: pre-processing, correlation operation and post-processing. Facial images were captured automatically by a camera-phone. Two points of eyes in these images are taken out. The size of the extracted image was normalized

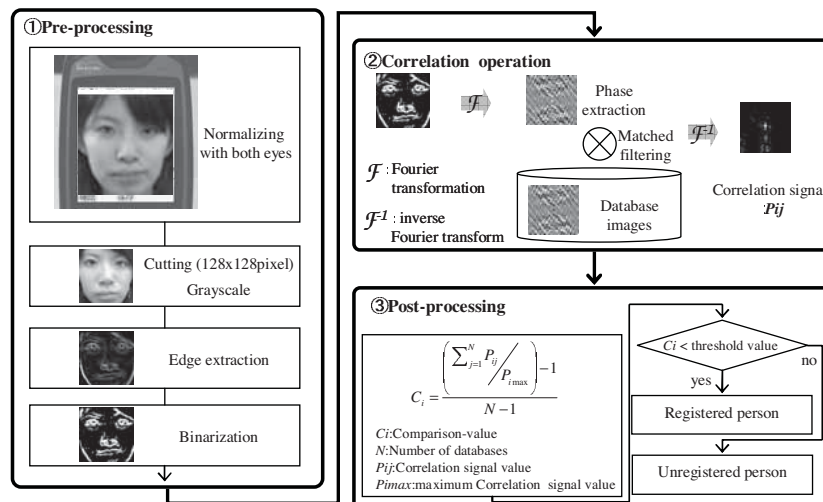


Fig.1 The face recognition algorithm for FARCO

to 128 x 128 pixel by the center. For input images taken at an angle, affine transformation was used to adjust the image and the image was normalized, fixing on the position of the eyes. This was followed by edge enhancement with a Sobel filter which binarized and defined the white area as 20%, and equalized the volume of transmitted light in the image. We have shown previously that binarization of the input (and database) image with appropriate adjustment of brightness is effective in improving the quality of the correlation signal. The correlation signal is classified by a threshold level. In practical applications, the threshold value must be customized. The threshold value varies depending on its security level, that is, on whether the system is designed to reject an unregistered person or permit at least one registered person. The optimum threshold value must be decided using the appropriate number of database images based on the biometrics guideline^[3] for each application. In this paper, the threshold value is fixed where equal error rate (EER) is at its lowest.

2.2 Application of online face recognition system

Applying the algorithm used for FARCO, a high-security online face recognition system was designed (Fig.2). The registration process for facial images has four steps. First, an administrator informs users of the URL, on which the online face recognition system is based. Then, the users access the URL. Several facial images were taken as reference images in their PCs or blogs on the internet. They were uploaded to the server together with their IDs, distributed at the time of registration in advance. Their facial images can be checked by the users themselves. Web page from an online face recognition is shown in Fig.2 (KEY images). The recognition process can be described as follows. When a facial image together with his/her ID is input, the pre-processed image will be checked with the stored images in the database. Recognition result will be displayed on the webpage as in Fig.2 (Recognition result). As the system interface was designed for a web-camera or a surveillance camera, it can be applied widely and introduced at various places such as school, office and hospital for multiple purposes.

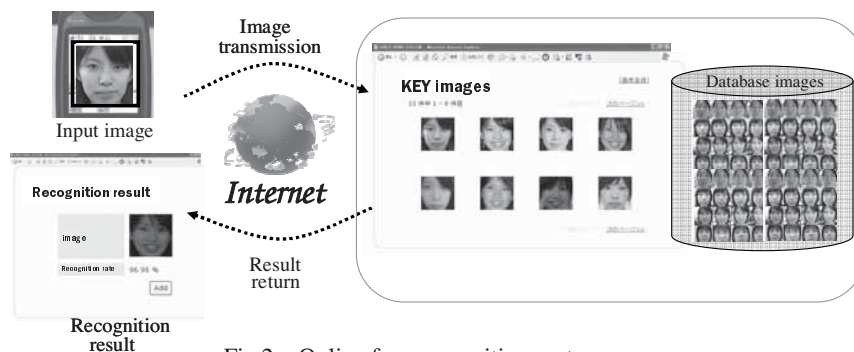


Fig.2 Online face recognition system

The online face recognition system based on the algorithm for FARCO was constructed as its software, with which simulation was conducted^[4,5]. If the intensity exceeded a threshold value, the input image would be regarded as a match with a registered person. Error rates divided by the total number of cases were given by the false rejection rate (FRR) and false acceptance rate (FAR). Results demonstrated considerably low error rates: 0 % as FAR, 1.0 % as FRR and EER.

However, in FARCO software, images are stored as digital data in the database such as Hard Disk Drive. As a result, an extra time is required for reading out data. In order to achieve high operation speed by optical processing, it is necessary to eliminate this bottleneck.

3. DEVELOPMENT OF HOLOGRAPHIC OPTICAL CORRELATOR SYSTEM

The constructed interface as an online face recognition system can be replaced by a holographic optical correlator, which is ultra high speed all optical correlation system^[6]. The system is potentially 100 times faster than the FARCO software. The FARCO software as well as ultra high speed all optical correlation system has been developed in parallel. Experiments were carried out using a holographic optical correlator.

3.1 Holographic optical correlator system — Ultra high speed all optical correlation system—

Using coaxial holography, two-dimensional page data can be recorded as volume holograms are generated by reference beam and signal beam that are bundled on the same axis and irradiated on the recording medium through a single objective lens^[7]. The holographic optical correlation system setup is shown in Fig.3. We applied the objective lens with specifications of NA=0.55 and focal length of 4.00mm for optical Fourier transformation. Photopolymer was used as holographic recording material. The structure of the holographic recording media has the reflection layer beneath the recording layer. We determine the thickness of recording layer as 500 μm . Correlation yielded results for 20 μm pitch multiplex recording. In this experiment, intensity values of correlation signals were obtained by CMOS sensor.

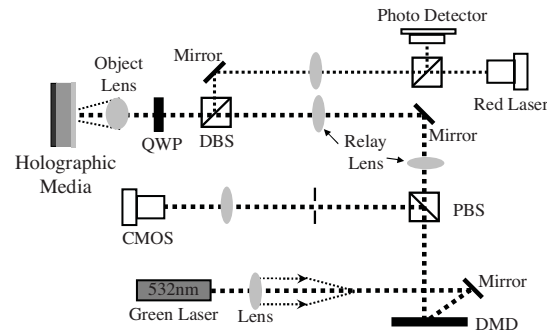


Fig.3 Holographic Optical correlation system

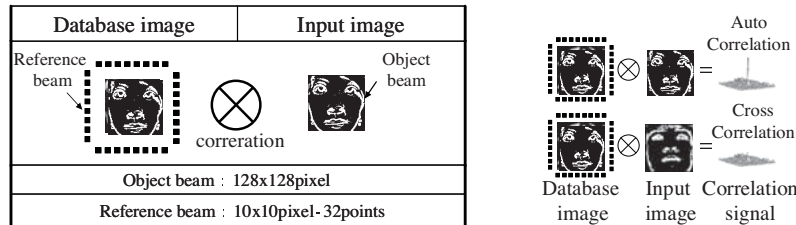


Fig.4 The experimental sample of face images

We performed a correlation experiment using facial images of 300 persons. Some of the facial images of input and database are shown in Fig.4. These images are normalized using our pre-processing method described in Section 2.1. The image of a multiplex record correlation result is shown in Fig.5, results demonstrated low error rates: 0 % as FAR, 4.67 % as FRR and EER.

4. CONCLUSION

The algorithm for previously-constructed FARCO system was applied to face recognition online, and the utility of the system was examined. The proof experiment with a holographic and optical correlator confirmed that the database containing large datasets could be processed and correlated at ultra high speed.

Optical correlation of 10μs/face is expected, assuming that 37,680 faces can be processed in one second with 20 μm pitch of hologram in one track rotating at 1,000 rpm. Applied as a face recognition system, it is then possible to correlate more than 314,000 faces per second. This system is also applicable to various image search engines. Based on the system, an ultra high speed attestation can further be achieved for larger database by using a holographic optical memory of the disk type and higher accuracy of the system will be sought in the future, in addition to its application to the online face recognition system.

Acknowledgement

This study is partly supported by the Cooperative Program of Practical Application of University R&D Results Under the Matching Fund Method (R&D) of NEDO.

References

- [1] E. Watanabe and K. Kodate, Appl. Opt. 44, 666-676 (2005).
- [2] R.Inaba, E.Watanabe and K.Kodate, Opt., Rev. 10, 4, 255 (2003).
- [3] A.J.Mansfield and J.L.Wayman, Biometric Testing Best Practices Version 2.01 (National Physical Laboratory, Teddington, 2002).
- [4] S. Ishikawa, E. Watanabe and K. Kodate, POF&MOC 2007 Technical Digest, G6, 130-131 (2007).
- [5] S.Ishikawa, E.Watanabe, M.Ohta and K.Kodate, 5th International Conference on Optics-photonics Design & Fabrication, 7PS4-49, 305-306 (2006).
- [6] E. Watanabe and K. Kodate, Jpn. J. Appl. Phys., 45, 8B, 6759-6761 (2006).
- [7] H. Horimai, X. Tan, and J. Li, Appl. Opt. 44, 2575-2579 (2005).

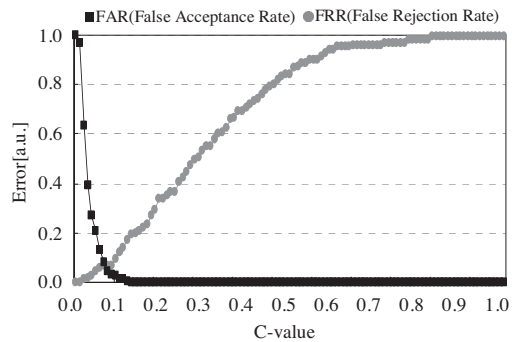


Fig.5 Experimental for holographic optical correlation system

Characteristic of the tracking error signal of a novel multi-level read-only disc

Mingming Yan^{*}, Jing Pei, Longfa Pan, Yi Tang
Optical Memory National Engineering Research Center,
Tsinghua University, 100084, Beijing, P. R. China

ABSTRACT

Multi-level run-length-limited technology could be employed to increase the capacity of the optical disc without changing the optical and mechanical unit. To improve the tracking servo characteristic of the ML-RLL read-only disc, a novel multi-level disc by using signal wave-shape modulation is proposed and realized on the DVD platform. The readout system for the novel multi-level read-only disc is also proposed. The uniformity and symmetry of the DPD signal of the novel multi-level read-only disc is better than the ML-RLL read-only disc and more close to the DVD read-only disc. The variance of the peak to peak value distribution of the DPD signal in open loop of the novel multi-level disc is nearly 1/5 of that of the ML-RLL read-only disc and is approximate to that of the conventional DVD read-only disc.

Keywords: optical storage, multi-level, run-length limited, DPD signal, tracking servo

1. INTRODUCTION

As the market size of HDTV program is growing very sharply, the optical disc with larger capacity and higher data transfer rate is required. Multi-level method is one of technology to increase the storage capacity and data transfer rate which can record more than two states in a mark and without changing the optical and mechanical unit.[1] Combining the multi-level (ML) method and run-length limited (RLL) technology, ML-RLL technology can achieve equivalent storage density with less level than only using multi-level method. The ML-RLL read-only disc employed amplitude modulation method to achieve multi-level has been reported. [2-3] However, influenced by the variation of the record mark and the crosstalk from adjacent tracks, the uniformity and symmetry of the DPD signal of the ML-RLL read-only disc is worse than that of the DVD read-only disc, which resulted in the instability of the tracking servo. [4]

In this paper, to improve the tracking servo performance, a novel multi-level read-only disc using signal wave-shape modulation (SWSM) is presented. The signal wave-shape modulation multi-level (SWSM ML) read-only disc is realized on the DVD platform. The uniformity and symmetry of the tracking signal of the SWSM ML read-only disc is better than that of the former ML-RLL read-only disc and more similarly with the conventional run-length limited read-only disc, such as DVD-ROM.

2. THE SIGNAL WAVE-SHAPE MODULATION ML DISC

The conventional DVD read-only disc uses the land/pit to generate the readout signal. Based on the record marks of the conventional DVD disc, sub-lands/sub-pits are inserted into the conventional DVD patterns as shown in Fig. 1. By inserting the sub-land/sub-pit in the different position of the DVD's pit/land or changing the length of the sub-land/sub-pit, it can generate different wave-shape readout signals which indicate the different levels. The sub-land/sub-pit is smaller than the DVD shortest pit/land. Fig. 2 shows the patterns of the SWSM ML read-only disc scanned by the atom force microscope.

The level number of the readout signal is determined by the location of the sub-land/sub-pit on the pits/lands and the length of the sub-land/sub-pit. One of the benefits of the SWSM ML read-only disc is the longer pit/land can yield more

^{*} Email: ymm@mails.tsinghua.edu.cn; Phone: +86-10-6278-8101; Fax: +86-10-6279-2828

levels, because the sub-land/sub-pit can be inserted in more position and its length can be varied more. For example, 14 levels can be realized on 10T and 11T while 6 levels can be realized on 6T and 7T signal. Another benefit of the SWSM ML read-only disc is that the tracking servo performance is better than the former ML-RLL read-only disc.

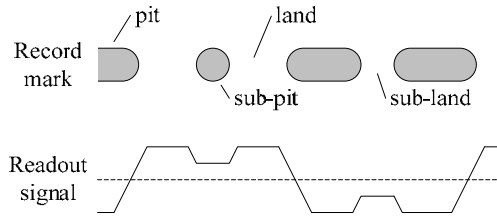


Fig. 1. Principle of the signal wave-shape modulation

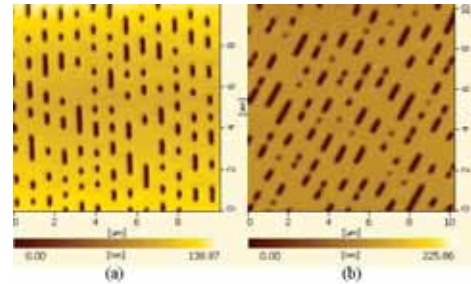


Fig. 2. Patterns of (a) the conventional DVD and (b) the SWSM ML read-only disc

3. READOUT SYSTEM AND SERVO PERFORMANCE

Fig. 3 shows the schematic diagram of the readout system for the SWSM ML read-only disc. The SWSM ML read-only disc uses the same wavelength, track pitch and number aperture (NA) with the conventional DVD read-only disc. That means it's possible to use the optical pickup of DVD-ROM. The system uses the commercial DVD read-only optical pickup and is controlled by the digital servo controller. The digital controller gets the analog signal, including focusing error (FE) signal and tracking error (TE) signal, from the 12-bit analog-to-digital converter (ADC) and outputs the signal to the 14-bit digital-to-analog converter (DAC) after executing the digital control algorithm. The digital servo controller is realized by the FPGA with an interior working clock of 150MHz. To minimize the discretization error, the sample frequency of the readout system is 125 kHz.

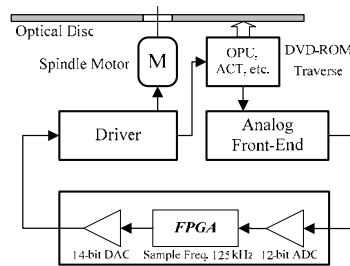


Fig. 3. Diagram of the readout system.

The astigmatic method is used to generate the FE signal while the DPD method is used to generate the TE signal. To compare with the DVD and the ML-RLL read-only disc, we made experiments on the three types of discs using the same readout system. Fig. 4 shows the DPD signal of the DVD read-only disc, the ML-RLL read-only disc, and the SWSM ML read-only disc when the focusing servo loop is closed. We recorded the DPD signals of crossing about 500 tracks of the three types of discs when the tracking loop is open for statistical analysis of the DPD signal quantity. The mean value of the DVD read-only disc is 1.91 while its variance is 0.010; the mean value of the ML-RLL read-only disc is 1.46 while its variance is 0.068; the mean value of the SWSM ML read-only disc is 1.43 while its variance is 0.011. The statistical result shows that the uniformity and symmetry of the DPD signal of the SWSM ML read-only disc is better than that of the ML-RLL read-only disc and is approximately the same as that of the conventional DVD read-only disc.

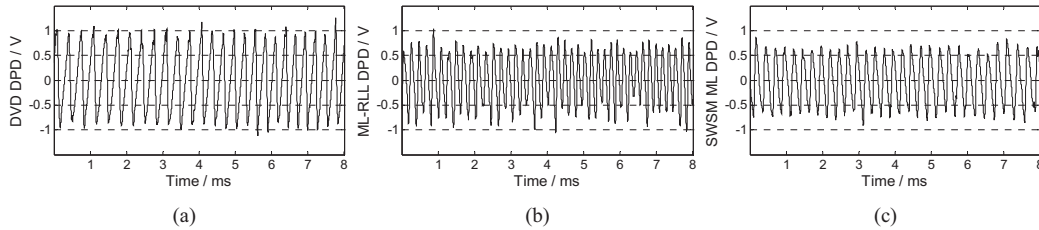


Fig. 4. DPD signal of (a) the DVD disc, (b) the ML-RLL disc and (c) the SWSM ML disc

Influenced by the variation of the width and depth of pits and the crosstalk from adjacent tracks, the uniformity and symmetry of the DPD signal of the ML-RLL read-only disc is rather worse than that of the DVD read-only disc, so it is hard to employ the DVD's tracking regulator and becomes more difficulty to design the tracking controller. However, the SWSM ML read-only disc achieves multi-level signal by inserting the small land/pit in the DVD pit/land instead of changing the width and the depth of the pit. The characteristic of the DPD signal of the SWSM ML read-only disc is almost as the same as that of the DVD read-only disc. So we can employ the DVD's tracking regulator with the lag-lead compensation method. Fig. 5 shows the residual tracking error signal of the DVD and the SWSM ML read-only disc when both using the DVD's tracking regular.

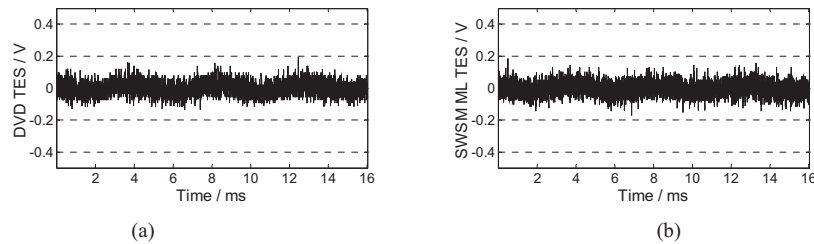


Fig. 5. Residual TES signal of (a) the DVD disc and (b) the SWSM ML disc

4. CONCLUSION

This paper proposes a novel multi-level disc by using signal wave-shape modulation, and discusses the tracking performance of the SWSM read-only disc. Compare with the conventional DVD disc and the former ML-RLL read-only disc, the uniformity and symmetry of the DPD signal of the novel multi-level read-only disc is better than the ML-RLL read-only disc and more close to the DVD read-only disc. The variance of the peak to peak value distribution of the DPD signal in open loop of the novel multi-level disc is nearly 1/5 of that of the ML-RLL read-only disc and is approximate to that of the conventional DVD read-only disc.

REFERENCES

- [1] T. Zhou, C. Tan, et al, "Multilevel amplitude-modulation system for optical data storage," in *Advanced Optical Storage Technology*, D. Xu, S. Ogawa, eds., Proc. SPIE 4930, 7-20 (2002).
- [2] Q. Zhang, Y. Ni, D. Xu, et al, "Multilevel run-length limited recording on read-only disc," in *Jpn. J. Appl. Phys.* 45(5A), 4097-4101 (2006).
- [3] J. Song, Y. Ni, D. Xu, et al, "Modeling and realization of a multilevel read-only disk," in *Optics Express* 14(3), 1199-1207 (2006).
- [4] Q. Shen, J. Pei, H. Xu, et al, "Analysis of the differential phase detection signal in multi-level run-length limited read-only disk driver," in *Jpn. J. Appl. Phys.* 45(7), 5764-5768 (2006).

Symmetric driving coils design for three-axis actuator with low interference force

Buqing Zhang, Jianshe Ma, Longfa Pan, Xuemin Cheng, Hua Hu, Yi Tang
 Optical Memory National Engineering Research Center, Tsinghua University, 10084, Beijing, China
 Graduate school at Shenzhen, Tsinghua University, 518055, Shenzhen, China
 Tel: 86-755-26036440 Fax: 86-755-26036439

1. Introduction

The lens actuator is an important mechanism in the optical pickup of an optical disk system. It is used for adjusting the attitude and position of the objective lens. It ensures that the focusing spot shall fall on the corresponding land/pit precisely. While the storage capacity and data transfer rate become higher, three-axis actuator with better dynamic performance is adopted to achieve high sensitivity and tilting function, which enhances the accuracy of the servo system and compensates the coma aberration caused by the leaning between the optical pickup and the disc. In order to improve the sensitivity of actuator, the magnetic flux density acting on the coils were raised by kinds of design methods such as Taguchi method and Finite element method [1-4]. Moreover, a new magnetization technology was used to improve the sensitivity [5]. However, the interference force along the main driving force (*i.e.* crosstalk force) was considered little during the sensitivity improvement process in the pervious researches. The crosstalk force should be reduced to improve the dynamic performance in the high accuracy three-axis actuator.

In this paper, a new magnetic circuit is proposed and analyzed to reduce the crosstalk force and improve the sensitivity. Experiment results show the feasibility of the configuration and design method.

2. New magnetic circuit with symmetric driving coils

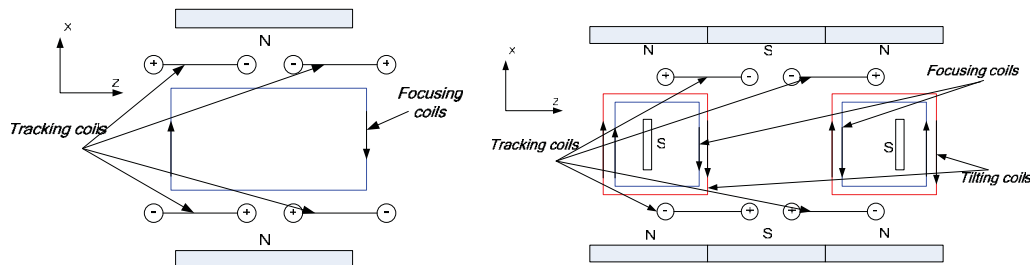


Fig. 1. Traditional magnetic circuit

Fig. 2. Novel magnetic circuit for high sensitivity actuator

In the traditional magnetic circuit for the lens actuator, there is only one group focusing coils in front of the single permanent magnet as shown in Fig.1. Although there are four group tracking coils, the effective force generation section is only 1/4 in each group. This kind of coils and magnets configuration can not provide high sensitivity, because the generation of driving force is limited by the magnetic circuit structure. In addition, the crosstalk force can not be neglected due to the nonlinearity of the magnetic filed. In our novel magnetic circuit as shown in Fig.2, two group focusing coils as well as two group tilting coils are put right in front of the N magnetic poles. To simplify the manufacture process, the tilting coils are enlaced around the focusing coils as shown in Fig.3. When the two group focusing coils are electrified in the same direction (*e.g.* both clockwise), the actuator will move in focusing direction. While the two groups of tilting coils are electrified in the opposite direction (*e.g.* one clockwise, the other counter-clockwise), the actuator will roll around the axis parallel to the suspension wire. Four rectangular tracking coils are attached to the moving part and for each group, half of the coils are in front of the N poles of the permanent magnets and the other half are in front of the S poles of the permanent magnets. The advantages of this design are as followings. Firstly, high driving force in tracking direction is achieved by the 2/4 force generation sections compared to the traditional 1/4, the main permanent magnets with special order and the auxiliary small magnets provide much efficient magnetic flux. Secondly, little crosstalk force in focusing and tracking direction is provided by the symmetric focusing/tilting coils and tracking coils. By improving the driving force as well as reducing the crosstalk force, the sensitivity and dynamic performance of the actuator can be improved at last.

In order to analyze the magnetic circuit especially for the driving force, finite element method based on the couple analysis is used. A special script program with the help of ANSYS Parameter Design Language (APDL) is used to carry out the magnetic flux density distribution and the node displacement analysis, which bases on the direct connection between the magnetic field and the structure filed. The magnetic flux density distribution on the driving coils is shown in Fig.4. The driving forces as well as the interference forces or moments distribution on each section of the focusing coils and tracking coils are shown in Fig.5 and Fig.6.

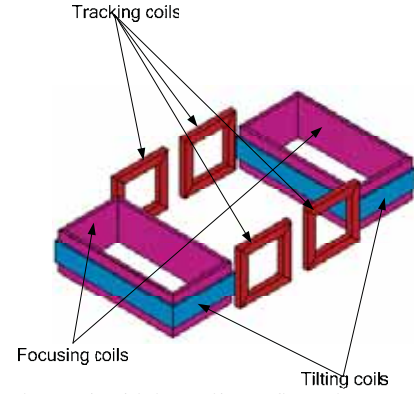


Fig. 3. The driving coils configuration

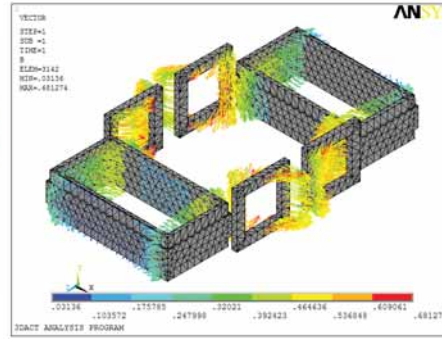


Fig. 4. The magnetic flux density distribution on driving coils

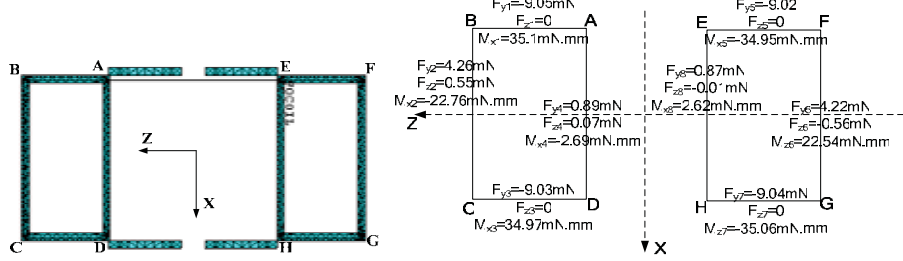


Fig. 5. The driving force and interference force on each section of the focusing coils

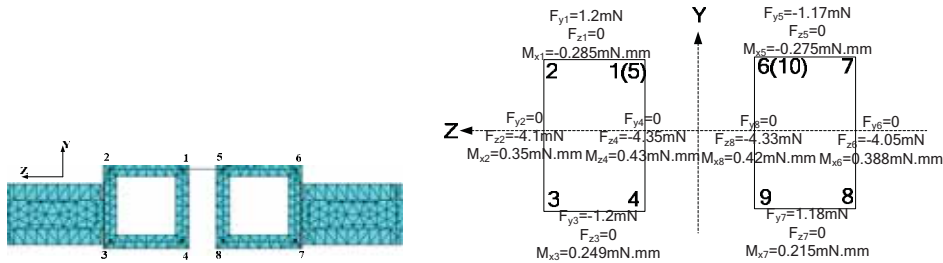


Fig. 6. The driving force and interference force on each section of the tracking coils

The driving forces in focusing direction are mainly from the sections 'AB','CD','EF' and 'GH', and the crosstalk forces come from the sections 'AD','BC','FG' and 'EH'. However, the direction of the crosstalk forces are opposite from the left coils to the right coils in Fig.5, and the total interference forces as well as the moments cancel out mostly, while the remain crosstalk force is 0.05 mN. In the tracking movement, there are also little crosstalk forces because of the symmetric coils configuration. It is because of the symmetric configuration of the coils and magnets, the interference forces in each section will cancel out at last even when the driving coils is off-centered, Figure 7 shows the DC tilt angle for the radial direction. The maximum tilt angle is no more than 0.2 deg. (DC tilt measurement conditions: focus range = ± 0.6 mm, track range = ± 0.4 mm). This proves the little crosstalk force moment in the actuator.

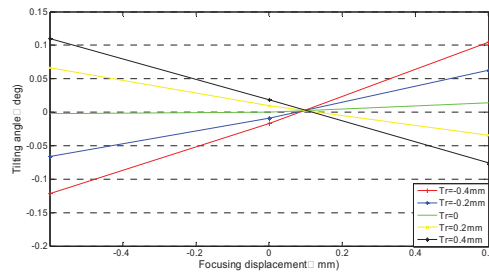


Fig. 7. Static tilting angle under different deviation in focusing and tracking direction

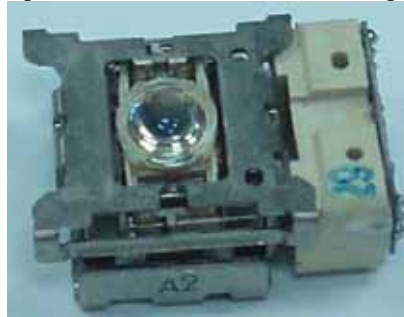


Fig. 8. Six wire suspension actuator

3. Experiment results

Several actuator samples are made and tested. Figure 8 shows the actual three-axis actuator. Table 1 gives the results of comparison of simulated specifications with experimental performance data. Results show satisfactory performance of the new actuator. The achievement has a great potential application for the super multi DVD drive.

Table 1. Comparison of simulation and experiment results

Item		Focusing		Tracking		Tilting	
		Simulation	Experiment	Simulation	Experiment	Simulation	Experiment
Sensitivity	5Hz(mm/v)	1.55	1.63	1.78	1.72	4.0deg/v	4.4deg/v
	200Hz(μ m/v)	75.6	86.8	86.6	93.0	0.7deg/v	0.8deg/v
1st resonance frequency(Hz)		43.5	45.6	43.6	45.7	78.2	86.9
Q-factor: gain(f1)-gain(5Hz) (dB)		9.9	10.62	9.59	10.5	12.59	12.78
2nd resonance frequency (k Hz)		28.8	28.8	28.7	29.8	31.1	34.6
Gain margin: gain(1kHz)-gain(f2)(dB)		58	58	56	55	55	52
Phase delay	at 1 kHz	-179.3	-183.1	-179.3	-180.9	-179.2	-181.6
	at 5 kHz	-180.2	-195.9	-179.5	-189.5	-179.2	-189.4

References:

- [1]I.H.Choi, W.E.Chung, Y.J.Kim, I.S.Eom, H.M.Park, J.Y.Kim, Jpn.J.Appl.Phys. 37(1998) 2189.
- [2]H.Fusayasu, Y.Yokota, Y.Iwata, H.Inoue, IEEE Trans on Magnetics, 34(1998) 2138.
- [3]C.Y.Ke, C.L.Chang, J.J.Ju, D.R.Huang, R.S.Huang, Journal of Magnetism and Magnetic Materials, 239(2002) 604.
- [4]K.T.Lee, C.J.Kim, N.C.Park, Y.P.Park, Microsystem Technologies, 9(2003) 232.
- [5]I.H.Choi, S.P.Hong, W.E.Chung, Y.J.Kim, M.H.Lee, J.Y.Kim, IEEE Trans on Magnetics, 35(1999) 1861.

Off axis astigmatic reflector for compact optical pickup

Ya-Ni Su*, Cheng-Huan Chen

Department of Power Mechanical Engineering, National Tsing Hua University, Taiwan, ROC

ABSTRACT

The request on miniaturization of pickup head has invoked the development of several new architectures and relevant optical components. An optical pickup with all its components stacked up layer by layer and based mostly on reflective optical components has been proposed as a compact and high efficiency solution. The optical component to generate focal error signal(FES) for the quadratic detector is also reflective type and has to work on off-axis fashion. Both the astigmatic reflector working on specular reflection and diffraction have been designed and analyzed to show a linear relationship between focal error signal and axial disc deviation within a range of 10 μ m deviation, which performance is sufficiently well as the feedback signal for the servo system to conduct focusing control.

Keywords: Optical pickup, astigmatic reflector

1. INTRODUCTION

Optical pickup is the key component in optical storage device and its weight and size will influence the bandwidth and application of the optical storage device. Reduction on the weight of the pickup helps to increase the responding speed of the servo system, and hence allowing a higher capacity of the storage device. In addition, with the increasing request on the reduced form factor of the information storage devices for portable application, the reduction on the size of the pickup becomes also important. The optical components in traditional optical pickup, such as collimation lens, beam splitter and astigmatic lens etc., are mostly refractive type and separate components[1]. Their function has been sufficiently well as commercial products, but the weight, size and assembly cost remains a large room for improvement. Several integrated type pickup with non-traditional optical components have been proposed for this issue, including free space micro-bench[2] and stack type[3] etc. Among which the stack type pickup as shown in Fig 1 features the smallest form factor, due to the light path from laser to disc and from disc to detector have been folded and restricted within a common space. In addition, all its components have been designed as layer structure and will be stacked up together in assembly, which significantly reduces the effort on alignment. The holographic optical element(HOE) in the stack type pickup plays two roles at the same time, one for splitting the forward and the backward light path, and the other for making astigmatic focusing of backward light beam on the quadratic detector. In order to maintain the efficiency, the surface relief of the holographic element needs a complex structure, and a birefringent layer coated on the HOE has to work with a quarter wave retarder to make the surface relief only visible for the backward light beam. The concept is feasible but difficult design due to multiple function of the HOE and expensive fabrication process to make piecewise smooth surface relief are inevitable. In this paper, an optical system which splits the function of the abovementioned HOE for two separate components has been proposed, one for splitting the light path and the other for making astigmatic focusing, yet these two components can still be made on a common substrate, which avoids further alignment job in assembly. Due to each component performing only one optical function, the design and structure can be largely simplified, which consequently makes the high efficiency stack type pickup more practical.

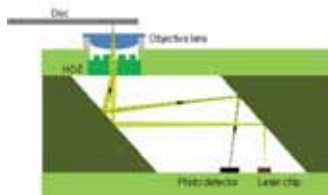


Fig. 1. Stack type pickup with holographic optical element.

2. OPTICAL ELEMENTS FOR STACK TYPE OPTICAL PICKUP

Fig 2 shows the configuration of the stack type pickup with separate beam splitter and astigmatic focusing element. The on-axis beam splitter has a blazed grating structure made of an isotropic material, as shown in Fig 3. A birefringent material is coated on the blazed grating, where the indices of the two material are matched in one of the two mutually orthogonal directions, namely the direction parallel and perpendicular to the groove of the blazed grating. A quarter wave retarder is attached on the top of the birefringent blazed grating with its optical axis 45 degree from the groove direction of the grating. The light beam emerging from the laser diode has a polarization state which sees the index matching and passes through the grating without any deflection. However, as the laser beam passes through the quarter wave retarder twice after reflected from the disc, its polarization state rotates by 90 degree, and will see the grating structure, hence being deflected by an angle based on the blazed angle and the index difference between the material for the birefringent grating. This deflection of the beam makes the splitting between forward and backward laser beam. The blazed grating can be easily made with diamond cutting, and the efficiency can be 100% theoretically, i.e. 100% of the backward propagating beam energy can be deflected to the desired direction. In addition, the coating of the birefringent material becomes much easier than the case of complex diffractive structure[4]. The deflected backward laser beam is then being focused onto the quadratic detector by an off-axis astigmatic reflector, as shown in Fig 2. This reflector can work on specular reflection with smooth surface or diffraction with microstructured surface. The on-axis beam splitter and the off-axis astigmatic reflector can also be made on a single substrate which is shown as the top layer component in Fig 2, so that their relative location has been well aligned in the fabrication, which brings no further effort in assembly.

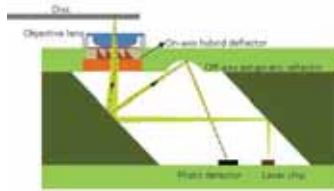


Fig. 2. Stack type pickup with separate beam splitter and astigmatic focusing element.

3. REFLECTIVE AND DIFFRACTIVE ASTIGMATIC REFLECTOR

The astigmatic reflector needs to make a astigmatic focusing of the light beam onto the quadratic detector with a sufficient focusing error signal(FES) upon the axial deviation of the disc within a range of $10\mu\text{m}$, normally from -5 to $+5\mu\text{m}$. And the relationship between the FES and disc deviation has to be linear. The off-axis reflector possesses inherent astigmatism, but a biconic surface is still required to produce a linear response of FES. The spot diagram of the biconic reflector corresponding to some axial disc deviation value is shown in Fig 4(a), which demonstrates a diamond spot shape instead of oval shape as in traditional pickup with refractive astigmatic lens. The FES diagram is shown in Fig 4(b), which indicates a linear relationship within the range of $\pm 5\mu\text{m}$ of disc deviation. This astigmatic reflector features a size of 1 mm diameter and can be made with diamond turning. In order to make the reflector more feasible in fabrication, a diffractive astigmatic reflector with a four level binary surface relief has also been proposed. The surface relief is shown in Fig 5(a), and the corresponding FES diagram is shown in Fig 5(b), which also shows a linear relationship within the range of disc deviation between $+5$ and $-5\mu\text{m}$. The binary diffractive optical element can be made with photolithography or reactive ion etching(RIE) with only two photo masks.

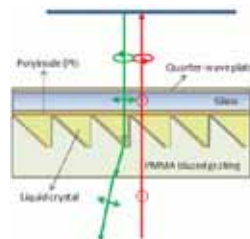


Fig. 3. On-axis beam splitter with a birefringent blazed grating.

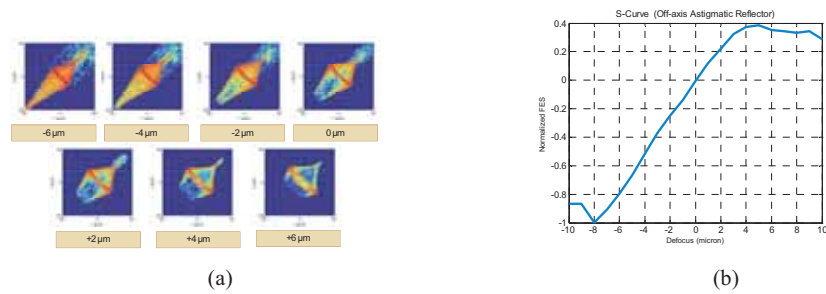


Fig. 4. (a) Spot diagram of biconic reflector. (b) FES diagram.



Fig. 5. (a) Diffractive astigmatic reflector with a four level binary surface relief. (b) FES diagram.

4. CONCLUSION

A stack type pickup with its beam splitter and detector optics as separating components has been proposed as a high efficiency and compact solution. These two components can be made on the same substrate as the top layer of the stack type pickup, hence with no further alignment in assembly. The astigmatic reflector for generating focal error signal on the quadratic detector has been designed with both reflective and diffractive type, and both have shown a linear relationship on the FES diagram within the range of axial disc deviation between +5 and -5 μm, which demonstrates the feasibility of the proposed architecture and associated components.

REFERENCES

- [1] Marchant, Alan B. : Optical recording (Addison-Wesley Publishing Company, 1990)
- [2] Lin, L. Y., J. L. Shen, et al. (1996). "Realization of novel monolithic free-space optical disk pickup heads by surface micromachining." *Opt. Lett.* **21**(2): 155.
- [3] Shih, H. F., C. L. Chang, et al. (2005). "Design of optical head with holographic optical element for small form factor drive systems." *IEEE Transactions on Magnetics* **41**(2): 1058-1060.
- [4] Wang, X., D. Wilson, et al. (2000). "Liquid-crystal blazed-grating beam deflector." *Applied Optics* **39**(35): 6545-6555.

Inorganic Reflective Achromatic Quarter-waveplate for OPU Applications

Kim L. Tan, Karen D. Hendrix, Curtis R. Hruska and Nada A. O'Brien*
JDSU Advanced Optical Technologies,

2789 Northpoint Parkway, Santa Rosa, California, USA

*Phone: (707) 525-7830; Fax : (707) 707-525-6840 ; E-mail: polarization@jdsu.com

1. INTRODUCTION

Many optical systems rely on the control of the polarization state of light. One such system is the optical pickup unit (OPU) for a 3-format optical data storage system, supporting compact-disc (CD), digital-versatile disc (DVD) and Blu-ray disc (BD) media. This next-generation OPU uses the blue-violet laser (405 nm wavelength) for high-density optical data storage while being backward compatible with legacy DVD and CD formats, accessed with red (650 nm) and near-infrared (NIR) lasers (780 nm), respectively. Double passing a quarter-waveplate (QWP) in this folded optical system allows for polarization sensitive optical elements to act on the first and second pass differently. For example, a polarization beam splitter (PBS) can be utilized to separate the reflected beam from the incident beam. Further, a polarizing hologram can be used to steer the return beam to an angular or spatial offset and not affecting the incident beam.

The conventional OPU incorporates a transmissive (T-) QWP to convert the linearly polarized laser beam to circularly polarized light prior to focusing at the optical disc. In some dual-path OPU designs, two QWPs are utilized: one for the blue-violet channel and another for the red and NIR channels. The red and NIR QWP is often a polymer-based retarder and the blue-violet QWP may be a birefringent crystal retarder. Due to the large difference in wavelength between the CD and the BD lasers (almost 2:1 ratio), it is difficult and/or expensive to fabricate a T-QWP that has achromatic quarterwave retardance for all three wavelength bands. Also, polymer-based retarders may not exhibit the necessary stability to operate at 405nm.

This paper discusses the design, fabrication and application of a single QWP element to address the reliability, retardance achromaticity and low-cost aspects of polarization controlling components in optical-pickup systems. The retarder is an all-inorganic reflective (R-) QWP that provides achromatic 90° retardance for the three laser wavelength bands and suitable for use in an OPU as described above. Measurements of a fabricated thin-film device are presented.

2. REFLECTIVE QWP DESIGNS

2.1 Operating Principles of Thin-film Retarders

Thin film coatings are out-of-plane (C-plate) retarders, having an optic axis normal to the device. The retardance can only be accessed at oblique incidence, with the tilt plane defining the fast and slow axes of the retarder. An optical admittance difference of the S-polarization (S-pol.) and P-polarization (P-pol.) light rays (i.e., linear polarizations that lie orthogonal and parallel to the plane of incidence, respectively) creates the retardance. In both transmissive [1] and reflective [2] thin-film retarders, one cannot decouple the plane of incidence from either the fast- or slow-axis. At a given off-axis illumination, the retardation properties of a uniform film is independent of the rotation of the device about its normal axis. At normal incidence, there is no retardance as the beam propagates along the optic axis. Hence, the retardance is only realized by the geometric configuration of the thin film vs. incidence direction.

In contrast to transmissive designs, reflective thin-film designs are not constrained by the cross-coupling of intensity and phase properties. Hence, the dispersion of the constituent thin-film materials can be mitigated such that true achromatic reflected retardance can be obtained over a broadband wavelength range or for multiple wavelength bands while maintaining a high reflectance. Whereas the transmissive C-plate is more commonly used to compensate for cone illumination of light, so that off-axis rays are made to accumulate a certain amount of retardance, reflective waveplates are best suited for non-normal, collimated illumination [3]. The reflective component can achieve very large retardances, e.g., 90° retardance at 45° angle of incidence (AOI).

A reflective waveplate must be configured off-axis in order to yield any retardance. Moreover, the input polarization must not coincide with the fast- and slow-axis of the inclined retarder. The fast and slow axes of the inclined retarder are aligned parallel and orthogonal to the plane of incidence, respectively, or vice versa, due to geometry. In common retarder applications of converting a linear polarization input to circular polarization output, the reflective retarder must be designed as a QWP. In addition, with a R-QWP, the input linear polarization must comprise equal amount of S-pol. and P-pol. components at zero relative phase. This means the input linear polarization is aligned $\pm 45^\circ$ vs. the local plane of incidence.

2.2 Applications of Thin-film R-QWP in OPU Systems

In the 3-channel high-definition disc-media access systems, the ratio of the long to the short wavelength is large (approximately 2:1). High light flux stability requirement is important for future high speed read/write-access. These requirements make a conventional T-QWP based on multi-layer birefringent crystals and organic foil retarders potentially unsuitable. A multi-layer achromatic crystal retarder is costly and a polymer retarder may not be durable under high flux exposure. A conventional polarization conversion element within the OPU system is schematically shown in Fig. 1(a). Light beams are multiplexed from one of the laser diodes (LD) into a common path by an array of PBS elements. These are folded by a regular mirror and deflected towards the optical disc. A T-QWP is inserted in the parallel beam section, between the fold mirror and objective lens. The T-QWP converts the linear polarizations in the source/detector segment to circular polarizations in the disc read/write segment. On double-passing the T-QWP, the return light beams are orthogonally polarized with respect to the LD output. These return beams can be separated by the same PBS array and are directed towards photodiodes (PD).

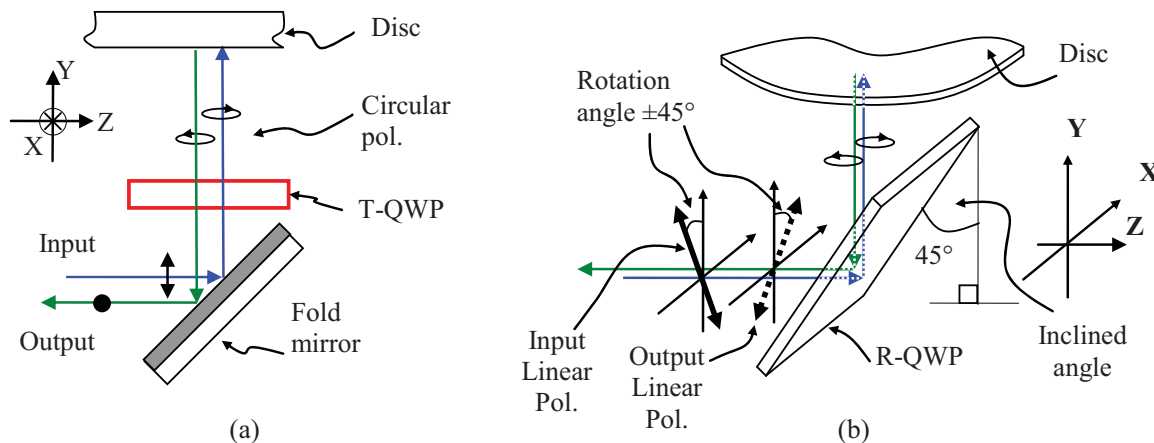


Fig. 1: (a) Conventional OPU sub-system utilizing a T-QWP component and a beam-folding mirror and (b) new OPU sub-system utilizing a R-QWP component for retardation and beam folding.

Using a modified setup as the conventional OPU layout, the functionality of QWP and fold mirror can be integrated into a single R-QWP, as shown by the OPU sub-system layout in Fig. 1(b). The incoming linearly polarized light has to be rotated about its Z-axis by $\pm 45^\circ$. In this way, the LD output sets up half P-pol. and half S-pol. at the reflective retarder. The 90° relative phase delay of P-pol. and S-pol. upon reflection from this reflective retarder converts the linearly polarized state into a circularly polarized one. On its return from the disc media, another polarization conversion takes place and the output light beam in the common path section is again orthogonally polarized versus the LD output for beam separation. In order to implement the required $\pm 45^\circ$ input linear polarization axis offset with the R-QWP plane of incidence, several OPU layout options are possible. These include using a rotated PBS or a co-packaged LD and PD. These potential layout options will be discussed at the conference.

3. COATED PART PERFORMANCE ATTRIBUTES

A R-QWP designed for an OPU must cover a wide wavelength range, but the required wavelength windows of operation are not continuous. The OPU incorporates short wavelength blue-violet laser ($\sim 405\text{nm}$ wavelength) and

legacy DVD red laser (650 and 660nm) and CD (780nm) NIR laser lines. The results of an example design for a R-QWP, targeting all three wavelength windows are shown in Fig. 2(a)–(c) plots for the blue, red and NIR channels. In each wavelength channel, the modeled and measured reflected retardance at 45° AOI are compared. The model yields a 90° retardance for each center wavelength and within a bandwidth of approximately $\pm 5\text{nm}$. The design has been fabricated as a dense sputtered thin film in JDSU Ucp-1 coating platform [4]. The measured retardance values at 45° incidence show a slight error in design targeting; these parts nevertheless show good achromatic retardance properties even for approximately 2:1 wavelength ratio (780nm vs. 405nm). Other results including reflected retardance within $90 \pm 5^\circ$ range for $45 \pm 2^\circ$ AOI range and an ellipticity of the output beam that is greater than 0.9 given an input linear polarization having a $\pm 5\text{nm}$ bandwidth of the center wavelengths and $45 \pm 2^\circ$ AOI range will be shown at the conference.

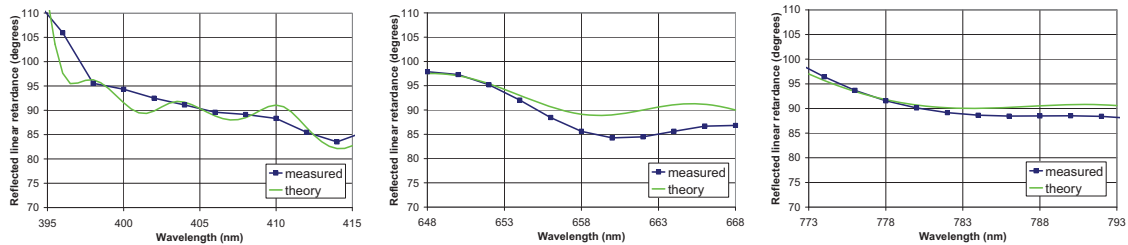


Fig. 2: Modeled and measured retardance at 45° AOI for a triple laser line R-QWP.

(a)Blue-violet band

(b)Red band

(c)NIR band

In addition to the reflected retardance performance, these retarder designs also produce high reflectance over the required bands. The flexible design allows for an optional transmitted tap output to be implemented in the component. These thin-film devices are very stable in high flux exposure and in adverse environmental conditions. Moreover, the high reliability birefringent component is engineered from thin-film designs, without the high cost of birefringent crystal growth. JDSU has demonstrated a less than 0.01 waves rms of surface distortion at 633nm wavelength over a 4.5mm square clear aperture.

4. CONCLUSIONS

JDSU has demonstrated the capability to design and fabricate all-inorganic reflective retarders. In high definition, 3-channel optical data storage systems, this R-QWP component provides retarder stability under high blue-violet light flux exposure and achieves true achromatic 90° retardance over all three diode laser wavelength bands. The all-inorganic R-QWPs developed by JDSU are flexible in design, durable and highly reliable under high light flux exposure and adverse environmental conditions. These retarders potentially offer a low cost solution for polarization conversion in optical data storage systems.

REFERENCES

- [1] P. Yeh, et al., “Compensator for liquid crystal display, having two types of layers with different refractive indices alternating,” US Pat. No. **5,196,953**, 1993.
- [2] W.H. Southwell, “High reflectivity coated mirror producing 90 degree phase shift,” US Pat. No. **4,312,570**, 1982.
- [3] K.L. Tan, et al., “Thin films provide wide-angle correction for waveplate components,” *Laser Focus World*, p. 59, Mar. 2007.
- [4] S. Sullivan, et al., “Bigger is not always better in optical coating production,” *Photonics Spectra*, pp. 86-92, Nov. 2005.

Estimation method of the archival lifetime for optical recordable disks

Mitsuru Irie^{*a}, Yoshihiro Okino^b and Takahiro Kubo^c

^a Faculty of Engineering, Osaka Sangyo University, 3-1-1 Nakagaito, Daito, Osaka 574-8530, Japan

^b High Tech Research Center, Kansai University, 3-3-35 Yamate-cho, Suita, Osaka 564-8680, Japan

^c T. Kubo Engineering Science Office, 3-8-1 Higashinada, Kobe, Hyogo 658-0072, Japan

ABSTRACT

This paper presents discussion of a simple estimating method for the archival life expectancy of optical disks in order to apply a rough clarification of archival grade disks based on the international standard. The performance of this method was examined using the Eyring acceleration test model with new four stress conditions and statistical analysis.

Keywords: Archival storage, Eyring acceleration test model, life expectancy, optical disk, reliability, DVD-R

1. INTRODUCTION

Recently, the users demand a stable preservation method of a huge digital information data in the internet-digital information society. Large-capacity optical disks have been expected the long-term and stability storage medium. Up to now, the method of presuming the life expectancy and a clarification of optical disk reliability for archival usage is researched¹⁾. This paper presents discussion of a simple estimating method for the archival life expectancy of optical disks in order to apply a rough clarification of archival grade disks based on the international standard^{2,3)}.

2. ACCELERATION TEST EVALUATION

We have adapted the Eyring acceleration test model for the presuming method of the optical disk life expectancy. Figure 1 shows a lifetime estimate model using the Eyring acceleration test. We used 16 times-speed specification of DVD-R, which is recorded at 8 times speed at middle area, and the modified consumer-type optical drive (EXA-16E; Pulstec) to evaluate the disks. The criteria used for determining a DVD disk's lifetime is the error number of ECC. The lifetime is assumed to be the time at which the parity inner (PI) error number of eight ECC blocks (PI sum 8) reaches 280. The layout of new stress condition on our Eyring method is shown in Fig.2. Table 1 presents a summary of the acceleration test conditions.

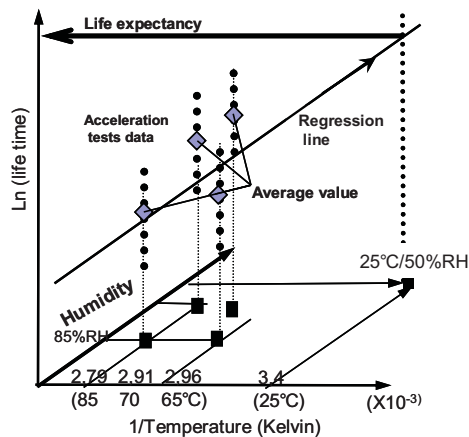


Fig.1. Lifetime estimate model using the Eyring acceleration test.

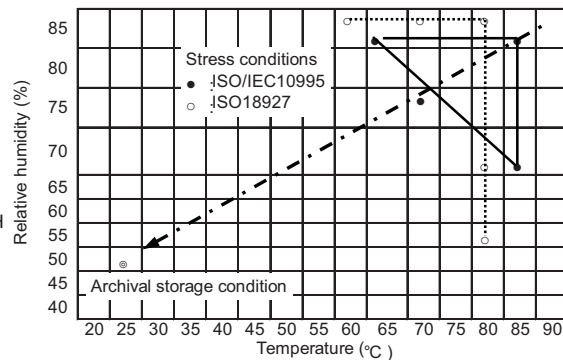


Fig. 2. Layout of new 4 stress conditions.

*irie@eic.osaka-sandai.ac.jp; phone 81 72 875 3001; www.osaka-sandai.ac.jp

3. DATA ANALYSIS FOR ESTIMATION OF THE ARCHIVAL LIFETIME

The following is steps to estimate the life expectancy value, as a function of ambient temperature and relative humidity.

1) Compute the predicted failure time

The failure time is calculated from the slope and intercept of the linear regression as the time at which the specimen would have a PI sum 8 of 280.

2) Data quality check for acceleration test

The relation between the median rank of lifetime data obtained for measurement and the natural logarithm of the lifetime data are shown in Fig. 3. Verify that the plots for all stress conditions are reasonably parallel to one another. The log mean and the log standard deviation at each stress condition were calculated using least-squares regression. Table 2 summarizes the log median at each stress condition. The time of the log median shows the natural logarithm of lifetime data for an optical disk with 50% survival probability.

3) Determination of Eyring model's equation

The Eyring model simplified equation in terms of temperature and relative humidity is ^{2,3)}

$$t = Ae^{\Delta H / kT} e^{B \times RH} \quad (1)$$

where t is the failure time data, T is the temperature in Kelvin, R is the relative humidity, k is the Boltzmann's constant, ΔH is the activation energy, and A and B are constants.

Constants A , B , and ΔH of eq. (1) were calculated using multiple linear regression analysis with failure time data and the respective stress conditions of temperature and relative humidity.

Through substitution of these values into the Eyring eq. (1), the Eyring acceleration model in DVD-R optical disk yields the following expression.

$$t = 5.12 \times 10^{-10} \cdot \exp\left(\frac{11.92 \times 10^3}{T}\right) \cdot \exp(-4.33 \times 10^{-2} \times R) \quad (2)$$

4) Standardized life expectancy

The log mean of a standardized life condition (25°C/50%RH) can be estimated using eq. (2). The life acceleration factor of each acceleration test can be calculated based on the lifetime of standardized life condition: 25°C/50%RH. The acceleration factor (α) of each stress is given by $\alpha = t_{50(usage)} / t_{50(stress)}$.

where $t_{50(stress)}$ is the lifetime of a stress condition at a 50% survival probability, $t_{50(usage)}$ is the lifetime of the standardized life condition (25°C/50%RH) at a 50% survival probability.

Table 1 Acceleration test conditions.

No.	Stress condition (temperature/relative humidity)	Number of specimen	Incubation duration (h)	Total test time (h)
1	85°C/85 % RH	15	150	2100
2	85°C/70 % RH	15	250	2000
3	65°C/85 % RH	15	250	2000
4	70°C/75 % RH	20	250	2000

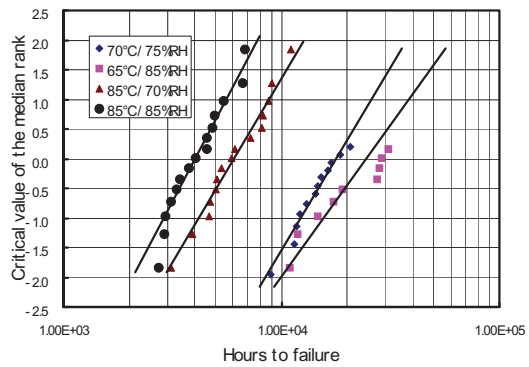


Fig. 3. Relation between the median rank of lifetime data and the natural logarithm of the lifetime data.

Table2 Log median at each stress condition.

Group	Log median	Temp. °C	1/T(Kelvin)	RH %
1	8.3175	85	0.002792	85
2	8.7094	85	0.002792	70
3	10.0121	65	0.002957	85
4	10.3478	70	0.002914	75

Table 3 summarizes the acceleration factor at each stress condition. The acceleration factor was used for normalization of lifetime data at each stress test. The relation between the median rank of the lifetime data and natural logarithm of the normalized lifetime data is shown in Fig. 4. All lifetime data in this figure show linearity. The statistical distribution of lifetime data is inferred to be a lognormal distribution.

A standardized life expectancy, $t_{50\%} = 13.7 \times 10^6$ (h) is calculated from the lognormal distribution of all lifetime data in Fig. 4. Figure 5 shows the reliability function ($R(t) = 1 - F(t)$) under the 90% confidence interval. The life expectancy by the 95% confidence interval can be presumed as 5.18×10^6 (h), when reliability (survival probability) is assumed as 95% at 25°C/50%RH.

4. CONCLUSION

We investigated a simple estimating method for the archival life expectancy of optical disks in order to apply a rough clarification of archival grade disks based on the international standard. To simplify the acceleration test, only four conditions were adapted. The performance of this method was examined using the Eyring acceleration test model with new four stress conditions and statistical analysis.

Consequently, we confirmed the capability of this method for estimating archival life expectancy of DVD-R as the minimum lifetime of 95% survival probability at 25/50%RH with a 95% confidence level.

Acknowledgements

We express our thanks to Junichi Nishiki and Kenichi Nakatani for help in the measurements. We would like to thank CDs21 solutions, Japan for supporting the work.

REFERENCES

- [1] M. Irie and Y. Okino, "Investigation on Life Expectancy of High-Speed Recordable Optical Disks," Jpn. J. Appl. Phys. 46 (2007) 3939.
- [2] ECMA 379, "Test Method for the Estimation of the Archival Lifetime of Optical Media," (2007).
- [3] ISO/IEC 10995, "Information technology - Test Method for the Estimation of the Archival Lifetime of Optical Media," in preparation for publication.

Table 3 Acceleration factor for each stress condition.

Stress condition	Calculated life-time (hours)	Acceleration factor (α)
85° C/85%RH	3,715.54	3690.29
85° C/70%RH	7,109.44	1928.62
65° C/85%RH	26,615.35	515.17
70° C/75%RH	24,540.60	558.72

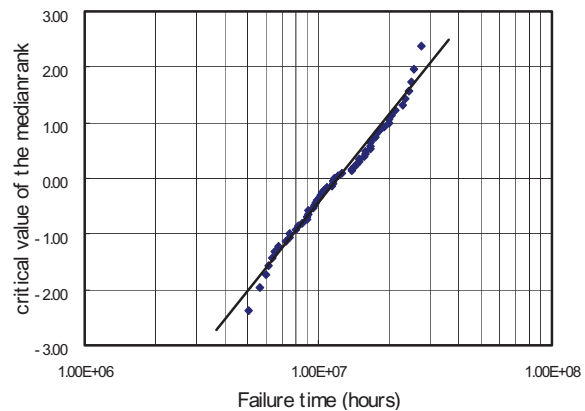


Fig.4. Combined lifetime data at 25°C/50%RH.

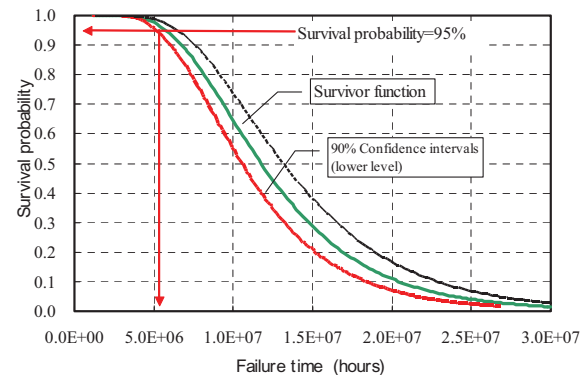


Fig.5. Survival Probability function at 25°C/50%RH .

Super-trellis based noise predictive detection for high-density optical storage

Xiao-Ming Chen Oliver Theis

Deutsche Thomson OHG, Karl-Wiechert Allee 74, 30625 Hanover, Germany
Phone: +49-511-418-2292/-2338, Fax: +49-511-4182483

1. INTRODUCTION

For high-density optical storage systems, partial-response (PR) maximum likelihood technique is employed for reliable bit detection. Thereby, a PR equalizer is used to shape the overall channel impulse response to a desired PR target. Noise samples at the equalizer output are correlated, and the performance degradation due to correlated noise becomes significant with increased storage density. Therefore, noise-predictive maximum likelihood was proposed to perform noise whitening.¹ In order to effectively exchange soft information with an outer soft-in soft-out (SISO) channel decoder, joint bit detection and runlength limited (RLL) decoding have been investigated.² Accordingly, the concatenation of RLL encoder, non-return-to-zero inverted (NRZI) precoder, and PR channel is interpreted as an equivalent RLL-NRZI-PR channel, which can be represented by an RLL-NRZI-PR super-trellis.

In this paper, we extend the concept of super-trellis for noise prediction and investigate its application to high-density optical storage. To keep the detector complexity reasonably low, reduced-state variations of the super-trellis based detector are also considered.



Figure 1. Transmission model for optical storage systems using noise prediction

2. SUPER-TRELLIS BASED NOISE PREDICTIVE DETECTION

Fig. 1 shows the transmission model for optical storage systems, where the Braat-Hopkins model³ is applied to optical storage channel using Blu-ray disc (BD) optics. Moreover, additive white Gaussian noise is present before PR equalizer. The PR-equalizer output signal is as follows:

$$y[k] = \sum_{l=0}^L h_l x[k-l] + e[k] = z[k] + e[k],$$

where $\{h_l\}$ denote PR-target coefficients with L as PR-channel memory length and $e[k]$ is colored noise.

Within this paper, we consider rate 2/3 RLL encoders that have $\mathbf{u}[n] = [u[2n], u[2n+1]]$ as infoword and $\mathbf{a}[n] = [a[3n], a[3n+1], a[3n+2]]$ as codeword. Given a phase reference $x[3n-1]$, the corresponding NRZI data symbols are obtained as $x[3n], x[3n+1], x[3n+2]$. Consequently, each infoword $\mathbf{u}[n]$ produces three noiseless PR channel outputs, $z[3n], z[3n+1], z[3n+2]$, which depend on \mathbf{x}_{3n-L}^{3n+2} (The notation \mathbf{x}_a^b denotes a sequence from time index a to b). Accordingly, the equivalent RLL-NRZI-PR channel has $\mathbf{u}[n]$ as input and \mathbf{z}_{3n}^{3n+2} as output. States in the RLL-NRZI-PR super-trellis can be defined as $S'[n-1] \triangleq [S[n-1], \mathbf{x}_{3n-L}^{3n-1}]$, where $S[n-1]$ is a state in the RLL decoding trellis and state transitions thereof determine data symbols \mathbf{a}_{3n}^{3n+2} . Therefore, state transitions $S'[n-1] \rightarrow S'[n]$ deliver NRZI data symbols \mathbf{x}_{3n-L}^{3n+2} . Note that the choice of \mathbf{x}_{3n-L}^{3n-1} in $S'[n-1]$ is not arbitrary due to RLL code constraints.

In the presence of a noise predictor (NP), the equivalent channel up to the bit detector is composed of RLL encoder, NRZI precoder, PR channel, and noise predictor, which is referred to as RLL-NRZI-PR-NP channel in the sequel, cf. Fig. 1. Let $\mathbf{p} \triangleq [p_1, \dots, p_M]$ denote the prediction vector, the RLL-NRZI-PR-NP channel can be described as

$$\mathbf{g} = \text{conv}(\mathbf{h}, [1, -\mathbf{p}]),$$

	$K = 1$	$K = 2$	$K = 3$	$K = 4$	$K = 5$	$K = 6$	$K = 7$
(1,7)PP	30/106	30/106	32/118	34/130	46/176	60/236	84/332
<i>d1k9r5</i>	18/60	18/60	18/60	18/60	60/234	60/234	60/234

Table 1. Number of states/branches in super-trellises for two rate 2/3 RLL codes

where $\text{conv}(\cdot, \cdot)$ stands for discrete-time convolution and \mathbf{h} represents the PR target. Moreover, the channel memory length of this equivalent channel is $L_p \triangleq L + M$. Accordingly, states in the RLL-NRZI-PR-NP super-trellis are defined as $S_p[n-1] \triangleq [S[n-1], \mathbf{x}_{3n-L_p}^{3n-1}]$. To control computational complexity of an RLL-NRZI-PR-NP super-trellis based detector, a reduced-state super-trellis can be constructed by a design parameter $K \in [1, L_p]$, where states are changed as $S'_p[n-1] \triangleq [S[n-1], \mathbf{x}_{3n-K}^{3n-1}]$. State transitions in the reduced-state super-trellis only provide data symbols \mathbf{x}_{3n-K}^{3n+2} . In order to obtain \mathbf{x}_{3n-K}^{3n-1} , delayed decision feedback sequence estimation¹ can be modified for super-trellis, where surviving paths for individual states in the reduced-state super-trellis are traced back by N_b steps. Since each step during tracing back provides three past decisions on NRZI symbols, $N_b = \lceil (L_p - K)/3 \rceil$, where $\lceil a \rceil$ denotes the smallest integer not less than a .

We have designed a (1,9) RLL code⁴ with a repeated minimum transition runlength constraint of 5 (shortly termed as *d1k9r5* code) and a remarkably low detector complexity. Table 1 compares the RLL-NRZI-PR-NP super-trellis complexity of the *d1k9r5* code to that of the (1,7)PP code adopted for BD standards, with respect to the number of states and branches. For $K \leq 4$, the super-trellis employing the *d1k9r5* code has a significantly lower complexity. In addition, the super-trellis employing the *d1k9r5* code has the same complexity for $K \leq 4$ and for $K \in [5, 7]$.

3. SIMULATION RESULTS

A linear equalizer based on the minimum mean square error (MMSE) principle with 19 coefficients is employed as PR equalizer, where the PR target is selected as $\mathbf{h} = [1, 2, 2, 1]$. For MMSE prediction, the prediction order is chosen as $M = 20$ resulting in $L_p = 24$, and bit detection is carried out using the Max-Log-MAP algorithm, which is appropriately modified for super-trellis based detectors. For simulations, signal-to-noise ratio (SNR) is defined as the reciprocal of the additive white Gaussian noise variance.

BER performance is compared between RLL-NRZI-PR-NP super-trellis based detectors and the RLL-NRZI-PR super-trellis based detector, where the complexity of the latter is similar to that of the former detectors with $K = 3$. As shown in Fig. 2 and Fig. 3, the performance gap between RLL-NRZI-PR-NP super-trellis based detectors and the RLL-NRZI-PR super-trellis based detector increases as the storage density increases from 25GB to 35GB. For the *d1k9r5* code, there is no performance difference for detectors with $K \in [1, 6]$, where the super-trellis structure is same for $K \in [1, 4]$.

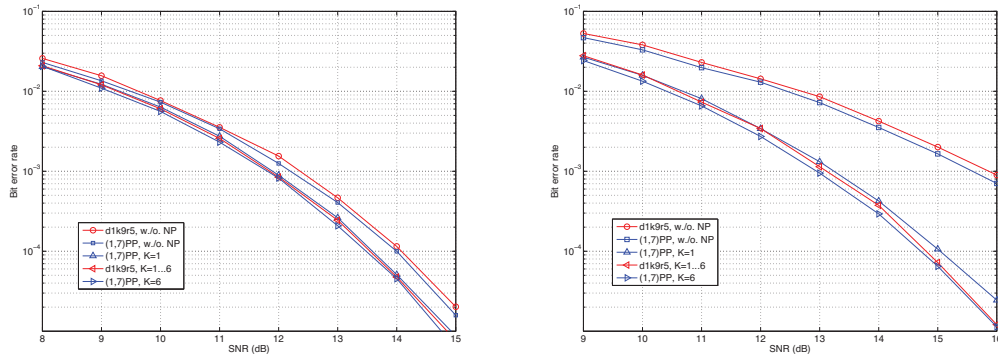


Figure 2. BER results for 25GB (left) and 30GB (right) storage capacity

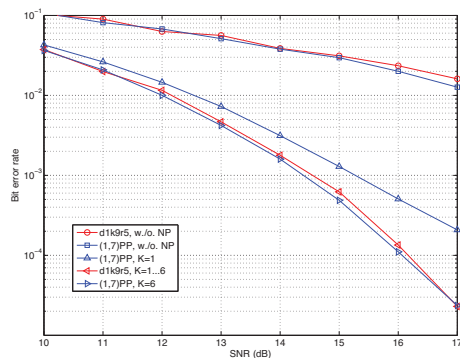


Figure 3. BER results for 35GB storage capacity

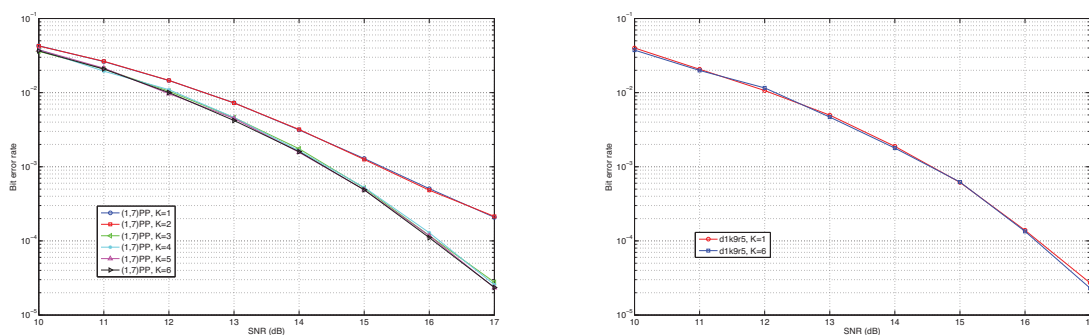


Figure 4. BER results for 35GB storage capacity under different complexities

Under the 35GB storage capacity, as shown in Fig. 4, for the (1,7)PP code no performance improvement is visible by increasing the detector complexity if $K \geq 3$. Although similar BER performance has been obtained for the (1,7)PP code with $K = 3$ and for the *d1k9r5* code with $K \leq 4$, the detector complexity of the *d1k9r5* code is only approximately one half of that of the (1,7)PP code as indicated in Table 1.

4. CONCLUSION

Incorporating noise prediction, RLL-NRZI-PR-NP super-trellis based bit detectors were investigated. With increased storage density, noise prediction based detectors provide increased performance gain. In the presence of an outer SISO channel decoder, an even larger performance gain is expected with the application of turbo principle. For the considered storage densities, systems employing the *d1k9r5* code with a lower detector complexity achieves a similar performance as systems employing the (1,7)PP code.

REFERENCES

- [1] J.D. Coker, E. Eleftheriou, R.L. Galbraith, and W. Hirt, "Noise-predictive maximum likelihood (NPML) detection," *IEEE Trans. Magnet.*, vol. 34, pp. 110–117, Jan. 1998.
- [2] M. Noda and H. Yamagishi, "An 8-state DC-controllable run-length-limited code for the optical-storage channel," *JJAP*, vol. 44, No. 5B, pp. 3462–3466, 2005.
- [3] K. Cai, G. Mathew, J. Bergmans and Z. Qin, "A generalized Braat-Hopkins model for optical recording channels," *Proc. IEEE ICCE '03*, pp. 324–325, 2003.
- [4] O. Theis, X.-M. Chen, D. Hepper, and G. Pilard, "Turbo equalization with RLL (1,9) and LDPC code for SuperRENS ROM discs with 60nm minimum mark length," submitted to *ISOM/ODS 2008*, Feb. 2008.

Channel coding and signal detection for multi-level DVD player system

Hua Hu*, Yi Tang, Haibo Yuan, Longfa Pan
Optical Memory National Engineering Research Center (OMNERC),
Rm. 4406, Bldg. 9003, Tsinghua University, Beijing 100084, P. R. China

ABSTRACT

Multi-level run-length-limited (RLL) recording is a novel way to significantly increase the recording density of current optical disc format without changing optical or mechanical components. In this paper, channel coding and signal detection for multi-level DVD player system are introduced, including error correction code (ECC), modulation code, timing recovery and adaptive partial-response maximum-likelihood (PRML) detection. The storage capacity of multi-level read-only DVD is designed to be 13 ~ 15 GB, so that it can record high-definition movie longer than two hours. Dynamic high-definition movie playback has been realized by using FPGA chips.

Keywords: Multi-level recording, error correction code, modulation code, PRML detection

1. INTRODUCTION

Current optical disc systems use binary signaling in conjunction with run-length-limited (RLL) modulation. However, we can use novel multi-level RLL modulation which combines RLL constraints and multi-level signaling to significantly increase recording density^[1]. This can be realized without changing optical or mechanical components of current optical disc systems. Up to now, multi-level recording has become a promising technology to be applied in CD, DVD, and Blu-ray disc systems.

As we know, read-only optical discs are very popular in movie distribution markets, and high-definition movie playback needs higher storage capacity than that of traditional DVD. If we develop a new format, multi-level read-only DVD, for high-definition movie playback, we can utilize current DVD production lines to manufacture high-definition products.

Recently, a multi-level DVD player system with conventional DVD optical pickup has been developed in Tsinghua University. Channel coding and signal detection for this multi-level system are introduced in this paper, including error correction code (ECC), modulation code, timing recovery and adaptive partial-response maximum-likelihood (PRML) detection. All of the coding and signal processing algorithms have been verified by FPGA chips.

2. CHANNEL CODING

The manufacture process of multi-level read-only DVD is depicted in Fig. 1. The first important process is error correction coding. We have designed an enhanced Reed-Solomon coding scheme for multi-level system, which has better burst error correction ability than that of Reed-Solomon Product-Code (RSPC) used in conventional DVD system.

Then the data blocks are translated into multi-level constrained sequences by multi-level RLL (d, k) modulation code. The constrained sequences are used for the power modulation of writing laser. Next, modified DVD mastering process is used to obtain several kinds of profiles of recorded marks (including pits and lands). Finally, Multi-level read-only DVD discs are obtained from the stamper by replication technology.

The profiles of pits and lands in four-level RLL read-only DVD is shown in Fig. 2. It can be seen the actual multi-level pits have different lengths and grey levels. The pit length corresponds to the run-length of channel symbols, and the grey levels means different depths and widths which correspond to the multi-level recording signals.

2.1 ECC scheme

The ECC used for multi-level read-only DVD system is modified from RSPC scheme. The data frame shall consist of 2060 bytes arranged in an array of 10 rows each containing 206 bytes. An ECC block is formed by arranging 16

* email: huhua@tsinghua.edu.cn

consecutive scrambled frames in an array of 160 rows of 206 bytes each. To each of the 206 columns, 16 bytes of parity outer (PO) code are added, then, to each of the resulting 176 rows, 10 bytes of parity inner (PI) code are added. Thus a complete ECC block comprises 176 rows of 216 bytes each. The maximum correctable consecutive errors are $216 \times 16 = 3456$ bytes, which is 18.7% higher than that of RSPC scheme ($182 \times 16 = 2912$ bytes). This new ECC has strong burst error correction ability, and can protect multi-level data against fingerprints and scratches on the disc surface.

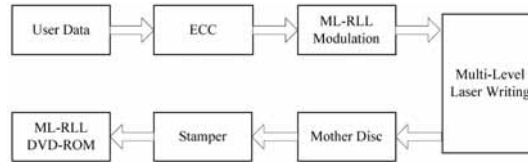


Fig. 1. The manufacture process of multi-level read-only DVD

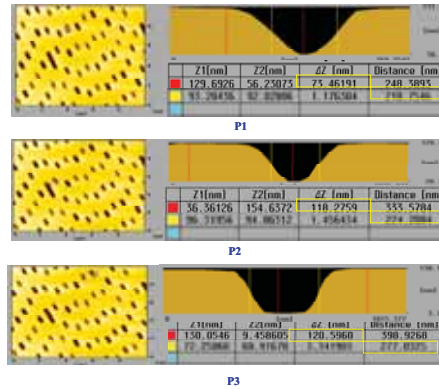


Fig. 2. The profiles of pits and lands in four-level RLL read-only DVD

2.2 Modulation code

As an extension of binary RLL codes, M-ary RLL (d, k) codes can be used for multi-level RLL modulation, which have at least d and at most k zeros between any two non-zero symbols in the constrained sequences [2]. However, these M-ary RLL codes usually result in consecutive multi-level pits on the optical disc. This will increase the difficulty of multi-level optical disc replication. Therefore, we proposed a new class of multi-level RLL codes to obtain spaced pits/lands (SPL) structure on multi-level optical disc [3]. The finite-state transition-diagram (FSTD) and transition matrix for multi-level SPL-RLL (d, k) codes are shown in Fig. 3 and Fig. 4. We calculated the capacities of multi-level SPL-RLL (d, k) codes with typical parameters, and designed some high efficient codes. As shown in Table 1, the four-level SPL-RLL (2, 9) code with rate of 8/12 is suitable for practical application [4]. This byte-oriented code has high efficiency of 94.0% and density ratio of 2.0 bits per minimum recorded mark, and the decoding window length is only two. The linear recording density can be directly increased by 33.3% if this code is applied instead of EFMPlus code in DVD systems.

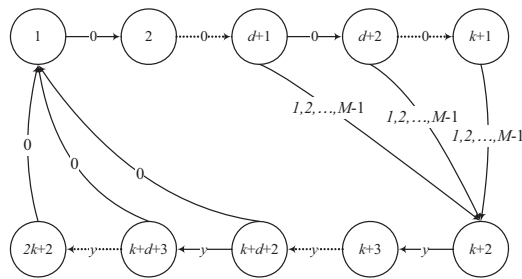


Fig. 3. The FSTD for multi-level SPL-RLL (d, k) codes

$$T = \begin{bmatrix}
 0 & 1 & 0 & 0 & 0 & 0 & 0 & 0 & 0 & 0 \\
 0 & 0 & \ddots & 0 & 0 & 0 & 0 & 0 & 0 & 0 \\
 0 & 0 & 0 & 1 & 0 & M-1 & 0 & 0 & 0 & 0 \\
 0 & 0 & 0 & 0 & \ddots & \vdots & 0 & 0 & 0 & 0 \\
 0 & 0 & 0 & 0 & 0 & 0 & M-1 & 0 & 0 & 0 \\
 0 & 0 & 0 & 0 & 0 & 0 & 0 & 1 & 0 & 0 \\
 0 & 0 & 0 & 0 & 0 & 0 & 0 & 0 & \ddots & 0 \\
 1 & 0 & 0 & 0 & 0 & 0 & 0 & 0 & 0 & \ddots \\
 \vdots & 0 & 0 & 0 & 0 & 0 & 0 & 0 & 0 & 0 & 1 \\
 1 & 0 & 0 & 0 & 0 & 0 & 0 & 0 & 0 & 0 & 0
 \end{bmatrix}$$

Fig. 4. The corresponding transition matrix

Table 1. Characteristic parameters of multi-level SPL-RLL (d, k) codes and binary RLL codes

M	(d, k)	R=m/n	DR=(1+d)*R	$\eta=R/C$	Note
2	(1, 7)	2/3	1.33	98.1%	(1, 7) code
2	(2, 10)	8/16	1.5	92.3%	EFMPlus code
4	(2, 11)	6/9	2.0	93.4%	Ref. [3]
4	(2, 9)	8/12	2.0	94.0%	Ref. [4]

3. TIMING RECOVERY AND PRML DETECTION

As shown in Fig. 5, the multi-level readout signals are much more complicated than that of conventional DVD. In addition, the readout signals are asymmetric due to multi-level RLL recording principle. In order to realize exact signal detection, we propose a feedback timing recovery and adaptive PRML detection scheme, which is depicted in Fig. 6. It consists of an ADC, a frequency synthesizer, a phase synthesizer, an interpolator, and a PRML detector. The ADC samples RF signal with fixed oversampling time. The interpolator interpolates sampling data with channel timing. The PRML detector includes a linear equalizer and an adaptive Viterbi detector. This read channel system is implemented with FPGA chips, and the symbol error rate (SER) of detected multi-level data can be achieved below 1.0×10^{-4} .

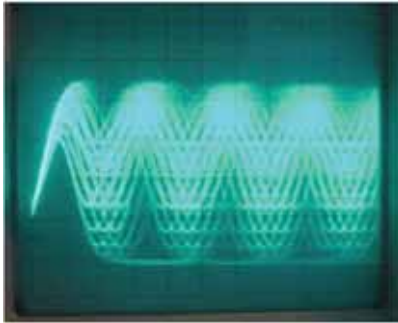


Fig. 5. Readout signal of multi-level disc

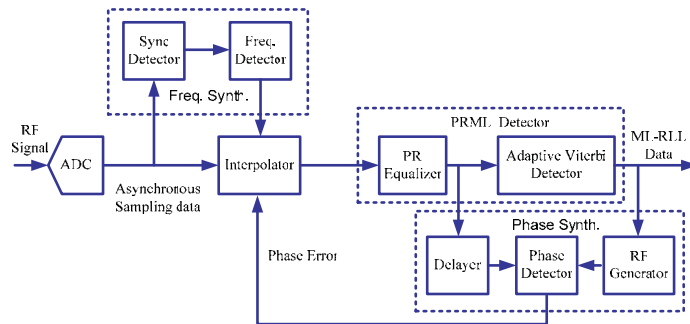


Fig. 6. Block diagram of timing recovery and adaptive PRML scheme

4. CONCLUSIONS

A four-level read-only DVD player system has been realized by advanced channel coding and signal detection. The storage capacity of single-side double-layer DVD can be increased to be 13 ~ 15 GB if we use novel multi-level SPL-RLL modulation and reduce a little of the track pitch or minimum recorded mark length. Therefore, this multi-level read-only DVD format has great potentials to be used for high-definition movie distribution.

REFERENCES

- [1] Howe, D. G. and Wu, K., "Recording of multilevel run-length-limited modulation signals," Proc. of SPIE 5380, Optical Data Storage, 562-575 (2004).
- [2] McLaughlin, S. W., "Five runlength-limited codes for M-ary recording channels," IEEE Trans. Magn., 33, 2442-2450 (1997).
- [3] Hu, H., Yuan, H. B., Tang, Y. and Pan, L. F., "New rate 6/9 RLL (2, 11) code with SPL constraint for four-level read-only optical disc," In: Technical Digest of ISOM, We-I-30 (2007).
- [4] Hu, H., Pan, L. F. and Ni, Y., "A new rate 8/12 run-length limited (2, 9) code for four-level read-only optical disc," In: Technical Digest of ODS, MD10 (2007).
- [5] Yuan, H. B., Xu, H. Z., Hu, H. and Pan, L. F., "Read channel for multilevel read-only optical disc system," In: Technical Digest of ISOM, We-I-27 (2007).

Error-Correcting Coded Indices for Multimode Balanced Conservative Codes for Holographic Storage

Yongguang Zhu and Ivan J. Fair

Dept. of ECE, Univ. of Alberta, Edmonton, AB, Canada T6G 2V4
Tel: 1-780-328-4543; Fax: 1-780-492-1811; E-mail: {ygzhu, fair}@ece.ualberta.ca

ABSTRACT

We present two error-correcting coding schemes for providing error protection for the control array indices required in multimode balanced conservative codes for holographic storage.

Keywords: Holographic storage, multimode coding, balanced, conservative, control array, index, Reed-Solomon codes

1. INTRODUCTION

Holographic storage is expected to play an important role in the data storage hierarchy due to its large storage capacity, short access time, and high data transfer rate [1-2]. In holographic storage, entire two-dimensional pages of binary data are optically recorded via an interference process such that numerous pages of data can be superimposed in the common volume of a holographic recording medium. In order to minimize interference between adjacent data pages recorded in the same volume, each data page is desired to be [3]: a) *balanced* ($N_1 = N_0$, where N_1 and N_0 denote the number of 1's and 0's within the data page, respectively) and b) *t-conservative* (there exist at least t transitions of the form $1 \rightarrow 0$ or $0 \rightarrow 1$, for a prescribed integer t , in each row and each column of the data page). Several coding schemes have been proposed to satisfy either one or both of these two constraints [3-6].

In our earlier work [6], we presented a multimode coding scheme for generating *t-conservative arrays* for holographic storage. In the multimode encoding procedure, each $m \times n$ binary input array U of source data is added to a set of control arrays $\mathcal{Z} = \{V_1, V_2, \dots, V_{(m+1)(n+1)}\}$ to form a selection set $\{U + V: V \in \mathcal{Z}\}$, where the set \mathcal{Z} is constructed such that each selection set contains at least one element that is guaranteed to be *t-conservative* [3, 6]. To retrieve the original input array U during the decoding process, at least $\lceil \log_2(m+1)(n+1) \rceil$ redundant bits are necessary to index $(m+1)(n+1)$ control arrays in the set \mathcal{Z} . This index information can be either appended as an additional column or row to the encoded array [3] or embedded into the encoded array [6]. As listed in Table 1, where the probabilities were obtained by simulating each setup 10^5 times, we have further found that the selection set $\{U + V: V \in \mathcal{Z}\}$ corresponding to each input array U contains at least one *pseudo-balanced t-conservative* array with bounded disparity $|N_1 - N_0| \leq B$, where B is a small constant. Therefore, by selecting a pseudo-balanced *t-conservative* array from each selection set, appropriately encoding the index of the control array, and using the remaining redundant bits in the appended column or row to jointly balance the numbers of 1's and 0's within the encoded array and to maximize the number of transitions within the appended column or row, we can enforce the final output of the multimode encoder to be both balanced and *t-conservative*. In [6], we have demonstrated several improvements that the multimode coding scheme can achieve over the original algorithms in [3].

In holographic storage, user data is usually encoded first by an error-correcting encoder that provides error protection for the input data from various noise sources, and then encoded by a constrained encoder to ensure that particular data patterns that violate the given channel constraints are not issued or to introduce certain desirable characteristics in the recorded data. One problem with the combined error-correcting and constrained coding schemes is that when using a multimode code (the cascaded codes in [3] can also be regarded as multimode codes) as the inner constrained code, clusters of errors caused by the inner constrained decoder may defeat the error-correcting power of the outer error-correcting decoder, especially when errors occur in the indices of control arrays. Since accurate recovery of the indices of control arrays is critical to the bit error performance of multimode codes, we propose the use of Reed-Solomon (RS) codes to encode these indices in order to provide error protection especially for them, while ensuring that the output arrays remain balanced and *t-conservative*. RS codes have strong burst-error correcting power and are therefore used in a large number of data storage systems [7].

Table 1: Probability that at least one pseudo-balanced t -conservative array with bounded disparity B exists in each selection set

$m \times n$	t	$B = 0$	$B = 2$	$B = 4$
15×16	4	0.50403	0.99942	1
31×32	8	0.50114	0.99989	1
63×64	16	0.50121	0.99995	1
127×128	32	0.49855	0.99999	1

2. RS CODING SCHEMES FOR THE INDICES OF CONTROL ARRAYS

Consider the indices of control arrays to be encoded by (k_1, k_2, l) RS codes, where k_1 denotes the number of symbols in each codeword, k_2 denotes the number of symbols in each source word, and l denotes the number of bits in each symbol. For simplicity, in this paper we only consider the cases where the final output arrays of the multimode encoders are of dimension $2^d \times 2^d$, for $d \geq 4$. For small arrays, there is not sufficient redundancy for both balancing the encoded arrays and correcting errors in the indices, but we can achieve this goal for larger arrays that are common in holographic storage, where a single data page may contain as many as one million bits [2].

2.1 Direct RS coding scheme

When encoding an arbitrary 1023×1024 input array into a 1024×1024 balanced 256-conservative array with the multimode coding scheme described above. There are 1024 bits in the appended row, where only 21 bits are needed to index 1049600 control arrays. The remaining 1003 redundant bits can be used not only for balancing the output arrays but for providing error protection for the index information. For instance, we can use the (23, 3, 8) RS code (it is often helpful to set $l = 8$ in order to utilize many commercially available RS encoders and decoders) to encode 24-bit indices, which can be obtained by simply appending the sequential 21-bit vectors from ‘00000000000000000001’ to ‘10000000010000000000’ with an arbitrary 3-bit sequence, into 184-bit RS encoded representations. The (23, 3, 8) RS code can correct any error patterns consisting of 10 bytes or fewer errors in any 23-byte block. In addition to the 184 RS encoded index bits, the remaining 840 bits can be used to both balance the final output arrays and ensure that there are as many transitions as possible in the extra row. Note that more powerful RS codes, such as the (33, 3, 8), (43, 3, 8) and (53, 3, 8) RS codes, can also be used to encode the indices of 1023×1024 control arrays, while ensuring the generation of 1024×1024 balanced 256-conservative arrays. Since the complexity of a high-speed implementation of an RS code grows with its redundancy, from our point of view, RS codes such as the (23, 3, 8) RS code provide a reasonable tradeoff between complexity and error-correcting capability, and should be powerful enough to correct errors that may occur in the indices of 1023×1024 control arrays.

For the 31×32 case, we have to use less powerful RS codes to encode the indices. The parameter l also needs to be smaller, such as $l = 4$, and the original index vectors must be selected appropriately in order to ensure that the final output array can be balanced by the remaining bits in the appended row and that the appended row will not violate the t -conservative constraint. We have verified that RS codes such as the (5, 3, 4) RS code can be used to adequately encode the indices of 31×32 control arrays.

2.2 Interleaving RS coding scheme for tiling small arrays to create a large array

Parallel detection and processing are strongly desired in holographic storage. It has been proposed to divide a large data page into relatively small blocks, such as 16×16 or 32×32 blocks, and then process these small blocks in parallel [2, 8]. Data patterns in each small block are desired to be balanced and t -conservative, which will ensure that the entire data page is balanced and satisfies a global conservative constraint. The multimode coding scheme described above is an appropriate approach for parallel detection and processing, where small multimode coded balanced conservative arrays can be easily tiled to create a large balanced conservative array.

When a large data page is divided into a number of 32×32 small blocks, it is straightforward to verify that the direct RS coding scheme can be combined directly with the multimode coding scheme to provide error protection for the indices of control arrays. However, for the 16×16 case, there is not sufficient redundancy for both balancing and error correction. To enable the creation of a large balanced conservative array by tiling error-protected multimode coded 16×16 arrays, we propose the following interleaving RS coding scheme.

Consider using the multimode coding scheme to encode 4096 15×16 unconstrained data array in parallel into 4096 16×16 balanced 4-conservative arrays, and then tiling these encoded arrays to form a 1024×1024 balanced 256-conservative array that is going to be recorded in a holographic medium. With the interleaving RS coding scheme demonstrated in Fig. 1, the 16 bits included as an extra row in each 16×16 encoded array consist of nine index bits, one parity bit, and six remaining bits. The indices from a number of small arrays are concatenated together and then encoded together using a powerful systematic RS code. The parity bits of this large codeword are then interleaved into the extra row included in each 16×16 array, along with other bits used for balancing and ensuring that the extra row in each 16×16 array has at least 4 transitions. In Fig. 1, we use the (80, 72, 8) RS code in systematic form to encode the indices of a row of 64 encoded arrays together, and then interleave the 8-byte parity bits into the 64 blocks by appending one bit to each original 9-bit index. The six remaining bits in each extra row can ensure the generation of 16×16 balanced 4-conservative arrays if we appropriately choose the 9-bit representations for the 272 indices of 15×16 control arrays. For instance, the 272 9-bit indices can be represented in a bi-mode manner, consisting of 173 ones with disparity either $+1$ or -1 and at least 4 transitions, 24 pairs with opposite disparities ± 1 and 3 transitions, and 75 pairs with opposite disparities ± 3 and at least 3 transitions. According to Table 1, by selecting a pseudo-balanced 4-conservative array with bounded disparity $|N_1 - N_0| \leq 4$ from each selection set and using the bi-mode representations of the 272 indices, the six remaining bits in each block can ensure that the encoded 16×16 arrays are balanced 4-conservative arrays. The interleaving (80, 72, 8) RS code provides protection for the index information of each 16×16 array from a certain amount of errors.

It is obvious to note that the interleaving RS coding scheme can also be applied for the 32×32 case. It will enable the use of more powerful RS codes to provide better error protection for the indices of control arrays than is possible if the indices are encoded individually.

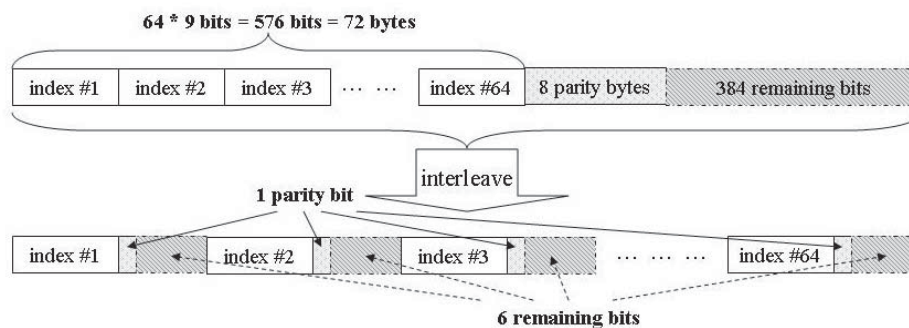


Fig. 1. Interleaving RS coding scheme for encoding the indices of a row of 64 multimode encoded 16×16 arrays with the (80, 72, 8) RS code in systematic form.

REFERENCES

- [1] J.F. Heanue, M.C. Bashaw, and L. Hesselink, "Volume holographic storage and retrieval of digital data," *Science*, 265, 749-752 (1994).
- [2] H.J. Coufal, D. Psaltis, G.T. Sincerbox (Eds.), *Holographic Data Storage*, Berlin, Germany: Springer-Verlag (2000).
- [3] A. Vardy, M. Blaum, P.H. Siegel, and G.T. Sincerbox, "Conservative arrays: Multidimensional modulation codes for holographic recording," *IEEE Trans. Inform. Theory*, 42 (1), 227-230 (1996).
- [4] W.Y.H. Wilson, K.A.S. Immink, X.B. Xi, and C.T. Chong, "Guided scrambling: A new coding technique for holographic storage," in *Proc. Opt. Data Storage Conf.*, 110-112 (2000).
- [5] J. Liu, C.C. Phua, T.C. Chong, Y. Wu, and V. Boopathi, "Effect of channel coding in digital holographic data storage," *Jpn. J. Appl. Phys.*, 38, 4105-4109 (1999).
- [6] Y. Zhu and I.J. Fair, "Multimode coding for generating conservative arrays for holographic storage," in *Proc. of 2007 IEEE Int. Symp. Inform. Theory*, 1181-1185 (2007).
- [7] S.B. Wicker and V.K. Bhargava (Eds.), *Reed-Solomon Codes and Their Applications*, IEEE Press (1994).
- [8] N.Y. Kim, J. Lee, Y. Hong, and J. Lee, "Optimal number of control bits in the guided scrambling method for holographic data storage," *Jap. J. App. Phy.*, 44 (5B), 3449-3452 (2005).

An Improved Chase Decoder for Turbo Product Codes over Partial-Response Channels

Zhiliang Qin, Songhua Zhang, Kui Cai, and Xiaoxin Zou

Data Storage Institute, Singapore, 117608

Tel: (65)68745219; Fax: (65) 67766527

E-mail: {qin_zhiliang; zhang_songhua; cai_kui; zou_xiaoxin}@dsi.a-star.edu.sg

1. Introduction

Turbo product codes (TPC) [1] based on iterative row-column Chase-II decoding [2] has been shown to achieve excellent bit-error-rate (BER) performance and requires no random interleavers in practical implementation, which makes it an attractive choice for optical/magnetic recording systems and fiber optical network applications.

In this work, we propose an improved Chase decoding algorithm that forms test patterns based on the local neighborhood of the least reliable bits in the received hard-decision sequence. Simulation results show that while using the same number of test patterns in algebraic decoding, the proposed decoder can provide significantly better BER performance compared with the original Chase-II decoder [1] over both additive white Gaussian noise (AWGN) channels and ideal partial-response channels.

2. Chase-II Algorithm for TPC Decoding

Given two systematic linear block codes C^1 with parameters (n_1, k_1, δ_1) and C^2 with parameters (n_2, k_2, δ_2) , where n_i, k_i, δ_i ($i=1,2$) denotes the codeword length, the data length, and the minimum distance, respectively, the product code $C^1 \otimes C^2$ is a $(n_1 n_2, k_1 k_2, \delta_1 \delta_2)$ code. The suboptimal soft-decision decoding algorithm developed in [1] is based on applying the Chase-II algorithm iteratively to row and column component codes of the product code. In summary, when applied to decode a $C(n, k, \delta)$ component code, the Chase-II algorithm first constructs a set \mathbf{e}_1 of 2^q n -tuple test patterns by identifying the q least reliable bits $y_{j_0}, \dots, y_{j_{q-1}}$ in the received hard-decision sequence \mathbf{y} and then forming all possible binary combinations on these q positions, where $\mathbf{y} = \text{sign}(\mathbf{r})$, $\mathbf{r} = \{r_i\}$, $i=0, \dots, n-1$, denotes the received noisy sequence, and the binary-phase-shift-keying (BPSK) modulation is assumed. Afterwards, the Chase decoder passes these 2^q test patterns into an algebraic decoder to obtain a set of candidate codewords $\hat{\mathbf{C}}$. Finally, the extrinsic information of code bits in the form of log-likelihood ratios (LLR) can be produced based on $\hat{\mathbf{C}}$ as,

$$w_i = \begin{cases} [(\mathbf{r} \cdot \mathbf{d} - \mathbf{r} \cdot \bar{\mathbf{d}})/2] \cdot d_i - r_i & \text{if } \bar{\mathbf{d}} \text{ exists} \\ \beta \times d_i & \text{otherwise} \end{cases} \quad (1)$$

where $i=0, \dots, n-1$, $\mathbf{d} = \{d_i\}$ ($d_i \in \{-1, +1\}$) is the decided codeword after Chase decoding, $\bar{\mathbf{d}} = \{\bar{d}_i\}$ is the most

likely competing codeword in $\hat{\mathbf{C}}$ with $\bar{d}_i \neq d_i$, the inner product operation is defined as $\mathbf{r} \cdot \mathbf{d} = \sum_{i=0}^{n-1} r_i d_i$, and

the reliability factor β is used to estimate w_i in case no competing codeword exists. Once the extrinsic information is determined, the soft input to the second-stage decoder can be updated as $r_i[2] = r_i + \alpha \times w_i$, where α is a weight factor to combat high standard deviation in w_i and high BER during the first few iterations. For the details of the list-based Chase-II algorithm for TPC decoding, please refer to [1].

3. Proposed Chase Decoder Based on the κ -opt Local Neighborhood

The proposed decoder differs from the Chase-II decoder in that it forms a list of test patterns based on the concept of the κ -opt local neighborhood of the q least reliable bits $\hat{\mathbf{v}} = \{y_{j_0}, \dots, y_{j_{q-1}}\}$, which is defined as,

$$N_\kappa(\hat{\mathbf{v}}) = \left\{ \mathbf{v} \in \{-1, +1\}^q \mid \|\mathbf{v} - \hat{\mathbf{v}}\|_H \leq \kappa \right\} \quad (2)$$

From a geometrical perspective, $N_\kappa(\hat{\mathbf{v}})$ represents a Hamming sphere with radius κ consisting of all possible

binary vectors with Hamming distance at most κ from the central vector $\hat{\mathbf{v}}$, and $\|\cdot\|_H$ denotes the Hamming weight of its vector argument. For all $\mathbf{v} \in N_\kappa(\hat{\mathbf{v}})$, \mathbf{v} differs from $\hat{\mathbf{v}}$ by at most κ elements. The size of a

complete κ -opt local neighborhood, however, is $|N_\kappa| = \sum_{i=0}^{\kappa} \binom{q}{i}$, which may be prohibitive for large values of

κ or q . To efficiently form a subset of the κ -opt neighborhood as a list of test patterns, the principle of the Lin-Kernighan local search (LS) algorithm [3], [4] for solving the traveling salesperson problem (TSP) can be applied. The basic idea is that we partition the κ -opt LS into several successive 1-opt LS procedures. At each step, a variable number of elements in the current solution are flipped to arrive at a better neighboring solution and form $q(q+1)/2$ trial solutions by flipping the bit associated with the highest gain. The trial solution in the sequence associated with the highest objective value is then accepted as the input for the next k -opt search step. This solution may differ in one up to q elements from the initial solution. For the sake of low computational complexities, we focus on the 1-step Lin-Kernighan algorithm in this paper, which results in a total of $1+q(q+1)/2$ test patterns for algebraic decoding. For clarity, the pseudocode of the proposed method is given as follows.

Algorithm 1. (Form test patterns for Chase decoding based on the 1-step Lin-Kernighan Algorithm)

1. Initialization: Obtain $\hat{\mathbf{v}} = \{y_{j_0}, \dots, y_{j_{q-1}}\}$ as the set of the q least reliable bits in the n -tuple received hard-decision sequence \mathbf{y} .
2. Generate a set $\mathbf{T} = \{0, \dots, q-1\}$ to record positions on which the elements of $\hat{\mathbf{v}}$ will be flipped.
 - a) Let a q -tuple vector \mathbf{v} denote the current trial solution $\hat{\mathbf{v}} \rightarrow \mathbf{v}$. Find the best neighboring solution \mathbf{v}_i by flipping elements recorded in \mathbf{T} , such as $\Omega(\mathbf{v}_i) \geq \Omega(\mathbf{v}_j)$, $\forall j \in \mathbf{T}$, where \mathbf{v}_i (\mathbf{v}_j , respectively) differs from \mathbf{v} by only the i th (j th, respectively) element. The objective function Ω is defined later.
 - b) Set $\mathbf{v}_i \rightarrow \mathbf{v}$ and exclude the i th position from \mathbf{T} as $\mathbf{T} = \mathbf{T} \setminus \{i\}$. Go to step 2.a) until $\mathbf{T} = \Phi$.
3. End. Substitute each q -tuple trial solution encountered in the search into \mathbf{y} on the q least reliable positions to form a list $\boldsymbol{\varepsilon}_2$ of $1+q(q+1)/2$ n -tuple test patterns, which are then passed to an algebraic decoder to obtain codeword candidates.

The objective function Ω is based on the correlation between the received signal \mathbf{r} and the trial solution \mathbf{v} as,

$$\Omega(\mathbf{v}) = \sum_{i=0}^{q-1} r_{j_i} v_i \quad (3)$$

Assuming $q=3$ and $\hat{\mathbf{v}} = \{y_{j_0}, y_{j_1}, y_{j_2}\}$, an example of all 7 trial solutions encountered in the search is given by $\{+y_{j_0}, +y_{j_1}, +y_{j_2}\}, \{-y_{j_0}, +y_{j_1}, +y_{j_2}\}, \{+y_{j_0}, -y_{j_1}, +y_{j_2}\}, \{+y_{j_0}, +y_{j_1}, -y_{j_2}\}, \{-y_{j_0}, -y_{j_1}, +y_{j_2}\}, \{+y_{j_0}, -y_{j_1}, -y_{j_2}\}, \{-y_{j_0}, -y_{j_1}, -y_{j_2}\}$. Correspondingly, the list $\boldsymbol{\varepsilon}_2$ of 7 test patterns can be obtained as,

$$\boldsymbol{\varepsilon}_2 = \begin{Bmatrix} y_0 & \cdots & +y_{j_0} & \cdots & +y_{j_1} & \cdots & +y_{j_2} & \cdots & y_{n-1} \\ y_0 & \cdots & -y_{j_0} & \cdots & +y_{j_1} & \cdots & +y_{j_2} & \cdots & y_{n-1} \\ y_0 & \cdots & +y_{j_0} & \cdots & -y_{j_1} & \cdots & +y_{j_2} & \cdots & y_{n-1} \\ y_0 & \cdots & +y_{j_0} & \cdots & +y_{j_1} & \cdots & -y_{j_2} & \cdots & y_{n-1} \\ y_0 & \cdots & -y_{j_0} & \cdots & -y_{j_1} & \cdots & +y_{j_2} & \cdots & y_{n-1} \\ y_0 & \cdots & +y_{j_0} & \cdots & -y_{j_1} & \cdots & -y_{j_2} & \cdots & y_{n-1} \\ y_0 & \cdots & -y_{j_0} & \cdots & -y_{j_1} & \cdots & -y_{j_2} & \cdots & y_{n-1} \end{Bmatrix} \quad (4)$$

, where each row of $\boldsymbol{\varepsilon}_2$ denotes an n -tuple test pattern. Note that for large values of q , the proposed decoder forms $1+q(q+1)/2$ test patterns, which is far fewer than 2^q test patterns generated in the exhaustive search as required by the Chase-II decoder.

4. Simulation Results

In this paper, we focus on the TPC with extended single-error-correcting BCH component codes (denoted by TPC/eBCH), which are especially suitable for applications requiring high code rates, low

encoding/decoding complexities, and low-cost implementations. Algebraic decoding for these codes involves very low computational complexities, since the non-zero syndrome solely specifies the bit-error location.

In Fig. 1, we present BER results of a rate-0.88 $(128,120,4)^2$ TPC/eBCH transmitted over AWGN channels. In order to provide a fair comparison between the proposed decoder and the Chase-II decoder, we set the number of test patterns used in algebraic decoding to be the same for both cases. For the Chase-II decoder, we first choose the number of the least reliable bits as $q=4$, resulting in $2^q=16$ test patterns. For the proposed decoder, the value of q is set to $q=5$, which also corresponds to $1+q(q+1)/2=16$ test patterns. When the value of q for the Chase-II decoder is increased to $q=5$ (i.e., $2^q=32$ test patterns), the proposed decoder can afford $q=8$ least reliable bit positions and generates a total of $1+q(q+1)/2=37$ test patterns. The first 32 test patterns in the list are then used in algebraic decoding for fair comparison purposes. Note that for the Chase-II decoder, the value of $q=8$ corresponds to $2^8=256$ test patterns, which involves a much higher complexity for algebraic decoding. In Fig. 1, all curves represent BER results obtained at the 4th row-column iteration. The weight and the reliability factor α and β [1] used in the simulation for each iteration are set to 0.5 and 1.0, respectively, as in [5]. Fig. 1 shows that with LS=16 test patterns, the proposed decoder can improve BER performance over the original Chase-II decoder at $E_b/N_o=4.2$ dB by *one order of magnitude*. Fig. 1 also shows that when the number of test patterns is increased to LS=32, the TPC decoder produces better BER performance. In this case, the proposed decoder still outperforms the Chase-II decoder by *one order of magnitude* at $E_b/N_o=4.1$ dB.

Next, we consider the TPC/eBCH transmitted over an ideal MEEPR4 channel corrupted with AWGN, where MEEPR4 channel coefficients are given by $\{5,4,-3,-4,-2\}$. The turbo equalizer at the receiver side consists of a 16-state BCJR channel detector [6] and the TPC decoder with extrinsic information exchanged in between for 3 outer iterations. For each outer iteration, four inner row-column iterations are performed in TPC decoding. In the simulation, the number of test patterns used in algebraic decoding is set to LS=16. Fig. 2 shows BER performance of turbo equalization from the 1st to the 3rd outer iteration, respectively. It is shown that for the third iteration, the turbo equalizer using the proposed decoding algorithm achieves better BER performance at $E_b/N_o=6.0$ dB by *one order of magnitude* compared with the scheme using the original Chase-II decoder.

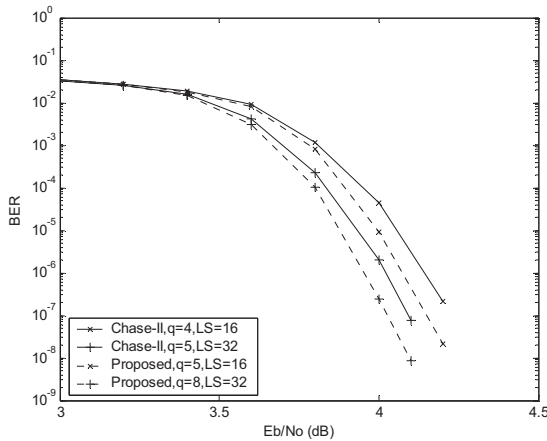


Fig. 1. BER results of $(128,120,4)^2$ TPC/eBCH transmitted over AWGN channels.

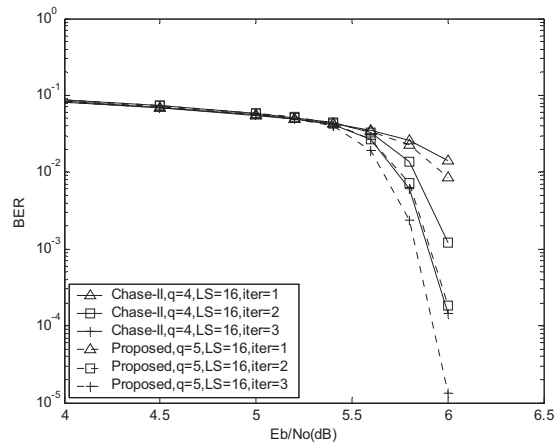


Fig. 2. BER results of $(128,120,4)^2$ TPC/eBCH transmitted over ideal MEEPR4 channels.

Reference

- [1] R. Pyndiah, "Near-optimum decoding of product codes: Block turbo codes," *IEEE Trans. Commun.*, vol. 46, pp. 1003–1010, Aug. 1998.
- [2] D. Chase, "A class of algorithms for decoding block codes with channel measurement information," *IEEE Trans. Inform. Theory*, vol. IT-18, pp. 170–182, Jan. 1972.
- [3] S. Lin and B. Kernighan, "An effective heuristic algorithm for the traveling salesman problem," *Operation Research*, vol. 21, pp. 498–516, 1973.

- [4] Z. Qin and K. C. Teh, "Reduced-Complexity turbo equalization based on local search algorithms for coded intersymbol interference channels," *IEEE Trans. Vehicular Tech.*, vol. 57, pp. 630-635, Jan. 2008.
- [5] C. Argon and S. W. McLaughlin, "An efficient Chase decoder for turbo product codes," *IEEE Trans. Commun.*, vol. 52, pp. 896-898, June 2004.
- [6] D. Raphaeli, "Combined turbo equalization and turbo decoding," *IEEE Commun. Lett.*, vol. 2, pp. 107-109, Apr. 1998.

Two-Dimensional 5:8 Modulation Code for Holographic Data Storage

Jinyoung Kim*, Bongil Lee, Jaejin Lee
 School of Electronic Engineering, Soongsil University, Seoul, Korea
 Phone: +82-2-820-0901, Fax: +82-2-821-7653
 E-mail: kijiyou@ssu.ac.kr*, bbong7258@ssu.ac.kr, zlee@ssu.ac.kr

ABSTRACT

We present a two-dimensional (2D) 5:8 modulation code without isolated pixel pattern for holographic data storage. We compare it with the 5:9 code and uncoded sequences. The bit error rates (BERs) are collected by the threshold detection and one-dimensional (1D) PRML collaborated with two-dimensional (2D) equalizer at the blur of 1.85. The proposed 2D 5:8 modulation code is very simple and removes all the isolated 2D ISI patterns. Despite of high code rate, the proposed 5:8 modulation code shows similar performance to the 5:9 modulation code.

Keywords: Holographic data storage, two-dimensional modulation code, PRML, 2D equalizer

1. INTRODUCTION

In the holographic data storage (HDS) system, there are two major concerns in the aspects of the lowpass frequency characteristics for the modulation code for HDS channel because data are recorded by pages into a volume of the storage medium [1, 2]. First, it causes the inter-page interference (IPI) for read/write processes. The IPI is severe to record more the number of pages. To avoid the IPI, the number of zero and one pixels must be almost equal in each page [3]. Second, to increase the capacity, it requires higher density of the recorded data. Thus, the two-dimensional (2D) inter-symbol interference (ISI) is severe in each page. Thus, it is necessary to find the modulation code having lowpass filtering effect. In this paper, we design a 2D modulation code having the same distribution of 1 and 0 in a page. It also has the lowpass filtering effect having no isolated pixel pattern. We compare the proposed 2D 5:8 modulation code with the 5:9 code [4] and the uncoded sequences.

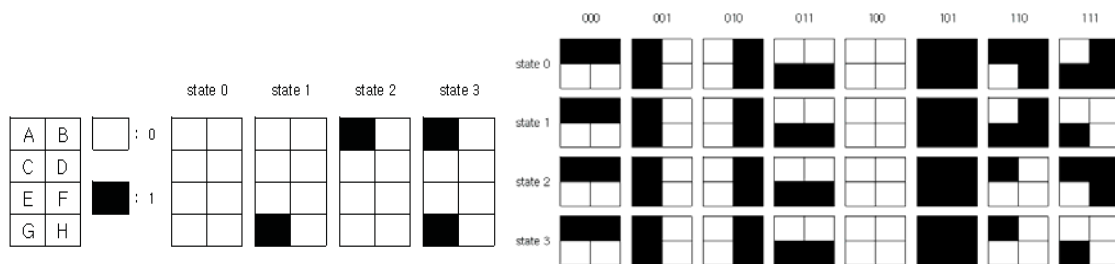


Fig. 1. Encoding scheme of the proposed 2D modulation code

2. A NEW 2D MODULATION CODE

Fig. 1 illustrates the encoding method. The rate of the proposed modulation code is 0.625 ($=5/8$). The codeword is 4 by 2 array and divided by two parts. One part that includes the pixels of A, B, G, H is to set a state using two input bits, and the other part that includes the pixels of C, D, E, F is four encoded output bits corresponding to the remaining three input bits. Each two pixel set {A, G} and {B, H} represents the previous state and next state, respectively. Without loss of generality, we assume that the state starts from 'state 0,' then {A, G} is initialized state 0 at first. As soon as we receive

the five input bits, the first two bits determine the next state using pixels of B and H. Then, the remaining three input bits determine the four bit pattern. When the next five input bits are received, the pixels A and G copy the previous codeword's pixel B and H, and the new state is determined by the first two input bits and recorded to the position of B and H. The remaining three bits similarly determines the four bit pattern in {C, D, E, F}. This is to remove the isolated 2D ISI patterns, and the encoding procedure is very simple. Fig. 2 illustrates a example of the proposed 5:8 modulation code.

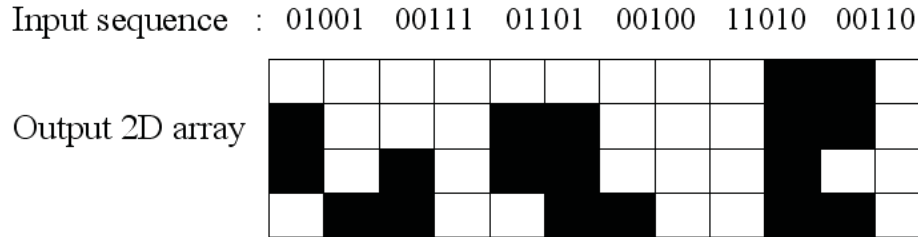


Fig. 2. An example of the proposed 5:8 modulation coded pattern

3. SIMULATION RESULTS

Fig. 3 and 4 show the performance of the bit separation characteristics. We can see that the coded sequence is more clearly separated than uncoded sequence. The separation performance of the proposed code has almost the same as that of the 5:9 code. (Because of the page limit, we cannot include the result.) Obviously, the bigger the grade of blur the more overlap occurs.

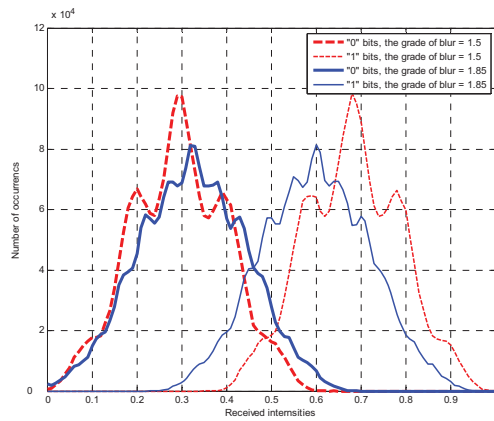


Fig. 3. Bit separation of uncoded sequences

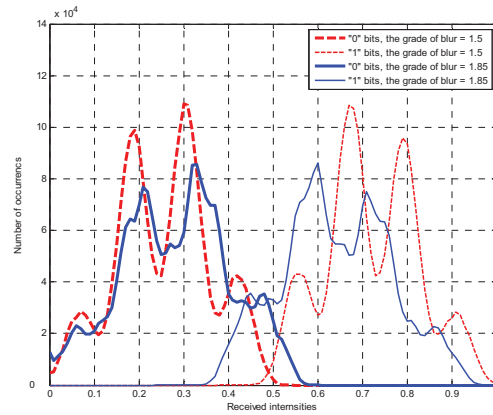


Fig. 4. Bit separation of the proposed 5:8 modulation code

Fig. 5 and 6 show the bit error rate (BER) performance when we use the threshold detection and the one-dimensional (1D) partial response maximum likelihood (PRML) detection with 2D equalizer. In Fig. 5, coded sequences are superior to uncoded sequence without concerning the high grade of blur. Meanwhile, the proposed 5:8 code and the 5:9 code show almost the same BER performance even if we increase the grade of blur to 2.1.

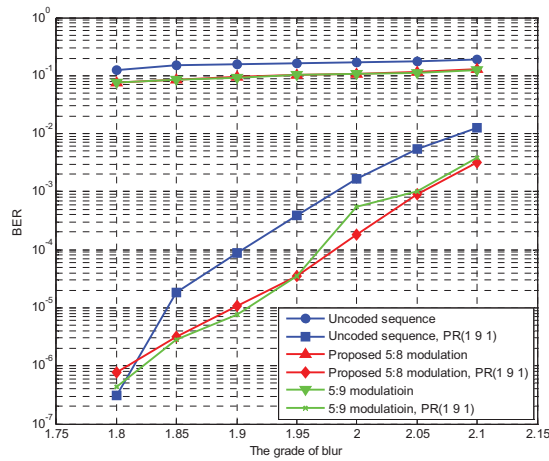
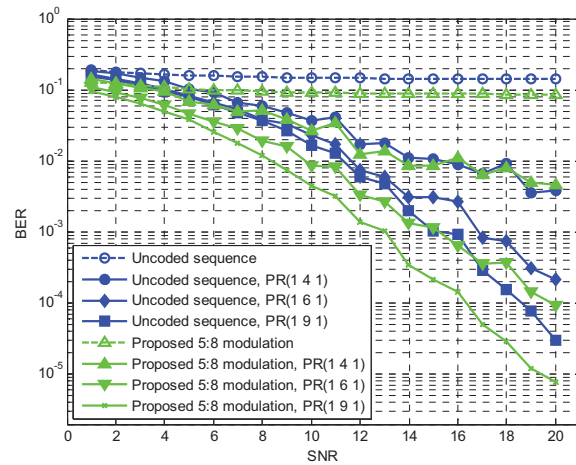


Fig. 5. BER performance without AWGN

Fig. 6. BER performance with AWGN ($\sigma_b = 1.85$)

When we change the PR target, the PR(1 9 1) target has the best BER performance for the proposed 5:8 code. This trend is also shown in the 5:9 code.

4. CONCLUSIONS

We introduced a 2D modulation code of rate 5/8 for HDS channel. It has almost the same performance as the 5:9 code. The proposed code has almost the same distribution of 1 and 0 to solve the IPI problem and no isolated pixel pattern to solve the ISI problem. Most of all, its encoding scheme is very simple.

REFERENCES

- [1] L. Hesselink, S. S. Orlov, M. C. Bashaw, "Holographic data storage systems," Proceeding of IEEE, 92, 8, 1231-1280 (2004).
- [2] V. Vadde and B. V. K. V. Kumar, "Channel Modeling and Estimation for Intrapage Equalization in Pixel-Matched Volume Holographic Data Storage," Appl. Opt. 38, 4374-4386 (1999).
- [3] W. Y. H. Wilson, K. A. S. Immink, X. B. Xi, and C. T. Chong, "An Efficient Coding Technique for Holographic Storage with the Method of Guided Scrambling," Proceedings of SPIE 4090, 277-786 (2000).
- [4] Nayoung Kim, Joohyun Lee and Jaejin Lee, "Rate 5/9 Two-Dimensional Pseudobalanced Code for Holographic Data Storage Systems," Jpn, J. Appl. Phys., 45, 2B, 1293-1296 (2006).

Hybrid image processing for Holographic Data Storage System

Jang Hyun Kim^{*a}, Hyunseok Yang^b, Jin Bae Park^c, and Young-Pil Park^b

^aDepartment of Electrical and Electronic Engineering, Yonsei University, Shinchon-dong, Seodaemoon-gu, Seoul, 120-749, Korea

E-mail: jhkim@control.yonsei.ac.kr

^bDepartment of Mechanical Engineering, Yonsei University, Shinchon-dong, Seodaemoon-gu, Seoul, 120-749, Korea

^cDepartment of Electrical and Electronic Engineering, Yonsei University, Shinchon-dong, Seodaemoon-gu, Seoul, 120-749, Korea

ABSTRACT

A holographic data storage system has the advantages of a high data rate, rapid access and a multiplexing method. The two-dimensional page-oriented nature of holographic data storage also utilizes the information capacity of an optical wavefront to allow data to be recorded and retrieved in parallel, a page at a time, rather than serially as in conventional storage. In this paper, we propose hybrid image processing method.

Keywords: Holographic data storage system, Image processing, Discrete Wavelet Transform(DWT), Digital mask

1. INTRODUCTION

Holographic data storage system(HDSS) is new generation technology in storage device. Moreover, it is one of the vital importance storage devices. Recently, Many research for holographic data storage system is in process however holographic data storage system does not has standard research direction[1]. Furthermore, image process for binary pattern is need that exact and real holographic data storage system is made for high quality of storage system. In this paper, we propose hybrid image processing method. Hence, we simulate image processing methods and experiment by our proposal method[6]. In order to obtain efficient results, we are going to do many experiments. Consequently, practical holographic data storage system is realized.

2. ARCHITECTURE OF HOLOGRAPHIC DATA STORAGE SYSTEM

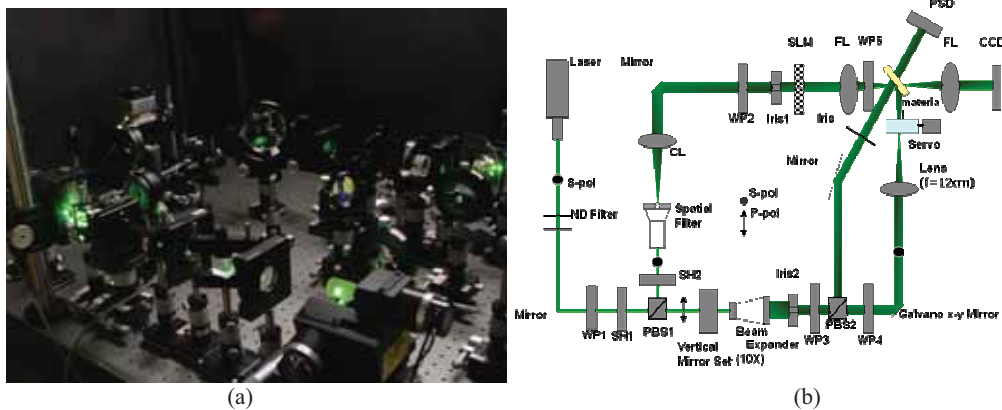


Figure 1 (a)Test bed of our HDSS (b)A structure of the HDSS

Figure 1 (a) shows our holographic data storage system and a structure of HDSS is shown in Figure 1(b). General Holographic data storage system have two laser source beams. However, It have three laser source beams in order that

servo control be control[3]. Important component specifications for holographic data storage system is shown in Table 1[1][2][4].

Table 1. shows specification of our holographic data storage system.

Components of our HDSS	Specification
Nd-YAG Laser(Compass 515, COHERENT)	532 nm wavelength, 150mW power
SLM	1024×768 pixels with 36 by 36 μm pixel pitch
Angle between the S-beam and R-beam	90°
NA of the collimating lens	0.38
Selectivity	4.9 μm
PSD	Kodenshi SD201
Servo motor	Faulhaber1717012R

3. HYBRID IMAGE PROCESSING METHOD IN HOLOGAPHIC DATA STORAGE SYSTEM

Hybrid image processing is composed of two image processing methods. One is wavelet based binary data compression and the other is digital mask method of image processing. Recorded binary data is compress by wavelet algorithm in our holographic data storage system. Moreover, digital mask decrease or increase bright of light in holographic data storage system[5][6].

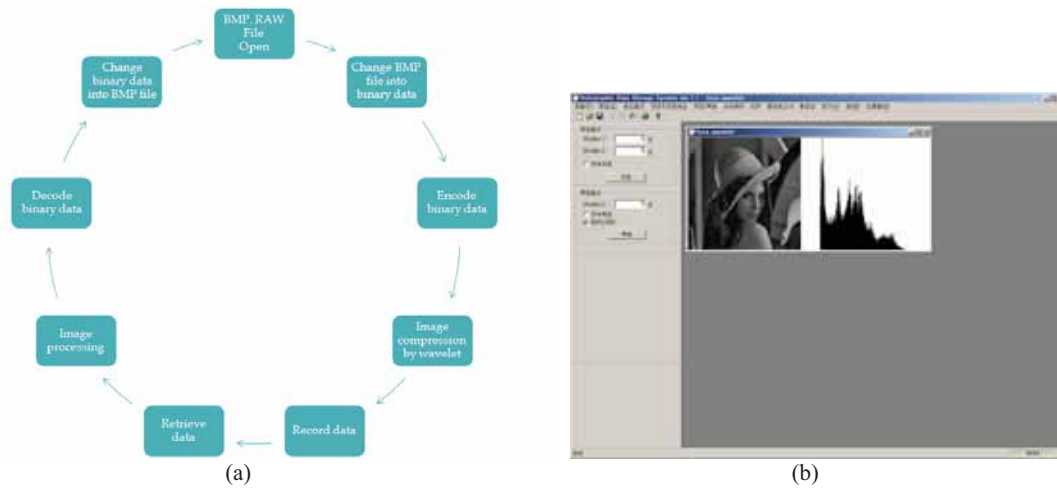


Figure 2 (a) Diagram box of process in HDSS (b) Image processing program GUI for holographic data storage system.

An overall process of holographic data storage system is shown in Figure 2(a). This equation is main equation of Discrete Wavelet Transform(DWT) in order to analysis or decomposition.

$$f(t) = \sum_{j \in Z} C_0 \phi_{0,j}(t) + \sum_{k \geq 0} \sum_{j \in Z} d_{k,j} \psi_{k,j}(t) \tag{1}$$

Here, $f(t) = \sum_{j \in Z} C_0 \phi_{0,j}(t)$ is coarse information of $f(t)$, $\sum_{k \geq 0} \sum_{j \in Z} d_{k,j} \psi_{k,j}(t)$ is detail information of $f(t)$.

4. SIMULATIONS AND EXPERIMENTS

Figure 2(b) show GUI program for image processing of our HDSS. GUI program is able to process original data page and show threshold value of each data page. Furthermore, It is able to many image processing and decode data page.



Figure 3. (a)Original image. (b)Modify image by mask method. (c)Compression image by wavelet. (d)Retrieved image by our hybrid image processing.

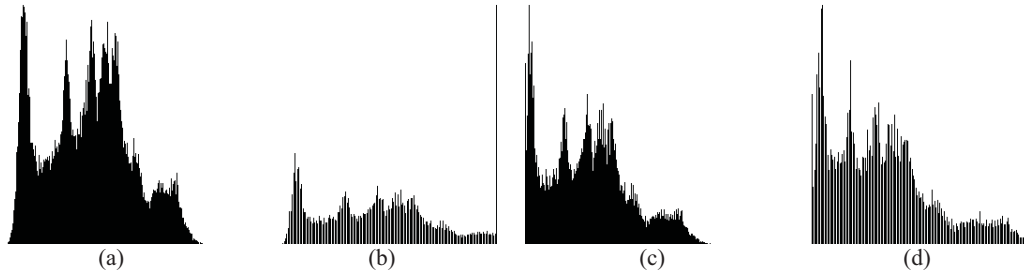


Figure 4. (a)Threshold of original image. (b) Threshold of modify image by mask method. (c) Threshold of compression image by wavelet. (d) Threshold of retrieved image by our hybrid image processing.

Figure 3 is shown recorded and retrieved data in HDSS. Figure 4 is shown threshold of each data which a boundary value of threshold is 128 between 0 and 255.

5. CONCLUSIONS

In this paper, we propose a hybrid image processing method in holographic data storage system. Hybrid image processing is consist of wavelet image compression and digital mask method. It is possible to realize recording and retrieving by hybrid image processing in holographic data storage system. Future plan of research in holographic data storage system include to optimize recorded and retrieved data page by image processing.

ACKNOWLEDGMENTS

This research was supported by the MOCIE (Ministry of Commerce, Industry and Energy) of Korea through the program for the Next Generation Ultra-High Density Storage (00008145).

REFERENCES

- [1] Hans J. Coufal, Demetri Psaltis and Glen T.Sincerbox, "Holographic Data Storage", Springer, New York, 2000.
- [2] E. Hecht and A. Zajac, "Optics", 1987, Addison-Wesley, Chapter 4.
- [3] George Barbastathis, Michael Levene, and Demetri Psaltis," Shift multiplexing with spherical reference waves", *Appl. Opt.* **35** (1996) 2403.
- [4] F. H. Mok, "Angle-multiplexed storage of 5,000 holograms in lithium niobate", *Opt. Lett.* **18** (1991) 915.
- [5] Kasra Rastani, "Storage capacity and cross talk in angularly multiplexed holograms: two case studies", *Appl. Opt.* **32** (1993) 3772.
- [6] Rafael G. Gonzalez, Richard E. Woods, "Digital Image Processing", ADDISON-WESLEY PUBLISHING COMPANY, 1993.

Gaussian Sum Approximation approach to Blu-ray Disk channel equalization

Gyuyeol Kong, Hyunmin Cho, Sooyong Choi
School of Electrical and Electronic Engineering, Yonsei University
134 Shinchon-Dong, Seodaemun-Gu, 120-749, SEOUL, KOREA

1. INTRODUCTION

As the recording density of optical storage systems increases, the partial response maximum likelihood (PRML) detection scheme becomes more practical for the improvement of the detection performance [1]. However, the PRML has a large complexity that performed equalization and ML and shows poor performance in high density recording channels. In this paper, we apply the Kalman filtering algorithm [2] for optical channel equalization and propose a new equalizer based on the Kalman filtering algorithm. Since the Kalman filtering algorithm exploits the orthogonality condition of linear least-mean-squares estimation, the Kalman algorithm provides an exact solution for linear Gaussian prediction and filtering problem while the Kalman filtering algorithm is not optimum for nonlinear systems. In addition, the Kalman filtering algorithm is limited due to the fact that it was derived with white Gaussian noise assumption. Therefore, the Kalman filtering algorithm performs poorly. In order to overcome these problems, the non-Gaussian signals in the state equation is approximated by a Gaussian sum based on the fact that non-Gaussian densities can be approximated reasonably well by a finite sum of Gaussian densities [3],[5]. Therefore the proposed equalizer incorporates the Gaussian sum approximation into a Kalman filtering algorithm [2] to mitigate inter-symbol interference.

2. OPTICAL SYSEMS AND EQUALIZATION

A. Optical recording channel [1]

The optical input signal can be modeled as

$$x(t) = \sum_{k=-\infty}^{\infty} a_k p(t - kT) \quad (1)$$

where $a_k \in \{-1, +1\}$ and $p(t)$ are an input sequence and a pulse with symbol duration T . The optical read back system is then given by

$$r(t) = x(t) \otimes h(t) + n_{AWGN}(t) + n_{jit}(t) \quad (2)$$

where $r(t)$ and $x(t)$ are the read back signal and the optical input signal, respectively. The noise can be represented summation of additive white Gaussian noise (AWGN) and jitter noise. The impulse response of the optical recording channel is given by

$$h(t) = \frac{2}{ST\sqrt{\pi}} \exp\left[-\left(\frac{2t}{ST}\right)^2\right] \quad (3)$$

In (3), S represents the normalized density of recorded data, and T is the symbol duration.

B. Equalization base on GSA

The input vector of the Kalman equalizer at time k which is the channel output vector $\mathbf{r}(k) = [r(k) \ r(k-1) \ \dots \ r(k-N+1)]$ is the sampled sequences of the readback signal, which can be written as

$$\mathbf{r}(k) = \mathbf{H}\mathbf{a}(k) + \mathbf{n}(k). \quad (4)$$

In order to apply an equalization problem to the Kalman framework, the channel is formulated by the observation equation (4) and the following state equation [2]:

$$\mathbf{a}(k) = \mathbf{F}\mathbf{a}(k-1) + \mathbf{G}a(k) \quad (5)$$

where \mathbf{F} is the $(N+M) \times (N+M)$ shift matrix and \mathbf{G} is the $(N+M) \times 1$ vector for the so called GSA-2 which use the range of 2 sequences in the state vector $\mathbf{a}(k)$.

$$\mathbf{F} = \begin{bmatrix} 0 & 0 & 0 & \cdots & 0 \\ 0 & 0 & 0 & \cdots & 0 \\ 0 & 0 & 1 & \cdots & \vdots \\ \vdots & \ddots & \ddots & \ddots & \vdots \\ 0 & \cdots & 0 & 1 & 0 \end{bmatrix}, \mathbf{G} = \begin{bmatrix} 1 & 1 & 0 & \cdots & 0 \\ 1 & -1 & 0 & \cdots & 0 \\ -1 & 1 & 0 & \cdots & 0 \\ -1 & -1 & 0 & \cdots & 0 \end{bmatrix}^T, \mathbf{a}(k) = \begin{bmatrix} 1 \\ 1 \\ 0 \\ \vdots \\ 0 \end{bmatrix}. \quad (6)$$

Therefore, 4 Kalman filters operate in parallel with the associated input vector according to the Kalman filtering algorithms. The state vector $\mathbf{a}(k)$ has 4 columns and the i -th column is denoted as $\mathbf{a}_i(k)$. Then, the i -th Kalman filter operates with the i -th column vector as the input vector. When the GSA equalizer using the range of n sequences, called the GSA- n equalizer, the GSA- n equalizer has a bank of 2^n Kalman filters. Each output is combined based on the GSA for $i=1, 2, \dots, L=2^n$, as follows :

$$\beta_i(k) = N[r(k) - \mathbf{H}^T \hat{\mathbf{a}}_i(k|k-1), \sigma_n^2 + \mathbf{H}^T \mathbf{P}_i(k|k-1) \mathbf{H}], \quad (7)$$

$$\alpha_i(k) = \frac{\beta_i(k)}{\sum_{i=1}^L \beta_i(k)}. \quad (8)$$

The estimated vector $\hat{\mathbf{a}}_i(k)$ of the state vector $\mathbf{a}_i(k)$ for the i -th kalman filter is given by the conditional expectation $E[\mathbf{a}_i(k) | \mathbf{r}(k)]$ with associated error covariance matrix $\bar{\mathbf{P}}(k)$ defined as $E[(\mathbf{D}(k) - \hat{\mathbf{D}}(k))(\mathbf{D}(k) - \hat{\mathbf{D}}(k))^T | \mathbf{r}(k)]$, which yields

$$\hat{\mathbf{a}}(k) = \sum_{i=1}^L \alpha_i(k) \hat{\mathbf{a}}_i(k), \quad (9)$$

$$\bar{\mathbf{P}}(k) = \sum_{i=1}^L \alpha_i(k) \cdot \{\mathbf{P}_i(k) + (\hat{\mathbf{a}}_i(k) - \hat{\mathbf{a}}(k))(\hat{\mathbf{a}}_i(k) - \hat{\mathbf{a}}(k))^T\}. \quad (10)$$

Therefore, it can be known from (9) that $\hat{\mathbf{a}}_i(k)$ is the combination of 2^n Kalman filters which operate in parallel based on the Kalman filtering algorithm and then the combined output for the estimated sequence can be obtained by (7)-(10). When $n=1$, the GSA-1 equalizer is the NKF equalizer in [5] and 2 Kalman filters operating in parallel. Therefore, the GSA- n equalizer is a generalized approach to the Kalman equalizer using the GSA.

3. SIMULATION RESULTS

Consider the Blu-ray Disk channel model (3) with 3.8 of S and the AWGN. Fig. 1 shows the bit-error-rate (BER) curves for the Kalman, GSA- n , partial response maximum likelihood (PRML) and the maximum likelihood sequence estimator (MLSE) bound. As the Blu-ray channel has a high density, the linear equalizer can't use any more. Fig. 1 shows that the proposed equalizer performs very well in the Blu-ray channel. The GSA- n approaches a BER performance of MLSE as n increases. Fig. 2 shows the required signal-to-noise (SNR) to obtain the BER of 10^{-3} for each equalizer when S is 3.5 to 5. From Fig. 3, as density increases, the GSA- n shows a small increment in SNR while the SNR of the PRML methods dramatically increases. Fig. 3 shows the histograms of the Kalman and GSA- n equalizers when the density is 3.8 and the SNR is 16dB. For the Kalman equalizer, the equalized signals have the large variance than the GSA- n equalizer. The variance of the GSA- n is getting smaller and the shape is getting sharper as n increases.

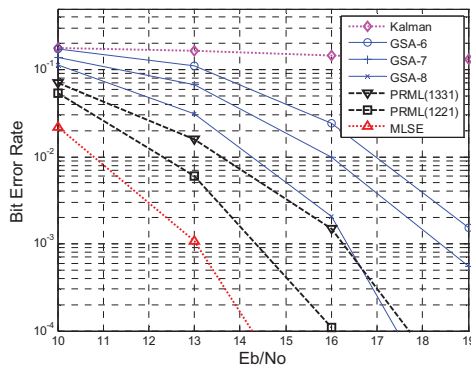


Fig. 1 BER curves of the Kalman, GSA-n, PRML and the MLSE bound when the density is 3.8

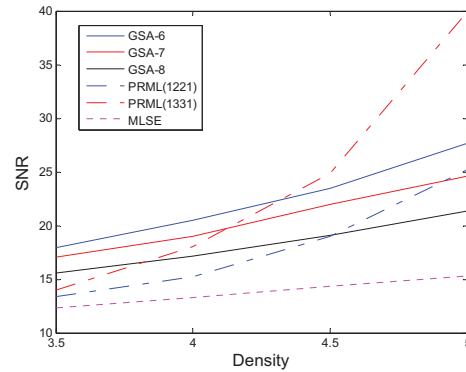


Fig. 2 Required SNR curves of the Kalman, GSA-n, PRML and the MLSE bound when the density is 3.5 to 5

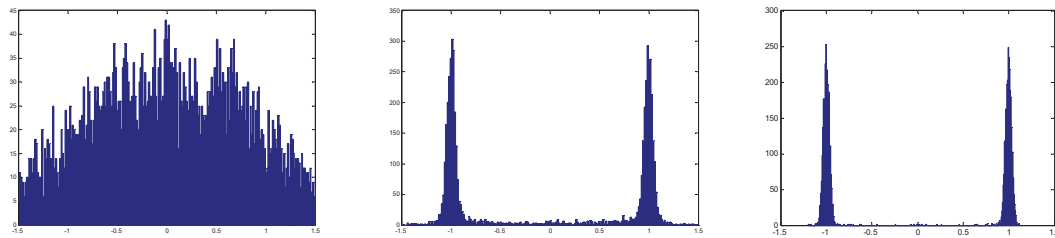


Fig. 3 Histograms of the Kalman, GSA-6, GSA-8 equalizers when the density is 3.6 in 16dB

4. CONCLUSION

A new equalization method for optical recording channels is proposed, which incorporates the Gaussian sum approximation into a Kalman filtering algorithm to mitigate inter-symbol interference in optical recording systems. Proposed equalizer consists of a bank of linear equalizers using the Kalman filtering algorithm and its output is obtained by combining the outputs of linear equalizers through the Gaussian sum approximation. The proposed equalizer shows a better bit-error-rate than a PRML method, and has complexity as low as the minimum mean square error (MMSE) linear equalizer in time-invariant channels.

REFERENCES

- [1] Joohyun LEE and Jaejin LEE, "Adaptive Equalization Using Expanded MLD for Optical Recording Systems", *Japanese Journal of Applied Physics*, vol. 44, no. 5B, 2005, pp. 3499-3502.
- [2] R. E. Kalman, "A new approach to linear filtering and prediction problems," *Transactions of the ASME—Journal of Basic Engineering*, vol. 82, no. Series D, pp. 35–45, 1960.
- [3] D. L. Alspach and H. W. Sorenson, "Nonlinear Bayesian estimation using Gaussian sum approximations," *IEEE Trans. Autom. Control*, vol. 17, no. 4, pp. 439–448, Aug. 1972.
- [4] S. J. Julier and J. K. Uhlmann, "Unscented filtering and nonlinear estimation," *Proc. IEEE*, vol. 92, no. 3, pp. 295–308, Mar. 2004.
- [5] S. Marcos, "A network of adaptive Kalman filters for data channel equalization," *IEEE Trans. Signal Process.*, vol. 48, no. 9, pp. 2620–2627, Sep. 2000.

One-Dimensional PRML Detection with Two-Dimensional Equalizer for Holographic Data Storage

Jinyoung Kim*, Donghyuk Park, Jaejin Lee
 School of Electronic Engineering, Soongsil University, Seoul, Korea
 Phone: +82-2-820-0901, Fax: +82-2-821-7653
 E-mail: kijjiyou@ssu.ac.kr*, mamak@ssu.ac.kr, zlee@ssu.ac.kr

ABSTRACT

We present a partial response maximum likelihood (PRML) detection with two-dimensional equalizer scheme for holographic data storage channel. The coefficients of the equalizer are composed and updated with two-dimensional array. We also search the partial response (PR) target for holographic storage channel varying the parameter of blur. The simulation results show that the proposed scheme outperforms the threshold detection.

Keywords: Holographic data storage, two-dimensional equalizer, 2D PRML

1. INTRODUCTION

The holographic data storage (HDS) system is a strong candidate for next generation storage in the aspects of the capacity and data transfer rate [1, 2]. Data are recorded by pages into a volume of the storage medium. It causes the inter-page interference (IPI) during the read/write processes. High density is essential to increase the capacity per unit area. Thus, the two-dimensional (2D) inter-symbol interference (ISI) is severe in each page. When the readback signal has ISI, the partial response (PR) equalization is used to eliminate the ISI of the readback signal in the serially recording storage systems. We introduce a 1D PRML detector collaborated with 2D equalizer and find the appropriate PR target for the channel.

2. THE PROPOSED DETECTION SCHEME FOR HDS CHANNEL

Fig. 1 shows the block diagram of the proposed detection system for HDS channel. It is similar to 1D PRML system. First, the input data $d[p, q]$ is the binary random or the 2D modulated data. The 2D modulation code used here is the 5:9 modulation code [4]. The 5:9 modulation code is to remove isolated 2D ISI patterns and has the low-pass filtering effect [5].

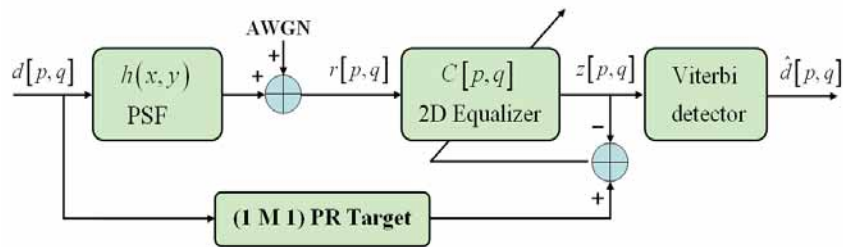


Fig. 1. Block diagram of the proposed detection scheme for HDS channel.

The received intensity $r[p, q]$ is the convolution of the point spread function $h(x, y)$ and the input data $d[p, q]$ in addition to the additive white Gaussian noise (AWGN) $n[p, q]$. We consider a holographic channel model that relates input data to the output data pixels through the charge-coupled detector (CCD) array. The data retrieval is illuminated by a suitable reference beam and the resultant diffracted signal is detected using the CCD array. Thus, $d[p, q]$ is expressed as a binary input data at (p, q) -position in a page, and the continuous point spread function (PSF) is modeled by

$$h(x, y) = \frac{1}{\sigma_b^2} \text{sinc}^2\left(\frac{x}{\sigma_b}, \frac{y}{\sigma_b}\right) \quad (1)$$

where σ_b is the grade of blur in resultant diffracted signals. When the pixel pitch between two nearest detectors is one, the received intensity $r[p, q]$ and the discrete PSF $h[p, q]$ are given by

$$r[p, q] = d[p, q] \otimes h[p, q] + n[p, q] \quad (2)$$

$$h[p, q] = \int_{q-\frac{\alpha}{2}}^{q+\frac{\alpha}{2}} \int_{p-\frac{\alpha}{2}}^{p+\frac{\alpha}{2}} h(x, y) dx dy \quad (3)$$

where α ($0 < \alpha \leq 1$) is the linear fill factor of the CCD pixels, and \otimes defines 2D convolution operation. We consider that α is 1 and range of the discrete PSF is 5×5 pixels.

Then it is passed to the 2D equalizer $C[p, q]$. The equalizer in the PRML system plays an important role. It makes the signal be the form of a given PR target. The 2D equalizer has 5×5 array coefficients and is implemented by 2D finite impulse response filter. Coefficients of the 2D equalizer are updated by the least mean square (LMS) algorithm. The update process is given by

$$C[p, q]_{k+1} = C[p, q]_k + 2\mu \varepsilon X_k \quad (4)$$

where $C[p, q]_{k+1}$ is the new coefficients, $C[p, q]_k$ is the current coefficients, μ is adaptation gain, ε is level error value, and X_k is the current filter input value. We set μ by 2×10^{-5} . The equalizer output $z[p, q]$ is given by

$$z[p, q] = r[p, q] \otimes C[p, q]. \quad (5)$$

Finally, the equalizer output is inputted to the Viterbi detector. Although the ISI affects 2D way, we use the 1D PR(1 M 1) target because the Viterbi detector is very simple in this case.

We define channel SNR as

$$SNR = 10 \log_{10} \left(\frac{1}{\sigma_w^2} \right) \quad (6)$$

where σ_w^2 is the AWGN noise power.

3. SIMULAION RESULTS

We simulated 1000 pages with a size of 480 by 480 pixels for each page. Fig. 2 shows the performance of the received signals without noise varying σ_b from 1.8 to 2.1. We see that the proposed one has a good performance. The uncoded sequence that includes the isolated 2D ISI patterns also has 10^{-6} BER at 1.8 grade of blur. Furthermore, the 5:9 modulation coded signal has better performance than the uncoded sequence. Fig. 2 shows the performance of the received signals with AWGN when σ_b is 1.85. The result shows that PR (1 9 1) is better than PR (1 6 1). In both coded and uncoded sequences, PR (1 9 1) is approximately 3dB better than PR (1 6 1) at 10^{-4} BER. The 5:9 modulation code is approximately 2dB better than the uncoded case at 10^{-4} BER.

4. CONCLUSIONS

We have presented the 1D PRML with 2D equalizer scheme for holographic data storage channel. We have shown the performance improvement, and the PR(1 9 1) target is better than PR(1 6 1) target. The BER performance of the modulation coded sequence is better than that of the uncoded one.

REFERENCES

- [1] L. Hesselink, S. S. Orlov, M. C. Bashaw, "Holographic data storage systems," Proceeding of IEEE, 92, 1231-1280 (2004).
- [2] V. Vadde and B. V. K. V. Kumar, "Channel Modeling and Estimation for Intrapage Equalization in Pixel-Matched Volume Holographic Data Storage," Appl. Opt. 38, 4374-4386 (1999).
- [3] W. Y. H. Wilson, K. A. S. Immink, X. B. Xi, and C. T. Chong, "An Efficient Coding Technique for Holographic Storage with the Method of Guided Scrambling," Proceedings of SPIE 4090, 277-786 (2000).
- [4] Nayoung Kim, Joohyun Lee and Jaejin Lee, "Rate 5/9 Two-Dimensional Pseudobalanced Code for Holographic Data Storage Systems," Jpn, J. Appl. Phys., 45, 2B, 1293-1296 (Feb. 2006).
- [5] J. J. Ashley and B. H. Marcus, "Two-Dimensional Low-pass Filtering Codes," IEEE Trans. Commun., 46, 009-6778 (1998).

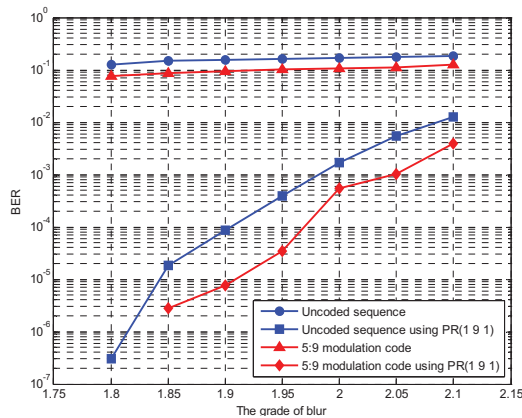


Fig. 2. Performance in accordance with the blur without AWGN

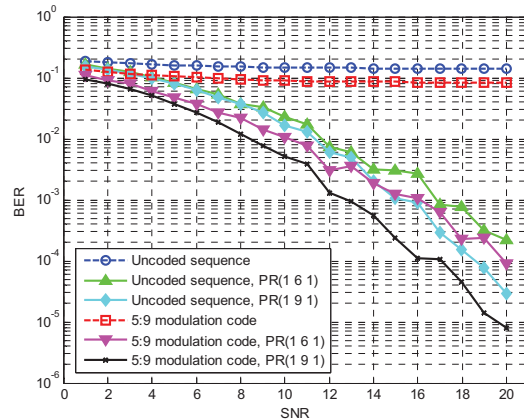


Fig. 3. Performance in accordance with the target with AWGN ($\sigma_b = 1.85$)

Optical Recording Channel Equalization Using a Bilinear Recursive Polynomial System

Hyunmin Cho, Gyuyeol Kong, Sooyong Choi
School of Electrical and Electronic Engineering, Yonsei University
134 Shinchon-Dong, Seodaemun-Gu, 120-749, SEOUL, KOREA

1. INTRODUCTION

In high density optical recording systems, a robust adaptive equalizer is necessarily required to compensate serious nonlinear intersymbol interference (ISI). Neural networks can be one of the alternative methods for channel equalization and signal reception because of their inherent nonlinear architectures. Almost all the equalizers using neural networks show good performance over conventional equalizers while their structures are much complex. Among them, equalizers using bilinear recursive polynomial (BRP) show good performance and have simple structures [1]. And the nonlinear mapping capability of a polynomial perceptron is investigated and the BRP is proposed in [2]. In order to improve the performance and simplify the structure of the BRP, a new equalizer, which is an equalizer using bilinear recursive polynomial model using decision feedback sequence (BRP-DF), is proposed. The recursive input of the BRP is the output while the BRP-DF uses the decision of the output as its recursive input. The proposed BRP-DF is applied to the optical recording channel. The optical recording channel is a digital storage system in which the primary interference element is nonlinear distortion. Also the BRP-DF is compared with the minimum mean square error (MMSE) equalizer, partial response maximum likelihood (PRML) detector and maximum likelihood sequential detector (MLSD) bound in terms of bit-error rate (BER) obtained by Monte Carlo simulations.

2. BILINEAR RECURSIVE POLYNOMIAL EQUALIZER

The proposed BRP-DF uses the modified output of the BRP as its recursive input. Fig.1 shows the simplified digital transmission system with the BRP-DF. $d(n) \in \{-1, 1\}$ is a bipolar modulated symbol at time n . The numbers of feedforward filter and feedback filter are denoted by N_{ff} and N_{fb} , respectively. The input to the feedforward filter at time n is $X(n)=[x(n), x(n-1), \dots, x(n-N_{ff}+1)]$, the sequences of the channel outputs added to additive white Gaussian noise (AWGN). The input to the feedback filter at time n is $\hat{Y}(n)=[\hat{y}(n-1), \dots, \hat{y}(n-N_{fb})]$, the previous decision output sequences. Therefore the output of the BRP-DF is

$$\hat{y}(n) = \text{sgn}(y(n)) = \begin{cases} -1, & \text{if } s_k < 0 \\ 1, & \text{if } s_k \geq 0, \end{cases} \quad (1)$$

where,

$$y(n) = f \left(\sum_{j=1}^{N_{fb}} a_j \hat{y}(n-j) + \sum_{i=1}^{N_{ff}-1} \sum_{j=1}^{N_{fb}} b_{ij} \hat{y}(n-j) x(n-i) + \sum_{i=0}^{N_{ff}} c_i x(n-i) \right) \quad (2)$$

where a_j , b_{ij} and c_i are the weights of the BRP-DF. The weights of the BRP-DF can be trained by many ways. Among them, the steepest descent gradient-based weight updating algorithm for the BRP-DF at time $n+1$ is given as follows:

$$a_j(n+1) = a_j(n) + \mu_a (1 - y^2(n)) e(n) \hat{y}(n-j) \quad \text{for } 1 \leq j \leq N_{fb} \quad (3)$$

$$b_{ij}(n+1) = b_{ij}(n) + \mu_b (1 - y^2(n)) e(n) \hat{y}(n-j) x(n-i) \quad \text{for } 1 \leq j \leq N_{fb}, 1 \leq i \leq N_{ff} \quad (4)$$

$$c_i(n+1) = c_i(n) + \mu_c (1 - y^2(n)) e(n) x(n-i) \quad \text{for } 0 \leq i \leq N_{ff} - 1 \quad (5)$$

where $e(n) = d(n) - y(n)$ and μ_a , μ_b and μ_c are the step sizes of the weights, $a_j(n)$, $b_{ij}(n)$ and $c_i(n)$, respectively. Therefore the total number of the weights for the BRP-DF is $N_{fb}N_{ff} + N_{ff} + N_{fb}$.

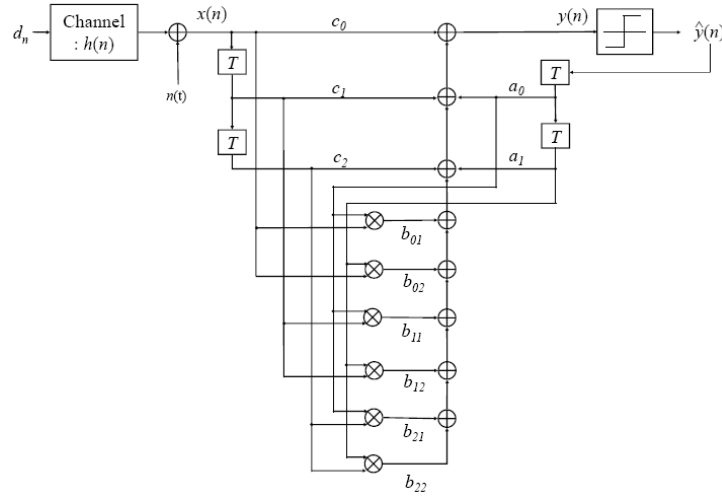


Fig. 1. Proposed BRP-DF equalizer with $N_{ff}=3$ and $N_{fb}=2$

3. CHANNEL MODEL

The optical input signal can be modeled as

$$x(t) = \sum_{k=-\infty}^{\infty} a_k p(t - kT) \quad (6)$$

where $a_k \in \{-1, +1\}$ and $p(t)$ are an input sequence and a pulse with symbol duration T . The optical readback system is then given in [3] by

$$r(t) = x(t) \otimes h(t) + n_{AWGN}(t) + n_{jt}(t) \quad (7)$$

where $r(t)$ and $x(t)$ are a readback signal and an optical input signal at time t , respectively. The additive noise can be represented by summation of AWGN and jitter noise. The impulse response of the optical recording channel is given by

$$h(t) = \frac{2}{ST\sqrt{\pi}} \exp\left[-\left(\frac{2t}{ST}\right)^2\right] \quad (8)$$

In (8), S represents the normalized density of recorded data, and T is the symbol duration [3].

4. SIMULATION RESULTS

The simulations are conducted at $S=3.8$ for the Blu-ray Disk (BD) recording channel [4]. The MMSE equalizer, the PRML, and the MLSD are examined as reference performances. Fig. 2 shows the BERs of the proposed BRP-DF equalizers when the number of feedback signal is from 1 to 5. The result shows that the performance increment is saturated when 3 or more feedback signals are used. Fig. 3 shows the BERs of the MMSE equalizer, BRP-DF using 3 feedback signals (BRP-3) scheme, PRML, and MLSE bound when $S=3.8$ and AWGN is considered. From the figure, we can identify that the proposed BRP-DF equalizers show the better BER performance than the MMSE equalizer. Fig. 4 shows the required signal-to-noise ratio (SNR) to get a BER of $1.0E-3$ for each equalizer when the normalized density $S=3.5$ to 5. The BER performance gap between PRML[1221] and BRP-3 is narrower as the normalized density goes to higher. At the density $S=5$, the PRML[1221] and the BPR-3 has the same BER performance.

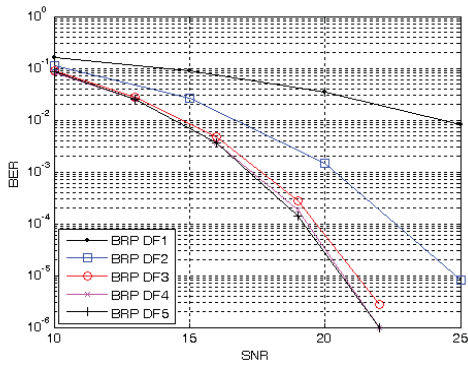


Fig. 2. BER performance of the proposed BRP-DF equalizer, $S=3.8$, jitter free channel

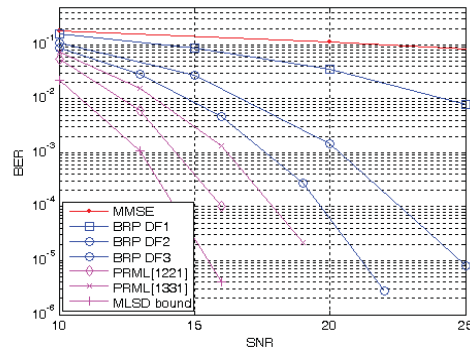


Fig. 3. BER performance of the proposed BRP-DF equalizers and other schemes, $S=3.8$, jitter free channel

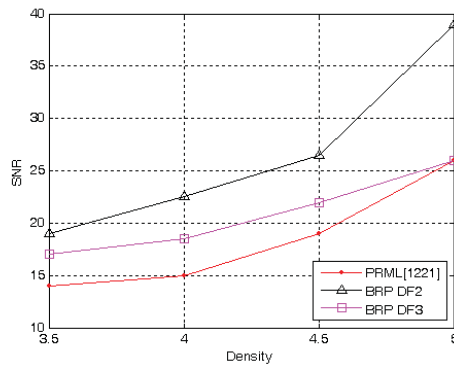


Fig. 4. BER performance of the proposed BRP-DF equalizers and other schemes, $S=3.8$, jitter free channel

5. CONCLUSION

The performance of BRP-DF is compared with the conventional equalizers and MLSD bound. The simulation results show that the performance of BRP-DF approaches to the PRML[1331] at $S=3.8$ even though the complexity of BRP-DF is much smaller than that of the PRML[1331] and the performance margin between of proposed BRP-DF and the PRML[1221] detector goes smaller as the normalized density goes higher.

REFERENCES

- [1] Zengjun Xiang, Guangguo Bi and Tho Le-Ngoc, "Polynomial Perceptrons and Their Applications to Fading Channel Equalization and Co-Channel Interference Suppression," IEEE Trans. on Signal Processing, vol.42, no.9, 2470-2479 (1994).
- [2] S. Chen, G. J. Gibson and C. F. N. Cowan, "Adaptive channel equalization using a polynomial-perceptron structure," Proc. IEE, pt. 1, vol.137, no.5, 257-264 (1990).
- [3] Joohyun Lee and Jaejin Lee, "Adaptive Equalization Using Expanded Maximum-Likelihood Detector Output for Optical Recording Systems," Jpn. J. Appl. Phys., vol. 44, no. 5B, 3499-3502 (2005).
- [4] Jing Pei, Heng Hu, Longfa Pan, Quanhong Shen, Hua Hu, and Duanyi Xu, "Constrained Code and Partial-Response Maximum-Likelihood Detection for High Density Multi-Level Optical Recording Channels," Jpn. J. Appl. Phys., vol. 46, no. 6B, 3771-3774 (2007).

Sum-Product Decoding of Multiple-Parallel-Concatenated Single-Parity-Check Codes over Partial-Response Channels

Xiaoxin Zou, Zhiliang Qin, Kui Cai, and Songhua Zhang

Data Storage Institute, Singapore, 117608

Tel: (65)68745219; Fax: (65)67766527

E-mail: {zou_xiaoxin; qin_zhiliang; cai_kui; zhang_songhua}@dsi.a-star.edu.sg

1. Introduction

In this paper, we consider the multiple-parallel-concatenated single-parity-check (M-PC-SPC) code [1], [2] as an efficient coding scheme for optical and magnetic recording systems. By viewing the M-PC-SPC code as a type of low-density parity-check (LDPC) codes, we propose a serialized decoding algorithm that significantly outperforms the conventional parallel sum-product algorithm (SPA) when used in turbo equalization [3] schemes.

2. M-PC-SPC codes

Fig. 1 shows the structure of an M-PC-SPC code, which takes the form of $P=3$ parallel branches of multiple SPC codes concatenated through random interleavers. In each branch, M blocks of $(t+1, t)$ SPC codewords are combined and interleaved together. Hence, the M-PC-SPC is a rate- $t/(t+P)$ $(tM+PM, tM)$ linear block code. In [1], [2], the M-PC-SPC code was viewed as a turbo code where the recursive systematic convolutional (RSC) component codes are replaced by SPC codes.

Since each branch of the M-PC-SPC code satisfies M parity checks, we may also consider it as a special type of LDPC codes whose parity-check matrix has a dimension of $PM \times (tM+PM)$. For example, the Tanner graph of a 3-branch M-PC-SPC code with each branch consisting of 2 $(3,2)$ SPC codes (i.e., $P=3$, $M=2$, $t=2$) is shown in Fig. 2. The parity-check matrix of this code in the systematic form is given by,

$$\mathbf{H} = \begin{bmatrix} 1 & 0 & 0 & 1 & 1 & 0 & 0 & 0 & 0 & 0 \\ 0 & 1 & 1 & 0 & 0 & 1 & 0 & 0 & 0 & 0 \\ 1 & 0 & 1 & 0 & 0 & 0 & 1 & 0 & 0 & 0 \\ 0 & 1 & 0 & 1 & 0 & 0 & 0 & 1 & 0 & 0 \\ 0 & 1 & 1 & 0 & 0 & 0 & 0 & 0 & 1 & 0 \\ 1 & 0 & 0 & 1 & 0 & 0 & 0 & 0 & 0 & 1 \end{bmatrix}$$

In the graph, the parity bit node has a degree of 1, while the data bit node has a degree of P and each check node has a degree of $t+1$.

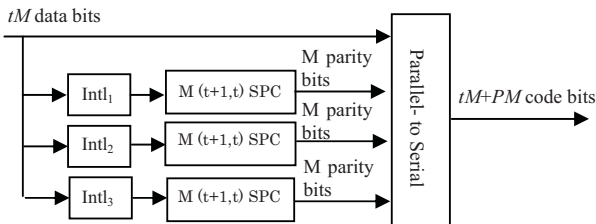


Fig. 1. Encoder of a 3-branch M-PC-SPC code.

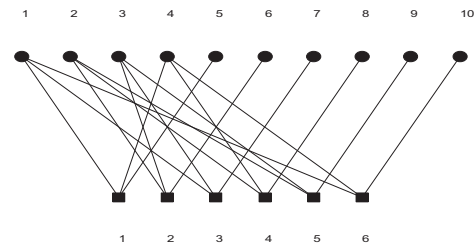


Fig. 2. Tanner graph of a 3-branch M-PC-SPC code with 2 $(3,2)$ SPC codes per branch.

3. M-PC-SPC Decoding

The observation that the M-PC-SPC code can be viewed as a LDPC code leads to a natural adoption of the sum-product decoding algorithm. In the following, we consider several algorithms that differ in message-passing schedules.

1) Conventional Fully Parallel Schedule

Let us denote the set of bits that participate in check m by $N(m)=\{n: H_{mn}=1\}$, and the set of checks in which bit n participates as $M(n)=\{m: H_{mn}=1\}$. Let $N(m)\setminus n$ represents the exclusion of n from $N(m)$, while $M(n)\setminus m$ represents the exclusion of m from $M(n)$. Let λ_n denote the *a priori* log-likelihood ratio (LLR) of bit n , which is delivered by the BCJR channel detector [3]. Let $\varepsilon_{mn}^{(i)}$ and $z_n^{(i)}$ denote the LLR sent from check m to bit n and the *a posteriori* LLR

of bit n at the i th LDPC decoding iteration, respectively. In the parallel SPA, all check nodes and, subsequently, all bit nodes pass extrinsic information to their neighbors. The implementation details can be found in [4].

2) Serialized Check-Updating Schedule

At the i th iteration, the parallel schedule updates all check-to-bit messages based on their values obtained from the $(i-1)$ th iteration, i.e., each $\varepsilon_{mn}^{(i)}$ is updated by using $\{z_{n'}^{(i-1)} - \varepsilon_{mn'}^{(i-1)} : n' \in \mathcal{N}(m) \setminus n\}$, i.e.,

$$\varepsilon_{mn}^{(i)} = 2 \tanh^{-1} \left(\prod_{n' \in \mathcal{N}(m) \setminus n} \tanh \left((z_{n'}^{(i-1)} - \varepsilon_{mn'}^{(i-1)}) / 2 \right) \right) \quad (1)$$

However, certain values of $z_n^{(i)}$ have already been updated based on a partial computation of $\varepsilon_{mn}^{(i)}$, and can be used instead in (1). The resulting serialized check-updating schedule can be described as,

$$\text{Check operation: } \varepsilon_{mn}^{(i)} = 2 \tanh^{-1} \left(\prod_{n' \in \mathcal{N}(m) \setminus n} \tanh \left((z_{n'}^{(i)} - \varepsilon_{mn'}^{(i-1)}) / 2 \right) \right) \quad (2)$$

$$\text{Bit operation: } z_n^{(i)} = \lambda_n + \sum_{m' \in \mathcal{M}(n), m' \leq m} \varepsilon_{m'n}^{(i)} + \sum_{m' \in \mathcal{M}(n), m' > m} \varepsilon_{m'n}^{(i-1)} \quad (3)$$

Since new updates are immediately used in decoding, speed-up of the convergence can be achieved. The serialization is particularly attractive for applications where the structure of a code makes the parallel SPA difficult to implement, e.g., high-rate M-PC-SPC codes whose parity-check matrices have a large number of 1s in each row. In the following, we further propose two techniques for the serialized algorithm that leads to an efficient implementation structure and better BER performance.

a. MacLaurin Series Approximation

The core element of the SPA decoding is the computation of the check-to-bit LLR as given in (2). Assuming that a and b denotes input LLRs to check c , the output LLR from the degree-2 check node c is give by the so-called tanh rule as $L = 2 \tanh^{-1}(\tanh(a/2) \tanh(b/2))$. In [4], an implementation based on the Jacobian algorithm was proposed, i.e.,

$$L = \text{sign}(a) \text{sign}(b) \min(|a|, |b|) + \log(1 + \exp(-|a+b|)) - \log(1 + \exp(-|a-b|)) \quad (4)$$

The underlying function $f(x) = \log(1 + \exp(-x))$ can be approximated by table lookup or by using a piecewise linear function. Saving results in a lookup table, however, would inevitably introduce quantization errors. In addition, to achieve optimal performance, multiple lookup tables are required over a wide range of signal-to-noise ratios (SNR). Accessing lookup tables repeatedly in the decoding process can be time-consuming. On the other hand, neglecting correction terms completely (i.e., the Min-Sum algorithm) introduces a noticeable performance loss.

It is noted that the function $\log(1 + \exp(-|x|))$ has a non-negligible value only when x is approximately zero. This suggests that the MacLaurin Series expansion [5] can be used to approximate the logarithmic term as $\log(1 + \exp(-|x|)) \approx \log 2 - |x|/2$. In this case, we can implement the tanh rule as,

$$L = \text{sign}(a) \text{sign}(b) \min(|a|, |b|) + \max\{0, \log 2 - |a+b|/2\} - \max\{0, \log 2 - |a-b|/2\} \quad (5)$$

, which can be realized in hardware very efficiently by using high-speed adders, comparators, and shift registers.

b. Normalization

For cycle-free graphs, it is well known that the SPA provides optimal performance and converges to maximum *a posteriori* (MAP) decoding. However, for a graph with cycles, there is no guarantee that the SPA is optimal. In this case, the outgoing LLRs from check nodes tend to have higher reliabilities compared with those obtained under the cycle-free assumption [6]. To compensate for the over-estimation of reliabilities, we introduce a multiplicative factor α in (2) to scale down check-to-bit LLRs generated in the serialized decoding algorithm as $\tilde{\varepsilon}_{mn}^{(i)} = \alpha \times \varepsilon_{mn}^{(i)}$ with $\alpha \leq 1$. The optimal value of α depends on SNR and the iteration number. For the sake of simplicities, we assume that α remains constant through the decoding process.

4. Simulation Results

To be applicable to optical and magnetic recording systems, we are interested in high-rate M-PC-SPC codes. The code used in the simulation consists of 4 parallel branches with each branch consisting of 128-block (33,32) SPC codes, thus resulting in an overall code rate of 0.89, the data frame size of 4096, and the codeword length 4608. We consider turbo equalization over an ideal coded MEEPR4 channel corrupted with additive white Gaussian noise

(AWGN), whose channel coefficients are given by $f=\{5,4,-3,-4,-2\}$. The turbo equalizer consists of a 16-state soft-in/soft-out (SISO) BCJR channel detector [3] and an outer SPA decoder with extrinsic information exchanged in-between for 5 outer iterations, each of which involves 2 local iterations inside the M-PC-SPC decoder.

Fig. 3 shows the BER performance at the 5th outer iteration of turbo equalization schemes using various message-passing schedules for M-PC-SPC decoding. In Fig. 3, we also include the performance of an alternative serialized decoding algorithm (curve labeled “Serial-Column”) that processes each bit node sequentially by using refined bit-to-check messages available at the current iteration in addition to the serial-check updating schedule as described above. It is shown that both serialized algorithms produce similar BER performance and outperform the conventional parallel SPA by 1.2 dB at the BER of 10^{-6} . For comparison purposes, we consider the Min-Sum and the MacLaurin Series approximations of the serial-check decoding algorithm, respectively. The latter is shown to perform better by 0.4 dB at the BER of 10^{-5} . Fig. 3 also shows that by combining normalization (with $\alpha=2$, i.e., a shift in the register) and the MacLaurin approximation, the proposed

low-complexity implementation of the serialized decoding algorithm performs better by 0.2 dB than the exact implementation at the BER of 10^{-6} . In this case, a performance gain of 1.4 dB is observed over the conventional parallel SPA decoder. Note that the M-PC-SPC code graph features a large number of short cycles. In this case, the exact SPA is by no means optimal and it is not surprising that the proposed decoder can achieve better BER performance over such code graphs.

Reference

- [1] D. Rankin and T. Gulliver, “Single-Parity-Check product codes,” *IEEE Trans. Commun.*, vol. 49, pp. 1354-1362, Aug. 2001.
- [2] J. S. K. Tee, D. P. Taylor, and P. A. Martin, “Multiple serial and parallel concatenated single-parity-check codes,” *IEEE Trans. Commun.*, vol. 51, pp. 1666-1675, Aug. 2001.
- [3] T. Souvignier, A. Friedmann, M. Oberg, P. Siegel, R. Swanson, and J. Wolf, “Turbo decoding for PR4: parallel vs. serial concatenation,” in *Proc. Intl. Conf. Commun.*, Jun. 1999, pp. 1638-1642.
- [4] J. Chen, A. Dholakia, E. Eleftheriou, M. P. C. Fossorier, and X. Hu, “Reduced-complexity decoding of LDPC codes,” *IEEE Trans. Commun.*, vol. 53, pp. 1288-1299, Aug. 2005.
- [5] S. Talakoub, L. Sabeti, B. Shahrava, and M. Ahmadi, “An improved Max-log-map algorithm for turbo decoding and turbo equalization,” *IEEE Trans. Instrument and Measurement*, vol. 56, pp. 1058-1063, Jun. 2007.
- [6] M. Yazdani, S. Hemati, and A. H. Banihashemi, “Improved belief propagation on graphs with cycles,” *IEEE Commun. Lett.*, vol. 8, pp. 57-59, Jan. 2004.

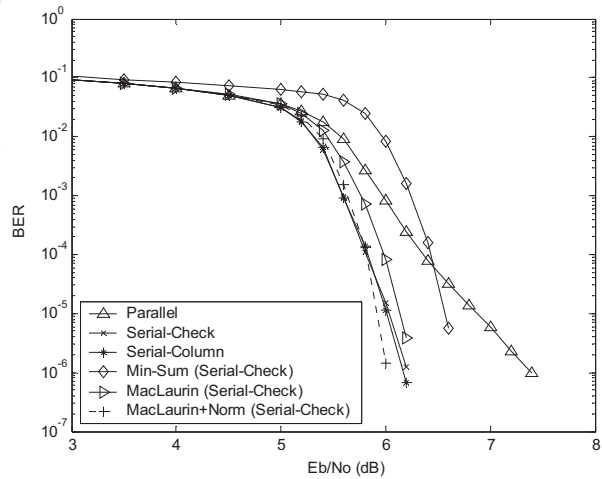


Fig. 3. BER performance of turbo equalization with various M-PC-SPC decoding algorithms over ideal MEEPR4 channels.

RMTR Constrained Parity-Check Codes for High-Density Blue Laser Disk Systems

Kui Cai¹, Kees A. Schouhamer Immink², Song Hua Zhang¹, Zhiliang Qin¹, and Xiao Xin Zou¹

¹Data Storage Institute, DSI Building, 5 Engineering Drive 1, Singapore 117608

²Turing Machines Inc., The Netherlands

¹E-mail: Cai_Kui@dsi.a-star.edu.sg

1. Introduction

Constrained codes, also known as modulation codes, have been widely applied in data storage systems [1]. In blue laser disk systems, in addition to the conventional minimum runlength constraint d and maximum runlength constraint k , a repeated minimum transition runlength (RMTR) constraint t has been adopted [2,3]. In particular, the t constraint stipulates the maximum number of consecutive minimum distance transitions (*i.e.* runs of 2T patterns in non-return-to-zero (NRZ) notation, and ‘1010’, ‘1010 10’, ‘10101010’, ‘101010101’ and so on patterns in non-return-to-zero-inverse (NRZI) format) in the channel bit stream. For example, the standard 17PP code [2] used for blu-ray disk (BD) is with a $t=6$ constraint, and the eight-two-twelve-modulation (ETM) code [3] proposed for high-definition digital versatile disk (HD-DVD) is with a $t=5$ constraint. The main reason for imposing the RMTR constraint lies in the aspect that for $d=1$ constrained blue laser disk systems, the most dominant error events at the output of the channel detector are caused by the consecutive 2T patterns. The RMTR constraint can eliminate the input data patterns that support some of these dominant error events, and therefore achieve a better performance [2,3, 4]. In addition, it has been found that the RMTR constraint can help to increase system tolerances, especially against tangential tilt [2,3,4].

In recent years, the parity-check (PC) codes and post-Viterbi error correction processing based detection approaches have shown high potential for high-density optical recording systems [5]. As illustrated in Fig. 1, the constrained PC code can detect dominant short error events at the output of the channel detector using only a few parity bits, and thereby significantly reduce the correction capacity loss of the error correction code (ECC). In the PC-code-based receiver, the task of locating the exact positions of the errors is done by a post-processor, which contains a bank of filters that are matched to the dominant error events of the system. Since RMTR codes can eliminate some of these dominant error events, the number of matched filters used for post-processing is reduced. Furthermore, the RMTR constraint can also effectively eliminate the non-dominant error events of the system. It has been found that most of these non-dominant error events consist of long consecutive 2T patterns [5]. To detect these events, more PC bits are required. They are also difficult to correct, since mis-correction of these long events will introduce many more errors. The RMTR constraint can prohibit the underlying data patterns that support these events and improve the performance of the PC-code-based receivers. The design of efficient constrained PC codes is key to the development of the PC-code-based receivers. Currently, no report has been found on the design of combined RMTR and PC codes.

In this paper, we first propose a new rate 8/12 RMTR code with $t=3$ constraint, which is found to be the minimum RMTR value associated with the rate 2/3 $d=1$ codes. We further propose a systematic method to efficiently combined the RMTR code with the PC codes for PC-code-based receivers.

2. A new RMTR code

The code design starts from computing the Shannon Capacity of the desired code. The Shannon Capacity is the theoretical limit of the code rate for given code constraints [1]. Based on the state transition diagram of a constrained system, the capacity can be computed as $C = \log_2 \zeta_{\max}$, where ζ_{\max} is the largest eigenvalue of the connection matrix of the state transition diagram. For $d=1$ codes with the RMTR constraint, we obtain

$$C(d=1, t=3) = 0.6793, \quad C(d=1, t=2) = 0.6509. \quad (1)$$

We thereby conclude that it might be possible to design a rate 8/12 $d=1$ code with the $t=3$ constraint. Furthermore, $t=3$ is the minimum RMTR constraint for $d=1$ codes whose code rates are comparable to that of the 17PP code and ETM code.

We propose an efficient finite state encoding method for designing the new code. As shown in Fig. 2, the main steps are as follows.

(1) Enumerate all valid $d=1$ constrained codewords of length $n=12$. Remove the codewords that contain more than 3 consecutive 2T patterns (*i.e.*, remove ‘...10101010...’ patterns in NRZI notation). Note that at this step, the k constraint is temporarily relaxed.

(2) Distribute the codewords obtained from Step (1) into a code table, according to the following principles. A codeword is a binary string of length n that satisfies the $d=1$ and $t=3$ constraints. The set of codewords, X , is divided into four subsets X_{00} , X_{01} , X_{10} and X_{11} . Codewords in X_{00} start and end with a ‘0’, codewords in X_{01} start with a ‘0’ and end with a ‘1’, *etc.* The encoder has s states, which are divided into two state subsets of a first and second type. The encoder has s_1

states of the first type and $s_2=s-s_1$ states of the second type. All codewords in states of the first type must start with a ‘0’, while codewords in states of the second type start with either a ‘0’ or a ‘1’. Codewords that end with a ‘0’, *i.e.*, those in subsets X_{00} and X_{10} , may enter any of the s encoder states. Codewords that end with a ‘1’ may enter the s_1 states only. Furthermore, the sets of codewords that belong to a given state must be disjoint. During decoding, by observing both the current and the next codewords, the decoder can uniquely decide the transmitted user word. That is, the decoder is a sliding block decoder with the least decoding window of length 2.

(3) Examine the code table obtained from Step (2), and remove codewords ending or starting with long runs of ‘10’s, which cause violations of the $t=3$ constraint during concatenation of the codewords.

(4) Tighten the k constraint of the designed code by optimizing the code table obtained from Step (3) by deleting codewords that start or end with long runs of ‘0’s, or by increasing the number of encoder states.

Following Steps (1) to (4), a new rate 8/12 RMTR code with 5 encoder states ($s=5$, $s_1=3$, and $s_2=2$) is designed, which satisfies the $d=1$, $t=3$, and $k=16$ constraints. By applying guided scrambling (GS) [1] to the new code, we can further reduce the k constraint (*e.g.* to $k=11$) and obtain satisfactory dc-free constraint.

3. A new RMTR constrained parity-check (PC) code

To further impose the PC constraints on the designed RMTR code for the PC-code-based receivers, we propose a systematic method to efficiently combine the RMTR code with the PC codes. The obtained codes are referred to as the RMTR constrained PC codes. As shown in Fig. 3, the proposed constrained PC codes include two component codes: the normal constrained code and the parity-related constrained code. The leading portion of the constrained PC code is a concatenation of the normal constrained codes, while at the end a parity-related constrained code is appended, to realize a specific PC constraint over the entire codeword.

In this work, we use the rate 8/12 RMTR code as the normal constrained code. In the design of the parity-related constrained code, we propose a novel approach to design sets of codewords with distinct parity bits, based on the same finite state encoding method of the normal constrained code. This enables the two component codes to be connected in any order without violating the modulation constraints. Furthermore, since the parity-related constrained code is also protected by parity-checks, error propagation is avoided. The design criteria are as follows. To design a parity-related constrained code with m user data bits and p parity bits, the number of codewords leaving a state set should be at least 2^{m+p} times the number of states within the state set. For each set of the codewords with the same parity bits, the number of codewords leaving a state set should be at least 2^m times the number of states within the state set. Following these criteria, a new 5-state ($s=5$, $s_1=3$, and $s_2=2$) rate 8/18 parity-related constrained code is designed, which satisfies the $d=1$, $t=3$, and $k=16$ constraints. It corresponds to a 4-bit PC code defined by the generator polynomial $g(x) = 1 + x + x^4$. With respect to the rate 2/3 $d=1$ codes, the rate 8/18 code achieves 1.5 channel bits per parity check, which is the minimum number of channel bits required per PC associated with the rate 2/3 $d=1$ codes. Concatenating the sequence of the rate 8/12 codewords with the rate 8/18 codeword, we obtain an RMTR constrained 4-bit PC code. Note that the size of input symbols for both the rate 8/12 code and the rate 8/18 code is matched with the byte-oriented ECC. This reduces the error propagation of the constrained decoder. During decoding, observing two consecutive codewords is sufficient to decode the transmitted user word. Finally, we remark that various RMTR constrained PC codes corresponding to different PC codes, such as the low-density parity-check (LDPC) code, can be designed in a similar fashion.

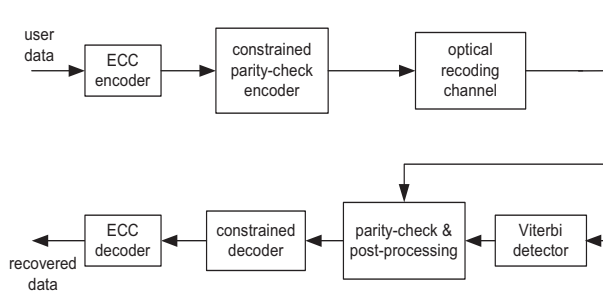


Fig. 1. Block diagram of a PC-coded optical recording system.

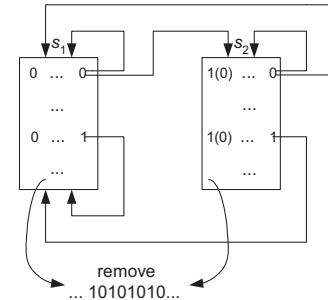


Fig. 2. Code design method for $d=1$ and $t=3$ constrained code.

4. Simulation results and discussion

The performance of the newly designed codes is evaluated using BD systems. Similar performance can be expected for the super-resolution near-field structure (super-RENS) disk systems. In the simulations, we assume that the optical read-out is linear and use the Braat-Hopkins model [5] to describe the channel. In the model, the normalized cut-off frequency $\Omega_u = f_c T_u$, where f_c is the optical cut-off frequency and T_u is the duration of one user bit, is a measure of the user

density. For a system using a laser diode with wavelength λ and a lens with numerical aperture NA , we get $\Omega_u = 2 NA L_u / \lambda$, where L_u is the spatial length of one user bit. For BD systems with $\lambda = 405 \text{ nm}$, $NA = 0.85$, the 17PP code, and at a high capacity of 30GB, we get $L_u = 93 \text{ nm}$ and $\Omega_u \approx 0.39$. The channel noise before equalization is assumed to be Gaussian and white. In the performance evaluations, a Viterbi detector that is matched to a 7-tap optimized channel partial response (PR) target is used, with the RMTR constraint being taken into consideration. The dominant error events turn out to be $\pm\{2\}$, $\pm\{2,0,-2\}$, $\pm\{2,0,-2,0,2\}$, $\pm\{2,0,-2,0,2,0,-2\}$, and $\pm\{2,0,-2,0,2,0,-2,0,2\}$, and the non-dominant error events are $\pm\{2,0,-2,0,2,0,-2,0,2,0,-2\}$, $\pm\{2,0,-2,0,2,0,-2,0,2,0,-2,0,2\}$, $\pm\{2,0,-2,0,2,0,-2,0,2,0,-2,0,2,0,-2\}$, etc [5]. It can be verified that all the dominant error events can be detected by the proposed RMTR constrained PC code. To correct these error events, 5 matched-filters are needed in the post-processor for the 17PP code. However, with the new RMTR constrained PC code, only 3 filters that match to the events $\pm\{2\}$, $\pm\{2,0,-2\}$, $\pm\{2,0,-2,0,2\}$ are needed. The codeword length of the RMTR constrained PC code is chosen to be $N=402$, since it achieves a trade-off between code rate loss due to PC and error correction power of the post-processor. The overall code rate is thus $R=264/402=0.6567$. Note that the capacity of the constrained PC code is given by $C_{pc} = C(d=1, t=3) - p/N$. Therefore, the rate of the new code is only 1.88 % below the capacity.

Fig. 4 illustrates the bit error rate (BER) comparison between the 17PP code and the newly designed codes. Comparison between Curves 1 and 2 shows that at $\text{BER} = 10^{-5}$, the rate 8/12 RMTR code performs around 0.25 dB better than the 17 PP code, since the $t=3$ constraint can eliminate the dominant error events $\pm\{2,0,-2,0,2,0,-2\}$ and $\pm\{2,0,-2,0,2,0,-2,0,2\}$. Comparison between Curves 3 and 4 shows that the RMTR constrained PC code gains 0.6 dB over 17PP code with ideal PC (i.e. no explicit constrained PC code, and the PC is done in a data-aided mode). This is due to the reason that the RMTR constraint can effectively eliminate most of the non-dominant error events. Overall, the new RMTR constrained PC code achieves a performance gain of 1.1 dB at high recording density.

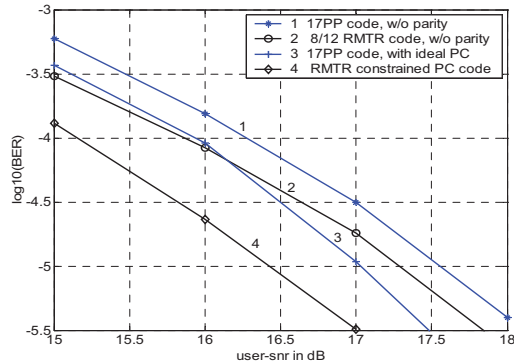
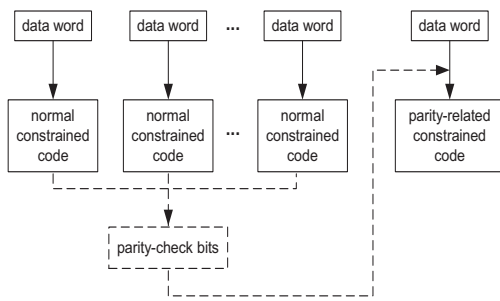


Fig. 3. Block diagram for encoding a RMTR constrained PC code. Fig. 4. BER comparison between the 17PP code and the new codes.

5. Conclusions

In this paper, a new RMTR constrained code has been first proposed for high-density blue laser disk systems. Compared with the codes used in standard systems, it imposes the minimum achievable RMTR constraint on the channel bit stream with the least decoding window length, without introducing additional code rate loss. A systematic method has been further proposed, which can efficiently combine the RMTR code with the PC codes. Simulation results show that the new RMTR constrained PC code achieves a performance gain of 1.1 dB over the 17 PP code, at $\text{BER} = 10^{-5}$ and high density.

References

[1] K.A.S. Immink, *Codes for Mass Data Storage Systems*, Shannon Foundation Publishers, The Netherlands, 1999.
 [2] T. Narahara et al., "Optical disc system for digital video recording," *JJAP*, pt. 1, vol. 39, No. 2B, pp. 912-919, 2000.
 [3] K. Kayanuma et al., "Eight to twelve modulation code for high density optical disk," in ISOM 2003, Technical Digest, pp.160-161.
 [4] W. Coene et al., "A new d=1, k=10 soft-decodable RLL code with r=2 MTR-constraint and a 2-to-3 PCWA mapping for dc-control," in ODS 2006, Technical Digest, pp.168-170.
 [5] K. Cai et al., "Constrained parity-check code and post-processor for advanced blue laser disc systems," *JJAP*, vol. 45, No.2B, pp. 1071-1078, 2006.

Parallel Multi-track Viterbi Detector for Two-Dimensional Optical Storage

Tim Yao*, Lee Yang^a, Qinyang Wu^a
 Dept. of ECE, Univ. of Texas El Paso, El Paso, TX, USA 79968;
^aSMIC, 18 Zhang Jiang Rd., Shanghai, PRC 201203

ABSTRACT

Two-dimensional optical system has been proposed to increase the capacity of traditional 1-dimensional system in recent years. However, the 2D optical systems also increase the complexity of signal processing including the channel modeling and bit detection. In this paper, we presented a parallel multi-track Viterbi detection algorithm to reduce the computation complexity and enhance the detection performance by proposing a 2D array of laser spot configuration.

Keywords: 2D Viterbi algorithm, multi-track recording, hexagonal lattice, 2D laser spots.

1. INTRODUCTION

Recently, many researches on the 2-dimensional (2D) optical disc storage systems were proposed to increase the capacity. [5][6] The 2D storage system can record higher track density over the conventional 1D optical system by reducing the track pitch [4], where adjacent tracks are group into broad spiral bit rows. According to the some research results, the 2D optical disc could have 2 times of capacity and 40% less of energy per bit comparing to the Blue-ray Disc (BD) [1]. By using multiple laser spots in array, the reading speed can increase several times. However the improvement also introduced news challenges to the signal processing, mainly due to the computation complexity jumping from 1D to 2D. From this perspective, the major characteristic of 2D format optical system include the resulting 2D inter-symbol interference (ISI), inter-track interference, and bit detection. To attack the problems resulted from the 2D optical format, the optimum detection algorithm requires a dramatic changes from the conventional 1D maximum likelihood detection implemented by Viterbi algorithm (VA). The research in the area of 2D or multi-D Viterbi detection for application of 2D optical storage system can be found in some recent publication [1],[2],[5]. Actually, 2D Viterbi algorithm has been applied to the 2-D signal processing such as the image years ago [3], although the problem does not involve the ISI and equalization, and any channel model. In the application of 2D VA on bit detection, two outstanding problems are the large number of states, and detection direction (axis) for different laser reader configuration. The number of trellis states in a 2-D equalizer is dependent on the interfering symbols surrounding on the target bit on the track, which is six and eight in hexagonal shape and rectangular shape respectively. Because the number of state is large, the research in [5] proposed an algorithm with reduced number of state while optimal performance is compromised. The moving direction of the Viterbi detector also plays an important role in the performance of the system. For a square lattice format optical disc, the detection has only 2 directions; while for hexagonal lattice, several moving direction can be exploited. This problem will be revisited in the next section. In this paper, several configurations of laser spot on the 2D disc surface and their effects on the VA processing speed and detection performance are investigated. We also propose the 2D array laser reader for the 2D optical storage system and present the parallel Viterbi bit detection performance based on the proposed configuration. The paper is organized as the following. The proposed algorithm and configuration are described in the next section. The simulation result is demonstrated in the third section, and the conclusion is made in the last section.

2. PARALLEL VITERBI DETECTOR

In a 2-D optical storage system, data are recorded in a meta-spiral ring, where each ring consist of several bit rows. The bit rows are arranged in hexagonal lattice and rectangular lattice (Figure 1), where the former has 15% of capacity advantage over the later one. This format is suitable for parallel read-out by a one-dimensional array of laser detector parallel to the Y direction. However this format put a few challenges to the bit detection process. The first is the increasing of inter-symbol interference (ISI), due to the optical interference coming from the increasing neighbors. In 1-dimensional format, the interference exists only in the X direction because the guard band separates each single track.

Research of the channel model of 2D optical system has been conducted in [4]. In this paper, we adopted the channel model used in [4], described as the following,

$$\mathbf{z}(n) = \sum_{k=0}^{N_h-1} \mathbf{H}_{k,n} \mathbf{a}(n-k) + \boldsymbol{\theta}(n) \quad (1)$$

where \mathbf{z} is the readback signal from the k -th track, \mathbf{a} is the bit sequence, $\boldsymbol{\theta}$ is the noise pick-up and laser spot, and \mathbf{H} is the 2D channel response. With the given channel, we propose a parallel Viterbi detector for the 2D systems. The parameter N_h is the number of bits that contribute to the signal level of the processing bit, surrounding bits and the target bit, which is 7 and 9 in hexagonal and square lattice. Since the hexagonal lattice has obvious advantages over the square lattice, we only focus the hexagonal lattice format in this paper.

The channel response is used for estimation of the current bit given the information of the surrounding bits. Since these bits are unknown on the trellis path, every possible combination, called *states* in Viterbi algorithm, must be tested. Therefore, the Viterbi detector algorithm requires total of 2^{N_h} states in the trellis tree. In conventional 1D optical storage system, the number of bits contributed to each bit is small, due to the single track nature, and thus the number of state of the trellis tree is also small. When the survival path move from the current state to next state, there is only one unknown input bit is, so the outgoing from each state is 2 (either the input 1 or 0). In 2D optical storage system, the picture of the Viterbi processing has totally changed. The performance will depend on the laser read-out devices configuration.

Case 1: Single Laser Spot

If only 1 laser spot is devised, then the processing sequence is either Y direction (Figure 2) or X direction (Figure 3). On the trellis diagram, each state has 2^3 or 2^2 outgoing branches, because each moving of the current bit to the next bit, three or two new input bits are introduced. The processing complexity therefore increases by large extend.

Case 2: 1D Laser Spot Array

To speed the Viterbi detection process, more laser spots are recommended for multi-track format in the 2D optical systems [1,2,3]. An array of laser spots is formed as shown in the Figure 4 to perform the multi-track and multi-sample reading. On the trellis diagram, each state will have 2^2 outgoing braches. Because the each read-out sample are correlated to the adjacent read-out sample, the number of braches can be reduced.

Case 3: 2D Laser Spot Array

Instead of use the 1D array laser spots, we proposed a 2D laser spots configuration as shown in Figure 5. This structure reduces the number of braches for some states and thus reduces the complexity of the algorithm. Suppose the sampled received at the k -th epoch is r_k and the corresponding data on the branch is $\alpha(\mu_k \rightarrow \mu_{k+1})$, which is derived by the equation (1), the branch metric is computed as

$$\lambda(\mu_k \rightarrow \mu_{k+1} | \mathbf{a}) = |r_k - \alpha(\mu_k \rightarrow \mu_{k+1}, \mathbf{a})|^2 \quad (2)$$

The Viterbi algorithm is more complicated then Case 1 and Case 2, however, it takes the advantage of parallel processing and better performance.

3. SIMULATION RESULT AND CONCLUSION

In this section, simulation of the 2D Viterbi detection algorithm is presented. We compare the performance for the Case 2 and Case 3, where the later configuration shows better performance than the former one (Figure 6). The algorithm in our simulation system has not yet been optimized yet, so the computing speed is slow. However, as the algorithm being optimized in the UTEP Lab, we believe that proposed configuration have practical application. Besides, this concept can be extended to a 3-dimensional Viterbi algorithm for multi-layers topical storage systems.

REFERENCES

- [1] Hekstra, A.; Coene, W.; Immink, A.; "Refinement of Multi-Track Viterbi Bit-Detection," IEEE Transactions on Magnetics, Page(s):3333-3339, July 2007.

- [2] Moinian, A.; Fagoonee, L.; Coene, W.; Honary, B.; "Sequence Detection Based on a Variable State Trellis for Multidimensional ISI Channels" IEEE Transactions on Magnetics, Page(s):580-587, Feb. 2007.
- [3] Miller, C.; Hunt, B.R.; Neifeld, M.A.; Marcellin, M.W.; "Binary image reconstruction via 2-D Viterbi search", International Conference on Image Processing, Page(s):181-184, 1997.
- [4] Li Huang; Mathew, G.; Tow Chong Chong; Channel Modeling and Target Design for Two-Dimensional Optical Storage Systems, IEEE Transactions on Magnetics, Page(s):2414- 2424, Aug. 2005.
- [5] Tosi, S.; Conway, T.; "Detector target response optimization for Multi-track digital data storage," IEEE Transactions on Magnetics, Page(s):1926-1928, July 2006.
- [6] W. Coene, "Two dimensional optical storage," in Proc. Int. Conf. Optical Data Storage (ODS), Vancouver, BC, Canada, May 2003, pp. 90–92.

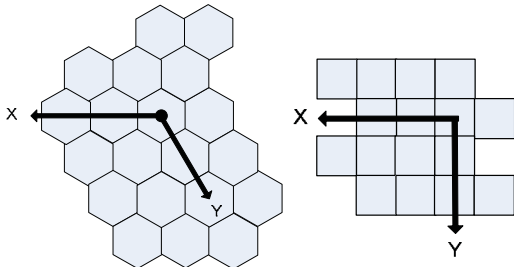


Figure 1. Hexagonal and square lattice on the 2D optical disc surface.

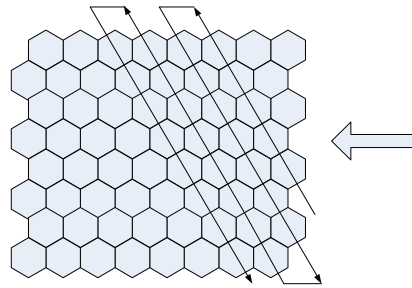


Figure 2. The read-out direction in Y axis for single laser spot.

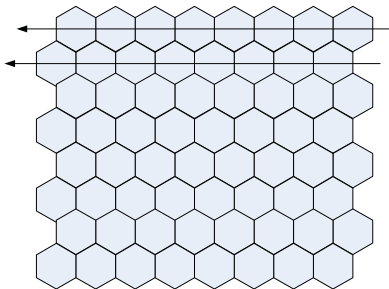


Figure 3. The read-out direction in X axis for single laser spot.

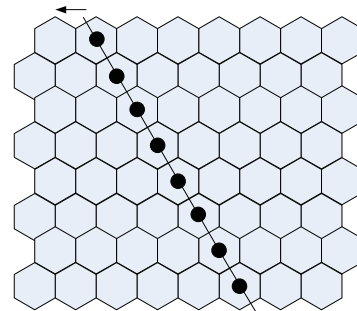


Figure 4. Configuration of 1D array of laser spot for 2D optical storage systems.

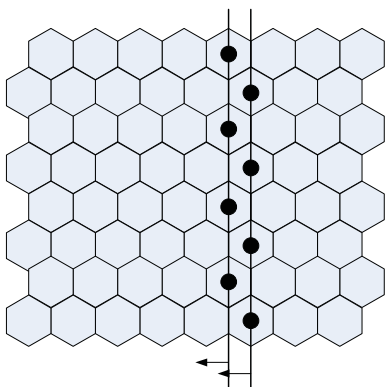


Figure 5. Proposed configuration of 2D array of laser spot for 2D optical storage systems.

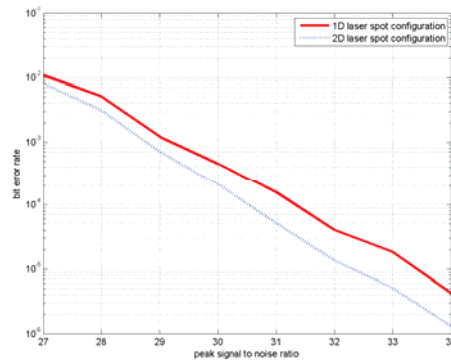


Figure 6. Viterbi detector Simulation result for 1D and 2D laser spot configurations.

Super-Resolution Near-Field Disk with Phase-Change Sn-doped GST mask layer

M.L. Lee*, K.T. Yong², C.L. Gan², S.M. Daud, L. H. Ting and L.P. Shi

¹Data Storage Institute, Agency for Science, Technology and Research (A*STAR), DSI Building, 5 Engineering Drive 1, Singapore 117608

²Nanyang Technological University, School of Materials Science and Engineering, Singapore 639798

E-mail address: Irene_LEE@dsi.a-star.edu.sg

Keywords: Super-Resolution, Near-Field Recording, Testing and Characterization, Media

Abstract: A new mask layer of $\text{Sn}_{7.0}\text{Ge}_{20.6}\text{Sb}_{20.7}\text{Te}_{51.7}$ was developed and used on Super-resolution near-field phase change optical disks. The thermal and optical properties of the mask layer were investigated. The recording performance of the new structure is discussed.

1. Introduction

One application of ultra-fast speed doped phase change material is in the use as a mask layer in rewritable aperture-type super-RENS disk. Mask layer as proposed by Tominaga et al. is incorporated above the recording layer to serve as a dynamic aperture just like a near-field probe to ‘sharpen’ the laser spot to enable mark sizes much smaller than the diffraction limit to be written [1-4]. Due to the nature of the diffusion of heat, the optical response of super-RENS optical disk is strongly dependent on the material properties of the masking layer. The limitation of aperture-type super-RENS is the lack of suitable mask material. In this paper, we demonstrate the performance of a newly developed $\text{Sn}_{7.0}\text{Ge}_{20.6}\text{Sb}_{20.7}\text{Te}_{51.7}$ as a mask layer in the super-RENS Blu ray structure.

2. Experimental Details

$\text{Sn}_{7.0}\text{Ge}_{20.6}\text{Sb}_{20.7}\text{Te}_{51.7}$ films were deposited by dc sputtering on a Si wafer, glass or PC (polycarbonate) substrates. $\text{Sb}_{70}\text{Te}_{30}$ films were also prepared for comparison studies. 50 nm thick films on glass substrate were annealed under Ar atmosphere at 220 °C for 15 mins. The structures of the films after annealing were characterized using X-ray diffraction (XRD, Philips X’pert MPD system). Differential scanning calorimetry (DSC) was employed to measure the crystallization and melting temperatures of the amorphous film stripped from the substrate. An in-house phase change temperature tester was used for isothermal reflectivity-time measurements. A blue laser static tester with 405 nm laser beam and numerical aperture (NA) of 0.6 was used to measure the crystallization speed of as-deposited films with dielectric protective layers. The recording and reading performances of Super-RENS disk with $\text{Sn}_{7.0}\text{Ge}_{20.6}\text{Sb}_{20.7}\text{Te}_{51.7}$ as the mask layer and $\text{Ge}_2\text{Sb}_2\text{Te}_5$ as the recording layer were measured using a Pulstec tester (DDU-100) of 405 nm laser beam and a numerical aperture of 0.85

3. Results and Discussion

Thermal property of $\text{Sn}_{7.0}\text{Ge}_{20.6}\text{Sb}_{20.7}\text{Te}_{51.7}$ phase change material was first studied by Dynamic Scanning Calorimeter (DSC). Thermal property of $\text{Ge}_2\text{Sb}_2\text{Te}_5$ material was also measured for comparison study. Figure 1 shows the crystallization (T_x) and melting (T_m) temperatures of both materials measured at a heating rate of $10\text{ }^\circ\text{C}/\text{min}$. The crystallization temperature of $\text{Sn}_{7.0}\text{Ge}_{20.6}\text{Sb}_{20.7}\text{Te}_{51.7}$ phase change material is close to that of $\text{Ge}_2\text{Sb}_2\text{Te}_5$ at $153\text{ }^\circ\text{C}$ while its melting temperature of $536\text{ }^\circ\text{C}$ is much lower than that of $\text{Ge}_2\text{Sb}_2\text{Te}_5$. Crystallization and melting temperatures of $\text{Ge}_2\text{Sb}_2\text{Te}_5$ were measured at $151.09\text{ }^\circ\text{C}$ and $574.77\text{ }^\circ\text{C}$, respectively. Kissinger's equation was used to calculate the activation energy of the films. Figure 2 shows the Kissinger plot for each single layer specimen. The activation energy for crystallization of $\text{Ge}_2\text{Sb}_2\text{Te}_5$ was estimated at 2.25 eV . $\text{Sn}_{7.0}\text{Ge}_{20.6}\text{Sb}_{20.7}\text{Te}_{51.7}$ phase change material has slightly higher activation energy of 2.54 eV . The higher crystallization temperature and activation energy of $\text{Sn}_{7.0}\text{Ge}_{20.6}\text{Sb}_{20.7}\text{Te}_{51.7}$ indicates that it has higher thermal stability compared to $\text{Ge}_2\text{Sb}_2\text{Te}_5$.

XRD pattern of $\text{Sn}_{7.0}\text{Ge}_{20.6}\text{Sb}_{20.7}\text{Te}_{51.7}$ films synthesized at $220\text{ }^\circ\text{C}$ showed diffraction peaks of (111), (200) and (222). These peaks correspond to rocksalt structure with a lattice parameter of 0.6057 nm , which is close to that of $\text{Ge}_2\text{Sb}_2\text{Te}_5$.

Isothermal crystallization process was carried out to understand the effect of Sn doping on the crystallization mechanism of $\text{Ge}_2\text{Sb}_2\text{Te}_5$. Figure 3 shows the reflectivity as a function of time for the as-deposited $\text{Ge}_2\text{Sb}_2\text{Te}_5$ and $\text{Sn}_{7.0}\text{Ge}_{20.6}\text{Sb}_{20.7}\text{Te}_{51.7}$ films kept at temperatures of $(T_x-10)\text{ }^\circ\text{C}$. The phase transformation for both films can be characterized by an S-shape curve. The crystallization of $\text{Ge}_2\text{Sb}_2\text{Te}_5$ proceeds by a low reflectivity amorphous regime (nucleation and structural relaxation regime), which lasted for about 520 s . This is followed by a relatively fast grain growth and completion of the crystallization process in about 120 s . The results show that crystallization mechanism of $\text{Ge}_2\text{Sb}_2\text{Te}_5$ is nucleation dominated as reported by H. J. Borg et al. [5]. For $\text{Sn}_{7.0}\text{Ge}_{20.6}\text{Sb}_{20.7}\text{Te}_{51.7}$ film, the nucleation regime was reduced to 400 s and crystallization process completed in 444 s . In comparison, crystallization of $\text{Sn}_{7.0}\text{Ge}_{20.6}\text{Sb}_{20.7}\text{Te}_{51.7}$ showed a more growth-dominated behavior. Reasons for the shorter incubation regime observed for crystallization of $\text{Sn}_{7.0}\text{Ge}_{20.6}\text{Sb}_{20.7}\text{Te}_{51.7}$ could be attributed to the lower activation energy for nucleation because of the weaker binding energy of Sn [6].

Laser-induced crystallization behavior of as-deposited $\text{Sn}_{7.0}\text{Ge}_{20.6}\text{Sb}_{20.7}\text{Te}_{51.7}$ films with dielectric protective layers were analyzed to study their crystallization speed using 405 nm laser beam with a numerical aperture of 0.6 . Figure 4 shows the change in reflectivity with time of $\text{Sn}_{7.0}\text{Ge}_{20.6}\text{Sb}_{20.7}\text{Te}_{51.7}$ film. Nucleation of the as-deposited film started after a pulse duration of 20 ns and crystal growth was completed in 60 ns .

Dynamic recording performance of the super-RENS blu ray disk with $\text{Ge}_2\text{Sb}_2\text{Te}_5$ as the recording layer and $\text{Sn}_{7.0}\text{Ge}_{20.6}\text{Sb}_{20.7}\text{Te}_{51.7}$ as the mask layer was evaluated. The reflectivity values of the as-deposited amorphous disk after bonding (R_a) and of the initialized crystalline (R_c) states were determined at 9% and 14% , respectively. This gave rise to an optical contrast of 36% , which is sufficient for blue laser recording. Mark trains with sizes of 80 and 50 nm were recorded at rotation speeds of 5.28 and 3.28 m/s respectively, on the super-RENS disk. Maximum carrier-to-noise ratio (CNR) values obtained of mark trains with sizes of 80 and 50 nm were 34.6 and 18 dB , respectively as shown in Figure 5. Figure 6 shows the readout stability for 50 and 80 nm mark sizes. Readout stability of more than $1,000$ cycles was obtainable for 50 nm mark sizes and more than $10,000$ cycles for 80 nm mark sizes. The reasons for the improvement in CNR and readout stability will be discussed in the conference.

4. Conclusions

Sn-doping in the form of $\text{Sn}_{7.0}\text{Ge}_{20.6}\text{Sb}_{20.7}\text{Te}_{51.7}$ showed similar crystallization temperature but lower melting temperature than $\text{Ge}_2\text{Sb}_2\text{Te}_5$ phase change material. It also exhibits the same crystallization structure as $\text{Ge}_2\text{Sb}_2\text{Te}_5$. Crystallization of as-deposited $\text{Sn}_{7.0}\text{Ge}_{20.6}\text{Sb}_{20.7}\text{Te}_{51.7}$ can be realized within 60 ns and showed a more growth-dominated behavior. The use of this phase change material as a mask layer in aperture-type Super-RENS had been realized. A CNR of 18 dB with more than 1,000 readout cycles were obtainable for 50 nm mark sizes.

References:

[1] J. Tominaga, T. Nakano, and N. Atoda, Appl. Phys. Lett. 73, 2078 (1998).
 [2] J. Tominaga, H. Fuji, A. Sato, T nakano, T. Fukaya, and N. Atoda, Jpn. J. Appl. Phys., Part 1 38, 4089 (1999).
 [3] T. Fukaya, J. Tominaga, T Nakano and N. Atoda, Appl. Phys. Lett. 75, 3114 (1999).
 [4] J. Kim, I. Hwang, D. Yoon, I. Park, D. Shin, T. Kikukawa, T. Shima and J. Tominaga, Appl. Phys. Lett. 83, 1701 (2003).
 [5] H.J. Borg, P.W.M. Blom, B.A.J. Jacobs, B. Tieke, A.E. Wilson, I.P.D. Ubbens, and G.F. Zhou, Proc. SPIE 3864, 191(1999).
 [6] D.R. Lide, Handbook of chemistry and Physics, 87th ed. (Chemical Rubber, Boca Raton, FL, 2006), pp. 9-52.

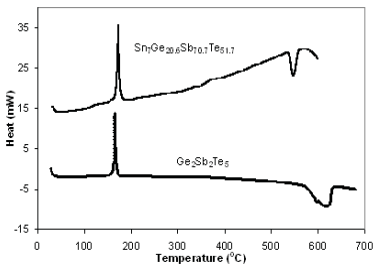


Fig.1. DSC results of $\text{Ge}_2\text{Sb}_2\text{Te}_5$ and $\text{Sn}_7\text{Ge}_{20.6}\text{Sb}_{20.7}\text{Te}_{51.7}$ at a heating rate of $10^\circ\text{C}/\text{min}$.

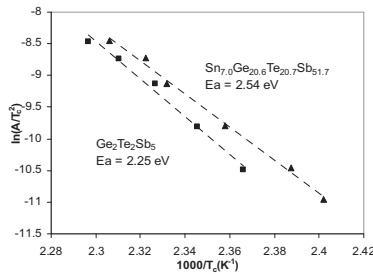


Fig. 2. Kissinger plot for $\text{Ge}_2\text{Sb}_2\text{Te}_5$ and $\text{Sn}_7\text{Ge}_{20.6}\text{Sb}_{20.7}\text{Te}_{51.7}$ films for crystallization.

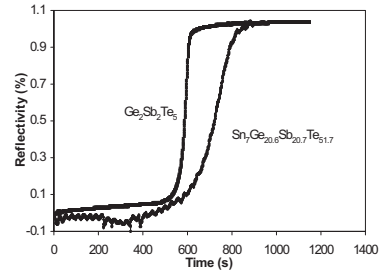


Fig.3. Isothermal reflectivity measurement for $\text{Ge}_2\text{Sb}_2\text{Te}_5$ and $\text{Sn}_7\text{Ge}_{20.6}\text{Sb}_{20.7}\text{Te}_{51.7}$ films.

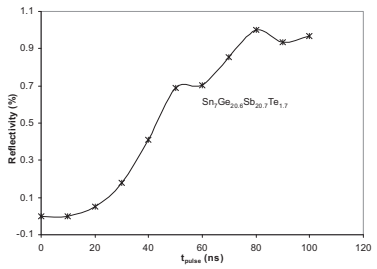


Fig. 4. Laser induced crystallization of $\text{Sn}_7\text{Ge}_{20.6}\text{Sb}_{20.7}\text{Te}_{51.7}$ film with protective dielectric layer.

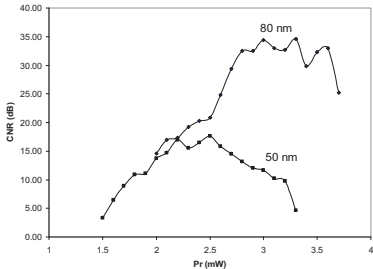


Fig. 5. Maximum carrier-to-noise ratio obtained for different mark trains at varying readout power.

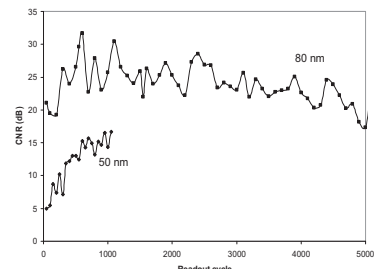


Fig. 6. Readout stability of super-RENS disk with $\text{Sn}_7\text{Ge}_{20.6}\text{Sb}_{20.7}\text{Te}_{51.7}$ used as the mask layer and $\text{Ge}_2\text{Sb}_2\text{Te}_5$ as the recording layer.

Nonlinear Modeling of Super-Resolution Near Field Structure

Manjung Seo^a, Sungbin Im^{*a} and Jaejin Lee^a

^aSchool of Electronic Engineering, Soongsil University,
511 Sangdo-dong, Dongjak-gu, Seoul 156-743, Korea

ABSTRACT

Reliable channel modeling becomes important measure in performance evaluation on various data detection algorithms. For this reason, correct and accurate modeling is required. This paper presents a nonlinear modeling of Super-RENS (Super-Resolution Near Field Structure) read-out signal using neural networks. The experiment results indicate that the NARX (Nonlinear AutoRegressive eXogenous) model considered in this study is superior to the NLMS (Normalized Least Mean Square) FIR (Finite Impulse Response) adaptive filter, which is one of linear modeling approaches. We verified the possibility that neural networks can be utilized for nonlinear modeling of Super-RENS systems. Furthermore, nonlinear equalizers can be developed based on the information obtained from this nonlinear modeling.

Keywords: Super-RENS, neural networks, nonlinearity, NARX, MSE

1. INTRODUCTION

Recently, various recording technologies are investigated for optical data storage. Super-RENS (Super-Resolution Near Field Structure) [1, 2] technique, which is capable of compatibility with other systems, is one of the next generation optical data storage techniques. In this paper, we apply the neural networks for nonlinear modeling of Super-RENS disc system. The model structure considered in this paper is the NARX (Nonlinear AutoRegressive eXogenous) [3] model, whose structure is depicted in Figure 1. The NARX model is a recurrent dynamic network, where feedback connections can enclose several layers of the network. Since it is based on the linear ARX model, which is commonly used in time series modeling, it has many desirable features. As shown in the figure, the NARX model consists of two layers; a feed-forward network with a tapped delay line at the input and an output layer. The function of Layer 1, f^1 , employs the tangent sigmoid function while that of Layer 2, f^2 , is the purely linear function. The various training algorithms in ref. [4-9] are applied. The physical conditions of obtaining the Super-RENS signal samples used in the experiments are as follows. The minimum mark size is 150 nm, the linear velocity of the disk is 4.92 m/s, the wavelength is 405 nm, and the numerical aperture (NA) is 0.85. More details of the disk properties can be found in ref. [10].

2. EXPERIMENTS AND RESULTS

Figure 2 shows the block diagram of the experiment setup employed in this work. Before training, we pre-process the RF signal in order to make more efficient modeling. In the pre-processing block, the target signal, that is, RF signal, is filtered to remove low frequency noise using a high-pass filter of stop band from D.C. to 2.5 MHz, and scaled into [-1, 1] by transforming the minimum and maximum values to -1 and +1, respectively. The DC component and the low frequency noise are located outside the information band because the lowest information frequency is 4.125 MHz for 8T signal. Figure 3 shows MSE (Mean Square Error) curves for various training algorithms. As shown in Figure 3, the Levenberg-Marquardt algorithm [4] achieves the minimum MSE. In Table 1, based on this training algorithm, the MSE's of the NARX model are listed depending on the input delay ranges from 3 to 25 with the output delay range from 1 to 2 in Layer 1. Layer 1 consists of 5 neurons while Layer 2 uses one neuron. As observed in Table 1, as the input delay range increases, MSE decreases, but the number of weights increases. Therefore, in this experiment, the input delay range covers from 0 to 10. IW (input weight matrices), LW (layer weight matrices) and b (bias vectors) sizes of the NARX model are summarized in Table 2. Figure 4 shows a part of the estimated and original waveforms of Super-RENS RF signal to demonstrate nonlinear modeling performance of the NARX model. The experiment results reveal that the MSE of NARX output signal with respect to the original RF signal is about 6.5×10^{-3} .

*sbi@ssu.ac.kr; phone +822-820-0906; fax +822-821-7653

For the purpose of comparison, we performed FIR (Finite Impulse Response) linear modeling with NLMS (Normalized Least Mean Square). Figure 5 shows the MSE curve for various step sizes of the NLMS FIR filter, where the number of filter taps is set to 76 and step size varies from 0 to 0.5. The experiment result reveals that the minimum MSE is 1.65×10^{-2} when the step size is 0.09. Figure 6 shows a part of the waveforms of the RF signal and the FIR filter output signal. Experiment results and comparing the waveforms of Figures 4 and 6 demonstrate that the linear modeling based on the FIR filter is not appropriate for modeling the Super-RENS disc system because of its limited properties.

Table 1. Mean square error according to the input delay ranges of the NARX model.

Number of neuron	Input delay ranges									
	0~3	0~4	0~5	0~6	0~7	0~8	0~9	0~10	...	0~25
Neuron : 5	0.0155	0.013	0.01	0.0085	0.008	0.0079	0.0074	0.0065	...	0.0055

Table 2. Sizes of the NARX model's weights and bias.

IW {1, 1}	IW {1, 2}	LW {2, 1}	b {1}	b {2}	Total
5×11	5×2	1×5	5×1	1×1	76

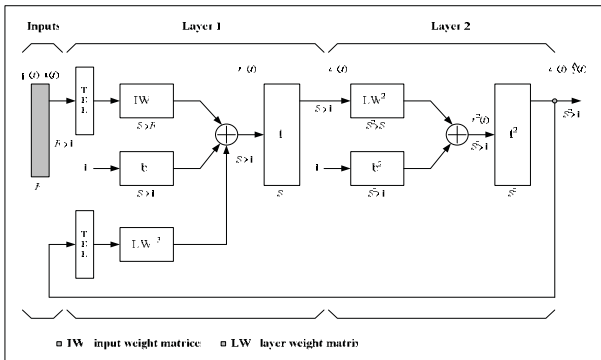


Fig. 1. Structure of the NARX model.

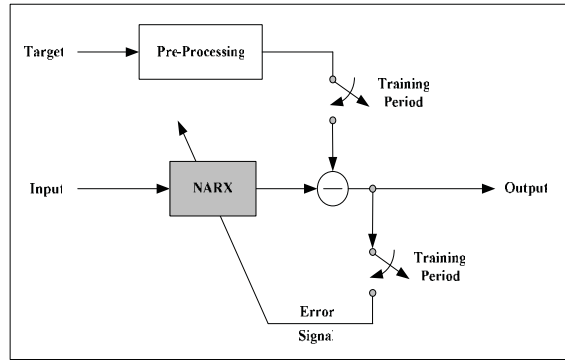


Fig. 2. Block diagram of the experiment setup.

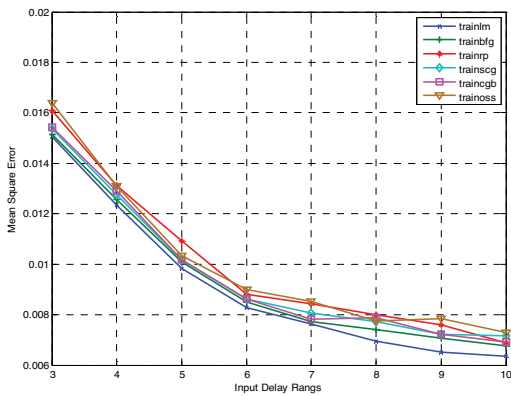


Fig. 3. MSE's vs. input delay ranges for various training algorithms.

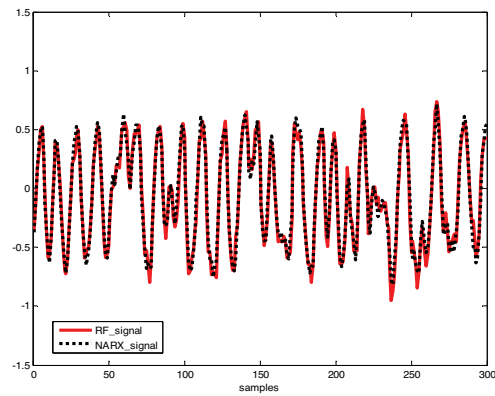


Fig. 4. Comparison of the RF signal and the NARX output signal.

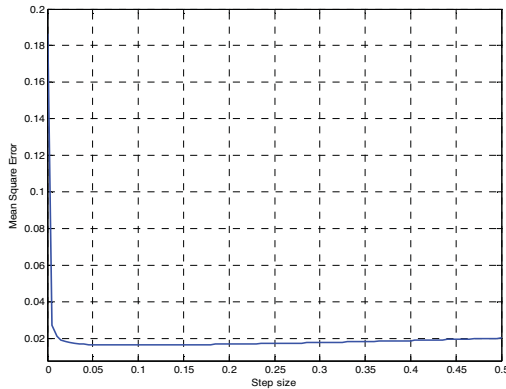


Fig. 5. MSE's for various step sizes of the NLMS FIR filter.

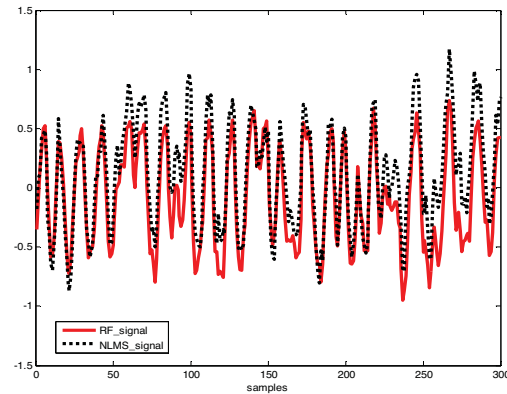


Fig. 6. Comparison of the RF signal and the FIR filter output signal.

3. CONCLUSION

This paper presents the results of applying the neural network to nonlinear modeling of Super-RENS disc system. According to the experiment results, the MSE between the RF signal and the output signal of the NARX model is less than that between the RF signal and the output signal of the NLMS FIR adaptive filter. This implies that the NARX model is more suitable for modeling of Super-RENS systems.

REFERENCES

- [1] J. Tominaga, T. Nakano and N. Atoda, "An approach for recording and readout beyond the diffraction limit with an Sb thin film," *Appl. Phys. Lett.*, 2078-2080 (1998).
- [2] T. Nakano, A. Sato, H. Fuji, J. Tominaga and N. Atoda, "Transmitted signal detection of optical disks with a super resolution near-field structure," *Appl. Phys. Lett.*, 151-153 (1999).
- [3] Feng, J., C.K. Tse, and F.C.M. Lau, "A neural-network-based channel-equalization strategy for chaos-based communication systems," *IEEE Trans. on Circuits and Systems I: Fundamental Theory and Applications*, Vol. 50, No. 7, 954-957 (2003).
- [4] Hagan, M.T., and M.Menhaj, "Training feed-forward networks with the Marquardt algorithm," *IEEE Trans. on Neural Networks*, Vol. 5, No. 6, 989-993 (1999).
- [5] Dennis, J.E., and R.B. Schnabel, *Numerical Methods for Unconstrained Optimization and Nonlinear Equations*, Englewood Cliffs, NJ: Prentice-Hall (1983).
- [6] Riedmiller, M., and H. Braun, "A direct adaptive method for faster backpropagation learning: The RPROP algorithm," *Proceedings of the IEEE International Conference on Neural Networks* (1993).
- [7] Moller, M.F., "A scaled conjugate gradient algorithm for fast supervised learning," *Neural Networks*, Vol. 6, 525-533 (1993).
- [8] Powell, M.J.D., "Restart procedures for the conjugate gradient method," *Mathematical Programming*, Vol. 12, 241-254 (1977).
- [9] Battiti, R., "First and second order methods for learning: Between steepest descent and Newton's method," *Neural Computation*, Vol. 4, No. 2, 141-166 (1992).
- [10] K. Kwak, S. Kim, C. Lee and K. Song, "New materials for super resolution disc," *SPIE Proceedings*, Vol. 6620, ODS2007 TuC5 (2007).

SESSION MC: Special Session: Nano-Photonics

Monarchy Ballroom
3:30 to 6:30 pm

Masud Mansuripur, College of Optical Sciences/The Univ. of Arizona
Kevin R. Curtis, InPhase Technologies Inc.

Recent Progress in Photonic Crystals for Manipulation of Photons

Susumu Noda

Department of Electronic Science and Engineering, Kyoto University,

Kyoto 615-8510, Japan

Email: snoda@kuee.kyoto-u.ac.jp

Photonic crystals, in which the refractive index changes periodically, provide an exciting new tool for the manipulation of photons and have received a keen interest from a variety of fields. In this presentation, I will describe present status of such manipulations of photons by photonic crystals.

First of all, I will describe ultrahigh Q nanocavities, which are very important for various applications including stopping or slowing light, nano-lasers, photonic nano-chips, single-photon emitters, and quantum information processing devices. I will at first describe an important concept [1] to realize ultrahigh Q nanocavities in 2D photonic crystal, where the form of the cavity electric field distribution should vary slowly, ideally as described by a Gaussian function, in order to suppress vertical photon leakage. Tuning of air holes at the cavity edge [1] or the formation of a photonic double-heterostructure [2] have been found to be very effective to satisfy the concept and to realize an ultrahigh- Q nanocavity. The cavity Q factor more than 2 million has been successfully realized [2-4]. Then, I will describe a new concept to control Q -factors dynamically [5]. When the Q factor becomes sufficiently large, next important issue is how to deliberately control storage and release photons from such a high Q nanocavity. When we introduce photons into a nanocavity, the Q factor should be low. Once the photons are introduced into the nanocavity, the Q factor should be increased rapidly, and when we want to release the photons from the nanocavity, the Q factor should be reduced. Thus, the dynamic control of the Q factor is very important. I will present the demonstration of dynamic control of the Q factor, by constructing a system composed of a nanocavity, a waveguide with nonlinear optical response, and a photonic-crystal hetero-interface mirror. The Q factor of the nanocavity is successfully changed from $\sim 3,800$ to $\sim 22,000$ within picoseconds.

Next, I will describe unique photonic crystal lasers, which are based on band-edge effect in photonic crystals. At the band-edge of photonic crystals, the group velocity of light becomes zero, which leads to a formation of two-dimensional broad-area stable single-cavity mode [12, 13]. The output beam can be emitted in the direction normal to the 2D crystal plane, which leads to the surface-emitting operation. I will show the present status of such unique lasers. I will describe that a broad-area single-mode surface-emitting operation has been successfully realized. In addition, various unique beam patterns including tangentially- or radially polarized doughnuts beams can be produced by engineering photonic crystal structures [14]. Finally, I will describe that lasing oscillation at the blue-violet wavelength regions has been successfully achieved [15]. These lasers are very important for various applications including next-generation information storage and micro- to nano-operation in biological and medical fields.

References:

- [1] Y.Akahane, T. Asano, B.S.Song, and S.Noda, *Nature*, 425 (2003) 944.
- [2] B.S.Song, S. Noda, and T. Asano. *Nature Materials*, 4 (2005) 207.
- [3] S.Noda, M.Fujita, and T.Asano, *Nature Photonics*, 1 (2007) 449.
- [4] Y. Takahashi, H.Hagino, Y.Tanaka, B.S.Song, T.Asano, and S.Noda, *Optics Express*, 15 (2007) 17206.
- [5] Y.Tanaka, J.Upham, T.Nagashima, T.Sugiya, T.Asano, and S.Noda, *Nature Materials*, 6 (2007) 862.
- [12] M.Imada, S.Noda, et al, *Appl.Phys.Lett.*, 75 (1999) 316.
- [13] S.Noda, M.Yokoyama, M. Imada, A.Chutinan, M. Mochizuki, *Science*, 293 (2001) 1123.
- [14] E.Miyai, K.Sakai, T.Okano, W.Kunishi, D.Ohnishi, and S.Noda. *Nature*, 441 (2006) 946.
- [15] H. Matsubara, et al, *Science*, 319 (2008) 445 (published on-line, 21 Dec. 2007).

Light-matter interaction in nanoscale optical devices

Marko Loncar

*School of Engineering and Applied Sciences, Harvard University,
33 Oxford Street, Cambridge, MA 02138,
loncar@seas.harvard.edu, <http://nano-optics.seas.harvard.edu>*

ABSTRACT: Mechanisms for light localization in nanoscale optical devices, including photonic crystals, metallic and semiconductor nanowires, will be reviewed. Our ability to understand and engineer light-matter interaction in these devices will open potential for further developments in areas such as optical/quantum information processing, high-density optical data storage, and bio-chemical sensing.

Optical manipulation of microscopic containers for chemistry with single molecules

Kristian Helmerson, Carlos Mariscal-Lopez, Jianyong Tang and Rani Kishore
Physics Laboratory, National Institute of Standards and Technology, Gaithersburg, Maryland,
20899-8424, USA
kristian@nist.gov, 301-975-4266 (tel), 301-975-8272 (fax)

The cell is arguably the basic building block and the fundamental chemical processing plant of living organisms. Inside the crowded environment of a cell chemical reactions, typically involving only a few, total number of molecules, take place in confining volumes. The transfer of these molecules from one compartment to another, as well as from cell to cell, constitute the flow of information necessary to perform and regulate the hierarchy of complex functions for sustaining life. Increasingly, researchers have found ways to study these chemical reactions with single molecule sensitivity in highly restricting volumes. These techniques open up new and exciting applications outside of the realm of biology and biochemistry, such as DNA computation and information storage.

One approach to working with small volumes focuses on the controlled flow of liquids through microchannels in glass, plastic and other solid substances. This approach is comparatively well developed and has met with significant successes. However, extrapolation of the fabrication techniques and fluid handling technology into the nano-scale regime has proven difficult. In addition, the large surface-to-volume ratios of the elongated channels can lead to troublesome surface interactions, a problem compounded in the nano-scale.

A second, complementary, approach to working with small volumes involves the use of small containers. Depending on the application, microscopic containers may be used in conjunction with or in place of microfluidic channels. In general, a miniature container for holding pico- to femtoliter volumes of liquid should satisfy three main requirements. (1) The container should be closed or sufficiently isolated from the environment that the substances held in the container do not escape into the surrounding medium, either by evaporation or diffusion. (2) It must be possible to access the contents of the container in order to add reagents as required by a given experimental protocol. (3) The contents of individual containers should be independently controllable so that distinct reactions can take place in separate containers.

Our group has been developing sub-micron sized water droplets as containers for single molecule manipulation [1]. The water droplets, which we call hydrosomes, are made in a perfluorinated liquid. The solubility of water in the perfluorinated liquid is at the level of a few ppm, thus the water droplets are essentially stable. Further stability, especially if the water droplets are at an elevated temperature, can be achieved by using a surfactant, such as Tween-20 or Triton X-100, in the water. Thus, the hydrosomes satisfy requirement (1) for use as a small volume container.

Formation of the hydrosomes is easily accomplished via ultrasonic agitation, which yields droplets with diameters in the range of 0.1 to 1 micron. Substances that are in the water during formation of the hydrosomes are readily incorporated into the hydrosomes, at the known concentration of the solution. Hence, encapsulation in hydrosomes is relatively easy and efficient compared to other types of containers which have membranes, such as liposomes.

We use optical tweezers to trap and remotely manipulate the hydrosomes. Optical tweezers rely on the increased polarizability of the object to be trapped compared to the surrounding medium, such that the energy of interaction between the object and the laser field is a minimum. That is, the object to be trapped must have an index of refraction, n , higher than the surrounding medium. The index of refraction of water ($n = 1.33$) is higher than the perfluorinated liquid (typically $n = 1.29$) therefore the hydrosomes are easily trapped and manipulated with optical tweezers, which satisfies requirement (3).

Hydrosomes readily fuse when brought into contact. Figure 1 is a sequence of video images showing the fusion of two hydrosomes, each held in independent optical tweezers. In addition, because of the immiscibility of water in the perfluorinated liquid, there should be no loss of the contents during the fusion of two hydrosomes. This is to be contrasted to the situation of a container with a material barrier, such as a lipid membrane based vesicle (liposome), where the barrier must be broken in order for the contents to mix, which often results in loss of some of the contents of the container to the surrounding medium. Thus, hydrosomes satisfy requirement (2).

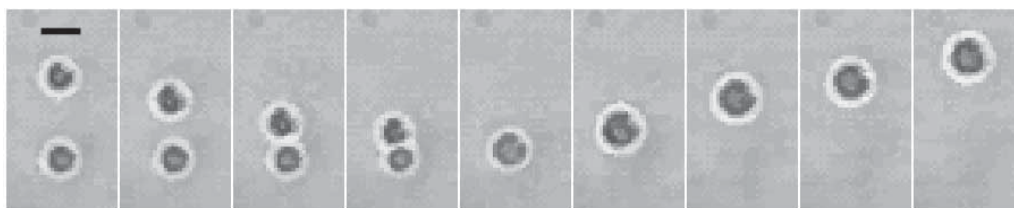


Fig. 1. Series of images showing the optical manipulation and fusion of two hydrosomes, initially held in independent optical tweezers. The upper hydrosome is translated by a mobile optical trap to the location of the other hydrosome held by a fixed trap, at which point the two droplets fuse into one. The fixed trap is then turned off and the single hydrosome is translated upwards by the mobile trap. The scale bar in the first image indicates 1 micron.

We have demonstrated confinement and detection of single dye, protein and DNA molecules in an optically trapped hydrosome. Figure 2(b) shows the light emitted from a single red fluorescent protein molecule confined in an optically trapped hydrosome. Using fluorescence correlation spectroscopy, we have determined that an encapsulated molecule spends a minimal amount of time at the water-perfluorinated liquid interface [2]. Hence the molecule can be considered as freely diffusing in the water droplet.

Reliable studies of molecular kinetics in small containers rely on accurate measurements of volumes and concentrations. This is especially true for mixing reactions due to the fusion of two containers where the final volume, and hence concentration, can be determined by a knowledge of the initial volumes, and hence concentrations, of the containers before fusion. The hydrosomes, however, are typically sub-micron in size, near or below the diffraction limit of a conventional optical microscope, which makes it difficult to accurately determine droplet sizes. This problem is compounded by the polydisperse sizes (0.1 to 1 micron) of the hydrosomes produced by ultrasonic agitation. In addition, the ultrasonic agitation technique produces thousands of droplets when typically only a few are required for any experiment.

Following the design of Ref. 3, we have recently demonstrated a nozzle capable of emitting single, sub-femtoliter hydrosomes, on demand. Our device consists of a piezo-electric tube holding a

hydrophobic coated, micropipette tip with a backing pressure from a precise pump. The micropipette tip is immersed into the perfluorinated liquid medium. The fast edge of a sawtooth-like driving voltage to the piezo leads to a quick retraction of the hydrophobic tip, resulting in the generation of a single droplet into medium. Using a stoichiometric measurement method, we have shown that the droplets generated are about 380 nm in diameter with a monodispersity better than 95%. Using two such hydrosome emitters, we have demonstrated the generation of two droplets on demand, which were then trapped by two independent optical tweezers and subsequently brought into contact to fuse.

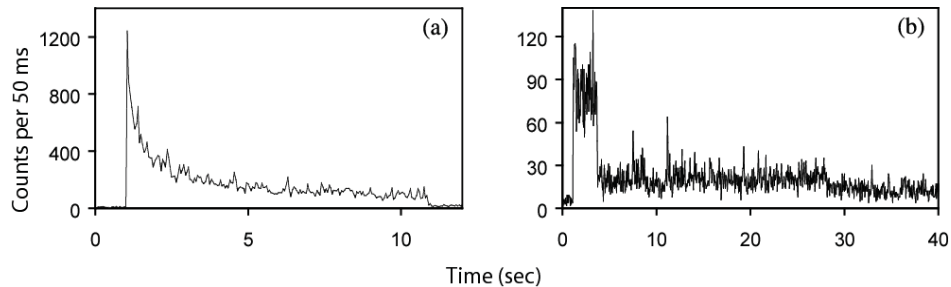


Fig. 2 Fluorescence collected from red fluorescent protein (RFP) encapsulated in optically trapped aqueous droplets. (a) At high concentration (1 μM), many molecules are fluorescing and the fluorescence decays exponentially. The droplet is removed from the optical trap at about 12 seconds. (b) At low concentration (10 nM), a step is observed in the fluorescence, characteristic of a single molecule photobleaching.

Our current set-up, with only two optical tweezers, only allows the manipulation of two hydrosomes simultaneously. Data acquisition rates could be greatly increased, and the technique could have greater application in other areas, if the process could be performed in parallel. We have recently implemented a holographic optical trapping [4] configuration, which allows for the creation of up to 100 traps simultaneously. The application of holographic optical tweezers for manipulation of hydrosomes is currently being investigated.

- [1] J. E. Reiner, A. M. Crawford, R. B. Kishore, Lori. S. Goldner, M. K. Gilson and K. Helmersen, *Appl. Phys. Lett.* **89**, 013904 (2006).
- [2] J. Tang, A. M. Jofre, G. M. Lowman, R. B. Kishore, J. E. Reiner, K. Helmersen, L. S. Goldner, and M. E. Greene, *Langmuir*, **24**, 4975 (2008).
- [3] W. Zhang, L. Hou, L. Mu and L. Zhu, *Microfluidics, BioMEMS, and Medical Microsystems II*. Edited by Woias, Peter; Papautsky, Ian. *Proceedings of the SPIE*, vol. 5345, p. 220, 2003.
- [4] E. R. Dufresne and D. G. Grier, *Rev. Sci. Instr.* **69**, 1974 (1998).

Applications of C-Apertures to Optical Data Storage

Lambertus Hesselink, J. Brian Leen, Paul Hansen, Yao-Te Cheng, Xiaobo Yin, and Yin Yuen.
Applied Physics Department, Stanford University, Stanford, California 94305

Abstract

This invited paper describes our latest work towards fully describing the operation of C-aperture light sources and using these sources to write nano-sized marks on optical recording media. During the last decade we have developed and refined a highly efficient nano-sized aperture that, under ideal conditions, increases power throughput by three orders of magnitude compared with round and square apertures producing the same optical spot size. As presented in ODS 2007, these apertures can be mounted on a solid state laser to produce a very high intensity nano-beam having a size of less than 80 nm [1]. In this paper we discuss the theoretical and practical aspects of applying C-apertures to optical data storage as well as our latest results related to using C-shaped nano apertures for optical data storage.

In recent years we have developed a resonant nano-sized aperture that has significantly better transmitted power performance than previously used square and round apertures [2]. The cross-sectional shape of the aperture resembles the letter C, suggesting the name: C-shaped aperture. We have found over the years that this particular shape is close to optimum, although many other shapes can be made to resonate [3].

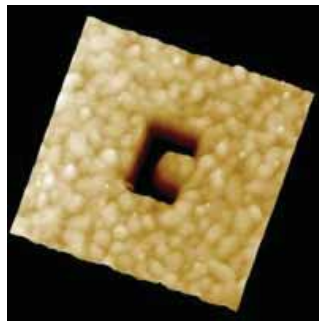


Figure 1. AFM image of a C-shaped nano-aperture manufactured in a gold metal plate.

The aperture, milled out in a metal such as gold, is illuminated from the bottom in Figure 1 by a linearly polarized light beam, with its polarization direction parallel to the horizontal edges of the C-shape. Photons interacting with the metal induce surface plasmons creating a current around the aperture. The boundary condition at the metal edges parallel to the linearly polarized incident light demand that the field at these boundaries is zero, inducing a strong driving force for the current in the metal. By appropriately choosing the C-shape the plasmon waves can be made to resonate, thereby significantly enhancing power throughput. Under realistic conditions with real metals, FDTD simulations performed by our group show that the enhancement factor for a gold medium of about 200 nm in thickness exceeds three hundred, producing a powerful sub-100 nm optical stylus of a spot size suitable for near-field optical recording.

In the presentation we will discuss in more detail the theoretical as well as practical details underlying these experiments, and recent progress we have made with regards to aperture fabrication, performance modeling of C-apertures, and applications to using these apertures to change the optical properties of recording media.

References

1. Rao, Z., Hesselink, L., Harris, J. S., "High-intensity bowtie nano-aperture Vertical-Cavity Surface-Emitting Laser for ultrahigh-density near-field optical data storage", Proceedings of SPIE, The International Society for Optical Engineering, 2007, v.6620; Optical Data Storage 2007, May 20-23 2007, Portland, OR, United States
2. Shi, X. and Hesselink, L., "Design of a C aperture to achieve $\lambda/10$ resolution and resonant transmission", J. Opt. Soc. of Am. B., **21** N. 7, p1305 (2004).
3. Sendur, K., Challener, W. and Peng, C., "Ridge waveguide as a near field aperture for high density data storage", J. App. Phys., **95**, N. 5, p. 2743-52 (2004)

Nanophotonics-based optical data storage

Min Gu

Centre for Micro-Photonics, Faculty of Engineering and Industrial Sciences
Swinburne University of Technology, VIC 3122, Australia
Tel: +61-3-92148776; Email: mgu@swin.edu.au

ABSTRACT

This talk will present our recent advance in the nanoparticle-assisted optical data storage technology where the information can be stored in five dimensions.

Keywords: Optical data storage, nanophotonics, quantum dots, nanoparticles

1. INTRODUCTION

Nanophotonics, defined as nanoscale optical science and technology, is a new frontier in photonics. It offers challenging opportunities for studying the interaction between light and matter on a scale much smaller than the wavelength of radiation, as well as for the design of novel nanostructural optical materials and devices. Furthermore, the use of such a confined interaction to spatially localise photochemical processes offers exciting opportunities for nanofabrication including optical data storage. The concept of optical data storage is based on the use of a laser beam that is focused onto a recording material to produce a spot where physical or chemical properties of the material are changed. In conventional two-dimensional (2D) optical data storage, data bits (spots) are recorded near the surface of a medium, which has led the CD and DVD technology. Two-photon-induced three-dimensional (3D) optical data storage systems have attracted significant interest due to a potential storage density of Tbits/cm³. Development of integrated optics compels the need for further expanding the current storage density by either breaking the diffraction limit of light or involving other physical dimensions. Here we introduce a new concept of multi-dimensional optical storage based on nanophotonics, in particular, involving nanostructured materials [1-7]. In this new technology, the information can be stored not only in different positions of a thick volume medium but also in a polarisation and spectral domains. The nanostructured materials comprise of semiconductor nanocrystal quantum dots (QDs) [1-5] and metallic nanorods [6-7]. The tuneability of optical properties of the QDs and the plasmonic properties of anisotropic gold nanorods provide the various erasable and non-erasable polarisation and spectral encoding mechanisms in the same spatial position to break the data density limit imposed by the 3D optical storage technology. This nanophotonic approach will lead to a horizon of the new-generation optical data storage technology.

2. QD-BASED OPTICAL DATA STORAGE

QDs have received so much attention because of their interesting properties such as the emission wavelength tunability with size, narrow emission bandwidths and discrete atom-like energy level structures. When two or more different sizes of QDs are mixed, the differences in energy level structures can be excited by different wavelengths of a recording beam. The excited energy can be used to induce physical and chemical processes or effects including photorefractivity, photochromism, photoisomerisation, photopolymerisation, photobrightening or photoionisation. The resultant change in refractive index, fluorescence, or structures can be used in optical storage as marks that can be recorded on one type of QDs at a certain wavelength without affecting the other QDs. This is the principle of spectral encoding. In addition, the shape of the QDs leads to a polarisation sensitivity, which is another physical dimension for data encoding. Fig. 1 shows the example of the QD-induced photorefractive polymer that is ready for two-photon excited optical data storage [4]. Fig. 2 shows the example of the QD-induced fluorescence energy transfer process under two-photon excitation, which is ready for polarisation multiplexing [5].

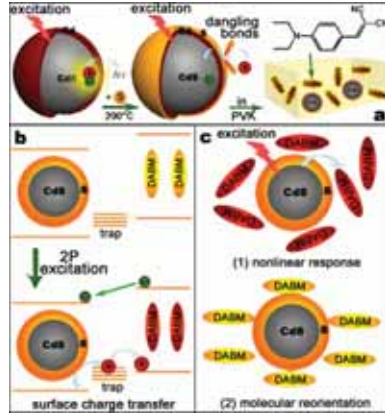


Fig. 1. Scheme of localised photorefractivity. a, Surface engineering of CdS QDs and incorporation of QDs into a photorefractive polymer. b, local charge transfer at the interface between QDs and DABM molecules. c, nonlinear response and enhancement by molecule reorientation.

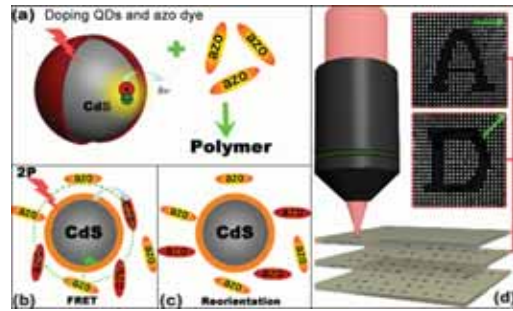


Fig.2. Scheme of multi-dimensional optical data storage. a, Incorporation of CdS QDs and azo dye into polymer. b, 2P-excited FRET process. c, Consequent reorientation of molecules. d, Polarisation multiplexed multilayer optical data storage.

3. ACKNOWLEDGEMENTS

The author acknowledges the support from the Australian Research Council and the important contribution from Dr. J. Chon, Mr. X. Li and Mr. P. Zijlstra.

REFERENCES

[1] X. Li, J. Chon, Min Gu, Nanoparticle-based photorefractive polymers, *Australian J. Chem.* (2008), in press.

- [2] James W. M. Chon, Peter Zijlstra, Min Gu, Joel van Embden, Paul Mulvaney, Two-photon induced photo-enhancement of densely packed CdSe/ZnSe/ZnS nanocrystal solids and its application to multi-layer optical data storage *Appl. Phys. Lett.*, 85 (2004), 5514-5516.
- [3] Xiangping Li, James Chon, Shuhui Wu, Richard Evans, Min Gu, Rewritable polarization encoded multi-layer data storage in 2,5-dimethyl-4-(p-nitrophenylazo)anisole doped polymer, *Opt. Lett.*, 32 (2007), 277-279.
- [4] Xiangping Li, Craig Bullen, James Chon, Richard Evans, Min Gu, Two-photon induced three-dimensional optical data storage in CdS quantum-dot doped photo-polymer, *Appl. Phys. Lett.*, 90 (2007), 161116.
- [5] X. Li, James Chon, Richard A. Evans, Min Gu, Two-photon energy transfer enhanced three-dimensional optical memory in quantum-dot and azo-dye doped polymers, *Appl. Phys. Lett.*, 92 (2008), 063309.
- [6] J. Chon, C. Bullen, Peter Zijlstra, Min Gu, Spectrally selective laser induced shape transition of gold nanorods and its application to optical data storage, *Adv. Functional Materials*, 17 (2007), 875-880.
- [7] Peter Zijlstra, James W. M. Chon, Min Gu, The effect of heat accumulation on the dynamic range of gold nanorod doped polymer nanocomposite for optical laser writing and patterning, *Opt. Express*, 15 (2007), 12151-12160.

SESSION TuA: Drive Technologies

Monarchy Ballroom

8:30 to 10:00 am

Ryuichi Katayama, NEC Corp. (Japan)

Kyunggeun Lee, SAMSUNG Electronics Co., Ltd. (South Korea)

Readout-Signal Amplification by Homodyne Detection Scheme

Hideharu Mikami*, Takeshi Shimano[†], Takahiro Kurokawa,
 Tatsuro Ide, Jiro Hashizume[‡], Koichi Watanabe, and Harukazu Miyamoto
 Central Research Laboratory, Hitachi, Ltd., 1-280, Higashi-koigakubo, Kokubunji 185-8601, Japan;
[‡] Mechanical Engineering Research Laboratory, Hitachi, Ltd., 8322-2, Horiguchi, Hitachinaka,
 Ibaraki 312-0034, Japan

ABSTRACT

We propose the use of a homodyne detection scheme to amplify optical disk readout signals. This scheme uses optical interference to amplify the signals. Additionally, to reliably obtain the amplified readout signal, we propose applying phase-diversity detection. We performed proof-of-principle experiments and observed that applying the scheme led to a 20-dB improvement in the S/N. We also designed an optical pickup where the scheme is applied in order to observe the amplified optical disk readout signal. The optical system was carefully designed so that a sufficiently amplified readout signal is obtained.

Keywords: homodyne detection, optical pickup, phase-diversity detection, multi-layer optical disk

1. INTRODUCTION

Multilayer recording is one of the most promising technical candidates for achieving larger capacity on optical disks. Currently, write-once disks with up to 6 layers and 8-layer ROM disks have been demonstrated [1,2]. Refined techniques such as using a layer-selective optical disk and a three-dimensional pit selection method have also been proposed [3, 4]. However, increasing the number of their recording layers results in low reflectivity for each layer, and with it a low signal level. On the other hand, maintaining practical data transfer times for larger capacity disks requires higher reading/writing speeds [5]. As measurement bandwidth becomes wider, higher-speed readout results in increased noise levels. For these reasons, larger capacity optical disks inevitably encounter the problem of low S/N. In this report, we propose applying a homodyne detection scheme [6] to an optical pickup to solve this problem.

2. PRINCIPLE

Figure 1 is a schematic diagram of an optical pickup to which a homodyne detection scheme is applied. Light from a laser diode (LD) is split into signal light and reference light by a polarization beam splitter (PBS₁). The signal light is irradiated onto an optical disk and returned to the PBS₁. The reference light is reflected by an optical element such as a mirror and returned to the PBS₁. The signal and reference lights become collinear after passing through the PBS₁ with their polarization orthogonal to each other. They pass through a half-wave plate (HWP) with its optical axis set as 22.5 degrees and are irradiated on another polarization beam splitter (PBS₂). Then the light fields of transmitted and reflected lights are expressed as $E_1 = (E_s + E_r)/\sqrt{2}$ and $E_2 = (E_s - E_r)/\sqrt{2}$, respectively, where E_s and E_r represents the signal and reference light fields, respectively. The split lights are detected by photodiodes (PD1, PD2) and their differential signal becomes

$$\eta|E_1|^2 - \eta|E_2|^2 = \eta\left(\frac{1}{2}|E_s|^2 + \frac{1}{2}|E_r|^2 + |E_s||E_r|\cos\Delta\phi\right) - \eta\left(\frac{1}{2}|E_s|^2 + \frac{1}{2}|E_r|^2 - |E_s||E_r|\cos\Delta\phi\right) = 2\eta\sqrt{I_s I_r} \cos\Delta\phi, \quad (1)$$

where η is the conversion efficiency of the detection system, $\Delta\phi$ is the phase difference of the signal and reference lights, I_s and I_r are the intensities of the signal and reference lights, respectively. Equation (1) has the maximum value $2\eta\sqrt{I_s I_r}$ when $\Delta\phi=0$. On the other hand, the signal level in a conventional direct detection scheme is ηI_s . Therefore, signal level is amplified by $2\sqrt{I_r/I_s}$ by applying the homodyne detection scheme.

*hideharu.mikami.kf@hitachi.com; phone +81-45-860-3035; fax +81-45-860-2322

[†]present affiliation: Development and Technology Division, Hitachi Maxell Ltd., 6139-1 Ohnogo, Joso-shi, Ibaraki 300-2595, Japan

This amplification effect leads to improved S/N when noise elements such as amplifier noise or common mode noise are dominant. For example, if the power of the reference light is 100 times higher than that of the signal light on detectors, S/N is ideally improved by 20 dB by applying the present scheme.

In the present scheme, $\Delta\phi$ is actually decided by the path length difference between signal and reference lights Δl as $\Delta\phi=4\pi\Delta l/\lambda$, where λ is wavelength of the light source. Then it is difficult to control $\Delta\phi$ to be near to 0 in order to maintain constant amplitude because sub-wavelength accuracy is required on Δl . Therefore we further apply phase-diversity detection. The schematic diagram of the scheme is shown in Fig. 2, which is a slight modification of the original one. In this scheme, the differential signal of PD1 and PD2 becomes the half that of the original, $\eta\sqrt{I_s I_r} \cos \Delta\phi$, and that of additional photodiodes, PD3 and PD4, becomes $\eta\sqrt{I_s I_r} \sin \Delta\phi$. Thus, the output signal of the scheme is the root sum squares of the two differential signals, $\eta\sqrt{I_s I_r}$, which is independent of $\Delta\phi$.

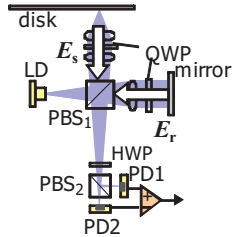


Fig. 1. Schematic of an optical pickup to which homodyne detection scheme is applied.

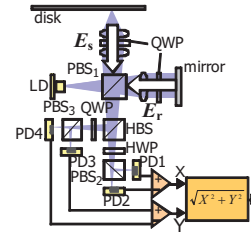


Fig. 2. Schematic of an optical pickup to which phase-diversity homodyne detection scheme is applied.

3. PROOF-OF-PRINCIPLE EXPERIMENT

Figure 3 is schematic diagram of the experimental setup we used to verify the effects of the phase-diversity homodyne detection scheme. We used a He-Ne laser as a light source. A mirror was used as a substitute for an optical disk. We adjusted the phase difference of signal and reference lights with a piezo actuator on which a mirror was mounted to reflect reference light.

The experimental result exhibiting the S/N improvement effect of the homodyne detection scheme is shown in Fig. 4. The signal pattern was generated by intermittently shielding the signal light path by an optical chopper. The noise mainly originated from the circuit of square root calculation. On the left side, the reference light and the lights irradiated on PD1, PD3, and PD4 were shielded. This situation corresponds to a conventional detection scheme. On the right side, the reference light was introduced, all the detectors were used, and thus the phase-diversity homodyne detection scheme was applied. The intensity of the reference light was 100 times higher than that of the signal light, and this corresponds to a 20-dB improvement in S/N.

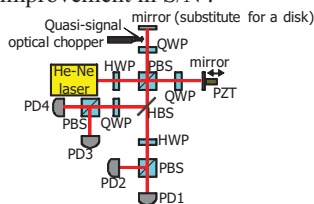


Fig. 3. Schematic of proof-of-principle experiment

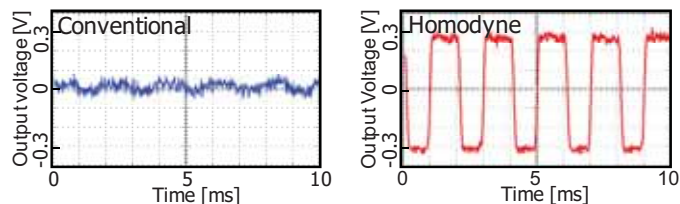


Fig. 4. Experimental result exhibiting the effect of homodyne scheme

4. DESIGN OF OPTICAL PICKUP

Our goal is to amplify readout signal of an optical disk by applying homodyne detection, and to demonstrate its effectiveness. For this purpose, first we designed an optical pickup to which homodyne detection is applied. The optical system should be carefully designed so that interference quality is kept high. Interference quality is decided by the difference between the signal and the reference lights in the following elements: first, light axis direction; second, optical path length; third, defocus; and four, wavefront aberration

The difference of the light axis directions is mainly caused by a tilt of the mirror for the reference light. The relative magnitudes of interference signal when the tilt changes (normalized by the case of no tilt), obtained by the setup of proof-of-principle experiment is shown in Fig. 5. In an actual optical pickup, the magnitude will be more sensitive to the tilt because the beam diameter of used lights will be larger than that of the experimental setup (~1 mm), and the

precision that is required for the tilt to obtain a reliable output signal is as small as 0.001 degree. This requirement is almost impossible to be satisfied because, as explained below, the mirror position should be actively controlled by an actuator. Therefore, we replaced the mirror by a corner cube prism shown in Fig. 6. A feature of this prism is that the reflected light is always parallel to the incident light. Therefore, the light axis direction of the reference light does not change and a stable signal output can be obtained.

Path length difference causes decrease of coherence. Figure 7 shows relative magnitudes of interference signal when path length difference changes (normalized by the case of no difference), experimentally obtained by using a blue laser diode. The precision required to obtain a reliable output signal on the path length difference is about 100 μm . In order to satisfy the requirement, we mounted an objective lens and a corner cube prism on one actuator. Therefore even if disk surface position fluctuates by 600 μm , path length difference caused by this fluctuation is canceled because the actuator follows the disk surface.

Differences in the level of defocus between the signal and the reference lights also cause the interference signal to degrade. To avoid this, we collimated reference light when it was incident on a corner cube prism. Moreover, wavefront aberrations of signal and reference lights also degrade the interference signal. However, components that are conventionally used in an optical pickup do not seriously degrade the wavefront.

The optical system we designed on the basis of the above design items is depicted in Fig. 8. The fabricated optical pickup and the results of experiments using it will be shown elsewhere.

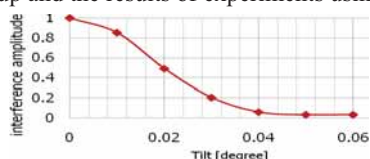


Fig. 5 Interference amplitude vs tilt of the reference light's mirror



Fig. 6. Corner cube prism



Fig. 7. Interference amplitude vs. path length difference

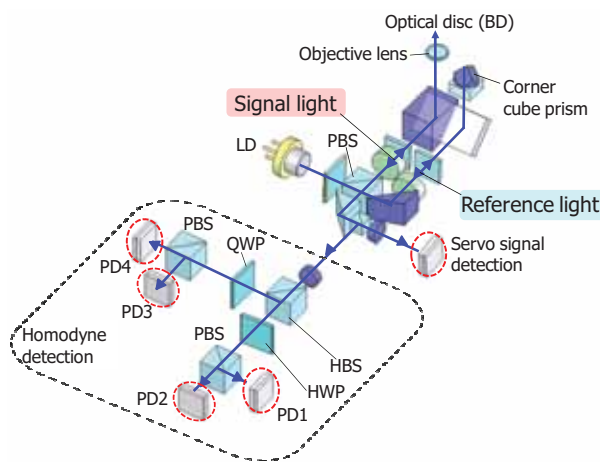


Fig. 8. Designed optical system.

5. CONCLUSION

We proposed a homodyne detection scheme for achieving higher signal-to-noise ratio in optical disk systems. We performed proof-of-principle experiments on the homodyne detection scheme and observed a 20-dB improvement in S/N by applying the homodyne detection scheme. Optical pickup to which homodyne detection is applied was designed in order to observe amplified readout signal of optical disk.

REFERENCES

- [1] K. Mishima *et al.*, "150 GB, 6-Layer Write Once Disc for Blu-ray Disc System," ODS 2006 (2006) TuA3.
- [2] I. Ichimura *et al.*, "Proposal for Multi-Layer Blu-ray Disc Structure," ISOM 2004 (2004) We-E-02.
- [3] K. Kojima and M. Terao, "Investigation into Recording on Electrochromic Information Layers of Multi-Information-Layer Optical Disk Using Electrical Layer Selection," *Jpn. J. Appl. Phys.* 45, 7058 (2004).
- [4] T. Shintani *et al.*, "Sub-Terabyte-Data-Capacity Optical Discs Realized by Three-Dimensional Pit Selection," *Jpn. J. Appl. Phys.* 45, 2593 (2006).
- [5] H. Minemura *et al.*, "High-Speed Write/Read Techniques for a Blu-ray Write-Once Disc," ISOM/ODS 2005 (2005).
- [6] T. Okoshi and K. Kikuchi, *Coherent Optical Fiber Communications*. KTK Scientific, 1988.

System technology for achieving 200GB drive with 5-layer disc (Invited)

Kyunggeun Lee, Inoh Hwang, Nakhyun Kim, Hyunsoo Park, Hui Zhao, Tao Hong and Insik Park

Digital Media R&D Center

SAMSUNG ELECTRONICS CO., LTD, Yeongtong-Gu, Suwon, 442-742, Korea

Tel: 82-31-200-4863, Fax: 81-31-200-3160, E-mail: kyglee@samsung.com

Abstract: We report the feasibility for achieving 200GB with 40GB per layer and 5-layer disc for the first time. bBER of lower than 10^{-3} were experimentally obtained respectively using this new data reproducing scheme which shows the possibility of reducing one order of bBER. With more improvement of media characteristics, less than 10^{-4} of bBER can be achieved.

1. Introduction

We have reported the feasibility of high capacity 40GB in a single layer and a dual layer Blu-ray Disc with a new data reproducing scheme by introducing a signal waveform phase detector [1,2]. There was a report to obtain 200GB with 6-layer [3], but it can be achieved with 5-layer by increasing the capacity to 40GB per layer. In this paper, we will report our system technology such as pickup and signal processing for achieving 200GB drive with 5-layer disc.

2. Experimental Procedure

Multi-layer disc up to 5 layers was made for experiment and the disc structure is depicted as Fig.1. Bi-(Ge)-O and TiO₂ were used for recording layer and protective layer, respectively. They are known as proper materials for multi-layer write once disc [3]. The disc was tested with an ODU-1000 dynamic tester made by Pulstec Industrial and an evaluator which has a pickup for multi-layer disc. The linear velocity was adjusted to increase the capacity to 40GB per layer, and RLL (1,7) random pattern was used for evaluation of bBER. The adaptive Viterbi decoder, the adaptive EQ and the pre-EQ & PLL were implemented on a FPGA board for the data reproducing.

3. Result and discussion

For multi-layer disc, thickness of each space layer is different to avoid the mirror effect, but it makes a lot of spherical aberration. Therefore, the optical pickup head should prepare a method for its compensation. A beam expander lens is employed to compensate the spherical aberration due to the thickness difference of each space layer. Fig.2 shows a pickup head which has a beam expander lens and stepping motor module. The thickness difference of +/-50um can be compensated by the beam expander lens driven by a stepping motor module as Fig.2.

In previous report, it was shown that bBER of 10^{-5} and 10^{-4} for 40GB per layer could be obtained with a commercial single layer and a dual layer Blu-ray disc and we confirmed that the recording and reproducing were possible with 40GB and 80GB, respectively. Using the parameters shown in Table 1, we obtained the bBER of lower than 10^{-3} for 40GB per layer with 5-layer disc with newly developed signal processing technology which will be explained at the next section. The result was almost same with an ODU-1000 dynamic tester and an evaluator with a pickup for multi-layer disc. It was confirmed that the main problem is the fluctuation of signal and this fluctuation of signal is known to come from the so-called mirror effect which is the result of the multi-interference between the layers [4]. Because the fluctuation of all

the layers are worse than that of a single layer disc, another factor such as the accumulation of the variation of the cover layer thickness can be thought to affect the fluctuation of signal. Improved result will be shown at the conference site.

4. Reduced State Sequence Estimation with Level Adaptation (RESSELA)

In case of multilayer disc, there are various kinds of noise and some of them come from multilayer structure. So in order to solve this problem, we add two kinds of idea.

First idea is two-stage equalizer, which has the function of gain-boosting and noise reduction. First equalizer has the block of target level supplier which gives desirable level value, and second equalizer has level adaptation block which gives average level value. If there's no noise, error signal between equalizer output and level value is zero. And filter coefficient keeps unit impulse response. Noisy case, filter coefficient of second equalizer can be changed in order to reduce noise component.

Two-stage equalizer has good performance of tilt case. Filter coefficient is updated by channel clock and a quick adaptation is possible. For tilt variation or another kind of disturbance, each coefficient changes optimally. So, always stable signal for maximum likelihood can be achieved.

Second idea is Reduced State Sequence Estimation with Level Adaptation algorithm(RESSELA). This algorithm uses feedback signal in order to reduce hardware size [5]. Total hardware size can be reduced by the number of feedback line roughly. If feedback line is 4, almost 1/16 hardware size is needed. Originally this idea was introduced in 1980's and we add our own idea. We combined this structure with level adaptation algorithm. In optical disc, there are various kinds of nonlinear component. Asymmetry is typical example of nonlinear component. In order to compensate this kind component, adjustable level is used for maximum likelihood algorithm. So level adaptation block calculates average level value, and feedback line is connected to select proper levels, and finally input of level adaptation is in front of second equalizer. This type of structure gets almost one order of bER improvement over 40GB capacity.

If we combine these two ideas and compare to our previous result [1,2], at least four times bER progress can be achieved as shown in Fig.5.

5. Conclusion

We have made 5-layer disc and tested 200GB capacity with 40GB per layer and got the bER of lower than 10^{-3} from each layer for the first time. Still there is a room to improve the characteristics as explained above, especially media characteristics. We will present improved results at the conference and are sure that this is a milestone for achieving 200GB optical Storage.

References

1. Hui Zhao et al, "A new data reproducing scheme for higher density Blu-ray disc", ISOM, Th-PO-04, 286 (2006)
2. Kyunggeun Lee et al, "Approach to high density more than 40GB per layer with Blu-ray disc format", ODS, TuB2 (2007)
3. Koji Mishima et al, "150GB, 6-layer write once disc for Blu-ray disc system", ODS, TuA3, 123 (2006)
4. Akemi Hirotsune et al, "Interlayer Crosstalk Reduced Multilayer Disk with Wide Fabrication Margin", ISOM, Tu-G-02(2007)
5. Alexandra duet-hallen, "Delayed decision-feedback sequence estimation", IEEE transactions on communications, Vol. 37, No. 5, May 1989

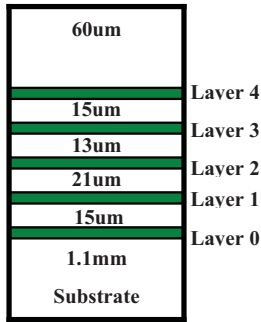


Fig.1 Disc structure



Fig.2 Pickup Head

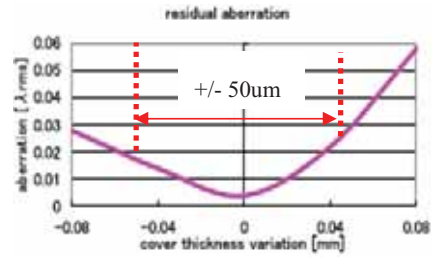


Fig.3 Aberration vs. cover layer thickness

	Layer 0	Layer 1	Layer 2	Layer 3	Layer 4
Reflectance (%)	2.3%	2.3%	3.4%	3.0%	3.4%
Pw / Pb (mW)	13.2 / 6.2mW	19.0 / 8.8mW	14.4 / 6.8mW	10.2 / 4.6mW	9.1 / 4.2mW

Table 1 Reflectance and recording powers using disc evaluation results with 40GB per layer

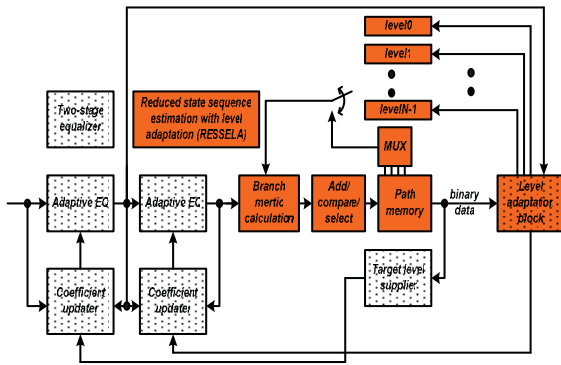


Fig.4 Diagram of RESELLA

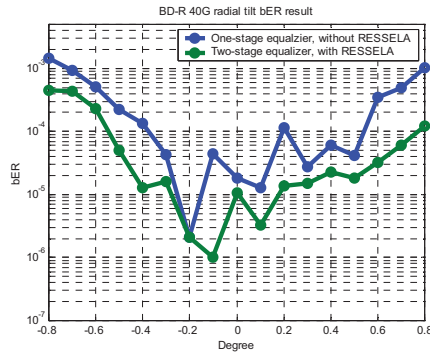


Fig.5 Tilt margin comparison

Stable Rotation of Optical Disks over 15000 rpm

T. Mukasa*, N. Goto, T. Takasawa, Y. Urakawa, N. Tsukahara
Sony Corporation, 5-1-12 Kita-shinagawa, Shinagawa-ku, Tokyo, Japan, 141-0001

ABSTRACT

Stable Rotation of optical disks and robust servo control are obviously needed to realize high data transfer rates of optical disk drives. But it is difficult to rotate polycarbonate optical disks over 15000 rpm without any vibrations. We analyzed disk vibrations at high rotational speed, and found a condition to suppress the vibrations. We confirmed high-speed rotation without vibrations up to 20000 rpm. We also made an experiment on high-speed-rotation with tracking servo control, and confirmed stable rotation at 17000 rpm using the double-boosted high-gain servo controller.

Keywords: optical disk, high-speed-rotation, vibration, disk case, double-boosted high-gain servo controller

1. INTRODUCTION

High data transfer rates are constant demand for optical disk drives to be used in computer peripherals and consumer electronic equipments. Stable rotation of optical disks and robust servo control are key technologies to realize the high data transfer rates. But it is difficult to rotate usual polycarbonate (PC) disks, whose diameters are 120 mm and whose thicknesses are 1.2 mm, over 15000 rpm without vibrations. The vibrations sometimes cause disk crush. Stable rotations with thin disks are reported [1,2], but stable rotation with the usual PC disks is still difficult. We analyzed the disk vibrations, and found a condition to suppress the vibrations. We confirmed high-speed-rotation of the disk without vibrations up to 20000 rpm under this condition. We also made an experiment on high-speed-rotation with tracking servo control, and confirmed stable rotation at 17000 rpm using the double-boosted high-gain servo controller [3].

2. ANALYSIS OF DISK VIBRATIONS

We analyzed the disk vibrations at high rotational speed with measuring the vibrations in time domain and in frequency domain. Figure 1 shows our experimental setup for analysis. PC disks are rotated in a disk case type-A shown in Fig.2 a), and the vibrations are measured by a laser Doppler vibrometer (LDV). Amplitude of the vibrations is measured with oscilloscope, and frequency elements of the vibrations are measured with fast Fourier transform (FFT) analyzer.

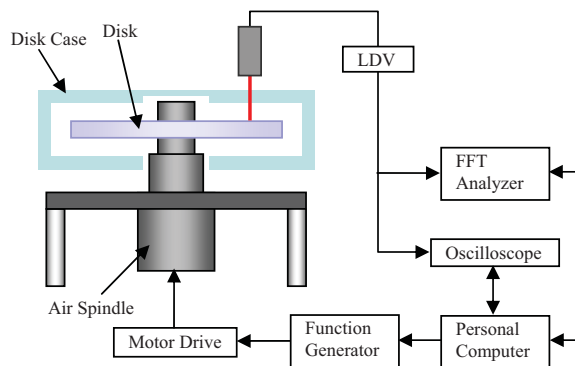


Fig.1 Experimental setup

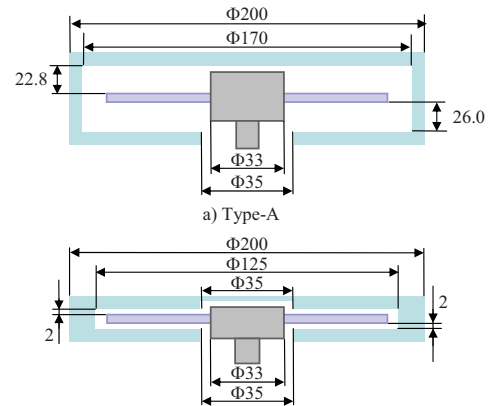


Fig.2 Disk case

*Tomoharu.Mukasa@jp.sony.com; phone 81 3 5448-4162; fax 81 3 5448-7868;

Figure 3 shows resonance amplitude of a BD-RE disk. The amplitude becomes larger gradually over 10000 rpm, and has a peak at 17500 rpm. Figure 4 shows the frequency elements of the vibrations. This graph shows three groups of trend of the frequency elements. The first one is group-1, which is caused by deformation of a disk. The frequency elements of the group-1 appear at integral proportion of the disk rotation speed, and makes lines which pass the origin. The second one is group-2, which represents natural modes of a disk, and makes lines which do not pass the origin. The last one is group-3, which make lines pass the origin, but not correspond to the group-1. The group-3 becomes pronounced over 14000 rpm. The amplitude seems to become large when the group-3 elements and the group-2 elements appear at the same frequency, such as 17500 rpm. We confirmed the size of the disk case gives effect to the frequency elements group-3. We guess air flow in the disk case affects the vibration.

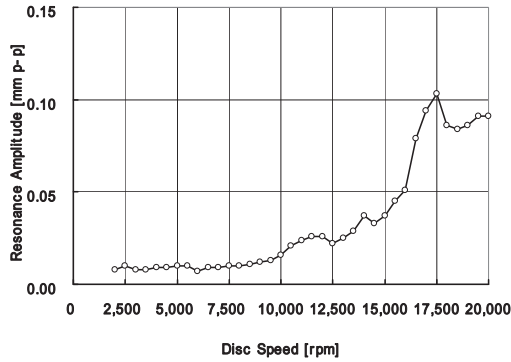


Fig. 3 Resonance amplitude [BD-RE] (Type-A)

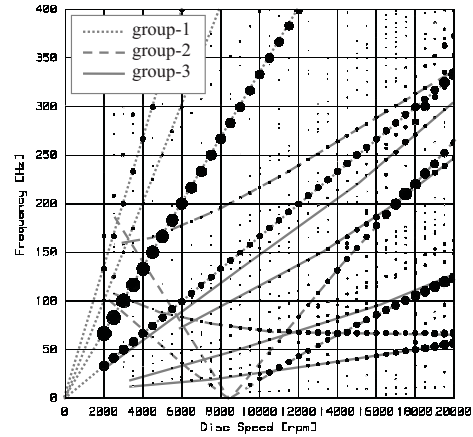


Fig. 4 Frequency elements of the vibrations (Type-A)

3. STABLE ROTATION

We changed the size of the disk case, and found that the disk case type-B shown in Fig.2 b) made the vibrations extremely small. Figure 5 shows resonance amplitude using two types of the disk case. The amplitudes using type-B are clearly smaller than the amplitudes using type-A up to 20000 rpm. Figure 6 shows frequency elements of the vibrations with the disk case type-B. We can confirm that the group-3 does not appear. We found the condition to suppress the vibrations which come from the air flow by changing the size of the disk case. We confirmed high-speed-rotation without vibrations up to 20000 rpm under this condition.

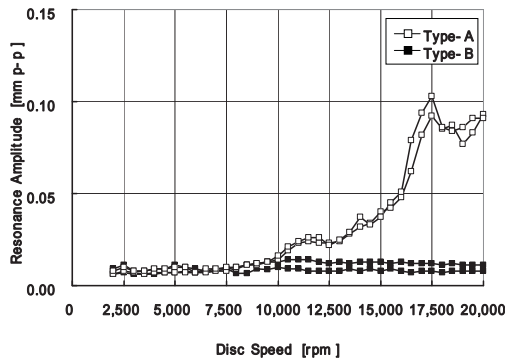


Fig. 5 Resonance amplitude [BD-RE] (Type-A and Type-B)

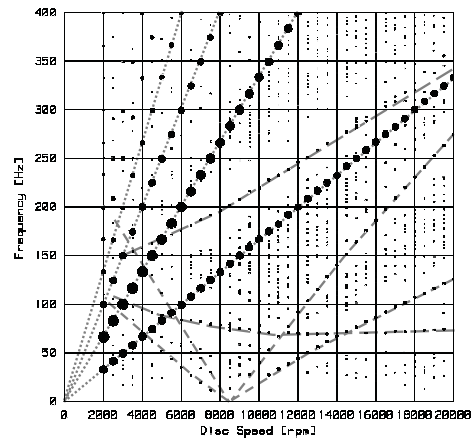


Fig.6 Frequency elements of the vibrations (Type-B)

4. SERVO CONTROL

We used the double-boosted high-gain servo controller for tracking servo control of this experimental high-speed-rotation optical disk drive [3]. Figure 7 shows a structure of the double-boosted high-gain servo controller. This controller consists of two low-frequency boosters and a lead-lag compensator in parallel. This controller increases a low-frequency gain extremely, as seen in Fig.8. We can suppress low-frequency disturbances caused by rotation of a disk with this controller.

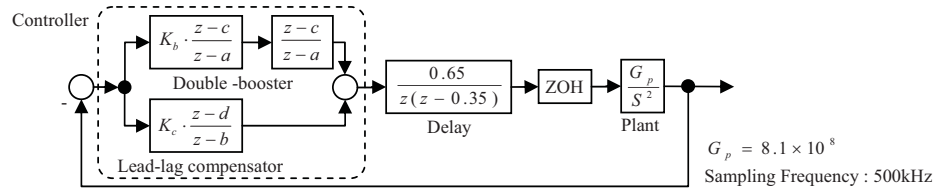


Fig. 7 Block diagram of the double-boosted high-gain servo controller

Parameters of the double-boosted high-gain servo controller are designed by the pole assignment method to have enough high gain at low frequency, similarly to the high gain servo controller [4]. We set four poles at -31416 rad/s. Open loop frequency characteristics are shown in Fig.8. We also draw simulated data of conventional controller. Much higher gain at low frequency is expected. Figure 9 shows the residual tracking error of the experimental system at 17000 rpm. Error from eccentric of a disk is well suppressed. We confirmed a tracking servo control at 17000 rpm with the double-boosted high-gain servo controller.

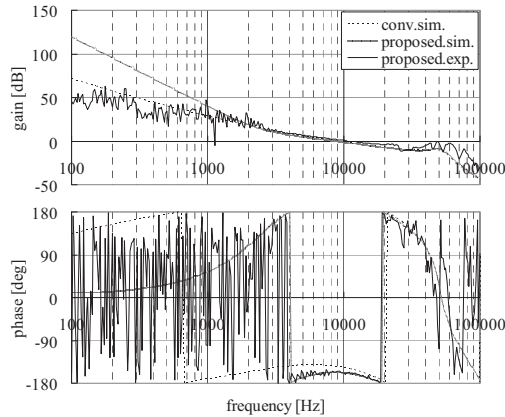


Fig. 8 Frequency response of the system with the double-boosted high-gain servo controller

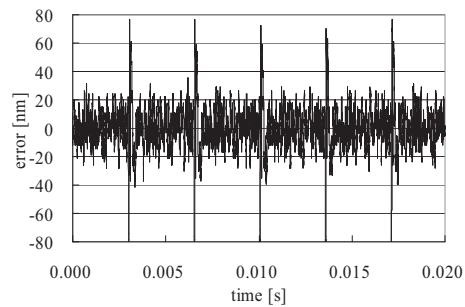


Fig. 9 Residual tracking error of the experiment at 17000 [rpm]

REFERENCES

- [1] D. Koide, Y. Takano, H. Tokumaru, N. Onagi, Y. Aman, S. Murata, Y. Sugimoto and K. Ohishi, "High-Speed Recording up to 15000 rpm Using Thin Optical Disk," Tech. Digest of ISOM2007, Tu-E-03, pp52-53(2007).
- [2] A. Inaba, H. Ido, H. Kishi, H. Yamanaka, S. Osawa, M. Tani, T. Uchida, Y. Watanabe, S.Arai, M. Yoshimoto, T. Iida, H. Awano, N. Ohta and T. Yoshida, "Tera Byte Optical Data Storage Demonstration of Advanced SVOD(Stacked Volumetric Optical Disks)," Tech. Digest of ISOM2007, Tu-E-01, pp48-49 (2007).
- [3] T.Mukasa and Y.Urakawa, "A Double-Boosted High-Gain Servo Controller for High-Rotation-Speed Optical Disk Drives," Tech. Digest of ISOM 2007, We-J-P02, pp246-247(2007).
- [4] Y. Urakawa and T. Watanabe, "High Gain Servo Controller with Complex Zeros for Optical Disk Drives," Tech. Digest of ISOM2004, Fr-K-03, pp232-233 (2004).

A High-density Recording by a Near-field Optical System using a Medium with a Top Layer with a High Refractive Index

A. Nakaoki^a, K. Saito^a, T. Yamasaki^a, T. Yukumoto^a, T. Ishimoto^a, S. Kim^a, T. Kondo^a,
T. Mizukuki^a, O. Kawakubo^a, M. Honda^b, N. Shinohara^b, and N. Saito^b

^a Sony Corporation, 4-14-1 Asahi-cho, Atsugi-shi, Kanagawa, 243-0014 Japan

^b JSR Corporation, 25 Miyukigaoka, Tsukuba, Ibaraki, 305-0841 Japan

ariyoshi.nakaoki@jp.sony.com; phone 81 46 201-4216; fax 81 46 202-6735

norihiko_saitou@jsr.co.jp; phone 81 3 5565-6607; fax 81 3 5565-6641

1. INTRODUCTION

100 GB can be stored on a 12 cm platter using near-field optical storage technology^[1]. We have proposed a super-hemisphere-type solid immersion lens (SIL) made of a high refractive index material of $n=2.075$, and achieved a high numerical aperture (NA) of 1.84^[2]. This NA is more than two times that of a Blu-Ray disc, and it makes possible to record at more than four times density of Blu-Ray. In return for this high-density performance, however, a disc-lens spacing less than 50 nm is necessary. C. Verschuren et al.^[3] demonstrated that a layer covering the medium is one solution. They adopted a UV-curable resin layer 3 μm -thick. The refractive index of the resin was 1.45 and a recording capacity of 75 GB was confirmed. We report here our use of a top-layer resin with a 1.83 refractive index to achieve high-density recording of 100 GB.

2. EXPERIMENTAL METHOD

Figure 1 shows the medium structure we used to evaluate the signal quality and collision resistance. Each of the six thin films comprising the phase-change recordable disc was deposited by sputtering on a polycarbonate substrate of 1.2 mm-thick and of 120 mm in diameter. To improve the refractive index of the topcoat material, we investigated resin comprised of inorganic fine particles with a high refractive index. First, light propagation inside the resin was simulated using the FDTD (finite-difference time-domain) method. The calculation parameters of an inorganic fine particle of $n=2.5$ were 70 nm and 20 nm, and that such a fine particle is dispersed in random order inside of a UV curable resin of refractive index $n=1.55$. A wavelength of 405 nm and NA of 1.7 were adopted as parameters for calculation. Figure 2 shows the light intensity distribution at the focal plane. It is clear that a more regular pattern can be obtained in the case of 20 nm particles than with 70 nm particles. We adjusted both the size and density of the inorganic fine particles to achieve a refractive index of $n=1.83$. The topcoat layer of 1.0 μm was made by spin coating.



Fig. 1. The medium structure with topcoat layer. Films such as the recording material (GeSbTe), two dielectric layers of Si_3N_4 and ZnS-SiO_2 , and the metal-reflection layer (Ag) were sputtered on a 1.2 mm polycarbonate substrate. The topcoat layer was made by spin-coating.

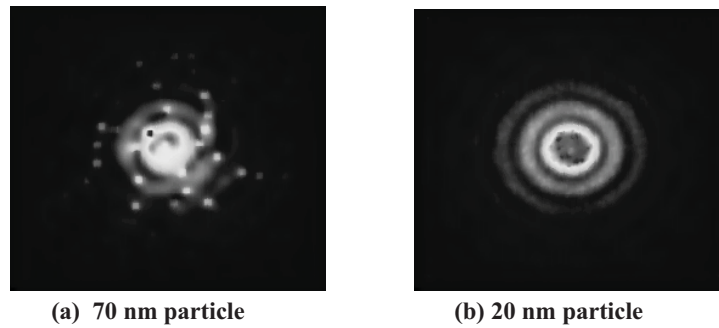


Fig. 2. FDTD simulation of light-intensity distribution inside the resin comprising fine particles. The particle size of (a) 70 nm, and (b) 20 nm are used as the calculation parameters.

3. RECORDING PERFORMANCE

The objective lens of NA 1.84 in which SIL was combined with an aspherical lens was adjusted for a topcoat layer of $n=1.83$ and $1.0\ \mu\text{m}$, and was loaded into the near-field tester ODU-1000 (Pulstec Industrial Co., Ltd.). Random data strings modulating according to 1-7 RLL code were recorded on the substrate of 160 nm pitch grooves in such a way as to adjust the minimum bit length to 62 nm and 56 nm. The reproduced waveform patterns are shown in Fig. 3, and jitter values of 7.69 % and 10.9 % were obtained respectively. We compared the jitter values from these media with those from non-coated media in order to estimate the signal quality. The result showed that only 1.65 NA was available if these coated media were adopted. This is not sufficient.

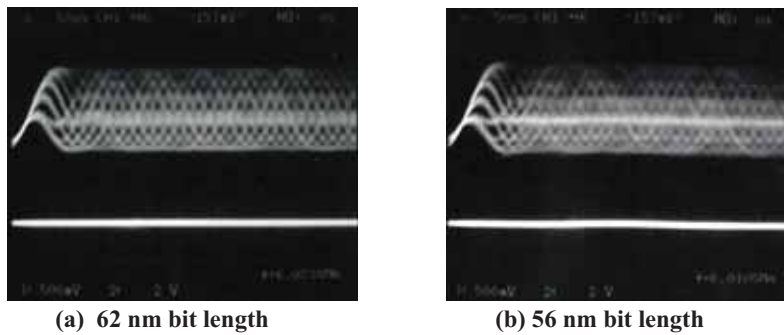


Fig. 3. Signal waveform of 1-7 RLL random data from the phase-change medium with the high refractive index topcoat. A recording bit density of (a) 62 nm and (b) 56 nm corresponding to the total capacity of 90 GB and 100 GB, respectively, was used.

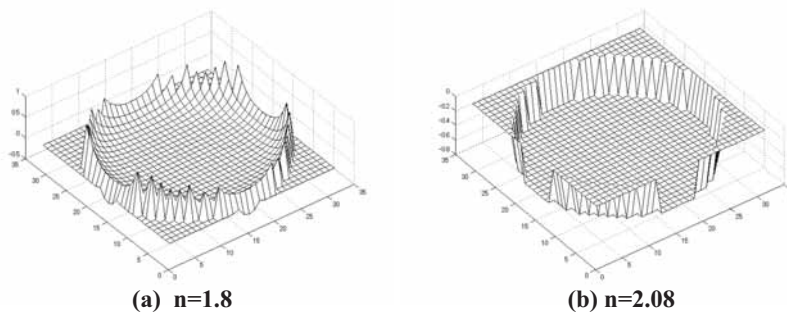


Fig. 4. 3D denotation of residual aberration on a pupil plane when both NA of 1.84 and a high refractive-index topcoat material of $1.0\ \mu\text{m}$ are adopted. A refractive index of (a) 1.8 and (b) 2.08 were calculated.

To explore this more in detail, we calculated the residual aberration when topcoat material with a different refractive index was used. The calculation results are shown in Fig. 4. Obviously, the residual aberration is not significant in the case of a refractive index of 2.08 (equivalent to SIL). On the other hand, a small residual aberration was found in the case of a refractive index of 1.8. We conclude that a material with a refractive index more than 1.95 is necessary to realize an NA of 1.84.

4. EVALUATION OF COLLISION RESISTANCE

Resistance in the face of an SIL collision with the medium surface was evaluated by a hand-made tester^[4]. The optical head is kept a fixed distance from disk surface while a disk is rotating. After power is applied to the two-axis actuator, the optical head will approach the disk. The optical head will collide with the disc under a controlled speed. The damage caused by the collision was estimated by measuring the defect noise level in the gap error signal. We found the maximum acceptable optical-head approach speed to be 0.05 m/s. We concluded that this topcoat has sufficient strength for practical use, because there was no damage to either the SIL or medium surface after a collision at this speed.



Fig. 5. Micrographic image of the SIL surface after a collision at an approach speed of 0.05 m/s. No scratch was found.

5. CONCLUSION

A coated medium comprised of resin with a high refractive index of 1.83 was examined using a near-field optical disc system of NA 1.84. The optical effect of fine particles dispersed into the resin was found to be negligible if the particle size is 20 nm. We succeeded in recording high-density data and found an acceptable level of jitter of 7.69 % at a recording capacity of 90 GB. The jitter at a recording capacity of 100 GB was 10.9 %. A collision test was applied to the topcoat, which was found to be sufficiently robust when the optical head approached the disc at a speed of 0.05 m/s.

REFERENCES

- [1] I. Ichimura, S. Hayashi, and G. Kino, "High-density optical recording using a solid immersion lens". *Appl. Opt.*, **36** (19), 4339 (1997).
- [2] M. Shinoda, K. Saito, T. Ishimoto, T. Kondo, A. Nakaoki, N. Ide, M. Furuki, M. Takeda, Y. Akiyama, T. Shimouma and M. Yamamoto, "High-Density Near-Field Optical Disc Recording", *Jpn. J. Appl. Phys.*, **44**, No. 5B, 3537 (2005).
- [3] C. Verschuren, D. Brules, D. Bruls, B. Yin, J. van den Eerenbeemd, and F. Zijp "High-Density Near-Field Recording on Cover-Layer Protected Discs Using an Actuated 1.45 Numerical Aperture Solid Immersion Lens in a Robust and Practical System", *Jpn. J. Appl. Phys.* **46**, 6B 3889 (2007).
- [4] T. Ishimoto, S. Kim, A. Nakaoki, T. Mizuguki, T. Kondo and O. Kawakubo, "Reliability for Lens Impact against Phase Change Recording Layer in a Near-Field Optical Disk Drive System", *Proc. of the 19th Symp on. PCOS 2007*, 27 (2007).

SESSION TuB: Components and Hybrid Recording

Monarchy Ballroom
10:30 am to 12:30 pm

Paul J. Wehrenberg, Apple Computer, Inc.
No-Cheol Park, Yonsei Univ. (South Korea)

Liquid crystal active optics and its application to optical pickups

Nobuyuki Hashimoto
NXG center, Citizen Technology Center Co., Ltd.
840 Shimotomi Tokorozawa Saitama, 359-8511 Japan.
hashimotono@citizen.co.jp

ABSTRACT

Liquid crystal devices are suitable devices for active optics since their half-wave voltage is only a few volts and can be driven directly by CMOS-ICs. In this paper, optical properties of liquid crystal active optics with segmented ITO patterns and their application to dynamically compensate optical aberrations are described. Optical properties of liquid crystal GRIN lens for AF applications and liquid crystals with sub-wavelength structures are also described.

Keywords: Active optics, Liquid crystal, Pickup, Adaptive optics, GRIN, Aberration,

1. INTRODUCTION

Though the market of the liquid crystal displays is widely spread, the liquid crystals are more suitable devices for active optics. We have paid attention to their characteristics and proposed to apply liquid crystal devices for adaptive optics or for optical pickups¹⁾. In 1991, we successfully demonstrated real-time 3D holography, one of the most complicated applications of waterfront modulations, using our own developed LCTV-SLMs as wave-front modulators²⁾. After that, we continued to study application of LCTV-SLMs to optical computing systems and application of segmented liquid crystal devices to an active optics using its phase modulation phenomenon.

On the other hand, as DVD devices which need severe aberration correction appeared, study of liquid crystal compensators and their application to DVD pickups have started especially in consumer electronics markets³⁾. Thanked to our long term of experiences in liquid crystal technologies, we have started to mass production of liquid crystal phase compensators for DVD pickups from year of 2000 and have got good reputations on their performance and quality for their cost. In this paper, we will describe characteristics of liquid crystal active optics and their application to optical pickups. Optical properties of liquid crystal GRIN lens for AF applications and liquid crystals with sub-wavelength structures are also presented..

2. OPTICAL PHASE MODULATION BY LIQUID CRYSTALS⁴⁾

Fig. 1(a) shows a sectional diagram of homogeneous-aligned liquid crystal cell ideal for optical phase modulations. Liquid crystals are sandwiched between ITO-coated glass substrates and their molecules are aligned in parallel by surface rubbing methods. For display applications, the molecules are usually twisted-aligned. The liquid crystal molecules have a nature of dielectric anisotropy so that a refractive index between long (n_e) and short (n_o) axis of molecules are different. In the figure, an ITO layer of a left side is divided into two segments and voltages are applied to liquid crystal layers of an upper segment. Then liquid crystal molecules of the upper segment tilt toward a direction of the electric fields. When Y polarized light passes through the cell, an effective refractive index of the upper layer is n_θ ($n_o < n_\theta < n_e$) and the lower layer is n_o . So that an optical pass difference between upper layer and lower layer becomes to $\Delta n (= n_\theta - n_o) d$ which causes an optical phase modulation. As the tilt angle of molecules can be adjusted by the electrical fields, continuous phase modulation can be possible. This means that we can make phase distribution patterns by making voltage distribution patterns using segmented ITO patterns. We can see from the figure that X-polarized light will not be modulated so that we should stack a pair of an orthogonal aligned liquid crystal cell to modulate random polarized light. A liquid crystal cell has a thin film structures so that thickness of an ITO or a rubbing layer is less than 100nm. Further more, an effective index of the molecules changes by electric fields, transmittance of the cell fluctuate. We can reduce this fluctuation to less than 1 % by optimizing their structures.

Fig. 1(b) shows phase modulation characteristics (retardation curve) of the homogeneous liquid crystal cell. The retardation reduces gradually in proportional to applied voltages but never becomes to zero since the molecules being nearby rubbing layers are surface anchored and will not tilt. The retardation also reduces rapidly when temperature exceeds around the point of 60°C. To enlarge the phase modulation capabilities, a cell gap (d) or Δn should be enlarged. But response time of the cell proportional to d^2 . For example, response time is around 30ms at 25°C and 100ms at 0°C in the case of simple operation. Usually, as liquid crystals show an rms voltage response and will be disintegrated by a DC field component, we should use AC voltages for driving the cell.

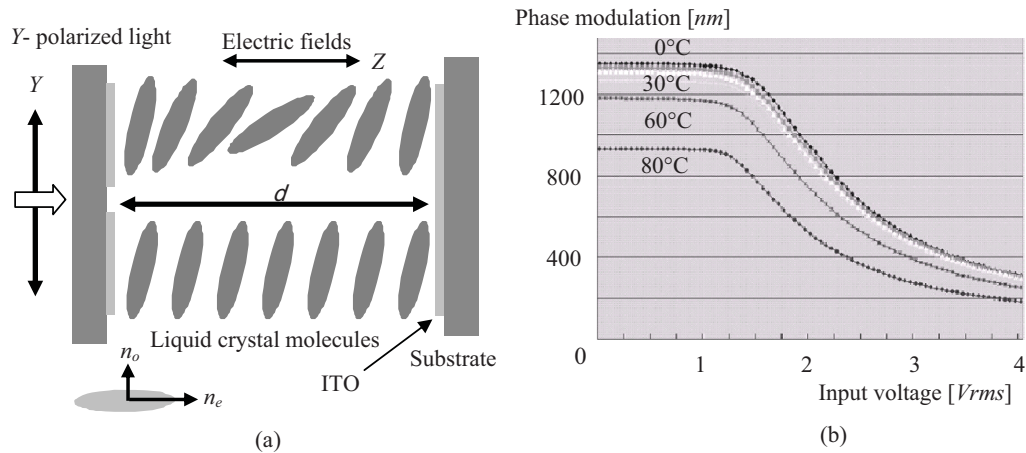


Fig.1 A schematic drawing of a homogeneous aligned liquid crystal cell (a) and its phase modulation characteristics (Retardation curve) (b) $\Delta n (= n_e - n_o) : 0.20, d = 6.8 \mu m$

3. APPLICATION TO OPTICAL PICKUPS

A liquid crystal active optics to compensate aberrations is widely used in DVD drives. Usually, Zernike aberration theorem based on Zernike polynomials is considered for correcting aberrations. Zernike polynomials are an orthogonal expansion normally defined in polar coordinate and its each term represents a waterfront aberration such as Coma, astigmatism or spherical⁵⁾.

Fig. 2 shows a schematic drawing which represents a concept of Coma aberration correction caused by disk tilt. For example, in DVD systems, disk tilt of 1 degree causes a 3'rd order Coma aberration of $100m\lambda rms$. Fig. 2(d) shows a 3'rd order Coma aberration profile in 3D. Fig. 2(a) shows a segmented ITO pattern of a liquid crystal cell which represents a quantized Coma aberration pattern in 2D. To place the liquid crystal cell in an entrance pupil of an objective, we can compensate Coma aberrations dynamically. Fig. 2(b) shows an aberration and its compensation profiles. Fig. 2 (c) shows residual aberrations after compensation. ITO segments are connected with smaller, highly resistive ITO links that produce voltage drops between the larger ITO segments. So voltage distributions can be generated by a simple 3-terminal input. Fig. 2(e) shows a photograph of liquid crystal optics which can compensate both Coma and spherical aberrations. Its segmented ITO pattern on one substrate is for Coma and on the other substrate is for spherical. We can drive each pattern independently according to orthogonality of Zernike aberrations. The thickness of the cell is $0.6mm$ and its flatness is over $\lambda/10$. An aperture diameter is $4mm$. Its response time is less than $700ms$ at $-20^\circ C$ and transmittance is over 95% at $650nm$. We can guarantee to drive the cell under the temperature range from $-20^\circ C$ to $75^\circ C$.

Fig. 3 shows photographs of RF signals (eye patterns) before and after correction of a 3'rd order Coma caused by disk tilt in DVD drives. A tilt angle is one degree and we can see that RF signals become clear after correction. This device is very attractive for a CD-DVD-BD compatible lens since there are no needs to tilt the lens for correcting a Coma.

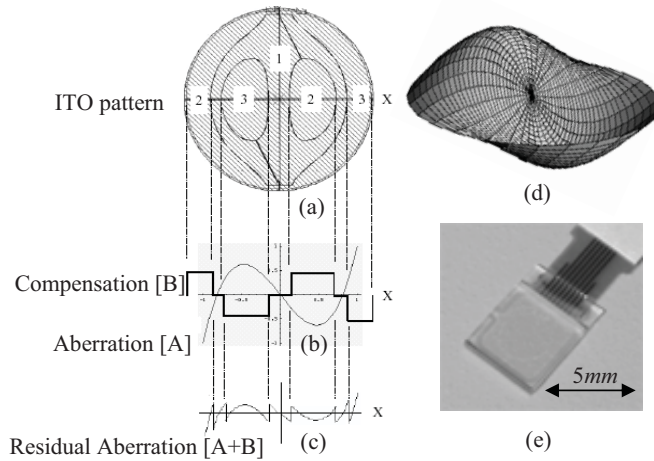


Fig. 2 Concept of Coma correction (a)~(c), a Zernike's Coma profile (d) and a liquid crystal optics (e).

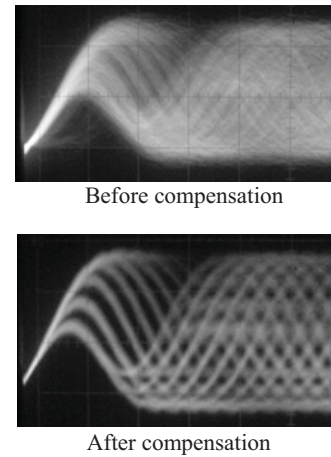


Fig. 3 RF signals under Coma aberration (DVD drive. Disk tilt: 1 deg.)

4. LIQUID CRYSTAL GRIN LENS⁶⁾

Fig. 4 shows a schematic drawing of segmented ITO patterns represent quantized a GRIN (Gradient Index) lens profile. We can change a focal length from $-45cm$ to infinity and infinity to $45cm$ in case of $2.5mm$ diameter, $\Delta n=0.24$ and a ell gap of $20\mu m$. Fig. 5 shows AF images before and after focusing by a liquid crystal GRIN lens. To construct sub-wave length structures inside the liquid crystal optics leads good effects such as polarization free and wavelength selectivity.

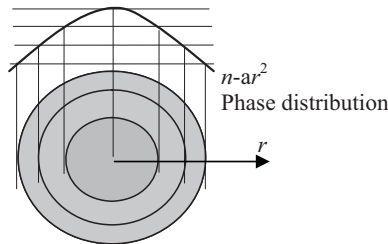


Fig. 4 Segmented ITO patterns represent a quantized GRIN lens

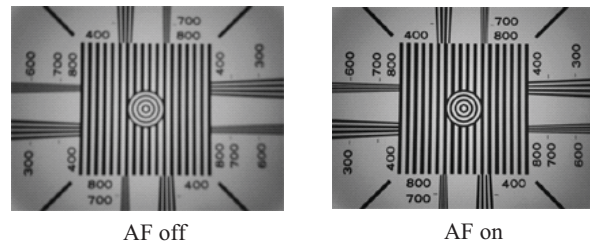


Fig. 5 AF images before and after focusing on by a liquid crystal GRIN lens

REFERENCES

- [1] N. Hashimoto, Japan patent:No. 63-249125(1988).
- [2] N. Hashimoto, K. Kitamura and S. Morokawa, "Real-time holography using high-resolution LCTV-SLM" Proc. SPIE 1461, 291-302 (1991)
- [3] S. Ohtaki, N. Murao, M. Ogasawara and M. Iwasaki, "The Applications of a Liquid Crystal Panel for the 15 Gbyte Optical Disk Systems", Jpn. J. Appl. Phys., 38, 1744-1749 (1999).
- [4] N. Hashimoto: "Optical applications of liquid crystals", ed. L. Vicari, 150-200, CRC press (2003)
- [5] Kim C.-J. and R. Shannon: "Applied Optics and Optical Engineering", ed. R. Shannon and J. Wyant, 193-221, Academic Press (1987)
- [6] N. Hashimoto and M. Kurihara, "Liquid crystal quantized GRIN lens and its application to AF systems" Proc. of 31'st. symposium in optics, pp.53-54(2006) in Japanese.

A Novel Deformable Mirror for Spherical Aberration Compensation

Sunao Aoki¹, Masahiro Yamada and Tamotsu Yamagami
 Storage System Development Division, Video Business Group, Sony Corporation
 5-1-12 Kitashinagawa Shinagawa-ku, Tokyo, 141-0001 Japan

ABSTRACT

By using conventional MEMS processes, we have successfully developed a highly accurate and easily controllable deformable mirror with a simple structure.

Keywords: deformable mirror, spherical aberration, MEMS, silicon wafer

1. INTRODUCTION

In high-density optical disc systems with high-NA objective lenses and multi-layered discs, it is important to reduce spherical aberration (SA). SA compensation devices such as beam expander type devices and liquid crystal type devices have been proposed so far. [1][2] By using our novel deformable mirror, we can reduce the number of components of the optical disc system and can devise a fast response system for SA compensation. Our experimental device compensates for SA by being deformed into the desired shape. The mirror is made of silicon and the mirror size is 3.8×5 mm which is suitable for an optical beam with a diameter of 2.4 mm. A conventional deformable mirror must be controlled by a lot of actuators to realize the desired shape; However with our deformable mirror, we can control the shape of the mirror surface using only one actuator because of the distributed strength on the back of the mirror surface. [3] Therefore, the control circuit for the SA compensator can be simplified and easy control is possible.

2. STRUCTURE AND FABRICATION PROCESSES

Figure 1 shows the backside of the mirror surface. There are seven concentric elliptical patterns, like a stairway on a small hill, which are arranged on the center of the back of the mirror. The shapes of the seven elliptical patterns are tuned carefully so that the optimal strength distribution for SA compensation is realized. The thickness of the thinnest area of the mirror device is $15 \mu\text{m}$, which is located at the outermost elliptical pattern. The shapes of the patterns in the device are elliptical, because the shape of the projected beam on the 45 degree mirror surface is an elliptical shape. Therefore, the deformed profile of the mirror surface is similar to the shape of a spoon. When setting each minor and major axis of the mirror to the X-axis and Y-axis respectively, the Z-axially-deformed ratio must be X:Y=2:1.

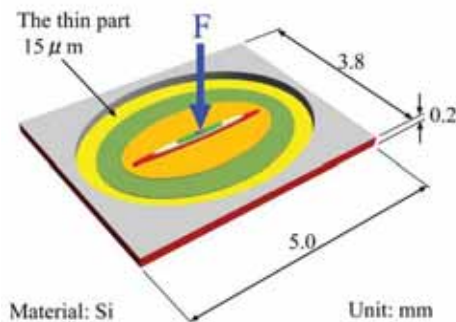


Fig. 1 Backside of mirror.

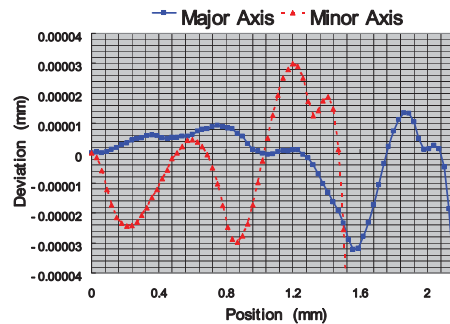


Fig. 2 Deviation from ideal curves.

¹ E-mail address: Sunao.Aoki@jp.sony.com; phone +81-3-5448-2442; fax +81-3-5448-7868

We used the finite-element-method (FEM) to obtain the desired strength distribution pattern. The diameter of each elliptical pattern, the step height of the patterns and the number of steps of the patterns are determined by evaluating the deviation from the ideal shape. Figure 2 shows the deviation of the simulated curve from the ideal curve. In the effective deformed area, both the deviation of the major axis section and the minor axis section are less than 60 nm p-p. The shape accuracy of the deformed mirror surface can be improved by reducing the deviation target as much as possible in the simulation.

The manufacturing processes of an elliptical pattern on the back of the mirror required by the FEM simulation is described as follows: The stair-like elliptical pattern can be realized in high accuracy by using the MEMS processes. The deformable mirror is fabricated on the 4-inch silicon wafer by using conventional photolithography and etching processes, and after the patterning processes the patterned silicon wafer is bonded with a flattened borosilicate glass plate by an anodic bonding method without glue. Finally, the devices are divided into pieces 3.8×5 mm in size. The flattened bonded glass plate keeps the flatness and rigidity of the surrounding area of the mirror, so the symmetry and the reliability of the deformed shape of the mirror can be improved. Figure 3 shows a photograph of the experimental deformable mirrors.

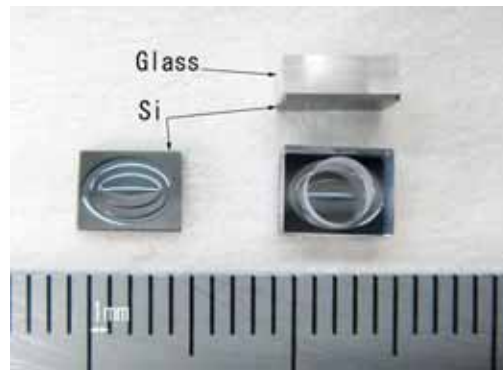


Fig. 3 Photograph of deformable mirror.

3. EXPERIMENTS AND RESULTS

The deformation can be obtained by pushing the center of the back of the mirror out with a piezoelectric actuator. In Figure 4, the measurement results of the actual deformation are shown, measured by a noncontact 3-dimensional measuring instrument scanning the mirror surface at $50 \mu\text{m}$ pitch resolution. The profile of the major axis section and the minor axis section are plotted in Figure 5. The broken line and the dashed-dotted line in the figure are the ideal curves; the residual aberration is caused by the difference between the ideal curve (broken line or dashed-dotted line) and the measured curve (solid line). As for our experimental deformable mirror, the shape error from the ideal shape was within ± 100 nm and the shape symmetry was excellent.

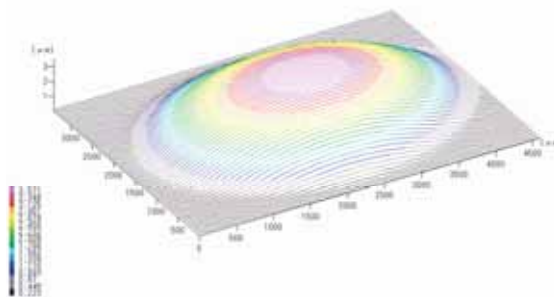


Fig. 4 Deformed shape (3-D).

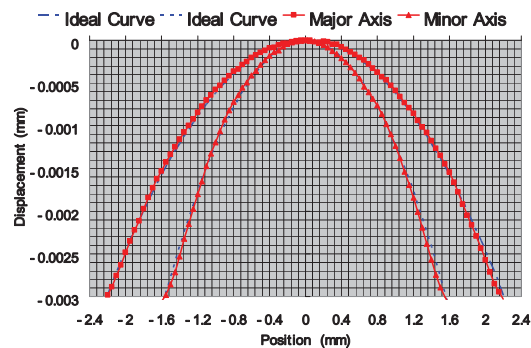


Fig. 5 Profile of mirror surface.

The SA is generated by changing the thickness of the cover glass which is located at the optical path in the experimental apparatus as shown in Figure 6. In Figure 7, we can see that the SA generated is compensated for sufficiently by the deformable mirror.

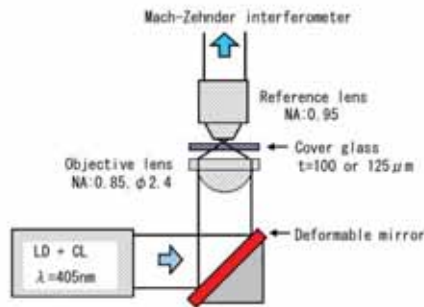


Fig. 6 Evaluation system.

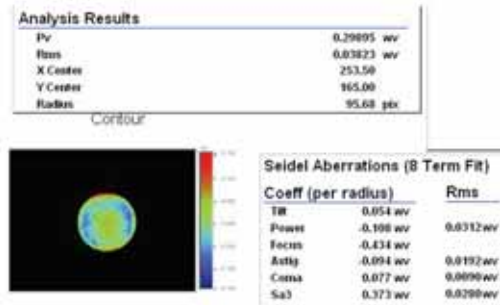


Fig. 7 Contour map of residual aberration.

The increased SA is approximately $0.25 \lambda_{\text{rms}}$, which is caused by a change of the cover glass thickness of $25 \mu\text{m}$. The deformable mirror can compensate for the SA to $0.038 \lambda_{\text{rms}}$ which is the same as that of conventional SA compensators.

4. CONCLUSIONS

We have developed a deformable mirror which has been able to compensate for SA with the novel idea that the deformation can be controlled by arranging the strength distribution on the opposite side of the mirror surface. Our deformable mirror is driven by only one actuator that can compensate for SA of various values by changing its radius of curvature.

REFERENCES

- [1] Isao Ichimura, Fumisada Maeda, Kiyoshi Osato, Kenji Yamamoto, and Yutaka Kasami, "Optical Disk Recording Using a GaN Blue-Violet Laser Diode", *Jpn. J. Appl. Phys.*, **Vol. 39**, pp.891-894, 2000.
- [2] Hironobu Tanase, Gakuji Hashimoto, Kenji Yamamoto, Tomomichi Tanaka, Takashi Nakao, Kotaro Kurokawa, Isao Ichimura, and Kiyoshi Osato, "Dual-Layer-Compatible Optical Head: Integration with a liquid-Crystal Panel", *Jpn. J. Appl. Phys.*, **Vol. 42**, pp.891-894, 2003.
- [3] Lijun Zhu, Pang-Chen Sun, Dirk-Uwe Bartsch, William R. Freeman, and Yeshaiah Fainman, "Adaptive control of a micromachined continuous-membrane deformable mirror for aberration compensation", *Applied Optics*, **Vol. 38**, pp.168-176, 1999.

Single longitudinal mode blue-violet laser diode for data storage

Christophe Moser, Lawrence Ho, Frank Havermeyer

Ondax, Inc. 850 E. Duarte Road, Monrovia, CA 91016, U.S.A

Phone: 626 357 9600 Fax: 626 357 9321

moser@ondax.com, lho@ondax.com, havermeyer@ondax.com

Introduction:

Commercially available blue-violet diodes near 405 nm for Blue-ray and HD-DVD disks lase with multiple longitudinal modes and have thus a sub-millimeter coherence length. Optical data storage technologies requiring coherent interference, such as holographic e.g., will benefit from having a compact blue-violet laser diode source with a long coherence length and some level of wavelength tuning.

Prior approaches, such as external cavities with diffraction gratings [1], have been used to generate single longitudinal mode tunable lasers near 405 nm. Such cavities require a very low reflectivity front facet coating, precise alignment, occupy a volume on the order of several cm³ and are prohibitively expensive for any mass markets. In contrast, we propose and experimentally demonstrate an ultra-short external cavity laser based on reflective volume holographic gratings. The main advantages of this laser is its sub mm³ volume, thermal wavelength tuning and compatibility with the existing high volume automated manufacturing lines of Blue-violet lasers because the external cavity can be passively aligned.

External cavity

It is well known that volume holographic gratings (VHG) have a narrow angular and spectral response [2]. Because of this unique property, a reflection-mode VHG will Bragg-match and strongly diffract only a narrow range of wavelengths anti-parallel to the incident beam. This property makes it possible to implement a compact external cavity laser diode without additional optical components, as shown in 1 [3]. The VHG is placed in the diverging beam of the laser diode. The distance between the VHG and the laser diode facet should be as small as possible. A narrow angular cone whose direction is normal to the grating vector provides the feedback to the laser cavity. Because the divergence of the laser beam is much larger than the cone surrounding the direction normal to the VHG, a misalignment of the VHG (i.e a change in the grating vector direction) by several degrees is automatically compensated by a different cone direction.

For a typical VHG with a thickness of 0.5 mm and Bragg wavelength of 405 nm, the FWHM angle selectivity is a cone subtending 3.3 degrees in air for close to anti-parallel diffraction. The laser diode (LD) emits light with a large divergence angle, dictated by the aperture of the LD's active area. The typical beam divergence of a blue-violet laser diode is 10 degrees in the slow axis and 20 degrees in the fast axis. The ratio of the area subtended by the diffracted cone and the laser beam is approximately 5%. This means that a fraction of 5% of the light contributes to the feedback to the laser. The other 95% of the light in the diverging beam can "escape" the grating without diffracting. The VHG acts as an angularly-spectrally sensitive output coupler.

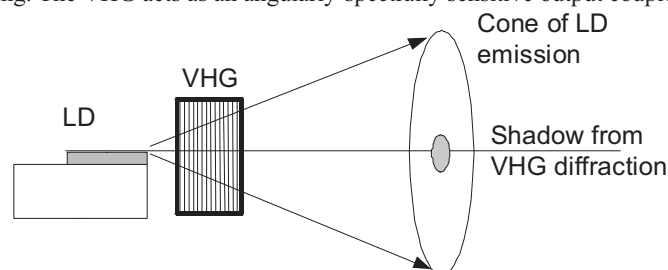


Figure 1: Ultra-short external cavity with a reflective volume holographic grating placed in the diverging beam of the laser diode.

Experimental results:

We manufactured volume holographic gratings in glass with center wavelengths of 403 nm and 407 nm to match the center wavelengths of commercially available blue-violet laser diodes. The spectral bandwidth of the

VHGs was approximately 0.15 nm FWHM. The VHGs were mounted close to the output facet of the laser diode (see fig.1).

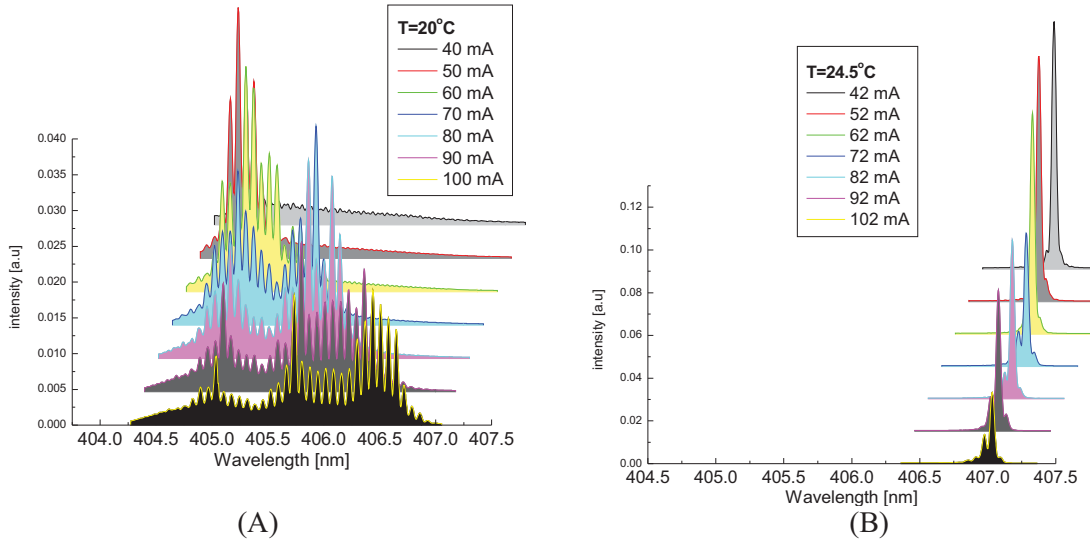


Figure 2: (A) Mode spectrum from the original blue-violet diode at different current level
 (B) Mode spectrum from the same blue-violet diode laser with feedback from a volume holographic grating mounted according to figure 1.

Figure 2 left shows the spectrum of the original blue-violet laser diode as a function of operating current. The threshold for the diode is 38 mA. A spectral resolution of 0.01 nm was achieved with a home-built spectrometer based on a rotating thick volume holographic grating. The diode is multimode longitudinal at all currents with a mode spacing of approximately 0.035 nm.

In contrast, after mounting the VHG, the spectrum of the diode is reduced to single mode for operating current below 65 mA (20 mW optical power) and four to five modes above 65 mA. The maximum number of modes oscillating in the cavity is limited by the bandwidth of the VHG (0.15 nm). We plan to use thicker VHGs to reduce the bandwidth and thus increase the maximum optical power for single longitudinal mode operation.

Single mode operation in the wavelength locked range was confirmed by the reading of a wavelength meter (Coherent Wavemaster, 1 pm resolution).

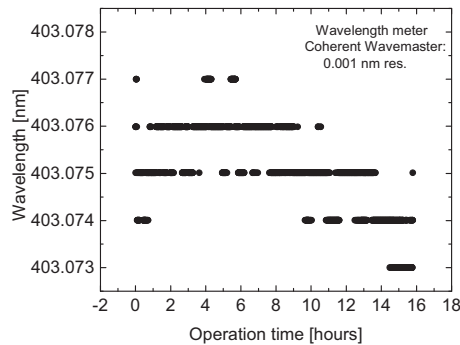


Figure 3: Wavelength stability of a single mode blue-violet laser wavelength stabilized with a volume holographic grating centered at 403 nm.

A second diode with 10 mW power was assembled with a 403 nm VHG. The laser diode was held at a constant temperature in a Thorlabs temperature and current controller. The laser diode had a single longitudinal mode within the locked temperature range. The wavelength stability was measured with a wavelength meter. The result is shown in figure 3. A 4 pm wavelength shift was observed during 16 hours of operation at constant current.

A michelson interferometer was used to measure the coherence length of the laser diode. The visibility of the interference fringes confirmed that the coherence length of the laser diode was larger than 1 meter.

The wavelength of the locked laser diode can be tuned by thermally tuning the semi-conductor laser and the VHGs independently. A schematic of a proposed implementation is shown in figure 4. Following the basic implementation of the fixed wavelength laser, the VHG is mounted against a low thermal conductor, itself mounted on the laser diode heatsink. Current flowing through the deposited metal on the side of the VHG provides heating and thus wavelength tuning. The small size of the VHG (0.2 mm³) is expected to provide relatively fast tuning and consume low electrical power.

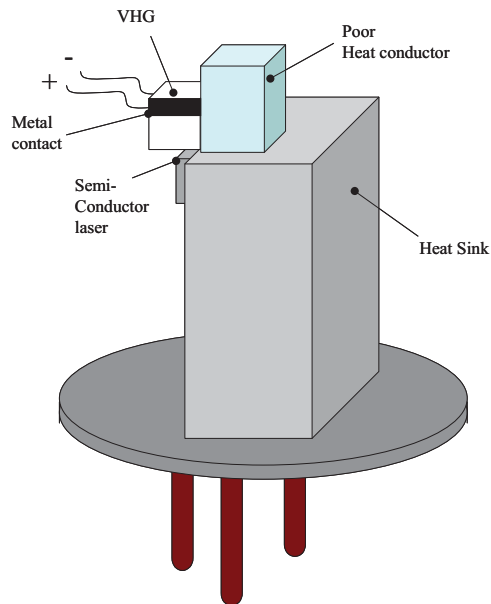


Figure 4: Schematic of a TO-can laser with wavelength tuning by heating the small VHG element.

We have shown that single longitudinal mode performance with a coherence length of over 1 meter can be obtained from a commercially available blue-violet laser with a passively aligned reflective volume holographic grating placed in the diverging beam of the laser diode. The ultra-short external cavity fits inside a TO-can 5.6 mm package. A method for tuning the wavelength of the laser is presented

References:

- [1] L. Hildebrandt et al, "Anti-reflection coated blue GaN laser diodes in an external cavity and Doppler free indium absorption spectroscopy," *Applied Optics*, 42 (12) : 2110-2118, 2003
- [2] H. Kogelnik, "Coupled wave theory for thick hologram gratings," *Bell Syst. Tech. J.*, 48:2909-2947, 1969.
- [3] G. Steckman et. al "Volume Holographic grating wavelength stabilized laser diodes", *IEEE J. Quantum Electronics*, 13 (3): 672: 678, 2007

Designs and tolerances of two-element NA 0.8 objective lenses for page-based holographic data storage systems

Yuzuru Takashima and Lambertus Hesselink
Department of Electrical Engineering, Stanford University
420 Via Palou Mall, Stanford, California 94305 USA

ABSTRACT

A two-element aspheric objective lens having an NA of 0.8 has been designed. The objective employs both an object and a pupil imaging in a diffraction limited manner which enables large field of view imaging as well as high NA focusing. With removable media in mind, tolerances on pixel miss-registration and drop in diffraction efficiencies of holograms have been related to lens design tolerances such as offence against the sine condition and geometrical spot size in root mean square of the object and reference beams. Within the tolerance, the design demonstrates the highest NA in the two-element configurations and long working distance of 20 % of the focal length which provides simple lens design solutions for both the page-based holographic data storages having removable media and holographic and surface recording compatible systems.

Keywords: Lens design, optical tolerance, diffraction efficiency, coupled wave theory, removable media

1. INTRODUCTION

A page-based holographic data storage system (HDSS) has demonstrated excellent performance such as a high recording density of more than one hundred bits/ μm^2 which leads to a hundred Giga-bytes capacity range per 120mm diameter disk having a very high readout data transfer rate of Gbytes/sec. The recording density of the page-based HDSS, as well as the tilt tolerance of recording media, scales quadratically with the NA of the optics, and the data transfer rate scales NA to the forth power. Therefore, it is preferable to have an objective having a high NA. Recently, an optical implementation such that an object and reference beam share single objective lens has been proposed and are widely adopted due to its simple implementation and robustness to environmental changes. The implementation in general requires high NA objectives to accommodate the reference beam within the objective lens [1-3].

In contrast to surface recording systems, few analytical researches on lens designs have been done for HDSS, except for spherical optics [4]. Although, many lens systems have been specially designed, it is not known what the minimum implementations having small number of elements and a large imaging NA are. Moreover, optical tolerance criteria of the objectives for HDSS has been seldom addressed in contrast to that of the Fourier transform lenses [5]. In the paper, we have analyzed how optical design tolerances such as offence against sine condition and aberrations of object and reference beams affect performances of HDSS such as pixel miss-registration, diffraction efficiency of holograms and energy spillover into adjacent detector pixels. Based on the tolerance analysis, we have designed high NA two-element objectives.

2. OPTICAL TOLERANCES OF FOR MEDIA-INTERCHANGEABLE SYSTEMS

2.1 Offence against the sine condition

The offence against the sine condition (OSC) is defined by, $OSC = f_i/\sin \theta_i - h_i$, where f_i is the focal length, θ is the incident angle with respect to the optical axis at the Fourier plane and h is the height at the SLM plane (Fig.1). The subscript i takes 1 or 2 for lens1 and lens 2, respectively. A ray intersects to a sphere having radius f_1 and $-f_2$, which are deduced to the second principal point H' of the lens 1 and the first principal point H of the lens 2 in the paraxial region, respectively. For the both systems, the displacement of the pixel image at the detector plane Δh is estimated by,

$$\Delta h = h_i \{ (OSC_1 - OSC_2) + (f_1 - f_2) \} / (OSC_1 + f_1) \sim NA (OSC_1 - OSC_2), \quad (1)$$

where $NA = \sin(\theta) = h_1/f_1$ and we assumed $f_1 = f_2 = f$ and $OSC_1 \ll f$. Assuming OSC_1 and OSC_2 are independent random variables, tolerance of the $OSC_{1,2}$ are given by $\Delta h / (2^{1/2} NA)$, where Δh is the pixel shift tolerance.

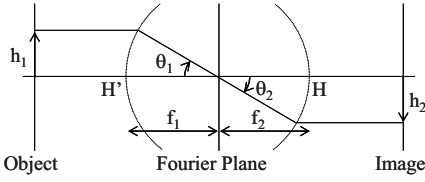


Fig. 1. Definition of quantities for pixel shift analysis.

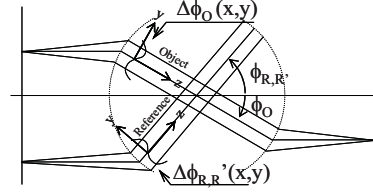


Fig. 2. Definition of quantities for diffraction efficiency drop analysis.

2.2 Drop of Diffraction efficiencies

Upon reconstruction of the recorded holograms, the relative diffraction efficiency η of thick hologram is given by $\eta = \text{sinc}^2(\chi)$, where $\text{sinc}(\chi) = \sin(\chi)/\chi$. χ is a Bragg detuning parameter, and is given by,

$$\chi = (\pi / \lambda) \Delta \theta d \sin 2(\theta_R - \psi) / \cos(\theta_R), \quad (2)$$

where λ is wavelength, d is a thickness of the hologram, θ_R and ψ are the incident angle of the reference beam and the slant angle of the grating with respect to the normal of the recording medium, respectively, and $\Delta\theta$ is deference between the recording reference and reconstructing reference beam [6]. We assume that the beams are aberrated but the wave fronts of the beams keep their shape during the propagation through the recording medium. We express aberrations of the recording object, recording reference and reconstructing reference beam in terms of local tilt of the wave front with respect to the reference sphere, and are given by $\Delta\phi_O(x,y)$, $\Delta\phi_R(x,y)$ and $\Delta\phi_{R'}(x,y)$, respectively, where (x,y) is transverse locations of the hologram in Cartesian coordinate system whose z axis is taken along the chief rays which angles with respect to the optical axis are ϕ_O , ϕ_R and $\phi_{R'}$, respectively (Fig. 2). It can be shown that relative diffraction efficiency drop due to aberrations of the reference and object beams are related to geometrical spot size in rms, and is given by,

$$\Delta\eta \approx \frac{A(\phi_O, \phi_R)^2}{48 f_{ideal}^2} \left\{ \frac{\cos^4 \phi_O}{n^2 - \sin^2 \phi_O} + 5 \frac{\cos^4 \phi_R}{n^2 - \sin^2 \phi_R} \right\} D_{rms}^2, \quad \text{where } A(\phi_O, \phi_R) = \frac{\pi d \sin \phi_R \sqrt{n^2 - \sin^2 \phi_O} - \sin \phi_O \sqrt{n^2 - \sin^2 \phi_R}}{\lambda_0 \sqrt{n^2 - \sin^2 \phi_R}}. \quad (3)$$

D_{rms} is a geometrical spot size in rms evaluated by an ideal lens having a focal length of f_{ideal} . We assume $D_{rms,O,R,R'}$ have the same value but a shape of the wave fronts of the beams are uncorrelated. Eqn. (3) provides aberration tolerance of the recording object, reference and reconstructing reference beam for a given tolerance of drop in diffraction efficiency, $\Delta\eta$.

2.3 Energy spill over into adjacent pixels due to blurring of image

A blurred pixel image causes additional energy spillover into adjacent pixels in addition to it due to the OSC and distortion, . The signal level detected by single pixel with aberrated imaging normalized by the signal level of the un-aberrated imaging is approximated by the Strehl intensity ratio, $1 - 4\pi\sigma^2/\lambda^2$, where σ is wave front aberration in rms [7].

2.4 Numerical examples of tolerances

Depending on the optical architecture, appropriate tolerances need to be taken into account during lens designs. For the optical architecture having auxiliary optics to deliver un-aberrated reference beam and readjustment of its angle upon reconstruction, the OSC and wave front aberration in rms of the object beam are relevant. The condition of $OSC_{1,2} < \Delta h / (2^{1/2} NA)$, gives $OSC < 0.0014$ for $NA = 0.5$ and $\Delta h = 1 \mu\text{m}$, and $\sigma < 0.044 \lambda$ at the Fourier plane is needed to restrict the energy spill over due to the blurring less than 10%. For the optical architecture such as the reference and object beams share the same objective lens, the tolerance of wave front aberrations expressed in D_{rms} at the Fourier plane is also relevant in addition to the OSC and wave front aberrations. Analysis shows that using an ideal lens of $f_i = 1\text{mm}$, $D_{rms} \sim 1 \mu\text{m}$ is required for the system with $\Delta\eta < 0.2$. The most severe degradation in diffraction efficiency happens at large angle between object and reference beam, or at the extreme field point opposite to the reference beam fields. The same criterion on OSC and σ as the previous case are applied for the imaging part of the system.

3. LENS DESIGN METHOD AND RESULTS

Aberration analysis of HDSS objective lenses shows that five aberrations such as spherical aberration and coma for focusing and the spherical aberration, coma and astigmatism for imaging need to be corrected for under a proper choice of Petzval curvature. It is known that such five aberrations are independent in the 4-f configuration in the third-order

region regime and therefore, optical system requires at least five degree of freedom to correct for all of the five aberrations [8]. Two-element systems have seven first order quantities such as four powers of surfaces and three thicknesses among which three parameters are determined by conditions on focal length, working distance and Petzval curvature. Therefore, 1st order design space is parameterized by four first order quantities. We used total power, thickness and power of one of two surfaces of the lens element II (pII, p3 and t, Fig. 4) as well as Petzval curvature as primary parameters, since manufacturability of the element II is of concern. Within the first order parameter space, we have evaluated a target function which is consisting of object and pupil aberrations using an expression of wave front error in rms containing up to fifth-order aberrations coefficients. The target function is minimized within the first-order parameter space. We found that the solutions exist within a narrow range of the first order parameter space, pII and p3 need to be about 0.5 and -0.5~1, respectively for unity system power. NA 0.8 solutions are derived from the fifth-order solution by ray-trace based optimization using higher order aspheric coefficients. Figure 3 and Table 1 show the design results for different glass materials. Design wavelength is 532 nm, the total power is unity and object NA is 0.035. In the designs, both object and pupil imaging are employed in a diffraction limited manner and the sign conditions are satisfied within the tolerance specified in the previous section.

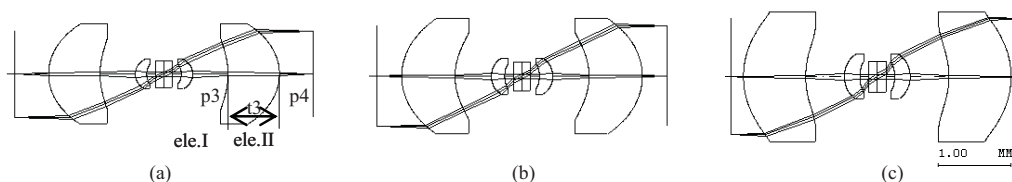


Fig. 3. Design results for (a) $N = 1.59219$, (b) $N = 1.85078$ and (c) $N = 2.15858$.

NA_{pupil}	N	PTZ	$\sigma_{pupil} \lambda$	$\sigma_{image} \lambda$	OSC
0.7	1.59219	0.416	0.0046	0.0036	0.0011
0.75	1.85078	0.337	0.0079	0.0041	0.0012
0.8	2.15858	0.333	0.0066	0.0042	0.0012

4. CONCLUSIONS

Optical tolerances such as offence against the sine condition, geometrical spot size in rms and wave front error in rms have been analytically related to pixel miss registrations, drop in diffraction efficiencies and signal levels with media interchangeable systems in mind. Based on the tolerances, objective lenses which employ both imaging and focusing with NA of up 0.8 are designed in two-element configurations for the page-based holographic data storages. The designs provide simple solutions for both the page-based holographic data storage systems having removable media and holographic and surface recording compatible systems.

REFERENCES

- [1] S. S. Orlov, W. Phillips, E. Bjornson, Y. Takashima, P. Sundaram, L. Hesselink, R. Okas, D. Kwan and R. Snyder, "High-transfer-rate high-capacity holographic disk data-storage system," *Appl. Opt.*, **43**, 4902-4914 (2004).
- [2] R. R. McLeod, A. J. Daiber, M. E. McDonald, T. L. Robertson, T. Slagle, S. L. Sochava and L. Hesselink, "Microholographic multilayer optical disk data storage," *Appl. Opt.*, **44**, 3197-3207 (2005).
- [3] Y. Takashima and L. Hesselink, "Media tilt tolerance of bit-based and page-based holographic storage systems," *Opt. Lett.*, **31**, 1513-1515 (2006).
- [4] M. A. Neifeld and M. McDonald, "Lens design issues impacting page access to volume optical media," *Opt. Commun.*, **120**, 8-14 (1995).
- [5] D. Casasent and T. Luu, "Phase error model for simple Fourier transform lenses," *Appl. Opt.*, **17**, 1701-1708 (1978).
- [6] H. Kogelnik, "Coupled wave theory for thick hologram gratings," *The Bell Sys. Tech. Journal*, **48**, 2909-2947 (1969).
- [7] Y. Takashima and L. Hesselink, "En-squared power based optical design for holographic storage systems," *Proc. SPIE*, **6342**, 63421B (2006).
- [8] Y. Matsui, S. Minami, "Fourier transform lens system," USP 4,189,214, (1980).

The Challenges of Heat Assisted Magnetic Recording Head Integration

Cal Hardie¹, Duane Karns, William Challener, Nils Gokemeijer, Tim Rausch, Michael Seigler, Edward Gage

Seagate Technology, 7801 Computer Ave, Bloomington, MN, 55435

¹Phone: (952)402-8393

¹E-mail: cal.hardie@seagate.com

ABSTRACT

The explosion of digital content has created a global demand for storage products that will only increase as the world becomes more digitally oriented and connected. This ever increasing demand for storage capacity has placed significant challenges on the magnetic recording industry. To extend recording densities to beyond 1Tb/in², the industry must find solutions to the superparamagnetic limit which imposes a signal-to-noise ratio, thermal stability, and writability tradeoff. Heat assisted magnetic recording (HAMR) is a technology for achieving these high areal densities. A successful integration of the HAMR technology will be shown. This integration process is compatible with existing thin film magnetic recording fabrication which includes thin film wafer process, slider lapping, and head/gimbal assembly. A demonstration of 200Gb/in² areal density will be shown as well as a path to increase the areal density capability of HAMR using Near Field Transducer (NFT) technology.

INTRODUCTION

HAMR provides a new degree of freedom to help solve the trilemma of magnetic recording media signal-to-noise ratio, thermal stability and writability. By temporarily heating the media during the recording process, the media magnetic strength can be lowered below the available applied magnetic write field. The heated region is then rapidly cooled in the presence of the applied head field whose orientation encodes the recording data. A sketch illustrating the HAMR writing process is shown in Figure 1.

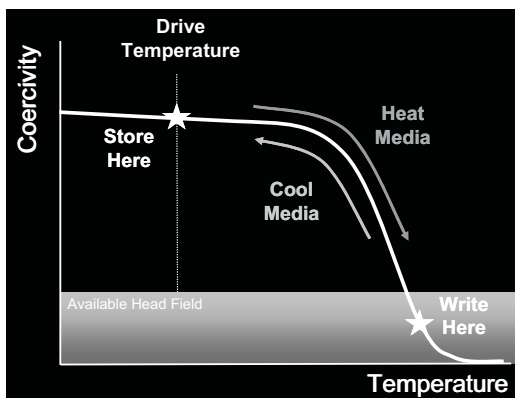


Figure 1

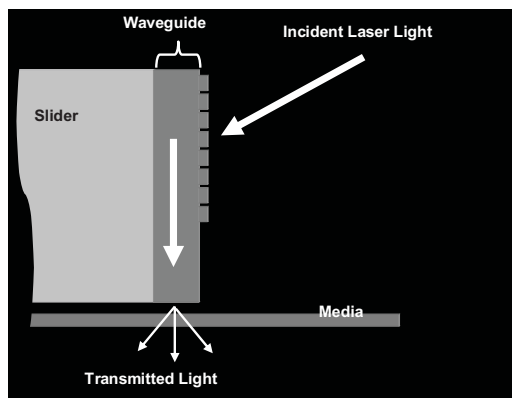


Figure 2

INTEGRATED HAMR HEAD DESIGN

With a focused laser beam heating the media, the write process is similar to magneto-optical recording, but in a HAMR system, the readout is performed with an integrated magneto-resistive element. The slider fabrication, air bearing, and the magneto-resistive reader are all borrowed from today's hard disc drive industry. A schematic diagram of a HAMR recording system is shown in Figure 2.

A waveguide is shaped to form a planar solid immersion mirror (PSIM), which focuses the light onto the recording medium. A grating for coupling light into the waveguide can be formed in the core of the waveguide using standard lithography and vacuum etching. The optical spot locally heats the media before it passes under the writing magnetic pole. See Figure 3.

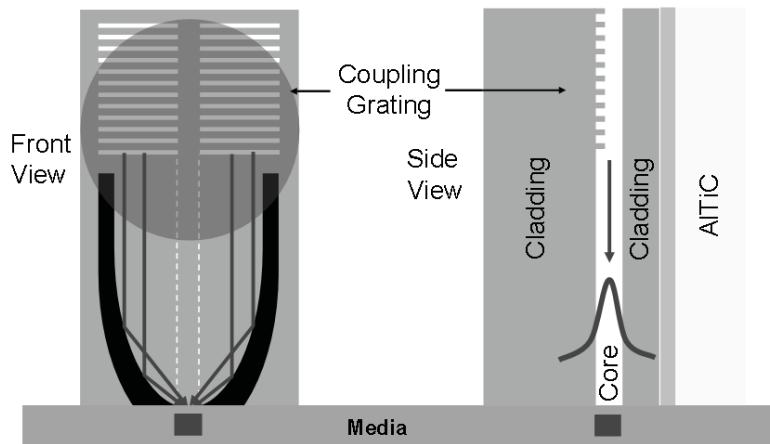


Figure 3

A considerable number of these heads have been built into sliders and lapped such that the focal point of the PSIM was located at the air bearing surface. Figure 4 illustrates cross-sections of finished HAMR sliders. Figure 5a shows an air bearing surface (ABS) view of the HAMR head, while 5b shows the focused light at the ABS after coupling into the waveguide. These HAMR heads were then fabricated into head gimbal assemblies (HGAs) for HAMR spin-stand testing.

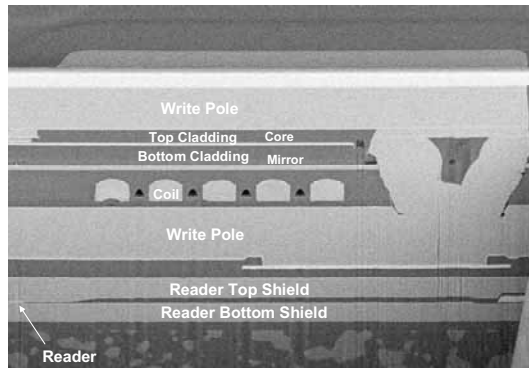


Figure 4 – Cross section of the HAMR slider

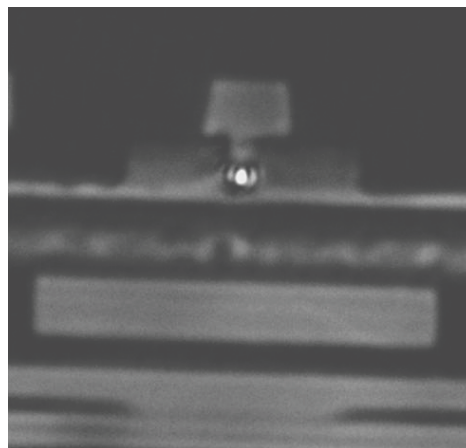
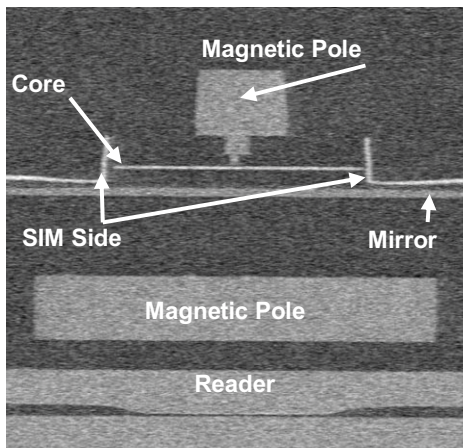


Figure 5 - An air bearing view of the HAMR slider a) SEM and b) optical with an optical aperture and the blue light spot shown

AREAL DENSITY DEMONSTRATION

The fully integrated HAMR HGAs were then tested on specially designed HAMR spin-stand that allows for full operation of the magnetic read and write head while the 488nm laser light is coupled into the waveguide and the slider is flying over the media at 15m/s.

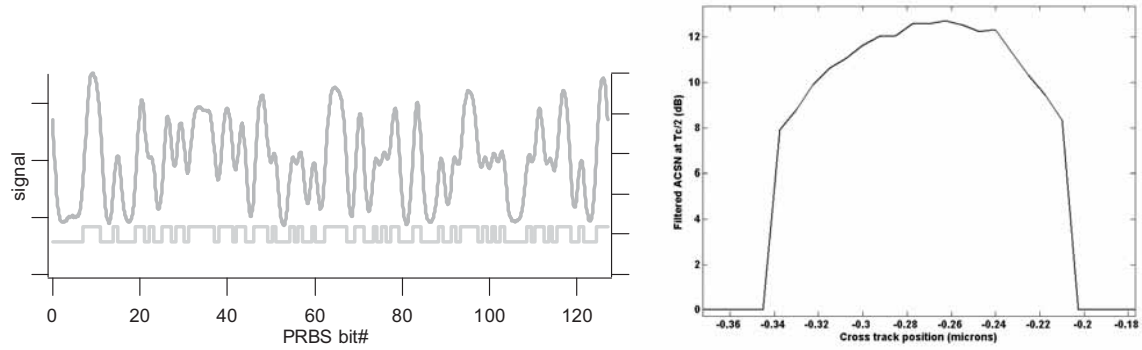


Figure 6 – a) Readback signal in the time domain for a HAMR head, b) ACSN cross-track profile

The data track was written by the fully integrated HAMR head and the read back was done with the reader on the same head. Figure 6a show the read back signal in the time domain for a fully integrated HAMR head for a 40Mhz tone and a pseudorandom bit sequence. An auto correlated signal-to-noise (ACSN) cross-track profile was then taken and is shown in Figure 6b. The calculated areal density of this HAMR demonstration is approximately 200Gb/in². The significance of this demonstration is that it will enable the exploration of HAMR recording physics studies including understanding of media exchange, composite media designs, thermal management, thermal/magnetic gradients, head disk interface robustness, and adjacent track aging.

HAMR EXTENDABILITY TO HIGH AREAL DENSITIES

In order to insure the extendibility of the HAMR technology to higher areal densities, a near field transducer (NFT) must be integrated into the optical portion of the device to focus the optical spot sizes to less than $\lambda/4$. Several NFT design exist in the literature and are shown in Figure 7. The focusing of the NFT is shown numerically in Figure 8.

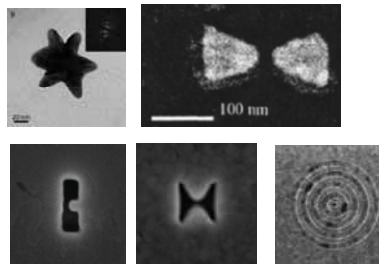


Figure 7

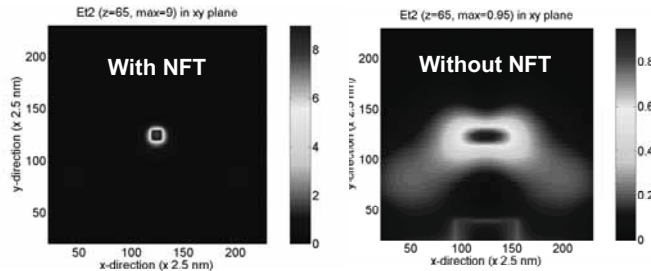


Figure 8

CONCLUSIONS

A fully integrated HAMR head design has been introduced. A light delivery path has been outlined. This design has been built into sliders and HGAs. Several HAMR heads have been tested for areal density capability. A cross-track profile for this fully integrated HAMR head shows an ACSN approximated areal density of 200Gb/in².

HAMR head with spot size converter and triangular aperture

Masakazu Hirata*, Manabu Oumi, Majung Park
Seiko Instruments Inc., 563 Takatsuka-Shinden, Matsudo-shi, Chiba 270-2222, Japan

ABSTRACT

Heat assisted magnetic recording (HAMR) technology needs integration of near-field element and magnetic pole. We proposed HAMR head with spot size converter (SSC) and triangular aperture for this requirement. It has high optical throughput with integrated optics and strong affinity to conventional HDD head. SSC, triangular aperture and mirror are formed in one structure so that there is no possibility to have optical loss caused by optical coupling of each component or misalignment. Simulation result of isolated SSC shows that it condensed spot to be $2.2 \times 1.8 \mu\text{m}$ (FWHM).

Keywords: HAMR, near field, hybrid recording, spot size converter, triangular aperture

1. INTRODUCTION

Heat assisted magnetic recording (HAMR) has been proposed as a future recording technology to achieve a density over 1 Tb/inch^2 . We think that the key matters for HAMR head are the following three points.

- (1) Near-field (NF) element as a micro heat generator
- (2) Light guide structure
- (3) Integrating near-field element and magnetic pole

We have focused on the key (1) and (2) so far. We have already proposed a triangular aperture as NF element and a light guide structure using horizontally placed optical fiber. In the previous study computer simulation showed that the triangular aperture has a NF peak on the edge perpendicular to the polarization of the incident light. Therefore it achieves less than 20 nm spot size (FWHM) localized NF in the direction of the polarization, which is not limited by the aperture size^[1]. Scanning near-field optical microscope and contact slider experiments also show that the triangular aperture is effective for localizing NF^[2]. Using light guide structure with optical fiber and micro optics can achieve a thin and small ($1.6 \times 1.6 \times 0.7 \text{ mm}$) NF flying head. The head was fabricated. Signal readout was demonstrated in flying operation^[1].

Concerning (3), distance between magnetic field and optical spot is important for HAMR. They must be very close to each other. Research of integrated structure of magnetic pole and optical spot is scarce yet. For example of the integrated structure, Gage et al. proposed integrated structure with the magnetic pole and planner SIM (solid immersion mirror) to concentrate the light^[3]. Miyanishi et al. proposed SMASH (surface plasmon and magnetic field applicable synchronously hybridized) head^[4] that has curved metallic wire and ledge structure. The wire generates magnetic field. NF is localized on the ledge structure.

In this paper, we will propose the integrated structure with the triangular aperture, the other optics and the magnetic pole.

2. HAMR HEAD WITH SPOT SIZE CONVERTER

Spot size converter (SSC) is well-known technology in optical telecommunication field. It makes the spot from an optical fiber smaller, and makes optical components connected to the fiber (ex. AWG (Arrayed Waveguide Grating)) smaller and more integrated. Nishida et al. have already proposed HAMR head with the SSC made of Si^[5].

Figure 1 shows schematics of our proposed HAMR head with SSC and triangular aperture. The SSC attaches to the existing magnetic writer of HDD. SSC core and clad are made of quartz and have different refractive indexes by doping. Light, which can have visible wavelength, propagates through the core. The core has triangular cross section that is reduced as closer to the magnetic pole, and is sharp-pointed. This triangular shape is formed by reactive ion etching. The sharp end of the core is covered with metallic film and NF enhanced film to be the triangular aperture. The other end is inclined to be mirror and is attached to optical fiber.

*masakazu.hirata@sii.co.jp; phone +81-47-891-2131

Incident light from the optical fiber is reflected at the mirror, condensed by the SSC, and NF is emerged by the triangular aperture very close to the magnetic pole.

Au, Ag, Al etc. can be chosen for the NF enhance film depending on wavelength of incident light and NF coupling with medium. When linearly polarized light perpendicular to the film is introduced, NF is localized at the border of triangular aperture and the NF enhance film.

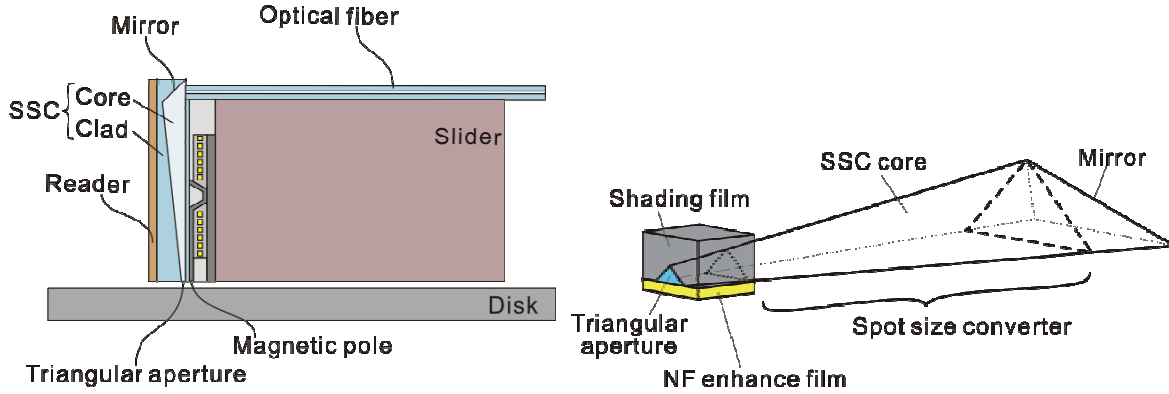


Fig. 1. HAMR head with spot size converter (SSC) and triangular aperture. (left)Schematics of the head structure (right)Enlarged view of SSC core and triangular aperture

Advantages of this structure are as follows.

(1) High optical throughput with integrated optics. : SSC, triangular aperture and mirror are formed in one structure so that there is no possibility to have optical loss caused by optical coupling of each component or misalignment. Since NF element becomes very small and assembling optics becomes difficult, this advantage will be important for practical use of HAMR technology.

(2) Strong affinity to HDD head. : The proposed head structure preserves conventional HDD head structure and just adds SSC. Concerning fabrication, the SSC is made by photolithography with reactive ion etching. We think it has strong affinity to conventional HDD head in both aspects of structure and fabrication.

It can also use optical fiber to introduce light for laser. We have proposed this technology and already demonstrated flying and light introduction.

3. SIMULATION OF SPOT SIZE CONVERTER

The behavior of isolated SSC was calculated. Figure 2 shows SSC core of the simulation model which has 10- μm -wide and 5- μm -high triangular entrance, and 3- μm -wide and 1.5- μm -high triangular exit. The length of the SSC is 300 μm . The z position 0 μm is the entrance of the SSC, and 300 μm is the exit. Refractive index of the clad is 1.45. Relative index differences are 1.5, 3.8, 6.9 and 10.3%. The wavelength of the light is 640 μm . The light is introduced by optical fiber whose mode field diameter (MFD) is 4.4 μm .

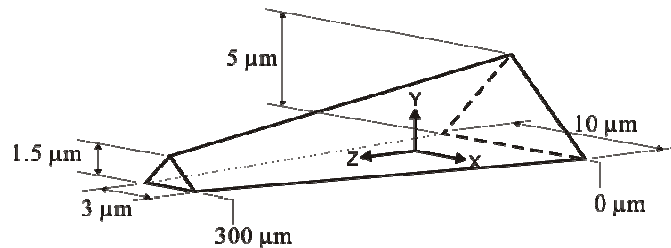


Fig. 2. Simulation model of SSC core

Figure 3 shows the result by BPM (Beam Propagation Method). Spot size becomes smaller with the SSC. Although spot size is smaller as the relative index difference is bigger, you can find each model with different relative index difference works as SSC. When relative index difference is 1.5%, the spot size at the exit is $2.2 \times 1.8 \mu\text{m}$ (FWHM). This result is for X polarization, and the result for Y polarization is almost same. In our previous study, introduced light to the triangular aperture was condensed by lens. Its focusing efficiency within $\phi 3 \mu\text{m}$ was 55~80%. It is estimated that spot size by SSC in front of the aperture is as almost same as the one by the lens, and therefore it is expected that the triangular aperture will work as well.

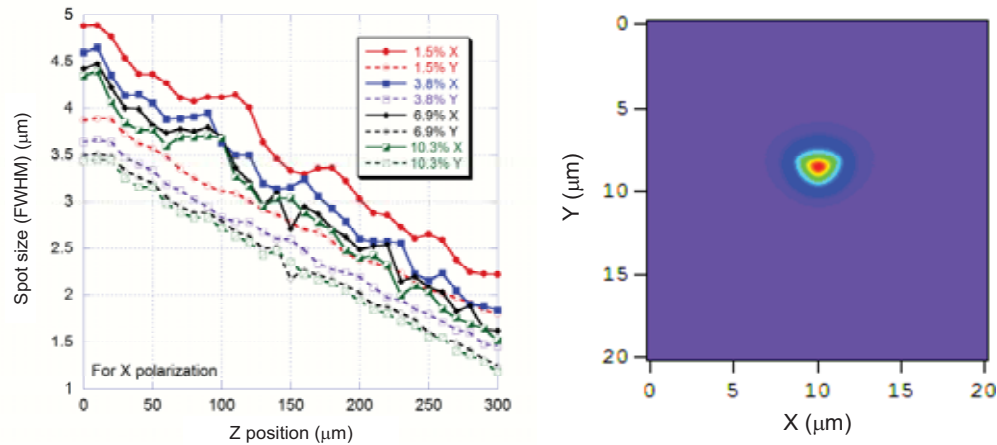


Fig. 3. Simulation result of SSC. (left)Spot size vs z position (right)Spot at $z=300\mu\text{m}$

4. CONCLUSION

HAMR head with SSC is proposed. It has high optical throughput with integrated optics and strong affinity to conventional HDD head. Simulation result of isolated SSC shows that it condensed spot to be $2.2 \times 1.8 \mu\text{m}$ (FWHM) when relative index difference is 1.5%.

ACKNOWLEDGEMENTS

A part of this paper belongs to "Terabyte optical storage technology" project that OITDA contracted with The Ministry of Economy Trade and Industry of Japan (METI) in 2002 and contracted with The New Energy and Industrial Technology Development Organization (NEDO) since 2003 based on funds provided from METI.

REFERENCES

- [1] M.Hirata, M.Park, M.Oumi, K.Nakajima, and T.Ohkubo, "Near-Field Optical Flying Head with A Triangular Aperture", *J.Magn.Soc.Jpn.*, 32, 158-161 (2008).
- [2] M. Hirata, M. Oumi, K. Shibata, K. Nakajima, and T. Ohkubo, "Triangular Aperture as Near-Field Element for High-Density Storage," *IEICE Trans. Electron.*, E90-C, 1, 102-109 (2007).
- [3] E. C. Gage, C. Peng, T. Rausch, W. Challener, B. Mihalcea, M. Seigler, K. Pelhos, and T. McDaniel : MORIS 2006 Workshop, (2006).
- [4] S. Miyanishi, N. Iketani, K. Takayama, K. Innami, I. Suzuki, T. Kitazawa, Y. Ogimoto, Y. Murakami, K. Kojima, A. takahashi: *IEEE Trans. Magn.*, 41, 10, 2817 (2005).
- [5] N. Nishida, H. Hatano, K. Sekine, K. Konno, M. Saka, and H. Ueda, "Novel TAMR head using focusing waveguide," MORIS 2007 Workshop, (2007)

SESSION TuP: Poster Session II

Queen's Ballroom
2:00 to 3:30 pm

Tuviah Ed Schlesinger, Carnegie Mellon Univ.
Yoshimi Tomita, Pioneer Corp. (Japan)
Yoshimasa Kawata, Shizuoka Univ. (Japan)

Misalignment compensation and equalization for holographic data storage

Haksun Kim*^a, Pilsang Yoon^{a,b}, Jooyoun Park^a, Heungsang Jung^a, Gwitae Park^b

^aDigital Media Lab., Daewoo Electronics Corp., 543, Dangjeong, Gunpo, Gyeonggi, Korea 435-733;

^bDepartment of Electrical Engineering, Korea Univ./5-1, Anam., Sungbuk, Seoul, Korea 136-701

ABSTRACT

In this paper, a misalignment compensation and equalization for holographic data storage are developed and evaluated. The proposed compensation algorithm removes a known contribution for pixel misregistration. The equalization technique helps to reduce the errors which are created due to bright 'Off' and dark 'On' pixels. Experimental results are shown to verify the proposed algorithm's effectiveness.

Keywords: Holographic digital data storage, misalignment compensation, equalization, 2D modulation code

1. INTRODUCTION

The channel of Holographic Digital Data Storage (HDDS) has intrinsic noises such as Inter Symbol Interference (ISI), non-uniform intensity distribution and Additive White Gaussian Noise (AWGN) due to optical and electrical components. The retrieved images from HDDS system usually have very low Signal-to-Noise Ratio (SNR). Therefore, it requires an effective signal processing algorithm for reliable data readout over noisy HDDS channel. [1] The compensation scheme for the error due to misalignment of data image at detector array is proposed in this paper. To improve SNR of the compensated data image, we have also developed equalization method based on 2D modulation code. The experiment results reveal that the proposed misalignment compensation and 2D equalization correctly recover the original data pattern from the corrupted data page.

2. MISALIGNMENT COMPENSATION AND EQUALIZATION

2.1 Compensation scheme for the misaligned data image

To determine the effect of misalignment, the reference patterns – 'On' pixel are inserted and distributed in the data page. Figure 1 describes the reference pixel and data pixels of the retrieved data page with misalignment. The compensation scheme is derived by an intuitive observation of the misalignment. When there are the misalignment between pixels of the retrieved data page and detector pixels, a neighboring pixel will receive unintended signal as shown in figure 1. The unintended signals I_x , I_y and I_{xy} at neighboring pixels of the reference pixel are used to calculate the leakage intensity of 'On' pixel. We can compensate the effect of misalignment by adding the leakage intensities to the considered pixel. The leakage intensity is given by $I_c \left((I_x + I_y + I_{xy}) / I_r \right)$, where I_c and I_r are intensity values of the considered pixel and the reference pixel, respectively. The intensity value of each neighboring pixel is updated by subtracting the leakage intensity.

2.2 Cancelation of the dark noise

Additional electrons can be generated within the CMOS sensor not by the absorption of photons but by the physical processes within the photo detector itself. This noise known as a dark noise can be thought of as unwanted signal which doesn't improve the quality of the detected image. During compensation processing, the intended pixel is compensated by adding the leakage intensity which is obtained by intensities of neighboring pixels adjacent to a reference 'On' pixel. If there are dark noises in the neighboring pixels, the compensation value includes error. To improve a performance of the compensation algorithm, we have tried to cancel the dark noise in a CMOS sensor. We can calculate the dark noise from the mean value of 'Off' pixels at the known pattern in the data page. After the dark noise level in the detected image is decided, it is subtracted from whole data pixels in the captured retrieving data page.

*hskim2@dwe.co.kr; phone 82 31 428-5331; fax 82 31 428-5321

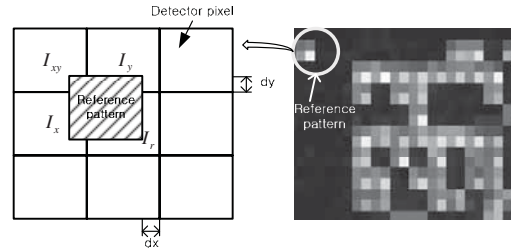


Fig. 1. Reference bit with the misalignment (left) and the retrieved image data (right)

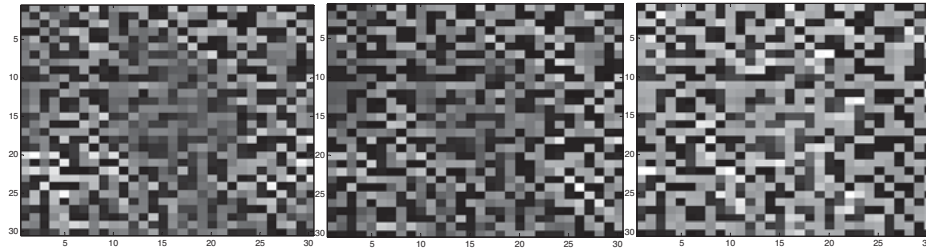


Fig. 2. Channel data (left), after the misalignment compensation (center), after equalizing (right)

2.3 Equalization for 2D modulation code

There are many variations in brightness for the ‘On’ pixels, ranging from white to gray. Such variations of the ‘On’ pixels are difficult to distinguish from the ‘Off’ pixels. The intensity variation of the ‘On’ pixels results high Bit Error Rate (BER) in the HDDS system. In this research, 2D modulation code which is the 6 bit data modulate as 3 by 3 pixels is proposed to solve this problem. The center bit is always 1, and outer 8 bits are obtained by the 6:8 balanced modulation. The proposed 2D 6:9 modulation code helps the equalization process. First, we define the target intensity value for ‘On’ pixels which is calculated by averaging intensities of the center ‘On’ pixel of the 3 by 3 modulation block in the retrieved data page. The equalization algorithm applied to 8 data pixels surrounding the ‘On’ pixel. Since these data pixels are modulated by balanced code, we can decide four ‘On’ pixels and four ‘Off’ pixels using the threshold value given by multiplying a scaling factor to the center intensity. As comparing the intensity of the ‘On’ pixels with the target intensity, we scale up the brightness of the dark ‘On’ pixels, and on the contrary the bright ‘Off’ pixels are scaled down.

The image data after equalizing is helpful for the decoding process such as error correcting algorithm. Especially the equalization is effective to the Low Density Parity Check (LDPC) decoding process that had been developed in reference 2. The LDPC decoding algorithm needed the information of the probability for the received channel data. The probability was calculated by using intensity difference between the ‘On’ and ‘Off’ pixel in the retrieved data page. For the successive decoding, the LDPC algorithm process iterative calculation. The proposed equalization algorithm can reduce the iteration number for the LDPC decoding process.

3. EXPERIMENT RESULTS

Actual experiments have been conducted to evaluate the proposed compensation algorithm and equalizer. For the test bed, an Nd-Yag laser with a maximum output power of 150 mW at 532 nm is used as a light source. The signal beam carries loaded data on the CRL XGA1L112 SLM with 800 by 600 pixels of 18 μm pitch. Then, the loaded data on the SLM is recorded on the photopolymer disk of 1mm thickness. The Mikrottron MC1310 CMOS camera with 1280 by 1024 pixels of 12 μm pitch is used to capture the retrieved data pages. Due to the difference of the SLM and CMOS pixel pitch, zoom optics was installed in the optical bed with 1.5 Nyquist rate aperture. The data images of 405 by 405 pixels were recorded and retrieved for the experiment. As shown in figure1, these data images consist of data sub-blocks

contained a 45 by 45 data. Each of the data sub-block has five 'On' pixels that are the reference pixel. Therefore, we can apply the proposed misalignment compensation scheme through the whole data pages.

Figure 2 describes the effect of the result for the proposed algorithms. In the figure 2, the left side image shows a 30 by 30 pixels block as it should ideally be received from the HDDS channel with the misalignment. The center of figure 2 shows the result after applying the compensation algorithm to the retrieved data image. And the right side in figure 2 represents equalized data image. Comparing to the left and right image in figure 2, the 'On' pixels in right image have fewer variations in brightness. As the result, the equalization algorithm correctly recovers the original data pattern.

For experiment, stacks of 54 multiplexed holograms in a spot were recorded along concentric circular tracks into the photopolymer disk. During read out from the disk, we injected noises into the control signal to generate arbitrary misalignments. Figure 3 shows the effect of the compensation and equalization on SNR. In this paper, SNR is defined by

$$\text{SNR} = 10 * \log\left(\frac{\mu_{on} - \mu_{off}}{\sqrt{\sigma_{on}^2 + \sigma_{off}^2}}\right) \quad (1)$$

where σ is the standard deviation of each 'On' and 'Off'. μ is the mean of each 'On' and 'Off' pixels.

4. CONCLUSION

We have confirmed the result of 2 by 2 oversampling method. Because of the result is effective through the Figure 2 and Figure 3, we think that the pre-processing methods in this paper will apply effectively to the other oversampling method. We will apply above pre-processing method to the other channel.

ACKNOWLEDGEMENTS

This research, conducted at DAEWOO Electronics Corp. has been supported by the MOCIE (Ministry of Commerce, Industry and Energy) of Korea through the Program for the Development of the Next Generation Ultra-High Density Storage (00008145)

REFERENCES

- [1] P. Yoon, E. Hwang, G. Kang, J. Park and G. Park, "Image compensation for sub-pixel misalignment in holographic data storage," ISOM 2004 Tech. Digest, 114-115 (2004)
- [2] B. Chung, P. Yoon, H. Kim, J. Park, J. Park and E. Hwang, "A modified low-density parity-check decoder for holographic data storage system," JJAP 46, 3812-3815 (2007)

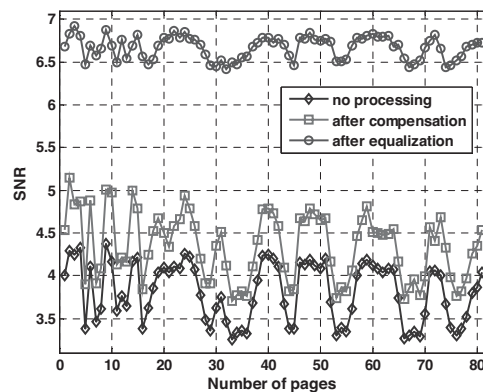


Fig. 3. SNR graph for the compensated and equalized data page.

Improvement of bit error rate by FIR filter based on genetic algorithm in holographic memory

Yuichiro Sasa, Hiroshi Oto and Manabu Yamamoto

Graduate School of Industrial Science and Technology, Tokyo University of Science, 2641 Yamasaki, Noda, Chiba, 278-8510 Japan Phone: +81-04-7122-9651

E-mail: ymanabu@te.noda.tus.ac.jp

Abstract: This paper studies the effects of FIR filter based on genetic algorithm. It is made clear that the best FIR coefficients can be provided by genetic algorithm.

1. Introduction

Recent increase and diversity of information demands larger and larger storage devices these days, and thus causes to attract general attention to hologram memory based on holographic recording technology. However, use of multiplex recording ends up with lower signal-to noise-ratio according to its multiplicity. One of the reasons to decrease SNR is the inter-symbol interference between each reproduced bit pattern. In order to improve this, this paper studied the effect of two dimensional FIR filter. The genetic algorithm was applied for deciding the best FIR filter coefficient. As a result, we succeeded in providing the best FIR coefficient corresponding to each reproduced images.

2. Two dimensional FIR filter

FIR filter is realized by applying convolution algorithm to the two dimensional filter and the CCD output wave. Following figure illustrates the two dimensional FIR filter.[1]

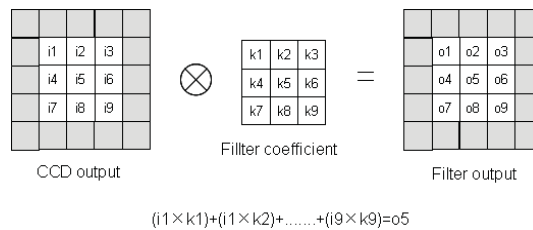


Fig.1 Two dimensional convolution algorithm by two dimensional filter

The experimental analysis employs the filter shapes of following 3x3 and 5x5 shapes.

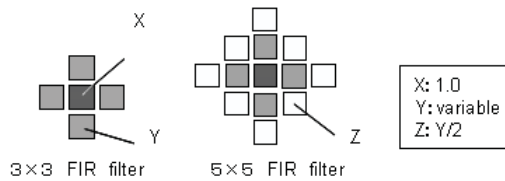


Fig.2 : FIR filter shape

In this paper, the FIR filter of following two models were designed.

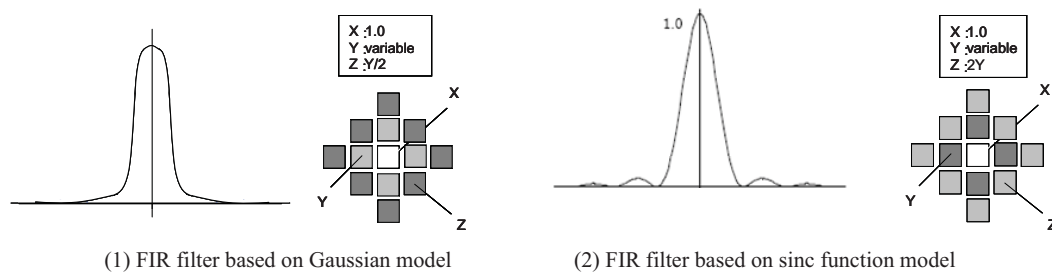


Fig.3 FIR filter model

3. Evaluation method for signal processing of reproduced data

The 2/4 modulation code is used for this experiment. Two times oversampling and expanded data of 600 bit size both vertically and horizontally are applied. Also this data is angularly multiplexed in one degree interval, and the recording media is photopolymer of medium thickness of 400 micrometers. Fig.4 shows the signal processing process.

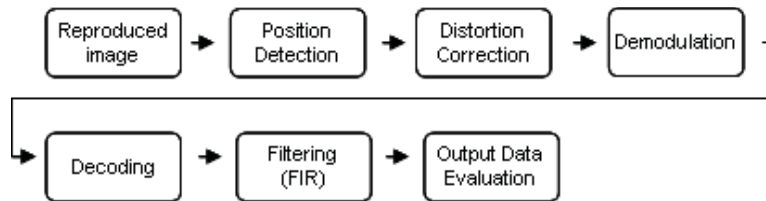


Fig.4 Evaluation process of reproduced data

4. Experimental results of FIR filter

The experimental results about 4 data samples are shown in Fig.5 and Fig.6.

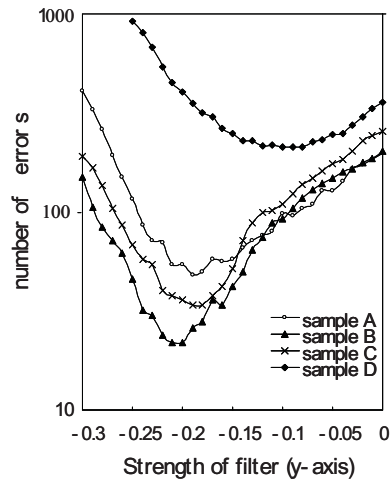


Fig.5 Results of gauss function model

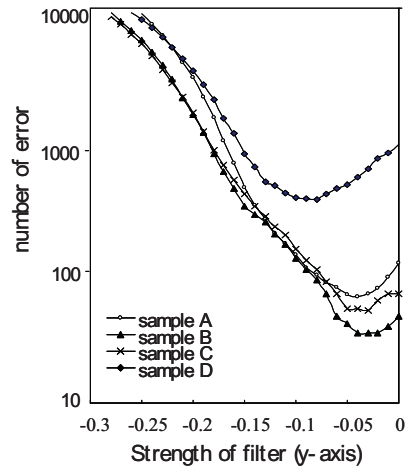


Fig.6 Results of sinc function model

The results indicate that the bit error rate decreases at sufficient FIR filter coefficient. For this experiment, we applied the genetic algorithm to decide best FIR filter coefficient.

Genetic algorithm is a method used to decide coefficient by applying “law of survival of the fittest” in the natural world. The flow chart is shown as Fig.7. The result of applying this genetic algorithm to FIR filter is shown in Fig.8. In this signal processing, the number of samples is 100, generation is 5 and probability of mutation evolution is 5%. After 3rd generation, the number of error bit becomes constant at minimum low level.

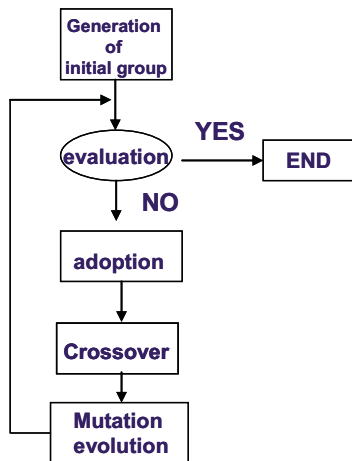


Fig.7 Flow chart of genetic algorithm

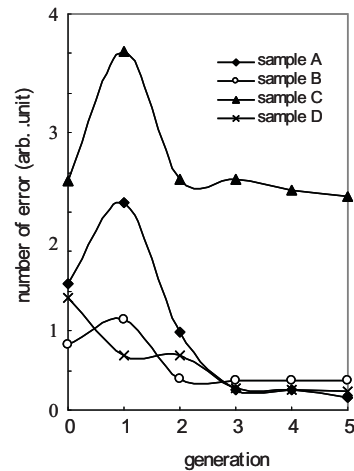


Fig.8 Genetic algorithm results

5. Conclusion

As for images which contain noises caused by neighboring inter-symbol interference, the experimental results show that their BER can be reduced and SNR can be increased by applying FIR filter. However, the

filter coefficient cannot be uniformly decided for each reproduced images.

In this paper, the genetic algorithm for deciding the best FIR filter coefficient is applied and it is made clear that the best coefficients corresponding to each reproduced image can be obtained by this genetic algorithm.

References

[1] H.Ootou, Y.Sasa and M.Yamamoto, "Improvement of signal-to-noise ratio by using two-dimensional signal processing", International Workshop on Holographic Memory 2007.10 (Malaysia).

Filter Structures of Write Compensation for Holographic Data Storage Systems

Takaya Tanabe, Ryu Suzuki and Iwao Hatakeyama
 Ibaraki National College of Technology, 866 Nakane, Hitachinaka, Ibaraki, 312-8508, Japan
 Phone: +81-29-271-2917, Fax: +81-29-271-2930
 E-mail: tanabe@ee.ibaraki-ct.ac.jp

1. Introduction

Volume holographic data storage is one of the promising ways to store the explosive digital data generated by IT society because of its ability of volume storage and parallel data transfer. Therefore, many holographic storage methods have been investigated to realize larger storage capacity and higher data transfer rate.¹⁻³

Several two dimensional page-data can be multiplexed on a volume of material using a spatial light modulator (SLM) and objective lens in volumetric holographic recording. To increase the data density, the SLM having a large number of the pixels is used. However, an optical system using the objective lens has some degrading factors, and they cause an intersymbol interference (ISI).

In this paper, several high pass filter structures of write compensation are compared and evaluated to suppression of ISI influence in simulations.

2. Filter Structures of Write Compensation

Figure 1 shows a write compensation method using a high pass filter. The method uses two pages, one is an original page of binary data to be recorded and the other is the compensation page extracted low frequency components from the original page using the high pass filter.

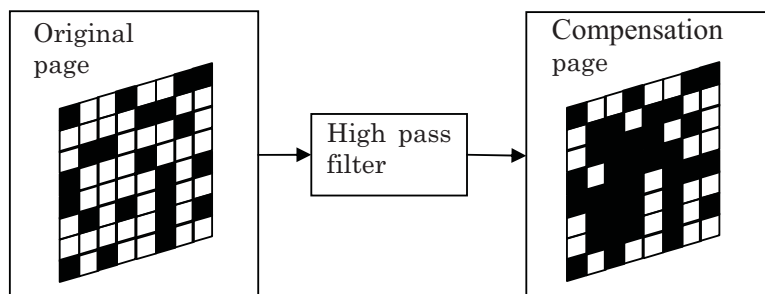
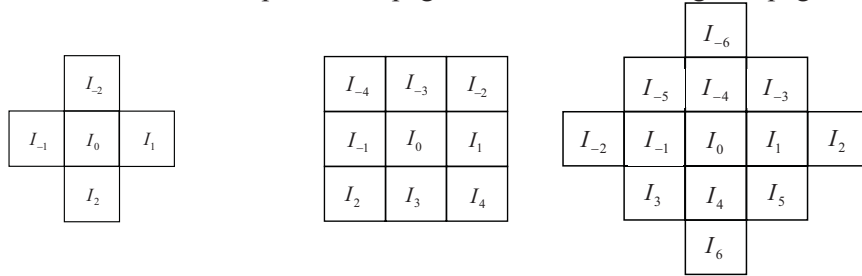


Fig.1. Write compensation method by using high pass filter.

Three pixel patterns used in the high pass filter are shown in Fig. 2. In case of the five-pixel pattern, each intended pixel of the compensation page is driven from the decision using five outputs from each intended pixel and four pixels adjacent to it of the original page. In cases of the nine-pixel and thirteen-pixel patterns, each intended pixel of the compensation page is driven from the decision using nine and thirteen outputs from the original page, respectively.

Figure 3 shows our simulated model of the four-focal-length holographic data storage system. An original page of binary data is displayed on the spatial light modulator (SLM), its Fourier transform and a reference beam wave front are recorded in the medium by interference in a certain exposure time. After that, the compensation page is recorded in the medium using the same

reference beam with a shorter exposure time. Here, we define the exposure time ratio as the ratio of the exposure time of the compensation page to that of the original page. Other pages



(a) Five-pixel pattern (b) Nine-pixel pattern (c) Thirteen-pixel pattern the Fig.2. Pixel patterns used in high pass filter of write compensation.

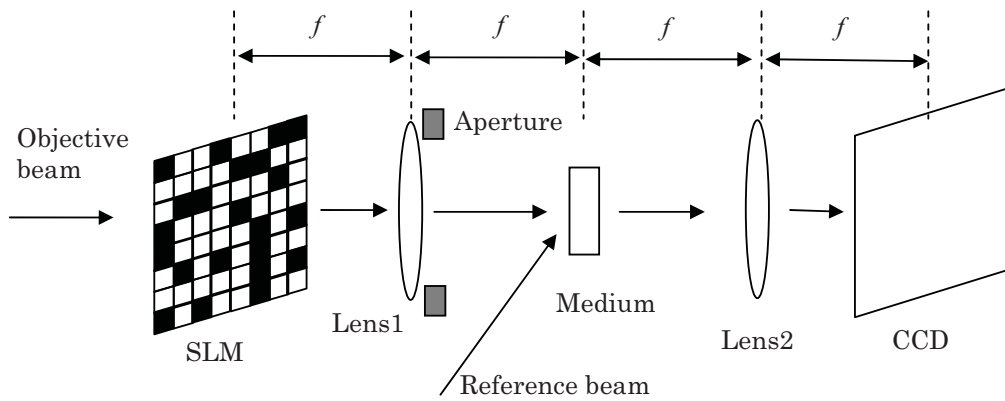


Fig.3. Schematic diagram of the 4-*f* holographic data storage system.

of binary data are recorded in the same way by changing the angle of the reference beam. To retrieve the data page, the reference beam with the appropriate angle illuminates the medium; then the readout page appears in front of the CCD. An aperture is used for considering the modulation transfer function (MTF) of the optical pass which is changed by the optical degradation like aberrations and servo errors.

3. Simulation Results

In our simulation a SLM page size of 100 x 100pixels is used and a laser wavelength $\lambda=500\text{nm}$ and a reference beam angle $\theta=83.65\text{degree}$ are selected. The cutoff frequency of the MTF is changed from $f_c=1.0 f_N$ to $2.0 f_N$, where f_N denotes the pixel frequency expressed as $f_N= d/\lambda f$. Here, f is the focal length of the Fourier transforming lens and d is the pixel pitch of the SLM.

To evaluate the relative quality of readout images, the SNR is defined as⁴

$$SNR = \frac{\mu_1 - \mu_0}{\sqrt{\sigma_1^2 + \sigma_0^2}},$$

where μ_1 and μ_0 are the mean values and σ_1 and σ_0 are the variances of the white and black bits.

Figure 4 shows the relationship between the exposure time ratio of the compensation page to that of the original page and the SNR. Here the cutoff frequency is set to $2.0 f_N$. The SNR has maximum value when the time ratio is 0.1 in each pixel pattern. This tendency depends mainly on

the changes of variance σ_1 . As the time ratio is increased, variance σ_1 is slightly decreased and then the SNR is improved. When the time ratio is greater than 0.1, variance σ_1 is increased rapidly and the SNR is decreased.

Figure 5 shows the relationship between the cutoff frequency of the MTF and the SNR, where the exposure time ratio in the write compensation is 0.1 in the case of nine-pixel pattern. Using the write compensation, the SNR is improved throughout the whole cutoff frequency.

Figure 6 shows relationship between the cutoff frequency of the MTF and the SNR improvement, where the exposure time ratio set to optimum value in each case. The write compensation with the five-pixel pattern shows the best in the SNR. When the cutoff frequency is $f_c=1.6f_N$, the SNR with the write compensation is 19.5% better than that without the write compensation.

4. Conclusions

The write compensation method, which the original page is recorded before or after the compensation page is recorded on the medium, is evaluated by using the simulations. The SNR is improved by using the write compensation with five-pixel pattern filter.

References

1. S. S. Orlov, W. Phillips, E. Bjornson, Y. Takashima, P. Sundaram, L. Hesselink, R. Okas, D. Kwan, R. Snyder, *Applied Optics*, **43**, pp. 4902-4914 (2004)
2. M.-P. Bernal, G. W. Burr, H. Coufal, M. Quintanilla, *Applied Optics*, **37**, pp. 5377-5385 (1998)
3. J. Park, J.-K. Cho, K. Nishimura, H. Uchida, M. Inoue, *Jpn. J. Appl. Phys. - Part 2 Letters* **43**, pp.4777-4780 (2004)
4. M. M. Wang, S. C. Esener, F. B. McCormick, I. Çokgör, A. S. Dvornikov, and P. M. Rentzepis, *Optics Letters*, **22**, pp. 558-560 (1997)

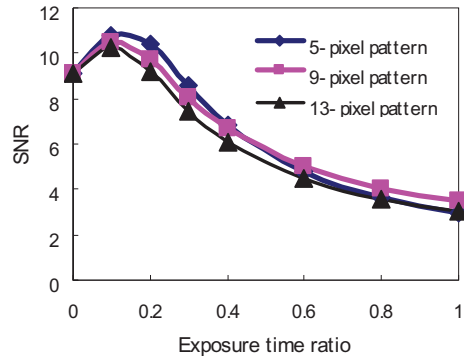


Fig. 4. Relationship between exposure time ratio and SNR.

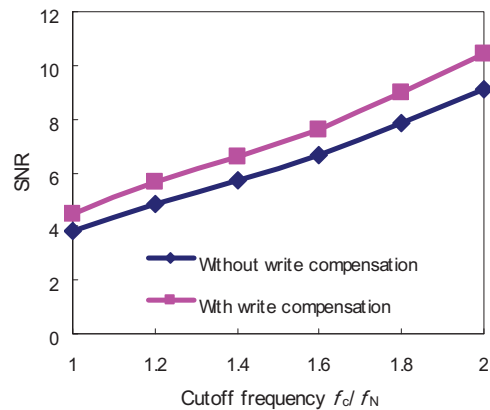


Fig. 5. Relationship between cutoff frequency of MTF and SNR in case of 9-pixel pattern.

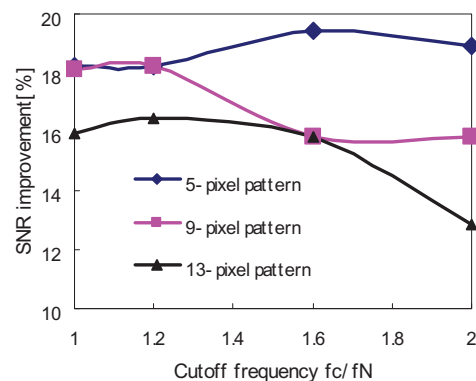


Fig. 6. Relationship between cutoff frequency of MTF and SNR improvement.

Inter-page cross-talk noise in collinear holographic memory

T. Shimura*, M. Terada, Y. Sumi, R. Fujimura, and K. Kuroda

Institute of Industrial Science, the University of Tokyo, 4-6-1, Komaba, Meguro-ku, Tokyo 153-8505, JAPAN

ABSTRACT

We estimated signal-to-noise ratio of reconstructed data image in collinear holographic memory depending on the number of multiplexed pages in the recording media. Inter-page cross-talk noise is considered theoretically and numerically. Both results well agreed and the signal to noise ratio of the multiplexed pages is inversely proportional to the square root of number of multiplexed pages.

Keywords: holographic data storage, signal-to-noise ratio, multiplexed pages, Monte-Carlo simulation

1. INTRODUCTION

Holographic memory is one of the promising candidates of post blu-ray optical data storage system. Major advantages are its large storage capacity as well as fast data transfer rate because of the page oriented reading and writing. One of the important factors which determine the storage density is degree of multiplexing of the hologram at the same volume. Dynamic range of the recording media, $M/\#$ or cumulative grating strength [1], and the inter-page cross-talk noise are limiting the degree of multiplexing of holograms. During the read out of one of the multiplexed holograms, reference beam hits other multiplexed pages. Because of the page selectivity of the holographic data storage system, the diffracted light from multiplexed pages excepting the target page are quite small, but when the degree multiplexing is large, we cannot ignore the accumulation of the residual diffracted light.

Effect of such phenomena, so called inter-page cross-talk noise, in the holographic data storage system was investigated and concluded that the noise level is proportional to the degree of multiplexing, M [2,3]. When we define the signal to noise ratio (SNR) as signal/noise, then it is inversely proportional to the noise level and M . However, in the holographic data storage system, SNR is usually defined as [4],

$$SNR = \frac{\mu_{ON} - \mu_{OFF}}{\sqrt{\sigma_{ON}^2 + \sigma_{OFF}^2}} \quad (1)$$

where μ_{ON} and σ_{ON} are the mean and standard deviations of the detected power for “ON” pixels, and μ_{OFF} and σ_{OFF} are the mean and standard deviations for “OFF” pixels. Then SNR is not always inversely proportional to M . The two different definitions of SNR cause confusion on the understanding of inter-page cross talk noise in holographic memory.

In this paper, we evaluate the effect of inter-page cross-talk noise in M multiplexed holograms and calculate SNR theoretically. We will show that SNR is proportional to $M^{-1/2}$, not M^{-1} when the sum of the intensity of the light diffracted by multiplexed holograms other than target holograms is much smaller than signal intensity. Then we show our results of numerical calculation for the collinear holographic memory system[5] and that results agree with our theory.

2. THEORETICAL ANALYSIS

We consider a holographic data storage system in which $M+1$ hologram pages are stored at the same volume. One is the target page and other M pages are multiplexed pages. Our theory is applicable to any multiplexing method, such as

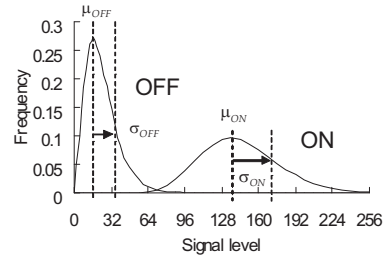


Fig. 1 An example of histogram of detected signal and definitions of variables.

polytopic [5] or collinear, under some assumptions stated bellow. For simplicity, we ignore the intra-page cross talk, that is, the image formation without multiplexing is ideal. Here, we will represent the image intensity at the imaging device, such as a CMOS camera, corresponding to the (m, n) pixel as,

$$I_{mn} = \left| E_{mn} + \sum_{k=1}^M E_k \right|^2 \quad (2)$$

where, E_{mn} is the amplitude of the diffracted light from the target page, and $E_{mn} = E_{sig}$ or 0 according to the pixel (m, n) is ON or OFF, and E_k is the amplitude of the diffracted light from the k^{th} multiplexed page. Here, we assume that residual diffracted light from overlapped pages has random amplitude, that is, E_k is a complex Gaussian random variable [7]. Now, let us calculate the μ and σ . From the definition of the standard deviations,

$$\sigma^2 = \langle |I_{mn} - \langle I_{mn} \rangle|^2 \rangle = \langle I_{mn}^2 \rangle - \langle I_{mn} \rangle^2. \quad (3)$$

where bracket $\langle \rangle$ denotes the ensemble average. The first term of eq.(3) is calculated as,

$$\langle I_{mn}^2 \rangle = \left\langle \left| E_{mn} + \sum_{k=1}^M E_k \right|^2 \left| E_{mn} + \sum_{k=1}^M E_k \right|^2 \right\rangle = E_{mn}^4 + 4ME_{mn}^2 \langle |E_k|^2 \rangle + (2M^2 - M) \langle |E_k|^2 \rangle^2. \quad (4)$$

To calculate eq.(4), we used equations which are derived using properties of complex Gaussian random variables;

$$\left\langle \sum_{k=1}^M E_k \right\rangle = 0, \quad \left\langle \left(\sum_{k=1}^M E_k \right)^2 \right\rangle = 0, \quad (5)$$

$$\left\langle \left| \sum_{k=1}^M E_k \right|^2 \right\rangle = \left\langle \sum_{k=1}^M |E_k|^2 \right\rangle = M \langle |E_k|^2 \rangle, \quad (6)$$

$$\left\langle \left| \sum_{k=1}^M E_k \right|^4 \right\rangle = \left\langle \sum_{k=l,p=q}^M E_k E_l E_p E_q \right\rangle + \left\langle \sum_{k=q,l=p,k \neq l}^M E_k E_l E_p E_q \right\rangle = (2M^2 - M) \langle |E_k|^2 \rangle^2. \quad (7)$$

Via the same way, we can obtain an equation,

$$\langle I_{mn} \rangle = \left\langle \left| E_{mn} + \sum_{k=1}^M E_k \right|^2 \right\rangle = E_{mn}^2 + M \langle |E_k|^2 \rangle. \quad (8)$$

By substituting eq.(4) and (8) to eq (3), then SNR is derived from eq.(1),

$$SNR = \frac{E_{sig}^2}{\sqrt{2M \langle |E_k|^2 \rangle \{ E_{sig}^2 + (M-1) \langle |E_k|^2 \rangle \}}} \quad (9)$$

When $E_{sig}^2 \gg (M-1) \langle |E_k|^2 \rangle$, that is, the summation of the intensity of diffracted light from all of the overlapped pages are much smaller than the signal intensity of the target page, SNR is expressed as,

$$SNR = \frac{E_{sig}}{\sqrt{2M\langle |E_k|^2 \rangle}}. \quad (10)$$

This result says the SNR defined as eq.(1) is inversely proportional to square root of the number of multiplexed pages, M when the inter-page cross talk is small.

3. NUMERICAL SIMULATION

We performed numerical simulation of inter-page cross-talk noise in the collinear holographic memory. The residual diffracted light E_k from k^{th} overwritten page is calculated with our model described in ref [8]. The effect of shift selectivity of the collinear holograms and partial overlap between the reference wave and the hologram is taken into account in our calculation. We ignored the influence of other pixels than (m, n) pixel in overlapped pages when we calculated I_{mn} , because it is a small value of second order. The Monte Carle simulation was executed with changing the ON or OFF state of (m, n) pixels in each page stochastically.

An example of the calculation is shown in Fig. 2. Pixel pitch of the Spatial Light Modulator (SLM) which provides data page and the reference waves was $13.68 \mu\text{m}$, and the focal length of the objective lens was 4 mm. Outer and inner diameters of the reference pixel area were 300 and 230 pixels. The pixel pattern of the reference area was radial lines of every 3 degrees. The Strait line indicated in the graph is proportional to shift pitch. As degree of multiplexing of the holograms, M , is inversely proportional to the square of the shift pitch, this result shows that the SNR is proportional to $1/\sqrt{M}$. We repeated this simulation with changing the diameters of the reference pixel area and reference pattern, the lines showed parallel shift and the dependency on the $1/\sqrt{M}$ did not changed.

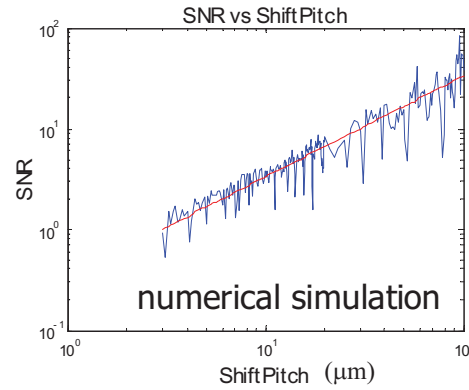


Fig. 2 An example of histogram of detected signal and definitions of variables.

4. SUMMARY

We analyzed the inter-page cross-talk in holographic data storage systems. The definition of SNR in holographic memory is not unique and SNR defined as eq.(1), which is frequently used in the holographic data storage, is inversely proportional to the square root of degree of multiplexing, \sqrt{M} , not M . From this result, we can estimate the limit of M under the assumption of the recording media is perfect, that is the response is linear, shrinkage is zero, and $M/\#$ is infinity, from the SNR measured or calculated for very low degree of multiplexing.

REFERENCES

- [1] Steckman, G. J., Solomatine, I., Zhou, G., and Psaltis, D., *Opt. Lett.*, **23** 1310-1312 (1998).
- [2] Gu, C., Hong, J., McMichael, I., Saxena, R., and Mok, F., *J. Opt. Soc. Am. A*, **9**, 1978-1983 (1992).
- [3] Coufal, H. J., Psaltis, D. and Sincerbox, G. T., eds., [*Holographic Data Storage*], Springer, Berlin (2000).
- [4] Pu, A., Curtis, K., and Psaltis, D., *Opt. Eng.*, **35**, 2824-2829 (1996).
- [5] Horimai, H. and Tan, X., *Appl. Opt.* **45**, 910-914 (2006).
- [6] Anderson, K. and Curtis, K., *Opt. Lett.*, **29** (2004) 1402-1404.
- [7] Goodman, J. W., [*Statistical Optics*], John Wiley and Sons, New York 40-56(1985).
- [8] Shimura, T., Ichimura, S., Fujimura, R., Kuroda, K., Tan, X., Horimai, H., *Opt. Lett.*, **31**, 1208-1210 (2005).

Design and test of channel board for holographic data storage

Pilsang Yoon^{*a,b}, Haksun Kim^a, Jooyoun Park^a, Heungsang Jung^a, Gwitae Park^b

^aDigital Media Lab., Daewoo Electronics Corp., 543, Dangjeong, Gunpo, Gyeonggi, Korea 435-733;

^bDepartment of Electrical Engineering, Korea Univ./5-1, Anam, Sungbuk, Seoul, Korea 136-701

ABSTRACT

The channel board has been designed and manufactured, and is use for real-time recording and reading process. The channel coding and decoding algorithm was implemented on Xilinx field-programmable gate array (FPGA) devices. For fast data transmission between the channel board and personal computer (PC), universal serial bus (USB) 2.0 interface is installed in the channel board. A developed firmware and device driver achieved a transfer rate of 34MByte/s. A holographic data storage system records a video stream, and it was successfully retrieved and reconstructed without error.

Keywords: Holographic data storage, channel en/decoder, data interface, FPGA

1. INTRODUCTION

The channel of holographic digital data storage (HDDS) has intrinsic noises such as inter symbol interference (ISI), non-uniform intensity distribution and additive noise due to optical and electrical components. The retrieved images from HDDS system usually have very low signal-to-noise ratio. Therefore, it requires an effective signal processing algorithm for reliable data readout over noisy HDDS channel. The channel board is designed to demonstrate real-time recording and reading process. Appropriate channel coding and decoding schemes is implemented with a FPGA chip for fast data processing. We made a hardware channel board which is installed interfaces to communicate with a host PC, complementary metal-oxide semiconductor (CMOS) camera, spatial light modulator (SLM). The hardware channel board is applied to HDDS prototype which is named DEPROTO-III. The channel board can successfully record and reconstruct user data without error.

2. ARCITECTURE OF CHANNEL BOARD

The channel board is designed to remove noise and error efficiently during reading and recording process, and consists of several functional blocks. Figure 1 describes a block diagram of the channel board for our HDDS prototype. In the following section, each functional block of the channel board is described sequentially.

2.1 Channel encoder and decoder

During data recording, channel encoder insert redundancy into recording data through 6:8 balanced modulation and low density parity check (LDPC) code for error correction. In HDDS channel, there is usually non-uniform noise variation in a retrieved data page. Therefore a block interleaving scheme was proposed to avoid this problem.[1] The encoded and interleaved data is construct 2D data page with the predefined page format.

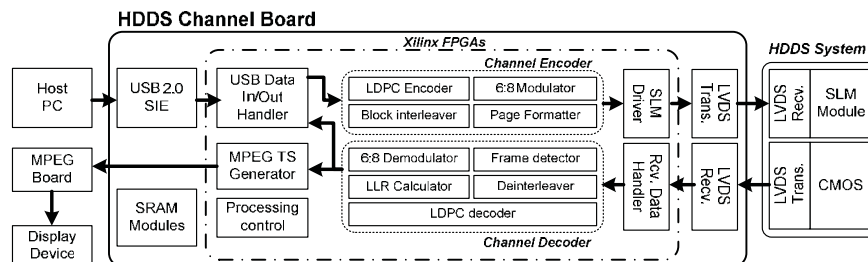


Fig. 1. Block diagram of the developed hardware channel board for HDDS system.

*psyoon@dwe.co.kr; phone 82 31 428-5326; fax 82 31 428-5321

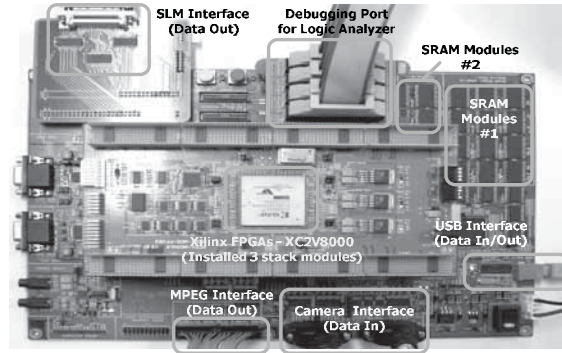


Fig. 2. Photo of the HDDS channel board with FPGAs and additional circuits.

The channel decoder had been designed to remove noise and error efficiently. It consists of some blocks – frame detector, deinterleaver, demodulator, log likelihood ratio (LLR) calculator, LDPC decoder.[2] The LDPC encoded data are interleaved and modulated, and then recorded. Therefore, the retrieved data pages from HDDS system requires deinterleaving, demodulating and LDPC decoding process. To improve LDPC decoding performance, we had proposed the LLR calculation scheme with demodulation.[1] Since the position of the retrieved data page on the image sensor can usually be altered during readout process. The frame detector is designed to search the special mark in the data page and determine the data region in the captured image.

2.2 SLM driver

After channel encoding process, the constructed data page transfers to display on the SLM panel. In DEPROTO-III, displaytech's 1280 x 768 SLM is used. It has register that each register bit is connected to a pixel driving circuit. If the register value is 0 and 1, then the corresponding pixel represents optically OFF and ON, respectively. The register values can be written through a 64 bit data bus with clock, sync and enable signals. The SLM driver generates these signals to transmit the two dimensional binary image data. The SLM panel is placed in the opto-mechanical assembly of DEPROTO-III apart from the channel board. Therefore, an additional circuit was needed to transmit all data and control signals from the SLM driver to the SLM. The DS90CR287 and DS90CR288A manufactured by National Semiconductor were adopted as data transmitter and receiver, respectively. The transmitter converts 28 bits data into four low voltage differential signal (LVDS) data streams, and the receiver converts the four LVDS signals back into 28 bits data.

2.3 Data interface

The developed channel board integrates the data interface circuits for transferring encoding / decoding data between the channel board and a host PC. The USB interface 2.0 is used for high transmission rate, high reliability of the data transmission and easy implementation. The designed channel board includes a Cypress CY7C68013A integrated USB 2.0 transceiver, serial interface engine (SIE) and 8051 processor. It supports high speed USB 2.0 transfer with a signaling bit rate of 480 Mbps. Firmware, Windows application program and device driver were developed to communicate between a host PC and the channel board.

Firmware has been programmed to analyze each incoming packet from the host PC and execute a control routine corresponding to the received packet, and to packetize the decoding data from the channel board and transfer the packet to the host PC. Windows application program has been developed in Visual C++ to easily link to the main control program. It has implemented functions for USB communication such as writing data file in the host PC and reading stored data file in the HDDS system, sending system control command, reading disk information, etc. A device driver was also developed so that application programs can interact with the USB device. Device driver is dependent on operating system installed on a host PC. In this research, a driver for Windows XP was programmed for USB interface.

3. IMPLEMENTATION AND EXPERIMENT

The channel board shown in figure 2 assembles various electronic components, such as three Xilinx XC2V8000 FPGAs for a fast signal processing, SRAM modules for temporary data storage, three LVDS receivers for camera interface, three LVDS transmitter for SLM interface and USB microcontroller for channel data interface. Using very high-speed

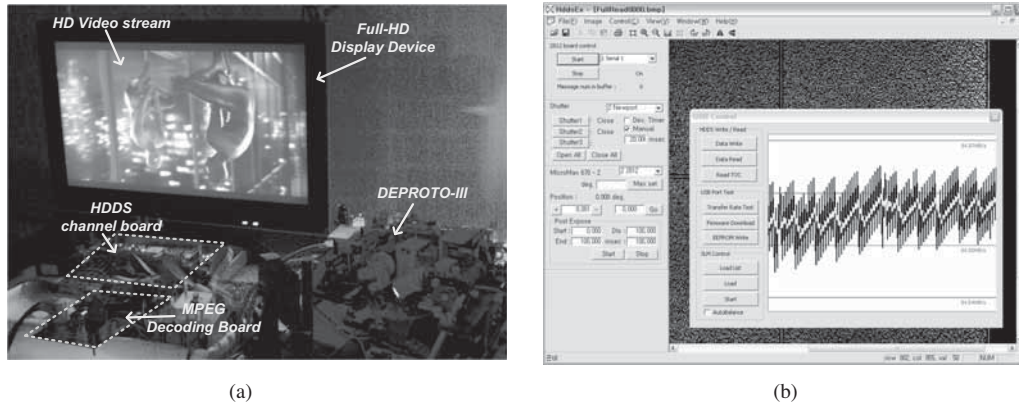


Fig. 3. (a) Video demonstration for testing performance of channel board, and (b) test of data transfer rate through USB interface.

integrated circuit hardware description language (VHDL), the functional blocks described in figure 1 are designed and divided into three parts efficiently, and then loaded to each FPGA chip. The LDPC decoding block has the largest portion of FPGA resources to implement the functional blocks. The proposed LDPC code is suited for fast processing based on parallel operation. However, the fully parallel architecture for high decoding throughput causes a huge hardware resource requirement. Therefore, the implementation of LDPC decoder is based on a trade-off between hardware complexity and decoding throughput.

In the actual recording and retrieving experiments, the recorded high-definition (HD) video stream was successfully reconstructed and stored in the host PC. Using an external MPEG decoding board, the reconstructed data was also displayed on a HD display device real-time, as shown in figure 3 (a). For testing data transmission through the integrated USB interface, a prepared data is stored in the memory module on the channel board and read back into the host PC. Bulk transfer mode is performed for this test. An averaged transfer rate is about 34MByte/s. Figure xx (b) shows a graph to display data transfer rate.

4. CONCLUSION

The channel board has been designed and built to record and retrieve data reliably in our HDDS prototype system. The channel coding and encoding algorithms are implemented in hardware with FPGAs. For transferring data between channel board and host PC, USB 2.0 interface chip was installed in the hardware board. In the experiments, the MPEG video clip in host PC is recorded and reconstructed successfully using the channel board.

ACKNOWLEDGEMENTS

This research, conducted at DAEWOO Electronics Corp. has been supported by the MOCIE(Ministry of Commerce, Industry and Energy) of Korea through the Program for the Development of the Next Generation Ultra-High Density Storage (00008145)

REFERENCES

- [1] B. Chung, P. Yoon, H. Kim, J. Park, J. Park and E. Hwang, "A modified low-density parity-check decoder for holographic data storage system," *JJAP* 46, 3812-3815 (2006)
- [2] P. Yoon, H. Kim, B. Chung and J. Park, "Design and implantation of channel decoder for holographic data storage," *IWHM 2007 Digests*, 27p17 (2007)

Tracking servo control using pole placement based on Luenberger observer for holographic data storage system

Yong Hee Lee*¹, Sang-hoon Kim¹, Jang Hyun Kim²,
Hyunseok Yang¹, Young-pil Park¹, Joo-Youn Park³

¹ Department of Mechanical Engineering, ² Department of Electrical and Electronic Engineering,
Yonsei University
134 Shinchon-dong, Sudaemoon-Ku, Seoul 120-749, Korea
³ DAEWOO Electronics Corp.,
543 Dangjeung-Dong, Kunpo-Shi, Gyonggi-Do, Korea

ABSTRACT

In this paper, we focus on effects of radial deviation on the disk and propose a tracking error compensation method for the holographic data storage system (HDSS) that uses a disk type media. In our HDSS, the tracking error is detected by a servo beam method, and the error compensation is achieved by a piezo actuator. A tracking servo controller is suggested, and the validity of the servo control is verified with simulation results.

Keywords: tracking servo controller, servo beam method, pole placement

1. INTRODUCTION

As high density recording becomes achieved, the tracking servo will be a significant factor like the tilt servo. The tracking margin will also be tightened. In this paper, we propose a tracking servo control for the HDSS. In the recording and the retrieving process, a tracking error signal (TES) is generated by a servo beam method. If the tracking error caused by the eccentricity of the disk is detected, the displacement of the piezo actuator moves the spindle motor stage to compensate the error. In order to achieve improved tracking performance, a pole placement based on state variable estimation and compensators are suggested for the controller. We demonstrate that the controller is properly designed and we evaluate the validity of the controller by means of experimental results such as SNR and BER [1].

2. THE TRACKING SERVO CONTROL SYSTEM

The tracking servo control system configuration of HDSS in CISD is shown in figure 1.

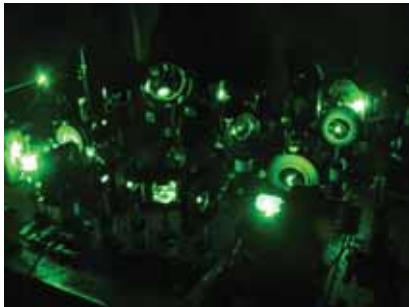
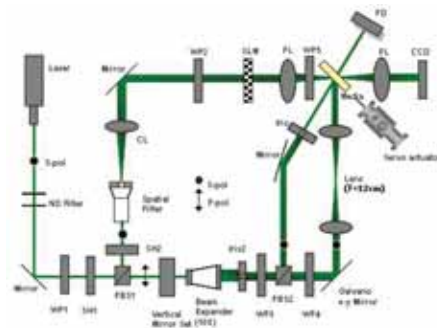


Fig.1. (a) HDSS in CISD



(b) Structure of HDSS

The error detection is achieved by a servo beam method. Servo tracks generated by the interference of an additional servo beam and a reference beam are formed on the circumference direction of the recording media. During both

*cion4242@yonsei.ac.kr; phone +82-2-2123-4677; fax +82-2-365-8460

recording and retrieving process, a servo signal is reconstructed by the reference beam illuminated on the recorded servo track. The servo signal is detected by a quadratic photodiode. When the disturbance occurs on the disk, the TES is generated by the detected servo signal through push-pull method like the conventional ODD [2].

In order to compensate the tracking error, we suggest using a piezo actuator in this tracking servo control system. Figure 2 shows the Frequency Response Function (FRF) of the piezo actuator. The experimental FRF are obtained with a Laser Doppler Velocimetry (LDV) and a Digital Signal Analyzer (DSA). A continuous transfer function of the plant (1) is derived by fitting in the experimental FRF. For applying controller based on state space, it's required that the transfer function should be converted to state space model. The state space model of the plant can be expressed as (2), and the state vector is composed of displacement, velocity, and acceleration.

$$G_{plant}(s) = \frac{3.341(10)^{10}}{s^3 + 1278s^2 + 2.215(10)^7s + 1.469(10)^{10}} \quad (1) \quad \dot{\mathbf{x}} = \begin{bmatrix} 0 & 1 & 0 \\ 0 & 0 & 1 \\ -1.469(10)^{10} & -2.215(10)^7 & -1278 \end{bmatrix} \mathbf{x} + \begin{bmatrix} 0 \\ 0 \\ 3.341(10)^{10} \end{bmatrix} u \quad (2)$$

3. SIMULATION

We designed a pole placement method based on state estimation as the tracking servo controller. State feedback gains (3) for full state feedback and observer gains (4) for estimation of state variables are calculated [3]. However, the steady state error did not converge to zero when we used only the pole placement based on an observer. Hence, 1 lead and 2 lag compensators are added in order to achieve better performance [4]. As a result, we can find that the system has 51.66dB of DC gain, 31.8 dB of gain margin and 35.6 phase margin as depicted in figure 3. In addition, the steady state error is diminished from 1.288 to 0.002 micron as shown in figure 5.

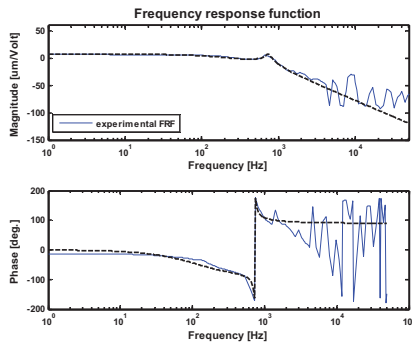


Fig.2. Frequency response function of plant

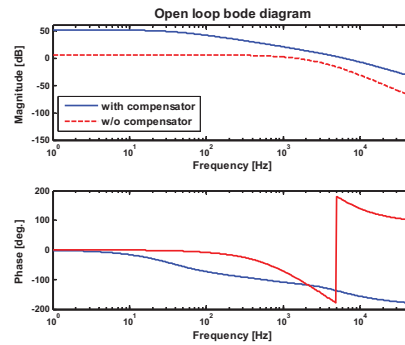


Fig.3. Bode diagram with compensator and without compensator

$$\mathbf{K} = [0.069 \quad 0.853(10)^{-4} \quad 2.311(10)^{-7}] \quad (3)$$

$$\mathbf{L} = [3.222(10)^3 \quad -1.952(10)^7 \quad -5.774(10)^{10}]^T \quad (4)$$

The block diagram of the tracking servo control system for HDSS in CISD is described in figure 4.

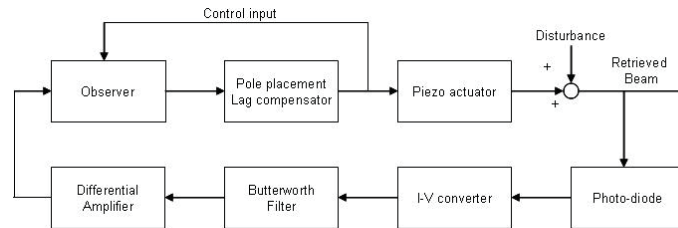


Fig.4. tracking servo control loop

The simulation result of tracking servo control is shown in figure 6. The simulation for tracking error compensation is performed in our HDSS with only 10 micron amplitude and 1Hz period because of the limitation of our spindle motor rotation speed and the small amount of eccentricity of the HDSS compared with conventional ODD. According to our simulation result, the tracking error is suppressed from 10 to 0.027 micron.

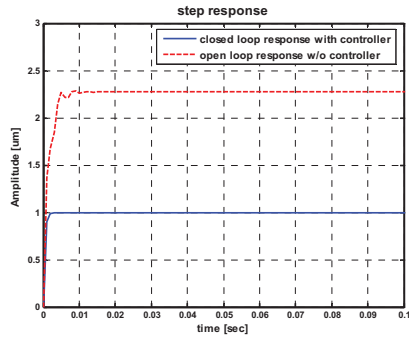


Fig.5. Step response with controller and without controller

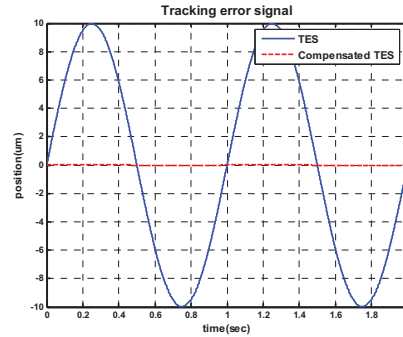


Fig.6. Response for tracking error signal

4. CONCLUSION

We suggested the method using a servo beam to generate the TES. A piezo actuator was applied on our HDSS to control the position of the spindle motor. In this tracking servo system, the piezo actuator covers only one track because of its short moving range. The estimation of state variables was designed to estimate the unmeasured state and a controller was designed using the pole placement and the lag compensator. The reduction of the TES was shown in the simulation results. The validity of the proposed method will be confirmed through experiments on our HDSS system. The experimental results will be presented at ISOM/ODS08'.

ACKNOWLEDGEMENT

This research was supported by the MOCIE (Ministry of Commerce, Industry and Energy) of Korea through the program for the Next Generation Ultra-High Density Storage (00008145).

REFERENCES

- [1] Coufal H. J., Psaltis D., Sincerbox G. T., 2000, Holographic Data Storage, Springer, Heidelberg, Germany.
- [2] Junho, Y., 2007, "Real time servo control of the holographic data storage with an additional servo beam", Microsystem Technologies.
- [3] Ogata K., 2002, Modern Control Engineering 4th ed., Prentice Hall, New Jersey, USA.
- [4] Nise N.S., 2004, Control Systems Engineering 4th ed., JOHN WILEY, Danvers, USA.

Tilt Error Measurement and Compensation Method for the Holographic Data Storage System

Sang-Hoon Kim^{*a}, Jang Hyun Kim^a, Yong Hee Lee^a, Hyunseok Yang^a,
Joo-Youn Park^b, Young-Pil Park^a

^aCenter for Information Storage Device (CISD), Yonsei University, 134 Sinchon-dong,
Seodaemun-ku, Seoul, 120-749, Korea;

^bDAEWOO Electronics Corp., 543, Dangjeong-Dong, Kunpo-Si, Gyonggi-Do, Korea

ABSTRACT

Tilt error can affect a serious effect to HDSS using angle(polytopic) multiplexing. Because the tolerance about tilt error is very tight it is important to measure the tilt error and compensate it. In this paper, tilt error measurement system using external photo detector is suggested and measuring experiments are conducted. A servo controller to compensate tilt error is designed and the performance of it is confirmed.

Keywords: Holographic storage, tilt error, angle multiplexing, galvano mirror

1. INTRODUCTION

Holographic Data Storage System(HDSS) can superimpose many data pages in one spot using various multiplexing methods. The polytopic multiplexing technique developed by InPhase tech. shows a good performance and is thought as one of promising multiplexing techniques. Because polytopic multiplexing is based on the angle multiplexing technique it is very weak to change of the incidence angle of reference beam into the media. As presented in ODS 2007 by InPhase tech., tolerances of the HDSS using polytopic multiplexing are $\pm 0.007^\circ$ about tangential tilt and $\pm 0.015^\circ$ about radial tilt. Recently photopolymer with disk type substrate is selected as a media of the holographic data storage system. Because shape of the media is a disk, a disk tilt must occur when the media rotates. When disk tilt is occurred the angle between the reference beam and the media is changed by the tilt, thus the data can not be recorded with a right angle or data page which was not wanted would be retrieved. The holographic data storage system is very weak to the tilt disturbance by the Bragg effect, therefore it is necessary to measure the tilt error and compensate it. In this study, we measure the amount of the tilt error using external photo detectors and compensate it by rotating the angle of the galvano mirror with designed controller.

2. TILT MEASUREMENT

2.1 Transmission geometry

Basic principle of the first tilt measurement method is Snell's law. A light wave transmitting the media with refractive index different from the air is refracted twice by Snell's law. Thus the direction of propagation vector of the transmitted light is not changed but the position is translated parallel to its original position. The light used for measurement the tilt error is called as servo beam. The amount of position change of the servo beam is determined by equation 1. Where, d is thickness of the media, n is refractive index of the media and θ_0 is the incidence angle of the servo beam.

$$x = \frac{d \times \left\{ \theta_0 - \sin^{-1} \left(\frac{\sin \theta_0}{n} \right) \right\}}{\cos \left\{ \sin^{-1} \left(\frac{\sin \theta_0}{n} \right) \right\}} \quad (1)$$

*urielk@yonsei.ac.kr; phone 82 2 2123-4677; fax 82 2 365-8460; mservo.yonsei.ac.kr

The servo beam can have any wavelength with corresponding photo detectors. Figure 1 shows layout of the tilt measurement scheme using Snell's law and measured tilt error signal with position sensitive detector when the disk with glass substrate is rotating at 30rpm. Tilt angle of about 0.1 degree can be measured using transmission geometry.

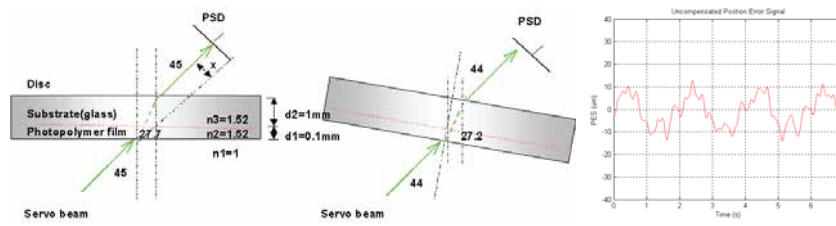


Fig.1. Transmission geometry and measured tilt error signal

Incidence angle of the reference beam is rotated by the galvano mirror to compensate the tilt error using designed controller. Equation 2 is transfer function of the galvano mirror and designed PID controller. Result of simulation is shown in figure 2.

$$G_{mirror}(s) = \frac{1.163 \times 10^8}{s^3 + 962.5s^2 + 5.958 \times 10^5 s + 1.16 \times 10^8} \quad (2)$$

$$G_c(s) = 1.0853 \times 10^{-4} \frac{s^2 + 5520s + 7.931 \times 10^6}{s}$$

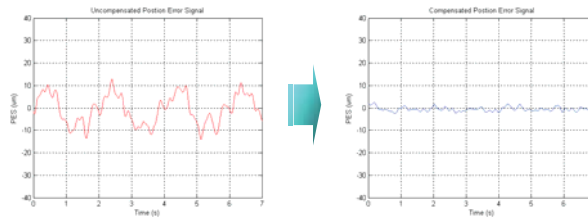


Fig.2. Measured tilt error signal and controlled tilt error signal

2.2 Reflection geometry

Tilt error can be measured by the transmission geometry but it has problems of low signal level and high noise component. In order to obtain high level and low noise tilt error signal, the layout of tilt measuring system is changed to a reflection geometry. Figure 3 shows a layout of the reflection geometry.

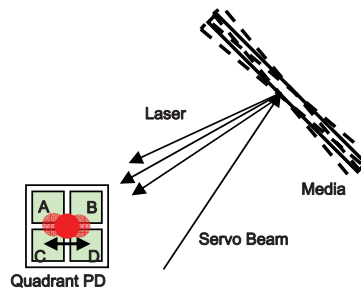


Fig.3. Layout of the reflection geometry

Change of tilt angle of the media by tilt disturbance changes angle of reflection of the servo beam and changes the position of servo beam on the quadrant photo detector at last. The amount of position change is determined by the distance between the media and the photo detector. For example, if the distance is 100mm, then 0.01 degree of tilt angle changes position of the servo beam about $17.45\mu\text{m}$. By using the quadrant photo detector array, radial and tangential tilt can be measured at once by a simple calculation.

To control the galvano mirror for tilt compensation the present angle of the mirror must be feedback to the control system. Though there is an encoder for the galvano mirror, when a high frequency input is entered the encoder can not tell us the exact value. Therefore the encoder is not suitable for precise servo control. Instead of the encoder, a Kalman filter estimator is used to obtain the feedback angle of galvano mirror. Figure 4 shows the experimental booth of HDSS in CISD and feedback signal from rotation of the galvano mirror using Kalman filter estimator.

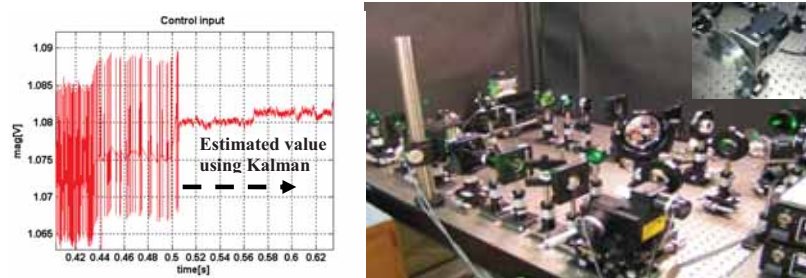


Fig.4. Experimental result of Kalman filter estimator and HDSS test bed in CISD

3. CONCLUSIONS

Tilt servo control is one of an important issue for HDSS. A tilt error measurement and compensation methods are suggested in this paper. The reflection geometry is thought better than transmission geometry and tilt error can be compensated by rotation of the galvano mirror. To control the galvano mirror precisely a Kalman filter estimator is used.

ACKNOWLEDGMENT

This research was supported by the MOCIE (Ministry of Commerce, Industry and Energy) of Korea through the program for the Next Generation Ultra-High Density Storage (00008145)

REFERENCES

- [1] Li H-YS, Psaltis D, "Three dimensional holographic disks", Applied Optics, Vol.33, No.17, 3764-3774 (1994).
- [2] Li H-YS, Psaltis D, "Alignment sensitivity of holographic three-dimensional disks", Journal of Optical Society of America, Vol.12, No.9, 1902-1912 (1995).
- [3] C-T Chen, Linear System Theory and Design, Oxford University Press (1999).
- [4] Normal S. Nise, Control Systems Engineering 3rd ed., Wiley (2000)

Design of a relay Lens with telecentricity in holographic storage system

Yung-Sung Lan^{1,2}, Kuang-Vu Chen², Ping-Jung Wu², Wen-Hung Cheng², Chih-Cheng Hsu², Chin-Tsia Liang², Kuo-Chi Chiu², Tzuan-Ren Jeng²

¹Department of Photonics and Institute of Electro-Optical Engineering, National Chiao Tung University, Hsinchu, Taiwan 300

²Electronics and Optoelectronics Research Laboratories, ITRI, Hsinchu, Taiwan 300

ABSTRACT

In this paper, we revealed a doubly telecentric Fourier 4f Relay for the holographic recording system, which is including six lenses and a PBS. It provides a zero distortion and the wavefront error within $1/4\lambda$ ($\lambda=532$ nm).

1. INTRODUCTION

There are two kinds of optical data storage systems (2D and 3D) which can be distinguished by how the data is recorded by one bit or one page. In the last few years we have witnessed the use of CD and DVD. Now BD (or HD-DVD) seems to play as an emerging technology. After that, holography is considered as one of several future data-storage paradigms that may answer our constantly growing need for higher-capacity storage and faster-access time. It breaks through the density limits of conventional storage by moving beyond recording only on the surface, to record through the full depth of the medium. Unlike other technologies that record one data bit at a time, holography allows a million bits of data to be written and read in parallel with a single flash of light.¹⁻³⁾

Despite the main advantages of the holographic storage, there are big challenges for the realization of systems. For such a storage technique, a special optical system containing a Fourier transform (FT) lens pair is adopted to store and retrieve digital data. In order to obtain a compact configuration and high information capacity, it is preferable to use short-focal-length FT lenses and a large spatial light modulator (SLM). There, however, is not enough space to put a spatial filter for lower consuming M# by applying the short-focal-length FT lenses. The solution is relay lens systems, they known up to now are without any distortion due to their symmetrical or substantially symmetrical set-up. This paper describes a study of telecentric relay lens in the holographic storage system. Finally a telecentric 4f relay lens is fabricated at the end of this paper.

2. LENS DESIGN

Telecentric lenses were discovered by I. Porro in 1848 and independently by E. Abbe in 1878.⁴⁾ In the last 120 years not much in depth literature has been published about the optical design of telecentric optical system. The published literature in the area of telecentric optical design methodologies are very elementary and lack much depth, when compared to the published literature on other lens design configuration methodologies.⁵⁾

A telecentric lens design optically corrects for parallax (perspective) errors by locating the entrance pupil at infinity. This correction makes imaging lenses with object-space telecentricity ideal for reducing dimensional-measurement errors caused by misfocusing and test-site vibration. It should be noted that beyond this parallax correction, high-quality telecentric imaging lenses usually offer uniform close-to diffraction-limited image resolution performance over the entire field of view, less than 0.1% distortion, and no vignetting across the whole image plane. If both entrance and exit pupils are located at infinity, the lens is called a "double-telecentric lens". A double-telecentric lens is actually an afocal optical system working as a finite-conjugate imaging lens. In a double-telecentric lens, both the object-space and image space chief rays are approximately parallel to the optical axis. A schematic of a telecentric lens, which is composed of three sections: front section A, iris diaphragm pupil, and rear section B, as shown in Fig. 1.

The specific requirements and the corresponding design parameter values of our objective are listed in Tab. 1. Here "object" refers to the SLM, and "image" refers to the CCD array as shown in Fig. 2. The objective presented in this figure has been designed by the commercial optical design software of ZEMAXTM. The magnification of the relay system is one, and the object and image are substantially equal in area. The design of a telecentric relay lens to be 4f Fourier configuration is due to the large field involved. However, the pixel size of the SLM that needs to be resolved at the detector array is much larger than the wavelength of light λ . This means that light from an individual pixel of the SLM is only diffracted into a small cone, which is $NA=0.038$. The distortion and field curvature of the telecentric 4f relay system are shown in Fig. 3.

3. CONCLUSION

The telecentric 4f relay lenses are made of Zeonex, the assembly of the system is shown in Fig. 4, and the profile of its reflecting surfaces is formed by diamond-turning machining (ULG-100CH). We successfully design the a telecentric 4f relay lens, which has a telecentric characterization in the object plane and Image plane, for the phase conjugate read out, in which a reproduction reference beam propagates in the direction opposed to the recording reference plane beam. In the full paper, we will carry out some experiment on it.

REFERENCES

- [1] J. W. Goodman, Introduction to Fourier Optics, 2nd Ed. (McGraw-Hill, New York, 1996).
- [2] J. F. Heanue, M. C. Bashaw, and L. Hesselink, "Volume holographic storage and retrieval of digital data" Science 265, 749-752(1994).
- [3] Sergei S. Orlov, William Phillips, Eric Bjornson, Yuzuru Takashima, Padma Sundaram, Lambertus Hesselink, "High-transfer-rate high-capacity holographic disk data-storage system" Applied Optics, Vol. 43, No.25, 2004.
- [4] M. Reiss, U.S. Patent 2,600,805, June 17, 1952.
- [5] M. Born & E. Wolf, Principle of Optics, 6th Ed. P. 1 86-7, Pergamon Press, NY, 1980

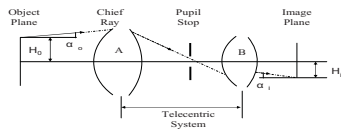


Fig. 1. A sketch of telecentric system

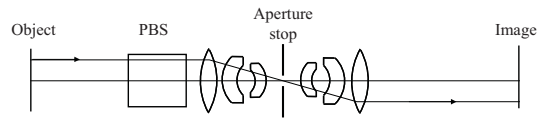


Fig. 2 The telecentric 4f relay system layout

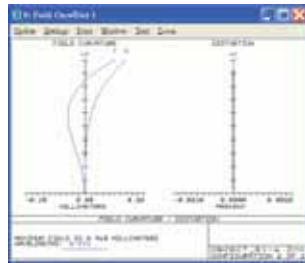


Fig. 3 The field curvature and distortion of the telecentric 4f relay system



Fig. 4 The telecentric 4f relay system

Table 1 First order requirements of the system

Geometric Parameters (mm)		Image Quality Parameters	
Track Length	244.69	Operational Wavelength (nm)	532
Object Size	8.96	MTF (lp/mm)	37
Image Size	8.97	Encircled Energy (on axis, on edge) (%)	(98.91, 98.89)
Pixel NA	0.038	Distortion over the full FOV (um)	0
Object Space Working Distance	53.49	Encircled Energy Uniformity total range over FOV	0.02 %
Image Space Working Distance	73.85	Object Space Telecentric (degree)	0.0235
Image Space Numerical Aperture	0.0356	Image Space Telecentric (degree)	0.0235

Optimal aperture size for maximizing the capacity of holographic data storage systems

Oliver Malki¹, Frank Przygodda, Joachim Knittel, Heiko Trautner, Hartmut Richter
 Deutsche Thomson OHG, Hermann-Schwer-Str. 3, D-78048, Germany
 Phone: +49-7721-85-2004, Fax: +49-7721-85-2241
¹E-mail: oliver.malki@thomson.net.

ABSTRACT

We suggest a new approach to determine the optimal spatial filtering of the object beam by an aperture placed in the focal plane in order to optimize the storage capacity of a holographic data storage system (HDSS). A capacity evaluation function $C(\xi)$ is introduced for which the maximum is searched by varying the aperture size. In our approach $C(\xi)$ depends on the code rate and the consumption of the holographic material, which is assumed to be placed in the focal plane. The code rate itself depends on the raw symbol error rate (SER) which is determined by the complete process of data page creation, simulation of the optical channel, and data detection. In addition we demonstrate the dependency of the optimal aperture size on the light intensity distribution in the focal plane, the detector sampling, and the noise level.

Keywords: holographic data storage, spatial filtering, material consumption, Nyquist aperture, data capacity

1. DATA CAPACITY VS APERTURE SIZE

In an HDSS typically a spatial light modulator (SLM) is used to generate two-dimensional digital patterns. These so-called data pages are stored via interference patterns of object and reference beam in the holographic medium and are retrieved from the medium by exposing it to the reference beam. The reconstructed data pages are then detected by a matrix detector [1]. Usually the data pages have to be spatially lowpass filtered before writing them into the medium in order to reduce the size of each hologram and therefore to increase the overall data capacity (see [2], [3]).

We will present an approach to optimize the data capacity in dependence on the size of a spatial filter realized by an aperture in the focal plane. Therefore we introduce the dimensionless aperture factor ξ with which the aperture size D can be written as $D=D_N \xi$. Here D_N is the Nyquist aperture [2] which is usually defined as $D_N=\lambda f/\Gamma$, where λ is the wavelength, f the focal length, and Γ is the size of one SLM pixel. By performing all calculations based on ξ we are independent of the particular choice of λ , f and Γ . Usually the data capacity C of an HDSS is assumed to be proportional to the inverse of the square of the aperture size $C\sim 1/D^2$ or $C\sim 1/\xi^2$ (see [1], [2], [3]). As an extension to this model we will present a more advanced capacity calculation, which enables to include an improved representation of the underlying optic concept.

1.1 Data capacity evaluation function

In order to calculate the optimal aperture factor ξ for spatial lowpass filtering we define a data capacity evaluation function $C(\xi)$ based on [1], [3] as the ratio of code rate $r_{\text{ECC}}(\xi)$ and material consumption function $M(\xi)$ to:

$$C(\xi) \propto \frac{r_{\text{ECC}}(\xi)}{M(\xi)} \quad (1)$$

More precisely $M(\xi)$ is proportional to an increase of the refractive index. A suitable code rate $r_{\text{ECC}}(\xi)$ for an HDSS is related to the raw SER. A higher raw SER requires more error correction coding (ECC) overhead which leads to a lower code rate. A lower raw SER enables less ECC and would lead to a higher $r_{\text{ECC}}(\xi)$. As a suitable approach for the relation of $r_{\text{ECC}}(\xi)$ to the raw SER we assume $r_{\text{ECC}}(\xi)\sim 1-b \text{ SER}(\xi)$ where b is a factor, which depends on the desired final SER and was set to 1 here. The actual SER is numerically determined considering the optical model. A result which will not be discussed in detail is that an increasing b leads to a slight shift of the maximum of $C(\xi)$ to higher ξ .

We assume $M(\xi)$ to be proportional to the integral of the two-dimensional intensity distribution $I(\xi)$ of a data page in the focal plane. This means that we implicitly assume a linear relation between the intensity and the modification of the refractive index of the holographic medium. Because of the symmetry of the square aperture the integral can be separated into the square of a one-dimensional integral

$$M(\xi) = a^2 \left(\int_0^\xi I(\xi') \cdot d\xi' \right)^2 \tag{2},$$

where a is a scalar constant. If the intensity distribution $I(\xi)$ is constant the integral leads to $M(\xi) = a^2 \xi^2$ or a capacity $C \sim 1/\xi^2$ which we already mentioned above. We consider two alternative functions for $I(\xi)$ which we assume to be an improved representation of the concerning optic concept. First the sinc function $\text{sinc}(x) = \sin(\pi x)/\pi x$, corresponding to the Fourier transform of a rectangular pixel. Secondly the Gaussian function $\text{gauss}(x, m, s)$ (or normal distribution with mean m and standard deviation s). The Gaussian function is a good approximation of the envelope of the intensity distribution in the focal plane, when using a random phase mask. In Fig. 1 the intensity distributions and the resulting material consumptions are displayed for these three cases.

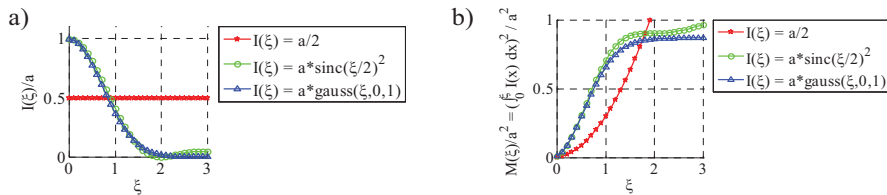


Fig. 1. a) Three different one-dimensional slices through the intensity distribution $I(\xi)$ in the focal plane. b) The material consumption $M(\xi)$, which is defined as the are integral of the intensity distribution (see eq.(2))

1.2 The simulation scheme

To determine how the SER depends on the aperture size, we apply the complete process of data page creation, the simulation of the optic channel, and the data detection. Then we compare the sent with the received data pages to calculate the SER. Here the SER means the raw SER without any application of ECC. We are using a block modulation where three white pixels are placed in each 4x4 block of SLM pixels. The pages for this simulation consist of 256x256 pixels.

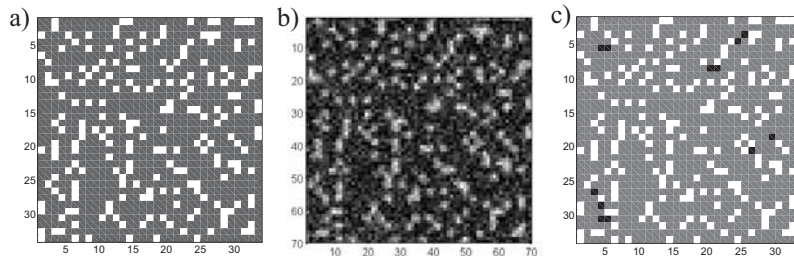


Fig. 2. a) Part of a data page on the SLM. b) The data page after filtering, sampling and noise addition is displayed ($\sigma \sim 2.1415$, $\xi = 1.6$, and $\text{PSNR} = 18$). c) The demodulated data page including erroneous pixel (SER ~ 7%).

Fig. 2a) shows a part of a data page used for simulation. The optic channel consists of spatial filtering, sampling of the detector and addition of Gaussian white noise. The spatial filtering was implemented by multiplying the Fourier transform of the original data page by an aperture function - in this case a square aperture - and afterwards applying the inverse Fourier transformation. For the detector we assumed a fractional sampling factor of e.g. $\sigma = 2.14$ and 100% fill factor, which was implemented by integral interpolation where the amount of light intensity on each detector pixel is calculated by the integral of light acquired by the corresponding sensitive pixel area. The noise level is defined by the PSNR [4] and is set to a value where the achievable raw SER is in a useful range - below 10% at the maximum of $C(\xi)$. Fig. 2b) shows the data page recorded by the simulated matrix detector after sending it through the optic channel. In the

first step of the demodulation procedure the positions of the synchronizing marks are detected. Afterwards the positions are used to determine the sampling factor in order to perform a linear sampling to the scaling of the SLM. Then the data are identified for each block by correlation detection. Fig. 2c) shows a part of the demodulated data page including some wrongly detected channel bits (marked as black squares).

2. RESULTS

In Fig. 3a) $C(\xi)$ is plotted for the three different kind of $M(\xi)$ in the case of $\sigma \sim 2.14$ and PSNR=18. The position and the significance of the maximum $C(\xi)$ depends on $M(\xi)$. The calculation of $r_{\text{ECC}}(\xi)$ for each ξ was performed by calculating the mean of 10 simulations as described in section 1.2. The resulting standard deviation of $C(\xi)$ was below 5%.

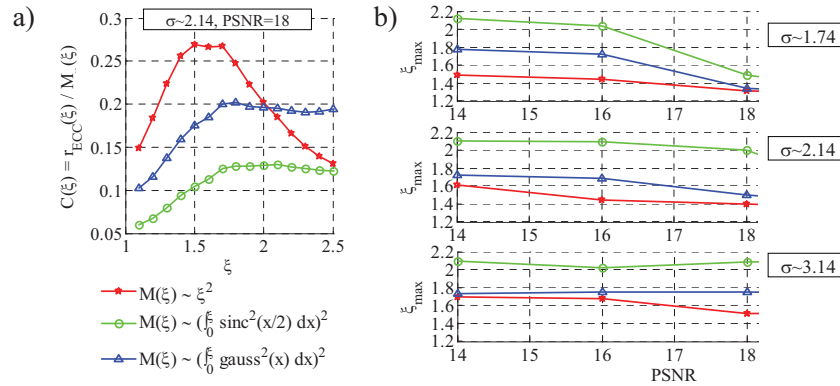


Fig. 3. Part a) shows the storage capacity in dependence on the aperture factor ξ for 3 different material consumption functions $M(\xi)$. In b) the values of ξ for maximum $C(\xi)$ are displayed vs. PSNR for 3 different sampling factors σ .

In Fig. 3b) the value of ξ at the maximum of the $C(\xi)$ denoted as ξ_{max} is displayed vs. PSNR. ξ_{max} has only a slight dependence on the PSNR and this dependence seems to be less significant for higher sampling factors. Generally it can be seen that ξ_{max} depends strongly on the material consumption function. The functions $M(\xi)$ based on the more realistic sinc and gauss functions lead to higher values of ξ_{max} .

3. CONCLUSION

We introduced a criterion to estimate the data capacity of an HDSS which considers the code rate and the material consumption depending on three different focal intensity distributions. Code rate and material consumption are related to the aperture size used for spatial low-pass filtering. We demonstrated that the optimal aperture size corresponding to maximum of $C(\xi)$ depends on the intensity distribution in the focal plane. In addition we showed the influence of system parameters like detector sampling and noise level. Further investigation may focus on the development of an improved model of $C(\xi)$ which enables to take more and advanced system parameters into account.

REFERENCES

- [1] Hesselink, L., Orlov, S. S., Bashaw, M. C., "Holographic data storage systems," Proc. IEEE, vol. 92, no. 8, pp. 1231-1280 (2004)
- [2] Bernal, M.-P., Burr, G. W., Coufal, H., and Quintanilla, M., "Balancing interpixel cross talk and detector noise to optimize areal density in holographic storage systems," Applied Optics . Vol. 37, No. 23, pp 5377-5385 (1998).
- [3] Burr, G. W. and Marcus, B., "Coding tradeoffs for high-density holographic data storage," Proc. SPIE 3802, pp. 18-29 (1999).
- [4] Malki, O., Knittel, J., Przygodda, F., Trautner, H., and Richter, H., "Two-dimensional modulation for holographic data storage systems," supplied to J.J.A.P Special Issue on Optical Memory ISOM 2007 (2008)

Angular interval scheduling for angle-multiplexed holographic data storage

Nobuhiro Kinoshita*, Tetsuhiko Muroi, Norihiko Ishii, Koji Kamijo, and Naoki Shimidzu
Science & Technical Research Laboratories, Japan Broadcasting Corporation (NHK)
1-10-11 Kinuta, Setagaya-ku, Tokyo, 157-8510 Japan

ABSTRACT

In angle-multiplexed holographic data storage, the full-width at half-maximum value of Bragg selectivity curves is dependent on the angle formed between the media and incident laser beams. We demonstrated an angular interval scheduling for closely stacking holograms into media even when the range of the angle is limited. We obtained bit-error-rates of the order of 10^{-4} under the following conditions: a media thickness of 1 mm, a laser beam wavelength of 532 nm, and an angular multiplexing number of 300.

Keywords: angular interval schedule, holographic memory, angle multiplexing, Bragg selectivity curve, bit-error-rate

1. INTRODUCTION

Holographic data storage has a high data-transfer-rate and large capacity because two-dimensional data array is accessed into / from media at once and the arrays are multiplexed in the same volume of media. Holographic data storage has applications where storing the large amount of video data is required, such as for HDTV and Ultra-HDTV [1].

Many multiplexing methods for holographic data storage have been developed. These methods include coaxial type multiplexing [2], phase coded multiplexing, angle multiplexing, etc. The angle multiplexing method will increase storage density by combining with phase conjugation reproduction and polytopic multiplexing [3].

In this paper, we demonstrate an angular interval scheduling for angle multiplexing that controls the angular intervals between adjacent holograms in order to increase the multiplexing number. We describe bit-error-rate (BER) characteristics using our angular interval scheduling under the following conditions: a media thickness of 1 mm, a laser beam wavelength of 532 nm, and an angular multiplexing number of 300. We also discuss modifying the angular interval scheduling in order to reduce the errors due to crosstalk from adjacent holograms.

2. OPTICAL SETUP

Figure 1 shows the optical configuration of our experimental equipment. The spatial light modulator (SLM) was a reflection-type liquid crystal on silicon (LCOS) that had 1400 x 1050 pixels and a pixel pitch of 10.4 μm . Each datapage contained 75,264 bits, which were coded in 2-4 modulation. The signal beam went through the Fourier-transform lens (FTL) and the square aperture eliminated the unwanted diffraction order on the Fourier-transform plane so that only the important components of the signal beam irradiated the recording media. The recording media was located at the offset from the Fourier-transform plane so as to avoid the local concentration of the DC components of the signal beam. The reference beam was irradiated from the FTL side when recording and from the opposite side when reproducing. We used InPhase media with a thickness of 1 mm as recording media, and it was mounted on a rotation stage. Angular multiplexing was performed with the media rotated on a plane that included signal and reference axes. The media rotation angle, θ_m , was set to zero, at which angle the signal beam axis is vertical to the media. The angle θ_m had a range from -3 to $+27$ degrees.

When reproducing, the diffracted beam from the hologram forms an image on the camera through the square aperture and the FTL. We used a CCD imager that had 2048 x 2048 pixels and a pixel pitch of 7.4 μm as a camera.

* e-mail: kinoshita.n-ee@nhk.or.jp; phone: +81 3 5494-3277; fax: +81 3 5494-3297

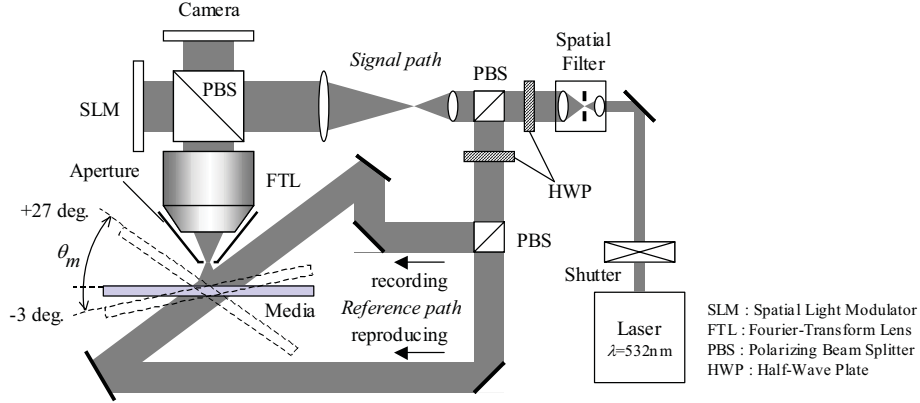


Fig. 1 Optical configuration of experimental equipment.

3. ANGULAR INTERVAL SCHEDULING

To investigate the fundamental characteristics of the angular width of each hologram, Bragg selectivity curves with media angles, θ_m , of -3 , 12 and 27 degrees were measured (See Fig. 2). In Fig. 2 (a), (b) and (c), the full-width at half-maximums (FWHMs) were 0.126 , 0.090 and 0.065 degrees, respectively. To stack many holograms as closely as possible into the media within the limited angle range of θ_m , it is necessary to adjust the angular intervals between adjacent holograms.

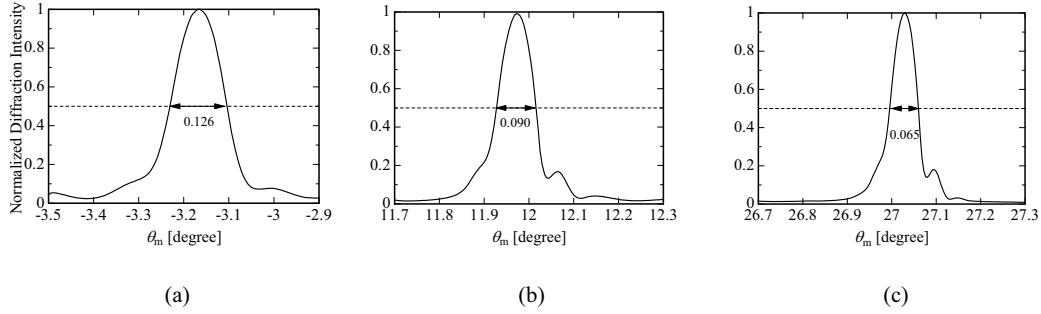


Fig. 2 Bragg selectivity curves where θ_m s are (a) -3 , (b) 12 and (c) 27 degrees when the media thickness is 1 mm. FWHMs are 0.126 , 0.090 , and 0.065 degrees, respectively.

Based on FWHMs of the Bragg selectivity curves, we assigned 300 datapages with angular intervals of $\Delta\theta_m$ between adjacent holograms. The n -th datapage's angular interval $\Delta\theta_m(n)$ was approximated to the following quadratic function that passes through three constant $\Delta\theta_m$ s,

$$\Delta\theta_m(n) \equiv an^2 + bn + s, \quad (1)$$

$$a \equiv \frac{2(s - 2t + u)}{N^2}, \quad (2)$$

$$b \equiv -\frac{3s - 4t + u}{N}, \quad (3)$$

where N is the total number of datapages ($N=300$), and s , t , and u denote three constant angular intervals $\Delta\theta_m(1)$, $\Delta\theta_m(N/2)$, and $\Delta\theta_m(N)$, respectively. Figure 3 (a) shows the angular interval $\Delta\theta_m$ as a function of the datapage number. We derived a schedule-A (dashed line in Fig. 3 (a)) from Eq. (1) by setting the three constant angular intervals $\Delta\theta_m(1)$, $\Delta\theta_m(N/2)$, and $\Delta\theta_m(N)$ to 0.136, 0.100, and 0.075 degrees, respectively, so that the sum of the $\Delta\theta_m$ corresponds to the full range of θ_m , 30 degrees.

After recording 300 datapages using the schedule-A, the bER characteristics was obtained (filled circles in Fig. 3 (b)). In the middle range of the page numbers the bERs are of the order of 10^{-5} . However, the bERs in the low datapage numbers are relatively high. Above the datapage number of 200, the bER gradually increased. For datapages with a high bER, the crosstalk noise from the adjacent hologram was significant. In such case, the angular intervals were too narrow.

To reduce the errors due to crosstalk noise, we modified the angular interval schedule. For the datapages with low and high numbers, the angular intervals were expanded. For datapages with numbers in the middle of the range, the angular intervals were narrowed so that the sum of the $\Delta\theta_m$ corresponded to the full range of θ_m , 30 degrees. We determined schedule-B (solid line in Fig. 3 (a)) by setting the three constant angular intervals $\Delta\theta_m(1)$, $\Delta\theta_m(N/2)$, and $\Delta\theta_m(N)$ to 0.148, 0.092, and 0.096 degrees, respectively. Using schedule-B, the bERs of 300 datapages (open circles in Fig. 3 (b)) were obtained. Though the crosstalk noises still remained in datapages with low and high numbers, bERs of the order of 10^{-4} were obtained across all the datapages.

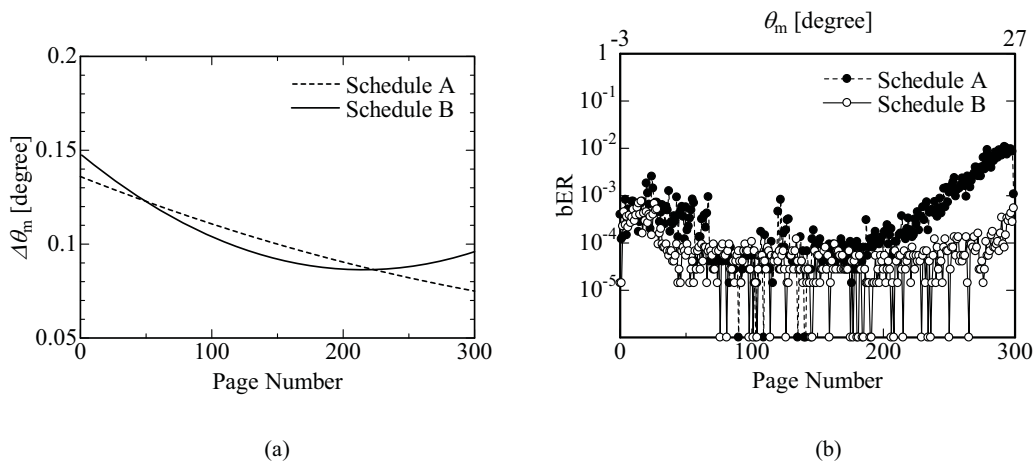


Fig. 3 (a) Angular interval schedules and (b) measured bERs without error correction.

4. CONCLUSION

We demonstrated an angular interval scheduling for closely stacking holograms into media even when the range of the angle is limited. With correctly assigned angular intervals, bERs of the order of 10^{-4} across all the datapages were obtained when using a media of thickness 1 mm, a laser beam wavelength of 532 nm, a media rotation range of 30 degrees and an angular multiplexing number of 300.

REFERENCES

- [1] T. Muroi, N. Kinoshita, N. Ishii, K. Kamijo, and N. Shimidzu, "Holographic Data Storage for Broadcasting Systems," *IWHM 2007 Digests*, 27o06.
- [2] K. Tanaka, H. Mori, M. Hara, K. Hirooka, A. Fukumoto, and K. Watanabe, "High density recording of 270 Gbits/inch² in a coaxial holographic storage system," *ISOM'07 Technical Digest*, Mo-D-03.
- [3] K. Anderson and K. Curtis, "Polytopic multiplexing," *Opt. Lett.*, **29**, 12, 1402-1404 (2004).

Shift selectivity of the collinear holographic storage system

Ye-Wei Yu, Chih-Yuan Cheng, Shu-Ching Hsieh, Tun-Chien Teng and Ching-Cherng Sun*
Department of Optics and Photonics, National Central University, Chung-Li 320, TAIWAN

Phone : +886-3-4276240, E-mail : ccsun@dop.ncu.edu.tw

ABSTRACT

The paraxial solution of the shift selectivity of the collinear holographic storage system is proposed, which is a powerful tool for simulation. We use the paraxial solution to simulate two-dimensional shift selectivity in a wide range so that the variation of shifting selectivity for different signal position can be figured out.

Keywords: paraxial solution, shift selectivity, collinear holographic, references pattern.

SUMMARY

Holographic Versatile Disc system using collinear algorithm has been shown large storage capacity, high transfer rate, short access time, and also compatible with existing disc storage system, such as CD and DVD [1-2]. Besides, small shift selectivity in both radial and tangential directions is also proposed [3]. The simulation of shift selectivity is necessary for it take an important role in storage capacity. In this paper, we propose a paraxial solution for shift selectivity, which can simulate the shift selectivity in two dimensions and in wide range easily. Thus, the effect of different reference patterns can be calculated in detail.

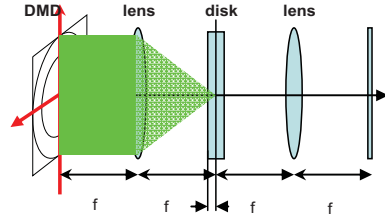


Fig. 1 (a)

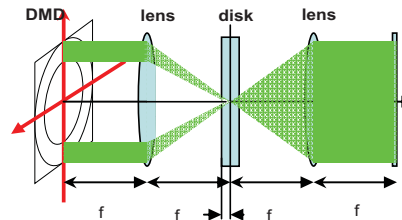


Fig. 1 (b)

Fig. 1. Transmission model of the collinear algorithm for (a) writing process and (b) reading process.

Recently, we have proposed a paraxial approximating analytic solution for the collinear system based on scalar diffraction theory and VOHIL model [4-5]. Which shown that the diffracted optical field on the CCD with different shifting $(\Delta u, \Delta v)$ can be written as

$$D_{\text{det}}(\xi, \eta, \Delta u, \Delta v) = \frac{2Te^{jk4f}}{(\lambda f)^2} \int_{-\infty}^{\infty} \int_{-\infty}^{\infty} \int_{-\infty}^{\infty} \left\{ \begin{array}{l} U_s(\xi_1, \eta_1) U_R^*(\xi_1 - \xi_2 + 2\xi, \eta_1 - \eta_2 + 2\eta) \\ U_p(-\xi_2 + \xi, -\eta_2 + \eta) \exp\left(-j \frac{2\pi}{\lambda f} (\Delta u \cdot \xi_2 + \Delta v \cdot \eta_2)\right) \\ \sin c \left[\frac{2T}{\lambda f^2} ((\xi_2 - 2\xi)(\xi_1 + \xi) + (\eta_2 - 2\eta)(\eta_1 + \eta)) \right] \end{array} \right\} d\xi_2 d\eta_2 d\xi_1 d\eta_1, \quad (1)$$

where U_p , U_R and U_S is the reading, reference and signal optical field distribution, respectively. T is the thickness of the recording media, k is the wave vector, λ is the wave length, f is the focal length of the lens, (ξ, η) is the coordinate on the CCD plane, (ξ_1, η_1) is the coordinate on the input SLM and (ξ_2, η_2) is the parameter come from convolution. The geometrical structure of the collinear storage system for the theoretical modeling is shown as Fig. 1.

To simply this formula, eq. (1) can be written as

$$D_{\det}(\xi, \eta, \Delta u, \Delta v) = \frac{2Te^{jk4f}}{(\lambda f)^2} \int_{-\infty}^{\infty} \int_{-\infty}^{\infty} \mathfrak{S} \left\{ \begin{array}{l} U_R^*(\xi_1 - \xi_2 + 2\xi, \eta_1 - \eta_2 + 2\eta) U_p(-\xi_2 + \xi, -\eta_2 + \eta) \\ \sin c \left[\frac{2T}{\lambda f^2} ((\xi_2 - 2\xi)(\xi_1 + \xi) + (\eta_2 - 2\eta)(\eta_1 + \eta)) \right] \end{array} \right\} U_s(\xi_1, \eta_1) d\xi_1 d\eta_1, \quad (2)$$

The pixel shift selectivity is the total intensity variation of one pixel, and can be written as

$$I_{\text{pixel}}(\Delta u, \Delta v) = \iint_{\text{pixel}} |D_{\det}(\xi, \eta, \Delta u, \Delta v)|^2 d\xi d\eta, \quad (3)$$

Then we get the pixel shift selectivity as

$$I_{\text{pixel}}(\Delta u, \Delta v) = \frac{2Te^{jk4f}}{\lambda^2 f^2} \iint_{\text{pixel}} \left| \iint \mathfrak{S} \left\{ \begin{array}{l} U_R^*(\xi_1 - \xi_2 + 2\xi, \eta_1 - \eta_2 + 2\eta) U_p(-\xi_2 + \xi, -\eta_2 + \eta) \\ \sin c \left[\frac{2T}{\lambda f^2} ((\xi_2 - 2\xi)(\xi_1 + \xi) + (\eta_2 - 2\eta)(\eta_1 + \eta)) \right] \end{array} \right\} U_s(\xi_1, \eta_1) d\xi_1 d\eta_1 \right|^2 d\xi d\eta, \quad (4)$$

Fig. 2(b) is the simulation result of eq.(4) with radial reference pattern shown in Fig.2(a). The parameter in this simulation is the same as what used in ref. 6, except that the integral pixel size of signal is $4\mu\text{m}^2$. And we get similar result. Generally, people who see Fig. 2(b) only anticipate that the diffracted intensity would be smaller as the disk shift more. However, Fig. 2(c) shows that the diffracted intensity is rising up in the displacement between $30\mu\text{m}$ and $40\mu\text{m}$.

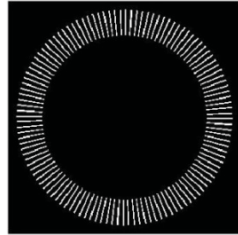


Fig.2 (a)

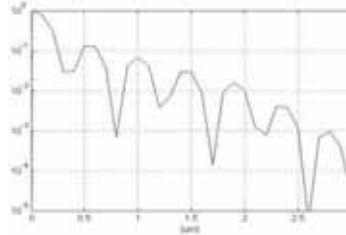


Fig. 2 (b)

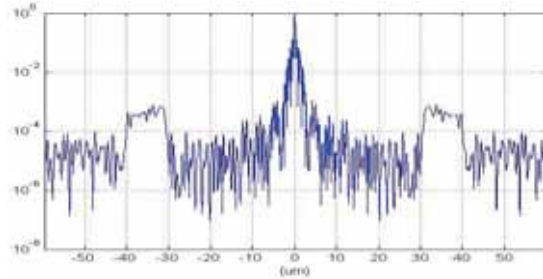


Fig. 2 (c)

Fig.2 (a) The radial reference pattern, (b) the shift selectivity in log scale, (c) the shift selectivity in log scale for displacement from $-60\mu\text{m}$ to $60\mu\text{m}$.

The two dimensional shift selectivity with large shifting can be simulated via two dimensional fast fourier transform. Fig. 3(a) is the two dimensional shift selectivity in log scale. To make it clear, we plot a new pattern which make what larger than 10^{-3} be white and what smaller than 10^{-3} be black Fig.3 (b). And we find a radial ring appear when

the displacement is around $15\mu\text{m}$. It shows that our calculation provides a powerful tool for the design of the reference pattern of the collinear optical holographic storage system.

This study was sponsored by the Ministry of Economic Affairs of the Republic of China with the contract no. 95-EC-17-A-07-S1-011 and the National Science Council with the contract no. NSC 96-2221-E-008-031. The authors would like to thank S. H. Lin and T. H. Yang for their comments on the study.

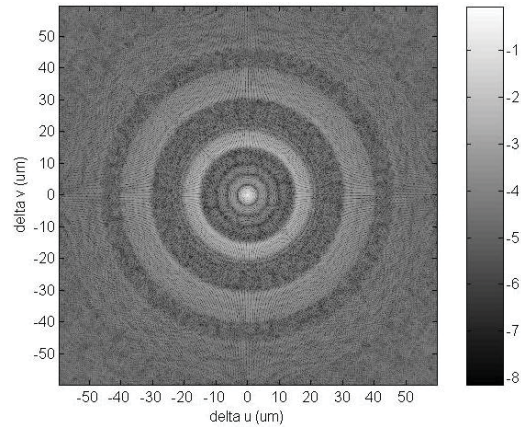


Fig. 3 (a)

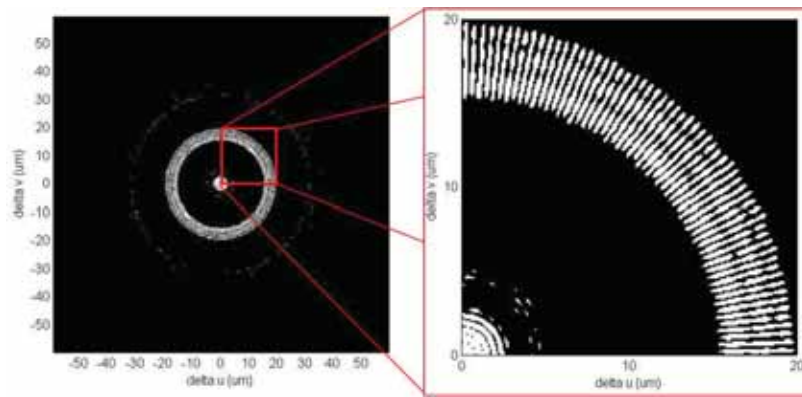


Fig. 3 (b)

Fig.3 (a) The two dimensional shift selectivity in log scale, (b) The binary pattern to highlight what larger than 10^{-3} .

REFERENCES

- [1] H. Horimai and X. Tan, "Advanced collinear holography," *Opt. Rev.* **12**, 90–92 (2005).
- [2] H. Horimai, X. D. Tan, and J. Li, "Collinear holography," *Appl. Opt.* **44**, 2575–2579 (2005).
- [3] H. Horimai and X. Tan, "Holographic versatile disc system," *Proc. of SPIE* **5939**, 593901(2005).
- [4] C. C. Sun, "A simplified model for diffraction analysis of volume holograms," *Opt. Eng.* **42**, 1184–1185 (2003).
- [5] C. C. Sun, Y. W. Yu, S. C. Hsieh, T. C. Teng and M. F. Tsai "Point spread function of a collinear holographic storage system," *Optics Express* **26**, 18111-18118 (2007).
- [6] T. Shimura, S. Ichimura, Y. Ashizuka, R. Fujimura, K. Kuroda, X. D. Tan, and H. Horimai, "Shift selectivity of the collinear holographic storage system," *Proc. of SPIE* **6282**, 62820s (2006).

Isoplanatic Lens Design for Phase Conjugate Storage Systems

Brad Sisson, Alan Hoskins*, Tolis Deslis, Kevin Curtis
InPhase Technologies, Inc., 2000 Pike Road, Longmont, CO 80501, USA
AlanHoskins@InPhase-Tech.com

Abstract: A new type of storage lens for holographic data storage systems is introduced that improves phase conjugation. This type of lens is characterized by a large isoplanatic patch. This enables relaxed assembly tolerances, asymmetric reader/writer architectures, and compensation for tilted plate aberrations in the media.

1. Introduction

Angle-polytopic phase conjugate Holographic Data Storage (HDS) systems [1-3] are useful for professional applications and are a leading candidate for 4th generation consumer optical storage. Phase conjugation allows simpler optics to be used due to aberration correction during hologram recovery. This aberration cancellation typically only occurs for the case when the recovered signal retraces the path it experienced during recording, and is limited in the cases of media misalignment or drive to drive interchange, where a completely different optical path is used in recovery. In this paper, we present the isoplanatic lens design concept that cancels aberrations in the presence of media misalignments and interchange between different lenses. This design concept is ideal for Holographic Read Only Memories (HROM) and consumer HDS systems where tolerances lead directly to cost. The design form is especially well suited for HROM systems as it allows asymmetric phase conjugate systems [4], holograms recorded with a complex, expensive mastering lens can be recovered and almost perfectly phase conjugated using a different, simpler, and cheaper reader lens.

The design form presented in this paper exploits the principle of isoplanatism or spatial invariance. This means aberrations to the point spread function of the lens do not vary significantly across the field [5]. Almost all lenses have limited isoplanatism due to the tiny "isoplanatic patches" required to linearize the response of the lens and allow it to perform a Fourier transform [6]. The size of these patches is typically slightly larger than the lens point spread function (PSF) [7], typically a few microns square. The lenses presented in this paper have isoplanatic patches on several millimeters square and are thus said to be extremely isoplanatic. The larger the isoplanatic patch, the more a shift of the storage lens with respect to the recorded hologram can be tolerated while phase conjugating the data perfectly.

2. Characteristics of Isoplanatic Lenses

A definition of extreme isoplanatism is readily obtained by extending existing definitions of "infinitesimal" isoplanatism as defined in the literature. Systems with infinitesimal isoplanatism have the following characteristics:

- Infinitesimal translations in object space produce infinitesimal translations in image space without change in quality of the corresponding image [8].
- Infinitesimal rotations in object space produce infinitesimal rotations in image space without changing the quality of the corresponding image [9].
- Wavefront aberration for a given point in the pupil is constant [10].
- The wavefront aberration corresponding to a given PSF in image space is constant [5].

To extend these definitions of infinitesimal isoplanatism to cover extreme isoplanatism we simply change all infinitesimal rotations and translations to finite and change all instances of the word point to patch. As mentioned in the introduction, extremely isoplanatic patches can be orders of magnitude larger in area than the infinitesimal patches associated with a lens PSF. These definitions, once modified to cover extreme isoplanatism, can be used as design time constraints when optimizing a lens with a modern lens design program [11].

In holographic data storage systems, the most convenient metric to measure the performance of the system is the signal to noise ratio (SNR). Because the SNR is largely a function of the PSF in the recording and recovering systems, we can reformulate the last characteristic of extreme isoplanatism; The SNR in a phase conjugate system is constant in the presence of finite shift or tilt of the system phase conjugation optics.

InPhase Technologies has developed an optical model of holographic storage systems which predicts the recovered page SNR by simulating the PSF using Huygens' method and the k-sphere formulation of volume holography. The model shows good correlation with experimental data for media shifts and rotation and has been adapted as a Zemax[®] plug-in and can be used to simulate the SNR during the design of HDS optics.

3. An Extremely Isoplanatic Holographic Storage Lens

Figure 1 shows an extremely isoplanatic Fourier transforming (FT) storage lens recently designed by InPhase Technologies. The lens was optimized for isoplanatism by constraining the lens performance using the definitions of Section 2. Using the 3rd characteristic of isoplanatic lenses listed above we can directly examine the size of the isoplanatic patches using the changes in Zernike polynomial coefficients or RMS wavefront error as a function of field.

Figure 2 shows the first nine Zernike coefficients as a function of field while Figure 3 shows the RMS wavefront error. The Zernike terms describe the first and third order wavefront properties for a single SLM pixel in the storage system. The slope of these curves can give insight into how the wavefront of the different SLM pixels changes across the lens field. Figure 3 shows how the RMS magnitude of the wavefront error changes across the lens field. An isoplanatic patch is the area where the wavefront shape and magnitude do not change significantly.

To evaluate the size of the isoplanatic patch for this lens, we introduce here the empirical criteria developed by InPhase Technologies of 1/50th wave RMS. While this value is much more stringent than the 1/14th wave Marechal criterion [13] for diffraction limited performance, it has been proven to adequately predict SNR constancy during phase conjugation. Note that this value gives SNR constancy for a SLM with 4.6 micron pixels and may be relaxed when larger pixels are used. Examining Figure 4, we see a large isoplanatic patch between 0 and 1.4 mm of field where there is less than 1/50th wave RMS variation. At the edge of the field the variation corresponds to an isoplanatic patch of 400 microns. We therefore conclude that over neighborhoods of order 400 microns wide, the wavefront shape and magnitude changes of Figures 2 and 3 are insignificant. This has profound consequences on phase conjugation in holographic data storage systems.

4. Examples – Symmetric and Asymmetric Phase Conjugation

In an ideal phase conjugate storage system, the SLM pixels with varying wavefront (see Figure 2 and 3) are recorded into holographic media using a reference beam. The recorded pixel wavefronts are then recovered using a conjugate beam and an identical storage lens. On readout the aberrations in each pixel are negated by reverse propagation through the FT lens resulting in perfect imaging. This is true for any lens, regardless of attributes such as isoplanatism. In practice however, phase conjugation involves an intermediate process where, after recording, the media may shift, tilt, and/or shrink. Additionally, the recording and recovering lens may not be identical due to manufacturing or assembly errors in different storage systems. In these instances, errors do not cancel out and in perfect phase conjugation results. These conditions can be greatly mitigated by using an extremely isoplanatic storage lens.

In the first example we consider tilt errors that introduce field shifts of about 400 microns (see Figure 4) in a symmetric phase conjugate system (the recording and recovery lens are identical). Because the tilt induced shift is less than the size of our isoplanatic patch, the performance of the system is still diffraction limited as predicted (see Figure 5). Tilt insensitivity is important when doing wavelength compensation for thermal effects although tilts encountered in a conventional LHD system are much smaller than 9.5 degrees [13].

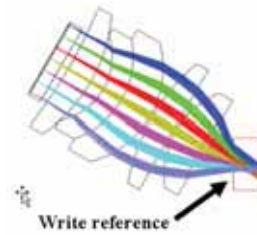


Figure 1. Extremely isoplanatic storage lens with an effective focal length of 2.4 mm and 1.7 mm field

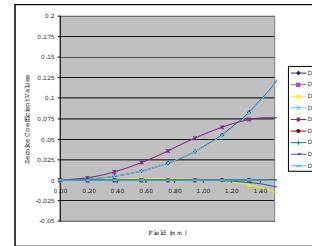


Figure 2. Zernike polynomial coefficients as a function of field for storage lens shown in Figure 2.

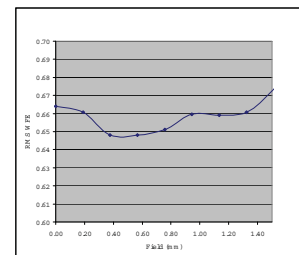


Figure 3. RMS wavefront error vs. Field for the isoplanatic storage lens shown in Figure 2.

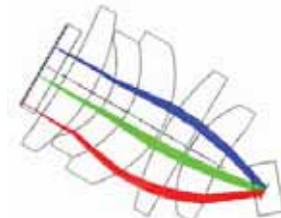


Figure 4. Symmetric readout using the lens in Figure 1 with a 9.5° media tilt.

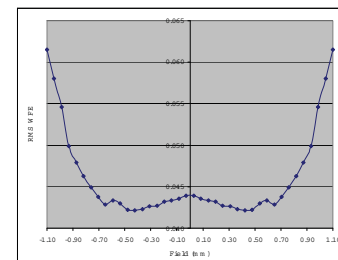


Figure 5. RMS wavefront in a symmetric system with 9.5° tilt error in media position.

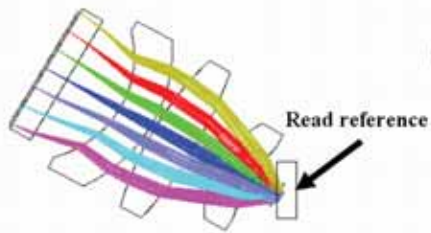


Figure 6. Asymmetric readout using 3 element lens to recover hologram s written with the lens in Figure 1.

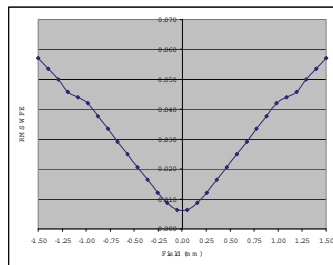


Figure 7. RMS wavefront error vs. field in asymmetric system with 80 μm axial shift in media

In the second example we investigate asymmetric phase conjugation (see Figure 6), where a simple 3 element lens is used to recover hologram s written with the 5 element lens in Figure 1. Without media shifts, tilts or rotations the 3 element lens was designed to perfectly phase conjugate the pixel wavefronts recorded by the lens in Figure 2. With a media axial shift of 80 μm , the lens is still diffraction limited over the lens field (Figure 7). This 3 element spherical lens assembly could be further simplified and replaced by a two element aspheric lens assembly without loss of performance.

5. Conclusions

In this paper we have shown a design concept that can be used to create extremely isoplanatic lenses ideal for use in phase conjugating holographic storage systems. This design form can increase the interchange, shift and tilt tolerances of the systems due to extremely large isoplanatic patches where changes in the HDS pixel wavefront shape and magnitude are insignificant. This design concept also allows for the design of asymmetric phase conjugating systems where different lens designs are used for recording and recovering hologram s. This property lends itself to HROM systems where the mastering system is made of expensive, near perfect lenses and the readers are built using simple inexpensive molded lenses and consumer HDS where media position tolerances generally lead to higher costs in manufacturing.

6. References

- 1) I. Redmond, "The InPhase Professional Archive Drive OMA : Design and Function," Invited talk, ODS Proceedings MA1 (2006).
- 2) A. Hoskins, et al, "Monocular Architecture" ISOM Conference (2007), Singapore.
- 3) E/ Chuang, et al, "Consumer Holographic ROM reader with Mastering and Replication Technology", Optics Letters Vol. 31 (8):1050-2.
- 4) E. Chuang, et al, "Demonstration of Holographic ROM Mastering, Replication, and Playback with a Compact Reader", ISOM Conference (2007), Singapore.
- 5) W.T. Welford, Aberrations of Optical Systems, Adam Hilger Ltd (1986).
- 6) J.W. Goodman, Introduction to Fourier Optics, 3rd ed., Roberts & Company (2005).
- 7) R.S. Longhurst, Geometrical and Physical Optics, Longman (1957)
- 8) T. Smith, Trans. Opt. Soc. London 24 (1922-1923) 31.
- 9) W.T. Welford, Optics Communications, 3 Num. 1 (1971) 1-6.
- 10) H.H. Hopkins, Japan. J. Appl. Phys. 4 (1965) Suppl. 1, 31.
- 11) W. Smith, Modern Optical Engineering, 2nd ed, McGraw-Hill Inc. (1990)
- 12) J. Wyant, K. Creath, "Basic Wavefront Aberration Theory for Optical Metrology", in Applied Optics and Optical Engineering Vol. XI, Ch 1.
- 13) A. Hoskins, et al, "Tolerances of a Page-Based Holographic Data Storage System," Proc. SPIE 6620, 662003 (2007).

Focus sensing method using far-field diffracted waves and its application to holographic data discs

Teruo Fujita and Hayato Horikoshi
Dept. of Electrical and Electronics Engineering, Fukui University of Technology
3-6-1 Gakuen, Fukui, Japan 910-8505
Telephone: +81-776-29-2517, Fax:+81-776-29-7891, E-mail: tfujita@fukui-ut.ac.jp

ABSTRACT

The basic characteristics of a focus sensing method using far-field diffraction were studied by simulation and experiment. A proposal is given for sampling 4 points, discretely separated from each other by a 1/4 pitch. Also proposed is a set of optics to be implemented with this focus sensing method for holographic data discs.

Keywords: Focus sensor, interference fringe, diffraction, fringe scanning, holographic data discs, collinear hologram

1. INTRODUCTION

To increase storage capacity using the thickness of the medium, focus shift recording for the collinear holographic data disc^[1] was proposed and its potential feasibility was reported recently^[2]. For a practical system to be realized, precise focus control of both the signal and reference beams must be implemented into the holographic data memory. In this paper we present a focus sensing method for this purpose and discuss its characteristics with simulations and basic experiments. In addition, a proposal is made for an optical control of each beam to the different focus position for realizing precise focus-shift recording.

2. PRINCIPLE OF PROPOSED METHOD

A one-dimensional periodical structure is common in optical discs, and diffracts the incident focusing beam into several diffracted orders. Interfering the 0th-order reflected beam with the 1st-order diffracted beams generates a well-known push-pull tracking error signal for the optical disc system. In the focus sensing method discussed in this paper, we use the same interference as the push pull method to create the focus error signal with a radially-modulated periodical structure on the disc. Figure 1 shows the interference between the 0th order reflected beam and the $\pm 1^{\text{st}}$ order diffracted beams on the objective lens' pupil in the presence of some defocus on the disc. When the wavefront aberration coefficient corresponding to the defocus is W_{20} , the phase difference between the 0th order and $\pm 1^{\text{st}}$ order (proportional to radial direction (y')) appears in the interference area as follows;

$$\Delta\theta_{\pm 1} = 2\pi W_{20} \left(\mp \frac{2y'}{q} + \frac{1}{q^2} \right), \quad (1)$$

where the pupil radius is normalized to unity and q is the normalized pitch by λ/NA (λ : wavelength, NA: numerical aperture of the objective lens). This phase produces the defocus fringe in the interference area, as shown in Fig. 1, in which spatial frequency increases proportionally to W_{20} . In the following we describe how our proposed method detects W_{20} in the real time operation.

In this method two detectors are placed in the interference area and the one dimensional periodical structure is modulated in the radial direction so that the relative distance between the optical spot and the periodical structure changes \pm one quarter pitch and half pitch, as shown in Fig.2. Assuming that the intensity distribution on the objective lens is uniform, the detector's outputs $I_{D1,D2}$ are described as follows;

$$I_{D1,D2} = I_0 + I_1 \cos \left[\beta_1 + \delta + 2\pi W_{20} \left\{ -\frac{2}{q} \left(y_1 \mp \frac{\Delta}{2} \right) + \frac{1}{q^2} \right\} \right], \quad (2)$$

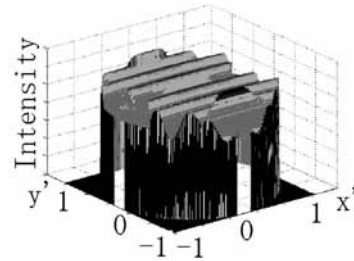


Fig. 1. Interference fringe caused by defocus on the objective pupil.

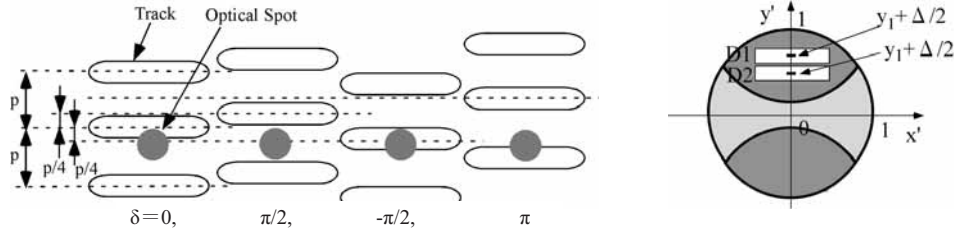


Fig.2. Spot position on the 1-D periodical/wobbled structure and detector (D_1 and D_2) location on the reflected/diffracted beams where β_1 is the initial phase, δ is the normalized W_{11} and Δ is the normalized spacing of the two detectors. If Δ and W_{20} is small enough, the difference and sum signals can be simplified as follows;

$$I_{DF} = I_{D1} - I_{D2} = 2I_1 \cdot 2\pi W_{20} \frac{\Delta}{q} \cdot \sin\left\{\beta_1 + \delta + 2\pi W_{20}\left(-\frac{2y_1}{q} + \frac{1}{q^2}\right)\right\}, \quad (3)$$

$$I_{SUM} = I_{D1} + I_{D2} = 2I_0 + 2I_1 \cdot \cos\left\{\beta_1 + \delta + 2\pi W_{20}\left(-\frac{2y_1}{q} + \frac{1}{q^2}\right)\right\}, \quad (4)$$

Although I_{DF} includes W_{20} , I_{DF} changes sinusoidally according to the radial position of the optical spot. Therefore the following operation (changing δ $-\pi/2$, 0 and $\pi/2$) picks up W_{20} to generate a focus error signal (FESa), because the subtraction of I_{SUM} s deletes the DC component and the first two terms (in curly brackets) are 90-degrees out-of-phase from the latter two terms;

$$FESa = \left\{I_{DF}\left(-\frac{\pi}{2}\right) + I_{DF}(0)\right\} \cdot \left\{I_{SUM}\left(-\frac{\pi}{2}\right) - I_{SUM}(0)\right\} + \left\{I_{DF}(0) + I_{DF}\left(\frac{\pi}{2}\right)\right\} \cdot \left\{I_{SUM}(0) - I_{SUM}\left(\frac{\pi}{2}\right)\right\} \propto W_{20}, \quad (5)$$

where $I_{DF}(\alpha)$ means the value of I_{DF} at $\delta = \alpha$. In the aforementioned method, we assume the intensity distribution of the incident beam on the objective pupil is uniform, whereas the focus offset occurs in the presence of a non-uniform intensity because the sum of I_{DF} produces the non-zero component and results in the offset. To suppress this focus offset we add another signal FESb given by Eq. (6) to the above FESa;

$$FESb = \left\{I_{DF}\left(\frac{\pi}{2}\right) + I_{DF}(\pi)\right\} \cdot \left\{I_{SUM}\left(\frac{\pi}{2}\right) - I_{SUM}(\pi)\right\} + \left\{I_{DF}(\pi) + I_{DF}\left(-\frac{\pi}{2}\right)\right\} \cdot \left\{I_{SUM}(\pi) - I_{SUM}\left(-\frac{\pi}{2}\right)\right\}, \quad (6)$$

$$FES = FESa + FESb. \quad (7)$$

As FESb generates the 180-degree out-of-phase offset component with respect to FESa, an offset-free focus error signal can be obtained even under non-uniform irradiation.

3. SIMULATION OF FOCUS ERROR SIGNALS

To make sure our method works well we have written MATLAB codes based on the Hopkins model^[3] because our idea is limited around the focus (W_{20} is small enough). Figure 3 shows a focus error signal obtained from Eq.(5) under uniform irradiation and a calculated FESa under typical LD irradiation. As we expected, the more the incident beam becomes non-uniform, the bigger the focus offset becomes. As well, the symmetry of the curve becomes worse and the offset fluctuates much more depending on the initial position of the optical spot relative to the periodical structure. Figure.4 is an offset dependency on the parallel radiation angle of an LD. It is confirmed that adding FESb to FESa produces an offset free focus error signal under typical LD irradiation, which is very similar to the one shown in Fig.3.

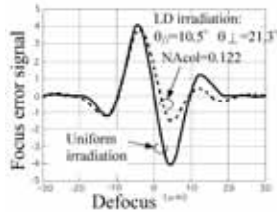


Fig.3. Calculated FES curves.

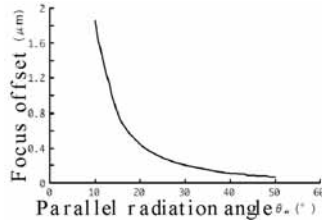


Fig.4: Offset dependence on the parallel radiation angle.

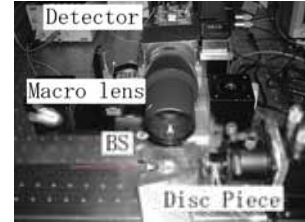


Fig.5. Photo of the bench optics.

4. EXPERIMENT USING BENCH OPTICS

An initial experiment was performed using simple bench optics shown in Fig. 5. We placed a piece of optical disc bonded on the 2-axis actuator in front of the objective lens ($NA_{obj}=0.53$) fixed to the bench optics. This actuator drove a disc piece up and down so that the actual disc movement was simulated. The intensity distribution on the objective-lens' exit pupil was magnified and projected through a macro lens (SIGMA MACRO 105mm F2.8) onto the detector plane. Figure 6 is a photo of an observed defocus fringe and Fig.7 presents the measured I_{SUM} and I_{DF} signals at $-2\mu\text{m}$ defocus and $2\mu\text{m}$ defocus. As expected, these signals varied sinusoidally for a period of $1.6\mu\text{m}$ and the phase of I_{DF} , differing from that of I_{SUM} by 90 degrees, was reversed against I_{SUM} . To detect the focus error signal, we sampled I_{SUM} and I_{DF} at various focus positions and 3 or 4 radial positions. Figure 8 is an obtained focus error signal.

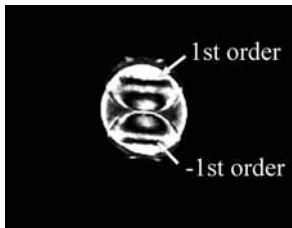


Fig.6. Photo of the defocus fringe.

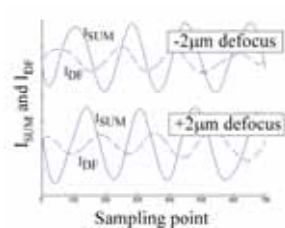
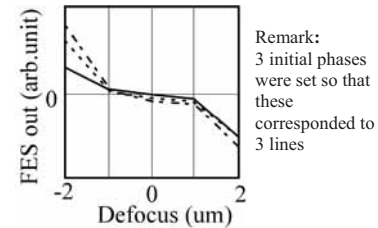
Fig.7. Observed I_{SUM} and I_{DF} (filtered by FFT).

Fig.8. Obtained FES by 4-point sampling.

5. APPLICATION TO HOLOGRAPHIC DATA DISC

Various multiplexing methods have been reported in hologram recording to increase its storage capacity. The focus-shift multiplexing method seems to be a promising one for holographic data discs over 1TB/12cm. However, to control both the signal and reference beams would require a new focus control system because the two beams have different depth focusing points. Because this proposed method can detect the focus error as long as the 0th order interferes with the 1st order, we will not need to have an additional optical path for conventional focus error detection. As well, the method requires neither a special optical component such as a cylindrical lens or a biprism nor accurate alignment. In Fig.9 we show how we can adjust the focus of each beam for focus-shift recording using this method.

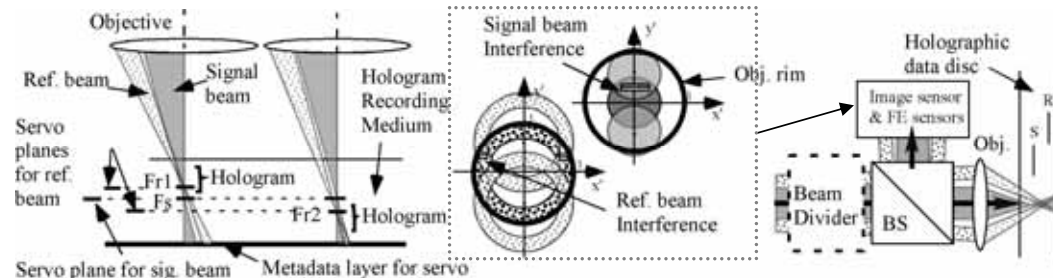


Fig.9. Optics implemented with the proposed focus sensing method. Only half beams are shown in the left figure. Signal and reference beams are focus-adjusted with the reference planes, and continuous servo beam is used for primary focusing/tracking.

6. CONCLUSIONS

We have proposed a focus sensing method using the defocus interference fringe at far-field and have studied its basic characteristics. The simulation confirmed that 4-point sampling was a very effective way to cancel the offset of this method. Furthermore we showed an example holographic data disc system where this method can be applied. In the next step we will determine how high-order aberrations and detector location, affect the focus error signal and we will design a focus control system using digital circuits and rotating disc with wobbled tracks.

REFERENCES

- [1] H. Horimai, X. Tan and J. Li, "Collinear Holography," *Appl. Opt.* 44, 2575-2579 (2005).
- [2] Y. Nagasaka et al., *Tech. Dig. ISOM2006, Th-I-28* or J. Minabe et al., *Tech. Dig. ISOM2007, We-J-P10*.
- [3] H. Hopkins, "Diffraction theory of laser read-out systems for optical video discs," *J. Opt. Soc. Am.* 69, 4-24(1979).

Aberration holograms and multiplexing – How to manage spherical aberration in microholographic data storage

Enrico Dietz, Sven Frohmann, Jonas Gortner, Alan Guenther, Jens Rass, Susanna Orlic

Optical technologies Lab, Technical University Berlin, Strasse des 17. Juni 135, 10623 Berlin, Germany

orlic@opttech.tu-berlin.de, www.opttech.tu-berlin.de

Abstract: Spherical aberration is a crucial issue in realizing high number of layers within the microholographic multilayer storage scheme. Different solutions on SA compensation have been investigated and to some extent practically implemented but they all suffer from a significantly increased complexity of the write/read system. Our current work addresses the problem of SA from the opposite direction, i.e. not by compensating but by utilizing the effect to improve the overall storage performance. For the first time we present the concept of so-called aberration holograms and experimental results that demonstrate its viability.

2007 Optical Society of America

OCIS codes: 210.2860 Holographic and volume memories, 090.7330 Volume holographic gratings, 090.2900 Holographic recording materials, 210.4590 Optical disks

1. Introduction

The microholographic data storage approach is based on the creation and detection of submicron sized reflection gratings. A significant increase in data density and overall capacity over the conventional optical disk technology results from the use of the third dimension, i.e. of the depth of a storage medium. Holographically recorded microgratings are strongly localized in all spatial directions and allow the technological implementation of multilayer storage with a relatively high number of data layers. For this purpose photopolymer samples of 300 micron thickness are used as storage media. As the microgratings are created by interfering two counterpropagating, diffraction limited beams, spherical aberration occurs when storage layers at different depth positions are addressed. As a consequence, both the beam spot and the written micrograting will blow up dramatically reducing the storage density. There have been lab demonstrations of techniques for reducing or compensating SA but none of these have come close to a practical system implementation. We investigate the impact of SA on spatial and diffraction properties of microgratings and present an entirely new concept of so-called aberration holograms for optical data storage.

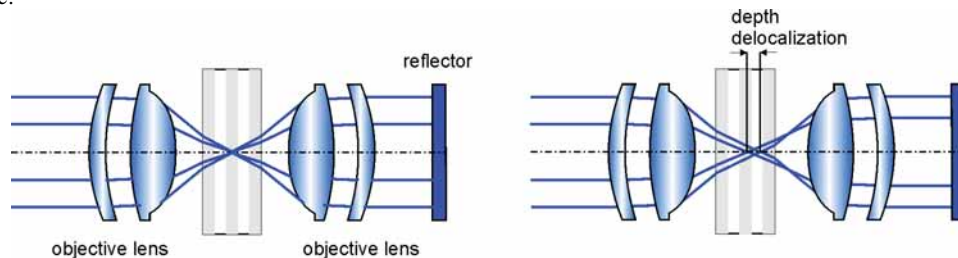


Figure 1. Microholographic recording scheme without (left side) and with spherical aberration (right side). SA results in a depth delocalization of the two write beam focus points and in a consequent distortion of the recorded grating structure.

2. Impact of spherical aberration on microholographic recording

In the case of perfectly corrected spherical aberration the interference pattern created by the two counterpropagating, strongly focused beams shows an ideal Gaussian shape with plane wave fronts at the waist and curved wave fronts at increasing longitudinal distance from the centre. The minimum achievable size of the area with enough energy to alter the structure of the photopolymer determines the size of the created gratings in the storage medium. The allowable spacing between adjacent micro gratings and hence the data density in each layer is limited by the lateral size of the gratings while their longitudinal size determines the minimum layer spacing and therefore the number of data layers in a certain medium. In the case of optimal correction of the spherical aberration, the laser beams are diffraction limited and the spot size and hence the size of the gratings is determined by the wavelength of the laser light and the numerical aperture of the focusing lenses.

However, if the correction of aberration is not trimmed correctly, the size of the spot increases both in lateral and in longitudinal direction. Normally, one would expect a decrease in data density as a result of this effect since the

layer spacing and the allowable data and track spacing would reduce. In a system that addresses many layers in a 300 μm thick polymer sample the described effect would make it necessary to alter the correction of the spherical aberration dynamically to make it fit the current addressed depth. This correction in a commercial drive would require additional shiftable or adjustable optical components and hence the device would become more complex and expensive.

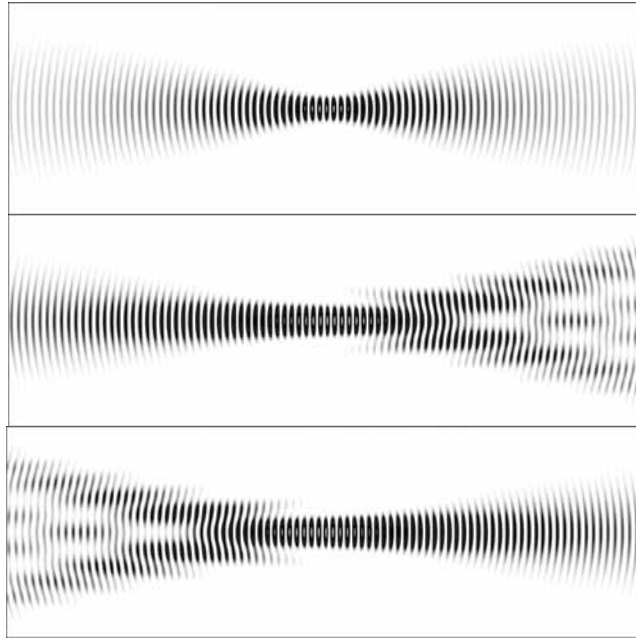


Figure 2. Impact of spherical aberration on the spatial modulation of a microholographic grating is calculated for three different aberration degrees obtained by defocusing the write beams, i.e. by shifting the focus point through the depth of the medium.

3. Concept of aberration holograms

We were able to demonstrate techniques that not only made such a dynamically correction unnecessary but that also proved to give as a new degree of freedom that could make the storage system more reliable and that might allow to increase the data density even further. With this concept it is not longer necessary to correct the spherical aberration of the two lenses to the current layer position in the photopolymer sample in the writing process. It is sufficient if both lenses together are adjusted to the thickness of the whole storage medium. If this is the case, then the second lens corrects the aberration produced by the first lens and the beam leaving the second lens is free of aberration. In the setup which is currently used and which promises to be the most stable and suitable for optical data storage this beam is then being reflected at a mirror and it is send back into the photopolymer medium through the second lens. Here, the same state of aberration as on the first pass is being reproduced by lens two and the interference pattern creates a grating in the sample that matches the phase fronts of the writing beams.

At this point one has to take into account the fact that the micro gratings are Bragg selective. This means that in the readout process the second write beam is being reproduced by the read beam (which also represents the first write beam). Since the sum of the lenses corrects the aberration, the reconstructed second write beam, which contains the information about the data stored in the photopolymer, is free of aberration when it leaves lens one. Therefore, it is possible to write and read gratings without the need to correct the spherical aberration.

As mentioned above the usage of laser beams with aberration leads to an increase of the size of the gratings. The grating formation does not take place in the focal range of a diffraction limited laser beam but in a large volume illuminated by the aberration deformed wave fronts of the write beam. Practically this implies that the write beam is no longer diffraction limited and the volume occupied by the grating increases dramatically. This reduces the power density needed during the writing process and it also relaxes the demanded degree of homogeneity of the photopolymer since now the grating is distributed over a larger area and the number of grating fringes increases,

allowing a lower diffraction efficiency of each fringe. This again means that the gratings are more Bragg selective and that the material dynamics are being spared. Hence the number of gratings that can be multiplexed (by means of wavelength multiplexing or other techniques) and written into the same volume increases.

Very important for the achievable data density is the fact that the gratings are Bragg selective. This means that only those gratings are being detected that match the phase fronts of the read laser beam. If during the recording process spherical aberration occurred, the wave fronts of the interference pattern and hence the microgratings are no longer planes or curves as in the ideal Gaussian beam. The aberration leads to a distortion of the wave fronts which is unique for the amount of aberration and therefore the depth of the layer in the medium where the current grating is written. Naturally the read beam shows the same amount of aberration as the write beam since they are identical. For the data density and the allowable spacing it is no longer decisive how small the micro gratings are, but how Bragg selective they are, i.e. in which distance to the point of perfect overlap between grating and readout beam the diffraction efficiency drops down.

It is important to point out that the optical resolution of the microholographic storage method does not suffer from heavy spherical aberration under the premises discussed above. Moreover, the resolution and selectivity remain nearly the same even if the hologram structure becomes very large in comparison to the diffraction limited microgratings. This large aberration distorted structure is however exactly coupled to the submicron sized focal range of the write beam and will rapidly change with movements in any spatial direction. The resulting change in the hologram structure is strongly spatially dependent with the same high resolution as in the case of diffraction limited microholograms. The spatial resolution and selectivity of the storage method can be improved dramatically by implementing optimized confocal filtering.

4. Aberration multiplexing

The primary advantage of the aberration hologram concept results from the fact that the recording takes place in a significantly larger volume of the photopolymer without any loss in optical resolution and spatial selectivity. This also implies that holograms possess a spatial selectivity concentrated on a few hundred nanometers sized focal range. The natural dependence of the light induced interference pattern on the local aberration of the two write beams coupled by the optical system is used as a unique identification of individual holograms. Any change in the aberration of the write beam will consequently alter the form and distribution of the created holographic grating fringes. The spatial selectivity of such holograms opens the possibility of an entirely new multiplexing method, the so-called aberration multiplexing. Practically, aberration multiplexing is performed by overlapping many holograms in the same volume while the aberration of individual holograms is used for their separate reconstruction. During readout a hologram is detected only when the aberration of its phase fronts exactly mirrors the aberration of the read beam. This way we open a fifth dimension to microholographic data storage as in addition of the three spatial dimensions and the spectrum as the fourth one, also the wave front aberration space becomes available for multiplexing.

5. Experimental results and verification

First results on high density recording of aberration holograms are presented. For this purpose the aberration of the write beam is additionally altered at different storage locations through the depth of a thick photopolymer sample. Current efforts address the aberration multiplexing, i.e. overlap recording and separate readout of several holograms that differ in their individual aberration.

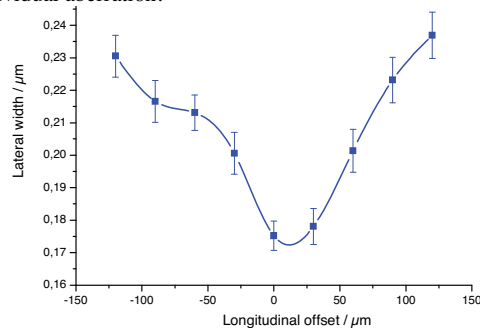


Figure 3. Dependency of the lateral grating width onto the longitudinal distance to the optically corrected focus depth in the polymer layer. It can be seen that an offset of $100\ \mu\text{m}$ in z -direction results in a reduction of the data density by half. This seems to be high, but the increase of size and the decrease of data density are much lower than the expected value if one ignores the effects of the Bragg selectivity.

Ultra-high Density Holographic Search Engine using Sub-Bragg and Sub-Nyquist Recordings

Joby Joseph*^a and David A. Waldman^b

^aDepartment of Physics, Indian Institute of Technology Delhi, New Delhi, INDIA 110016

^bDCE Aprilis, 5 Clock Tower Place, Suite 200, Maynard, MA, USA 01754

ABSTRACT

We propose and demonstrate a holographic data storage device which is suitable for search only purposes. This “Holographic Google” can provide pointers or addresses such that by using these pointers one may retrieve the original data that is stored elsewhere. In comparison to conventional holographic data storage-cum-retrieval system, the holographic search only engine can have exceptionally large data density by use of sub-Bragg 2D multiplexing and sub-Nyquist holographic recordings. An areal density of >600Gbits/sq.inch has been achieved in a CROP photopolymer of only 400 μ m thickness.

Keywords: Holographic Recording, Systems and Applications

1. INTRODUCTION

Searching of data from large data banks is an important aspect of many applications such as database management, financial records, medical records, biometrics, interactive video, library etc. Currently such data are stored in magnetic tape drives, magnetic disks or optical disks. Search speeds in such databases are generally limited by the I/O characteristics of the system, especially when the data banks become huge, and are reliant upon indexing methods. To improve upon the search speed of such large data bank systems, massively parallel search operations are necessary. It is difficult to achieve such massive parallelism using current storage devices, because data are stored and recovered in serial manner in these devices. However, parallel search capability is an inherent feature of a holographic data storage system, using the principle of optical correlation and also because of its multiplexed recording feature. Multiplexed recording in a common volume, allows one to carry out search operation of all the contents at a location, in a single step by performing simultaneous multiple correlations between a stored data page and a search argument (query). Apart from the ability to carry out parallel, multiple searches among the stored data, the page oriented nature combined with multiplexing capability gives volume holographic memories an edge over other bit oriented memories, in terms of large data capacity and fast transfer rates.

Most of the recent advanced developments in holographic storage have so far been done with prime importance given to data recovery, to obtain minimum BER and maximum SNR for the recovered data pages. There have also been many studies on holographic data search; however most of these were done in conjunction with data recovery aspects, such that the system is primarily meant for data recovery [1,2]. In the present paper, we present a holographic storage system which is primarily meant for search only purposes, in which data recovery from the same system may not even be possible, but the data recovery is readily achieved from other storage means..

This search engine herein provides a means for extremely fast and parallel retrieval of address information from a holographic data base, such that, by using these addresses one may retrieve the original data or information that is stored elsewhere. For example, the original information may be stored in hard disks, tape drives, CDs, DVDs or even other holographic disks, for data recovery using the addresses. In short, the system works like an ‘Internet Search Engine’ such as “Google”, where one carries out a search operation for a query and the search engine provides pointers to the places or sites where the queried information is available for retrieval. Similar to such internet search engines, the “Holographic Google” can provide pointers or addresses as well as the amount or degree of match between queried information and the stored information.

2. HOLOGRAPHIC SEARCH ONLY SYSTEM

In this section, we discuss about a holographic storage system which is meant only for search purposes, hence will not be used for read-out of the data from the stored hologram. It is known that the multiplexing factor, of a volume holographic storage system that is meant for data recovery, is generally governed by Bragg conditions, leading to the requirement of thicker materials for achieving large storage density. In the conventional holographic data storage and recovery system, during data read-out, reference beams at the corresponding angles (addresses) illuminate the holographic medium for the recovery of the corresponding data. In order to recover the data pages with minimum cross talk, the multiplexing should satisfy various conditions depending on the multiplexing method employed. For example: Bragg angle detuning for in-plane angle multiplexing, Bragg wavelength detuning for wavelength multiplexing, phase of the reference beams for phase-code multiplexing, size of data page for peristrophic & out-of-plane (fractal) multiplexing, size of the Fourier spectrum (Nyquist size) for spatial multiplexing and so forth.

We propose a novel storage procedure for search only purpose, in which the multiplexing is not governed or limited by such conditions, leading to exceptionally high data density at the cost of data recovery. Multiplexing is carried out through sub-Bragg angle tuning in in-plane as well as out-of-plane directions (Sub-Bragg 2D multiplexing) and also using sub-Nyquist aperture size at the recording surface. Here, the multiplexing factor is governed by the capability of the system to resolve or discriminate the correlation peaks and not by the material thickness.

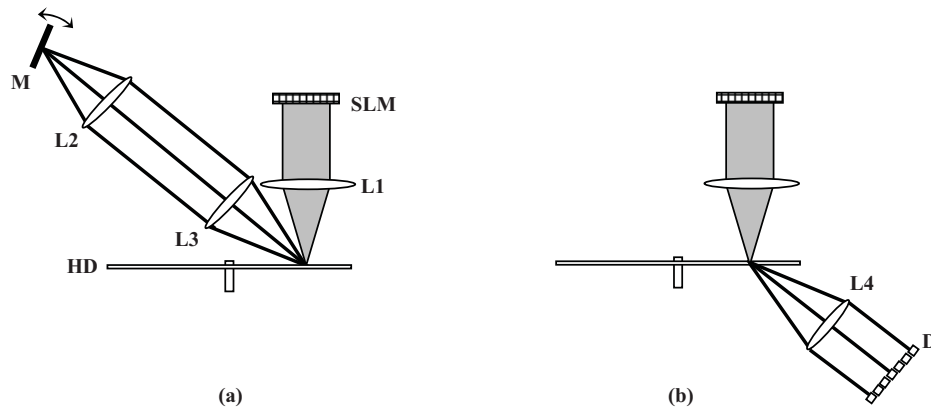


Fig. 1. Holographic search only system showing (a) storage procedure and (b) search procedure. SLM: Spatial light modulator for data display, L1-4: lenses, M: Rotating mirror for angular multiplexing, HD: Holographic disk, D: Detector array for the detection of correlation peaks.

Figure 1 shows the general schematic of a transmission geometry based holographic data storage and search only system, using angular multiplexing. Combining the Figs. 1 (a) and (b), the system has a $2f$ optical set-up in the object arm and a $6f$ optical set-up in the reference arm. During the storage procedure as shown in Fig. 1(a), multiple data pages are holographically stored in the recording medium (which could be in the form of a disc) through interference with plane wave reference beams incident at different angles (which function as addresses for each of the stored data pages).

During the search only procedure as shown in Fig. 1 (b), the digital data page (search page), or portion thereof, corresponding to the search information (query) is displayed on the SLM and the multiplexed holograms at storage location are illuminated by the search object beam, leading to the simultaneous reconstruction of multiple reference beams. The directions of the reconstructed reference beams correspond to the addresses of the stored data and the intensity of these beams correspond to the match between the search data and the stored data. The amount of power diffracted into each of the reference beams is governed by the correlation between the search data page and the stored data page. It is important to note the following operational advantages of such a holographic search only system:

- 1) No requirement of the problematic pixel-to-pixel matching of SLM and CCD
- 2) No requirement of thicker material. Thin material with high dynamic range is preferred.
- 3) Less stringent requirements for servo and for signal-to-noise ratio of recorded holograms
- 4) No CCD or CMOS array needed. An array of fast photo detectors is preferred.
- 5) A prerecorded holographic search only engine has a simple optical architecture, as shown in Figure 1(b).

2.1 Sub-Bragg 2D multiplexing and Sub-Nyquist recording and search

As described earlier, the angular multiplexing factor, of a holographic storage system meant for search engine, is not limited by Bragg detuning conditions. Hence, even for a thin recording material, very small angle differences can be used for multiplexing in in-plane as well as out-of-plane directions. The reference beam angle difference is instead limited by the size of the correlation spots at the detector plane. It is important to note that the system can no longer exploit the shift invariance in both x and y directions, even when a thin recording material is used. The mirror M of Fig. 1(a) has the provision to rotate the reference beam in both in-plane as well as out-of-plane angles. Rotation of the mirror in both directions leads to scanning of the focused reference beam spot on the detector plane (the correlation plane) in 2-D directions. Hence, we refer to this sub-Bragg in-plane plus out-of-plane multiplexing as 2D multiplexing. A similar multiplexing scheme has been employed by Liao et al [3] for face recognition using thick photorefractive crystal.

In conventional holographic data storage disc systems, for better SNR and BER of the recovered data page, peak-to-second null angle separation is preferably used. For the search only engine, sub-Bragg angle multiplexed holographic recordings have been done with reference angle separations corresponding to 1/5th of peak-to-second null Bragg detuning angle, for a photopolymer medium of thickness 400 μ m using a laser at wavelength 532nm. Figure 7 shows the auto-correlation peaks from recording of 180 sub-Bragg holograms using 2D multiplexing.



Fig. 2. Results of sub-Bragg and sub-Nyquist holographic search. (a) 180 auto-correlation peaks from sub-Bragg 2D multiplexing. (b) Part of 600 auto-correlation peaks from sub-Nyquist & sub-Bragg recording.

In a conventional holographic data storage system, the size of the aperture at the hologram recording plane optimized with respect to BER and other desirable parameters, is usually more than or equal to 1.2 times Nyquist size [4]. However, such an aperture size is needed only when the data is to be recovered back. Hence for the search engine, the aperture size can be much smaller than this limit. Figure 2 (b) shows the result of auto-correlation peaks [A small part of 150x4=600 correlation peaks], using a rectangular aperture whose vertical width is around 1/5th and horizontal width is 1/2 of Nyquist size. As can be noticed, the correlation peaks are elongated in the vertical direction, because of diffraction due to restricted vertical width at the recording plane. Reference beam angles need to be adjusted accordingly during the recording stage, keeping in view of the width of these elongated correlation peaks.

Combining the above features, 600 binary data page holograms were recorded in one location in 400 μ m thick DCE Aprilis Type D photopolymer using sub-Nyquist and sub-Bragg 2-D multiplexing. This corresponds to an areal density of >600 Gbits/sq.inch in a thin recording medium and the signal-to-noise limits were not reached. Through better optimization, it is possible to achieve 800-1000 holograms in one location. As per our knowledge, this is the highest data density per unit volume reported in literature, for any type of applications. Another feature of a search only system is that the data pages need not incorporate error correction codes, since the data is not intended for recovery. The whole user data can be displayed on the SLM during storage, leading to substantially higher end user data density.

REFERENCES

- [1] G.W. Burr, G. Maltezos, F. Grawert, S. Kobras, H. Hanssen and H. Coufal., "Using volume holograms to search digital databases," Proc. SPIE 4459, 311-322 (2001).
- [2] X. Li, F. Dimov, W. Phillips, L. Hesselink and R. McLeod., "Parallel associative search by use of a volume holographic memory," 29th Applied Imagery Pattern Recognition Workshop (AIPR'00), p.78-83 (2000).
- [3] Y. Liao, Y. Guo, L. Cao, X. Ma, Q. He and G. Jin., "Experiment on parallel correlated recognition of 2030 human faces based on speckle modulation," Opt. Express 12, 4047-4052 (2004).
- [4] B. Das, J. Joseph and K. Singh., "Performance analysis of content-addressable search and bit-error rate characteristics of a defocused volume holographic data storage system," Appl. Opt. 46, 5461-5470 (2007).

Detection of Reproduced Image Distortion using FFT Cross-Correlation Method in Holographic Memory

Yuta Kajiwara, Takumi Sano and Manabu Yamamoto

Department of Applied Electronics, Tokyo Univ. of Science, 2641 Yamasaki, Noda, Chiba, Japan

ymanabu@te.noda.tus.ac.jp

Abstract: This paper studies the analysis method of reproduced image distortion. The image distortion was made visible by the marker detection using FFT cross-correlation method.

1. Introduction

Various recording methods are proposed for volume holographic memory. These recording methods use two-dimensional digital data, and several markers for data position detection are placed at the data area. In these recording methods, the distortion of reproduced images is caused by the optical system aberration or medium shrinkage by the polymerization process. With the increase in the volume of page data, these distortions caused by the medium shrinkage increase the bit error rate. Therefore, it is needed to study precise characteristics of the image distortion in the multiplexed recording.

In this paper, we studied reproduced image distortion with multiplex recording by measuring the transfer vector of marker using the FFT (Fast Fourier Transform) cross-correlation method.

2. Detection of Reproduced Image Distortion by FFT Cross-Correlation Method

In this study, we detected the reproduced image distortion by the FFT cross-correlation method. The FFT cross-correlation method involves locally the similarity of the brightness patterns [1]. For the calculation of the cross-correlation value, FFT was used. The processing procedure is shown in Figure 1. One $N \times N$ pixel template image was used as the reference image, and the reproduced marker image of the same size was placed at an area of investigation. Correlation calculation was performed for these two images. With the direct cross-correlation method, the size of the investigation area can be set freely, but with the FFT cross-correlation method, the template image area and the investigation area are of the same size. From the function $C_{fg}(x, y)$ obtained by inverse FFT of the function $F^*(\xi, \eta) \cdot G(\xi, \eta)$, the shift value $(\Delta x, \Delta y)$ was determined. By transforming this vector into an image, we detected the peak value of the cross-correlation.

To detect the high-accuracy position coordinates of the marker by FFT cross-correlation method, the image is enlarged by sub sampling method. The sub sampling process is shown in Figure 2. In order to observe how the points on the input image correspond to the output image, the four points $\phi 1$, $\phi 2$, $\phi 3$, and $\phi 4$ are properly weighted, and their mean values are calculated, as shown in Fig. 2(b). The position coordinates after mapping and signal value of the point are calculated by using the formula shown below.

$$x = \frac{(\phi 1 \times x 2 + \phi 2 \times x 1) \times y 2 + (\phi 3 \times x 2 + \phi 4 \times x 1) \times y 1}{(x 1 + x 2) \times (y 1 + y 2)}$$

3. Experimental results

We detected the distortion with reproduced images by coaxial-type multiplexed holographic recording experiment. Recording was carried out by the shift multiplexed recording method which is linear multiplexing. The data format examined in this study is shown in Figure 3. The data page consists of one page sync mark at upper left and 51 sub-pages, and a sync marker is embedded in each sub-page midmost. Each sub-page size is $24H \times 24V$ bits and the 3/16 modulation code was used for data symbols. The marker size is 4×4 bits. In this study, the number of total shift multiplexed holograms is twenty-three.

We calculated shift value of each marker about all reproduced images provided with shift multiplex recording by the FFT cross-correlation method. Figure 4 shows the distribution about transfer quantity of each marker, which was provided from the 23rd multiplexing reproduced image with $2\mu\text{m}$ shift multiplex recording. The shift quantity is plotted with a normalized value in Fig. 4. Without depending on multiplex number, the tendency that the reproduced image distortion in the left and upper part of data area become larger was obtained. The diagram of transfer vector difference between the 23rd multiplex recording and non-multiplex recording is shown in Figure 5. The white blocks show original marker positions, and the arrows express for increase of the marker transfer vector. In every reproduced image, each marker is shifted generally in the left direction of horizontal axis from an original position. However, as the multiplex number became bigger, a nonlinear distortion occurring in reproduced image became more remarkable. The cause of distortion is thought to be the advance of polymerization by the increase of the multiplex recording process.

4. Conclusion

We were able to detect the detailed marker position using FFT cross-correlation method and sub sampling method. By measuring the transfer vector of marker positions, the reproduced image distortions caused by the medium shrinkage can be analyzed precisely in multiplexed hologram recording.

References

- [1] R.Suzuki, F.Naitou, S.Yoshida, T.Mori and M.Yamamoto, *Jpn. J. Appl. Phys.*, 47 (2008) 183.

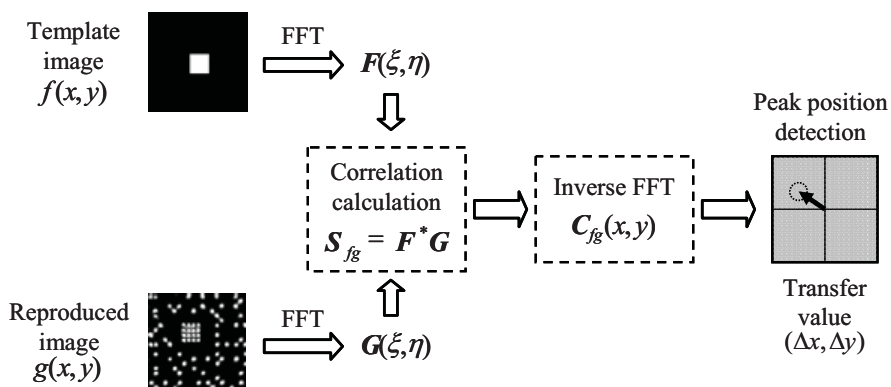


Fig. 1. Procedure of FFT cross-correlation method

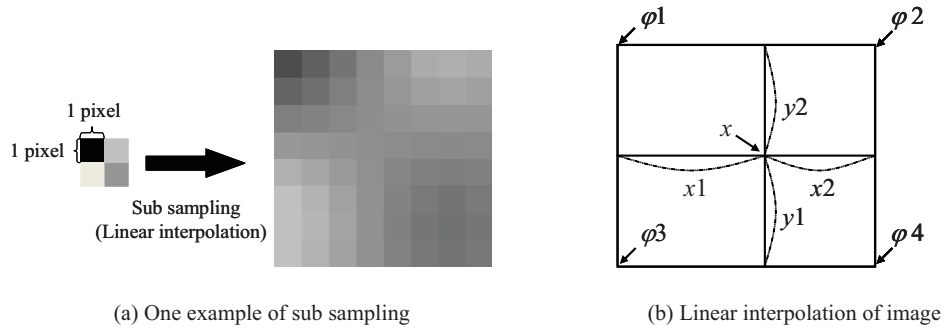


Fig. 2 Sub sampling method

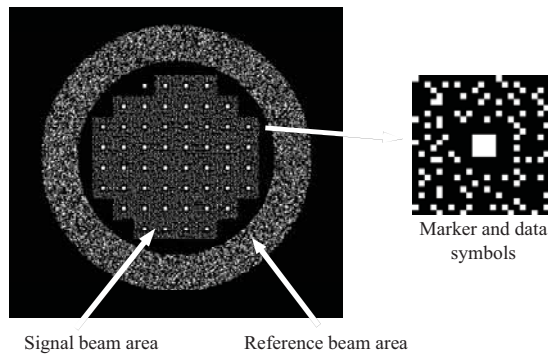


Fig. 3. Input data format with marker embedded

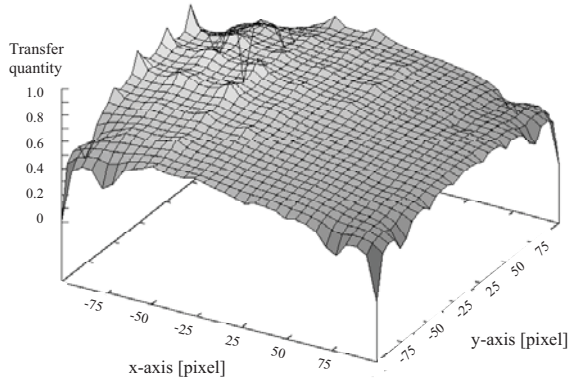


Fig. 4 Distribution about transfer quantity of each marker in the data area

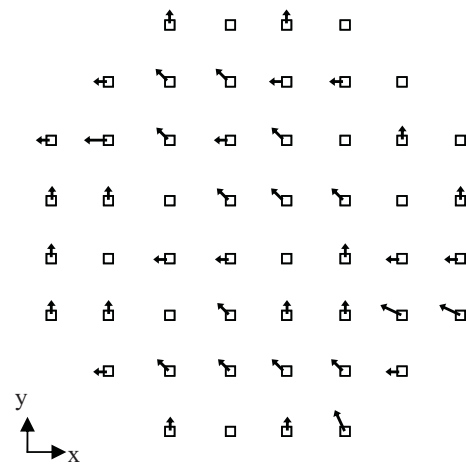


Fig. 5 Transfer vector differences between the 23rd multiplexing and non-multiplexing

Tilt compensation method for Holographic Data Storage

Sang-Woo Ha, Jae-Sung Lee, Na young Kim,
Jeong-Kyo Seo, In Ho Choi and Byung Hoon Min
Digital Storage Research Lab., LG Electronics Inc.
360-5 Yatap-Dong, Bundang-Gu, Sungnam-Si, Kyunggi-Do, 463-828, Korea
Phone : +82-31-789-4042, Fax : +82-31-789-4204, E-mail: felixha77@lge.com

ABSTRACT

The page-oriented angle-multiplexing holographic data storage system is one of the promising techniques for high capacity and data transfer rate, but its narrow tilt margin has been pointed out as a demerit. To overcome this weak point, we have already proposed the 2-axis deck mechanism employed to the CHDS (Compact size Holographic Data Storage) system [1]. In this paper, we propose the way to detect and compensate the radial/tangential disc tilt. The compensation result by this method is also demonstrated.

Keywords: holographic data storage, radial/tangential disc tilt, tilt detection, tilt compensation.

1. INTRODUCTION

With a rapid increase of various multimedia contents such as movie, music, digital photo and etc, current storage technologies are struggling to keep up with high capacity, fast access and long archive life. Aside from high density magnetic storage device and semiconductor memory, many kinds of optical storage technologies such as near field recording, holographic storage and super resolution techniques are under development. Among them, holographic data storage has been noticed as one of the promising technologies with the potential for vast capacity and high data rates. The development of a viable storage material and high performance optical components such as SLM, CIS, LD which have been considered as the major challenges for commercialization is advanced recently, but a narrow system margin such as radial/tangential tilt still remains especially in the Page-oriented angle-multiplexing Holographic data storage system. [2][3]

To overcome this weak point, we have already proposed the 2-axis deck mechanism employed to the CHDS system and showed the improvement of radial/tangential tilt margin [1]. In this paper, we propose the way to detect and compensate the radial/tangential disc tilt. The compensation result by this method is also demonstrated.

2. TILT DETECTION AND COMPENSATION

Since a disc tilt error occurred during exchanging disc in the drive can not be avoided in all kinds of the ODD system, the tilt compensation should be performed in the holographic data storage system, which has a narrow tilt margin. For compensation, the exact tilt error detection is essential. Relative angle between objective lens and disc of each holographic storage system might have a deviation, so the tilt compensation by using SNR or BER of reconstructed data page as a tilt error signal would be the most accurate way to compensate. However, for using BER or SNR as a tilt error signal, image processing for calculating SNR and BER takes time, and this leads to a decline of data transfer rate [4].

For a fast tilt detection and compensation, we apply the fact that the partial intensity of reconstructed data page is changed by radial and tangential tilt generated. Because the intensity of several sections of reconstructed data page is used for tilt detection, this detection method using intensity is much faster than calculating SNR or BER.

2.1 Intensity variation of reconstructed data page by disc tilt

In Fig. 1, reconstructed data pages are listed in the ascending order of radial and tangential disc tilt around the reference data page (fig 1.5) without a disc tilt. The amount of radial and tangential disc tilt is given by a 2-axis deck, and data page is composed of 320x288 pixels for the experiments [1][5]. Fig.1 shows that the intensity distribution of each data

page varies according to the amount of radial/tangential disc tilt. With operating the average intensity of 4 sections (A, B, C and D in fig.1), disc tilt can be detected accurately.

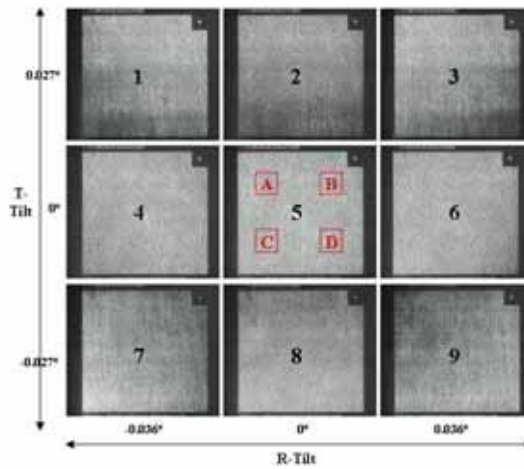


Fig.1 Intensity variation of reconstructed data page by radial/tangential tilt

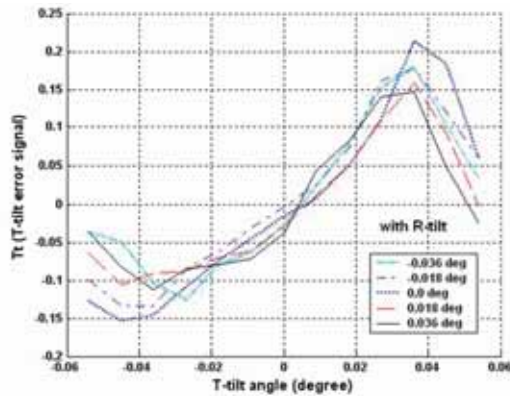
2.2 Disc tilt detection with the intensity variation of reconstructed data page

Fig. 2 represents the relation between disc tilt angle and tilt error signal. Each of 5 curves on a graph in fig.2(a) shows the relation between tangential disc tilt angle and Tt(tangential tilt error signal) when the radial disc tilt angles are -0.036, -0.018, 0, +0.018 and +0.036 degree respectively, and 2 curves on a graph in fig.2(b) shows the relation between radial disc tilt angle and Rt(radial tilt error signal) when the tangential disc tilt angles are -0.01 and +0.01 degree respectively.

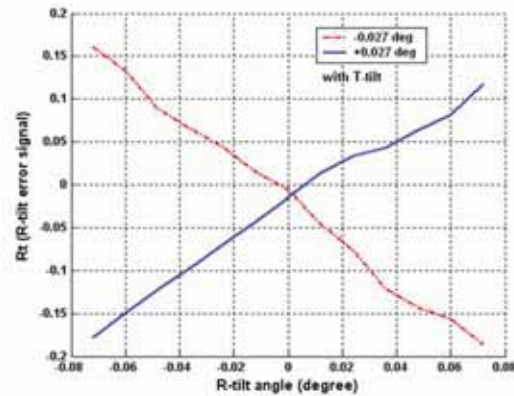
Rt and Tt are calculated with the intensity of section A, B, C and D in fig.1. The formulas for Rt and Tt are represented in (1-1) and (1-2)

$$T_t = \frac{(a+b)-(c+d)}{a+b+c+d}, \quad (1-1) \qquad R_t = \frac{(b+d)-(a+c)}{a+b+c+d}, \quad (1-2)$$

where a, b, c and d is an average intensity of the section A, B, C and D respectively.



(a)Relation between tangential disc tilt angle and Tt



(b) Relation between radial disc tilt angle and Rt

Fig. 2 Disc tilt angle and tilt error signal

It shows that the relation between tangential tilt angle and Tt is well matched, although there is a little difference among the points where Tt is zero according to given radial tilt in Fig.2(a). Also, the relation between radial tilt angle and Rt is well matched as well.

2.3 Tilt compensation procedure

Fig.3 shows the tilt compensation procedure by using Rt and Tt and the SNR improvement of reconstructed data page according to the tilt compensation. Since a tangential tilt is more sensitive than a radial tilt and the SNR degradation by radial tilt is hard to detect with this proposed method when a tangential tilt is zero, it's better to correct radial tilt as the first step, and correct tangential tilt. A procedure for correcting tilt includes detecting tangential tilt, detecting radial tilt, correcting radial tilt and correcting tangential tilt.

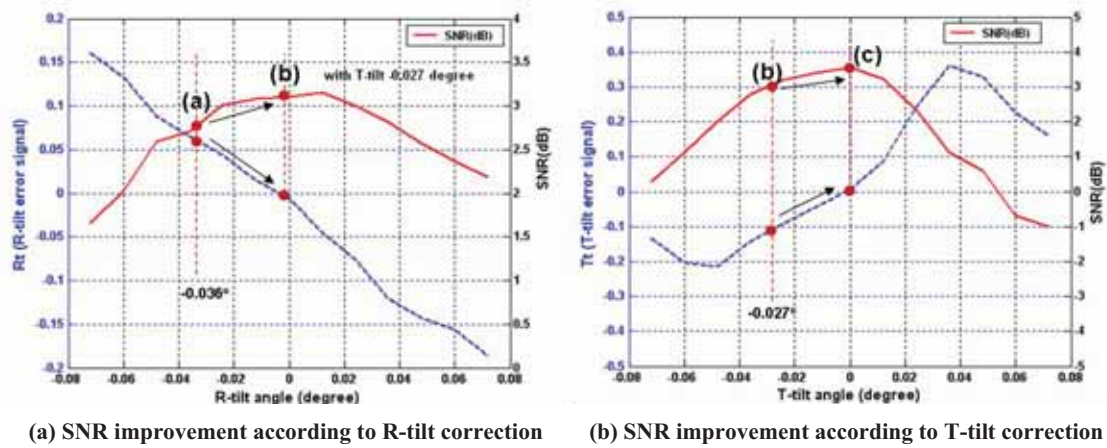


Fig.3 Schematics for tilt compensation procedure

When the disc has a tangential tilt of -0.027 degree and a radial tilt of -0.036 degree, the SNR of reconstructed data page is shown at point (a) in fig 3.(a). After radial tilt correction, the SNR is improved from point (a) to point (b) in fig 3.(a), and further improved from point (b) to point (c) in fig 3.(b) according to tangential tilt correction. Although the SNR of data at point (b) is not the highest value in fig 3.(a), the difference is under 0.05 dB, and therefore, it is acceptable.

3. CONCLUSION

In this paper, we propose the tilt detection method and show how to compensate disc tilt with detected tilt error for solving the narrow disc tilt margin problem which is one of the major challenges for commercialization in the Holographic Data Storage system. Since tilt compensation with a tilt error signal calculated by SNR or BER of reconstructed data page takes time leading to a decline of data transfer rate, we use the partial intensity variation of reconstructed data page as a tilt error signal. As a result, we can achieve fast and accurate tilt compensation with the proposed method and we expect that this method and 2-axis deck mechanism we have proposed previously can contribute to the commercialization of the holographic data storage system.

REFERENCES

- [1] I.S. Song, et al, "Compact size Holographic Data Storage technology", ISOM Invited (2007)
- [2] I. Redmond, "The Inphase Professional Archive Drive OMA : Design and Function." Invited talk, ODS Proceedings(2006)
- [3] A. Hoskins, et al, "Tolerances of a Page-Based Holographic Data Storage System," ODS Proceedings(2007)
- [4] S.H. Lee, et al, "The angle align method of reference beam for holographic data storage", ODS Proceedings(2006)
- [5] J.S. Lee, et al, "Efficient Balanced Code Using Viterbi Algorithm and Section Division for Holographic Data Storage", Jpn. J. Appl. Phys., Vol. 46, No. 6B, 2007, pp.3797-3801

Dynamic Recording and Readout of Micro-holograms in GE Dye-doped Thermoplastic

Zhiyuan Ren, Victor Ostroverkhov, Xiaolei Shi, Mark Cheverton, James Lopez, Brian Lawrence,
and Michael Durling

General Electric Global Research, One Research Circle, Niskayuna, NY, 12309 USA
Telephone: 518-387-4776, Fax: 518-387-5164, ren@research.ge.com

ABSTRACT

We have implemented recording and readout of micro-holograms in dye-doped thermoplastic in our new dynamic system that utilizes five-axial servos to compensate rotating tilting/run-out.

Keywords: Holographic recording

1. INTRODUCTION

Static recording of micro-holograms in GE dye-doped thermoplastic medium for holographic data storage was reported in [1]. Since then, we have constructed a new dynamic system for recording micro-hologram tracks in a rotating medium. This paper reports our result on tone recording in the new dynamic system. To obtain precise location and alignment of focal spots of counter-propagating recording and reference beams inside the medium during the recording process, we utilize servo in five axes to dynamically compensate axial/radial/tangential disc run-out/tilting.

2. RECORDING MEDIUM AND DYNAMIC SYSTEM

The recording medium has a bonded structure shown in Figure 1. A reference polycarbonate disc with grooves and reflective coating is bonded to a recordable disc of GE dye-doped thermoplastic through adhesive.

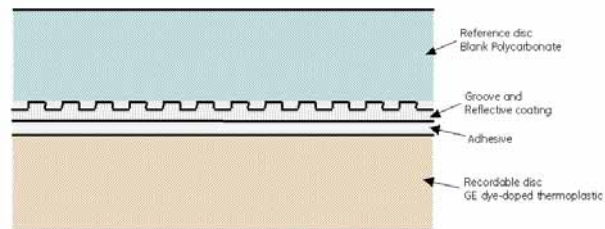


Figure 1: Bonded structure of the recording medium

The dynamic system is shown in Figure 2. During the recording process, focusing (or axial) and tracking (or radial) servos of objective lens L3 are done using the conventional astigmatic focusing and push-pull tracking servo signals generated from red (658nm) laser beam, reflected from the grooves and reflective coating layer of the recording medium, going through various optics, and eventually hitting quad-detector QD-R; Axial- and radial-following servos of objective lens L4 and tangential-following (galvo) servo are done using servo signals generated from green (532nm) recording laser beam, going through various optics including galvo, L4, recording medium and L3, and finally hitting quad-detector QD-G; Through these servos in five axes, the focal spots of counter-propagating green reference and recording laser beams pulsed through EO modulator EOM intersect precisely on a spiral at a preset depth inside the thermoplastic. During the readout process, only focusing and tracking servos of L3 are needed to make L3's focal spot of CW green reference laser beam follow the recorded spiral micro-hologram tracks in the preset depth; Reflected/diffracted light from micro-holograms on the track goes through various optics and at last hits a con-focal detector.

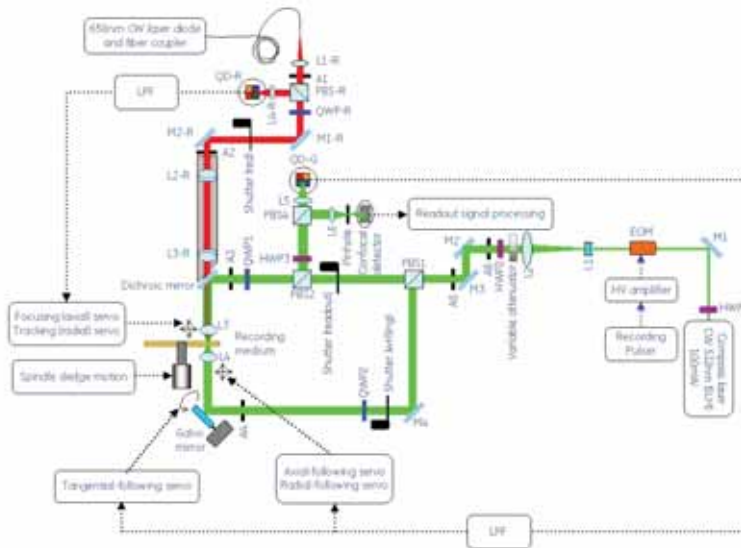


Figure 2: GE dynamic system

3. DYNAMIC RECORDING AND READOUT RESULTS

Figure 3 shows the monotone readout signal on the con-focal detector. Various parameters used in the recording and readout are: $NA=0.2$, recording power= $2 \times 15mW$, readout power= $0.5mW$, disc rotation speed= $30RPM$, recording radius= $35mm$, monotone frequency= $10KHz$, hologram feature size ($W \times L$) = $1.7\mu m \times 5.5\mu m$, diffraction efficiency= 0.0003 .

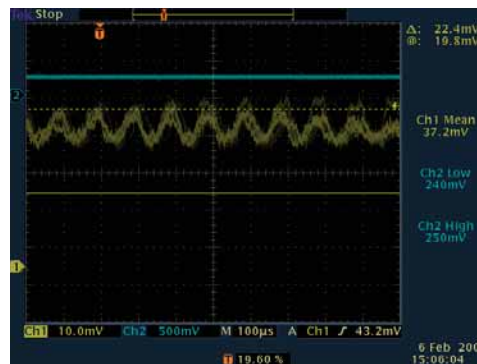


Figure 3: oscilloscope capture of the readout monotone signal on the con-focal detector

Figure 4 illustrates the effects of various following servos during the recording process. In (A), all following servos were off, and disc rotation run-out/tilting causes power level variation of transmitted recording green laser beam on con-focal detector; Subsequently in (B), (C) and (D), this variation is gradually reduced to minimum through introduction of tangential-following (galvo), radial-following and axial-following servos. Our servo system is designed and implemented using control prototyping software and hardware from dSPACE Inc. and The Mathwork Inc.

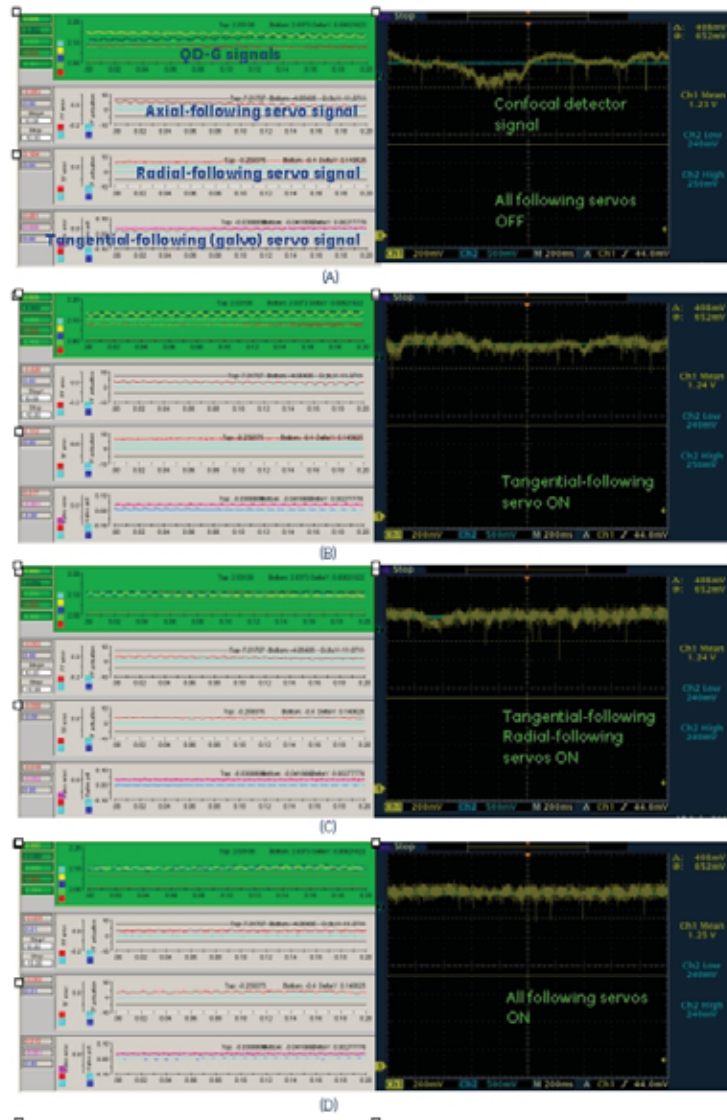


Figure 4: Effect of servos for objective lens L4 and galvo

4. CONCLUSIONS

We have successfully implemented dynamic tone recording and readout of micro-hologram in GE dye-doped thermoplastic medium. We are currently experimenting on multilayer recording with higher NA.

REFERENCES

- [1] Pingfan Wu, Xiaolei Shi, Brian Lawrence, Zhiyuan Ren, Joseph Smolenski, Chrisoph Erben, Eugene Boden, and Kathryn Longley, "Micro-holograms Recorded in a New Thermoplastic Medium for Holographic Data Storage," GE Report 2006grc268, also ODS'06.

Subwavelength Focus by Radial Polarization through Metallic Thin Film with Annular Illumination

Tzu-Hsiang Lan^{*a}, Chung-Hao Tien^b

^aDepartment of Photonics & Institute of Electro-Optical Engineering,

^bDepartment of Photonics & Display Institute Engineering,
National Chiao Tung University, Hsinchu, Taiwan

ABSTRACT

We proposed a simple setup to generate a non-diffraction sharp focus via metallic thin film illuminated by radial polarization (RP) with annular pupil. The penetrated electric field is excited by the surface-plasmon-polariton on the bottom of gold-air interface. In the case of NA = 0.75 with 85% apodized annular pupil, the non-diffraction focused beam, 0.37 λ full width at half maximum (FWHM), propagates more than 2λ as the intensity drops to half.

Keywords: numerical aperture, annular pupil, diffraction limit, radially polarized beam, surface-plasmon-polariton

1. INTRODUCTION

Recently, radial polarization is attracting more attention in high numerical aperture (NA) systems due to its novel subwavelength focused spot, which is expected to increase the spatial resolution in high recording density system.^[1] However, smaller focused spot by RP than other states of polarization merely exists in strong focusing circumstance (NA > 0.9) which could increase the cost of the objective lens and the complication of the system.^[2]

Meanwhile, the localized surface-plasmon-polariton (SPP) excited by focusing beam on a flat metallic thin film provides a route to accentuate the longitudinal component of RP (called non-diffraction Bessel beam) on the bottom of metallic thin film.^[3] The surface plasmon resonance may provide strong field enhancement at particular incidence angle. In this paper, we studied the focusing of radial polarization through gold thin film with annular illumination. The relation between the apodized pupil and the optical behavior through the metallic thin film will be given.

2. SIMULATION

Figure 1 (a) schematically shows the used model with Kretschmann-Raether configuration in this paper. A radially polarized beam illuminating the pupil plane of an aplanatic lens (NA = 0.75) produces a spherical wave converging toward a dielectric-metal interface. A solid or liquid immersion material is used to match the index of refraction with the dielectric substrate. In this paper, the refractive indices of the immersion material and the substrate are $n_1 = 1.5$. All geometry dimensions are normalized by $\lambda_0 = 632.8\text{nm}$ throughout this paper.

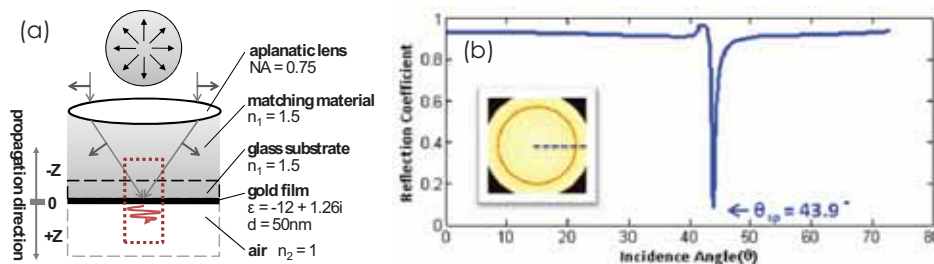


Fig. 1. (a) schematic diagram of the focusing system with Kretschmann-Raether configuration. (b) the reflection and transmission coefficient curves versus incident angle are calculated for this multilayer.

*allenblue.eo94g@nctu.edu.tw; phone +886-3-5712121#59209; fax +886-3-5735601

A 50 nm gold film ($\epsilon = -12+1.26i$) is deposited on the bottom of the dielectric substrate. The medium below the gold layer is air with $n_2 = 1$. Figure 1(b) shows the curves of reflection coefficient versus incident angles. It can be seen that the surface Plasmon resonance (SPR) is occurred at $\theta_{sp} = 43.9^\circ$ and the critical angle is located at $\theta_c = 41.4^\circ$. Because radial polarization is cylindrical-symmetric, the entire entrance beam is p-polarized with respect to the incidence plane. Therefore, a dark ring will appear on the exit pupil of the aplanatic lens which reveals the active region of SPR.

Base on the vector diffraction theory, we calculated the penetrated field distribution in the vicinity of gold layer (dotted square in Fig.1). The annual pupil is introduced to select the angles of the incidence beam which can excite SPR.

3. DISCUSSION

In the following, the FWHM and longitudinal to transverse ratio (L-T) are two merit indices for identifying the shape of focused spot. Figure 2 shows the field distribution of focused RP with circular (a - c) and with annular (d - f) illumination. The intensity of the focused field is reasonably decreased about 1~1.5 order as passing through. The film acts as a 'beam shaping filter' which is able to suppress the transverse component and preserve the longitudinal component. Accordingly, it yields a smaller focused spot.

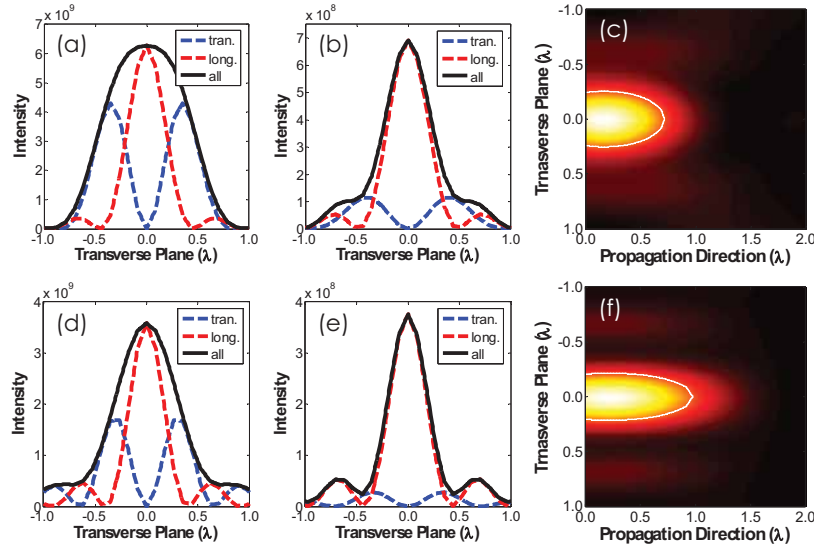


Fig. 2. Focusing RP on the glass-gold interface with circular (a - c) and with (d - e) annular illumination. The cross-section of decomposed field distribution are observed at the top (a), (d) and bottom (b), (e) of the gold thin film. The third column depicts the total intensity distribution of the light passed through the gold layer, where the white contour is the position of half intensity.

The level of penetrated transverse component is always lower than that of focused on the glass-gold interface. The gold layer at least provides 75% relative reduction power on the strength of the transverse component, and this power will increase when annular pupil illumination takes into account. On the other hand, the longitudinal component (red dashed lines) presents relatively unchanged shape as exposing under this setup. Therefore, the total shape (black solid lines) of the focused spot is almost dominated by the longitudinal component due to enlarged L-T ratio caused by the filter-like metallic film.

The third column of Fig. 2 depicts the total intensity distribution of the beam after passing through the gold layer, where the white line is the contour of its half intensity. The annular illumination not only reduces the FWHM of the focused spot but also extends the depth of the penetration in the air. According to our simulation, 64% apodized annular illumination can keep the same shape (0.42λ FWHM) to propagate 0.97λ along the optical axis until the peak intensity dropped to half. This feature could be further improved by increased the ratio of apodized annular.

In order to further investigate the role of metallic film, we depicted the field distribution in the vicinity of the gold layer

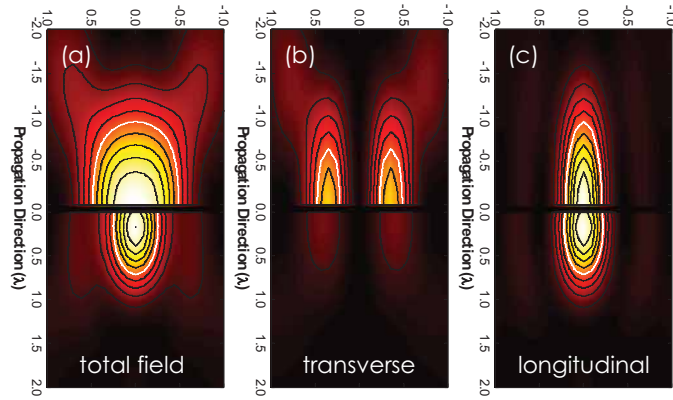


Fig. 3. Field distribution of focused RP in the vicinity of gold layer, where the middle black bar represents the gold thin film and the contours are increased by step of 10% and the half position is labeled by white lines. From left to right depicts (a) total field, (b) transverse component, and (c) longitudinal component.

and decomposed it into transverse and longitudinal component, as shown in Fig. 3. The intensity of each component is normalized and ignores the decreased factor caused by the film. It is clear that the dramatic reduction of the total field is due to vanish of the transverse component after passing through the gold layer. Only longitudinal component could survive after passing through the metallic film and maintain the beam shape with high L-T ratio.

Finally, we concluded with sketching Fig. 4 which shows (a) the FWHM and the L-T ratio versus different ratio of apodized annular illumination and (b) field distribution of the case with 85% apodized annular illumination. The increased pupil apodized ratio will be followed by the larger L-T ratio and smaller FWHM. In the case with 85% apodized annular illumination, the beam can keep the shape and propagate more than 2λ .

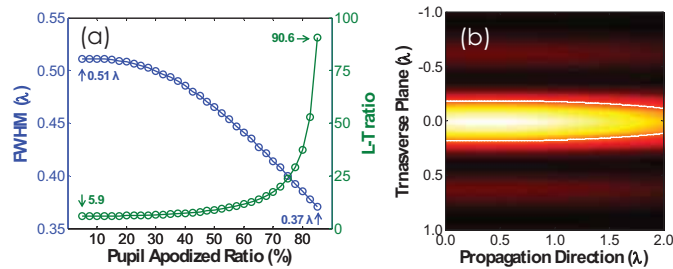


Fig. 4. (a) the FWHM and the L-T ratio of penetrated field versus different ratio of apodized annular illumination. (b) the total intensity distribution in the case of 85% apodized annular illumination.

4. CONCLUSIONS

We proposed a Kretschmann-Raether configuration with annular RP illumination to yield a subwavelength focus spot. With objective of $NA = 0.75$ and 85% apodized annular pupil, a non-diffraction focused beam has FWHM of 0.37λ and more than 2λ penetration depth. The mechanism can easily accompany with solid immersion lens (SIL) and expected to be applicable to optical data storage system.

REFERENCES

- [1] S. Quabis, et al., "Focusing light to a tighter spot," *Opt. Commun.* **179** (2000)
- [2] T. Z. Lan, et al., "Study on the Focusing Mechanism of Radial Polarization with an Immersion Objective," *Pros. ISOM'07*
- [3] Q. Zhan, "Evanescent Bessel beam generation via surface plasmon resonance excitation by a radially polarized beam," *Opt. Lett.* **31** (2006) 1726.

Surface Plasmon Antenna Nano-source

Haifeng Wang¹, Baoxi Xu¹, Towchong Chong^{1,2}

¹Data storage Institute (DSI), Agency for Science, Technology and Research, DSI Building, 5 Engineering Drive 1, Singapore 117608

²Optical Crystal Lab, Department of Electrical & Computer Engineering, National University of Singapore, 4 Engineering Drive 3, Singapore 117576
E-mail: wang_haifeng@dsi.a-star.edu.sg

1. Introduction

Recent advances in optical data storage, magnetic data storage and nano lithography requires the generation of nano-sized light sources. In optical data storage system, the focused beam size is determined by the numerical aperture of the pickup and the wavelength of the incident light source with a relationship of $\text{FWHM}=\lambda/(2\text{NA})$, [1] thus to reduce the beam size, one can either reduce the wavelength or increase the numerical aperture of the pickup, the current blue ray disk uses 405nm light source, and a pickup with a numerical aperture of 0.85. To further increase the capacity of the disk, one can only reduce the beam size by increasing the numerical aperture, because the blue light source is already quite expensive. While the increase in the numerical aperture of the pickup is also limited by the availability of high refractive index material, the highest numerical aperture that is achievable for blue light is 2.34 using diamond. [2] Therefore the minimum beam size is calculated as $405/(2*2.34)=86.5\text{nm}$, which corresponds to a disk capacity of around 200GB. However the expensive blue light source and the diamond sil-lens will sure make the cost hike. To further increase the disk capacity to beyond 1TB and reduce the cost, new solutions has to be found. In the heat assisted magnetic recording (HAMR) system, a light source with beam size of around 30nm is expected to act as a heater to warm up the stable recording media during writing, this is to reduce the what's called superparamagnetic effect and increase the capacity of a disk to beyond 1TB. In the photolithography technique, advanced deep UV (193nm) photolithography can now offer sub-100 nm resolution, further decreasing the wavelength to EUV (13.5nm) does not provide the expected advances because of the EUV related defects, and therefore the line width can not be controlled below 40nm. [3] To meet the requirement, surface plasmon related technique that takes advantage of the collective behavior of free electrons on the surface of some noble metals has been demonstrated, and sub 50nm spot size has been verified experimentally. [4-6] This is benefited from the resonance antenna structures, i.e., aperture type and resonant arms type antennas. There are three kind of aperture type antennas, C-shaped [7-10], H-shaped [11-12] and bow-tie shaped apertures [13-17]. The H-shaped aperture appears like the combination of two C-shaped aperture, and it can also be taken as a special case of the bow-tie shaped apertures with two arms change from triangular shape to rectangular shape. The resonant arms structure consists of two separate metal arms, the surface plasmon resonance between the arms provide very strong field confinement, like the behavior of antenna [18-19] where the length of the arms are limited and which has significant effect on the resonance between the arms. Here we propose a new type of plasmon antenna nano-source, which utilizes the surface plasmon resonance between the outer boundaries of a rectangular shape metal film and the inner boundaries of a rectangular shaped aperture inside the rectangular shape metal film. This type of surface plasmon antenna nano-source has simple structure, when excited with red laser, around 30nm beam size can be obtained, which is applicable to terabyte optical recording, heat assisted magnetic recording (HAMR) and nano-lithography.

2. Theory

We chose gold as the metal to excite surface plasmon. The material model for gold is the widely accepted Drude model.

$$\varepsilon(\omega) = \varepsilon_r + i\varepsilon_i = 1 - \frac{\omega_p^2}{\omega^2 + \gamma^2} + i \frac{\gamma}{\omega} \frac{\omega_p^2}{\omega^2 + \gamma^2}, \quad (1)$$

Where $\omega_p = \left(\frac{4\pi e^2 N}{m}\right)^{1/2}$ is the plasma frequency and γ is the frequency of collisions. From formula (1)

we have

$$\epsilon_r = 1 - \frac{\omega_p^2}{\omega^2 + \gamma^2}, \quad (2)$$

$$\epsilon_i = \frac{\gamma}{\omega} \frac{\omega_p^2}{\omega^2 + \gamma^2}, \quad (3)$$

Thus plasma frequency and the collision frequency can be obtained as:

$$\omega_p = \omega \left[1 - \epsilon_r + \frac{\epsilon_i^2}{1 - \epsilon_r} \right]^{1/2}, \quad \gamma = \frac{\omega \epsilon_i}{1 - \epsilon_r} \quad (4)$$

3. Results & discussion

As is shown in Fig.1, the structure we modeled is a 360nm×360nm×40nm gold film with 100nm×20nm rectangle aperture in it; this film is deposited on a silica substrate shown in Fig.2, Gaussian beam with wavelength of 650nm is focused onto the center of the gold film through the substrate by a NA=0.5 lens, the maximum amplitude of the beam on the focal plane is taken as 1.0, and as a result, a nano-source with intensity full-width-half-maximum of 69nm×30nm size is generated at 5nm away from the bottom surface of the gold film, which is shown in Fig.3 and Fig.4. By dividing the field intensity integration on the plane at 5nm away from the bottom surface with that on the top surface of the gold cubic, a efficiency of 69% is obtained, this is achieved with the help of surface plasmon generated on the top and bottom surface of the gold cubic. Surface plasmon resonances between the boundaries of the large cubic and the boundaries of the aperture like the behavior of a antenna, which squeezes the light through a small aperture.

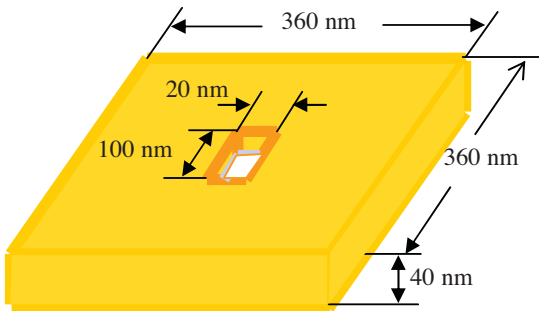


Fig. 1 the structure of the gold film

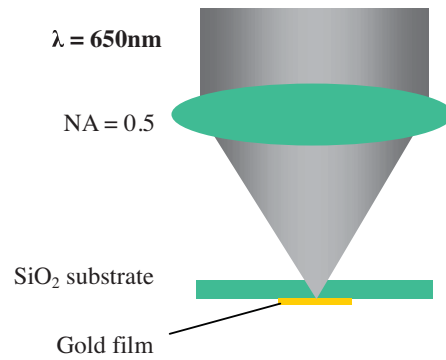


Fig.2 Intensity image at 5nm away from bottom surface

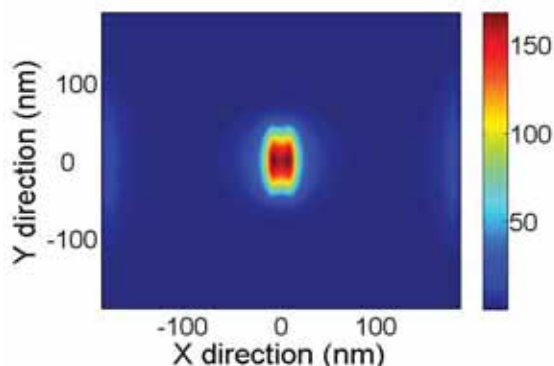


Fig.3 Intensity at 5nm below gold film

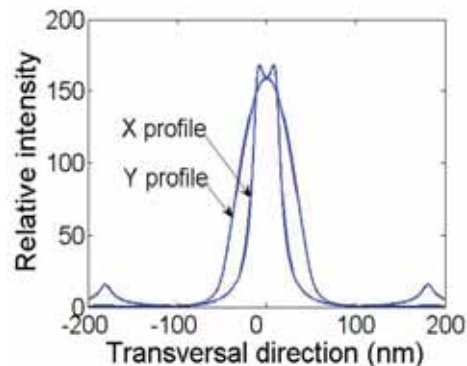


Fig.4 Intensity X- and Y-profile of Fig.3

4. Conclusions

In conclusion, We have proposed a new type of surface plasmon antenna nano-source, which consists of a finite size metal film and a rectangular aperture it, the surface plasmon resonance between the outer boundary of the film and the boundary of the aperture results in a very high field enhancement and extremely tight field confinement. As a result, a nano-source with FWHM of $30\text{nm} \times 69\text{nm}$ size and with high field enhancement at 5nm away from the end surface of a plasmon antenna. The field intensity at 5nm distance is enhanced by 170 fold, the optical efficiency calculated at this distance is as high as 69%. This kind of source may be applicable to near field recording, imaging and lithography.

References

- 1 Haifeng Wang, Gaoqiang Yuan, Weilian Tan, Luping Shi, Tow Chong Chong, *Opt. Eng.* **46**, 065201(2007)
- 2 No-Cheol Park, Near-field Recording Technologies, 4th Annual Optical Storage Symposium, 5 Oct, (2006).
- 3 http://en.wikipedia.org/wiki/Extreme_ultraviolet_lithography
- 4 Liang Wang, Sreemanth M. Uppuluri, Eric X. Jin, and Xianfan Xu, *Nano Lett.*, **6** (3), 361 -364, (2006).
- 5 Arvind Sundaramurthy, P. James Schuck, Nicholas R. Conley, David P. Fromm, Gordon S. Kino, and W. E. Moerner, *Nano Lett.*, **6** (3), 355 -360, (2006).
- 6 Zhao-Wei Liu, Qi-Huo Wei, and Xiang Zhang, *Nano Lett.*, **5** (5), 957 -961, (2005).
- 7 Kursat Sendur William Challener and Chubing Peng, *J. Appl. Phys.*, **96**, (2004) 2743.
- 8 Liang Wang, Eric X. Jin, Sreemanth M. Uppuluri, and Xianfan Xu, *Opt. Express*, **14**, (2006) #72378.
- 9 Fang Chen, A. Itagi, J. A. Bain, D. D. Stancil, and T. E. Schlesinger L. Stebounova and G. C. Walker B.B. Akhremitchev, *Appl. Phys. Lett.*, **83**, (2003) 3245.
- 10 Xiaolei SHI and Lambertus HESSELINK, *Jpn. J Appl. Phys.*, **41**, (2002) 1632.
- 11 E.X. Jin and X. Xu, *J. Quantitative Spectroscopy & Radiative Transfer*, DOI: 10.1016/j.jqsrt.2004.08.019.
- 12 Eric X. Jin and Xianfan Xu, *Jpn. J. Appl. Phys.*, **43**, (2004) 407.
- 13 E.X.JIN and X XU, *Appl. Phys. B* **84**, (2006) 3.
- 14 K. SENDUR & W. CHALLENGER, *J. Microsc.* **210**, (2003) 279.
- 15 Eric X. Jin and Xianfan Xu, *Appl. Phys. Lett* **86**, (2005) 111106.
- 16 Jiying Xu, Jia Wang and Qian Tian, *Proceeding of SPIE*, **5635** DOI: 10.1117/12.570913.
- 17 Kunihiro Ishihara, KeiShi Ohashi, Tomofumi Ikari, Hiroaki Minamide, Hiroyuki Yokoyama, Jun-ichi Shikata and Hiromasa Ito, *Appl. Phys. Lett.* **89**, (2006) 201120.
- 18 Robert D. Grober, Robert J. Schoelkopf, and Daniel E. Prober, *Appl. Phys. Lett.* **70**, (1997)1354.
- 19 Ertugrul Cubukcu, Eric A. Kort, Kenneth B. Crozier, and Federico Capasso, "Plasmonic laser antenna," *Appl. Phys. Lett.* **89**, (2006) 93120.

Picometer-scale accuracy in Position Measurements of NanoDots

Donald A. Chernoff* and David L. Burkhead

Advanced Surface Microscopy Inc., 3250 N. Post Rd., Ste. 120, Indianapolis IN 46226 USA

ABSTRACT

Current and new formats for optical and magnetic data storage require nanometer control of track pitch and feature size variation. Nanometer control implies picometer metrology. We use an ordinary open-loop AFM with additional offline calibration and measurement software to measure pitch and pitch variation. In demonstration measurements on a 144 nm pitch 2-Dimensional square grating (31 G dot/in²) we measured average pitch to an accuracy of 40 pm (1σ). Accuracy was confirmed by optical diffraction measurements at a national standards laboratory. This method also works with SEM and can be applied to denser patterns of interest for 4th generation optical disc and for patterned magnetic media.

Keywords: patterned media, pitch variation, jitter, period, picometer, AFM, SEM, traceable calibration.

1. INTRODUCTION

Many nanofabrication processes require controlling both the mean pitch of a regular pattern and the variation of pitch within that pattern. In optical discs, specified ranges for individual pitch values correspond to $\sigma = 1-1.5\%$ of track pitch. In magnetic hard disks (HDD), which are not intended to be interchangeable between drives, the budget for “write to write track misregistration” is typically $\sigma = 3-7\%$ of the pitch.¹ The gauge should be at least 3x more precise than the objects being measured, so we require (for HDD) gauge $\sigma = 1-2\%$ of pitch. Although this is looser than for optical discs, the smaller pitch values used may increase the challenge. Researchers aiming for a data density of 1 terabit/inch² are using physically patterned media having track pitch of 50 nm or less. At 50 nm pitch, a good pattern should have $\sigma < 1.7-3.3$ nm. In turn, the gauge should be able to measure a perfect 50-nm pitch pattern with $\sigma < 0.5-1$ nm.

We show here that existing microscopes **can** meet these gauge requirements. The microscopes are high-quality, general purpose microscopes, not purpose-built metrology research instruments or expensive critical dimension tools labeled as “CD-SEM” or “CD-AFM”. We also show how one can extend these techniques to qualify traceable calibration standards with pitch values of 50 nm or less, with useful uncertainty limits. Finally, we demonstrate the measurement of various size and position parameters needed for bit patterned magnetic media.

2. MATERIALS AND METHODS

The calibration standard was a 292-nm pitch 1-dimensional grating (Ti lines on Si, Advanced Surface Microscopy Models 292UTC or 301BE). The test specimen was a 144-nm pitch 2-dimensional grid (Al bumps on Si, Advanced Surface Microscopy Models 150-2DUTC or 150-2D). See figure 1. The mean pitch of each pattern was measured by optical diffraction at Physikalisch-Technische Bundesanstalt (PTB), the German national standards laboratory equivalent to NIST in the U.S. The pitch values were 292.096 ± 0.015 nm (95% confidence limit) and 143.928 ± 0.015 nm (X axis), respectively. These values are traceable to the international meter.

AFM. We used a Veeco/Digital Instruments Dimension 3100 AFM with NanoScope IIIA controller. For high accuracy pitch measurements, we used contact mode (5x5 μm scans, 512x512 pixels). We placed both specimens in the AFM at one time and alternated image capture between the two specimens. In a series of 21 images, the odd-numbered images were captured at various spots on the 292 nm grating and the even-numbered images were captured at various spots on the 144 nm grating. For measurements of the size, shape and position of individual nanodots, we used TappingMode™ 3x3 μm scans of the 144 nm grating alone.

SEM. We used a Hitachi S4700 Field Emission SEM at 5 kV, with nominal magnification 25 kx.

Data analysis. We analyzed the data using DiscTrack Plus™ software (Advanced Surface Microscopy).

* phone: +1-317-895-5630; www.asmicro.com

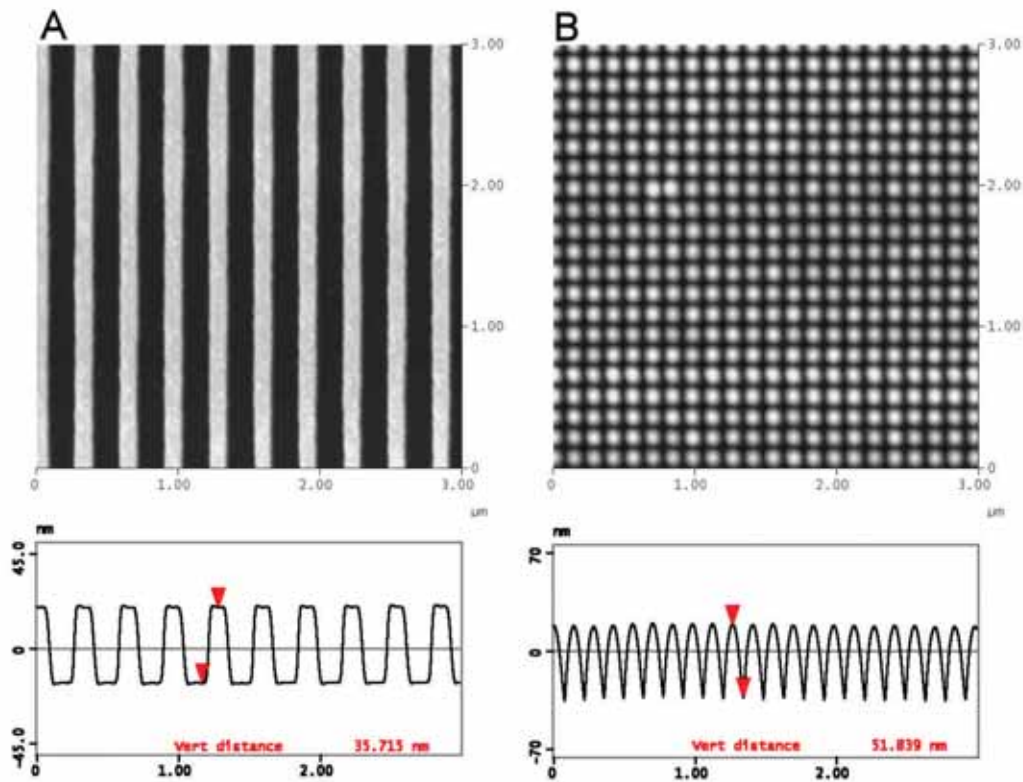


Fig. 1. 3 μm AFM height images of the 292-nm 1D grating (A) and the 144-nm 2D grating (B). The graphs are height profiles made by averaging all scan lines. The ridge height for the 1D grating was 36 nm and the bump height for the 2D grating was 88 nm. The average height of the columns of bumps was 52 nm.

3. RESULTS

3.1 AFM Pitch Measurements

Details of the measurement process, statistical analysis and uncertainty budget have been described in prior work, which also describes the optical diffraction setup.^{2,3,4,5,6} Here we highlight results of interest to media researchers.

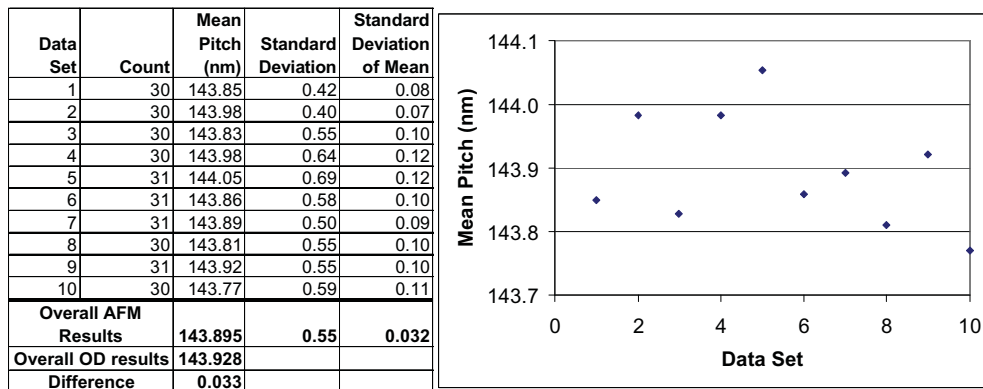


Fig. 2. Summary of AFM pitch results.

The overall run of 11 calibration and 10 ‘test’ images was divided into 10 data sets, each analyzed separately. For a given data set, we measured the pitch using one test specimen image and two images of the calibration standard, one captured before and one captured after the test image. This procedure (“interleaved calibration”) increases accuracy by correcting for short term drift in the AFM’s magnification and increases the precision of nonlinear scale corrections by using redundant calibration data. Figure 2, a table and graph of pitch statistics for each data set, shows there was no significant difference in mean pitch from spot to spot. The overall standard deviation of individual pitch values was 0.55 nm, just 0.38% of the pitch. We found this random effect dominated all other sources of uncertainty at the individual pitch level.

The corresponding standard deviation of the overall mean was 0.032 nm (32 picometers), an improvement by the factor $\sqrt{304}$, the number of pitch values measured. The next largest effect, a cosine error (possible sample orientation difference 1°) was 22 pm, so the uncertainty of the mean pitch was 40 pm. The 95% confidence limit for mean pitch was therefore 80 pm; which is just 0.056% of the pitch. Since the AFM mean value differed from the OD (optical diffraction) mean by only 33 pm, we can say with confidence that the two methods gave identical results within experimental uncertainty, i.e. no important systematic errors were neglected. The AFM results are therefore traceable to the international meter.

We have measured the pitch standard deviation of other 2-D gratings, with pitch of 292 and 700 nm. In those cases, we also found individual pitch $\sigma = \text{ca. } 0.4\%$ of pitch. Assuming that this standard deviation holds also for a pitch of 50 nm, one would obtain a precision of about 0.2 nm. This is more than twice as good as the gauge requirement for patterned hard disk drive media we indicated above. Applying the same uncertainty model, the mean pitch uncertainty would be 15 pm after measuring 300 pitch values (expanded uncertainty = ± 30 pm or 0.06% of the pitch).

3.2 SEM Pitch Measurements

Self-calibrated images of the 144 nm grating had pitch variation $\sigma = 0.43$ nm. The full paper will give details.

3.3 AFM Position Measurements

Center to center position variation of individual nanodots is a basic measure of jitter in bit patterned magnetic media. For the 144 nm 2-D grating, we found center to center $\sigma = 2.64$ nm. This is equivalent to “data to clock” jitter $\sigma = 1.3\%$, where $T=144$ nm). The full paper will give details.

4. CONCLUSIONS

In this work, we used Optical Diffraction measurements as a high-accuracy foundation for pitch metrology, showing that it is possible to get high precision measurements of pitch variation using a general purpose microscope (here, an ordinary AFM). This is an important result because optical diffraction is not presently available to measure pitch < 140 nm. For that range, we can use microscopes instead and still get high accuracy after a moderate number of measurements.

REFERENCES

- ¹ “Patterned Magnetic Media”, <http://www.hitachigst.com/hdd/research/storage/pm/index.html>.
- ² Donald A. Chernoff, Egbert Buhr, David L. Burkhead, and Alexander Diener, “Picometer-scale accuracy in pitch metrology by optical diffraction and atomic force microscopy”, in “Metrology, Inspection, and Process Control for Advanced Lithography XXII”, edited by John Allgair, Proceedings of SPIE Vol. 6922, to be published 2008.
- ³ Buhr, E., Michaelis, W., Diener, A., and Mirandé, W., “Multi-wavelength VIS/UV optical diffractometer for high-accuracy calibration of nano-scale pitch standards”, *Meas. Sci. Technol.* 18, 667-674 (2007).
- ⁴ Chernoff, D. A. and Burkhead, D. L., “Automated, high precision measurement of critical dimensions using the Atomic Force Microscope”, *J. Vac. Sci. Technol. A* 17, 1457-1462 (1999).
- ⁵ Chernoff, D. A. and Lohr, J. D., “High precision calibration and feature measurement system for a scanning probe microscope”, U.S. Patent 5644512 (1997).
- ⁶ Chernoff, D. A. and Lohr, J. D., “High precision calibration and feature measurement system for a scanning probe microscope”, U.S. Patent 5825670 (1998).

Study on transparency mechanism of bimetallic Bi/In film

Sihai Cao, Chuanfei Guo, Zhuwei Zhang, Yongsheng Wang, Junjie Miao, Qian Liu*

National Center for Nanoscience and Technology, China.

No.11, Beiyitiao, Zhongguancun, Beijing 100080, China

* Corresponding author: liuq@nanoctr.cn; Phone: +86-10-82545585 ; Fax +86-10-62656765

1. INTRODUCTION

Bimetallic Bi/In film has been regarded as one of candidate materials used to nano-optical storage medium, photomask, thermal resist for microfabrication and transparent conducting oxides^[1-5]. When exposed to laser with power density above threshold, which is dependent on modification of the composition, bimetallic Bi/In thin film turned transparent and the optical density varied almost linearly with exposure power density^[3].

Laser exposure process of bimetallic Bi/In film was earlier regarded as thermal-induced alloying process^[2, 6, 7]. Therefore the eutectic composition for Bi-In binary system was selected in the initial design to realize the laser exposure at lower temperature, *i.e.* lower power density^[7]. Recently, it was thought to be related to oxidation of the film. It is necessary to understand the transparent mechanism of the film, for developing recording materials with better performance. Since bimetallic Bi/In film's laser exposure is closely related to thermal-induced process, systematic study on the heat treatment of the film would help understand the exposure process. At the same time, laser exposure experiments would benefit the understanding of the behavior in optical storage process.

2. EXPERIMENT

Bimetallic Bi/In thin films were deposited on slide glass by magnetron sputter ACS-4000-C4. Indium was first deposited at 50W with Ar flow 25sccm under the pressure of 0.1Pa. Next Bismuth was deposited at 20W with Ar flow 50sccm under the pressure of 0.2Pa. The as-deposited films were heated to designed temperature in tube furnace and kept for 3h in air, and then cooled naturally to ambient temperature in furnace. The film was exposed for 1s by CW laser in Renishaw Micro-Raman Spectroscopy System with $\lambda=785\text{nm}$ and single pulsed ($\sim 7\text{ns}$) Nd:YAG laser (Spectra Physics Pro-230, $\lambda=532\text{nm}$).

Optical properties test was carried out by Lambda950 UV/VIS from 400nm to 800nm. XRD analysis was performed on X'Pert Pro. The composition of the films was analyzed by Auger Electron Scan on PHI-700. During the test process, the film was in-situ sputtered by Ar ion gun at a reference speed of 2nm per minute. Field emission scanning electron microscope (FESEM) images were taken on field emission scan electron microscope Hitachi S-4800 at high voltage of 5kV.

3. RESULTS AND DISCUSSION

Optical properties for bimetallic Bi/In thin films are shown in Fig.1. Here OD (optical density) is defined as $\lg I_0 / \lg I$, with I_0 as incident intensity of the beam and I as transmitted intensity. The as-deposited bimetallic Bi/In film exhibits higher OD than those heat treated. Compared with previous reports^[3], OD value of the as-deposited bimetallic Bi/In film is relatively lower. This maybe relates to the higher oxygen concentration in the film

fabrication. In addition, present Bi/In mole ratio off the eutectic point composition (Bi=53at %) is maybe another reason which will be discussed later. When the treatment temperature increased from 150°C to 350°C, OD value of the films decreases obviously, as shown in Fig.1. This means the films get more and more transparent. When temperature was further increased to 400°C, there was almost no change for OD value. Therefore the as-deposited and heat treated films at 350°C for 3h in air were studied next based on the largest change of OD value for the film.

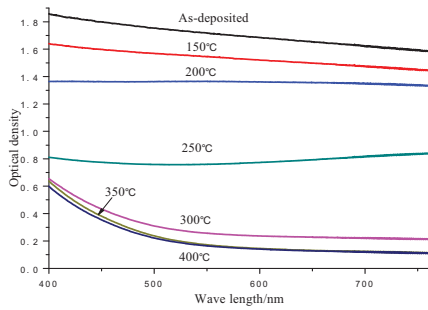


Fig.1 OD curves of Bi/In films

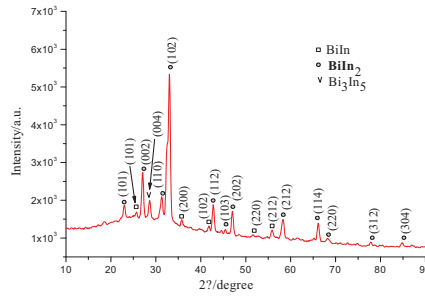


Fig.2 XRD of as-deposited Bi/In film

XRD profiles of as-deposited and heat treated bimetallic Bi/In film are shown in Fig.2 and Fig.3. It can be seen that BiIn and BiIn₂ alloys have been formed in bimetallic film except trace amount of Bi₃In₅. After heat treatment, diffraction peaks of Bi₂O₃ and In₂O₃ were found and were confirmed by XPS analysis. That is to say when heat treated at 350°C for 3h in air, the film converted to oxides and turned transparent. This is similar to the behavior of transparent conductive oxide such as ITO [8], ZAO and ZMO [9].

Figure 4 shows that there was more Indium than Bismuth on the top of the film although In was first sputtering deposited on slide glass. This indicates Bi and In films do not existed as two separate layer, accordant to XRD results. Partial oxidation is observed in the as-deposited films, which is presumably the reason for smaller optical density than that in other references [3]. After heat treatment, both oxygen content and the mole ratio of O/(In+Bi) have an increase, demonstrating oxidation process of the bimetallic film.

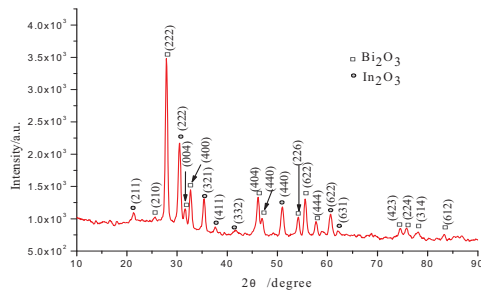


Fig.3 XRD of Bi/In film heat-treated at 350°C

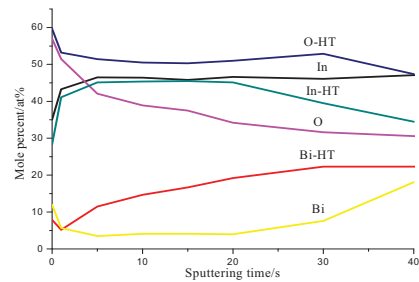


Fig.4 Auger results of as-deposited and heat treated (HT) Bi/In

Based on above results it can be concluded that the transparent conversion of bimetallic Bi-In film under heat treatment is attributed to oxidation rather than alloying process. As for exposure power's dependence on composition ratio, it should relate to the different oxidation energy for Bi and In. Therefore, the selection of composition at the eutectic point of Bi-In is not necessary. Further study bimetallic Bi-In thin films with different composition on their threshold of exposure power are still needed.

For the area exposed for 1s, which marked within ellipse in Fig.5, in-situ microscope image shows it turned transparent. FESEM image shows it looks obscure relative to unexposed area around because of the charging effect of oxide. However, laser ablation was observed without traces of oxidation at the outer margins of the hole ablated, for the area (see Fig.6) exposed with single pulse of 7ns. This may be due to the untimely heat transfer under an ultra short pulse laser.

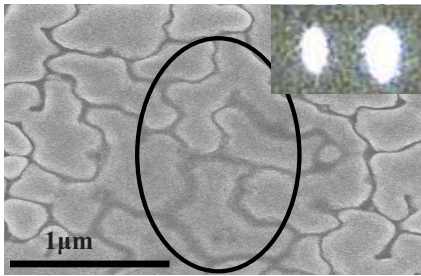


Fig.5 SEM and microscope images of exposed area

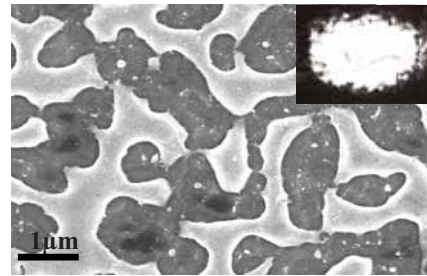


Fig. 6 SEM and microscope images of ablated area

4. CONCLUSION

Oxidation of the bimetallic Bi/In thin film replaces alloying process in transparent mechanics. The optical density of the film has a decrease after heat treatment; this is similar to the long pulse laser exposure. For laser exposure with ultra short pulse, for example ~ 7 ns, laser ablation is the main reason for the transparent conversion. The conversion indicates that it is possible that the film have a potential application in optical storage.

REFERENCES

- [1] M.V. Sarunic, G. H. Chapman, Y. Tu. A Prototype. Proc. SPIE, 2001, 4274:183-193
- [2] G. H. Chapman, Y. Tu, M.V. Sarunic. Proc. SPIE, 2002, 4690: 465-476
- [3] D. Poon, G. H. Chapman, Y. Tu et al. Proc. SPIE, 2005, 5992: 59920k1-11
- [4] Y. Tu, M. Karimi, N. Morawej et al. Mat. Res. Soc. Symp. Proc, 2002, 745: 73-78
- [5] M. Karimi, R. Tu, J. Peng et al. Thin Solid Films, 2007, 515 (7): 3760-3765
- [6] Y. Tu, G. H. Chapman. Proc. SPIE, 2003, 4979: 87-98
- [7] Marinko V. Sarunic. Master thesis. Simon Fraser University, 2001
- [8] K.L. Chopra, S. Major, D.K. Pandya. Thin Solid Films, 1983,102:1-46
- [9] C.G. Granqvist. Solar energy materials and solar, 2007, 91:1529-1598

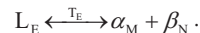
Strategies for employing nano-heterostructures in a near-field enhanced super-resolution optical disk

Yang Wang, Qingling Qu, Yiqun Wu and Fuxi Gan

Shanghai Institute of Optics and Fine Mechanics, Chinese Academy of Sciences,
PO Box 800-211, Shanghai 201800, China, Tel.: 86-21-69918562, Fax: 86-21-69918800

The drive for increased optical storage density and capacity has stimulated much interest in the field of optical super-resolution that offers the capability for operation beyond the diffraction limit. A kind of self-masking super-resolution optical disk based on an instantaneously formed “nano-aperture” and near-field interaction was developed by J. Tominaga et al.¹. In this so-called super-resolution near field structure (Super-RENS) optical disk, confined light and near-field enhancement was considered to be the origin of simultaneously getting high resolution and carrier-to-noise ratio (CNR). Enhanced near-field is the key advantage of Super-RENS when compared with traditional “iris eclipse” super-resolution optical disk technique. As we know, the optical transmission from a “bare aperture” with size of sub-wavelength or smaller will be enormously attenuated, which will not result in a sufficient signal in principle. Nobel metallic nano-particle induced local surface plasmon^{2,3} and photo-thermally induced graded refractive index^{4,5} were reported to be responsible for the near-field enhancement of Super-RENS optical disk. In this paper, new strategies to obtain enhanced near field transmission by embedded nano-heterostructure induced by eutectic transition are proposed. Numerical simulations demonstrate that periodic eutectic microstructures formed on binary eutectic alloy thin film during irradiation of a laser beam can result in a prominent near-field enhancement. Results can give important information to understand the microscopic mechanism of eutectic-binary-alloy-type super-RENS disk (highest CNR can be achieved when the composition ratio is near the eutectic point of a binary-alloy mask layer)⁶ from a near-field optics view and may provide a potential new approach to develop functional subwavelength- or nano- heterostructures for nano-photonics and plasmonics applications⁷.

When irradiated by a Gaussian beam, the center of the focused spot on the eutectic binary alloy mask layer melted into liquid for the photo-thermal effect. After the laser beam has passed or turned off, the liquid region is cooled to be solid. At a certain temperature (T_E) during this process, the eutectic transition should take place. This transition process can be expressed as:



As shown in a typical phase diagram of binary alloys (Fig.1), two different solid phases α_M (phase α with composition M) and β_N (phase β with composition N) can be produced simultaneously from L_E (melted liquid with composition E) and regular eutectic micro-/nano-structures (such as periodic lamellar structures) will be formed⁸. Like the transient “aperture” formation during phase-changing or melting of mask layer, the eutectic micro-/nano-structure maybe also formed transiently under a certain solidification conditions.

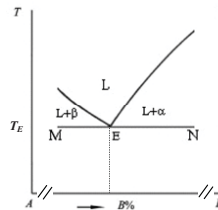


Fig.1 Typical phase diagram of binary alloys

Simplified three-dimensional finite-difference time-domain (3-D FDTD)^{4,5} geometrical models (Fig.2(a),(b)) of the eutectic microstructure on binary-alloy thin film are established according to a representative lamellar eutectic structure of Al-Cu alloy formed after laser irradiation (Fig.2(c))⁹. For calculation convenience, the periodic micro-/nano- structure is embedded in the center of a 60-nm-thick perfect electric conductor (PEC) thin film. The incident light propagating along the +z is a homogeneous plane wave with a wavelength of 650nm and

its polarization is along y axis direction. The dimension of each cell is $\Delta x = \Delta y = 2\text{nm}$, $\Delta z = 4\text{nm}$. The time step is $4.447 \times 10^{-18}\text{s}$ according to the stability criteria of FDTD algorithm.

Near-field optical intensity profiles of the lamellar periodic structure along the x and y axis direction for different z are presented in Fig. 3(a) and (d), respectively. For comparison, the other two cases: bare aperture and homogeneous structure (uniformly filled with α phase) are also given. From Fig.3, it is easy to see that there exit a great enhancement of the near-field optical intensity for the lamellar structure with periodic refractive index distribution compared with those of bare aperture and homogeneous structure. During readout process, the enhanced near field interacts with the recorded marks and the higher spatial frequencies beyond the diffraction limit may be included into the propagating far field³. Therefore, the higher-CNR super-resolution readout may be realized.

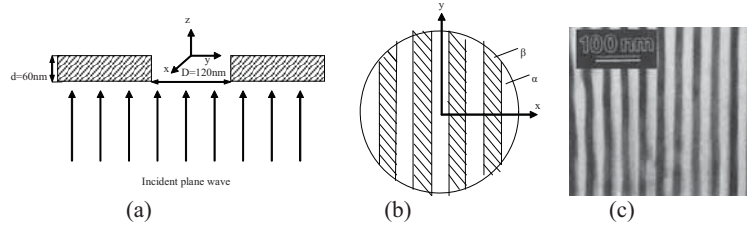


Fig.2 Simplified FDTD geometrical model (a,b) and an actual microstructure of Al-Cu eutectic alloy formed after laser irradiation (c) (cited from ref.9 after area cutting)

The Near-field optical intensity of the lamellar periodic structure is very sensitive to the width ratio and refractive index ratio of phase α and β (Fig. 4 (a)). And there is an obvious influence of the azimuth angle between the polarization direction of incident light and the arranging direction of lamellar slices on the enhancement of near field (Fig.4 (b)). Fig.4 shows the intensity ratio of the subwavelength aperture filling with nano-structured alloy and that of bare aperture. It is clearly shown that the intensity can be magnified several thousand times. It looks more effective on near field enhancement than Sb thermal lens with graded refractive index distribution, which can get 400~700 times magnification under similar circumstances⁵.

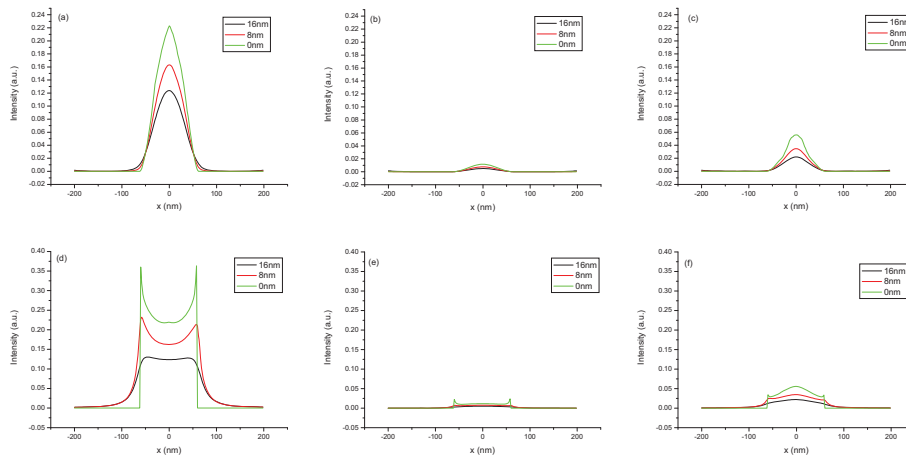


Fig.3 Near-field optical intensity profiles of various structures along x (a,b,c) and y axis (d,e,f) for different z:(a,d) lamellar periodic structure; (b,e) bare aperture; (c,f) homogeneous structure

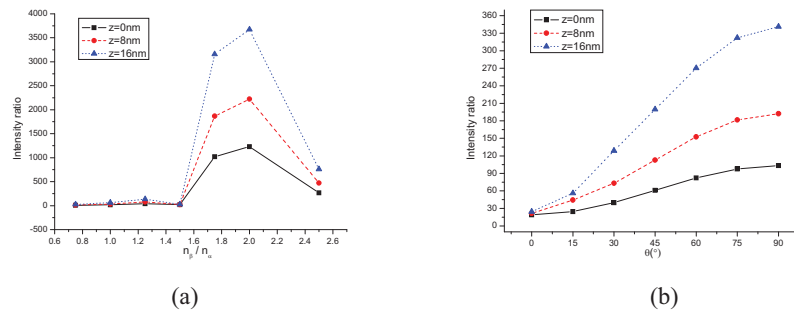


Fig. 4 Intensity ratio of the lamellar periodic structure to the bare aperture with different refractive index ratio of phase α and β (a), and with different azimuth angle between the polarization direction of incident light and the arranging direction of lamellar slices (b)

It should be pointed out that the laser-induced periodic micro-/nano-structures on the eutectic-binary-alloy mask layer are totally different with directly prepared periodic multilayer or lamellar thin films. The eutectic micro-/nano-structure only formed in the center part of focused area. It is highly localized (with size of about tens or hundreds of nanometers) and have special near field characteristics. The eutectic micro-/nano-structure maybe only formed transiently under a certain solidification conditions (such as at a specific temperature or stress state) during the laser irradiation process. Although the accurate control of structure geometry and refractive index distribution is not easy, but maybe it will become a potential effective method to prepare localized periodic lamellar micro-/nano-structure especially for near-field enhanced super-resolution, nano-photonics and plasmonics applications.

References

1. J. Tominaga, T. Nakano, N. Atoda, An approach for recording and readout beyond the diffraction limit with an Sb thin film, *Appl. Phys. Lett.* 1998, 73(15): 2078-2080
2. T. Kikukawa, T. Nakano, T. Shima, and J. Tominaga, Rigid bubble pit formation and huge signal enhancement in super-resolution near-field structure disk with platinum-oxide layer, *Appl. Phys. Lett.*, 2002, 81(25): 4697-4699
3. T. Chu, W. Liu, D. Tsai, Enhanced resolution induced by random silver nanoparticles in near-field optical disks, *Opt. Commun.*, 2005, 246: 561-567
4. J. Wei, F. Zhou, Y. Wang, F. Gan, Y. Wu, Optical near-field simulation of Sb thin film thermal lens and its application in optical recording, *Journal of Applied Physics*, 2005, 97:073102
5. F. Zhou, W. Xu, Y. Wang, F. Gan, Optical transmission enhancement by a sub-wavelength film lens, *Chin. Opt. Lett.*, 2006, 4(1): 52-55
6. T. Shima, T. Nakano, J. Tominaga, An approach to lower the threshold laser power of super-resolution-readout optical disk using silver telluride layer, *Jpn. J. Appl. Phys.*, 2004, 43(11B): L1499-L1501
7. B. Wang, G. Wang, Directional beaming of light from a nanoslit surrounded by metallic heterostructures, *Appl. Phys. Lett.* 2006, 88: 013114
8. J. Yu, W. Yi, B. Chen, *Gallery of Binary Alloy Phase Diagram*, Shanghai Scientific and Technical Publishers, Shanghai, 1987, pp. 35.
9. M. Zimmermann, A. Karma, M. Carrard, Oscillatory lamellar microstructure in off-eutectic Al-Cu alloys, *Phys. Rev. B*, 1990, 42(1):833-837

Recovery and Reconstruction of the Intensity Distribution of Nano-sized Light Field Obtained with NSOM

H. X. Yuan, B.X. Xu, Sofian MD, T. C. Chong
Data Storage Institute, DSI building, 5 Eng. Dr.1, NUS, Singapore, 117608
Tel: 65-68748412 Fax: 65-67778517 Email: Yuan_hongxing@dsi.a-star.edu.sg

Abstract

Blurring effects of finite NSOM tip on the directly reconstructed image are modeled with assumption of Gaussian light distribution and circular aperture of NSOM tip. Analysis shows that when the interested light field is of the similar size with NSOM tip, 50nm to 80nm in general, the retrieved field width will different substantially with actual one. Deconvolution technique, traditionally adopted for digital signal process and image process to improve the contrast, is proposed here to improve characterization precision of the nano-sized light field. Comparison is also made between the directly retrieved image and processed image in this paper.

Key words: near-field optics, NSOM, deconvolution, nano-optics, surface plasmon (SP)

Model and Experiments

Near-field Scanning Optical Microscopy (NSOM) is able to circumvent the diffraction limit and push the optical resolution as high as 100nm and below, so it gets wide applications in optical engineering and bio-engineering. However, with plasmonics coming into sight of both scientists and engineers[1][2], the collection mode of NSOM becomes an popular way to reconstruct the sub-mircon near field distribution. With further squeezing into nano-size, the raw data or raw image directly obtained by NSOM system comes to susceptible since the aperture size of NSOM tip now can only reach 50 to 100nm. If the light field is within the same order or even just tens of nanometers, the raw data or raw image is actually the convolution result of the light field and comparably bigger aperture of NSOM tip and thus is substantially different with the actual light field distribution. In order to recover and reconstruct the nano-sized light field from the raw data without tightening the request of finer aperture of tip, the technique of deconvolution, which has been widely utilized to for digital signal process and special image process to improve the image contrast[3], is proposed in this paper to improve the characterization precision by post processing the raw NSOM image. The light field derived from the resultant image, therefore, is much closer to the original field.

In order to get a general picture of how much impact of hundred nanometer sized NSOM tip excises on the image, a simplified model is built firstly. Assuming that the interesting nano-sized light field is of Gaussian distribution and FWHM is d_f , so

$$\sigma = d_f / 2\sqrt{2\ln 2} \approx 0.391d_f, \quad (1)$$

and the light intensity distribution can be described as

$$f(x, y) = A e^{-\frac{x^2+y^2}{2\sigma^2}} \quad (2)$$

where A is a constant. Another assumption is the aperture of NSOM tip is of circular shape of diameter d_t , and its function can be described as

$$g(x, y) = 1, \text{ when } \sqrt{x^2 + y^2} \leq d_t / 2. \quad (3)$$

So the raw data of raw image of NSOM is actually the convolution of both functions.

$$I(x, y) = A \int_{-d_t/2}^{d_t/2} \int_{-\sqrt{(d_t/2)^2 - \beta^2}}^{\sqrt{(d_t/2)^2 - \beta^2}} e^{-\frac{(x-\alpha)^2 + (y-\beta)^2}{2\sigma^2}} d\alpha d\beta \quad (4)$$

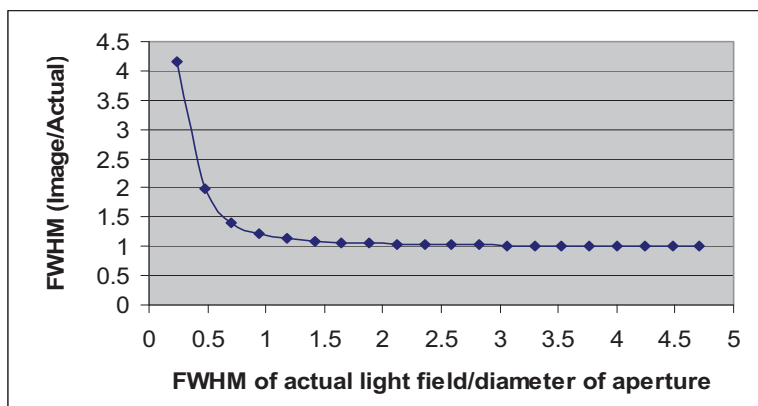


Fig.1 Evolution of ratio between FWHM of light field derived from NSOM image and the FWHM of actual light field vs. the ratio between the actual FWHM of light field and the tip size

Just as mentioned above, the actual FWHM of the light field may differentiate prominently with that derived from NSOM image when the size light field comes close to the aperture size dt of NSOM tip. If normalized to the NSOM aperture size dt , FWHM derived from the image can be obtained from the convolution result of Equ.(4). Shown in Fig.1 is the evolution of FWHM (Image/actual), the ratio between FWHM of the field derived from the NSOM image and actual FWHM of light field, vs. FWHM (actual/tip size), the ratio between the actual field size and tip size. Obviously, when the size of the actual field is around 2 times of the NSOM tip aperture size, the derived FWHM is just 4% different from actual one, but when both comes to the same size, the difference between derived FWHM and actual one can reach 20%. With further size reducing of the light field to half of the tip size dt , the error between derived FWHM and actual one can be as high as nearly 100%. The above estimation is carried out without consideration of noise. If noise is taken into account, the deviation of FWHM derived directly from NSOM image from the actual one maybe worse. This implies the necessity to correct the derived FWHM. As long as the actually size of the tip aperture can be characterized with AFM or other equipments, the aperture function of certain experiments can be obtained in advance, and the directly achieved NSOM image can be deconvoluted into the actual light field distribution.

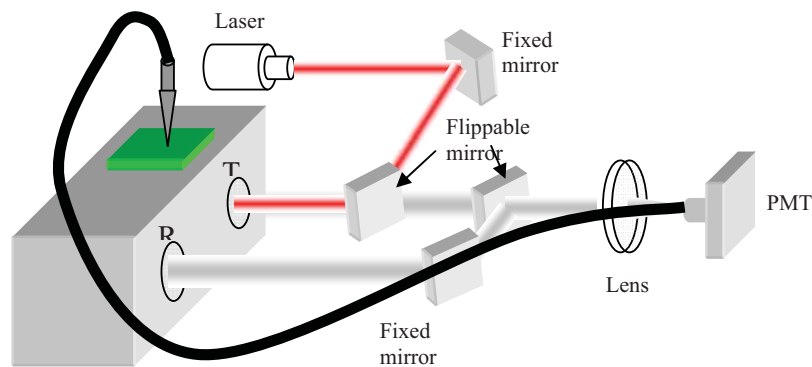


Fig.2 Schematic of the collection mode of NSOM

A series of nano-sized apertures fabricated with FIB on 100nm thick Ag thin film on glass substrate, on which surface plasmonic effects present, are shined with focused laser of 650nm wavelength from the bottom of the sample. Shown in Fig.2 is the schematic of the collection mode of NSOM for this experiment. The NSOM image directly obtained with NSOM for the aperture of 400nm is shown in Fig.3. The ticks for both directions are just sampling counters. The actual spatial sampling step is 12.5nm. Shown in Fig.3(a) is NSOM image directly taken with NSOM. With consideration of tip size round 80nm in diameter and the NSOM tip model as Eq.(3), deconvolution technique with iterative method is applied to the raw image, and the resultant image

after 40 times iteration has been verified to be stabilized and is shown in Fig. 3(b). Unit for both directions are sampling counter, spatial resolution is 12.5nm. The FWHM of light spot derived from raw image is around 510nm, while that from processed image is only 475nm. This difference is around 7%, slightly bigger than the previous prediction. The possible reasons are from several aspects. The most probable one is the background of raw image is too noisy as the result of poor splicing of fiber tip with extension fiber cable, so FWHM derived from raw data may appear to be bigger than actual one. While the processed image suppress the noise efficiently at the vicinity of the light spot, thus the FWHM is supposed to be much closer to the actual one.

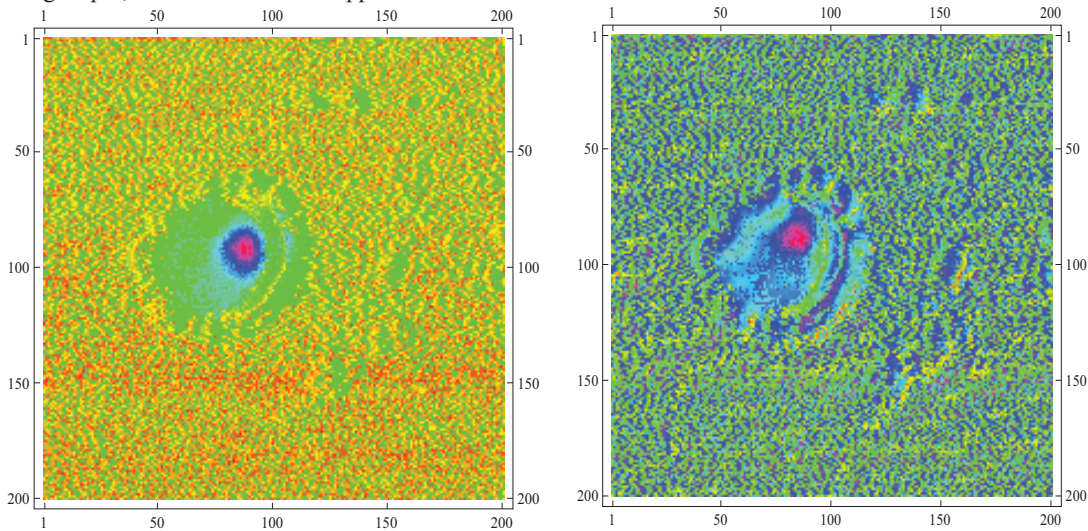


Fig.3 NSOM raw image and deconvoluted image for aperture of 400nm. Unit for both directions sampling counter, spatial resolution is 12.5nm.

Discussion and Conclusion

FWHM width of the light field derived from NSOM image working at collection mode maybe substantially different from the actual one when the FWHM of the actual light field comes to the same order of the tip size. Such error may reach 100% of the actual field size. To increase the creditability of the NSOM image for nano-sized light field distribution with the NSOM collection, deconvolution technique has been verified as a useful tool to recover the actual field distribution. Of course, the assumption of uniform tip aperture function can be further improved and how to overcome the impact of the sampling noise is another challenge for achieving high-fidelity reconstruction of the actual light field.

Reference

- [1]. J. R. Krenn, A. Dereux, J. C. Weeber, E. Bourillot, Y. Lacroute, and J. P. Goudonnet, "Squeezing the Optical Near-Field Zone by Plasmon Coupling of Metallic Nanoparticles", APL, Vol.83, p2590 (1999).
- [2]. H.X. Yuan, B.X. Xu, B. Lukiyanchuk, T.C. Chong, "Principle and design approach of flat nano-metallic surface plasmonic lens", APA, Vol 89, P397 (2007).
- [3]. Kwang Eun Jang and Jong Chul Ye, "Single channel blind image deconvolution from radially symmetric blur kernels", Optical Express, Vol.15, p3791(2007).

Pupil Plane Characteristics and Filtering for Optical Data Storage Using Circular Polarization

Junyeob Yeo¹, Moonseok Kim¹, Narak Choi¹, Tom D. Milster² and Jaisoon Kim¹

¹School of Physics and Astronomy, Seoul National University

San 56-1 Sillim-Dong, Kwanak-Gu, Seoul, 151-747, Korea

Phone/Fax: 82-2-873-7372/82-2-884-3002, Email : jskim@phya.snu.ac.kr

²College of Optical Sciences, University of Arizona,

Tucson, Arizona 85721, USA

1. Introduction

To improve capacity, a near field solid immersion lens (SIL) system is an excellent candidate for future technology. Previous research on SIL technology focused on the analysis of total light intensity signal for handling (writing, reading) data, gap control and developing media. For a high-NA system, characteristics of the reflected signal beam show big differences from that of previous systems based on far-field optical analysis. In a SIL system, the properties of reflected signal seen at the exit pupil strictly depend on the gap thickness between the SIL and the top surface of the medium.¹⁾

Previously, our concern was focused on the optical spot sizes and signal contrasts for a NA~1.1 linearly polarized optical system according to the different gap thicknesses. In this case, the signal contrast can vanish for specific index modulation of the medium, and it can be improved by using an appropriate filter.²⁾

In this paper, our interest is concentrated on the exit pupil characteristics in high-NA SIL optical systems using circular polarization.

2. Pupil characteristics and high-NA system.

Signal contrast depends on variation of recording media refractive index that is mainly limited by quantum effects related to the material. After writing, the complex refractive index of a recording layer is changed to n' from an original value of n_0 . The refractive index difference Δn is $n_0 - n'$. In this case, data signal contrast is directly related to the modulation of $\Delta n/n_0$. Contrast is large when n_0 is small. However, it becomes worse as n_0 increases. To improve signal contrast in high NA systems, especially for the near field system, pupil plane characteristics are investigated by analyzing various combinations of polarization states, including linear and circular polarization. Several new ideas for pupil filtering are suggested.

3. Pupil plane characteristic and filtering

In the system layout shown in Fig. 1, a circularly polarized Gaussian Laser beam of 650nm/405nm wavelength is focused, reflected from different recording media and collimated again through OBJ/SIL. Wavelength 650nm system is an example of for high modulation signal and 405nm system is an example of for low modulation signal.

OBJ's NA, refractive index of SIL and the effective NA of SIL for 650nm/405nm are 0.6/0.7, 1.843/2.086 and 1.1/1.45, respectively.^{3),4),5)} For any particular change in medium during data access, the readout signal contrast using specific wavelength (650/405nm) source is defined as $V = (I_x - I_n)/(I_x + I_n)$, where I_x and I_n are the max/min detector signals corresponding to the change of the medium states that can be represented by complex refractive index.^{6),7)}

To realize the pupil plane filtering without disturbing the optical path from the light source to the recording medium, a 4- f (focal length) imaging system is used. The specific optical filter is located on the plane where the image of the original pupil is formed.^{2), 3)}

Total irradiance difference between crystalline (max) and amorphous (min) at NA=1.1, 650nm and using the same medium as previous research³⁾ ($n_0 = 3.38 + 3.4i$) is shown in Fig. 2. To choose the proper filter for the improvement of signal contrast, pupil plane characteristics are analyzed. The irradiance difference distribution on depth of a gap is shown, Fig. 2(a), and a simplified figure of the irradiance difference distribution is shown in Fig 2(b). Rotational symmetry in pupil plane is observed. Therefore, a rotationally symmetric filter is designed. The signal contrast is improved using this filter. The result is illustrated in Fig. 3.

Similarly, total / x component / y component irradiance distributions at the pupil plane for a NA=1.45, 405nm system ($n_0 = 2.2724 + 2.566i$)⁴⁾ are shown Fig. 4. To improve the signal contrast, several different types of pupil filters are suggested by analyzing pupil plane characteristics for the case of circular polarization. Two appropriate

pupil filters with multi-transmittance and polarization variations are shown in Fig. 5. The filter using polarization variation is chosen, because it showed the best performance improvement, which is illustrated in Fig. 6. Likewise, the filter using polarization variation is also used for a NA=1.1, 650nm system ($n_0=3.38+3.4i$)³⁾, and the result presented as a dotted line graph is added on the Fig. 3.

More complex filters that can change shape according to the gap thickness variation will be presented at the conference.

3. Conclusion

Data signals in high-NA data storage systems are enhanced by using optical filters that block, truncate or apodize certain segments of the pupil that would otherwise produce negative contributions in the signal read out. System NA and material characteristics are the important variation factors for the investigation.

To design optimized shape of the pupil filter, a deep understanding of the intensity distribution, polarization state at the pupil and detail simulation results based on the polarization induced pupil aberration are needed. More detail results in pupil characteristics and advanced suggestion for filtering will be presented at the conference.

4. Reference

[1]T. D. Milster, J. S. Jo, K. Hirota and K. Shimura and Y. Zhang: Jpn. J. Appl. Phys. 38(1999) 1793.
 [2]T. D. Milster, K. Shimura, J. S. Jo and K. Hirota: Opt. Lett. 24 (1999) 605.
 [3]K. Shimura, T. D. Milster, J. S. Jo and K. Hirota: Jpn. J. Appl. Phys. 39(2000) 897.
 [4]Jack van den Eerenbeemd, "Near-Field Optical Recording on Cover Protected Discs.", 2008, Philips Electronics N.V.
 [5]K. Hirota and G. Ohbayashi: Jpn. J. Appl. Phys. 37(1998) 1847.
 [6]D. G. Flagello, T. D. Milster and A. E. Rosenbluth: J. Opt. Soc. Am. A13 (1996)53.
 [7]T. D. Milster, J. S. Jo and K. Hirota: Appl. Opt. 38(1999)5046.

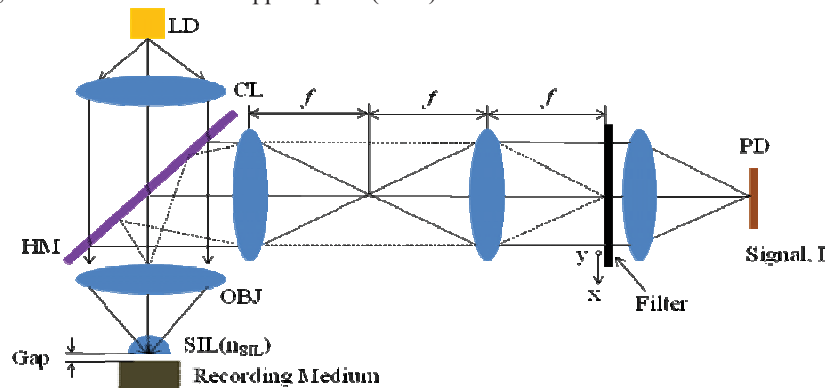


Fig. 1. Optics layout for pupil plane characteristic and filtering. LD: Laser Diode, CL: Collimator, HM: Half Mirror, OBJ: Objective Lens, SIL: solid immersion lens, PD: Photo Detector.

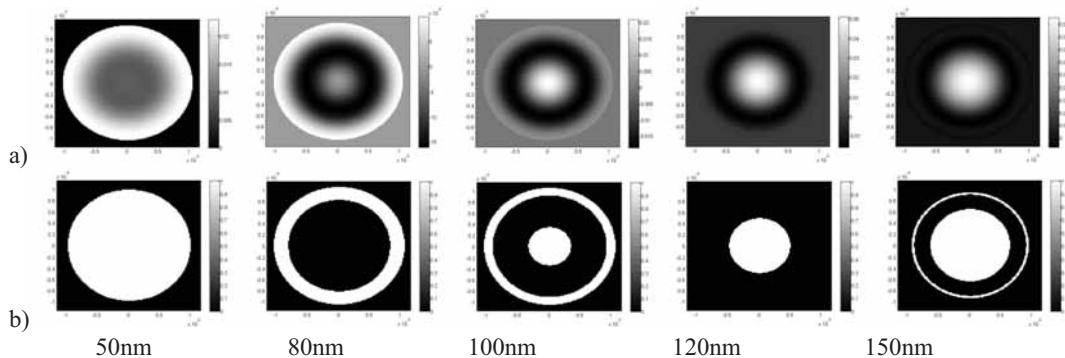


Fig 2. (a) Irradiance difference distribution, 650nm: Ix-Ia. (b) Irradiance difference distribution having the value above/ below zero is white/black.

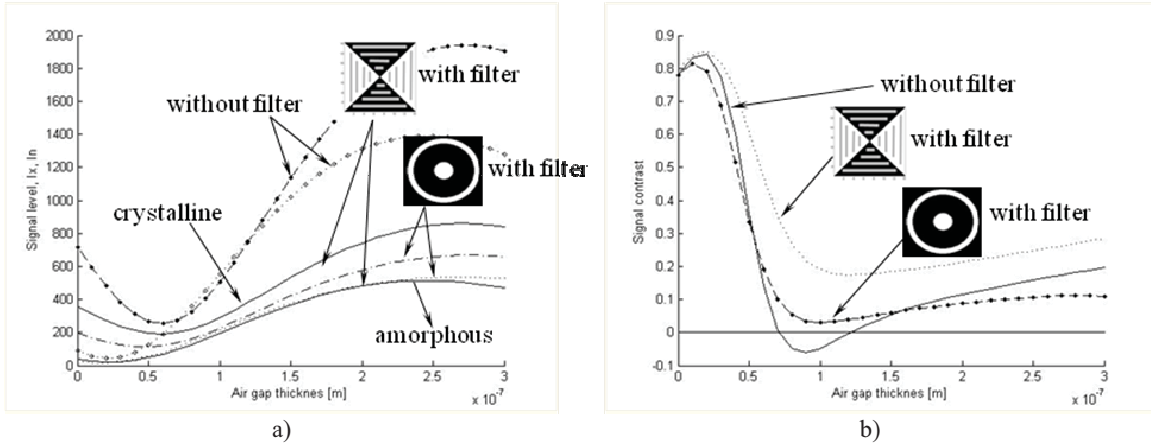


Fig. 3. NA = 1.1, $\lambda = 650\text{nm}$. Signal level (a) and signal contrast and filter pattern used in the calculation (b) on the air gap thickness between the solid immersion lens and the recording medium using filter.

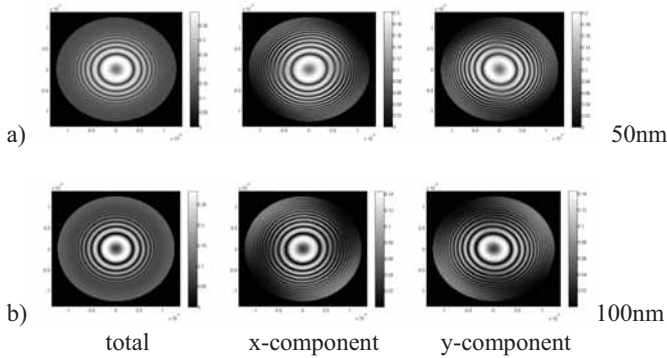


Fig. 4. Total / x component / y component irradiance distribution of pupil plane at 405nm and NA = 1.45.

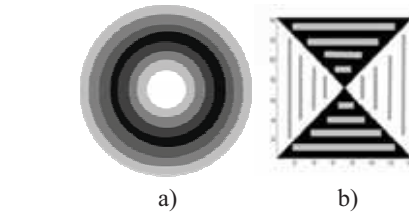


Fig. 5. The filter with multi - transmittance (a), The filter using polarization variation (b)

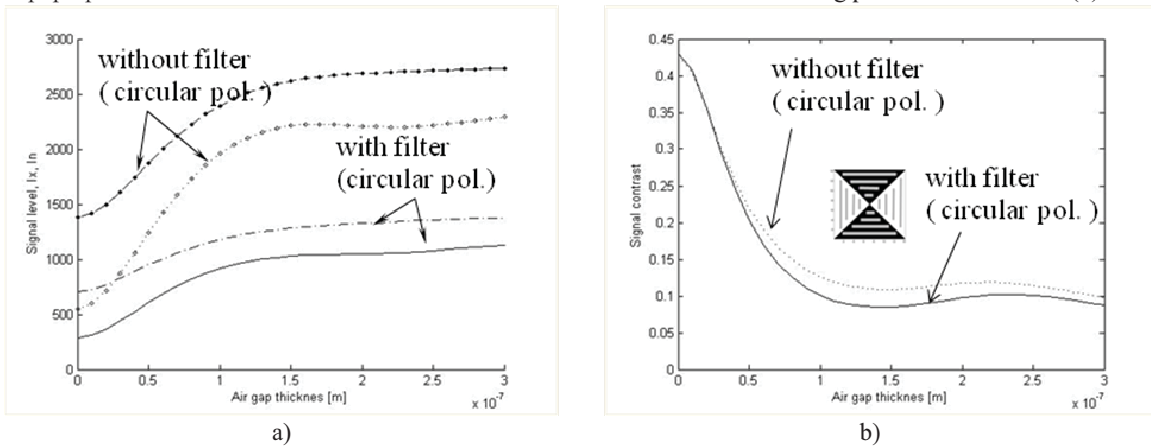


Fig. 6. NA = 1.45, $\lambda = 405\text{nm}$ Signal level (a) and signal contrast and filter pattern used in the calculation (b) on the air gap thickness between the solid immersion lens and the recording medium using filter.

Aberration Compensation in Near Field Optics for Multi-layer Data Storage

Kwanhyung Kim¹, Kitak Won¹, Hyeongryeol Park¹, Narak Choi¹, Sam-Nyol Hong², Jeongkyo Seo²,
Kwang-Sup Soh¹ and Jaisoon Kim¹

¹Department of Physics and Astronomy, Seoul National University
San 56-1 Sillim-Dong, Kwanak-Gu, Seoul, 151-747, Korea
Phone/Fax +82-2-873-7372/+82-2-884-3002, Email : jskim@phya.snu.ac.kr
²Digital Storage Research Laboratory, LG Electronics
360-5, Yatap-Dong, Bundang-Gu, Sungnam-Si, Kyunggi-Do 463-828, Korea
Phone /Fax +82-31-789-4213/ +82-31-789-4205

1. Introduction

In Optical data storage, the devices have been developed to obtain high data capacity. Among the numerous methods, near-field recording (NFR) becomes a matter of interest. By using solid immersion lens (SIL) in NFR, the optical system can achieve high numerical aperture (NA) value and, therefore, reduce the spot size which is important factor to determine the data capacity¹⁾. Multi-layer structure of a media is the one of the various methods to obtain high data capacity. The multi-layer structure of a media is used in present high capacity media such as DVD and BD. The multi-layer structure in NFR system using SIL is considered in this study.

To access the data at multiple layers, there are two matters that should be considered. One is the change of focus depth position among the recording layers and the other is compensation of proper spherical aberration (SA) induced by recording medium according to the previous change²⁾⁻⁴⁾. In far-field system, recording layer can be controlled by adjusting objective lens position and the proper amount of SA can be compensated by moving collimator lens or applying some correction wave plate as like liquid crystal plate (LCP). However, in near-field SIL system, not even the thin air gap between SIL and top of media but also the spacer thickness between objective lens and top of SIL cannot be varied easily because of its high sensitivity in on and off axial fluctuation. Thus, it is necessary to find suitable methods that work for moving the best focused beam spot among the recording layers and compensating appropriate SA according to the corresponding layer, simultaneously.

In previous research, there is a study for using LCP compensator in NFR multi-layer system with NA 1.45 and 405 nm wave-length⁵⁾. In this paper, SA compensation using LCP with system NA value 1.7 including newly suggested optimum sectioning design is investigated and two different types of afocal compensator lens systems are also studied. Lastly, as one of the best optimized compact and simple design, all-in-one collimator and objective combined system design is introduced.

2. Changing Recording Layer and Compensating SA

In this study, two main ideas of different approach are investigated in detail for changing the recording layer and compensating SA simultaneously at an appropriate near field SIL system. One is using LCP for cancelling proper optical path difference error on ray trajectory. The other is using compensator lens system such as Keplerian Telescope Type, Galilean Telescope Type⁶⁾ and compact combined all-in-one system.

The media has 3-layer structure except a few micrometer thickness cover layer on top of it and its index of refraction is 1.75 at 405 nm wave-length. Best focus is formed inside 3 μ m from the top surface of the media. The first and the third layer are located at $\pm 1 \mu$ m from the position of best focus (Fig. 1).

Objective part consists of an objective lens (OL) and 0.5 mm radius LaSF35 Hemi-SIL which makes 1.7 effective NA. The entrance pupil diameter of the OL is 2.5mm and the field angle is also considered up to 0.2 degree. Due to it arouse only insignificant amount of wavefront aberration, detail analysis of minute vectorial diffraction phenomena and gap induced reflection effect occurring from the infinitesimally thin air gap between bottom of Hemi-SIL and top of media is ignored in this paper. The boundary value of root mean square (RMS) wave-front error that can sustain system performance in the aberration consideration is decided as 30 m λ .

2.1 Liquid Crystal Plate (LCP) and defocus System

In multi-layer structure, when the NA value is increased, SA introduced by changing recording layer is also increased²⁾. So, it is difficult to use only LCP in order to compensate the SA with system NA value 1.7 which is higher than previous research with system NA value 1.45. By changing incident beam from parallel beam to converging or diverging incident beam, LCP can compensate the wave-front error³⁾. Since the LCP cannot change

optical path continuously, the wave-front error also cannot be compensated perfectly. Thus, it is necessary to design the LCP to reduce the residual wave-front error as small as possible (Fig. 3).

Compensation ability of LCP determined by manufacturing factors based on material and structure characteristics is limited as maximum 1 wave-length optical path difference (OPD) in this paper. There are more restrictions in the specifications of LCP and it can be manufactured with free shaped areas on it that have electric circuit boundary. Proper stepped OPD values for each bounded area are obtained by applying corresponding voltages to those circuits that bound specific patterned area. And so, there exist stepped gap of OPD between adjacent regions and the width of that circuit is $3\mu\text{m}$. Since the width of that patterned circuit on LCP is $3\mu\text{m}$ and the regions that are corresponding to that area cannot change the optical path (Fig. 2).

Simulation result shows that, if the width of electric circuit regions can be neglected, increasing the number of bounded compensation regions is more effective for reducing wave-front error and it also shows that LCP with at least six separated compensation regions is good enough to reach the $30\text{ m}\lambda$ RMS wave-front error boundary condition. However, there exist electric circuit regions fairly and increase the number of bounded region results in widening the area of electrode region which cannot contribute to the compensation. Since the shadow effect of electric circuit regions are so strong relative to the detail fitting to the aberration envelope by finely dividing of compensation regions, there exists an optimized number of dividing compensation regions to get the best result.

In this study, using four fold divided compensation regions shows the best performance at $66.4\text{ m}\lambda$ RMS wave-front error (Fig. 4).

2.2 Compensator Lens System.

Keplerian and Galilean telescope type are considered in order to compensate SA^{2), 6)}. Keplerian telescope type compensator consists of two aspheric positive lenses. The entire length of the system is constant because it is designed that the compensator can balance the aberration by moving the second lens conjugated with first compensator lens (Fig. 5). The layout of Galilean telescope type compensator composed of two lenses is shown in Figure 6. Keplerian type achieves good performance under the $30\text{ m}\lambda$ RMS wave-front error. The compensating result of RMS wave-front error is $16.6\text{ m}\lambda$ at the first layer, $7.7\text{ m}\lambda$ at the second layer and $8.9\text{ m}\lambda$ at the third layer.

The Keplerian and Galilean type systems are composed of a total of 5 lenses including the collimator. A system which includes many lenses has various disadvantages such as cost and difficulty of fabrication. Therefore Compact Combined (Collimator + Objective) System is considered in order to make lens system compact. An attempt was made to reduce the number of lenses and surprisingly it was possible to reduce the number of lenses to three in an NA 1.7 system (Fig. 7).

This result indicates that designing a three lenses system may be possible in other systems with different limitation conditions. The best focus is formed inside $9\mu\text{m}$ from the top surface of the media with reflective index 1.9 and the reflective index of SIL is about 2.4 at 405 nm wave-length. The compensation is possible up to $2\mu\text{m}$.

3. Summary

In this study, three types of compensating method are investigated. Keplerian and Galilean telescope type compensation system reveal enough optical performance for the multi-layer recording. Lastly, compact combined all-in-one system is suggested as an alternative design which can nicely abstract all the advantages of telescope type compensation systems.

4. References

- [1] Narak Choi, Seongbo Shim, Tom D. Milster, and Jaisoon Kim "Optical Design for the Optimum Solid Immersion Lens with High Numerical Aperture and Large Tolerance" *JJAP*. Vol. **46**(6B) pp. 3724-3728 (2007)
- [2] Tom D. Milster, Robert S. Upton and Hui Luo "Objective lens design for multiple-layer optical data storage" *opt.eng* **38**(2) 295-301 (Feb. 1999)
- [3] V.N. Mahajan Optical Imaging and Aberrations pp. 247-364
- [4] Edwin P. Walker, Jacques "Spherical aberration correction for two-photon recorded monolithic multilayer optical data storage" *Optical Data Storage* 154-156 (April 2001)
- [5] Ji Yeon Lee, Sam Nyol Hong, Yun Sup Shin, Kyun Taek Lee, Kwan Woo Park, Jeong Kyo Seo, In ho Choi, Eui Seok Ko, Byeong Hoon Min "Applying Liquid Crystal Panel for SA compensation in NRF multi-layer System", 2007 International Symposium on Optical Memory, Tu-F-03
- [6] Jaisoon Kim, Tomas D. Milster "Design aspects of waveguide hybrid advance MEMS (WHAM)" *Optical Data Storage* 447-456 (January 2002)

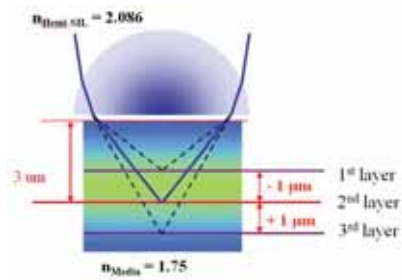


Fig. 1. The multi-layer structure of the media

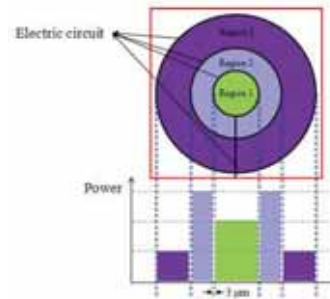


Fig. 2. The compensating and electrode regions of LCP

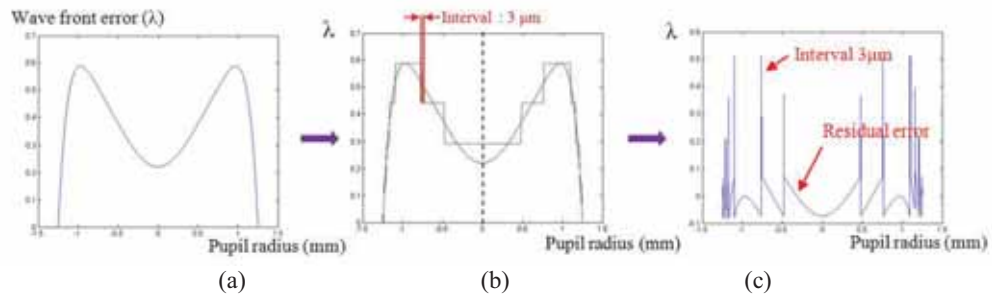


Fig. 3. LCP compensation (a) Before compensation (b) LCP design for compensation (c) After compensation

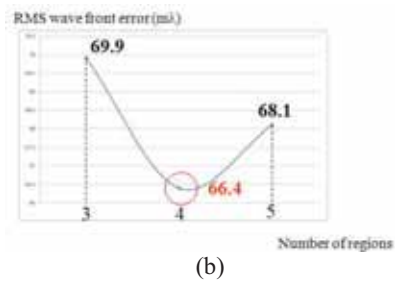
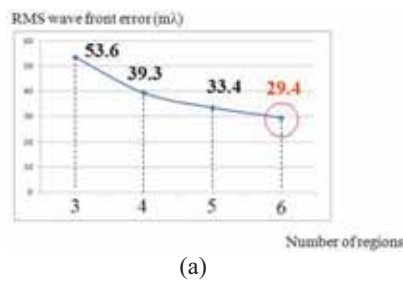


Fig. 4. The compensating results as increasing regions (a) Ignoring electric circuit regions (b) Considering electric circuit regions

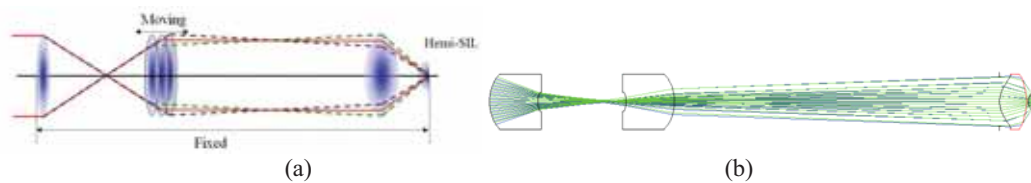


Fig. 5. The Keplerina Telescope type (a) The layout (b) The design

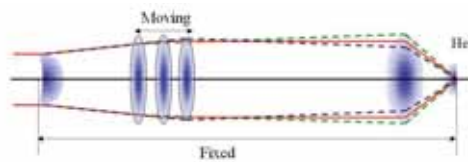


Fig. 6. The layout of Galilean telescope type

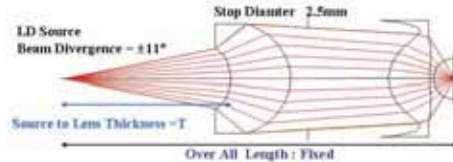


Fig. 7. The layout of compact combined System

GaP Solid Immersion Lens Based on Diffraction

Youngsik Kim, Jun Zhang and Tom D. Milster

College of Optical Sciences, University of Arizona, Tucson, AZ, 85721, USA

yskim@optics.arizona.edu

Abstract: Hybrid solid immersion lens system(SIL) with a spherical lens attached micro gallium phosphide SIL and a diffractive optical element, and its aberration correction mechanisms are discussed.

Keywords: Near-Field Recording, Super-Resolution, New or Related Technologies

1.Introduction

Various techniques involving near field optics have been introduced for resolution enhancement in fields such as optical data storage, microscopy and lithography. Solid immersion lens(SIL) system has attracted much attention because the diffraction-limited spot size is reduced by the factor of refractive index of the SIL, and thus produces a high-performance with a high numerical aperture(NA).[1][2][3] By using highly refractive index materials like GaP with $n(650\text{nm})=3.3$ for the SIL, a high-performance SIL system can be obtained.[4] However, tolerances associated with the geometrical aberrations of the high-performance SIL system must be considered. In general, a SIL is placed in an optical path between a focusing objective lens and the data and/or imaging layer, like which is shown in Fig. 1. In this paper, diffraction based hybrid SIL system with a focusing objective lens using a diffractive optical element (DOE) to compensate for an aberration induced from spherical lens and its chromatic aberration is investigated. We assume that the laser diode wavelength is nominally 650nm with the range of 640nm to 660nm.

2.Diffraction based hybrid SIL design

To apply a micro-sized SIL to the system, it is necessary to mount it on the flat surface of a concentric spherical lens. If the epoxy which has the same refractive index as a support lens is used, simple hemispherical lens is sufficient to construct an aberration free SIL system, and incident converging beam is required.[5][6] However if a plane wave is used for illumination, the aberration induced from a spherical lens can be corrected by using a DOE. Fig. 2 shows a hemisphere SIL system with simple spherical lens and a DOE that is used to correct sphere-induced aberrations. Spherical lens induced OPD aberration curve is positive and shown in Fig. 3 (a), whereas OPD aberration curve of a DOE to compensate for it is negative and shown in Fig. 3 (b). We design hybrid SIL system with a 650nm light, 10th even aspherical

phase DOE, 2mm radius LaSFN9, 1.5 refractive index epoxy, and 114um radius GaP micro-SIL. The NA of SIL system is 1.7. Fig. 4 shows a DOE phase profile as a function of radius.

3. Optical performances and tolerance analysis

The optical performance of the designed hybrid SIL system is good enough to be applied to fields such as optical data storage, microscopy and lithography. In the center of the field of view, the wavefront aberration is below 2 mλ RMS at 650nm,. DOE has complementary dispersion characteristics to that of optical glasses and plastics. In the visible spectrum, DOE has an Abbe number of -3.5. Because, as the laser wavelength changes, spherical lens has the positive focus shift, whereas a DOE shows the negative focus shift, the chromatic aberration that has been critical issues in the high NA system can be compensated with the DOE.[7] The smallest zone spacing on the DOE is about 10um, which is well within the range of smooth-zone mastering techniques that produce better than 90% diffraction efficiency.

The independent tolerance analysis is performed. The decenter tolerance is the most sensitive factor of errors. However, since the misaligned range can be controlled using an improved centering technique, we expect that the SIL system would be assembled within tolerance margin. By using the Monte Carlo tolerance analysis, the optical performance on synthetic error conditions can be evaluated. We can estimate the large tolerance to make the SIL system more useful.

4. Conclusions

We designed diffraction based hybrid SIL system using a spherical lens which micro GaP SIL is attached and a DOE, and obtained a numerical aperture of 1.7 and good tolerance . A DOE can be used to correct the spherical aberration as well as chromatic aberration due to a spherical lens. Because the numerical aperture of DOE is relatively low, the minimum zone spacing is about 10um, thus its fabrication is relatively easy. Hopefully, we will show a DOE fabrication and its application testing results at the conference.

References

- [1] S. M. Mansfield and G.S. Kino, Appl. Phys. Lett. **57**, 2615(1990)
- [2] C. D. Poweleit, A. Gunther, S. Goodnick, and J. Menendex, Appl. Phys. Lett. **73**, 2275(1998)
- [3] R. Brunner, M. Burkhardt, A. Pesch, and O. Sandfuchs, J. Opt. Soc. Am. A, **21**, 1186(2004)
- [4] Qiang Wu, G. D. Feke, R. D. Grober, and L. P. Ghislain, Appl. Phys. Lett. **75**, 4064(1999)
- [5] M. Lang, T. D. Milster, T. Minamitani, G. Borek. and Brown, Jpn. J. Appl. Phys. **44**, 3385(2005)
- [6] M. Lang, T. D. Milster, S. K. Park, B. McCarthy, and D. Sarid, Opt. Eng. **45**, 103002(2006)
- [7] T. D. Milster, Jpn. J. Appl. Phys. **38**, 1777(1999)

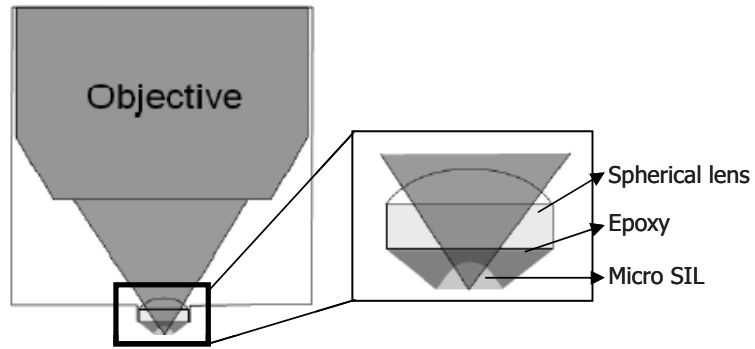


Fig. 1 Two-step SIL system with simple spherical lens and a DOE that is used to correct sphere-induced aberrations

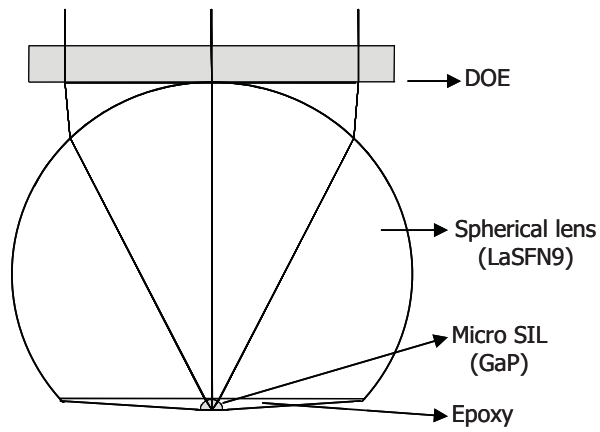


Fig. 2 Hybrid SIL system with a spherical lens which micro SIL is attached, and a DOE

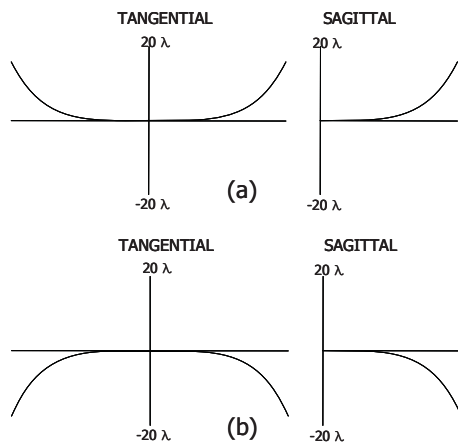


Fig. 3 Optical path length aberration curves of spherical lens (a) and DOE (b)

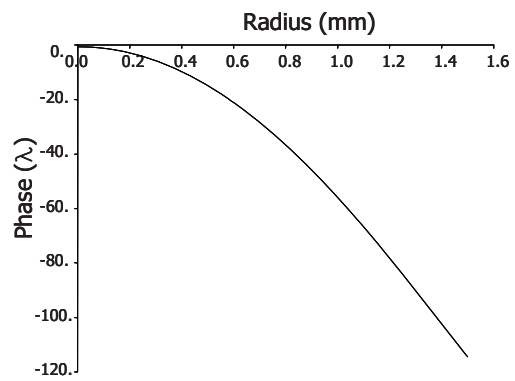


Fig. 4 DOE phase as a function of radius

Assembly and Evaluation of SIL Optical Head for High NA Cover-Layer Incident Near Field Recording

Yong-Joong Yoon^a, Taeseob Kim^a, Cheol-Ki Min^a, Wan-Chin Kim^a, No-Cheol Park^{*a},
Young-Pil Park^a, Tao Hong^b, Kyunggeun Lee^b

^aCenter for Information Storage Device, Yonsei University, 134 Shinchon-dong Seodaemun-ku,
Seoul 120-749, Korea

Phone: +82-2-2123-4677, Fax: +82-2-365-8460

E-mail: pnch@yonsei.ac.kr

^bDigital Media R&D Center, SAMSUNG ELECTRONICS CO., LTD, Suwon, 442-742, Korea

ABSTRACT

For increasing a data recording density and reducing a spherical aberration in cover layer incident near field recording (NFR), a high refractive index cover layer is needed and the assembly and evaluation technology of a solid immersion lens (SIL) optical head for a high numerical aperture (NA) cover layer incident NFR is also required. In order to assemble and evaluate the SIL optical head for the high NA cover layer incident NFR, a modified Twyman-Green interferometer is developed. In this paper, we show the assembly and evaluation results of the SIL optical head with the high refractive index cover layer disc and compare them with simulation ones. Through this research we can improve the effective NA as 1.84 which is the highest NA that has been reported and we can also increase the data recording density per layer such as the surface recording NFR in cover layer incident NFR.

Keywords: cover layer incident near field recording, solid immersion lens, Twyman-Green interferometer

1. INTRODUCTION

As one of the next generation optical storage devices, a NFR technology has been developed by many researchers. Recently, for the high data recording capacity, the cover layer incident NFR with multiple recording layers has been reported [1]. Comparing with the surface recording NFR, the cover layer incident recording NFR has the limitation of increasing the effective NA of the SIL optical head due to the limited refractive index of the cover layer materials. That means the data recording capacity per layer of the cover layer incident recording NFR is lower than that of the surface recording NFR. In order to improve the data recording capacity per layer with the high NA in the cover layer incident NFR, a high refractive index cover layer is needed. In addition to the development of a high refractive index cover layer material, the assembly and evaluation technology of the SIL optical head for the high NA cover layer incident NFR should be developed. Thus assembly setup based on Twyman-Green interferometer is developed to assemble and evaluate the high effective NA SIL optical head with the high refractive index cover layer disc. In this paper, we represent the assembly and evaluation results of the SIL optical head whose effective NA is higher than 1.8 for the cover layer incident NFR and compare the results with simulation ones for feasibility.

2. SIL OPTICAL HEAD FOR COVER LAYER INCIDENT NFR

The SIL optical head for the cover layer incident NFR should be designed with considering the spherical aberration introduced by the cover layer [2] as shown in Fig. 1. As shown in Fig. 1, to achieve the high effective NA and to reduce the spherical aberration introduced by the cover layer, it is better to use the cover layer whose refractive index is as high as that of the SIL. However, in practice, it is impossible to choose the cover layer material that has high refractive index as the SIL. Thus, in order to obtain the effective NA higher than 1.8, we choose the refractive index of the cover layer as 1.9 which is developed for the feasibility study on the high NA cover layer incident NFR by Samsung electronics. Figure 2 is the schematic diagram of the designed SIL optical head for the high NA cover layer incident NFR. In this design, the effective NA is 1.84 with the objective lens NA of 0.77 and the refractive index of SIL is 2.3837. The specifications of

the designed SIL optical head are summarized in Table 1. Figure 3 (a) and (b) show the reflected intensity distributions at the exit pupil for E_x and E_y , respectively. Figure 3 (c) depicts the interferogram of the SIL optical head in the case of contact between the bottom of the SIL and the disc. When we perform the simulations, the cover layer thickness is set as 910nm and the spherical aberration introduced by the cover layer is compensated. We also consider the various coating layers as well as the cover layer for the accurate simulation. Because of the interference between multiple reflections inside the cover and other coating layers, the concentric rings are observed as shown in Fig. 3 (a) and (c).

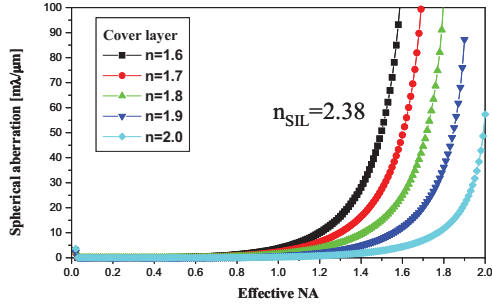


Fig. 1 Spherical aberration as a function of NA for the different refractive indices for the cover layer

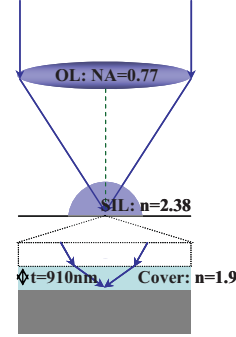


Fig. 2 Schematic diagram of SIL optical head for the high NA cover layer incident NFR

Table 1. Specifications of SIL optical head

Effective NA		1.84
SIL	Diameter	1.0mm
	Index	2.38
	Cone angle	70deg.
Wavelength		405nm
Effective focal length		1.33m (in air)
Magnification		0
Cover layer incident type		

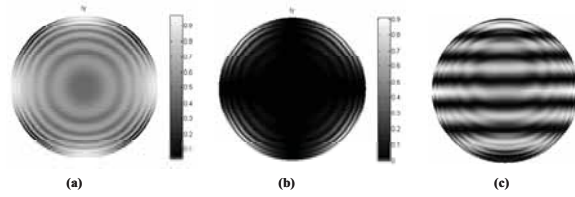


Fig. 3 Simulation results of intensity distribution for E_x (a), E_y (b) and interferogram (c) with disc contact

3. ASSEMBLY AND EVALUATION

In order to assemble the SIL optical head for obtaining good quality, it is essential to adjust the distance between the SIL and the objective lens, shown in Fig. 4 (a) and (b). Because, even though the decenter and tilt tolerance between the SIL and the objective lens can be provided by the holder, shown in Fig 4 (c), the distance tolerance between the SIL and the objective lens is so tight that it can not be met the tolerance with just controlling the mechanical tolerance of lenses and holder [3]. Thus, interferometer is needed for the precision assembly of the SIL optical head with measuring the aberrations. Figure 5 shows the assembly setup which is based on the Twyman-Green interferometer. We assemble the SIL optical head and measure its aberrations with this modified interferometer while the disc, shown in Fig 4 (d), whose cover layer thickness is 910nm is contacted with the bottom surface of the SIL. Figure 6 is the interferogram with disc contact at the exit pupil. As similar to the simulation results, the concentric rings are observed because of the multiple beam interference as previously mentioned. The measured aberrations are summarized in Table 2. When we measure the total aberration, the defocus aberration is subtracted because this can be compensated by the zoom optics in NFR system. The measured total aberration is about $26m\lambda_{rms}$ which is less than Marechal criterion of $70 m\lambda_{rms}$ for the good image quality.

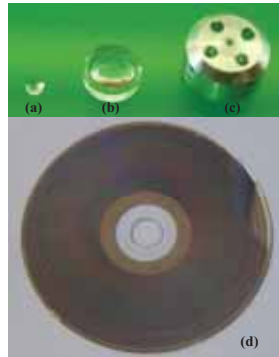


Fig. 4 SIL optical head components: (a) SIL, (b) OL, (c) holder, and (d) high refractive index cover layer disc

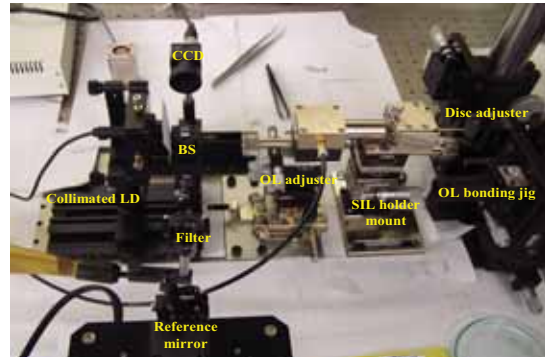


Fig. 5 Modified interferometer for SIL assembly

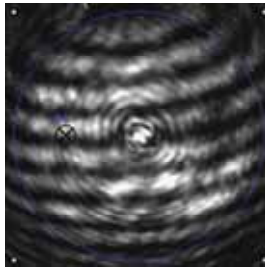


Fig. 6 Experiment results of interferogram with disc contact

Table 2 Measured aberrations

Aberrations	Value [λ]
Total	0.026
Defocus	0.0403
X Astigmatism	0.0032
Y Astigmatism	0.0257
X Coma	-0.0035
X Coma	0.0079
Spherical	0.022

4. CONCLUSIONS

In this study, we presented the modified Twyman-Green interferometer to assemble and evaluate the SIL optical head for the high effective NA cover layer incident NFR. We also optimized the high refractive index and thickness of cover layer through the geometrical optics simulation. By using this assembly setup and the high refractive index cover layer disc, the SIL optical head, which is capable of applying to the high effective NA cover layer incident NFR, was developed. This SIL optical head has good optical performance and its total aberration is lower than Marechal criterion. Thus, the cover layer incident NFR can have the high effective NA (>1.8). As consequence, the data recording density per layer can be increased such as the surface recording NFR in the cover layer incident NFR.

REFERENCES

- [1] Jack M. A. van den Eerenbeemd, Dominique M. Bruls, Coen A. Verschuren, Bin Yin, and Ferry Zijp, "Towards a Multi-Layer Near-Field Recording System: Dual-Layer Recording Results," *Jpn. J. Appl. Phys.*, 46, 3894-3897 (2007)
- [2] Sjoerd Stallinga, "compact description of substrate-related aberrations in high numerical-aperture optical disk readout," *Appl. Opt.*, 44, 849-858 (2005)
- [3] Y. J. Yoon, H. Choi, W. C. Kim, T. Song, N. C. Park, "Thickness tolerance compensation of SIL first surface near-field recording with replicated lens on SIL," *Microsyst Technol.*, 13, 1289-1295

Improvement of Protection Process using Observer for SIL Based Near-Field Recording

Hyunwoo Hwnag^a, Sang-Hoon Kim^a, Joong-Gon Kim^a, Tae-Wook Kwon^a, Hyunseok Yang^{*b},
No-Cheol Park^a, Young-Pil Park^b, Jeong Kyo Seo^c, In Ho Choi^c and Byeong Hoon Min^c

^aCenter for Information Storage Devise, Yonsei University 134 Shinchon-Dong,
Seodaemun-gu, Seoul, 120-749

^bDept. of Mechanical Engineering, Yonsei University 134 Shinchon-Dong,
Seodaemun-gu, Seoul, 120-749, Korea

Phone: +82-2-2123-2824, Fax: +82-2-365-8460 E-mail: hsyang@yonsei.ac.kr

Digital Storage Research Laboratory, LG Electronics, 360-5, Yatap-Dong,
Bundang-Gu, Sungnam-Si, Kyunggi-Do 463-828, Korea

ABSTRACT

In the NFR system, there always exists possibility of collision between SIL and media by dust, scratches on the media, and external shock because of its extremely small gap distance. The kinetic energy which concerns damage from shock is in direct proportion to the square of velocity. And the phase of velocity is faster than the phase of displacement. So, it is effective to predict a collision with velocity information. The velocity of the actuator in NFR system should be estimated by an observer without using a velocity sensor. In this paper, we propose an improved protection process with a mode switching servo method using a Luenberger observer. The gap distance state can be estimated earlier by detecting the velocity state yielded by external shock. Through simulations and experiments, we confirm that the protection process based on velocity and gap distance is more powerful than the protection process based only on the gap distance.

Keywords: Near field recording system, SIL, Protection process, Luenberger observer

1. INTRODUCTION

Solid immersion lens (SIL) based near-field recording system is the next generation optical data storage with over 100 GB on a single layer. Development of near-field recording system is almost completed with precise and advanced technology. However, reliability in user's environments should be guaranteed in order to be commercialized.

Control of the gap distance between the SIL and the media is very important. There are many researches for the control of gap distance [1][2]. But, because of its extremely small distance, there always exists possibility of collision by dust, scratches on the media, and external shock. The NFR system is very weak even to small amount of external shock because of its extremely small gap between the SIL and the disk. To solve this problem, we represented a NFR system that includes a safety mode and a protector [3].

In this paper, we propose an improved protection process with a mode switching servo method by using a Luenberger observer. Generally, the phase of velocity is faster than the phase of displacement. Also, the kinetic energy which concerns damage from shock is in direct proportion to the square of velocity. Hence, avoiding collision with velocity information is more effective than with displacement information. However, since a common NFR system cannot directly sense the velocity of the actuator, a Luenberger observer is designed to estimate the velocity. The change of the gap distance can be estimated in advance by detecting velocity variation which is occurred by external shock. This protection process based on both velocity and gap distance is more powerful than the protection process that depends only on gap distance.

2. PROTECTION PROCESS

When we design a controller for gap and tracking servo, first of all we should identify the transfer function of the actuator. The transfer function of the system in focus direction is obtained as equation (1) with displacement output. To

design an observer, we should convert the transfer function into a state space model. The state space model has two state variables which are coupled with displacement and velocity. The block diagram of the servo system that includes the observer is described in Fig. 1. The observer uses the gap error signal and the control input from the real plant to estimate the states of the plant.

The observer estimates all the states of the observable system using a control input and an output. It compensates the error of estimation with information of the difference between the estimated output and the real output. This process can operate in real time [4]. The observer is designed in discrete domain with 100 KHz sampling frequency, and the observer gain is determined to place the observer's pole in z-plane zero for the fastest compensation. The dynamics of the observer and the observer gain is shown in equation (2). The state x_j is the estimated velocity state.

$$\frac{X}{V} = \frac{18540000}{s^2 + 62.92s + 72430} (\mu m/V) \quad (1)$$

$$\begin{aligned} \begin{bmatrix} \hat{x}_1(k+1) \\ \hat{x}_2(k+1) \end{bmatrix} &= \begin{bmatrix} 0.9994 & -0.7241 \\ 9.997 \times 10^6 & 1 \end{bmatrix} \begin{bmatrix} \hat{x}_1(k) \\ \hat{x}_2(k) \end{bmatrix} \\ &+ \begin{bmatrix} 9.997 \times 10^6 \\ 4.999 \times 10^{11} \end{bmatrix} u(k) \\ &+ \begin{bmatrix} 0.0054 \\ 0 \end{bmatrix} [y(k) - \hat{y}(k)] \\ \hat{y}(k) &= \begin{bmatrix} 0 & 1.854 \times 10^7 \end{bmatrix} \begin{bmatrix} \hat{x}_1(k) \\ \hat{x}_2(k) \end{bmatrix} \end{aligned} \quad (2)$$

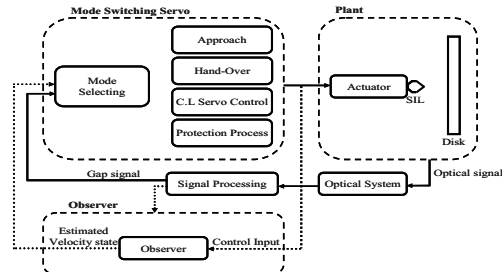


Fig. 1 Gap servo with shock detected using observer

When the gap distance is much lower than the final air gap distance, or when the velocity of the actuator changes rapidly, the protection process moves the actuator to the original place to prevent collision between SIL and disk.

3. SIMULATION AND EXPERIMENT RESULTS

3.1 Simulation results

The simulation is executed with 6 KHz cutoff frequency controller and a sine wave disturbance with 10 micrometer amplitude. Through the simulation results of the observer, it is proved that the output of the observer and the output of the plant are almost the same. An impulse signal is added to the disturbance to simulate the unusual situation caused by external shock. In these situations, gap signal that was sensed changed rapidly. Thus, modeling as an impulse disturbance is a reasonable analysis. The estimated velocity state of the observer is added to the reference of the protection process. It is used as information with the gap distance to detect the dangerous state. When the estimated velocity state reaches the limit velocity that corresponds to limit distance, the improved protection process moves the actuator to the initial position to avoid collision. The limit velocity is obtained through simulations. When the state of the actuator becomes unstable, the protection process moves the actuator to the initial position to avoid collision. Then, the pull-in process takes the actuator back to the closed loop gap servo. This process will extend the durability, and will enhance the robustness of the system. The gap distance and the estimated velocity state during the protection process that depends only on the gap distance is shown in Fig. 2(a), and those based on both velocity and gap distance is shown in Fig. 2(b).

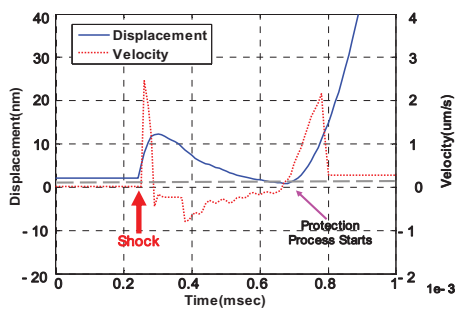


Fig. 2 (a)

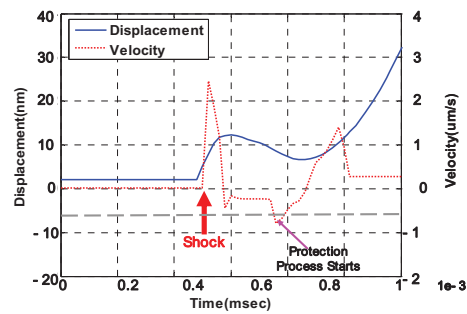


Fig. 2 (b)

Fig. 2 (a) The protection process simulation depends only on the gap distance
 (b) The protection process simulation based on both the velocity and the gap distance

In this simulation, we confirm that given signal and estimated signal is almost same. And the protection process based on both velocity and gap distance is faster and more stable than the protection process that depends only on gap distance.

3.2 Experiment Results

The estimated velocity state of the observer is added to the reference of the protection process. It is used as information with the gap distance to detect the dangerous state. There are some problems in these experiments. If test bed is directly damaged by shock, the NFR system is broken. To protect NFR system, we use rubber damper in bottom of test bed. So, when the change of disturbance by shock is biggest, there is shown the rough shaking of the actuator with delay. The gap distance and the estimated velocity state during the protection process that depends only on the gap distance is shown in Fig. 3(a), and those based on both velocity and gap distance is shown in Fig. 3(b). The reference distance is 20nm, the limit distance is 10nm, the limit velocity is $111\mu\text{m/s}$, and the magnitude of the applied shock is 1G. In these experimental results, the real output from the system and the estimated gap distance are exactly the same. The estimated velocity state is faster than displacement state. Above all, the position of the limit velocity that corresponds to limit distance is located in front of the limit distance in time domain. Hence, the protection process based on both velocity and gap distance is faster and more stable than the protection process that depends only on gap distance. Therefore, the performance of the NFR system with an observer could be considered to be better than without the observer with respect to external shock.

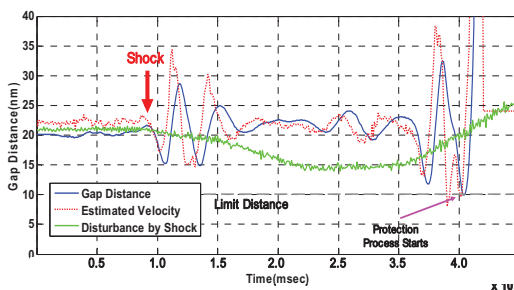


Fig. 3 (a)

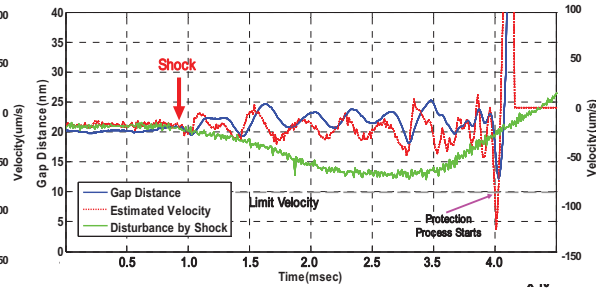


Fig. 3 (b)

Fig. 3 (a) The protection process depends only on the gap distance
 (b) The protection process based on both the velocity and the gap distance

4. CONCLUSION

In the general environment, dusts, scratches on the media, and external shocks may cause failure of the servo and may also degrade the performance of the NFR system. In this paper, we proposed an improved protection process for the SIL based NFR system to solve this problem by using a Luenberger observer. The velocity state is estimated with the observer. A reliability of the observer is proved with simulation and experiment results. The performance of the protection process for the unpredicted situation is improved, and the possibility of collision is lessened since the change of the estimated velocity state is faster than the change of the distance.

REFERENCES

- [1] Tsutomu Ishimoto, K. Saito, M. Shinoda, T. Kondo, A. Nakaoki and M. Yamamoto, "Gap servo system for a biaxial device using an optical gap signal in a near field readout system," Jpn. J. Appl. Phys. Vol. 42 (2003) pp. 2719-2724.
- [2] Ju-Il LEE, Michael VAN DER AA, Coen VENSCHUREN, Ferry ZIJP and Martin VAN DER MARK, "Development of an air gap servo system for high data transfer rate near field optical recording," Jpn. J. Appl. Phys. Vol. 44 (2005) pp. 3423-3426.
- [3] Yong-Joong Yoon, Sang-Hoon Kim, Woong Seol, Joong-Gon Kim, No-Cheol Park and Hyunseok Yang, "Analysis on Effect of External Shock in Near-Field Recording System", JJAP, Vol. 46, No. 6B. 2007. pp. 3997-4002
- [4] Katsuhiko Ogata, Modern Control Engineering (Prentice Hall, 1970), Chapter 12.

Improved Air Gap Controller for SIL based Near-Field Recording Servo System

Joong-Gon Kim^a, Min-Seok Kang^a, Won-Ho Shin^a, No-Cheol Park^{*a},
Hyun-Seok Yang^b, and Young-Pil Park^b

^aCenter for Information Storage Device, Yonsei University 134 Shinchon-Dong, Seodaemun-gu,
Seoul, 120-749 Korea

Phone: +82-2-2123-4677, Fax: +82-2-365-8460 E-mail: pnch@yonsei.ac.kr

^bDept. of Mechanical Engineering, Yonsei University 134 Shinchon-Dong, Seodaemun-gu, Seoul,
120-749 Korea

ABSTRACT

An improved gap servo controller for solid immersion lens (SIL) based near-field recording (NFR) system is suggested to improve robustness and performance. To improve control performance on the dynamic disturbances of the NFR system, the internal model principle (IMP), which is one of the advanced control methods rejecting periodic disturbance at the specific frequency, is implemented to the conventional NFR servo system. Furthermore, to maintain extremely small air gap avoiding collision between the SIL and the media when the external shock is applied, the air gap servo system with the dead-zone controller is applied. Experimental results show that the residual gap error is reduced from 0.7951nm to 0.5796nm with IMP based controller, and anti-shock control performance is improved by 88% with dead-zone controller.

Keywords: gap error signal, internal modeling principle, dead-zone control, anti-shock

1. INTRODUCTION

In the last decade, the SIL based NFR technology has been studied actively resolving its critical issues on systemization. The near-field air gap servo is the one of essential technologies to guarantee system reliability. In general, in order to increase the near field coupling efficiency, it requires maintaining constant air gap distance between the SIL and the disk less than $\lambda/20$ without collision. The near-field air gap control is highly susceptible to dynamic disturbances such as disk vibration and external shock due to its extremely small air gap [1]. Therefore, the SIL based NFR servo system should be able to reject aforementioned dynamic disturbances. In this paper, we introduce the improved air gap controller using the internal model principle and the dead-zone controller, which have superior dynamic disturbance rejection performance to that of conventional air gap controllers which are generally composed of the lead-lag compensator and the PID controller.

2. DESIGN OF ADVANCED CONTROLLER

Figure 1 shows the air gap servo system for the SIL based NFR system which uses a 405 nm blue laser diode, gap sensing photo diode, SIL assembly, voice coil motor actuator, polycarbonate disk and digital signal processor. Our conventional air gap servo controller has the cut-off frequency at 7.02 KHz with phase margin 38.4 degree, gain margin 8.19 dB and DC gain over 80 dB. The precedent air gap controller used the lead-lag compensator and PID controller with the feedback NFR servo system. However, the control performance of precedent air gap controller is not enough to cope with the dynamic periodic disturbance and the external disturbances in axial and radial direction. Therefore, the air gap controller should be robust to the dynamic periodic disturbance and the external shock for the protection of the SIL and data on media. With IMP based controller, the specific dynamic disturbance with a certain frequency can be cancelled out faster and more accurately than conventional air gap controllers [2]. The dominant disturbance, which is caused by the vertical run-out of the rotating disk, to the gap controller has a frequency of 675 Hz in our system. In order to reduce the residual gap error due to the high frequency periodic disturbance, the improved controller with IMP control block is designed to have higher gain at the frequency of 675Hz without affecting the system stability as shown in Fig. 2. And the

dead-zone controller is a non-linear control method which improves anti-shock performance by suppressing the disturbance due to the external shock. [3]. As shown in Fig. 3, the proposed improved controller contains the IMP and the dead-zone control blocks in addition to the conventional air gap controller.

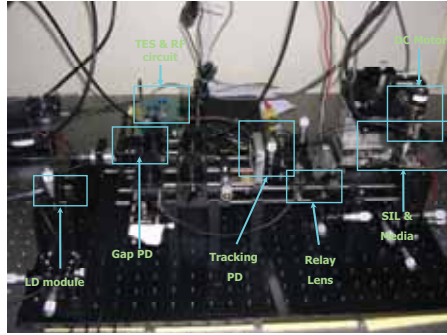


Fig. 1. Experimental setup of the SIL based NFR servo system

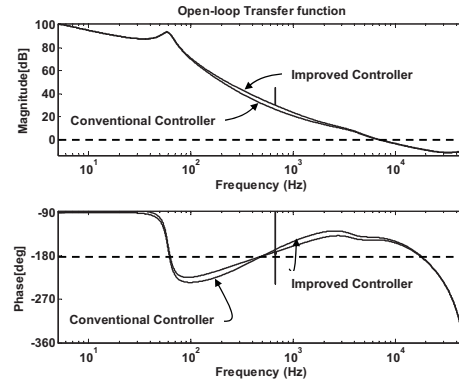


Fig. 2. Open loop transfer function of the comparing controller

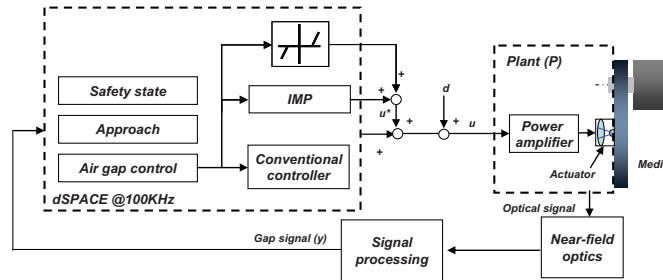


Fig. 3. Schematic diagram of advanced control methods for NFR servo system

3. EXPERIMENTAL RESULTS OF ADVANCED CONTROL METHODS

Figure 4 (a) and (b) show the residual gap errors in frequency domain around 675Hz, where the dominant disturbance lies, for the conventional gap controller and the proposed improved controller, respectively. The target air gap is 20 nm. As shown in Fig. 4, the residual gap error at 675Hz is reduced from 0.80 nm to 0.58 nm by applying the improved controller. Figure 5 shows the transient response for the external shock with amplitude of 1 G. As shown in Fig. 5 (a), there are large amount of fluctuations even including collision between the SIL and the media in the transient response right after the external shock is applied for the conventional gap controller. By applying the improved controller, the initial amplitude of fluctuation is reduced by 80% and the collision can be avoided as shown in Fig. 5 (b).

4. CONCLUSIONS

In this paper, we proposed the improved air gap controller using the internal model principle and the dead-zone controller, which have superior dynamic disturbance rejection and anti-shock performances to the conventional air gap controllers. Experiments show the effectiveness of the proposed controller. The residual gap error at the frequency of the dominant disturbance is reduced from 0.80 nm to 0.58 nm and the amplitude of initial transient response due to the external shock is also reduced by 80% in addition to avoiding collision.

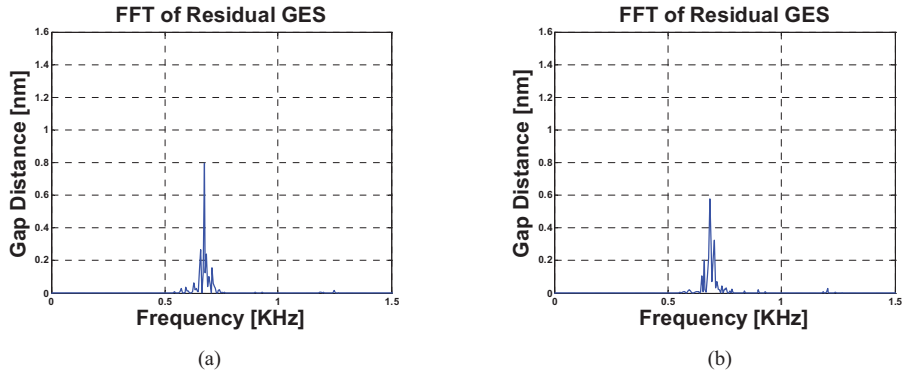


Fig. 4. FFT of residual GES (a) the conventional air gap controller and (b) the improved controller

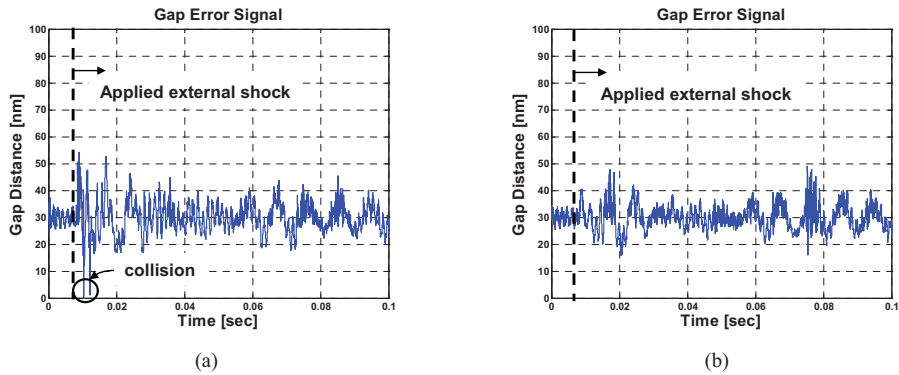


Fig. 5. Residual GES when applied external shock (1g) (a) the conventional air gap controller and (b) the improved controller

ACKNOWLEDGMENT

We would like to acknowledge that LG, Philips, SAMSUNG, and Sony Corporations have kindly provided us with technical supports on our experiments.

REFERENCES

- [1] T. Ishimoto, S. M. Kim, T. Yamaskik, T. Yukumoto, A. Nakaoki, M. Yamamoto, "Approach of Improving Disk Performance to High-Quality Gap Control in Near-Field Optical Disk Drive System", Jpn. J. Appl. Phys., 46, 3981-3986 (2007)
- [2] J. G. Kim, T. H. Kim, H. Choi, Y. J. Yoon, J. Jeong, N.C. Park, H. S. Yang, and Y. P. Park, "Improved Gap Control for SIL Based Near Field Recording System", Technical Digest of ISPS07, Santababara, USA(2007)
- [3] Y. Zhoua, M Steinbuchb, M. Van Der Aac, H. Ladegaarda, "Anti-shock controller design for optical drives", Control Engineering Practice 12, 811-817 (2004)

Effects of Surface and Mechanical Properties of Cover-layer on Near-Field Optical Recording

Jin-Hong Kim, Jun-Seok Lee, Jungshik Lim, Ki-Chang Song, and Jung-Kyo Seo¹

Devices and Materials Lab., LG Elite

16 Woomyeon-Dong, Seocho-Gu, Seoul 137-724, Korea

Phone: + 82-2-526-4574, FAX: +82-2-526-4959

E-mail: jinhkim@lge.com

¹*Digital Storage Research Lab., LG Electronics*

360-5 Yatap-Dong, Bundang-Gu, Sungnam-Shi, Kyunggi-Do, 463-828, Korea

Abstract: Polymer, nanocomposite, and dielectric cover-layers are fabricated with a spincoating and a sputtering method. Polymer cover-layer does not show any significant problems in the gap between a solid immersion lens (SIL) and a media surface but it has a limited magnitude in the refractive index. Nanocomposite cover-layer enhances the refractive index, which can be matched with the effective numerical aperture of the optics with the SIL, but it shows scratch problem in the cover-layer during a gap-servo process. The surface roughness and the mechanical properties of the nanocomposite are the origin of the problem. An alternative to avoid the scratch problem is to prepare the cover-layer with a hard material, and a dielectric cover-layer is fabricated by the sputtering. Even though a stress problem is remained in the dielectric cover-layer, it shows some positive evidences for the application.

1. Introduction

It is possible to expect that near-field recording (NFR) technology is one of the most promising candidates for next generation optical data storage. Solid immersion lens (SIL) system can be implemented to increase recording density by enhancing the effective numerical aperture (NA_{EFF}). In this technology, one of the most important things to be considered is the gap distance between the SIL and media surface controlled by the variation of the reflected light at the surface.¹ The gap distance should be a few tens nm, which yields some serious problems such as, collision², contamination, and heat at the gap.³ Therefore, cover-layer incident NFR configuration is preferable in this approach. The refractive index of the cover-layer should be matched with the NA_{EFF} to avoid the total reflection of the laser beam at the gap.⁴ Additionally, not only the mechanical properties such as, the hardness and toughness but also the surface roughness are critical for the NFR technology owing to the narrow gap distance. In this study, a few types of cover-layers were prepared and compared in their properties especially, mechanical and surface characteristics as well as the optical properties.

2. Types of Cover-layer

Three types of cover-layer could be possible in this study, for example, a polymer, a nanocomposite, and a dielectric cover-layer. Basically, the polymer and the nanocomposite cover-layer could be fabricated by a spincoating with a UV curing, and the dielectric cover-layer should be prepared by a sputtering method. When the thickness of the cover-layer for cover-layer-incident NFR application is considered, the spincoating seems to be an adequate technique for a few μm -thick cover-layers. The nanocomposite consists of polymer binder and nano particles can increase the refractive index, in which the difference between the polymer and the nanocomposite is attributed to the nano particles.⁴ A limitation of the refractive index of polymer material requires dispersing nano particles into the polymer since the nano particles have high refractive index. Some optical problems for the application such as, the optical absorption and the haze can be avoided by choosing TiO_2 nanoparticles. Inorganic dielectric materials also can be considered for the NFR cover-layer but, the sputtering technique seems not to be an appropriate method for such a thick cover-layer since the preparation process induces much stress. Fortunately, the sputtering method has not only many species of materials to choose but also many parameters to control the layer properties.⁵

3. Sample Preparation and Measurement

Around 3 μm -thick polymer cover-layer and nanocomposite cover-layer could be coated by the spincoating and cured by UV irradiation. The thickness was dependent on the viscosity of the resin and the rotating speed of the spincoater. The uniformity of the thickness should be controlled carefully owing to the shape of disc, which prevents the resin from being dosed at the center. The dielectric cover-layer was coated by the sputtering, which is used for thin film, in general. However, a few μm -thick layers were fabricated using the technique even if it includes some problems. The thickness and the refractive index of the cover-layers were measured by a spectrophotometer and an ellipsometer. The surface morphology and the mechanical properties of the cover-layer were measured by an AFM and a pencil hardness tester.

4. Results and Discussion

It is necessary to increase the refractive index of the cover-layer in NFR so that the total reflection can be reduced for the large NA_{EFF} . Fig. 1 shows the refractive index of polymer and nanocomposite cover-layer as a function of wavelength. It is clear that the refractive indices of the nanocomposite are higher than those of the polymer cover-layer since the nanocomposite contains TiO_2 nano particles. The refractive index of the polymer at blue wavelengths is around 1.75, and about 1.8 is the largest value for a pure polymer material can achieve. Even though the refractive index of the nanocomposite is over 1.9 at blue wavelengths, it can be enhanced more by adding the nano particles more.

It was confirmed that the polymer cover-layer did not show any significant problem for the gap-servo process. However, some serious problems of the nanocomposite cover-layer during the gap-servo test were observed. Specifically, surface characteristics and mechanical properties of the material seem to cause the gap-servo problem, which is turned out to be making scratches in the cover-layer.⁵ The surface morphology of the nanocomposite cover-layer is shown in Fig. 2. The peak-to-valley roughness of the nanocomposite cover-layer is about 30 nm which is a similar magnitude with the gap distance while the roughness of the polymer cover-layer is less than 10 nm. Additionally the mechanical properties such as, the hardness and the toughness of cover-layer also should be considered to avoid such damages in the cover-layer when the collision between the SIL and the media occurs.

One of the best solutions to meet the requirements for the cover-layer could be the dielectric cover-layer prepared by the sputtering technique. Basically, the refractive index of the dielectric films can be tailored especially, the refractive indices of aluminum oxynitride (AlO_xN_y) on the preparation condition are shown in Fig. 3. The refractive index can be tuned from about 1.75 to 2.2 in the figure, which can cover all required range of the application. On the other hand, the sputtering seems not to be a proper method to achieve such a few μm -thick cover-layer, because not only such a thick layer induces much mechanical stress but also the polycarbonat substrate brings about the stress owing to the thermal expansion during the preparation. Fig. 4 shows a NFR media image with about 3 μm -thick dielectric cover-layer, in which the trace of buckling can be observed. The stress in the media can be released by buckling especially, for the thick dielectric layer. Therefore, it seems to be difficult to fabricate a successful dielectric cover-layer by sputtering. However, there are many dielectric materials besides AlO_xN_y , some of the materials show possibilities from the viewpoint of the buckling, and it could be discussed in the presentation.

5. Conclusion

Several types of cover-layers were prepared for NFR application. Polymer and nanocomposite cover-layers were fabricated with the spincoating, and a dielectric cover-layer by sputtering. Polymer cover-layer showed good gap-servo performance, but the refractive index of the polymer is limited to match the effective numerical aperture of NFR. The refractive index of the nanocomposite cover-layer could be enhanced by adding the nano particles. However, a scratch problem was observed in the nanocomposite cover-layer after a gap-servo test, which was attributed to the surface characteristics and the mechanical properties of the material. As an alternative, a dielectric cover-layer was prepared by a sputtering, which showed a buckling problem owing to the stress of the thick dielectric film and the thermal expansion of the substrate during the sputtering. However, the stress problem seemed to be solved, which implies that this approach shows some possibilities for the application.

References

- 1) T. Ishimoto, K. Saito, M. Shinoda, T. Kondo, A. Nakaoki, and M. Yamamoto, Jpn. J. Appl. Phys. "Gap Servo System for a Biaxial Device Using an Optical Gap Signal in a Near Field Readout System" **42** (2003) 2719.
- 2) D. Bruls, C. Verchuren, J. van den Eerenbeemd, B. Yin, and F. Zijp, ISOM Tech. Dig., "Practical and Robust Near Field Optical recording System" 2006, p. 22.
- 3) Jin-Hong Kim, Opt. Eng., "Cover-layer with High Refractive Index for Near-Field Recording Media" **46** (2007) 045201.
- 4) Jin-Hong Kim and Jun-Seok Lee, Jpn. J. Appl. Phys., "Cover-layer with High Refractive Index for Near-Field Recording Media" **46**, No. 6B (2007) 3993.
- 5) Jin-Hong Kim, Jun-Seok Lee, Jungshik Lim, and Jung-Kyo Seo, "Improvement of Cover-layer Surface Properties for Near-Field Optical Recording" Technical Digest of ISOM 2007, p. 182.

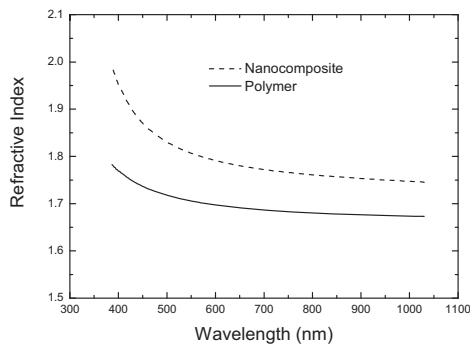


Fig. 1. Refractive indices of nanocomposite and polymer cover-layers on wavelength.

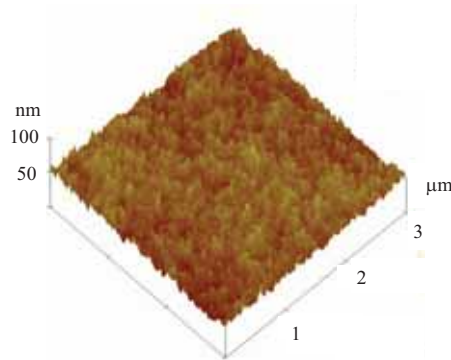


Fig. 2. Surface morphology of nanocomposite cover-layer.

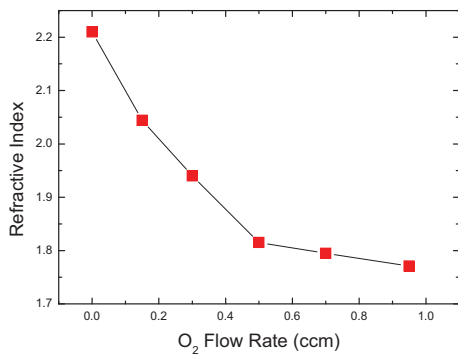


Fig. 3. Refractive index of AlO_xN_y dielectric film as a function of O₂ flow rate during sputtering.



Fig. 4. Image of buckling after deposition of 3 μm-thick AlO_xN_y dielectric layer.

Design of Compatible Optics for Near-field Recording and Blu-ray Disc Using Relay Lens

Hyun Choi^a, Jong-Pil Kim^a, Yong-Joong Yoon^a, Wan-Chin Kim^a, No-Cheol Park^{*a}, Young-Pil Park^a

^aCenter for Information Storage Device, Yonsei University, 134 Shinchon-Dong, Sudaemun-gu, Seoul, Korea, 120-749

Phone: +82-2-2123-4677, Fax: +82-2-365-8460

E-mail: pnch@yonsei.ac.kr

ABSTRACT

We designed compatible optics for solid immersion (SIL) based near-field recording system and Blu-ray disc (BD). The working distance, numerical aperture (NA) and cover-layer thickness of SIL based NFR system differ from the BD. Therefore, for compatibility of NFR and BD, we use the relay lens which is composed two low NA lenses. Wavefront errors of this system are $0.0148\lambda_{\text{rms}}$ and $0.0064\lambda_{\text{rms}}$ for NFR and BD, respectively. In NFR system, tolerance of SIL thickness is $\pm 1\mu\text{m}$ under the criterion of wavefront aberration $0.035\lambda_{\text{rms}}$.

Keywords: solid immersion lens, near-field recording, blu-ray disc, compatibility

1. INTRODUCTION

Near field recording (NFR) technology has been considered as a strong candidate of next-generation optical storage device. Solid immersion lens (SIL) based NFR is highlighted for the reason of similarities with present ODD and less complexity of optical system than other NFR technologies. There have been great achievements in the research on resolving technical issues of SIL based NFR including the matters of mechanical reliability as well as improving fast near-field air-gap servo and manufacturability of the SIL assembly. Recently, to prevent recording layer from the scratches and to adapt multiple-layered media, cover-layer incident SIL based NFR concept is proposed. C.A. Verschuren et al. designed and tested the SIL optics with an effective NA of 1.45 to demonstrate the feasibility of a near-field system using cover-layer incident concept. [1] And T. Yamasaki et al. developed new cover-layer material with refractive index over 1.75 for application to NFR system with higher NA optics. [2] However, for becoming certain next-generation optical storage device, SIL based NFR system has to be compatible to conventional optical storage device such as Blu-ray disc (BD). There have been many researches of compatible optics for various types of optical storage device such as compact disc (CD), digital versatile disc (DVD), high definition DVD (HD-DVD), and BD. S.J. Kim *et al.* developed BD optical pickup with a twin-objective lens actuator which is compatible with CD and DVD. [3] And Y. Tanaka *et al.*, I. Morishita *et al.* and M. Miyauchi *et al.* introduced compatible optical pickup using the phase matching optics such as diffractive optical element (DOE), hologram optical element (HOE) and multi ring zones. [4]~[6] In this study, for compatibility of NFR and BD, we propose design of compatible optics for SIL based NFR and BD using the relay lens.

2. DESIGN OF COMPATIBLE OPTICS

The relay lens is adapted multi-layered NFR system for shifting focal point to each recording layer. Therefore, we designed compatible optics using the existing optical component. Table I indicates designed NFR/BD specifications. In order to realize NFR/BD compatibility using a single optics, the difference of the cover-layer thickness, change of numerical aperture (NA) and working distance have to be compensated. Figure 1 shows the configuration for the NFR/BD compatible optics. The relay lens 2 moves back and forth for correcting aberration and adjusting the working distance and NA for compatibility of NFR and BD.

Table I. specifications for the NFR/BD compatible optics

	NFR	BD
Wavelength	405nm	405nm
NA	1.45	0.85
Wavefront error	$0.0148\lambda_{\text{rms}}$	$0.0064\lambda_{\text{rms}}$
Thickness of cover-layer	$5\mu\text{m}$	$100\mu\text{m}$
Working distance	-	$40\mu\text{m}$
Entrance pupil diameter	2.4mm	1.2mm

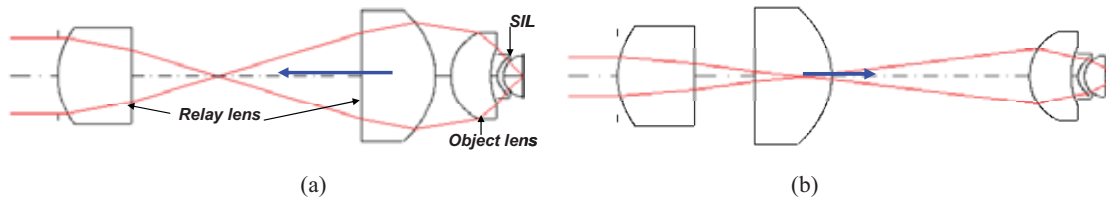


Fig. 1. Configuration for the NFR/BD compatible optics; (a) NFR (b) BD

The relay lens which changes the focus point according to NFR and BD is combined with same aspherical–plano type lens. The relay lens can be produced by the plastic material, because effective NA is only 0.285. Designed maximum moving distance is 4.833mm. Table II shows the specifications of relay lens. The SIL optical head is combined with objective lens, hemisphere lens and replicated lens as shown in Fig. 2. Objective lens is bi-aspherical type lens. Refractive index of hemisphere lens is 2.086. Radius and thickness of hemisphere lens are $640\mu\text{m}$. For manufacturability of replicated lens, its center thickness and edge thickness have to be thinner than $200\mu\text{m}$ and thicker than $50\mu\text{m}$. [7] In this design, center thickness and edge thickness of replicated lens are $185\mu\text{m}$ and $56\mu\text{m}$, respectively. In case of NFR, working distance is almost zero because evanescent wave can be propagated near the $\lambda/4$ region. But, working distance of BD optical head is determined as far as possible for protection of optical head and media. In this design, working distance is $40\mu\text{m}$. Wavefront errors are $0.0148\lambda_{\text{rms}}$ and $0.0064\lambda_{\text{rms}}$ for NFR and BD, respectively.

Table II. Specification of relay lens

Type	Aspherical-plano
Thickness	2.36mm
NA	0.285
EFL	4.28mm
Moving distance	4.833mm

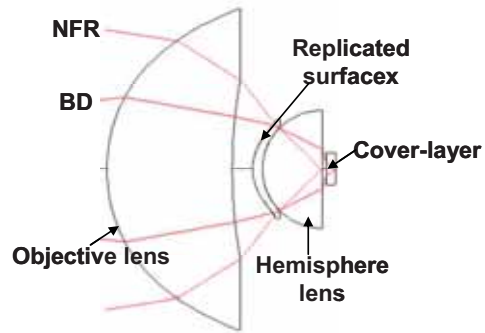


Fig. 2. Configuration for SIL optical head

In general super-hemisphere SIL, SIL thickness tolerance is below $0.5\mu\text{m}$ under the criterion of wavefront aberration $0.035\lambda_{\text{rms}}$. [7] Therefore, SIL thickness tolerance is key issue for improving manufacturability. In this design, SIL thickness tolerance is $\pm 1\mu\text{m}$ under the criterion of wavefront aberration of $0.035\lambda_{\text{rms}}$ in NFR case as shown in Fig 3. In case of BD, SIL thickness error does not matter because it is compensated by focusing servo actuator.

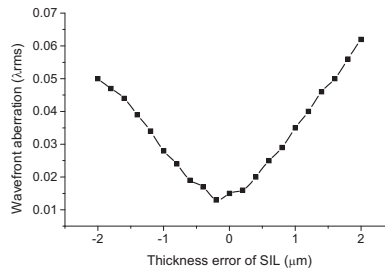


Fig. 3 SIL thickness tolerance

3. CONCLUSIONS

For various optical media such as CD, DVD and BD, the compatibility is essential for next-generation optical storage device. Therefore, for SIL based NFR is considered as next-generation optical storage device, compatibility of SIL based NFR has to research. In this study, we designed compatible optics for SIL based NFR and BD and verified feasibility compatibility of NFR and BD. The designed system compensated aberration which is induced by difference of focus point between NFR and BD by moving the simple relay lens. And we analyzed the SIL thickness tolerance in NFR case. Designed system has better SIL thickness tolerance than general super-hemisphere SIL.

REFERENCES

- [1] C.A. Verschuren, et al. "Near-Field Recording with a Solid Immersion Lens on Polymer Cover-layer Protected Discs", Japanese Journal of Applied Physics, Vol. 45, No. 2B, 1325–1331 (2006)
- [2] T. Yamasaki, T. Yukumoto, S. Kim, T. Ishimoto, A. Nakaoki, F. K. Bruder, R. Oser and K. Hildenbrand, "Evaluation of top coated media for near-field optical disc system of NA 1.84", Technical digest, ISOM06, Takamatsu, Japan (2006).
- [3] S.J. Kim, T. Y. Heor, T. K. Kim, Y. M. Ahn, C.S. Chung and S. H. Park, "High Response Twin-Objective Actuator with Radial Tilt Function for Blu-ray Disc Recorder", Japanese Journal of Applied Physics, Vol. 44, No. 5B, 3393–3396 (2005)
- [4] Y. Tanaka, Y. Komma, Y. Shimizu, T. Shimazaki, J. Murata and S. Mizuno, "Lens Design of Compatible Objective Lens for Blu-ray Disc and Digital Versatile Disk with Diffractive Optical Element and Phase Steps", Japanese Journal of Applied Physics, Vol. 43, No. 7B, 4742–4745 (2004)
- [5] I. Morishita, H. Shindo, N. Takeya, H. Jeong, Y. Yoon, I. Chang, H. Kim, D. Lee and C. Kyong, "Blu-ray Disc/Digital Versatile Disc Recording and Reproducing Compatible Use Technology in the 2nd Generation Pick Up for Blu-ray Disc", Japanese Journal of Applied Physics, Vol. 43, No. 7B, 4746–4751 (2004)
- [6] M. Miyauchi, T. Kanai, Y. Mitsui, Y. Makino, Y. Sugi, T. Maruyama, M. Mukoh and T. Shimano, "A compatible optical system for Blu-ray/HD-DVD/DVD/CD", Technical digest, ISOM07, Singapore, Th-PP-02 (2007)
- [7] Y.J. Yoon, H. Choi, W.C. Kim, T. Song and N. C. Park, "Thickness tolerance compensation of SIL first surface near-field recording with replicated lens on SIL", Microsyst Technol, 13 1289–1295 (2007)

COLLISION BETWEEN MEDIA SURFACE AND SOLID IMMERSION LENS IN NEAR FIELD RECORDING

Hyo Kune Hwang, Jin Moo Park, Sung Hoon Lee, Jung Kyo Seo, Seung Hun Yoo, In Ho Choi,
Byung Hoon Min
Digital Storage Research Laboratory, LG Electronics,
360-5 Yatap-Dong, Bundang-Gu, Sungnam-Si, Kyunggi-Do 463-828, Korea

ABSTRACT

Mechanical (Physical) interface between Head and Media is one of the important issues in SIL based near field storage. Especially harsh collision between media surface and SIL is one, because it can make permanent deformation causing optical issues. In this paper, the method to predict reaction of cover layer material, studied in LGE in recent years, is discussed to reduce this permanent deformation. To develop this method, correlation the collision test and the virtual tests have been the main topic of structural part.

Keywords: Indentation, collision, nano-indentation test, virtual collision test, virtual nano-indentation test, CAE

1. INTRODUCTION

Mechanical (Physical) interface between Head and Media is one of the important issues in SIL based near field storage. Thus, research on mechanical issue has been continued to improve the stability of the system. This issue can be largely categorized into three parts: structure, flow/contamination, and thermal issues. Studies have been done on how nano-gap system is influenced by each of three parts. For this research, structural part deals with the protection of media from the collision of SIL and media caused by external disturbance, and flow/contamination part is about the prevention of contaminants from attaching to the media by using airflow [1]. Lastly, thermal part is about the research on the material stability with respect to thermal field including SIL [2].

In structural part, collision happens due to lack of homogeneity on media surface and external disturbance by feeding vibration and external shock. Sometimes harsh collision of SIL makes indentation mark on cover layer, which causes optical troubles when read and write. (Fig. 1) Thus it became one of issues in structural part. NFR system is design to be operated in nano-gap, so the collision is unavoidable. Because of this reason, defining the threshold condition to prevent indentation and developing cover layer material are important. To overcome this issue, the process to extract mechanical properties which can be used in virtual test and the process for making specification have been studied in our lab.

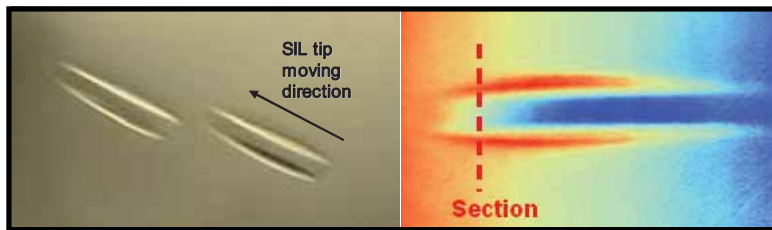


Fig. 1. Indentation mark on media surface by harsh collision

2. COLLISION EXPERIMENT AND VIRTUAL TEST

2.1 Correlation between collision and virtual collision gap error signals (CAE Feasibility test)

It's very hard to measure the reaction force and study the mechanism of collision in NFR system, so CAE is one of best solutions to analysis harsh collision. Most of FEM solvers are known that they can handle the MEMS problem, but NFR system is the problem between MEMS and nano-scale. So the feasibility of the solver should be verified before using

CAE tool for virtual collision test. Since glass is somewhat free from strain rate effect, glass disk and SIL collision test was done to correlate real and virtual collision experimental gap error signals. Virtual collision model was based on the inclined SIL collision in the paper[3]. As a result, the gap error signals from two experiments are almost the same. (Fig. 2)

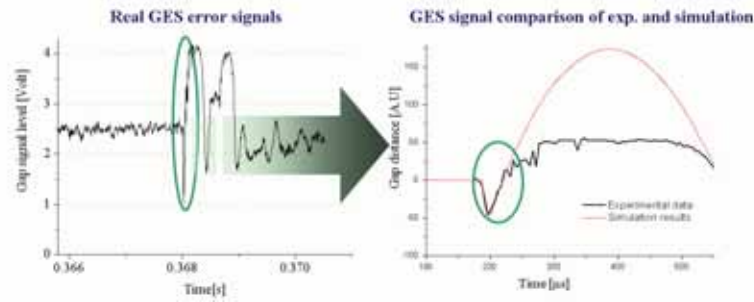


Fig. 2. GES Comparison of real and virtual collision result with glass disk

2.2 Indentation mark analysis

Virtual collision test with polycarbonate disk and SIL was modeled to analyze the indentation mechanism. As shown in Fig. 3, indentation mark was well simulated after collision and profile curves represented good correlation with real ones. Because it is a virtual test, it is easy to do case study. SIL inclined angle and linear velocity were put in this model as design factors, then the reaction force data was calculated as shown in Fig. 4. In the simulation result, indentation mark remains after collision with more than 300mN. If reliable material properties are put in this model, it is expected that the reasonable cover material can be specified quantitatively.

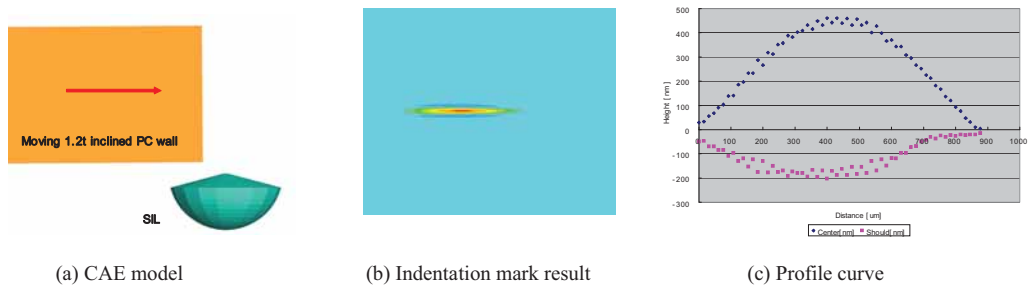


Fig. 3. Indentation mark simulated by collision CAE.

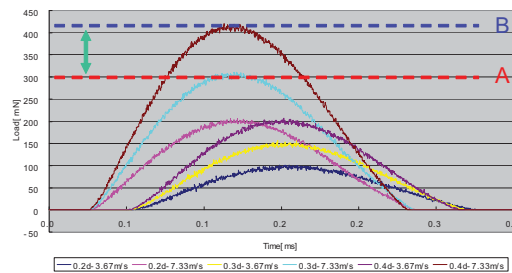


Fig. 4. Indentation force on media surface by collision of SIL with various linear velocities

2.3 Nano-indentation test and material property estimation

Nano-indentation test [4] is developed to measure film and coating hardness in nano-scale these days. By this test, hardness data and displacement-force curves of NFR and BD disk was evaluated with Berkovich tip. (Fig. 5) Then the hardness data are listed in Table 1.

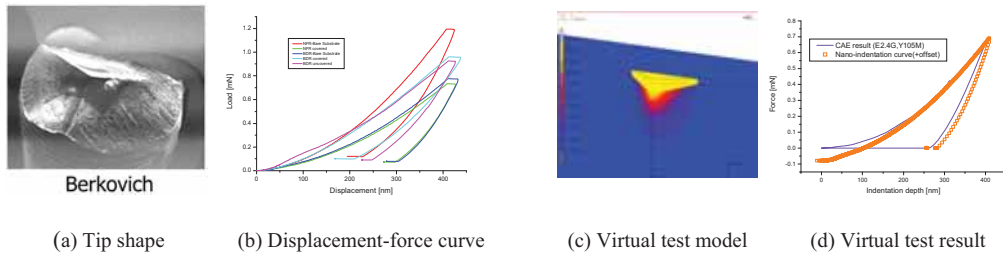


Fig. 5. Nano-indentation test

Table 1. Hardness data by nano-indentation test

Sample Name	Depth	100 - 110nm	200 - 210nm	300 - 310nm	400nm
Transparent Disk (front side)	Hardness	0.577	0.522	0.496	0.486
	Std. Dev.	0.032	0.009	0.030	0.020
Transparent Disk (back side/Covered)	Hardness	0.385	0.302	0.273	0.258
	Std. Dev.	0.043	0.021	0.013	0.007
Covered BD	Hardness	0.680	0.543	0.472	0.410
	Std. Dev.	0.028	0.011	0.007	0.000
Uncovered BD	Hardness	1.280	0.637	0.467	0.390
	Std. Dev.	0.220	0.039	0.021	0.014
Center BD (Bare PC substrate)	Hardness	0.393	0.307	0.285	0.273
	Std. Dev.	0.064	0.027	0.013	0.000

To simulate collision exactly, the conversion process from nano-indentation test result to the mechanical properties should be established. For this purpose, virtual nano-indentation method as shown in Fig. 5(c) has been developed to estimate the mechanical properties of the cover layer material (e.g. Young's modulus, yield stress). The feasibility of this method has been verified by comparing displacement-force curves. (Fig. 5(d))

It is estimated that the yield strength of BD cover layer is twice as high as PC substrate by this method. This means that there will be no indentation marks on media surface during the test of LGE NFR system, only if the cover layer material has mechanical properties as high as BD's.

3. FUTURE WORKS

Because the cover layer material used in NFR system should have high optical capability, it is hard to develop the material which has high mechanical properties either. But the method to evaluate cover layer mechanical properties with virtual test may be the first step to actualize NFR system into commercial one. The verification and correlation of this method are still in progressing and improved result will be introduced in the conference in detail.

REFERENCES

[1] Jung Eung Park and Jin Moo Park, "Airflow Analysis in a Near Field Optical Disc System" ISOM/ODS 05. Tech. Digest, MP4 (2005).
 [2] Jin Moo Park and Ho Chul Ryu, "THE THERMAL EFFECT AT THE INTERFACE BETWEEN DISC AND SOLID IMMERSION LENS IN NEAR FIELD RECORDING" ISOM 2007. Tech. Digest, (2007).
 [3] Do Hyeon Son and Mi Hyeon Jeong, "THE SMALL-SIZED OPTICAL MODULE AND THE SLED MOVING METHOD OF A GAP SERVO NEAR FIELD RECORDING" Technical digest, Topical meeting, ODS, Portland, USA (2007).
 [4] ISO 14577-4: Part 4: Test method for metallic and non-metallic coatings

THE NEAR FIELD OPTICAL MODULE AND THE TILT COMPENSATION METHOD OF GAP SERVO NEAR FIELD RECORDING SYSTEM

Do Hyeon Son, Bong-Sik Kwak, Mi Hyeon Jeong, In Gu Han, Jeong Kyo Seo,
In Ho Choi, and Byung Hoon Min

Digital Storage Research Laboratory, LG Electronics, 360-5 Yatap-Dong, Bundang-Gu, Sungnam-Si, Kyunggi-Do 463-828, Korea

Phone : +82-31-789-4028, Fax : +82-31-789-4204, E-mail : sondo@lge.com

ABSTRACT

We presented the NF optical module (the near field optical module) for a commercialized gap servo near field technology in ODS 2007. Since then, we redesigned and improved the previous NF optical module to produce the upgraded NF optical module in the optical, electrical and mechanical areas. The latest experiments show that it is possible to acquire the improved RF readout signals, which are better than results presented in ODS 2007. To enhance the system stability, we propose the tilt compensation method of the NF system for compensating the amount of disc tilt on the NF deck mechanism. By applying the proposed method, we acquire the stable servo signals of the NF optical module on the deck mechanism.

Keywords: NF optical module, gap servo, gap jumping, tilt compensation, near field recording

1. INTRODUCTION

As one of strong candidates after a BD (Blu-ray Disc) era, gap servo NFR technology has many merits: the use of active servo method^{[1][2]} for axial direction, the possibility of using the existing conventional optical drive actuator and the similarity of the existing conventional optical drive layout.

With regards to gap servo NFR technology, LGE already presented the relevant technologies and experimental research results in the electrical^[3], optical^[4], and mechanical^[5] areas. For commercialization of technology, we studied and presented the NF optical module^[6] and the deck mechanism^[6] of gap servo NFR. The rough RF readout signals^[7] of the NF optical module were presented in ODS 2007, but there remain many rooms of improvement in signal quality. The improvements of the RF readout signals of the NF optical module are indispensable for commercialization. In this paper, we present the latest experimental results of the upgraded NF optical module.

We already presented the gap jumping method^[7] for sled moving and showed the effectiveness of reducing the collisions by applying the proposed method. Nevertheless, because of small mechanical tilt margin between SIL (Solid Immersion Lens) and a disc, the gap servo NF technology requires and needs to maintain the optimal contact condition for preventing or reducing the collisions of SIL lens and a disc. For the optimal contact condition on NF deck mechanism, we have to compensate the tilt amounts caused by a disc. Based on the above reasons, in this paper we propose the tilt compensation method for compensating the amount of disc tilt automatically. The effectiveness of the proposed compensation method is shown by the NF optical module experiments mounted on the deck mechanism.

2. DESIGN & EXPERIMENT

The improvement points of RF readout signals of the previous NF proto module were selected based on investigation of electrical, optical and mechanical parts of the NF optical module. For the electrical part, the work for increasing the S/N (signal to noise) ratio of servo and RF readout signals started. We redesigned and improved the previous NF optical

module with the rearrangement of components, precise assembly and aligning performance of optical components and enhancing adjustment capability in the optical and mechanical parts.

Fig. 1 shows the newly designed modeling of the upgraded NF optical module. The GES (Gap Error Signals) & RF PD (Photo Diode) of the upgraded NF optical module has a different mounting position with respect to the optical beam axis for enlarging room of adjustment and mounting space of PD. This newly designed concept gives much more space to PD components comparing to the previous one. The upgraded NF optical module also includes the motorized expander module used in the previous one for accurate controlling expander lens. For increasing the capability of adjusting and assembling, we upgraded the adjustment system for adjusting PD and optical components. The newly upgraded adjustment system is shown in fig. 2. We apply the concept of enlarging adjusting degree of freedom of components.

Gap servo NFR technology requires an optimal contact condition between SIL lens and disc for preventing the collision caused by a small mechanical margin. In this paper, we propose the tilt compensation method of gap servo NFR system. LGE presented the NF deck mechanism including radial, tangential moving mechanism for making a contact condition. The proposed tilt compensation method is realized by using these moving mechanisms. Fig. 3 shows the relation of GES variance to disc tilt angle at a disc rotating and the characteristics of greater GES variance to greater tilt angle. Using this relation, we propose the compensating tilt angle by monitoring GES variance as adjusting moving mechanisms. The realized deck mechanism including the previous NF optical module and control system for the tilt compensation during a disc rotating shows the stable servo signals after the compensation is finished, and finally, we can acquire the RF readout signals.

3. EXPERIMENTAL RESULTS AND DISCUSSION

The experiments using the improved and upgraded NF optical module are in progress and show better S/N ratio of the electrical signals comparing to the previous one. The relevant experiments are in progress as well, and consequently, the latest experimental results will be presented at the conference. For making the optimal contact condition between the NF optical module and a disc rotating on NF deck mechanism, the experiments applying the proposed tilt compensation method shows that it is possible to acquire the stable servo signals. Based on these results, we can acquire the RF readout signals on the NF deck mechanism. Fig. 4 shows the NCS (Number of Collision-like Signals) during the gap distances. We will present additional results at the conference.

4. CONCLUSION

We present newly designed and upgraded NF optical module by improving LGE the previous one. The upgraded NF optical module shows better S/N ratio of signals, and from this result, we expect that the upgraded NF optical module can acquire the improved RF readout signals.

For making the optimal contact condition between the NF optical module and a disc mounted on the realized half-inch sized NF deck mechanism, we propose the tilt compensation method using the GES variance, which shows that we can acquire stable servo signals in the NF deck mechanism. Additionally, the experiments show that it is effective in acquiring the RF signals and moving a long distance of sled moving on the NF deck mechanism by the stable servo signal with the proposed tilt compensation and the gap jumping method. We expect to make an improved performance of the RF readout signals hereafter on the NF deck mechanism with the application of the upgraded NF optical module.

REFERENCES

- [1] C. A. Verschuren, J. M. A. van den Eerenbeemd, F. Zijp, J. I. Lee, D. M. Bruls, "Near-Field Recording with a Solid Immersion Lens on Polymer Cover-layer Protected Discs", Technical digest, 2005 Topical meeting, ISOM/ODS, Honolulu, HA, USA (2005).

- [2] M. Shinoda, K. Saito, T. Ishimoto, A. Nakaoki, M. Yamamoto, O. Maeda, T. Hashizu, T. Asano, K. Aga, K. Takagi, M. Tazoe, "High Density Near-Field Optical Disc System", Technical digest, 2005 Topical meeting, ISOM/ODS, Honolulu, HA, USA (2005)
- [3] J. K. Seo, J. U. Lee, Y. S. Shin, J. M. Park, I. H. Choi and J. Y. Kim, "TRACKING SERVO METHOD FOR THE GAP SERVO NEAR FIELD OPTICAL STORAGE SYSTEMS", Technical digest, ODS, Montreal, Canada(2006)
- [4] Y. S. Shin, J. U. Lee, J. M. Park, J. K. Seo, I. H. Choi and J. Y. Kim, "CROSS-TALK EFFECTS BETWEEN GAP ERROR AND TRACK ERROR SIGNALS IN A GAP SERVO NEAR FIELD OPTICAL STORAGE SYSTEM", Technical digest, ODS, Montreal, Canada (2006)
- [5] Y. S. Shin, J. U. Lee, D. H. Son, J. M. Park, J. K. Seo, I. H. Choi and B. H. Min, "NFR RESEARCH FOR OVER 200 GB CAPACITY (Invited)", Technical digest, ISOM, Takamatsu, Japan (2006)
- [6] J. U. Lee, J. K. Seo, G. S. Park, J. K. Lee, J. M. Park, S. K. Kim and J. Y. Kim, "Recording and Readout Performance of Swing Arm OPU for Small Form Factor Optical Drive System", Technical digest, 2004 Topical meeting, ODS, Monterey, CA, USA (2004)
- [7] D. H. Son, M. H. Jeong, G. A. Kim, S. H. Lee, I. G. Han, J. K. Seo, I. H. Choi and B. H. Min, "THE SMALL-SIZED OPTICAL MODULE AND THE SLED MOVING METHOD OF A GAP SERVO NEAR FIELD RECORDING", Technical digest, ODS, Portland, OR, USA(2007)

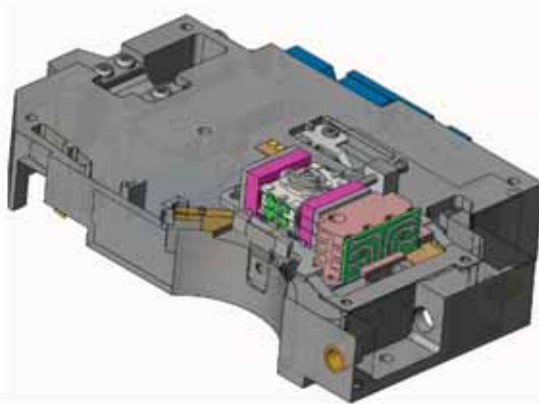


Fig. 1. The design model of the upgraded NF optical module

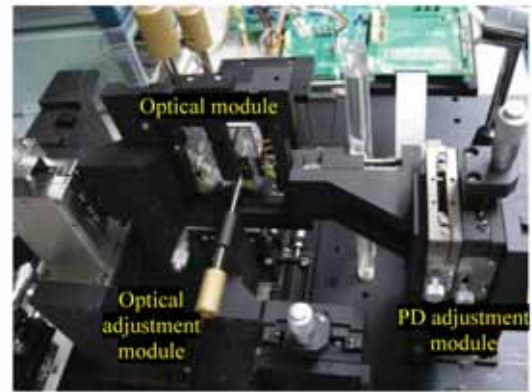


Fig. 2. The newly upgraded adjustment system

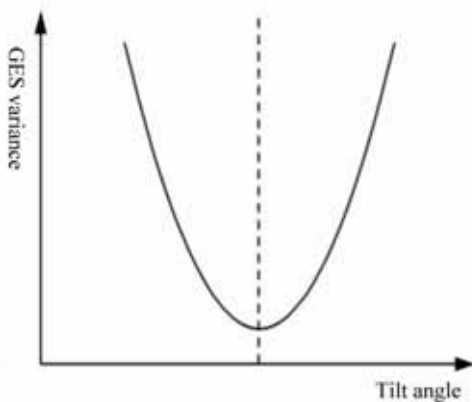


Fig. 3. The relation of GES variance to disc tilt angle

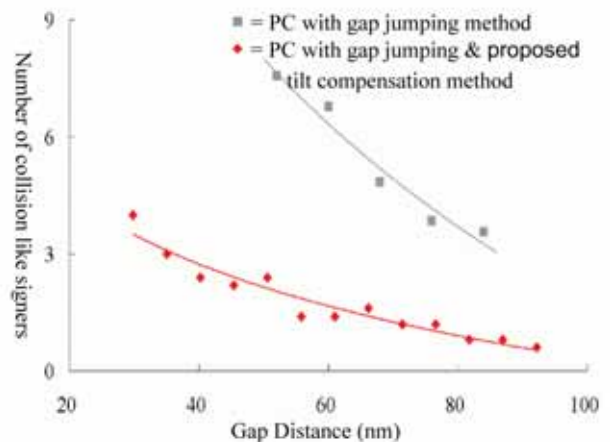


Fig. 4. NCS according to the gap distances

L1₀ ordering of (001)-oriented FePt thin films and its possible application in hybrid recording

B. Ma, C. L. Zha, Z. Z. Zhang, Q. Y. Jin,

State Key Laboratory for Advanced Photonic Materials and Devices, and Department of Optical Science and Engineering, Fudan University, Shanghai 200433, China

Tel: 86-21-65642059, Fax: 86-21-65641344, E-mail: qyjin@fudan.edu.cn

$L1_0$ ordered FePt thin films have been intensively investigated in recent years,¹⁻⁵ because of their potential applications for ultrahigh density perpendicular recording media. It should be also a candidate for the opto-magnetic hybrid recording, especially when its thermal property is improved using a proper multilayered structures.

We have prepared four kinds of stoichiometric FePt alloy films (sample A, B, C and D), with thickness about 8 nm, by dc magnetron co-sputtering of Fe and Pt from elemental targets. Sample A is grown on in-situ heated MgO (100) single crystal substrate. Sample B, C and D are films deposited at room temperature (RT) on SrTiO₃ (100), MgO (100) and 2-nm-thick FeO_x covered Si wafer, respectively, and then annealed for 10 minutes at temperatures from 300 to 750 °C in vacuum. For FePt/TbFeCo sample, the FePt was first deposited onto a single crystalline MgO (100) substrate at 650 °C, then TbFeCo on the top at room temperature. The composition of the films, Fe₅₀Pt₅₀, is determined by x-ray fluorescence spectrometer (XRF), and their detailed structures are studied by x-ray diffraction (XRD) with Cu K_α radiation in geometry of symmetric scan ($\theta \sim 2\theta$). The magnetic properties of the films are measured by vibrating sample magnetometer (VSM) with a maximum applied field of 18 kOe.

Figure 1 shows the XRD θ - 2θ spectra of four FePt samples, with left column for as-deposited films (except for (a) $T_S = 100$ °C) and right column for 600 °C-deposited or annealed films. For the films grown on heated MgO (see first row of Figure 1), no obvious FePt (001) superlattice peak is observed, and thus a disordered $A1$ structure is found when $T_S = 100$ °C. However, the (001) superlattice peak appears when $T_S = 600$ °C, which indicates the formation of $L1_0$ ordered structure. For the films on SrTiO₃, MgO and Si substrates (sample B, C and D), all the as-deposited films exhibit disordered $A1$ structure. Especially, the film deposited on Si/FeO_x shows a (111)-preferred orientation. When annealed at 600 °C, the $L1_0$ structure has formed for all the samples, and their c -axis is perpendicular to the film plane, irrespective of their epitaxial or non-epitaxial growth. For the film on Si/FeO_x, the (111) peak disappears entirely after annealing.

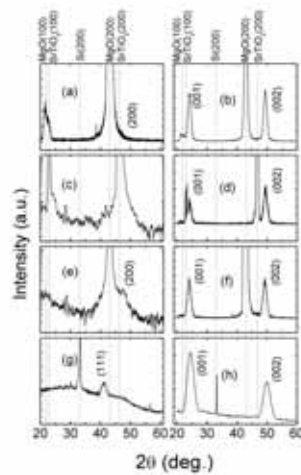


Fig. 1 The XRD θ - 2θ spectra of FePt films deposited onto heated MgO substrate with (a) $T_S = 100$ °C and (b) $T_S = 600$ °C, and onto SrTiO₃ ((c) and (d)), MgO ((e) and (f)), Si/FeO_x ((g) and (h)). Except for (a) and (b), the spectra in left column are for as-deposited samples prepared at RT, and those in right column for films annealed at $T_A = 600$ °C. The diffraction peak positions of substrates are labeled on the top of the figures, and those peaks of FePt films are shown inside.

Their in-plane and perpendicular hysteresis loops (not shown here) confirm that the magnetic anisotropy is out-of-plane for all the samples deposited or annealed at 600 °C. Table I lists the details of their structural and magnetic properties. The chemical ordering parameter S is calculated from the ratio of integrated intensities of (001) to (002) peaks by formula in Ref.5, and the grain size D , along the normal direction, from the above diffraction peaks by the Scherrer formula. It is found that the S values of the three epitaxial films on heated MgO, SrTiO₃ and MgO after annealing (sample A, B and C) are smaller than 1, which indicates that these films are not fully ordered though they grow in an epitaxial way. But for the film on Si/FeO_x (sample D), the ordering parameter $S = 1$. Its lattice constant along c -axis exhibits the maximum compression of all samples, resulting in the largest anisotropy field H_k ; almost twice the values of the other three samples. Its perpendicular coercivity reaches about 6.4 kOe, and the out-of-plane hysteresis loop has a high squareness. In addition, the calculated grain sizes of FePt films on MgO and SrTiO₃ are twice as large as that on Si/FeO_x. This is reasonable because the epitaxial growth favors the formation of a fine crystalline structure and large grains.

Table I Structural and magnetic properties of FePt films deposited and annealed at $T_A = 600$ °C, with c the lattice constant along c -axis, D the grain size calculated from the diffraction peaks by the Scherrer formula, S the chemical ordering parameter calculated from the ratio of integrated intensities of (001) to (002) peaks by formula in Ref.5.

Sample	Substrate	c (nm)	D (nm)	S	$H_C(\perp)$ (kOe)	H_k ($10^6 \times \text{erg/cc}$)	M_r/M_s
A	Heated MgO	0.377	12.3	0.67	2.65	35	0.93
B	SrTiO ₃	0.3703	13.3	0.69	5.95	30	0.94
C	MgO	0.3683	11.1	0.81	3.40	32	0.85
D	Si/FeO _x	0.3658	6.4	1	6.25	65	1

Figure 2 shows the influence of temperature on the chemical ordering of FePt films. The temperature is the substrate temperature for sample A, but the annealing temperature for sample B, C and D. The chemical ordering parameter S increases with temperature. At the same time, the lattice parameter c compresses, accompanying the $A1$ to $L1_0$ transformation. However, their $L1_0$ kinetic ordering processes are very different. The film on heated MgO (sample A) starts the phase ordering earlier, and the ordering parameter S follows a linear relationship with temperature, but is still not very large (less than 0.7) when T_S reaches 600 °C. Though the lattice mismatch between the FePt film and SrTiO₃ substrate (sample B) is very small (1.5%), quite suitable for epitaxial growth, its ordering process does not proceed effectively in comparison with the behavior of the FePt film on MgO (sample C) with lattice mismatch as large as 9.3%. This indicates that an appropriate large lattice mismatch (thus an adequate induced stress) is required to achieve a better ordered fct phase with the c -axes of all grains out of plane, because the lattice in the film plane needs to be expanded so that the lattice along c -axis compresses more. Among these samples, the ordering behavior of the non-epitaxial film deposited on Si/FeO_x (sample D) seems quite good. Its ordering process begins above 300 °C, later than sample A but 100 °C earlier than sample B and C. The ordering parameter S is already 0.7 when $T_A = 400$ °C, the temperature at which ordering starts for samples B and C.. When T_A increases to 600 °C, S equals 1, suggesting the completion of the $L1_0$ phase ordering; At this point the fct phase is fully ordered.

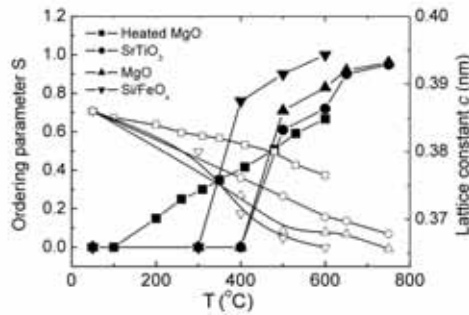


Fig. 2 The influence of in-situ substrate or annealing temperature on the chemical ordering parameter S (closed symbols) and lattice constant c (open symbols) of FePt thin films deposited on heated MgO (square), SrTiO₃ (circle), MgO (upper triangle) and Si (with FeO_x underlayer) (down triangle) substrates. The line is guide for eyes.

In order to find suitable media for hybrid magnetic recording based on FePt ordering alloy, the properties of FePt/TbFeCo

bilayer will be also discussed.

References

¹ R. F. C. Farrow, D. Weller, R. F. Marks, and M. F. Toney, A. Cebollada, G. R. Harp, J. Appl. Phys. **79**, 5967 (1996)
² T. Shima, T. Moriguchi, S. Mitani, K. Takahashi, Appl. Phys. Lett., **80**, 288 (2002)
⁴ Y. F. Xu J. S. Chen and J. P. Wang, Appl. Phys. Lett., **80**, 3325 (2002); J. S. Chen. B. C. Lim, and J. P. Wang, Appl. Phys. Lett., **81**, 1848(2002)
⁵ T. Suzuki, Materials Transaction, **44**(8), 1535 (2003)
¹¹ B. E. Warren, *X-Ray Diffraction* (Dover, New York, 1990), p. 208

Nano-Optical Characteristics of Double-sided Grating Structure for HAMR Application

Dong-Soo Lim, Hyun-Suk Oh and Young-Joo Kim*
 Center for Information Storage Device (CISD), Yonsei University
 134 Shinchon-dong, Seodaemun-Ku, Seoul 120-749, Korea

ABSTRACT

The surface plasmon phenomenon of double-sided grating structure with nano-slit aperture was studied to understand the enhancement of near-field optical throughput for HAMR application. Based on the FDTD simulation, the near-field optical intensity through 50x300 nm aperture with an aid of the double-sided grating structure showed 10 times higher value than that of the nano-slit aperture without grating pattern. In addition, it was found that the light penetrated through the nano-slit aperture in the asymmetric double-sided grating could be confined locally around the thin layer area to increase the optical intensity.

Keywords: grating, surface plasmon, near-field optics, high near-field optical throughput, heat assisted magnetic recording

INTRODUCTION

Recently, near-field optics having extraordinary high optical throughput with subwavelength spot size is desirable in many applications, such as waveguide, microscopy, biological detection, optical data storage and heat assisted magnetic recording (HAMR). In the HAMR technology, one of most critical requirements is related to the high near-field optical throughput with nano spot size which heats the media locally to Curie temperature to reduce its coercivity sufficiently to switch magnetization. However the optical throughput decreases exponentially when the aperture size is much smaller than the wavelength of the incident light. To overcome this drawback, many researches have been suggested special aperture designs including metal nano-hole array [1] and 'C' shaped nano apertures [2]. In our previous work [3], we proposed the grating structure with nano-slit aperture based on the surface plasmon effect for HAMR head. The coupled diffracted light with grating structure can promote the surface plasmon wave when its wavevector coincides with that of surface plasmon. In this paper, the near-field optical behavior in the double-sided grating structure was investigated using finite differential time domain (FDTD) simulation. The effect of magnetic media on the near-field characteristics was also analyzed for the HAMR application.

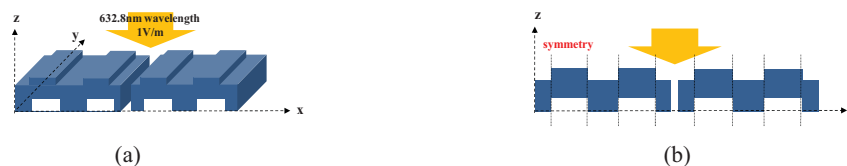


Fig. 1. Schematics of the double-sided grating with nano-slit aperture (a) isometric view (b) front view

SIMULATION RESULTS AND DISCUSSION

Figure 1 shows the schematics of the double-sided grating with nano-slit aperture. The incident light is guided to the nano-slit aperture which is formed on the metal grating. Using grating, it is expected to enhance the near-field optical throughput through nano-slit aperture by the excitation of surface plasmon. From our previous research [3], we optimized the configurations of nano-slit, film material, film thickness and single-sided grating structure. The optimized nano-slit showed 50nm in width and 300nm in length. In addition, the thickness of metal film showed the best optical efficiency with 210nm for silver.

*yjkim@yonsei.ac.kr; phone 82-2-2123-6852; fax 82-2-365-8460

The pitch, width and depth of Ag single-sided grating were decided as 450nm, 210nm and 90nm, respectively. To increase the near-field optical throughput, we have tried to design the double-sided grating structure which has grating patterns on both sides of metal plate as shown in Fig 1. For the FDTD simulation (XFDTD, Remcom Inc.), the linearly x-polarized plane wave was assumed to propagate to the -z-direction. A simulation cell size was kept in 5nm x 5nm x 5nm. The double-sided grating structure is shown in Fig. 2(a) where the separation of top and bottom grating patterns was fixed as 130nm. For the understanding of asymmetric effect, the grating pattern in the bottom side was translated from 0 to 95nm in the x-direction from the symmetric position. In the case of symmetric double-sided grating structure, the near-field optical intensity is similar to that of the single-sided grating structure as shown in Fig. 2(a). However, as the translation of bottom grating was occurred, the near-field optical intensity increased as shown in Fig. 2(b). We believe that the wavevector interaction between top and bottom grating patterns leads to the large enhancement of near-field optical intensity in the asymmetric grating structure. The maximum enhancement of near-field optical intensity was found at the 80nm translation.

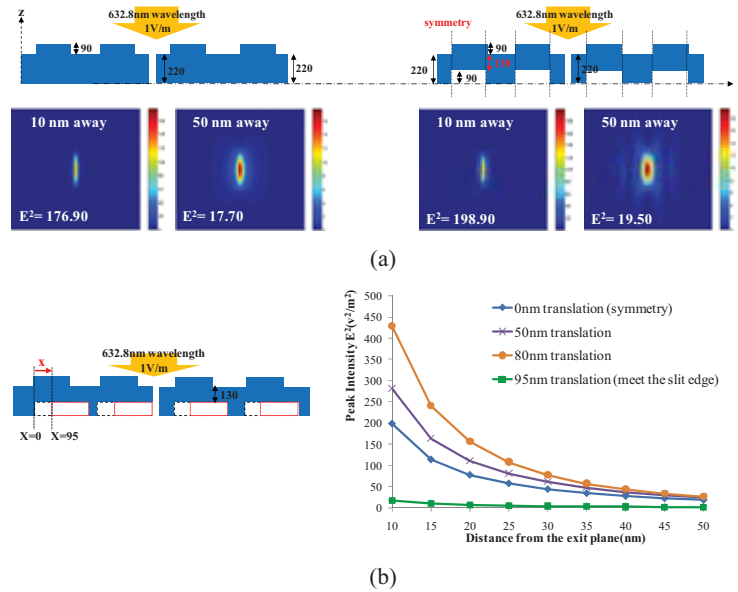


Fig. 2 (a) Comparison of field distribution of xy-plane for the single-sided grating structure and symmetric double-sided grating structure (b) The effect of translation of bottom grating pattern for double-sided grating structure

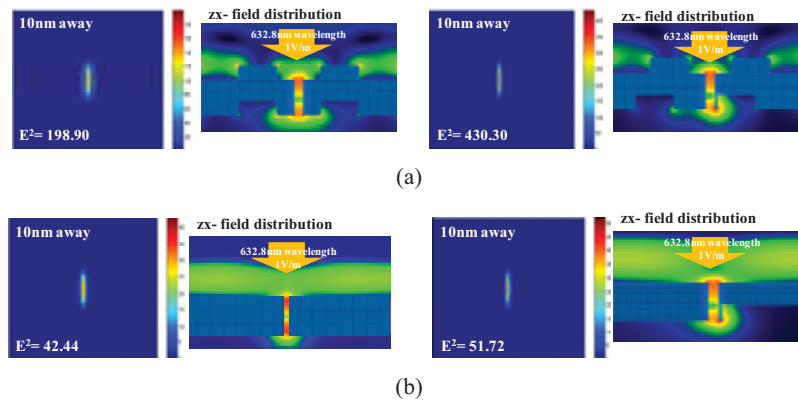


Fig. 3 The near-field distribution of (a) symmetric and 80nm translated double-sided grating and (b) nano-slit and asymmetric nano-slit

For 80nm translated double-sided grating structure as shown in Fig. 3(a), the light is mainly confined around the thin layer area in the right side of bottom grating at the exit plane. We believe that the local confining of near-field optics as well as wavevector matching of both grating patterns could induce the enhancement of near-field optical throughput. This local confining phenomenon of near-field optics could be also explained only with the nano-slit aperture having asymmetric exit plane without grating pattern as shown in Fig. 3(b). It was found that the near-field optical intensity of the 80nm translated double-sided grating structure showed about 2.2X higher value than that of the symmetry case. This means 10 times higher value than that of the nano-slit aperture without grating pattern. To apply double-sided grating structure for HAMR head, we also analyzed the near-field interaction with the magnetic media. In this simulation, the magnetic media was assumed as cobalt thin film of 35nm thickness and the gap between double-sided grating structure and media was fixed as 10nm as shown in Fig. 4. Based on the simulation results, the near-field optical intensity at the surface of Co media showed around 80% lower value than that of the case without media. Because the propagation wave was absorbed by the Co media, the near-field optical intensity through the double-sided grating structure decreases as the light propagates into the Co media. More detailed results with the media will be discussed in the presentation.

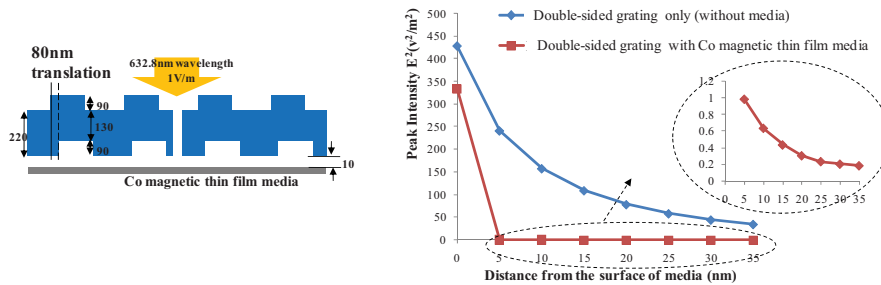


Fig. 4 The near-field optical interaction between double-sided grating structure and magnetic media

SUMMARY

To increase the near-field optical throughput, the double-sided grating structure combined with nano-slit aperture was investigated by using FDTD simulation. The near field optical intensity through 50x300 nm aperture with an aid of the double-sided grating structure showed 10 times higher value than that of the nano-slit aperture without the grating pattern with the careful control of asymmetry of both grating patterns. For the asymmetric double-sided grating structure, the local confining of near-field optics around the thin layer area at the exit plane as well as the wavevector matching of both grating patterns may enhance the surface plasmon excitation, resulting in the enhancement of near-field optical throughput. The near-field interaction between double-sided grating structure and magnetic media was also investigated for the HAMR application. Since new double-sided grating structure has an advantage of high near-field optical throughput with small spot size, it can be applied to the HAMR head in the near future.

ACKNOWLEDGEMENT

This work was supported by the Korean Research Foundation Grant funded by the Korean Government (MOEHRD, Basic Research Promotion Fund) (KRF-2006-331-C00124).

REFERENCES

- [1] C. Genet and T. W. Ebbesen, "Light in tiny holes", *Nature* **445**, 39 (2007)
- [2] Xiaolei Shi and Lambertus Hesselink, "Design of a C aperture to achieve $\lambda/10$ resolution and resonant transmission", *J. Opt. Soc. Am. B.* **21** No.7 1305 (2004)
- [3] Dong-Soo, Lim and Young-Joo Kim, "Light Delivery for the Heat Assisted Magnetic Recording (HAMR) Head with Grating Structure", ODS 2007, MD4 (2007)

Magnetic and Magneto-optical Properties of Hybrid Recording Media on Porous Alumina Underlayer

J B Yan, Z Y Li , F Jin , K F Dong, G Q Lin, X S Miao *

(Dept. of Electronic Science & Technology, Huazhong Univ. of Science & Technology, Wuhan.430074,China)

1. Introduction

Hybrid recording or heat assisted magnetic recording (HAMR) has attracted much attention as a promising candidate for next generation magnetic recording technology beyond 1Tb/in²[1-4]. The rare-earth transition metal (RE-TM) alloys usually are applied as a media for magneto-optical recording^[5-6], it can also be considered for the hybrid recording due to its large perpendicular uniaxial magnetic anisotropy with amorphous structure and an extremely high coercivity H_c . However, the desirable recording characteristics were not reported in any literature using amorphous RE-TM media, the strong exchange coupling of these media has been believed to reduce the resolution of the magnetic recording, because magnetic transition is distorted due to domain-wall motion. Actually, the magnetic boundary of a small-sized domain shifts or vanishes through the displacement of the magnetic domain wall during the high-density magnetic recording. Magnetic pinning sites, which impede the motion of a magnetic domain wall, are hence required to improve the resolution of magnetic recording. Several papers had demonstrated that the formation of the magnetic pinning sites induced by intermediate layers played a significant role in the magnetic media and enhanced the resolution of magnetic recording.^[7-9]

In this study, we employed a chemical method to fabricate the underlayer, which possess the nano-scale hole structure, in order to induce magnetic pinning sites in magnetic recording film. The relationship between the surface morphology and the magnetic properties was investigated for TbFeCo films with/without the anodic Al oxidation (AAO) underlayer as an example of hybrid recording media.

2. Experiment

A 500nm thick Al layer with high-purity were deposited onto water-cooling glass substrate by r.f. magnetron sputtering system. This Al film was anodized in sulfuric acid using a two step anodic oxidation process with the voltage from 6 to 20V and temperature from 0 to 40°C for evaluating the pore size and density^[10], the crystal structure of the film was analysed by x-ray diffractometry (XRD), the surface of the anodized alumina was observed by a scanning electron microscope (SEM).

Then TbFeCo film with a thickness of around 90nm was deposited onto this porous structure by RF magnetron sputtering, and subsequently was overcoated with 10nm SiN for the protection from surface oxidation. The background pressure was below 2×10^{-6} Torr and the Ar sputtering pressure was 2mTorr. A composite target consisting of an FeCo

Corresponding Author(Email:miaoxs@mail.hust.edu.cn)

TbFeCo layer. The sputtering parameters, such as forward power, argon pressure, and sputtering time, were optimized for better magnetic properties. For comparison with the properties of the film on the flat surface, TbFeCo thin film was sputtered onto clean glass substrate using the same sputtering parameters in the same chamber, Magnetic properties were measured by using a vibrating sample magnetometer(VSM) and Magneto-optical Kerr Effect (MOKE) tester.

3. Results and Discussion

The x-ray diffraction studies show that no other defined diffraction peak for anodic oxidation Al can be detected and confirm that anodic oxidation Al is in amorphous state. Figure 1 shows the planar-view and cross-section scanning electron microscopy (SEM) images of nanoporous anodic alumina substrate at various anodic voltages and temperature.

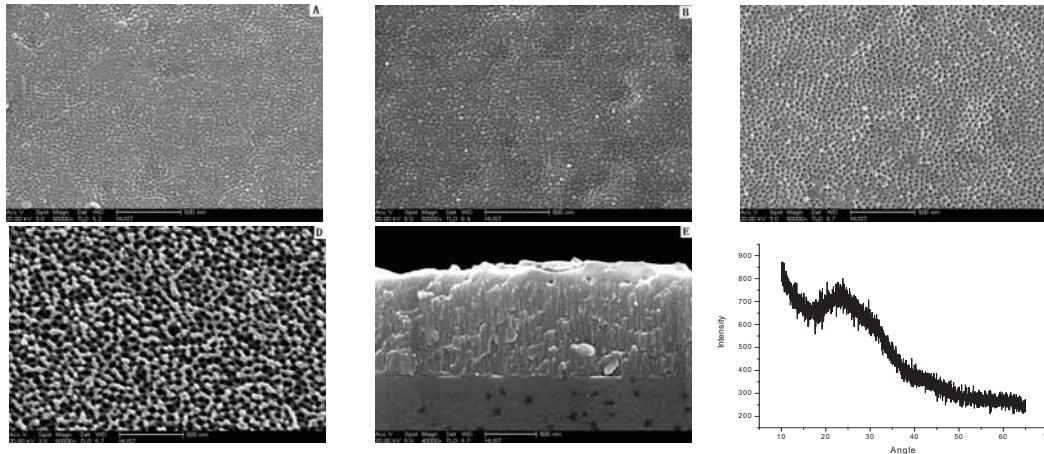


Fig1. SEM photograph of the surface and section of porous alumina with the applied anodic potential and temperature. A(5°C 10V) , B(5°C 14V), C(5°C 18V),D(40°C 18V),E is SEM photograph of the cross section of porous. F is XRD pattern of porous alumina substrate

The average distance of the nearest nanoporous decreased with the anodic voltage, it is 15 nm at the anodic voltage of 10 V and temperature of 5°C, while 50 nm at the anodic voltage of 18 V and temperature of 40°C. The regularity of nanohole arrays depends on the anodization time and concentration of the acid used. With a decrease in the anodization voltage and temperature, the anodization speed gets slower and a time needed for self-organization becomes longer in general^[11]. The diameter of the nanohole could be adjusted by the anodization voltage and temperature.

Figure 2 shows the magnetic hysteresis loops of TbFeCo films on the AAO and on the glass when the measured magnetic field is perpendicular to the film surface. The coercivity (H_c) of TbFeCo films on the AAO is larger than that on the glass, this is due to the fact that the nanoporous structure of AAO can pin the magnetic domain wall of TbFeCo films, but the squareness of TbFeCo on the AAO gets poorer than that on the glass, this maybe bring from the deviation of the granular perpendicular anisotropy axis as growth in the nanoholes. From the magnetic loops, it seems that there are no significant changes in M_s .

The Kerr loops of TbFeCo at wavelength of 780nm are shown in Fig3, the Kerr loops were measured from film side by using the polarizing modulation method. The Kerr rotation angle is 0.2 degrees for the film on the glass substrate, 0.18 degrees for the film on the AAO respectively. From the residual Kerr rotation of each film, it seems that there are no

significant changes.

The dependence of the coercivity (H_c) of TbFeCo film on the AAO hole diameter is shown in Fig. 4. The H_c decreases with the increase of the hole diameter. The maximum coercivity was found to be 5.6 kOe at the AAO hole diameter of 15nm, but it was only about 3.5 kOe for the TbFeCo film on the glass. This is due to the fact that the

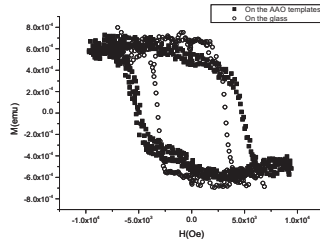


Fig2. Magnetic hysteresis loops of TbFeCo films with and without AAO underlayer measured along the directions perpendicular.

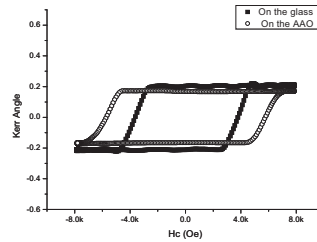


Fig3. Kerr loops of TbFeCo films with and without AAO underlayer

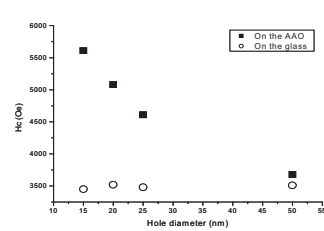


Fig4. Dependence of coercivity with the hole diameter of AAO nanoporous

nanoporous structure of AAO can pin the magnetic domain wall of TbFeCo films. When the AAO hole diameter increase, the effect of pinning would be reduced. Although the coercivity is not enough for realizing ultra high density magnetic recording, it is possible to increase by adjusting the Al anodization condition and TbFeCo film composition.

4. Conclusion

A self-ordered hexagonal array of nanopores was fabricated by anodizing a thin film of Al on glass and the magnetic properties of TbFeCo on this underlayer were studied. The results show that AAO nanopores could increase the coercivity of TbFeCo films without significant changes in M_s and Kerr rotation angle. The coercivity of the system can be controlled by the anodization condition. These results are valuable for the ultrahigh density hybrid recording.

5. Acknowledgments

This work was supported by the Major Project of National Natural Science Foundation of China (No.60490290).

Reference

- [1] M. Alex, A. Tselikov, T. McDaniel, N. Deeman, T. Valet, and D. Chen, IEEE Trans. Magn. **37**, 1244, 2001.
- [2] J. J. M. Ruigrok, J. Magn. Soc. Jpn. **25**, 313, 2001.
- [3] H. Saga, H. Nemoto, H. Sakeda, and M. Takahashi, Jpn. J. Appl. Phys., Part 1 **38**, 1839, 1999.
- [4] H. Katayama, S. Sawamura, Y. Ogimoto, J. Nakajima, K. Kojima, and K. Ohta, J. Magn. Soc. Jpn. **23**, 233, 1999.
- [5] H. Saga, H. Nemoto, H. Sakeda, and M. Takahashi, J. Magn. Soc. Jpn. **23**, 225, 1999.
- [6] H. Katayama, S. Sawamura, Y. Ogimoto, J. Nakajima, K. Kojima, and K. Ohta, J. Magn. Soc. Jpn. **23**, 233, 1999.
- [7] C.-H. Chang and M. H. Kryder, J. Appl. Phys. **75**, 6864, 1994.
- [8] K. Ozaki, K. Matsumoto, I. Tagawa, and K. Shono, J. Magn. Soc. Jpn. **25**, 322, 2001.
- [9] K. Matsumoto, H. Kawano, T. Morikawa, and K. Shono, Jpn. J. Appl. Phys., Part 2 **41**, L691, 2002
- [10] Gapin A. I., Ye X. R., Aubuchon J. F., et al., Journal of Applied Physics, **99**, 08G902, 2006.
- [11] H. Masuda, F. Hasegawa, and S. Ono, J. Electrochem. Soc. **144**, L127, 1997.

Study of recorded mark width change with laser power in HAMR

B.X. Xu¹, H.X. Yuan¹, Sofian MD¹, R. Ji¹, J. Zhang¹, Q.D. Zhang¹ and T.C. Chong^{1,2}

¹Data Storage Institute, A-Star, Singapore

5, Engineering Drive 1, Singapore 117608

²National University of Singapore

Phone: 65-68748512, Fax: 65-67778517, xu_baoxi@dsi.a-star.edu.sg

Abstract

The dependence of the recorded mark width on the laser power for heat assisted magnetic recording is studied experimentally and theoretically. With the laser power increase, the recorded mark width of the perpendicular magnetic media will deviate from its dependence on the beam spot and increase faster. The simulation result with the model including thermal conduction and convection shows that the temperature related thermal conductivity of the material is main reason to cause this deviation.

Key words: heat assisted magnetic recording, thermal effect

Heat assisted magnetic recording (HAMR) has attracted more interests due to its ability to overcome the superparamagnetic effect and push the magnetic recording density to beyond 1Tb/in². In this approach, the laser is used to heat the magnetic media to reduce its coercivity so that the magnetic field of the available magnetic head is strong enough to switch the magnetic domain. During the recording process, the media's thermal profile caused by laser heating may seriously affect the recording performance. Theoretical analysis with thermal Williams-Comstock model showed that the existence of the thermal gradient causes the transition location changes along track direction and cross-track direction with assuming the thermal profiles as Gaussian shapes [1][2]. The broad track widths were caused by higher central temperature and broader temperature distribution [2][3]. The track width broadening with laser power increase was observed in experiment [4], but the trend of track width broadening was not quantified. Thermal erasure on the neighboring tracks is another serious problem in HAMR. It was shown that the erasure was primarily determined by the temperature profile on the media after shining of the laser beam. The sharper the thermal profile is, the more the recording performance improvement can be achieved.

All of above researches show that the thermal profile caused by laser beam affects the recording performance seriously. In this paper, the dependence of the recorded mark width on the laser power for heat assisted magnetic recording is studied experimentally and theoretically.

In the experiment, a perpendicular media with the recording material of CoCrPt is used. The laser beam with wavelength of 405nm is focused on the recording layer. The perpendicular magnetic field is applied from the opposite side of the laser beam through the glass substrate. Fig.1 shows the measured beam spot size and its fitted curve which indicates a good Gaussian shape. The focused beam spot size (FWHM) is 1.5 μ m. In this experiment, the big beam spot

does not affect this study since the dependence of the recorded mark width on laser power is the main concern. The coercivity of the media is 3050Oe. The applied magnetic field is adjustable below 4000G, but in this experiment, the field is set to 2000G which ensures no magnetic domain switched. The media is rotated with the linear speed of 6.5m/s at the focused laser spot position. The recorded marks are measured with magnetic force microscope (MFM).

Before recording, the media is processed by dc-magnetization where the magnetization direction is opposite to the applied magnetic field direction. The laser is modulated to show the contrast of the recorded mark. To avoid the overlapping of the written pattern, the laser is controlled so that its shining only happens during the one complete round of disk rotation.

Fig.2 shows the MFM images of recorded marks at different laser powers and applied magnetic field of 2000G. The dependence of the mark width on the laser power is plotted in Fig.3. As the laser power increases, the mark width increases, and the increase rate changes from large to small, and then large again.

In order to understand the dependence of recorded mark width on laser power, a theoretical model including the thermal conduction and thermal convection is built. In most analysis, the recording material's thermal conductivity is considered constant. In this case, the simulated the recorded mark width is plotted in Fig.3. At the lower laser power, the simulation result is consistent with experimental one. However, at high laser power, the obvious difference between experimental data and theoretical result can be observed. Actually, for most alloy material, as the temperature increase, the material thermal conductivity will increase [5]. This variable thermal conductivity will cause the media's temperature distribution change, and further causes the recorded mark width change. The simulation result with variable thermal conductivity is plotted in Fig.3 too. It is obvious that the experimental result is consistent with the simulation result in all laser power range.

It is concluded that with the laser power increase, the recorded mark width will deviate from its dependence on the beam spot and increase faster. Temperature related thermal conductivity of the material gives main contribution. In the perpendicular magnetic recording with HAMR technology, the single-pole write head will be adopted and the main pole width is wider than the laser beam spot. Therefore, in the cross track direction, the writing magnetic field is constant within the laser spot. This is same with this experiment situation and the conclusion of this study is applicable to it.

Reference

- [1] T. Rausch, J.A. Bain, D.D. Stancil, and T.E. Schlesinger, *IEEE Trans. Magn.* 40, 137(2004)
- [2] M.F.Erden, T.Rausch, and W.A.Challener, *IEEE Trans. Magn.* 41, 2189(2005)
- [3] A. Lyberatos and J. Hohlfeld, *J. Appl. Phys.* 95, 1949(2004)
- [4] K. Kojima, M. Hamamoto, J. Sato, K. Watanabe, and H. Katayama, *IEEE Trans. Magn.* 37, 1406(2001)
- [5] See some alloy's thermal data sheets on website:
<http://www.hightempmetals.com/technicaldata.php>

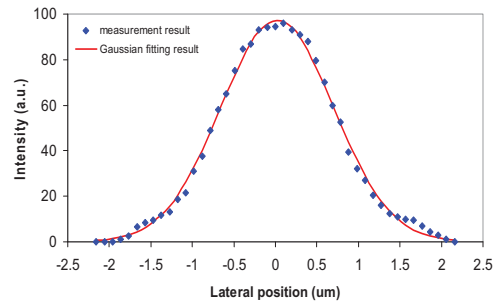


Fig.1 Focused laser beam spot

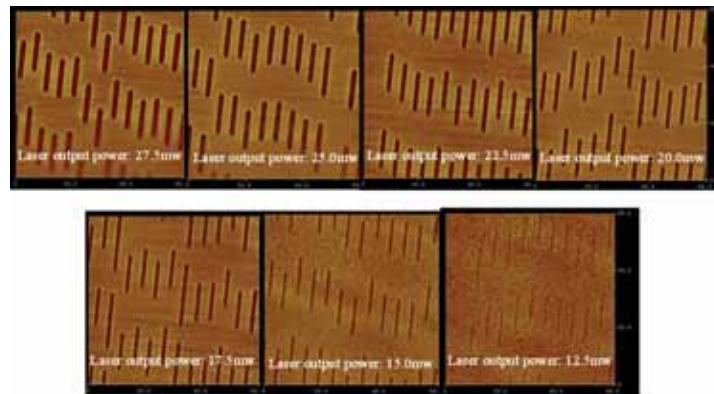


Fig.2 MFM images of recorded marks at magnetic field of 20000e

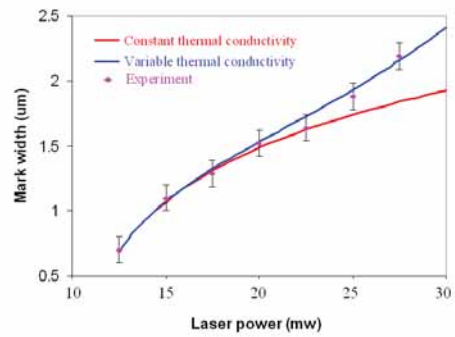


Fig.3 Experiment mark widths and simulation results at different laser powers

Near-Field Optical Coupling and Enhancement in the Surface Plasmon Assisted HAMR (SPAHS) Media

Dong-Soo Lim and Young-Joo Kim*
Center for Information Storage Device (CISD), Yonsei University
134 Shinchon-dong, Seodaemoon-Ku, Seoul 120-749, Korea

ABSTRACT

New structure of ‘surface plasmon assisted HAMR (SPAHS) media’ was studied to increase the near-field optical throughput with an aid of the metal and dielectric interface in the magnetic media. Since the near-field light from HAMR head can be coupled and enhanced easily at the metal-dielectric interface of the SPAHS media, it is expected to increase the optical efficiency for the hybrid recording. Based on the FDTD simulation, the optical intensity of near field light through nano-slit aperture resulted in 23 times higher value inside the SPAHS media than that of inside the conventional magnetic media. The media geometry was also optimized with the consideration of fabrication process.

Keywords: surface plasmon, near-field optics, heat assisted magnetic recording (HAMR), grating, HAMR media, patterned media, discrete track media

INTRODUCTION

The heat assisted magnetic recording (HAMR) and bit patterned media (BPM) are considered as a promising candidate for the realization of the high density magnetic recording to overcome the superparamagnetic limit. However, high resolution patterning process and the high near-field optical throughput with very small spot size are critical challenges to realize over 1 Tb/in² areal density for the BPM and the HAMR technology, respectively. As a solution for the fabrication difficulty in the BPM as well as the low near-field optical throughput in HAMR head, we proposed the ‘Surface Plasmon Assisted HAMR (SPAHS) media’ using the surface plasmon (SP) effect on the magnetic media [1]. Figure 1 shows the schematic diagram of SPAHS structure, which is based on the discrete track media (DTM) structure with the metal and dielectric thin films to generate the surface plasmon excitation at the edge interface of them. This near-field coupling can increase the optical intensity and induce the desired light power to heat the magnetic region locally. In this paper, we investigated the effect of incident light on the surface plasmon enhancement with Au and Ag metal films on the SiO₂ dielectric material. The near-field optical characteristics inside the SPAHS media as well as the interaction between nano-slit aperture and SPAHS media were also studied and analyzed using finite differential time domain (FDTD) simulation.

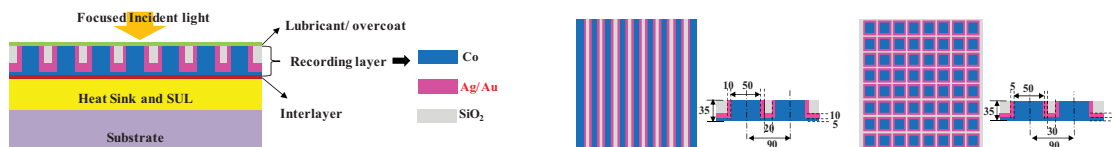


Fig. 1 Design concept of surface plasmon assisted HAMR media

SIMULATION RESULTS AND DISCUSSION

Both types of patterned media such as DTM and BPM can be applied in the SPAHS media as shown in Fig. 1. Since the surface plasmon would be excited at the interface of metal-dielectric film, we reported that both DTM and BPM type of the SPAHS media showed surface plasmon enhancement, resulted in stronger optical intensity, compared to the case of conventional DTM and BPM in the previous report [1]. Because the fabrication of the DTM has a few limitations compared with the BPM as explained above, we have focused on the DTM type SPAHS media in this paper.

*yjkim@yonsei.ac.kr; phone 82-2-2123-6852; fax 82-2-365-8460

To understand the effect of wavelength of the incident light for the surface plasmon enhancement in the SPAH media, the visible range of light was used with the real metals such as cobalt for magnetic layer, silver or gold for metal layer and SiO₂ for dielectric layer. Since the real metals have complex permittivity at optical frequencies [2], a modified Debye model [3] was used to calculate the surface plasmon enhancement in this research. For the FDTD simulation (XFDTD, Remcom Inc.), the linearly x-polarized plane wave was assumed to propagate to the -z-direction as shown in Fig. 2(a). A simulation volume was divided into 2.5nm x 2.5nm x 2.5nm cell unit and the optical intensity was measured at the surface of SPAH media. We have used two different metal layers of Au and Ag with the thickness of 10nm and changed the wavelength of light from 400 to 800 nm. From this simulation, we found that the maximum enhancement occurred at 650 nm wavelength for Ag film and 670 nm for Au film, as shown in Fig. 2(b). Thus, we decided the metal layer as Ag and the light wavelength as 650nm for the calculation of near-field interaction in this research. The optical field distribution on the surface of SPAH media was shown in Fig. 2(c) which resulted in the strong field at the interface of metal and dielectric layers.

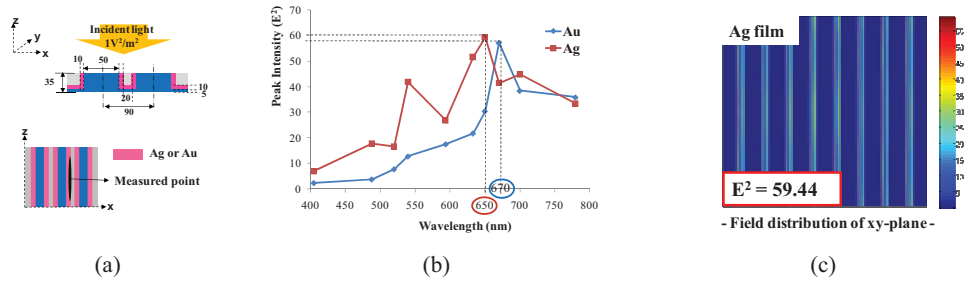


Fig. 2 (a) the schematic diagram of SPAH media for the simulation. (b) The effect of wavelength of incident light on optical intensity for Au and Ag metal film (c) the field distribution on the SPAH media surface with Ag film

The near-field optical interaction between near-field light from nano-slit and SPAH media was examined and shown in Fig. 3. A nano-slit aperture in the perfect conductor material (PEC) was considered as a typical model of the aperture type HAMR head in this research. With the consideration of the flying height, the flying gap of 10nm between the nano-aperture and magnetic media was assumed to calculate the optical intensity and field distribution. To understand the effect of nano-slit size at the inside of SPAH media, we have varied the width of nano-slit aperture from 50 to 90 nm with the fixed length of 300nm. The nano-slit size was studied with the grating structure for the application to the HAMR head in the previous report [4]. These 50nm, 70nm and 90nm width of the nano-slit aperture mean the Co track width, width of Co track with Ag film and track pitch of the proposed structure, respectively. Because near-field optics through the aperture is coupled with the Ag-SiO₂ interface of the SPAH media, the surface plasmons are excited at the near-field region and it provides about 7 times higher intensity at the surface of the SPAH media than that of the case without media. Although small nano-slit size of 50nm x 300nm is preferred, the optical intensity and spot size with the nano-slit apertures of 70nm x 300nm and 90nm x 300nm showed similar enhancement, which means that this SPAH media is less sensitive to the nano-slit size to give more tolerance for the HAMR head fabrication.

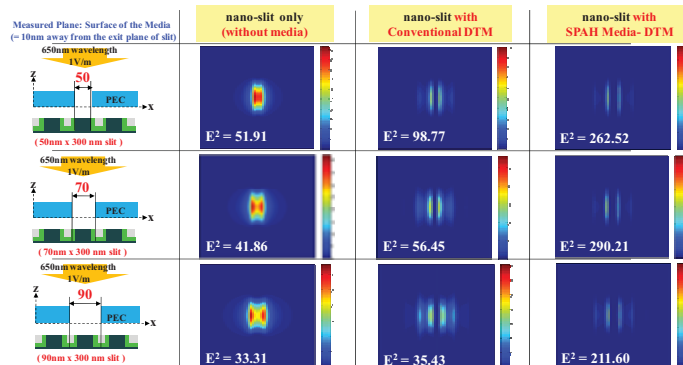


Fig. 3 Near-field optical interaction between HAMR Head and SPAH media

The near-field coupling interaction between the near-field optics and SPAH media was also examined and resulted in the enough tolerance in the relative position of the nano-slit aperture and SPAH media. Another important issue of the HAMR technology is that the light through the HAMR head should be sufficiently propagated into the media to increase the temperature of the track. Figure 4 shows the propagation of light through nano-slit aperture into the SPAH media, which compares with the conventional DTM. Using 70nm x 300nm nano-slit aperture, the optical intensity at the inside of SPAH media increases about 23 times in the maximum compared to the value of the conventional DTM. The optical intensity through the nano-slit aperture decreases as the light propagates into the magnetic media as shown in the conventional DTM. However, the surface plasmon wave at the surface of the SPAH media propagates through the interface to increase the optical intensity at the inside of the SPAH media. Thus, this propagation wave is absorbed by the magnetic layer to increase the media temperature locally which is essential for reducing the coercivity of magnetic media for the HAMR application.

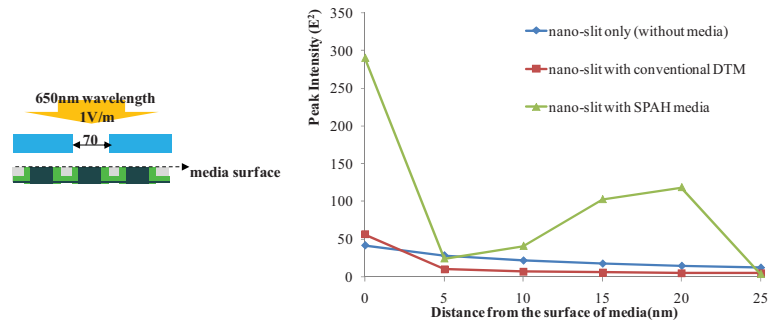


Fig. 4 The near-field optical intensity in the inside of SPAH media as being propagated into the media

SUMMARY

New structure of ‘Surface Plasmon Assisted HAMR (SPAH) Media’ was studied to understand the near-field optical interaction between HAMR head and SPAH media. Since the near-field light through the nano-slit aperture excites surface plasmon at the Ag-SiO₂ interface and is propagated through the interface, new proposed structure can generate the enhanced and confined optical intensity at the inside of media. Based on the FDTD simulation, the optical intensity of near-field light through nano-slit aperture resulted in 23 times higher value at the inside of SPAH media than that of inside the conventional magnetic media which is essential for reducing the coercivity of magnetic media for the HAMR application. Moreover, since it is possible to fabricate the SPAH media with an additional metal and dielectric layer deposition from the current DTM processing, it is expected that this SPAH media is very attractive to be applied to the HAMR technology.

ACKNOWLEDGEMENT

This work is supported by the Seoul R&BD Program NT070126.

REFERENCES

- [1] Dong-Soo Lim and Young-Joo Kim, “Proposal and design of new HAMR media using surface plasmon enhancement”, MORIS 2007, PB4 (2007)
- [2] Edward D. Palik, [Handbook of optical constants of solids], Academic Press, San Diego, Vol. I, pp. 294, 356 (1998)
- [3] Karl S. Kunz and Raymond J. Luebbers, [The Finite Differential Time Domain Method for Electromagnetic], CRC press, New York, Chap 8, p. 123 (1993)
- [4] Dong-Soo Lim and Young-Joo Kim, “Enhancement of Near-Field Optical Throughput using Double Grating Structure for HAMR Head”, APMRC 2006, BS-01-01 (2006)

Design and Performance Evaluation of Light Delivery for Heat Assisted Magnetic Recording

Eunhyoung Cho*, Sung-Mook Kang³, J Brian Leen², Sung-Dong Suh¹, Jin-Seung Sohn¹,
Lambertus Hesselink², No-Cheol Park³, Young-Pil Park³

1. Samsung Advanced Institute of Technology (SAIT), P.O.Box 111, Suwon 440-600, Korea
Phone: +82+31+280-8048, Fax: +82+31+280-6879

*E-mail: cchoeh@samsung.com

2. Dept. of Applied Physics, Stanford University, 420 via Palou Mall, Stanford, California 94305
USA

3. Center for Information Storage Device, Yonsei University, 134 Shinchondong, Seodaemungu,
Seoul, Korea, 120-749

ABSTRACT

In this paper, we present a description of the design, fabrication and evaluation of light delivery using a C-shaped nano-aperture for optically-assisted magnetic recording. A light delivery which had a C-shaped nano-aperture for HAMR was designed, with respect to the resonance characteristic related to the geometry and the metal layer, by XFDTD simulation tool. And also, it was fabricated by using focused ion beam (FIB) lithography. Finally, we evaluated the performance of a fabricated light delivery system utilizing a nano-aperture.

Keywords: HAMR(Heat Assisted Magnetic Recording), FDTD(Finite Difference Time Domain), Power throughput

1. INTRODUCTION

There is an ever growing demand for data storage devices that can store more data in a smaller area [1]. Heat Assisted Magnetic Recording (HAMR) provides a means of increasing the data recording density by combining realistic write fields with very-high-coercivity and thus stable medium to achieve very-high-density magnetic recording [2]. In order to enhance the areal density of thermally-assisted recording with light, optical resolution beyond the diffraction limit can be achieved by using a metallic nano-aperture in a near-field system [3].

In this study, the goal is to investigate the feasibility of combining a GMR head with a high optical throughput nano-apertures developed to create an efficient HAMR system. Therefore, we present a description of the design, fabrication and evaluation of light delivery using a C-shaped nano-aperture for optically-assisted magnetic recording. To determine the dimensions of a C-shaped nano-aperture configuration, an optimal design parameter α was used (see Fig. 1) and calculated by simulation with commercial FDTD code 'XFDTD v6.3'. The resonance characteristics of a nano-aperture under thickness variation of the metal layer were analyzed to facilitate design and fabrication of light delivery having enhanced power throughput and a spot size under 100nm. Lastly, we evaluated the performance of a fabricated light delivery system utilizing a nano-aperture

2. DESIGN OF A LIGHT DELIVERY WITH C-SHAPED NANO-APERTURE

A C-shaped nano-aperture for HAMR light delivery was designed with a focus on the cutoff frequency's relation to ridge height variation and the resonance property's relation to thickness variation of the metal. As a first design step, we find that the cutoff frequency increases as the design parameter α decreases (shown in Fig. 1). This shows that the choice of α will depend on the device's operating wavelength. We have chosen to use laser diodes at a wavelength of 780nm and the simulation indicates that, for this wavelength, an α value of 90nm should be used in the fabrication of the structure. The

frequency response of the $\alpha = 90\text{nm}$ aperture in a 10nm thick gold film is shown in Fig. 2, with a maximum peak at the design frequency of 651.5[THz].

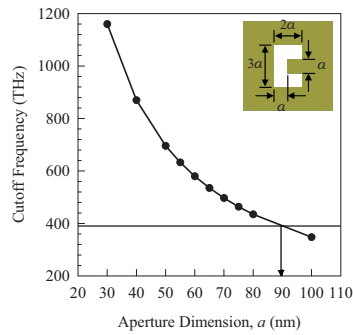


Fig.1 Relation of the optimal design parameter α and the cutoff frequency

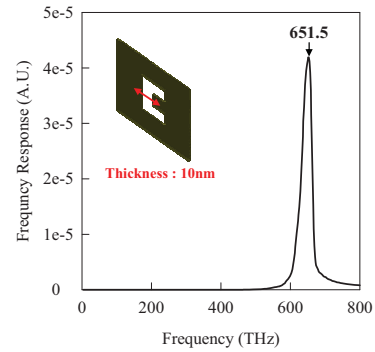


Fig.2 Frequency response at 651.5 [THz]

Next, we analyzed the relation of the frequency response characteristics and the Metal layer thickness. Through FDTD simulation, we find that more transmission modes are generated as the thickness of the metal layer is increased (shown in Fig. 3). Examining the electric field intensity, we find that the $\alpha = 90\text{nm}$ nano-aperture has a maximum at a thickness of 280 nm (see Fig. 4). The effect of ridge height was also simulated and to achieve a large power throughput (PT) and a small spot size, we selected a ridge height of 70nm. The simulation result of the relation between a PT and a ridge height are shown in Fig. 5.

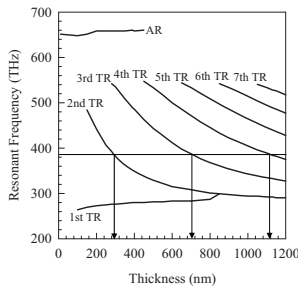


Fig.3 Relation of the resonance frequency and the metal thickness

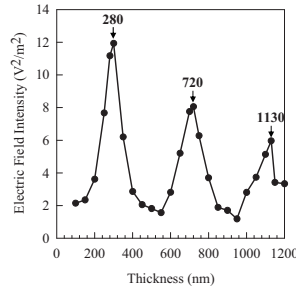


Fig.4 Electric field intensity with respect to the metal thickness

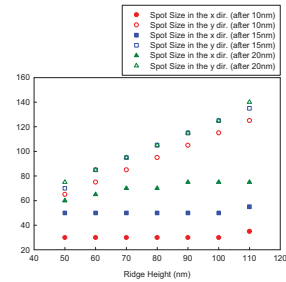


Fig. 5 Spot size due to ridge height

3. FABRICATION AND EVALUATION

The waveguide fabrication procedure is shown like Fig. 6. Figure 7 (a) shows the fabrication by focused ion beam (FIB) lithography of the initial design for light delivery with a C-shaped nano-aperture. Figure 7 (b) shows the improved aperture attached to a polymer waveguide. The polymer waveguide and nano-aperture were fabricated at a low temperature to demonstrate compatibility with the low temperature fabrication requirements of magnetic write heads. The C-shaped nano-aperture fabricated by FIB presents two possible problems: the rounding of edges/corners and the degradation of the ridge due to overdosing. However, we have shown by FDTD simulation that the round edges/corners have no effect on the performance of a nano-aperture. However, degradation of the ridge does reduce performance and thus it is important to select the optimal dose time during the fabrication process. To evaluate the performance of the

fabricated nano-aperture we used a rotating a probe to determine spot size variation with respect to source angle. Figure 8 is showing NSOM image. The orientation of the C with respect to the elliptical probe aperture will have an important effect on the recorded spot size and so image were recorded at several relative orientations. Figure 9 is showing the spot size variation for various probe orientations.

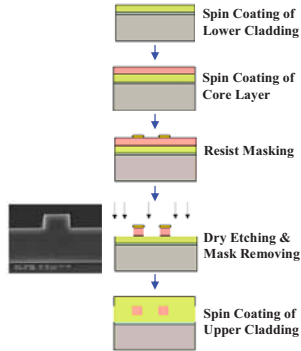


Fig. 6. Waveguide fabrication procedure

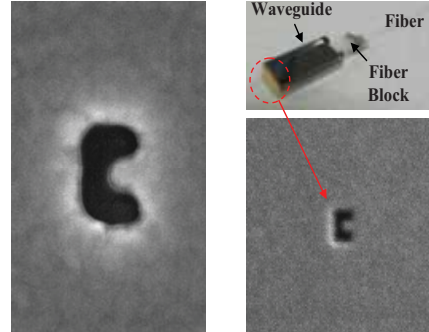


Fig. 7 (a) Initial fabricated C-shape nano-aperture (b) Improved C-shape nano-aperture and light delivery system

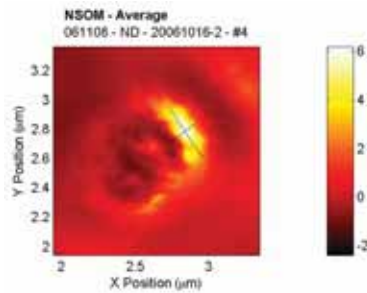


Fig.8. NSOM image with waveguide at 45 degree

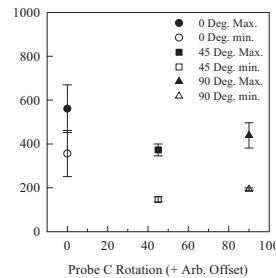


Fig. 9 Spot size according to the orientation variation of the probe

4. CONCLUSIONS

We have developed and evaluated an optimal light delivery system with the C-shaped configuration that has the maximum electric field intensity and throughput for optically-assisted magnetic recording. We have shown that the resonance modes of a C-shaped nano-aperture are related to the geometry and the metal layer thickness. Obtaining an optical intensity maximum is a vital factor in selecting the metal layer thickness. Finally, we have found that it is important to choose the optimal dose time for reducing degradation of the ridge during fabrication.

REFERENCES

[1] Michael A. Seigler et al., "Progress and Prospect in Heat Assisted Magnetic Recording", Optical Data Storage 2007, TuA1
 [2] Jaap, J. M. Ruigrok "Limits of conventional and thermally-assisted recording", J. Magn. Soc. Japan, 25, 313-321 (2001)
 [3] Xiaolei Shi and Lambertus Hesselink, "Ultra light transmission through a C-shaped nanoaperture", OPTICS LETTERS / Vol.28, No. 15 / August 1, 2003

Patterning for ultra-high density multi-dimensional multi-level ROM storage

J.Y. Sze*¹, L.P. Shi¹, D. N. Sutanto², C. Y. Chong¹, J. M. Li¹, G. Q. Yuan¹, L. D. Ng¹, C. L. Gan² and T.C. Chong^{1,3}

¹Data Storage Institute, Agency for Science, Technology and Research (A*STAR), 5 Engineering Drive 1, Singapore 117608

²School of Materials Science and Engineering, Nanyang Technological University, Nanyang Avenue, Singapore 639798

³Department of Electrical and Computer Engineering, National University of Singapore, 4 Engineering Drive 3, Singapore 117576
Phone: +65 6874 5091, Fax: +65 67778517
Email: SZE_Jia_Yin@dsi.a-star.edu.sg

1. INTRODUCTION

Multi-dimensional multi-level (MDML) recording is one of the methods to achieve ultra-high density data storage in optical media. Multi-level signal recording has been proposed earlier as an effective method for increasing disk capacity and data transfer rate [1]. However, current multi-level technologies use only one parameter of the light, such as reflection or polarization. In order to enhance the capability of multi-level recording, MDML recording technology has been proposed [2]. The proposed MDML disc has a structure that makes use of both multi-level reflection and the change in orientation of the elliptical shape mark. The angle, θ of the orientation of the elliptical shape with the track provides one dimension signal with multi-level signals of $\theta_1, \theta_2, \theta_3, \dots, \theta_n$. The reflection provides another dimension with multi-level reflection signals $R_1, R_2, R_3, \dots, R_m$ caused by the multi-depth pits. An optical system has been designed to control the elliptical shape of laser beam and the angle of pattern [2]. The system can also be used to determine the readout signal. As for realizing MDML ROM substrates, the novel use of different phase change materials for formation of multi-depth pit structure is being explored in this paper.

The formation of multi-depth pit structure is investigated by the use of phase change lithography and a MDML optical writing strategy. This technology utilizes the difference in etching rates for amorphous and crystalline states of phase change materials. The etching rate of the crystalline regions is greater than the amorphous regions and this selectivity etching of crystalline regions enables the formation of marks after etching. To achieve multi-depth pit structure, two or more phase change materials can be used to form a thin film stack. If the crystallinity of these phase change materials is controlled, then this structure can be used to form multi-depth pits after etching. The phase change process depends on the crystalline temperatures of the phase change materials. Thus, the wet etching characteristics of different phase change materials are first investigated at their crystallinity temperature (T_c). Suitable materials are chosen to be investigated in the design and fabrication of multi-level pit depths for MDML ROM master disc.

2. EXPERIMENTS

The crystallinity temperature of phase change thin films, $Sb_{70}Te_{30}$, $GeSb_4Te_7$, $Ge_2Sb_2Te_5$, $GeTe$ and $AgInSbTe$ were investigated by differential scanning calorimetry (DSC). Thick films of about 500 nm of each type of phase change materials were sputtered on polycarbonate substrates using Balzer sputtering system. The films were carefully removed from the polycarbonate into the aluminum crucible. The sample was placed beside an empty crucible (reference sample) in the DSC and the materials changed from amorphous to crystalline phases when the temperatures were increased from room temperature to 600 °C. For wet etching, the thin films of at least 100 nm were first deposited on silicon wafers. Samples were placed in a high temperature furnace and annealed at their T_c for 15 minutes. Both as-deposited and annealed samples were placed in NaOH solvent of different concentrations

for similar amount of time. The concentrations are 0.025 wt%, 0.4 wt% and 4 wt%. The samples were then rinsed with deionised water and blow dry with N₂ gas before being examined under atomic force microscope (AFM, Veeco 3100).

It was found that the annealed samples were easily lift off from the substrates as it appeared from the initial experiments that the annealing process had introduced stress into the films' structure. During etching, the films delaminated easily from the substrate. The use of an adhesion layer to prevent delamination between the phase change film and the substrate was examined. A thin layer of ZnS-SiO₂ was sputtered first on the Si before the phase change materials was sputtered. The etching rates changed significantly with a layer of adhesive layer.

The design and fabrication of the thin film stack was carried out. The thin film stack consisted of two or three layers of phase change materials. An adhesion layer was also sputtered on a planar polycarbonate disc. Multi-pulse writing strategy with varying power levels were used to write the disc using a MDML optical tester and writing strategy developed earlier [3]. The disc was etched in two different concentration of NaOH etchant. The resultant marks were analyzed by AFM.

3. RESULTS AND DISCUSSION

Table 1 shows the T_c and T_m obtained from the DSC measurements. From these data, the phase change materials with a wide range of T_c were selected for further investigations. GeSb₄Te₇, Ge₂Sb₂Te₅ and GeTe have been investigated for their wet etching characteristics. The etch depth with different etch times of Ge₂Sb₂Te₅ in 0.4 wt% is shown in Fig. 1. At concentration of NaOH of 0.4 wt% or higher, it was found that some of the annealed films were etched off very easily in 10 minutes. This resulted in difficulty in obtaining an accurate profile with the AFM and poor selectivity. Thus, using etchant of lower concentrations 0.025 wt%, the selectivity for Ge₂Sb₂Te₅ and GeSb₄Te₇ has been obtained.

Material	Crystalline temperature, T _c			Melting Temperature, T _m		
	Onset T _c (°C)	Peak T _c (°C)	Offset T _c (°C)	Onset T _m (°C)	Peak T _m (°C)	Offset T _m (°C)
Sb ₇₀ Te ₃₀	126.1	141.7	159.2	520.1	528.1	540.6
GeSb ₄ Te ₇	136.5	147.9	159.9	574.6	591.2	600.1
Ge ₂ Sb ₂ Te ₅	149.4	165.1	179	572.1	597.4	-
AgInSbTe	168.9	179	191	509.9	524.6	540
GeTe	171.4	193	209.6	-	-	-

Table 1 Different crystallinity and melting temperatures of phase change materials obtained from DSC measurements

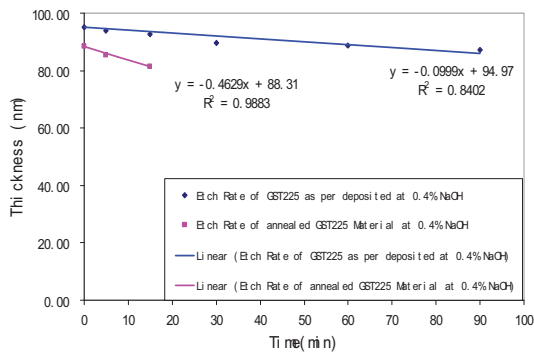


Fig. 1 Etching rate of Ge₂Sb₂Te₅ using 0.4 wt% NaOH

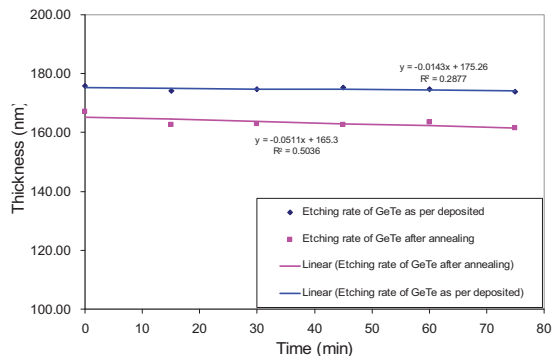


Fig. 2 Etching rate of GeTe (with ZnS-SiO₂) using 0.025 wt% NaOH

A thin layer of adhesion layer, ZnS-SiO₂ was sputtered below the phase change films in order to reduce delamination and improve selectivity. From the measurement of the etch depth using AFM, there is not much etching on both as-deposited and annealed samples at same concentration of 0.4 wt% even after 30 minutes. This shows that the layer of ZnS-SiO₂ has retarded the etching process. As for GeTe, with the adhesion layer, the AFM results, as shown in Fig. 2, showed the etching was gradual and uniform. The etching time was up to 70 minutes and the selectivity was 3.53. The delamination of the films was not observed.

Three types of phase change materials were sputtered on top of the adhesion layer on a polycarbonate planar substrate. Marks with varying power levels were written on the thin film stack. The thin film stack is shown in Fig. 4. The top layer of GeTe was sputtered thicker than the other layers to ensure that as the lower crystalline regions were etched away, the top layer of GeTe will not be fully etched away. Multi-level pulses with varying powers were used to write the marks with equal spaces. The input writing strategy for the multi-level pulse is illustrated in Fig. 5. This caused the amorphous thin film stacks to have different levels of crystalline regions. The crystalline regions were then etched in 0.4 wt% concentration to leave behind the amorphous regions. The resultant profiles with varying pit depth were analyzed using AFM.

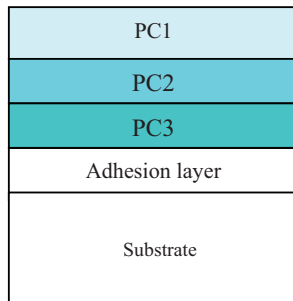


Fig. 4 Design of multi-layer structure

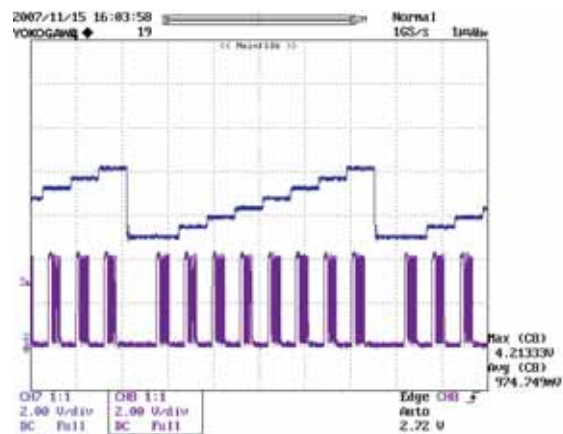


Fig. 5 Input source writing strategy

4. SUMMARY

Phase change materials were thermally annealed and their wet etching characteristics in NaOH at different concentrations were determined. This technology has been proposed as a mastering technology to fabricate multi-depth pits for MDML ROM discs by using several layers of phase change materials. Experiments were carried out to show the feasibility of the proposed methodology to form multi-depth pits using a multi-level pulse with varying writing power. Together with the optical system for controlling the elliptical shape of the mark, the MDML ROM disc can be realized.

REFERENCES

1. B. D. Terris, H. J. Marnin, and G. S. Kino, Appl. Phys. Lett. **65**, 388 (1994).
2. L.P. Shi *et al.*, ISOM'07, We-J-20, Singapore (2007)
3. W. L. Tan *et al.*, ISOM'07, We-I-36, Singapore (2007)

Application of Polynomial Regression and Re-sampling Method to Estimate Life Time of Optical Disk

Kunimaro Tanaka, Keisuke Fujiwara
 Teikyo Heisei university
 2289-23, Uruido, Ichihara, Chiba, 290-0193, Japan

Abstract

Re-sampling and linear regression is used for optical disk life estimation. However, Arrhenius plot bends sometimes. Experimental result of application of polynomial regression is reported.

1. Introduction

The digitization of cultural heritage is one of important methods to preserve present culture to our posterity. There are type of culture which can be preserved by digitization like music and video. The optical disk is most promising long term storage media for this purpose. In order to keep digital heritage longevity of storage media is important. This paper explains application of polynomial regression method to estimate life time of optical disks.

2. Life Test Project on DVD

The Digital Contents Association of Japan (DCAj) has needs to preserve own contents. It conducted the project to evaluate life time of DVD available in the market in order to collect information for improving life time of optical disks. The fund was from Keirin race. Tested disks were DVD-RAM 5 brands, DVD-RW 5 brands and DVD-R 8 brands. They were bought at a large electronic store in Tokyo. Following initial items were measured before the life test. They were PI error, BER, Jitter Reflectivity, Modulated amplitude, Asymmetry of signal and disk tilt. Xenon Lamp test and Hydrogen sulfide test were also conducted. [1]

3. Arrhenius method and Re-sampling method

In order to estimate life time of optical disks, Arrhenius method was used for simplicity. The life time was defined for the worst case storage condition as 30 degree centigrade and 80 % RH. It means the the worst case expected life time was measured. The stress conditions for measurement were 85 degree, 80degree, 75 degree and 65 degree in centigrade. The humidity was 80%RH in all cases. The end of life was defined as the time when number of Inner parity errors (PI error) reaches 280 for DVD-RW and DVD-R disks and 10^{-3} Byte error rate for DVD-RAM disks. There were brands of disks showed life time of more than 30 years. However, not all brand showed good result. There were disks which did not conform to criteria of DVD forum from the beginning. Following life time study was

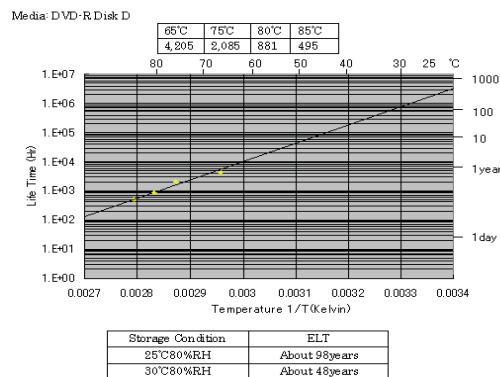


Fig.1 Arrhenius plot of DVD-R D

conducted to selected good quality disks.

Figure 1 show the Arrhenius plots of DVD-R D brand for example. Points are average value of life time at each stress condition. Data number at each stress condition were 6 except 10 discs at 65 degree.

The re-sampling method was introduced to analyze Arrhenius plot, It's advantage is (1). Interval estimation becomes possible.(2) Unlike traditional static estimation, distribution function of universe does not have to be defined. [2][3]

The regression was done using formula (1).

$$y = a + bx \tag{1}$$

y stands for es plynomal regression was applied.

repeated 1000 histogram was shown in figure 2. The interval estimation is possible from the histogram. Because this method is powerful statistical method, the bootstrap method was proposed to Ecma International meeting and employed in Ecma life expectancy standard .and ISO/IES life expectancy standard later on.[4][5]

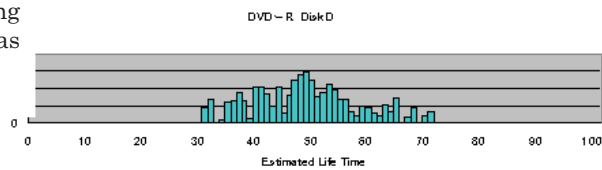


Fig.2 The distibution of ELT of DVD-R D

4. Polynomial regression

When we observe the figure 1 carefully, the plot line tends to bend at lower temperature.

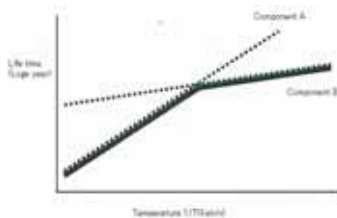
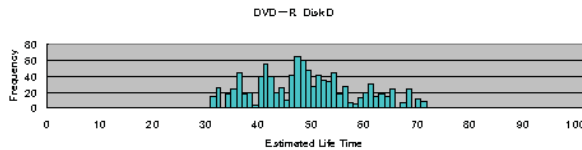


Fig.3 The bent Arrhenius plot



The histogram of ELT obtained by polynomial regression (Evaluator1)

Fig.4 Histogram by polynomial regression

Originally Arrhenius plot is straight line, but the plot tend to bend at lower stress condition sometimes. The cause of this bent is as follows. The recording layer of the optical disk has composed of multiple type of layers. Each layer has different activation energy. The accelerated life time (ALT) at each stress condition is decided by the component of the layer which has the shortest ALT. Figure 3 explains the situation. The component A has shorter ALT than component B at high stress region and vice versa at lower temperature. The polynomial regression instead of linear regression was tried. The regression formula was shown in formula 2.

$$y = a + bx + cx^2 \tag{2}$$

The obtained histogram using formula 2 is shown in figure 4.

The median and standard variation of histograms were compared. They are shown in table 1.

The histogram of polynomial regression was shifted to shorter life time a little bit than linear regression's one. However, shift was very small because bent was small. In order to get better estimation using polynomial regression the data at lower stress conditions have to be measured. However, this measurement gives another burden to us. The measurement at 65 degree has consumed about three years. When a discs whose Arrhenius plot bent more than DVD-R D will appear in the future, the polynomial regression will gives better result than linear regression. Because the space of the summary is very small, I can not show all results. I hope we can discuss more data at the conference..

Table 1 Comparison of regression (years)

	Median	Standard variation
Linear regression	48	89
Polynomial regression	47	193

5. Conclusion

Arrhenius plot is often used to estimate life expectancy test of optical disks. However, the plot tends to bend sometimes because optical disk is composed of materials whose activation energies are different. The combination of re-sampling method and polynomial regression might be useful tool for such case.

6. Acknowledgement

Authors wish to express our appreciation to useful guidance by Dr. Prof Giichiro Suzuki of Teikyo Heisei University. All data used in this study was supplied from project of DCAj. Authors wish to thank for kind offer of those valuable data.

This study was subsidized by the Japan Keirin Association through its Promotion funds from KEIRIN RACE and was supported by the Mechanical Social Systems Foundation and the Ministry of Economy, Trade and Industry.

Reference

- [1] "A Feasibility Study on Development of Optical Disk Medium for Long-Term Storage," report of The Mechanical Social System Foundation and The Digital Content Association of Japan, 16-F-9 March 2005.
- [2] A.C. Davison, D.V. Hinkley and G.A. Young, "Recent developments bootstrap methodology", Statistical Science 18-2, 141-157, 2003
- [3] "Interval Estimation of Optical Disks Life Time Using the Boot Strap Method", pp. 134 – 142, Feasibility study on development of Optical Disk, Medium for Long-Term Storage, report of The Mechanical Social System Foundation and The Digital Content Association of Japan, 17-F-5 March 2007 (in Japanese)
- [4] Ecma 379 (2007)
- [5] ISO/IEC-JTC1 IS10995 (2008)

Crystallization Kinetics and Recording mechanisms of *a*-Ge/Ni Bilayer for Write-once Blue-ray Disk

Yung-Chiun Her and Jyun-Hung Chen

Department of Materials Science and Engineering, National Chung Hsing University, 250 Kuo-Kuang Rd., Taichung 40227, Taiwan
Tel: +886-4-22859112, Fax: +886-4-22857017, E-mail: ycho@dragon.nchu.edu.tw

1. Introduction

Amorphous Si (*a*-Si) film, demonstrating the advantages of environmental friendliness and simple fabrication process, has been adopted as the recording layer for write-once blue-ray disk.¹⁾ However, the recording sensitivity and crystallization temperature of *a*-Si (~700°C) recording film need to be reduced to increase the recording speed and lower the recording power.²⁾ It is well-known that metal induced crystallization can dramatically reduce the crystallization temperature and shorten the crystallization time of *a*-Si. As a result, the *a*-Si/Cu and *a*-Si/Ni bilayer recording films were proposed for use in the write-once blue-ray disk, in which the crystallization temperatures of *a*-Si films induced by thin Cu and Ni metal layer were reduced to 480 and 350°C, respectively.^{2, 3)} Germanium (Ge) has similar physical and chemical properties as Si, however the crystallization temperature of *a*-Ge (~400-420°C) is much lower than that of *a*-Si.⁴⁾ Accordingly, lower recording power and higher recording speed will be expected for the write-once blue-ray disk with a *a*-Ge/metal bilayer recording film. In this work, we investigated the crystallization kinetics of *a*-Ge/Ni bilayer recording film under thermal annealing. The microstructural changes of *a*-Ge/Ni bilayer at different heating temperatures were examined to illuminate the recording mechanism for write-once blue ray recording.

2. Experimental procedures

a-Ge/Ni bilayer recording films with thickness ratios of 20:1 and 10:1 were deposited on Corning 7059 glass substrates by an ion beam assisted deposition system. The thickness of *a*-Ge layer was fixed at 20 nm, while the thicknesses of Ni ultrathin films were controlled at 1 and 2 nm. The crystallization kinetics of the as-deposited *a*-Ge/Ni bilayer recording films under nonisothermal annealing was analyzed quantitatively by monitoring the reflectivity variation with temperature or time during the heating process. The crystalline structures of the *a*-Ge/Ni bilayer before and after thermal annealing at various temperatures were identified by the grazing incident x-ray diffractometer (GIXD) and transmission electron microscopy (TEM).

3. Results and discussion

Figures 1(a) and 1(b) show the reflectivity variations with temperature for the as-deposited *a*-Ge/Ni bilayer recording films with thickness ratios of 20:1 and 10:1, respectively, at heating rates of 5, 10, 20, and 40°C/min. For the *a*-Ge/Ni bilayer recording film with a thickness ratio of 20:1, a steep reflectivity increase was found to take place at temperatures around 410°C, representing that a structural change occurred. As the thickness ratio was decreased to 10:1, the *a*-Ge/Ni bilayer recording film exhibited a three-stage reflectivity change during the heating process. The first one with a slow decrease in reflectivity occurred in the temperature range between 90 and 190°C, the second one with an increase in reflectivity took place in the temperature range between 210 and 245°C, while the third one with an abrupt increase in reflectivity arose in the vicinity of 390°C, implying that three different structural changes occurred during the heating process. To identify the structural phase transition corresponding to each reflectivity change, the structures of *a*-Ge/Ni bilayer recording films before and after annealing at various temperatures were examined by GIXD and TEM. Figures 2(a) and 2(b) show the GIXD diffraction patterns of the *a*-Ge/Ni bilayer recording films with thickness ratios of 20:1 and 10:1, respectively, before and after annealing at 200, 300, and 500 °C. For the *a*-Ge/Ni bilayer recording film with a thickness ratio of 20:1, the microstructure of the bilayer recording film was amorphous in the as-deposited state and remained amorphous after annealing at 200°C. After annealing at 300°C, the formation of NiGe phases was observed. As the annealing temperature was further increased to 500°C, in addition to the existing NiGe phases, crystalline Ge could also be observed. Obviously, the steep reflectivity increase at ~ 410°C observed in the *a*-Ge/Ni bilayer recording film with a thickness ratio of 20:1 can be attributed to the crystallization of *a*-Ge. For the *a*-Ge/Ni bilayer recording film with a thickness ratio of 10:1, the microstructure of the bilayer recording film was also amorphous in the as-deposited state. After annealing at 200°C, the Ni₅Ge₃ phases were observed. After annealing at 300°C, the metastable Ni₅Ge₃ phases would disappear and transform to the stable NiGe phases. As the annealing temperature was further increased to 500°C, the crystallization of *a*-Ge could occur. Figures 3(a)-3(d) also show the TEM bright field images and selected area diffraction (SAD) patterns of the *a*-Ge/Ni bilayer recording film with a thickness ratio of 10:1 before and after annealing at 200, 300, and 500 °C for 3 min. Similar to GIXD's results, amorphous Ge and Ni were observed in the as-deposited *a*-Ge/Ni bilayer recording

film. After annealing at 200°C, different grains with size less than 30 nm in diameter could be distinguished and new diffraction rings corresponding to a Ni₅Ge₃ phase were found. However, Ge still remained as an amorphous phase. As the annealing temperature was increased to 300°C, new NiGe phases were identified from the diffraction patterns. Meanwhile, no *c*-Ge phase was detected. As the annealing temperature was further increased to 500°C, in addition to the existing NiGe phases, the crystalline Ge (*c*-Ge) phases were observed. It is evident that as the *a*-Ge/Ni bilayer recording film with a thickness ratio of 10:1 was heated above ~ 90°C, *a*-Ge would start to react with Ni to form Ni₅Ge₃ phases, giving rise to the slow decrease in reflectivity. As the temperature was increased, the metastable Ni₅Ge₃ phases would transform to the thermodynamically favored end phase, NiGe, leading to the increase in reflectivity in the temperature range of 210-245°C. As the temperature was further increased to ~ 390°C, the unreacted *a*-Ge would crystallize to *c*-Ge, resulting in the steep rise of the reflectivity.

Figures 1(a) and 1(b) also show that as the heating rate was increased, the occurrence of reflectivity changes in the *a*-Ge/Ni bilayer recording film shifted to higher temperatures. The formation temperatures of Ni₅Ge₃ and NiGe phases and the crystallization temperature of *a*-Ge were defined as the temperatures at the midpoints of reflectivity changes. As the heating rates were increased from 5°C/min to 10, 20, and 40°C/min, for the *a*-Ge/Ni bilayer with a thickness ratio of 10:1, the formation temperatures of Ni₅Ge₃ were increased from 134°C to 141, 146, and 157°C, respectively, the formation temperatures of NiGe were increased from 215°C to 220, 227, and 248°C, respectively, and the crystallization temperatures of *a*-Ge were increased from 385°C to 390, 396, and 402°C, respectively. Meanwhile, the crystallization temperatures of *a*-Ge for the *a*-Ge/Ni bilayer with a thickness ratio of 20:1 were increased from 407°C to 413, 419, and 428°C, respectively. These temperature shifts with increasing heating rate can be related to the activation energies for the Ni₅Ge₃ and NiGe phase formations and crystallization of *a*-Ge using Kissinger's equation. From the slopes of Kissinger's plots, as shown in Figure 4, the activation energies for the Ni₅Ge₃ and NiGe phase formations and the crystallization of *a*-Ge for the *a*-Ge/Ni bilayer with a thickness ratio of 10:1 were determined to be 1.31±0.14, 1.81±0.22, and 4.53±0.12 eV, respectively, while the activation energy for the crystallization of *a*-Ge for the *a*-Ge/Ni bilayer with a thickness ratio of 20:1 was determined to be 3.96±0.28 eV.

In general, the crystallization of the *a*-Ge film was completed at 400-420°C. Inserting a Ni metal thin layer can only slightly reduce the crystallization temperature of *a*-Ge. Nevertheless, the crystallization temperature of *a*-Ge/Ni bilayer is still ~85°C lower than that of *a*-Si/Cu bilayer,⁵⁾ which is currently adopted by the commercial write-once blue-ray disk. However, the activation energy for crystallization of *a*-Ge induced by Ni is ~1.2 eV higher than that of *a*-Si induced by Cu. Therefore, higher archival stability and lower recording power and data-transfer-rate may be expected in the write-once blue-ray disk adopting *a*-Ge/metal bilayer as a recording film.

4. Conclusion

As the *a*-Ge/Ni bilayer recording film was heated, *a*-Ge would start to react with Ni to form Ni₅Ge₃ phases at ~ 90°C, and then the metastable Ni₅Ge₃ phases would transform to the thermodynamically favored NiGe phase in the temperature range of 210-245°C. Finally, the unreacted *a*-Ge would crystallize to *c*-Ge at ~ 390°C. The activation energies for the Ni₅Ge₃ and NiGe formations and the crystallization of *a*-Ge for the *a*-Ge/Ni bilayer were determined to be 1.31±0.14, 1.81±0.22, and 4.53±0.12 eV, respectively. The results show that inserting a Ni metal layer can only slightly reduce the crystallization temperature of *a*-Ge. The crystallization temperature of *a*-Ge/Ni bilayer is ~85°C lower than that of *a*-Si/Cu bilayer. However, the activation energy for crystallization of *a*-Ge induced by Ni is ~1.2 eV higher than that of *a*-Si induced by Cu. Therefore, the write-once blue-ray disk with a *a*-Ge/Ni bilayer recording film may have a higher archival stability and lower recording power and data-transfer-rate than that with a *a*-Si/Cu bilayer recording film.

5. References

1. S. Ohkubo, T. Ide and M. Okada, "Basic study of write-once media for blue-violet laser", Tech. Dig. Optical Data Storage, 34-36 (2001).
2. Y.C. Her and C.L. Lin, "Feasibility of Cu/a-Si Bilayer for High Data-Transfer-Rate Write-Once Blue-Ray Recording", Jpn. J. Appl. Phys. Part 1 **43**, 1013-1017 (2004).
3. Y.C. Her, S.T. Jean, and J.L. Wu, "Crystallization kinetics and recording mechanism of a-Si/Ni bilayer for write-once blue-ray Recording", J. Appl. Phys. **102**, 093503 (2007).
4. F. Oki, Y. Ogawa, and Y. Fujiki, "Effect of Deposited Metals on the Crystallization Temperature of Amorphous Germanium Film", Jpn. J. Appl. Phys. Part 1 **8**, 1056 (1969).
5. Y.C. Her and C.L. Wu, "Crystallization kinetics of Cu/a-Si bilayer recording under thermal and pulsed laser annealing", J. Appl. Phys. **96**, 5563-5568 (2004).

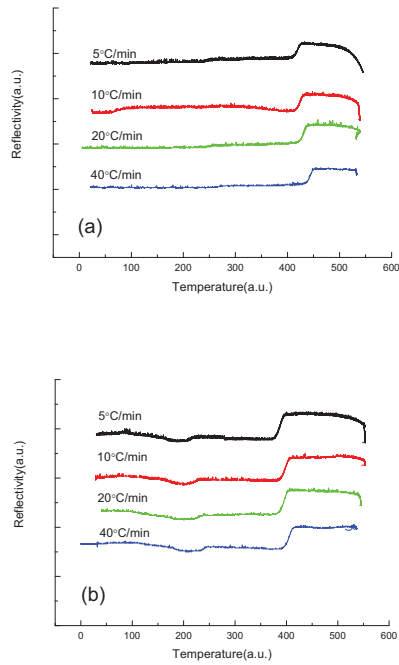


Figure 1 Reflectivity variations with temperature for the as-deposited a-Ge/Ni bilayer recording films.

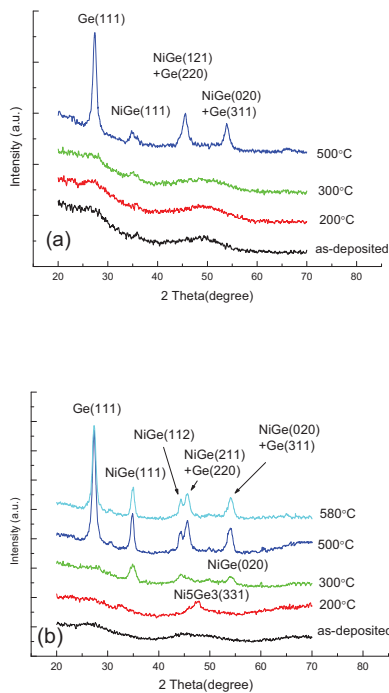


Figure 2 GIXD patterns of the a-Ge/Ni bilayer recording films with thickness ratios of (a) 20:1, (b) 10:1.

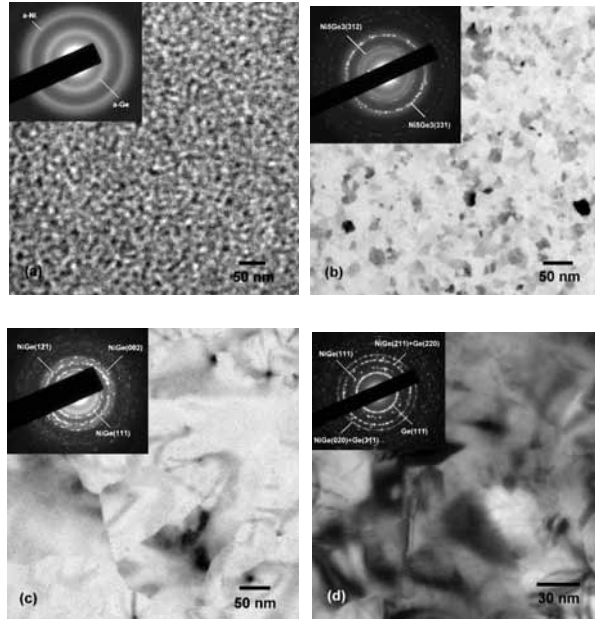


Figure 3 TEM images and diffraction patterns of the a-Ge/Ni bilayer recording film with a thickness ratio of 10:1 (a) before and after annealing at (b) 200, (c) 300, and (d) 500 °C for 3 min.

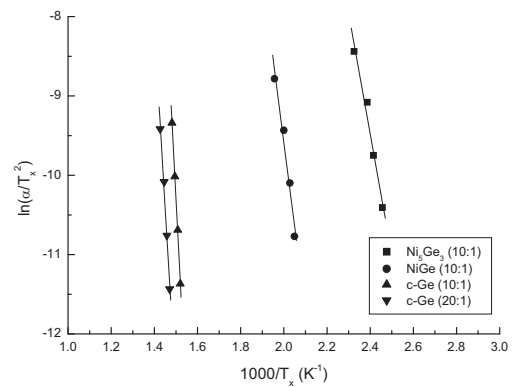


Figure 4 Kissinger's plots for a-Ge/Ni bilayer recording films with thickness ratios of 10:1 and 20:1.

Preparation and optical storage properties of novel metal hydrazone organic materials for recordable blu-ray disc

Yiqun Wu^{a,b}, Zhimin Chen^{a,b}, Donghong Gu^a, Yang Wang^a and Fuxi Gan^a

^a Shanghai Institute of Optics and Fine Mechanics, Chinese Academy of Sciences, PO Box 800-211, Shanghai 201800, China, Tel and Fax: 0086-21-69918087

^b Lab of Functional Materials, Heilongjiang University, Haerbin 150080, China

As the need for ever-increasing storage capacities continues to grow, high-density Optical storage technology which uses a 405 nm short wavelength laser and an objective lens of high numerical aperture (NA) of 0.85 is developing rapidly due to its high capacity over 23 GB on a single layer of a 120mm-diameter optical disc and great commercial demand¹. For recordable discs, the recording material can be a spin-coated dye, a phase-change layer, or an inorganic alloy². In such discs, a simple and cost-effective organic dye layer can possibly replace the more complex phase-change or inorganic alloy recording stack³⁻⁴. For this purpose, a dye material has to be developed that responds sensitively to the wavelength of a blue-violet laser. Moreover, it has to be highly soluble in organic solvent for easy production by a spin-coating process, during which it should perfectly fill narrow grooves, and it should decompose under blue-laser irradiation without melting. Consequently, intensive efforts are now being increasingly made to seek for new organic storage materials with short wavelength absorption and new preparation approaches to obtain high quality recording films in recent years⁴⁻⁷. As a very important kind of functional materials, hydrazones and their corresponding metal compounds, have attracted much attention over the past years in synthetic chemistry and inorganic chemistry due to their diverse biological activities and various chelating forms⁸. In this paper, several new organic materials: metal chelated hydrazones as recording media for recordable blu-ray disc have been developed, and their optical, thermal and recording properties were investigated.

Fig.1 shows the synthetical schemes and the chemical structures of the metal chelating hydrazones. Their structures were characterized and confirmed by elemental analysis, FT-IR, ¹H-NMR and MALDI-FT-ICR-MS analysis, respectively. The thermal properties of the synthesized compounds were investigated by TGA-DSC (Fig. 2). It is found that most of the metal hydrazones have high and sharp thermal decomposition temperature (>250°C) with high weight reduction over 30% and narrow temperature region, which are helpful to fabricate small recording marks using 405 nm blue laser.

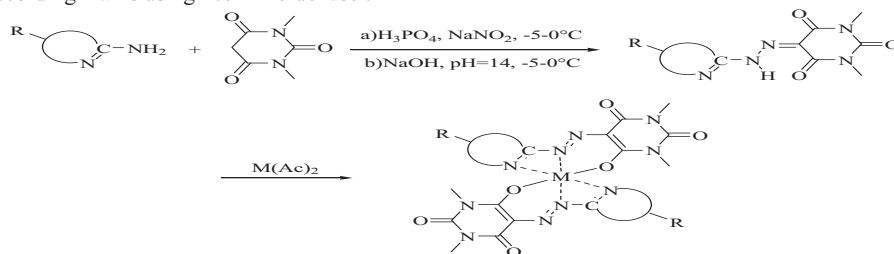


Fig. 1 Synthetical schemes and the chemical structures of the metal chelated hydrazones

These new materials have good solubility ($\geq 2.0\text{wt}\%$) in 2,2,3,3-tetrafluoro-1-propanol (TFP), which is a specific organic solvent for disc manufacture, and smooth films can be prepared easily by the spin-coating method. The root-mean-square (RMS) surface roughness is measured to be as low as 0.6 nm within $5\mu\text{m}\times 5\mu\text{m}$. Fig.3 shows the absorption spectra of the complexed films, the λ_{max} can be classified into two groups: one is around 350-380 nm and the other is located in 430-460nm. The absorption spectra of materials can be adjusted by modulating the metal ions, diazo heterocycles, coupling components, substituent groups of the compounds.

As is known, organic recordable optical storage is based on the changes of irreversible local thermal decomposition or thermal deformation (pit formation) of the organic dye (recording layer) induced by the modulated laser, so the suitable optical properties, i.e., absorption, refractive indices, extinction coefficients and reflectivity, etc., of the organic dye layer used in optical discs can have great impacts on their performance^{3,9}. In this work, the optical constants (complex refractive indices $N=n+ik$, where n is refractive index and k is extinction coefficient) of the films were determined. The results show that the refractive index n values are in the range of 1.81-1.95 and 1.22-1.36, extinction coefficient k values are located in 0.17-0.27 and 0.35-0.51, the absorption coefficient α values (α can be calculated from the expression $\alpha=4\pi k/\lambda$, where λ is the wavelength.)

are 0.53×10^5 - $0.93 \times 10^5 \text{ cm}^{-1}$ and 1.09×10^5 - $1.58 \times 10^5 \text{ cm}^{-1}$. The results indicated that these dye films can be divided into two types: one possesses relatively higher refractive index and lower extinction coefficient and absorption coefficient (typel) comparing the other (typell). It was implied that two types of dyes may be suitable for different recording models.

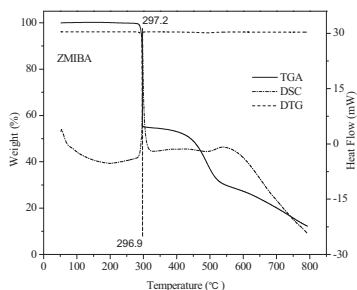


Fig.2 TGA-DSC curves of the new complex

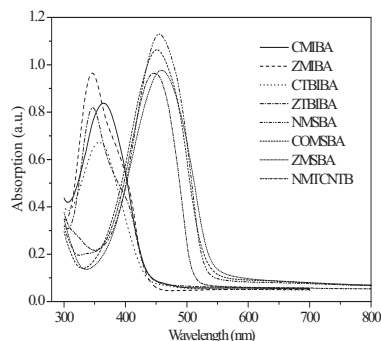


Fig.3 Absorption spectra of some new complexes

The static optical recording properties of above two types of the dyes were measured on a static optical recording tester¹⁰ using 406.7nm laser and an objective lens of NA 0.90. For typel, from before to after recording marks were formed, the reflectivity of the area irradiated is changed from high to low, so the dyes of typel belong to the recordable blu-ray “High to Low (HTL)” model¹¹. High reflectivity contrast ($C \geq 50\%$) (Fig.4) and clear recording marks ($\sim 150\text{nm}$, Fig.6) were obtained. $[C = 2R_b - R_a / (R_b + R_a) = 2I_b/I_0 - I_a/I_0 / (I_b/I_0 + I_a/I_0)]$, where R is the reflectivity, I is the reflective intensity, and b is before and a is after]. For typell, change of reflectivity on the irradiated area is just opposite to typel from low to high, so the dyes of typell belong to the recordable blu-ray “Low to High (LTH)” model¹¹. High reflectivity contrast ($C \geq 60\%$) (Fig.5) and clear recording marks ($\sim 170\text{nm}$, Fig.7) were obtained. Recording marks on the two types of the dye layers are stable after readout times reach to 15000.

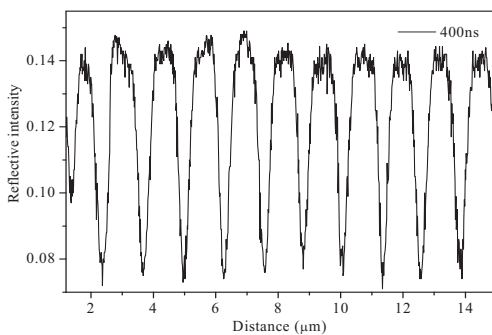


Fig.4 Test result of reflectivity contrast of a new dye spin-coating film under the conditions of writing power: 3mW; pulse width: 400ns; reading power: 0.5mW

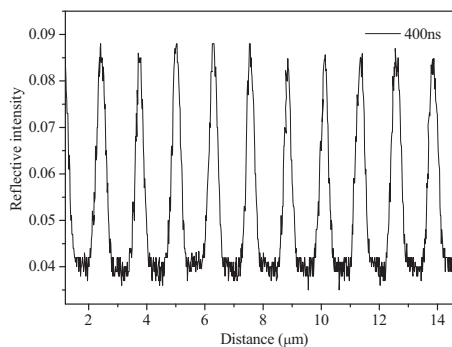


Fig.5 Test result of reflectivity contrast of a new dye spin-coating film under the conditions of writing power: 3mW; pulse width: 400ns; reading power: 0.5mW

Two types (HTL and LTH) of new metal hydrazone organic dyes as recording media for recordable blu-ray disc have been synthesized. These dyes have good solubility ($>2.0\text{wt}\%$) in 2,2,3,3-tetrafluoro-1-propanol (TFP) and smooth spin-coating films have been easily prepared. Excellent thermal decomposition properties with high and sharp thermal decomposition temperature ($>250^\circ\text{C}$), high weight reduction over 30% and narrow temperature region have been found. The absorption peaks (λ_{max}) of the films are located in 350-380 nm for typel and 430-460nm for typell. And typel has relatively higher refractive index and lower extinction coefficient and absorption coefficient comparing the typell. Both of them respond sensitively to blue-violet laser, clear stable static recording marks and high reflectivity contrast ($\geq 50\%$) were obtained.

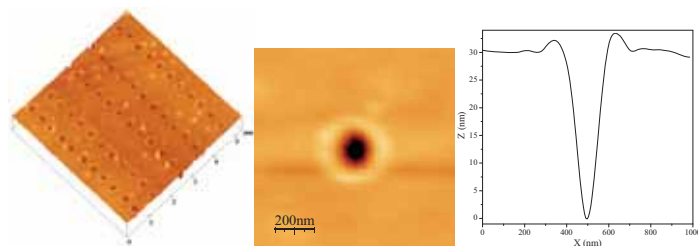


Fig.6 Recording marks on the typeldye film (AFM)

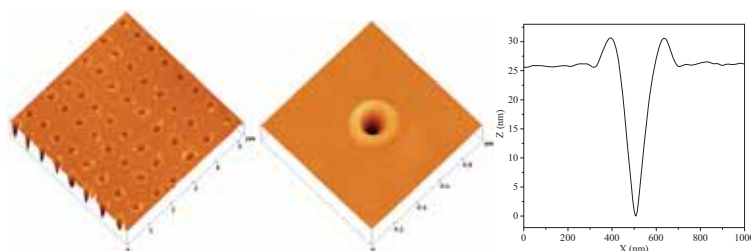


Fig.7 Recording marks on the typell dye film (AFM)

REFERENCES

1. B. Stek, R. Otte, T. Jansen and D. Modrie, "Advanced signal processing for the Blu-ray disc system", *Jpn. J. Appl. Phys.* 2003, 42, 912-914.
2. A.E.T. Kuiper, L. Van Pieterse, *Materials Issues in Blue Recording*, *Mrs Bulletin*, 2006, 31(4): 308-313.
3. H. Mustroph, M. Stollenwerk, V. Bressau, *Current developments in optical data storage with organic dyes*, *Angew. Chem. Int. Edit.*, 2006, 45(13): 2016-2035.
4. Y. Sabi, S. Tamada, T. Iwamura, M. Oyamada, F. Bruder, R. Oser, H. Berneth and K. Hassenruck, "Development of organic recording media for blue high numerical aperture optical disc system", *Jpn. J. Appl. Phys.* 2003, 42, 1056-1058.
5. Y. Usami, T. Kakuta, T. Ishida, H. Kubo, N. Saito and T. Watanabe, "Blue-violet write-once optical disc with spin-coated dye-based recording", *SPIE Proceeding* 2003, 5069, 182-189.
6. F. Huang, Y. Wu, D. Gu, F. Gan, "Progress of the organic materials used for the new generation high density recordable digital versatile disc", *Progress in Physics*, 2003, 23(3): 312-32.
7. F. Huang, Y. Wu, D. Gu, F. Gan, "Synthesis, spectroscopic and thermal properties of nickel(II)-azo complexes with blue-violet light wavelength", *Dyes and Pigments*, 2005, 66: 77-82.
8. MC Rodriguez-Arguelles, MB Ferrari, F Bisceglie, C Pelizzi, G Pelosi, S Pinelli, M Sassi, "Synthesis, characterization and biological activity of Ni, Cu and Zn complexes of isatin hydrazones" *J. Inorg. Biochem.* 2004; 98: 313-321.
9. A.H.M. Holtslag, E.F. Mccord, G.H. Werumeus Buning: "Recording Mechanism of Overcoated Metallized Dye Layers on Polycarbonate Substrates" *Jpn. J. Appl. Phys.* 1992, 31, 484-493
10. X. Gao, W. Xu, F. Zhou and F. Gan, "Static testing system for blue-ray optical data storage properties", *SPIE Proceeding* 2005, 5966-66.
11. K. Takazawa, N. Morishita, Y. Ootera, K. Umezawa, N. Nakamura, S. Morita, *HD DVD-R Disc With Organic Dye Having Low to High Polarity Recording*, *ISOM/ODS 2005*, OSA Technical Digest Series, Honolulu, Hawaii, paper ThB3.

Crystallization and Melting Kinetics of Zn-doped Fast-Growth Sb₇₀Te₃₀ Phase-Change Recording Films

Yung-Sung Hsu^{*a}, Ying-Da Liu^a, Yung-Chiun Her^a, Shun-Te Cheng^b and Song-Yeu Tsai^b
^aDepartment of Materials Science and Engineering, National Chung Hsing University,
 Taichung 40227, Taiwan. ^bMaterials Research Laboratory, ITRI, Hsinchiu 31040, R.O.C.

ABSTRACT

In order to obtain sufficiently high recording sensitivity and archival stability, while maintain adequate initialization ability for the rewritable optical memories, the optimum Zn concentration in Sb₇₀Te₃₀ recording film should be located between 5.3 and 17.9 at.%.

Keywords: Crystallization kinetics, fast-growth, melting kinetics, thermal annealing, Zn-Sb-Te.

1. INTRODUCTION

For the rewritable optical memories, specific foreign element(s) have been frequently doped into the fast-growth Sb₇₀Te₃₀ recording film to enhance its recording sensitivity and archival stability.[1,2] It has been found that the crystallization and melting properties of the element-doped Sb₇₀Te₃₀ recording films play important roles in the erasing and recording characteristics.[3,4] In this paper, we investigated the crystallization and melting kinetics and crystallization mechanisms of various Zn-doped fast-growth Sb₇₀Te₃₀ recording films.

2. EXPERIMENTAL

Various Zn-doped Sb₇₀Te₃₀ (hereafter denoted as ZST) recording films of 35 nm in thickness are deposited on Corning 1737 glass and silicon substrates by DC magnetron co-sputter of an alloyed Sb₇₀Te₃₀ and a pure Zn targets. The sputtering power of the Sb₇₀Te₃₀ target was fixed at 100W, and the co-sputtering power of the Zn target was controlled at 0 to 60W. The argon gas flow rate was fixed at 20 sccm, while the background pressure and work pressure were 5×10^{-6} and 3×10^{-5} Torr, respectively. The chemical compositions of ZST recording films prepared at different sputtering powers were analyzed by an inductively coupled plasma-mass spectrometer (ICP-MS). The samples were heated at heating rates of 5, 10, 20, 40 and 80°C/min, and the reflectivity variations with temperature were monitored in real time. The crystallization and melting kinetics of the ZST recording films were quantitatively studied. The crystalline structures of the ZST films annealing at various temperatures were examined by transmission electron microscope (TEM) to understand the crystallization mechanisms.

3. RESULTS AND DISCUSSION

The chemical compositions of the ZST recording films prepared at sputtering powers of 0, 20, 40, and 60W were measured to be Sb_{69.9}Te_{30.1}, Zn_{5.3}Sb_{64.9}Te_{29.8}, Zn_{17.9}Sb_{58.0}Te_{24.2}, and Zn_{34.7}Sb_{44.4}Te_{20.9}, respectively. It was found that most Zn atoms replaced Sb atoms, while only small fraction of Te atoms was replaced by Zn atoms.

Fig. 1 shows the reflectivity variations with temperature for various ZST recording films at a heating rate of 10°C/min. All the curves showed an abrupt reflectivity rise in the temperature range from 135 to 275°C, and a rapid reflectivity drop in the vicinity of 450°C. For the pure Sb₇₀Te₃₀ recording film, we have concluded that the abrupt reflectivity increase in the first stage is due to the crystallization of amorphous Sb₇₀Te₃₀ to crystalline Sb. As the temperature was increased, the crystalline Sb phase would gradually transfer to Sb₂Te₃ phase. After the temperature was increased above 400°C, parts of the pseudo-eutectic Sb–Sb₂Te₃ alloy started to melt. As the temperature kept increasing, more pseudo-eutectic Sb–Sb₂Te₃ would melt, resulting in a steep reflectivity decrease.[3] Figs. 2(a)-(d), 3(a)-(d), 4(a)-(b) show the bright-field (BF) TEM images and diffraction patterns of Zn_{5.3}Sb_{64.9}Te_{29.8}, Zn_{17.9}Sb_{58.0}Te_{24.2}, and Zn_{34.7}Sb_{44.4}Te_{20.9} films before and after annealing at various temperatures for 1 min. The crystalline phase transitions and constituent phases of various ZST recording films at various temperatures were summarized in Table I. Similar to Sb_{69.9}Te_{30.1}, the ZST recording films were amorphous in the as-deposited state, and would firstly crystallize to rhombohedral Sb phase. For the Zn_{5.3}Sb_{64.9}Te_{29.8} film, part of the crystalline Sb phase would transfer to rhombohedral Sb₂Te₃ phase as the temperature was higher than 200°C. For the Zn_{17.9}Sb_{58.0}Te_{24.2} film, only crystalline Sb phase was found after annealing at 250°C. However, the crystalline Sb and Sb₂Te₃ phases and a new face-centered cubic (FCC) ZnTe phase were observed after annealing at 300°C. For the Zn_{34.7}Sb_{44.4}Te_{20.9} film, it would remain amorphous up to 250°C, and only crystalline Sb phase was formed after annealing at 300°C. The Sb, Sb₂Te₃, and ZnTe phases would coexist after annealing at 400°C. After annealing at 500°C, most of the ZST recording films were melted. The grain size of the Sb phase was found to decrease substantially from ~ 600 to 200, 30, and 15 nm, respectively, as Zn content was increased from 0 to 5.3, 17.9, and 34.7 at.%. It is evident that the addition of Zn would retard the crystallization of Sb and the formation of Sb₂Te₃ phases in the ZST films.

The crystallization temperature (T_c) was defined as the temperature at the midpoint of the reflectivity increase, and the melting temperature (T_m) was defined as the temperature at the beginning of the reflectivity drop. As the Zn content was increased from 0 to 5.3, 17.9, and 34.7 at.%, T_c was found to increase from 136 to 147, 212, and

*g8966014@mail.nchu.edu.tw; phone: +886-4-2285-9112; fax: +886-4-2285-7017

274°C, respectively, and T_m increased from 396 to 449, 468, and 477°C, respectively. It is evident that the addition of Zn could effectively increase T_c and T_m of the $Sb_{70}Te_{30}$ recording film so that the archival stability can be improved, however, the recording sensitivity may be sacrificed. As the heating rate was increased, the crystallization and melting temperatures of the recording films also increased. The activation energies for crystallization (E_c) and melting (E_m) could be calculated from the Kissinger's formula: $\ln(\alpha/T_x^2) = C - (E_a/RT_x)$, where α is the heating rate, T_x is the absolute phase transformation temperature, E_a is the activation energy, and C and R are constants.[5] Fig. 5 shows the plots of $\ln(\alpha/T_x^2)$ vs $1/T_x$ for various ZST recording films. As the Zn content was increased from 0 to 5.3, 17.9 and 34.7 at.%, E_c and E_m were determined to be 2.08 and 3.33 eV/atom, 2.19 and 2.46 eV/atom, 4.09 and 2.25 eV/atom, 4.15 and 2.14 eV/atom, respectively, giving rise to the reduced activation energy (E_c/E_m) increased from 0.63 to 0.89, 1.82, and 1.94. The increases of T_c and E_c due to Zn addition may be explained by the confusion principle. Normally, an alloy system involving more elements will have a lower chance to select viable crystal structures and a higher chance of glass forming.[6] and therefore, will be more resistant to crystallization. In addition, the $Zn^{+2}Te^{-2}$ nuclei are expected to restrain the formation of the $Sb_2^{-3}Te_3^{+2}$ phase due to the opposite electricities of the Te atoms, which will also lead to higher T_c and E_c . The increases of T_m and decrease of E_m may be explained by the decrease of covalent character of the alloy system and the decrease of latent heat of fusion, respectively. An alloy or a compound system with a higher covalent character of a bond tend to reduce the heat of fusion by stabilizing discrete units in the melt, which in turn reduces the number of bonds that have to be broken during melting, leading to a lower melting temperature.[7] The percentage covalent characters of the Sb-Te, Zn-Sb, and Zn-Te bonds are estimated to be 99.9, 96.1, and 95.1%, respectively. As a result, the bonding energies of the Zn-Te and Zn-Sb bonds are expected to be higher than those of the Sb-Sb, Sb-Te, and Te-Te bonds that explain the increase of melting temperatures of the $Sb_{70}Te_{30}$ alloy with increasing the Zn content. Meanwhile, the latent heats of fusion of Sb, Te and Zn are about 19.8, 17.5, and 7.3 KJ/mol, respectively. The addition of Zn atoms will decrease the latent heat of the ZST recording films, resulting in the decreased of E_m .

Normally, the pulsed laser spot exhibits a Gauss spatial intensity distribution with an approximately top-hat profile in bulk materials.[8] For nano-scaled thin films, the active region is limited and similar as a 2D situation with large plane temperature gradients depending on the laser power. Uhlmann et al. have asserted that for congruently melting glass-forming materials, the crystallization velocity at low temperature will be limited by the viscosity of the glass forming liquid. E_c can be interpreted as low temperature viscous flow, and regarded as the dynamic driving force for crystal front propagation. E_m could be interpreted as the high temperature viscous flow, and regarded as the dynamic driving force for melt front propagation.[9,10] It is expected that, as Zn atoms are doped into $Sb_{70}Te_{30}$, the laser powers required to initiate crystallization may increase, while the laser powers required to form the melt-quenched amorphous marks will decrease. Based upon our previous studies, E_c/E_m should be controlled at ~1 to achieve smoothly reversible switching between the amorphous and crystalline marks. [3,4] As a result, the Zn concentration should be located between 5.3 and 17.9 at.% to prevent the divergent of crystalline and melting phases.

4. CONCLUSIONS

Adding Zn into the fast-growth $Sb_{70}Te_{30}$ recording film can enhance the formation of ZnTe compound which will retard the crystallization of Sb and formation of Sb_2Te_3 phase, leading to the increase of crystallization temperature and the activation energy for crystallization. The addition of Zn can also increase the melting temperature but decrease the activation energy for melting. Accordingly, doping Zn into $Sb_{70}Te_{30}$ can improve the archival stability and recording sensitivity. However, the initialization of the as-deposited ZST recording film will also become more difficult. Therefore, it should have an optimization Zn doping concentration for the $Sb_{70}Te_{30}$ film to obtain sufficiently high recording sensitivity and archival stability, while still maintain adequate initialization ability. Base upon our results, the optimum Zn doping concentration in the $Sb_{70}Te_{30}$ recording film should be located between 5.3 and 17.9 at.%.

REFERENCES

- [1] H. Inoue, H. Hirata, T. Kato, H. Shingai, and H. Utsunomiya., "Phase Change Disc for High Data Rate Recording" Jpn. J. Appl. Phys., 40, 1641-1642 (2001).
- [2] K. Kiyono, M. Horie, T. Ohno, T. Uematsu, T. Hashizume, M. P. O'Neill, K. Balasubramanian, R. Narayan, D. Warland, and T. Zhou., "Rewritable Multilevel Recording by Mark-Size Modulation on Growth-Dominant Phase-Change Material" Jpn. J. Appl. Phys., 40, 1855-1856 (2001).
- [3] Y. S. Hsu, Y. C. Her, S. T. Cheng, and S. Y. Tsai., "Thermal- and Laser-Induced Order-Disorder Switching of Ag-Doped Fast-Growth $Sb_{70}Te_{30}$ Phase-Change Recording Films" Jpn. J. Appl. Phys., 46, 3945-3951 (2007).
- [4] Y. S. Hsu, Y. C. Her, S. T. Cheng, and S. Y. Tsai., "Thermal- and Laser-Induced Order-Disorder Switching of In-Doped Fast-Growth $Sb_{70}Te_{30}$ Phase-Change Recording Films" IEEE. Trans. Mag., 43, 936-938 (2007).
- [5] H. E. Kissinger. Anal. Chem., 29, 1702-1706 (1957).
- [6] A. L. Greer., "Confusion by design" Nature (London), 366, 303-304 (1993).
- [7] M. W. Barsoum. Fundamentals of Ceramics. McGRAW-HILL Inc. Int. Ed. pp. 96-101 (1997).
- [8] G. K. L. Ng, P. L. Crouse, and L. Li., "An analytical model for laser drilling incorporating effects of exothermic reaction, pulse width and hole geometry" Int. J. Heat Mass Transfer 49, 1358-1374 (2006).
- [9] P. J. Vergano and D. R. Uhlmann., "Crystallisation kinetics of germanium dioxide: the effect of stoichiometry on kinetics" Phys. Chem. Glasses. 11, 30-38 (1970).
- [10] D. W. Henderson., "Thermal analysis of non-isothermal crystallization kinetics in glass forming liquids" J. Non-Cryst. Solids 30, 301-315 (1979).

Table I. The crystalline phase transitions of various Zn-doped $Sb_{70}Te_{30}$ recording films at various temperatures.

Compositions	135~185°C	200~250°C	275~300°C	350~400°C
$Sb_{69.9}Te_{30.1}$	Sb	$Sb+Sb_2Te_3$	$Sb+Sb_2Te_3$	$Sb+Sb_2Te_3$
$Zn_{5.3}Sb_{64.9}Te_{29.8}$	Sb	$Sb+Sb_2Te_3$	$Sb+Sb_2Te_3$	$Sb+Sb_2Te_3$
$Zn_{17.9}Sb_{58.0}Te_{24.2}$	amorphous	Sb	$Sb+Sb_2Te_3+ZnTe$	$Sb+Sb_2Te_3+ZnTe$
$Zn_{34.7}Sb_{44.4}Te_{20.9}$	amorphous	amorphous	Sb	$Sb+Sb_2Te_3+ZnTe$

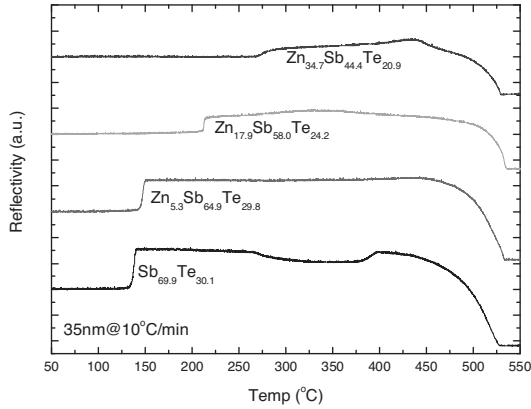


Fig. 1. Reflectivity variation with temperature for the ZST recording films at a heating rate of 10°C/min.

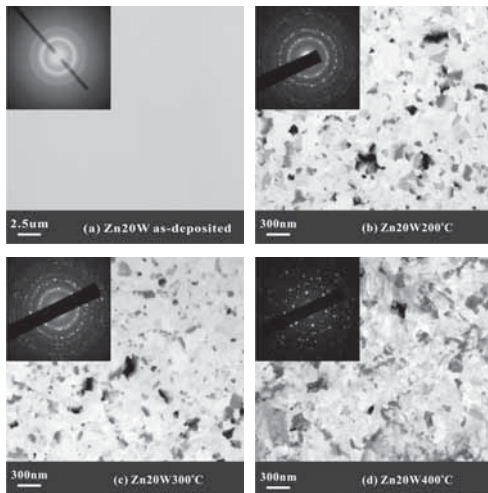


Fig. 2 TEM images of the $Zn_{5.3}Sb_{64.9}Te_{29.8}$ film (a) as-deposited, and annealed at (b) 200°C, (c) 300°C, and (d) 400°C, respectively.

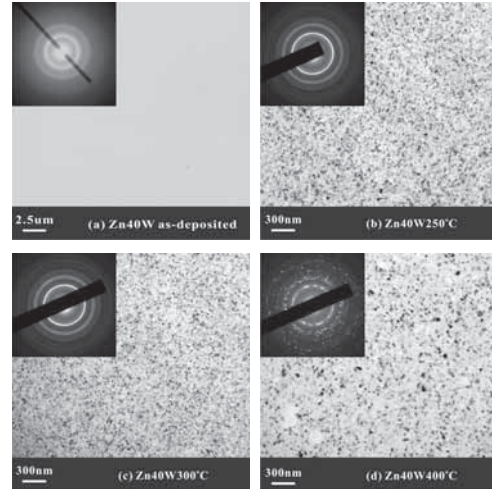


Fig. 3 TEM images of the $Zn_{17.9}Sb_{58.0}Te_{24.2}$ film (a) as-deposited, and annealed at (b) 250°C, (c) 300°C, and (d) 400°C, respectively.

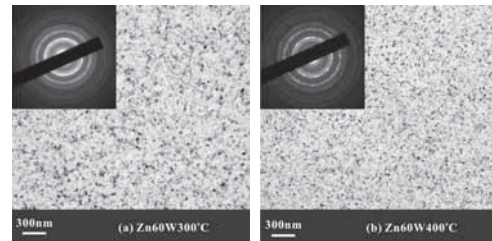


Fig. 4 TEM images of the $Zn_{34.7}Sb_{44.4}Te_{20.9}$ film annealed at (a) 300°C and (b) 400°C.

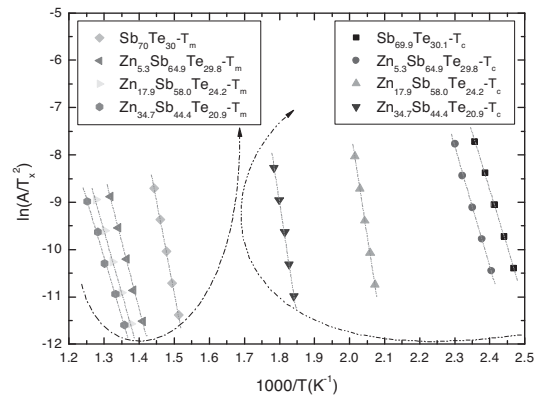


Fig. 5. $\ln(a/T_x^2)$ versus $1/T_x$ for both crystallization and melting of various recording films.

Crystallization Time Dependence on SbTe based Phase Change Films Measured by Rotating Disc Techniques

R. E. Simpson, P. Fons, A. Kolobov, M. Kuwahara, J. Tominga
Center for Applied Near-Field Optics Research (CAN-FOR), National Institute of Advanced
Industrial Science and Technology (AIST), Tsukuba Central 4, 1-1-1 Higashi, Tsukuba 305-8562
Japan

Abstract

Dynamic measurements of growth dominated and nucleation dominated materials are presented as a function of mark length and film depth. Bismuth doping of these films is found to increase the crystallization rate of the growth dominated materials through a corresponding decrease in the material's viscosity.

Keywords: Phase Change, Bismuth, Antimony Telluride, Dynamic Disc Measurement, Viscosity, Bulk Modulus

1. Introduction

Fast growth phase change compositions have been identified as potentially interesting materials for future nanoscale data storage devices and media[1]. The crystallization time of such materials is dominated by the time necessary for the crystalline region to grow from quenched in crystalline nuclei or from the interfaces surrounding the amorphous region. For this reason, these materials are quite different to the well known nucleation dominated compositions which for Ge:Sb:Te tend to exist along the Sb₂Te₃-GeTe pseudo-binary. An attractive feature of these materials is their intrinsic crystallization time scalability with mark size. As the mark radius is decreased, the crystallization time scales correspondingly. In contrast, static measurements of the nucleation dominated GeSbTe compositions, show crystallization times with little dependence on mark size[2,3]. Thus, their scaling to smaller dimensions has no positive effect on the crystallization. In fact the crystallization time has been shown to slightly increase with decreasing film thickness[3, 4]. This was attributed to interfacial effects. In this manuscript similar results are reported by use of a rotating disc set-up. New phase change compositions based on growth dominated crystallization are sought. Pure Sb shows explosive growth dominated crystallization, but it cannot retain the amorphous marks under normal operating conditions. SbTe materials with high Sb concentration are known to show growth dominated crystallization.

There exists three common ways to measure the phase change time: (1) using a non-rotating disc, known as a static tester, to measure the change in reflection as a function of incident optical power and duration[2, 5] (2) measuring the time to crystallize amorphous marks of fixed length as a function of disc linear velocity using a dynamic disc tester[6] or (3) measuring the time to electrically crystallize phase change materials embedded in an electrical test chip as a function of voltage and pulse length and monitoring the change in electrical resistance of the chip[7]. For the measurement of doped Sb₈Te₂ films, reported here, the dynamic disc tester system has been adopted. However, a novel methodology which allows measurement of the crystallization velocity is used to characterize the crystallization time of the re-amorphised state. The methodology and measurements obtained are described herein.

Bi has been reported to reduce the crystallization time of Ge₂Sb₂Te₅ phase change films by a corresponding reduction in the crystallization activation energy[7]. Recently it has been shown that the growth dominated, Sb₈Te₂ phase change films, also show a reduction in crystallization time of the as-deposited film without any significant change in crystallization activation energy or crystal structure[8]. This decrease was attributed to a reduction in the materials viscosity. It is possible to understand how the viscosity changes with Bi concentration through consideration of the material's bulk modulus. The bulk modulus of a material is a measurement of its resistance to compression; it scales with viscosity. The bulk modulus of a material can be obtained from first principal, density functional, calculations. Such simulations have been performed for the crystalline phase of Sb₈Te₂:Bi compositions. These results are discussed and related to crystallization time data.

2. Methodology

Optical disc suitable for dynamic measurements of the write and erase properties at 650nm were fabricated by sputter deposition at 0.5Pa. The disc structure was (Polycarbonate Substrate)/(ZnS-SiO₂)/(PCM)/(ZnS-SiO₂)/(AlCr), with films depths 130nm/X/20nm/50nm respectively. Two sets of discs have been fabricated for different material systems. The first set of Ge₂Sb₂Te₅ discs were fabricated with X varying from 10 to 100nm. For the second set of disks, X was kept constant at 40nm but the composition was varied such that increasing proportions of Bi was added to the Sb₈Te₂ composition.

Two different disc rotation techniques have been used to measure the crystallization time of the Sb₈Te₂ materials. The first, somewhat more conventional method, is now described. The conditions for initialization of the as-deposited structure are found for a disc linear velocity of 2ms⁻¹. The minimum power of the erase laser required for saturation of reflectivity increase is found by monitoring the voltage across the detector. The discs are then initialized with these conditions. 0.5μm marks are written by increasing the disk linear velocity to 6ms⁻¹ and recording at a frequency of 6MHz with a 50% duty cycle. The necessary writing power is found by increasing the power of the laser diode until the increase in signal strength is saturated. The signal strength is measured with a RF analyzer. The 0.5μm marks are then written to the initialized disc. The signal intensity after an erasure is then measured as a function of disk linear velocity. The laser wavelength was 650nm, the maximum write power was 15mW, whilst the maximum erase power is 8mW. The read power was fixed at 1mW. The maximum disc velocity was 17ms⁻¹. This method has been applied to Ge₂Sb₂Te₅ for films of depths ranging from 10nm to 100nm.

The same dynamic disc testbed has been used to make non-conventional measurements of the erasure time for marks with varying length; hence making possible an estimate of the crystal growth speed for growth limited phase change compositions. To do this, both the disc linear velocity and the write frequency were varied such that marks of different length could be written. The erasability of the marks was then measured. This method has been applied to doped, growth limited, Sb:Te, phase change compositions.

3. Results

The erasability of 0.5μm marks, recorded on the groove as a function of disk linear velocity for various Ge₂Sb₂Te₅ film depths is given in figure 1. It can be seen that the erasability has some dependance on the film depth. Films of depth greater than 40nm seem to show similar erasure properties. Decreasing the depth below 40nm decreases the maximum velocity at which data can be erased. A Ge₂Sb₂Te₅ film of depth 20nm was also used to measure the ability of the film to crystallize amorphous marks of different lengths at a fixed disc linear velocity of 6ms⁻¹. This measurement has been compared with Sb₈Te₂ and (Sb₈Te₂)₉₇:Bi₃ films.; the results are displayed in figure 2. Adding just 3% Bi to the Sb₈Te₂ was found to reduce

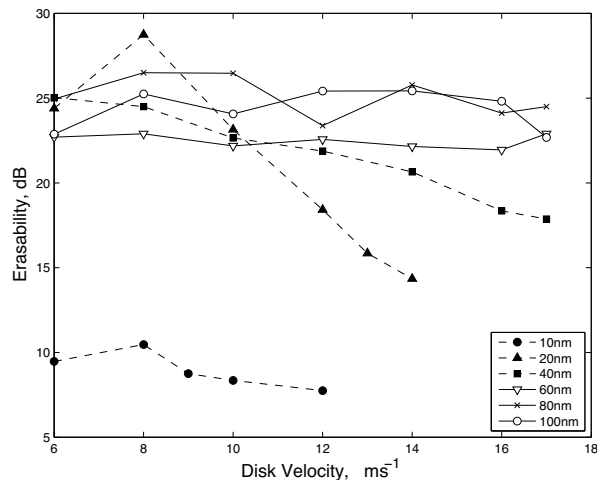


Figure 1: Erasability of Ge₂Sb₂Te₅ as a function of Disc Velocity for different film depths

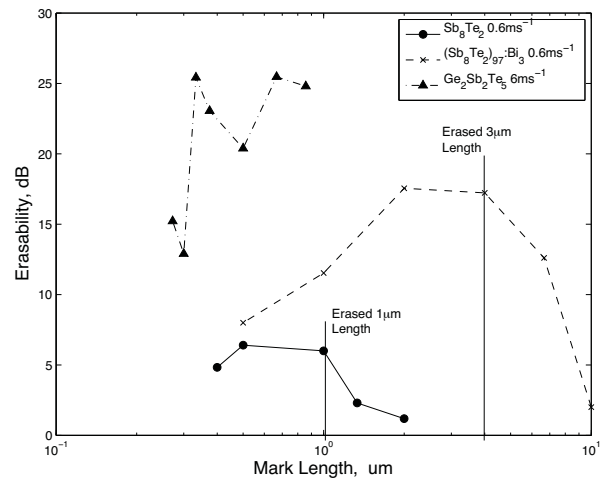


Figure 2: Erasability for Ge₂Sb₂Te₅ and doped Sb₈Te₂ films as a function of mark length

the crystallisation time by a factor of 3. This is depicted in figure 2 by the fact that marks could be erased in the Bi doped Sb_8Te_2 film which were more than 3 longer than those in the pure Sb_8Te_2 film.

4. Discussion

The crystallization speed of $\text{Ge}_2\text{Sb}_2\text{Te}_5$ shows some dependence on its depth. It can be seen in figure 1 that decreasing the depth below 40nm reduces the speed that data can be erase from the disc. This might be counter-intuitive since, one might think that greater depths would require a longer period to crystallize. However, it is known that $\text{Ge}_2\text{Sb}_2\text{Te}_5$ is a nucleation limited phase change material. Similar reports which analyze the phase change of $\text{Ge}_2\text{Sb}_2\text{Te}_5$ using a static tester are in good agreement with these measurements[4]. For films of 40nm or less, the affect of the ZnS-SiO_2 interface must be considered. It seems that there is a critical film depth of around 40nm, below which the interface effect has a detrimental impact on the crystallization time.

The measurements of Bi doped Sb_8Te_2 show that adding a small proportion of Bi increases the speed of crystallization. This effect was also noticed in our previous study of the as-deposited state. The viscosity of growth dominated materials is clearly of importance since it partially determines the speed of atomic migration. The faster the atoms can move, the quicker atoms can join a nucleated crystal or join an amorphous-crystalline interface. In our previous study we suggested that the materials viscosity is reduced by adding Bi. In $\text{Ge}_2\text{Sb}_2\text{Te}_5$, Bi has been also reported to reduce the erasure time only by reducing the crystallization activation energy. We reported an activation energy insensitivity to Bi and consequently it was inferred that this reduction was due to a viscosity reduction. To help support this idea, a simulation of the material's bulk modulus was carried out using density functional theory and assuming the Local Density Approximation (LDA). The Sb_8Te_2 :Bi films have been shown to hold an A7-type structure with the constituent atoms occurring randomly on each site. These condition were simulated in order to calculate the material's bulk modulus. Table 1 shows the results. It can be seen that adding a small amount of Bi to the structure does, indeed, decrease the material's bulk modulus and therefore its viscosity. However, there appears to be a threshold Bi concentration above which the bulk modulus is increased. It is a topic of future research to use these simulations to discover the Bi concentration at which the bulk modulus is minimized.

Composition	Bulk Modulus
$\text{Sb}_{75}\text{Te}_{25}$	63.5 GPa
$\text{Sb}_{66}\text{Te}_{25}\text{Bi}_9$	56.1 GPa
$\text{Sb}_{50}\text{Te}_{25}\text{Bi}_{25}$	65.65 GPa
$\text{Te}_{25}\text{Bi}_{75}$	67.35 GPa

Table 1: Simulation of bulk modulus

5. Conclusions

The crystallization speed of $\text{Ge}_2\text{Sb}_2\text{Te}_5$ and Bismuth doped Sb_8Te_2 has been investigated using two different rotating disc methods. Bi doping has been found to reduce the crystallization speed of growth dominated materials thus decreasing the erasure time in growth dominated phase change media or devices. Adding just Three atomic percent Bi, increases the rate of crystallisation by a factor of three. The increase in crystallization speed has been shown, using density functional simulations, to be related to a decrease in bulk modulus.

References

1. M. Lankhorst, B Ketelaars, et al., 'Low-cost and nanoscale non-volatile memory concept for future silicon chips', Nature Materials, 4 (4), 2005
2. J. H. Coombs, A. P. J. M. Jongenelis, et al., 'Laser-induced crystallization phenomena in GeTe-based alloys. I. Characterization of nucleation and growth', Journal of Applied Physics, 78 (8), 1995
3. G Zhou and Bernardus A. J. Jacobs, 'High performance media for phase change optical recording', Japanese Journal of Applied Physics, Part 2: Letters, 38 (3B), 1999
4. G Zhou, 'Materials aspects in phase change optical recording' A304-A306, 2001
5. A. W. Smith, 'Imnjction laser writing on chalcogenide films', Applied Optics, 13 (4), 1974
6. K. Wang, D. Wamwangi, et al., 'Influence of Bi doping upon the phase change characteristics of $\text{Ge}_2\text{Sb}_2\text{Te}_5$ ', Journal of Applied Physics, 96 (10), 2004
7. R. E. Simpson, P. Fons, et. al., 'Reduction in crystallisation time of Sb:Te films through addition of Bi', Accepted for Publication: Journal of Applied Physics.

Cyclability improvement on Super-Resolution BD-like ROM disks based on the high-contrast semiconductor InSb

J. Pichon^{*}, F. Laulagnet, M-F. Armand, O. Lemonnier, B. Hyot and B. André
CEA-Léti MINATEC, 17 rue des martyrs, Grenoble cedex 9, F-38054, France

^{*} E-mail : joseph.pichon@cea.fr, Phone: 33 4 3878 2554

ABSTRACT

We present our recent improvements of InSb-based Super-Resolution BD-like ROM disks in terms of cyclability, as investigated by dynamic and static testing.

Keywords: Super-Resolution, testing and characterization

1. INTRODUCTION

Several solutions are currently being investigated in order to satisfy the needs in storage capacity linked to the emergence of the High Definition market. Among them, Super-Resolution (SR) technology [1], based on an extension of the capacity of existing optical disks formats, appears as a credible candidate to ensure the transition towards ultra-high capacity optical storage technologies. The recent progress in SR media development, for both write-once and read-only disks, has made possible the retrieval of signals that can be considered as acceptable for commercial applications when treated with high performance PRML detection algorithms [2,3].

Nevertheless, SR disks usually exhibit a relatively poor cyclability, which can be considered as a problem that needs to be solved in the optics of SR format standardization. The explanation of this poor cyclability is thought to find its source in the intrinsic readout mechanism of SR disks, based on the local and reversible modification of the optical properties of the active layer. One can assume that the high laser power required to generate this optical nonlinear phenomenon may result, through absorption, in a local elevation of temperature in the active layer. Heating of the materials, repeated at each readout cycle, is thought to induce undesirable structural modifications of the stack, potentially affecting the optical nonlinear process and, consequently, the efficiency of the readout mechanism in a significant way.

We recently reported the semiconductor InSb as a high-potential material to play the role of the active layer in SR disks, because of the high sensitivity and the signal quality delivered by InSb-based disks [4]. We proposed a model based on the reversible local metallization of InSb [5], induced by the photo generation of free electrons in the conduction band, in order to explain the increase in reflectance observed during the readout process. The huge optical nonlinearity of InSb was characterized by way of static pump-probe measurements of reflectance [6] which also pointed out the important role played by temperature in the nonlinear process. Complementary X-ray diffraction analysis exhibited the influence of the crystalline microstructure of InSb on the readout mechanism [7].

In this paper we report our recent improvement on the cyclability of InSb-based SR disks, made possible by the use of interface layers. We also analyze the evolution of the optical nonlinearity of InSb after several excitations through static pump-probe characterization of its optical properties.

2. EXPERIMENTS

2.1 Dynamic testing: evaluation of the quality of BD-like SR ROM disks

The structure of our Super-Resolution BD-like ROM disks is represented on figure 1. A thin film stack was deposited by RF magnetron sputtering techniques on a pre-recorded substrate moulded from a stamper mastered by Sony using electron beam lithography techniques. The pre-recorded substrates comprise single tone sequences of 80nm 2T pits (resolution limit: 120 nm) as well as random (1,7)RLL coded sequences. Two thin-film stacks were studied: a classical 3-layer stack ZnS-SiO₂(50nm) / InSb(20nm) / ZnS-SiO₂(50nm), and a 5-layer stack including interface layers ZnS-SiO₂ / interface layer / InSb / interface layer / ZnSiO₂. The quality of the signal retrieved from these disks, read out at a speed of 2.65 m/s, was evaluated by way of basic CNR measurements on single tone sequences and bit Error Rate (BER) evaluation on random sequences using the adaptive DF-PRML method (Ricoh). The cyclability was evaluated as a first step by observing the evolution of the carrier-to-noise ratio (CNR) after several readouts of the same track.

2.2 Static testing: characterization of the optical nonlinearity of InSb

We used a classical pump-probe static tester in order to achieve real-time measurements of the optical properties of samples excited by tuneable laser pulses ($\lambda=405\text{nm}$), focused with a 0.75-NA objective lens. The evolution of the sample reflectance before, during and after the excitation pulse was detected using a probe beam ($\lambda=440\text{nm}$). The stacks tested have exactly the same design as those of the SR disks, except that they were deposited on plain glass substrates and that no cover layer is required for our static testing setup. The protocol adopted to evaluate the amplitude of the dynamic optical contrast is illustrated on figure 2. A first pulse is used to crystallize the InSb layer, making the semiconductor switch from the amorphous as-deposited state (reflectance: R_a) to a crystalline state (reflectance: R_c). Once the material is stabilized in this crystalline state, an excitation pulse (fixed duration of 200 ns, which is approximately the time necessary for the spot to fly over a 80 nm mark at a speed of 2.65m/s) is delivered to induce the reversible nonlinear effect. If the pulse power is sufficiently low to prevent any irreversible degradation of the stack, the InSb layer goes back to the crystalline state at the end of the pulse since the absence of a heat sink in the disk structure prevents the layer from re-amorphizing. An investigation of the reproducibility of the phenomenon was also carried out by measuring the evolution of the optical contrast ($\Delta R/R_c$) after a high number of excitation pulses, until the stack exhibited a deterioration (loss of optical contrast and/or evolution of reflectance in the crystalline state).

3. RESULTS

3.1 Correlation between the signal amplitude of SR disks and the reversible optical contrast of the active stack

Figure 3 represents the evolution of CNR with increasing readout power, obtained during readout of a monotone 80nm 2T pits sequence. The introduction of interface layers did not show any significant influence on the signal which reaches around 37 dB at a power of 1.4 mW. A bER as low as $9.3 \cdot 10^{-4}$ was obtained on the classic 3-layer stack during readout of random sequences comprising 80 nm 2T pits, read out at a speed of 2.65 m/s. Figure 4 represents the evolution of the reversible optical contrast $\Delta R/R_c$ in response to 200ns-duration pulses of various powers. The introduction of interface layers induces a slight loss in stack sensitivity, but both stacks (with and without interface layers) exhibit a huge gain in reflectance, higher than 100%. Despite the slightly different thermal configuration between static and dynamic testing, implied by the use of a glass substrate instead of a polycarbonate substrate, a strong correlation between static and dynamic testing results can be observed, which suggests that the optically-induced nonlinearity of InSb is the main phenomenon involved in the readout mechanism of InSb-based SR disks.

3.2 Correlation between dynamic and static results in terms of cyclability

Figure 5 represents the evolution of CNR with the number of cycles, measured during readout of a monotone 80nm 2T pits sequence at a power of 1.4 mW. For both stacks (with and without interface layers), no significant evolution of signal was observed before 3 000 readout cycles. The use of interface layers significantly slows down the degradation of CNR which remains higher than 30 dB after 30 000 cycles. The same CNR value is reached after only 12 000 cycles for disks comprising the classical 3-layer stack. Figure 6 represents the evolution of contrast in reflectance with increasing number of excitation pulses. The 50 ms delay applied between two pulses is comparable to the delay between two cycles for a disk read-out at a speed of 2.65 m/s. For both stacks, the contrast in reflectance slowly decreases as the number of excitation pulses increases. It was observed that the 3-layer stack completely deteriorates after around 500 pulses. Just as in a dynamic case, the use of interface layers causes the loss of contrast to slow down, since no such abrupt loss of contrast is observed before around 7 000 pulses.

4. CONCLUSION

The cyclability of InSb-based SR disks, evaluated by CNR measurements, was significantly improved by adding interface layers between the active InSb layer and the dielectric ZnS-SiO₂ layers. Some bER measurements will be performed on random sequences in order to determine if the loss of signal for 2T marks, observed after 3 000 cycles, can be corrected by adaptive PRML detection algorithms. It was pointed out that the use of interface layers significantly improved the cyclability of our disks. Static pump-probe measurements of reflectance, which give direct access to the physical phenomenon(s) optically-induced in the stacks, exhibited that the use of interface layers causes the degradation of the optical nonlinear effect to slow down. From the observed correlation between static and dynamic configurations, we can speculate that the decrease of the optical contrast after several pulses is the main phenomenon involved in the decrease of signal amplitude observed after reading out the InSb-based disks for a long time. The static tester then appears as a complementary but essential tool for optimizing the SR disks structure and will be used in further SR media development.

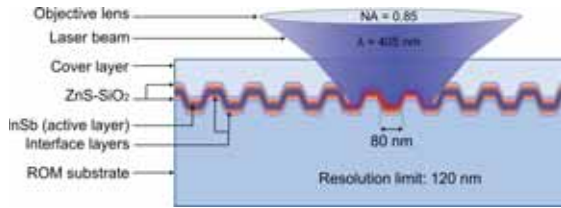


Fig. 1. Representation of the BD-like ROM disk including a 5-layer stack based on the active semiconductor InSb

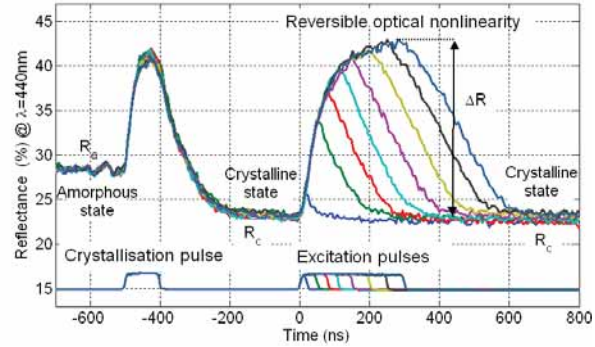


Fig. 2. Protocol used to evaluate the amplitude of the optical contrast induced by laser pulses on the static tester.

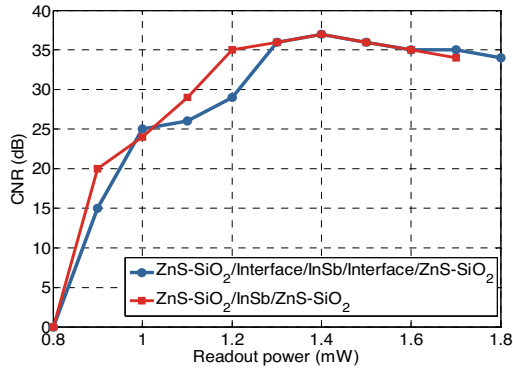


Fig. 3. CNR dependence on readout power measured during the readout process of monotone sequence of 80 nm marks

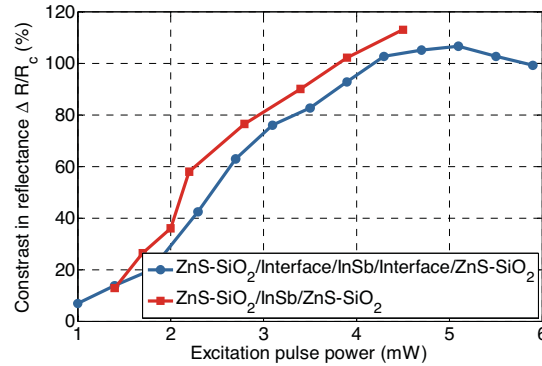


Fig. 4. Contrast in reflectance dependence on the excitation pulse power (pulse duration: 200ns), measured on the static tester

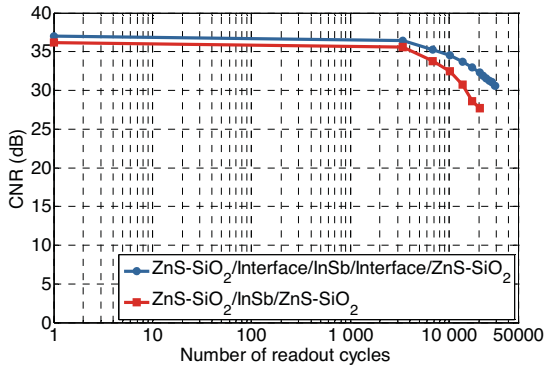


Fig. 5. Evolution of the CNR with the number of readout cycles during the readout process of monotone sequence of 80 nm marks at power of 1.4 mW and a speed of 2.65 m/s

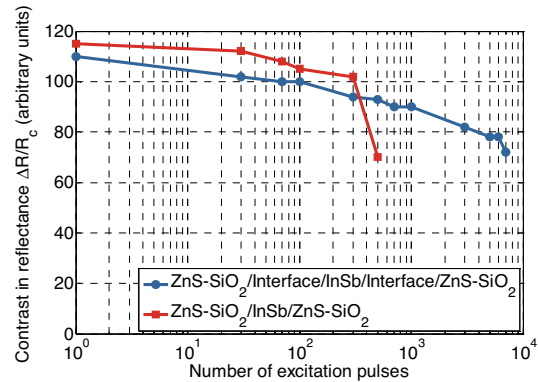


Fig. 6. Evolution of the dynamic contrast in reflectance (arbitrary units) with the number of excitation pulses, measured on a static tester

REFERENCES

- [1] J. Tominaga *et al.*, JJAP vol. 39, p 957, (2000)
- [2] J. Kim *et al.*, JJAP vol. 46 p 3933(2007)
- [3] H. Tajima *et al.*, Technical digest of ISOM'07, MB-03, (2007)
- [4] B. Hyot *et al.*, Technical digest of ISOM'07, MB-03 (2007)
- [5] B. Hyot *et al.*, Technical digest of ODS'06, p206 (2006)
- [6] B. Hyot *et al.*, Technical digest of ISOM'07, MB-06 (2007)
- [7] B. Hyot *et al.*, Technical digest of ISOM'07, WE-I-06 (2007)

Improvement of Aerodynamic Stability in Flexible Optical Disk System with Cylindrically Concaved Stabilizer

Yasunori SUGIMOTO†, Shozo MURATA†, Yasutomo AMAN†, Masaru SHINKAI†, Nobuaki ONAGI†, Daiichi KOIDE‡, Yoshimichi TAKANO‡, and Haruki TOKUMARU‡

† Core Technology Research and Development Group RICOH COMPANY, LTD.
1005 Shimo-Ogino, Atsugi City, Kanagawa-Pref. 243-0298, Japan

‡ Science & Technical Research Laboratories, Japan Broadcasting Corp. (NHK)
1-10-11 Kinuta, Setagaya-Ku, Tokyo 157-8510, Japan

1. Introduction

A flexible optical disk (FOD) system, comprised of a flexible disk and a stabilizer, was previously reported^{1,2)}. Due to the aerodynamic effect of the stabilizer, an axial runout of less than 10 μm at 15000 rpm was achieved, and thus, high-density recording with a high numerical aperture (NA) pickup was also realized^{3,4)}.

However, a problem still exists in the difficulty in setting the clearance between the disk and the stabilizer (Cbd). A narrower Cbd setting is better for stabilization. However, if the Cbd is too narrow, the disk and stabilizer will collide; if it is too wide, the Cbd setting may cause the axial runout to increase rapidly. Furthermore, the margin of the Cbd setting is reduced at higher rotating speeds. In this paper, to expand the margin of the Cbd setting in order to improve aerodynamic stability, the effects of both disk thickness and material on the aerodynamic stability were investigated.

2. Details of cylindrically concaved stabilizer

The top view of the cylindrically concaved stabilizer is shown in Fig. 1 (a), and the mounted status of the rotating flexible disk is shown in Fig. 1 (b). As depicted in Fig. 2 (a), the shape of the top surface is almost cylindrically concave with a 1000-mm radius, which can entirely cover the flexible disk. The clearance (Cbd) set between the disk and the base of the stabilizer is defined in Fig. 2 (b).

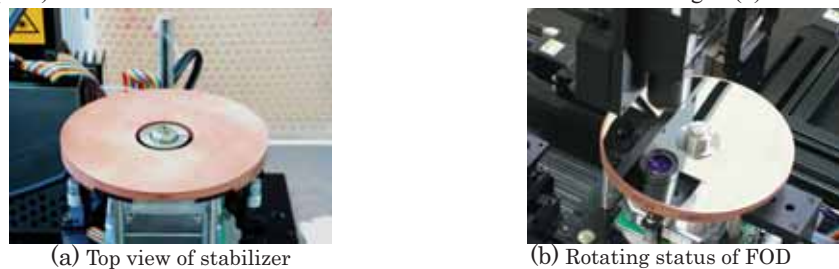


Fig.1 Layout of FOD system

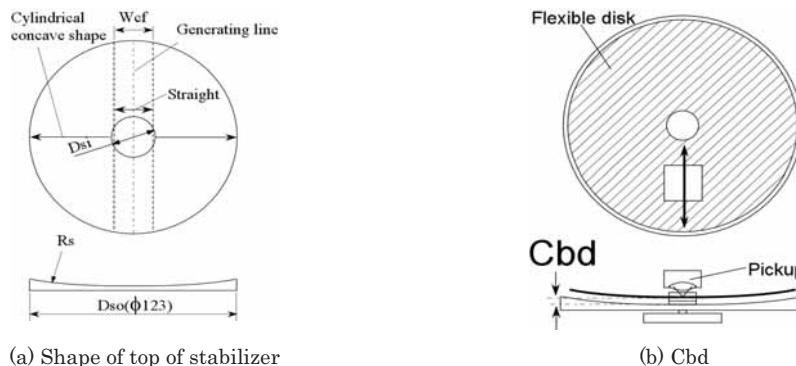


Fig.2 Detailed schematic diagram of stabilizer

Material	Thickness (μm)
polycarbonate(PC)	50,72,95,120,200
polyethylene terephthalate (PET)	50,75,100,125

3. Experiments and Results

Table.1 Disk types

Several types of flexible optical disks were prepared, as listed in Table 1. All of the disks were 120 mm in diameter and were deposited with an Ag layer.

As shown in Fig. 3, after sandwiching the flexible disk between two hubs, 25 mm in diameter and 0.6 mm in thickness, the disk was placed on the spindle motor. When the disk starts rotating, the disk rotation generates a flow of air through the axial clearance between the disk and the stabilizer. The air is taken in from the inside radial clearance (RCsc) and vented around the outer rim of the disk. When the clearance setting of the Cbd is appropriate, the disk rotates along the stabilizer surface while maintaining a constant gap, even though the surface is curved. The gap fluctuation becomes the axial runout of the disk. A narrower Cbd setting is better for stabilization. In fact, the narrowest practical setting was around 0.1 mm, because a setting that was too narrow caused the disk and stabilizer to collide.

The axial runout, the performance of aerodynamic stability, was evaluated on the line of a pickup radial scan from 25 to 58 mm by a laser displacement sensor (LC-2430, Keyence).

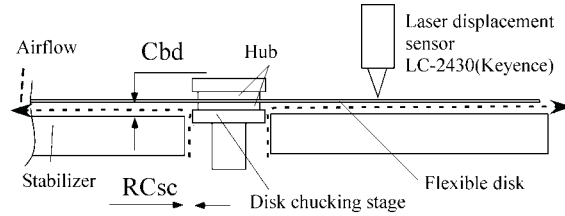


Fig.3 Cross-section of flexible optical disk drive

The effect of thickness on axial runout is indicated in Fig. 4. In this case, an axial runout of less than 10 μm is achieved among radii from 25 to 58 mm no matter what the disk thickness and disk rotation speed were.

On the other hand, Fig. 5 shows a radial profile of suppressed axial runout at 15000 rpm. In this case, an axial runout of less than 10 μm is achieved among radii from 25 to 58 mm no matter what the disk material was. This result shows that axial runout is unaffected by disk thickness or disk material. These results indicate that the system has a wide allowable range of disk thickness and disk material.

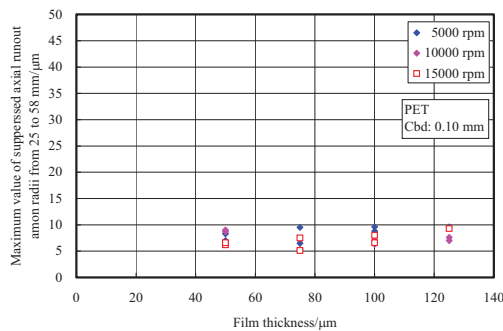


Fig. 4 Axial runout among radii from 25 to 58 mm

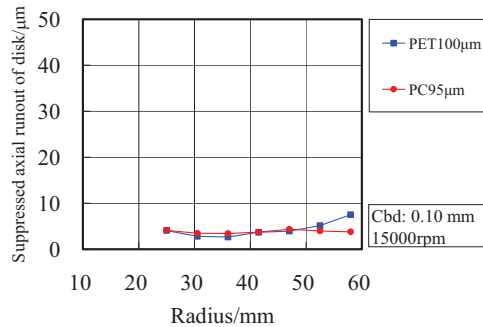


Fig. 5 Radial profile of suppressed axial runout

The effect of Cbd setting on suppressed axial runout is plotted in Fig. 6. This result shows that there is a “turning” Cbd setting at which the axial runout increased rapidly. For example, the turning Cbd setting of PC 120 μm is around 0.24 mm, and the turning Cbd setting of PET 75 μm is around 0.38 mm. The turning Cbd setting is defined as the active Cbd range of the stabilizer.

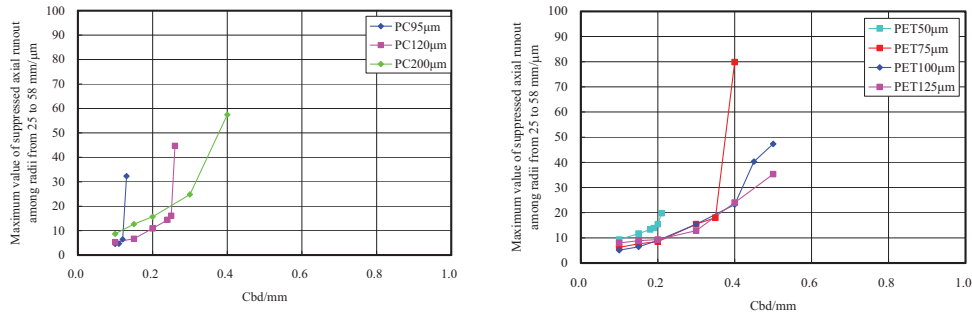


Fig. 6 Change in suppressed axial runout at 15000 rpm with Cbd setting

The effect of disk thickness on active Cbd range is indicated in Fig. 7. This result shows that the active Cbd range is proportional to disk thickness. An active Cbd range was not obtained in the 50-μm or 72-μm PC disks. Therefore, it is imperative that PC disk thickness be more than 72 μm.

Flexible optical disk thickness is now about 150 μm, and with dual layers, the disk thickness is around 200 μm. This result indicates that a flexible optical disk that is 100-200 μm thick has a sufficiently active Cbd range at 15000 rpm.

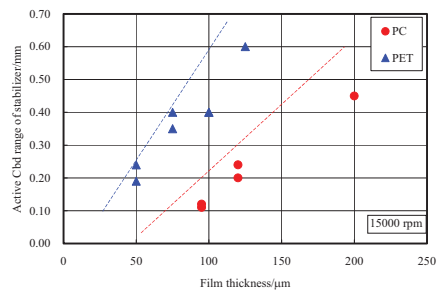


Fig. 7 Change in active Cbd range at 15000 rpm with disk thickness

4. Conclusion

The aerodynamic stability of flexible disks that varied in thickness and material was investigated. As a result, it was found that the aerodynamic stability at 15000 rpm could be improved by increasing the disk thickness. This high rotational speed provides a maximum data transfer rate of more than 600 Mbps for the recording density of a Blu-ray Disc. This rotational speed seems to be sufficiently high for a professional HDTV video disk recorder.

References

- [1] N. Onagi, et al.: Jpn. J. Appl. Phys. **43** (2004) 5009
- [2] N. Onagi, et al.: IEEE. **41** (2005) 1004
- [3] D. Koide, et al.: Tech. Dig. of ISOM, 2007, Tu-E-03
- [4] Y. Aman, et al.: Jpn. J. Appl. Phys. **46** (2007) 3750

Multi-level Read-only DVD Using Signal Waveform Modulation

Yi Tang*, Jing Pei, Longfa Pan, Hua Hu, Haibo Yuan, Buqing Zhang, Mingming Yan
Optical Memory National Engineering Research Center, Tsinghua Univ., 100084, Beijing, China

ABSTRACT

A novel multi-level read-only DVD using signal waveform modulation is introduced in this paper. By inserting sub-pit/sub-land in the recording track, we can obtain multi-level waveform of readout signal. This multi-level waveform modulation has been implemented on a DVD platform. For the signal detection of run-length and recording levels, a digital timing recovery system and a pattern recognition method with feedback are adopted. This readout system can achieve raw error rate of less than 10^{-4} .

Keywords: Optical Storage, Multi-level, Signal Processing, Timing Recovery, Pattern Recognition

1. INTRODUCTION

A recognized advantage of optical storage is the low-cost mass-production of read-only memory (ROM) media. Multi-level (ML) technology can increase the storage capacity without changing the readout optics. Studies on multi-level read-only recording have been carried out^[1,2]. Variation of pit width and/or depth was employed to achieve variation of readout signal amplitude. The essence of the previous multi-level is a so-called amplitude modulation (AM) method.

In this paper, a novel multi-level read-only recording is presented. In this method, a sub-land/pit is inserted to the original pit/land, leading to variations in wave-shape of readout signal. Using the wave-shape to differentiate the levels, a signal waveform modulation (SWM) ML method is realized. This innovative ML method is implemented on the DVD platform. Signal processing, including timing recovery and level detection, is also presented in this paper.

2. PRINCIPLE

The readout of ROM media is based on phase-modulation resulting from constructive and destructive interference of light from the pits and the adjacent land. Because of the size limit of focusing light spot, if the land/pit is too short, the corresponding signal amplitude change will be too small for run-length detection. Therefore, conventional 2-level recording employs a run-length-limited (RLL) coding, which formulates the smallest length of pit and land.

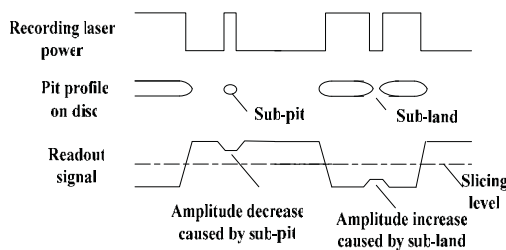


Fig. 1. principle of SWM ML recording

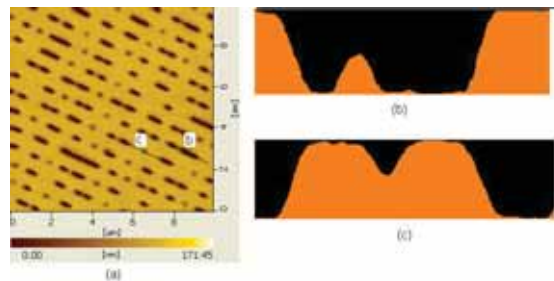


Fig. 2. AFM image of SWM ML disc

However, in the proposed ML method, we make use of those pits/lands shorter than the formulated smallest length. They are called sub-pits/lands here. A sub-pit/land is inserted to the original land/pit, modifying the wave-shape of the readout signal. Using the wave-shape to differentiate the levels, one run-length can have more than 2 states. So a SWM ML method is realized. Changing the length and/or position of the sub-pit/land, the number of realized levels can be increased. A long pit/land has more space for the sub-land/pit to change length and/or position, so it can realize more levels. Contrarily, a short pit/land will have fewer levels. The principle is shown in figure 1.

* tangyi00@mails.tsinghua.edu.cn, phone: 861062788101, postal address: Room 4406, Building 9003, Tsinghua Univ., Beijing, China, 100084

3. RECORDING

This ML recording is implemented on commercially available DVD mastering and injection molding equipment. All the process parameters are the same as those of conventional DVD, which can be seen in ref. 1. The only change is the writing pulses. An ESP-7000 formatter (by ECLIPSE) is employed to generate the expected writing pulses.

A write strategy (WS) optimization is needed. The first target of WS is determining appropriate sub-pit/land length and position, ensuring levels shall be easily differentiated. The second one is compensating the run-length deviation caused by sub-pit/land insertion. Theoretical calculation is used to help the WS optimization. A lithography model [3] is used to predict pit profiles. A diffractive model is used to calculate the readout signal. The timing parameters can be preliminarily determined by theoretical calculation, and then fine adjustment is done according to experiment result. The atom force microscope (AFM) scanning image of molded discs is shown in figure 2, where, sub-figure (b) is the cross-section of a pit with a sub-land, and (c) is that of a land with a sub-pit.

As discussed in the 2nd section, different level numbers are realized by different run-length. Here, 5T realizes 4 levels, 6T and 7T realize 6 levels, 8T and 9T realize 10 levels, 10T and 11T realize 14 levels.

4. READOUT

A commercial DVD pick-up and servo electronic is employed to read the disc. A DVD-like linear equalizer is used to decrease jitter. The equalized readout signal of random data is shown in figure 3. The waveforms of typical run-lengths, 6T and 11T, are shown in figure 4 and 5, where, TxLy means level y of xT land and TxPy means level y of xT pit.

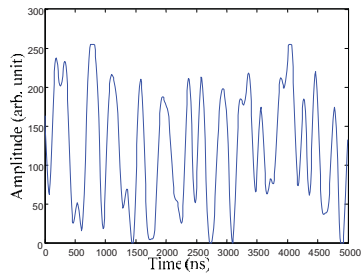


Fig. 3. readout signal of random data

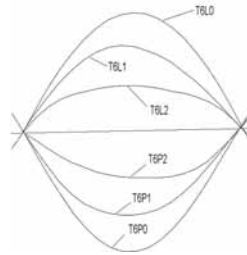


Fig.4. waveforms of 6T

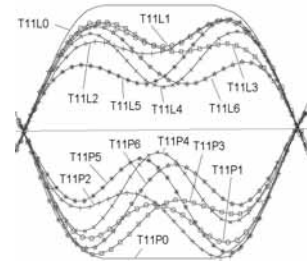


Fig.5. waveforms of 11T

A digital signal processing based on FPGA is used to retrieve the run-length and level data. Analog RF signal is sampled by an analog-to-digital converter with a fixed sampling frequency of 100MHz, which is nearly 3 times of the channel bit frequency. This asynchronous sampled data is equalized by a DVD-like linear equalizer. The timing recovery and level detection are followed. The diagram is shown in Fig. 6.

Timing recovery is regenerating data synchronous with the channel clock from the asynchronous sampled data. It is realized by linear interpolating. The interval of interpolating positions is determined by frequency detection. A sync pattern, 14T pit-3T land-3T pit, is used for frequency detection. There are always 1472 channel bits between every two sync patterns. After the amount of samples between two sync patterns N_{freq} is counted, the interpolating interval is calculated as $N_{freq}/1472$. So, the kth interpolating position can be expressed as $k*N_{freq}/1472$. However, experimental results show that the accuracy is not good enough. So, a phase detection and adjustment are carried out during interpolating. The principle of which is shown in Fig.7. Phase error, ε , is calculated as below

$$\varepsilon = (a - b) / 2(a + b) \approx (c - d) / 2(c + d) \quad (1)$$

When $|\varepsilon|$ is bigger than a threshold, θ , a fine adjustment, Φ , is executed as shown in Fig. 7. Usually, Φ is smaller than θ . Values of Φ and θ should be tried and carefully selected in order to minimize the residue phase error and run-length error rate. Because of the waveform modulation, equation (1) sometimes cannot indicate the actual phase error. It can be seen in Fig. 8 that $d \neq c$ while there is no phase error. To avoid this, a condition that $d+c > \Psi$ (Ψ is a predetermined value) is purposed to satisfied. Otherwise, the adjustment will not be executed. After timing recovery, the run-length is calculated by comparing the synchronous data with the slicing level.

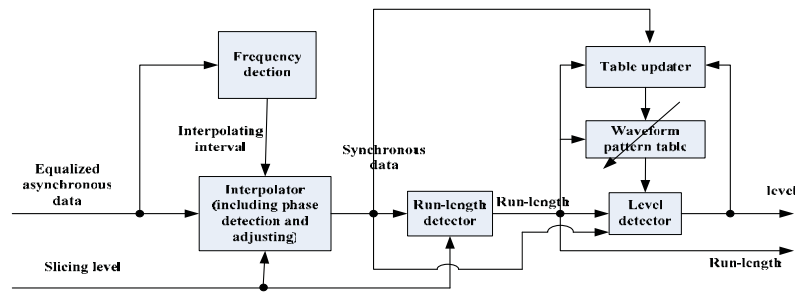


Fig. 6. diagram of timing recovery and level detection

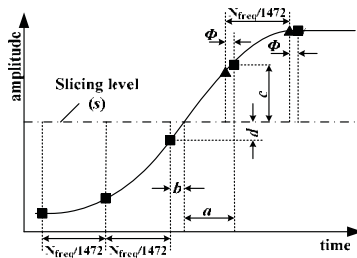


Fig.7. phase detection and adjustment

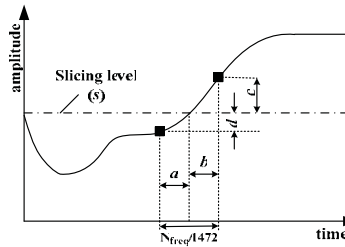


Fig.8 influence of waveform on phase detection

Level detection is done by a pattern recognition method. Waveform pattern table provides standard waveform values for every run-length and level. Euclid distances between the actual waveform and standard waveforms of every level are calculated. The detected level is who has the minimal Euclid distance. Adaptive adjustment is needed to compensate the processing parameter drifting of different disks and readout instability. It is done by updating the waveform pattern table. After the level is detected, the actual waveform values are feedback and compared with the corresponding values in the pattern table. The table values are updated and become closer to the actual ones. So, the deviation of table values form the actual ones can be gradually reduced.

5. CONCLUSION AND DISCUSSION

The readout system achieves a raw bit error rate of less than 10^{-4} . The feasibility of this method is experimentally demonstrated. Compared with conventional AM ML, this new SWM ML has some significant merits. Now 2-level-to-multi-level mapping modulation coding is employed in our method. It can realize the same transfer rate and capacity as that of (0, 6) run-length limited coding. Its density ratio (DR) is 2.25 bits per minimum run-length, while corresponding value of AM ML is only 2^[4]. Furthermore, in SWM ML, both land and pit can realize multi-level. It is naturally land-pit-spacing, which can facilitate the injection molding and DC-free control. In additional, experiments shows that our SWM ML has the same track-following servo performance as conventional 2-level DVD, while the AM ML encounters the tracking error detection problem^[5].

REFERENCES

- [1] SONG J, NI Y, Xu D Y., et al.. *Optics Express*, 14(03) : 1199-1207 (2006)
- [2] ZHANG Q C, NI Y, XU D Y, et al.. *Jpn. J. Appl. Phys*, 45: 4097-4101(2006)
- [3] H. Yuan, D. Xu, et al.. *Optics Express*, 15, 4176-4181 (2006)
- [4] H. Hu, H. Yuan, et al.. *ISOM 2007 technical digest*, We-1-30 (2007)
- [5] Q. Shen, J. Pei, et al.. *Jpn. J. Appl. Phys*, 45: 5764-5768(2006)

SESSION TuC: Special Session: Applications

Monarchy Ballroom
3:30 to 6:30 pm

Susanna Orlic, Technische Univ. Berlin (Germany)
Mitsuru Irie, Osaka Sangyo Univ. (Japan)

Toward Adoption of Optical Disks for Preservation of Digitized Cultural Heritage

Kunimmaro Tanaka
Teikyo Heisei university
2289-23, Uruido, Ichihara, Chiba, 290-0193, Japan

Abstract

Digital archive is important for preservation and usage of present culture. Recent status and requirement for optical disks for this purpose is described.

1. Introduction

Digital archiving is considered useful method to preserve present culture. Digital archives are being developed in various organization. In addition to it, digitally born art such as computer graphics, photograph taken by digital camera, computer music have to be preserved in digital form. Our concern is which storages are suitable for storing digital archives. There are various candidates as magnetic tapes, hard discs, optical discs semiconductor tips and even micro film. This paper describes present status of optical discs for archival use and requirement to make optical discs penetrate into this field.

2. Life time of DVD available in the market

Because measurement of life time of optical disks takes very long time, there are not enough data in the industry except in the laboratories of manufactures. This situation makes consumers uncertain. I would like to introduce project of Digital Contents Association of Japan. DCAj is tackling various issues to facilitate production, distribution and usage of attractive, high-quality content welcomed by the market. DCAj established the committee which evaluate the life time of DVD. The members of committee were from industry, user groups and academia. The committee conducted life test and regular performance test also. The committee bought 8 brands DVD-R disks, 5 brands DVD-RAM disks, and 5 brands DVD-RW disks from a large electronic store in Tokyo. The results of the life test are reported below. The end of life time was defined as the time when number of Inner Parity errors (PI error) reaches 280 for DVD-RW and DVD-R disks and 10^{-3} byte error rate for DVD-RAM disks. The combination of Arrhenius plot and jack knife were used.[1] The stress condition were 65 degree, 75degree, 80degree and 85degree in centigrade. The humidity was 80 %RH at all cases for the worst case measurement. The test results were shown in Table 1. Because there were disks which did not satisfy DVD criteria from the beginning or data spread too much, the life of not all brands disk were able to be measured. Those data are not written in the table. The unit of the value in Table 1 is year, and value is median value. Although each type of disk has same brand name A,B,C,...., in table 1, their actual brand are different from each other. Some brand showed life time of more than 30 years, while others did zero year.

Table 1. The life time of various (year)

	DVD-R	DVD-RW	DVD-RAM
Brand A	64.380	6576.405	256.736
Brand B	23.122	31.198	181.658
Brand C	10.278	14.976	166.619
Brand D	15.836		50.760
Brand E			61.024

3. The international standard for archival optical disks

As shown in DCAj test, the life time of the DVD in the market spreads very much. It means the standard life time measurement of optical disks is necessary. Table 2 shows necessary optical disk standards for digital archives and existing standards.

Table 2 Optical Disk Standards for digital archive

Standards	Standard no.	Status
Life estimation	10995 (DVD) 18921 (CD-ROM) 18925 (Optical disk) 18926 (MO) 18927 (CD-R)	Already made.
Error monitoring and data migration	12142 (SCSI command set) 29121 (DVD)	29121 is under discussion.
Media handling	18938 (Optical disk) 18934 (Multiple type media)	Already made.
Standard drive	---	Not yet started
Drive carrillation	---	Not yet started
Accreditation	---	Not yet started

4. Archival grade optical disk for consumer use.

Video, audio, documents and photograph in consumer fields have been digitized now a days . It means media for storing those digital data are necessary. Because optical disk has long life, it is prominent candidate for preservation of such digital data. When accreditation systems for long life optical disk are made using above mentioned standards, it will be very helpful.

5. Digitization of cultural heritage

Libraries and museums preserves digital cultural heritage. For what type of information is suitable for digital preservation is important issue. Digital equipment becomes obsolete quickly. Format, equipment and media have to be renewed. Information has to be migrated. The those renewal cost has to be considered. Figure 2 shows focused cost comparison of various factors. The data is from Swedish national archives. [2] Percentage of staff, premises and support will become 12 times of equipments. The cost for storage media is negligible small. In order to reduce staff cost of digitization,

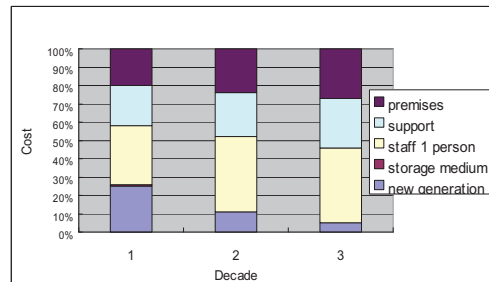
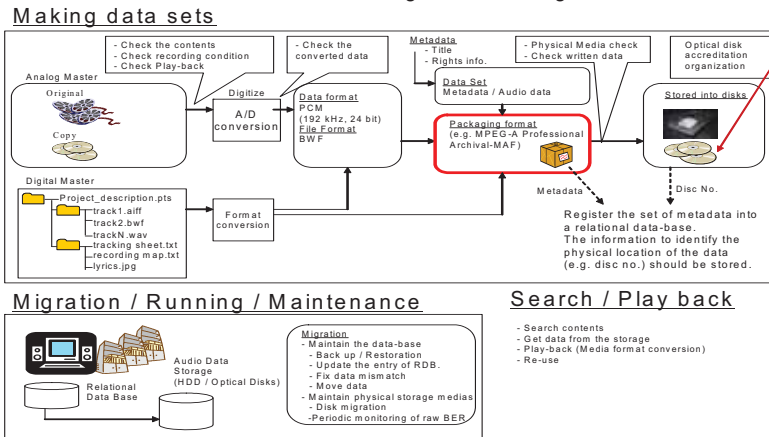


Figure 1

microfilm was selected for preservation in Swedish national archival. However, in order to let people access to the archive through network, digitization is inevitable. Audio and video are type of cultural heritage that digitization is very effective for preservation. It means necessity of digitization depends on type of information.

An over view of digital archiving



6. Professional audio digital heritage

Figure 2 shows concept of digitization of professional audio data. The standardization of packaging format is necessary.

When it is tried to make digital archives separately from daily workflow, it is very difficult to achieve it. Work flow has to be changed such as digital archives are made automatically and re-used in daily operation in order to establish digital archive.[3]

Historical Records Archive Promotion Conference was formed by six record and broadcasting companies in Japan. HRAPC is digitizing Japanese historical sound source recorded between 1900 and 1950. Those sound sources has been stored in SP records and metal stampers. There are 70000 titles to be digitized in total.

7. Document preservation

Electronic documents are stored in both microfilm and digital storage.

National Diet Library in Japan has stored 143,000 books, 46000 precious pictures in it's digital archive system. They are accessible from outside through internet. Storage system conforms to OAIS.

National Archives of Japan has to preserve governmental documents. They are stored in paper format. However, mportant documents are converted into microfilms and digital data. There are 180 million pictures in it's digital archive system. There ate two sections in the Digital archives system. They "Digital Archive System" and "Digital Gallery". Digital information are stored in the form of JPEG2000 ISO/IEC 1544-1 Lossless format. Then they are converted again to PDF ISO/IEC 15444-6 or JPEG2000 lossy format for review purpose.[4]

The e-document law was established in Japan. This might stimulate to use digital document. JIS Z6017-2006 specifies management method of electronic document stored in DVD.

8. Conlusion

Digitization is very effective method to preserve present culture to our descendant. Optical disk is one of the most prominent storages. However, there are lots of formidable competitors. In order to make optical disks penetrate into this field, 1) Accredit system of present optical disk has to be established, 2) Data management system have to be developed and improved in order to support usage me optical disk. 3) Bit cost has to be lowered. It means recording density has to be increased. 4) Transfer rate has to be improved.

9 . Acknowledgement

This study was subsidized by the Japan Keirin Association through its Promotion funds from KEIRIN RACE and was supported by the Mechanical Social Systems Foundation and the Ministry of Economy, Trade and Industry.

The data and information were supplied from project of DCAj, National archives of Japan, National Diet Library, Recording industry association of Japan, and NTT. Author wishes to thank for kind offer of those valuable data.

9. Reference

[1] "A Feasibility Study on Development of Optical Disk Medium for Long-Term Storage," report of The Mechanical Social System Foundation and The Digital Content Association of Japan, 18-F-10 March 2007.

[2] Jonas Palm, "The Digital Black Hole," <http://www.tape-online/technology/.html-palm>

[3] Klaus Heidrich (chair) "Digital Archive Strategies and Solutions for Radio Braodcasting," J.Audio Eng. Soc. Vol 52, No. 11 pp 1180-1184, Nov. 2004.

[4] National Archives of Japan "Introduction of NAJ Digital Archive," from ppt of NAJ, June 2007.

Trends in the Digital Home

Why “IMG0064.jpg” is the new blinking 12:00

T. Rausch, S. Iren, D. Seekins and E. Riedel
Seagate Research, 1251 Waterfront Place, Pittsburgh, PA, 15222

ABSTRACT

Technology has become more ubiquitous and accessible than ever before, but it still remains out of reach of many everyday individuals. People struggle with technology and content management in the home on a regular basis. Using design research techniques, we went into the homes of families and spent time with them, observing their successes and failures with digital data. As a result of the study we identified several trends in the digital home and barriers between individuals and their technology.

Keywords: Usability, technology barriers, digital home

1. INTRODUCTION

When the videocassette recorder was introduced to the home in the 1970s and 1980s it was hailed as a marvel in technology. Consumers could watch the latest Hollywood blockbusters in the comfort of their own homes, or record a late night episode of Mary Tyler Moore and watch it at their convenience. It is no wonder that VCR home ownership in the United States increased from less than 1% in 1980 to over 50% by 1987¹; outpacing the adoption rates of color and cable television introduced two decades earlier. The VCR, like the television and radio before it, was a technological marvel that promised to change people’s lives by allowing them to digest video content on their terms. Imagine, being able to start/stop, fast-forward, re-watch and even record video whenever and wherever you wanted. However, for a generation of consumers that grew up using rotary dial telephones many of the features of the VCR were just too complicated to use and were often ignored. No one feature exemplifies this more than the digital clock integrated into most VCRs. Early VCRs in the United States did not take advantage of WWVB signals (or other time signals embedded in broadcasts), which are common in some newer electronic devices and instead required users to manually set the time on their devices. The clock would need to be reset manually when the device was first powered on or whenever power was lost. The systems were designed to notify the user that the correct time needed to be set by simply blinking “12:00” at infinitum. Setting the clock became one of the burdens of modern life and a symbol of the failings of technology due to its complexity. Being able to set the clock became a symbol of one’s technical prowess and oneness with technology. Ironically, for many years the most common “hack” for fixing this problem was to use a small piece of black electrical tape to obscure the clock from view.

Today, the digital landscape looks very different. The VCR is well on its way to extinction thanks to the DVD and the digital video recorder. People carry with them small portable devices for reading email, listening to music and watching video. We have digital photo and video cameras with storage so cheap no one thinks about the cost of capturing images. Yet, through all this the “blinking 12:00” still survives, albeit in a different form. Consumers today live in a world with multiple, and often incompatible, digital rights management (DRM) schemes that not only serve the interests of the content creators but also seek to lock consumers to a specific brand. It is a world of multiple file formats for photos, videos, music and documents where incompatibilities abound. Even the language of the technology is so sophisticated that it is cryptic to all but the most sophisticated users. These things are barriers to the usefulness of technology in the everyday lives of consumers. For this generation the complexity is no longer embodied by the blinking “12:00” but by the barriers between individuals and their content. Given the popularity and ubiquity of digital cameras, this is perhaps best exemplified by the meaningless default file names used for digital photos. Rather than automatically describe a digital photo file by the contents therein, today’s technology uses an incremental counter to index the image file names. In a recent home study project we conducted, the majority of participants did not take the time to change the name of the photos to something more representative of the content or in many instances gave any thought to organizing their photos. This is not surprising given the volume of pictures being taken. It is simply not practical to manually rename or tag every photo. Even when photos are tagged, much of the information is stored in a separate file or database unique to the

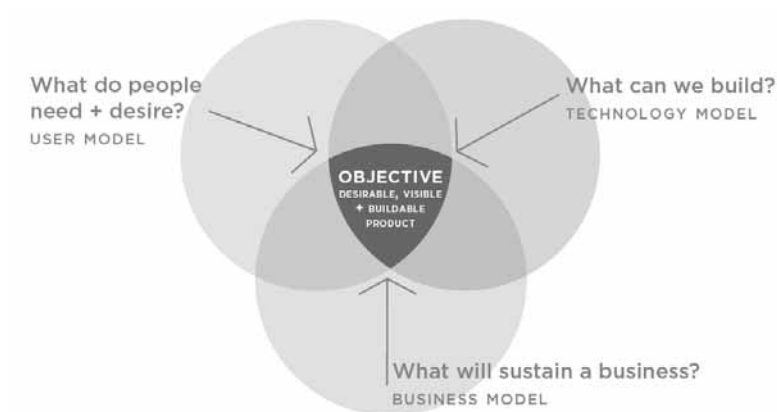


Figure 1 Ingredients for Success - find the balance between user needs, technology and business.

photo application and is not easily shared with friends or family or between different applications or devices. This limits the usefulness of personal photo libraries and many complained how difficult, if not impossible, it was to find a particular photo. In this instance, the cryptic file names like “img0064.jpg” represent a significant barrier between individuals and their content; this is the new blinking “12:00” for this generation.

In a world where we manufacture more transistors than grains of rice, and at a lower cost, we should focus some of this processing power to making the technology more accessible to consumers². This can be accomplished by designing solutions for consumers rather than individual products. Including consumers early on in the design process, and at various stages during development to seek a balance between technology, business and the needs of the consumer, greatly increases the likelihood of a product being successful (see Figure 1). At one company, user centered design methodologies cut development costs by 33-50%³. Studies show that correcting user centered design flaws during development costs 10 times as much as correcting them early on in the process and nearly 100 times when the product has been released⁴.

2. HOME VISITS PROJECT

In 2007 we conducted a series of home visits where we went into people’s homes and talked to them about their interactions with digital data and observed them succeeding and failing at these interactions. The homes we visited represent a cross section of the American family. We visited two homes with children under the age of ten, a home with two teenagers, a couple where the children had already moved out and finished college, a home of a young couple who just moved in together and a home where most of the children had moved off to college but still had a young child in the house. The purpose of the project was to better understand how consumers are interacting with their digital data and how storage can be better designed to meet these needs. During the visits we observed numerous trends in the digital home and saw many barriers between individuals and families and their technology and digital content. From these observations we extracted four major themes common to nearly all the families we visited.

Theme 1 - There is no such thing as a simple product

Most product designs assume a single user interacting with a single device. In reality, devices are part of a large ecosystem and must work together, seamlessly, with many other devices. Consumers have to deal with many different interfaces, from software to physical connections. They must become fluent in the language of the technology and they must spend a great deal of time configuring devices. People have different ways of dealing with these barriers such as avoiding the technology all together, using it in a limited capacity, or relying on someone else to help them.

Theme 2 - Content management is a village affair

Again, remember that most product designs assume a single user interacting with a single device. In most households, more than one person is interacting with the devices and the content. This requires negotiation on configuration,

acquisition, and management of new devices and new content within a home. It raises questions as to who is in control of the data and the technology; who owns it and who is allowed to use it? Rather than make things easier, often technology becomes an additional source of friction in an already complex dynamic social structure. If only children possess the knowledge to set the VCR clock or choose programs to record, how can parents manage access to inappropriate content?

Theme 3 - No one single way of organizing content will do, and organizing content requires special knowledge

For photos, movies and music, most application software provides some kind of default organization scheme: Photos by date, movies by genre, title, rating, etc., music by artist, album, track and genre. Many people live with these defaults; sometimes because the defaults are acceptable, but often because they lack the knowledge, desire or will to invest in what it takes to organize the way they really want. However, content means different things to different people and people's priorities and activities shift over time. In many instances the rigid file structures people use to organize their content fails them. For example, people acquire more and more content over time and often find that their organization system, which was created when they only had a few files, does not scale to thousands of digital pictures and music files. In addition, the value of individual content changes over time and today's fun-shot or top 40-hit becomes tomorrow's precious scrapbook entry or tie to an important memory. People require organization systems that can adapt to these changes.

Theme 4 - Different goals require different support

During our home visit project we met viewers, collectors and makers. Each has different goals and required different things from their technology. While viewers simply sit and enjoy the content, collectors enjoy building a systematic collection of content and derive pleasure from the activities of amassing and organizing the collection. Collectors need storage and organization schemes that can support large or even massive content collections: storage capacity, visualization at multiple levels of detail, and effortless reliable backup. Makers use content to make something new (e.g. photo albums, a family history, scrapbooks, movies). They love the actual process of "making" something as much as, if not more than, the end product. Each content item is precious to them and makers need storage and organization schemes that can support good version control (original scan, black and white version, low-res version), organic "piles" of work in progress, multiple media formats, effortless backup, and a good balance between ease of use and full control.

3. CONCLUSION

Using design research techniques we went into the home of six families. We observed many trends and barriers between people and their technology and content. People dealt with the barriers in different ways from ignoring the technology, relying on someone else to do it for them or only using a limited set of the features. To solve these problems product designers need to change from designing products to providing solutions for people and involve consumers in every stage of the solution development. Although technology exists to address many of these problems, solutions must balance user attention with technology solutions

REFERENCES

¹ See for example Everett Rogers, "Video is Here to Stay," *Media & Values* **42** (1988)

² Quote is widely attributed to Sam Palmisano from IBM and first appeared in "A Law of Continuing Returns", *LA Times*, April 17, 2005. The complete quote was as follows "Last year more transistors were produced, and at a lower cost, than grains of rice, according to the Semiconductor Industry Association. Moore estimates that the number of transistors shipped in 2003 was 10 quintillion, or 10 to the 18th power -- about 100 times the number of ants estimated to be stalking the planet."

³ J. L. Bosert, "Quality functional deployment: A practitioner's approach." In Bias, R. G. & Mayhew, D. J. (Eds.), *Cost-Justifying usability*. Boston: Academic Press. (1991)

⁴ T. Gilb, "Principles of software engineering management" In *Usability is good business*. Retrieved October 15, 2001, from <http://www.compuware.com>. (1988).

Applications for 4th Generation Optical Storage

T.E. Schlesinger, B. Krogh and T. Chen

Department of Electrical and Computer Engineering

Carnegie Mellon University

Pittsburgh, PA, USA 15213

ed@ece.cmu.edu

Abstract: Optical data storage provides inexpensive, removable, easily replicated medium. Only applications requiring these will use optical storage. Advanced imaging and control systems are applications that could require the next generation of optical data storage systems.

1. Introduction

Any successful technology must solve a problem or provide a new capability that is highly desired by the user. The three generations of optical data storage technology, namely, CD's, DVD's, and high definition technology did just that. In each case the capacity of the medium along with the unique characteristics of optical storage systems, namely, inexpensive substrates that can be efficiently replicated at low cost and which can be removed from the player made this technology uniquely suited to address certain markets. CD's were well suited for the distribution of audio content, DVD's for video, and third generation HD DVD's for high definition movies. It is the application that determines the technology requirements in terms of storage capacity, data rates, acceptable error rates, archivability, acceptable cost etc. Without a well defined application driving the development of technology the justification for the investment as well as the required measures of performance become unclear. This is the challenge currently faced by fourth generation optical storage.

It is not clear at this time what need or new capability is driving the development of fourth generation optical storage technology. In addition extrapolations of current market needs indicate that current DVD systems will continue to dominate the market in terms of units shipped [1] well into the next decade even before high definition systems take over the majority of the market. Thus it is important that those organizations working on the development of fourth generation technology begin to identify and focus on the types of applications that would require this technology.

2. Discussion

One answer to the challenge facing fourth generation optical data storage technology could be an attempt by optical storage systems to displace other information storage technologies such as magnetic hard disk drives, tape systems, or solid state memory. While this may be possible in principle and certainly defines the performance metrics required of any fourth generation technology, it is generally difficult to displace an incumbent technology without offering a disruptive advantage in the field. It is not clear that the advantages of optical systems, the inexpensive substrate, fast and economical replication for content distribution, and removability provide this disruptive advantage.

In a previous publication [2] we offered multi-thread multi-view imaging technology as an example of an application that requires the particular features of optical data storage while at the same time demanding orders of magnitude more storage capacity. This technology is based on the convergence of image processing, computer vision and computer graphics which has lead to an emerging area of research referred to as image-based rendering (IBR). IBR allows a 3D scene to be captured and stored as 2D images, and these 2D images

in turn can be processed to render the 3D scene from arbitrary viewpoints. If used in photography, television, or movies, IBR enables the viewer to choose any arbitrary viewpoint to watch the picture. Hence this technology is also referred to as "free viewpoint TV." Research in this area focuses on the rendering procedure, as well as the capturing process which is equally, if not more, important. In addition this technology requires the ability to store vast amounts of data in an inexpensive and removable medium. For professional applications this medium would be used as a content distribution system. One challenge in identifying this as the driving application for optical data storage is that we are likely many years away from the development of products capable of capturing a multi-view image or that the cost of producing studio content for multi-view and multi-thread systems would be prohibitive. While we still believe that such a system can and will be a driving application for fourth generation optical storage technology eventually we note that other fields are also developing systems that would benefit from the unique capabilities of optical data storage. One such development is the new methods for control that will require massive amounts of storage that can be accessed in real-time.

One such example is the concept of "just-in-time system identification", initially proposed in Stenman et al. [3]. System identification refers to the use of empirical data to construct models of dynamic systems for control system design. For complex systems, many models need to be constructed to cover the full range of nonlinearities and operating conditions. Just-in-time system identification replaces off-line modeling with quick access to a huge database of input-output behaviors to create useful models for the current operating point. This approach avoids the need to anticipate the full set of models that will be needed online and assures the models are based on the latest available data, which is critical when the dynamics change over time due to factors such as aging of materials that change the responsiveness of the system. Just-in-time system identification and other proposals for data-mining approaches to system modeling require the acquisition and storage of massive amounts of operational data [4]

A second development in control that also requires massive on-line storage is what is becoming known as "explicit model predictive control" [5]. In this work the concept is to replace real-time in-the-loop optimization in standard model-predictive control (MPC) with off-line computations of the control laws that result from the optimizations over the entire state space. This leads to different feedback control laws for different regions of the state space. The retrieval of these control laws in real-time brings the power of MPC to applications for which in-the-loop optimization is impossible. The number of regions explodes as the dimension (number of state variables) grows, however. The ability to store and retrieve control laws in real-time for massive numbers of regions in the state space would be a significant boost for what has been demonstrated to be an extremely effective approach to real-time control [6].

Building up the necessary data bases for such applications is not a trivial task and would require the constant monitoring of complex systems over a great deal of time. One mechanism to accomplish this would be to monitor many identical systems over shorter periods of time. Each individual system would report its collected data to a central aggregator which would merge and build the much larger data base needed for these applications from the individual data sets. However, while it might be practical for each individual system to upload its information to the central aggregator through some communications link it would not be practical to send the much larger data set back to the individual systems via the same communications link. It is the delivery of this large data set to many systems that could benefit from a fourth generation optical disk of far greater capacity than those available today. In applications such as this where there is an inherent asymmetry in the collection and distribution of data that favors the use of optical storage systems.

3. Conclusion

A driving motivation in any technology is that it solves a problem or offers a new capability that did not previously exist. In the case of previous generations of optical storage technology their use was clearly

defined even as they were being developed. This is not the case today for fourth generation optical storage technology. In this paper we reiterate the description of one possible application that could drive the development of fourth generation optical storage, namely, multi-view multi-thread imaging systems. We also describe a second application area in modern control systems that would also benefit from the ability to distribute vast amounts of data inexpensively replicated to numerous end users. Both offer a potential use for the unique characteristics of optical storage technology; inexpensive substrates, economical replication for content distribution, and removability.

4. References

- [1] W. Schlichting, in INSIC Optical Data Storage Roadmap, 2006
- [2] T.E. Schlesinger, T. Chen, “*Application Driven Optical Storage*”, Proc. SPIE Vol. **6620**, 66200U (Jul. 11, 2007)
- [3] A. Stenman, F. Gustafsson, and L. Ljung. “*Just in time models for dynamical systems*”, Proceedings of the 35th IEEE Conference on Decision and Control, Kobe, Japan, 1996.
- [4] S. Saitta, B. Raphael, I.F.C. Smith, “*Data mining techniques for improving the reliability of system identification*”, Advanced Engineering Informatics **19**, 289(2005).
- [5] A. Bemporad, M. Morari, V. Dua, and E. N. Pistikopoulos, “*The explicit linear quadratic regulator for constrained systems*” Automatica **38**, 3(2002)
- [6] Maeder Urban, Raphael Cagienard, Manfred Morari, “*Explicit model predictive control, Advanced strategies in control systems with input and output constraints*”, Lecture Notes in Control and Information Sciences, **346**, 237(2007).

DVD-Download

Shoji Taniguchi

Disc Systems Department, Devices Research Center, Corporate R&D Laboratories, R&D Group,
PIONEER CORPORATION
1-2, Fujimi 6-Chome, Tsurugashima-Shi Saitama 350-2288, Japan

ABSTRACT

DVD-Download format provides a new distribution channel of DVD-Video discs, such as that for a small quantity and large variety of DVD-Video titles according to consumer's demand via internet download and centralized production. This paper describes its concept, distribution models, benefits, and disc physical characteristics to realize high playback compatibility with existing DVD-Video players in the market.

Keywords: DVD-Download, DVD-Video, CSS, MOD, EST, DVD-R

1. INTRODUCTION

Recently, several internet downloading services have been started for video content. In many cases, video contents are downloaded only with anti-ripping software and in order to keep security of data transmission, such anti-ripping software has to be frequently renewed. This situation makes difficult to verify playback compatibility of the downloaded video content.

Under the circumstances described above, there was a big demand in the DVD industry to create a new DVD recordable disc format to enable to record CSS (Content Scramble System) encrypted DVD-Video content. Since CSS is used as the content protection method for conventional DVD-Video discs, it was expected that the recorded discs would realize high playback compatibility with existing DVD-Video players.

1.1 Concept and features

In order to respond the demand in the DVD industry, the new DVD format; **DVD Download Disc for CSS Managed Recording (DVD-Download disc)** has been introduced by the DVD Forum to realize the following concept.

- 1) To provide the recording capability of CSS encrypted DVD-Video content via internet download and centralized production
- 2) Recorded (final) discs have high playback compatibility with existing DVD players
- 3) No security damage to existing DVD business

2. DISTRIBUTION MODEL OF DVD-VIDEO CONTENT

The CSS Managed Recording is a general term to create a disc which records CSS encrypted DVD-Video content onto a blank DVD-Download disc. This section introduces some typical models to distribute DVD-Video content and to create the recorded (final) DVD-Download discs.

To divide broadly into two categories, so called MOD (Manufacturing On Demand) and EST (Electronic Sell Through) are taken into consideration as the typical content distribution models as shown in Figure 1. The basic definitions of those two models are as follows.

- 1) **MOD:** A final disc will be sold as a recorded disc to consumers directly from service providers.
- 2) **EST:** A blank disc will be purchased by consumers and video image data will come via a network from service providers to be recorded on the disc by consumers.

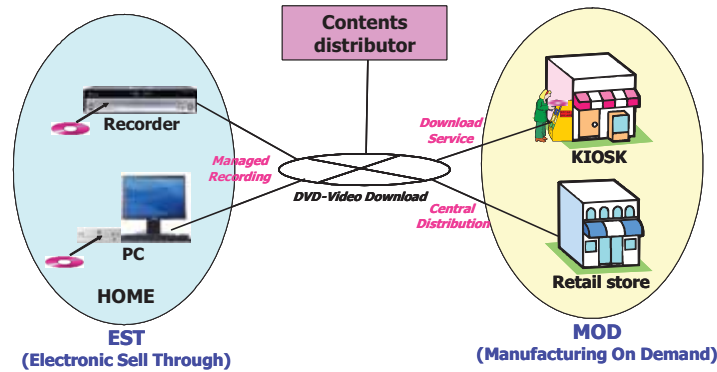


Fig. 1. Scope of distribution model

2.1 MOD

A final disc is created by service providers or by special recording machines managed by service providers, and a blank disc is never recorded by consumer's machines such as Home PC and other devices at home. MOD model includes the following two typical models.

- 1) **MOD-1:** Service providers create the final DVD-Download disc and distribute the disc to consumers
- 2) **MOD-2:** Service providers make the CSS protected image data of DVD-Video content and transfer it into their special recording machines. Consumers select content(s) and get the final disc(s) by using the special machines.

2.2 EST

Service providers provide only the content electronically to consumers (e.g. through internet), and the final disc is created by consumer's machines. EST model includes the following two typical models.

- 1) **EST-1:** Service providers provide CSS protected image data of DVD-Video content to consumers and the data is recorded onto a blank DVD-Download disc without any processing by consumer's machines.
- 2) **EST-2:** Service providers provide elementary Video data of DVD-Video content and its scenario to consumers. The image data of DVD-Video content is created by consumer's machines by using the elementary data according to the provided scenario. The image data is protected by CSS and recorded onto a blank DVD-Download disc by using the consumer's machines.

3. PLAYBACK COMPATIBILITY

DVD-Download disc format was created based on DVD-R (DVD-Recordable) disc format. In the case of CSS encrypted DVD-Video recording on a DVD-R disc, format modifications were essentially required to realize high playback compatibility with existing DVD players in the market. The following preconditions were taken into consideration.

- 1) Until now, recordings of CSS encrypted contents have been prohibited on DVD recordable media by the Recordable Media Playback Control rule (CSS compliance rule). Therefore conventional DVD playback devices are designed not to play CSS encrypted video contents on the current DVD-R discs.
- 2) Recently, the CSS compliance rule has been changed to permit the "CSS Recordable DVD" (DVD-Download disc). Taking account of the conventional device design, the current DVD-R discs can not be applied for DVD-Download.

3.1 Improvement of playback compatibility

In order to improve playback compatibility, playback tests were conducted using several kinds of sample discs with format modifications. Figure 2 shows the typical results of playback compatibility tests among existing DVD playback devices. Based on those results, it was confirmed to change the DVD-R physical specifications concerned with the following disc identification.

- 1) Bit setting of Book type field in the Control Data zone
- 2) Groove wobble specification
- 3) Other necessary modifications to keep consistency with Read-only DVD-Video discs as much as possible

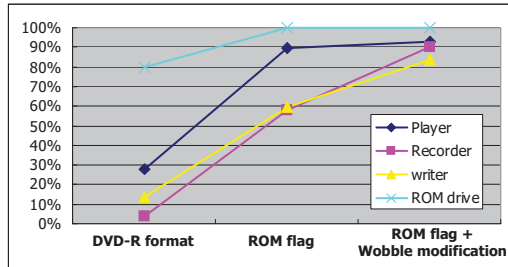


Fig. 2. An example of playback compatibility ratio (not the final results)

3.2 General parameters of DVD-Download disc

Based on the experimental results and the requirements for CSS Recordable DVD, DVD-Download specifications were created. Table 1 shows the general parameters of the DVD-Download disc compared with the conventional DVD-R disc.

Table. 1. Comparison of general parameters between DVD-R and DVD-Download discs

	DVD-R for General	DVD-Download (MOD)	DVD-Download (EST)
Pre-recorded area	Pre-recorded Control Data Zone (with no CSS Key)	Non pre-recorded Lead-in area *	Pre-recorded Lead-in area with CSS Disc Key sets
Recording speed	1x to 16x	6x and 8x *	2x, 4x, 6x and 8x
Book Type in CDZ	0010b (DVD-R)	0000b (DVD-ROM)	
RMA & P-Physical format information Zone	specified	not specified	
Push-pull specifications	0.22 < PPb < 0.44	0.20 < PPb < 0.40, PPa < 0.40	
Wobble frequency	8 times of Sync frame frequency	16 times of Sync frame frequency	

* DVD-Download for EST disc is also available for MOD use.

4. SUMMARY

DVD-Download format gives the following benefits to the DVD-Video business.

- 1) **For Consumers:** Easy to find and/or buy favorite DVD-Video movies that may not be found in DVD video stores.
- 2) **For Video Stores:** Solution of the problem of limited shelf space that allows only a selection of DVDs such as New Release movies
- 3) **For Replicators:** No need to maintain all glass masters and stampers
- 4) **For Studios and video industries:** Expansion of DVD business dealing with a small quantity with sporadic orders that is not economical in conventional manufacturing, inventory keeping, and distribution management

It is expected that the DVD-Download business will become widespread and provide consumer friendly pro-competitive benefits.

REFERENCES

- [1] DVD Specifications for DVD Recordable Disc for General Part1 / Optional Specifications DVD DOWNLOAD DISC for CSS Managed Recording Revision 1.0, February (2007)
- [2] The DVD DORUM NEWS Vol. 30, July (2007)

Optical Storage in 2008: Where is the Competition Heading?

Barry H. Schechtman

Information Storage Industry Consortium (INSIC)

3655 Ruffin Road, Suite 335; San Diego, CA 92123-1833, USA

email: barry@insic.org phone: (858) 279-8059

fax: (858) 279-8591 internet: <http://www.insic.org>

Introduction

Optical storage products have become well established and pervasive for certain applications. Well-known examples include:

Consumer applications

- Sale or rental of published entertainment content (audio, video)
- Dissemination of published information (software, databases)
- Recording of content in mobile devices (music players, camcorders)
- Backup and retention of personal information (second copies, archiving)
- Sharing and interchange among users and computer systems (the new floppy disk)

Enterprise applications

- Archiving of business information (regulatory compliance, long-term retention)
- Dissemination of published information (software, databases)

Optical storage has succeeded in these application areas because it offers the following combination of attributes:

- A large installed base of standardized inexpensive drives to record and play back content
- Inexpensive media in versions that are permanent, recordable or rewritable
 - The WORM function of recordable media has been especially important
- Large information capacity on a single physical volume of media
- Media which is robust for handling and relatively durable for long-term storage
- Sufficient data transfer rates for the applications

In recent years, developers of other technologies have recognized that the above applications represent attractive markets that they wish to pursue (or in some cases defend) in competition with optical storage. As a result, every one of the listed applications has significant competition from one or more of the following non-optical technologies:

- Direct downloading of information
- Magnetic hard disk drives (HDDs)
- Magnetic tape
- Nonvolatile solid-state memory (flash memory)

This paper will review the status, in the context of the above applications, of these other technologies that compete with optical storage, and provide an outlook of where they are heading in the future.

Dissemination, Sale or Rental of Published Information

This area has been undergoing a significant transformation because of the impact of direct downloading of information. The rapid penetration of increased communications bandwidth to both homes and business locations provides users with alternatives to purchasing or renting their digital content on pre-published physical volumes of optical media. This direct downloading model has already become prevalent for software purchases and upgrades, it is well established for music file access, and it is presently emerging for access to entertainment videos. Figure 1 indicates how broadband penetration to homes in the US has occurred more quickly than has the adoption of several other new technologies [1], and the penetration rate has been even faster in other countries. In addition, as of October 2007, the average advertised download speed in the US was 8.8 Mb/s, and significantly faster speeds were offered in at least a dozen other countries in Asia and Europe, ranging up to over 90 Mb/s in Japan [2]. As of June 2007, Japan and Korea led the world in percentage of their broadband connections using optical fiber (36% and 31%, respectively) [3] and other nations are likely to follow the trend towards increased fiber usage.

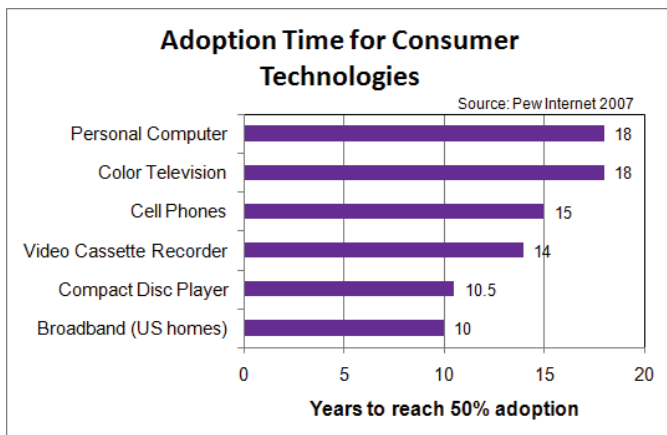


Figure 1: Adoption time for various consumer technologies.

expected to drive acceleration of bandwidth requirements, such as video surveillance, video telephony, and decentralized “cloud” computing.

Also in this category of distributing recorded information, optical disk has been used to provide and update map databases for automobile navigation systems, but the technology for those applications has shifted away from optical, first to hard disk drives and more recently to flash memory.

Recording of Content in Mobile Devices

In this application segment, optical disks have been used in some portable music players and camcorders as the primary storage medium to capture information. As the capacity and performance requirements for these devices have grown, accompanied by the desire for more compact form factors, optical technology is being displaced by small HDDs and flash memory.

Backup and Retention of Personal Information

As consumers now generate, modify and accumulate vast amounts of digital information, there is an increasingly important need to safeguard that information so it can be accessed over the long term. Recordable optical technology has served well for this application, especially during the past decade when inexpensive CD or DVD burners have been incorporated into many personal computers. The extremely low media cost and the ubiquitous presence of drives have helped to drive this usage of optical disks. However, as the amount of information to be retained has grown, optical technology has not kept pace with the capacity and performance needs of many users, and HDD technology has made significant inroads. External HDD products offer hundreds of GB of capacity (compared to a few GB on a DVD volume) and transfer speeds up to 60 MB/s (compared to 25 MB/s or less for DVD recorders). The capacity, performance and cost of HDDs have also made this the technology of choice for the digital video recorder (DVR) integrated into television set-top boxes.

Magnetic hard disk drive technology continues to advance, despite the well-recognized concerns with superparamagnetic effects that occur at very small bit volumes. A significant worldwide research effort is underway to work around those concerns by adoption of more complex recording methods, for example using heat assisted magnetic recording (HAMR) and/or bit patterned media (BPM). The HDD industry aims to maintain areal density progress at an annual growth rate of at least 40%, reaching a density of 10 Tb/in² in 2015. During this period, HDDs will continue to offer an attractive combination of high capacity, high performance and low cost per gigabyte that will favor them over optical disk where one or more of these attributes are important. On the other hand, for small consumer personal devices such as music players and cell phones, neither HDDs nor optical disks are expected to have much future success in competition with nonvolatile solid-state storage.

Sharing and Interchange Among Users and Computer Systems

The ubiquitous nature of standardized optical drives in most computer systems, coupled with the low cost of optical media, established the optical disk as the technology that displaced the magnetic floppy disk for interchange applications. However, optical disk use for interchange is declining under competitive pressure from flash memory. Flash memory drives, packaged with the commonplace USB interface, have rapidly declined in cost and advanced in

The use of this available bandwidth for movie downloading is being offered by numerous companies. This segment of the industry is still in an early stage. Several business models are being pursued, some of which use physical optical media for manufacturing on demand or electronic sell through, as described in the paper by S. Taniguchi at this conference [4]. Other offerings bypass the use of optical media and permit direct downloading to a computer hard drive and viewing the movie on a PC or a large screen TV. It remains to be seen which, if any, of these download-based approaches will succeed commercially. However, it is likely that the bandwidth availability to support them will continue to grow. Aside from the entertainment video downloading application, there are a number of other applications that are

both capacity and performance. By virtually all measures, such drives are a more natural technology than optical for interchange, and it is likely that flash will continue to grow its relative share of this application.

Archiving of Business Information

Magnetic tape technology remains the dominant technology for long term storage of the information to support large enterprises. Tape also continues to have a sizable market in medium-size enterprise environments, but it has declined rapidly in the small system environment, and has virtually disappeared from personal systems. The applications domain, in which tape competes most directly with optical storage, is for archival storage of data. This is a market that is strongly growing, driven partly by the rapidly increasing amount of digital data being generated (especially so-called “fixed content” data), and partly by the requirements of regulatory laws to retain data for as long as many decades. Archive applications are generally implemented in automated library configurations with a high ratio of media units to drives. Optical storage is presently represented here primarily by the UDO product family from Plasmon, and it will also be represented by the emerging holographic data storage products from InPhase Technologies. For archive applications, tape has capacity, data rate and cost advantages, and optical has advantages in offering physical write-once media and faster time to first data. An important variable in this market is the reliability and longevity of the archived data. The optical companies suggest that their media are better in this respect than magnetic tape; however, there has not yet been a standardized test methodology developed that has been applied to both optical and tape media to provide a quantitative basis for the comparison.

The tape industry recognizes the importance of the archival application to its future success, and has been investing in significant development to maintain tape technology’s capacity and performance advantages. The tape technology roadmap for the next ten years proposes to double capacity per tape cartridge every two years and advance data rate by 22% per year [5]. These expectations are shown in Figures 2(a) and 2(b), which for comparison include the capacity per disk and data rate parameters for the Plasmon UDO™ and InPhase Tapestry™ holographic technologies. It is apparent that the optical technologies need to significantly improve to compete directly with tape in these attributes. It would also be useful if the optical media suppliers would take the lead in developing a standardized test methodology to establish the archival quality of their media, along the lines of what has recently been implemented for consumer DVD media [6].

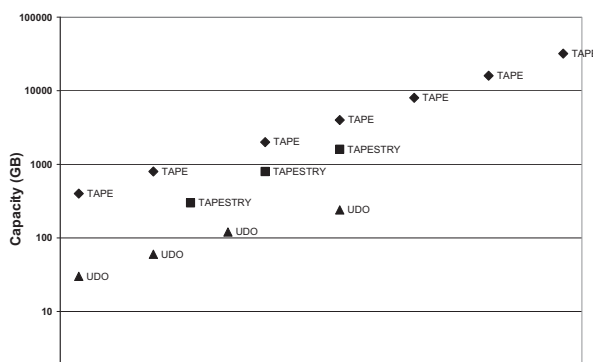


Figure 2(a): Comparison of capacity roadmap for traditional optical (UDO), holographic (TAPESTRY) and magnetic tape technologies.

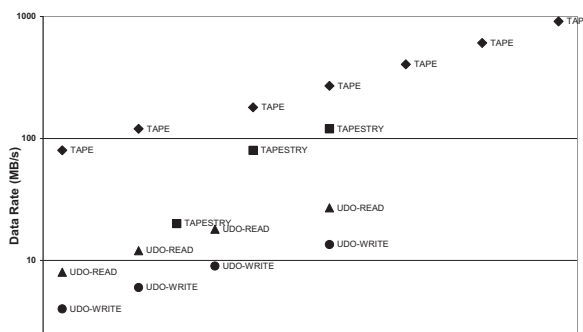


Figure 2(b): Comparison of data rate roadmap for traditional optical (UDO), holographic (TAPESTRY) and magnetic tape technologies.

Conclusion

Virtually every application of optical disk storage faces strong competition from alternative technologies. In order to remain competitive and successful, optical storage technology must retain the attractive attributes it has historically offered, and it must continue to significantly improve upon them.

[1] <http://www.websiteoptimization.com/bw/0712/>

[2] <http://www.websiteoptimization.com/bw/0711/>

[3] <http://www.oecd.org/dataoecd/21/58/39574845.xls>

[4] S. Taniguchi, “DVD-Download” ISOM-ODS 2008, Waikoloa, HI

[5] INSC International Magnetic Tape Storage Roadmap (2008)

[6] Ecma International Standard 379 (June 2007) and ISO/IEC Standard 10995 (February 2008) “Test Method for the Estimation of the Archival Lifetime of Optical Media”

SESSION WA: New and Related Technologies

Monarchy Ballroom
8:30 to 10:00 am

Thomas D. Milster, College of Optical Sciences/The Univ. of Arizona
Jooho Kim, SAMSUNG Electronics Co., Ltd. (South Korea)

Fundamental exploration of the solutions for ultra-high density optical recording

L. P. Shi^{1*}, T. C. Chong^{1,2}, B. S. Luk'yanchuk¹, J. M. Li¹, H. F. Wang¹, G. Q. Yuan¹ and J. Y. Sze¹

¹Data Storage Institute, A*STAR (Agency for Science, Technology and Research), Singapore 117608

²Electrical Computer Engineering Department, National University of Singapore, Singapore 117576

Summary

1. Introduction

Optical storage offers a reliable and removable storage medium with excellent robustness, long lifetime, low cost and non-contact data retrieval and provides read only, write once read many and rewritable three functions. They have been widely used in multimedia to store digitized audio, video, animation and images. Tremendous efforts have been put to search for high density, fast data transfer rate, high performance, high reliability, and low cost optical media. Till now three generations of optical media have been developed, CD, DVD and High-Definition DVD (HD DVD) and Blu-ray (BD). CD with 650 MB capacity adopts laser diode with wavelength $\lambda = 780$ nm, numerical aperture (NA) of focus lens 0.45 and 1.6 μm track pitch. DVD uses smaller track pitch of 0.74 μm wide by using laser with $\lambda = 650$ nm and NA = 0.6. BD uses a $\lambda = 405$ nm blue-violet laser technology, 0.85 NA and track pitch of 0.32 μm . For decades, the major driving force for optical disc is to increase the density by reducing the spot size through shorter wavelength and larger NA. Current BD with 25 GB/side uses $\lambda = 405$ nm and NA = 0.85. To increase the disc capacity, possible approaches are to reduce the wavelength from laser diode and increase NA of objective lens. However, for 4th generation optical storage, it is not practical to further increase the density by using shorter wavelength because almost all of the component will be changed if UV LD is used though it has not been developed yet. Researchers are seeking alternative options for the next generation optical storage. Till now, a few solutions have been proposed and listed in INSIC optical roadmap 2006 [1] and ISOM optical disc roadmap 2006 [2] including near field recording, volumetrical recording, holography recording, and super resolution near field optical recording. Each technology has its advantages and drawbacks. In this paper the possible solutions to achieve ultra-high density optical recording are explored fundamentally. The challenges and limitations are discussed.

2. Overcoming diffraction limit

In order to further reduce spot size, several methods have been adopted such as using subdiffractive optics with radially polarized light and Bessel-Gaussian beams. These methods refer to light focusing with high numerical aperture lenses. In contrast to usual light with linear polarization which was used within the previous technologies the new optical using e.g. circular or radial polarization and additional phase modulation elements, e.g. binary optic elements [3, 4]. Schematic for this technique is shown in Fig. 1. With this technique one can reach optical resolution above 0.4λ .

High field localization can be achieved with field-enhancement by laser illuminated tip [5], the effect by combining scan near field optical microscope with femtosecond lasers, optical resonances and near-field effects with transparent particles [6], and plasmonic nanoparticles

[7]. These methods permit to localize laser light on the scale beyond 100 nm, however they need great modification of the optical part of storage device. For example, experiments were done using an atomic force microscope (AFM) tip illuminated by a laser, see in Fig. 3.

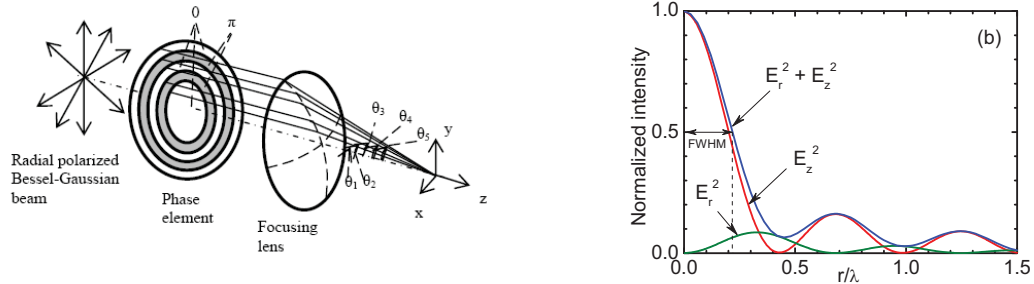


Fig. 1. Schematic diagram of the setup, phase modulation optical element and focusing lens.

longitudinal component and the total field on the focal plane of the NA = 0.95 lens for radial polarized Bessel-Gaussian beam with additional phase modulation [4].

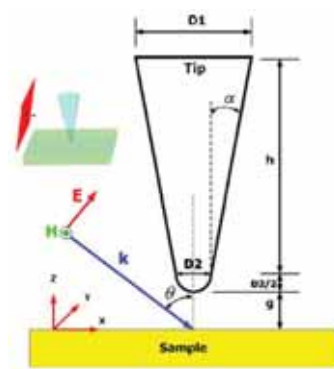


Fig. 2. Intensity profile of the radial component,

Fig. 3 Schematic of the tip-sample system simulated. this scheme permits achieve field localization on a scale 40-50 nm with gold tip and 532 nm laser.

3. Other Solutions

Beside the methods to further reduce size and overcome diffraction limit, there are also some solutions which can be used in future technologies. For example one can use modification of scattering effect during laser modification of sizes of nanoclusters, embedding into the transparent media. This technique permits at least in principle use multibit recording [8]. With weakly dissipating plasmonic materials it is possible to produce very fast variations of scattering diagram from forward scattering to back scattering, see in Fig. 4.

In order to increase further capacity, several other methods can be used including volumetric recording using real space, imagine space and parameter spaces, and making use of the

interaction effect of light and matters. These methods are summarized schematically in Fig.5. The method can be combined and achieve higher density and capacity.

By using different light parameter a new optical recording technologies can be developed. Optical storage using light with multi parameters distinguish it from other memory technologies. One possible solution is multi-dimensional multilevel recording (MDML) [9]. MDML make use of different parameters (such as reflection, modulation amplitude, frequency, polarization, refraction, time, mark width, mark length, electronic spin and so on) of light to detect multi-dimensional multilevel signals.

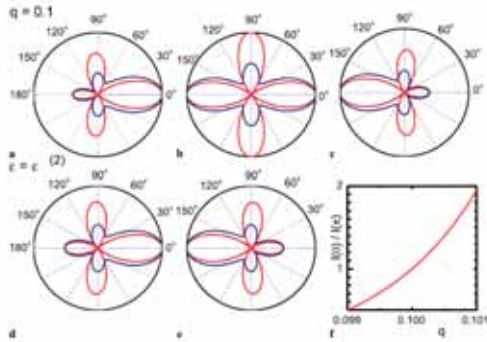


Fig. 4. The exact Mie solution; variation in the scattering diagram near quadrupole resonance for the particle with Size parameter $q = 2\pi a/\lambda = 0.1$. With small variation of the size parameter (about 1%) one can reach big modification in the ratio of forward to backward scattering intensities [8].

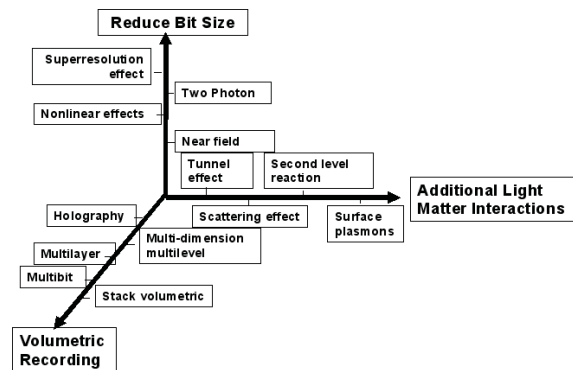


Fig. 5. Schematic for Technical Solutions for Future Generation.

References

1. INSIC optical storage roadmap 20062. ISOM optical storage roadmap 2006.
3. Wang H.F., Shi L. P., et al., *Appl. Phys. Lett.* 89, 171102 (2006)
4. Wang H. F., Shi L.P., et al., *arXiv:0709.2748v1* [physics.pop-ph], 18 Sept. 2007
5. Wang Z. B., Luk'yanchuk B. S., et al., *Appl. Phys. A* **89**, 363 (2007)
6. Hong M.H., Lin Y., et al., *Journal of Physics: Conf. Series* **59**, 64 (2007)
7. Wang Z. B., Luk'yanchuk B. S., et al., *Phys. Rev. B* **70**, 032427 (2004)
8. Luk'yanchuk B. S. et al., *Appl. Phys. A* **89**, 259 (2007)
9. Shi L.P. et al, *Digest of ISOM 2006*, 226 (2006).

Plasmonic Nano-structures for Optical Data Storage

Masud Mansuripur,[†] Aramais R. Zakharian,[‡] Andrey Kobayakov,[‡] and Jerome V. Moloney[†]

[†]College of Optical Sciences, The University of Arizona, Tucson, Arizona 85721

[‡]Corning Incorporated, Science and Technology Division, One Science Center Drive, Corning, New York 14831

masud@optics.arizona.edu

Abstract: We describe a method of optical data storage that exploits the small dimensions of metallic nano-particles and/or nano-structures to achieve high storage densities. The resonant behavior of these particles (both individual and in small clusters) in the presence of ultraviolet, visible, and near-infrared light may be used to retrieve pre-recorded information by far-field spectroscopic optical detection.

Metallic nano-structures exhibit strong resonances when illuminated with ultraviolet, visible, or near-infrared light in the vicinity of their surface plasmon polariton (SPP) frequencies. These SPP frequencies are sensitive to the geometry and dimensions of the nano-structure, e.g., diameter and depth of a pit or a hole in a metal film, diameter and length of a metallic nano-rod, axial dimensions of an ellipsoidal nano-particle, etc. The resonances are also dependent on the orientation of the nano-structure relative to the polarization state of the incident light. In addition to sensitivity to polarization and wavelength, metallic nano-structures exhibit strong interactions with their environment and with each other; for example, optical transmission through one nano-hole is strongly modulated by the presence of other nano-holes in the neighborhood.^{1,2}

This paper describes a method of optical data storage that exploits the small dimensions of metallic nano-particles to achieve high data densities. The proposed method employs the resonant behavior of these particles (both individual and in small clusters) for the purpose of retrieving the stored information using spectroscopic far-field detection. The nano-particles should be arranged in such a way as to imprint their signature in a unique way on the optical spectrum of the readout laser beam. It should be emphasized at the outset that the large-scale fabrication of such nano-structures in a reliable and cost-effective way is far from trivial for the present-day manufacturing technologies. It is our hope, however, that an exploration of plasmonic nano-structures in the context of optical data storage will bring attention to the unique properties and potential advantages of such structures, thus spurring the development of tools and techniques for their large-scale fabrication.

Fig. 1. In one realization of the proposed concept, plasmonic features are nano-holes and/or nano-slits in a thin metallic film. A group of such features constitutes a bit-cell, within which several bits of information are encoded in a small (micron-sized) region of the storage medium. Much like the organization of data on a conventional optical disk, these bit-cells are arranged sequentially along parallel data tracks.

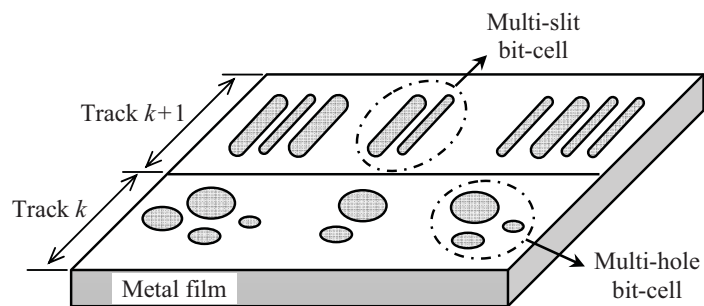


Figure 1 shows a possible realization of an optical storage medium that incorporates nano-holes and/or nano-slits in a thin metallic film. The data bits are grouped together in small clusters and placed within individual bit-cells, each cell containing several bits of information. As an example, a typical bit-cell may occupy a $0.5 \times 0.5 \mu\text{m}^2$ area on the surface of a $0.2 \mu\text{m}$ -thick silver film, each bit-cell containing ten or more nano-holes whose individual diameters could range from, say, 20 to 100 nm. If, in a given cluster, the presence or absence of a nano-hole of a specific-size is associated with a single information bit (“0” or “1”), then m nano-holes can encode an m -bit sequence within each bit-cell. Transmission of light through

a nano-hole (or nano-slit) is a strong function of the aperture diameter and film thickness, as well as the size, shape, and location of the neighboring nano-apertures. For a given state of polarization of the incident beam, certain wavelengths couple strongly to the guided mode through a nano-aperture and reach the opposite side, while other wavelengths are either reflected from the metallic surface or resonantly transmitted through adjacent nano-apertures; see Fig. 2. It is this property of the nano-holes and nano-slits that provides a mechanism for readout of the stored information. (Although Fig. 1 shows one track containing nano-holes and an adjacent track containing nano-slits, there is no a priori reason for distinguishing between the two; in other words, it should be possible to mix nano-slits with circular as well as elliptical nano-holes in arbitrary combinations and arrangements.)

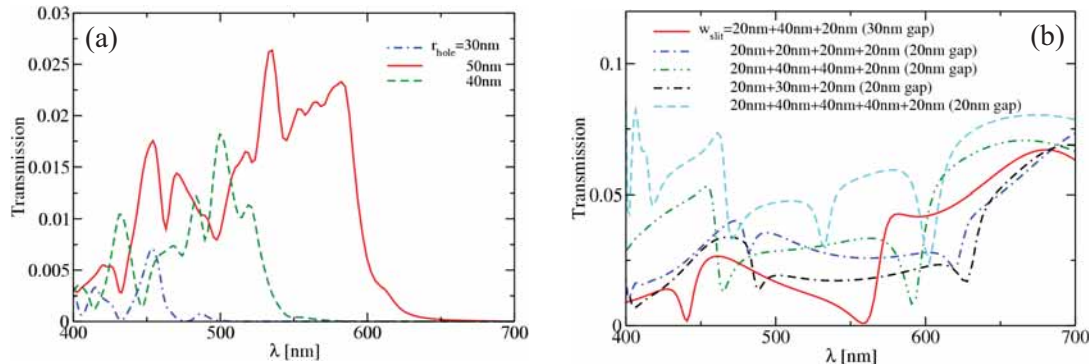


Fig. 2. Computed transmissivity versus the vacuum wavelength λ for nano-holes and nano-slits in a silver slab. The Finite Difference Time Domain (FDTD) method has been used to solve Maxwell's equations; transmissivity is defined as the fraction of total incident optical power at each wavelength. The regions on both the incidence and transmission sides of the silver slab are free-space ($n = 1$), and the Drude model is used to simulate the dispersion of the complex dielectric constant $\varepsilon(\omega)$ of silver. (a) Three cylindrical nano-holes with diameters $d_1 = 60\text{nm}$, $d_2 = 80\text{nm}$, and $d_3 = 100\text{nm}$, each filled with a transparent dielectric of refractive index $n_o = 2.0$, within a 200nm -thick silver film. The incident beam is a focused, linearly-polarized Gaussian, having $\text{FWHM} = 1\mu\text{m}$. (b) Multiple air-filled slits ($n_o = 1$) having widths $W_1 = 20\text{nm}$, $W_2 = 30\text{nm}$, and $W_3 = 40\text{nm}$. Different combinations of these slits are embedded within a 400nm -thick silver film and illuminated with a focused Gaussian beam. Each cluster of slits has a unique transmission spectrum, which could be exploited for identification of the cluster during readout.

A readout method for the nano-apertures depicted in Fig. 1 is shown in Fig. 3. Here a short pulse from a femtosecond laser is focused on a bit-cell, and the transmitted beam is subsequently sent to a spectrum analyzer. The pulse is short enough ($\sim 10\text{--}20\text{fs}$) that its spectrum covers the entire range of visible frequencies. Each cluster of nano-apertures is thus uniquely identified by its spectral signature, and the entire content of the bit-cell is retrieved upon analyzing the spectrum of the transmitted light. Assuming linear track-velocity of 100m/s and focused spot-size of $0.5\mu\text{m}$, the dwell time on each bit-cell is $\sim 5\text{ns}$, thus requiring a repetition rate of $\sim 200\text{MHz}$ from the femtosecond light source. If one further assumes that a maximum of 10 bits can be stored within a bit-cell, the resulting data-rate will be $\sim 2\text{Gbit/s}$.

Unless the number of stored bits in individual cells can reach 10 and beyond, it is difficult for the proposed device of Fig. 1 to surpass the storage capacity of a conventional Blu-Ray disk (25GB per layer on a 12cm platter). A variation on the same theme, however, is shown in Fig. 4, where information is stored in metallic nano-rods embedded in a transparent substrate. Each nano-rod resonates with one or more wavelengths from the UV, visible, and near-IR range, scattering the resonant wavelength(s) out of the main optical path.³ The transmitted light's spectrum is thus endowed with the collective signature of the cluster of rods embedded within individual bit-cells. This alternative method has the advantage that a large fraction of the incident light can pass through each storage layer, thus allowing the stacking of several such layers.

Fig. 3. Proposed readout scheme for the plasmonic disk depicted in Fig. 1. A femtosecond laser pulse is focused by a diffraction-limited objective onto the disk surface. The pulse has a broad spectrum, covering the entire visible range ($\lambda = 400\text{nm}$ to 700nm). The size of the focused spot at the disk surface, $\sim 0.5\mu\text{m}$, is comparable to the bit-cell dimensions. Although the nano-holes within a given cell are not individually resolved in a conventional sense, their collective signature, imprinted upon the spectrum of the transmitted light, can be used to identify the presence or absence of various holes within a cell. With a maximum of 10 nano-holes placed in each cell, the total number of distinct spectral patterns will be $2^{10} = 1024$. The spectral patterns can be further optimized by adjusting the nano-holes relative to each other and also relative to the direction of polarization of the incident beam.

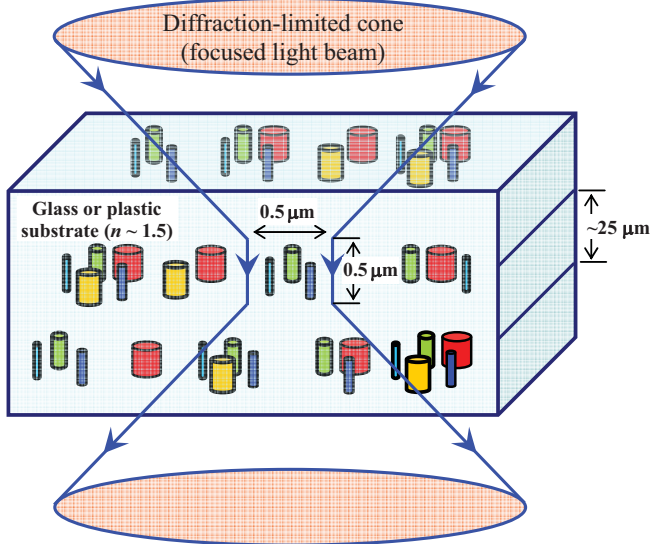
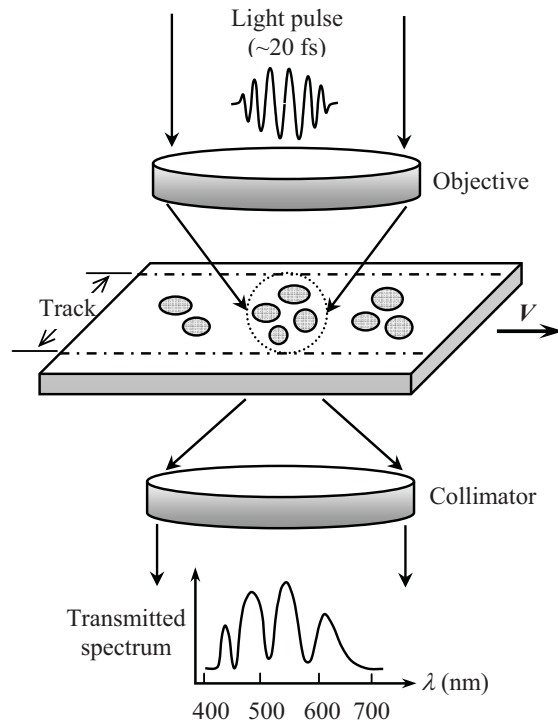


Figure 4. An alternative realization of the concept of plasmonic data storage. Each bit-cell is a collection of metallic nano-rods (diameter $\sim 20\text{--}100\text{nm}$, height $\sim 1.0\mu\text{m}$) embedded in a transparent substrate. Identical rods appear in different cells, although a given cell may or may not contain a specific-sized rod. Each cell stores m information bits in the form of the presence or absence of a given rod (0 or 1). The incident beam is a diffraction-limited cone of light with a spot diameter of $\sim 0.5\mu\text{m}$ and a duration of $\sim 10\text{--}20\text{fs}$. Since nano-rods of differing dimensions resonate at different wavelengths, the scattering cross-section of each rod is a strong function of the incident wavelength. Provided that attenuation is not too severe, the light pulse may pass through several layers of nano-rods before focusing on a specific cell. The transmitted spectrum thus carries the signature of the bit-cell located under the focused spot.

Acknowledgement. Supported by the Air Force Office of Scientific Research under contract number FA 9550-04-1-0213.

1. A. R. Zakharian, M. Mansuripur, and J. V. Moloney, "Transmission of light through small elliptical apertures," *Optics Express* **12**, 2631 (2004).
2. Y. Xie, A. R. Zakharian, J. V. Moloney, and M. Mansuripur, "Transmission of light through slit apertures in metallic films," *Optics Express* **12**, 6106 (2004).
3. J. Mock, S. Oldenburg, D. Smith, D. Shultz, S. Shultz, "Composite Plasmon Resonant Nanowires," *Nano Lett.* **2**, 465 (2002).

Towards femto-Joule nanoparticle phase-change optical memory

A. I. Denisyuk, K. F. MacDonald and N. I. Zheludev

Optoelectronics Research Centre, University of Southampton, SO17 1BJ, United Kingdom
 niz@orc.soton.ac.uk; www.nanophotonics.org.uk/niz
 Tel. +44 (0)23 8059 3566; Fax +44 (0)23 8059 3142

Phase-change functionality in gallium nanoparticles offers an innovative conceptual basis for the development of high density, low energy, non-volatile optical memories.

Phase-change materials, wherein structural forms with differing electronic and/or optical properties are used to encode digital information or control signal propagation, have recently attracted great interest due to their potential to address growing challenges of size and power consumption in data storage and memory applications, and to enable innovative photonic and plasmonic functionalities [1-4]. Their functionality may enable the shrinking of optical switching and memory devices all the way down to the nanoscale, thereby helping to achieve the ultimate goal of nanophotonics - that is, to create devices smaller than or comparable in size to the wavelength of the signals they handle (a relationship of proportions that is easily achieved in most electronic circuits).

Several problems hinder the nanoscale miniaturization of photonic circuits and data storage technologies: the need to guide optical signals in narrow and sharply bending waveguides; and the need to modulate these signals and encode information in very small active regions. The use of surface-plasmon-polariton waves as information carriers may address the guiding issue [5, 6] but the optical modulation and information storage problems seems to be much more difficult to tackle. In essence, both require very strong changes in the absorption or refraction of nanoscale volumes of material in response to external control excitations, be they temporary changes to effect signal modulation or more permanent bi- or multi-stable changes in the logic state of memory elements. Such large changes in absorption and refraction are only possible in media where there is something substantial to change, and in this respect metals fit the bill.

Large changes in the optical properties of metals can only be achieved through a phase change, and some metals, notably gallium, can exist in several phases with markedly different optical properties. Indeed, the properties of gallium's various phases range from those of the almost semiconductor-like, partially covalent solid α phase to those of the almost ideally metallic liquid [7, 8]. While electronically very different, many of gallium's phases are energetically very close to each other; for example the δ and β crystalline phases (normally metastable, but preferred to the α phase in the confined geometry of a nanoparticle [9]) are only separated by 3×10^{-4} eV/atom [10]. This is of considerable benefit for nanophotonics applications because it means that the energy requirements for switching are very low. Consider for example a 50 nm particle: to completely transform the particle from the δ to the β phase requires only ~ 20 fJ of energy – around three orders of magnitude less than the energy required to achieve a nonlinearity through the electronic excitation of every atom (assuming one 1 eV photon per atom).

Of crucial importance to the optical memory and switching functionality of metallic nanoparticles is the nature of the phase transition process itself (Fig. 1). Transitions in bulk materials are characterized by a

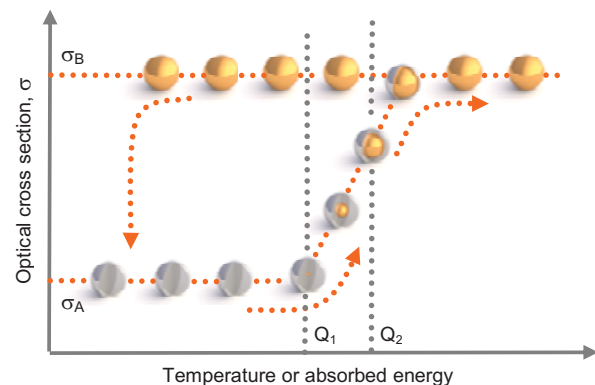


Fig. 1: Phase-change optical functionality in a nanoparticle. Dependence of optical cross-section on absorbed energy for a nanoparticle undergoing a phase transition. At low temperature particle is in phase A. Reversible changes in cross-section occur in the excitation range between Q_1 and Q_2 during the continuous transition to phase B (indicated by the mixed-phase shell structures). Excitation levels above Q_2 lead to a memory effect: once the transformation to phase B is complete, the particle remains in this phase even if the excitation is withdrawn. A transition back to phase A occurs abruptly only after overcooling. (After Ref. [3])

discontinuous change in the state of the body, a sudden (irreversible) rearrangement of the crystalline lattice at a specific temperature. In nanoparticles however, transitions from lower to higher energy phases proceed through a surface-driven dynamic coexistence of forms across a size-dependent range of temperatures [11-13]. Where, as in gallium, the two forms involved have different dielectric coefficients, this gives rise to a continuous change in optical properties. With decreasing temperature, the reverse phase transition occurs only after substantial overcooling. The resulting hysteresis in their optical properties forms the basis of gallium nanoparticles' memory functionality.

We report here on phase-change memory functionality in films of gallium nanoparticles and in single particles, demonstrating that data can be written to bi- and multi-stable memory elements both optically and via electron-beam excitation, and that logic states can be identified through measurements of the particles' reflectivity and cathodoluminescent (CL) emission. Together these results offer an innovative conceptual basis for the development of high density phase-change memories.

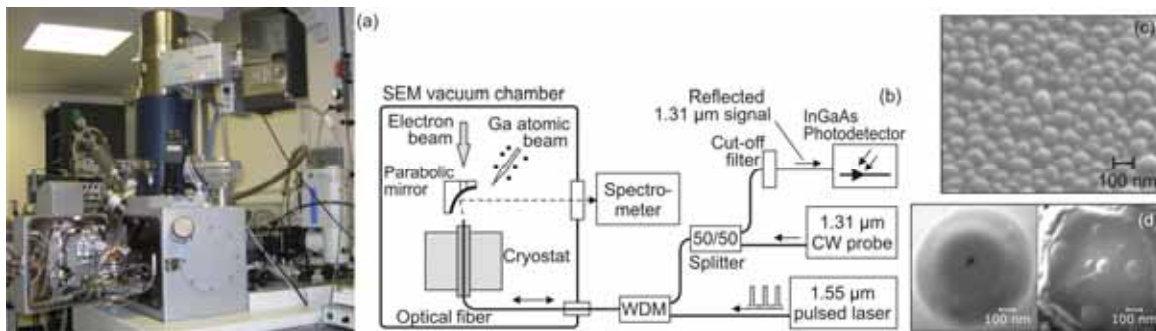


Fig. 2: (a and b) Integrated system, based on a modified scanning electron microscope, for growth, imaging, cathodoluminescence study, and optical interrogation of gallium nanoparticle films; (c) Secondary electron image of part of a gallium nanoparticle film grown on the core area of a single-mode fibre end face; (d) Scanning electron microscope images of the nano-aperture at the tip of a near-field microscopy probe before (left) and after (right) gallium deposition. A single nanoparticle is formed in the aperture.

In the experiments reported here, nanoparticle growth, imaging, optical measurements, and CL studies were all performed under high vacuum inside a scanning electron microscope (SEM) equipped with an effusion cell for gallium deposition and a nitrogen-cooled cryostat to control sample temperature in the 100–305 K range (Fig.'s 2a and b).

Monolayer films of gallium nanoparticles were grown on the end faces of cleaved single-mode fibres using the light-assisted self-assembly technique [14]. With the fibre tip held at a temperature of 100 K, gallium was deposited at 0.3 nm/min for 50 min (giving a mass thickness of 15 nm) while 1 μ s pulses from a 1550 nm diode laser (19 mW, 1 kHz repetition rate) were launched into the fibre from outside the SEM chamber. This process produces a monolayer of particles with a mean diameter of 60 nm on the optical core area of the fibre end face (Fig. 2c).

Single, isolated nanoparticles were formed by depositing gallium, typically for 30 min. at a rate of 0.3 nm/min., onto near-field optical microscopy probes - tapered, gold-coated fibres with nano-apertures at their tips. Here, they are ideally located for optical interrogation and excitation via the fibre (Fig. 2d).

The integrated experimental system allows for particles to be imaged in situ by the SEM and for their cathodoluminescence to be probed, with the emitted light being directed out of the chamber by a bespoke parabolic mirror to a spectrum analyzer comprising a Horiba Jobin-Yvon CP140 spectrograph and a liquid nitrogen-cooled CCD array for wavelength-sensitive detection in the 400-1000 nm range. Samples' reflective optical properties can also be studied via the fibre, and phase transitions can be stimulated in the particles by both optical and electron beam excitations.

Bistable memory functionality, engaging transformations between the solid (logic '0') and liquid (logic '1') states, has been demonstrated in films of nanoparticles on cleaved fibre tips (Fig. 3). In this case, the state of the nanoparticles can be read via measurements of film reflectivity using a low power optical probe beam, measurements of nonlinear reflective response to pulsed optical excitation (this technique discriminates strongly between the phases because their responses have opposite signs), or measurements of cathodoluminescent emission

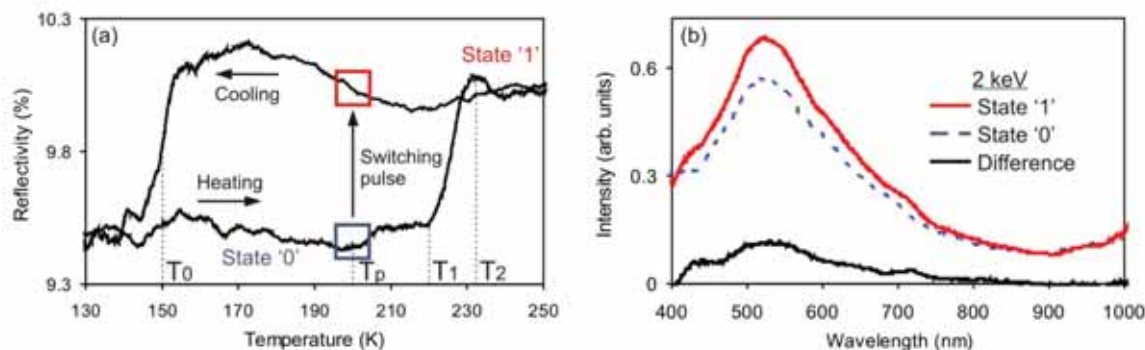


Fig. 3: (a) Reflectivity hysteresis of a gallium nanoparticle film on a fibre end face (measured via the fiber) as function of cryostat temperature. Single optical or electron beam pulses can be used to induce abrupt phase (memory state) switching at $T_p = 200$ K ($T_0 < T_p < T_1$); (b) Chodoluminescence spectra obtained at T_p before and after excitation-induced switching between the two phase states, together with the difference spectrum.

in response to low energy electron beam excitation (Fig. 3b, the advantage here being that an electron beam can probe small regions within the particle film).

At a fixed temperature (T_p in Fig. 3a) within the hysteresis loop, single $1 \mu\text{s}$, 1550 nm optical pulses with a fluence of $>0.3 \text{ fJ/nm}^2$ can irreversibly switch the nanoparticles from the low reflectivity solid phase ('0') into the high reflectivity liquid phase ('1'), thus providing memory 'write' functionality. Single electron beam pulses with a fluence of $>35 \text{ fJ/nm}^2$ can also be used to perform the write function, with the advantage that they can selectively address small areas within a large film of particles. The 'erase' function is achieved by cooling the particles down to below their solidification point (T_0 in Fig. 3a), either by cooling the sample as a whole (non-volatile mode) or, in the case where the bistable operating temperature is maintained by the local heating effect of continuous probe laser illumination, simply by switching the laser off (volatile mode).

Single, isolated nanoparticles, free from the inhomogeneous broadening effects of the size distribution found in a particle film, show more complex phase change behaviour. Here, transitions between different crystalline solid states, and ultimately between solid and liquid, are observed. This multi-stable system has facilitated the first demonstration of a quaternary logic resonatorless optical memory element. Single pulse energies of just a few pJ are required to encode information in the phase state of the particle, and read-out is achieved through reflective optical pump-probe measurements.

To summarize, particulate phase-change memory elements offer the possibility of very high data storage densities. For example, if individual binary (two-phase) elements within a close-packed array of 60 nm particles could be addressed, as they might with a steerable tightly focused electron beam, a storage density of $\sim 0.2 \text{ Tbit/in.}^2$ could be achieved. Smaller particles and higher-base logical elements would obviously further increase this value (for comparison, today's 'BluRay' disks offer an optical storage density of $\sim 0.015 \text{ Tbit/in.}^2$).

References:

- [1] M. Wuttig, "Towards a universal memory?," *Nat. Mater.* **4**, 265-266 (2005).
- [2] H. F. Hamann, M. O'Boyle, Y. C. Martin, M. Rooks, and H. K. Wickramasinghe, "Ultra-high-density phase-change storage and memory," *Nat. Mater.* **5**, 383-387 (2006).
- [3] N. I. Zheludev, "All change, please," *Nat. Photon.* **1**, 551-553 (2007).
- [4] A. V. Krasavin, and N. I. Zheludev, "Active plasmonics: Controlling signals in Au/Ga waveguide using nanoscale structural transformations," *Appl. Phys. Lett.* **84**, 1416-1418 (2004).
- [5] R. Zia, J. A. Schuller, A. Chandran, and M. L. Brongersma, "Plasmonics: the next chip-scale technology," *Mater. Today* **9**, 20-27 (2006).
- [6] E. Ozbay, "Plasmonics: Merging Photonics and Electronics at Nanoscale Dimensions," *Science* **311**, 189-193 (2006).
- [7] M. Bernasconi, G. L. Chiarotti, and E. Tosatti, "Ab initio calculations of structural and electronic properties of gallium solid-state phases," *Phys. Rev. B* **52**, 9988-9998 (1995).
- [8] N. R. Comins, "The optical properties of liquid metals," *Phil. Mag.* **25**, 817-831 (1972).
- [9] A. Di Cicco, "Phase transitions in confined gallium droplets," *Phys. Rev. Lett.* **81**, 2942-2945 (1998).
- [10] A. Defrain, "Etats metastables du gallium, surfusion et polymorphisme," *J. Chim. Phys.* **74**, 851-862 (1977).
- [11] R. S. Berrv, and B. M. Smirnov, "Phase stability of solid clusters," *J. Chem. Phys.* **113**, 728-737 (2000).
- [12] M. Wautelet, "Phase stability of electronically excited Si nanoparticles," *J. Phys.: Condens. Matter* **16**, L163-L166 (2004).
- [13] P. Buffat, and J.-P. Borel, "Size effect on the melting temperature of gold particles," *Phys. Rev. A* **13**, 2287-2298 (1976).
- [14] K. F. MacDonald, V. A. Fedotov, S. Pochon, K. J. Ross, G. C. Stevens, N. I. Zheludev, W. S. Brocklesby, and V. I. Emel'yanov, "Optical control of gallium nanoparticle growth," *Appl. Phys. Lett.* **80**, 1643-1645 (2002).

Nanophotonic Hierarchical Hologram: demonstration of the physical hierarchy

Naoya Tate^a, Wataru Nomura^a, Takashi Yatsui^b, Makoto Naruse^{a,c}, Motoichi Ohtsu^a

^aThe University of Tokyo,
2-11-16 Yayoi, Bunkyo-ku, Tokyo 113-8656, Japan,
Phone: +81-3-5841-1670, Fax: +81-3-5841-1140,
e-mail: tate@nanophotonics.t.u-tokyo.ac.jp;

^bSORST, Japan Science and Technology Agency,
2-11-16 Yayoi, Bunkyo-ku, Tokyo 113-8656, Japan;

^cNational Institute of Information and Communications Technology,
4-2-1 Nukui-kita, Koganei, Tokyo 184-8795, Japan

Many anti-counterfeiting techniques have been proposed in the fields of security and product authenticity verification [1]. For example, holography, which generates natural three-dimensional images, is the most common anti-counterfeiting techniques [2]. The surface of the hologram is ingeniously designed into a complicated structure, and it diffracts incident light in a specific direction, and a number of diffracted lights can form an arbitrary three-dimensional image. Because the structures are recognized as being difficult to duplicate, a hologram has been widely used in the anti-counterfeiting of bills, credit cards, etc. However, conventional anti-counterfeiting methods based on the physical appearance of holograms are less than 100% secure [3]. Although they provide ease of authentication, adding another securing feature without causing any losses to the appearance is quite difficult.

Recently, advances in nanophotonics, by utilizing optical near-field interactions, allow optical devices and systems to be designed at densities beyond those conventionally constrained by the diffraction limit of light [4]. Because several physical parameters of “propagating” light are not affected by nanometric structures, conventional optical responses in the far-field also are not affected by these structures. This means another functional hierarchy in an optical near-field regime can be added in conventional optical devices and systems without any loss of the primary quality, such as reflectance, absorptance, refractive index, and diffraction efficiency. We describe our application of the nanophotonics techniques to holography: a “nanophotonic hierarchical hologram.” We also describe our demonstration of the concept using commercial optical devices.

Our “nanophotonic hierarchical hologram” is defined as a hologram that has multiple observing layers. It can be created by adding a nanometric structural change (< 100 nm) to a conventional hologram (> 100 nm). Figure 1 shows the basic composition of the hierarchical hologram. In principle, the phenomenon occurring at a subwavelength scale does not affect the function induced by propagating light. Therefore, the visual aspect of the hologram is not affected by such a small structural change on the surface, and additional data can be written-in to the nanometric layer without any incident. Generally, distribution of the optical near-field is observed by scanning a

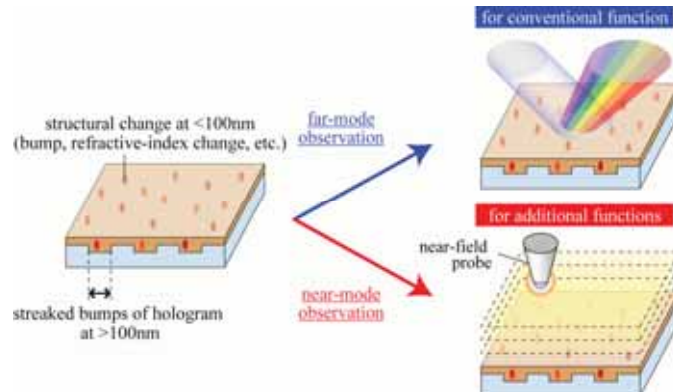


Fig. 1. Basic concept of functional hierarchy of hierarchical hologram. In principle, no interference occurs between the two layers, “far-mode” and “near-mode”. By controlling vertical position of the near-field probe in the near-mode observation, multiple layers can be utilized.

near-field probe on the material surface. Moreover, the number of layers can be increased in the “near-mode” observation to further extend the hierarchical function. An optical near-field interaction between multiple nanometric structures causes characteristic spatial distribution depending on the size, the alignment, etc. Therefore, various optical signal patterns can be observed, and another layer is added in the “near-mode” observation [5,6]. By applying this hierarchy, new functions can be added to a conventional hologram as distribution of nanometric structures.

We used a commercially available embossed hologram in our experiment as a sample of nanometric fabrication. Because an embossed hologram is easily mass produced at a low cost, it is the type used in most security applications, such as credit cards and bank bills [7]. In our experiment, a 40-nm-thick Au layer was coated on the sample surface of the hologram at the nanometric level. Then, 40 nanometric holes were fabricated in a 10 μm x 10 μm region using a focused ion beam (FIB) system. Optical responses in the far-field are not affected by these fabrications [8]. Optical responses during a near-mode observation were detected using a near-field optical microscope (NOM). A NOM was operated in an illumination-collection mode with a near-field probe having a tip with a curvature radius of 5 nm. The fiber probe was connected to a tuning fork. Its position was finely regulated by sensing of shear force with the tuning fork and was fed back to a piezoelectric actuator. The light source used was a laser diode (LD) with an operating wavelength of 785 nm, and scattered light was detected by a photomultiplier (PMT). Figure 2 shows a scanning electron microscope (SEM) image of three nanometric holes that were fabricated on a hologram. The diameter of each hole is less than 100 nm, and some structural changes were observed on the rim of each hole. The optical response during the near-mode observation is shown in Fig. 2. Evident optical responses were observed, which were attributed to an optical near-field generated on the rim of each hole. These results indicate that conventional functions of a hologram at the far-field were not adversely affected by adding another functional layer in the near-field.

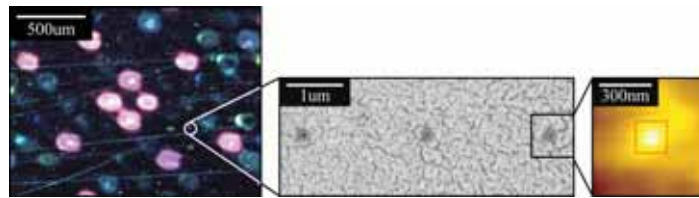


Fig. 2. SEM image of fabricated nanometric holes on hologram (left), and corresponding optical response observed by NOM (right).

We replaced the embedded hologram with a diffraction grating for a quantitative evaluation of the independence between nanometric fabrications and a far-mode observation. After fabricating nanometric holes on the surface of the grating, we measured the diffraction efficiency and compared the efficiency with that of grating with no holes. A grating was coated with a 40-nm-thick Au layer on the surface (600 lines/mm) and 25 nanometric holes ($\phi=100$ nm) were fabricated using a 100 μm pitch with an FIB system. The fabricated region was illuminated by the light from the LD ($\lambda=532$ nm), and the diffracted light intensity was measured. Figures 3(a) and (b) show the experimental results. For example, the first-order diffraction intensity of each result was 30.9% and 29.6%, respectively, and the difference was only about 10%. No differences were evident recognized in other orders of diffraction lights, as well. This means that the nanometric fabrications do not have a profound effect on the optical devices.

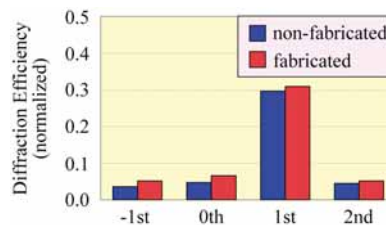


Fig. 3. Diffraction efficiencies of non-fabricated grating and fabricated grating [8].

In order to demonstrate the variation of hierarchy in the near-mode observation, we grew Ag aggregates from a colloidal solution and detected the hierarchical distribution of the optical near-field in several detecting distance.

The distance is controlled by changing sensitivity of the near-field probe against to the shear force. Figure 4 shows schematic diagram of the experiment and experimental results as the distributions of the detected optical responses along the line in the diagram. Evident difference is observed between each layer, and each aggregate represented their strongest optical response in different detecting distances. This means that at least two layers were created in this experiment. Applying well-controlled growth method, accurate alignment technique of aggregates, and several

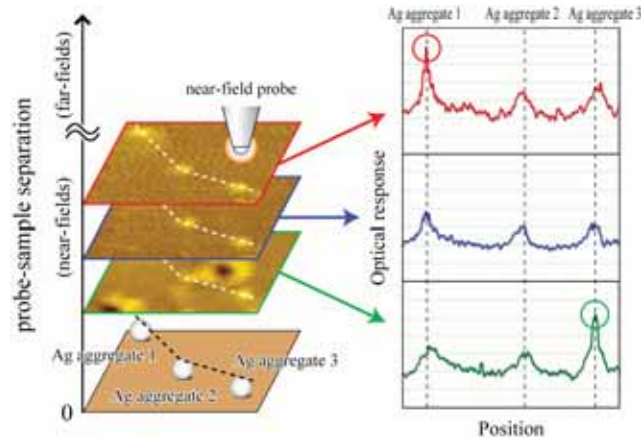


Fig. 4. Schematic diagram of the detection of hierarchical properties of Ag aggregates, and experimental results as the distribution of the detected optical responses in each layer along the line in the diagram.

combinations of materials can realize various hierarchical distributions, and the number of layers can be extremely increased.

In this paper, we described a demonstration of the concept of our “hierarchical hologram” and an experiment involving two hierarchical layers using a far-mode and near-mode observation. Moreover, the basic property of hierarchical distribution attributed to Ag aggregates is demonstrated. Our concept can be applied not only to a hologram but also any other media, such as lens and jewelry. Adding extra functions creates value-added media with only a few deficits in the primary functions. However, a trade-off occurs between the conditions of nanometric fabrications (e.g., size and pitch) and deficit of the primary functions. For actual use to several media, the trade-off in each media is under investigation by the authors.

This work was supported by the research project of the New Energy and Industrial Technology Organization (NEDO), Japan, and Special Coordination Funds for Promoting Science and Technology, Japan.

REFERENCES

- [1] Fagan, W. F. (ed), [Optical security and anti-counterfeiting systems], Society of Photo Optical Instrumentation Engineers (1990).
- [2] Van Renesse, R. L. (ed), [Optical document scanning], Altech House Optoelectronics Library, 69-225 (1998).
- [3] McGrew, S. P., "Hologram counterfeiting: problems and solutions," Proc. SPIE, Optical Security and Anticounterfeiting Systems, William F. Fagan, Ed., 1210, 66-76 (1990).
- [4] Ohtsu, M., "Near-field nano-optics toward nano/atom deposition," Tech. Dig. 18th Congr. Int. Commission for Optics, SPIE, 3749 (1999).
- [5] Naruse, M., Yatsui, T., Nomura, W., Hirose, N., and Ohtsu, M., "Hierarchy in optical nearfields and its application to memory retrieval," Opt. Exp., 13, 9265-9271 (2005).
- [6] Naruse, M., Inoue, T., and Hori, H., "Analysis and synthesis of hierarchy in optical near-field interactions at the nanoscale based on angular spectrum," Jpn. J. Appl. Phys., 46, 6095-6103 (2007).
- [7] Lancaster, I. (ed), [Holopack holoprint guide book], Reconnaissance International Publishers and Consultants, 139-154 (2000).
- [8] Tate, N., Nomura, W., Yatsui, T., Naruse, M., and Ohtsu, M., "Hierarchical hologram based on optical near- and far-field responses," Opt. Exp., 16, 607-612 (2008).

Higher sensitivity for the analysis of bio-entities with changes in thicknesses of multilayered BioDVD structure

Subash C. B. Gopinath^a, Koichi Awazu^a, Penmetcha K. R. Kumar^b,
and Junji Tominaga^{*a}

^aCenter for Applied Near Field Optics Research (CAN-FOR), National Institute of Advanced Industrial Science and Technology (AIST), Tsukuba, Japan

Phone: +81-29-861-2911, Fax: +81-29-851-2902, E-mail: j-tominaga@aist.go.jp

^bFunctional Nucleic Acids Group, Institute for Biological Resources and Functions, National Institute of Advanced Industrial Science and Technology (AIST), Tsukuba, Japan

Phone: +81-29-861-6085, Fax: +81-861-6095

ABSTRACT

As a sequel to our earlier investigations on the analysis of biomolecular interactions on multilayered structures of BioDVD, herewith, we have manipulated the thicknesses of ZnS-SiO₂ layers as predicted by computational simulations. With the changes in two ZnS-SiO₂ layers from 45, 85 nm to 60 and 65 nm, respectively, we have checked the optical reflections with spotted samples having single strand DNA, hybrid DNA, DNA-RNA hybrid and DNA, RNA and protein complexes. The obtained signals from these molecules are compared with previous multilayered BioDVD and found that the changes in the ZnS-SiO₂ layer promote the reflected signal as prominent. These results will give a way to improve our previous DVD based bionanosensor with higher sensitivity.

Keywords: Bio-DVD, ZnS-SiO₂, Bio-molecules, multilayer

1. INTRODUCTION

At present several devices are available for the analysis of nucleic acid and ligands, including flowcytometry, affinity probe capillary electrophoresis, enzyme-linked immunosorbent assay (ELISA)-like assays (1). DNA chip technology is now-a-days widely used in various fields of biology as the powerful analytical tool with fluorescence associated scanning system. Eventhough these kinds of array based techniques having several advantages, scanning systems are expensive especially high density chips are preferred (2). As the alternate to this technique, in the past CD (Compact Disc) or DVD (Digital Versatile Disc) are introduced for the analysis of bio-molecules with wide surface and high speed scanning, in addition low cost in preparation and processing (3,4). These kinds of disc has multilayered structure with combinations of alloys and phase shifting materials. The phase shifting materials present in these multilayered structure will facilitate the higher reflection of detecting molecules and help to addressing.

Presently two major classes of phase-change materials are used in optical recording. One is based on the ternary GeSbTe (GST); the other is a quaternary AgInSbTe (AIST). The AIST-based material exhibit a higher signal-to-noise ratio during the readout and have several other favorable characteristics (5) because of these properties, we previously explored the quaternary-AIST phase-change materials for biosensing (3). In our preliminary analysis, SiO₂ was deposited as thin films on the sensor surface. The reflection intensity increased linearly with increasing thickness of the SiO₂ film ranging from 2-10 nm. The same surface was subsequently used for analyzing biotin and streptavidin interactions and found that the binding events can be detected on a rotating disc substrate at a constant velocity of 4.0 m/s (3). In the present study, we have manipulated the multilayer structures of BioDVD based on predictions as obtained by computer stimulations.

2. EXPERIMENTAL

Before spotting the recognition molecules on the Bio-DVD, the desired track was marked with the DVD-writing mode (0.2 mm lesser than desired track). All measurements were taken from the arrow head manually marked on the center of the DVD and the surface need to be analyzed was facing to the laser beam. The reflection intensity was measured from the multilayer side by an optical disk drive tester (DDU-1000, Pulstec Industrial Co., Ltd.) equipped with a 635 nm diode laser and a pickup lens with a NA of 0.6. The laser beam was irradiated from the multilayer side of BioDVD by inserting a dummy plate with a thickness of 0.6 mm between BioDVD and the pickup lens. The readout laser power P_r was adjusted to $P_r = 1.0$ mW, and the BioDVD was rotated at a constant linear velocity of 4.0 m/s during the measurements. The measurements were carried out in auto-focus and auto-tracking modes. The reflection intensity signal was measured at a sampling rate of 10 MS/s, and smoothed by 50-point boxcar averaging.

5' thiolated DNA is prepared chemically with 20 deoxythiamine residues (dT)₂₀ with protected thiolated group. To deprotect the thiolated group, oligos were treated with DTT (60 mM) and Tris HCl (250 mM, pH 8.0) for 16 hr at room temperature. After the reaction, the SH-poly-dT₂₀ oligo was subjected to purification by passing through TSK-gel in HPLC system (Shimadzu, Japan) running with 2.5 mM TEAA and eluted with the linear concentration by using TEAA and Acetonitrile in the ratio of 40:60. The solution from peak area was collected and dialyzed for 5 hrs against double distilled water with twice. Dialyzed sample was further concentrated in speed-vacuum dried and measured the concentration of DNA. RNA molecules are enzymatically synthesized as described before (6). Human Factor IX was purchased from American Diagnostica (Stamford, CT, U.S.A.).

3. RESULTS AND DISCUSSION

In this study, we have improved the sensitivity to detect the bio-molecules on DVD surface with changes in the thicknesses of the multilayered structure. As shown in the figure 1 we have modified two ZnS-SiO₂ layers deposited. In our previous BioDVD system, we had ZnS-SiO₂ layers with 45 and 85 nm on either side of phase-shifting materials (Figure 1). Using these layers and reflections obtained with bio-entities, we have modeled the new structure by computational simulations. To improve the optical reflection as suggestion created with computational simulations, these layers are modified from 45 and 85 nm to 60 and 65 nm, respectively (Figure 1).

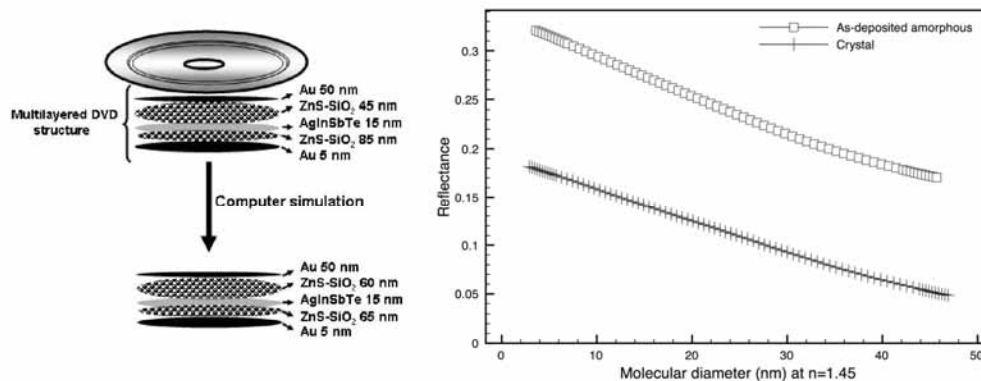


Fig.1. Multilayered structures on BioDVD system before and after adjusting the thicknesses (left) and reflection curves simulated using molecule immobilized on new multilayered structure (right).

The reflection curves simulated using molecule immobilized on the disc with 60 and 65 nm dielectric layer thickness is shown in Figure 1 (right). In both amorphous and crystalline state of the AIST film, the detection ranges of molecules are more expanded than that of the previous disc. Using the modified multilayered BioDVD, we have

examined the optical reflection with the attachment of single stranded DNA molecules. As shown in the figure 2, we could find the clear differences between two different sputtered discs. The new multilayered structure has shown very prominent signals compared with old one. In addition, due to higher reflected signal, the baseline was adjusted nicely and formation of wavy signal can be avoided with new multilayered disc. During fabrication of DVD disc, bit relaxed condition by loosening the screw at the center of sputtering plate, is also reduced the baseline alignment. The signal-to-noise ratio between these two different multilayered structures was found to improve with new multilayered structure as 20:1, whereas in old pattern it was 10:1.

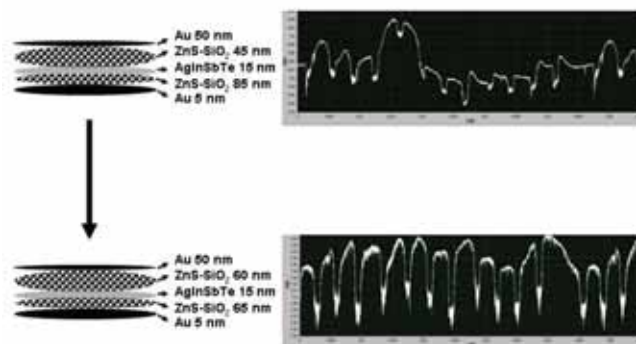


Fig. 2. Signal obtained with single stranded DNA molecules on two different multilayered structures

To expand with further application, we have also analyzed the formation of DNA-DNA duplex, DNA-RNA duplex and DNA-RNA-Protein complexes. As we expected, we could see the clear discrimination with different molecules in respective to their sizes. The comparison between two different multilayers have also shown the different reflection levels and new disc was displayed with higher sensitivity. In summary, the new disc created in the present study has the potential to become a label-free and high-throughput multi-analyte platform for the detection of a wide range of bio-entities.

References

- [1] Gopinath, S.C.B., Misono, T. and Kumar, P.K.R. Prospects of ligand-induced aptamers. *Critical reviews Anal. Chem.* 38, 34-47 (2008).
- [2] Perraut, F., Lagrange, A., Pouteau, P., Peyssonneaux, O., Puget, P., McGall, G., Menou, L., Gonzalez, R., Labeye, P. and Ginot, F. A new generation of scanners for DNA chips. *Biosen. Bioelectron.* 17, 803-813 (2002).
- [3] Arai, T., Gopinath, S.C.B., Mizuno, H., Kumar, P.K.R., Rockstuhl, C., Awazu, K. and Tominaga, J. Toward biological diagnosis system based on digital versatile disc technology. *Japanese Journal of Applied Physics.* *Jpn. J. Appl. Phys.* 46, 4003-4006 (2007).
- [4] Zhao, M., Nolte, D., Cho, W., Regnier, F., Varma, M., Lawrence, G. and Pasqua, High-speed interferometric detection of label-free immunoassays on the biological compact disc. *J. Clin. Chem.* 52, 2135-2140 (2006).
- [5] Liang, R., Peng, C., Nagata, K., Daly-Flynn, K., and Mansuripur, M. Optical characterization of multilayer stacks used as phase-change media of optical disk data storage. *Appl. Opt.* 41, 370-378 (2002).
- [6] Rusconi, C.P., Scardino, D., Layzer, J., Pitoc, G.A., Ortel, T.L., Monroe, D. and Sullenger, B.A. RNA aptamers as reversible antagonists of coagulation factor IXa. *Nature* 419, 90-94 (2002).

SESSION WB: Media and Applications

Monarchy Ballroom
10:30 am to 12:30 pm

Rie Kojima, Matsushita Electric Industrial Co., Ltd. (Japan)
Chong-Tow Chong, Data Storage Institute (Singapore)

Challenge to Snap Shot Structural Visualization of the Phase Change

Y. Tanaka^a, Y. Fukuyama^b, N. Yasuda^b, J. Kim^b, H. Murayama^b, S. Kimura^b, K. Kato^{a,b}, S. Kohara^b,
Y. Moritomo^c, T. Matsunaga^d, R. Kojima^e, N. Yamada^e, H. Tanaka^b and M. Takata^{*a,b,f}

^aSPRING-8/RIKEN, Hyogo 679-5148, Japan; ^bJapan Synchrotron Radiation Research Institute/SPRING-8, Hyogo 679-5198, Japan; ^cUniversity of Tsukuba, Ibaraki 305-8571, Japan;
^dMaterials Science and Analysis Technology Center & ^eAV Core Technology Development Center, Matsushita Electric Industrial Co., Ltd., Osaka 570-8501 Japan; ^fDepartment of Advanced Materials Science, The University of Tokyo, Kashiwa 227-8561 Japan

ABSTRACT

Of particular importance is the microscopic direct investigation of the data storage process in DVD or Blu-ray Disc media to develop a faster phase-change optical recording system. Thus, an *in-situ* structural observation by the time resolved X-ray diffraction has been required to uncover the fast phase-change phenomena. Here, we report the time resolved X-ray diffraction measurement of the simulated erasing process (amorphous-crystal phase change) with the model DVD media sample using synchrotron radiation (SR) pulse X-rays and synchronized laser irradiation for $\text{Ge}_2\text{Sb}_2\text{Te}_3$ (GST) and $\text{Ag}_{3.4}\text{In}_{3.7}\text{Sb}_{76.4}\text{Te}_{16.5}$ (AIST). A coupled *in-situ* photo reflectivity measurements were concurrently carried out to reveal the time-dependent structure-property relationship of the sample DVD media. The significant difference in crystallization process between GST and AIST as cast amorphous was found by both the photo reflectivity change and the X-ray diffraction peak intensity. The steep rise in crystallization of AIST is ascribed to its characteristic crystallization process; its X-ray diffraction profile shows a significant sharpening during the crystallization process, whereas the peak width of GST remained unchanged. The present findings suggest that crystal growth control is another key for designing faster phase-change materials. Our challenge of snap shot structural visualization of phase change phenomena by the time-resolved X-ray diffraction in SPRING-8 will be presented.

Keywords: phase change phenomena, DVD, time resolved experiment, X-ray diffraction, synchrotron radiation, GST,

1. INTRODUCTION

With the development of the digital information technologies, data storage with high-recording speed and high-recording density has been a large demand for storing and efficient using of the daily increasing data. Rewritable optical media such as a DVD-RAM (digital versatile disc-random access memory) is a typical solution to respond to the strong demand. The idea to apply an amorphous-crystal reversible phase-change phenomenon for memory devices proposed by Ovshinsky in the 1960s is a memory switch originally based on changes in the electrical properties of the both phases in chalcogenide materials[1], but materials developed in early stage yielded the problems in the phase-change speed and the repetition of cycle number in the phase-change process for optical memories. However, two landmark studies reported by Chen et al.'s on GeTe[2] and Yamada et al.'s on Au-Ge-Sn-Te[3] demonstrated that a single crystalline phase is a key to produce good phase-change materials. These approaches discovered the way to develop new phase-change materials and led to the discovery in 1987 of GeTe-Sb₂Te₃[4] and in 1992 of $\text{Ag}_{3.5}\text{In}_{3.8}\text{Sb}_{75.0}\text{Te}_{17.7}$ [5]. The development of these materials has allowed us not only to produce rewritable CDs (compact discs), DVDs, and Blu-ray discs, but also to promote the today's drastic development of nonvolatile solid memories. Thus, the phase-change materials are well-established media; however, the understanding of the fast phase-change mechanism, is remaining unclear.

2. X-RAY PINPOINT STRUCTURAL MEASUREMENT

The crystal growth process in DVD media induced by laser irradiation should also be a key to govern the recording speed, hence, various TEM studies as well as FEM study, optical, electronic and structural studies have been reported

*takatama@spring8.or.jp; phone +81-791-58-2942; fax +81-791-58-2717

and the crystallization behavior of the amorphous phase was discussed. The recent DVD materials can complete the phase change with a 20 ns laser irradiation[6], however, we are not aware any studies on the real-time observation of the crystal growth process probed by both structure and optical properties measurements in nano-seconds time scale. In the present study, we developed a time-resolved X-ray diffraction apparatus coupled with *in situ* photo reflectivity measurement, in order to obtain the findings on the crystallization process of GST and AIST, which are thought to exhibit different crystallization behavior. To reveal the crystallization process of the amorphous phase in the fast phase-change materials, we have developed the x-ray pinpoint structural measurement system as shown in Fig.1 at BL40XU in SPring-8[7].

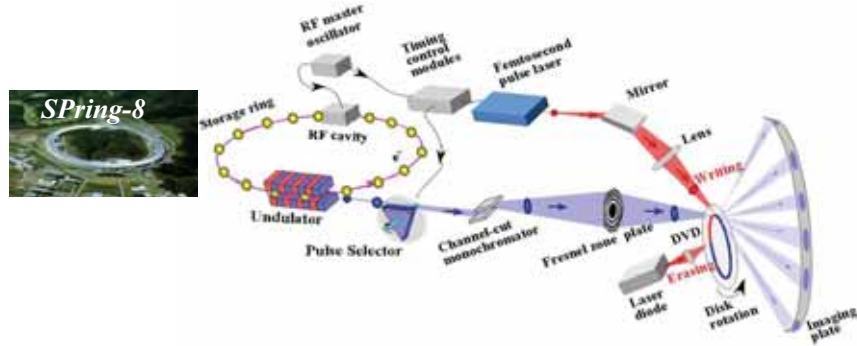


Fig. 1. The schematic design of X-ray pinpoint structural measurement system at SPring-8 BL40XU beamline. The system was developed for 40 pico second time-resolved structural study with sub-micron spatial-resolution.

3. PUMP & PROBE MEASUREMENT OF PHASE CHANGE PHENOMENA

In order to observe (i) the time constants of both crystallization and optical reflectivity change, and (ii) crystallization behavior. We employed APD (Avalanche Photodiode) / MCS (multi-channel scaling) measurement coupled with photo reflectivity measurement for (i) and IP/Pump & probe for (ii), respectively as shown in Fig. 2.

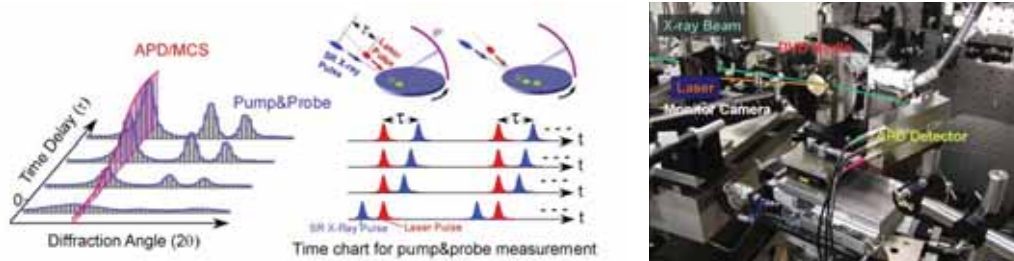


Fig. 2. The Schematic diagram of APD/MCS and IP/Pump & probe measurement and scheme of DVD rotating system and the time chart of pump & probe measurement with photograph of the time-resolved experiment apparatus for APD/MCS measurement.

These measurements can be achieved by the use of pulse characteristic and highly coherent X-ray beam. A combination of 40 picoseconds X-ray pulses generated by SPring-8 and synchronous femto-second laser pulses allows us to perform time-resolved X-ray diffraction measurements in nano-seconds time scale, which probes the crystallization process of the amorphous phases. Fig. 2 shows the scheme and photograph of time-resolved experiment apparatus, respectively. A DVD disc is rotated during the measurement to supply the virgin amorphous surface.

4. TIME RESOLVED OBSERVATION OF CRYSTALLIZATION

The time-resolved photo reflectivity profiles of 300 nm-thickness GST and AIST samples are shown in Fig. 3(a). Both profiles exhibit a rapid increase of the photo reflectivity between 100 and 200 ns. Wei and Gan reported the photo reflectivity change of 30 nm-thickness GST film deposited by d.c.-magnetron sputtering and found 3 stages for the crystallization[8]. Similar stages can be observed in the photo reflectivity profile of GST as indicated by red arrows, whereas AIST does not show separated distinct onset stage. The X-ray diffraction intensity profiles of all Bragg peaks (black and blue lines) show good accordance with those of the reflectivity profiles (red lines). Fig. 3(b) shows the diffraction patterns obtained by IP/Pump & probe method with a 40 picoseconds snapshot. Since the intensity of each diffraction peaks have time-dependent increase, there is no crystal phase transition in GST and AIST during the crystal growth. However, the position of diffraction peaks shift to higher angle corresponding to about 1% lattice parameter shrinks due to the time-dependent temperature decrease. As shown in Fig. 3(c), the peak width of GST, estimated from the curve fitting of Bragg peaks using a pseudo-Voigt remains the same while that of AIST has a time dependent decrease. These our findings imply the different crystallization process of AIST from that of GST whose detail will be presented in the talk.

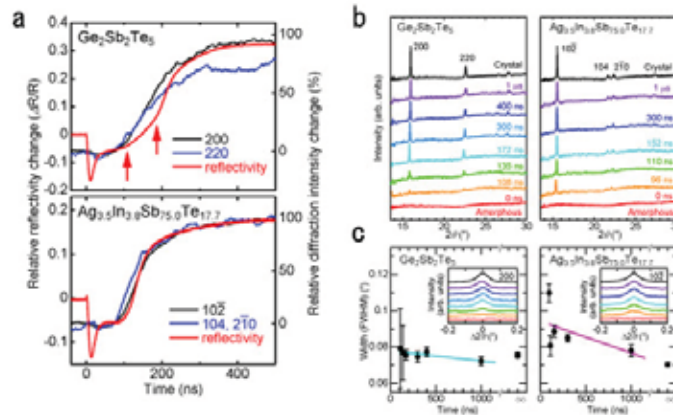


Fig. 3 (a) Photo reflectivity and time-resolved X-ray diffraction profiles of GST and AIST obtained by APD/MCS method. (b) Time-dependent X-ray diffraction patterns obtained by IP/Pump & probe method. (c) The peak width changes calculated for 200 reflection of GST and 10-2 reflection of AIST.

REFERENCES

- [1] Ovshinsky, S.R. "Reversible electrical switching phenomena in disordered structures." *Phys. Rev. Lett.* 21, 1450-1453 (1968).
- [2] Chen, M., Rubin, K. A. and Barton, R. W. "Compound materials for reversible, phase-change optical data storage." *Appl. Phys. Lett.* 49, 502-504 (1986).
- [3] Yamada, N., Takenaga, M. and Takao, M. "Te-Ge-Sn-Au phase change recording film for optical disk." *Proc. of SPIE, Optical Mass Data Storage II*, 695, 79-85 (1986).
- [4] Yamada, N. et al. "High speed overwriteable phase change optical disk material", *Proc. Int. Symp. on Optical Memory*. *Jpn. J. Appl. Phys.* 26, Suppl. 26-4, 61-66 (1987).
- [5] Iwasaki, H., et al., "Completely erasable phase change optical disk." *Jpn. J. Appl. Phys.* 31, 461-465 (1992).
- [6] Yamada, N. "Potential of Ge-Sb-Te phase-change optical disks for high-data-rate recording in the near future." *Proc. of SPIE, Optical Data Storage 1997*, 3109, 28-37 (1997).
- [7] Kimura, S. et al. "X-ray pinpoint structural measurement for nanomaterials and devices at BL40XU of the Spring-8." *AIP conference proceedings*, 879, 1238-1241 (2007).
- [8] Wei, J. & Gan, F. "Theoretical explanation of different crystallization processes between as deposited and melt-quenched amorphous Ge₂Sb₂Te₃ thin films." *Thin Solid Films* 441, 292-297 (2003).

What is the origin of activation energy in phase-change film?

J. Tominaga*, T. Shima, P. Fons, R. Simpson, M. Kuwahara, and A. Kolobov
 Center for Applied Near-Field Optics Research (CAN-FOR), National Institute of Advanced
 Industrial Science and Technology (AIST), Tsukuba Central 4, 1-1-1 Higashi, Tsukuba 305-8562
 Japan

ABSTRACT

Activation energy of phase-change films is one of the basic parameters to estimate the physical and chemical feature. However, the origin of the energy has never been discussed because of the simple model of randomness in the amorphous structure. In this paper, we reveal the origin of the activation energy, which initiates the transition from the amorphous to crystalline state, based on a GeSbTe-superlattice model by *ab-initio* local density approximation (LDA).

Keywords: phase-change film, activation energy, amorphous, crystal, GeSbTe

1. INTRODUCTION

Chalcogenide phase-change materials are highly attractive sources not only for optical data storage but also future solid-state memories. Among them, GeSbTe alloys and Sb-rich Te alloys with or without additives are the central materials in research. High-speed switching functionality, long-term durability at high-temperature or many read-write cyclability is required for each application. In optimizing such physical requirements, basic parameters and physical constants in the materials are highly important. “Activation energy” is one of the intrinsic and typical parameters to evaluate the crystallization, and a wide range of values have been estimated for the last 40 years by some methods such as Kissinger’s plot [1,2]. The values reported so far almost converge between 2 and 3 eV, although the meaning in the phase-transition has not been discussed well. What determines this value? According to the random model, a highly-random arrangement of the Ge, Sb and Te atoms may show a different value (probably higher) at each level of randomness, resulting in a large deviation. As a result, the energy would take a stronger correlation with the film fabrication condition rather than with the composition ratio. Reconsideration of the activation energy from a perspective of physics to chemistry, the definition becomes much clearer. In chemistry, activation energy is strongly related to an intermediate state of reaction, such as collision factor of starting molecules to form a final product [3]. But, it should be noticed that the Gibbs free-energy of formation is only determined by the difference of the initial and final states: not by the activation energy. For example, the formation energy of water is only the difference of $\Delta G_f = G_f(\text{H}_2\text{O})_{\text{gas}} - G_f(\text{H}_2) - G_f(\text{O}_2)$. However, the gas mixture of O_2 and H_2 does not produce H_2O without a trigger, of which energy is defined as activation energy.

In ISOM07, we provided a super-lattice model of $\text{Ge}_2\text{Sb}_2\text{Te}_5$ phase-change alloy and discussed that the alloy is composed of two main compartments: a Ge_2Te_2 layer unit and a Sb_2Te_3 layer unit due to in principle, the Kolobov model of Ge-switching between octahedral and tetrahedral coordination [4, 5]. In addition, we could clearly reproduce a large refractive index change at a longer light wavelength (~ 600 nm) and a relatively small index change at a short wavelength (~ 400 nm) by a computer simulation based on the first principle local density approximation. In this paper, we further step forwards in evaluating the activation energy based on our super-lattice model and the LDA simulation.

2. MODEL OF ACTIVATION STATE

As already discussed in ISOM07, the specific index change of refraction in $\text{Ge}_2\text{Sb}_2\text{Te}_5$ is only generated by the replacement of Ge layer and Te layer in between the two states: $[-(\text{Te-Sb-Te-Sb-Te})-(\text{Te-Ge---Ge-Te})-]_n$ and $[-(\text{Te-Sb-Te-Sb-Te})-(\text{Ge-Te-Te-Ge})-]_n$ [5]. The former corresponds to so-called amorphous and the latter to so called crystal. Both have *A-7* like structures but the volume of the amorphous is slightly bigger than the crystal [6]. This is due to a small space or an imaginary layer for charge-balance is generated between two *Ge* layers. To generate the reaction, the *Ge* and *Te* layers mutually defuse into their respective layers. As both states have the energy minimum by the LDA simulation, it is thought that the superimposed state of the layers is the transition point providing the energy maximum in the phase transition. The reaction is depicted in Fig. 1.

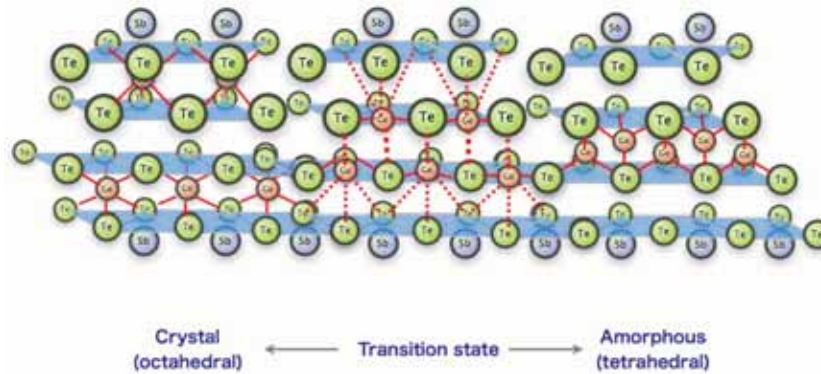


Fig.1 Three phases of $\text{Ge}_2\text{Sb}_2\text{Te}_5$ super-lattice structures. Left: crystal state composed of Ge octahedral coordination (6 bonds), Center: transition state, and Right: amorphous state composed of Ge tetrahedral coordination (4 bonds).

It should be noticed that in the transition the 1st Ge layer moves downwards and superimpose on the 2nd Te layer, and 2nd Ge layer moves upwards and superimposes on the 3rd Te layer. The 1st Ge layer makes a new bond with the 3rd Te layer, and the 2nd Ge layer oppositely makes a new bond with the 2nd Te layer.

3. LDA SIMULATION FOR ACTIVATION ENERGY

We constructed three super-lattices in the simulation as shown in Fig. 2. All simulations were carried out using the local density approximation (LDA) with a plane wave basis. Ultrasoft pseudopotentials were employed. Spin polarization was neglected. There were 9 atoms in total in the primitive unit cell used for the calculations. The valence electrons in the s - and p -orbitals: $4s^2 4p^2$ for Ge, $5s^2 5p^3$ for Sb and $5s^2 5p^4$ for Te were adapted in the basis set, but d-electrons were not included. The self-consistent total energies were obtained using a density-mixing scheme in connection with a conjugated gradient technique. The total energy was calculated to take into account the relaxation of the lattice constants and internal atomic positions in the amorphous and crystal structure, while the relaxation of internal atomic positions was constrained in the transition structure. Atomic positions were optimized by means of the quasi-Newton method within the Broyden-Fletcher-Goldfarb-Shanno scheme. The forces on each atom were relaxed to less than $0.01 \text{ eV}/\text{\AA}$. [7].

The calculated total energy of the crystal was -1650.62 eV with a unit volume of 256.13 \AA^3 . Those of the amorphous model were respectively -1650.26 eV and 261.21 \AA^3 . The difference of the energies was just 0.37 eV (40.6 meV/atom), which was very close to 36 meV calculated by the transition between a distorted cubic model and spinel model as amorphous [8]. The volume change between the two states was about 2%, which was smaller than one reported with the single non-super-lattice film. In contrast, the estimated total energy and volume in the transition model were -1647.92 eV and 285.33 \AA^3 . The volume was +11.4% as large as the crystal one and +9.4% as large as the amorphous one, respectively. In addition, the energy difference between the transient activated state and the amorphous state was 2.34 eV , which agreed well with ones experimental results reported. In another calculation, with free-lattice and free-atomic positions, from the constrained transition point, it was observed that the transition model gradually transformed into the crystal structure with the tetrahedral coordination of Ge atoms. The total energy change in the procedure is shown in Fig. 3. In comparison, activation energy by the replacement of Te and Sb layers in the Sb_2Te_3 layer unit was estimated 6.52 eV . According to the results, it is thought that the activation energies experimentally reported with as-deposited films are probably of the Ge-Te layer exchange to produce the crystalline state. Oppositely, it was found that higher activation energy is required to initiate the crystallization of $\text{Sb-Sb}_2\text{Te}_3$ phase change films.

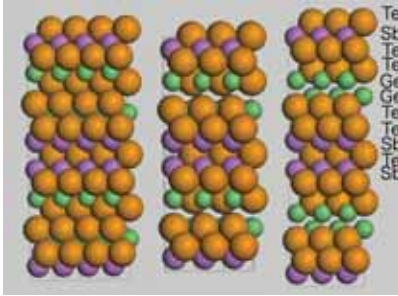


Fig. 2 Three computer models for crystal (left), transition (center) and amorphous (right) states. Big, middle and small balls are Te, Sb and Ge, respectively.

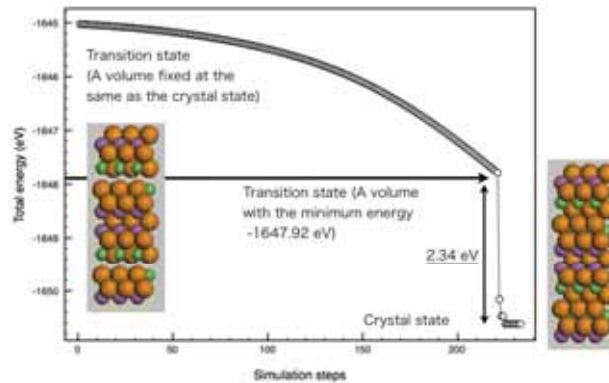


Fig. 3 Energy transition from the transition structure into the crystalline structure. After the transition energy obtained, the energy state was recalculated under free-lattice and free-atomic position.

4. CONCLUSIONS

We estimated activation energy of $\text{Ge}_2\text{Sb}_2\text{Te}_5$ based on the Kolobov model by the first principle computer simulation. A calculated value by the exchange of *Ge-Te* layers was 2.34 eV, which was very much compatible to ones reported experimentally, while that by the exchange of Sb-Te layers was 6.52 eV. According to the results, the activation energy from GeSbTe amorphous to crystal or vice versa is probably attributed to a transition state to exchange Ge and Te layers in the film.

REFERENCES

1. H. E. Kissinger, Reaction kinetics in different thermal analysis, *Analytical Chemi.* **29**, 1702-1706 (1957).
2. J. Tominaga, T. Nakano and N. Atoda, Doubleoptical phase transition of GeSbTe thin films sandwiched between two SiN layers, *Jpn. J. Appl. Phys.* **37**, 1852-1854 (1998).
3. P. W. Atkins, Physical Chemistry, Oxford, 1998.
4. J. Tominaga, T. Shima, P. Fons, A. Kolobov, L. P. Shi, R. Zhao, T.C. Chong, The role of Ge switch in phase transition – An approach using atomically controlled $[\text{GeTe}/\text{Sb}_2\text{Te}_3]$ superlattice, *Tech. Digest ISOM07*, pp. 22-23, Singapore, 2007.
5. Kolobov *et al.*, Understanding the phase-change mechanism of rewritable optical media, *Nature Mater.* **3**, 703-708 (2004).
6. N. Yamada and T. Matsunaga, Structure of laser-scystallized $\text{Ge}_2\text{Sb}_{2.5}\text{Te}_5$ sputtered thin films for use in optical memory, *J. Appl. Phys.* **88**, 7020-7028 (2000).
7. J. Tominaga, T. Shima, P. Fons, A. Kolobov, L. P. Shi, R. Zhao, T.C. Chong, *Jpn. J. Appl. Phys.* *submitted*.
8. W. Welnic *et al.*, Unravelling the interplay of local structure and physical properties in phase-change materials, *Nature Mater.* **5**, 56-62 (2004).

Acknowledgement: A part of the work was carried out under *Nanoelectronics Project* supported by METI.

Reliable measurement of optical constants for molten phase-change thin film

Daisuke Eto*, Kazuhiko Aoki and Shuichi Ohkubo
System Jisso Research Laboratories, NEC Corporation
1753 Shimonumabe, Nakahara-ku, Kawasaki, 211-8666 Japan

ABSTRACT

In ISOM2007, we reported on the first measurement in the world of optical constants for molten InSb film. Subsequently, we performed more detailed measurement with changing the thickness of InSb layer or the interface layer material. As a result, we have ascertained that the optical constants are almost independent of the thickness of InSb layer or the interface layer material. This result implies reliability of our measurement. Moreover, we found that the melting point of InSb thin film decreases and gets away from that of bulk InSb as the thickness of InSb decreases. This result can be attributed to large surface area compared to volume in thin film.

Keywords: Optical constants, Molten InSb thin film, Interface layer, Thickness, Material, Melting point

1. INTRODUCTION

Super-Resolution (SR) optical disc system is one of the promising candidates as the next generation's optical storage system and it has been intensively researched.^{[1][2][3]} In the SR media, mask layer of which optical constants are changed by temperature rise is used. Phase-change material exhibiting large change of optical constants accompanied by the phase transition between the solid crystalline and the molten phases is suitable for the SR mask layer. The SR signal depends on the contrast between reflectance in molten area and that in the solid crystalline area. Therefore, reliable measurement of optical constants for molten phase-change thin film is a key issue to design the SR media.

In ISOM2007, we reported on the first measurement in the world of optical constants for molten InSb thin film as a post-deadline paper.^[4] By sandwiching InSb layer between protective layers which were composed of metal oxide, we succeeded in the measurement without evaporation, oxidization and mutual diffusion of thin film. In this paper, we will present more detailed measurements to confirm its reliability by changing the thickness of the InSb layer or the interface material.

2. EXPERIMENTS

Figure 1 schematically describes the experimental setup for measuring the optical constants. It consisted of a laser diode emitting blue laser beam toward a sample, one photo diode (PD#1) detecting reflected beam from the sample, another photo diode (PD#2) detecting transmitted beam through the sample. Wavelength of the blue laser beam was 405 nm. The laser beam was collimated and its diameter was 1mm. The irradiated laser power was lower than 1.0mW. Since the laser beam was not focused, energy density was so low that temperature rise generated by laser beam was negligible. The optical constants were determined by finding parameter sets of refractive index n and extinction coefficient k so that the calculated T and R become closest to the measured T and R .

*d-eto@cc.jp.nec.com; phone +81-44-431-7581; fax +81-44-431-7592

The calculation of T and R was based on the Jones matrix.^[5] The sample was set on a heater which could heat the sample up to 600 °C.

Figure 2 describes the sample structure. InSb layer was sandwiched between interface layers. InSb thin film, interface layer thin films and ZnS-SiO₂ thin films were deposited on a glass substrate by using magnetron sputtering. We prepared three samples changing the thickness of InSb layer; 10 nm, 30 nm and 50 nm. Moreover, we prepared four samples changing material which composes interface layers; Ga₂O₃, Ta₂O₅-based, Cr₂O₃-based and GeN.

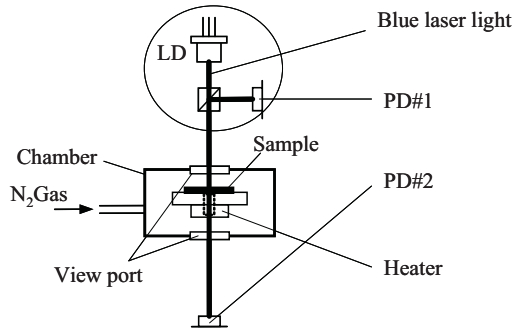


Figure 1 Experimental setup for measuring optical constants

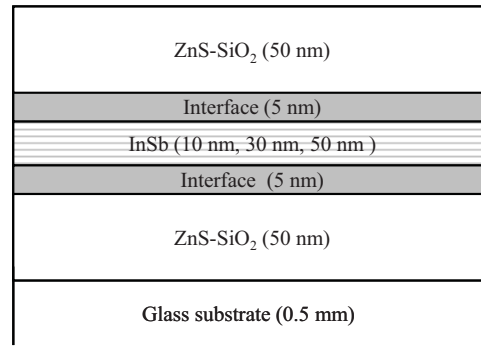


Figure 2 Sample structure

3. RESULT & DISSUSSION

Figure 3 describes an example of the measurement; temperature dependence of transmittance (T) and reflectance (R) of a sample which contained 10-nm-thickness InSb layer and Ga₂O₃ interface layer. R shows step changes and saturation around 490 °C which imply fusion and solidification of thin film. And in low temperature region less than 300 °C, both T and R in cooling process are almost the same as those in heating process. This means that the InSb thin film is quite stable even after experiencing fusion and solidification. No evaporation, no oxidization or no mutual diffusion was observed.

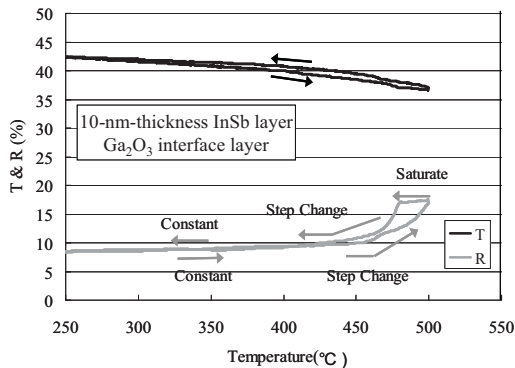


Figure 3 An example of the measurement; temperature dependence of T & R

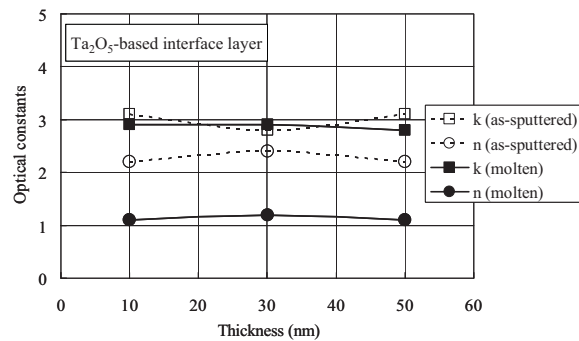


Figure 4 Thickness dependence of optical constants of InSb thin film

Figure 4 describes thickness dependence of optical constants of InSb thin film. Optical constants were almost independent of the thickness of InSb layer both in as-sputtered state and in molten state, which means reliability of our measurement.

Figure 5 describes thickness dependence of melting point of InSb thin film. As the thickness decreased, the melting point of InSb thin film decreased and got away from that of bulk InSb, i.e. approximately 520 °C. This result indicates the difference of melting point between thin film and bulk material can be attributed to large surface area compared to volume in thin film.^[6]

Figure 6 describes material dependence of optical constants of molten InSb thin film. In these four materials, optical constants were almost identical. This result indicated that all these four materials are suitable for interface layer in our measurement. Moreover, they must be suitable for interface layer on SR media to increase thermal stability in phase-change layer.

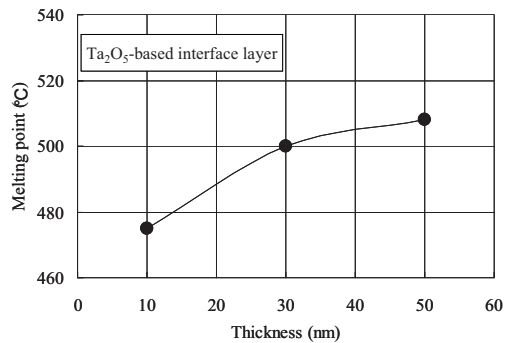


Figure 5 Thickness dependence of melting point of InSb thin film

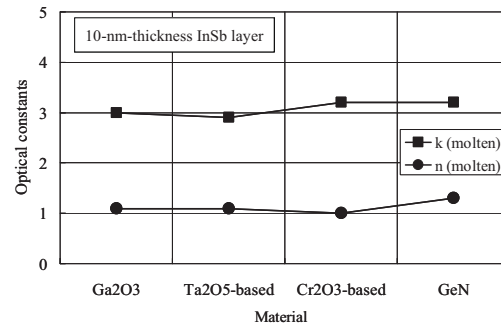


Figure 6 Material dependence of optical constants of InSb thin film

4. CONCLUSION

We have stably measured optical constants of molten InSb thin film under various conditions. It is clarified the optical constants are almost independent of both the thickness of InSb layer and interface layer material. This result implies reliability of our measurement. Moreover, the melting point of InSb thin film decreases and gets away from that of bulk InSb as the thickness of InSb decreases. This result can be attributed to large surface area compared to volume in thin film. By using these results, we can analyze the near-field optical distribution more correctly, and optimize the structure of the SR media to maximize the SR media performance.

REFERENCES

- [1] K. Yasuda et al.: Jpn. J. Appl. Phys. **32** (1993) 5210
- [2] T. Shima et al: Jpn. J. Appl. Phys. **44** (2005) 3631
- [3] K. Aoki et al: Int. Symp. on Optical Memory, 2006, p.10
- [4] D. Eto et al: Int. Symp. on Optical Memory, 2007, p.180
- [5] R. C. Jones: J. Opt. Soc. A **31** (1941) 488
- [6] M. Wautelet: Nanotechnology **3** (1992) 42

A two-color photopolymer system for high-capacity multilayer optical data storage

Benjamin A. Kowalski

Department of Electrical and Computer Engineering, University of Colorado, Campus Box 425, Boulder, CO 80309
kowalski@colorado.edu

Robert R. McLeod

Department of Electrical and Computer Engineering, University of Colorado, Campus Box 425, Boulder, CO 80309
robert.mcleod@colorado.edu

Timothy F. Scott

Department of Chemical and Biological Engineering, University of Colorado, Campus Box 424, Boulder, CO 80309
timothy.scott@colorado.edu

ABSTRACT

A novel two-color photopolymer system is demonstrated, which suppresses polymerization at the periphery of recording while maintaining high writing sensitivity at the focus. This enables both increased storage density and increased signal via suppression of out-of-focus exposure.

1. INTRODUCTION

Multilayer 3D methods such as microholograms are an appealing candidate for high capacity optical data storage [1, 2]. Highly sensitive photopolymer storage media are commercially available and are optimized for high writing transfer rates using low laser powers. However, in a single-photon medium, 3D bit density is limited, not only by the diffraction-limited beam waist and Rayleigh range of the focused writing beam, but also by the fact that the accumulation of out-of-focus exposure wastes the majority of the polymer dynamic range. It has been shown that the read-out efficiency of each layer is inversely proportional to the square of the total number of layers [3]. One common approach to reducing out-of-focus exposure is to use a two-photon initiation process. Although two-photon exposure is tightly confined to the focused spot, two-photon systems typically absorb at longer wavelengths, so that the overall achievable feature size is not appreciably smaller than for one-photon processes. Furthermore, the low sensitivity of two-photon processes typically requires high intensities achievable via a large, expensive pulsed laser [4] or very low write rate. Here we demonstrate a novel hybrid two-color photopolymer that has the high sensitivity of a single-photon process, but with spatial confinement of polymerization not limited by the physics of diffraction. This approach has advantages over established photochromic systems, in which photoinitiation occurs only in the simultaneous presence of two colors [5].

2. OVERVIEW OF TWO-COLOR SYSTEM

The photopolymer we have developed is photoinitiated by one wavelength and photoinhibited by another wavelength. Simultaneous application of both wavelengths provides precise spatial control of the polymerized region. For example, to decrease the transverse bit size, a Gauss-Laguerre inhibiting beam is superimposed over the Gaussian writing beam (fig.1, left). Polymerization is suppressed at the edges of the writing beam; thus, the region of polymerization is transversely confined to smaller than the diffraction-limited spot size. Our scheme is conceptually similar to super-resolution optical storage, in that a traveling mask limits the exposure volume to less than the diffraction limit. However, the super-resolution mask only achieves confinement in the two transverse dimensions, whereas our system can achieve sub-diffraction-limit confinement in all three dimensions by manipulating the inhibiting beam into a so-called bottle beam [6].

The polymer system consists of a monomer, triethylene glycol dimethacrylate (TEGDMA), a photoinitiator system, camphorquinone / ethyl 4-(dimethylamino)benzoate (CQ/EDAB), and a photoinhibitor, tetraethylthiuram disulfide (TED). When the photoinitiator is excited by light at the writing wavelength (473 nm), it initiates radical polymerization, so that the monomer begins to form a crosslinked polymer network. In the presence of the inhibiting wavelength (365 nm), however, the inhibitor produces radicals that terminate growing polymer chains faster than they can form. Figure 1 (right) illustrates this effect for uniform illumination of a large area. When the inhibiting beam is turned off, the inhibiting radicals rapidly recombine to form inert products; therefore, this system exhibits no memory

effects even at high write speeds. This is in contrast with photochromic materials, in which decay back to the nonabsorbing species is thermally driven and thus often takes minutes at room temperature.

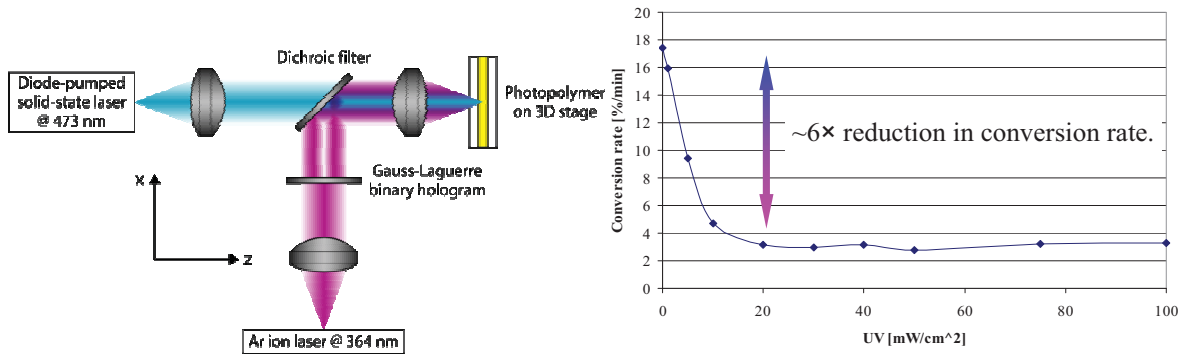


Figure 1. Layout of two-color writing optics (left) and polymerization rate under constant blue and variable UV exposure (right).

3. MODELING AND EXPERIMENT

The polymerization rate, R_p , as a function of the writing and inhibiting intensities, I , is expected to be

$$R_p \approx (I_{\text{writ}} - k I_{\text{inhibit}})^{0.5}$$

where k is a ratio of rate constants, and where the half-power dependence is due to the bimolecular termination of the polymer chains. Our model also does not allow the polymerization rate to drop below the “floor” value of $R_p \approx I_{\text{writ}} / 6$ specified by fig. 1, right. As shown in Figure 2, this model reveals that roughly 50% reduction of both radial and depth size are achievable with equal density of initiating and inhibiting radical species. Greater confinement factors are expected to be possible as the inhibition is increased, up to a limit indicated by the “floor” of the polymerization rate.

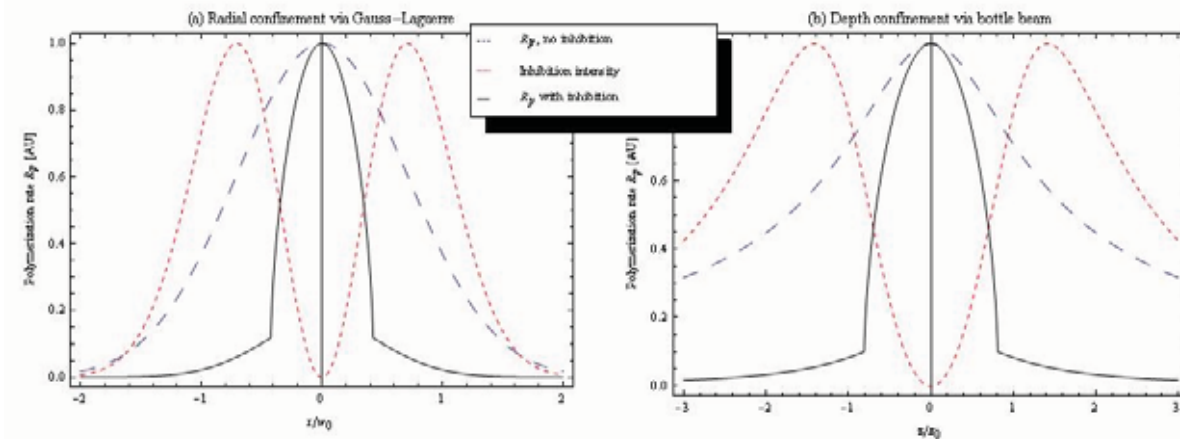


Figure 2. Modeling of polymerization rate R_p , showing confinement transversely with a Gauss-Laguerre inhibiting beam (a) and in depth with a bottle inhibiting beam (b). The pedestal character of the confined R_p profiles is due to the “floor” of the conversion rate (fig. 1, right)

Several features of these predictions are worth highlighting. First, the features are both smaller and much sharper than the smooth Gaussian illumination due to the fact that polymerization is related to the difference of the two intensities. This is in contrast to multi-photon approaches such as two-photon or photochromic absorption in which the polymerization is proportional to the product of the two intensities. Second, the strong suppression of polymerization above and below focus in Figure 2(b) may enable multi-layer data storage in which the majority of the dynamic range is available at each layer, yet maintains the high writing rate at low power of a one-photon absorption process. Figure 3 shows preliminary experimental results in which polymerized features were written at the boundary of liquid monomer and a glass cover layer. In (a), a phase-contrast microphotograph shows three point exposures, with one of the

spots completely suppressed by a Gaussian inhibiting beam. In (b) and (c), a scanning-electron micrograph was obtained after a sample was washed with a solvent. The features on the right, created only with the initiating light, are broad and smooth as expected. The features on the left show the impact of inhibition with a Gauss-Laguerre “donut” mode that has completely suppressed the peripheral polymerization. The resulting features are both much smaller and have well-defined, sharp edges, consistent with the model predictions.

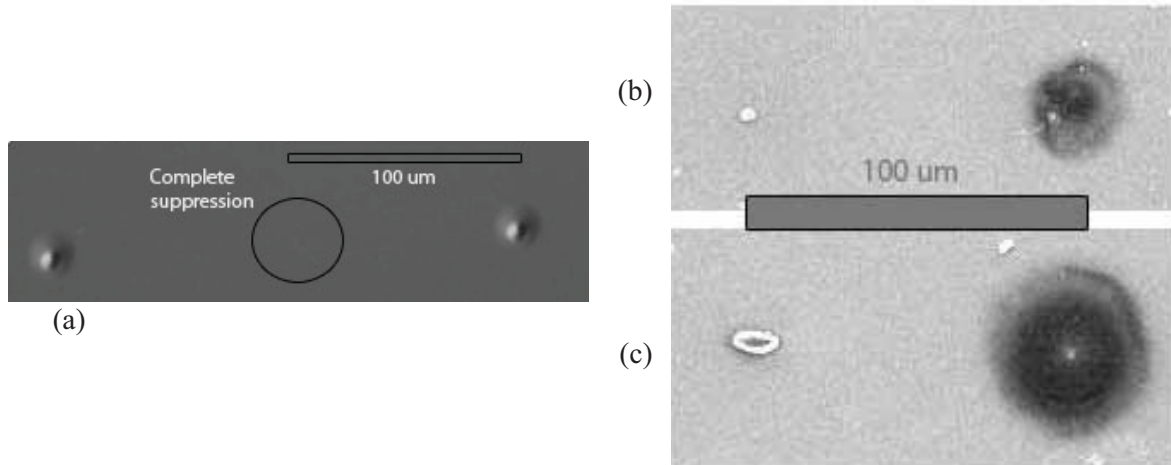


Figure 3 (a) Phase-contrast microphotograph of three point exposures, showing complete suppression of a single spot by a Gaussian inhibiting beam. (b) Scanning electron micrograph of point exposures. The spot on the left shows strong transverse confinement by a Gauss-Laguerre inhibiting beam, relative to the spot on the right with no inhibition. All other writing parameters are identical. (c) As in (b), but with longer exposure times. The asymmetry in the confined spot is due to slight decentering of inhibiting beam relative to writing beam.

4. CONCLUSION

We developed a novel two-color photopolymer system that simultaneously achieves both high sensitivity and suppression of peripheral and out-of-focus exposure. We experimentally demonstrate radial confinement of the polymerized region; modeling indicates that the system can also achieve depth confinement, thereby enabling higher recording densities and more efficient use of material dynamic range for multilayer optical data storage.

References

- [1] H. J. Eichler, P. Kuemmel, S. Orlic, and A. Wappelt, “High density disk storage by multiplexed microholograms,” *IEEE J. Sel. Top. Quantum Electron.* **4**, 840–848 (1998).
- [2] S. Orlic, S. Ulm, and H. Ju. Eichler, “3D bit-oriented optical storage in photopolymers,” *J. Opt. A* **3**, 72–81 (2001).
- [3] R. R. McLeod, A.J. Daiber, M.E. McDonald, S. L. Sochava, T.L. Robertson, T. Slagle, L. Hesselink, “Micro-holographic multi-layer optical disk data storage,” *Appl. Opt.* **44**, 3197-3207 (2005)
- [4] Wu, En-Shinn, James H. Strickler, WR Harrell, Watt W. Webb. “Two-photon lithography for microelectronic application,” *Proceedings of SPIE* 1674,776 (1992)
- [5] Lee, Suk-Kyu, and D.C. Neckers, “Two-photon radical-photoinitiator system based on iodinated benzospiropyrans”, *Chem. Mater.* **3**, 858-864 (1991)
- [6] Arlt, J. and M.J. Padgett, “Generation of a beam with a dark focus surrounded by regions of higher intensity: the optical bottle beam”, *Opt. Lett.* **4**, 191-193 (2000)

Phase aberration limits to three-dimensional optical data storage in homogeneous media

Robert R. McLeod*

Department of ECE, University of Colorado, Boulder, Colorado, 80309-425

ABSTRACT

Various multi-layer optical data storage methods have been proposed in which bits are written in an initially homogeneous material. Writing methods include one- or two-photon absorption at a single or two counter-propagating foci followed by polymerization, diffusion, photochromism or conformational change, while reading methods include transmission deflection, reflection, absorption or fluorescence. To varying degrees, all of these methods will be constrained by phase aberrations that decrease the Strehl ratio as the number of layers and index perturbation of each bit are increased. Although the complete problem is theoretically and numerically intractable, statistical derivations of the impact are possible. These analytic expressions are derived and validated with simulations of low-capacity disks, then used to establish limits in the interesting high-capacity case.

Keywords: Holographic and volume memories, Optical data storage, Optical aberrations

1. INTRODUCTION

The desire for large layer count and simple disk manufacture motivates the use of a homogeneous optical disk volume in which bits are recorded at “virtual layers” determined only by the focal depth¹. Recording systems in this class can be organized by three characteristics: the linearity of the absorption during recording, the physical recording mechanism and the readout technique. These characteristics can be chosen somewhat independently leading to a large number of combinations and a correspondingly large body of literature. During recording, the linearity of the absorption determines the 3D localization of the material response which in turn impacts in-plane and out-of-plane crosstalk, consumption of material dynamic range and accumulation of phase aberrations. The physical recording mechanism can induce molecular conformational change to modify absorption, birefringence or fluorescence, initiate polymerization for direct or diffusion-drive index change, excite free-carriers which induce index change via the photorefractive effect or, in the case of high-power lasers create voids or other localized material changes. Finally, detection includes one or two-photon fluorescence and coherent transmission or reflection scattering with various microscopy techniques such as confocal filtering and homodyne detection [2] to increase signal quality.

2. THEORY

For sake of generality, this paper will assume that there is an index change, δn , with a peak index change of Δn which depends on the time integral of intensity raised to a material-dependent power α . This response parameter would be unity for an ideal linear process, two for an ideal two-photon process and less than unity for radical-initiated photopolymers. Assuming a Gaussian beam with Rayleigh range z_0 is used to write either isolated bits or long marks, the on-axis phase delay can be shown to be

$$\begin{aligned}
 S(\tilde{z}_1, \tilde{z}_2) &= \int_{z_1}^{z_2} \delta n(0,0,z) dz = \Delta n z_0 \left[\tilde{z}_2 {}_2F_1\left(\frac{1}{2}, \bar{\alpha}, \frac{3}{2}, -\tilde{z}_2^2\right) - \tilde{z}_1 {}_2F_1\left(\frac{1}{2}, \bar{\alpha}, \frac{3}{2}, -\tilde{z}_1^2\right) \right] \\
 &= \Delta n z_0 \begin{cases} \sqrt{\pi} \Gamma(\bar{\alpha} - \frac{1}{2}) / \Gamma(\bar{\alpha}) & \text{if } -\tilde{z}_1 = \tilde{z}_2 \rightarrow \infty \\ \arctan(\tilde{z}_2) - \arctan(\tilde{z}_1) & \text{if } \bar{\alpha} = 1 \\ \pi & \text{if } \bar{\alpha} = 1, -\tilde{z}_1 = \tilde{z}_2 \rightarrow \infty, \end{cases} \quad (1)
 \end{aligned}$$

* mcLeod@colorado.edu

where the $\tilde{z} \equiv z/z_0$ is a normalized depth coordinate, ${}_2F_1$ is Gauss's hypergeometric function and Γ is the Gamma or generalized factorial function and $\bar{\alpha}$ equals α for an isolated bit and $\alpha/2$ for an infinitely long mark. Equation 1 reveals that for long marks in a linear material with $\bar{\alpha} = 1/2$, the phase aberrations are not well-confined in depth – we will therefore only consider pulsed OOK keying. The equation also shows that material nonlinearity has only a moderate impact on peak phase aberration – a two-photon absorber has just half the phase delay of a one-photon material.

The Strehl ratio of the reading or writing focus after propagating through a large number of such index perturbations is related to the standard-deviation of the optical path delay (OPD) [3]. To find how the peak delay of a single bit (Eq. 1) relates to the standard deviation of a volume of such bits, we first find the standard deviation of the OPD of a single layer by noting that the shape of the index profile in the focal plane, $\delta n(r, z=0) = \Delta n \exp(-2\alpha r^2/w_0^2)$, will dominate the statistical properties of the projected OPD. Assuming that the index perturbation due to each bit is confined to a rectangular cell of size $B w_0$ along track and $T w_0$ across track where w_0 is the beam waist radius, the variance of the OPD for a single layer normalized to $\Delta n = 1$ can be calculated as

$$\begin{aligned} \sigma_{layer}^2 &= \left(\beta \langle \delta n^2 \rangle - \beta^2 \langle \delta n \rangle^2 \right) / \Delta n^2 \\ &= \frac{\pi\beta}{4BT\alpha} \operatorname{erf}(B\sqrt{\alpha}) \operatorname{erf}(T\sqrt{\alpha}) - \left(\frac{\pi\beta}{4BT\alpha} \operatorname{erf}(B\sqrt{\alpha/2}) \operatorname{erf}(T\sqrt{\alpha/2}) \right)^2, \end{aligned} \quad (2)$$

where $\langle \rangle$ indicates averaging over one transverse unit cell of the grid and β is the fraction of bits that are “1”s. This expression assumes no overlap of bits so is expected to underestimate σ_{Layer} for small B or T . It will be shown in the next section that the OPD of layers tends to be uncorrelated and thus the variance of the OPD of individual layers add. Assuming that the disk is sufficiently thick that the majority of layers are far from the edges, we can take the approximation in Eq 1 that $-\tilde{z}_1 = \tilde{z}_2 \rightarrow \infty$ and, for sake of definiteness we will assume a linear material, $\alpha = 1$. This enables the calculation of the Strehl ratio of the focus propagating through M total layers:

$$SR \approx 1 - (2\pi/\lambda_0)^2 \sigma_{Total}^2 = 1 - (2\pi/\lambda_0)^2 M (\Delta n z_0 \pi)^2 \sigma_{Layer}^2 \quad (3)$$

3. VALIDATION WITH NUMERICAL CALCULATION

Equation 3 and the assumptions leading to it can be verified for low storage density by direct numerical integration of index perturbations in a 3D space. As illustrated in Figure 1 (a), this requires the integration of δn along the ray paths of the Gaussian beam which turn out to be at radial coordinates proportional to the beam radius $w(z)$. Equivalently, the ray paths can be transformed to straight lines which warps the index space as shown in part (b). The variable magnification of each layer is what decorrelates their OPD.

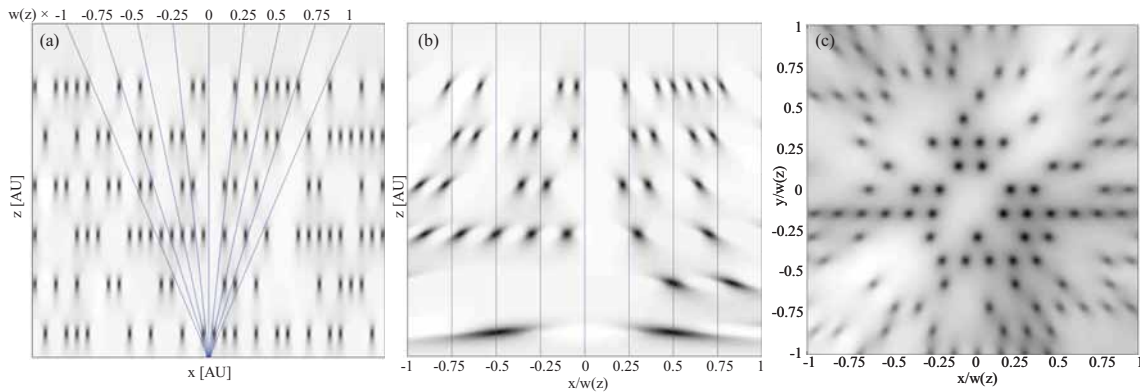


Figure 1. Slice through a 3D simulation of a 6-layer disk showing ray paths and index before (a) and after (b) transformation. Calculated OPD of the third layer from the top (c) shows a characteristic warping.

Figure 2 (left) compares the numerically and theoretically calculated standard deviation of the OPD for a single disk layer as function of the bit density. As expected the accuracy degrades at high bit density due to the simple method of calculating the variance within the layer. Figure 2 (right) shows that the standard deviation of the OPD is accurately predicted by the square root of the number of layers, verifying the assumption of statistical independence from layer to layer.

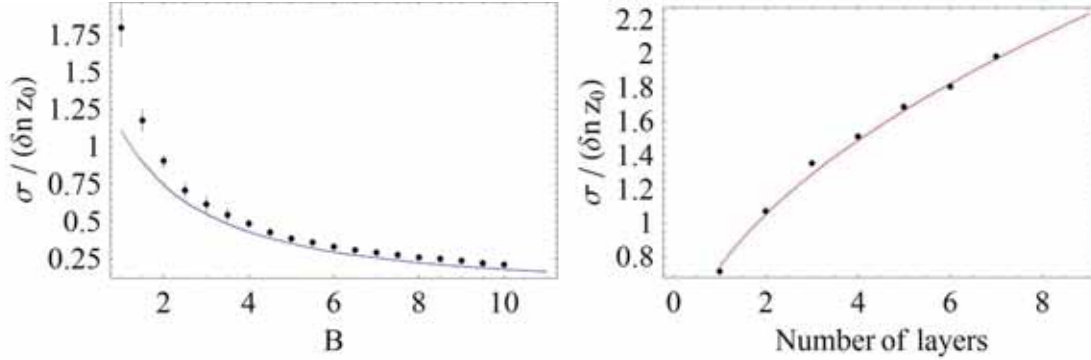


Figure 2. Comparisons of theory and numerics. The left figure plots equation 2 versus the average (circles) and standard deviation (bars) of 20 simulations for a square ($B=T$) grid of 0.2 NA bits placed half way between the surface and the focus $500 z_0$ into a linear ($\alpha=1$) material. The right figure shows the standard deviation of the entire disk for $T=B=2.5$ (circles) and the square root of M normalized to $M=1$.

4. CONCLUSIONS

Equation 3 can be used to predict explicit limits on the number of possible layers if the peak index perturbation of each bit is known. Taking the specific case of microholograms, the confocal reflection efficiency of a bit is given by

$$\eta = \left[\left(\frac{\pi}{\lambda_0} \right) \Delta n \left(\frac{\pi z_0}{2} \right) \right]^2 . \quad (4)$$

Δn in this expression is the zero-to-peak amplitude of the microholographic grating at the origin. When integrating the OPD, this is also the average over the fringes and thus is the proper value for Eq. 1. Assuming typical values for the a high-density storage system of $B=T=2$, $\alpha=1$ and $\beta=0.5$, $\sigma_{\text{Layer}} \approx 1/4$, yielding the remarkably simple result

$$SR \approx 1 - M\eta . \quad (5)$$

This equation concisely shows the trade-off of optical focus quality, number of layers and reflection efficiency. Remarkably, it does not depend on many of the details of the system including numerical aperture or wavelength. Since Strehl ratio is typically required to be larger than 0.9, a $M=100$ layer disk (for example) can not have individual bit efficiencies in excess of 0.001. Photochromic, fluorescent or other multi-layer methods in which index change is not directly coupled to readout strength must obey this same limit for any induced index change.

-
- 1 G. W. Burr, "Three-dimensional optical storage," Proc. SPIE Int. Soc. Opt. Eng. 5225, 78 (2003).
 - 2 F. Guattari, G. Maire, K. Contreras, C. Arnaud, G. Pauliat, G. Roosen, S. Jradi, and C. Carré, "Balanced homodyne detection of Bragg microholograms in photopolymer for data storage," Opt. Express 15, 2234-2243 (2007)
 - 3 M. Mansuripur, *The Physical Principles of Magneto-optical Recording*, pp 675-676, (Cambridge University Press, 1995).

Application of ODS Technology to Lithography

Tom D. Milster

College of Optical Sciences, University of Arizona, Tucson, AZ, 85721, USA

Email: milster@arizona.edu

As demands for ever smaller and more powerful computer circuits increase, technologists are planning to decrease the minimum feature size fabricated on Si wafers to less than 16 nm by 2020. This Herculean task may be accomplished with exposure tools operating at the soft x-ray wavelength of 13.5 nm and advanced processing techniques. A significant problem with this plan is that, as the minimum feature size decreases, the cost of the exposure and processing systems increases. This paper addresses the possibility of applying optical data storage (ODS) technology to lithographic exposure, in order to reduce cost of the components and provide a path for fabrication of 10 nm features.

In many ways, ODS and lithographic systems are striving to achieve the same goal, which is to *produce the smallest feature size possible at the fastest data rate possible*. With ODS systems, high performance single-laser-beam systems are mass produced with near-ultra-violet wavelengths to scan inexpensive rotating disc platters. Control of the spot position over the disc is maintained with advanced optical servo feedback mechanisms. In lithography, massive single lenses are designed to cover a large image field and expose areas corresponding to the area of a computer chip. Control over the exposure position is accomplished with extremely fine environmental control and sophisticated stages and metrology. The technical hypothesis of this paper is *by changing the paradigm of lithographic systems from massive, large-field exposure devices to small-field devices operating in parallel, ODS technology can be applied to realize economies of scale and performance to reach lithographic goals in the next several decades*.

This summary contains a brief review of lithographic technology. Then, several relevant ODS technologies are discussed for this application. Finally, a system concept is displayed.

An International Technology Roadmap for Semiconductors (ITRS) is published periodically by the semiconductor industry. It is an assessment of semiconductor technology requirements.[1] Figure 1 shows the 2007 ITRS, where the vertical axis is indexed by the node corresponding to the smallest feature size that is fabricated on a computer chip. Note that significant innovation is required in order to satisfy the technology requirement starting at the 22 nm node. Conventional optical lithographic techniques with 193 nm wavelength technologies will not be able to produce the required feature size. Therefore, new and innovative technologies, such as extreme ultra-violet (EUV), could play a major role in realizing the 32 nm and smaller nodes. The ITRS indicates that 16 nm features will be required in computer chips by 2019.

The conventional lithographic system exhibits a powerful light source, illumination optics, mask and projection camera, as shown in Fig. 2. Deep ultra violet (DUV) ArF lasers operating at an emission wavelength of 193 nm are used as a powerful light source. Typically, 30W to 40W of output power are used in each instrument. The laser beam is passed through a complicated beam shaping system and homogenizer that controls polarization, uniformity and spatial coherence of the illumination on the mask. Homogenizers often employ fly's eye lenslet arrays that form multiple images of the source in the pupil of the projection camera. The mask is an enlarged image of the print that will be made on the Si wafer. DUV systems use a transmissive mask, where mask features are computed with complicated algorithms that take into account vector diffraction and photoresist properties. A demagnified image of the mask transmission is formed on the wafer by the projection camera. Typical magnification factors are 5:1 and 4:1. After exposure of one chip area, the mask and wafer are repositioned to scan over an adjacent area on the 300 mm diameter wafer.

Resolution of the smallest printable feature at the wafer (which is called the *critical dimension*) is given by

$$\text{Resolution} = k_1 \frac{\lambda}{NA}, \quad (1)$$

where k_1 is a process parameter, λ is the wavelength of the light source in air and NA is the numerical aperture of the projection camera. Equation (1) is derived from the phenomenon of diffraction and from special processing characteristics of the photoresist. By using liquid immersion techniques, NA can be 1.3

or higher with DUV systems. With $k_1 = 0.3$ through special illumination and resist processing techniques, the critical dimension of DUV systems is less than 45 nm.

The projection camera is an outstanding optical component, which is capable of providing $NA = 1.3$ over a 26 mm by 33 mm area at a wavelength of 193 nm. The shear number of resolution elements is daunting – over 420 billion pixels per exposure, which is more pixels than the display of a 452 by 452 array of HDTV screens viewed simultaneously at 1,920 x 1,080 pixels per screen.

This performance comes at a cost of over \$20M per instrument. However, optical lithography systems are cost efficient, because many wafers can be exposed for each mask and the throughput in terms of the number of wafers per hour is high. Most exposure tools can process 100 wafers per hour or better.

Next generation EUV lithography systems, using a source wavelength of 13.5 nm, $NA = 0.25$ and $k_1 = 0.6$, could provide fabrication at the 32 nm critical dimension node, but will likely be significant only at the 22 nm node. EUV exposure systems and masks are extremely expensive, because they operate in vacuum and must use reflective components. Also, the source power is an important concern, due to contamination and limited reflectivity of mirror components. In order to achieve higher NA , EUV systems must use more mirrors, which decreases throughput.

It is known that ODS systems can produce feature sizes nearly equal to the goal of the ITRS. For example, Ito *et al.* have demonstrated writing an 11 nm line between data marks in a TeO_x -based film.[2] Ito's system used an argon laser wavelength of 351 nm and $NA = 0.9$. The nonlinear nature of the TeO_x -based film allowed fabrication of well-controlled 80 nm lines and spaces, which are much smaller than the full-width-at-half-maximum (FWHM) spot size calculated from $0.6\lambda/NA = 234$ nm. At least, Ito's demonstration illustrated that features on the order of 10 nm can be fabricated in nonlinear films with a thermal threshold. Similarly, the 11 nm feature size is close to the ultimate recording limit in GST materials, as discussed by Tanaka.[3] Phase-change random access memory (PRAM) has achieved even better resolution with a cell size of 3 nm by 20nm.[4] In addition, the super-RENS effect is being investigated in PtO_x films for nano-fabrication at AIST.[5]

Consider an ODS-like system using a diamond SIL and an exposing wavelength of 248 nm. The estimated minimum feature size is 18.6 nm, which is four times smaller than the FWHM spot size at $NA = 2.0$. Effectively, the thermal resist produces a k_1 factor of 0.15. With the addition of a high-efficiency concentrator, it is reasonable to assume that the spot size could be reduced by another factor of two in order to meet the 10 nm target.[6]

Finally, a system concept of a massively-parallel ODS-based lithography tool is shown in Fig. 3.

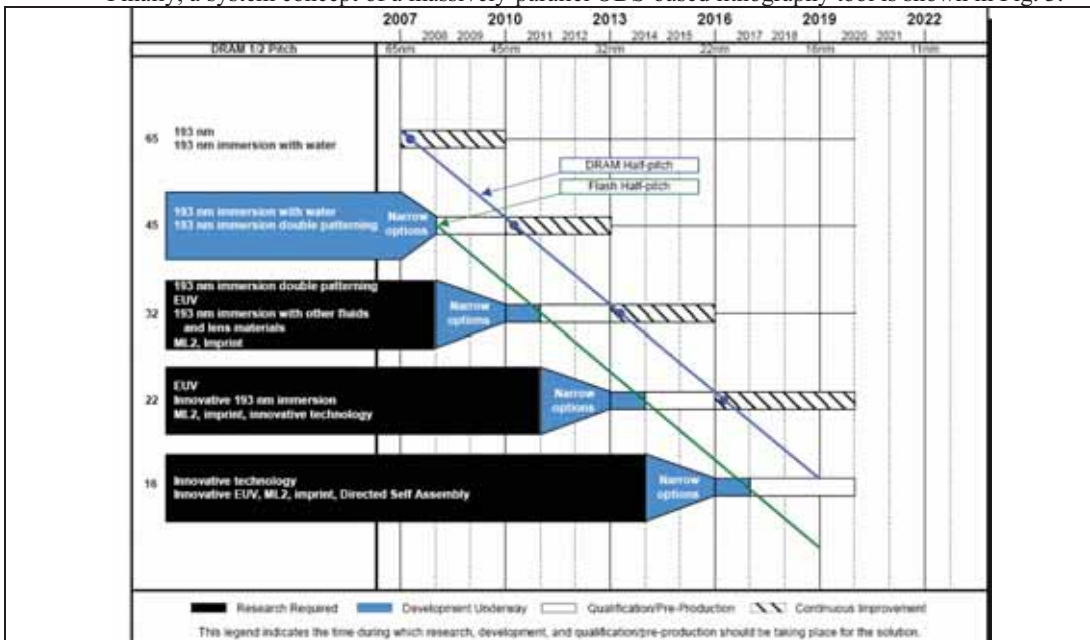
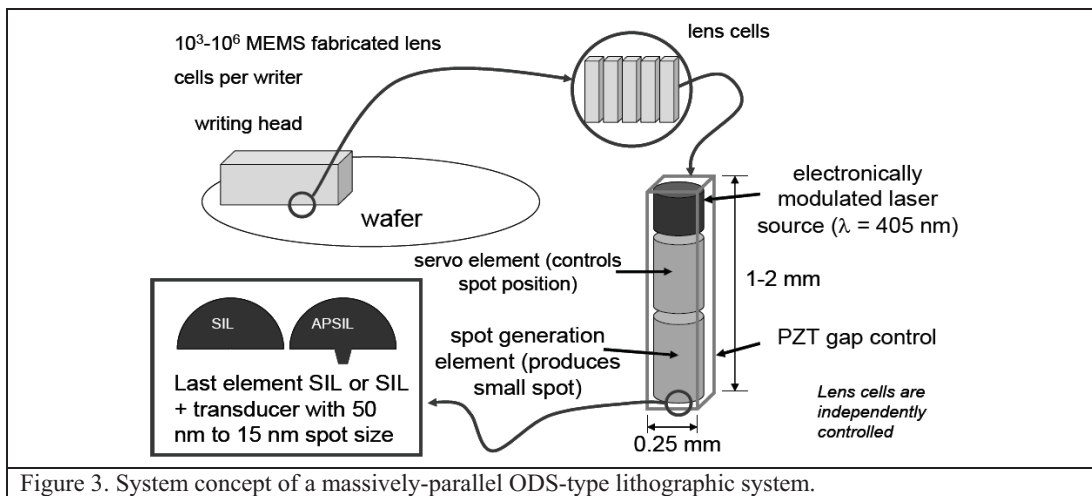
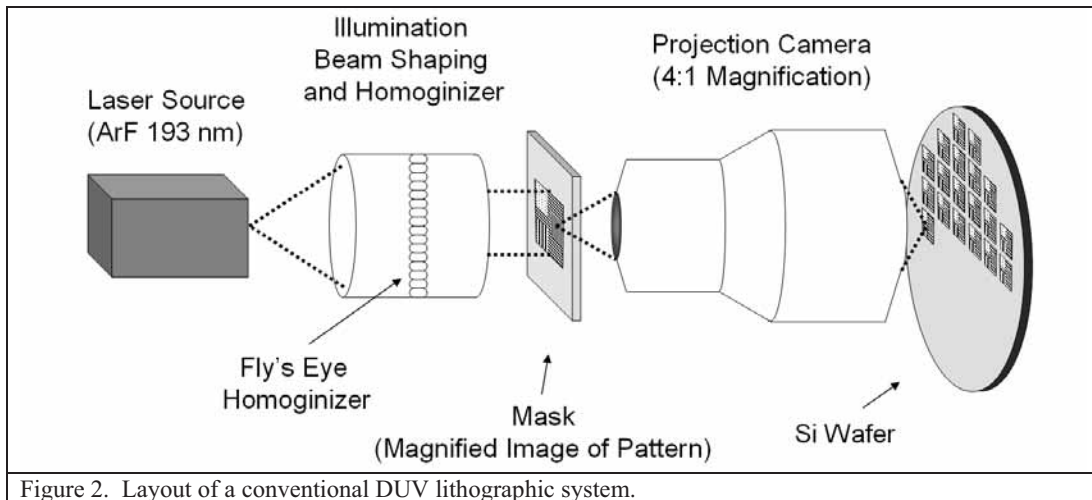


Figure 1. The 2007 ITRS (from Reference 1.)



References:

1. http://www.itrs.net/Links/2007ITRS/2007_Chapters/2007_Lithography.pdf
2. E. Ito *et al.*, *JJAP*, 44, 3574, 2005
3. Tanaka, Paper MO-C-05, ISOM 07
4. *Nature* **445**, 362-363 (25 January 2007).
5. K. Kurihara *et al.*, *J. Opt. A: Pure Appl. Opt.* **8** (2006) S139-S143
6. S. G. Tang *et al.*, *Opt. Lett.*, **26**(24) p. 1987 (2001).

SESSION ThA: Coding and Signal Processing

Monarchy Ballroom
8:30 to 10:00 am

Satoru Higashino, Sony Corp. (Japan)
Seiji Kobayashi, Sony Corp. (Japan)

Signal-Readout System for Optical Pickup with Homodyne Detection Scheme

Takahiro Kurokawa*, Hideharu Mikami,
Tatsuro Ide, Koichi Watanabe, and Harukazu Miyamoto
Central Research Laboratory, Hitachi, Ltd., 1-280, Higashi-koigakubo, Kokubunji 185-8601, Japan;

ABSTRACT

We developed a signal-readout system suitable for optical pickups using a homodyne detection scheme, which is used to amplify signal lights by using optical interference. The system consists of two optical-signal detectors and a readout-signal generator. The optical-signal detector, which contains two photodiodes connected in series, successfully cancels large DC-current components arising from a reference light. It is able to avoid output signal saturation of a current-to-voltage amplifier and to raise the upper limit of a signal amplification rate. By using the detector, a signal amplification rate of 3.6 was obtained on a practical disc. The readout-signal generator generates a readout signal on the basis of the phase-diversity method. In order to stabilize the amplitude of the readout signal, the amplitudes of two detection signals should be precisely balanced.

Keywords: homodyne detection, optical pickup, phase-diversity method, multi-layer optical disc, optical-signal detector

1. INTRODUCTION

As one of the most promising technologies for achieving data storage with capacities of 100-200GB, the multi-layer Blu-ray Disc (BD), which has four or more recording layers, has been proposed [1-3]. However, on the multi-layer BD, the reflectance of each recording layer is very low and thus a signal light reflected from a disc is very weak. This causes a low readout signal-to-noise ratio (SNR). In order to solve the problem and to realize the practicality of the multi-layer BD system, we have been developing optical pickups using the homodyne detection scheme, which can amplify weak signal light by using optical interference [4]. In this paper, we report on the development of a signal-readout system suitable for the homodyne detection scheme and a demonstration of signal amplification on a commercially available disc.

2. PRINCIPLE OF HOMODYNE DETECTION

Figure 1 shows a basic configuration of an optical pickup with the homodyne detection scheme. A signal light reflected from a disc interferes with a reference light, which is not irradiated to the disc, and the interference light is differentially-detected with two photodiodes. The differential-detection signal D is described as

$$D = \eta I_1 - \eta I_2 = \eta \left(\frac{1}{2} I_{sig} + \frac{1}{2} I_{ref} + \sqrt{I_{sig} I_{ref}} \cos \Delta\phi \right) - \eta \left(\frac{1}{2} I_{sig} + \frac{1}{2} I_{ref} - \sqrt{I_{sig} I_{ref}} \cos \Delta\phi \right) = 2\eta \sqrt{I_{sig} I_{ref}} \cos \Delta\phi,$$

where I_{sig} and I_{ref} are the intensities of the signal and reference lights respectively, η is the conversion efficiency of the detector, and $\Delta\phi$ is the phase difference between the signal and reference light. The differential-detection signal D can be amplified by increasing the intensity of the reference light. However, the amplitude of the differential-detection signal fluctuates due to fluctuation of $\Delta\phi$. To solve this problem, the phase-diversity method [4] has been introduced. The configuration of an optical pickup with this method applied is shown in figure 2. Two differential-detection signals D_1 and D_2 become

$$D_1 = \eta I_1 - \eta I_2 = \eta \left(\frac{1}{4} I_{sig} + \frac{1}{4} I_{ref} + \frac{1}{2} \sqrt{I_{sig} I_{ref}} \cos \Delta\phi \right) - \eta \left(\frac{1}{4} I_{sig} + \frac{1}{4} I_{ref} - \frac{1}{2} \sqrt{I_{sig} I_{ref}} \cos \Delta\phi \right) = \eta \sqrt{I_{sig} I_{ref}} \cos \Delta\phi,$$

$$D_2 = \eta I_3 - \eta I_4 = \eta \left(\frac{1}{4} I_{sig} + \frac{1}{4} I_{ref} + \frac{1}{2} \sqrt{I_{sig} I_{ref}} \sin \Delta\phi \right) - \eta \left(\frac{1}{4} I_{sig} + \frac{1}{4} I_{ref} - \frac{1}{2} \sqrt{I_{sig} I_{ref}} \sin \Delta\phi \right) = \eta \sqrt{I_{sig} I_{ref}} \sin \Delta\phi.$$

Thus, the readout signal I_{out} generated on the basis of the operation below is independent of $\Delta\phi$.

$$I_{out} = D_1^2 - D_2^2 = \eta^2 I_{sig} I_{ref} \cos^2 \Delta\phi + \eta^2 I_{sig} I_{ref} \sin^2 \Delta\phi = \eta^2 I_{sig} I_{ref}.$$

*takahiro.kurokawa.nb@hitachi.com; phone +81-45-860-3028; fax +81-45-860-2322

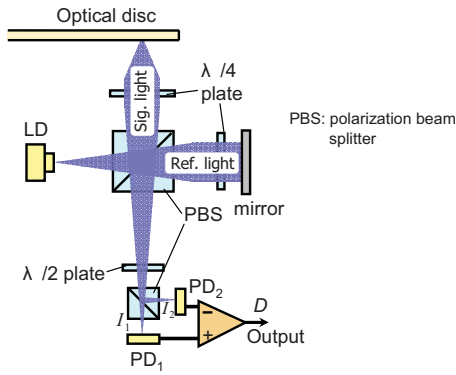


Fig. 1. Basic configuration of optical pickup using homodyne detection scheme.

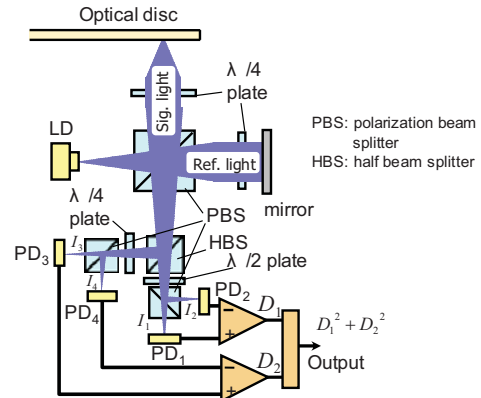


Fig. 2. Configuration of optical pickup using homodyne detection scheme with phase-diversity method applied.

3. DEVELOPMENT OF SIGNAL-READOUT SYSTEM

The developed signal-readout system for the homodyne detection scheme based on the phase-diversity method consists of two optical-signal detectors and a readout-signal generator. The optical-signal detector generates the differential-detection signal. Figure 3 shows a previous configuration of the detector. It had a problem of output-signal saturation of a current-to-voltage amplifier (I-V amplifier) due to input of large DC-current component arising from the reference light. The saturation had limited the signal amplification ratio. To solve this problem, the differential-current-detection method using a "balanced photodiode", shown in figure 4, was introduced. The balanced photodiode consists of two photodiodes connected in series. From the connecting point a differential current of two photodiodes can be extracted. Therefore, the DC-current components of two photodiodes are successfully canceled and the limitation of the signal amplification ratio is drastically relaxed. The readout-signal generator generates the readout signal from two differential-detection signals, D_1 and D_2 , based on the phase-diversity method. The configuration of the developed signal-readout system is shown in figure 5.

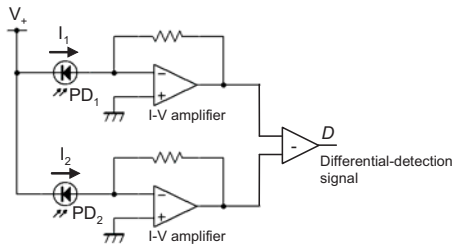


Fig. 3. Previous optical-signal detector.

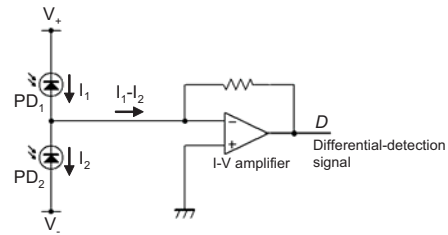


Fig. 4. Optical-signal detector with balanced photodiode.

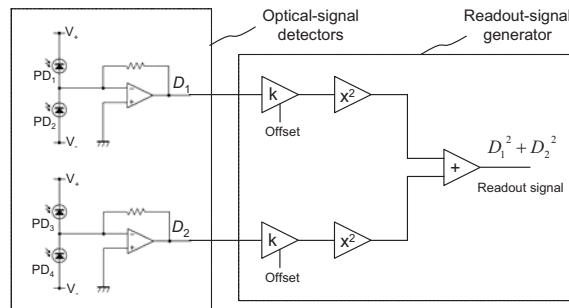


Fig. 5. Configuration of signal-readout system consisting of optical-signal detectors and readout-signal generator.

4. SIGNAL-READOUT EXPERIMENT

Readout-signal amplification was demonstrated using our developed signal-readout system. The upper waveform in figure 6 shows a single differential-detection signal D_1 observed on a single-layer BD-R disc. The amplitude of the signal was 3.6 times larger than that of a conventional detection signal shown as the lower waveform. Therefore, the signal amplification effect by homodyne detection scheme was verified on a commercially available disc.

At this time, however, stable readout signals based on the phase-diversity method have not been obtained. The cause of the instability is the imbalance of the amplitudes between two differential-detection signals. If there is an imbalance, the phase-difference-dependent terms in the operation formula based on the phase-diversity method cannot be canceled. Therefore, in order to suppress fluctuations of the readout signal within a required amount for reliable data readout, the amplitudes of two differential-detection signals should be precisely balanced.

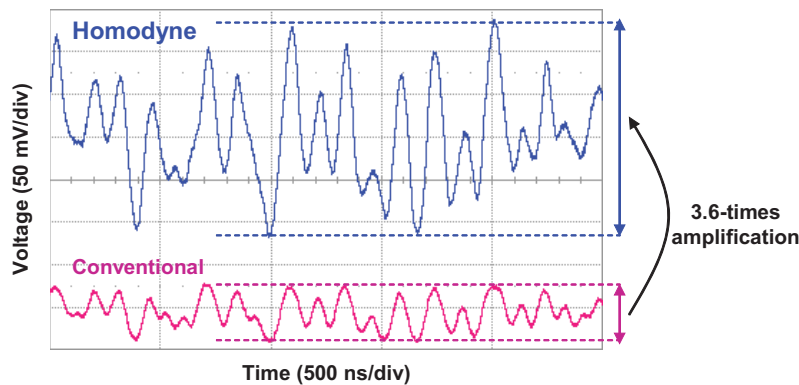


Fig. 6. Readout-signal waveforms of homodyne and conventional detection signals.

5. CONCLUSION

We developed a signal-readout system suitable for optical pickups using a homodyne detection scheme. The optical-signal detector with a balanced photodiode, which consists of two photodiodes connected in series, successfully cancels large DC-current components arising from a reference light and passing through two photodiodes. It is able to avoid output signal saturation of current-to-voltage conversion amplifier and to raise the upper limit of the signal amplification rate. By using the detector, a signal amplification rate of 3.6 was obtained on a single-layer BD-R disc. To stabilize the amplitude of readout signals based on the phase-diversity method, the amplitudes of two differential-detection signals should be precisely balanced.

REFERENCES

- [1] I. Ichimura *et al.*, "Proposal for Multi-Layer Blu-ray Disc Structure," ISOM 2004 (2004) We-E-02.
- [2] K. Mishima *et al.*, "150 GB, 6-Layer Write Once Disc for Blu-ray Disc System," ODS 2006 (2006) TuA3.
- [3] H. Habuta, *et al.*, "Century Stable Quadruple-Layer BD-R Using Te-O-Pd Based Films," ISOM 2006 (2006) Mo-B-05.
- [4] H. Mikami *et al.*, "Readout-Signal Amplification by Homodyne Detection Scheme," ODS 2007 (2007) MA4.

Turbo equalization with RLL (1,9) and LDPC code for SuperRENS ROM discs with 60 nm minimum mark length

Oliver Theis^{*a}, Xiao-Ming Chen^a, Dietmar Hepper^a, Gaël Pilard^b

^aDeutsche Thomson OHG, Karl-Wiechert-Allee 74, 30625 Hannover, Germany;

^bDeutsche Thomson OHG, Hermann-Schwer-Straße 3, 78048 Villingen, Germany

*Phone: +49 511 418-2338, Fax: +49 511 418-2483

1. INTRODUCTION

Following the demand of ever-increasing storage capacity of optical discs, the partners in the French-German project 4GOOD (4th-Generation, Omni-purpose Optical Disc-system) [1] are developing fundamental technologies for high-density optical data storage in order to achieve at least 200 GB on a dual-layer 12-cm disc. The 4GOOD project is funded by the German Ministry of Economy and Technology (BMWi) and the French Ministry of Economy, Finance and Industry (MINEFI).

The fundamental technology chosen for disc readout beyond the diffraction limit is super-resolution near-field structure (SuperRENS) [2], which adds a mask layer on top of the data layer with the advantage of keeping the traditional working distance between disc and pick-up. Both the linear density and the track pitch are being decreased in order to increase the storage density by a factor of 4 compared to Blu-ray Disc (BD).

First SuperRENS test discs with a minimum mark length of 60 nm and track pitch 320 nm have been manufactured, which means a gain factor of 2.5 in linear density compared to BD. As more severe ISI and lower SNR are observed, turbo equalization techniques are applied to lower the bit error rate (BER). This gives rise to the demand for runlength limited (RLL) modulation codes with low decoder complexity.

A new RLL (1,9) code is presented together with BER results of super-trellis detection incorporating turbo equalization in loop with low-density parity-check (LDPC) decoding for measured data from 60-nm SuperRENS discs.

2. TURBO EQUALIZATION USING RLL (1,9) CODE

A turbo equalization scheme iteratively exchanging extrinsic information between a joint partial response (PR) detector / RLL demodulator (super-trellis) and an outer soft-in soft-out error correction decoder with application to optical storage has been proposed in [4]. The complexity of the super-trellis, i.e. the number of states and branches, should be kept at a minimum. According to [5] there are 34 states and 130 branches for the super-trellis of the 17pp code with PR memory length $L=4$, i.e. five-tap targets. This is why another (1,7) code having only 20 states and 74 branches for $L=4$ is presented there as well.

A new RLL (1,9) code with rate 2/3 is developed having 18 states and 60 branches in the super-trellis for $L \leq 4$. The code is derived from a (1,7) code presented in [6] and modified to incorporate repeated minimum transition run (RMTR) $r=5$ limitation by relaxing the maximum runlength constraint to $k=9$. The code is therefore referred to as d1k9r5 in the following. Figure 1 depicts the signal processing chain for an optical storage channel employing a d1k9r5 encoder and a super-trellis detector. A message-passing LDPC decoder can for example be used for extrinsic information feedback as well as a turbo product code (TPC) decoder or any other soft-decision decoder.

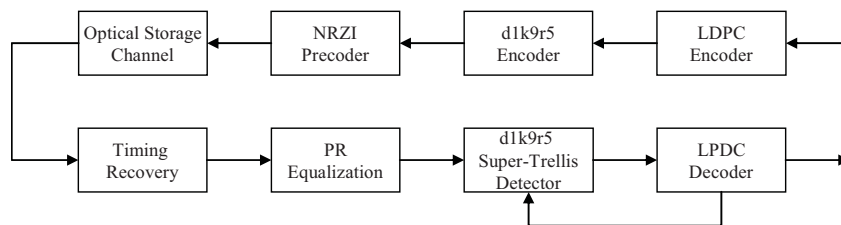


Figure 1. Optical storage channel signal processing chain incorporating the d1k9r5 modulation and turbo equalization

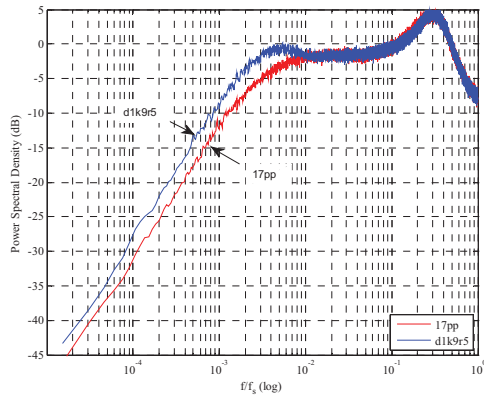


Figure 2. Normalized power spectral density comparison between d1k9r5 code and 17pp code

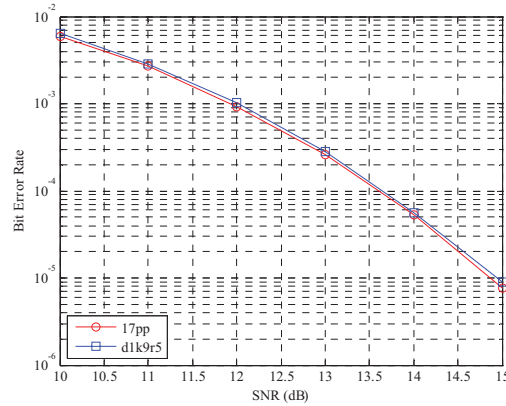


Figure 3. Super-trellis detector bit error rate of d1k9r5 vs. 17pp code for the 25 GB channel with Braat-Hopkins model equalized to PR target [0.17, 0.5, 0.67, 0.5, 0.17]

A DC-control method with 2 control bits preceding a block of channel data bits in such a way that the digital sum variation is minimized is added to the d1k9r5 encoder to decrease low-frequency content. As shown in Figure 2, the power spectral density for the d1k9r5 code is just about 2.5 dB higher than for the 17pp code in the low-frequency region for equal control bit redundancy, since d1k9r5 does not provide the parity preserving (pp) property.

Figure 3 reveals only minor differences in the BER performance between a d1k9r5 and a 17pp Max-Log-MAP super-trellis detector for the Braat-Hopkins channel model [8] with target [0.17, 0.5, 0.67, 0.5, 0.17] equalization [9]. Noise prediction techniques can be incorporated into the d1k9r5 super-trellis detector as well, without increasing the number of states and branches in order to combat colored noise after PR equalization especially for high-density channels [7].

3. MEASUREMENT RESULTS

The semiconductor material InSb for the mask layer so far shows the best performance with respect to aperture size, read-out bandwidth and speed of changing its physical properties for ROM discs [3]. The mask layer is stacked on top of a single data layer having 60 nm minimum mark length and a track pitch of 320 nm (Figure 4).

Turbo equalization BER results according to Figure 5 are obtained from asynchronously measured HF samples read at a laser power of 2.0 mW and a linear velocity of 4.92 m/s while timing recovery, PR equalization, d1k9r5 super-trellis detection and LDPC decoding are carried out through software in an offline mode.

The BER after super-trellis decoding without turbo equalization amounts to 10^{-2} and is used as a reference for a comparison to simulation results. Turbo iterations are performed in loop with a Sign-Min message-passing decoder carrying out 4 inner iterations on a rate 0.96 quasi-cyclic LDPC code with column weight 2.

BER after LDPC decoding is lowered from $7 \cdot 10^{-3}$ without turbo equalization down to $2 \cdot 10^{-5}$ after the 5th iteration. These results have been embedded in the plot of BER simulations given in Figure 5. Measured results correspond well with the simulation results although convergence is somewhat slower.

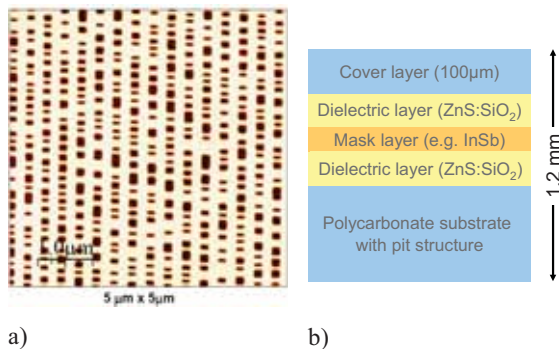


Figure 4. (a) AFM image of a substrate with 60 nm minimum mark length and 320 nm track pitch and (b) layer stack of SuperRENS discs

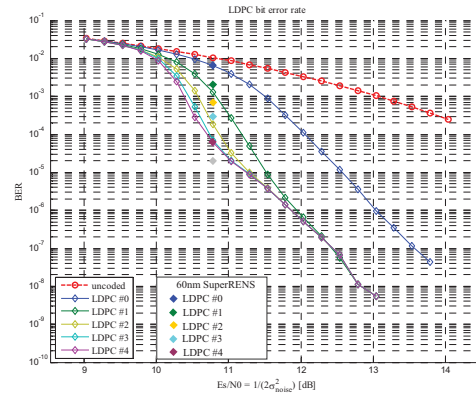


Figure 5. Results of simulated vs. measured BERs for turbo equalization with a d1k9r5 and a LDPC code

4. CONCLUSIONS AND OUTLOOK

The d1k9r5 RLL modulation code with minimum runlength $d=1$, maximum runlength $k=9$ and RMTR limitation of $r=5$ has been developed with emphasis on low decoder trellis complexity for use within turbo equalization schemes in a 4th generation optical disc system. Simulations show that BER performance over PR channels is similar to the 17pp code while the super-trellis detector complexity is reduced.

BER results for measured data obtained from a 60-nm SuperRENS disc, using turbo equalization and a high-rate quasi-cyclic LDPC code, correspond well to simulation results. Continuously decreasing BERs down to $2 \cdot 10^{-5}$ after 5 iterations show that a turbo equalization scheme incorporating d1k9r5 super-trellis detection can be successfully applied in SuperRENS storage systems together with an LDPC code.

Future publications will cover details about the LDPC code and alternatives like TPC more in-depth.

REFERENCES

- [1] D. Hepper, H. Richter, S. Knappmann, R. Eyberg, et al, "4GOOD – Technology and Prototype for a 4th-Generation Omni-Purpose Optical Disc System," Conf. Rec. ICCE 2008 (IEEE International Conference on Consumer Electronics), Session 2.3: Optical Storage: Present and Future, paper 2.3-4, pp. 57–58.
- [2] J. Tominaga, T. Nakano, N. Atoda, "An approach for recording and readout beyond the diffraction limit with an Sb thin film," Appl. Phys. Lett. 73, 2078 (1998).
- [3] B. Hyot, F. Laulagnet, O. Lemonnier, A. Fargeix, "Super-Resolution ROM Disc with a Semi-Conductive InSb Active Layer," Proc. of ISOM 2007, October 21–25, 2007.
- [4] E. Yamada, T. Iwaki, T. Yamaguchi, "Turbo Decoding with Run Length Limited Code for Optical Storage," Jap. J. Appl. Phys., Vol. 41, pp.1753–1756 (2002).
- [5] M. Noda, H. Yamagishi, "An 8-State DC-Controllable Run-Length-Limited Code for the Optical Storage Channel," Jap. J. Appl. Phys., Vol. 44, pp. 3462–3466 (2005).
- [6] G. V. Jacoby, R. Kost, "Binary Two-Thirds Rate Code with Full Word Look-Ahead," IEEE Trans. Mag., Vol. 20, No. 5, 1984.
- [7] X.-M. Chen, O. Theis, "Super-trellis based noise predictive detection for high-density optical storage," submitted to ISOM/ODS 2008.
- [8] K. Cai, G. Mathew, J. Bergmans and Z. Qin, "A generalized Braat-Hopkins model for optical recording channels," Proc. IEEE ICCE '03, pp. 324–325, 2003.
- [9] J. Bergmans, et al., "Asynchronous LMS adaptive equalizer," Signal Processing, Vol. 85 pp. 1301–1313 (2005).

Study of ITR-PLL with Linearly Constrained Adaptive Pre-Filter for High Density Optical Disc

Yoshiyuki Kajiwara, Junya Shiraishi, Shohei Kobayashi and Tamotsu Yamagami
AS Development Department, Recording System Development Division,
Video Business Group, Sony Corporation
5-1-12 Kitashinagawa Shinagawa-ku, Tokyo, 141-0001 Japan
Yoshiyuki.Kajiwara@jp.sony.com

ABSTRACT

Digital Phase Locked Loop with Linearly Constrained Adaptive Pre-Filter (LCAPF) has studied for high linear density optical discs. LCAPF has implemented before Interpolated Timing Recovery (ITR) unit in order to improve the quality of phase error calculation by using adaptive equalized Partial Response (PR) signal. Coefficients updates of asynchronous sampled adaptive FIR filter with Least-Mean-Square (LMS) algorithm are constrained by Projection Matrix in order to suppress phase drift of adaptive filter. We had developed Projection Matrices which are suit for Blu-ray disc (BD) and FPGA board for experiments. The results show that the LCAPF improve the tilt margins of 33GB BD ROM with enough stability.

Keywords: Blu-ray disc, interpolated timing recovery, PLL, Linearly Constrained, adaptive filter, LMS, Volterra

1. INTRODUCTION

Advanced systems of Blu-ray disc (BD), which have higher areal density and multilayer structures [1], are one of potential candidates of higher recording density optical storage in future. Those approaches should face some deterioration of the read back signal inevitably. Especially, higher linear density BDs cause lower signal level of the high frequency components by the restriction of the modulation transfer function (MTF), and multilayer structures cause noisy read back signal by inter layer interferences. In order to discuss the feasibilities of such higher recording density BD, stable and accurate Phase Locked Loop (PLL) system would be a vital for successive data reading. Interpolated Timing Recovery (ITR) algorithm [2, 3] has been investigated as effective Digital PLL systems because of its simple mathematical expression and accuracy. On the other hand, the one of key factor of improved PLL schemes are combination of adaptive equalization of the read back signal before calculation of the phase error [4, 5]. If calculations of phase error are done by well equalized signal, the precision of phase errors could improve. Although those structures [4, 5] exhibited good performances for higher linear density BD, there still have large loop delays for PLL which exaggerates their phase-lock performance. Because adaptive equalizers were placed between PLL unit and phase error calculator, there were some fixed loop delay within the feedback loop. In order to minimize those loop delays, Minimum Mean Square Error (MMSE) ITR scheme [6] was presented. The theory showed how channel-rate-asynchronous adaptive FIR filter place before ITR by computations of linear interpolation of the channel-rate-synchronous Least-Mean-Square (LMS) error using ITR numerical phase information. The MMSE ITR scheme, which has minimum loop delay and accurate direction of phase error calculated by adaptive equalized signal, has performed very well. From LMS adaptive equalizer theory perspective [7], while sign (direction) of LMS errors has enough credibility, LMS algorithm works well with adequate step-gain parameter. But MMSE ITR scheme had some problems, which were called phase drift and related instability of adaptive filter, while implementing in practice. There were two feedback loops, PLL and LMS, which were interfering both on phase control of read back signal. As a result, values of adaptive FIR tap coefficients would corrupt and read channel system would be instable.

In this paper, we proposed MMSE ITR scheme with Linearly Constrained Adaptive Pre-Filter (LCAPF) for higher density BDs. Linearly Constrained Adaptive Filter (LCAF) algorithm [8, 9] provides the limitation of the updates of the adaptive filter's components within the frequency domain. We utilize this LCAF algorithm in order to improve stabilities

of the MMSE ITR scheme by fixing 8T component's update of adaptive filter within frequency domain. We also implemented channel-rate-asynchronous adaptive Volterra filter (AVF) [10] for asymmetry compensation before ITR-PLL.

2. THEORY OF MMSE ITR SCHEME WITH LCAPF

Fig. 1 exhibits a block diagram of the MMSE ITR with LCAPF components of this report. Sampled reproduced signal $r(k)$ is sampled by ITR frequency f_s which is higher than data rate frequency f_d . Sampled signal's envelope is adjusted by Auto Gain Control (AGC), and signal is adaptive equalized by asynchronous sampled LCAPF and 2nd order AVF [10]. Both LCAPF and AVF are asynchronous sampled adaptive equalizers, asynchronous LMS errors are calculated by ITR⁽⁻¹⁾ Error generator [6]. And LMS modules are implemented by Error-Signed-LMS algorithm. In the study, reference signal for LMS is generated by Viterbi Detector (VD). Then, Adaptive equalized signal is inputted to ITR block. In order to improve the qualities of the Phase error, FDTS (Fixed Delay Tree Search) detector [4, 10] has adopted for assumed PR Class of adaptive equalized signal. FDTS is a detector which has better bER performance for PR equalized signal than threshold level detector and it has shorter decision delay than VD. Phase error is calculated by the method of decision directed timing detection method [4, 11] for PR equalized signal. LCAF LMS algorithm (Gradient Projection algorithm) is expressed as below [8, 9],

$$\vec{h}(k+1) = \vec{h}(k) + \mu \cdot V [e_{async}(k) \cdot \vec{x}(k)], \quad (1)$$

where $\vec{h}(k)$ is FIR filter tap coefficients vector of LCAPF, μ is step-gain-parameter of LMS algorithm, $e_{async}(k)$ is asynchronous LMS error generated by ITR⁽⁻¹⁾ Error generator [6], $\vec{x}(k)$ is LMS signal vector. And V is a Projection Matrix of LCAF gradient projection algorithm which can constrain update of the LMS tap coefficients. We can determine V through setting parameters of steering-vector matrix S [8]:

$$V = I - S[S^T S]^{-1} S^T. \quad (2)$$

We chose parameters of S for fixing the update of 8T components of Pre-Filter in order to inhibit phase drift of 8T signal. The effect of fixing 8T signal component, the largest power component of the signal, depresses phase drift for all frequency components of signal. We examined MMSE ITR Scheme with LCAPF through computer simulations, LCAPF equalized well, and phase drift of the Pre-Filter had restricted. We had proved that steering vector matrix S can control some frequency components of the adaptive filtering adequately.

3. EXPERIMENTAL RESULTS OF FPGA EVALUATION BOARD

An FPGA board had developed for bER evaluation of the BD. Although block diagram of the read channel is as same as Fig. 1, we designed LCAPF and LMS module as 8 parallel architectures for reducing area of digital circuit. For comparison, we utilized two experimental setups shown on Fig. 2, LCAPF and Conventional ITR Read Channel Models. Figs. 3 and 4 are results of Tangential and Radial Tilt Skew of 33GB BD ROM which has 10% asymmetry. We employed Viterbi Detector (PR12221) for bER evaluations and reference signal of LMS algorithm. LCAPF performed very well because the results of both Tilt Skew tests showed improvement of effective adaptive equalizing and asymmetry compensation qualities of LCAPF and AVF. In addition, their tap coefficients of LCAPF are stable enough for product requirements and phase drifts had restricted effectively. As a result, Tangential skew margin has widen to $-0.8 \sim +0.8$ degrees and Radial skew margin has widen to $-0.8 \sim +0.8$ degrees below bER criteria ($3.1E-4$).

4. CONCLUSION

In conclusion, we investigated MMSE ITR Scheme with LCAPF for stable equalization before ITR (PLL) in order to utilize LCAPF read channel for advanced BD which has higher areal density and multilayer structure. We had examined the performances of the channel both equalization and stability through computer simulations. In addition, we developed the channel by FPGA board and experimented with BD-ROM 33GB. As a result, the bER performances of Tangential and Radial Tilt Skews were wide enough, and the stability of LCAPF was good enough to utilize commercial implementation.

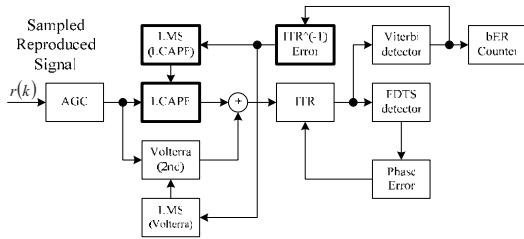


Fig. 1. Block Diagram of MMSE ITR Scheme with LCAPF

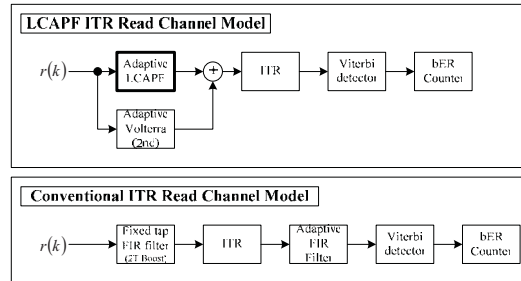


Fig. 2. ITR Read Channel models for experiments

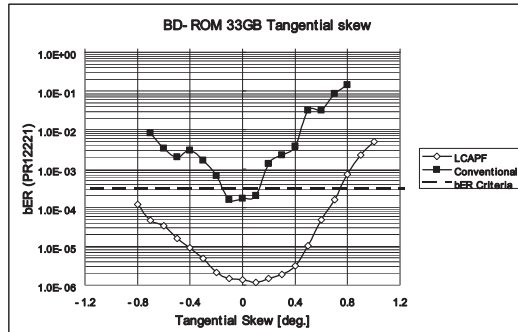


Fig. 3. Tangential Tilt Skew of BD-ROM 33GB

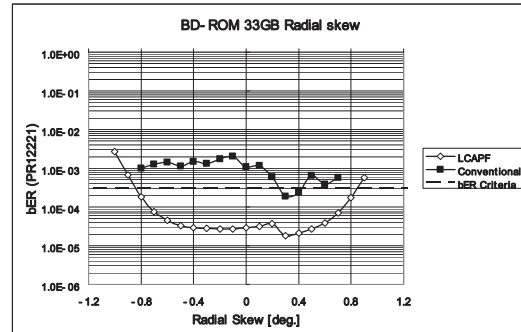


Fig. 4. Radial Tilt Skew of BD-ROM 33GB

REFERENCES

- [1] I. Ichimura, T. Maruyama, J. Shiraishi, and K. Osato, "High-density multilayer optical disc storage," *Proc. Of SPIE* Vol. 6282, 628212, (2006).
- [2] F. M. Gardner. "Interpolation in Digital Modems - Part I: Fundamentals," *IEEE Trans. on Communications*, VOL 41, NO.3, 501-507 (1993).
- [3] S. Higashino, S. Kobayashi, T. Yamagami, "A Parallel Architecture of Interpolated Timing Recovery for High-Speed Data Transfer Rate and Wide Capture-Range," *Tec. Dig. Of Optical Data Storage Topical Meeting, Portland, TuB5* (2007).
- [4] S. Higashino, Y. Kajiwara, S. Kobayashi, "Hybrid Equalized Partial Response Path-Feedback Maximum Likelihood for 35.4GB Blu-ray Disc ROM," *Jpn. J. Appl. Phys.* **44**, 3474-3476 (2005).
- [5] K. Lee, H. Zhao, I. Hwang, W. Park, C. Chung and I. Park, "Approach to high density more than 40GB per layer with Blu-ray disc format," *Tec. Dig. Of Optical Data Storage Topical Meeting, Portland, TuB2* (2007).
- [6] Z. Wu, J. M. Cioffi, K. D. Fisher, "A MMSE Interpolated Timing Recovery Scheme for The Magnetic Recording Channel," *Communications, 1997. ICC '97 Montreal, Towards the Knowledge Millennium. 1997 IEEE International Conference on*, VOL 3, 1625 -1629 (1997).
- [7] S. Haykin, "ADAPTIVE FILTER THEORY", 4th edition, Prentice Hall (2002).
- [8] L. Du, M. Spurbeck, R. T. Behrens, "A linearly constrained adaptive FIR filter for hard disk drive read channels," *Communications, 1997. ICC '97 Montreal, Towards the Knowledge Millennium. 1997 IEEE International Conference on*, VOL 3, 1613 - 1617 (1997).
- [9] O. L. Frost III, "An Algorithm for Linearly Constrained Adaptive Array Processing," *Proc. Of the IEEE*, VOL 60, NO 8, 926-935 August (1972).
- [10] Y. Kajiwara, S. Higashino, T. Yamagami, "Asymmetry Compensation by Nonlinear Adaptive Partial Response Equalizer for 31.3 GB Blu-ray Disk ROM," *Jpn. J. Appl. Phys.* **44**, 3482-3486 (2005).
- [11] K. H. Mueller, M. Müller, "Timing Recovery in Digital Synchronous Data Receivers," *IEEE Trans. on Communications*, VOL.COM24, NO.5, 516-531 (1976).

Adaptive Writing Strategy Based on Bits-Indexed Writing Parameters

Hui Zhao, Hyunsoo Park, Inoh Hwang, Kyunggeun Lee, and Insik Park

Digital Media R&D Center

SAMSUNG ELECTRONICS CO., LTD, Yeongtong-Gu, Suwon, 442-742, Korea

Tel: 82-31-200-6611, Fax: 81-31-200-3160, E-mail: hui.zhao@samsung.com

Abstract: A new writing parameters' organization method is proposed, in which the writing parameters are indexed by bits patterns being recorded. An adaptive writing strategy based on these bits-indexed writing parameters is also proposed to automatically optimize recoding for high-density Blu-ray Disc. Experiment's results on a commercial Blu-ray Disc with 40GB capacity prove the performance of this method.

1. Introduction

As optical data recording density increases, writing strategy performance is more correlated to bit error rate (bER). Several attentions were paid to adaptive writing strategy technology in order to optimize writing pulses' parameters according to various medium. Although some adaptive methods were proposed for PRML detection to reduce errors caused by edge-shift [1], no method can reduce errors caused by high frequency signals such as 2T-signal-shift errors yet, which are dominant in high density optical disc signal detection errors. To solve the problem, we propose an adaptive writing strategy for high density recording, which comes with a new writing parameters' organization method. Current widely used writing parameters' organization method indexes writing parameters by lengths of two continuous symbols (mark and space) being recorded. Different from that, the method proposed in this paper indexes writing parameters with a fixed length bits-pattern being recorded.

2. Principle of proposed writing parameters' organization method

During recording, to control the position of recorded marks' edges, two parameters shall be adjusted: first writing pulse's start time (TSFP) and last pulse's end time (TELP). Each parameter, TSFP or TELP, influences the position of a mark edge. During recording process, a NRZI sequence is being recorded in a medium. Each bit inverting ("01" or "10") in the NRZI sequence represents a mark edge (front or tail). In other words, each bit inverting corresponds to a writing parameter (TSFP or TELP). Based on above knowledge, a bits pattern of a fixed width can be used to index that writing parameter. The bits pattern includes the two inverting bits and several adjacent bits before and after the two inverting bits, as shown in Fig.1. Therefore, all the TSFP and TELP parameters can be organized in a look up table: the index for each parameter is a bits pattern with a fixed width. Fig.2 shows an example writing parameters' look up table based on this idea. All the indexing bits patterns in Fig.2 share the same characters: fixed width and two inverting bits in center. There are two advantages in this writing parameters' organization method. It offers a writing strategy decision window with a selectable width. Wider decision window means more controllable of writing strategy and more complex circuit. It is easier to select window width for balance with this method than currently used method. Moreover, it establishes relation between writing parameter and a section of RF waveform, instead of a mark edge.

3. Principle of adaptive writing strategy based on bits-indexed writing parameters

The function of adaptive writing strategy is to update a writing parameters' look up table like Fig.2. For PRML detection, to minimize the RF signals' deviations from their corresponding reference levels can be effective to reduce bER. The RF signals' deviations are caused by noises and residual inter-symbol interference (ISI). The residual ISI is caused by symbol interference out of the PRML detection window. If the writing strategy decision window is wider than PRML detection window, it offers a possibility to compensate the residual ISI by adjusting writing pulses' parameters. The presented adaptive writing strategy is achieved by a series repeating circles of recording and reproducing. If $W_n(k)$ represents a writing parameters at position k ($k = 0, 1, \dots$) for recording a sequence of bits at n th recording. $E_n(k)$ represents a sequence of RF signals' errors from their reference levels when the n th recorded signal is reproduced. Then, to minimize the RF signals' deviations, $W_n(k)$ should be changed in the inverse direction of gradient:

$$\frac{\partial \left(\sum_k \text{mean}(E_n(k))^2 \right)}{\partial W_n(j)} = 2 \cdot \sum_k \left(\left[\text{mean}(E_n(k)) \right] \cdot \frac{\partial (\text{mean}(E_n(k)))}{\partial W_n(j)} \right) < 0 \quad (j = 0, 1, 2, \dots) \quad (1)$$

$$\frac{\partial (\text{mean}(E_n(k)))}{\partial W_n(j)} = \frac{\partial (\text{mean}(RF(k)) - \text{ref_level}(k))}{\partial W_n(j)} \quad (2)$$

The $ref_level(k)$ represents the reference level for PRML detection. To presume that the reference level is constant against writing parameters adaptation, an iterative form of $W_{n+1}(k)$ can be deduced from (1) and (2) in a least mean squares (LMS) form:

$$W_{n+1}(j) = W_n(j) - 2 \cdot \mu \cdot \sum_k [E_n(k) \cdot h(k-j)] \quad (3)$$

The μ is an updating ratio with small value to guarantee the convergence of writing strategy adaptation process. $h(\cdot)$ is the impulse response of channel before Viterbi detector. The good point in equator (3) is that no detailed knowledge of storage medium is necessary. The presumption of constant reference level is only exactly true for fixed reference levels. For adaptive reference levels, the presumption will not cause problems because the reference levels are always adapted in the direction to minimize RF deviations from reference level. In practice, some $W_n(k)$ s are not available because there may not be a writing parameter (TSFP or TELP) at each position k . And because different recording positions may correspond to the same writing parameter, an available $W_n(k)$ shall be updated by the summation of the feedback errors all related to it.

Fig.3 shows the system structure for adaptive writing strategy. Several recording and reproducing circles are necessary to writing strategy adaptation. Firstly a sequence of bits is recorded in an area of the optical disc with current writing parameters. The RF signal is reproduced and processed by pre-equalizer [2] and an adaptive equalizer. After that, the RF signal is detected to a bits sequence by a Viterbi detector. With detected bits sequence and reference levels, ideal RF signal sequence can be generated. By subtracting ideal RF signal from delayed real RF signal, RF erroneous signal can be calculated. Then, the RF erroneous signal is processed by a finite impulse response (FIR) filter, coefficients of which are impulse response coefficients of the channel before Viterbi detector. The writing strategy feedback errors memory accumulates errors outputted from FIR filter for each writing parameter. The memory cells for accumulation are addressed by bits pattern from the detected bits sequence. A delay line keeps the writing parameter in being addressed memory cell corresponding to the processed error signal outputted from FIR filter. The corresponding relation is expressed in equator (3). After the feedback errors are accumulated enough, the writing parameter feedback error in each memory cell is used to update the writing parameter memory (that is writing parameter look up table) with the same indexing bits patterns. Equator (3) explains the updating rule. After that, the updated writing parameters will be used for the next recording. After several circles recording and reproducing, optimized writing parameters can be obtained.

4. Experiment results and analysis

The presented adaptive writing strategy is verified by an experiment on Blu-ray Disc. A commercial recordable disc is recorded with channel bit length of 46nm, corresponding to 40GB capacity per layer. A Viterbi detector with detection window width of 8 and an LMS adaptive equalizer with 21 taps are adopted to detect signal. The writing parameters are indexed by bits pattern with 16 in length. The initial writing strategy parameters are set to the values same to a conventional writing strategy. The high frequency band gain of the pre-equalizer is 6dB, as shown in Fig.7. After writing strategy is adapted with 10 recording and reproducing circles, bER (average value of 5 different tracks) is improved from 1.5×10^{-4} to 2×10^{-5} , as shown in Fig.4. The decreasing of normalized mean squared value of RF errors is shown in Fig.5. RF waveform is reformed less fluctuant after 10 circles' writing strategy adaptation, as shown in Fig.6. Power spectrum density (PSD) of the RF signal before and after writing strategy adaptation is shown in Fig.7. There is a small difference between the two PSD: After 10 circles' writing strategy adaptation, RF signal power under 4MHz are boosted and RF signal power between 4MHz and 8MHz are suppressed. One possible explanation for the bER improvement is given by considering frequency domain. Because of the low SNR in high frequency band of optical disc channel, the pre-equalizer's high frequency gain amplifies noisy signal. That introduces RF deviations. After 10 circles' writing strategy adaptation, in time domain, RF deviation is minimized by adapted writing strategy. The equivalent change in frequency domain is that the high frequency gain is suppressed by adapted writing strategy. It proves that adaptive writing strategy can adapt writing parameters according to channel character. Due to the low pass character of optical storage channel, additional benefit can be obtained by suppressing RF signal high frequency band in recording stage and boosting high frequency band in reproducing stage.

5. Conclusion

A new adaptive writing strategy based on a new writing parameters' organization method is proposed. An experiment on a commercial Blu-ray Disc of 40GB capacity proves that the proposed adaptive writing strategy can adapt writing parameters according to channel character and improve bER about 10 times.

References

1. Akihito Ogawa, et al, "New Write Shift Compensation Method Modified for Optical Disk Systems to Which Partial Response Maximum Likelihood (PRML) Detection Is Applied" ,J.J.A.P., Part1 42, (2003) 919
2. Kyunggeun Lee et al, "Approach to high density more than 40GB per layer with Blu-ray disc format", ODS, TuB2(2007)

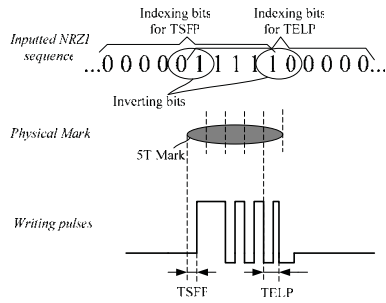


Fig.1 Relation between recorded bits and writing parameters

Indexing bits pattern	TSFF
0000 000C	0.50
0000 001	0.51
0000 100C	0.49
0000 111C	0.52
...	...
Indexing bits pattern	TELP
0001 0001	1.00
0001 0011	0.98
0011 0000C	0.98
0011 0001	0.97
...	...

Bits inverting

Fig.2 Writing parameters' look-up table

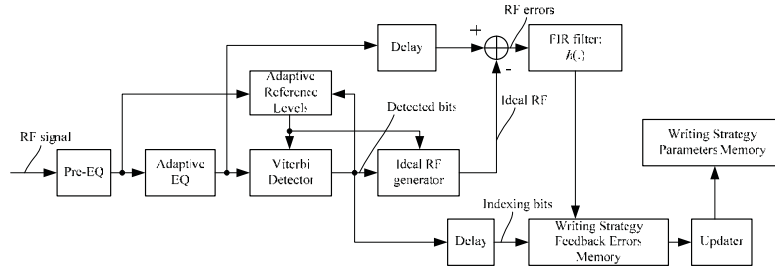


Fig.3 Writing strategy updating circuit structure

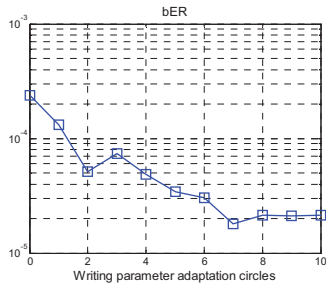


Fig.4 Experiment results: bER improvement

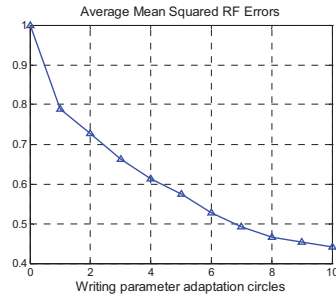


Fig.5 Experiment results: decreasing of average mean squared RF errors (normalized value)

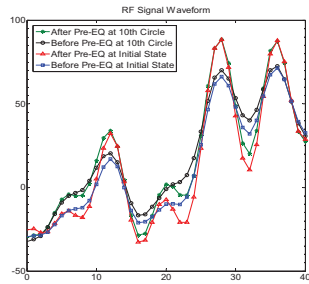


Fig.6 RF waveform before and after 10 circles' writing strategy adaptation

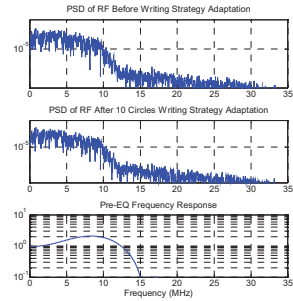


Fig.7 PSD of RF signal and frequency response of Pre-EQ

Reduced state sequence estimation with level adaptation (RESSELA) for high density disc

Hyunsoo Park, Hui Zhao, Inoh Hwang, Kyunggeun Lee, and Insik Park

Digital Media R&D Center

SAMSUNG ELECTRONICS CO., LTD, Yeongtong-Gu, Suwon, 442-742, Korea

Tel: 82-31-200-3134, Fax: 81-31-200-3160, E-mail: greenbee@samsung.com

Abstract: We report the new data reproducing scheme for high density over 40GB with a commercial Blu-ray recordable disc. bER of 1×10^{-6} and 1.3×10^{-4} and 2.6×10^{-3} and 9×10^{-3} with 40GB, 45GB, 47.5GB and 50GB were experimentally obtained respectively using this new data reproducing scheme which shows the possibility of achieving 50GB with a commercial single-layer Blu-ray disc.

1. Introduction

During last few years, we reported a novel data reproducing scheme by introducing a signal waveform phase detector. [1] As a result, the phase locked loop (PLL) circuit showed a good working even at 50GB capacity and bER of 5×10^{-5} has been achieved at 40GB capacity using a commercial single-layer Blu-ray disc.

In this paper we will describe our new data reproducing algorithm for capacity over 40GB. With our new algorithm, great bER improvement can be achieved without increasing hardware size too much.

2. Experimental Procedure

A commercial single-layer BD-R disc of which capacity is 25GB and an ODU-1000 dynamic tester made by Pulstec Industrial were used for the experiment. The linear velocity was adjusted to increase the density and RLL (1,7) random pattern was used for evaluation of bER. Viterbi decoder which has the algorithm of reduced state sequence estimation with level adaptation and two-stage equalizer were used in order to increase bER performance. Fig.1 shows the block diagram for the data reproducing.

3. Two-stage equalizer

Two strong candidate structures for data reproducing of high density optical disc are adaptive equalizer and Viterbi decoder. Adaptive equalizer makes input waveform as proper one that is suitable for Viterbi decoder. Viterbi decoder can get optimal binary sequence in the presence of inter-symbol interference. In this paper basic structure of equalizer is the same as previous one. [2] But in order to increase bER performance, we used two-stage equalizer.

Two-stage equalizer has two kinds of equalizer. One is adaptive equalizer for gain boosting (First equalizer). The other is adaptive equalizer for noise reduction (Second equalizer). Both equalizers have same structure except for adapting filter coefficient. First equalizer updates filter coefficients by the difference between equalizer output and target level supplier. Target level supplier includes desirable frequency characteristics. So, first equalizer has the function of optimal gain boosting. On the other side, second equalizer updates filter coefficients by the difference between equalizer output and level value that comes from input of second equalizer. Level adaptation block makes proper level value from the input signal of second equalizer. If there's

no noise, error signal between equalizer output and level value is zero. And filter coefficients keep unit impulse response. Noisy case, filter coefficients of second equalizer can be changed in order to reduce noise component.

If this type of equalizer is used, bER improvement can be achieved in case of tilt presence. From our experiment, bER performance of two times can be achieved by the use of two-stage equalizer.

4. Reduced state sequence estimation with level adaptation(RESSELA)

Reduced state sequence estimation is the detection algorithm that provides a direct tradeoff between complexity and performance in the presence of inter-symbol interference channels [3]. In optical disc, channel characteristics is determined by the relation of channel bit length, laser wavelength, and numerical aperture. Unfortunately, good bER result of high density mainly depends on the structure of Viterbi algorithm. Most case, complex structure makes good bER result. But complex structure gives rise to various kinds of problems. For example, hardware size increases significantly by the factor of the length of inter-symbol interference. Hardware size between PR(a,b,c) type and PR(a,b,c,d,e) is 4 times difference in worst case.

In order to overcome these problems, reduced state sequence estimation can be one of the solutions. This algorithm uses determined data again in order to reduce hardware size. Of course, more feedback degrades system performance. In 50GB capacity, from our experience, Viterbi decoder with window size 13 is suitable to eliminate the severe inter-symbol interference. But it needs too much hardware area. So we used Viterbi decoder with window size 9 and 4 bits feedback structure. With this structure, performance is almost same as that of window size 13, but hardware size is almost same as that of window size 9.

In addition, optical channel has its own characteristics. For example, asymmetry signal can be observed from most common Blu-ray discs. Those kinds of nonlinear component drop system performance. We solve those problems by the use of level adaptation. [2] Level adaptation block gets the signal in front of second equalizer, and calculates average level value from the relation between the binary signal and the signal in front of second equalizer. Average levels are used for calculation of branch metric and error signal generation for second equalizer. Multiplexer which is connected to feedback signal selects proper levels in order to calculate branch metric. Detailed structure of level adaptation block is Fig.2.

5. Test result

Combination of two-stage equalizer, feedback algorithm and level adaptation block makes the performance of detector as best one. Fig.3 shows the experimental results of the bER according to the capacity using this reproducing scheme. bER of 1×10^{-6} and 1.3×10^{-4} and 2.6×10^{-3} and 9×10^{-3} with 40GB, 45GB, 47.5GB and 50GB were experimentally obtained respectively.

Fig.4 shows the bER difference between previous structure and current structure. Previous structure has only one kind of adaptive equalizer and window size of Viterbi decoder is 9. [1] With radial tilt, bER performance between previous one and current one is 7 times in average. Especially, with high tilt case the difference is big. That may come from the adaptation of each equalizer.

6. Conclusion

bER of 10^{-6} and 10^{-3} for 40GB and 50GB were obtained using a commercial BD-R disc with the new reproducing scheme including two-stage equalizer and reduced state sequence estimation with level adaptation. These results can give a hint to achieve 50GB per single layer with just tuning composition or layer structure of current available commercial discs.

References

1. Hui Zhao et al, "A new data reproducing scheme for higher density Blu-ray disc" ISOM, Th-PO-04, 286 (2006)
2. Junghyun Lee et al, "Advanced PRML data detector for high density recording" ODS, TuC2, 234 (2004)
3. Alexandra duet-hallen, "Delayed decision-feedback sequence estimation" IEEE transactions on communications, Vol. 37, No. 5, May 1989

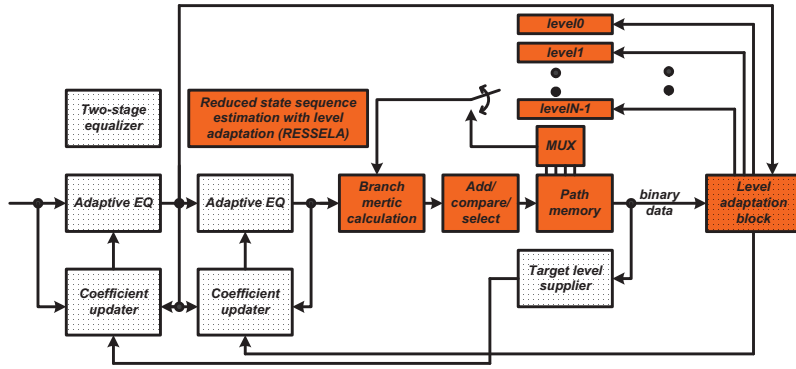


Fig.1 Structure of data reproducing scheme

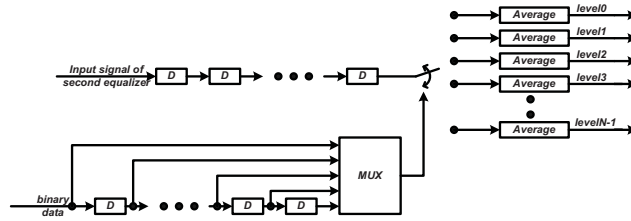


Fig.2 Structure of level adaptation block

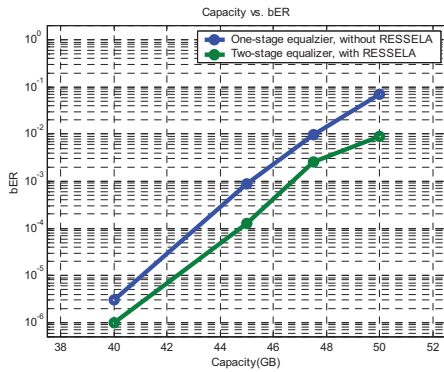


Fig.3 BER vs. capacity

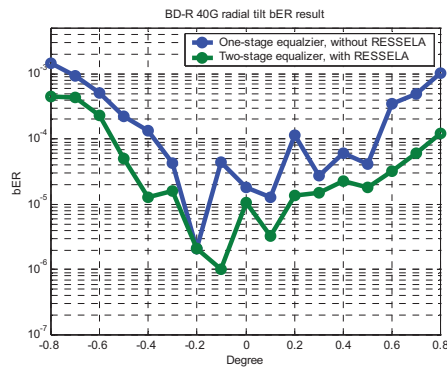


Fig.4 BER vs. tilt variation

Analysis on SNR improvement by multi-tone demodulation

Atsushi Kikukawa*, Hiroyuki Minemura

Central Research Laboratory, Hitachi Ltd., 1-280 Higashi-koigakubo, Kokubunji, Tokyo Japan, 185

ABSTRACT

The use of multi-tone demodulation (MTD) to improve read signal SNR was theoretically investigated. It was discovered that as the SNR improvement is balanced between the read signal amplitude gain and the noise converted from the harmonic bands, extending the input bandwidth to an extreme value was not necessary. We also found that the clock jitter in the analog to digital converter is a major factor that limits the efficiency of MTD and that the clock jitter should be taken into account when deciding on properties of a system, such as its input bandwidth and its pulse duty.

Keywords: drive technologies, multi-tone demodulation, under-sampling

1. INTRODUCTION

A promising way to expand the data storage capacity of an optical disc system beyond that provided by the Blu-ray Disc (BD) is increasing the number of the recording layers beyond two. However, the reflected light intensity from multi-layered discs is only a fraction of that of single layered ones because it is absorbed or reflected by other layers on the return path. Therefore, it is very likely that optical disc systems that use multi-layered discs will suffer from an insufficient signal to noise ratio (SNR). The linear recording density might also be simultaneously increased in order to lessen the number of the recording layers; however, this will also lead to a shortage in the SNR because margins, such as the tilt margins, will be more critical.

We have proposed the multi-tone demodulation (MTD) as a way of increasing the SNR, and have experimentally demonstrated on a spin-stand that it may improve the bit error rate by over two magnitudes [1]. In conventional read systems, the incident laser beam is pulse modulated at several hundred megahertz to suppress laser noise, and only the baseband component is extracted using the bandwidth limitations of the photo-detector and current amplifier. Thus, the signal energy included in the higher-order harmonics is lost and the amplitude of the signal is considerably decreased. However, as the MTD also uses the signal energy included in the harmonic components of the modulated read signal, it means that we can increase the signal amplitude, and consequently the SNR. However, any overall theoretical discussions useful for estimating the system performance have not been given. We consider the basic operation of the MTD and effects on the SNR improvement of the some parameters are numerically calculated basing on it.

2. THEORY OF MTD OPERATION

The MTD operation in the time domain picture is illustrated in Fig. 1(a). That is, a peak in the pulsed read signal is captured and held until the next peak appears. Thus, a step-like continuous signal is obtained when this process is repeated. The step-like distortion can be removed using an appropriate low-pass filter. Such operation can be done using a pair of an analog to digital converter (ADC) and a digital to analog converter (DAC) [1].

When we look at this process in the frequency domain, it may be referred to as “multi-tone demodulation”. For simplicity, we assume the original read signal is a sinusoidal one with a sufficiently low frequency. When this signal is pulse modulated, its spectrum will look like as shown in Fig. 1(b). It consists of the baseband read signal and its harmonics. When the pulsed read signal is sampled at the modulation frequency f_{HF} , all the harmonic components are under-sampled because their frequencies are above the Nyquist frequency. Under-sampling by the modulation frequency is equivalent to demodulation. In this case, all the harmonic components within the input bandwidth are demodulated into the baseband at once, so we call this conversion the MTD. The demodulated signals are equivalent to the baseband read signal except for the amplitude, thus they are added coherently. Then, the amplitude of the MTD converter output can be expressed as the sum of the harmonic signal amplitude as expressed in Equation (1).

*atsushi.kikukawa.vk@hitachi.com; phone +81-42-323-1111

$$A = a_0^+ + \sum_{i=1}^M (a_i^+ + a_i^-) \quad (1)$$

Here, M is the number of the harmonics within the input bandwidth, and $a_i^{+(-)}$ is the amplitude of the positive (negative) harmonic component around the i th harmonic (a_0^+ represents baseband amplitude). We call the signal amplitude gain by the MTD (A/a_0^+) as “pulsed gain”.

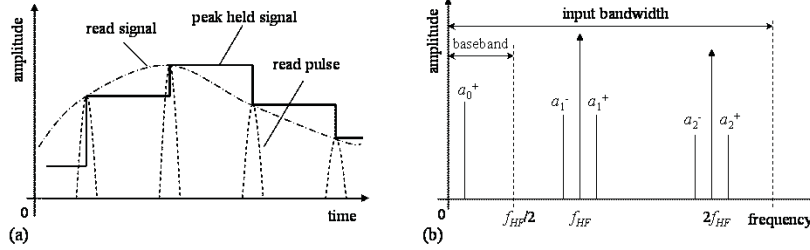


Fig. 1. MTD operation and pulsed read signal spectra. (a) MTD operation in the time domain picture. Peaks of pulses in pulsed read signal are held until next peak. (b) Pulsed signal spectrum. Read signal is assumed to be sinusoidal, thus its spectrum and harmonics are line-like. Segments with arrow represents the modulation carrier and its harmonics.

In the MTD, the noise components in each harmonic band are also converted onto the baseband. If we consider the noise included in an infinitesimal bandwidth, its frequency is converted to the corresponding frequency in the baseband and super imposed on the noise of that frequency. However, as the phases of the each noise component in the individual harmonic bands are incoherent, thus the composed noise amplitude at the baseband will be the root of squared sum of their amplitude. If we assume that the average noise amplitude is uniform throughout the input bandwidth, the average output noise amplitude can be expressed as Equation (2).

$$N = \sqrt{2M}n \quad (2)$$

Here, n is the average input noise amplitude. It is possible to gain the SNR if the signal amplitude increases more rapidly than the noise stated by Equation (2) does.

The above description explains how the SNR of the MTD is fundamentally determined if an ideal ADC is used under perfect conditions. However, actual ADCs have an internal noise source as a result of the clock jitter, which may limit the performance of the MTD. That is, the sampled value will be different from the true value if the clock jitter causes the sampling timing of the ADC to fluctuate. The amplitude of the noise (error) at the i th order harmonic can be described by Equation (3), where a_i is the signal harmonic amplitude, f_{HF} is the modulation frequency, and δt is the instantaneous jitter.

$$\delta v_i = 2\pi a_i i f_{HF} \cos(2\pi i f_{HF} t) \delta t \quad (3)$$

Note that the total noise will be the root of the squared sum of all the noise from every harmonic and the total uniform noise given by Equation (2). It should also be noted that the noise amplitude caused by the clock jitter is proportional to the amplitude and the order of the harmonic.

3. RESULTS OF NUMERICAL ANALYSIS

On the basis of the above considerations, we numerically analyzed the effects of the input bandwidth and the ADC clock jitter. For simplicity, the read signal was regarded as a sinusoidal signal and its carrier to noise ratio (CNR) at the converter output was evaluated. We shall refer the change in the CNR between the input and the output as “CNR gain”. The CNR gain is equal to the improvement in the SNR.

We first investigated the effect of the input bandwidth. The pulsed gain (signal amplitude gain), the average output noise amplitude, and the CNR gain relative to the input bandwidth are shown in Fig. 2(a). The input bandwidth B_w is normalized with the modulation frequency f_{HF} . The output average noise amplitude is normalized with the input average

noise amplitude. The pulse duty and the ADC jitter were set to 4/32 and 0, respectively. A 12th order Butterworth low-pass filter was used to limit the bandwidth.

The pulsed gain increases rapidly where bandwidth is below 4 (B_w/f_{HF}) because the major harmonics are included in the lower bands. As the bandwidth is increased further, the pulse gain increments become smaller while the average noise amplitude continuously increases in accordance with Equation (3). Therefore, the CNR gain grows rapidly at the low frequency region, then saturates at the region over 4 (B_w/f_{HF}). This means that there is no need to increase the bandwidth of the PD and amplifier to an extreme value. Thus, assuming the modulation frequency as 400 MHz, an input bandwidth around 1 GHz is reasonable for the purposes of making a practical design.

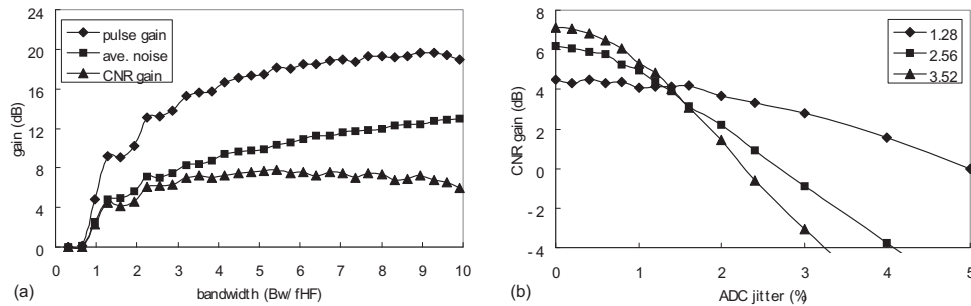


Fig. 2 (a) Pulsed gain, noise, CNR gain relative to the input bandwidth (b) CNR gains with various input bandwidth relative to ADC jitter.

Next, we investigated the effect of the ADC clock jitter. Shown in Fig. 2(b) are the CNR gains relative to the ADC jitter with input bandwidth of 1.28, 2.56, and 3.52 (B_w/f_{HF}). The pulse duty was 8/32. As shown above, the CNR gain is larger for the wider input bandwidth when the jitter is around 0, however, as the jitter increases, the CNR gains decrease more rapidly. This is because, as indicated by Equation (4), the higher harmonics are more strongly affected by the ADC clock jitter. Therefore, the input bandwidth should be determined by also considering the ADC clock jitter. Further, the clock jitter should be considered when deciding the pulse duty because the energy distribution ratio to the harmonics depends on it.

4. CONCLUSION

We clarified that the SNR improvement in the MTD is obtained by the amplitude gain difference between the signal and the noise. That is, the signal amplitude is gained by coherent addition of the demodulated signal harmonics while noise amplitude is gained by incoherent addition. The effects of the input bandwidth and the ADC drive clock jitter was examined by the numerical analysis. It was found that the input bandwidth need not be of an extreme value, but should be able to pass through the major harmonics in the pulsed read signal. Thus, making an effective MTD system with a reasonable input bandwidth of around 1 GHz is possible. We also found out that the jitter of the ADC drive clock significantly limits the MTD, and it should be taken into account when designing system properties such as input bandwidth and pulse duty.

REFERENCES

- [1] Kikukawa, A. and Minemura, H., "Novel HF-pulse read signal converter for increasing read signal SNR" Tech. Digest ISOM'07, Th-PP-04, 302-303 (2007).
- [2] Eynde, F. O. and Sansen, W., [Analog Interfaces for Digital Signal Processing Systems], Kluwer Academic Publishers, Boston, Dordrecht & London, 91-92 (1993).

SESSION ThB: Holographic I

Monarchy Ballroom
10:30 am to 12:30 pm

Lambertus Hesselink, Stanford Univ.
Tsutomu Shimura, The Univ. of Tokyo (Japan)

Linear Signal Processing for a Holographic Data Storage Channel using Coherent Addition

Masaaki Hara*, Kazutatsu Tokuyama, Kenji Tanaka, Kazuyuki Hirooka, and Atsushi Fukumoto
Tera Bytes Memory Development Department, Core Technology Development Group,
Sony Corporation, 5-1-12 Kitashinagawa, Shinagawa-ku, Tokyo 141-0001, Japan

ABSTRACT

A linear channel model and linear signal processing are available for a holographic data storage channel when coherent addition is applied in a reproduction process.

Key words: Linearity, Interpixel Interference, SNR, Equalization, HDS channel, Channel Model

1. INTRODUCTION

A holographic data storage (HDS) channel is generally a nonlinear channel. However, coherent addition of DC components in a reproduction process avoids the loss of phase information by an intensity sensor. A linearly reproduced signal is retrieved by calculating the square root of the intensity and subtracting the added DC components, as suggested in ISOM2007[1].

In this report, we propose a simple channel model realized by coherent addition, and theoretically demonstrate that linear equalization is effective in the HDS channel.

2. LINEAR CHANNEL MODEL OF A HOLOGRAPHIC DATA STORAGE SYSTEM

Figure 1 shows the HDS system modeled as a communication channel that consists of a spatial light modulator (SLM), a Fourier transform (FT) lens, an optical aperture, an inverse FT lens, and a CMOS image sensor (CIS).

For a coaxial configuration, coherent addition is realized using the signal area of the SLM occupied by the DC components in the reproduction process. It is equivalent to adding the DC components directly onto the pixels of the CIS, as shown in Fig.1.

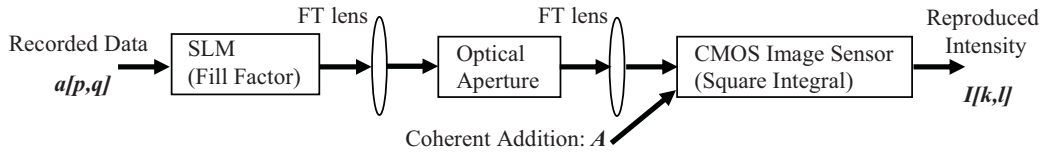


Fig. 1. Communication Channel model of a HDS System using the Coherent Addition

The output intensity $I(k, l)$ at the (k, l) th pixel of the CIS, can be calculated as follows[2]:

$$I(k, l) = \int_{-\infty}^{\infty} \int_{-\infty}^{\infty} \left| \sum_p \sum_q a[p, q] \text{rect}\left(\frac{x - p\Delta s}{\delta s}, \frac{y - q\Delta s}{\delta s}\right) \right|^2 \text{sinc}\left(\frac{xw}{\lambda f_L}, \frac{yw}{\lambda f_L}\right) + A^2 \text{rect}\left(\frac{x - k\Delta c}{\delta c}, \frac{y - l\Delta c}{\delta c}\right) dx dy. \quad (1)$$

The recording data $a[p, q]$ have two levels $[0, 1]$ without a phase mask or three levels $[-1, 0, +1]$ with a random binary phase mask. δs and Δs are the pixel pitch and width of the SLM, respectively. The impulse matrix of the recording data becomes a pulse matrix $\sum_p \sum_q a[p, q] \text{rect}\left(\frac{x - p\Delta s}{\delta s}, \frac{y - q\Delta s}{\delta s}\right)$ according to the linear fill factor of the SLM, $\Delta s / \delta s$, where $\text{rect}(x, y) = 1$ for $-0.5 \leq x, y \leq +0.5$ and zero otherwise.

The impulse response of the optical aperture in the image plane is $\text{sinc}(xw/\lambda f_L, yw/\lambda f_L)$, which is the inverse Fourier transform of a two-dimensional ideal low pass filter in the frequency plane, where f_L is the focal length of

*Masaaki.HARA@jp.sony.com; phone +81-3-5448-6698; fax +81-3-5448-3257

the FT lens, λ is the wave length of coherent light source, w is the width of the square optical aperture, and $sinc(x, y)$ is defined as $[\sin(\pi x)/(\pi x)][\sin(\pi y)/(\pi y)]$. The Nyquist aperture width is defined as $w_N \equiv \lambda f_L / \delta_s$.

The convolution of the pulse matrix and sinc function is projected onto the CIS with added coherent DC light of amplitude A . After rectification and squaring to calculate the intensity of incident light, $I(k, l)$ is obtained by integration according to the fill factor of the CIS, $\Delta c / \delta c$, where δc and Δc are the pixel pitch and width of the CIS, respectively.

Assuming that the amplitude of DC light satisfies the following condition:

$$[\sum_p \sum_q a[p, q] \text{rect}(\frac{x - p\Delta s}{\delta s}, \frac{y - q\Delta s}{\delta s})] * \text{sinc}(\frac{xw}{\lambda f_L}, \frac{yw}{\lambda f_L}) + A > 0, \quad (2)$$

the linearly reproduced signal $r[k, l]$ can be retrieved by calculating

$$r[k, l] \equiv C_1(\sqrt{I[k, l]} - C_2 A), \quad (3)$$

where C_1 and C_2 are constant values proportional to Δc . Above is the brief summary of our previous report[1] from a theoretical point of view.

On the other hand, if a linearly reproduced signal is obtained, a simple linear channel model defined as

$$h_L(k, l) \equiv \int_{-\infty}^{\infty} \int_{-\infty}^{\infty} \{ \text{rect}(\frac{x}{\delta s}, \frac{y}{\delta s}) * \text{sinc}(\frac{xw}{\lambda f_L}, \frac{yw}{\lambda f_L}) \} \text{rect}(\frac{x - k\Delta c}{\delta c}, \frac{y - l\Delta c}{\delta c}) dx dy \quad (4)$$

should be effective to deal with the HDS channel. We now estimate the difference between $r[k, l]$ and linear superposition of $a[p, q]$ and $h_L(k, l)$, because integration is performed after the components are squared in Eq.(1).

Figure 2 shows a linearity comparison of simulation results. As shown in Fig. 2(a), even when the phase mask is not in use, the negative amplitude generated in the signal is rectified in conventional reproduction ($A = 0$). When using a random binary phase mask, the linearity is quite low, as shown in Fig. 2(b). However, when using coherent addition ($A = 2$), $r[k, l]$ is almost equal to the linear superposition as expected (Figs. 2(c) and (d)). Figure 3 shows the normalized mean squared error (NMSE), which is defined as (mean squared error between linear superposition and $r[k, l]$)/(mean power of linear superposition). This result clearly reveals that by applying coherent addition, a simple linear channel model in Eq. (4) is made available for a HDS channel because NMSE is less than $1.0E-3$ for linear reproduction ($A = 2$).

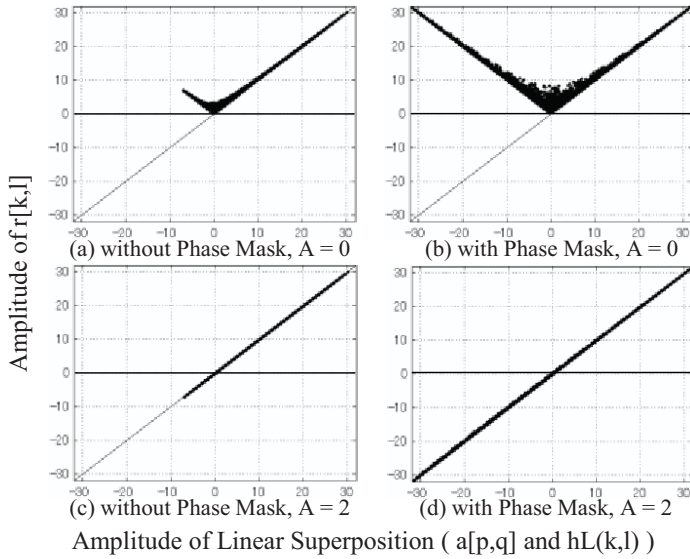


Fig. 2. Linearity Comparison (Aperture : Nyquist Size×1.2)

<Common Simulation Condition>

Number of SLM pixel: 48×48
 pixel resolution : 16×16
 SLM fill factor: $\Delta s / \delta s = 15/16$
 CIS fill factor: $\Delta c / \delta c = 5/8$

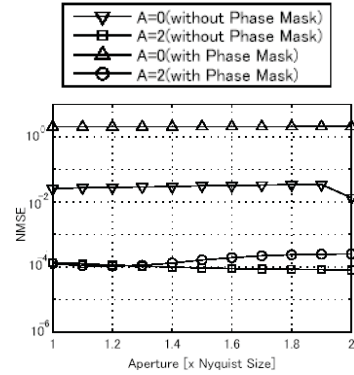


Fig. 3. Normalized Mean Squared Error

3. LINEAR EQUALIZATION OF HOLOGRAPHIC DATA STORAGE CHANNEL

A smaller aperture size is more effective in achieving a higher recording density because it decreases the size of hologram pages and suppresses the consumption of medium dynamic range. However, to compensate for interpixel interference (IPI) and improve SNR, a carefully designed equalizing filter must be used. In general, "Nyquist's first criterion" is used as a zero intersymbol interference (ISI) equalizing target in conventional data storage and digital communication systems. A typical function in the frequency domain is given as follows:

$$H(f, \alpha) = \frac{1}{2} \left[1 - \sin\left(\frac{\pi(f - f_N)}{2\alpha f_N}\right) \right] \text{ for } |f - f_N| < 2\alpha f_N, \quad 0 \text{ for } |f| > (1 + 2\alpha f_N), \quad 1 \text{ for } |f| < (1 - 2\alpha f_N), \quad (5)$$

where f is frequency, f_N is the Nyquist frequency, and α is the roll-off factor with a range of $0 \leq \alpha \leq 1$.

Let $nq1_{1D}$ be a row vector of zero ISI impulse response, which is the inverse Fourier transform of H . Then a two-dimensional zero IPI impulse response is obtained as an outer product of $nq1_{1D}$, i.e., $nq1_{2D} \equiv nq1_{1D}^T nq1_{1D}$, where $nq1_{1D}^T$ is the transposed column vector of $nq1_{1D}$. A characteristic of the zero IPI equalizer for $r[k, l]$ can be calculated by $eql_{2D} = FFT^{-1}[FFT\{nq1_{2D}\} / FFT\{h_L\}]$, using the linear channel model of Eq. (4). Note that $2f_N$ is equal to the Nyquist size, w_N , in the frequency plane.

Figure 4 shows the relationship between aperture size and SNR before and after equalization. The roll-off factor α is set to be $\alpha = (Aperture\ Size / Nyquist\ Size) - 1$. Before equalization, SNR is changed with or without the phase mask regardless of the coherent addition (Fig. 4(a)). After equalization (Fig. 4(b)), SNR is greatly improved in linear reproduction ($A = 2$), which shows the effectiveness of linear equalization for a holographic data storage channel.

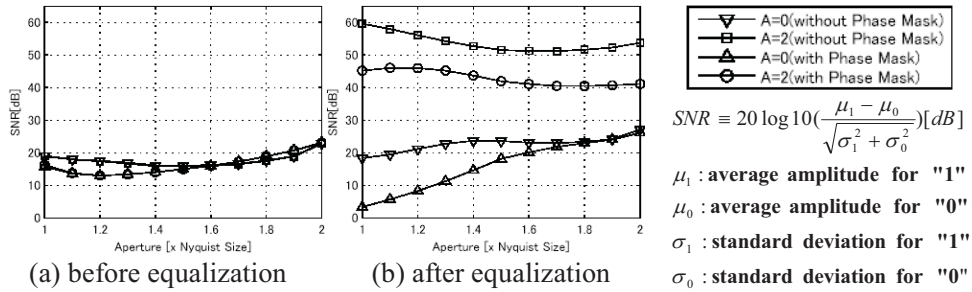


Fig. 4. Aperture Size and SNR before and after Equalization

4. CONCLUSION

By applying coherent addition, a simple linear channel model and conventional linear equalization are made available for a HDS channel. We expect that the recording density and transfer rate of holographic data storage systems will improve dramatically by applying those technologies and knowledges of signal processing that have been already developed in the field of digital communication and digital mass storage systems.

REFERENCES

- [1] M. Hara, K. Tanaka, K. Tokuyama, M. Toishi, K. Hirooka, A. Fukumoto, and K. Watanabe, "Linear Reproduction of a Holographic Storage Channel using Coherent Addition of Optical DC Components," to be published in Jpn. J. Appl. Phys.
- [2] V. Vadde and B. V. K. V. Kumar, "Channel modeling and estimation for intrapage equalization in pixel-matched volume holographic data storage," Appl. Opt. **38**, 4374 (1999)

Homodyne detection of holographic data pages

Mark R. Ayres*, Kevin Curtis
InPhase Technologies, Inc., 2000 Pike Rd., Longmont, CO, USA, 80501

ABSTRACT

The first generation of holographic data storage (HDS) devices rely on direct detection of the holographic signal by a photodetector array. Significant performance improvements could theoretically be realized by applying a coherent detection method such as homodyne detection. Homodyne performance improvements could potentially increase storage density and data transfer rates simultaneously. Homodyne detection would further enable PSK (*phase shift keying*) modulation of the signal beam, conferring great benefits by homogenizing the recording intensity at the Fourier plane and reducing intra-signal noise. However, homodyne detection is difficult and expensive to implement because of the need to phase-align the local oscillator beam to the signal beam. We present an alternative method of algorithmic phase alignment that could potentially enable homodyne detection in a low-cost second-generation HDS product.

Keywords: Holographic and volume memories, Optical data storage, Homodyne, Heterodyne, Coherent detection

1. INTRODUCTION

For page-oriented HDS, homodyne detection can be formulated for a 2D spatially-varying signal rather than the traditional 1D time-varying signal. We write the photocurrent, i_{PD} , detected by photodetector array element g, h as

$$i_{PD}[g, h] \sim |E_{LO}[g, h] + E_S[g, h]|^2 = |E_L|^2 + |D[g, h]E_C|^2 + 2D[g, h]|E_L||E_C|\cos(\Delta\phi[g, h]) \quad (1)$$

where $E_{LO}[g, h] = E_L \exp(j\phi_L[g, h])$ and $E_S[g, h] = D[g, h]E_C \exp(j\phi_C[g, h])$ are the scalar monochromatic optical fields of the local oscillator and the signal respectively. Each is presumed to have constant amplitude (E_L and E_C , respectively), and spatially varying phase ϕ_L and ϕ_C , with difference $\Delta\phi = \phi_C - \phi_L$. The signal is composed of a carrier modulated by a data pattern, $D[g, h]$. The benefits of homodyne detection accrue when $|E_L| \gg |E_C|$ so that the third interference term dominates over the second direct term. Then the factor of $|E_L|$ provides optical amplification, and the sign, as well as the magnitude, of $D[g, h]$ may be ascertained. However, this feat requires dealing with the phase factor. While optical methods have been proposed [1], it seems likely that environmental robustness would require expensive adaptive optics to dynamically maintain the $\Delta\phi = 0$ relationship across the whole page. Instead, we propose a method that allows $\Delta\phi$ to vary and generates the phase-matched image algorithmically.

Coherent optical detection is often employed to boost the signal level above detector thermal noise, and so to approach the shot noise limit. In the case of HDS, coherent optical scatter noise typically dominates detector noise. However, the linearization of this optical noise by the coherent detection process should result in 3 dB of SNR improvement [2]. Furthermore, switching from ASK to PSK signal modulation will provide another 3 dB SNR increase [3]. Finally, the use of PSK modulation will address several holographic issues by eliminating the need for a phase mask to attenuate the D.C. component of ASK-modulated data, and by greatly reducing intra-signal modulation noise [4].

2. QUADRATURE HOMODYNE DETECTION

Consider an HDS system wherein the reconstructed signal beam is mixed with a co-propagating plane wave local oscillator from the same laser source, perhaps using a non-polarizing beam splitter. If the optical axes of the two components are sufficiently well aligned (and if the data page was originally modulated onto a flat carrier wavefront), then the detected image will contain coarse fringes produced as the signal drifts in and out of phase with the local oscillator – i.e., $\Delta\phi$ will be limited to a relatively low spatial bandwidth. Now suppose that a switchable retarder – one that selects between two path-lengths that differ by one quarter wavelength – is inserted in one of the beam paths. Then

* email: markayres@inphase-technologies.com; website: inphase-technologies.com

we can take two different detector images of the same hologram. The images – call them P and Q images – will have similar fringe patterns, except that the phase of the entire pattern shifts by 90° since $\Delta\varphi$ was changed by 90° between exposures. Figure 1 below shows such a “quadrature pair” of images. The high contrast regions occur where the local oscillator is in phase with the signal ($\cos \Delta\varphi \approx 1$), and the gray, low-contrast regions indicate the local oscillator is $\pm 90^\circ$ different than the signal ($\cos \Delta\varphi \approx 0$). In other regions, the contrast is high, but the image is inverted ($\cos \Delta\varphi \approx -1$, indicated by the light border). Because of this quadrature relationship of the fringe patterns, each data pixel appears in high contrast in at least one of the two images, although it may be inverted. And if the optical amplification is sufficiently high, both images may be detected with far shorter total exposure time than a single directly-detected image.

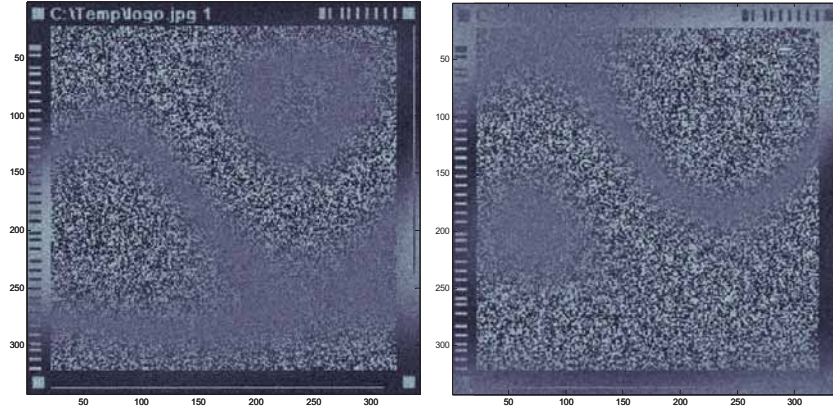


Figure 1. Simulated P and Q detector images of a hologram showing quadrature relationship between the fringe patterns.

The quadrature image pair can be blended into a single high-contrast, positive polarity image if the fringe pattern can be characterized across the images. This can be accomplished in practice by embedding known data patterns, or *reserved blocks*, within the page, and then performing a cross correlation between the detected image and the known pattern. The cross correlation will exhibit a strong peak where the contrast is high and the local oscillator is in phase with the signal, and a very weak peak where the contrast is low. In the inverted regions, the cross correlation will produce a strong negative-going peak. This results in two maps, $X_P[i,j]$ and $X_Q[i,j]$, indicating the cross correlation peak strength at each i,j reserved block position within the P and Q images.

We have previously described the use of reserved block cross correlation maps in the context of oversampled image detection [5]. The present usage is basically similar, except that the strength of each cross correlation peak is required rather than its position. The reserved blocks are 8×8 pixels in size, distributed on a 64×64 grid. The pattern equalization method for enhancing position accuracy in the previous work serves to enhance peak strength measurement accuracy here. In fact, quadrature homodyne may be practiced with oversampled detection, with the operations combined so that a single cross correlation is used to determine both the position and strength of each peak.

Once the $X_P[i,j]$ and $X_Q[i,j]$ maps are established, they are spatially up-sampled by 64 to determine interpolated peak strengths at every detector pixel location. This can produce an accurate result as long as the reserved block grid adequately samples the low-frequency fringe pattern. Then, the combined image is calculated by

$$\hat{E}_S[g,h] = \frac{X_P[g,h]}{\sqrt{X_P^2[g,h] + X_Q^2[g,h]}} \tilde{I}_P[g,h] + \frac{X_Q[g,h]}{\sqrt{X_P^2[g,h] + X_Q^2[g,h]}} \tilde{I}_Q[g,h] \quad (2)$$

where $\hat{E}_S[g,h]$ is the estimated signal optical field impinging on detector element g,h , and $\tilde{I}_P[g,h]$ and $\tilde{I}_Q[g,h]$ are the A.C.-filtered quadrature image intensities (i.e., the P and Q images with their D.C. components removed). Equation (2) is the noise-minimizing linear solution for estimating $E_S[g,h]$ when the noise power in the P and Q images are taken to be equal. The numerators blend the two terms in proportion to their projections onto the local oscillators, naturally correcting the negative polarity of the inverted regions. The denominators serve merely to normalize by the local image intensities, and might be omitted in an actual hardware implementation.

3. TEST RESULTS

The quadrature homodyne detection algorithm was tested on simulated images and compared to direct detection and ideal homodyne detection. Simulated detector images of a 752×752 pixel data page oversampled by 4:3 were generated. The resampling channel was re-optimized by generating different coefficients for each case. For the homodyne images, a local oscillator with $100 \times$ signal power was introduced, and in the quadrature homodyne case, two waves of phase tilt were also applied. The results of the tests are summarized in Figure 2:

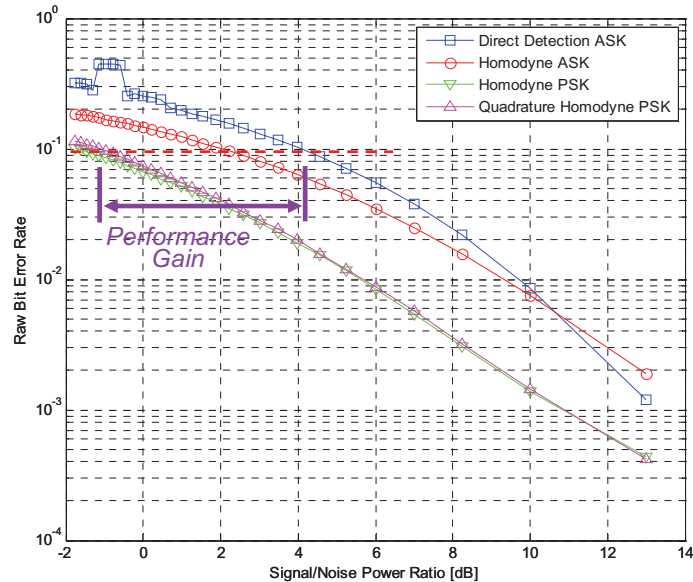


Figure 2. Results of simulated PSK quadrature homodyne detection compared to direct ASK detection, and standard (phase-matched local oscillator) homodyne detection of ASK and PSK modulated signals.

The x axis represents the proportion of pseudorandom coherent noise added to the signal, and the y axis is the raw bit error rate determined by threshold detection after resampling. As expected, the quadrature homodyne plot differs little from the ideal PSK homodyne plot, deviating slightly at low SNR where the phase estimates become noisy. The homodyne PSK plots show about 5 dB of improvement over the direct detection plot in the region of interest, which is in good agreement with the 6 dB prediction. Improvements from holographic considerations (intra-signal modulation, etc...) were not modeled, and so would further improve on this performance.

4. CONCLUSIONS

We have presented an algorithmic method for performing homodyne detection in a page-oriented HDS system without the need for expensive adaptive optics. Modeling confirms that such a system would enjoy significant performance improvements over direct detection, thus providing the promise of increased storage capacity and faster data transfer rates in a second-generation HDS device.

References

- [1] M. Hara, et. al., "Linear Reproduction of a Holographic Storage Channel using the Coherent Addition of the Optical DC Components," ISOM (2007).
- [2] M. R. Ayres, *Signal Modulation for Holographic Memories*, Ph. D. Dissertation, University of Colorado at Boulder, (2007).
- [3] L. Kazovsky, S. Benedetto, A. Willner, *Optical Fiber Communications Systems*, Artech House Inc., 151-152 (1996).
- [4] M. R. Ayres, R. R. McLeod, "Intra-signal modulation in holographic memories," ISOM/ODS (2008).
- [5] M. Ayres, A. Hoskins, K. Curtis, "Image oversampling for page-oriented optical data storage," *Appl. Opt.* **45**, 2459-2464 (2006).

Development of a coaxial holographic data recording system

Atsushi Fukumoto

Tera Bytes Memory Development Department, CTDG, Sony Corporation,
5-1-12 Kitashinagawa, Shinagawa-ku, Tokyo 141-0001, Japan.
Atsushi.Fukumoto@jp.sony.com; phone +81 3 5448 6698; fax +81 3 5448 3257

ABSTRACT

Based on our recent progress in high-density and high data-transfer-rate recordings using coaxial holographic recording testers, the prospects for performance improvement in future systems are discussed.

Keywords: coaxial holographic recording, recording density, data transfer rate

1. INTRODUCTION

Coaxial holographic data recording is an attractive candidate for the next generation of optical storage systems, because it allows us to easily combine the optical disk technologies to realize a large storage capacity and a high data-transfer rate [1, 2]. We have developed a static tester and a dynamic tester employing the coaxial method, to demonstrate high-density and high data-transfer-rate recordings, respectively. By introducing newly developed techniques in these testers, the density and data-transfer rate have been improved. In this paper, development of a coaxial holographic data recording system using these testers is described.

2. STATIC TESTER FOR HIGH DENSITY RECORDING

The static tester, shown in Fig. 1, demonstrates high-density recording. Its coaxial optical system includes several unique devices; a random phase mask, an external cavity diode laser (ECDL) as a light source, a polarizing beam diffractor (PBD), and a high NA objective lens [3]. The random phase mask is placed on the optical conjugate plane of a spatial light modulator (SLM) for pixel matching. It suppresses the large DC component of the diffraction pattern on the focal plane and promotes interference between the signal and reference beams. The 407-nm wavelength ECDL, developed in-house, maintains a stable single-mode oscillation with CW output power of up to 80 mW [4]. Since the reference and retrieving signal beams propagate along the same optical axis and are close to each other, the scattered reference beam degrades the retrieving signal quality. Then, the PBD selectively diffracts the reference beam away from the optical axis. Finally, an objective lens of 0.85 NA is designed to minimize the size of a recording hologram on the focal plane.

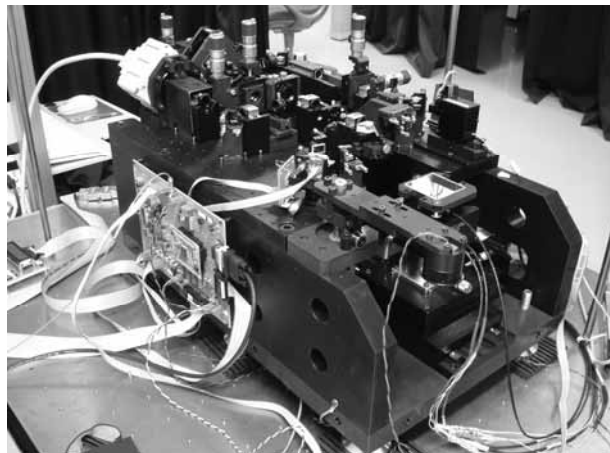


Fig. 1 Photograph of the static tester

The amount of data in one hologram (page data capacity) and the NA of the objective lens are important factors for high-density recording. When the diameter of the objective is fixed, the page data capacity increases as the SLM pixel size decreases. Designing a high NA objective lens for small pixels is difficult. Thus, the page data capacity is actually limited by the above-mentioned trade-off issue. In the static tester, the page data capacity of 135 Kbits is obtained using an effective pixel size of $11.2 \mu\text{m}^2$.

Multiplex-recording for recording density evaluation is performed using a two-dimensional shift multiplexing technique. A recording media fixed on an x-y PLZT stage is moved with an assigned shift pitch during recording intervals. The number of recording (multiplexing) pages, determined by the shift pitch and the recording hologram size, almost satisfies the $(2n - 1)$ regime where n is the minimum integer beyond the value obtained by the hologram size divided by the shift pitch. Consequently, the multiplexed pages are distributed widely over the x-y plane. The symbol error rate of the retrieved signal from the center-positioned page is an index for recording the density evaluation. Using this scheme, we recently demonstrated a recording density of 270 Gbits/inch² with an error rate less than 10 % [5].

Our next course for furthering high-density recording is to employ a coherent addition technique [6]. This technique dramatically improves the SNR of the retrieval signal, and increases the current recording density by a factor of 3–4; therefore, we intend to apply this technique to the static tester.

3. DYNAMIC TESTER FOR HIGH DATA-TRANSFER-RATE RECORDING

The dynamic tester, shown in Fig. 2, demonstrates high data-transfer-rate recording. Unlike the static tester, the dynamic tester is equipped with several servo techniques, which enable recording and retrieving holograms under rotating disk-type recording media. Image stabilizing (IS) is a unique servo technique developed for the coaxial recording and retrieving [7]. Using the IS technique, a recording/retrieving laser beam is maintained at a constant position on continuously rotating media during recording/retrieving. The laser beam is moved to the next recording/retrieving position during recording/retrieving intervals. Thus, shift multiplexing on continuously rotating media is performed successfully with appropriate exposure energy, even when using a relatively low-power ECDL. The focusing and tracking servo techniques are similar to those of a conventional optical disk system. While detecting the servo signals using an additional red diode laser, the objective lens, which is mounted on a two-axis actuator, is moved vertically and horizontally to control the position of the recording/retrieving laser beam.

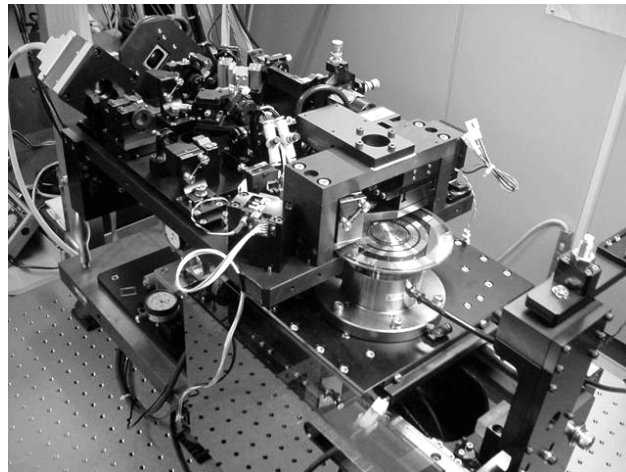


Fig. 2 Photograph of the dynamic tester

A high-speed image sensor with a large pixel number is a key device for high data-transfer-rate recording, since the retrieving data-transfer rate is determined by the frame rate of the image sensor and the page data capacity. In this study, we used a 1.5-Kfps CMOS image sensor (CIS) with 512×512 pixels. Adopting 2×2 times oversampling, the page data capacity is set to be 63.5 Kbits. Using the CIS, 100 multiplexed pages with a $15\text{-}\mu\text{m}$ shift pitch were retrieved successfully with a 92-Mbps data-transfer rate. In addition, we investigated the recording data-transfer rate. 100 pages recorded with various data-transfer rates were retrieved with a 92-Mbps data-transfer rate. As a result, we achieved a

recording data-transfer rate of up to 107 Mbps, which is limited by available laser exposure energy, with an average symbol error rate of less than 10 % [8].

For achieving data-transfer rate of the order of Gbps, some technical issues must be resolved. Developing a CIS with higher speed and a larger pixel number, and a lower oversampling rate, is essential for increasing the retrieving data-transfer rate. We have developed a data resampling method for lower oversampling rates, which is yet to be applied to the dynamic tester [9]. The recording data-transfer rate is increased by improving the laser exposure energy and the recording sensitivity of the media. Our next target is to double the current data-transfer rate using a high-speed CIS and high-power ECDL.

REFERENCES

- [1] S. S. Orlov, W. Phillips, E. Bjornson, Y. Takashima, P. Sundaram, L. Hesselink, R. Okas, D. Kwan, and R. Snyder, "High-transfer-rate high-capacity holographic disk data-storage system," *Appl. Opt.* **43**, 4902–4914 (2004).
- [2] H. Horimai, X. Tan, and J. Li, "Collinear holography," *Appl. Opt.* **44**, 2575–2579 (2005).
- [3] K. Tanaka, M. Hara, K. Tokuyama, K. Hirooka, K. Ishioka, A. Fukumoto, and K. Watanabe, "Improved performance in coaxial holographic data recording," *Opt. Express* **15**, 16196–16209 (2007).
- [4] T. Tanaka, K. Takahashi, K. Sako, R. Kasegawa, M. Toishi, K. Watanabe, D. Samuels, and M. Takeya, "Littrow-type external-cavity blue laser for holographic data storage," *Appl. Opt.* **46**, 3583–3592 (2007).
- [5] K. Tanaka, H. Mori, M. Hara, K. Hirooka, A. Fukumoto, and K. Watanabe, "High density recording of 270 Gbits/inch² in a coaxial holographic storage system," in *Technical Digest of International Symposium on Optical Memory 2007*, pp. 38–39.
- [6] M. Hara, K. Tanaka, K. Tokuyama, M. Toishi, K. Hirooka, A. Fukumoto, and K. Watanabe, "Linear reproduction of a holographic storage channel using coherent addition of optical DC components," in *Technical Digest of International Symposium on Optical Memory 2007*, pp. 36–37.
- [7] K. Hirooka, K. Takasaki, S. Kobayashi, H. Okada, S. Akao, S. Seko, A. Fukumoto, M. Sugiki, and K. Watanabe, "Development of a coaxial type holographic disc data storage evaluation system, capable of 500-fps-consecutive writing and reading," in *Technical Digest of Optical Data storage 2006*, pp. 12–14.
- [8] K. Takasaki, K. Hirooka, T. Takeda, T. Hori, H. Okada, M. Hara, K. Tokuyama, S. Yamada, S. Seko, A. Fukumoto, and K. Watanabe, "High-speed data recording and retrieving using the image-stabilizing technique in a coaxial holographic disc system," in *Technical Digest of Optical Data storage 2007, post deadline paper*.
- [9] K. Hirooka, M. Hara, K. Tanaka, S. Seko, A. Fukumoto, and K. Watanabe, "Two-dimensional clock extraction method for data pixel synchronization in holographic data storage," in *Technical Digest of International Symposium on Optical Memory 2007*, pp. 40–41.

A reflective counter-propagating holographic setup

Joachim Knittel*, Frank Przygodda, Oliver Malki, Heiko Trautner, Hartmut Richter
Deutsche Thomson OHG, Hermann-Schwerstr. 3, D-78048 Villingen-Schwenningen, Germany

ABSTRACT

We present a reflective counter-propagating holographic setup for optical data storage. The part of the reference beam that is transmitted through the holographic medium, strikes the spatial light modulator and is reflected to interfere with the original reference beam. Thus the system makes efficient use of the laser light. We investigate the shift selectivity and compare experimental and theoretical results that were obtained with a 2D FFT-Volume integral method.

Keywords: Holographic storage, shift-selectivity, capacity, optical storage.

1. INTRODUCTION

Holographic data storage is one of several competing optical storage technologies to reach storage capacities beyond 1 Tbytes on a 12cm disc. Although the idea of using holography for optical data storage is relatively old, it is not yet clear, which optical concept is most suitable for a practical holographic system [1, 2]. In the following paragraphs we present an alternative optical concept that features light efficiency. This will be proven by experimental investigations including a comparison of measured shift-selectivity data with theoretical results.

2. THE REFLECTIVE COUNTER-PROPAGATING COLLINEAR SETUP

A schematic layout of a reflective counter propagating collinear setup is shown in Figure 1. To record a hologram, the medium is illuminated with a reference beam that is focused into the holographic medium (H) by objective lens (OL₁). The transmitted portion of the reference beam is recollimated by a second objective lens (OL₂) and directed towards a reflective spatial light modulator (SLM). The SLM modulates the wavefront of the reflected light and directs it back into the holographic medium. At this stage the reference beam is turned into a signal beam. The additional lenses (L₁ and L₂) are used to shift the location of the reference beam focus to improve the overlap in the holographic medium. As the lenses are placed in the front and back focal plane of the 4f imaging system formed by the objective lenses OL₁ and OL₂, the beam diameter on the SLM does not change.

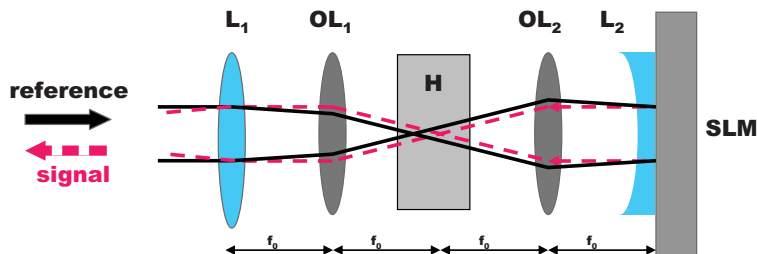


Fig. 1. Schematic of the holographic setup that consists of 2 objective lenses (OL₁ & OL₂) and two additional lenses (L₁ & L₂) that are used to shift the focus of the reference beam relative to the Fourier plane of the signal beam.

As shown in Figure 2 a nearly perfect overlap between signal and reference beam is achieved provided that the reference beam shift Δf in the medium is adapted to the diameter of the hologram, meaning that

$$\Delta f \frac{Na}{n} = \frac{\lambda f_0}{d} \quad (1)$$

*joachim.knittel@thomson.net, phone: ++49-7721-85-2070, fax: ++49-7721-85-2241.

with SLM pixel size d and focal length f_0 of the objective lenses. The focal lengths f_1 of lens L_1 and f_2 of lens L_2 are related by $f_1 = -2 f_2$ and thus the two lenses compensate each other. Therefore, the (reflected) signal beam is not influenced by the additional lenses and the diameter of the hologram in the Fourier plane does not change.

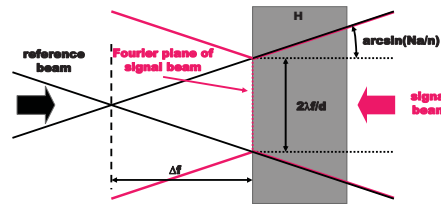


Fig. 2. Schematic showing the overlap of signal and reference beam within the holographic medium (H). The focus shift Δf is chosen in such a way that the overlap is optimal. The diameter of the hologram in the Fourier plane is determined by the pixel size d of the SLM and the focal length f_0 of the objective lens.

3. EXPERIMENTAL SETUP

A simplified schematic of the experimental setup is shown in Figure 3. Briefly, the laser source is a laser diode with external cavity and a wavelength of 405nm. The two objective lenses OL_1 and OL_2 are commercial microscope objective lenses with numerical aperture of 0.6 and focal length $f_0 = 5$ mm. Photopolymer coupons with 0.5mm thick cover glasses and a 0.3 mm thick photopolymer layer are used as holographic medium. The SLM has a pixel size of $22.4\mu\text{m}$. Lenses L_1 and L_2 have a focal length of 200mm and -400mm or alternatively of 100mm and -200 mm. This leads to a reference beam shift in the medium of about $190\mu\text{m}$ or $380\mu\text{m}$ respectively. The ideal shift according to equation (1) would be $220\mu\text{m}$. Linear polarized light is used. The holographic medium is placed in the position shown in Figure 2.

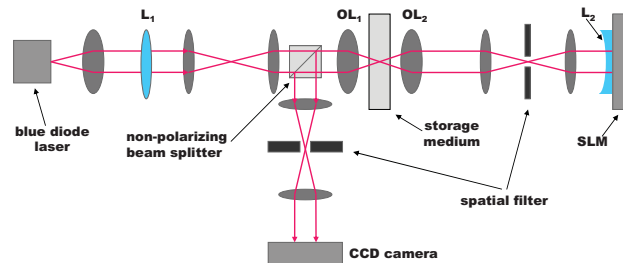


Fig. 3. The experimental setup used for measuring the shift selectivity of a reflective counter-propagating system.

4. RESULTS AND DISCUSSION

Figure 4 shows typical data page recorded with our setup. We are using a block modulation, where 3 white pixels are placed in each 4×4 block. The circular interference pattern in the center is due to reflections from the uncoated holographic disc and the objective lens, which has just a standard AR-coating for visible light.

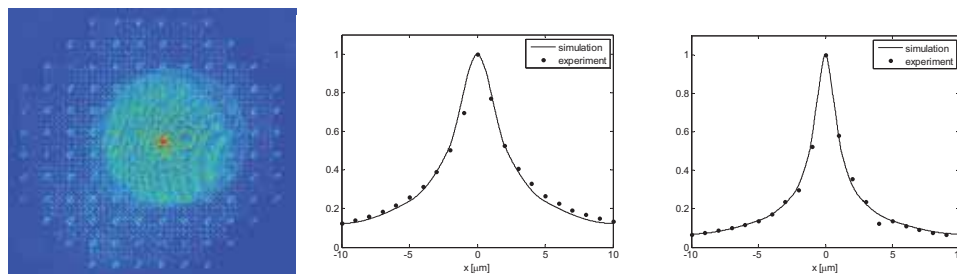


Fig. 4. Data page recorded and read-out with our experimental setup (left). Measured and simulated shift-selectivity curves for $f_1 = 100$ mm (center) and $f_1 = 200$ mm (right).

The shift-selectivity curves for two different lens combinations L_1 and L_2 is shown in Figure 4. As expected the shift selectivity for the $L_1=200\text{mm}$ is better than for $L_1=100\text{mm}$ (Larger L_1 means smaller z_0 in equation (2)). The measurements agree quite well with the simulation results that were obtained with a 2D FFT-volume integral method [3].

In Figure 5 it is shown that after a lateral hologram shift of $5\ \mu\text{m}$ a stripe like data region remains. By using a data page that has no data in this stripe like region, the shift selectivity can be significantly improved. This is clearly visible in the diagram of Figure 5. The phenomena can be explained with the following equation that yields an approximated value for the shift selectivity [4]:

$$\delta_{\text{Bragg}} = \frac{\lambda z_0}{L \tan(\alpha)} \quad (2)$$

Here λ denotes the wavelength of light in vacuum, z_0 the distance between the focus spot of the reference beam and the center of the recording region, L the thickness of the medium and α the angle between the average propagation direction of the signal and reference beam. For signal beams close to the center α is nearly 0, and so the shift length is very large. Therefore, by eliminating regions with small α the shift selectivity can be improved. Another method currently under investigation is to improve the shift selectivity with a random phase plate [5].

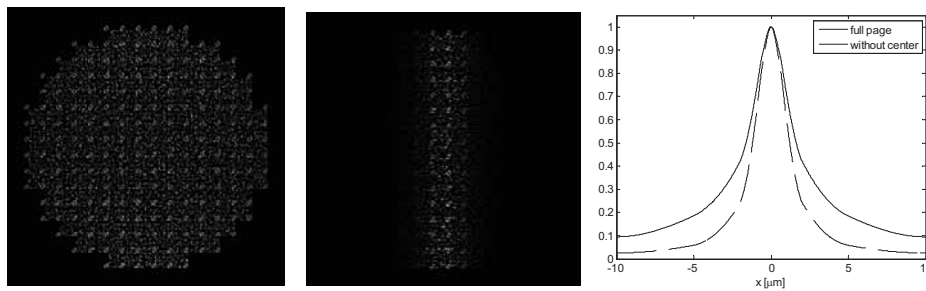


Fig. 5. Simulated data page (left) and after a lateral shift of $5\ \mu\text{m}$ (center). Comparison of shift-selectivity curves for a data page with a blank two block wide stripe through the center and without the blank stripe (right).

5. SUMMARY

We described a novel reflective counter-propagating concept for holographic data storage. There is a perfect agreement between experimental and simulated shift-selectivity curves. A special data page was presented that improves the shift selectivity of the system.

REFERENCES

- [1] H. J. Coufal, D. Psaltis, and G. T. Sincerbox, eds., *Holographic Data Storage*, Springer Series in Optical Sciences (Springer Verlag, 2000).
- [2] L. Hesselink, S. Orlov, and M. C. Bashaw, "Holographic data storage systems," *Proc. IEEE* **92**, 1231 (2004).
- [3] B. Gombkőto, P. Koppa, aA. Sūto, and E. Lőrincz, "Computer simulation of reflective volume grating holographic data storage," *JOSA* **24**, 2075 (2007).
- [4] G. Basbasthatis, M. Levene, and D. Psaltis, "Shift multiplexing with spherical reference waves," *Appl. Opt.* **35**, 2403 (1996).
- [5] O. Matoba, Y. Yokohama, K. Nitta, and T. Yoshimura, "Reflection-type holographic disk memory with random phase shift multiplexing," *Appl. Opt.* **45**, 3270 (2006).

Practical Holography

**Ken Anderson, Edeline Fotheringham, Friso Schlottau, Paul Smith,
Keith Farnsworth, Jason Ensher, Kevin Curtis**
InPhase Technologies, Inc., 2000 Pike Rd., Longmont, CO, 80501
kenanderson@inphase-tech.com

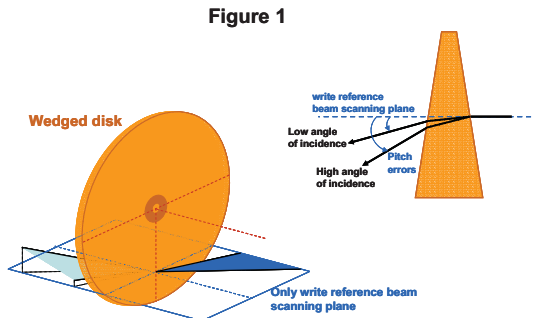
Abstract: We review the evolution of InPhase Technologies’ holographic storage drive and discuss technical obstacles that we have overcome to bring our product to market.

1. Introduction

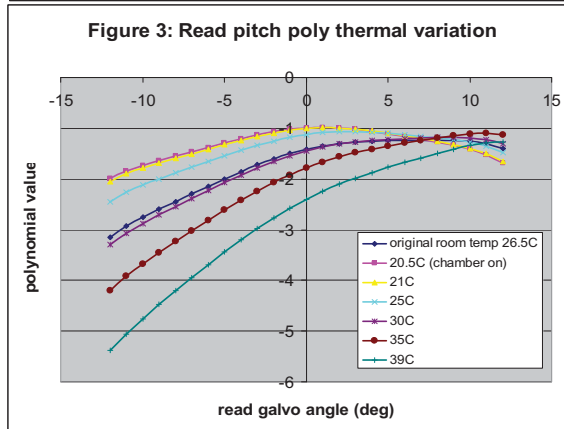
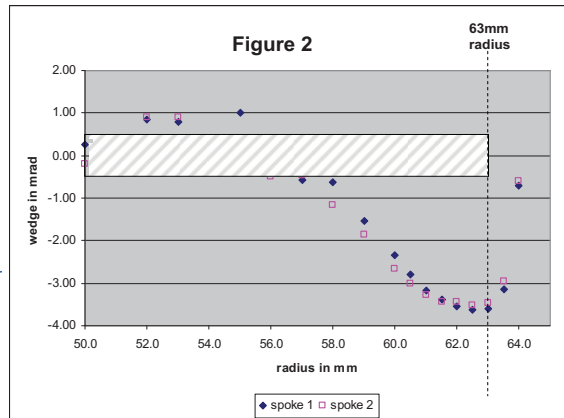
InPhase Technologies has been at work for over 7 years in developing the world’s first holographic data storage product. During this period, we have created over 7 distinct architectural development platforms. This paper focuses on the lessons learned from the last two preproduction prototype platforms: Engineering Validation and Testing (EVT) and Design Validation and Testing (DVT)[1] and the advances that have been made as a result. There are a multitude of physical effects that must be considered when designing a drive to work in real world conditions: temperature, vibration, interchange, etc. While many effects were taken into account in the design phase, there were several more subtle effects that needed to be discovered to fully develop a robust drive. Some of these effects have been discussed previously[2]. This paper gives an overview of the most challenging (and not so obvious) effects that InPhase has encountered from the perspective of what it takes to design and build a practical holographic storage drive.

2. Pitch and Angular sensitivity

Holographic sensitivity to pitch (the holographic Bragg degenerate dimension) is on the order of 0.5 milliradians.[3] This means if the accumulated mirror tilt is greater than this we start to lose SNR in the holograms. There are a few effects that can



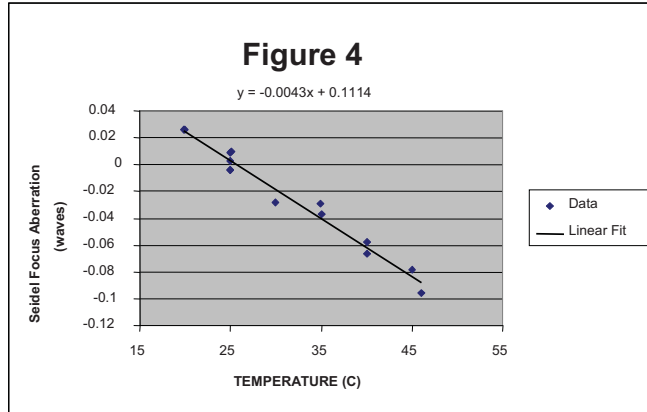
contribute to a pitch variation: Pointing changes of reference beam at the media due to thermal expansion or contraction of upstream components, reference beam mirror axis not parallel to rotational axis, or disk wedge at the outer diameter of the disk (See Figure 1 and 2). Pointing changes due to thermal expansion or contraction are typically caused by some asymmetric thermal expansion of glue joints in mirrors. Extreme care and analysis of mechanical designs and gluing techniques must be taken to ensure thermal sensitivity is minimized. The problem is exacerbated by the fact that there are tens of mirrors in the optical path; each of which contributes one part of the variation. For



this reason, InPhase developed our own proprietary spherical mounts for mounting mirrors and glue bonding procedures to ensure even expansion during thermal cycling. In addition, we developed a automate pitch corrector that can be placed in the optical path before the write reference galvo mirror and used to calibrate out any residual pitch that is left over after all of the above techniques are applied. Figure 3 illustrates the amount of pitch correction compensated for with the pitch corrector for temperatures ranging from 20.5 C to 39C.

3. Wavefront sensitivity

The planarity of the reference beam will determine the ultimate quality of the reconstructed holograms and therefore this must be tightly tolerated. Athermalization of the optomechanics is quite important in order to maintain adequate wavefront, and one of the most sensitive optics is laser diode collimating lens. The main reason this is so sensitive is the high numerical aperture of the collimating lens. Very small changes in optical path length led to enough wavefront variation to degrade SNR. Figure 4 illustrates the Seidel focus error as a function of temperature between 17 and 46 degrees C for our first generation of lasers. This graph shows that the collimator is shifting slightly with respect to the laser diode. A focus change of 0.12 waves results in a SNR degradation at the media on the order of 1 to 2dB. For this reason, we spent considerable time optimizing the optomechanics to minimize wavefront error over temperature.



4. Laser robustness

Isolating vibration from the external environment has always been a big concern for holographic storage. However, it has proven to be easily controllable with good servo engineering, proper isolation, and the help of short (~1.5ms) exposure times. On the other hand, a small shutter vibration internal to the laser due to its proximity to the grating was detrimental. Because of an earlier decision to forego pathlength matching (since

Figure 5A

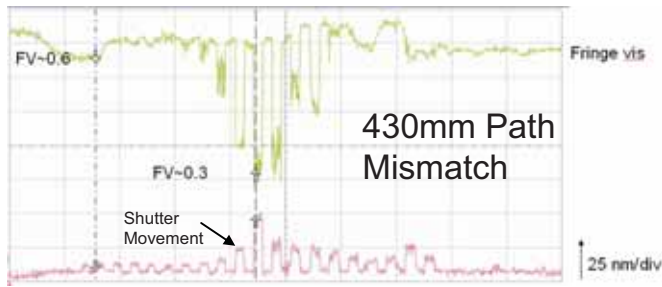
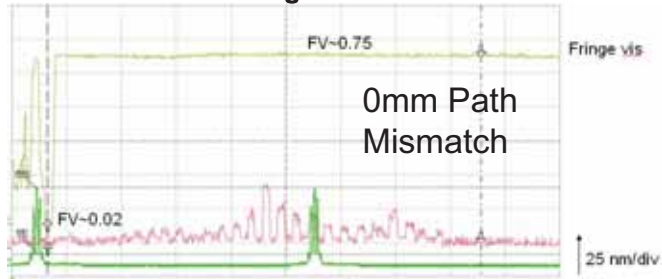


Figure 5B

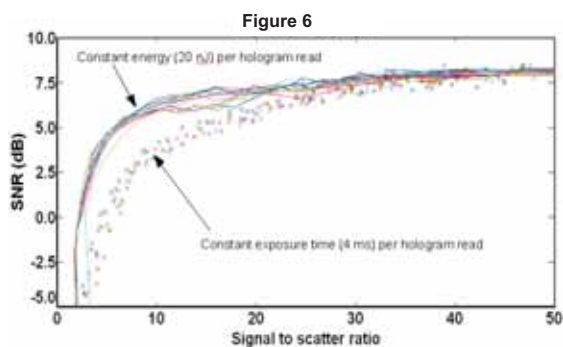


there was a very large coherence length), the drive became very sensitive to tiny motions of the laser grating. For example, a path length mismatch of about 430mm caused the drive to be susceptible to fluctuations on the order of a 10 nanometers of motion. It turned out that the tiny mechanical shutter that we are using in the laser was vibrating the grating on that order, and that was enough that the laser wavelength would shift fast enough that the path length mismatch would induce enough delay between object and reference paths that coherence would be lots at the media. The allowable grating motion is given by $\delta d = 2\Delta f_{tol}d^2\Delta t/\Delta xq$, where δd is the maximum grating movement during exposure interval Δt , Δf_{tol} is the tolerable frequency shift which is on the order of 100Hz, Δx is the path length difference, d is the cavity length of the ECDL, and q is the mode number.

As a result, we made a decision to retrofit pathlength matching into the drive. The experimental validation of the improvement of path length matching is given in Figure 5. Figure 5A shows the fringe visibility when the path length mismatch is 430mm. The data on the top of the figure is the fringe visibility, and the data on the bottom of the graph is the measured displacement of the grating. The visibility remains constant when the system is path length matched.

5. Media

There are many media related factors that must be taken into account when optimizing a holographic system. The most fundamental of these is media scatter from the polymer itself. Media scatter ultimately limits how much diffraction efficiency is required to obtain a good SNR. At InPhase, we commonly use a term we call Signal to Scatter Ratio (SSR). We use the SSR to determine the level of necessary signal strength of the holograms and from this calculation and the available M#, we can also determine the maximum number of holograms allowed in a single location. An experimental plot of SNR versus SSR is shown in Figure 6. There is a very strong knee in the curve around an SSR of around 10. For this reason, at 350Gbit/in² density, we typically operate around a SSR of 12 to 15.



Media bubbles are also very detrimental to performance. Our current data shows that bubbles about 20 to 30um can degrade SNR by a few tenths of a dB. We discovered that the reason such a small bubble could impact SNR so greatly was because a bubble acts like a scattering source and not like an absorptive particle. Scatter from a bubble is much more harmful than a black particle of identical size. A bubble can quickly take the SSR of the book below the SSR threshold. A hologram and the scatter from a bubble 123um in diameter are shown in Figure 7. Even though bubbles are very harmful, the process for making disks is quite good and can produce disks

with less than 20 bubbles per disk, most of which are quite large and therefore easily detectable by the scatter signal. A couple of different techniques are being used to mitigate the effects of bubbles. The first and most desirable method is to produce a defect map during manufacture of the disks that is stored in the RFID chip. This requires that the defects are mapped quite accurately to enable “keep out” zones. A backup approach is to measure the scatter at individual locations of the media and compare this to a threshold value. This is a more difficult solution due to the complexity of mapping scatter levels of the disk that vary. It also takes more overhead to measure the scatter that can impact transfer rate, pre-exposing the disk, etc.

6. Conclusions

We have discussed several hurdles that InPhase has faced in the development of a practical holographic storage device, and we have described solutions to each. We have encountered many problems and have developed many solutions that will allow us to manufacture the worlds first commercially available holographic storage device.

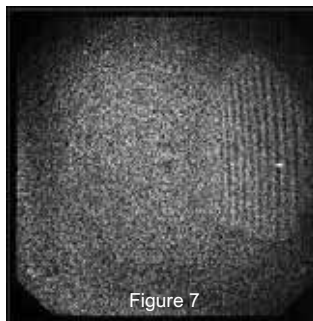


Figure 7

7. References

1. Kevin Curtis Tom Wilke, Invited Talk, "InPhase Professional Archive Drive Architecture" International Workshop on Holographic Memory, October 26-28, 2007 Penang Malaysia.
2. Alan Hoskins, et al, "Using Bragg Effects to Determine Media Orientation and Wavelength Detuning in a Holographic Data Storage System", Workshop on Holographic Memory, October 26-28, 2007 Penang Malaysia.
3. Alan Hoskins, et al, "Tolerances of a Page-Based Holographic Data Storage System," Proc. SPIE 6620, 662003 (2007).

Material consumption and crosstalk characteristics of different holographic concepts

Frank Przygodda*, Joachim Knittel, Oliver Malki, Heiko Trautner, Hartmut Richter
Deutsche Thomson OHG, Hermann-Schwer-Str. 3, D-78048 Villingen-Schwenningen, Germany

ABSTRACT

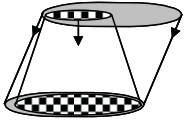
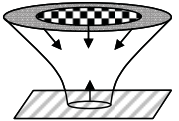
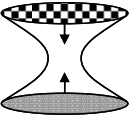
Holographic data storage is considered to be one of the most promising technology for high capacity data storage. Currently several holographic concepts are suggested and investigated in detail by many companies. The concepts differ primarily in the way of superimposing object and reference beam inside the holographic medium. At present time the most relevant concepts are the plane wave concept [1,2], the collinear concept [3,4] and a concept with counter-propagating beams [5]. We compare all three concepts regarding their beam overlap, the efficiency of material consumption, diffraction efficiency and crosstalk characteristics. The investigation is performed by numerical simulations which enable to use the same conditions in all setups and to be independent from experimental uncertainties like the non-linear behavior of the mediums sensitivity, influences by light scattering or reflections.

Keywords: Holographic Recording, Media

1. INTRODUCTION

The efficiency of holographic data storage in a photosensitive material depends on the physical material parameters like sensitivity and dynamic range as well as on the used holographic setup. Apart from technical aspects the setups also differ in terms of the efficiency of utilizing the holographic medium. An obvious criterion is the beam overlap of object and reference beam: regions of the material, which are illuminated by only one of the beams, do not contribute to data storage and waste dynamic range. In this article three holographic setups, a plane wave setup, a collinear setup, and a concept based on counter-propagating beams are investigated regarding their capability of storing maximal information by minimal utilization of dynamic range. Furthermore the inter-hologram crosstalk is investigated, which is desired to be low in order to maximize the data density inside the medium. For comparability the focused beams have the same numerical aperture of $NA=0.6$ in all three models. Suppression of the DC-peak in the Fourier plane is obtained by a pixelated phase mask applied in all cases, for similarity also in the plane wave model where the Fourier plane itself is located outside the medium. The medium thickness was set to $300\ \mu\text{m}$. For the collinear setup a reflective layer was assumed. A list of the geometrical model parameters are given in Table 1.

Table 1: Geometrical parameters of the three investigated holographic setups.

Plane wave setup	Collinear setup	Counter-propagating setup
 <p>medium: $300\ \mu\text{m}$ $NA_{\text{obj}} = 0.6$ focal length: $5\ \text{mm}$ data page: $160\ \text{kpix}$ white rate: 0.2 pixel size: $12\ \mu\text{m}$ phase cells: $12\ \mu\text{m}$ phase shift: $0, \text{Pi}$ Nyquist filter: 1.5 ref.: plane wave ref. diam.: $550\ \mu\text{m}$ ref. angle: $40\ \text{deg}$</p>	 <p>medium: $300\ \mu\text{m}$ with mirror at Fourier plane $NA_{\text{ref,obj}} = 0.6$ focal length: $5\ \text{mm}$ data page: $100\ \text{kpix}$ white rate (obj.): 0.2 white rate (ref.): 0.5 pixel size: $12\ \mu\text{m}$ phase cells: $12\ \mu\text{m}$ phase shift: $0, \text{Pi}$ Nyquist filter: 1.5</p>	 <p>medium: $300\ \mu\text{m}$ $NA_{\text{obj}} = 0.6$ $NA_{\text{ref}} = 0.6$ focal length: $5\ \text{mm}$ data page: $160\ \text{kpix}$ white rate: 0.2 pixel size: $12\ \mu\text{m}$ phase cells: $12\ \mu\text{m}$ phase shift: $0, \text{Pi}$ Nyquist filter: 1.5</p>

*frank.przygodda@thomson.net; phone +49 77 21 85 20 84; fax +49 77 21 85 22 41

2. SIMULATIONS AND RESULTS

2.1 Medium consumption

Fig. 1 shows schematically an object and reference beam superimposed inside the holographic medium together with a cut through the resulting refractive index modulation. We define the total volume V_t of the hologram by the region where at least one of the beams causes an increase of refractive index Δn . Note, that in general the beam borders have a smooth intensity transition. Therefore a threshold refractive index level of 1% of the mean refractive index at a given z -coordinate is used to determine the border of the volume. The region where reference and object beam causes a refractive index level above the 1% threshold defines the overlapping volume, here denoted with V_o . In addition to the refractive index change Δn also the fringe modulation n_f is of interest. It is calculated as the absolute difference between the coherent and incoherent sum of the two beams. These parameters vary along the depth of the holographic volume. In Fig.1 (right) the numerically determined overlap of reference and object beam and $n_f/\Delta n$ at a given z -coordinate are plotted for the three models. Note that the setup with counter-propagating beams shows a nearly 100% overlap and a maximal fringe modulation independent from the z -coordinate.

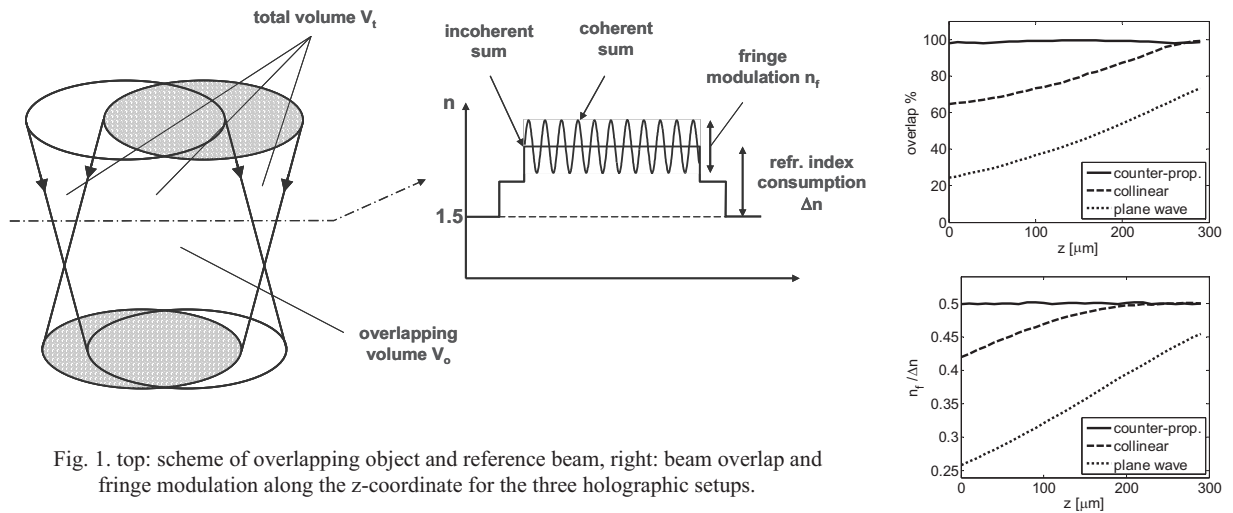


Fig. 1. top: scheme of overlapping object and reference beam, right: beam overlap and fringe modulation along the z -coordinate for the three holographic setups.

2.2 Hologram efficiency

The beam propagation method (BPM) [6,7] based on scalar diffraction theory is an effective technique for simulating the diffraction process of light at the refractive index modulations of a hologram. This method was used for simulating the plane wave and the collinear setup where the object and reference beam propagate in basically the same direction. The reflective layer of the collinear concept was considered by simulating a transmissive optical setup with a 600 micron thick material. For holograms produced by object and reference beam propagating in opposite directions the BPM cannot be applied because in this case the diffracted light is scattered backwards (reflection hologram). Here, the 2D-FFT volume integral method [7,8] was used. Table 2 gives an overview over the obtained diffraction efficiencies η together with the parameters V_t , V_o/V_t , and mean Δn and n_f within the total hologram volume. As a measure for the efficiency of the hologram in relation to its material consumption the ratio $\sqrt{\eta}/(\Delta n)$ is listed in the table. Regarding this parameter the counter-propagating setup is the most efficient concept. As

Table 2. Parameters obtained by numerical simulation.

medium: 300 μm thick sens.: $S = 2 \times 10^{-6} \Delta n / (\text{mJ}/\text{cm}^2)$ dosis: $E = 2 \times 0.5 \mu\text{J}$	Plane wave setup	Collinear setup	Counter- propagating setup
total volume V_t (μm^3)	7.75e7	2.61e7	1.75e7
beam overlap V_o/V_t	46%	77%	99%
mean Δn within V_t	0.778e-6	4.58e-6	3.41e-6
mean n_f within V_t	0.276e-6	2.18e-6	1.70e-6
diffraction efficiency η	0.19e-4	6.3e-4	8.0e-4
$\sqrt{\eta} / (\Delta n)$	5.60e3	5.48e3	8.31e3
$\sqrt{\eta} / (\Delta n \cdot V_t)$	0.72e-4	2.09e-4	4.75e-4

real holographic materials have a saturation level Δn_{\max} the number of holograms each consuming Δn is limited. Thus a high parameter $\sqrt{\eta}/(\Delta n)$ means that the holographic concept exploits the materials M-number efficiently. We do not take into account that different concepts per se need different diffraction efficiencies for example to overcome the systems noise (probe beam scatter, reflections, etc.). Since it is desirable that a hologram occupies a small volume also the parameter $\sqrt{\eta}/(\Delta n \cdot V_i)$ is of interest. The counter-propagating concept shows again best performance followed by the collinear concept. The advantage of the counter-propagating concept becomes even bigger if the data page size of 160 kpix compared to the smaller page of the collinear concept (100 kpix) is taken into account.

2.3 Shift-selectivity and inter-hologram crosstalk

The selectivity of a holographic concept influences crosstalk characteristics and multiplex performance. In Fig. 2 and 3 selectivity curves obtained by numerical simulation are shown. In the tables below the residual diffracted intensity is listed for larger shift distances and tilt angles respectively. Although it is hard to compare shift and angle selectivities it can be seen that the counter-propagating setup produces less residual light compared to the plane wave setup and also the collinear setup. This suggests that the inter-hologram crosstalk of the counter-propagating concept is lower compared to the other setups. A direct comparison of the inter-hologram crosstalk produced by shift-multiplexed holograms is shown in Fig. 4. The ratio of the cumulative intensity resulting from an increasing number of one-dimensional multiplexed holograms with respect to the intensity of a single hologram is plotted. In case of the counter-propagating setup the crosstalk is about 12% lower compared to the collinear setup.

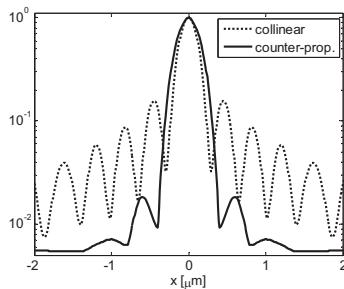


Fig. 2. Shift-selectivities

	$\eta_{\text{shift}}/\eta_0$	
	Collinear	Counter-prop.
2 μm	24.7e-3	5.5e-3
20 μm	5.5e-3	4.9e-3

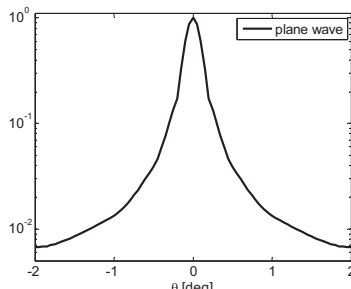


Fig. 3. Plane wave angle-selectivity

	$\eta_{\text{tilt}}/\eta_0$
	Plane wave
2 deg	6.6e-3
10 deg	5.6e-3

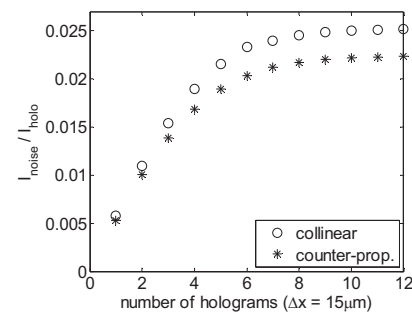


Fig. 4. Inter-hologram crosstalk build-up for collinear and counter-propagating setup. Holograms multiplexed at a distance larger than the diameter of a single hologram do not contribute to the cumulative crosstalk.

3. CONCLUSION

Numerical simulations have been performed to study material consumption and crosstalk characteristics of three different holographic setups. It could be shown, that a setup based on counter-propagating beams provides a better utilization of the holographic medium, a higher diffraction efficiency and a lower inter-hologram crosstalk than collinear and plane wave setups. From this point of view the counter-propagating setup seems to be a very interesting concept for a future holographic storage system.

REFERENCES

- [1] H. J. Coufal, et al., eds., "Holographic Data Storage" (Springer 2000)
- [2] K. Anderson and K. Curtis: Opt. Lett. 29, 1402.
- [3] H. Horimai, X. Tan, and J. Li: Appl. Opt. 44 (2005) 2575.
- [4] Tanaka et al.: Optics Express Vol 15 No. 24 (2007) 16196.
- [5] O. Matoba, et al., Appl. Opt. 45 (2006) 3270.
- [6] M. D. Feit and J. A. Fleck Jr.: Appl. Opt. 17 (1978) 3990.
- [7] J. W. Goodman: Introduction to Fourier Optics (McGraw-Hill, Singapore, 1996) 2nd ed.
- [8] Balázs Gombkötő, et al.: JOSA A, Vol. 24,7 (2007) 2075.

SESSION ThC: Holographic II and Super Resolution

Monarchy Ballroom
2:00 to 4:00 pm

Robert R. McLeod, Univ. of Colorado at Boulder
Satoru Tanaka, Pioneer Corp. (Japan)

Wobble alignment for angularly multiplexed holograms

Mark R. Ayres^{*}, Alan Hoskins, Paul C. Smith, John Kane
InPhase Technologies, Inc., 2000 Pike Rd., Longmont, CO, USA, 80501

ABSTRACT

Holographic data storage (HDS) devices derive their capacious storage density from highly selective physical processes such as the Bragg effect. A consequence of this selectivity is the requirement for very precise alignment during data recovery. In an angularly-multiplexed system, optimal recovery may require dynamic alignment in the Bragg-perpendicular direction (readout beam pitch) as well as the Bragg-selective direction (readout beam angle). Furthermore, while alignment information is not readily available from a recovered hologram, high speed recovery demands that each hologram be read in a single, well-aligned exposure. We present a wobble-tracking method that allows readout beam angle, pitch, and wavelength misalignment to be measured and corrected by a closed-loop servo during the readout of sequential holograms.

Keywords: Holographic and volume memories, Holography, Optical data storage

1. INTRODUCTION

Angle-multiplexed holograms are recorded in a volume medium by varying the reference beam angle in small increments. However, upon playback, misalignment, medium shrinkage, thermal expansion, and other distortions cause a displacement of the optimal recovery angles from their recording angles. This displacement typically contains a dominant low-frequency component, along with much smaller high-frequency excursions. The low-frequency component is a characteristic since the holograms are all subject to the same dimensional distortion. Attempting to recover the holograms at the original recording angles would result in errors and/or reduced margin in locations where the displacement is high.

The purpose of this algorithm is to provide an estimate of the optimal position for the next hologram in sequence using information available from previously recovered holograms. The available information consists only of a scalar quality metric (for example SNR or brightness) of the previous holograms. The method can be described as using two conceptual steps: 1) derive a feedback error signal which is an estimate of the displacement from the optimal recovery position for each hologram; 2) apply the feedback signal as input to a compensation algorithm that produces one or more axis control commands to be applied for the recovery of subsequent holograms. In this analysis, the method resembles a servo control system, and many of the techniques of analysis and implementation for that field of study are applicable, and hence will not be developed in this brief overview.

2. THE WOBBLE ERROR SIGNAL

The SNR quality metric is used as the basis for the displacement error signal. SNR is calculated by embedding known data patterns within each hologram (referred to as “reserved blocks” [1]), and measuring the fidelity of the detected

pattern according to a formula, e.g., $SNR = 20 \log_{10} \left(\frac{\mu_1 - \mu_0}{\sigma_1 + \sigma_0} \right)$ where μ_1 and μ_0 are the measured means of the

detected ones and zeros in the reserved blocks, and σ_1 and σ_0 are their respective standard deviations. SNR for a given hologram as a function of readout beam angle generally has the form of a sharp peak, with SNR reaching a maximum value at an optimal angle and falling off steeply as the angle deviates from optimal, e.g., approximating

$$SNR(\phi) = SNR_0 - C (\phi - \phi_0)^2, \quad (1)$$

^{*} email: markayres@inphase-technologies.com; website: inphase-technologies.com

where ϕ is the external reference beam angle with respect to the medium normal, ϕ_0 is the optimal readout beam angle, and C is a constant defining the quadratic peak shape. SNR_0 , the peak SNR of the hologram, is not known in advance and indeed varies somewhat from hologram to hologram. An alignment error indicating both the sign and magnitude of the readout beam angle error, $err = \phi - \phi_0$, cannot be determined from a single SNR sample.

However, from the SNR peak model it is apparent that the *derivative* of $SNR(\phi)$ is proportional to err . The readout beam angle error can thus be determined from two SNR samples offset in ϕ :

$$err = \phi - \phi_0 = \frac{SNR(\phi - \Delta\phi) - SNR(\phi + \Delta\phi)}{4 C \Delta\phi} \quad (2)$$

where $\Delta\phi$ is a constant readout beam angle offset. In order to estimate err while recovering a sequence of holograms with only one exposure which is near the SNR peak for each hologram, it is necessary that 1) $\Delta\phi$ be small; and 2) each err sample is calculated from the difference in SNR of *two different* holograms within the sequence, i.e.,

$$err_h \approx \frac{(-1)^h [SNR_h(\phi_h - (-1)^h \Delta\phi) - SNR_{h-1}(\phi_{h-1} + (-1)^h \Delta\phi)]}{4 C \Delta\phi} \quad (3)$$

where the subscript denotes the hologram number in the sequence. The nominal readout beam angles ϕ_h and ϕ_{h-1} should be separated by the true spacing between holograms h and $h-1$ in order to produce the most accurate estimate. Furthermore, the alternating sign factor $(-1)^h$ has been introduced so that even-numbered holograms are always sampled at $-\Delta\phi$ from their nominal positions, while odd-numbered holograms are sampled at $+\Delta\phi$. Thus, an error sample can be generated with every new hologram when the alternating “wobble” offset $\Delta\phi$ is applied to the sequential recovery angles. The method is analogous to “wobble tracking” employed for track following by some optical disk drives [2].

3. PITCH AND WAVELENGTH ERROR SIGNALS

In addition to the angle error signal, a wobble imparted to the readout beam recovery angles can be used to determine other misalignments. This is possible because the presence of these angular misalignments causes the wobble offset to produce a shift in the best Bragg-matched region of the holographic image. This shift can be detected as a change in the position of the intensity centroid of the detected image.

The principle for this measurement is illustrated in Figure 1. The wave vectors \vec{k}_{p1} and \vec{k}_{p2} for two readout beams at slightly different angles are indicated by the arrows, and the locus of the polarization density distribution created by the interaction of a readout beam with the hologram is indicated by the red patch. In a perfectly aligned system, the polarization density patch would lie entirely on the surface of the k-sphere (area in dashed lines), but in the figure a tilt error has been introduced. This is manifested as a clock-wise rotation of the patch about an axis parallel to \vec{k}_x passing through the tip of the readout beam wave vector, as indicated by the circular arrow. The rotation causes the vertical edges of the polarization density patch to separate from the surface of the k-sphere, indicating a Bragg-mismatch. This causes diminished diffraction efficiency at the edges of the holographic image, as illustrated by the paler shading.

When holographic exposures are taken at the two angular readout beam offsets indicated by wave vectors \vec{k}_{p1} and \vec{k}_{p2} , the polarization density patch translates up and down as though it were rigidly attached to the tip of readout beam wave vectors. This causes the line of intersection between the patch and the k-sphere to shift rightwards (for \vec{k}_{p1}) or leftwards (for \vec{k}_{p2}), and hence the bright, best Bragg-matched part of the image to shift from right to left. This may be detected as a shift in the centroid of the image intensity pattern in the y direction. Conversely, if the rotation is counter clock-wise instead of clock-wise, then the intensity centroid will shift from left to right instead of right to left, with the amount of centroid shift proportional to the degree of rotation.

In a similar manner, the centroid shifts in response to media rotation, or rotation about an axis parallel to \vec{k}_z . In fact the method cannot actually distinguish between these two rotation components, but instead it will indicate a ‘zero’ alignment error (i.e., no centroid shift) when the hologram is optimally Bragg-matched. Thus, a small media rotation misalignment can be corrected by a small readout beam tilt, and vice-versa. Furthermore, in a real-life system, the optimal medium

rotation angle/readout beam tilt angle settings will change within an angle-multiplexed hologram stack due to out-of-plane errors in the beam steering optics, etc... In the preferred embodiment, one of these axes (say, media rotation) is set to some nominal, invariant value for a hologram stack, and the other (say, readout beam tilt) is dynamically adjusted in response to the centroid feedback signal in order to optimize the Bragg-matching of each hologram.

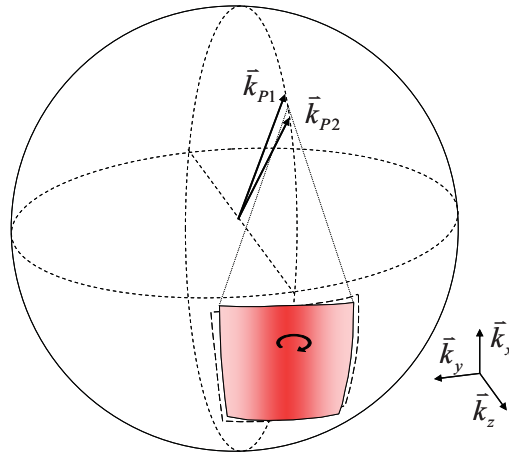


Figure 1. Principle of centroid shift error signal in k-space.

In yet another embodiment, a centroid shift in the x direction (as opposed to the y direction as above) can be used to indicate a wavelength or dimensional mismatch. Again referring to Figure 1, a wavelength mismatch would be indicated graphically by changing the radius of the k-sphere and the length of wave vectors \vec{k}_{p1} and \vec{k}_{p2} , and an isotropic dimensional mismatch (caused, say, by thermal expansion or contraction of the medium) would be graphically indicated by changing the radius of curvature of the red polarization density patch. In either case, the curvature of the k-sphere would no longer match the curvature of the polarization density patch, and so the polarization density patch would separate from the k-sphere at the *top and bottom* of the patch when best Bragg-matched in a horizontal locus across the middle. Thus, the readout beam angle wobble will cause the locus of highest intensity to shift *up and down*, which may be detected as a shift in the x centroid of the intensity in the detected images.

In an integrated system, the wobble offset can be used to derive all three error signals, which are in turn used to close all three servo loops. Because changes in the alignment of sequential holograms are slowly-varying, and because the error signals are relatively noisy, a low-gain servo compensator is required. We have demonstrated a readout angle servo that recovers sequential holograms with less than 0.15 dB average SNR loss per hologram when compared to careful optimal alignment. The servo uses a recursive least squares filter to predict the positions of subsequent holograms based on a linear LS fitting to the previous hologram positions estimated from the error signal.

4. CONCLUSIONS

We have presented a method for dynamic alignment in an angle-multiplexed HDS system. The method allows for the simultaneous measurement of readout beam angle, pitch, and wavelength misalignment by imparting an alternating “wobble” offset in the sequential recovery angles. A low-gain servo compensator is used to correct the slowly varying alignment errors.

^[1] M. Ayres, A. Hoskins, K. Curtis, “Image oversampling for page-oriented optical data storage,” *Appl. Opt.* **45**, 2459-2464 (2006).

^[2] A. B. Marchant, *Optical Recording: A Technical Overview*, pp. 180-181, Addison-Wesley Publishing (1990).

Three-dimensional Fourier Optics analysis of holographic optical data storage systems

George Barbastathis

Department of Mechanical Engineering
Massachusetts Institute of Technology

ABSTRACT

A theoretical method for analysis and design of holographic memories is presented. The memory is expressed as a 3D pupil in an imaging system. It is shown how practical memory performance metrics, such as interpage—intrapage crosstalk and defocus tolerance, can be understood and optimized using this approach.

Keywords: Holographic data storage, volume holography, 3D Fourier Optics

1. INTRODUCTION

The analysis of holographic data storage systems is typically carried out either using Bragg theory,¹ or Coupled Mode theory.² Bragg theory is appropriate for weakly diffracting holographic memories, whereas Coupled Mode theory can also handle strongly diffracting cases. Both approaches typically assume holograms that have finite thickness in the longitudinal (axial) dimension but are infinite in the lateral dimension. Thus, volume diffraction effects such as Bragg angular and wavelength selectivity can be accounted for, but the more common diffraction effects on the reconstructed pages due to the finite aperture of the optical system cannot. A simple formula expressing the blur in the diffracted field due to the finite 3D size of the hologram as convolution with a “grating vector cloud” is given in section 9.7.4 of Goodman.³ Alternatively, diffraction effects due to the finite aperture can be decoupled from Bragg effects, and quantities such as “resolution” (*i.e.*, discriminating ability between grayscale values of adjacent pixels) defined based on the (paraxial) Rayleigh criterion.⁴

In this paper, we describe an approach that can model *coupling* effects due to Bragg diffraction and diffraction from the finite aperture. We show that, under certain conditions, the coupling is non-trivial, and may result in either reduced or enhanced diffraction artifacts in the reconstructed image. Our approach is based on a generalization of Fourier Optics to three-dimensional (3D) pupils; therefore, we refer to this approach as “3D Fourier Optics.” A holographic memory is a special case of a 3D pupil; other cases include various volume holographic imaging lenses.^{5–7} 3D Fourier Optics relies upon the weakly diffracting approximation, which is appropriate for multiplex holographic data storage because of the efficiency scaling laws of most holographic data storage materials.^{8,9} The development of the theory presented here uses the paraxial approximation and leads to intuitive closed-form results. However, the paraxial approximation is not necessary; indeed, 3D Fourier Optics has been used to compute non-paraxial effects, such as Seidel aberrations, in volume holographic imaging systems albeit at higher computational expense.¹⁰

2. BASIC THEORY

2.1 Geometry and notation

The geometry for recording and readout of a Fourier-plane holographic memory is shown in Figure 1(a). The volume holographic material is located at the pupil plane of a telescope consisting of lenses with focal lengths f_1 , f_2 , respectively. The hologram is assumed to be a slab of thickness L and aperture a . The slab cross-section is arbitrary; we will consider rectangular and parallelepiped shaped slabs as shown in Figure 1(b–c) in section 3.1, and cylindrical shaped slabs in section 3.2.

E-mail: gbarb@mit.edu; Mailing address: MIT 3-461c, 77 Massachusetts Ave., Cambridge, MA 02139, USA

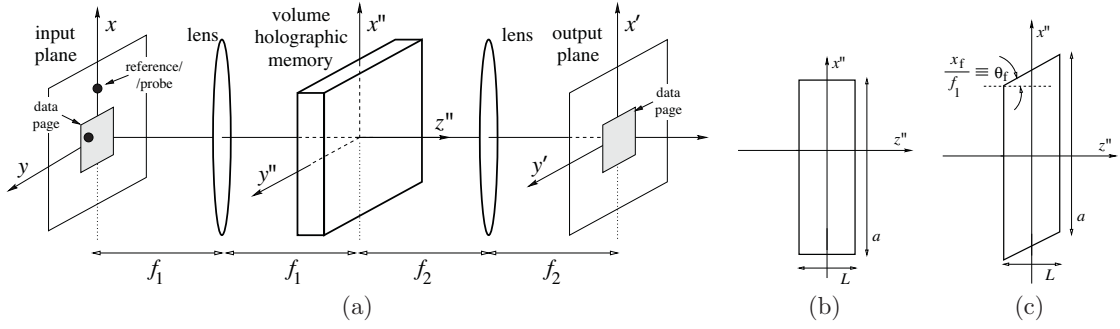


Figure 1. (a) Holographic memory recording and readout geometry. (b) Cross-section of a rectangular slab-shaped holographic memory. (c) Cross-section of a parallelepiped slab-shaped holographic memory.

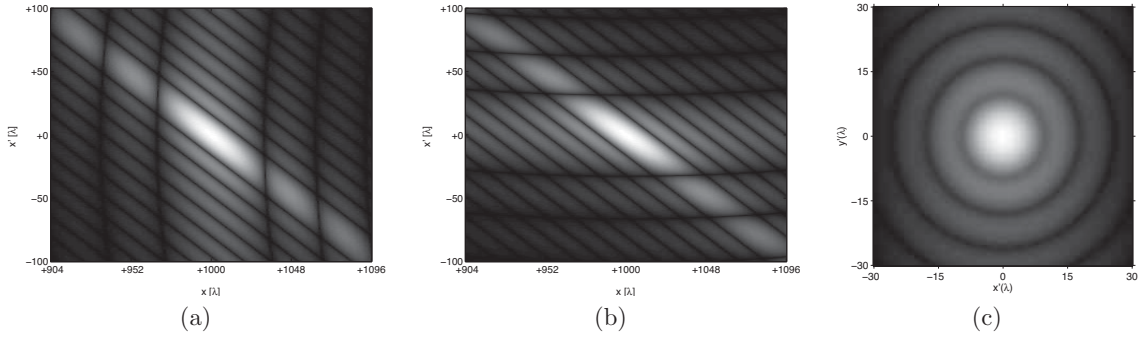


Figure 2. (a) Point-spread function of the memory shown in Figure 1(b) in response to angular detuning of the reference beam for $a = 250\lambda$, $L = 500\lambda$, and $f_1 = f_2 = 4 \times 10^3\lambda$. (b) Point-spread function of the memory shown in Figure 1(c) in response to angular detuning of the reference beam for the same parameters used in Figure 2(a). (c) Defocused response for a cylindrical slab-shaped hologram with the same parameters used in Figure 2(a), and longitudinal defocus of 64λ . The brightness plotted in this figure is $|q(x', y')|^{1/2}$.

2.2 The point-spread function

During recording, the fields generated by mutually coherent off-axis reference and on-axis signal (data page) beams $r(x, y)$ and $s(x, y)$, respectively, interfere at the pupil plane to record a hologram $\Delta\varepsilon(x'', y'', z'')$. For example, if the reference and signal fields are both point sources at coordinates (x_f, y_f) , (x_s, y_s) respectively on the input plane (denoted as solid dots in Fig. 1a) then the hologram consists of planar fringes. During readout, the signal beam is turned off, and the hologram is probed by a field $p(x, y)$. Our objective is to compute the field distribution $q(x', y')$ resulting at the output plane.

In the special case of a point source object, $q(x', y')$ is the *point-spread function (PSF)* of the holographic memory. Let

$$P(x'', y'', z'') = \exp\left\{i2\pi\frac{z''}{\lambda}\right\} \iint p(x, y) \exp\left\{-i2\pi\frac{xx'' + yy''}{\lambda f_1}\right\} \times \exp\left\{-i\pi\frac{(x^2 + y^2)z''}{\lambda f_1^2}\right\} dx dy. \quad (1)$$

represent the field generated by the probe in the vicinity of the pupil plane, and let $g(x'', y'', z'') = P(x'', y'', z'') \times \Delta\varepsilon(x'', y'', z'')$. The key result of 3D Fourier Optics is that

$$q(x', y') = \sqrt{\eta} G\left[\frac{x'}{\lambda f_2}, \frac{y'}{\lambda f_2}, \frac{1}{\lambda}\left(1 - \frac{x'^2 + y'^2}{2f_2^2}\right)\right], \quad (2)$$

where $\eta \ll 1$ is the diffraction efficiency, and $G(u, v, w)$ denotes the 3D spatial Fourier transform of $g(x'', y'', z'')$. An important consequence of this result is that the point-spread function of the holographic memory is strongly

shift variant. This is due to the Bragg selectivity of the 3D pupil (volume hologram.) Therefore, the readout field can be represented as a superposition integral but *not* as convolution of the signal field with the PSF.

3. APPLICATION TO HOLOGRAPHIC DATA STORAGE SYSTEMS

3.1 Inter–page and intra–page crosstalk

Result (2) allows a convenient representation of inter–page and intra–page crosstalk, as shown in Figure 2(a–b) for the on–axis data page pixel $x_s = 0$ and a plane–wave reference originating at $x_f = 10^3\lambda$. The horizontal axis is the probe coordinate x while the vertical axis is the output space coordinate x' (both in units of wavelength λ). Therefore, a vertically oriented cross–section of this diagram centered at the Bragg–matched location $x \equiv x_f$ represents the inter–page crosstalk; whereas a horizontally oriented cross–section of the diagram centered on the pixel’s Gaussian image location $x' \equiv x_s$ represents the intra–page crosstalk. Note the strong dependence of the two types of crosstalk on the hologram cross–section. The parallelepiped hologram, which results often in practice from the overlap between reference and signal beams in the holographic material during recording, produces stronger intra–page crosstalk sidelobes than the rectangular hologram. The opposite is the case for inter–page crosstalk.

3.2 Effects of defocus

The same formulation may be used to evaluate the results of defocus. An example of a rather severe case is shown in Figure 2(c). This diagram is the intensity produced at the output plane (x', y') for the on–axis data page pixel read out by a defocused reference. The familiar Fresnel rings appear in the defocused PSF, but they are masked by a vertically oriented aperture due to the Bragg selectivity of the volume holographic memory.

4. CONCLUSIONS AND DISCUSSION

The 3D Fourier Optics formulation provides a useful and intuitive framework for analysis and optimization of holographic memories under rather general conditions. Since (2) takes into account the wavefronts of the reference, signal, and probe fields in predicting the response, the approach is also compatible with optical design software to include Seidel and higher–order aberration effects due to the memory recording and readout optics.

REFERENCES

- [1] Leith, E. N., Kozma, A., Upatnieks, J., Marks, J., and Massey, N., “Holographic data storage in three-dimensional media,” *Appl. Opt.* **5**, 1303–1311 (August 1966).
- [2] Kogelnik, H., “Coupled wave theory for thick hologram gratings,” *Bell Syst. Tech. J.* **48**, 2909–2947 (November 1969).
- [3] Goodman, J. W., [*Introduction to Fourier Optics*], Roberts & Company, 3rd ed. (2005).
- [4] Yi, X. M., Yeh, P., and Gu, C., “Statistical analysis of cross–talk noise and storage capacity in volume holographic memory,” *Opt. Lett.* **19**(9), 1580–1582 (1994).
- [5] Barbastathis, G., Balberg, M., and Brady, D. J., “Confocal microscopy with a volume holographic filter,” *Opt. Lett.* **24**(12), 811–813 (1999).
- [6] Sinha, A., Sun, W., Shih, T., and Barbastathis, G., “Volume holographic imaging in the transmission geometry,” *Appl. Opt.* **43**(4), 1533–1551 (2004).
- [7] Sinha, A., Liu, W., Psaltis, D., and Barbastathis, G., “Imaging with volume holograms,” *Opt. Eng.* **43**(9), 1959–1972 (2004).
- [8] Brady, D. and Psaltis, D., “Control of volume holograms,” *J. Opt. Soc. Am. A* **9**(7), 1167–1182 (1992).
- [9] Moser, C., Maravic, I., Schupp, B., Adibi, A., and Psaltis, D., “Diffraction efficiency of localized holograms in doubly doped LiNbO₃ crystals,” *Opt. Lett.* **25**(17), 1243–1245 (2000).
- [10] Watson, J. M., Wissman, P., Oh, S. B., Stenner, M., and Barbastathis, G., “Computational optimization of volume holographic imaging systems,” in [*Proceedings of the OSA Topical Meeting on Computational Optical Sensing and Imaging (COSI)*], (2007).

Intra-signal modulation in holographic memories

Mark R. Ayres^{*a}, Robert R. McLeod^b

^aInPhase Technologies, Inc., 2000 Pike Rd., Longmont, CO, USA, 80501;

^bDepartment of Electrical and Computer Engineering, University of Colorado, Campus Box 425, Boulder, CO 80309

ABSTRACT

Holographic memories record an interference pattern between a signal beam and a reference beam. Interference between different signal modes – *intra-signal modulation* – may be recorded as well. These spurious cross-terms can cause diffraction noise in the recovered holograms. We analyze intra-signal modulation and show that the noise magnitude is strongly impacted by the signal beam data modulation scheme, as well as other factors. Coherent and incoherent bounds for the noise magnitude are estimated and related to ideal binary ASK (amplitude-shift-keying) and PSK (phase-shift-keying) signal modulation.

Keywords: Holographic and volume memories, Holography, Optical data storage

1. INTRODUCTION

Data in holographic memories are typically recorded in a photo-sensitive medium that develops a volumetric dielectric modulation pattern, $\Delta\epsilon(\vec{r})$, in response to the integrated optical intensity, $I(\vec{r})$, of the recording illumination, i.e.,

$$\Delta\epsilon(\vec{r}) = ST I(\vec{r}) = ST \left[E_R(\vec{r})^2 + |E_S(\vec{r})|^2 + E_R^*(\vec{r})E_S(\vec{r}) + E_R(\vec{r})E_S^*(\vec{r}) \right], \quad (1)$$

where S is the sensitivity of the recording medium, T is the exposure time, and $\vec{r} = \{x, y, z\}$ is the spatial coordinate vector. E_S and E_R are the scalar optical fields of the signal and reference beams, respectively. The third and fourth terms of equation (1) represent the desired data-bearing fringes. The first and second terms (sometimes known as the *ambiguity*) are completely spurious from the standpoint of data retention. It is the second, intra-signal, term, $ST|E_S(\vec{r})|^2$, which is both densely-modulated and Bragg-matched to the signal beam, that concerns us here.

Holographers have long been concerned with the effects of the intra-signal term, especially in the Fourier-plane recording geometry favored by data storage researchers. For traditional binary ASK data modulation where each data bit is represented by a pixel in either an ‘on’ or ‘off’ state, the intra-signal term contains a large D.C. component which is manifested as an intense ‘hot spot’ in the Fourier plane. Large intensity inhomogeneities like this prevent the faithful reconstruction of the signal beam both because of non-linear recording (e.g., the medium’s inability to develop a large local $\Delta\epsilon(\vec{r})$), and because diffraction is itself non-linear in the strongly-modulated regime. This problem is typically addressed by using a phase mask to homogenize the recording intensity [1]. We show here, however, that even linear-regime intra-signal noise may severely degrade the reconstructed signal in cases where the intra-signal noise terms are mutually coherent.

2. ANALYSIS

The recorded intra-signal dielectric modulation pattern and its interaction with the reconstructed signal beam may be represented in *k-space*, i.e., the Fourier transform space of the three dimensional optical fields and dielectric modulation patterns involved. The *k-space* representation of a signal beam field, $E_S(\vec{k})$, composed using an SLM with square pixels of size p on a square grid of spacing d may be given by

* email: markayres@inphase-technologies.com; website: inphase-technologies.com

$$E_S(\vec{k}) = \frac{A}{k_0/f} \sum_g \sum_h D(g,h) \text{rect}\left(\frac{k_x - k_0 g d/f}{p k_0/f}\right) \text{rect}\left(\frac{k_y - k_0 h d/f}{p k_0/f}\right) \text{sinc}\left[\left(k_z - \sqrt{(k_0 n)^2 - \left(\frac{k_0 g d}{f}\right)^2 - \left(\frac{k_0 h d}{f}\right)^2}\right) \frac{L}{2}\right], \quad (2)$$

where A is the signal amplitude, k_0 is the recording wave number in free space, and f is the focal length of the objective lens, which forms a Fourier plane in the middle of the recording layer with thickness L . The k-space coordinate vector is $\vec{k} = \{k_x, k_y, k_z\}$, and g and h are SLM pixel coordinate indices. $D(g,h)$ is the data pattern, where $D(g,h) \in \{0,1\}$ for binary ASK, and n is the homogeneous refractive index. Fourier filtering of the signal has been neglected.

The intra-signal dielectric modulation pattern $\Delta\varepsilon_S(\vec{k})$ is proportional to the intensity of the signal beam, which is distributed as the 3D autocorrelation of the optical field in k-space, i.e.,

$$\Delta\varepsilon_S(\vec{k}) = ST E_S(\vec{k}) \otimes E_S(\vec{k}), \quad (3)$$

where \otimes is the cross correlation operator. We are interested in the diffraction of a reconstructed signal pixel, $E_{g,h}(\vec{k})$, by $\Delta\varepsilon_S(\vec{k})$. In the weak (Born) limit, this diffraction noise field can be written as a convolution in k-space: [2]

$$E_N(\vec{k}) = \frac{j k_0^2}{2 k_z} \Delta\varepsilon_S(\vec{k}) * E_{g,h}(\vec{k}) \Big|_{|\vec{k}| = n k_0}. \quad (4)$$

Equations (2), (3) and (4) are graphically represented in Figure 1. Figure 1 (a) shows the locus of $E_S(\vec{k})$ propagating within the media volume, with each data pixel represented as a square patch on the surface of the k-sphere with a k_z uncertainty determined by the sinc-shaped transform of the media slab. $\Delta\varepsilon_S(\vec{k})$, the autocorrelation of $E_S(\vec{k})$ is shown in Figure 1 (b). The dots represent individual inter-pixel gratings arrayed in a manifold that is extremely dense near the origin, and increasingly sparse at higher frequencies. Finally, Figure 1 (c) shows the convolution of $\Delta\varepsilon_S(\vec{k})$ by reconstructed pixel $E_{g,h}(\vec{k})$. This represents an inhomogeneous polarization density within the medium, and those components that lie on the k-sphere (indicated by the dotted red line) constitute propagating optical noise.

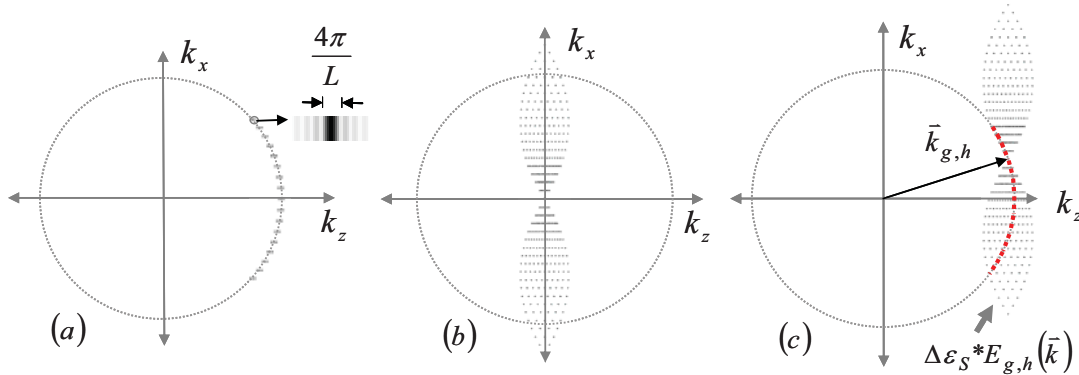


Figure 1. Graphical representations in k-space of (a) signal field, $E_S(\vec{k})$; (b) intra-signal modulation pattern, $\Delta\varepsilon_S(\vec{k})$; and (c) evaluation of optical noise from single reconstructed signal pixel g,h diffracted by $\Delta\varepsilon_S(\vec{k})$.

Each reconstructed pixel radiates noise into every other reconstructed pixel mode, and conversely, each pixel mode receives noise from every other pixel. There are very many very weak inter-pixel gratings overlapping within the intra-signal manifold. We can make an order-of-magnitude approximation of the total noise power by estimating the diffraction efficiency of each inter-pixel grating, the effective number of inter-pixel gratings lying on the k-sphere, and the phase relationship among the contributing inter-pixel fields. We relate the diffraction efficiency η_{ISM} of a single

inter-pixel gating to the hologram diffraction efficiency, η , by $\eta_{ISM} = \eta / \rho N_{pix}^2$ where N_{pix} is the number of signal pixels and ρ is the reference to signal beam intensity ratio. The effective number of inter-pixel gratings contributing to the noise is determined by estimating how densely they overlap at the intersection with the k-sphere (as illustrated in Figure 2), and then summing over the overlapping positions.

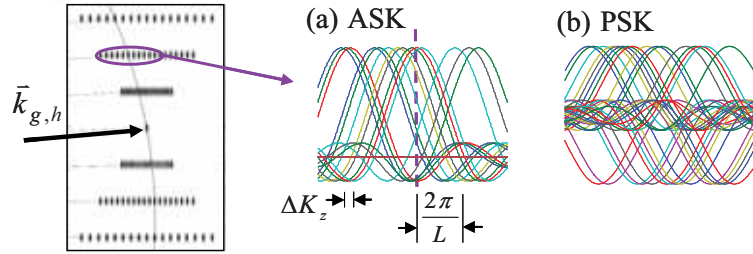


Figure 2. Detail of Figure 1 (c) illustrating sinc-shaped inter-pixel polarization terms densely overlapping in k_z near the k-sphere summing (a) coherently for ASK signal modulation; and (b) incoherently for PSK signal modulation.

Applying suitable approximations to equation (3), we find that the spacing of inter-pixel grating overlap, ΔK_z , falls inversely with distances Δg and Δh from the center of the modulation pattern. Selecting the center g, h SLM pixel as representative, we sum over the whole pattern to obtain an approximation for the effective number of gratings:

$$N_{eff} \approx 4 \sum_{\Delta g=1}^{\frac{1}{2}N_{pix}^{1/2}} \sum_{\Delta h=1}^{\frac{1}{2}N_{pix}^{1/2}} \frac{2\pi/L}{(\Delta g + \Delta h)(k_0 d^2/n f^2)} \approx \frac{2.76 n f^2 \lambda}{L d^2} N_{pix}^{1/2}. \quad (5)$$

N_{eff} indicates the coherent sum of the inter-pixel noise fields as in the ideal ASK-modulated signal of Figure 2 (a). Alternatively, in a binary PSK-modulated signal where zeros and ones are transmitted with opposite phases ($D(g, h) \in \{-1, +1\}$), the inter-pixel noise fields would largely cancel, yielding an RMS sum rather than a coherent sum of the contributing noise fields as illustrated in Figure 2 (b). Further assuming that N_{eff} is the number of components for this RMS sum, we arrive at expressions for the weak diffraction efficiency of the noise process:

$$\eta_{ASK} = \frac{1}{4} \beta^4 [M N_{eff}]^2 \frac{\eta}{\rho N_{pix}^2}, \quad \eta_{PSK} = \frac{1}{4} \beta^4 [M N_{eff}] \frac{\eta}{\rho N_{pix}^2} \quad (6)$$

where β is the pixel ‘on’ rate and M is the number of multiplexed pages. These may differ by a factor of $>10^8$ in a high density system. For a hypothetical megapixel system with $M=1000$, we find $\eta_{ASK} \approx 67$ (i.e., stronger than Born-regime diffraction), and $\eta_{PSK} \approx 5 \times 10^{-7}$, representing the difference between a feasible and an infeasible HDS system.

3. CONCLUSIONS

We have estimated the strength of intra-signal modulation noise and demonstrated that it can be very large when the inter-pixel gratings add coherently, and very small when they add incoherently. Ideal binary ASK and PSK signal modulation were shown to exemplify the two cases. Real systems will likely fall between these two extremes, with phase masks, shift multiplexing, and other opto-mechanical perturbations serving to decohere otherwise coherent intra-signal noise in a traditional ASK-modulated system.

References

- [1] C. B. Burckhardt, “Use of a Random Phase Mask for the Recording of Fourier Transform Holograms of Data Masks,” *Appl. Opt.* **9**, 695-700 (1970).
 [2] M. R. Ayres, *Signal Modulation for Holographic Memories*, Ph. D. Dissertation, University of Colorado at Boulder, (2007).

Sparse modulation codes for channel with media saturation

Lakshmi D Ramamoorthy*, B. V. K. Vijaya Kumar
Carnegie Mellon University, 5000 Forbes Avenue, Pittsburgh, PA, USA 15232

ABSTRACT

Channel model with media saturation was built to simulate data pages. We observed a trade off between the relative write transfer rates and bit error rate.

Keywords: Sparse modulation codes, reverse concatenation, relative write transfer rate

1. INTRODUCTION

Sparse modulation coding is an encoding scheme so that the number of ones is much smaller than the number of zeros in any small region of a data page. Sparse modulation codes have been proposed in the past [1-3] for holographic data storage (HDS) because the appropriate sparse code can increase the total storage capacity by about 15%. A HDS channel is modeled to have an output signal-to-noise ratio (SNR) that decreases with number of stored pages M as $\text{SNR} \propto 1/M^2$ [1]. As more pages are stored, the diffraction efficiency decreases as the square of the number of pages, thus setting a limit on the number of pages that can be stored and reliably retrieved. It was also established in [1] that, as fewer “on” pixels occurs in a data page, the diffraction efficiency per pixel increases. The motivation for sparse codes has been that, by reducing the number of “on” pixels per page of N pixels we can store more pages before the diffraction efficiency once again limits the reconstruction fidelity. While increasing sparsity will facilitate the storage of more pages this will be at the expense of reducing the user information per page due to the code rate loss associated with sparse encoding. This suggests a tradeoff between storing more pages while reducing user information per page. It has been shown in refs. [1,2] that the overall effect will be a net gain in storage capacity for some choices of the ratio of ones to the total pixels in the page (which is 25%).

2. CHANNEL MODEL WITH MEDIA SATURATION

Channel simulator described in [4] with modification to accommodate media saturation is used to simulate data pages for the experiments. The conventional HDS optical system is a two lens arrangement where a page of binary data is placed in the spatial light modulator (SLM) plane and its Fourier transform (obtained with the first lens system) is recorded in the holographic medium. This is called the 4-focal length architecture. During readback, a reference beam illuminates the medium at the specified angle and the hologram is deflected off. Inverse FT is taken by the second lens and the output appears on the camera. The channel simulator parameters used are amplitude contrast ratio = 10, light drop from center to corners = 10%, SLM non-uniformity = 1%, SLM fill factor = 95%, frequency plane aperture = Nyquist size, camera fill factor = 40%, optical noise variance = 0.017, optical noise mean = 0, electronic noise variance = 0.0014, electronic noise mean = 0.43, dark noise variance = 1%, dark noise mean = 0 and quantization = 10 bits. These parameters are opted because they closely match the real data.

In the Fourier plane of the data page huge intensity peaks are present at the zero spatial frequency since the data page contains only positive values. Recording such wavefronts requires an extremely large dynamic range from the holographic material or the high intensity at the Fourier plane saturates the recording material. We adopt the saturation modeling scheme for the azobenzene polymers (candidate HDS recording materials) described in ref. [5]. In this reference, experimental results on the saturation behavior of the holographic material were studied. The applicability of the experimental results and also its usefulness during computer simulations for the holographic channel is shown. From their studies, the expression for diffraction efficiency takes the form

*lakshmidr@gmail.com; phone 1 412 268-4108; fax 1 222 555-876

$$\eta = C \frac{I_{obj} \times I_{ref}}{\left(1 + F \times (I_{obj} + I_{ref})\right)^2} \quad (1)$$

where I_{obj} is the object beam intensity and I_{ref} is the reference beam intensity. C and F are media parameters with optimal values of $C = 2.8$ a.u. and $F = 0.15 \text{ cm}^2/\text{W}$.

Next, we discuss the application of this saturation model in our channel simulator. After the aperture is applied to the 2D-Fast Fourier Transform (FFT) of the input data page we apply the saturation model. The diffraction efficiency is calculated from the reference beam intensity and the 2D-FFT (after aperture effect) of the input data page. The reference beam is given by $Re^{j2\pi\phi(x,y)}$. The intensities of the object and reference beams are used for calculating the diffraction efficiency. This diffraction efficiency is multiplied pointwise with the reconstructed wavefront, which effectively means the 2D-FFT after the aperture effect is multiplied pointwise with the calculated diffraction efficiency. The inverse FT is taken after that and the other channel impairments such as optical noise, camera fill-factor, electronic noise, dark noise and quantization are applied. We choose $R = 1000$ in our simulation and $\phi(x, y)$ is given by $\sin\theta_x x + \sin\theta_y y$, where we assume the angle of incidence in the x and y direction are θ_x and θ_y , respectively. For the angle of incidence, we can choose values ranging from $-\pi$ to π and the simulation results do not change much. However, varying the parameter R affects the SNR. Results are presented for the choice $R=1000$ as benefits of sparseness is predominantly observed because the data page (of size 1024×1280) SNRs are reasonable and of a varied range.

3. SIMULATION RESULTS

3.1 Importance of sparseness

We study the necessity for sparseness by simulating data pages with a range of sparseness and observing their SNRs. There is also a rate loss associated with the data pages that have other than 50% zeros and ones. We can compensate for that rate loss by multiplexing more number of pages in such cases. First, we find the associated rate loss then calculate the number of pages that need to be multiplexed to achieve the same capacity. This reflects in the page diffraction efficiency which gets multiplied by square of the rate of the code used to achieve the percentage of ones and zeros in the page. This is because diffraction efficiency equals $(M\#/M)^2$, where $M\#$ is the HDS recording medium's dynamic range parameter [6] and M is the number of pages multiplexed in a given volume of the media. Hence, in our channel simulator depending on the rate of the modulation code we multiply the associated constant to the Fourier transform of the data page. The rate of the modulation code is determined by computer search for the highest rate code for a maximum codeword length of 100 and the precision of the binomial coefficients to perform the encoding/ decoding to be up to 10^{15} (details in [1]). The SNR (defined in [4]) for data pages simulated with media saturation and the multiplication factor for the diffraction efficiency to compensate for the modulation code rate are plotted in Fig. 1a.

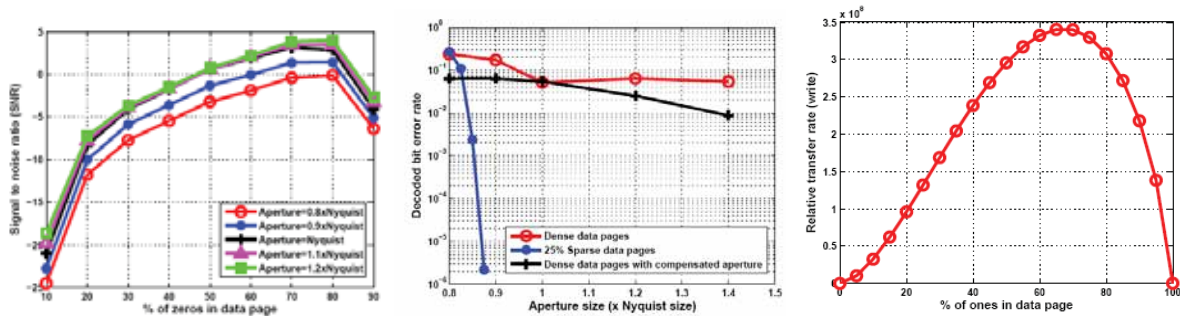


Fig. 1. (a) Channel with media saturation and modulation code rate compensation, (b) Sparse modulation and LDPC ECC performance on sparse data pages generated with media saturation and (c) Relative write transfer rate for various sparsity in the data page.

3.2 Reverse concatenated sparse modulation code and low-density parity-check (LDPC) code

Usually the sparse modulation decoder followed by the LDPC decoder appears in the read channel of HDS system. However, the output of the sparse modulation code is hard bits and the LDPC decoder required soft information hence we resort to reverse concatenation of the modulation code and error correction code (ECC). The sparse modulation code

used is a rate 17/24 code that produces 25% ones in each codeword. The ECC used is a rate 1/2, regular, quasi-cyclic LDPC code with column weight of 3 [7]. The decoder performance comparison for sparse and dense data pages (pages with 50% zeros and ones) simulated using a channel with media saturation (described in Section 2) is provided in this section. However, there is a rate loss of 17/24 in the case of sparse data pages due to the rate of the sparse modulation codes. To compensate for that rate loss, we multiply the aperture size by 24/17 for dense data page case. Because of the larger aperture, the ISI is lower for the dense data pages compared to the sparse data pages. The overall capacity for the dense and the sparse data pages would also be about the same in this case. The results are shown in Fig. 1b. The sparse data pages have superior BER compared to both the dense data pages and the aperture compensated dense data pages. The sparse data pages decodes with no errors at aperture of $0.875 \times \text{Nyquist}$ size whereas there are several errors even at an aperture of $1.4 \times \text{Nyquist}$ size for both the other two cases. The dense data pages exhibits no decrease in BER at the apertures greater than Nyquist size up to $1.4 \times \text{Nyquist}$ size, this is because the media saturation causes the SNR to be about the same for apertures in the range of Nyquist to $1.4 \times \text{Nyquist}$ size. This is seen in Fig. 1a.

3.3 Relative write transfer rate

For different sparsity in data pages, the relative recording rate (RR) varies which in turn affects the relative write transfer rate [8]. Though sparse data pages yield good performance in terms of BER compared to dense data pages, the relative transfer rate is also an important figure of merit. Assuming that the modulation ratio (ratio of the reference beam intensity to the object beam intensity) is constant, the relative recording rate depends on the energy in the page. Page with all ones in it has the highest energy ($z=1$). Pages with other percentages of zeros and ones in them get less energy ($z < 1$) to the media and hence they will record slower. The modulation ratio of one is assumed for example purpose to illustrate the effects on transfer rate. Assuming certain values for reference and signal transmission like 0.9 and $0.4z$, respectively, and using the split of signal and reference as n , then $0.9 \times n = (1-n) \times 0.4 \times z$ for modulation ratio =1. Total energy to the medium is $2 \times \text{reference beam intensity}$ and $RR = E(z)/E(1)$, where $E(z)$ is the energy as a function of the level of sparsity (z) and $E(1)$ is the energy when $z=1$. $RR = E(z)/E(1) = 2 \times 0.9 \times n / (2 \times 0.9 \times (0.4/1.3)) = 0.4z / (0.31 \times (0.9+0.4z))$. We now have RR as a function of z . The relative write transfer rate (TR_w) is equal to $RR \times (\text{information in a page}) / (\text{average page delay})$. There are several factors that determine the average page delay, for illustrating an example we choose it to be 1 ms. The number of message bits in a data page (with equal ones and zeros) of size 1000×1000 is 5×10^5 because of the rate 1/2 ECC. Hence, for the different page sparsity the amount of information in terms of the number of message bits is the entropy normalized for a page of 1000×1000 pixels. We can now plot relative write transfer rate as a function of page sparseness, as shown in Fig. 1c. The relative write transfer rate peaks at about 70% ones in the data page.

4. CONCLUSION

Channel model with media saturation was used to simulate data pages which were used to demonstrate the importance sparseness in data pages by an increase in SNR for sparser data pages. We also concluded that, we can achieve high transfer rates if there are more ones (70%) in the page and low BER can be achieved if there are more zeros (75%) in the page. There is a trade off between the relative write transfer rates and BER.

REFERENCES

- [1] B. M. King and M. A. Neifeld, "Sparse modulation coding for increased capacity in volume holographic storage," *Applied Optics*, vol. 39, no. 35, pp. 6681–6688, 2000.
- [2] —, "Low-complexity maximum-likelihood decoding for shortened enumerative permutation codes for holographic storage," *IEEE Journal on Selected Areas in Communications*, vol. 19, no. 4, pp. 783–790, 2001.
- [3] B. M. King, G. W. Burr, and M. A. Neifeld, "Experimental demonstration of gray-scale sparse modulation codes in volume holographic storage," *Appl. Opt.*, vol. 42, no. 14, pp. 2546–2559, May 2003.
- [4] L. Ramamoorthy, S. Nabavi and B. V. K. Vijaya Kumar, "Physical Channel Model for Holographic Data Storage Systems," in *IEEE Lasers and Electro-Optics Society* (IEEE, 2004), pp. 997-998.
- [5] P. Varhegyi, A. Kerekes, S. Sajti, F. Ujhelyi, P. Koppa, G. Szarvas, and E. Lorincz, "Saturation effect in azobenzene polymers used for polarization holography," *Appl. Phys. B*, vol. 76, pp. 397–402, 2003.
- [6] G. B. F. Mok and D. Psaltis, "System metric for holographic memory systems," *Opt. Lett.*, vol.21, pp.896–898, 1996.
- [7] Z. Li and B. V. K. V. Kumar, "A class of good quasi-cyclic low-density parity check codes based on progressive edge growth graph," in *IEEE Asilomar Conference on Signals, Systems, and Computers*, vol.2, November 2004, pp.1990–1994.
- [8] K. Curtis, private communication, 2008.

Optical Super-Resolution through Super-Oscillations

Nikolay Zheludev

Optoelectronics Research Centre, University of Southampton, Highfield, Southampton, SO17 1BJ,
United Kingdom

www.nanophotonics.org.uk/niz

ABSTRACT

To achieve optical sub-wavelength concentrations of light beyond the near-field, the concept of super-oscillations recently flagged by Berry and Popescu, and demonstrated by our group using a quasi-crystal array of holes, provides a viable and less technologically challenging alternative to the approach based on negative-index super-lenses exploiting recovery of the evanescent fields.

Keywords: Optical super-resolution, nano-hole arrays, super-oscillation

1. THE QUEST FOR A SUPER-LENSE

Research on artificial photonic materials engineered on the sub-wavelength scale was catalyzed a few years ago by the incredible promise of a Veselago-Pendry optical negative refraction super-lens¹, capable of resolving features beyond the wavelength limit and imaging object located in the far-field into the far-field on the other side of the super-lens. The superlens is based on the recovery of the quickly fading evanescent fields close to the object by amplifying them in a slab of a negative-index material. Such evanescent, non-propagating fields are commonly believed to be the necessary components to form sub-wavelength field concentrations and to achieve sub-wavelength resolution. Indeed, it is accepted by the photonics community that the resolving power of optical instruments imaging objects located in the far-field, where evanescent waves have faded, cannot be far from that given by the Abbe/Rayleigh well-known rule, according to which the smallest distance between two points that can be seen as distinct with a lens is about the wavelength of light.

The bulk negative index material required for the super-lens should simultaneously exhibit negative permeability μ and a negative electric permittivity ϵ . Apparently, achieving super-resolution when the object and its image are placed in the sub-wavelength vicinity of the “lens” is a much simpler task than imaging a remote object. In this case only one material property (ϵ or μ) of the “lens” needs to be negative. The single-negative superlens suitable for the near-field was branded by John Pendry a “poor-man’s super-lens”. It was the silver nano-layer film “poor-man’s super-lens” which was used to demonstrate sub-wavelength resolution in the optical part of the spectrum independently by the groups of Richard Blaikie and Xiang Zhang. This was a remarkable and fundamental achievement which excited the research community. However, it had limited practical importance: the object and the image would have to be restrictively close - at a nanometer proximity to the metal film. This is why a lot of effort is being concentrated on the development of proper negative index materials – ones that exhibit both negative ϵ and μ values. In spite of recent numerous successful demonstrations of such *double-negative* optical materials, there is still substantial scepticism that such materials can, in the near future, be developed for use in the manufacturing of practical super-lenses. The resonance nature of the negative index that is coupled to the problem of losses inheritably limiting the optical bandwidth and transmission of the super-lens is the main fundamental obstacle.

This is why many researchers are now seeking alternatives to the negative index super-lens. For instance the Zhang group in Berkley came up with an ingenious idea of de-coupling evanescent waves on the image side of the “poor-man’s super-lens” with a grating to achieve a near-field to far-field imaging device. Another detour to the use of bulk negative index materials is to employ anisotropic materials with hyperbolic dispersion (the Engheta and Nurimanov groups): when evanescent waves enter such anisotropic media, their wavevectors are gradually compressed until they become propagating waves that could project a magnified image into the far-field. Although the “NIM detour” superlens has

demonstrated the unique ability of overcoming the “diffraction limit” the main limitation of all such designs is that *object still has to be in the near-field of the superlens*.

2. SUPER-RESOLUTION WITHOUT EVANESCENT FIELDS

However, there is a solution that can provide sub-wavelength concentrations of light beyond the near-field. For several decades the microwave community contemplated the idea of achieving antennas that beat the diffraction limit for directivity. In 1943, S. A. Shelkunoff published an analysis of the radiation pattern of a linear array of dipoles and proved that by properly adjusting the individual radiating elements, it is possible to achieve a much narrower radiation pattern than that of a conventionally-uniform array. Soon after that Bouwkamp and Bruijn and then Woodward and Lawson were able to prove that there were no theoretical limits to directivity whatsoever.

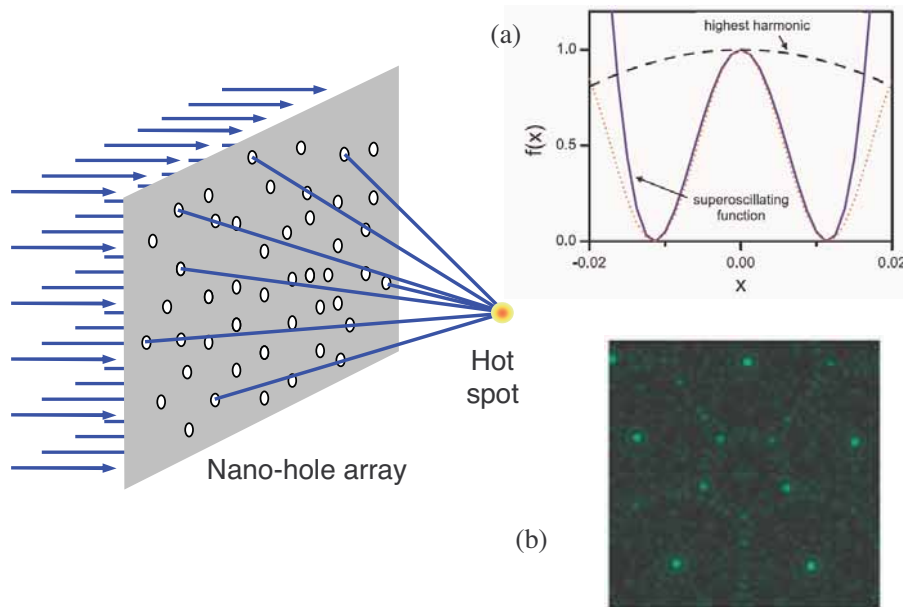


Figure 1. An array of nano-holes in a screen as a generator of super-oscillating field. It can create a sub-wavelength hot-spot when illuminated by a plane monochromatic wave. Inset (a) shows a function Eq. 1, super-oscillating at $x = 0$. Inset (b) shows an example of “photonic carpet” generated by quasi-periodic array of holes when sub-wavelength, super-oscillating hot spots have been observed

The idea of achieving super-resolution without evanescent fields recently had an independent revival in the domain of optics: Berry and Popescu, starting from earlier works on quantum mechanics, predicted that diffraction on a grating structure could create sub-wavelength localisations of light that propagate further into the far field than more familiar evanescent waves². They relate this effect to the fact that band-limited functions are able to oscillate arbitrarily faster than the highest Fourier components they contain, a phenomenon now known as superoscillation. The superoscillation idea challenges the well-established beliefs that a function whose Fourier spectrum is bounded can vary no faster than its highest frequency component.

This astonishing claim is clearly counter-intuitive to many and goes against all common experience. However, many examples of simple super-oscillating functions have been identified. For instance a limited series

$$f(x) = \sum a_n \cos(2\pi \times nx).$$

can generate super-oscillating functions relevant to optical scattering and microwave emission. For instance, $f(x)$ with $a_0 = 1$, $a_1 = 13295000$, $a_2 = -30802818$, $a_3 = 26581909$, $a_4 = -10836909$, $a_5 = 1762818$ and $a_n = 0$ is a super-oscillating function. It is plotted in Fig. 1 (solid curve) alongside with the highest frequency component (dashed curve). At $x = 0$, the function has a feature that oscillates times faster than its highest frequency component.

Aside from the fact that the super-gain antenna aims to create a narrow beam of electromagnetic radiation while the super-oscillation generator aims to achieve sub-wavelength localization of light at a distance from the grating, both ideas have the same underlying physics: the tailored interference of several coherent sources. However, the task of designing super-oscillation in optics could be a much easier problem than designing a super-gain microwave antenna. An array of nano-holes may be used in such a way that super-oscillation is achieved a few tens of microns away from it by tailored interference of light penetrating through the holes.

An optical generator of super-oscillating fields has recently been demonstrated with the use of a Penrose type quasi-crystal array of nano-holes in a thin metal film³. When illuminated with a coherent light source it creates a complex diffraction pattern on the other side of array - a few tens of microns away. At certain distances these patterns show well-defined, sparsely distributed sub-wavelength light localisations. Moreover, as such sub-wavelength localisations are formed by propagating far-fields, they can be projected to the far-field by a conventional lens⁴ or used as a sub-wavelength source in a scanning imaging device for imaging object located far beyond the near-field area. The question now is, whether such a pattern, or for that matter any super-oscillating grating-type field generator, could be used as a proper far-field to far-field super-resolution lens and whether it can achieve a sub-wavelength resolution.

A detailed analysis of these issues will be given in the talk.

REFERENCES

¹ J. B. Pendry, *Phys. Rev. Lett.* **85**, 3966 (2000)

² M. V. Berry and S. Popescu, *J. Phys. A: Math.Gen.* **39**, 6965 (2006)

³ F. M. Huang, N. Zheludev, Y. Chen, and F. J. Garcia de Abajo, *Appl. Phys Lett.* **90**, 091119 (2007)

⁴ F. M. Huang, Y. Chen, F. J. Garcia de Abajo, and N. I Zheludev, *J. Opt. A* **9**, S285-S288 (2007)

Comparison of a semiconductor and a phase-change material for application in a super-resolution ROM disk

G. Pilard, L. Pacearescu, H. Hölzemann, C. Féry

Deutsche Thomson OHG

Hermann-Schwer-Strasse 3, 78048 Villingen-Schwenningen, Germany

Phone: +49-7721-85-2766, Fax: ++49-7721-85-2241, E-Mail : christophe.fery@thomson.net

Abstract: Super-resolution ROM disks were manufactured with a semiconductor material (InSb) or a phase change material (AgInSbTe). A good CNR value of 40dBm was measured on a single tone pattern with 80nm pits for both materials. On random pattern with RLL (1,9) encoding and a channel bit length of 40nm, a bER of 1.10^{-3} was found for the InSb disk. However, it was impossible to decode from the AIST based disk. This is due to the unexpected reflectivity modulation that occurs when 2T marks are read-out.

Keyword : Super-Resolution

1. Introduction

Since Tominaga *et al.* have reported about the recording and the detection of marks below diffraction limit using a Sb mask layer [1], the super resolution technology appears to be a promising candidate for the 4th generation optical storage. Beside the potential for read-only, recordable or rewritable formats, its backward compatibility with BD format is a strong advantage.

It has been demonstrated that the super-resolution detection based on phase change or semiconductor material is related to a local change of the optical properties of the so called mask layer or detection layer. Further it is common understanding that a temperature increase due to the focused laser spot is required for the super-resolution effect of phase change materials [2][3]. Among them, chalcogenide materials like AgInSbTe have shown high CNR values of single-tone patterns below the diffraction limit [2]. This is a priori due to a low thermal conductivity and a strong optical non-linearity.

Recently, Hyot *et al.* disclosed a super-resolution ROM disk with a low band gap semiconductor InSb as a detection layer [4]. The bit error rate (bER) measured on a random pattern with a channel bit length of 40nm and Blu-ray tester was about 2.10^{-3} . It was observed that the super-resolution originates from a strong increase of the reflectivity when the laser intensity was above a threshold [5]. It is interesting to observe that this behavior is opposite to the “aperture mechanism” ascribed to chalcogenide materials like AIST where the transmittance of the mask layer is enhanced through the formation of a small aperture [2].

In order to compare the benefits of the “local metallization” to the “aperture formation”, super-resolution ROM disks were deposited with either $\text{In}_{0.5}\text{Sb}_{0.5}$ or $\text{Ag}_3\text{In}_5\text{Sb}_{71}\text{Te}_{21}$. We found that for both materials the CNR measured on a single tone pattern with 80nm pits is about 40dB. However, for the random pattern a bER of about 1.10^{-3} was calculated for the semiconductor based disk while it was impossible to decode from the phase-change based disk. A careful examination of the HF signal can explain this behavior. While the reflectivity decreases on 2T pits for InSb based disks, it increases for AIST based disk. Thus, the position of the smallest marks can be mistaken in the later case. The calculation of the far-field intensity using a Finite Element Method (FEM) ascribes the opposite signature for the smallest marks to the nature of the optical transition.

2. Experimental conditions and results

The super-resolution near-field structures (super-RENS) are sputtered on substrates where several patterns are pre-recorded. The results reported here are related to the following two stacks: substrate / ZnS:SiO₂ (70nm) / InSb (20nm) / ZnS:SiO₂ (50nm) / cover layer (0.1mm) and substrate / ZnS:SiO₂ (100nm) / AIST (25nm) / ZnS:SiO₂ (50nm) / cover layer (0.1mm). The various layer thicknesses are chosen after optimization of the CNR measured on single tone pattern.

The electrical characterization was performed on a Blu-ray tester (NA=0.85, $\lambda=405\text{nm}$), while the disk rotation speed was fixed at 4.92 m.s^{-1} . CNR measurements were made on a single tone pattern with 80nm pits. The spectral measurements are obtained on random pattern with (1,7) PP encoding and a channel bit length of 40 nm. The bER is measured from a random pattern with (1,9) RLL encoding with the same channel bit length.

Figure 1 shows the CNR as a function of the read-out power for AIST and InSb based disks. For both types of detection layers a CNR of >40dB could be achieved, whereas the super resolution behavior of InSb occurs at lower laser power. However, the situation is quite different when looking at the spectral response of the two recorded discs (Figure 2 and Figure 3). For the phase-change detection layer, the strength of the signal above the cut-off frequency of approx. 20 MHz is significantly lower. For instance, at 30.7 MHz (i.e. for 80nm marks), a power of 15 dBm is found for InSb while AIST shows 10 dBm. It is also interesting to notice the dip that appears in the AIST spectrum close to the cut-off frequency. This feature is discussed below.

In order to confirm that InSb forms a better detection layer than AIST, the bit error rate was measured for the two systems. For the semiconductor based disk a bER as low as 1.10^{-3} was found while no decoding was possible for the disk with phase-change material using the layer stack with optimum CNR.

The reason for the discrepancy between the read-out of single and multi-tones can be found on Figure 4. It shows the HF signal of a sequence of 20 pits with $2T=100\text{nm}$ between a 19T space and a 20T mark for both InSb and AIST disks. As expected, for marks with minimum feature size of 150nm, the reflectivity on lands is higher than the reflectivity on pits. The situation can be different for the marks below 150 nm. Whereas InSb allows to properly detect the 20 x 2T pits, only 19 of them are found using AIST. Moreover the HF signal shows inverted pit and land signal levels for AIST and InSb. This explains why the random sequences from AIST disks could not be decoded.

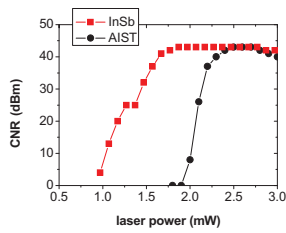


Figure 1 : CNR vs. read power measured on 80nm marks for InSb and AIST based disks

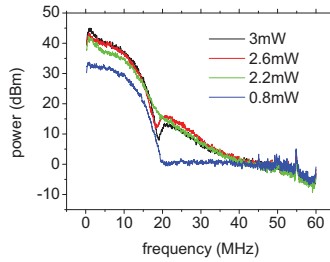


Figure 2 : power spectrum of the read-out signal for several read-out power levels (AIST disk)

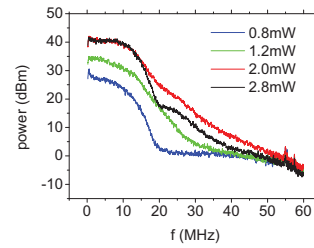


Figure 3 : power spectrum of the read-out signal for several read-out power levels (InSb disk)

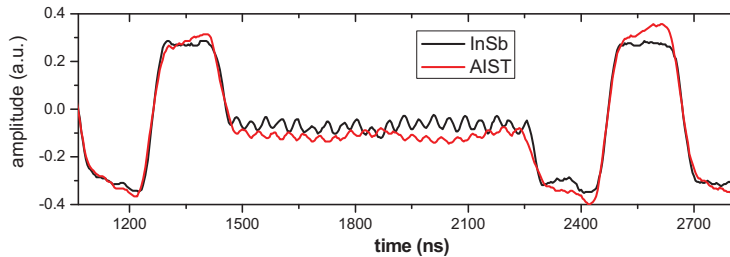


Figure 4 : HF signal from AIST and InSb disks read by Blu-ray tester at elevated laser power above the super-resolution level. The ROM pattern in the substrate is a sequence of 20x100nm marks between a 19T space and 20T marks.

3. Numerical computation and discussion

The results above show that the super-resolution read-out is dramatically affected whether the reflectivity goes low to high or high to low. To help in understanding this phenomenon, the light reflected from a pit/land structure was calculated using a FEM.

Figure 5 shows how the Super-Resolution ROM disk has been implemented in the 2D simulation model. A 3-layer stack comprising one active layer sandwiched between two dielectrics layers covers a ROM substrate with a monotone sequence of 100 nm 2T pits, which is smaller than the resolution limit of the Blu-ray optics with a laser wavelength of 405 nm and a numerical aperture of 0.85.

The pit geometry implemented into the calculation is obtained from AFM measurements of actual sample discs. The refractive indexes at low read power are taken from literature. The super-resolution regime is modeled by inserting a “probing area” into the detection layer. It consists in either an amorphous AIST or “metallic” InSb. For this study the width of the probe is arbitrarily fixed to 100nm.

Figure 6 gives the calculated reflectivity obtained when the beam is moving from pit to land. It is seen that for an “aperture” probe type material the reflectivity changes from high to low. For a “metallic” probe type material it changes from low to high. This result explains the experimental observations of the previous section. Furthermore, for the AIST mask layer and marks below 150 nm a competition exists between the diffraction mechanism and the super-resolution mechanism. This explains the “dip” in the read-out spectrum around the cut-off frequency and the decoding issue of the AIST disc.

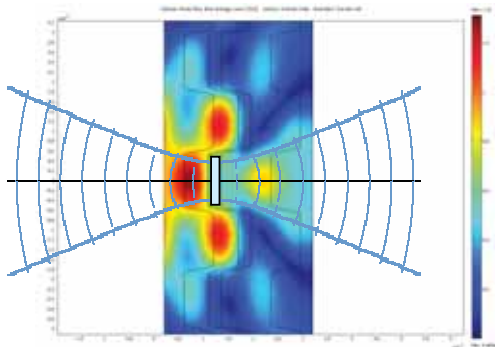


Figure 5 : 2D representation of the Super-Resolution ROM disk. The 3 layers on top of the substrate represent the 2 dielectric layers encapsulating the active thin layer where the aperture has been opened. The focused laser beam is supposed to be a Gaussian-shaped TE-polarized plane wave moving across the pits.

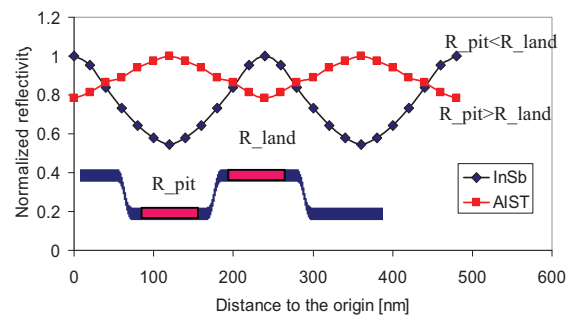


Figure 6 : Calculated reflectivity for a moving beam and for a probing mark inserted into InSb or AIST at the center of the beam (i.e. super-resolution regime)

4. Summary

We compared the super-resolution read-out of random patterns obtained with InSb (semiconductor) or AIST (phase-change) mask layers. While a good bER was found for the semiconductor based disk, it was impossible to decode data from the current phase-change based disk. We confirmed that this is due to the nature of the optical transition inducing the super-resolution effect. In case of AIST, where the super-resolution mechanism is based on an aperture formation, the position of the smallest pits and lands might be mistaken due to the opposite signal caused by the diffraction and the reflectivity change. Thus, materials with a low to high optical transition are better suited for super-resolution application.

5. References

- [1] J. Tominaga, T. Nakano, N. Atoda, Appl. Phys. Lett. 73, 2078 (1998)
- [2] M. Kuwahara, T. Shima, P. Fons, T. Fukaya, J. Tominaga, J. Appl. Phys. 100, 43106 (2006)
- [3] J.M. Li, L.P. Shi, H.X. Yang, K.G. Lim, X.S. Miao, Jpn. J. Appl. Phys. 46, 4148 (2007)
- [4] B. Hyot, X. Biquard, F. Laulagnet, in Technical Digest of ISOM 2007
- [5] J. Pichon, M.F. Armand, F. Laulagnet, B. Hyot, in Technical Digest of ISOM 2007

Super resolution media with significantly high read stability

S. Ohkubo*, K. Aoki, E. Kariyada, and D. Eto
System Jisso Research Laboratories, NEC Corporation
1753, Shimonumabe, Nakahara-ku, Kawasaki, Kanagawa 211-8666, Japan

ABSTRACT

Read stability is the most critical issue in the super-resolution (SR) media for practical use. We have confirmed the read stability of 10^6 times for SR ROM media with the phase change mask layer. Improvement of the read stability is achieved by reducing sulfur concentration of the protective layer and the use of the newly developed $\text{Ga}_2\text{O}_3\text{-Cr}_2\text{O}_3$ interface layer which can suppress mutual diffusion between the phase change and the inter-face/protective layers.

Keywords: Read stability, Super-resolution, Phase change, $\text{Ga}_2\text{O}_3\text{-Cr}_2\text{O}_3$, inter-face layer

1. INTRODUCTION

As the conventional manner to increase the recording capacity, *i.e.*, shortening wavelength (λ) of laser-diode or increasing numerical aperture (NA), approaches the limit, super-resolution (SR) technique has been intensively studied.^{[1]-[3]} In the SR media, the mask layer exhibiting change of the optical constant in accordance with temperature change is used. The temperature distribution in the mask layer creates the smaller detection aperture than the actual focused laser beam. This allows the reproduction of the signal beyond the cutoff frequency determined by λ and NA. Several kinds of mask layer such as ZnO, GeAl and chalcogenide phase change materials have been proposed. The phase change material is most attractive in terms of recording capacity, because the optical constants of the phase change material drastically change in the crystalline-to-molten phase change. However, the use of the molten phase causes the severe issue of the read stability which was 10^5 times at most so far. The read stability of 10^6 times is necessary for the practical use.

This paper describes the improvement of read stability of SR media. With the newly developed protective and inter-face layers, the 10^6 times read stability has been achieved. Also, based on the actual measurement of the optical constants of the molten phase, we have designed the SR media with high reflectivity contrast between the molten and the crystalline areas and confirmed the feasibility of doubling the recording capacity.

2. MEDIA CHARACTERISTICS

2.1 Layer structure

Figure 1 schematically describes the cross sectional view of the SR media. Each layer was successively deposited on polycarbonate substrate by magnetron sputtering. In the SR media with the phase change mask layer, read operation is almost equivalent with write operation in the rewritable media because the mask layer is molten in every read operation. In other words, read operation in the SR media can be regarded as the DC write operation which causes much severe thermal damage than in the rewritable media. Considering the fact that DOW is 10^5 times at most in the very sophisticated rewritable media, read stability of 10^6 times in the SR media seems quite challenging. We have addressed this big issue by developing the new protective and inter-face layers. It is well known that the main cause limiting the DOW cycle in the rewritable media is the degradation of crystallization speed caused by the sulfur diffusion from the protective layer (typically ZnS-

*s-ohkubo@ab.jp.nec.com; phone 81-44-431-7582; fax 81-44-431-7592

SiO₂). The SR media also uses the reversible transition between the molten and crystalline phases, the degradation of the crystallization speed is the most critical issue. In order to suppress sulfur diffusion, we have reduced sulfur concentration less than 40 mol%. Instead of ZnS, Ta₂O₅ has been added in order to maintain sufficient sputtering rate which is one of the most attractive features of ZnS-SiO₂. Inter-face layer has a role of both suppression of sulfur diffusion and promotion of crystallization speed. We have tried several oxide inter-face layers and have found that Ga₂O₃-Cr₂O₃ inter-face layer can significantly improve the read stability.

Ag-alloy
ZnS-SiO ₂ -Ta ₂ O ₅
Ga ₂ O ₃ -Cr ₂ O ₃
InSb
Ga ₂ O ₃ -Cr ₂ O ₃
ZnS-SiO ₂ -Ta ₂ O ₅
Substrate

Figure 1. Cross sectional view of the layer structure.

2.2 Optical properties

Optical properties of the media are summarized in Table 1. We actually measured the optical constants of InSb including molten phase^[4]. It has been found that the extinction coefficient, k , of InSb in the molten phase is larger than that in the crystalline phase. This property is quite different from the conventional phase change materials such as GeSbTe. However, it is helpful to design rear aperture detection (RAD) type SR which is more suitable for improving signal amplitude of the small recording pit compared with front aperture detection (FAD). Also, the low melting temperature of InSb is effective in improving read stability by reducing thermal damage of the media.

Table 1. Optical properties of the developed media.

Phase of InSb	Optical constants (n, k)	Reflectivity (designed)
Molten	(1.1, 3.0)	29.8 %
Crystalline	(2.5, 1.7)	7.9 %

3. RESULTS AND DISCUSSION

Figure 2 shows comparison of the frequency characteristics between the normal (read power: 0.5 mW) and SR (3.2 mW) detections for the ROM media with ETM encoded^[5] random data at linear velocity of 6.6 m/s. In these measurements, optical head with $\lambda=405$ nm and NA=0.65 was used. The minimum pit length and the track pitch were about 200 nm and 400 nm, respectively. Although the recording density itself is not so high, significant improvement of signal resolution can be seen in Fig. 2. If we set the criteria of the resolution of -30 dB for the limit of the data detection with a signal processing technique such as PRML, the results in Fig. 2 imply the possibility of doubling the recording capacity. This large enhancement can be attributed to the high reflectivity contrast between the aperture (molten) and mask (crystalline) areas listed in Table 1.

The results on the read stability are shown in Fig. 3 and Fig. 4. As can be seen from each figure, PRSNR

remained almost the same up to 10^6 times read operation, and the enlarged 2T signal amplitude can be clearly identified even after 10^6 times SR readout. Thus, it can be concluded that the read stability of 10^6 times is feasible.

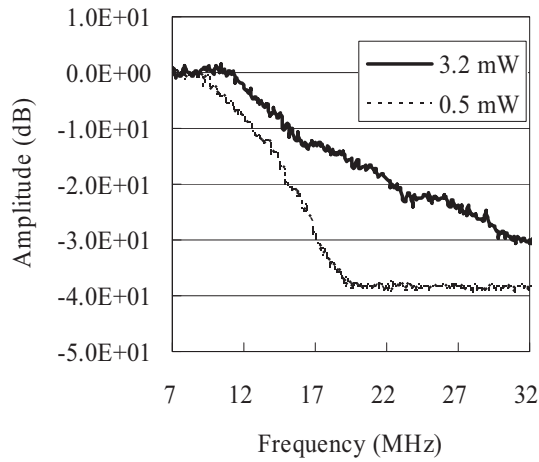


Figure 2. Comparison of frequency characteristics between the normal (0.5 mW) and SR (3.2 mW) readout.

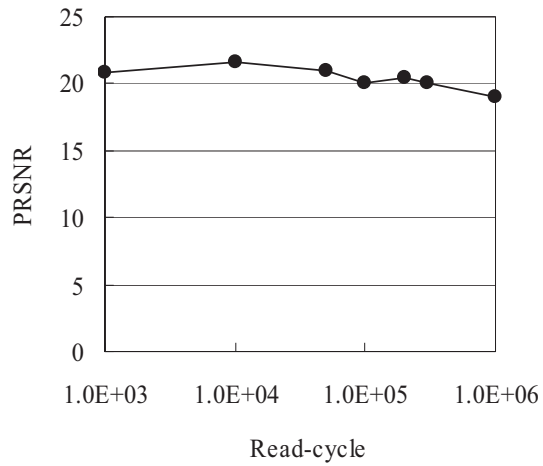


Figure 3. PRSNR vs read-cycle for the read power of 3.2 mW.

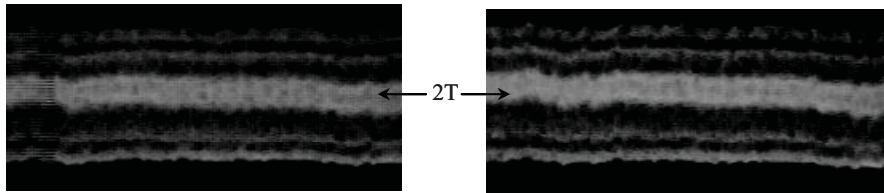


Figure 4. Example of SR reproduced waveform; in early stage (left), and after 10^6 times read (right).

4. CONCLUSIONS

We have confirmed the feasibility of 10^6 times read stability and increasing the recording capacity by a factor of 2. These improvements have been achieved by (1) protective layer with low sulfur concentration, (2) Ga_2O_3 - Cr_2O_3 inter-face layer, (3) InSb mask layer and actual measurement of its optical constants including molten phase.

REFERENCES

- [1] K. Yasuda, M. Ono, K. Aratani, A. Fukumoto, and M. Kaneko, Jpn. J. Appl. Phys., Part 1 **32**, 5210 (1993).
- [2] T. Shima, T. Nakano, J. Kim, and J. Tominaga, Jpn. J. Appl. Phys., Part 1 **44**, 3631 (2005)
- [3] G. Mori, M. Yamamoto, H. Tajima, N. Takamori, and A. Takahashi, Jpn. J. Appl. Phys., Part 1 **44**, 3627 (2005)
- [4] S. Ohkubo, K. Aoki, and D. Eto, Appl. Phys. Lett. **92** 011919 (2008)
- [5] K. Kayanuma, C. Noda, and T. Iwanaga, Tech. Digest ISOM2003, pp. 160 (2003)

Key to Authors and Presiders

A

Akiyama, Reiko [TD05-64]SMP
Aman, Yasutomo [TD05-149]STuP
Anderson, Ken E. [TD05-51]SThB
André, Bernard [TD05-148]STuP
Aoki, Kazuhiko [TD05-37]SWB,
[TD05-59]SThC
Aoki, Kazuko [TD05-60]SMP
Aoki, Sunao [TD05-20]STuB
Armand, Marie-Françoise [TD05-148]
STuP
Ashida, Sumio Review
Ayres, Mark R. [TD05-48]SThB,
[TD05-53]SThC, [TD05-55]SThC

B

Bain, James A. SC918 Inst
Barbastathis, George [TD05-54]SThC
Bell, Bernard W. SympComm, Review
Bhagavatula, Vijayakumar Review,
[TD05-56]SThC
Bletscher, Warren L. [TD05-77]SMP
Boden, Eugene P. [TD05-06]SMB
Burkhead, David L. [TD05-122]STuP

C

Cai, Kui [TD05-91]SMP, [TD05-97]
SMP
Cao, Liangcai [TD05-67]SMP
Cao, Sihai [TD05-123]STuP
Challener, William A. [TD05-23]STuB
Chen, Cheng-Huan [TD05-85]SMP
Chen, Jyun-Hung [TD05-144]STuP
Chen, Kuang-Vu [TD05-109]STuP
Chen, Tsuhan [TD05-27]STuC
Chen, Xiao-Ming [TD05-42]SThA,
[TD05-88]SMP
Chen, Zhimin [TD05-145]STuP
Cheng, Chih-Yuan [TD05-112]STuP
Cheng, Shun-Te [TD05-146]STuP
Cheng, Wen-Hung [TD05-109]STuP
Cheng, Xuemin [TD05-84]SMP
Cheng, Yao-Te [TD05-13]SMC
Chernoff, Donald A. [TD05-122]STuP
Cheverton, Mark A. [TD05-119]STuP
Chiu, Kuo-Chi [TD05-109]STuP
Cho, Eun-Hyung [TD05-141]STuP
Cho, Hyunmin [TD05-94]SMP,
[TD05-96]SMP
Choi, Hyun [TD05-133]STuP
Choi, In-Ho Review, [TD05-118]STuP,
[TD05-130]STuP, [TD05-134]
STuP, [TD05-135]STuP
Choi, Narak [TD05-126]STuP, [TD05-
127]STuP
Choi, Sooyong [TD05-94]SMP, [TD05-
96]SMP
Chong, Chong-Tow SympComm,
Review, TD05 SWB SessChr,
[TD05-30]SWA, [TD05-61]SMP,
[TD05-65]SMP, [TD05-121]STuP,
[TD05-125]STuP, [TD05-139]
STuP, [TD05-142]STuP
Chong, Chun Yang [TD05-142]STuP
Coblentz, Kenneth D. [TD05-03]SMB
Curtis, Kevin R. SC917 Inst, TD05
SMA SessChr, TD05 SMC
SessChr, TD05 S SessChr, TD05
Chr, [TD05-48]SThB, [TD05-51]
SThB, [TD05-113]STuP

D

Daud, S. M. [TD05-100]SMP
Davies, Clare E. Review
Davies, David H. SympComm,
Review
Denisyuk, Andrey I. [TD05-32]SWA
Deslis, Tolis [TD05-113]STuP
Dietz, Enrico [TD05-08]SMB, [TD05-
76]SMP, [TD05-115]STuP
Dong, K. F. [TD05-138]STuP
Dozor, David M. [TD05-79]SMP
Durling, Michael R. [TD05-119]STuP
Dvornikov, Alexander S. [TD05-03]
SMB

E

Ensher, Jason R. [TD05-51]SThB
Eto, Daisuke [TD05-37]SWB, [TD05-
59]SThC

F

Fair, Ivan J. [TD05-90]SMP
Farnsworth, Keith W. [TD05-51]SThB
Feid, Timo [TD05-76]SMP
Féry, Christophe [TD05-58]SThC
Fons, Paul [TD05-36]SWB, [TD05-
147]STuP
Fotheringham, Edeline [TD05-51]
SThB
Frohmann, Sven [TD05-08]SMB,
[TD05-76]SMP, [TD05-115]STuP
Fujimura, Itaru TD05 S SessChr
Fujimura, Ryushi [TD05-105]STuP
Fujita, Goro [TD05-07]SMB
Fujita, Teruo [TD05-114]STuP
Fujiwara, Keisuke [TD05-143]STuP
Fukumoto, Atsushi Review, [TD05-47]
SThB, [TD05-49]SThB
Fukuyama, Yoshimitsu [TD05-35]SWB

G

Gage, Edward C. [TD05-23]STuB
Gan, Chee Lip [TD05-100]SMP,
[TD05-142]STuP
Gan, Fuxi [TD05-124]STuP, [TD05-
145]STuP
Gokemeijer, N. J. [TD05-23]STuB
Gortner, Jonas [TD05-08]SMB, [TD05-
115]STuP
Goto, Naofumi [TD05-17]STuA
Gruber, Matthias [TD05-71]SMP
Gu, Donghong [TD05-145]STuP
Gu, Min [TD05-14]SMC
Guenther, Alan [TD05-08]SMB, [TD05-
115]STuP
Guo, Chuanfei [TD05-123]STuP

H

Ha, Sangwoo [TD05-118]STuP
Han, In Gu [TD05-135]STuP
Hanazawa, Makoto [TD05-60]SMP
Hansen, Delbert [TD05-77]SMP
Hansen, Paul [TD05-13]SMC
Hara, Masaaki [TD05-47]SThB
Hardie, Cal [TD05-23]STuB
Hasegawa, Shin-ya Review
Hashimoto, Nobuyuki [TD05-19]
STuB
Hashizume, Jiro [TD05-15]STuA
Hatakeyama, Iwao [TD05-104]STuP
Havermeyer, Frank [TD05-21]STuB
He, Qingsheng [TD05-67]SMP
Helmerson, Kristian [TD05-12]SMC
Hendrix, Karen D. [TD05-86]SMP
Hepper, Dietmar [TD05-42]SThA
Her, Yung-Chiun [TD05-144]STuP,
[TD05-146]STuP

Hesselink, Lambertus Review, TD05
SThB SessChr, [TD05-13]SMC,
[TD05-22]STuB, [TD05-141]STuP
Hidaka, Motohiko [TD05-62]SMP
Higashino, Satoru Review, TD05
SThA SessChr
Higuchi, Takanobu [TD05-04]SMB
Hirao, Akiko Review
Hirata, Masakazu [TD05-24]STuB
Hirooka, Kazuyuki [TD05-47]SThB
Ho, Lawrence [TD05-21]STuB
Hoelzemann, Herbert [TD05-58]SThC
Honda, Miwa [TD05-18]STuA
Hoskins, Alan C. [TD05-53]SThC,
[TD05-113]STuP
Hruska, Curtis R. [TD05-86]SMP
Hsieh, Shu-Ching [TD05-112]STuP
Hsu, Chih-Cheng [TD05-109]STuP
Hsu, Yung-Sung [TD05-146]STuP
Hu, Hua [TD05-84]SMP, [TD05-89]
SMP, [TD05-150]STuP
Huang, Der-Ray SympComm, Review
Hwang, Hyokune [TD05-134]STuP
Hwang, Hyun-Woo [TD05-130]STuP
Hwang, Inoh [TD05-16]STuA, [TD05-
44]SThA, [TD05-45]SThA
Hyot, Béangère [TD05-148]STuP

I

Ichimura, Isao SympComm, Review
Ichimura, Shuichi Review
Ide, Tatsuro [TD05-15]STuA, [TD05-
41]SThA
Iida, Tetsuya Review, [TD05-04]SMB
Im, Sungbin [TD05-101]SMP
Immink, Kees A. S. [TD05-98]SMP
Inoue, Mitsuteru [TD05-60]SMP
Iren, S. [TD05-26]STuC
Irie, Mitsuru TD05 STuC SessChr,
Review, [TD05-87]SMP
Ishii, Norihiko [TD05-111]STuP
Ishikawa, Sayuri [TD05-82]SMP
Ishimoto, Tsutomu [TD05-18]STuA
Itoh, Kazunori Review
Itonaga, Makoto M. Review

J

Jeng, Tzuan-Ren Review, [TD05-109]
STuP
Jeong, Mi Hyeon [TD05-135]STuP
Ji, Rong [TD05-139]STuP
Jin, Fang [TD05-138]STuP
Jin, Guofan [TD05-67]SMP
Jin, Qingyuan [TD05-111]STuP
Joseph, Joby [TD05-116]STuP
Jung, Heungsang [TD05-102]STuP,
[TD05-106]STuP

K

Kajiwara, Yoshiyuki [TD05-43]SThA
Kajiwara, Yuta [TD05-117]STuP
Kaiman, Erika [TD05-81]SMP
Kamijo, Koji [TD05-11]STuP
Kane, John [TD05-53]SThC
Kanemura, Takashi [TD05-60]SMP
Kang, Min-Seok [TD05-131]STuP
Kang, Sung-Mook [TD05-141]STuP
Kannan, Swetha [TD05-77]SMP
Kariyada, Eiji [TD05-59]SThC
Karns, Duane C. [TD05-23]STuB
Kasanavesi, Sashi K. [TD05-77]SMP
Katayama, Ryuichi SympComm,

Review, TD05 STuA SessChr,
[TD05-09]SMB
Kato, Kenichi [TD05-35]SWB
Katsumata, Akiyoshi [TD05-68]SMP
Kawakubo, Osamu [TD05-18]STuA
Kawata, Yoshimasa TD05 STuP
SessChr, TD05 SMB SessChr,
Review
Khulbe, Pramod K. [TD05-77]SMP
Kikukawa, Atsushi [TD05-46]SThA
Kikukawa, Takashi Review, TD05
SMP SessChr
Kim, Haksun [TD05-102]STuP, [TD05-
106]STuP
Kim, Jaisoon [TD05-126]STuP, [TD05-
127]STuP
Kim, Jang Hyun [TD05-93]SMP,
[TD05-107]STuP, [TD05-108]
STuP
Kim, Jin-Hong [TD05-132]STuP
Kim, Jinyoung [TD05-92]SMP, [TD05-
95]SMP
Kim, Jong-Pil [TD05-133]STuP
Kim, Jooho SympComm, Review,
Review, TD05 SWA SessChr
Kim, Joong-Gon [TD05-130]STuP,
[TD05-131]STuP
Kim, Jungeun [TD05-35]SWB
Kim, Jungshik [TD05-132]STuP
Kim, Kwan-Hyung [TD05-127]STuP
Kim, Moon-Seok [TD05-126]STuP
Kim, Na Young [TD05-118]STuP
Kim, Nakhyun [TD05-16]STuA
Kim, Sang-Hoon [TD05-107]STuP,
[TD05-108]STuP, [TD05-130]
STuP
Kim, Sunmin [TD05-18]STuA
Kim, Taeseob [TD05-129]STuP
Kim, Wan-Chin [TD05-129]STuP,
[TD05-133]STuP
Kim, Young-Joo Review, [TD05-137]
STuP, [TD05-140]STuP
Kim, Youngsik [TD05-128]STuP
Kim, Yullin [TD05-79]SMP
Kimura, Shigeru [TD05-35]SWB
Kinoshita, Nobuhiro [TD05-111]STuP
Kishore, Rani B. [TD05-12]SMC
Kitano, Motoki [TD05-72]SMP, [TD05-
73]SMP
Knittel, Joachim [TD05-50]SThB,
[TD05-52]SThB, [TD05-110]STuP
Kobayashi, Seiji TD05 SThA SessChr,
[TD05-07]SMB
Kobayashi, Shoei [TD05-43]SThA
Kobyakov, Andrey [TD05-31]SWA
Koda, Sokoh [TD05-62]SMP
Kodate, Kashiko [TD05-64]SMP,
[TD05-82]SMP
Kohara, Shinji [TD05-35]SWB
Koichi, Awazu [TD05-34]SWA
Koide, Daiichi [TD05-149]STuP
Kojima, Rie Review, TD05 SWB
SessChr, [TD05-35]SWB
Kokenyesi, Sandor J. [TD05-81]SMP
Kolobov, Alexander [TD05-36]SWB,
[TD05-147]STuP
Komatsu, Yuichi [TD05-09]SMB
Kondo, Takao [TD05-18]STuA
Kong, Gyuyeor [TD05-94]SMP, [TD05-
96]SMP
Kowalski, Benjamin A. [TD05-38]SWB
Krogh, Bruch H. [TD05-27]STuC
Kubo, Takahiro [TD05-87]SMP
Kui, Cai [TD05-98]SMP
Kuroda, Kazuo [TD05-105]STuP
Kurokawa, Takahiro [TD05-15]STuA,
[TD05-41]SThA
Kuwahara, Masashi [TD05-36]SWB,
[TD05-147]STuP
Kwak, Bong-Sik [TD05-135]STuP
Kwon, Tae-Wook [TD05-130]STuP

Key to Authors and Presiders

L

lan, Tzu-Hsiang [TD05-120]STuP
Lan, Yung Sung [TD05-109]STuP
Laulagnat, Fabien [TD05-148]STuP
Lawrence, Brian L. [TD05-06]SMB,
[TD05-75]SMP, [TD05-119]STuP
Lee, Bongil [TD05-92]SMP
Lee, Irene [TD05-100]SMP
Lee, Jaemin [TD05-92]SMP, [TD05-95]
SMP, [TD05-101]SMP
Lee, Jae-Sung [TD05-118]STuP
Lee, Jun-Seok [TD05-132]STuP
Lee, Kyunggeun Review, TD05
STuA SessChr, [TD05-16]STuA,
[TD05-44]SThA, [TD05-45]SThA,
[TD05-129]STuP
Lee, Sung Hoon [TD05-134]STuP
Lee, Xuan-Hao [TD05-66]SMP
Lee, Yong Hee [TD05-107]STuP,
[TD05-108]STuP
Leen, J. B. [TD05-13]SMC, [TD05-
141]STuP
Lemonnier, Olivier [TD05-148]STuP
Li, Jianming [TD05-30]SWA, [TD05-
142]STuP
Li, Minghua [TD05-61]SMP, [TD05-65]
SMP
Li, Y. [TD05-77]SMP
Li, Zuoyi [TD05-138]STuP
Liang, Chin-Tsia [TD05-109]STuP
Liang, Xinan [TD05-61]SMP, [TD05-
65]SMP
Lim, Dong-Soo [TD05-137]STuP,
[TD05-140]STuP
Lim, Pang-Boey [TD05-60]SMP
Lin, Gengqi [TD05-138]STuP
Liu, Pengfei [TD05-63]SMP
Liu, Qian [TD05-123]STuP
Liu, Tzong-Shi [TD05-78]SMP
Liu, Ying-Da [TD05-146]STuP
Loncar, Marko [TD05-11]SMC
Longley, Kathryn L. [TD05-06]SMB
Lopez, James [TD05-119]STuP
Luk'yanchuk, Boris S. [TD05-30]SWA

M

Ma, Bin [TD05-136]STuP
Ma, Jianshe [TD05-84]SMP
Ma, Qiang [TD05-67]SMP
Ma, Shih-Hsin [TD05-66]SMP
MacDonald, Kevin F. [TD05-32]SWA
Maeda, Takeshi SympComm, Review
Malki, Oliver [TD05-50]SThB, [TD05-
52]SThB, [TD05-110]STuP
Mansuripur, Masud Review, TD05
SMC SessChr, [TD05-02]SMA,
[TD05-31]SWA
Mariscal-Lopez, Carlos [TD05-12]
SMC
Matsuda, Nami [TD05-60]SMP
Matsunaga, Toshiyuki [TD05-35]SWB
McLeod, Robert R. Review, TD05
SThC SessChr, [TD05-38]SWB,
[TD05-39]SWB, [TD05-55]SThC
Miao, Junjie [TD05-123]STuP
Miao, X. S. [TD05-138]STuP
Mikami, Hideharu [TD05-15]STuA,
[TD05-41]SThA
Milster, Thomas D. SympComm,
Review, TD05 SWA SessChr,
[TD05-40]SWB, [TD05-79]SMP,
[TD05-128]STuP, SC920 Inst,
[TD05-77]SMP, [TD05-126]STuP
Min, Byung-Hoon [TD05-118]STuP,
[TD05-134]STuP, [TD05-135]
STuP, [TD05-130]STuP
Min, Cheol-Ki [TD05-129]STuP
Minemura, Hiroyuki Review, [TD05-
46]SThA

Mitsumori, Ayumi [TD05-04]SMB
Miyagawa, Naoyasu SympComm,
Review
Miyamoto, Harukazu Review, [TD05-
15]STuA, [TD05-41]SThA
Miyamoto, Hirotaka [TD05-07]SMB
Mizukuki, Takeshi [TD05-18]STuA
Moloney, Jerome V. [TD05-31]SWA
Moritomo, Yutaka [TD05-35]SWB
Moser, Christophe [TD05-21]STuB
Mueller, Christian [TD05-76]SMP
Mukasa, Tomoharu [TD05-17]STuA
Murata, Shozou [TD05-149]STuP
Murayama, Haruno [TD05-35]SWB
Muroi, Tetsuhiko [TD05-111]STuP,
[TD05-195]S
Muto, Shinzo [TD05-68]SMP

N

Nagy, Peter [TD05-81]SMP
Nakamura, Toshihiro [TD05-62]SMP
Nakaoki, Ariyoshi [TD05-18]STuA,
[TD05-183]S
Naruse, Makoto [TD05-33]SWA
Ng, Lung Tat [TD05-142]STuP
Ni, Kai [TD05-67]SMP
Nishikawa, Koichiro Review
Noda, Susumu [TD05-10]SMC
Nomura, Wataru [TD05-33]SWA

O

O'Brien, Nada A. [TD05-86]SMP
Ogasawara, Masakazu [TD05-04]SMB
Ogawa, Koichi TD05 S SessChr
Oh, Hyun-Suk [TD05-137]STuP
Ohishi, Kiyoshi SC919 Inst
Ohkubo, Shuichi [TD05-37]SWB,
[TD05-59]SThC
Ohmori, Kentaro [TD05-62]SMP
Ohmura, Kohji [TD05-62]SMP
Ohtsu, Motoichi [TD05-01]SMA,
[TD05-33]SWA
Okamoto, Atsushi [TD05-69]SMP,
[TD05-70]SMP, [TD05-72]SMP,
[TD05-73]SMP
Okino, Yoshihiro [TD05-87]SMP
Okumura, Tetsuya Review
Onagi, Nobuaki [TD05-149]STuP
O'Neill, Michael SympComm, Review
Orlic, Susanna TD05 STuC SessChr,
Review, [TD05-08]SMB, [TD05-
76]SMP, [TD05-115]STuP
Ostroverkhov, Victor P. [TD05-06]
SMB, [TD05-75]SMP, [TD05-119]
STuP
Oto, Hiroshi [TD05-103]STuP
Oumi, Manabu [TD05-24]STuB

P

Pacearescu, Larisa [TD05-58]SThC
Pan, Longfa Review, [TD05-83]SMP,
[TD05-84]SMP, [TD05-89]SMP,
[TD05-150]STuP
Park, Donghyuk [TD05-95]SMP
Park, Gwitae [TD05-102]STuP, [TD05-
106]STuP
Park, Hyeong-Ryeol [TD05-127]STuP
Park, Hyun-Soo [TD05-16]STuA,
[TD05-44]SThA, [TD05-45]SThA
Park, Insik Review, [TD05-16]STuA,
[TD05-44]SThA, [TD05-45]SThA
Park, Jin-Bae [TD05-93]SMP
Park, Jinmoo [TD05-134]STuP
Park, Joo Youn [TD05-102]STuP,
[TD05-106]STuP, [TD05-107]
STuP, [TD05-108]STuP
Park, Majung [TD05-24]STuB
Park, No-Cheol Review, TD05 STuB
SessChr, [TD05-129]STuP,

[TD05-130]STuP, [TD05-131]
STuP, [TD05-133]STuP, [TD05-
141]STuP
Park, Young-Pil SympComm, Review,
[TD05-93]SMP, [TD05-107]STuP,
[TD05-108]STuP, [TD05-129]
STuP, [TD05-130]STuP, [TD05-
131]STuP, [TD05-133]STuP,
[TD05-141]STuP
Pei, Jing [TD05-83]SMP, [TD05-150]
STuP
Penmetcha, Kumar K. R. [TD05-34]
SWA
Pichon, Joseph [TD05-148]STuP
Pilard, Gael [TD05-42]SThA, [TD05-
58]SThC
Przygodda, Frank [TD05-50]SThB,
[TD05-52]SThB, [TD05-110]STuP

Q

Qin, Zhiliang [TD05-91]SMP, [TD05-
97]SMP, [TD05-98]SMP
Qu, Qingling [TD05-124]STuP

R

Ramamoorthy, Lakshmi D. [TD05-56]
SThC
Rass, Jens [TD05-08]SMB, [TD05-76]
SMP, [TD05-115]STuP
Rausch, Tim SympChair, Review,
TD05 S SessChr, [TD05-23]STuB,
[TD05-26]STuC
Reiko, Akiyama [TD05-82]SMP
Ren, Zhiyuan [TD05-119]STuP
Rentzepis, Peter M. [TD05-03]SMB
Richter, Hartmut [TD05-50]SThB,
[TD05-52]SThB, [TD05-110]STuP
Riedel, Ernest P. [TD05-26]STuC
Ross, Fergus J. [TD05-75]SMP

S

Saito, Kimihiro SympChair, Review,
TD05 S SessChr, TD05 SMB
SessChr, [TD05-07]SMB, [TD05-
18]STuA
Saito, Norihiko [TD05-18]STuA
Sano, Takayuki [TD05-69]SMP,
[TD05-73]SMP
Sano, Takumi [TD05-117]STuP
Sasa, Yuichiro [TD05-103]STuP
Sato, Kunihiro [TD05-69]SMP
Satoh, Isao SympComm, Review
Satoh, Kazuyuki [TD05-60]SMP
Schechtman, Barry H. SympComm,
Review, TD05 SThD SessChr,
[TD05-29]STuC
Schlesinger, Tuviah E. SympComm,
Review, TD05 STuP SessChr,
[TD05-27]STuC, [TD05-78]SMP
Schlottau, Friso [TD05-51]SThB
Scott, Timothy F. [TD05-38]SWB
Seekins, D. [TD05-26]STuC
Seigler, Michael A. [TD05-23]STuB
Sekiguchi, Tohru [TD05-68]SMP
Seo, Jeong-Kyo [TD05-118]STuP,
[TD05-127]STuP, [TD05-130]
STuP, [TD05-135]STuP
Seo, Jung-Kyo [TD05-132]STuP,
[TD05-134]STuP
Seo, Manjung [TD05-101]SMP
Shi, L. P. [TD05-100]SMP
Shi, Luping TD05 Chr, TD05 SMP
SessChr, TD05 S SessChr,
[TD05-30]SWA, [TD05-142]STuP
Shi, Xiaolei [TD05-06]SMB, [TD05-75]
SMP, [TD05-119]STuP
Shima, Takayuki [TD05-36]SWB
Shimano, Takeshi SympComm,
Review, [TD05-15]STuA

Shimidzu, Naoki [TD05-111]STuP
Shimura, Tsutomu TD05 SThB
SessChr, Review, [TD05-105]
STuP
Shin, Dongho Review
Shin, Won-Ho [TD05-131]STuP
Shin, Yun-Sup SympComm, Review,
Review, TD05 SMP SessChr
Shinkai, Masaru [TD05-149]STuP
Shinoda, Masataka Review
Shinohara, Noriyasu [TD05-18]STuA
Shiraishi, Junya [TD05-43]SThA
Simpson, Robert E. [TD05-36]SWB,
[TD05-147]STuP
Sissom, Bradley J. [TD05-113]STuP
Smith, Paul C. [TD05-51]SThB, [TD05-
53]SThC
Sofian, M. D. [TD05-125]STuP, [TD05-
139]STuP
Soh, Kwang-Sup [TD05-127]STuP
Sohn, Jin-Seung [TD05-141]STuP
Solanki, Sanjeev [TD05-61]SMP,
[TD05-65]SMP
Son, Do-Hyeon [TD05-135]STuP
Song, Ki-Chang [TD05-132]STuP
Su, Ya-Ni [TD05-85]SMP
Subash Chandra Bose, Gopinath
[TD05-34]SWA
Sugimoto, Yasunori [TD05-149]STuP
Suh, Sung-Dong [TD05-141]STuP
Sumi, Yojiro [TD05-105]STuP
Sun, Ching-Cherng [TD05-66]SMP,
[TD05-112]STuP
Sutanto, Diana N. [TD05-142]STuP
Suzuki, Ryu [TD05-104]STuP
Sze, Jia Y. [TD05-30]SWA, [TD05-
142]STuP

T

Takabayashi, Masanori [TD05-70]SMP
Takano, Yohimichi [TD05-149]STuP
Takasawa, Takeharu [TD05-17]STuA
Takashima, Yuzuru [TD05-22]STuB
Takata, Masaki [TD05-35]SWB
Taktas, Viktor [TD05-81]SMP
Takeda, Minoru Review
Tamura, Reiji Review
Tan, Kim L. [TD05-86]SMP
Tanabe, Norihiro [TD05-07]SMB
Tanabe, Takaya [TD05-104]STuP
Tanaka, Hitoshi [TD05-35]SWB
Tanaka, Junya [TD05-72]SMP
Tanaka, Kenji [TD05-47]SThB
Tanaka, Kunimaro Review, [TD05-25]
STuC, [TD05-143]STuP
Tanaka, Satoru TD05 SThC SessChr,
Review, [TD05-04]SMB
Tanaka, Yoshito [TD05-35]SWB
Tang, Jianyong [TD05-12]SMC
Tang, Yi [TD05-83]SMP, [TD05-84]
SMP, [TD05-89]SMP, [TD05-150]
STuP
Taniguchi, Shoji [TD05-28]STuC
Tao, Shiquan [TD05-63]SMP
Tate, Naoya [TD05-33]SWA
Teng, Tun-Chien [TD05-66]SMP,
[TD05-112]STuP
Terada, Masaru [TD05-105]STuP
Theis, Oliver [TD05-42]SThA, [TD05-
88]SMP
Tien, Chung-Hao Review, [TD05-120]
STuP
Ting, L. H. [TD05-100]SMP
Tokumaru, Haruki TD05 Chr, TD05
S SessChr, TD05 SMA SessChr,
[TD05-149]STuP
Tokuyama, Kazutatsu [TD05-47]SThB
Tominaaga, Junji Review, TD05 SThD
SessChr, [TD05-34]SWA, [TD05-
36]SWB, [TD05-147]STuP
Tominaga, Shin [TD05-09]SMB
Tomita, Yasuo [TD05-62]SMP

Key to Authors and Presiders

Tomita, Yoshimi Review, TD05 STuP
SessChr
Tomiyama, Mizuho [TD05-09]SMB
Trautner, Heiko [TD05-50]SThB,
[TD05-52]SThB, [TD05-110]STuP
Trunov, Mihail [TD05-81]SMP
Tsai, Din Ping SympComm, Review
Tsai, Meng-Yen [TD05-78]SMP
Tsai, Song-Yeu [TD05-146]STuP
Tsujioka, Tsuyoshi Review, [TD05-80]
SMP
Tsukahara, Nobuhiko [TD05-17]STuA

U

Uchiyama, Hiroshi [TD05-07]SMB
Ueyanagi, K. Review
Urakawa, Yoshiyuki [TD05-17]STuA

V

Vieth, Udo [TD05-71]SMP

W

Waldman, David A. [TD05-116]STuP
Walker, Edwin P. [TD05-03]SMB
Wan, Xiaojun [TD05-63]SMP
Wang, Haifeng [TD05-30]SWA, [TD05-
121]STuP
Wang, Huanyong [TD05-63]SMP
Wang, Shyhyeu Review

Wang, Yang [TD05-124]STuP, [TD05-
145]STuP
Wang, Yongsheng [TD05-123]STuP
Watanabe, Eriko [TD05-64]SMP,
[TD05-82]SMP
Watanabe, Koichi [TD05-15]STuA,
[TD05-41]SThA
Wehrenberg, Paul J. TD05 STuB
SessChr, Review
Welles, Kenods [TD05-75]SMP
Won, Kitak [TD05-127]STuP
Wright, David C. Review
Wu, Feipeng [TD05-63]SMP
Wu, Ping-Jung [TD05-109]STuP
Wu, Qingyang [TD05-99]SMP
Wu, Yiqun [TD05-124]STuP, [TD05-
145]STuP

X

Xu, Baoxi [TD05-121]STuP, [TD05-
125]STuP, [TD05-139]STuP
Xu, Xuewu [TD05-61]SMP, [TD05-65]
SMP

Y

Yagi, Shogo Review
Yamada, Masahiro [TD05-20]STuB
Yamada, Noboru Review, [TD05-35]
SWB
Yamagami, Tamotsu [TD05-20]STuB,
[TD05-43]SThA

Yamamoto, Manabu [TD05-74]SMP,
[TD05-103]STuP, [TD05-117]
STuP
Yamanaka, Yutaka Review
Yamasaki, Takeshi [TD05-18]STuA
Yamatsu, Hisayuki [TD05-07]SMB
Yan, Junbing [TD05-138]STuP
Yan, Mingming [TD05-83]SMP,
[TD05-150]STuP
Yanagisawa, Takuma [TD05-04]SMB
Yang, Hyunseok [TD05-93]SMP,
[TD05-107]STuP, [TD05-108]
STuP, [TD05-130]STuP, [TD05-
131]STuP
Yang, Lee [TD05-99]SMP
Yao, Timothy S. [TD05-99]SMP
Yasuda, Nobuhiro [TD05-35]SWB
Yatsui, Takashi [TD05-33]SWA
Yeo, Junyeob [TD05-126]STuP
Yin, Xiaobo [TD05-13]SMC
Yokoi, Kenya Review
Yong, K. T. [TD05-100]SMP
Yoo, Seung Hun [TD05-134]STuP
Yoon, Pilsang [TD05-102]STuP,
[TD05-106]STuP
Yoon, Yong-Joong [TD05-129]STuP,
[TD05-133]STuP
Yoshida, Shuhei [TD05-74]SMP
Yu, Ye-Wei [TD05-66]SMP, [TD05-
112]STuP
Yuan, Gaoqiang [TD05-30]SWA,
[TD05-142]STuP

Yuan, Haibo [TD05-89]SMP, [TD05-
150]STuP
Yuan, HongXing [TD05-125]STuP,
[TD05-139]STuP
Yuen, Yin [TD05-13]SMC
Yukumoto, Tomomi [TD05-18]STuA

Z

Zakharian, Aramais R. [TD05-31]SWA
Zha, Chaolin [TD05-136]STuP
Zhang, Buqing [TD05-84]SMP, [TD05-
150]STuP
Zhang, Jun [TD05-79]SMP, [TD05-
128]STuP
Zhang, Jun [TD05-139]STuP
Zhang, Qide [TD05-139]STuP
Zhang, Songhua [TD05-91]SMP,
[TD05-97]SMP, [TD05-98]SMP
Zhang, Zhuwei [TD05-123]STuP
Zhang, Zongzhi [TD05-136]STuP
Zhao, Hui [TD05-16]STuA, [TD05-44]
SThA, [TD05-45]SThA
Zhao, Yuxia [TD05-63]SMP
Zheludev, Nikolay I. [TD05-32]SWA,
[TD05-57]SThC
Zhu, Yongguang [TD05-90]SMP

CALL FOR PAPERS

SUBMISSION
DEADLINE:

19 DECEMBER
2008

THE
**OPTICAL
DATA
STORAGE**

TOPICAL
MEETING

1 0 - 1 3 M A Y 2 0 0 9

BUENA VISTA PALACE RESORT & SPA

LAKE BUENA VISTA,
FLORIDA USA



IEEE



OSA[®]
Optical Society of America



SPIE